

Multi-scale Digital Rock: Application of a multi-scale multi-phase workflow to a Carbonate reservoir rock

Andrew Fager¹, Hiroshi Otomo¹, Rafael Salazar-Tio¹, Ganapathi Balasubramanian¹, Bernd Crouse¹, Raoyang Zhang¹, Hudong Chen¹, and Josephina Schembre-McCabe²

¹Dassault Systèmes, USA

²Chevron, USA

Abstract. In some of the challenging digital rock applications the trade-off between model resolution and representative elemental volume is not captured in a single resolution model satisfying the minimum requirements for both aspects. In the wide range of lithofacies found in carbonate reservoir rocks, some facies fall in this category, where large pores, ooids or vugs, are connected by small scale porous structures that could have orders of magnitude smaller pores. In these cases a multi-scale digital rock approach is needed. We recently developed an extension to a digital rock workflow that includes a way to handle sub-resolution pore structures in single phase and multi-phase flow scenarios in addition to regular resolvable pore structures. Here we present an application of this methodology to a multi-scale limestone carbonate rock. A microCT image captures the large pores for this sample, but does not resolve all the pores smaller than the pixel size. A three phase image segmentation that considers pore, solid and under-resolved pores or porous media (PM) is generated. A high resolution confocal image model is obtained for a representative region of the smaller pores or PM region. A set of constitutive relationships (namely permeability vs. porosity, capillary pressure vs saturation and relative permeability vs saturation) are obtained by simulation from the high resolution confocal model. The low resolution segmented image, a porosity distribution image, and the constitutive relationships for the PM are input in an extended LBM multi-scale multi-phase solver. First we present results for absolute permeability and show a parametric study on PM permeability. The model recovers the expected behaviour when the PM regions are considered pore or solid. A consistent value of permeability with experiments is obtained when we use the PM permeability from the high resolution model. To demonstrate the multi-phase behaviour, we present results for capillary pressure imbibition multi-scale simulations. Here a small model for a dual porosity system is created in order to compare single scale results with the multi-scale solver. Finally, capillary imbibition results for the whole domain are shown and different wettability scenario results are discussed. This application illustrates a novel multi-scale simulation approach that can address a long standing problem in digital rock.

1 Introduction

Petrophysical properties are critical to understand and forecast oil & gas production. In particular, properties related to single-phase and multi-phase fluid flow are required. These properties represent effective macroscopic constitutive relationships for flow; such as absolute permeability vs porosity, J-function capillary pressure and relative permeability vs. saturation. Laboratory measurements are typically done for this purpose, but another option is to use digital rock to simulate petrophysical properties directly using the particular rock 3D structure, obtained using x-ray micro-tomography (microCT) [1]. Properties directly depend on the internal pore structure, and different type of structures have different constitutive relationships; for example; random porous media, packed spheres, parallel planes, bundle of tubes, heterogeneous sandstones, shale rocks, carbonate rocks. No single property model is good for all porous media types, therefore the need of laboratory measurements or simulation on the actual 3D image of the

particular rock. Samples that belong to one porous media type will share similar constitutive relationships. This is the reasoning behind core sampling per porous media type.

A typical microCT image resolution can be few micrometer per pixel. For most sandstones this resolution may capture the main percolation pore space, while small crevices and some clay porosity are not captured. Since the main percolating path is primarily responsible for fluid flow, this image could still represent the flow properties of the rock. But in many other cases the pores (bodies and throats) that form the interconnected pore structure can vary in size in the same rock by orders of magnitude. This case can be found in some carbonate rock lithofacies, which are complex structures form by recrystallization of micro-organisms, where larger pores are many times connected only through pores smaller than the typical microCT image resolution, which is not able to capture the main percolating pore structure and is not suitable for flow simulation. An increase in imaging resolution can enable percolation, but with more magnification, the larger pores are not going to be captured properly by the image. This

* Corresponding author: Andrew.FAGER@3ds.com

is a genuine example where a multi-scale approach is needed to enable simulation.

In the digital rock literature, there are several publications on multi-scale extensions of multi-phase pore-network models [26-27]. Regarding voxel based models, like LBM, there are several publications [2-6, 24-25] on single-phase multi-scale fluid flow simulations, where formulations for a viscous force with the permeability has been provided by the Brinkman equation and the permeability value was derived from simulations at finer resolutions, but extensions to the multi-phase flow simulation are not discussed. Two recent publications [7, 8] consider multi-phase fluid flow in multi-scale pore structures. In [7] relative permeability from under-resolved regions was computed by solving the transport equation for the total energy, Helmholtz free and kinetic energy, but without considering other important physical properties such as the capillary-pressure curves. On the other hand, in [8], the capillary saturations are calculated in the finer scale using a Young-Laplace relationship and used for estimating capillary pressure in under-resolved regions, but no fluid flow simulation was performed involving pore structure connectivity and relative permeability was also not considered.

We present in this paper an application of a recently developed [9-10] extension to the Shan-Chen multi-phase Lattice Boltzmann model [11-15] that introduces numerical models for treating multi-scale porous media, such as carbonate rocks, which includes under-resolved pores as well as resolved pores. The flow behaviour of under-resolved pores (porous media) is described by a complete set of multi-phase constitutive relationships, which includes single phase permeability-porosity correlation, relative-permeability-saturation, and capillary-pressure-saturation curves. This approach allows for local variability of porosity and saturation in under-resolved regions, while fluid forces are applied locally satisfying the constitutive relationships in the porous media. In the rest of this section we describe our general workflow for multi-scale simulations, as well as describe the carbonate sample selected for this application. In the next section we demonstrate the workflow steps, including image segmentation, porosity estimation, and porous media characterization, all required inputs for the multi-scale multi-phase simulation. Finally we discuss the results for single-phase and multi-phase and present our conclusions.

1.1 Multi-scale modelling

Current microCT technologies focus on imaging one single scale, and requires one to choose this scale by balancing the trade-off between image resolution and representative elemental volume (REV). Image resolution must be at least small enough to resolve a percolating pore structure, while REV must be at least large enough to statistically represent all sizes of pores found in the sample. Unfortunately, the number of pixels in microCT imaging systems is limited, and constrains the pixel size and REV to each other. In cases where pore sizes vary by orders of magnitude, like carbonate rocks, a compromise between pixel size and REV cannot be found, and porous media (PM) pixels

have to be considered. PM pixels represent regions where pores are present but smaller than the pixel size. An example of a Carbonate rock [21] image is shown in figure 1 (top), where some regions showing as intermediate grey can be identified as PM, with pores sizes smaller than the pixel size. The intermediate grey value can be interpreted as the pore fraction or sub-resolution porosity, between 100% pore (darkest regions) and 0% pore (brightest regions). In general the sub-resolution porosity of PM pixels can be different, even if the pixels belong to the same PM-type. In a similar way that core samples can be classified by porous media types, PM pixels can also be classified by PM PM-types if they share similar constitutive relationships, or equivalently similar 3D pore structure, as illustrated in figure 1. High resolution imaging, like scanning electron microscopy (SEM) can be used to identify and select representative sample images for a PM-type, for instance in a carbonate rock like the one in figure 1, we could find that all the under-resolved pixels belong to a single PM-type, that we could call "carbonate PM-type 1" for instance.

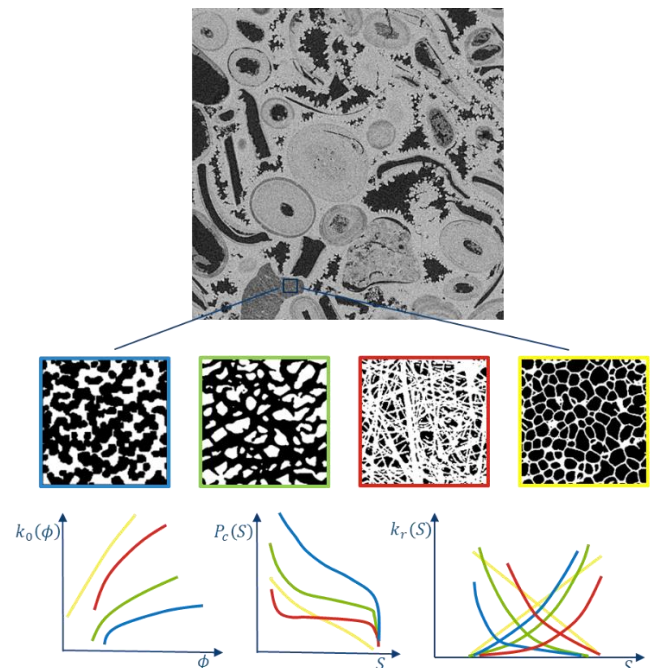


Fig. 1. Modelling of under-resolved pore structures using the concept of PM-types classification and characterization.

In general, it could be possible to have more than one PM-type present in an image, corresponding to different sub-resolution pore structures. A rock can have few clay minerals, with distinct microscopic pore structure, like kaolinite that exhibits typical booklet or book-like structures, grown diagenetically inside pores, Illite is hairy grain coating, and chlorite forms flakes. Microporous carbonates can be also present in rocks, as well as partially dissolved feldspars and other metamorphic microporous rocks. In shale rocks organic content, like kerogen also have a microporous structure. Each of these PM-types will behave differently under fluid flow and their identification is part of the image segmentation process. In many cases, like the carbonate rock example in figure 1, a single PM-type can be sufficient.

In order to sample 3D structures of a given PM-type, a combination of high resolution imaging techniques can be used, for example: SEM, focus ion-beam (FIB), laser confocal scanning microscopy (LCSM), X-ray nanotomography are the most common. By performing simulations using 3D images of these PM samples, it is possible to obtain a suitable set of constitutive relationships that represents well the corresponding PM-type as illustrated in figure 1 (bottom). In a sense, the constitutive relationships for these PM-types can be seen in turn as the result of high resolution digital rock simulations of micron size models. These relationships, absolute permeability vs porosity, J-function capillary pressure and relative permeability vs. saturation, describe a continuum behaviour where porosity, saturation and other properties are described as continuum variables in contrast to a discrete representation where each pixel is pore or solid. It is feasible that some representative PM-types can be characterized and collected into PM libraries that could be used in the same way as core samples called “analogues” are used in core analysis, in this case as a convenient complement to high resolution imaging.

These PM pixels with their local porosity estimated from the images and corresponding constitutive relationships should be sufficient input for a continuous solver that simulates the interaction between such PM pixels. Moreover, the challenge is on extending the current digital rock solvers from only pore/solid pixels to include also PM pixels in the algorithms. Here, we use a solution based on the lattice Boltzmann method (LBM), although the methodology itself is not limited to LBM, for this issue by employing a new workflow [9-10] with effective computational models for flows in under-resolved porous regions. In a fluid-flow simulation at a certain resolution level, flow contributions from under-resolved porous regions are properly taken into account by applying numerical models at each location using local information of geometry and fluids. The models reproduce proper forces acting on the fluids such as viscous, pressure, and capillary forces, using local representative physical properties captured by the PM-type constitutive relationships.

There are various ways to define numerical models for fluid forces in the under-resolved region. We show here one possible example [9-10]. The viscous force $\vec{F}_{PM_vis}^\alpha$ can be defined using the absolute permeability K_0 and relative permeability K_r^α as,

$$\vec{F}_{PM_vis}^\alpha = -\frac{\nu^\alpha}{K_0 K_r^\alpha} \rho^\alpha \vec{u}^\alpha \quad (1)$$

where α is an index for fluid phases and ν is the kinematic viscosity. Here, ρ and \vec{u} are density and velocity of fluid flow, respectively. Also, K_0 and K_r^α are functions of the porosity ϕ and density ratio of fluid phases under an assumption of homogeneous structure for under-resolved porous region. On the other hand, an example for definition of capillary force $\vec{F}_{PM_cap}^\alpha$ can be written as,

$$\vec{F}_{PM_cap}^\alpha = -\frac{2\sigma \cos\theta J}{\sqrt{K_0 K_r^\alpha / \phi}} (\nabla \rho^{\alpha_1}) \cdot H(At, |\partial_x(At)|) \quad (2)$$

where the hat notation indicates the unit vector and θ is the fluid-solid contact angle in the under-resolved porous structure. Here, J is the Leverett J-function, $P_c \sqrt{K_0 K_r^\alpha / \phi} / \sigma \cos\theta$, is the normalized capillary function of density ratio of fluid phases, and α_1 is an index of a corresponding fluid phase. A function H is a switch function depending on the local multi-phase interface information. Here, $At = (\rho^{\alpha_1} - \rho^{\alpha_2}) / (\rho^{\alpha_1} + \rho^{\alpha_2})$. This switch function is necessary for the diffusive multi-phase model because its non-zero interface thickness may cause excessive artificial force. Moreover, this definition cannot cover a scenario where a fluid phase is confined in an under-resolved pixel. In order to mitigate this problem, an additional model can be implemented using the Leverett J-function and local pressure. Since the saturation is almost insensitive to the local pressure force in this scenario, the local expected saturation level can be computed accurately using the local pressure and the Leverett J-function. Accordingly, the local saturation is controlled without significant deviation from the expected value. Accurate wettability can be realized with the Shan-Chen model in the LBM approach, which naturally constructs the inter-component force using the fluid potential from neighboring sites [9-13]. On the solid boundary, the proper wall potential is assigned so that the targeted contact angle is achieved. By simply extending this model, the wettability originated from solid parts in the porous media can be properly taken into account. Specifically, the potential in the porous media is constructed by both fluid density and solid wall potential weighted by local porosity.

1.2 Test sample

For this study, we use an Indiana limestone rock sample with porosity and permeability measurements in a 1.5 inch diameter core-plug sample, summarized in table 1. Mercury Intrusion Porosimetry (MIP) characterization was done in a 0.25 inch end-trim for this sample and results are shown in figure 2, including the saturation vs. pressure measured data and the derived pore throat size distribution, where two pore size families are clearly appreciated. To study the oil-water behaviour in this Indiana limestone core-plug sample, a spontaneous counter-current imbibition experiment in a decane-saturated and decane-aged sample was done, yielding a remaining decane saturation of 38%.

Table 1. Porosity, permeability laboratory measurements.

	un-stressed	800 psi
Klinkenberg Permeability, mD	12.5	6.68
Permeability to Air, mD	14.6	7.94
Swanson Permeability, mD	10.3	-
He Porosity, fraction	0.17	0.16

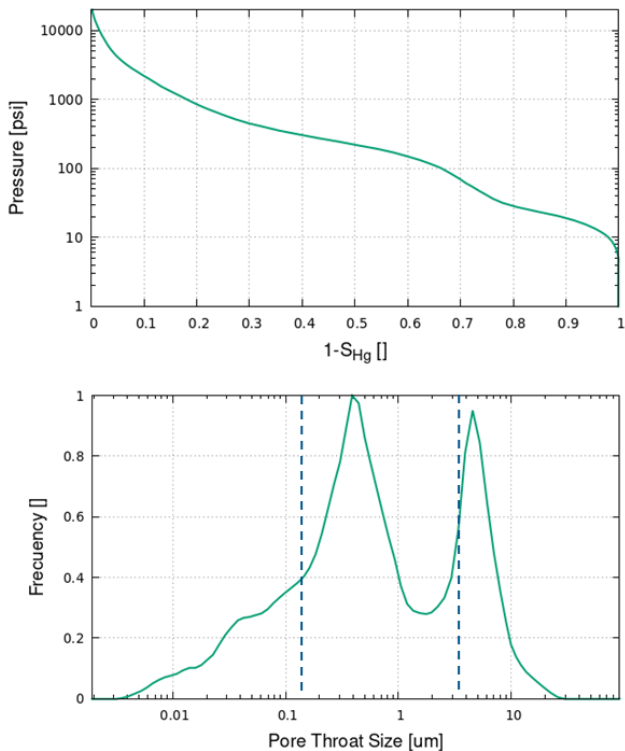


Fig. 2. Mercury intrusion porosimetry data, and derived pore throat size distribution of Indiana limestone sample

Imaging was acquired at two resolutions, $3.5 \mu\text{m}/\text{pixel}$ x-ray micro-tomography 3D imaging, shown in figure 3 for a selected 600^3 volume, and laser confocal scanning microscopy at $0.128 \mu\text{m}/\text{pixel}$, shown in figure 4. A statistical reconstruction algorithm [22] used a set of 2D confocal images focused at a typical micro-porous region as input to build a representative 3D model. The multi-point statistical (MPS) reconstruction method [22] was developed, validated and used extensively for geomodeling applications, and is well known by his capability to capture high order correlations beyond 2-point correlation functions or variograms. Although, we have not done and extensive validation for pore-scale modeling applications, the MPS reconstruction is not a required element in our workflow, which can use in general any other type of higher resolution 3D imaging, like nanoCT and FIB.

We show with vertical dashed lines in figure 2, these two imaging resolutions as a reference of what pore sizes can be captured and modelled using each of these imaging techniques.

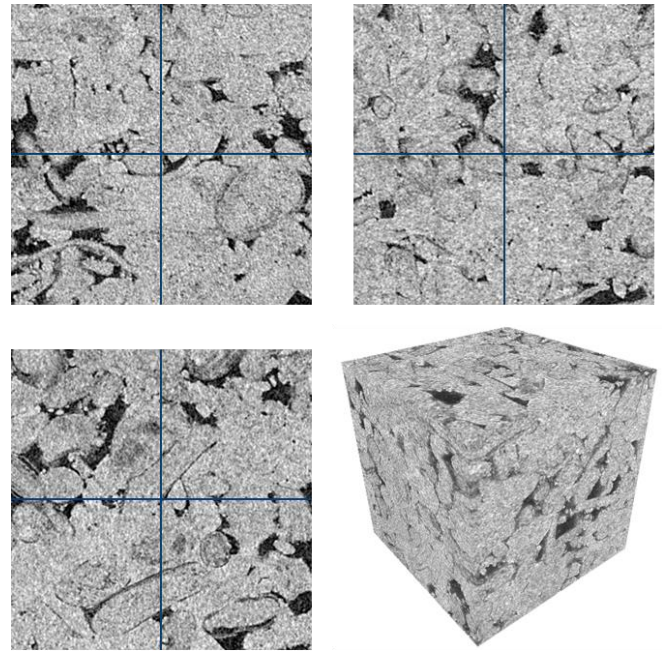


Fig. 3. Cross-sectional view and 3D view of the microCT image for our application sample, Indiana Limestone.

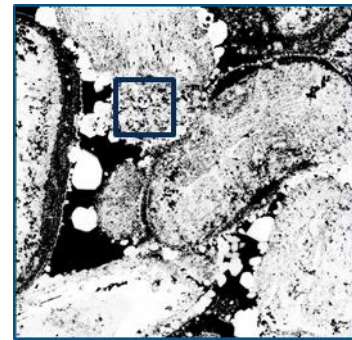


Fig. 4 View of a slide of confocal image in the Indiana Limestone sample, at nominal resolution of $0.128 \mu\text{m}/\text{pixel}$.

2 Multi-scale workflow

In this section we follow the multi-scale workflow steps for the carbonate sample described in the previous section. A summary of the workflow steps is shown in figure 5, which includes: large scale modelling: segmentation, porosity estimation, small scale modelling: PM samples selection, properties simulation using digital rock, and generation of constitutive relationships for the PM-type. We perform our multi-scale flow simulations using these inputs from both scales, and the results are presented and discussed in the following section.

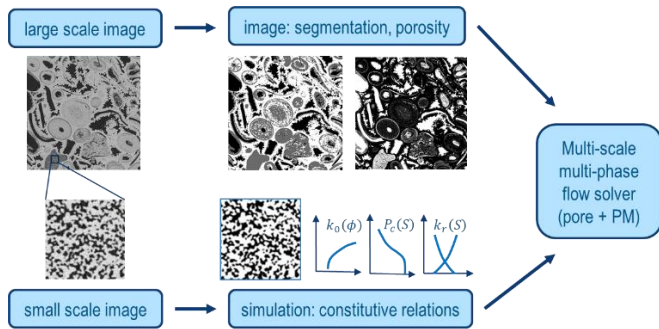


Fig. 5. Multi-scale workflow.

2.1 Image segmentation, porosity

MicroCT images show a grey scale that quantify the x-ray attenuation coefficient of the material contained in each pixel. Different pure materials (minerals and fluids) have different attenuations values and show as different grey scale values. If each pixel contains only one type of material, segmentation reduces to locate the best thresholds that separate grey scale values corresponding to different materials. However, when a pixel contains pores smaller than the pixel size, a.k.a a PM pixel, there is a partial volume effect and the x-ray attenuation is an average of the solid and pore fractions within the PM pixel.

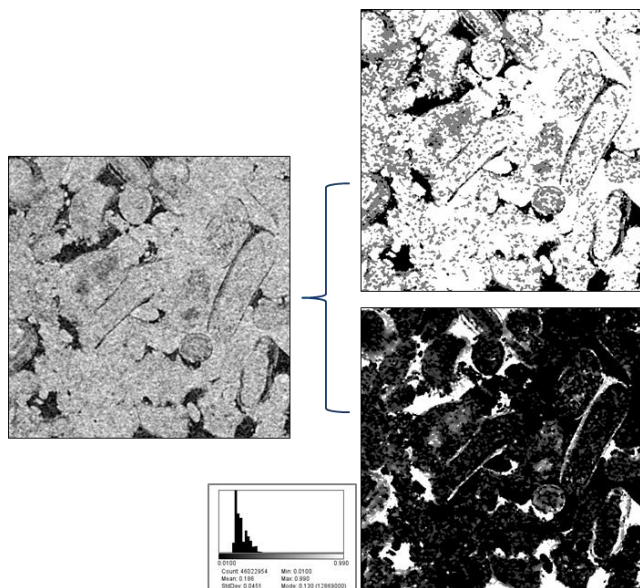


Fig. 6. Generation of image segmentation and image porosity.

Depending on the how different the PM pixel grey values are compared to other materials present on the image, it may be possible to use only thresholding to segment the PM pixels from the other pure materials. If grey scale is not enough, textural features can also be used to segment out PM pixels of different PM-types. In the Indiana Limestone sample presented in the previous section, we identify one PM-type, corresponding to a crystalline micro-structure sometimes referred as micrite. We show in figure 6 (top-right) a possible segmentation for our Indiana Limestone image, where pixels of pore/solid show as black/white, while pixels for the PM-

type “micrite” are marked with a single shade of medium grey. The volume fraction of pore pixels in the image is 7%, while the volume fraction of PM pixels is 21.3%.

Next, we estimate the values for the local porosity in each of the pixels marked as PM. We use the segmented image to mask out each of the three sub-sets of pixels in the original grey scale image in figure 6 (left). We compute the average grey scale value for the two sub-sets corresponding to pore and solid pixel labels. These two grey scale values should correspond to the values of porosity 1.0 and 0.0 respectively. A linear transform between grey scale values and porosity is calibrated using these two reference points. Notice that this transformation is only possible in cases with only one type of mineral. In general, a linear transform can also be applied using an estimation for the mean value and standard deviation of the porosity in the PM region. In addition to the calibration of grey scale to porosity, a masked Gaussian smoothing filter can be applied to reduce the noise level for the PM porosity. The result for the local porosity image is shown in figure 6 (bottom-right), with a PM porosity mean and standard deviation of 0.186 and 0.05 respectively and a histogram distribution shown next to the porosity image. Notice that the porosity values in the pixels labelled as pore and solid are 1.0 and 0.0 respectively, this is enforced by the masking criteria. A quick calculation of the total porosity for this sample image, including the two contributions from pore and PM is: $7\% + 0.186 \cdot 21.3\% = 11\%$. A more accurate way to map the under-resolved porosity is by direct measurement, using an x-ray attenuating contrast agent like Iodine in a brine solution that is vacuum saturated in the sample. A reference dry-microCT (unsaturated) is performed first, and used later to subtract from the wet-microCT (saturated). This differential imaging technique has demonstrated quantitative accuracy for estimating the under-resolved porosity [30-32] and robustness regarding different mineralogy, therefore it is not limited by lithology. However, the availability of this imaging technique seem to be mainly in research laboratories, being a less common capability in commercial microCT facilities. If only dry microCT is available, the method described earlier can still be used.

These two images: (1) PM-type label and (2) sub-resolution porosity, can be sufficient input for a complete description of flow behaviour of the PM pixels; assuming that a PM library of constitutive relationship curves is accessible for the LBM solver to fetch the corresponding flow response of each PM pixel given its pair values of: PM-type and sub-resolution porosity. In the next sub-section we present the required PM library of constitutive relationship.

2.2 Porous media models

Based on [28-29], “micrite” particles are classified in three classes; fine, medium and coarse micrites, with a diameter (or maximum side length of the crystal) of 0.1-3 μm , 3-6 μm and 6-10 μm , respectively. They exhibit a relation between micropore classes and micrite microtextures: Very fine micropores (0.1 – 2 μm) are found in compact anhedral micrites (like shown in figure 7), coarse micropores (6 – 10 μm) are found in microrhombic and polyhedral micrites. Care

should be taken to choose the correct PM-type representative sample if direct imaging is not available. In this application, for modelling the identified micrite PM-type, a model was obtained by LCSM microscopy imaging in a selected representative location of the identified micrite PM-type in the Indiana Limestone sample. A 3D model was constructed from those confocal images with a resolution of 200 nanometres. An image of the confocal model is shown in figure 7.

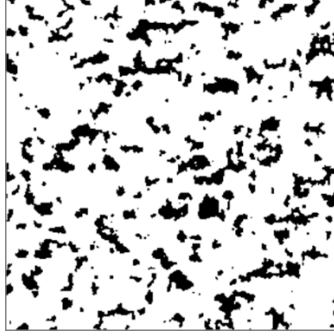


Fig. 7. PM model for the micrite PM-type, based on confocal imaging

The porosity, permeability values for the confocal model are 18.2%, 1.7mD. We use the confocal model for micrite as it comes from a high resolution image of the actual sample. Fluid flow simulations using our single-scale LBM solver produce a set of constitutive relationships, as illustrated in figure 8, absolute permeability vs porosity, capillary pressure vs. saturation and relative permeability vs. saturation, for the micrite PM-type represented by the confocal PM model, shown in figure 7.

In order to capture the single phase absolute permeability correlation with porosity we consider the simulation results from eight sub-volumes and fit a parametric relationship as show in figure 8 (top). The fitting quality can be affected by the functional form used, and the limited data range, however the application range is also limited, 12%-24% from the porosity distribution in figure 6, with the maximum of the distribution where the actual data is found. For two-phase flow simulations, we consider in this case an imbibition setup (inlet water, outlet oil) and fit similar parametric relationships in order to capture continuous functions of saturation conveniently, figure 8 (P_c middle, K_r bottom). The wettability condition was set to water wet, with a water-contacted angle of 10° , oil-contacted angle 30° , a water-oil interfacial tension of 30 dynes/cm, and an initial water saturation of approximately 35%. The set of curves in figure 8 will be use as the constitutive relationships that represent the flow behaviour of the PM pixels classified as belonging to the PM-type identified as micrite for our Indiana Limestone sample in the multi-scale simulations presented in the next section.

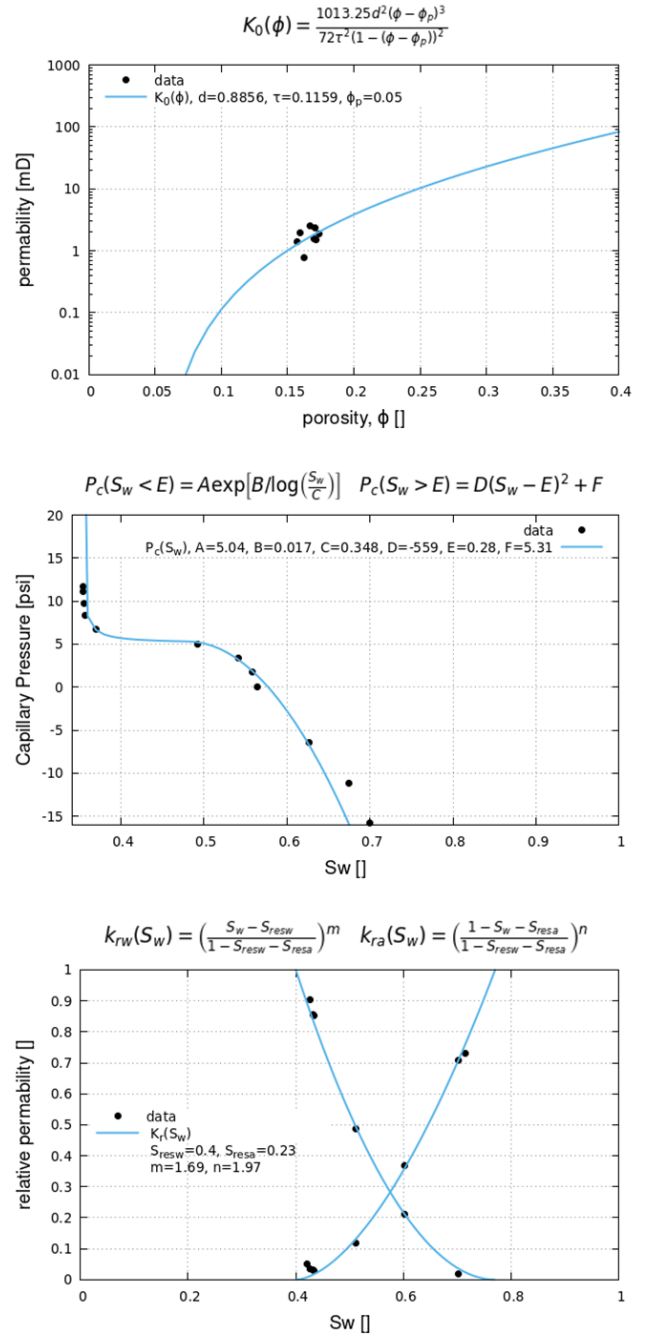


Fig. 8. Constitutive relationships for the confocal model of micrite PM-type.

3 Results and discussion

As a baseline for comparison we would like to consider two references: (1) A single resolution model, where in figure 6 (top-right) all the pixels marked as PM are re-labelled as solid, and (2) a registered model, which is a full resolution dual porosity model, constructed by scaling the microCT model by a factor of $10\times$, and replace the PM regions by copies of the 3D PM model, shown in figure 7, using periodic mirror boundaries that enforce full connectivity of the PM pore structure.

In figure 9 we show an illustration of this registered model constructed using the confocal model pore structure. The top image shows a slice from the resulting 6000^3 pixels

model, with a resolution of $0.35 \mu\text{m}/\text{pixel}$, which is 10 times smaller than the original microCT image resolution. The full model shown in figure 9 is too large to be used in a simulation, therefore we will use sub-volumes or coarsened versions of this model for comparison.

In this section we discuss the single-phase and multi-phase multi-scale simulation results for our Indiana Limestone sample and compare them with the available experimental measurements and our baseline simulation results.

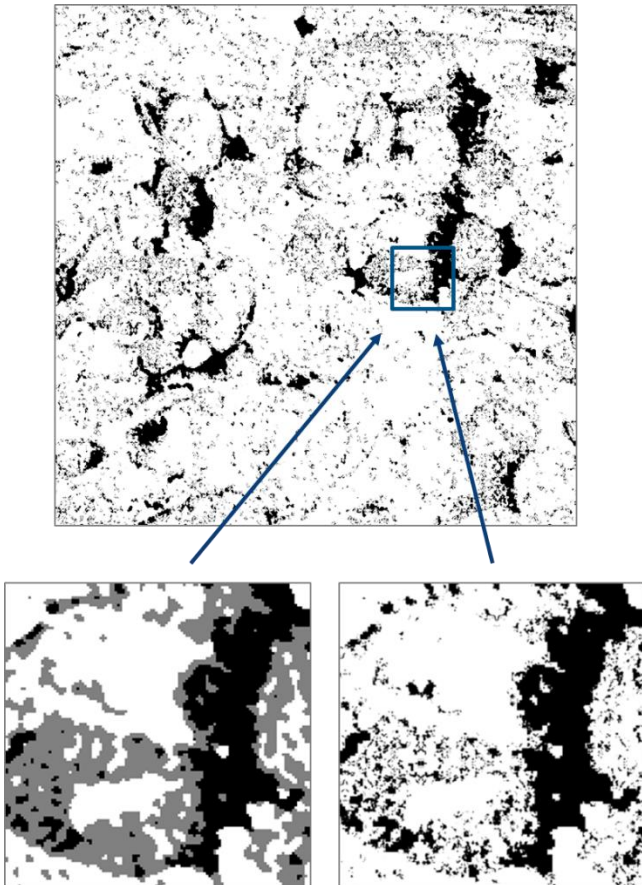


Fig. 9. Registered confocal model, 6000^3 .

3.1 Single phase

As shown in the pore size distribution from figure 2 (bottom), the microCT resolution of $3.5 \mu\text{m}$ can only fully resolve the larger pores of this Indiana Limestone sample, not the micropores. Moreover, when we analyse the connectivity of the fully resolved percolating pore structure, we find that the critical pore throat is just 1 pixel. This means that the single-scale pore structure (PM considered solid), is barely connected. In order to obtain a numerically stable estimation of the baseline permeability for the single resolution model, we increase the resolution in the model by a factor of $2\times$. The single-scale single-phase LBM solver simulation result for absolute permeability using the $2\times$ model is 7.7 mD (the $1\times$ model result is 6.0 mD). We select a representative direction (k_x) in order to facilitate the comparison between different results. The velocity flow paths for this single resolution

model are shown in figure 10 (left). Next, we consider the registered large size model described in the introduction of this section. We utilize a surface element based LBM modelling capability [16-20] to capture features below the nominal pixel resolution by using as input geometry a grey scale image of the pore-solid boundary. This grey scale boundary interface is actively used to locate a pore-solid surface out of the original pixel restricted grid, allowing us effectively to resolve pore structures smaller than the nominal pixel size, and avoid “stair case” related artefacts in the flow. We nominally coarsen our 6000^3 registered by a $5\times$ factor, however the grey scale resulting model could be considered equivalent to a 2400^3 model. The registered confocal model simulation result for absolute permeability is 8.2 mD . Velocity flow paths for this registered model are shown in figure 10 (right). This small increment in the registered model result relative to the single resolution model permeability indicates that the role of the under-resolved porosity for single-phase flow is secondary in the case of this sample.

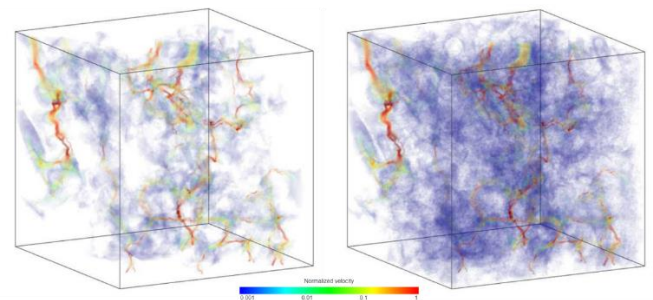


Fig. 10. Velocity flow lines for single resolution model (left) and registered confocal model (right).

For the multi-scale single-phase simulation in this Indiana Limestone sample, following the workflow in figure 5, we use as geometry input the pair of images for the segmentation and porosity, figure 6 (right), and the porosity vs permeability relationship for the confocal model of micrite PM-type shown in figure 8 (top). The multi-scale simulation result for absolute permeability is 7.8 mD , which is a value consistent with the results from the single resolution model and registered model simulations.

Finally we want to discuss a parametric study for the overall single-phase flow in this sample as a function of a varying value of the PM permeability. The goal of this exercise is to verify the consistency between our single-scale solver and our multi-scale solver: for a small enough value of k_{PM} used in our multi-scale solver we should recover the same results as in our single-scale solver when PM pixels are re-labelled as solid. Similarly, for a large enough value of k_{PM} used in our multi-scale solver, we should recover the same results as in our single-scale solver when PM pixels are re-labelled as pore. The results of this parametric study are shown in figure 11. As expected we recover with our multi-scale solver the respective end member results of the single-scale solver for the overall permeability. Moreover, we show in figure 11 that the range of the permeability expected from laboratory measurements, table 1, is consistent with the result obtained with the confocal model we use for micrite PM-type.

This kind of response function in figure 11, can also be useful to understand the ranges of permeability for the under-resolved porosity where a significant impact in the overall flow can be expected. This response function is not trivial and depends on the complexity of the PM plus pore connected structure.

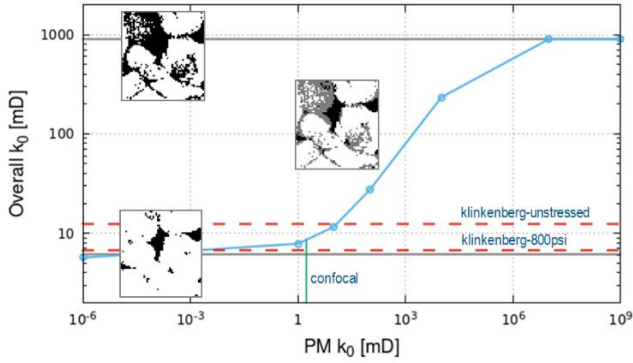


Fig. 11. Single-phase multi-scale flow permeability prediction as function of PM permeability

3.2 Multi-phase drainage

Although it is entirely possible to use it for drainage, we will delay the use of our multi-scale multi-phase LBM extension until the next sub-section for imbibition, which represent a more interesting scenario for oil-water behaviour, and has some experimental data to compare with, while in the other hand for drainage we have only MIP experimental data to compare with, therefore we take this as an opportunity to describe our MIP multi-scale extension for this type of simulation. We use the well-known percolation invasion method for MIP simulation [23], which uses the maximal inscribed sphere map on the pore space and the Young-Laplace inverse relationship between pore radius and pressure for capillary equilibrium. In the maximal inscribed sphere map, each pore pixel is assigned a radius value equal to the largest sphere radius that can be inscribed in that region of the pore space and includes this pixel inside the sphere. This map can be used to represent the local capillary equilibrium inter-phase between ideally wetting and non-wetting fluids, given that the contact angle of the inscribed sphere is 180°. This is a good approximation for mercury intrusion porosimetry (MIP), between the inter-phase of liquid mercury and vapour mercury. In order to minimize the surface-to-volume ratio effect given the small size of digital rock models as compared to real core samples used in the laboratory, we do not surround the whole model with mercury, but we restrict the mercury to be in contact with only one face of the rectangular prism model. For an initial low applied pressure (large applied radius), all pixels marked with radius larger or equal to the “applied radius” and connected with the inlet are marked as invaded by mercury. The applied pressure is increased and this percolation invasion process is repeated until all the pore structure is invaded. A saturation can be computed as the pore pixels invaded fraction, and recorded for each pressure. In figure 12 we show the results of this method applied to the single resolution case in our Indiana Limestone model. For the registered cases, due to the

size limitations of the method, we show a 2× coarsened version of the registered model using the confocal micrite PM-type model, figure 12. For comparison, we include the experimental MIP data. We also use an experimental total porosity value of 16.5% to normalize the simulated saturations.

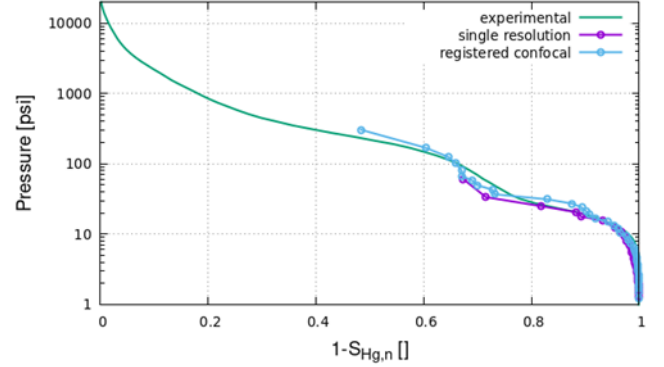


Fig. 12. Drainage results, pressure vs. normalized mercury saturation for single resolution model and registered model compared to experimental MIP.

Notice in figure 12 that the simulation results have an intrinsic maximum pressure limit associated with the minimum pixel size of the model, due to the Young-Laplace relationship. In order to extend this method to include the PM pixels, we consider the extension of the Young-Laplace relationship to radius smaller than the pixel size for a saturation S and pressure P

$$P(\phi_i, S) = \frac{2\sigma \cos \theta J(S)}{r_e(\phi_i)} \quad (3)$$

where the effective radius of a PM pixel of porosity ϕ_i , is $r_e(\phi_i) = \sqrt{k(\phi_i)/\phi_i}$, σ is the interfacial tension, θ is the contact angle, and $J(S)$ is the Leverett J-function that can be computed from the single-scale MIP simulation results on a 3D PM sample, like the micrite PM-type sample shown in figure 7. The results of this extended method that considers capillary behavior in PM pixel is shown in figure 13, where we show the MIP-PM simulation results using the confocal PM model.

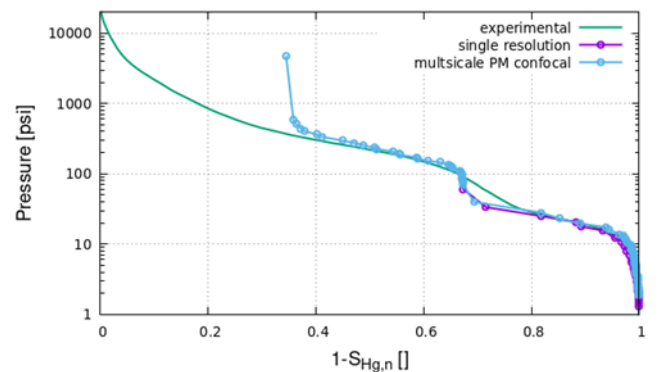


Fig. 13. Drainage results, pressure vs. normalized mercury saturation for single resolution model and multi-scale PM confocal MIP model compared to experimental MIP.

Similarly to what was done for the registered model, the saturation calculation is done using a total experimental porosity value of 16.5%, instead the total image porosity, which is 11% when one uses the micrite PM-type confocal model. The difference in total image porosity comes from a rescaling of the porosity input image, figure 6 (bottom-right), to have a mean value of 0.186 in order to be consistent with the porosity (and resolution) of the micrite confocal PM model used. In the case shown in figure 13, we were able to recover the location of the second entry pressure corresponding to the under-resolved micrite porosity, down to the limit imposed by the resolution of the PM model used, which is around $0.2 \mu\text{m}$.

3.3 Multi-phase imbibition

This sub-section covers the application of our multi-scale multi-phase LBM method to the Indiana Limestone model. A full size single-scale multi-phase simulation was not possible due to the limited connectivity of the full size microCT model (critical radius of 1 pixel). A full size registered model is also impractical. Therefore, we decide to test first a smaller 100^3 sub-volume for methodology comparison, as shown in figure 14, microCT image, multi-scale PM model segmentation and porosity, single resolution model, and registered confocal model.

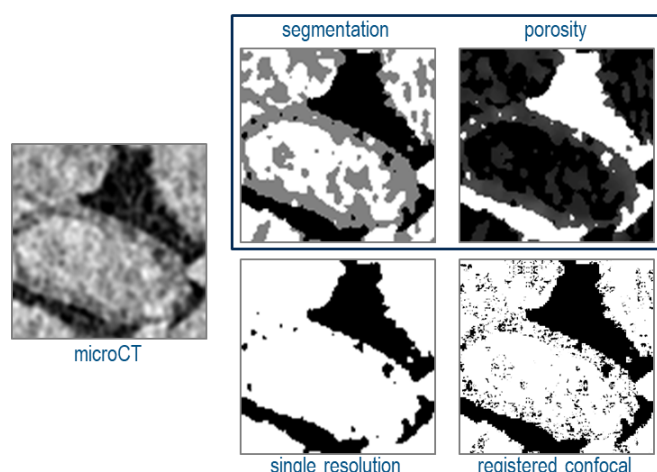


Fig. 14. Model images for the sub-volume 100^3

We considered an imbibition setup (inlet water, outlet oil) and the wettability condition was set to water wet, with a water-contacted angle 10° , oil-contacted angle 30° , and an interfacial tension water-oil 30 dynes/cm. It was difficult to have a comparable initial water saturation value between models, since each one has a different effective porosity, but we tried to set it around 10%, relative to a common total porosity value used to normalize saturations to be comparable with each other. For the single resolution model and registered confocal model the 10% water saturation was set from a maximal inscribed sphere based drainage (section 3.2) and we use our single-scale LBM solver. For the multi-scale PM model the initial conditions were set with no water in the resolvable pore and a partial constant initial water saturation around 40% in the PM and our multi-scale LBM solver extension was used, with inputs: segmented and porosity

images, figure 14 (top-middle and top-right), constitutive relationships for imbibition in the confocal PM model for micrite PM-type, figure 8.

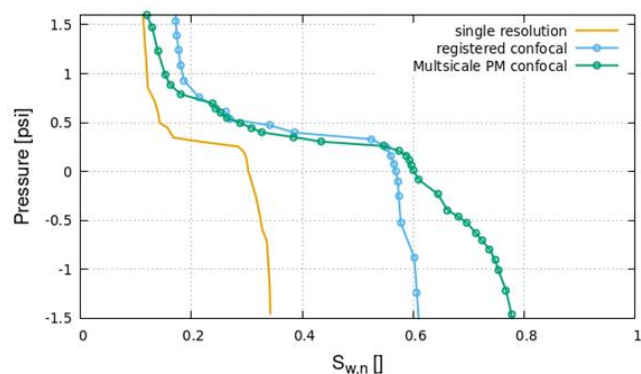


Fig. 15. Comparison of imbibition results for the sub-volume 100^3

A comparative plot with the three results is shown in figure 15, where there is a clear distinction between the single resolution model result that ignores under-resolved porosity contributions and the other two results that consider the under-resolved porosity contribution. The main difference relates to the capacity to mobilize more of the remaining oil in the pore space when the additional connectivity provided by the under-resolved porosity is considered. Notice that even though there is some variability with the registered result, there is an important consistency trend with the results obtained using the multi-scale PM-pore-solid model. The results in figure 15 provide some validation that our multi-scale multi-phase LBM extension is reasonably capturing the multi-phase behaviour as compared with some high resolution dual porosity model results, registered-confocal.

Moving up in model size, we consider next a 250^3 sub-volume scaled by $2\times$ to a 500^3 size that shows more heterogeneity, but still keeping a minimal resolved pore connectivity, with a critical radius of 2 pixels. While not yet of REV size to compare with laboratory data, this model still gives us some additional insight on the fluids distribution at different stages of the imbibition process. This time we run only single resolution model and multi-scale model simulations. Registered models become impractical at this point. Same wettability conditions were set as in the previous case, and initial conditions were set with no water in the resolvable pore and a constant initial water saturation around 40% in the PM. In this case we use the laboratory total porosity, 16.5% to normalize all saturations.

The simulation results are shown in figure 16. First, we compare the single resolution model result (dotted yellow line) to the multi-scale result (green line), similarly to what we observed in the previous 100^3 case, the addition of the PM connectivity enables a better oil mobilization in the resolvable pores. Next, we calculate separately the saturation contributions to the multi-scale total saturation results from the resolvable pore (purple) and from PM (blue). The pore contribution starts at zero saturation, but for better visualization we move the curve to start at the same location as the PM curve. We can see that at the beginning of the simulation the PM saturation increases more than the pore

saturation, while at later stages of the simulation the order is reversed. In the bottom of figure 16 we show four stages of the fluid distribution corresponding to the green circles that also show visually the same interplay between the pore and PM water saturation evolution along the simulation.

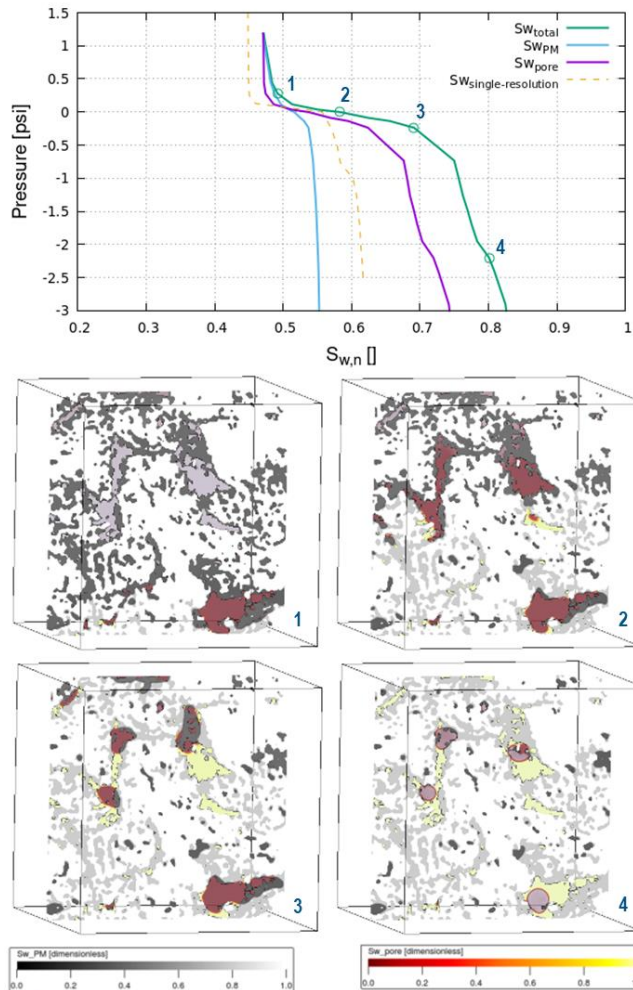


Fig. 16. Comparison of imbibition results for the 500³ case.

Finally we run our multi-scale multi-phase simulation in the whole model 600³ at the original resolution 3.5 $\mu\text{m}/\text{pixel}$, where the structure of only resolvable pore is barely connected by 1 pixel. We use the same initial conditions and porosity normalization as in the previous sub-volume 500³ case. In addition to the same water-wet setup used in the two previous cases (100³ and 500³), we also test a mix-wet condition in which the resolvable pore is considered oil-wet, with a water-contacted angle 10°, oil-contacted angle 150°, while the PM wettability is maintained as water-wet, this is done by using the same constitutive relationships as in figure 8. In general if a different wettability condition for the PM is to be used, a new set of constitutive relationships would need to be created where the desired wettability conditions for PM are used in the simulation of the corresponding PM model.

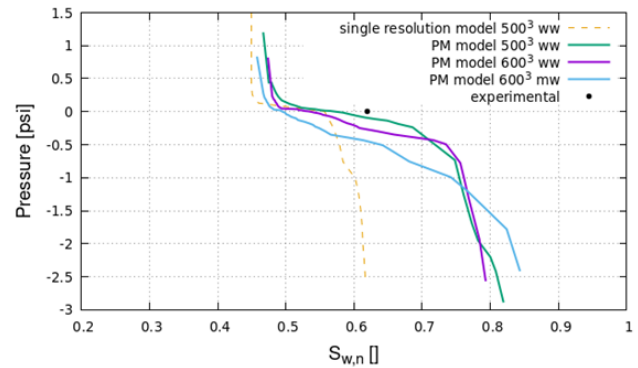


Fig. 17. Comparison of imbibition results for the 600³ case.

Four results are shown in figure 17, a 600³ water-wet case result (purple), two results for the sub-volume high resolution 500³ water-wet case: single resolution model (dashed yellow) and multi-scale (green), and the 600³ mix-wet case just described (blue). As for the water-wet cases, they are deemed to be in good agreement for the whole volume 600³ and the 500³ sub-volume as well as consistent with the water saturation of 62% from laboratory spontaneous imbibition measurement. Next, the mix-wet scenario behaves in the expected way relative to the water-wet case, most of the blue curve is below the purple curve, except at the end of the curve where the order is inverted. Finally, our initial observation holds: the multi-scale results show a larger mobilization of remaining oil as compared with the single-scale results.

4 Conclusions

In this paper we show a new method for multi-scale flow simulations, single-phase and multi-phase, and an application to a multi-scale carbonate rock, where under-resolved pores are believed to play an important role for oil production. We show consistency between our single-scale LBM solver and the new multi-scale LBM solver extension. In addition to an extension to the LBM solver, we also show a possible extension to include under-resolved pores to the percolation invasion method for MIP simulation that uses the maximal inscribed sphere map. It is worth noticing too that we discuss a complete workflow where a systematic identification and characterization of PM-types play a central role. Additionally, this framework allows for internal variation of porosity within the same PM-type. We believe this complete workflow represent a significant advancement in the application of digital rock methods to a difficult class of multi-scale rocks, such as carbonates. By including the simulation of flow in under resolved pores, the LBM extension solver is not limited to a minimal pixel size anymore. Given the relaxation of the resolved percolating pore space, which extend now to the join pore + PM space, other possible applications of this workflow could include plug-size sample simulation and whole core medical CT based simulation when heterogeneity is not captured properly by plug-size samples. A critical requirement could be, being able to identify PM-type classes that can be represented well by few samples at the right scale. A future workflow for core-plug and whole-core would definitely require several scales for which this workflow can be used progressively to connect pairs of adjacent scales. Multiple scales of images and other

experimental data would be necessary for testing and validation of this workflow at core-plug scale and above. The current multi-scale workflow is more suitable for isotropic uniform cases, when the under-resolved pores are much smaller than the pixel-size. Cases where the under resolved pores are close to the pixel-size would need local directionality. This limitation can be important to capture properly for instance under-resolved pore throats. We are working on an improvement that uses the image itself to compute local directionality and rotate the PM-type permeability tensor accordingly. This extension to the workflow will be the subject of a follow up publication.

References

1. G.R. Jerauld, J.T. Fredrich, N.M. Lane, Q. Sheng, B. Crouse, D.M. Freed, A. Fager, R. Xu, Abu Dhabi Int. Pet. Exhib. Conf., Society of Petroleum Engineers SPE-188688-MS (2017)
2. D.M. Freed, International Journal of Modern Physics C **09**, 1491 (1998)
3. N.S. Martys, J.G. Hagedorn, Materials and Structures **35**, 650 (2002)
4. I. Ginzburg, G. Silva, L. Talon, Phys Rev E **91**, 023307 (2015)
5. J. Li, D. Brown, Geofluids, 1740693 (2017)
6. J. Zhu, J. Ma, Scientific Reports **8** 5826 (2018)
7. A. Demianov, O. Dinariev, N. Evseev, The Canadian journal of chemical engineering **89**, 206 (2011)
8. M. Suhrer, X. Nie, J. Toelke, Proceedings of international petroleum technology conference, 20035 (2020)
9. H. Otomo, H. Chen, R. Zhang (to be published)
10. H. Otomo, R. Salazar-Tio, H. Chen, R. Zhang, A. Fager, G. Balasubramanian, B. Crouse, H. Fan, J. Yang, US patent application filing number 17/136,259 (2020)
11. H. Otomo, H. Fan, R. Hazlett, Y. Li, I. Staroselsky, R. Zhang, H. Chen, C. R. MECANIQUE **343** 559 (2015)
12. H. Otomo, H. Fan, Y. Li, M. Dressler, I. Staroselsky, R. Zhang, H. Chen, J. Comput. Sci. **17** 334 (2016)
13. H. Otomo, B. Crouse, M. Dressler, D.M. Freed, I. Staroselsky, R. Zhang, H. Chen, Comput. & Fluids **172** 674 (2018)
14. H. Chen, R. Zhang and P. Gopalakrishnan, US Patent 9576087 (2013)
15. H. Chen, R. Zhang and P. Gopalakrishnan, Phys. Scr. **95** 034003 (2020)
16. H. Chen, C. Teixeira, K. Molving, Int J Mod Phys C **9** 1281 (1998)
17. Y. Li, R. Zhang, R. Shock, H. Chen, Eur. Phys. J. Special Topics **171** 91 (2009)
18. Y. Li, R. Shock, R. Zhang, H. Chen, J.Fluid Mech **519** 273 (2004)
19. H. Fan, R. Zhang, H. Chen, Phys. Rev. E **73** 066708 (2006)
20. B. Crouse, D. M. Freed, N. Koliha, G. Balasubramanian, R. Satti, D. Bale, S. Zuklic, The Society of Core Analysis conference SCA2016-058
21. T. Bultreys. Savonnières carbonate. Digital Rocks Portal <http://www.digitalrockportal.org/projects/72> (2016)
22. S. Strebelle, Mathematical Geology **34** 1 (2002)
23. D. Silin, T. Patzek, Physica A **371** 336 (2006)
24. A. Fager, R. Salazar-Tio, G. Balasubramanian, and B. Crouse, RMAG/DWLS FALL SYMPOSIUM. Denver (2019)
25. M. Zhang, R. Salazar-Tio, A. Fager, B. Crouse, Unconventional Resources Technology Conference URTeC (2020)
26. S. K. Masalmeh, X. Jing, S. Roth, C. Wang, H. Dong, M. Blunt, Society of Petroleum engineers SPE-177572-MS (2015)
27. L. C. Ruspini, G. Lindkvist, S. Bakke, L. Alberts, A. M. Carnerup, and P. E. Øren, Society of Petroleum Engineers SPE-180268-MS (2016)
28. R. L. Folk, American Association of Petroleum Geologist Memoir **1** 62 (1962)
29. M. H. Rahman, B. J. Pierson, W. I. Yusoff, International Petroleum Technology Conference, IPTC 14583 (2011)
30. A. Ghous, T. J. Senden, R. M. Sok, A. P. Sheppard, V. W. Pinczewski, M. A. Knackstedt, Society of Petrophysicists and Well Log Analysts Symposium, Abu Dhabi, SPWLA-MERS-2007-E (2007)
31. M. A. Boone, T. De Kock, T. Bultreys, G. De Schutter, P. Vontobel, L. Van Hoorebeke, V. Cnudde, Materials Characterization, **97**, 150 (2014)
32. Q. Lin, B. Bijeljic, H. Rieke, M. J. Blunt, Water Resources Research **53**, 7457 (2017)

Combining high-resolution core data with unsupervised machine learning schemes for the identification of rock types and the prediction of reservoir quality.

Christophe Germy^{1,*}, Tanguy Lhomme¹, and Paul Bisset²

¹EPSLOG, Liege, Belgium

²Core Technical Services, Aberdeen, UK

Abstract. CoreDNA is an integrated core analysis solution combining transdisciplinary, high resolution, non-destructive measurements on whole cores, for an early yet objective description of cores and the rapid estimation of formation properties. Whole cores, which may still be in their half-open liners, are mounted on one unique table-top equipment and submitted to a battery of tests, all sharing the same depth reference and compatible resolution ranges. A key enabler of CoreDNA is the capability to create a smooth and flat surface along whole cores, which is obtained with a succession of dry cut with a PDC cutter, each removing a sub-millimetre thick layer of rock. On a 4-inches diameter core, removing a 3mm-thick layer of rock suffices to create a 3cm wide flat surface. Such a surface is too small to hinder further sampling and plugging, yet large enough for many different types of sensors, and therefore suitable to take many high-fidelity measurements, which would normally require slabbed cores. Technologies including ultra-high-resolution pictures, elemental composition and the direct measurement of geomechanical properties such as strength and acoustic velocities, are all deployed on the same mini-slab surface along entire cores. Ultra-high resolution panoramic pictures (1.8 μ m/px) are processed to extract textural and colour features but also continuous grain size distribution from wavelet analysis. Grain size distributions calculated from images are backed-up by analysis of 3D topographical maps created with a laser scan. Results of these fast tests (3ft per hour) are analysed real-time and turned into high resolution, continuous profiles of properties (petrophysical, geomechanical and geochemistry). This knowledge is fed into (unsupervised) machine learning algorithms for the automated identification of lithofacies, the design of fit-for-purpose plug selections and the programming of subsequent steps in core analysis programs, even remotely. Measured core properties are stored under one unique format for all discipline, which eases interdisciplinary work, from the QC of standard tests (Routine Core Analysis, Rock Mechanical Test) to the upscaling of core data and the calibration of robust predictive models from well logs. Such data bases are also formatted for machine learning and can therefore be used to train AI models with reliable data from large numbers of legacy cores, where sedimentological descriptions and plug data are available. The case study of a well drilled in a North Sea field underlines the benefit of this disruptive technology in core analysis when run on intact cores prior to slabbing or taking any sample (plugs and preserved)..

1 Introduction

Because most branches of core analysis rely heavily on plug samples, the competition for intact core material is tough. In practice, not only these samples consume a significant fraction of the material available but also, the selection of sample sites is based on not much *a-priori* information. Indeed, little is known before permanent damage is done to the core by plugging and cutting. In this paper we promote a new approach of core analysis, which is focused on finding practical ways to bypass this issue.

To this end we designed an integrated core analysis concept that combines several non-destructive tests to produce multi-disciplinary data sets continuously along whole cores. The primary purpose of this concept is to equip core specialists with quantitative, high resolution logs of real

rock properties as early as possible in their core analysis workflows, without causing any irreparable damage to cores.

2 Methodology

CoreDNA is an integrated core analysis solution combining transdisciplinary, high resolution, non-destructive measurements on whole cores, for an early yet objective description of cores and the rapid estimation of formation properties (Figure 1). Whole cores, which may still be in their half-open liners, are mounted on one unique table-top equipment and submitted to a battery of tests, all sharing the same depth reference and compatible resolution ranges.

The complete CoreDNA test series includes the following tests:

- portable XRF measurements for elemental composition,
- then high resolution photo for panoramic viewing of the cores,

* Corresponding author: tanguy.lhomme@epslog.com

- ultra-high resolution photos for the rock texture and grain properties,
- probe permeability,
- laser scan for grain properties,
- ultrasonic velocity logging,
- strength from the scratch test.
- The MiniSlab is also a suitable surface for sedimentological descriptions.

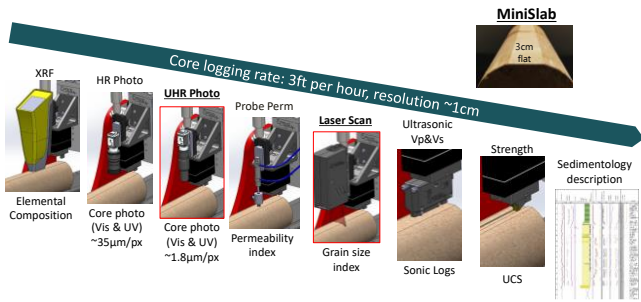


Figure 1: CoreDNA test sequence.

Results of these fast tests (3ft per hour) are analysed real-time and turned into high resolution, continuous profiles of properties (petrophysical, geomechanical and geochemistry). This data is fed into (unsupervised) machine learning algorithms for the automated identification of lithofacies, the design of fit-for-purpose plug selections and the programming of subsequent steps in core analysis programs.

2.1 Mini-Slab

The MiniSlab is created with a succession of dry cuts with a PDC cutter (Figure 2), each removing a sub-millimetre thick layer of rock. On a 4-inches diameter core, removing a 3mm-thick layer of rock suffices to create a 3cm wide flat surface. Such a surface is too small to hinder further sampling and plugging, yet large enough for many different types of sensors, and therefore suitable to take many measurements, which would normally require slabbed cores. Technologies including ultra-high-resolution pictures, elemental composition and the direct measurement of geomechanical properties such as strength and acoustic velocities, are all deployed on the same mini-slab surface along entire cores.

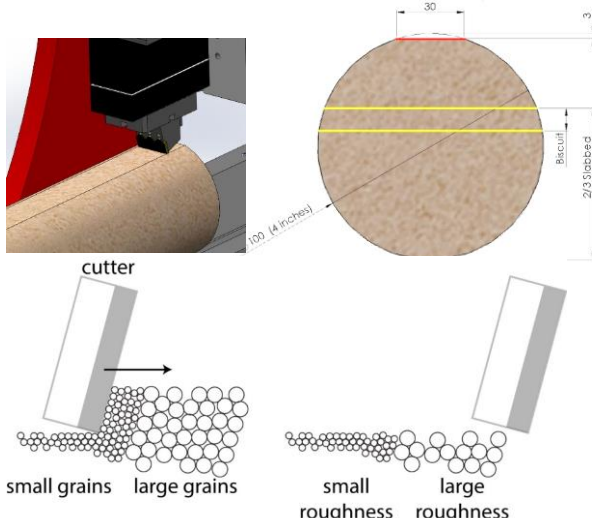


Figure 2: Creation of a MiniSlab surface with a PDC cutter.

2.2 Portable XRF

An Olympus Vanta XRF system is integrated on the CoreDNA bench. The X-Ray detector faces the MiniSlab and reports the elemental composition once the X-Ray source is triggered. Elemental compositions are calculated from the factory-standard Geochem calibration available on portable XRF devices from Olympus. The spot size is 1cm and continuous logs can be created by moving the XRF by steps of 1cm along the core. The measurement time can be chosen or automatically adapted to measure the elemental composition of rock cores with a specified accuracy.

2.3 High Resolution Pictures

High-definition panoramic core pictures (35µm/pixel) of the MiniSlab are taken under white light or UV light. The acquisition of core images is performed while the samples are fastened onto the test bed to guarantee an accurate depth match between the different measurements and core photographs. The camera system is calibrated in order to ensure a consistent picture quality despite varying testing environments and testing setups.

Principal Component Analysis are run on images of the RGB pixels of high-definition core photographs for every centimetre. The two first principal components respectively represent the picture brightness and a log of color differences. They provide useful information for the identification of rock facies.

2.4 Ultra-High Resolution Pictures

Photos of core samples are taken with telecentric lenses giving a resolution of less than 2 microns per pixel. The depth of field these lenses is limited to about 0.3mm, which is too small to fully capture the topographic features related to grain size in most clastic reservoir rocks. We combine stacks of several pictures of the same zone taken at different altitudes in order to increase the sharpness of a single reconstructed picture across the entire depth range (**Error! Reference source not found.**). The actual depth range is measured on the MiniSlab surface by the laser and used to determine the optimal number of pictures per stack.

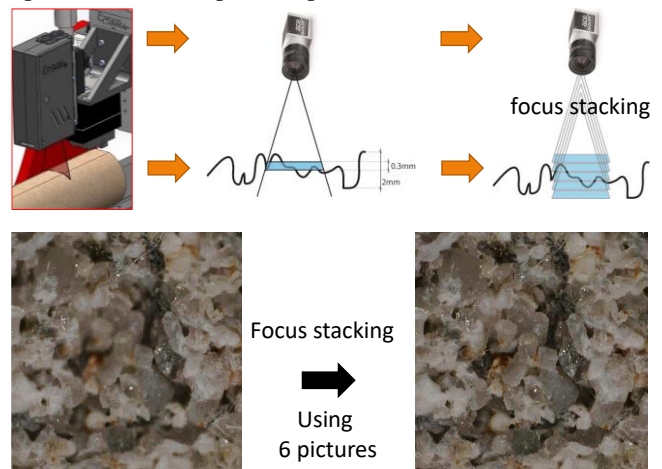


Figure 3: Acquisition and stacking of ultra-high-resolution images.

2.5 Wavelet Analysis

These pictures are turned into grey-scale images and analysed using wavelet transforms according to the following sequence (**Error! Reference source not found.**):

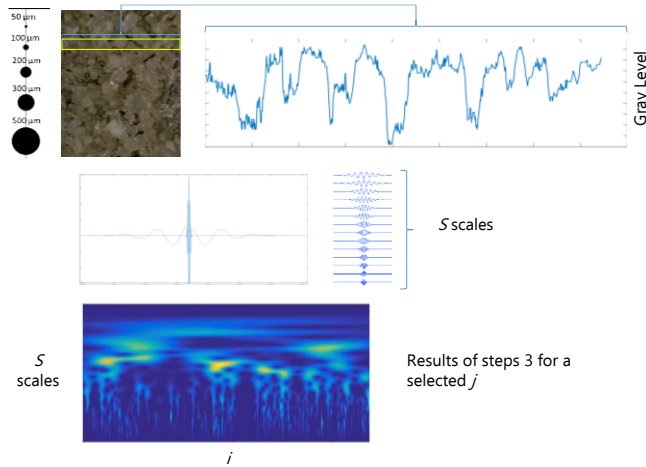


Figure 4: Wavelet analysis of Ultra-High Resolution Images for grain size distribution mapping.

1. First we extract lines of pixel intensity, and then
2. we calculate convolution products of these intensity vectors by wavelets of different scales s .
3. Then we calculate the norm of these convolution products. At this point, for every line in the working window we have created such a map where the horizontal axis is the position of the pixel on the line and the vertical axis is the scale of the wavelet used in the convolution product. A high value at the coordinate (i,s) , shown with a green colour in (Figure 4), shows a good match between local features of the intensity profile centered on the i th pixel and a wavelet of scale s .
4. We average the norm of the convolution products over the entire line
5. And over the number of lines in the working window
6. We normalize the product to create a cumulative distributed function (cdf) in scale and
7. Transform this cdf into another one in terms of grain diameter
8. Finally we use a Cahn-Fullman transform to turn this results into a cdf in grain volume [1].

There are a few limitations in the technique using ultra high resolution images for Grain size distributions mapping. First the wavelet transform often ends up with non-zero low frequency residues, which are interpreted as large particles. Although in small numbers, these large ghost particles amount for a significant fraction of the cumulative grain volume. We therefore need a low-frequency filter, or a maximum grain size cut-off value to remove these ghost particles from the distributions.

These is also the matter of bedding planes and fractures which sometimes come with high contrasts and are interpreted as large particles. Strong colour contrasts may also amplify the detectability of some grains with respect to others. Windows of investigation are 1cm wide, which means that particle larger than 5mm will be hardly visible with this method.

For these reasons, the best option to obtain reliable grain sizes is two combine two independent data sources, which are the laser scans and the ultra-high resolution pictures.

Practically, maximum grain size cut-off values can be determined from laser scans and the QA/QC of results can be greatly improved such that spotting outliers and invalidating dubious results becomes much easier.

2.6 Laser Topography

The laser scan technology uses a laser beam to map the topography of the MiniSlab surface continuously along whole cores, with a vertical accuracy of 1 micron and a horizontal resolution of 20*20 microns (Figure 5).

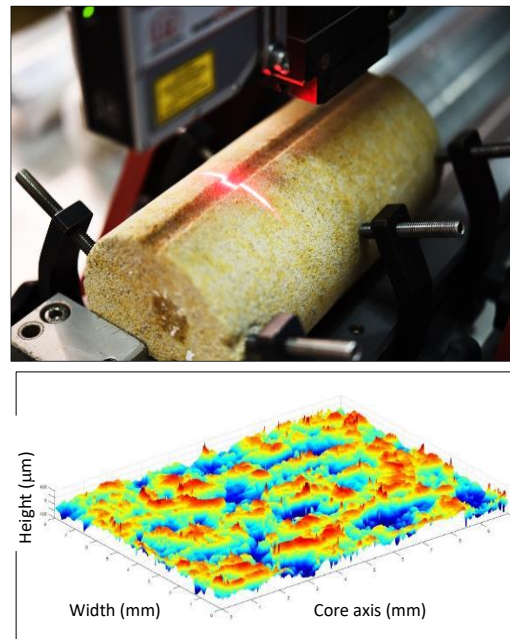


Figure 5: - Laser topography: acquisition.

The fundamental assumption here is that the topographic features of the Mini-Slab surface are related to the size of constitutive grains.

This is mostly the case in clastic rocks, unless large grains embedded in a strong matrix are sheared by the PDC cutter during rock cutting, which blurs the correlation of the measured surface roughness with the size of large grains.

2.7 Strength and Ultrasonic Velocities

Continuous high resolution profiles of rock strength profile and ultrasonic compressional velocity (V_p) profile are acquired on fresh cores. Details on the scratch tests can be found in [2] and [3].

2.8 Grain Size From Autocorrelation of Laser Profiles

Topographic maps are analysed for the purpose of deriving continuous grain size distributions along tested cores.

First we compute 1D autocorrelation functions along lines perpendicular to the core length, which are then averaged over a 1cm window. A proprietary transform, which has been calibrated on more than 10 outcrop rock samples, is then used

to turn the average autocorrelation function into a cumulative distributed function in volume of the grain size (Figure 6).

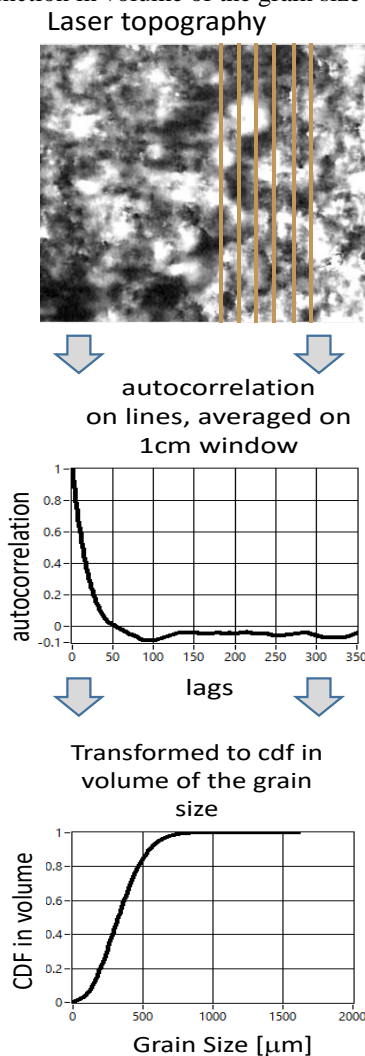


Figure 6: - Grain size from autocorrelation of laser profiles.

2.9 Estimated Permeability from Grain Size

An estimate of permeability is obtained with an empirical transform of grain size data from laser scans. This strong link between CoreDNA and conventional core data had already been demonstrated in other case studies involving other formations, as seen for example in the two charts in Figure 7: the blue curves show CoreDNA data (strength and grain size), while the red dots show porosity and permeability values measured on plug samples much later [4].

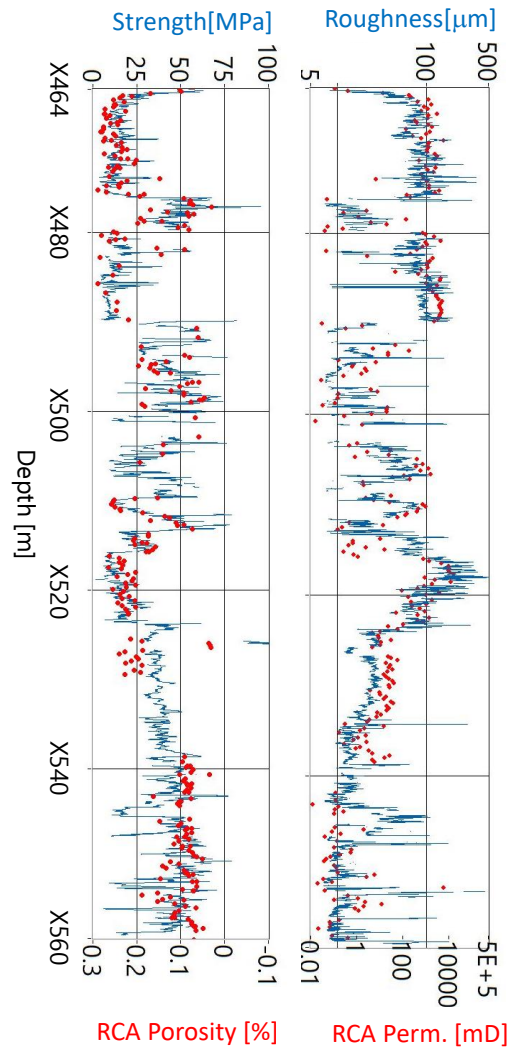


Figure 7: - Reservoir quality indexes derived from CoreDNA data

3 Applications

CoreDNA data was acquired on two cores from an observation well drilled by Neptune Energy in a North Sea prospect [5].

3.1 Data Recovery

The two cores had about similar lengths of 37m each, although Core1 had been subject to intensive plugging, including seal peels, prior to being tested with CoreDNA, while Core 2, which was tested immediately after opening its barrel, had not been plugged and was therefore in much better condition overall. CoreDNA data recovery was significantly lower in Core1 than in Core2, as seen in Figure 8, where coloured intervals correspond to sections where CoreDNA data could be retrieved, while blank intervals are seen where core material was too sparse even for CoreDNA sensors.



Figure 8: Data recovery on Cores 1 and 2

This difference in recovery advocates for continuous, non-destructive core measurements such as CoreDNA to be taken as a first step in core data acquisition programs, before any core material is spent in more destructive tests.

3.2 Missing data points

If the presence of specific elements in the cores is such that their concentrations cannot be detected wherever it is lower than the limit of detection (LOD) of the XRF device, the core data analyst has the two following options:

- the dataset only covers sections where all selected vectors are defined, or;
- the data set is completed with values equal to 10% of the device LOD wherever measured element concentrations were found below the LOD.

3.3 Data Coherence

The internal coherence of CoreDNA data is visible in the 2 cross-plots seen in Figure 9.

Brightness and color index values are normalized over the entire core depth range. High values of the brightness index means brighter formations under UV light.

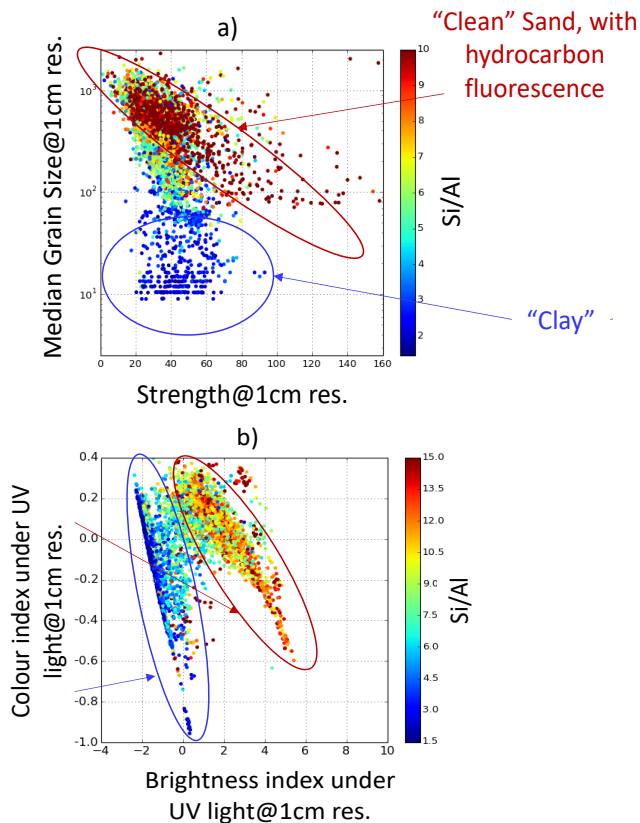


Figure 9: a) P50 of grain size distribution vs Rock Strength@1cm resolution vs. b) Colour index under UV light vs Brightness index under UV light. Colours indexed on Si/Al concentration ratios given by the portable XRF measurements.

Sections with low Si/Al concentration ratios have strength limited below 80MPa and smaller median grain sizes. They are also darker, although their colour index under UV light span across the entire range. These attributes are all compatible with the properties of clays.

Conversely, sections with higher Si/Al concentration ratios have strengths varying across the whole range but always have large grain sizes. They also appear brighter under UV light, with a slightly tighter range of colour index under UV lights than “clay” sections. These sections therefore have attributes compatible with those of clean, hydrocarbon-bearing sands.

The data organisation visible in Figure 9 prompts for a data analysis scheme based on the following data vectors:

- Strength,
- Grain Size P50 from Laser Scan,
- Elemental Compositions from XRF ,
- Brightness and colour index from high resolution core photos.

3.4 Identifying Lithofacies

A K-mean clustering scheme was run on the CoreDNA data set consisting of selected vectors, all at a 1cm resolution. The clustering analysis is performed in the multidimensional space defined by the principal components of the original data vectors. The number of selected components is adjusted to capture a meaningful fraction of the total variance. The results of the clustering algorithm are visualized with a colour scheme specifically built to represent the degree of proximity of clusters centroids. To this end, the RGB bits of each cluster colours are related to the position of cluster centroids in a 3D space defined by the three first principal components of the data space analysed by clustering (Figure 10).

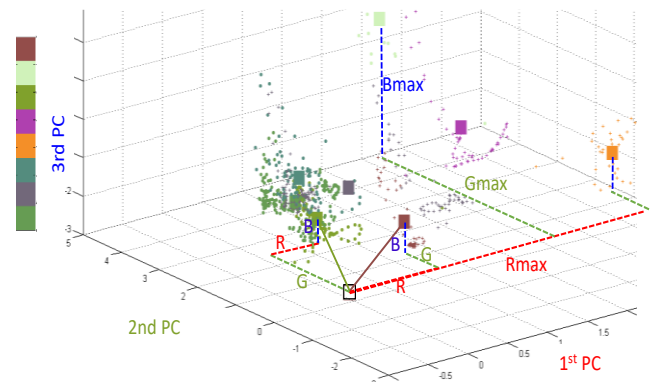


Figure 10: RGB colour scheme indicative of cluster centroid proximity.

The adequate number of clusters required to describe the spatial distribution of lithofacies detected along the tested core is determined with the use of a stabilisation diagram, synthesizing colour-based clustering results obtained for the same data set with an increasing number of clusters. The optimal number of cluster is set equal to the minimum number of cluster above which the colour-based representation of facies does not change anymore.

Statistical properties of lithofacies identified as clusters are shown using the logic depicted in Figure 11.

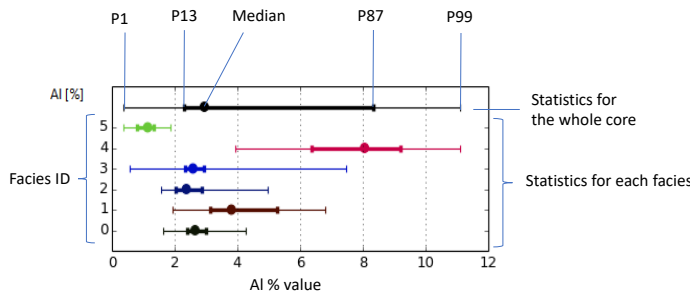


Figure 11: Statistic box example

The vertical axis of the statistic box corresponds to the facies number, while the horizontal axis corresponds to the range for one of the physical properties used in the clustering scheme. The topmost line shows the statistics for the physical property displayed by the statistic box for the entire core. Each facies is shown on a different line below, with its specific colour, extending from the 1st to the 99th percentiles for the physical property being displayed. The dot on this bar corresponds to the median value of the physical property for this facies. The left hand side extremity of the thick bar shows the 13th percentile while the right hand side of the thick bar shows the 87th percentile. In a normal distribution, the range covered by the thick bar would correspond to the median plus or minus the standard deviation.

3	34%	Weak	Medium to coarse	High Si/Al ratio, low Ca, low S, low Fe
4	9%	Weak	Medium to coarse	High Al, High Fe
5	10%	Strong	Medium to coarse	High Si, low Ca,
6	13%	Strong	Small	High Al, high Fe, High S

3.5 Results

Clustering analysis for lithofacies identification was run on the two cores separately.

3.5.1 Core1

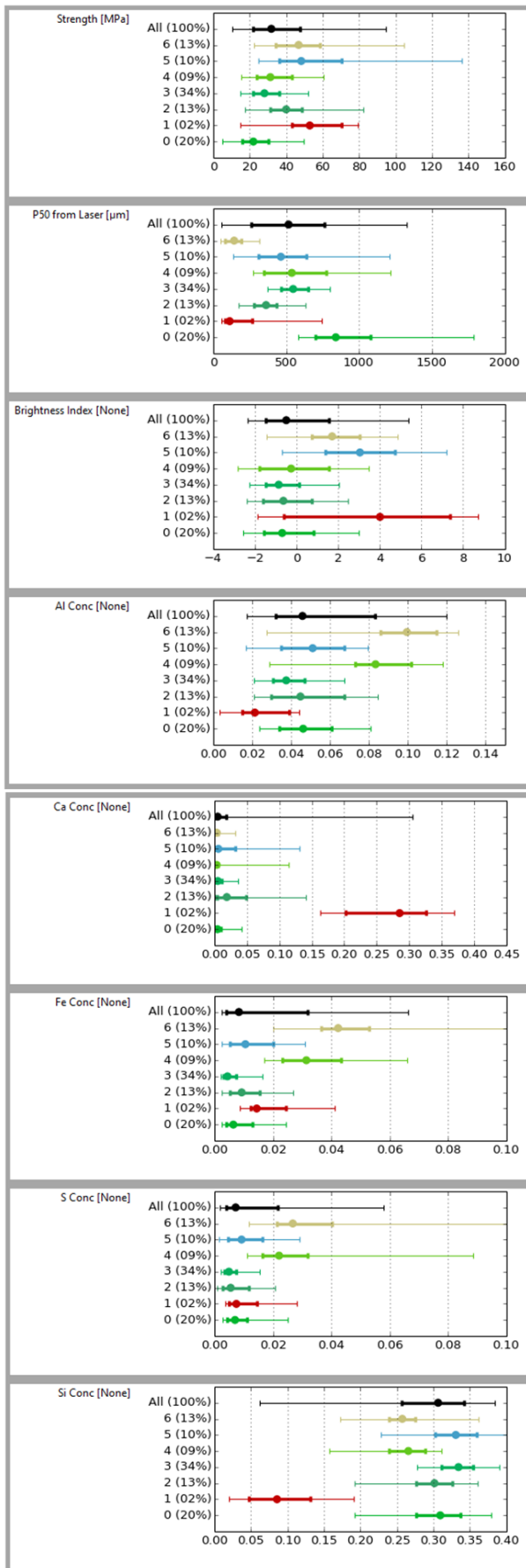
The first core was analysed using the following CoreDNA vectors:

1. Strength;
2. Brightness Index;
3. P50 of GSD from Laser;
4. Al, Ca, Fe, S & Si concentration

A total of seven different lithofacies were identified in Core1. Statistic boxes are shown in Figure 12 for each of the physical properties used in the clustering scheme. The main characteristics of the 7 lithofacies identified in Core1 are described in Table 1.

Table 1: Lithofacies identified in Core1

Facies	Core coverage	Strength	Grain size	Mineralogy
0	13%	Weakest	Coarse to very coarse	Low Al
1	2%	Strong	Small	High Ca, low Al, low Si
2	13%	Intermediate	Medium	High Si, low Ca, low Al, low S



3.5.2 Core2

The second core was analysed using the following CoreDNA vectors:

1. Strength;
2. P50 of GSD from Laser;
3. Al, Ca, Fe, S & Si concentration.

A total of six different lithofacies were identified in Core2. Statistic boxes are shown in **Error! Reference source not found.** for each of the physical properties used in the clustering scheme.

Figure 12: Lithofacies identified by clustering; Core1.

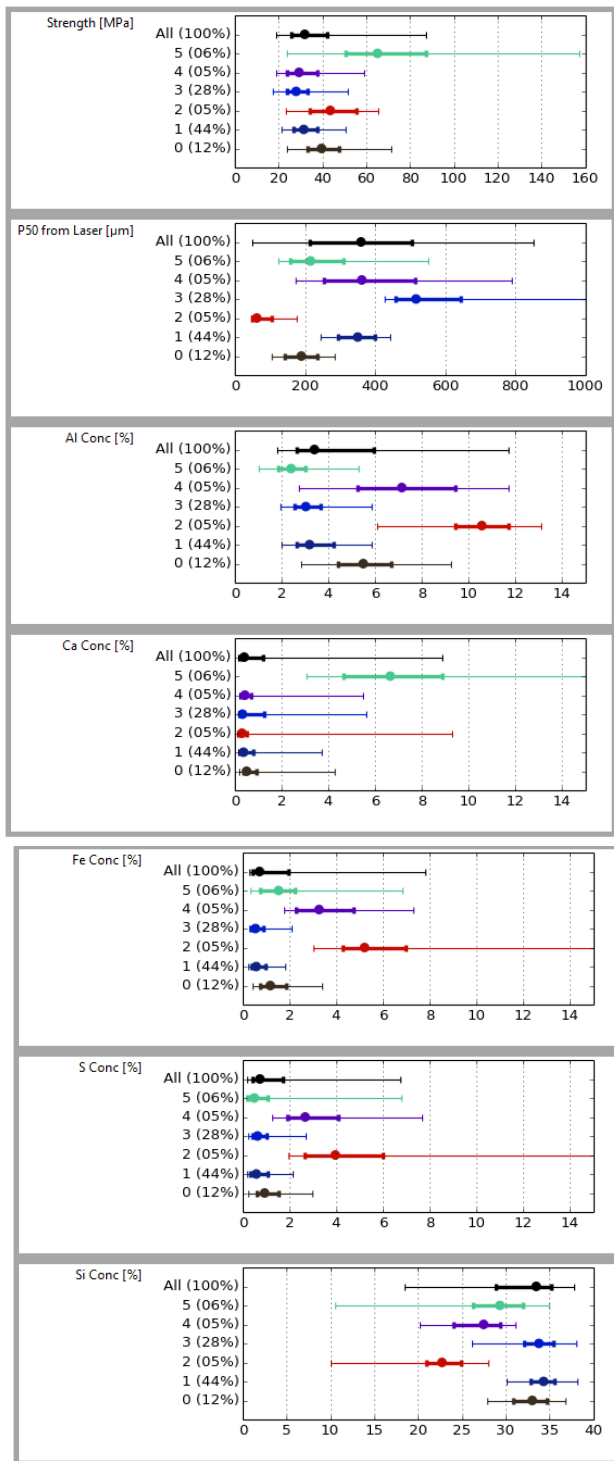


Figure 13: Lithofacies identified by clustering: Core2.

The main characteristics of the 6 lithofacies identified in Core2 are described below:

Table 2: Lithofacies identified in Core2

Facies	Core coverage	Strength	Grain size	Mineralogy
0	12%	Intermediate	Very fine	Low Si/Al ratio
1	44%	Weak	Medium	High Si/Al ratio, low Ca

2	5%	Intermediate	Very fine	Very low Si/Al ratio
3	28%	Weak	Coarse to very coarse	High Si/Al ratio, low Ca, low Al
4	5%	Weak	Medium to coarse	Low Si/Al ratio, large S
5	6%	Strong	fine	Large Ca, High Si/Al ratio

3.5.3 Facies groups

Facies identified above are grouped by types of lithology, using the information synthesized in Table 2. For instance, the aluminium concentration detected by the XRF measurements is indicative of the presence of clay, and therefore of the sand cleanliness. Facies can therefore be grouped according to their position with respect to a mid-range threshold (Figure 14).

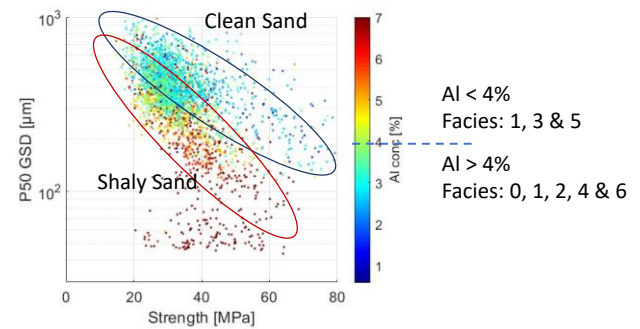


Figure 14: Distinction between shaly sand and clean sand based on the average Al concentration in each facies.

Using this classification, we group lithofacies as seen in Figure 15.

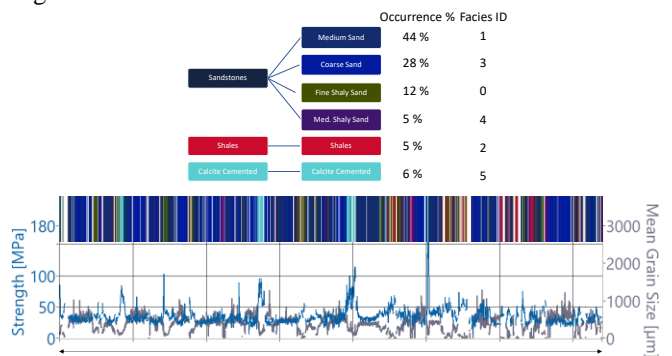


Figure 15: Lithofacies identified and grouped along Core2.

4 Conclusions

The complete CoreDNA array of transdisciplinary, high resolution, non-destructive tests was deployed as an integrated core analysis package on cores from one observation well drilled by Neptune Energy in a North Sea prospect.

One of the two cores from this well was tested with CoreDNA prior to any other testing program and was therefore virgin

from any sample hole, which allowed for maximum CoreDNA data recovery along its 37 meter of length.

A comprehensive data set ranging from textural and colour features of the rock to grain size distribution statistics, elemental concentrations, elastic wave velocities and rock strength was fed in an unsupervised machine learning algorithm for the early yet objective identification of lithofacies.

Six different lithofacies were identified in the 37m core interval, ranging from coarse clean sand to fine grain shaly sands, including limited thin calcite cemented layers.

In less than 24 hours following the testing campaign, a detailed sequence of rock facies with associated properties including reservoir quality index was provided to sedimentologists and core analysis specialists.

Such a detailed and comprehensive knowledge of the distributions of core properties, available under one unique format for all discipline, eases interdisciplinary work and significantly improves existing core analysis standards. It also provided a sound basis to train AI rock reservoir property predictors linking well-log data to well established core-based lithofacies signatures.

References

- [1] J. W. Cahn and R. L. Fullman, "On the use of Lineal Analysis for Obtaining Particle Size Distribution Functions in Opaque Samples," *Trans. AIME* 206, 610, 1956.
- [2] C. Gernay, T. Richard, C. Lindsay and H. T. Woo, "SPE-174086-PA The Continuous Scratch Profile: A High Resolution Strength Log for Geo-Mechanical and Petro-Physical Characterization of Rocks," *SPE Reservoir Evaluation & Engineering-Formation Evaluation*, publication pending.
- [3] T. Richard, F. Dagrain, E. Poyol and E. Detournay, "Rock Strength determination from scratch tests," *Engineering Geology*, pp. 91-100, 2012.
- [4] C. Gernay, L. Perneder and T. Lhomme, "Combining the analysis of ultra-high resolution images with continuous direct measurements to identify rock types," in *IRIS Rock Imaging SUMMIT*, Aberdeen, 2020.
- [5] C. Gernay, "Technical Talk: Epslog Engineering: Early Trans-Disciplinary High Resolution Core Logs To Steer The Core Analysis Workflow," 2nd December 2020. [Online]. Available: https://www.afes.org.uk/wp-content/uploads/2020/12/EPSLOG_GENERAL-CORE-DNA-AFES-2020.pdf.

NMR Core Analysis On Whole Core Samples

M. J. Dick^{1,*}, D. Veselinovic¹, R. Krumm², R. Antle² and D. Green¹

¹Green Imaging Technologies, Fredericton, NB, Canada

²Baker Hughes – Oklahoma City, OK, USA

Abstract. Nuclear Magnetic Resonance (NMR) has proven to be an important tool in the core analysis laboratory. Traditional NMR core analysis is restricted to core plug sizes (1” to 1.5” in diameter and ~2” in length). NMR analysis of whole core has been restricted by the size of typical NMR instruments and, more importantly, signal interference from portions of the core sample that are outside the probe’s field of view. This overestimates NMR porosity and creates unusable images and profiles with 2-D and 3-D measurements.

In this paper, new methods for performing quantitative NMR core analysis on whole core samples are presented. For bulk measurements, such as T_2 distributions or T_1 - T_2 maps, one method accounts for the signal outside the field of view through calibration using a sample of known volume that is larger than the probe field of view. The NMR volume of the sample is then compared with the known volume of the sample. Any difference between the two volumes is due to signal being folded in from outside the field of view. The ratio of the observed NMR volume to the known volume of the calibration sample is a correction factor, this can be applied to all whole core measurements done with the NMR probe. This technique has been successfully applied to measurements of T_2 and T_1 - T_2 maps on different whole core samples.

This calibration method works well for bulk measurements but is ineffective for imaging because the signal from outside the field of view spatially interferes with the signal within the field of view. This spatial interference leads to image distortion and erroneous results. NMR pulse sequences suppressing signal from outside the field of view improve profile measurements and maintain quantitative capabilities while eliminating sample blurring.

1 Introduction

NMR rock core analysis is an important tool in reservoir evaluation. Coring oil and gas deposits extract long sections (normally 4” diameter) of core from the well to the surface. Care is taken to preserve the core in its native state by sealing it with wax and storing it for core studies in a core analysis lab. Most core analysis is performed on plug samples extracted from the larger core. Typically, these plugs are taken at strategic locations obtaining standard 1” or 1.5” diameter samples for testing. Depending on rock type, plugging a core can be a challenge due to cracking, fracturing, or even pulverization by the plugging drill bit; it can be difficult to obtain proper cylindrical core plugs of sufficient length. Additionally, friction between the bit and the core generates considerable heat causing fluids in the preserved rock to evaporate and problems with saturation measurements. Also, obtaining plugs from whole core can involve drilling fluids that can change the original saturation. Whole core NMR analysis is appreciated for its ability to quantify fluids in an undisturbed state.

Depending on the plugging interval, core plugs can be affected by heterogeneity, skewing the description of the core and upscaling efforts. The ability to measure porosity and saturations continuously along whole core is

advantageous compared to discrete plug samples, especially when trying to match core to logs.

Addressing issues arising from plugging whole core, we propose using long sections of whole core for NMR analysis. Using the whole core comes with its own set of unique challenges: a larger NMR spectrometer is required, increasing complexity with moving the bulky core through the NMR field of view, and sample preparation is more difficult because of its increased size.

Our approach to NMR long core experiments consists of two parts, bulk measurement – to measure porosity of a section; and an image measurement – to measure saturations along the section. Bulk measurements are obtained by using an NMR T_2 [1] test determining the signal in the maximum field of view. Details on how this is achieved and calibrated is explained in the following section. Image measurements can be obtained by using one-dimensional saturation profile tests [2, 3]. For imaging long core samples, an out of field of view signal suppression technique is required because the sample exceeds the length of the NMR probe. A specialized pulse sequence [4] suppresses signal folding in from outside the field of view. This specialized sequence is outlined in the following section.

* Corresponding author: mjdick@greenimaging.com

2 Experiment

All NMR data for this experiment is recorded with an Oxford Instruments 8 MHz NMR spectrometer [5] using a 100 mm diameter probe. The spectrometer has a magnetic gradient in all three directions (X, Y and Z) allowing full profile measurements. Gradients allow for localized measurements of small volumes by dephasing protons outside the volume of interest; this allows for “scanning” data acquisition where volumes or “slices” are acquired sequentially. Green Imaging Technologies software was employed for data acquisition, inversion, reconstruction, and analysis [6].

Two pieces of whole core (from the same core) were used for this study, one long (40 cm) and one short (10 cm). The core was from a well from the Sweetwater region of Wyoming at a depth range of 7140-7145 feet. Table 1 summarizes the physical properties of each sample and Figure 1 shows an image of the longer core. Prior to the NMR scans, each piece of core was saturated with 2% KCl brine. 2% KCl was chosen to prevent dissolution of the sample by pure water. Saturation was performed in a high-pressure vessel with an overburden pressure of 10,000 PSI. The porosity data summarized in Table 1 was derived from the NMR data. This is the most accurate measure of porosity recorded on these samples. Porosity derived from mass data is prone to error such as grain loss which can affect the porosity derived. A hydraulic lift was employed to control the movement of the longer core through the spectrometer.

Core Sample	Short	Long
Core Diameter (cm)	6.70	6.66
Core Length (cm)	10.18	40.0
Bulk Volume (mL)	358.9	1393.4
Porosity (p.u.)	11.94	11.52

Table 1: Sample Information



Figure 1: Long Sample

3 Results

3.1. Calibration of field of view

The first step of bulk measurements on whole core is mapping the probe field of view. A 10 cm diameter and 1 cm long glass vial is filled with a calibration fluid containing a mixture of CuSO₄ in water. CuSO₄ is paramagnetic and reduces the bulk relaxation time of the fluid. The pancake shaped calibration sample is laid flat in the magnet’s field and is moved along its vertical axis in 1 cm steps. At each step, a T₂ test is used to measure the observed volume. The change in observed volume vs. displacement along the vertical axis (Figure 2 – Red Trace)) shows that the probe does not have a field of view

with sharp edges. Instead, the observed signal rolls off more gradually along the vertical axis of the magnet. This makes assigning a fixed field of view more difficult. Based on the map plotted in Figure 2, the probe field of view is estimated to be 14 cm (±7 cm) (Figure 2 – Blue Box). Clearly, this is just an estimate of the field of view because samples > 14 cm will have some fraction of their total observed signal from contributions beyond the field of view estimated as ±7 cm. The derivative also shows that samples within the field of view do not uniformly contribute to the total observed signal. For example, material at a displacement of -5 cm contributes only 75% of the equivalent amount of material at 0 cm of displacement.

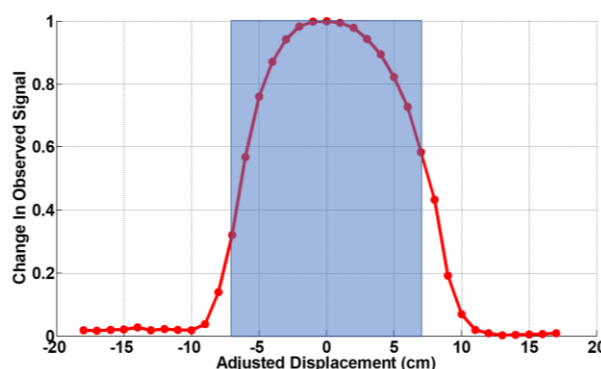


Figure 2: Probe field of view measurement profile.

To complete a bulk NMR measurement on a long piece of core, varying contributions to overall signal intensity along the vertical axis of the magnet need to be calibrated. To do this, a Teflon tube (62 cm in length and 3.71 cm in diameter) is filled with calibration fluid (CuSO₄) and centred within the field of view. A T₂ acquisition then measures the observed volume of the fluid in the tube within the field of view. As shown in Equation 1, the observed NMR volume was compared to the geometric cylinder volume whose diameter is the same as the Teflon vial and length is in the field of view of the NMR probe. This is the effective volume the NMR measurement should observe.

$$\frac{NMR\ Volume}{Geometric\ Vol} = \frac{NMR\ Volume}{\pi r^2 l} = \frac{156.44\ ml}{151.3\ ml} = 1.03367 \quad (1)$$

The ratio of the observed NMR volume to the geometric cylinder volume is the correction factor applied to any NMR measurements taken of core longer than the field of view of the magnet. In other words, the observed NMR volume overestimates the true geometric volume by approximately 3%. As a result, the observed NMR volume should be divided by this calibration factor to compensate the true volume of core within the field of view. Because the calibration constant was determined using a long uniform liquid calibration source, this method assumes that the core sample is also homogeneous along its length and is longer than the field of view of the magnet. However, this method can be applied to any rock type (conventional or unconventional) if it is homogeneous. If the sample was very inhomogeneous

this calibration method would lead to an overestimate of porosity of no more than 3.4 percent. In addition, experimental conditions such as pressure or temperature will have no effect on the calibration.

3.2. Porosity measurement of long core using calibration factor

To test the validity of employing a correction factor to determine the porosity of long core samples, validation measurements are performed on the two samples described in Table 1. First, the short sample is placed in the magnet and its T_2 distribution is measured (Figure 3 – red trace). The derived pore volume is then divided by the samples' bulk (geometric) volume to give a porosity of 11.94 p.u. The length of the short sample is completely within the field of view of the NMR probe, so no correction factor is needed to account for signal contributions outside the field of view.

Next, the long sample is placed in the magnet and its T_2 -distribution is measured (Figure 3 – Blue Trace). The measured pore volume is divided by the geometric volume of the field of view (Geometric Volume = $\pi r^2 l = \pi(6.66 \text{ cm})^2(14 \text{ cm}) = 487.7 \text{ ml}$). Note that we are dividing by the geometric volume of the field of view here and not the bulk volume of the sample. This is necessary because the sample extends beyond the field of view of the magnet. Because the sample length is beyond the NMR probe field of view, the pore volume is also divided by the correction factor. The porosity of the long core sample is determined to be 11.52 p.u. The good agreement between the porosity derived for the long and short samples validates employing the calibration method for bulk measurements on samples longer than the probe's field of view.

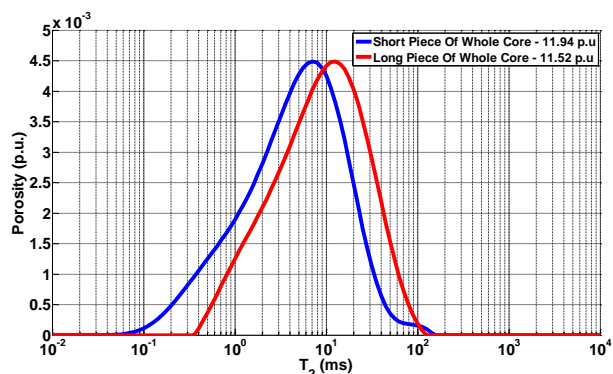


Figure 3: T_2 relaxation time distribution of long and short core samples

Figure 4 shows the T_1 - T_2 distributions of the long and short samples. T_1 - T_2 maps are also bulk measurements so the same calibration factor employed to correct the T_2 distributions can be employed to rectify the long core data. Employing the correction factor the porosity determined for the long sample from the T_1 - T_2 data was 12.07 p.u. which was in good agreement with the porosity derived from the T_1 - T_2 data of the short sample (12.53 p.u.) More importantly, the two maps plotted in Figure 4 are almost identical. This means T_1 - T_2 maps can be

effectively employed for core analysis such as fluid typing.

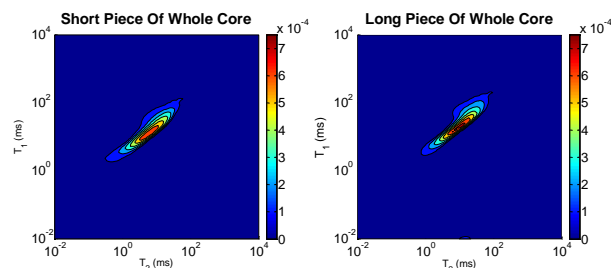


Figure 4: T_1 - T_2 maps of long and short core samples. The similarity between the plots validates the normalization techniques for samples exceeding the NMR's probe field of view.

While employing a correction factor to NMR relaxation measurements on whole core samples is effective and accurate, it is far from ideal. As mentioned earlier, it assumes homogenous core samples and any heterogeneity will lead to inaccurate results. For example, the small differences observed in the T_2 distributions (Figure 3) and the T_1 - T_2 maps (Figure 4) for the long vs. short core samples can be attributed to inhomogeneity of the sample. Figure 1 shows that our sample was not perfectly homogeneous. Additionally, correction factors cannot be applied to NMR images, i.e. it's not effective for regions close to the ends of the core. The correction method assumes that there is sufficient material on either side of the field of view. If not, then the assumptions made in determining the correction factor are invalidated.

3.3. Region of interest selection for whole core measurement

Because of the shortcomings of the calibration method just outlined, an exploration of a method for a region of interest selection of long core samples was examined based on insights developed by Vashee et al. [4]. These techniques can be applied to any NMR/MRI pulse sequence allowing any bulk or imaging technique to be adapted for long core samples. In our case, validation began by applying it to one-dimensional saturation profiles. Saturation profile measurements produce a 1D image of a rock core by collapsing (or summing) the signal in the 2nd and 3rd dimension. There are several different methods to acquire a one-dimensional profile [2,3] and an out of volume suppression technique can be applied to most of them. Without this suppression, samples that extend beyond the useable volume of the probe and/or linear region of the magnetic field gradients will create profiles that are unusable, as signal from outside the probe folds back into the measured profile, making the profile useless. The black trace in Figure 5 shows a saturation profile acquired on the long core sample without the out of volume suppression turned on.

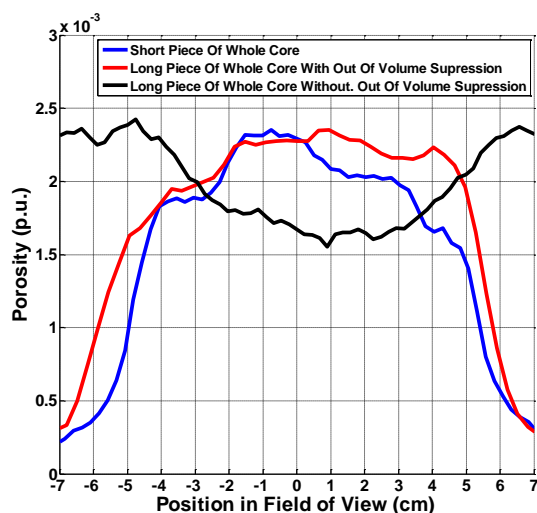


Figure 5: Saturation profiles of long and short core samples. Also shown is the saturation profile recorded for the long core sample without the use of volume suppression.

Out of volume suppression mitigates signal from outside the volume of interest. This works by taking two profiles, one normally and one with a spatially selective inversion pulse on the front end [4]. The spatial inversion pulse is performed in the presence of a magnetic field gradient to excite the desired region of the profile. The two profiles are then subtracted (in the time domain) and only signals from within the selected inversion slice are added, all other signals are subtracted. The selective inversion pulse is a slice selective adiabatic inversion pulse (hyperbolic secant pulse [4]). The adiabatic nature of the pulse ensures correct inversion even in the presence of radio-frequency (RF) inhomogeneity due to limitations of the RF coil. The duration between the normal profile sequence and the inversion pulse is about 1 ms. Therefore, if the T_1 of the sample is less than about 3 ms, this technique will fail to fully suppress out of volume signal. The technique also doubles the scan time, although the extra scan increases signal to noise by a factor of the square root of two. This is because in the volume of interest the signal is measured twice (once with the normal saturation profile and once with the spatially selective inversion pulse). When the two profiles are then subtracted, the profile has an increase in signal to noise of the square root of two as any signal does when you measure it twice.

A saturation profile of a long sample with out of field suppression is shown in Figure 5 (red trace). In this profile example, the region of interest is chosen as 11.2 cm or eighty percent (80%) of the field of view (14 cm). Also shown in Figure 5 (blue trace) is a saturation profile recorded on the short core sample without the suppression technique applied. Out of volume suppression was not necessary with the shorter sample as it did not extend beyond the field of view of the probe. The good agreement between the porosity per cm of both core sample lengths support that out of volume suppression techniques give accurate results. The length of the short sample as determined by the saturation profile (Figure 5 – blue trace) is also accurate. The length of the short core sample

is known to be 10.18 cm and should fall within the region of interest (11.2 cm) probed by the out of volume suppression measurement of the long core sample (Figure 5 – red trace).

4 Conclusion

We have successfully measured the T_2 relaxation time distribution and T_1 - T_2 maps of long core samples by employing a calibration method for handling signal from outside the field of view. The T_2 relaxation time and T_1 - T_2 map measured from a long core sample were identical to those measured with a short sample (shorter than the probe's field of view) taken from the same core validating the method.

The bulk calibration method has some shortcomings; it requires a homogeneous sample and cannot be applied to NMR images. To circumvent these problems, an NMR pulse sequence that suppresses contributions to the observed signal from portions of the sample outside the probe field of view is used. We have successfully employed this out of volume suppression technique to measure a saturation profile on a long core sample. Next steps include expanding the out of volume suppression for use beyond one dimensional saturation profiles to two- and three-dimensional images. Additionally, volume suppression methods to T_2 distributions and T_1 - T_2 maps to create slice selective version of these bulk measurements are being implemented.

References

- [1] Meiboom, S. and Gill, D., "Modified Spin-Echo Method for Measuring Nuclear Relaxation Times", *Review of Scientific Instruments* (1958), 29, 688-691
- [2] Halse M, Goodyear D J, MacMillan B, Szomolanyi P, Matheson D and Balcom B J 2003 Centric scan SPRITEmagnetic resonance imaging *J. Magn. Reson.* 165 219–29.
- [3] L. Li, H. Han and B. Balcom, "Spin echo SPI methods for quantitative analysis of fluids in porous media" methane storage capacity in organic-rich shales," *J. of Magn. Reson.*, vol. 198, pp 252-260, 2009.
- [4] S. Vashae, O.V. Petrov, B.J. Balcom, and B. Newling, "Region of Interest Selection of Long Core Plug Samples by Magnetic Resonance Imaging: Profiling and Local T_2 measurement", *Measurement Science and Technology*, vol. 25, pp 1-10, 2014.
- [5] *Geo-Spec 2-75 Rock Core Analyzer User Manual*, Version 1.8, Oxford Instruments, Tubney Woods, Abingdon, Oxon, UK, 2018.
- [6] *GIT Systems and LithoMetrix User Manual*, Version 1.9, Green Imaging Technologies, Fredericton, NB, Canada, 2016.

Digital Core Analysis as an Efficient Tool for Acid Treatment Optimization

Evgeny Ivanov^{1*}, Dimitry Korobkov¹, Igor Varfolomeev¹, Alexander Demianov¹, Alexander Sidorenkov¹, Anna Beletskaya², and Mikhail Stukan¹

¹Schlumberger, 125171 Leningradskoe shosse 16A, build. 3, Moscow, Russian Federation

²Schlumberger, 555 Industrial Boulevard, Sugar Land, TX 77478, USA

Abstract. Digital rock workflow for acid treatment optimization is developed. It includes construction of a digital rock model based on X-ray microtomography, running a set of multiscale digital experiments and a number of acid flooding experiments on rock samples for the model tuning. Here, we present results of application of the developed workflow for Austin chalk rock treatment by hydrochloric acid on core samples of 8 mm in diameter. Pore-scale simulations were performed using high-resolution 3D microCT models to determine the dependencies of rock permeability, active surface area and effective reaction rate on actual porosity. These properties were used to populate the laboratory-size core models, and Darcy-scale numerical approach was applied to simulate the dissolution at different injection rates. The core-scale simulations demonstrated inhomogeneous character of dissolution process leading to wormhole development in a certain range of injection rates. In parallel to numerical simulations, laboratory experiments on the same rock samples were performed at flow rates close to the optimal regimes followed by microCT imaging of wormhole structures. This information was then used to tune the model parameters. After that, the dependencies of the number of pore volumes injected until the breakthrough (PVBT) on the injection rate were obtained numerically for all the cores considered.

1 Introduction

Acidizing is one of the approaches widely used to increase the rate of hydrocarbons production from carbonate reservoirs. The effect is achieved due to partial dissolution of matrix rock by acid solution injected under pressures below the formation fracture pressures. Depending on parameters, such as reactive fluid composition, rate of fluid injection, and rock mineral composition, different dissolution patterns can be created. Face dissolution is observed when the acid is spent before penetrating deep into the rock. While uniform dissolution takes place, when the acid is evenly distributed along the treatment zone leading to uniform increase of rock porosity. The optimal inflow of hydrocarbons toward the wellbore or fracture is achieved, when the acid creates a set of thin channels, or so-called wormholes.

The treatment efficiency is crucially dependent on the acid composition and injection scenario. Since the optimal parameters are determined by geology and lithology of the reservoir, to achieve the best effect, each treatment should be preceded by experiments on representative rock samples.

One of the key characteristics determined in the framework of acidizing job design is the pore volume to breakthrough (PVBT). Which is defined as the amount of treatment fluid (measured in core pore volumes) required to be injected before the appearance of macroscopic channel on the opposite side of the core. PVBT dependence on the treatment fluid injection rate goes

through the minimum, which reflects the optimum injection rate [1, 2].

Standard design of acidizing job heavily relies not only on laboratory experiments, but also on the simulation of treatment fluid impact on transport properties of the rock. Among the parameters to be optimized are the treatment fluid composition, sequence of injected fluids, amount of the fluid to be injected, and the injection rate. These simulations base on geology model of the near wellbore zone of the collector and account for fluid-rock interactions via such effective parameters as PVBT, which have to be determined in core experiments. Unfortunately, the amount of the core material available is usually not sufficient for comprehensive laboratory analysis of various fluids and treatment scenarios. Moreover, the destructive nature of acidizing experiments imposes the fundamental limitation: experiments are performed on different core samples, which makes impossible any direct comparison of different acidizing scenarios. Conventional laboratory acidizing experiments performed using insufficient number of samples are less conclusive, since it is hard to distinguish the effects caused by the changes in the treatment scenario from those related to the variation in sample properties without averaging over a sufficiently large collection of samples. Therefore, a potential added value of simulation-based screening of acidizing scenarios for performance of acidizing technology can hardly be overestimated. Development of numerical models applicable for acidizing optimization have been of high interest during the past decades [3, 4]. According to the recent review [5], most available acidizing models do not provide acceptable accuracy in prediction of the optimum

* Corresponding author: Eivanov7@slb.com

injection rate. One of the possible reasons is that due to the limitations in computational resources, reactive transport models cannot simultaneously account for spatial heterogeneity at different scales: from macro scale, down to the pore scale. Thus, to make predictions on scales interesting from a practical point of view, the well-mixed condition is often assumed at scales smaller than the model discretization size. Similarly, many semi-empirical models assume the existence of dominant wormhole and ignore fine-scale acidizing patterns [3]. Therefore, using those models, one cannot properly reproduce the actual wormhole patterns and hence identify the optimum acid composition and fluid injection rates. We believe that a proper digital acidizing model should be able to reproduce the laboratory results scales, under a wide range of experimental conditions — only then such a model can be considered as a verified one and used at practically interesting scale.

There are definite indications that rock pore structure is a critical factor in carbonate acidizing job design [6, 7, 8]. Dubetz et al. [6] have shown that pore size distribution functions can correlate with optimal acidizing parameters better than porosity or permeability.

In acidizing processes, the transport phenomenon interferes with the chemical reaction. This determines the size and the resolution of a model required — it must capture the pore space geometry before and after the treatment and describe the whole physical sample.

Here, we propose a combined two-scale approach based on detailed digital rock models obtained using X-ray microCT. The pore scale approach used in this work is based on a combination of principles of thermodynamics and density functional theory applied for hydrodynamics (DFH) [9]. This approach allows to estimate the effective reactive and transport properties of the rock directly from the pore geometry and the treatment fluid properties [10] and is not restricted to any specific treatment fluid or mineral. The inhouse simulation software (Direct Hydrodynamics (DHD)) we use for pore-scale simulations, proved to be applicable in many problems of HC recovery from the porous media [11-13].

In our previous work [12], we described implementation of the heterogeneous chemical reactions at pore scale accounting for the evolution of pore geometry during reactive flow. However, accounting for all the fundamentals of treatment process makes the developed algorithm computationally expensive. Therefore, it was applied at small models of porous media sufficient to capture just few connected pore channels.

In the current work the pore-scale simulations were used in assumption of fixed pore geometry just to calculate the transport and reactive properties in each individual sub model, obtained from detailed microCT scan of carbonate rock. Results of numerous calculations were used to correlate the relative active surface and permeability to porosity in order to use these correlations in core-scale modeling.

The continuum model was utilized to simulate the reactive fluid flow using the Darcy equation on core scale. To capture the mineral dissolution process, the closing relations for the effective reaction rate and evolution of

rock transport properties were defined from the direct hydrodynamics modeling at pore scale.

The developed approach allows to effectively account for the core-scale phenomena and the presence of fine pores in low-permeable matrix in the models, which contain high permeable structures like fractures and wormholes. It also allows to upscale the treatment fluid–mineral rock chemical reaction from pore scale to the continuous Darcy-scale modeling.

In this work, we demonstrate an application of the suggested approach on example of Austin chalk core samples treatment with aqueous solution of hydrochloric acid.

This paper is organized as follows. First, the summary of laboratory core tests is presented. Then the microCT scan equipment and digital model construction technique is described, followed by numerical model description. Finally, the results of laboratory tests together with numerical simulations are discussed and followed by conclusions.

2 Experimental setup

While analyzing heterogeneous reservoir rocks, it is important to perform laboratory measurements and microCT imaging on the same core plug. Taking into account the constrains of both techniques the Ø8 mm plug with 10-20mm length looks like an optimal tradeoff between the image quality and the suitability of the sample for the laboratory experiments. We use existing routine core analysis (RCAL) and special core analysis (SCAL) methodology and equipment adapted for the cores of such size [14].

A special configuration of 3-phase core flooding setup was assembled for the test (Fig. 1). For flooding experiments on mini-plugs, we built a Hassler-type core holder with electrodes for electrical properties measurements by two-wire method. In the mini plug flooding experiment, the pressure drop can be measured between inlet and outlet only because of small plug length.

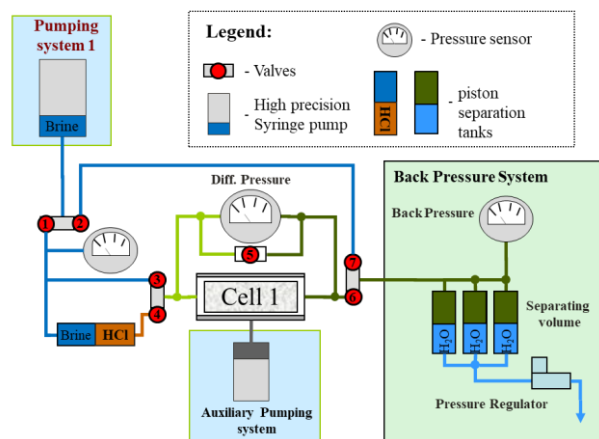


Fig. 1. Hydraulic scheme of coreflooding setup.

The outer part of the core holder is connected to auxiliary pumping system to maintain confining pressure.

Core flooding setup consists of the following main parts (see Fig. 1):

- Main pumping system with two precision syringe pumps for constant pulseless fluid injection with the flow rate range 0.001 to 30 ml/min at pressure up to 40 MPa.
- Separation tank connected through valve 4 to core inlet. Prior to the experiment, it is filled with acid. During the experiment, acid is displaced into the line and comes to the core.
- Inlet fresh line connected through valves 1 and 3 to core inlet. It is used for the initial core flooding, stabilization of the flow and for flash after acid pumping.
- Auxiliary line between valves 2 and 7. It is used to fill up back pressure system before the test.
- Back pressure system to maintain pore pressure at core outlet at constant level in range 1 to 40 MPa.
- Differential pressure measurement system (includes a couple of gauges and safety bypass with valve 5) placed between inlet and outlet of the core holder for precision pressure drop measurements (± 0.0003 MPa) along the studied core.

Multiphase core flooding system was simplified for the acidizing test. It was found that a single pumping system that provides the constant flow rate directly (for brine injection) or through a separation tank (for acid) is much better than two independent pumping systems for injection of brine and acid. At the single pump configuration, one can benefit from pulseless swap of flow from brine to acid and back.

3 Acid flooding experiments on Austin Chalk core samples

For acidizing experiments, we chose well known carbonate outcrop called Austin chalk. This rock is rather homogeneous in terms of mineralogy and void space geometry at least on millimetre to centimetre scale. Gas permeability values of the studied carbonate miniplugs were in range 11.3 to 18.0 mD at porosity 23.2 to 28.6 %.

As a model brine we used 2 %wt solution of NaCl, while solution containing 15 %wt of HCl and 2 %wt of NaCl was used for acidizing.

Before acidizing test, a mini-plug was fully saturated with model brine using vacuum saturator and then loaded into the core holder. Temperature, as well as confining and pore pressures were gradually increased to the target values in a course of one hour. The described series of the experiments was done at ambient temperature ($\sim 27^\circ\text{C}$), 70 bar pore pressure (i.e. back pressure in Fig. 1) and 110 bar confining pressure. Listed pore pressure was chosen to reduce the effect of the evolved CO_2 gas while acidizing.

Experiment was started with measurement of single-phase water permeability (100 % of brine in flow) at different flow rates. After flow stabilization at the required flow rate (i.e. pressure drop along the core became constant), the inlet valves 3 and 4 (Fig. 1) were switched to allow acid flow instead of brine flow.

After injecting the required amount of acid solution, the valves were switched again to injection of brine to flash out and stop the acidizing process. Upon completion

of the experiment and drying the sample, amount of dissolved/removed mineral was calculated based on the sample weight before and after the experiment.

Electrical resistivity of the core was measured by two-point method during all flooding experiments and the measured value was used to estimate the time when the acid front came to the miniplug inlet.

It is extremely important for miniplug acidizing to reduce dead volume of tubes at core inlet, i.e. between outlet of valves 3, 4 and miniplug inlet. Otherwise, mixing of the acid solution and brine leads to the decrease of the acid concentration at the front. This can significantly influence the results of the rock dissolution. In our test we minimized the dead volume to 0.3 ml to guarantee close to a step-function rapid increase of acid concentration at the core inlet.

Mutual analysis of pressure and electrical resistivity data during the experiment allowed to determine the basic parameters of carbonate acidizing process, including the beginning of the wormhole generation and its breakthrough at the opposite end of the sample. When the acid front approaches the core inlet, the electrical resistance begins to decay. In general, the acid injection is stopped as soon as the differential pressure drops to zero, indicating that the core is fully penetrated by high permeable dissolved wormhole. Depending of the flooding test purpose, the acid flow could be stopped early. Early stop of the acid injection gave us opportunity to study using microCT the wormhole structure at different stages of its evolution.

Two carbonate miniplugs (Exp2, Exp3 – target samples) were chosen for laboratory test and for digital model constructions and simulation, while one additional miniplug (Exp1 – trial sample) was prepared from a similar rock sample for preliminary measurements of PVBT and possible adjustment of experiment scenario for the target cores. Parameters of the core samples and experiment scenarios are listed in Table 1.

Table 1. Description of core samples and laboratory tests

	Exp1*	Exp2	Exp3
Core size L / \varnothing mm	17.7 / 7.6	16.7 / 7.7	16.4 / 7.7
Porosity	23.2 %	24.3 %	26.6 %
Permeability	9.1 mD	12.2 mD	15.8 mD
Pore volume	0.187 ml	0.186 ml	0.204 ml
Pre-test measurements		High-res. microCT	
Acid flooding test scenario	1) saturation with brine		
	2) flow stabilization		
	3) injection of 15 % HCl @ 0.4 ml/min		
	until BT reached	0.2ml injected	0.1ml injected
	4) cleanup		
Post-test measurements	Porosity measurement and microCT to determine wormholes structure		

*Trial sample

Standard PVBT measurement implies acid injection until the rapid pressure drop at inlet gauge, which

conforms to corresponding permeability increase. Unfortunately, the acid located within the core and line at that moment dissolves additional mineral during the cleanup stage, resulting in overdeveloped wormholes structure. To minimize this effect, we measured an approximate value of PVBT on the trial sample and adjusted the volumes of acid injected on the target cores.

Electrical resistivity measurement allows to detect acid front approaching the face of core sample, where electrode is placed, and thus eliminates the effect from dead zone of holder before the core. Fig. 2 demonstrates a resistivity decrement after approximately 0.33 to 0.35 ml of acid is injected.

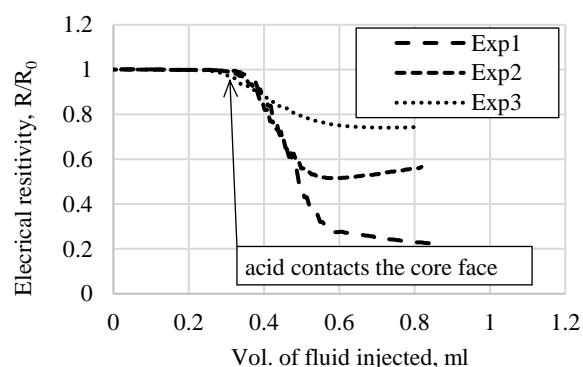


Fig. 2. Electrical resistivity of the cores during fluid injection. The start of resistivity decrease corresponds to the contact of acid front with the core face (shown by callout).

Pressure profiles during acidizing process (difference between inlet and outlet valves) are shown in Fig. 3. The moments the acid front contacted the cores faces are marked to demonstrate the difference between the amount of acid required to breakthrough the core and the total volume of acid injected to the moment. For the trial sample, BT was achieved at 0.58 ml of acid injected, but only ~0.24 ml actually came into the core at that time. Experiments on the target cores were adjusted and only 0.2 and 0.1 ml of acid were injected; sharp pressure leaps at the corresponding moments (see Fig. 3) indicate valves switching. The actual acidizing of target cores took place during the cleanup phase, when brine was injected into core holder. Brine injection lasted for about tens of pore volumes until the core properties became stable.

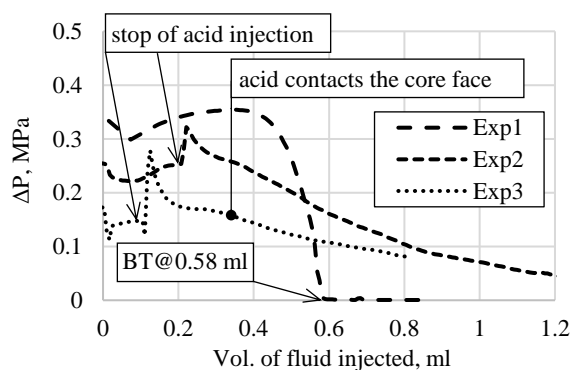


Fig. 3. Differential pressure (between inlet and outlet valves) as measured during acidizing process in all experiments. Acid injection was started at zero and stopped at specific for each core volume (shown by callouts).

The post-acidizing core parameters were measured after full cleanup on dried cores (see Table 2).

Table 2. Core measurements after acid flooding experiments

	Exp1*	Exp2	Exp3
Core size L / Ø mm	17.7 / 7.6	16.7 / 7.7	16.4 / 7.7
PVBT	2.4 ml (1.3 PV)		
Porosity (increment)	31.7 % (+8.5 %)	26 % (+1.7 %)	27.6 % (+1 %)
Permeability (relative incr.)	>10 D ×1000	1.4 D ×115	980 mD ×62

* For the trial sample the values of porosity and permeability don't correspond to the wormhole breakthrough, since the acid injection wasn't stopped at BT, full amount of acid injected was ~3.5PV

4 Core imaging and pore-scale calculations

For all samples 3D images both before and after the acid treatment were obtained using Bruker™ SkyScan™ 1172 microCT scanner with a maximum 10 W tube power and 100 kV tube voltage, at “step and shoot” sample rotation type and 0.1° rotation of sample per step. For the Ø = 7.7 mm, L = 16.4 mm miniplug, we achieved ~2.2 μm voxel size. It means that the whole sample comprises of ~4000×4000×8000 voxels in total. It should be noted that the charge-coupled device (CCD) detector installed in this microCT got 4000×2096 pixels, and the conventional circular scanning trajectory [15] was used – each sample was scanned as a sequence of overlapping vertical segments that were stitched together after the Filtered back projection (FBP) reconstruction. We compensated for gentle slow changes in X-Ray tube brightness and beam hardening artefacts using spatially smoothed histogram matching for large cylindrical regions.

The core flooding process was performed outside of the microCT; thus, the acquired images were not spatially aligned. We used in-house developed software [16] to spatially register the “before acid” and “after acid” images. Spatial registration allows direct voxel-to-voxel image comparison (Fig. 4), as well as comparison of actual and simulated wormhole geometries.

We built binary pore/void models (Fig. 5) for both “before acid” and “after acid” images using a modified image segmentation method, based on indicator kriging [17]. In this work, we assumed that the regions of the sample that were far enough from the wormhole were not affected by the acid. This allowed to automatically optimize the “after acid” image segmentation parameters by minimizing the pixelwise mismatch between both binary images within such a region. The binary models of the wormholes were built based on the difference between

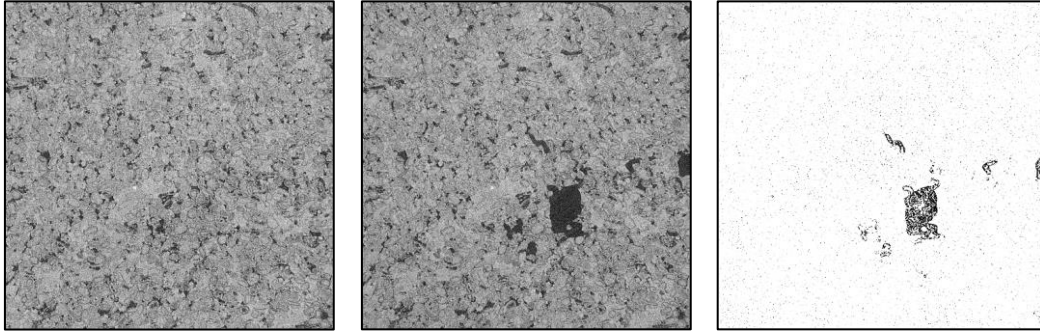


Fig. 4. Fragments of the spatially registered microCT images (from left to right): before acid treatment, after the treatment, and their absolute difference.

spatially registered models of core before and after acidizing experiment (Fig. 4).

Each full-sample model was cropped into a regular grid of 425 non-overlapping 396^3 sub-blocks, which were used to model numerically the rock properties using the in-house developed software for high-resolution digital model analysis based on the principles of DFH [9]. An example of 396^3 block with noticeable changes on its top face is shown in Fig. 5.

The permeability calculation implies obtaining the steady-state solution for velocity distribution within resolved pores with proper (no slip) boundary conditions on the faces of rock cells together with holding fixed overall flow rate through the model. Such calculation requires iterations and may be computationally expensive for big models of large core sample. But, for the needs of the current work, we calculated velocity distribution on cubic models of moderate size (see Fig. 6) to investigate statistics of properties distribution, so permeability calculations were relatively cheap in terms of computational resources and could be processed in parallel. In addition, we calculated porosity and active surface of mineral over the same sub-models, to construct proper correlations in order to utilize them for construction of the core-scale model.

Automatic parameters finetuning improves overall results consistency. Even though for some individual sub-blocks the data obtained looked counterintuitive, e.g., the open porosity decreased after the acid treatment (Fig. 7).

Although this is physically possible, e.g., due to non-dissolvable particles migration, in the current study it is likely that such events should be attributed to image imperfections (e.g., noise). Provided that such effects are inevitable, fairly large statistics are required to mitigate their influence on the final result.

It should be noted that all “before acid” blocks had porosity between 7.5 to 15% (Fig. 8). That is significantly below the lab measurement results (Table 1), which can be associated with large amount of below-resolution porosity. However, the calculated permeability remained within 5 to 50 mD range (Fig. 8), which aligns with the laboratory data fairly well. Thus, we assumed that the larger-pores network, responsible for the most part of the flow rate was resolved well enough for adequate transport modeling. This allowed us to limit ourselves to simple binary models on this stage, avoiding additional higher-resolution scanning, multiscale model construction, and calibration steps [13].

An example of 396^3 block with significantly altered porous structure is shown in Fig. 5 and Fig. 6. The “before acid” permeability of this block is only 8 mD, while the “after acid” permeability is 75 mD. Meanwhile, the resolved porosity changed from 10 % to 13 %, and the open porosity changed from 6 % to 11 %. Note the high-velocity region next to the (local) tip of the wormhole — this was the major flow channel even before the acid treatment, and the local flow rate significantly increased after the treatment.

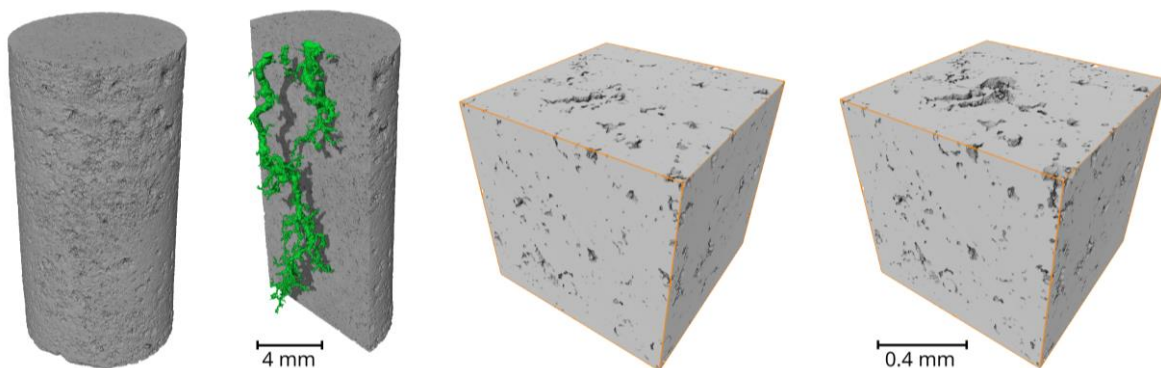


Fig. 5. 3D renders of the binarized microCT images of Exp3 sample (from left to right): full $\sim 4000 \times 4000 \times 8000$ voxel “before acid” state, spatially registered “after acid” state (with wormhole shown in green), example of inner 396^3 voxel cube in “before acid” state, the same cube in “after acid” state.

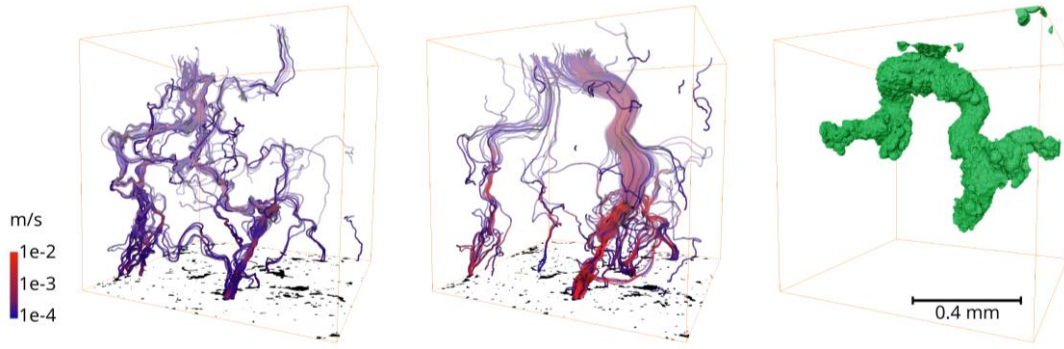


Fig. 6. Streamlines from single phase digital flow simulations on two spatially registered 396^3 voxel binary models, shown in Fig. 5: “before acid” (left) and “after acid” (middle). Semi-transparent part of the flowlines next to the top face of the cube correspond to the flow source. Fluid velocity is color-coded in logarithmic-scale units. The dissolved volume is visualized on the right.

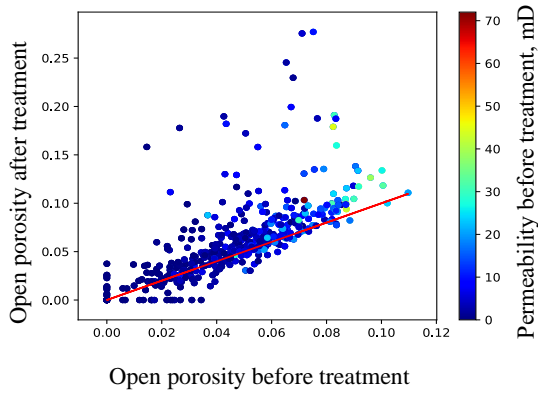


Fig. 7. Crossplot open porosity before and after the acid treatment, with color-coded permeability for individual 396^3 blocks. Note that mostly-dissolved blocks featured higher porosity and permeability even before the acid treatment. Red line is $y = x$.

5 Pore-scale model

Reactive flow modeling is computational resource intensive. Thus, we downscaled full sample $\sim 4000 \times 4000 \times 8000$ voxel binary models to just $\sim 200 \times 200 \times 400$ voxel models, where each voxel encoded local porosity (Fig. 9) (that is, the average of the corresponding $20 \times 20 \times 20$ region of the original image). Instead of binary pore/mineral representation of the core, each voxel in such a model is associated with an initial permeability value in accordance with its intrinsic porosity, based on the porosity-permeability correlation plots obtained on pore-scale models.

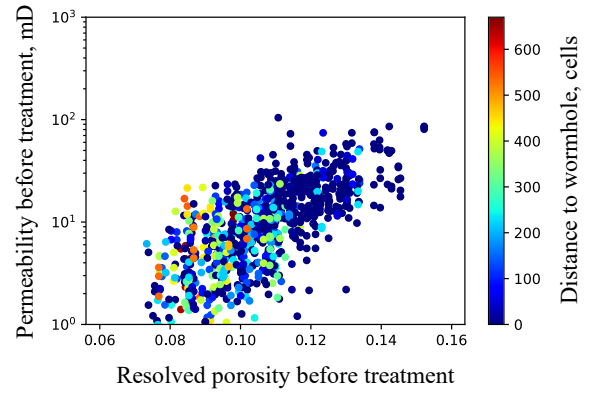


Fig. 8. Permeability vs porosity crossplot, with color-coded distance to wormhole for individual 396^3 blocks. Note that wormhole is generally passes through blocks with high porosity and high permeability.

As it was mentioned above, parameters of the pore-scale model were adjusted to represent spatial inhomogeneity of core properties and its evolution during dissolution process.

Resolved porosity (φ_{res}), as it follows from the results of numerical analysis of core models, constitute only $\sim 1/3$ of total porosity (φ_{tot}) measured. Deficient unresolved porosity (φ_{unres}) was distributed uniformly over the solid mineral; the new total porosity, given by the following equation, should match the value measured in laboratory experiment (see Table. 1):

$$\varphi = \varphi_{res} + (1 - \varphi_{res}) \cdot \varphi_{unres}$$

In actual work, we adopted the correlation proposed by Maheshwari et al. [2]. The properties of porous media were assumed to be linked to the open porosity according to the two-parametric dependence:

$$\frac{K}{K_0} = \left(\frac{\varphi}{\varphi_0}\right)^\gamma \left(\frac{\varphi(1-\varphi_0)}{\varphi_0(1-\varphi)}\right)^{2\beta} \quad (1)$$

$$\frac{r_p}{r_{p0}} = \sqrt{\frac{K\varphi_0}{K_0\varphi}} \quad (2)$$

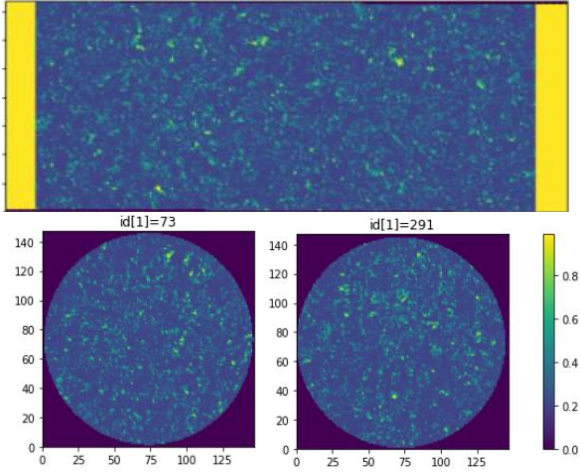


Fig. 9. Downscaled model of Ø8 mm core (Exp3) before acidizing. The porosity (after correction to account for the unresolved pores) distribution is shown by color within longitudinal and cross sections, dark zones are impermeable walls of coreholder, bright yellow are spacers between inlet/outlet sides of coreholder and core faces. Voxel size is 50 μm .

$$\frac{a_v}{a_{v0}} = \frac{\varphi r_{p0}}{\varphi_0 r_p} \quad (3)$$

Here, φ is porosity including unresolved one, K is absolute permeability, r_p is average pore radius, and a_v is active surface area available for heterogeneous reaction per unit volume of porous media. Variables with index 0 denote values with respect to initial (reference) state of the porous media. Exponents β and γ are pore-broadening and pore-connectivity parameters; they are estimated using the properties of the rock. It should be noted that permeability increases infinitely while mineral dissolving, while porosity converges to 1.0 as defined by eq. (1). In order to avoid infinite values in equations, the actual value of permeability should be limited at some reasonable level. In the current work we applied upper limit for permeability at level of the 75-90% of dissolved porosity.

Table 3. Parameters of the pore-scale model described by eqs. (1-3)

	Exp2	Exp3
$\varphi_{unresolved}$	18.3%	20.2%
φ_0^*	27%	
K_0 , mD	19	
a_0 , m^{-1}	$1.8 \cdot 10^4$	
β	2	
γ	1	

6 Core-scale reactive flow model

For core scale modeling we utilized continuous media approach instead of direct hydrodynamics within complex pore space geometry, used for pore scale simulations.

In the current work, reactive flow modeling is formulated in accordance with well-known continuous model of transport in porous media, assuming the local mass velocities to be defined by Darcy law. Our formulation accounts for chemical reactions, which are responsible for the porosity increase due to dissolution of mineral, and changes in the solution composition, due to spent of active component of acid. The reactions are governed by kinetic law defined by reaction rate in dependence on local concentration of acid, relative area of active surface of the mineral in contact with acid, and in general it may vary with flow rate and pore channels structure.

Before providing governing equations, let us specify basic variables used in continuum mechanics to describe instantaneous state of mixture: component molar densities n_i (index i denotes the component number ($i = \text{Mineral, Water, Acid, reaction Product}$)), pressure P , spatial Cartesian coordinates $a = x, y$ or z , and time coordinate t . We considered isothermal processes, so the temperature was assumed to be fixed, and dependence of certain variables on temperature was omitted. We will use the shortened notation $\partial_t B \stackrel{\text{def}}{=} \partial B / \partial t$ for partial derivatives with respect to coordinates and time, as well as the summation over repeated indexes is implied hereinafter (e.g., $\partial_a I_{ia} \stackrel{\text{def}}{=} \frac{\partial}{\partial x} I_{ix} + \frac{\partial}{\partial y} I_{iy} + \frac{\partial}{\partial z} I_{iz}$).

Upscaling from distinguished individual pores to Darcy description implies reformulation of transport properties, reaction kinetics, and mineral dissolution to continuous representation of porous media [18, 19]. In the framework of this approach, the common conservation equations are the following:

$$\partial_t(\varphi n_i) + \partial_a I_{ia} = q_i = \eta_i r_{eff}, \quad (4)$$

$$I_{ia} = n_i U_a + Q_{ia},$$

$$U_a = -\frac{K_{ab}}{\mu} \partial_b P, \quad Q_{ia} = -\varphi D_{i,ab} \partial_b n_i,$$

$$\partial_t \varphi = -\eta_M v_M r_{eff}, \quad (5)$$

where $r_{eff} = r_{eff}(n_i, S_a, u)$ is the rate of the effective chemical reaction of mineral dissolution, which accounts for mixture composition, mineral-acid contact area S_a , and the flow rate u . Here, U_a is the seepage velocity component along the axis a ; $D_{i,ab}$ is the effective diffusion tensor, including dispersion of velocity within porous media; η_M and v_M are stoichiometric coefficient and mineral molar volume, respectively.

In the current work, we used a simplified model of fluid components (pseudo components) and reaction kinetics. First, we assumed the reaction rate to be dependent on a single component (acid) only. Therefore, calculation of the transport equation for the other components could be avoided, since the distribution of reaction products didn't affect the result. Also, the fluid was considered as incompressible; hence, any change of the fluid volume is either due to porosity increase or due to generation of new volume of fluid during reaction. This can be expressed by a source term in continuous equation:

$$\partial_t \varphi + \partial_a U_a = \eta_i v_i r_{eff}, i \in \{W, A, P\}$$

That is solved in form of general elliptic problem on pressure distribution:

$$\frac{1}{\mu} \partial_a (K_{ab} \partial_b P) = -\eta_i v_i r_{eff}, i \in \{M, W, A, P\} \quad (6)$$

The sum $V_r = \eta_i v_i$ could vary depending on the experiment conditions and, moreover, during the dissolution process (if non-ideal solution model is applied), since molar volumes of components are functions of mixture composition.

The certain form of permeability K_{ab} and dispersion $D_{i,ab}$ tensors, as well as the effective reaction rate as a function of rock properties and flow rate serve as the closing relation for eqs. (4)-(6) and should be obtained from experiments and pore-scale modeling.

7 Numerical approach to core-scale reactive flow modeling

Our implementation of the reactive flow in porous media modeling can be divided into two computationally expensive parts: pressure distribution calculation and solution of mass transfer equations with chemical reactions. The problem of pressure determination inside each voxel of the simulation domain can be reduced to the solution of a system of linear equations (6). In the current implementation, we used generalized minimal residual method (GMRES) solver with multigrid preconditioner from NVIDIA AmgX library, which gives an opportunity to utilize GPU accelerators.

We utilized an explicit algorithm for mass transfer calculations. The developed algorithm had first-order approximate precision for space and time steps and was implemented both for parallelized calculations on CPUs or GPUs. CPU realization used Numba library for python and was tested on 48 cores. GPU version utilized a single graphical card for better performance – enabling parallelization on several GPUs allowed to enlarge the grid size, but on the price of calculation speed. The CPU version showed good performance while using up to 12 cores. With larger core count, it became less effective. GPU utilization significantly improved mass transfer calculation performance: modern GPUs showed approximately 9 times speed up compared to 12 CPU cores (see Table 4 and Fig. 10).

Table 4. GPU calculation performance.

GPU	Execution time (ms per call)	GPU memory usage (GB)
Pressure calculation step		
Tesla V100	180	1.065
Tesla P100	260	1.052
Tesla K40	670	0.666
Transport+reaction calculation step		
Tesla V100	0.97	0.125
Tesla P100	1.10	0.125
Tesla K40	3.98	0.125

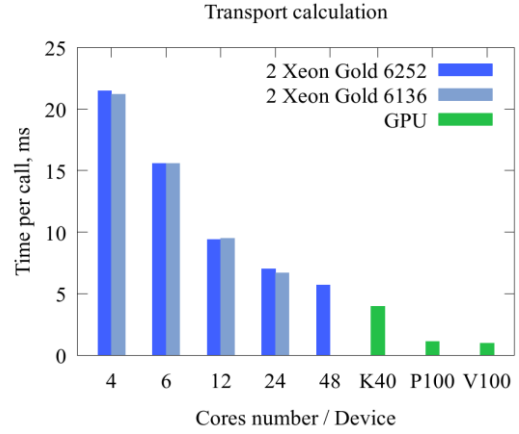


Fig. 10. Time required for transport equations calculation procedure at different CPUs and GPUs.

We performed several tests to determine performance of our code on different hardware. For tests, we used model with $184 \times 75 \times 75$ grid cells. Since pressure calculation is the most computationally expensive part of the algorithm (see Table 4), it was performed once per certain number of simulation steps according to the changes in permeability due to chemical reactions. In the test case, 10000 transport steps were made, and it required 54 pressure updates. This proportion (54:10000) heavily depends on the simulated domain structure and can vary starting from 1:10000 to 1:10 reflecting the wormhole propagation.

According to the tests performed, a GPU version is preferable for better calculation speed, however, the grid size is limited by GPU's memory capacity. For modern P100 and V100 accelerators, it is about $13.8M$ ($\sim 440 \times 176 \times 176$) voxels in a simulation domain. Preferable solution to overcome this limitation is optimization of algorithm for pressure solver to minimize possible performance lost on parallelized GPUs.

8. Acidizing modeling and results analysis

Core-scale digital models of each of the sample cores (see Table 1) were constructed and tuned as described in the previous sections. Results of laboratory tests were used to adjust such parameters as effective reaction rate and diffusion, which are hard to be measured experimentally. Although it is possible to estimate the dependence of the effective reaction rate on active surface area (and indirectly, porosity), acid concentration and fluid injection rate from the digital models, the exact value of the effective reaction rate cannot be defined without additional experiments. Similarly, the construction of acid diffusion/dispersion model, which accounts for heterogeneity of fluid velocity and mixing of fresh acid and reaction product with brine, also requires labor-intensive experiments. Though such highly elaborated approach, which requires a series of laboratory and numerical experiments for parameters tuning is known [20], in the current work, we decided to utilize simplified reaction/diffusion models, taking into account only the mobility of the components and effective

interaction between them at given experimental condition, without considering their chemical nature. This enabled building a practically applicable model that reproduced the experimental result without numerous laboratory experiments; however, its application is limited to certain combination of acid, mineral and experiment conditions. Therefore, the respective models should be adjusted for each study.

Equations for reaction and diffusion applied in the current work are as follows:

$$r_{eff} = k_{eff} S_a n_A \quad (7)$$

$$D_{i,ab} = D_{acid} I_{ab} \quad (8)$$

Where k_{eff} is the heterogeneous reaction rate coefficient, S_a is the active surface area per unit volume of porous media, while n_A is calculated as concentration of acid per unit volume of fluid, D_{acid} is the diffusion coefficient of the effective component of the acid solution, and I_{ab} is the identity matrix.

The simulation parameters (see Table 5) were determined based on the experiment conditions or tuned iteratively for the best match between the simulation results and respective experimental data for treated cores.

Table 5. List of simulation parameters.

Parameter	Unit	Value
brine/acid solution viscosity, μ	mPa*s	0.84
acid component diffusion, D_{acid}	m ² /s	$1.5 \cdot 10^{-9}$
stoichiometric coefficients		
mineral η_M		-1
acid η_A		2
water η_W		-4
reaction products η_P		1
molar volume	m ³ /mole	
mineral v_M		0.06357
acid v_A		0.03064
water v_W		0.018
reaction products v_P		0.1501
heterogeneous reaction rate, k_{eff}	m/s	$4 \cdot 10^{-3}$

In the simulations the moment wormhole break through the core outlet was determined geometrically, unlike to the experimental approach, where PVBT was measured by pressure difference. The connected region(s) of core, where porosity is increased up to the limit (determined in the separate sensitivity study) of 95-99%, was defined as wormhole(s), and the length of such region(s) from the inlet face to its farthest tip was the parameter indicating the wormholed part of the core.

Simulation of the acidizing process on each of digital core models was performed in accordance with experimental workflow. Trial sample was acidized at fixed acid flow rate (0.4 ml/min) and PVBT value was measured and compared with the experimental value. Variations of the reaction rate and acid component diffusion coefficients allow to amend the wormholes structure and resulting PVBT value in a wide range. However, in the current study the values close to the reported in literature [19,21] worked rather well.

After the acidizing model parameters were determined at the cores-scale digital model of the first trial core, experiments on target cores were performed with limitation of injected acid volume in agreement with the laboratory workflow.

As the result for each core model, the PVBT value, final porosity distributions, total amount of dissolved rock, permeability, and wormhole geometry were obtained and compared with the experimental data.

Table 6 summarizes the result of experiments and respective simulations in terms of PVBTs and core after-treatment porosities and permeabilities. The observed systematic deviations between experimental and simulated permeability may be caused by neglecting transition from Darcy to Navier-Stokes flow in big caverns and dissolved wormholes. The correct accounting for viscous effects in open channels would require solution of vector non-linear Navier-Stokes equation in such regions which would result in overconsumption of memory and computational time. The necessary optimizations and improvements are the subject of further research.

Table 6. Simulation results and respective experimental data

	Exp1	Exp2	Exp3
Volume of acid injected	PVBT measure	0.2 ml 1.1 PV	0.1 ml 0.5 PV
Laboratory measurements on treated core			
PVBT	1.3PV		
Porosity		26%	27.6%
Permeability		1.4 D	980 mD
Simulation			
Porosity		25.6%	27.5%
Permeability		1.1 D	760 mD
PVBT at 0.4ml/min		1.1PV	1.34PV

The final wormhole structures obtained for two target cores in simulations and in experiments (build based on microCT interpretation) are shown in Figs. 12 and 13.

Pairwise comparison of wormholes images corresponding to simulations and experiments shows qualitatively similar patterns, however plenty of disturbances in details are also clear. In general, it may be explained by insufficient quality (resolution and noise) of models obtained from microCT and applied for numerical simulation and due to the fact that in numerical simulations we did not account for Navier-Stokes flow in channels. However, it is possible to assume that the major heterogeneous features of rock were properly captured in the digital models, since the trends are reproduced fairly well, and integral characteristics after the acid treatment are close to the ones measured on physical core samples.

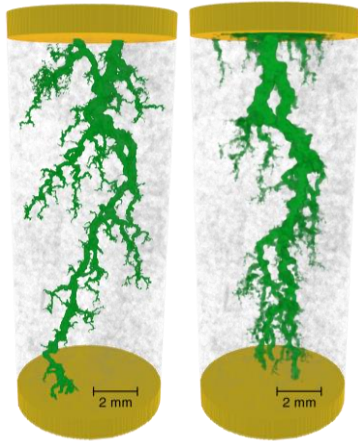


Fig. 12. Wormhole patterns obtained after Exp2 laboratory acidizing experiment (left) and the corresponding digital simulation (right). Yellow zones represent inlet/outlet space.

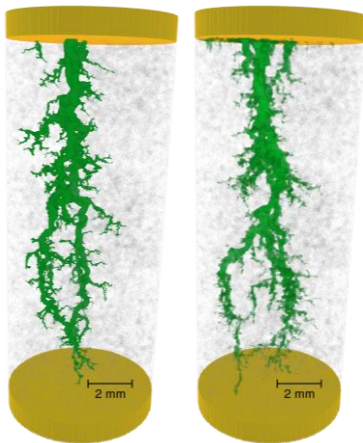


Fig. 13. Wormhole patterns obtained after Exp3 laboratory acidizing experiment (left) and the corresponding digital simulation (right). Yellow zones represent inlet/outlet space.

The simulated streamlines (Fig. 14) within core/wormhole show the flow distribution during the acidizing experiment. As the wormhole propagation approached the end, the maximum velocity speed increased for several orders of magnitude. Because of that, the calculation performance also drastically decreased closer to the end of simulation, due to limitation on the time step of explicit scheme.

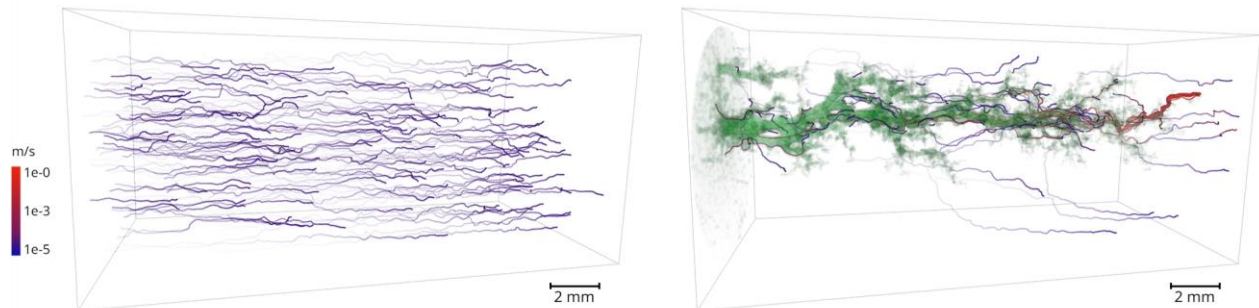


Fig. 14. Simulated streamlines from single-phase core-scale flow modelling (Exp3) with color-coded velocity and semi-transparent simulated wormhole (in green), before the acid treatment (left) and after (right).

Digital experiment allows to repeat simulations at varying fluid injection rates in a wide range from 0.04ml/min to 1ml/min. As the result, the PVBT curves for two cases were obtained (see Fig. 15).

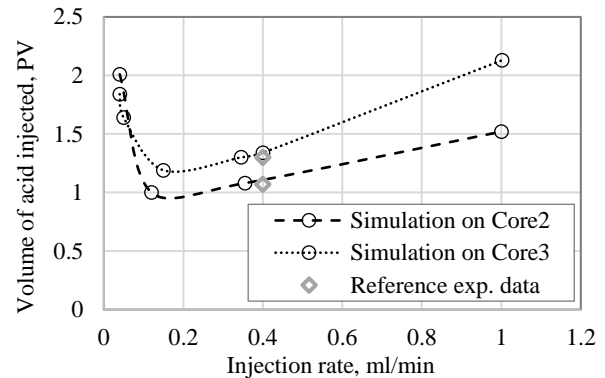


Fig. 15. PVBT curves obtained on digital cores together with reference laboratory data.

Conclusions

In this study, we analyzed carbonate acidization process using the two-scale continuum model. We simulated reactive flow of acid in carbonate rock at Darcy scale, while the accounting for the underlying physics at the pore level was performed through direct pore-scale simulation of transport properties on micromodels of real rocks. To tune rock models and demonstrate predictive capability of the present approach, the PVBT and dissolution patterns were obtained from numerical simulations and compared with experiments on Ø8mm cores of Austin Chalk. Also, PVBT curves in a wide range of injection rates were calculated on the same core models, which would be impossible in the laboratory due to the destructive nature of the experiments. The suggested approach opens the way for improvements in acidizing job design by increasing the consistency between the models used for reactive flow modeling and actual pore-scale structure of the real rocks.

References

- 1 C.N. Fredd, H.S. Fogler, *SPE Formation Damage Control Symposium*, SPE-31074-MS (1996)
- 2 P. Maheshwari, R.R. Ratnakar, N. Kalia, V. Balakotaiah, *Chem. Eng. Science* 90 258–274 (2013)
- 3 G. Glasbergen, N. Kalia, M.S. Talbot, *8th European Formation Damage Conference, Scheveningen*, SPE-121464-MS (2009)
- 4 C.I. Steefel, et al, *Computat Geosci.* 19 (3): 445–478 (2015)
- 5 O.O. Akanni, H.A. Nasr-El-Din, *SPE Middle East Oil & Gas Show and Conference*, SPE-172575-MS (2015)
- 6 D. Dubetz, et al, *SPE Annual Technical Conference and Exhibition*, SPE-181725-MS (2016)
- 7 J. Etten, D. Zhu, A.D. Hill, *EUROPEC SPE-174314-MS* (2015)
- 8 M.E. Ziauddin, E. Bize, *SPE Middle East Oil and Gas Show and Conference*, SPE-104627-MS (2007)
- 9 A. Demianov, O. Dinariev, N. Evseev, *Introduction to The Density Functional Method in Hydrodynamics* (Moscow: Fizmatlit, 2014)
- 10 E. Ivanov, et al., *SPE Russian Petroleum Technology Conference*, SPE-202016-MS (2020)
- 11 A. Demianov, O. Dinariev, N. Evseev, *Can. J. Chem. Eng.* 89 (2): 206–226, (2011)
- 12 A. Beletskaya, et al., *SPE Russian Petroleum Technology Conference*, SPE-187805-RU (2017)
- 13 O. Dinariev, N. Evseev, D. Klemin., *E3S Web Conf.* 146 01001 (2020)
- 14 D. Korobkov, A. Goncharov, *Society of Core Analysts*, SCA2014-081, (2014)
- 15 Andrew M. Kingston, et al., *Proceedings Volume 9967, Developments in X-Ray Tomography X*; 996712 (2016)
- 16 A. Nadeev, “Method For Evaluating Material Sample Structural Changes Resulting From Acting Upon Sample”, WO2016013955
- 17 W. Oh, B. Lindquist, *IEEE Transactions on Pattern Analysis and Machine Intelligence*, Volume: 21, Issue: 7, (1999)
- 18 M.K.R. Panga, M. Ziauddin, V. Balakotaiah, *AIChE Journal* 51 3231–3248 (2005)
- 19 M. Ghommem, et al., *Journal of Petroleum Science and Engineering* 131: 18-33 (2015)
- 20 M. Ghommem, W. Zhao, S. Dyer, *Journal of Modeling and Simulation Vol.5*: 63-71 (2014)
- 21 M. Gautelier, E.H. Oelkers, J. Schott, *Chemical Geology* 157 (1-2): 13–26 (1999)

Advanced core characterisation to improve multiphase flow prediction in heterogeneous sandstone and carbonate rocks

Nele Wenck¹, Samuel Jackson^{2,1}, Ann Muggeridge¹, and Samuel Krevor¹

¹Department of Earth Science and Engineering, Imperial College London, United Kingdom

²CSIRO Energy, Private Bag 10, Clayton South, Victoria 3169, Australia

Abstract Characterisation of multiphase flow properties is crucial in predicting large-scale fluid behaviour in the subsurface, for example CO₂ plume migration at CCS storage sites. One gap in conventional reservoir simulation workflows is the field scale representation of the impact of small-scale capillary heterogeneities. We present an approach to characterising rock samples, which combines core flood experimental data with a numerical optimisation scheme, developed by Jackson et al. (2018). We apply the characterisation effort to a carbonate and two sandstone cores with distinct types and length scales of heterogeneities. The Bentheimer and Bunter sandstones exhibit parallel and perpendicular layering, respectively, whereas the Edwards Brown dolomite is characterised by isotropic, multi centimetre cementation. We use the digital core models to predict the relative permeability of both phases at distinct flow rates. The isotropic heterogeneity in the Edwards Brown dolomite resulted in non-monotonic behaviour as the flow rate was reduced; initially the gas relative permeability increases, and subsequently decreases with approach to the capillary-limit. This work highlights the significant contrast in fluid behaviour between sandstones and carbonates caused by variations in capillary characteristics and underscores the importance of characterising these small-scale heterogeneities for field studies.

1 Introduction

1.1 Introduction to multiphase flow properties

The characterisation of multiphase flow properties is crucial in predicting large-scale fluid flow behaviour, for example for the prediction of plume migration at carbon capture and storage (CCS) injection sites or in field development plans for hydrocarbon production. Subsurface fluid flow is governed by the multiphase Darcy law [1,2]:

$$q_p = \frac{-Kk_{rp}}{\mu_p} (\Delta P_p - \rho_p g) \quad 1$$

where q is the Darcy velocity (m s^{-1}), K is the permeability (m^2), μ is the viscosity (Pa s), P is the pressure (Pa), ρ is the density (kg m^{-3}) and g is gravity acceleration (m s^{-2}). k_{rp} is the relative permeability of phase p and the subscript p refers to the property of a phase. Relative permeability is one of the key parameters controlling fluid behaviour. Historically, flow calculations assumed rocks to be homogeneous, see for example [3]. However, the work from [4] demonstrated that permeability heterogeneity significantly impacts the relative permeability and should thus be incorporated in flow models.

More recently it has become apparent that rocks may be heterogeneous in terms of spatially varying relative permeability and capillary pressure functions. The type and length scale of heterogeneity plays a key role on the observed fluid behaviour [5-7]. For example, layering parallel to flow may result in capillary crossflow, which can be observed as an increase in the phase permeabilities [8].

The ratio of capillary to viscous forces controls the importance of capillary heterogeneity. At the low flow potentials typically encountered in reservoirs, capillary pressure heterogeneity has been shown to significantly alter fluid flow [5-7]. Its importance can be quantified using the capillary number. Throughout this work, we use the definition first proposed by [9] for capillary heterogeneity formed of layers parallel to flow:

$$N_c = \frac{H \Delta P}{L \Delta P_c} \quad 2$$

where H [m] is a length scale associated with the heterogeneity, L [m] is the sample length along the flow axis, ΔP [Pa] is the pressure differential across L , and ΔP_c [Pa] is

* Corresponding author: nele.wenck15@imperial.ac.uk

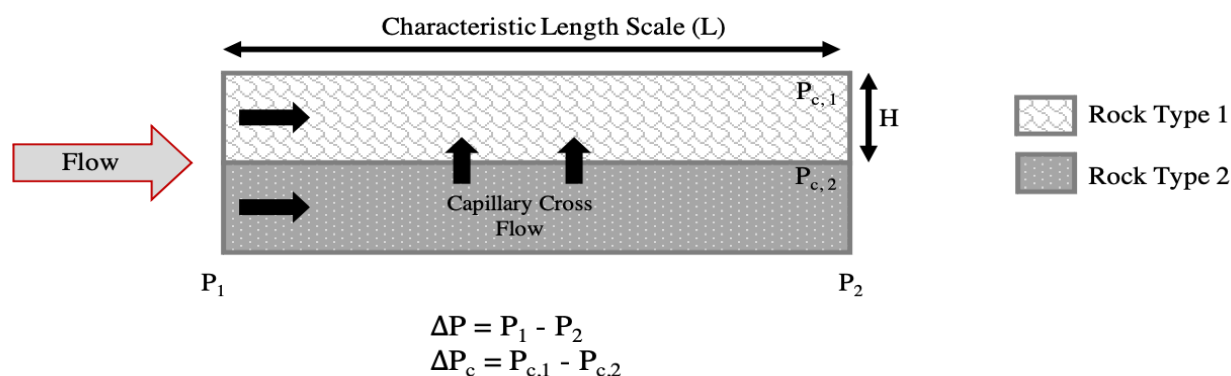


Figure 1: Schematic of layer cross flow arising from capillary heterogeneity in a 2-layer system. The governing parameters from Equation 2 are also depicted.

the contrast in capillary pressure imposed by the heterogeneities (Figure 1).

1.2 Capillary Heterogeneity Characterisation

To model capillary heterogeneity, [10] developed a method, which used capillary pressure and J-function scaling to infer the 3D permeability distribution within a core. The workflow enabled the authors to build a 3D model of the sandstone rock sample, which was verified by comparing experimental and simulation saturation distributions. [11] and [12] built on these results and developed the method further by analysing a wider range of samples. It emerged that gas relative permeability anisotropy was also mainly caused by the presence of capillary heterogeneity within a rock sample.

Even though studies thus far have demonstrated the importance of capillary heterogeneity as one of the dominant fluid distribution mechanisms on a sub-core scale for both brine-oil and brine-gas systems, the established analytical methods used for calculating relative permeability, until recently, failed to incorporate this mechanism. This was the main motivation behind the work of [13]. Two sandstone samples were characterised on a sub-core scale based on the methodology presented in [10]. Thereafter, the authors determined the core-average effective relative permeability using the digital models in a numerical simulation. The work also investigated the factors influencing the rate dependency of relative permeability, which had been observed for many years. They concluded that capillary forces and end effects control this behaviour.

[14] noted that [13] primarily focused on deriving an effective, viscous-limit relative permeability for each sample. This does not describe fluid behaviour at flow rates typically encountered in the subsurface [15]. Instead, fluid flow in these applications is largely in the capillary-limit regime. Hence, the authors proceeded to use the method developed by [13] as a basis to numerically characterise the rock heterogeneity on two samples with differently orientated heterogeneities. Rather than solely deriving the effective relative permeability, the characterisation effort allowed the authors to simulate flow and predict the characteristic relative permeability for a range of capillary numbers (spanning 4 orders of magnitude). Additionally, they removed experimental constraints such as boundary effects.

[16] simultaneously also developed a workflow to characterise heterogeneity in carbonates, but instead, used multi-rate core-flood experiments. The use of multiple rates enabled them to introduce a multi-objective optimization, incorporating both, saturation and pressure. Their goal was to characterise relative drainage capillary pressure curves as well as scaling factors, which quantitatively describe the distribution of heterogeneity within a core. Using three different rock samples, they applied their workflow and presented a close match between simulation and experiment, thereby verifying the method.

1.3 Focus of this study

The aforementioned studies have demonstrated the importance of capillary action as a fluid distribution mechanism. However, the majority of reservoir simulation workflows have thus far failed to incorporate the impact of small-scale heterogeneities on the field scale, leading to incorrect flow predictions, for instance at the Sleipner injection site [17]. This is partly driven by the uncertainty surrounding the characterisation of capillary heterogeneity in reservoir samples and the predicted impact on relative permeability anisotropy. The majority of characterisation studies have focused on well-behaved sandstones. However, reservoirs typically exhibit more complex sedimentary structures.

In this work, we have applied the workflow developed by [14] to three rock samples, two sandstones and one carbonate. The sandstones exhibit distinct planar bedding, one parallel to the axis of flow and one perpendicular to the axis of flow. The carbonate rock is characterised by isotropic heterogeneity - a low-permeable, multi-centimetre, cemented region towards the outlet of the core. Using the methodology, we have produced digital models of the three samples, which incorporate capillary heterogeneity. These models enabled us to predict the relative permeability at a range of flow rates and analyse the varying fluid behaviour in distinct flow regimes.

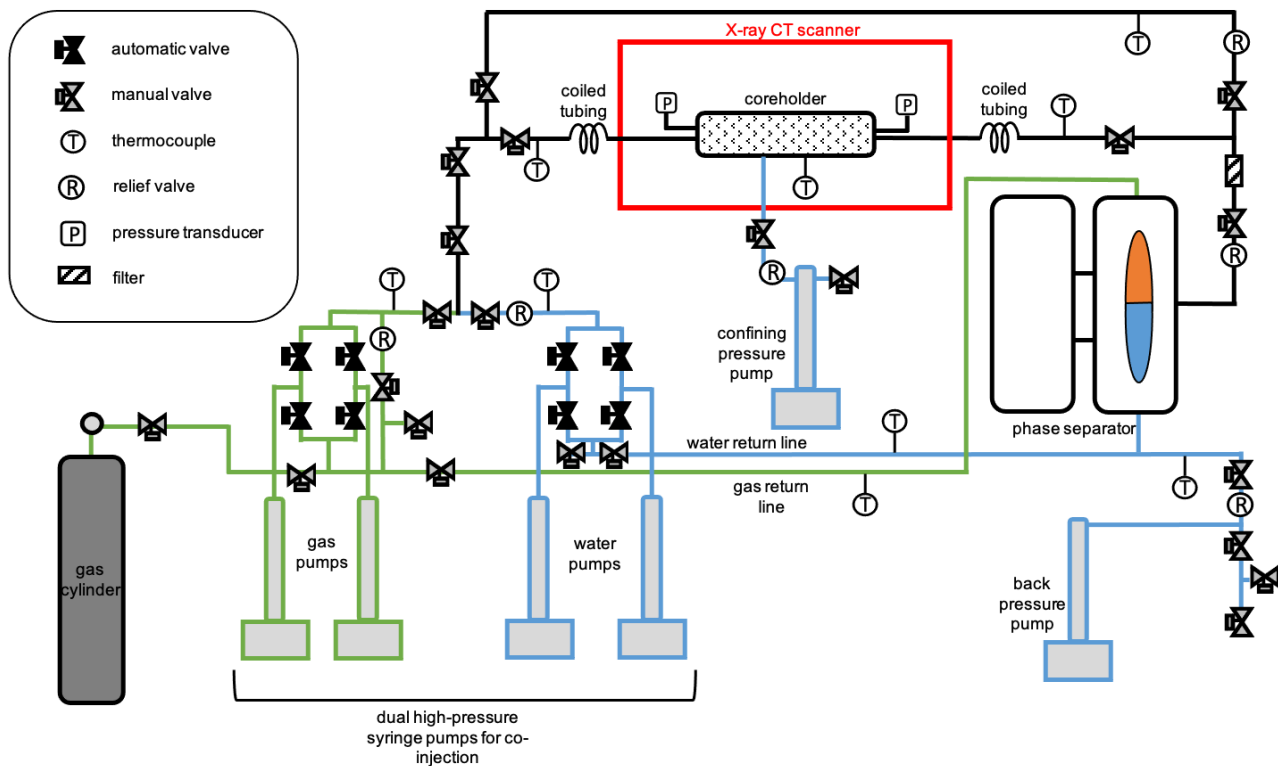


Figure 2: A schematic of the flow loop used for the drainage core flood experiments.

2. Methodology

In this section, we first introduce the rock samples analysed and we then describe the experimental method. This is followed by a detailed description of the numerical modelling, which forms the second part of the rock characterisation workflow.

2.1. Rock types

Three rocks were chosen due to their distinct depositional features and heterogeneities. The Bentheimer sandstone was deposited in a shallow marine environment and is known for its homogeneity [18]. Its composition was mainly quartz (95%), followed by feldspars (4%) and clays (1%) [19]. Our sample was characterised by a single planar bedding parallel to the principal axis of flow.

The Bunter sandstone is a reservoir sample from a previously proposed CCS site in the Southern North Sea. It is a permeable, porous formation [20], thus was evaluated as a potential storage site for the 2008 CASSEM project (CO₂ Aquifer Storage Site Evaluation and Monitoring project) [21]. The sample exhibited a similar composition to the Bentheimer sandstone, with a majority of quartz and some feldspars and clays [22]. However, this sandstone was more porous and heterogeneous than the former, with distinct layers perpendicular to the principal axis of flow.

The Edwards Brown dolomite represented the most heterogeneous rock we studied. It was quarried from the Upper Cretaceous formation in Texas (USA) [23]. The

sample was composed primarily of dolomite and calcite with some quartz [23-24]. The core exhibited isotropic porosity variations with a large ~4cm low-permeable region.

2.2. Core flood experiments

Cylindrical rock samples were plugged with lengths of $\sim 15\text{cm} < L < \sim 20\text{cm}$ and a radius of 1.9cm. Prior to the experiment, the samples were dried in a vacuum. A drainage core-flood was performed on each individual sample in a closed flow loop at constant temperature and pressure. The sample was initially saturated with the wetting fluid (brine or DI water). Chemical equilibrium between the wetting fluid and the rock was ensured by passing several pore volumes of the wetting fluid through the core at high pressure. Thereafter, the core was left saturated for hours. Subsequently, the wetting and non-wetting fluids were co-injected at a constant fractional flow until steady state was reached (stable pressure drop across the core). A medical X-ray CT scanner was then used to image the rock core, thereby measuring the fluid saturations within the sample. The pressure drop across the core was also recorded using pressure transducers. The fractional flow of the non-wetting fluid was increased, and the previous steps were repeated. This continued until the fractional flow of the non-wetting phase reached 1. The fractional flows were chosen to cover a large range of water saturations. The experiment was performed at two flow rates to collect data near the viscous-limit and capillary-limit flow regimes. See Figure 2 for a schematic of the flow loop and Table 1 for a summary of the experimental parameters.

Table 1: Summary of the experimental conditions for the three rock samples.

Experimental Parameters	Bentheimer	Bunter	Edwards Brown
Experimental core length (m)	0.198	0.151	0.148
Experimental core radius (m)	0.019	0.019	0.019
Pressure (MPa)	15.5	13.1	10
Temperature (°C)	50	53	20
Wetting fluid	Deionised Water	Brine	Deionised Water
Non-wetting fluid	Nitrogen	Carbon Dioxide	Nitrogen
Wetting fluid salinity (molkg ⁻¹)	-	1	-
Total flow rate low (mlmin ⁻¹)	7	2	0.5
Total flow rate high (mlmin ⁻¹)	40	20	5
Number of fractional flows high rate	10	8	10
Number of fractional flows low rate	6	6	16

2.3. Core characterisation

Mercury-intrusion porosimetry (MIP) was performed on all the samples to obtain a core-average intrinsic P_c - S_w curve. For the Bentheimer, a sample was taken from the end of the core. For the Bunter and Edwards, sister samples were analysed.

We use a Brooks-Corey model to describe the data, with parameters obtained by minimising the misfit between the MIP data and the model given by Equation 3 [25]:

$$P_c(S_w) = P_e \left(\frac{1 - S_{wirr}}{S_w - S_{wirr}} \right)^{\frac{1}{\lambda}} \quad 3$$

where P_c [Pa] is the capillary pressure as a function of water saturation (S_w [-]), P_e [Pa] is the entry pressure, S_{wirr} [-] is the irreducible water saturation and λ [-] is the pore size distribution factor. A maximum P_c cutoff was applied to the MIP data before fitting. S_{wirr} was determined from the experimental voxel saturations. The values for the parameters from Equation 3 are summarised in Table 2.

The CT images were cropped and coarsened, primarily to reduce the uncertainty in the voxel-scale experimental saturation and speed up the numerical simulations. The amount of coarsening applied to the images was also governed by the REV. It is important to choose a voxel size under which a continuum property has meaning. We verified the REV for porosity by estimating the number of pores present within each voxel using the maximum pore radius obtained from MIP. We recognise that the REV for capillary pressure may be different, however challenging to quantify using the available data. Jackson et al. (2020) and Zahasky et al. (2020) showed that the correlation length scales of capillary pressure and porosity are of a similar order of magnitude. From this, we assumed that capillary pressure is also a valid continuum property at the chosen voxel scale. The image coarsening reduced the standard deviation for the voxel saturation to under 4%. Please refer to [16] for further detail, including a more detailed discussion on REV.

To obtain 3D porosity maps of the rock cores, the CT images were processed using the standard method described in [27]. See Figure 3 for 2D profiles.

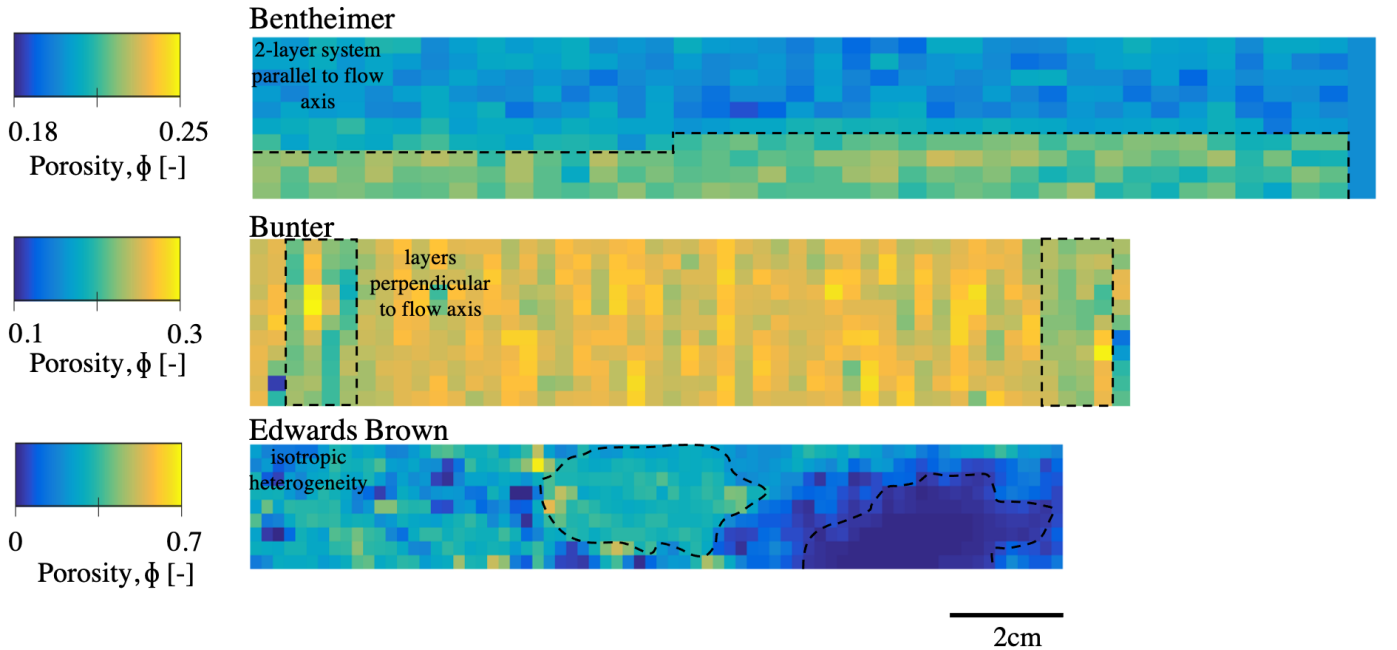


Figure 3: 2D porosity profiles from the central slices for the Bentheimer (top), Bunter (middle) and Edwards Brown (bottom) obtained from the CT images. The key features of each sample are indicated with the black dashed lines. Core dimensions are provided in Table 1.

The core-average pressure drops and saturations recorded at each fractional flow during the high-rate experiment are used to model a viscous-limit, characteristic relative permeability for each sample. This describes the fluid behaviour unaffected by capillary heterogeneity. For the two sandstones, the 1D fluid simulator SENDRA was used to history match the experimental slice average saturation profiles and pressure drops across the core. For the Edwards Brown dolomite, the history match failed to converge to a solution with an acceptable residual error. Hence, Matlab's built-in *fmincon* optimisation tool was used to directly fit the core averaged relative permeability data. In this study, we fitted the relative permeability with the Chierici functional form [28]:

$$k_{rg} = k_{rg}(S_{wirr})e^{-BR_w^m} \quad 4$$

$$k_{rw} = k_{rw}(S_{gc})e^{-AR_w^L} \quad 5$$

$$R_w = \frac{S_w - S_{wirr}}{1 - S_{gc} - S_w} \quad 6$$

where k_{rg} [-] and k_{rw} [-] are the gas and water relative permeabilities, respectively. S_w [-], S_{wirr} [-] and S_{gc} [-] refer to the water saturation, irreducible water saturation and critical gas saturation, respectively. A, B, M and L are the Chierici parameters that control the shape of the curves. The modelling parameters for each sample are summarised in Table 2.

2.4 Characterisation of capillary heterogeneity

To characterise the capillary heterogeneity, we applied the method developed by [14]. The workflow will be briefly described in the following. For further detail, please see [14]. The method is an iterative optimisation scheme, which uses the experimental core flood observations to infer the capillary pressure characteristics within a rock sample. It is an inverse process, which uses the experimental 3D saturation distribution to obtain voxel-scale capillary pressure heterogeneity information. Thus, it was assumed that the capillary heterogeneity can be characterised on a grid block scale. After obtaining an initial guess of the capillary heterogeneity, numerical simulations mimicking the core flood experiment were run to iteratively calibrate the digital model until the residual error reached a certain threshold. Throughout, a mismatch between the simulation and experiment saturations and capillary pressures was assumed to stem from an incorrectly assigned capillary characteristic.

For the initial guess, the capillary pressure within each slice was assumed to be constant and was mapped to the core-average characteristic Brooks-Corey curve obtained in the routine characterisation workflow. A deviation of a voxel-scale saturation from the slice value was assumed to stem from capillary heterogeneity.

Thus, a scaling factor κ was assigned to that voxel, which scales the core-average characteristic curve as the following:

$$P_{c,i}(S_i) = \kappa_i P_{c,avg}(S_i) \quad 7$$

where $P_{c,i}$ is the individual voxel capillary pressure, $P_{c,avg}$ is the average capillary pressure curve, S_i is the experimental voxel saturation and κ_i is the voxel's scaling factor, which represents the capillary heterogeneity. The goal here was to minimise the mismatch between the slice and voxel P_c - S_w values by scaling the capillary pressure curve:

$$\theta = \sum_i^{N_v} \sum_f^{N_f} \sqrt{(K_i P_{c,avg}(S_{if}^{exp}) - P_{c,i}(S_{if}^{exp}))^2} \times \sqrt{(S(K_i P_{c,avg}) - S_{if}^{exp})^2} \quad 8$$

where S_{exp} is the experimental voxel saturation, K_i is the individual voxel scaling parameter, N_v is the total number of voxels, N_f is the total number of fractional flows and $S(K_i P_{c,avg})$ represents the saturation of the average capillary pressure curve after it has been scaled (using the slice-average capillary pressure).

Upon completion, a 3D digital model of the sample can be built with this initial guess of the capillary heterogeneity as well as the 3D porosity distribution and the viscous-limited relative permeability, found previously. This is then used in the CMG IMEX fully implicit simulator to simulate the experiment.

Table 2: Summary of experimental and numerical modelling parameters for the three samples

Parameters	Bentheimer	Bunter	Edwards Brown
Experimental core length (m)	0.198	0.151	0.148
Experimental core radius (m)	0.019	0.019	0.019
Entry pressure Pe (kPa)	3.51	1.62	9.18
Pore distribution, λ [-]	2.3	1.43	0.48
Permeability, K_{abs} (D)	1.86	2.20	0.046
Chierici A/L [-]	3/0.75	3/0.9	15.7/1.06
Chierici B/M [-]	5/0.56	3.75/0.4	2.66/0.54
S_{wirr}/S_{gc} [-]	0.08/0.0	0.08/0.0	0.0/0.0
Core-average porosity, ϕ [-]	0.21	0.25	0.23
Coarsened voxel size, $\Delta x, \Delta y$ (m)	0.0032	0.00277	0.00246
Coarsened voxel size Δz (m)	0.005	0.003	0.002

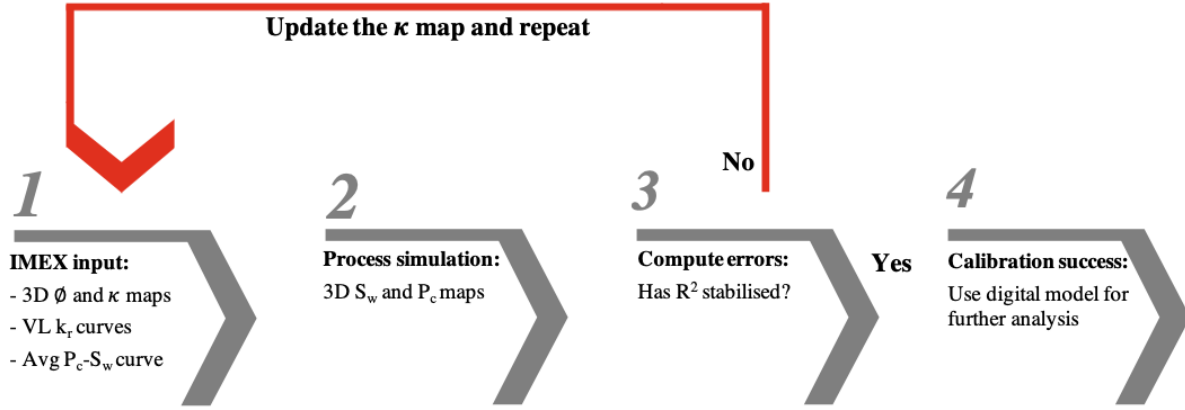


Figure 4: Flow chart summarising the iterative optimisation scheme to characterise the capillary heterogeneity from [14]. VL refers to the viscous limit, high-rate conditions.

A deviation between the experimental and simulation voxel saturations was assumed to stem from an incorrectly assigned κ value. The assumption of constant capillary pressure within each slice was now relaxed. The digital model of the rock core was updated by adjusting the κ values to minimise the following objective function, where S_{if}^{exp} was replaced by S_{if}^{sim} , which represents the voxel-scale simulation saturation:

$$\theta = \sum_i \sum_f \sqrt{(K_i P_{c,avg}(S_{if}^{exp}) - P_{c,if}(S_{if}^{sim}))^2} \times \sqrt{(S(K_i P_{c,avg}) - S_{if}^{exp})^2} \quad 9$$

The optimisation is said to have converged when the error in the voxel saturations, R^2 , has stabilised. See [26] for further details. The calibration scheme is summarised graphically in Figure 4.

3. Results and discussion

3.1 Advanced core characterisation

Using the workflow presented in Section 2, the three rock cores were characterised successfully. The success of the models was determined by comparing the voxel saturations and relative permeabilities from the experiment to a core flood simulation. The simulation used the digital, calibrated model and mimicked the core flood performed in the laboratory. The resultant error then provides an indication whether the rock core was adequately characterised using the calibration scheme. See Figure 5 and Table 3 for the resultant errors.

Table 3: Percentage errors of the core-average saturation and pressure drop recorded in the experiment and the core-flood simulation for the three rock samples.

Gas fractional flow	% Error ΔS_w (-)	% Error ΔP (kPa)
Bentheimer		
0.14	4.29	22.16
0.40	0.14	9.75
0.71	5.28	1.81
0.99	10.50	48.58
Bunter		
0.1	6.52	23.87
0.31	12.33	13.53
0.85	4.93	1.19
1.0	5.44	15.92
Edwards		
0.11	2.17	22.77
0.36	0.32	17.57
0.83	1.83	12.17
1.0	3.64	19.44

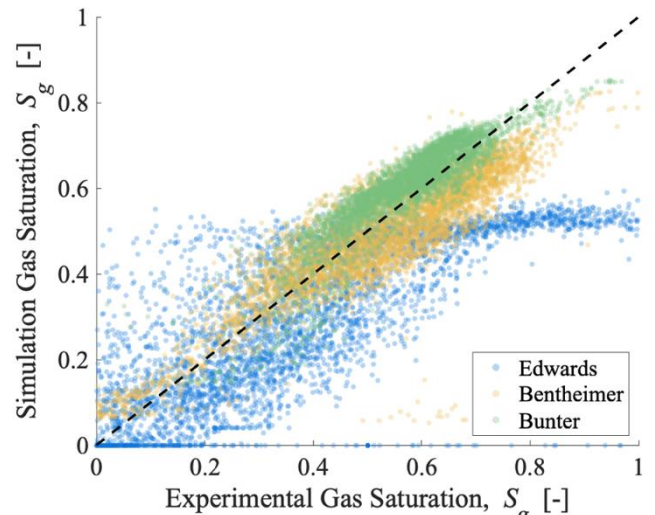


Figure 5: This plot compares the voxel saturation observations from the experiment to the results from the simulation at the final fractional flow. The simulation mimics the core flood experiment using the digital calibrated model. The outliers in the Edwards at high S_g stem from uncertainties in the end effect model in the simulation. These become most prominent at the last fractional flow plotted here.

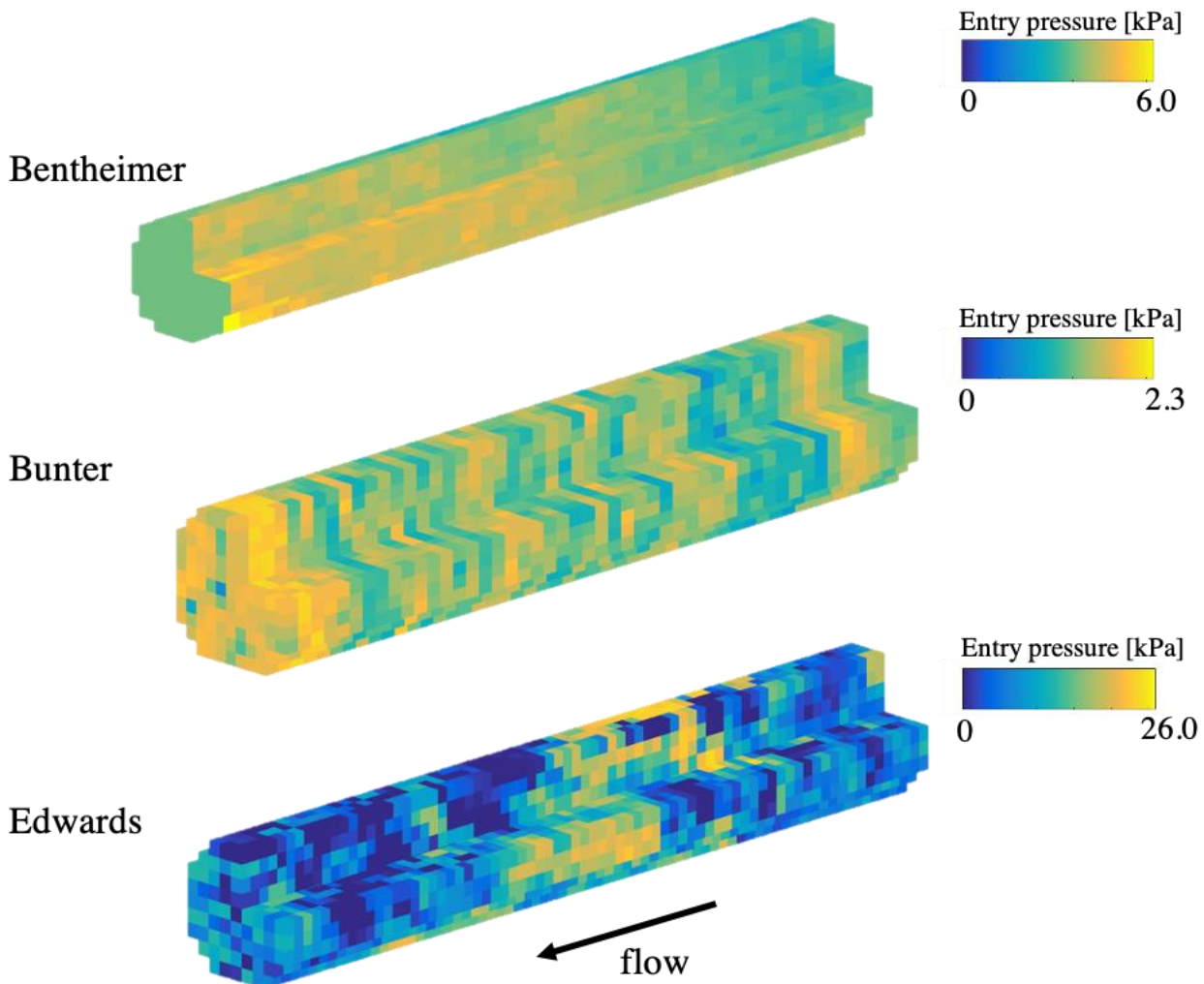


Figure 6: 3D entry pressure maps for the three samples obtained from the workflow described in Section 2.

Pore entry pressure distributions from the final, calibrated models are plotted in Figure 6. As shown, the Edwards Brown has the largest range of entry pressures, followed by the Bentheimer with the Bunter last. The homogeneity of each of the layers in the Bentheimer is clearly visible: each of the two layers displays a relatively uniform entry pressure of 4kPa and 5kPa, respectively. In comparison to this, the perpendicular bedding observed in the porosity map of the Bunter is clearly visible. The entry pressures cluster into distinct layers of low (1kPa) and high (2kPa) regions. Overall, this sandstone sample appears significantly more heterogeneous than the Bentheimer sandstone. Lastly, the Edwards Brown displays the most severe heterogeneity with regions reaching nearly 26kPa. Pressures can be clustered into large vug-shaped regions as was sketched on the 2D porosity profile. The core characterisation workflow has thus allowed us to characterise the spatial distribution of capillary heterogeneity.

3.2 Fluid dynamics

To investigate, in more detail, the varying flow dynamics caused by capillary heterogeneity within each sample, we used the digital models from Section 3.1 to run core flood simulations at varying flow rate. The core-average pressure drops and saturations were used to determine the relative permeability at each rate using Darcy's law, Figure 7. 3D saturation maps were plotted for two of the samples to further illustrate the value these digital models add to our understanding of flow dynamics in heterogeneous rocks (Figures 8 and 9).

From Figure 8 it can be seen that the parallel layering in the Bentheimer sample resulted in capillary cross-flow in the low rate case, enhancing gas flow. After invading the sample, the gas preferentially flows laterally first into the low P_c region, and only then migrates towards the outlet. This resulted in a raised gas relative permeability at high water saturations ($S_w > 0.6$) compared to the viscous-limit curve as the flow rate was lowered, whereas the water relative permeability was reduced (Figure 7, top). At lower water saturations, the end effect is artificially lowering the relative

permeability, see [14] for a detailed discussion. The high-rate simulation results in a homogeneous saturation distribution and thus a lower gas relative permeability.

In comparison to the Bentheimer, the distinct bedding perpendicular to the axis of flow in the Bunter sample hindered fluids from migrating efficiently through the sample. This is observed as a significant reduction of both phase permeabilities with decreasing flow rate (Figure 6, centre).

The Edwards Brown, characterised by isotropic heterogeneity, displays non-monotonic behaviour with increasing rate (Figure 7, bottom). Initially, the relative permeabilities increased with increasing flowrate, after which they decreased again, in agreement with the analytical work by [9]. Referring to the 3D saturation maps from a low-rate simulation (0.5mlmin^{-1}) and a high-rate simulation (100mlmin^{-1}) shown in Figure 9, it emerges that the isotropic heterogeneity leads to the formation of connected pathway flow, where the gas forms a channel through the low P_c regions in the sample. This results in an increased gas permeability. In contrast to this, the high-rate core flood resulted in a very uniform saturation map, which translates to a lower permeability.

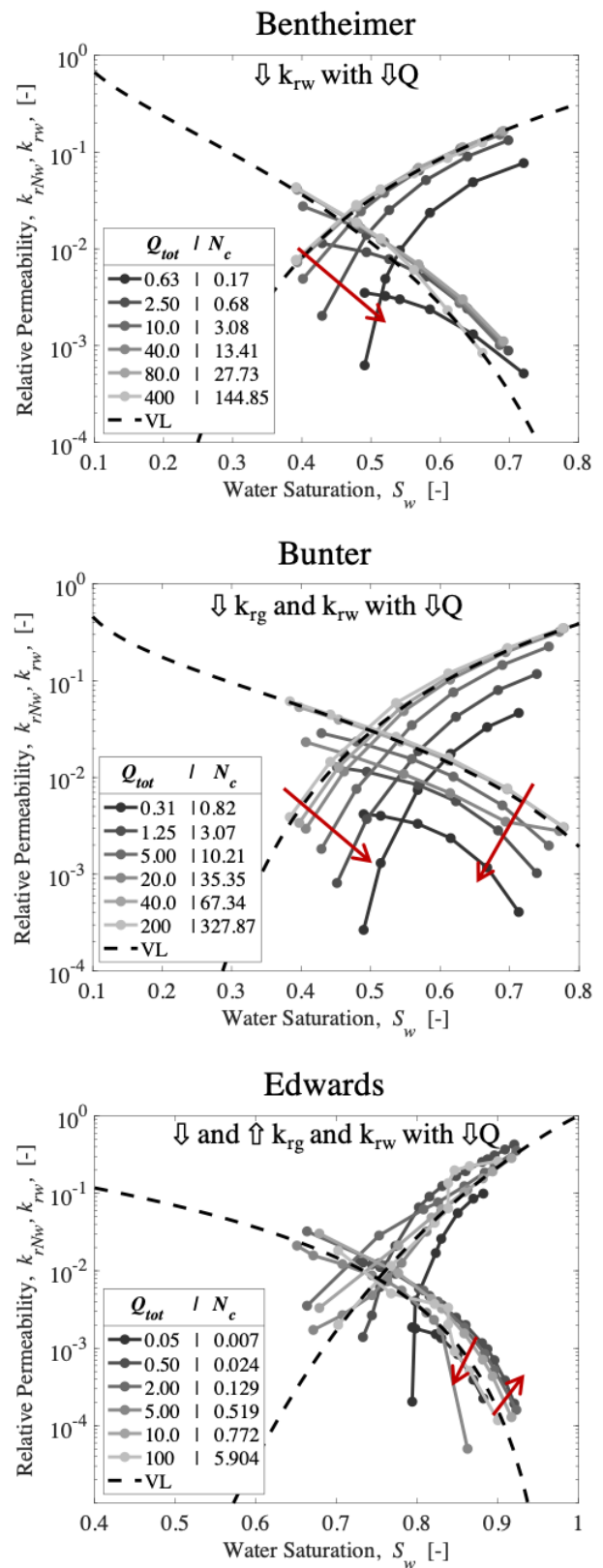


Figure 7: Predicted drainage relative permeabilities at a range of flow rates obtained using the digital models from Figure 6.

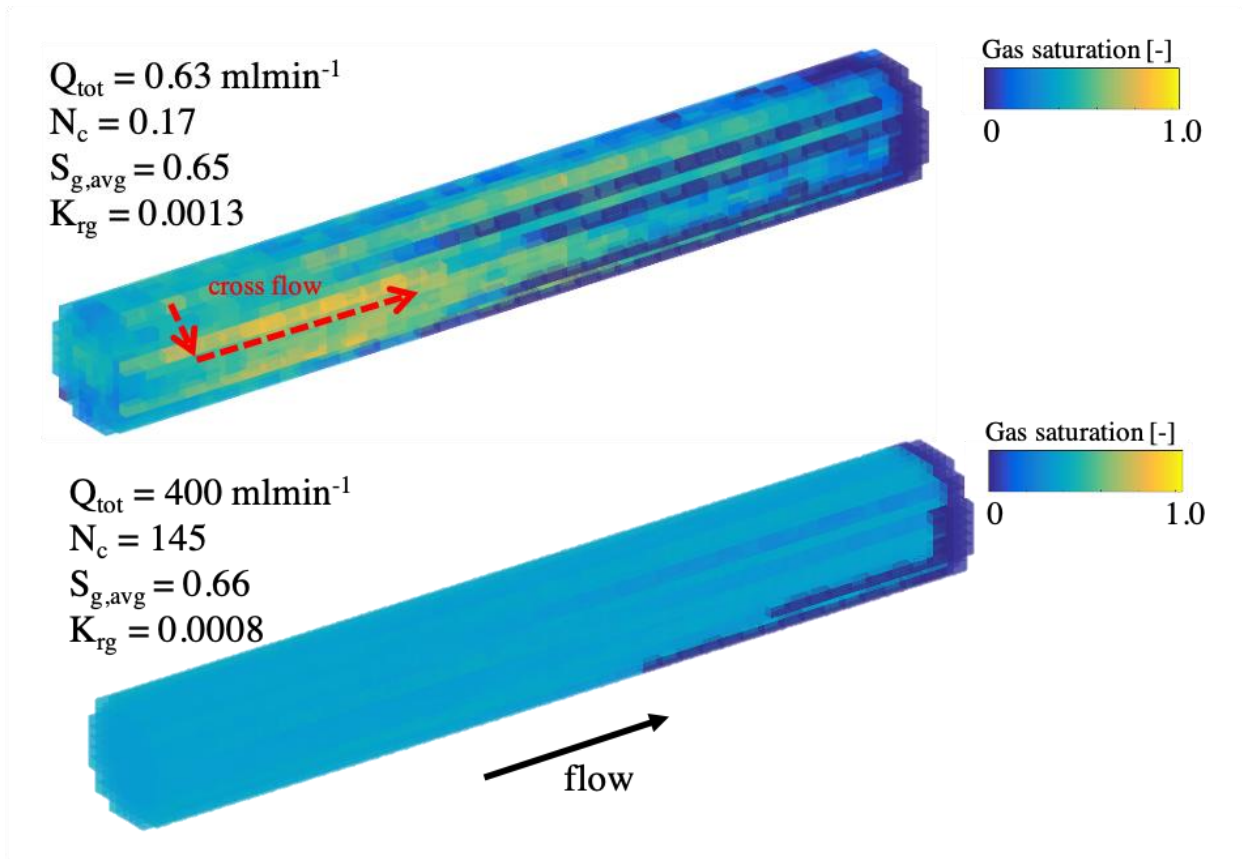


Figure 8: 3D saturation map of the Bentheimer at two distinct simulated flow rates.

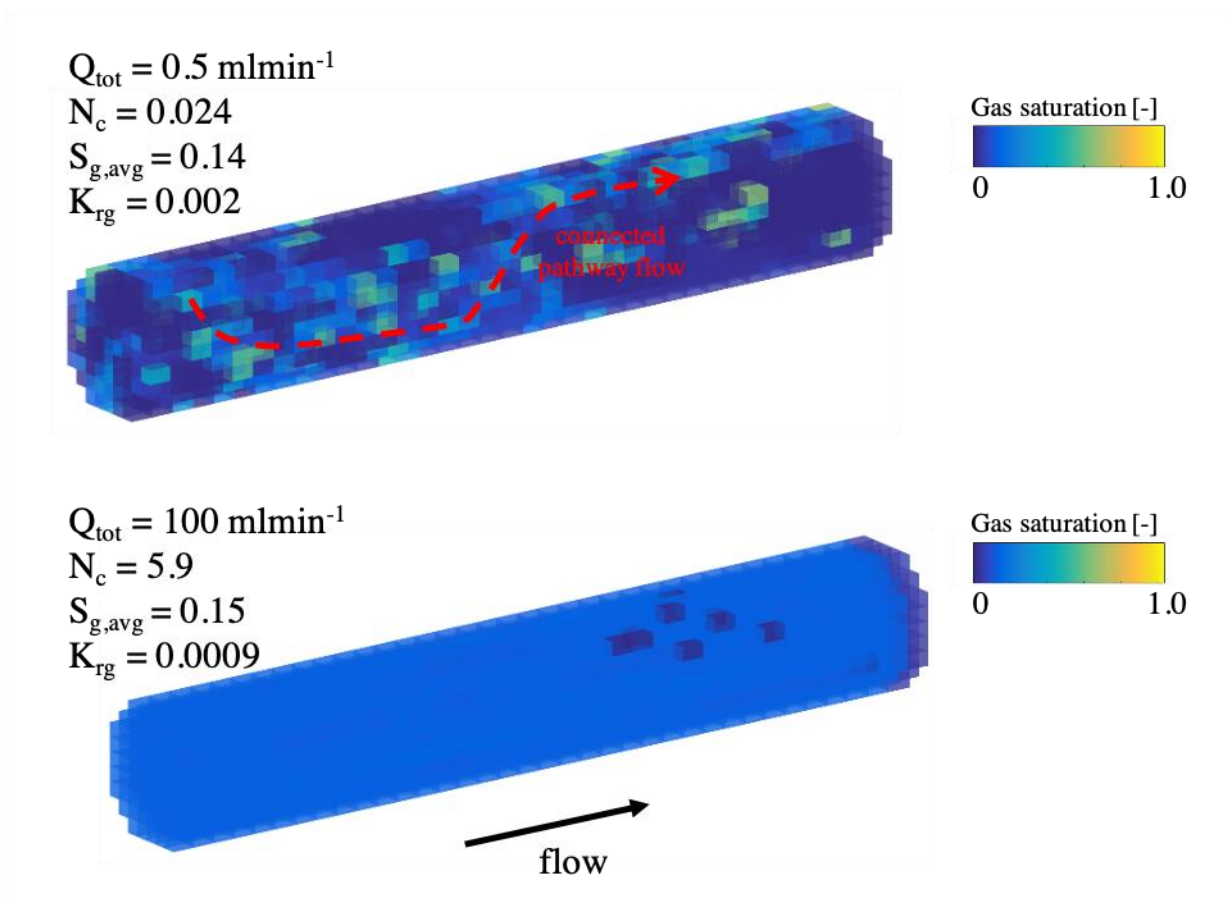


Figure 9: 3D saturation map of the Edwards Brown at two distinct simulated flow rates.

4. Conclusion

We have presented an advanced core characterisation workflow that combines observations from core flood experiments with an iterative numerical optimisation scheme developed by [14]. Three rock samples were selected for this study, two sandstones and one carbonate, with a range of heterogeneity types and length scales. This work represents the first step in an upscaling procedure, whereby the digital models can be used to infer the upscaled impact of capillary heterogeneity at the field scale, as demonstrated in [30].

Drainage core flood experiments were performed on each of the samples [22-23, 29]. A medical X-ray CT scanner was used to image the core saturation and the core-average pressure drops were recorded with pressure transducers. The experiments were performed at two distinct flow rates to obtain multiphase flow parameters in the capillary and viscous flow regimes. After routinely characterising the samples, the experimental core data was used in combination with the optimisation scheme. This was essentially a history match of the core flood experiment, with the voxel-scale saturation distribution as a matching target and the voxel-scale capillary pressure heterogeneity as a fitting parameter. Through this, a 3D digital model of each sample was built incorporating spatial variability in porosity and capillary pressure. The 3D models illustrated the contrasting entry pressure distributions in each sample. The Bentheimer and Bunter sandstones exhibited parallel and perpendicular layering, respectively. The entry pressures in the Edwards Brown were isotropically distributed and could be clustered into large vug-like regions.

Using the digital models, core flood simulations were run at a range of flow rates to investigate the varying flow dynamics in each of the samples. Strong rate dependency of relative permeability was observed in all samples. The parallel layering in the Bentheimer allowed for the phases to cross flow between the layers, which raised the gas relative permeability. In contrast, the Bunter sandstone, with layers orientated perpendicular to the axis of flow, inhibits the flow of both phases, thus the relative permeabilities decreased in the capillary flow regime. Lastly, the Edwards Brown with isotropic heterogeneity exhibited non-monotonic behaviour, where the relative permeability did not display a clear relationship with flowrate. The results illustrate the importance of incorporating rock heterogeneity into flow simulations and the value added from producing these digital models.

5. References

- 1 M. Muskat, M. Meres, *Phys.*, **7**, 9 (1936)
- 2 M. Muskat, R. Wyckoff, H. Botset, M. Meres, *AIME*, **123**, 1 (1937)
- 3 H. Welge, *J. Pet. Technol.*, **4**, 4 (1952)
- 4 A. Corey, C. Rathjens, *J. Pet. Technol.*, **8**, 12 (1956)
- 5 T. Kortekaas, *Soc. Pet. Eng. J.*, **25**, 6 (1985)
- 6 A. Hove, V. Nilsen, *SPE Reserv. Eng.*, **5**, 4 (1990)
- 7 R. Dawe, M. Wheat, M. Bidner, *Transp. in Porous Media*, **7**, 1 (1992)
- 8 Y. Debbabi, M. Jackson, G. Hampson, P. Salinas, *Transp. in Porous Media*, **124**, 1 (2018)
- 9 G. Virnovsky, H. Friis, A. Lohne, *Transp. in Porous Media*, **54**, 2 (2004)
- 10 M. Krause, J. Perrin, M. Benson, (2011), *SPE J.*, **16**, 4 (2011)
- 11 M. Krause, *SPE Annu. Tech. Conf.* (2012)
- 12 M. Krause, S. Krevor, S. Benson, *Transp. in Porous Media*, **98**, 3 (2013)
- 13 M. Krause, S. Benson, *Adv. Water Resour.*, **83**, (2015)
- 14 S. Jackson, S. Agada, C. Reynolds, S. Krevor, *Water Resour. Res.*, **54**, 4 (2018)
- 15 P. Ringrose, K. Sorbie, P. Corbett, J. Jensen, *J. Pet. Sci. Eng.*, **9**, 2 (1993)
- 16 S. Hosseinzadeh Hejazi, S. Shah, R. Pini, *Chem. Eng. Sci.*, **200**, (2019)
- 17 J. Cavanagh, J., B. Nazarian, *Energy Procedia*, **63**, (2014)
- 18 A. Peksa, K. Wolf, P. Zitha, *Mar. Pet. Geol.*, **67** (2015)
- 19 M. Andrew, B. Bijeljic, M. Blunt, *Int. J. Greenh. Gas Control*, **22** (2014)
- 20 M. Stephenson, *Elsevier*. (2018)
- 21 M. Smith, D. Campbell, E. Mackay, D. Polson, *SCCS*, (2012)
- 22 C. Reynolds, M. Blunt, S. Krevor, *Water Resour. Res.*, **54**, 2 (2018)
- 23 S. Manoorkaar, S. Jackson, S. Krevor, *Water Resour. Res.*, **57**, 4 (2021)
- 24 P. Lai, K. Moulton, S. Krevor, *Chem. Geol.*, **411**, (2015)
- 25 R. Brooks, A. Corey, *Colorado State University: Hydrology Papers*, **3**, 1 (1964)
- 26 N. Wenck, S. Jackson, A. Muggeridge, S. Krevor, *Water Resour. Res.*, (In review)
- 27 E. Withjack, *SPE Form. Evaluation*, **3**, 4 (1988)
- 28 G. Chierici, *SPE J.*, **24**, (1984)
- 29 C. Reynolds, S. Krevor, *Water Resour. Res.*, **51**, 12 (2015)
- 30 S. Jackson, S. Krevor, *Geophys. Res. Letters*, **47**, 18 (2020)

3D Multiclass Digital Core Models via microCT, SEM-EDS and Deep Learning

Igor Varfolomeev^{1*}, Vladimir Svinin^{1,2}, and Ivan Yakimchuk¹

¹Schlumberger Moscow Research, Reservoir Potential Department, 125171 Moscow, Russia

²NRNU MEPhI, ICIS, 115409 Moscow, Russia

Abstract. We describe an integrated methodology for constructing a 3D multiclass model of a rock sample, based on X-ray microtomography (microCT) and quantitative evaluation of minerals (QEMSCAN) by automated SEM-EDS (Scanning Electron Microscopy, Energy Dispersive Spectroscopy). We focus on building an automated operator-independent workflow, allowing to distinguish between voxels featuring substantially different physical properties, such as void, quartz, denser and less dense clay aggregates. The workflow is demonstrated using a set of five $\varnothing 8$ mm Berea sandstone miniplugs. For each miniplug, a $\sim 4000^3$ voxel microCT image is acquired. Next, each miniplug is cut into smaller pieces, and the 45 resulting polished surfaces are subjected to the QEMSCAN analysis, producing $\sim 4000^2$ pixel mineral maps. Each mineral map is automatically spatially registered with the corresponding microCT image using an in-house surface-based algorithm. Further, the ground truth images for the supervised multiclass segmentation are constructed from the mineral maps. We compare 3D and 2D convolutional neural network (CNN) architectures with the baseline Naïve Bayes classifier, which is roughly equivalent to the approaches commonly used in practice today. We find that supervised CNN-based segmentation is fairly stable, despite microCT image quality non-uniformness and achieves higher quality scores compared to feature based and baseline approaches.

1 Introduction

Nowadays, the Digital Rock approach is a well-known technique for core analysis. Generally, it consists of numerical simulation of physical phenomena on a digital representation of a core sample.

Centimetre-scale Digital Rock models are usually created via X-ray microtomography (microCT) imaging and subsequent image segmentation. Binary solid/void segmentation using methods like Indicator Kriging [1] and Active Contours [2] is still most commonly used in practice. Such models proved to be suitable for estimating single-phase and multi-phase permeabilities of some rock samples, like Berea sandstone [3], where spatial resolution of the modern microCT scanners easily allows to resolve the pore throats. One major drawback, associated with these segmentation methods is the significant operator involvement; the operator's choices might greatly influence the ultimate result, and it might be not clear which segmentation parameters are more appropriate. Due to the nature of the hydrodynamics, the required parameter selection precision increases dramatically as the pore throat sizes get closer to the microCT resolution limit. Another drawback is that the substances featuring sub-resolution porosity could not be appropriately represented in such models. This might limit the ability to model, for example, clayey sandstones

or carbonates. Both difficulties could be handled through the use of multiclass operator independent segmentation process and a suitable physical properties simulator.

Modern sophisticated simulation techniques allow to take into account a sizeable set of physicochemical properties (e.g., mineralogy, sub-resolution porosity, wettability) with respect to their volumetric spatial distributions [4,5]. In this paper, we focus on the segmentation part.

2 Related works

One of the first works, discussing the possibility of combining SEM and microCT images is [6,7]. The authors acquired microCT and QEMSCAN images of a sandstone sample, and spatially registered them. However, the segmentation technique, described by the authors is limited to a direct correlation between the microCT grayscale values and mineral types. Although such approach allows to distinguish minerals with significantly different X-ray effective linear attenuation coefficients, like quartz and pyrite, it is usually unreliable in most practical cases, like when distinguishing quartz and dense kaolinite. The contrast between different practically important minerals tends to be low on regular microCT systems, equipped with ~ 100 kV X-Ray tubes,

* Corresponding author: ivarfolomeev@slb.com

although it could be significantly higher on monochromatic lower-kV synchrotron-based systems.

2.1 Extracting features

Some works highlight the possibility to use additional features instead of just the grayscale value for CT image segmentation, for example, image gradients in [8]. The operator selects an area, attributed to a specific class on a 2D intensity-gradient histogram, which improves segmentation quality, compared to grayscale-only methods.

It is natural to assume that the segmentation quality could be further improved by increasing the number of the features (e.g. local average, median, variance, ...) taken into account. However, as the number of features grows, it becomes problematic to manually select ranges, attributed to specific classes. Thus, instead, operator directly specifies a set of voxels, attributed to each specific class, and the machine learning (ML) supervised segmentation task arises. The [9] was one of the first works to utilize the Fiji Trainable Weka Segmentation tool [10] for the microCT image segmentation task. The authors demonstrate that this approach allows better particle separation than the traditional, grayscale-based binary segmentation.

Nowadays, multiple software packages, similar to the Fiji Trainable Weka Segmentation are available, namely ilastik [11] and Zeiss Zen IntellesisTM[12]. However, they share the same basic idea — using manual brush strokes as a training set for a ML classifier. Each tool provides a different set of feature extraction filters. Their common drawback is increased memory requirements due to in-memory architecture. Two more tools to mention are Thermo ScientificTM Amira-AvizoTM (including the XImage PAQ plugin) and ORSTM DragonflyTM, which also provide the ability to train pre-configured CNN models.

2.2 Training data

Some authors use semi-automatic segmentation results to train their ML models. In [13] authors train 2D SegNet CNN [14] using a set of 20 images, 256×256 each. The classes they consider are mostly easily distinguishable by their grayscale values, except a single phase, that got its own distinct microstructure. In [15] authors also use a “mainly grayscale-based” method to create a training set for their CNN, even though they do have two QEMSCAN images of the same sample. The motivation for such a decision is that those two slices do not provide a large enough training set. Some image registration difficulties are also mentioned. The CNN is able to almost perfectly reproduce that ground truth labeling, achieving ~99% accuracy. However, it is not entirely correct to directly compare this score with the score achieved with an independent ground-truth data (such as QEMSCAN-based).

Considerable efforts were spent on inventing a better ground truth segmentation, suitable for training ML models. Some works, discussing microCT image

segmentation use an “image degradation” approach to create a ground truth segmentation and the “image to be segmented” from a single source. In [12] an already segmented volume is forward-projected into the projection domain, then shadow projections are blurred, and Gaussian noise is added to them; and finally a new volumetric image is reconstructed from these shadow projections. According to the authors, this emulates the real noise generating processes, taking place in a microCT device. However, it should be mentioned that this simple model does not take many other possible imperfections of the real microCT device into account. In [16] the ground truth segmentation is produced from real full-quality X-ray projections, while the “image to be segmented” is produced from the decimated or downsampled subset of the same projections — this emulates faster microCT acquisition.

Although such approaches are well-suited for development purposes, we believe that the usage of a naturally higher-resolution SEM data represents a more promising approach.

In [17] authors use SEM-EDS to create a mineral map of the edge of a rock sample cylinder. This might not be the best option, because microCT images typically feature significant artefacts next to the outer edges of the sample being scanned, especially flat edges. In [18] both sample cylinder edge and a flat cut surface are scanned before the microCT, which might produce similar issues. The authors of the [19,20] also perform SEM-EDS on the top part of the cylindrical sample after the microCT measurement. They mention the imperfectness of the result, even after the histogram matching [19]. The authors utilize 2D SURF-based image registration [20] and also mention the imperfectness of the result, even though their sample contains large distinctive features. They conclude [19] that the feature based ML segmentation was unable to improve the quality, as compared to the grayscale-based segmentation. This result is also partially associated with the classes in question — all 3 classes being considered are easily distinguishable by their grayscale level.

In [21] authors use spatially registered QEMSCAN images of internal miniplug cross-sections to construct the ground truth labelling. They mainly focus on a feature-based segmentation of a coarse-grained sandstone via per-grain classification. Indeed, for larger, easily separable (using a watershed transform) and fairly uniform grains, this provides an ability to accumulate a massive amount of statistics that characterizes each grain. The non-zero threshold rotation-invariant Local Binary Patterns (LBP) [22] feature extraction technique was recognized as one of the most robust, allowing to distinguish even such a similar minerals, like quartz and albite. The demonstrated proof-of-concept per-pixel feature-based segmentation result considers 5 classes, and the whole experiment uses a single QEMSCAN image.

3 Imaging

3.1 X-ray microCT imaging

We use Bruker™ SkyScan™ 1172 cone-beam microCT scanner to obtain images of the five similar $\varnothing 8$ mm Berea sandstone miniplugs with ~ 2.2 μm voxel size, using 100 kV tube voltage and the maximum available 10 W tube power. Each sample is also ~ 8 mm high, which results in $\sim 4000^3$ voxel microCT image. It must be noted that the CCD detector being used got 4000×2096 pixels, and the conventional circular trajectory is used. Thus, the sample is scanned as two independent vertical segments, that are later stitched together by the scanner's image reconstruction software. We would later discuss how this affects the segmentation quality.

3.2 Sample slicing

After the acquisition of the microCT images, we use a precision diamond saw to cut each sample into smaller blocks and embed them into epoxy resin. Each block undergoes standard SEM-EDS sample preparation procedures, namely polishing and carbon deposition. The resulting geometry is illustrated in Fig. 1. Each cutting plain is roughly orthogonal to the plug cylinder axis, but up to 5° errors are possible, due to overall mechanical tolerances. We avoid using original outer miniplug edges for the SEM-EDS mapping, not only because these areas are associated with significant artifacts, but also because we would like to use 3D CNN receptive field later.

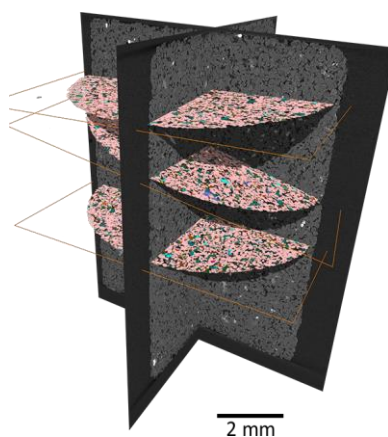


Fig. 1. Positions of the surfaces scanned with the SEM and the miniplug, imaged with microCT (purely schematic).

Furthermore, once the first set of the SEM images is acquired, we re-polish all blocks, to remove few extra microns, and repeat the imaging process. This allows us to obtain numerous slices from a limited physical volume. In this paper, about 9 slices were imaged from each of 5 miniplugs. A total of 45 slices allows to investigate the segmentation quality as a function of the size of the training set, and the effects, associated with non-uniformity of the microCT image quality.

In a daily practice, the “densely packed cross-sections” geometry allows to efficiently utilize the volume of the scanned sample, to save the most of the miniplug intact, e.g., for the subsequent laboratory experiments.

3.3 SEM imaging

We use Thermo Scientific™ QEMSCAN™ 650F SEM to acquire $\sim 4000 \times 4000$ mineral maps of each cross-section.

The bundled iMeasure® software acquires EDS spectra with about 1000 counts for each pixel of the mineral map and independently classifies each pixel in accordance with the pre-built mineral library [23]. We would refer to this image as QMS-mineralogy. Simultaneously, the BackScattered Electrons (BSE) image with the same resolution is acquired, we would refer to it as QMS-BSE. The software automatically moves the SEM table to sequentially cover the whole $\varnothing 8$ mm area of the sample with $\sim 0.3 \times 0.3$ mm frames. The example mineral map is shown in Fig. 4a.

We also utilize Thermo Scientific™ Maps™ software, to obtain a higher-resolution BSE (Backscattered Electrons) image of the same surface, we would refer to it as Maps-BSE.

4 Image registration

To utilize classic supervised ML segmentation approaches, we must first spatially register the microCT and the SEM images. This task is complicated by the large size of the data (a single 4000^3 8-bit image takes 64 GB), and the lack of reliable “special” points — the whole image could be viewed as a semi-stochastic texture. Thus, most modern image registration techniques either incur a large computation cost [24], associated with the direct area-based registration, or require a rather fine manually selected initial starting point.

In this work, each mineral map is automatically spatially registered with the corresponding microCT image using the following in-house registration approach, which consists of the three steps.

4.1 Surface-based registration

The aim of the initial step is to roughly locate the global minima, with the precision, comparable with the size of the grain (or pore), as required for the subsequent area-based optimization process to start in the vicinity of the global minima.

The general rigid-body image registration problem could be formulated as an optimization of six translation-rotation parameters, and a scale parameter:

$$T_m = [x_m, y_m, z_m, \varphi_m, \theta_m, \psi_m, s_m].$$

Here, x_m, y_m, z_m are related to image shift along corresponding axes; $\varphi_m, \theta_m, \psi_m$ are x-y-z Euler angles; and s_m is image scaling.

In this notation, we can significantly reduce the volume of the parameter space to look through. For the binarized versions of the images, namely I_{3D} and I_{2D} , we extract the “center of mass” points. That is (x_{2Da}, y_{2Da}) for the 2D image. For 3D image, we use a number of z-slices and the least-squares approach to estimate the cylinder axis position $(x_{3Da}(z_{3D}), y_{3Da}(z_{3D}))$ for each z_{3D} within the 3D image.

The key point is the extraction of the outer contours of the images, as illustrated in Fig. 2. For 3D image, they could be formalized as

$$\begin{aligned}
 R_{2D}(\varphi_{2D}) &= \max(r):(I_{2D}(x_{2D}, y_{2D}) = 1) \\
 R_{3D}(\varphi_{3D}, z_{3D}) &= \max(r):(I_{3D}(x_{3D}, y_{3D}, z_{3D}) = 1) \\
 x_{2D} &= x_{2Da} + r\sin(\varphi_{2D}) \\
 y_{2D} &= y_{2Da} + r\cos(\varphi_{2D}) \\
 x_{3D} &= x_{3Da}(z_{3D}) + r\sin(\varphi_{3D}) \\
 y_{3D} &= y_{3Da}(z_{3D}) + r\cos(\varphi_{3D})
 \end{aligned}$$

Having the surface profiles, we can estimate s_m using the average radius values. The x_m and y_m could be calculated based on the axis position, once the rest of the parameters would be known.

Thus, we would only need to optimize 4 parameters: $[z_m, \varphi_m, \theta_m, \psi_m]$, out of which for φ_m and θ_m we may consider only a quite limited discrete set of their values, because, in accordance with the assumption about the cutting geometry, they should not exceed 5°.

By the simple geometrical means, the $[z_m, \varphi_m, \theta_m, \psi_m]$ parameterize the sine-like R_{2D} curve position on the R_{3D} surface (Fig. 3), and the aim is to find the matching set of parameters, that would define the correct position of the R_{2D} curve (some additional details could be found in [21]).

Due to relatively small size of the R_{2D} and R_{3D} arrays, which is unlikely to exceed 10 Mbytes, and a limited number of options to consider, even the exhaustive grid search only takes a few seconds on a modern CPU.

According to our practice, the surface profiles are good unique descriptors, and the rock sample surface is never smooth, which allows to automate the whole image registration process.

Moreover, the method works even if the outer surface of the sample is partially damaged. One could notice a perfectly smooth and round part of the surface in the top-right area of the sample shown in Fig. 4b. This artefact resulted from a sample being slightly outside the cylinder-shaped microCT reconstruction volume. Nevertheless, the surface-based registration works in this case as well.

4.2 Area-based registration

The aim of the second image registration step is to improve the result of the first step, still sticking to the rigid-body assumption. This is implemented as a direct iterative “black-box” optimization of all T_m parameters,

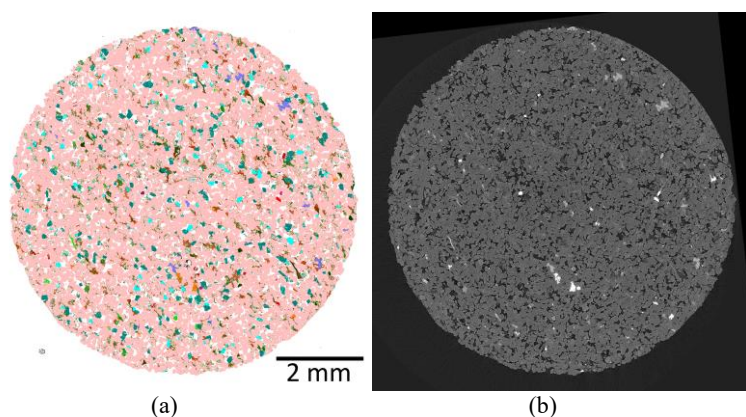


Fig. 4. Example 3D-to-2D image registration procedure result: (a) de-warped QMS-mineralogy image; (b) spatially corresponding microCT cross-section

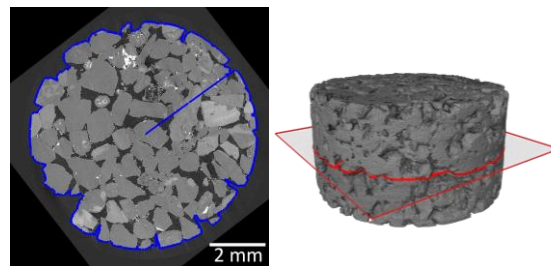


Fig. 2. Surface profiles of a miniplug sample (coarse-grained sandstone is used for readability).

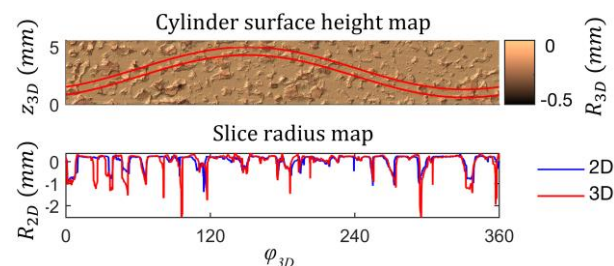


Fig. 3. Matching 2D and 3D surface profiles of a miniplug

using area-based registration norm. To compare discrete-index mineral map with continuous grayscale microCT image, we use mosaic-image Put’ev matching score [25] (or similarly, the explained variance score, calculated after assigning each mineral the grayscale value equal to the average of all the microCT image pixels, matching to that mineral, according to current T_m).

4.3 Smooth non-rigid distortions compensation

Although the miniplug usually represents a fairly good example of a rigid body, the rigid body approximation is insufficient for pixel-perfect SEM-microCT image registration. The issue arises mainly due to acquisition hardware imperfectnesses — even tiny sub-pixel SEM lens distortions tend to accumulate to several pixels—large smooth distortions, when multiple SEM images are stitched together.

One possible workaround is to calibrate the SEM distortions using a special regular sample, and later apply the corresponding de-warping to all SEM images [7]. One of the drawbacks of this method is that it assumes that the distortions would not change after the calibration.

Another drawback is that this method is unable to compensate the distortions, that arise from a limited SEM stage movement precision and the SEM image stitching algorithm glitches.

Instead, we directly apply an Optical Flow estimation method [26] to the pair of images in question. We use smooth large-scale components of the resulting vector field to de-warp the SEM image. This ensures that small artefacts, like mechanically damaged grains would not result in major image distortions. The transformation is so smooth, that for each small sub-area, containing a few grains, it could be viewed as a plain translation.

It must be noted that this de-warping step only considers the 2D distortions in the plane of the SEM image. Thus, it is unable to fully replace

the area-based registration step, which is fully 3D, even if the surface-based registration step provides a very good initial approximation.

The ultimate result of the image registration procedure is shown in Fig. 4. Finally, to allow calculating features on the original microCT data, we scale the SEM image to match the original microCT voxel size. Also, for ML needs, we not only export a single matching microCT cross-section (Fig. 4b) but a 401-slices thick 3D block (e.g. ± 200 slices around the matching cross-section).

5. Relabelling

In [27] it was demonstrated that the QEMSCAN classification result could be misleading sometimes and not agree with the optical petrography results — the issues generally arise for minerals that are very close in their elemental concentration proportions, but considered very different from a petrography point of view. One simple example is the quartzite and quartz pair. These two minerals are usually easily visually distinguishable on a BSE image, but might be indistinguishable from the QEMSCAN’s “independent pixels” point of view. This particular pair could be separated via a joint QMS-mineralogy and QMS-BSE images post-processing,

honouring some minimal neighbourhood of the pixel in question. In this work, we do not question the accuracy of the QEMSCAN image. However, the original QEMSCAN image is still poorly suitable for direct use as a ground truth labelling, mainly due to the noise-like patterns, shown in Fig. 5.

Firstly, we note a number of single-pixel grains, that are definitely too small to be recognizable on a microCT image (Fig. 5a) — even though QEMSCAN pixel size ($2\ \mu\text{m}$) is very close to microCT voxel size ($\sim 2.3\ \mu\text{m}$), the physical resolution of the SEM is significantly higher. Moreover, such objects would hardly influence any physical properties of the Digital Rock model anyway. However, the underlying grain still might be real, and might influence the microCT image somehow. Thus, the general principle we use is not to “smooth-out” such objects with a median filter or equivalent, but to re-assign them to the “Unknowns” class, which is later ignored by all the ML classifiers we use. The mask, highlighting such objects, is shown in the rightmost column in Fig. 5a.

Areas featuring high concentrations of such single-pixel grains are trickier. We found that removing relatively large areas around them stabilizes many classifiers, most probably because such objects are usually outliers in the ML sense. One might note that the

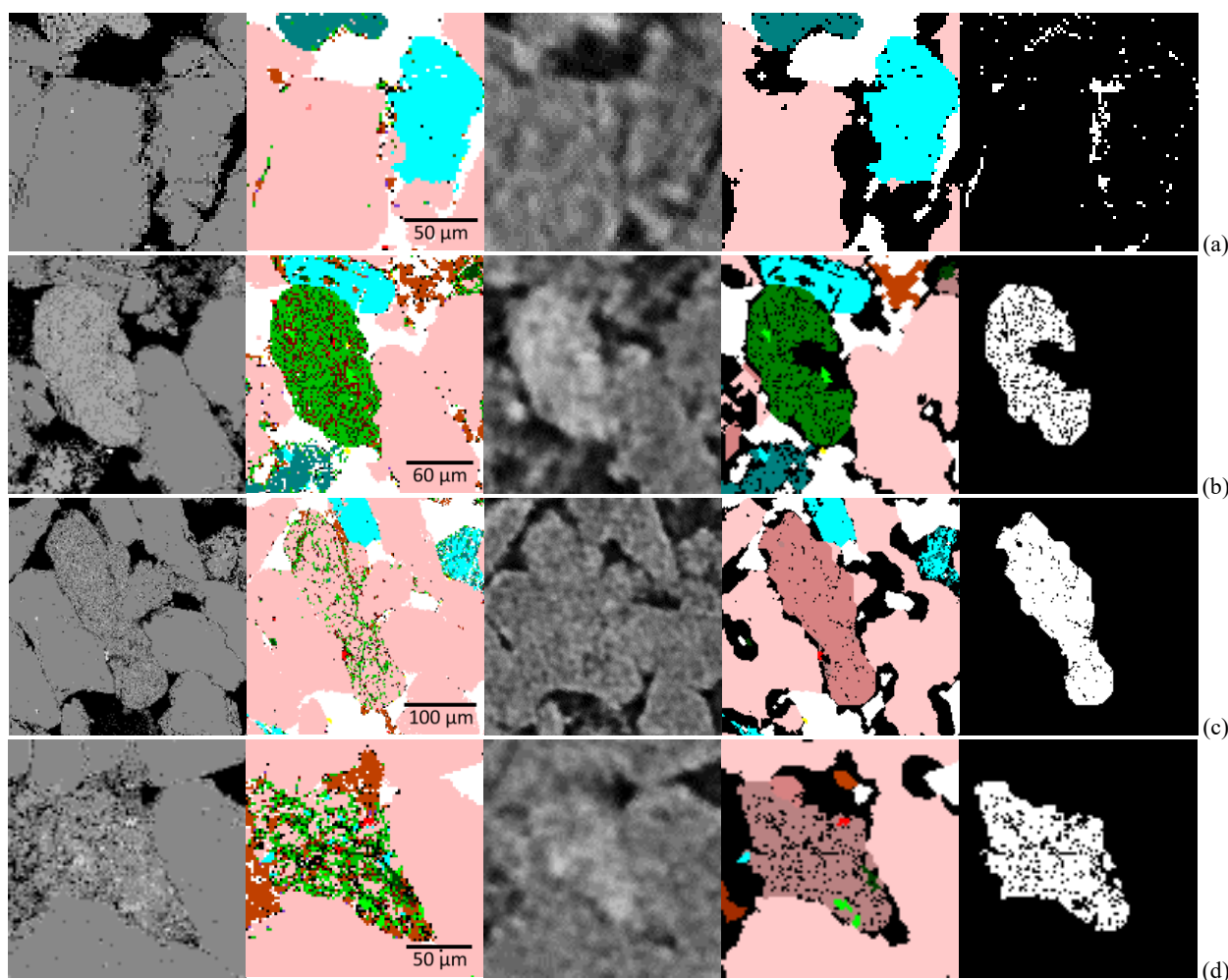


Fig. 5. QEMSCAN mineral map relabeling examples: 1st column - QMS-BSE image; 2nd column - QMS-mineralogy image; 3rd column - spatially registered microCT image; 4th column - relabeling result; 5th column - the relabeled pixels in question (see text); (a) small objects; (b) Clay_mixture class; (c) Quartz_with_clay class; (d) Quartz_clay_cement class.

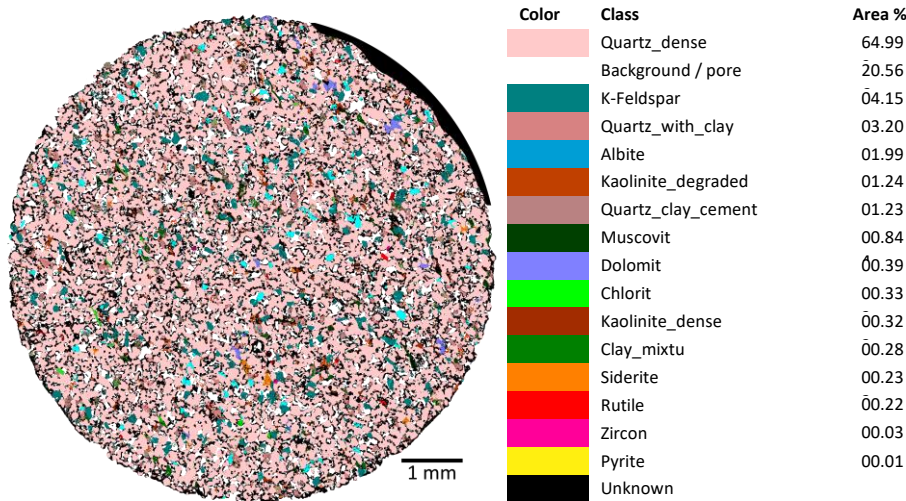


Fig. 6. The ground truth image of the validation slice — the result of the relabeling procedure for the image, shown on Fig. 4a. The legend result and the area percentage for all the classes on the relabeled image.

relabelled image in Fig. 5a contains more Unknowns than just the “small objects” mask, discussed in the previous paragraph.

More importantly, there is a multitude of clay-related classes. The Fig. 5b-d demonstrate that some grains look fairly uniform on the scale of tens of pixels (especially on the BSE image) but produce single-pixel noise-like patterns on both mineral map and BSE.

We relabel such objects, aiming to also distinguish the most important types of conglomerates. Most of them could be easily categorized into broad classes, each containing at least tens of such objects per a single QEMSCAN image. Namely, the grain shown in Fig. 5b is assigned to the Clay_mixture class. The grain, shown in Fig. 5c is assigned to the Quartz_with_clay class. The grain, shown in Fig. 5d is assigned to the Quartz_clay_cement class. Such relabelling not only makes sense from the further Digital Rock physical properties modelling point of view (and could be viewed as an upscaling step), but also greatly simplifies the

segmentation task — now pixelwise classification losses begin to make sense.

All the said relabelling was implemented using basic morphological image processing operations, and carefully hand-tuned for the specific dataset in question (but not for individual slices). Theoretically, such a “clustering” operation could be automated to avoid operator involvement, but that would require considerable additional research.

Finally, slices are inspected manually, and the broad Unknown class strokes (black) are placed where major artefacts are noticed. An example of such a manual intervention is clearly visible in Fig. 6 on the top-right part of the image. The reason for this is the same artefact (resulting from a sample being slightly outside the cylinder-shaped microCT reconstruction volume) that was already discussed above. We also automatically detect the sample circle radius and fill the out-of-sample-circle area with Background/pore class colour (white). We ignore this area in all further area-percentage calculations, including segmentation accuracy calculations.

6. Feature-based segmentation

For the feature-based segmentation results, demonstrated below, we build on the results, demonstrated in [21,28]. We only use 2 QEMSCAN slices for training and a single QEMSCAN slice (shown in Fig. 6) for validation — feature-based approaches require less data before the result quality stops to increase, compared to the CNN-

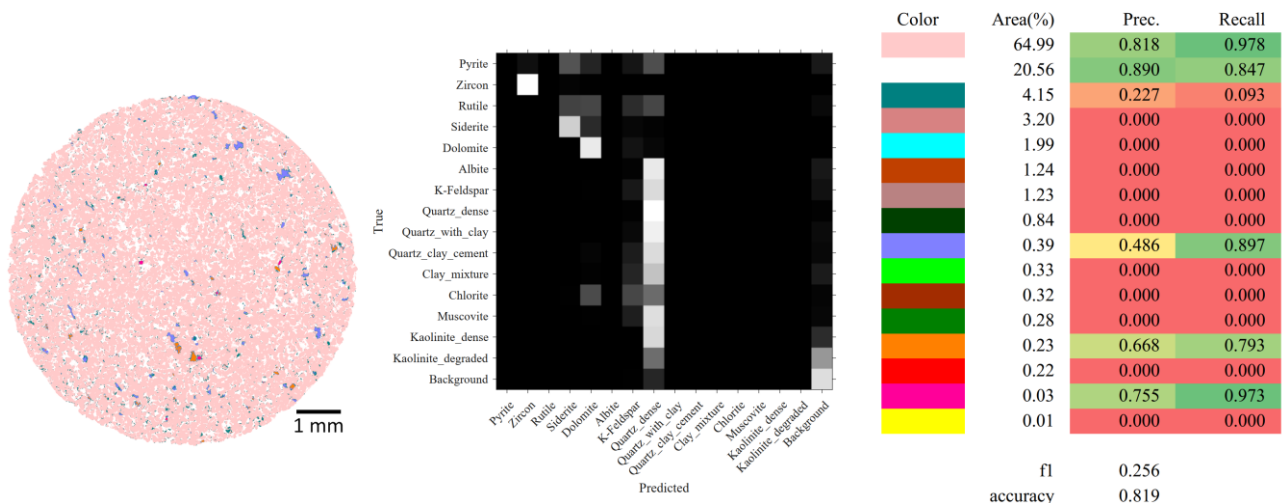


Fig. 7. The result of the “Naïve Bayes” segmentation approach: validation slice segmentation (see legend in Fig. 6), confusion matrix (row-normalized), Precision and Recall (green-yellow-red palette highlights good-average-poor values).

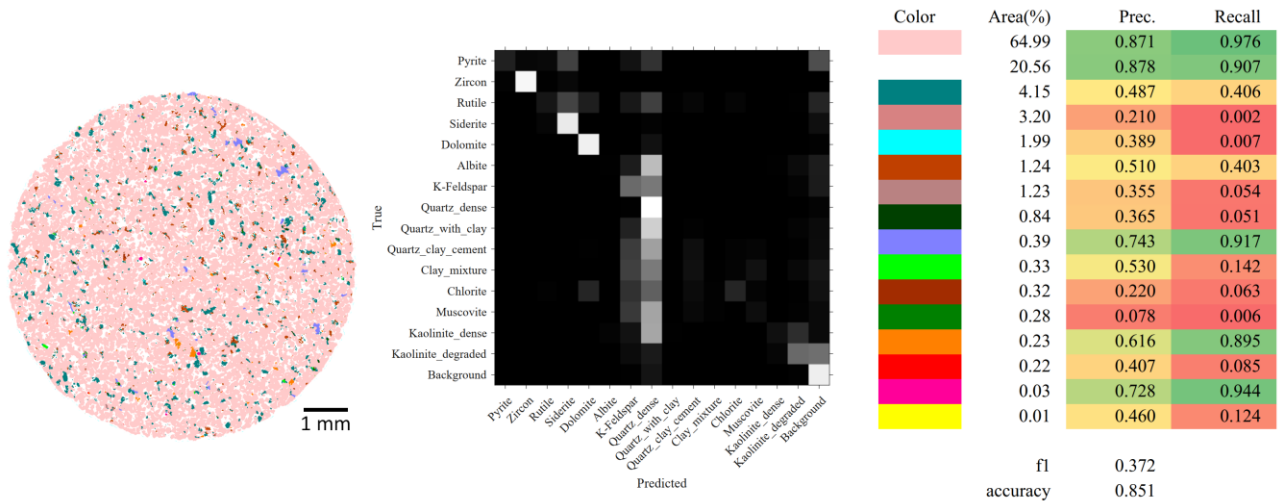


Fig. 8. The result of the “LightGBM” segmentation approach. Designations are equal to Fig. 7.

based. Depending on the circumstances, this could be either a strength or a weakness.

6.2 Naïve Bayes

Our baseline “Naïve Bayes” approach actually utilizes only a single feature channel – the original microCT image, filtered with the manually tuned bilateral filter to suppress noise. We use parametric Naïve Bayes classifier assuming normal distribution. This is roughly equivalent to manually choosing a set of a threshold values after image pre-filtering. The result, shown in Fig. 7 highlights a set of substances that are easily distinguishable by their grayscale values with green background in Precision and Recall columns (definitions of the “Precision”, “Recall”, “accuracy” and “ F_1 ” terms could be found in [29]). A visual comparison with Fig. 4b confirms this assumption.

Still, Naïve Bayes looks significantly better than the binary Otsu segmentation approach (Fig. 15, Fig. 16) which only achieves 0.813 accuracy and 0.109 F_1 , (we use micro-averaging) assuming that it distinguishes Quartz_dense and Background classes.

6.3 LightGBM

LightGBM [30] is a modern gradient boosting framework, providing both high performance and state-of-the-art classification accuracy in many benchmarks. We combine it with two 3D 8-bit cube-shaped rotation-invariant LBP patterns and a local window statistics feature vector (e.g. average, median, variance, skew, kurtosis, ...). We fine-tune LBP meta-parameters using cross validation (namely histogram windows size, pattern scale and threshold value). Also, we post-process the soft-classification result, provided by the LGBM using the Graph Cut approach [31] to make it a bit smoother. The result demonstrated in Fig. 8 achieves higher scores compared to Fig. 7.

7. CNN-based segmentation

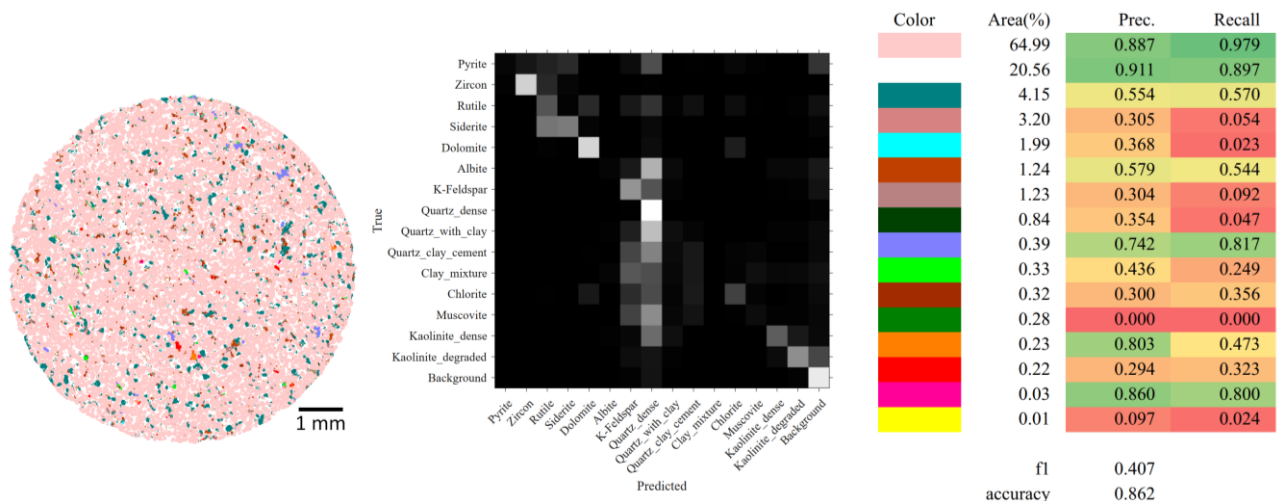


Fig. 9. The result of the “3-slice U-net” segmentation approach. Designations are equal to Fig. 7.

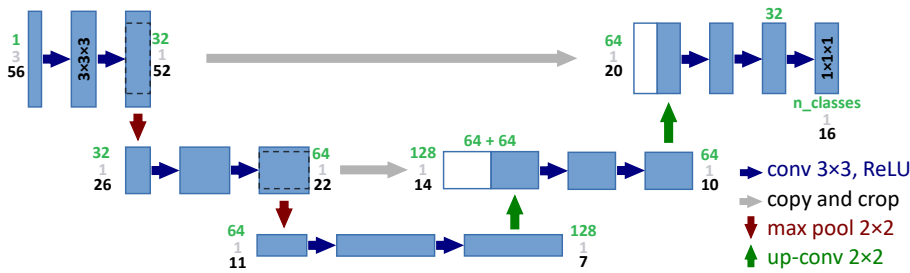


Fig. 10. The 3-slice U-net architecture. The number of feature channels is indicated in green; z-size is indicated in gray; x and y sizes are equal and are indicated in black.

The CNN-based segmentation results, demonstrated below, utilize the U-net architecture [32]. For the experiments in this section, we use the same single QEMSCAN slice for validation, and 44 slices for training. We use 3D receptive field, valid-mode convolutions and dense 2D output labelling (except that some pixels belong to the Unknown class). We argue that such a geometry is more efficient than sparse 3D labelling [33]. The training epoch corresponds to a number of randomly selected patches with a total area equal to the total area of the training set. We do not perform training data rebalancing or hard negative mining, despite severe imbalance. We use cross-entropy loss and Adam optimizer with learning rate 0.0002, $\beta_1=0.5$, $\beta_2=0.99$. Our experience suggests

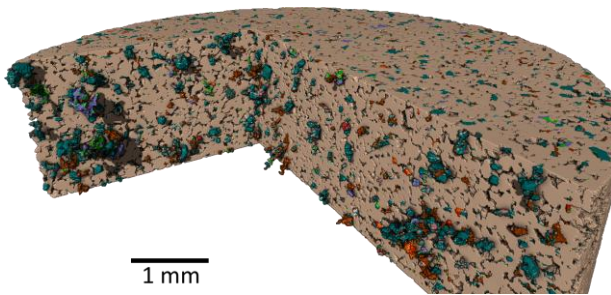


Fig. 11. The 3D render of the 3-slice U-net segmentation result

that further fine-tuning only provides specific minor improvements. Although they might be valuable in specific cases, they are out of the scope of the present article, aiming at a more general comparison.

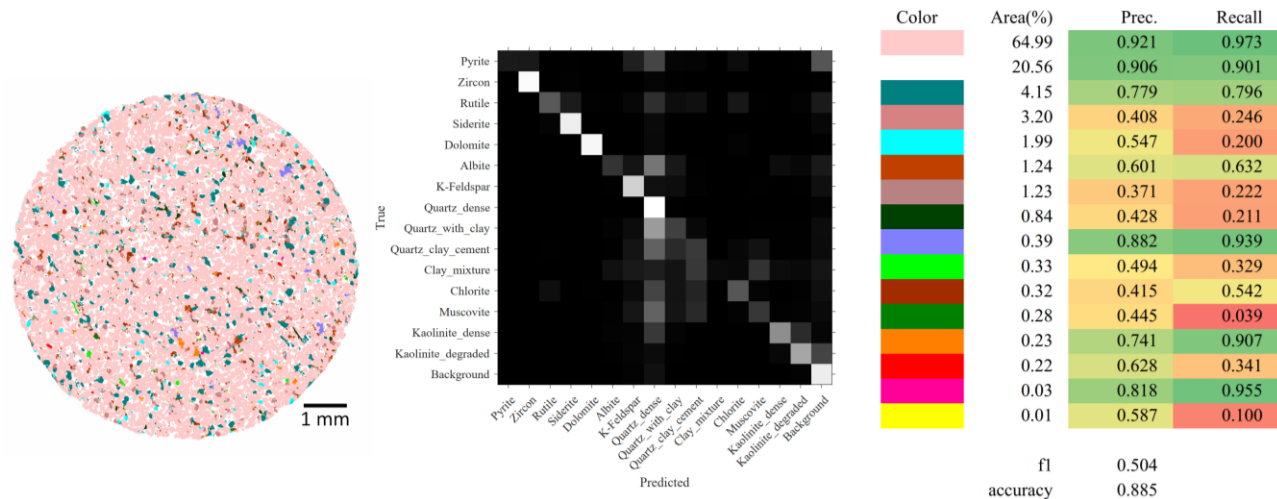


Fig. 12. The result of the “3D U-net” segmentation approach. Designations are equal to Fig. 7.

7.1 3-slice U-net

Our first, most lightweight U-net model uses 3-slice [34] architecture (Fig. 10), that is — only the first single convolution is $3 \times 3 \times 3$, while the rest are 3×3 , thus being almost 2D. Some additional details are available in [28]. The training performance is about 100 epochs per day, on a single GK210 chip of the Nvidia[®] K80 GPU. The Fig. 9

demonstrates the 1000-epoch training result, but scores only marginally improve after 200 epochs. On the large scale, this result is visually similar to the LightGBM result (Fig. 8), but the scores are significantly higher. Some differences could be seen in the Fig. 15 — the CNN generally produces less small infeasible details. The 3D rendering (Fig. 11) demonstrates adequate 3D geometry of the grains despite the “almost 2D” nature.

7.2 3D U-net

Our second U-net model (Fig. 13) is fully 3D and all 3 spatial dimensions are (almost) equal. It uses $204 \times 204 \times 92$ input patches and 112×112 output patches. Specific patch sizes are used to ensure full symmetry in max pooling and up-convolution layers. Additional $3 \times 3 \times 1$ convolution layer is added for the same purpose. Each convolution, except the last one, is followed by PReLU activation with 0.25 activation parameter. The last convolution uses softmax activation. Up-convolution layers use transposed convolutions and halve the number of the feature channels. The training performance is, again, about 100 epochs per day, but now a GPU server with $7 \times \text{RTX2080Ti}$ is used. The training batch size is 7 (a single patch per a GPU) due to GPU memory limitations. After the first

100 epochs, accuracy score, calculated on our only validation slice, oscillates in [0.088, 0.0885] range.

For the Fig. 12, we select a result with the maximum accuracy observed. This result demonstrates a significant step forward, as compared to

our previous results — the confusion matrix now looks much more like a clean diagonal. One exception is the most-common Quartz_dense class that is thus considered “the safest choice” when the U-net is not certain about a specific pixel. The Precision score is above 0.37 for all classes, but the Recall is still below 0.25 for the most difficult-to-distinguish classes, including clays. However, the confusion matrix suggests that in many cases clays are mostly mixed with other clays, which might be acceptable for many practical scenarios. Classes like Quartz_with_clay and Quartz_clay_cement are similar in their nature — there is no clear boundary between them.

The fact that Pyrite is commonly mixed with Quartz and Background could be attributed to the small size of the Pyrite grains and mechanical damage of the sample surface during polishing.

7.2 3D U-net+GAN

The Generative Adversarial Networks (GAN) are algorithmic architectures that use two neural networks, competing against each other, e.g., while the first one attempts to generate realistic synthetic images, the other

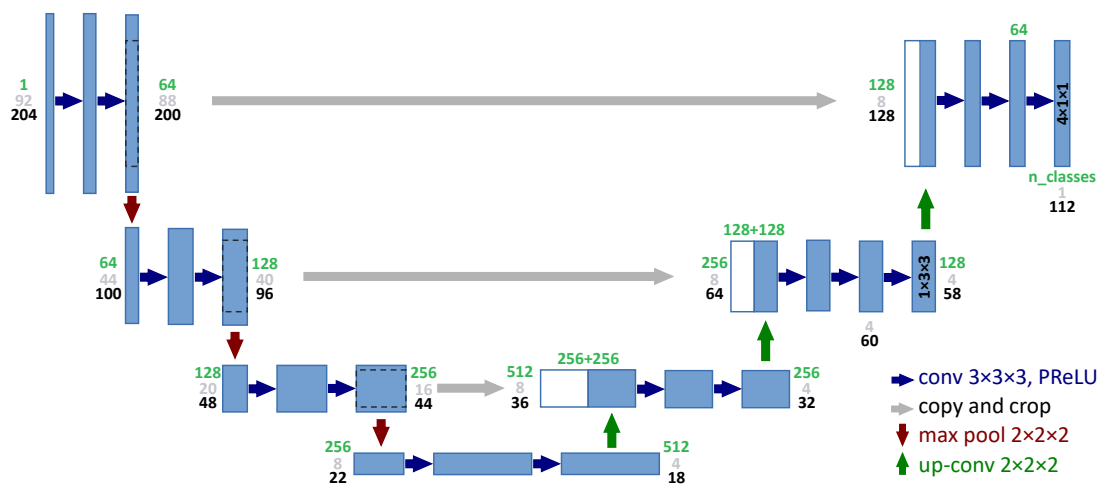
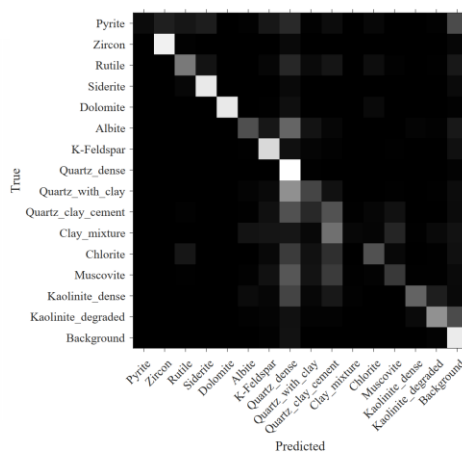
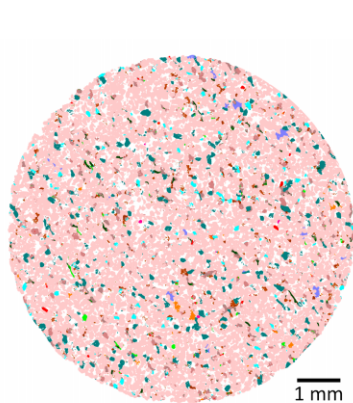


Fig. 13. The 3D U-net architecture. Designations are equal to Fig. 10.

one attempts to distinguish between the synthetic and real images. This concept, originally proposed in [35], proved to be very successful for continuous data generation tasks, like grayscale or RGB image generation, including image-to-image translation [36]. But only a limited success should be expected, when directly applying GANs to discrete data generation tasks, like the image segmentation task in question. The issue arises from a limited amount of information, available to the generator network through the argmax layer.

Last but not least, almost all ground truth patches contain at least one Unknown (black) pixel (see Fig. 16b), while our segmentation methods are designed to produce none (see Fig. 16e-k). If we blindly pass such “real” and “fake” patches to the discriminator, it would be able to distinguish between them by just that. Thus, it would not provide any meaningful information about the “fake” patch quality to the generator. To fix this, we make generated patches look like real in terms of the Unknown class distribution, by copying the Unknown pixels from the ground truth image.

Our third U-net model utilizes effectively the same architecture as the previous one, but features an additional 14-layer discriminator network, attached to its output.



Color	Area(%)	Prec.	Recall
	64.99	0.924	0.973
	20.56	0.905	0.897
	4.15	0.797	0.826
	3.20	0.470	0.265
	1.99	0.622	0.301
	1.24	0.650	0.553
	1.23	0.305	0.313
	0.84	0.454	0.217
	0.39	0.929	0.886
	0.33	0.507	0.308
	0.32	0.493	0.380
	0.28	0.260	0.030
	0.23	0.765	0.888
	0.22	0.531	0.462
	0.03	0.862	0.920
	0.01	0.727	0.043
f1 accuracy		0.542	0.887

Fig. 14. The result of the “3D U-net+GAN” segmentation approach. Designations are equal to Fig. 7.

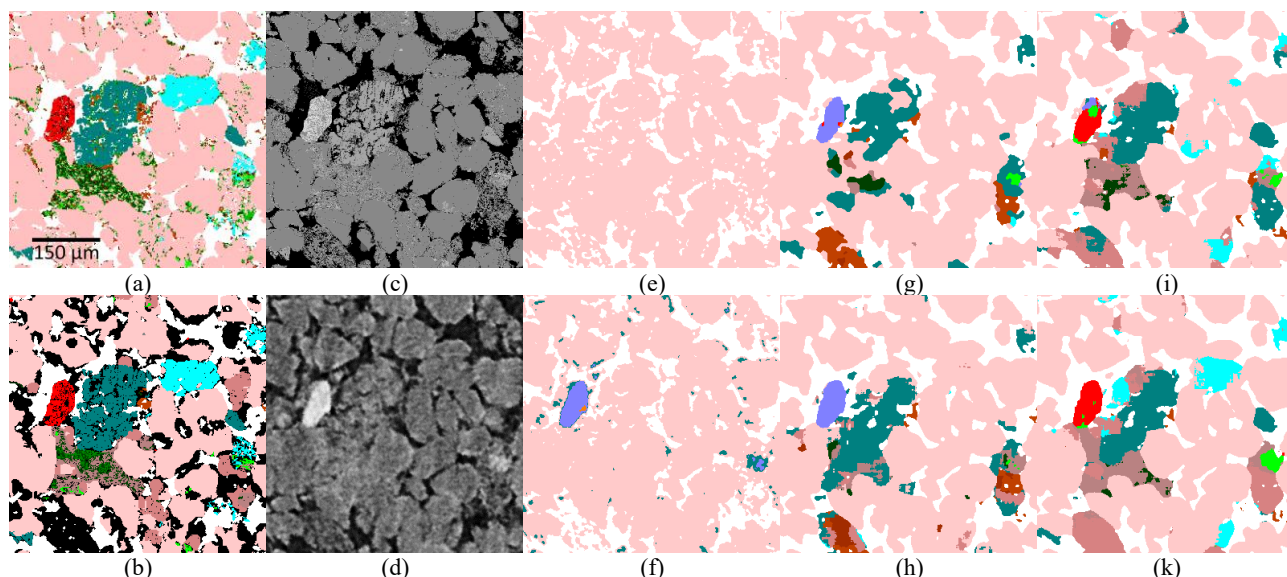


Fig. 15. Comparison of the different segmentation results for the fragment one: (a) original QMS-mineralogy; (b) Relabeling result (segmentation ground truth); (c) original QMS-BSE; (d) microCT; (e) Otsu; (f) Naïve Bayes; (g) LightGBM; (h) 3-slice U-net; (i) 3D U-net; (k) 3D U-net+GAN.

Only 2D 3×3 convolutions are used, because we lack 3D ground truth data. For the 4th, 7th and 10th convolutions, stride equals 2, for the rest stride equals 1. The number of feature channels first doubles after each filter, starting from 32 and ending up at 512, and then halves back down to 32. Each convolution is followed by a LeakyReLU activation with 0.2 parameter and instance normalization. The last convolution is rather followed with a sigmoid activation. During the training phase, generator and discriminator are updated with 1:1 ratio, using minimax GAN loss. Dropout and hard-negative mining are not used. The training performance drops to about 60 epochs per day.

Once again, in the Fig. 14 we just present the best result achieved. However, we must admit that in this case, the training performance is less stable, and results vary way more across different epochs, which is a typical for the architecture used. One promising point, however, is

that this result is significantly better than those on Fig. 12 in terms of the F_1 score. Another promising point is that careful inspection of the smaller crops (Fig. 15) indicate some progress towards smoother, more realistic grains, with less unfeasible mineral mixtures. Even though this “smoothing” hardly ever provides a truly realistic result and sometimes results in an even more incorrect classification, like for a K-Feldspar grain in Fig. 16.

8. Image quality uniformness

To assess the microCT image quality uniformness, and the possible associated effects, we train 3-slice U-net on various sets of slices, and simultaneously evaluate it on all available slices (Fig. 17). One simple effect to mention is that training sets below 10 slices seem to be insufficient in terms of the F_1 score.

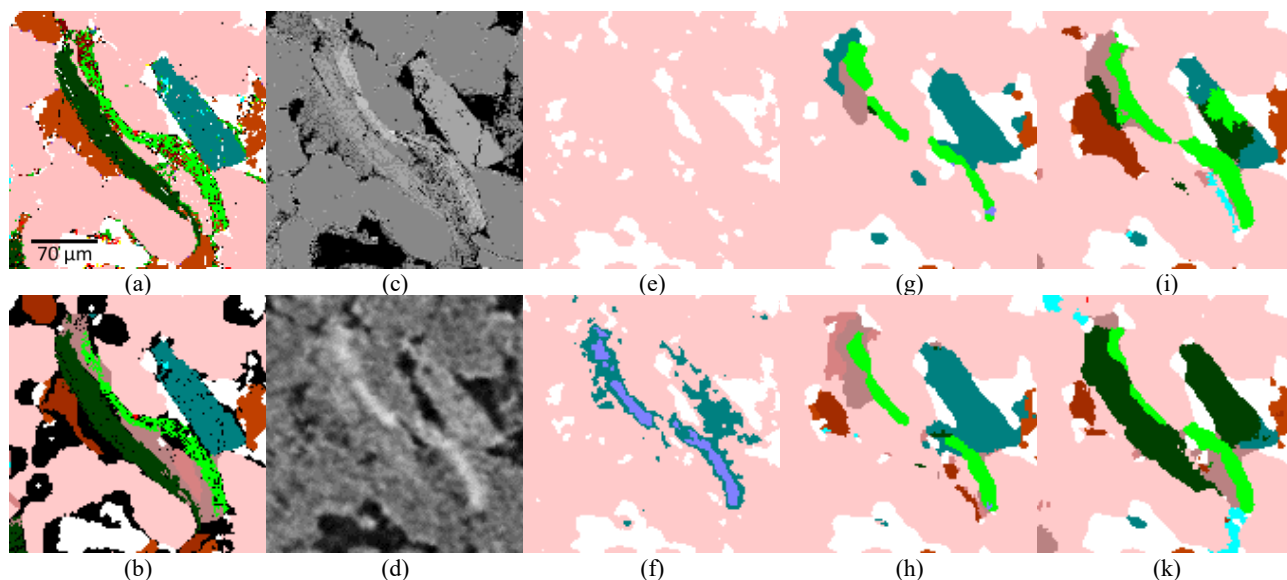


Fig. 16. Comparison of the different segmentation results for the fragment two: (a) original QMS-mineralogy; (b) Relabeling result (segmentation ground truth); (c) original QMS-BSE; (d) microCT; (e) Otsu; (f) Naïve Bayes; (g) LightGBM; (h) 3-slice U-net; (i) 3D U-net; (k) 3D U-net+GAN.

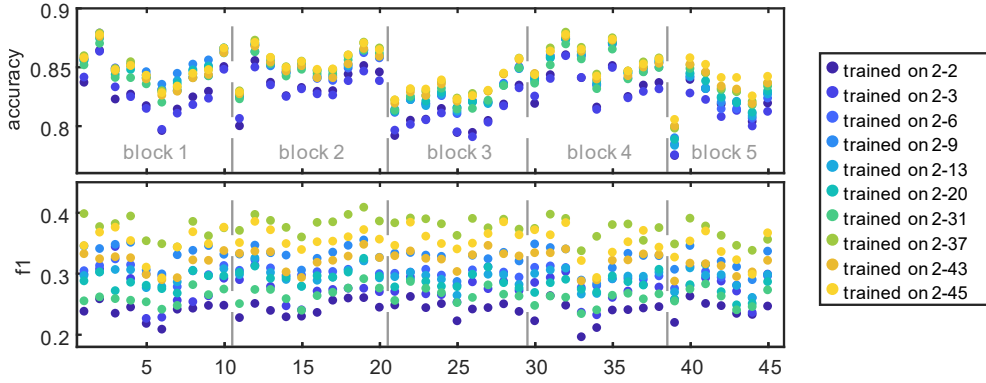


Fig. 17. The effect of the training set selection. Each block corresponds to a physical miniplug.

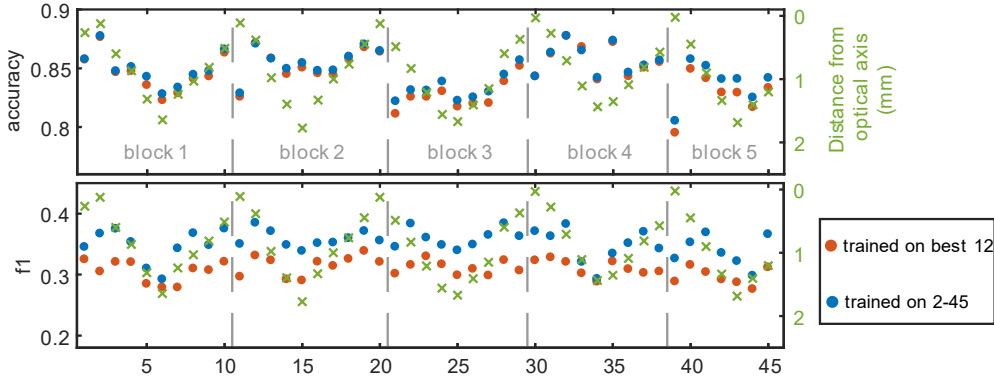


Fig. 18. The “distance from the optical axis” effect.

The second, more interesting effect we notice in Fig. 17 is that the segmentation quality is not growing monotonously when adding training slices. In particular, it significantly drops (in terms of the F_1 score) for most slices, when we add slices 38-43 to the training set. This might suggest that there are some “bad” slices, negatively affecting the segmentation quality. To assess this hypothesis, we train the same classifier using 12 best-accuracy slices, however, the segmentation quality decreases on all slices (Fig. 18). Thus, one might conclude that there are no “bad” slices, just an intrinsic non-uniformness, which is partially associated with microCT image quality non-uniformness.

We found a strong correlation between the distance from a slice to the microCT optical axis (central slice) and the segmentation quality for that slice (the fact that the first slice from each block demonstrates lower segmentation quality than the second one should be probably attributed to the sample preparation issues). Gradual minor quality drop in the areas further from the optical axis is the expected effect for conventional cone-beam circular-trajectory microCT scanners, utilizing Filtered Back Projection (FBP) reconstruction algorithm. The multiclass segmentation relies on barely visible tiny features and thus it is highly sensitive to such effects. However, this is certainly not the only source of imperfectnesses. We assume that the only feasible mitigation measure is to train models on a larger datasets, covering more-or-less all possible imperfectnesses. Later,

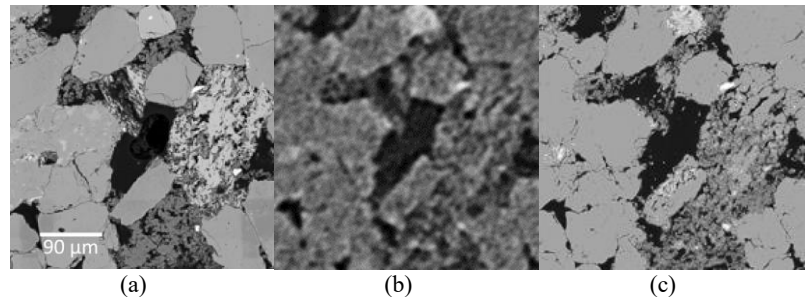


Fig. 19. Super-resolution experiment image fragments comparison: (a) original Maps-BSE image; (b) microCT image; (c) super-resolution result

such model could be fine-tuned for a specific smaller practical job.

9. Learned super-resolution

The ability of the CNN to resolve meaningful details in the microCT image could be also studied by using effectively the same CNN architecture and input data for a learned super-resolution task. For this purpose, we use a single full-slice Maps-BSE image for training, and another Maps-BSE image, from a different slice, for the visual comparison (Fig. 19). The result demonstrates that

although our model is unable to reconstruct the Maps-BSE image exactly, and locations of specific tiny features may not match real in a pixel-perfect manner, on a larger-scale, the overall morphology and substance types are mostly reproduced correctly (which is actually more important than pixel-perfect positions for the subsequent physical properties modeling). Moreover, infeasible patches are uncommon. This is partially associated with the fact that continuous data generation task is more suitable for the modern GANs. This looks promising in a sense that there is still potential for segmentation quality improvement.

It should be noted that such a super-resolution tool is also valuable by itself. In [37] authors discuss microCT-to-microCT super-resolution and provide the visual comparison of the result with an SEM image. This super-resolution task is also close to the conditional image generation [38], which could be viewed as effectively the same task with a weaker preconditioning.

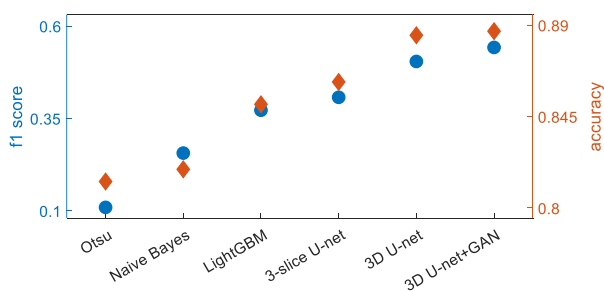


Fig. 20. The comparison of the segmentation quality scores.

10. Conclusions

Convolutional neural networks allow multiclass microCT image segmentation with a quality far beyond more traditional methods (Fig. 20). Larger 3D receptive fields are beneficial for the segmentation quality, but the associated computation cost is higher. Basic supervised training could be considered fairly stable and thus production ready. However, a tightly spatially matching sizable operator-independent ground truth labelling is required. The 3D GAN-based approaches have not demonstrated their full potential yet and are currently less stable in general. However, they already provide slight improvements and represent a promising subject for further research.

References

- W. Oh et al., IEEE Transactions on Pattern Analysis and Machine Intelligence **21**, 590–602 (1999)
- A. P. Sheppard et al., Physica A: Statistical Mechanics and Its Applications **339**, 145–151 (2004)
- D. A. Koroteev et al., in *Proc. of International Symposium of the Society of Core Analysts* (California, USA, 2013), 12
- O. Dinariev et al., in *Proc. of International Symposium of the Society of Core Analysts* (Pau, France, 2019)
- J. Goral et al., Sci. Rep. **10**, (2020)
- M. Knackstedt et al., in *Soc. Pet. Eng. - SPE Asia Pac. Oil Gas Conf. Exhib., APOGCE* (2010), 1589–1597
- T. K. Varslot et al., US20110181701 A1 (2011)
- A. C. Jones et al., Biomaterials **28**, 2491–2504 (2007)
- Y. Wang et al., Minerals Engineering **83**, 185–191 (2015)
- I. Arganda-Carreras et al., Bioinformatics **33**, 2424–2426 (2017)
- C. Sommer et al., in *2011 IEEE International Symposium on Biomedical Imaging: From Nano to Macro* (2011), 230–233
- M. Andrew, Computational Geosciences **22**, 1503–1512 (2018)
- S. Karimpouli et al., Computers & Geosciences **126**, 142–150 (2019)
- V. Badrinarayanan et al., IEEE Transactions on Pattern Analysis and Machine Intelligence **39**, 2481–2495 (2017)
- Y. Da Wang et al., ArXiv:2002.05322 (2020)
- I. A. Varfolomeev et al., Computers **8**, 21 (2019)
- M. Andrew et al., Microscopy and Microanalysis **23**, 156–157 (2017)
- M. R. Ball et al., Microscopy and Microanalysis **25**, 410–411 (2019)
- G. Tiu, Classification of Drill Core Textures for Process Simulation in Geometallurgy: Aitik Mine, Sweden, Master's thesis in Natural Resources Engineering, Luleå University of Technology, (2017)
- P. I. Guntoro et al., Minerals Eng **142**, 19 (2019)
- I. A. Varfolomeev et al., in *Proceedings of the 3rd IAPR Asian Conference on Pattern Recognition – ACPR* (Kuala Lumpur, Malaysia, 2015), 346–350
- M. Pietikäinen et al., in *Computer Vision Using Local Binary Patterns* (Springer, London, 2011), 13–47
- A. R. Butcher et al., in *Seventh Mill Operators' Conference* (The Australasian Inst. of Mining & Metallurgy, 2000), 267–271
- S. Latham et al., in *Proc. of International Symposium of the Society of Core Analysts* (Society of Core Analysts, Abu Dhabi, UAE, 2008)
- Yu. P. Pyt'ev et al., *Methods of Morphological Analysis of Images [In Russian]* (Fizmatlit, Moscow, 2010)
- C. Liu, Beyond Pixels: Exploring New Representations and Applications for Motion Analysis, PhD thesis in Electrical Engineering and Computer Science, Massachusetts Institute of Technology, (2009)
- I. A. Varfolomeev et al., in *Proceedings of the SPE Russian Petroleum Technology Conference and Exhibition* (Society of Petroleum Engineers, 2016)
- I. A. Varfolomeev et al., VKIT [In Russian] (**7**), 3–9 (2019)
- D. M. W. Powers, ArXiv:2010.16061 (2010)
- G. Ke et al., in *Advances in Neural Information Processing Systems* (2017), 3149–3157
- Y. Boykov et al., Pattern Analysis and Machine Intelligence, IEEE Transactions On **23**, 1222–1239 (2001)
- O. Ronneberger et al., in *Medical Image Computing and Computer-Assisted Intervention – MICCAI 2015* (Springer, Cham, 2015), 234–241
- Ö. Çiçek et al., ArXiv:1606.06650 (2016)
- M. Lai, ArXiv:1505.02000 (2015)
- I. J. Goodfellow et al., ArXiv:1406.2661 (2014)
- P. Isola et al., in *IEEE Conference on Computer Vision and Pattern Recognition – CVPR* (2017), 5967–5976
- Y. D. Wang et al., Water Resources Research **56**, e2019WR026052 (2020)
- L. Mosser et al., in *Proc. of 80th EAGE Conference and Exhibition* (EAGE, 2018), 1–5

Large two phase Digital Rock Physics simulations for relative permeability uncertainty assessment

Mohamed Regaieg^{1*}, Igor Bondino², Clément Varloteaux³, Tilty Farhana Faisal⁴, Jianhui Yang⁵ and Richard Rivenq¹

¹ TotalEnergies SE, Pau, France

² TotalEnergies SE, Feluy, Belgium

³ Computational Hydrocarbon Laboratory for Optimized Energy Efficiency, Pau, France

⁴ National Institute for Research in Computer Science and Automation, Pau, France

⁵ TotalEnergies E&P, Aberdeen, United Kingdom

Abstract

Recent numerical developments in digital rock physics, known as Generalized Network Modelling (GNM) [25], allow to reconstruct an upscaled version of the 3D segmented image of a rock in the form of a network of pore elements where the single-phase flow conductances in each pore are derived by solving the Stokes equation in the original geometry. In engineering terms, this hybrid solution allows to capture relevant flow information from the original Micro-CT image whilst keeping the overall cost of multi-phase computation manageable. In this work, OpenFOAM is called for the Stokes flow solution inside a pore network extraction platform called GNextract developed with Imperial College, London, during a 8-year collaboration [25], and TOTAL's pore-scale network simulator DynaPNM [27] is used in quasi-static mode after having been made fully parallel. All codes are run on TOTAL's supercomputer PANGEA.

In the first part of this paper we give an overview of TOTAL's two-phase flow simulation workflow. We then continue on the physics side reporting a new major finding with respect to assumptions that have been used so far by the majority of authors for the modelling of water layers in mixed-to-oil wet rocks. This is seen to have a very large impact on simulation accuracy, especially in terms of relative permeability trends versus wettability. Subsequently, we validate our simulation workflow against three relative permeability experiments performed on microplugs and against a SCAL dataset. The comparison against all datasets gave satisfactory results. On the computational side, we describe how we are able to extract and simulate large networks thanks to a newly developed stitching algorithm and to the parallelization of our pore scale simulator. This allowed us to perform large uncertainty studies (thousands simulations / day) on images as large as (8480x8480x10000) voxels representing a rock volume of 46 cm³. Being able to simulate large networks allowed us to study the impact of the image size on the spread of the simulated residual oil saturation. We show that simulations on images as small as 1200x1200x1200 are dominated by finite size effect and result on large variability of the simulations. This finite size effect is drastically reduced by simulating much larger images, greatly improving the precision of the numerical result.

1- Introduction

Digital Rock Physics (DRP) has been an appealing technology to the oil and gas industry in the last 25 years. In fact, oil and gas companies have dreamt of using DRP as a mean to predict multi-phase properties of Reservoir Rocks (such as Kr and Pc) numerically without the need to perform SCAL experiments. However, the problem has proved more complex than what researchers have expected, and the weakest points of the technology have been the limitation of image resolution [29], rock/fluids wettability characterization [7, 32] and sometimes an over-simplification of the physics. DRP could also be criticized for computing properties on usually small rock volumes without proving neither that the Representative Elementary Volume (REV) for single phase and two-phase flow is reached nor that the simulations are not dominated by finite size and boundary effects.

Advances in Micro-CT imaging have allowed the characterization of wettability from images of multiphase flow experiments. Andrew et al [4] have measured the contact angles manually in scCO₂-Brine-Carbonate system by tracing vectors tangential to the solid surface and the scCO₂-brine interface. This was done at 300 locations on an image of scCO₂ trapped as a residual phase in the pore-space of the scCO₂. In more recent works, other researchers have developed automatic contact angle computation methods [3, 30]. These methods were used to compute contact angles either at residual oil saturation Sor [2] or after stabilization of co-injection of water and oil [13].

Several simulation techniques have been developed to study single and two-phase flow in porous media. Direct numerical simulation (DNS) methods such as finite volume method and Lattice Boltzmann have been widely used to compute petrophysical properties of rocks directly on Micro-CT images [24, 35]. However, these methods

* Corresponding author: regaieg.mohamed@gmail.com

are computationally expensive for two-phase and capillary dominated flow regime which characterizes most oil reservoirs. Pore Network modelling (PNM) technique, on the other hand, simplifies the pore structure and idealizes its geometry through a pore network extraction [10] that is later used in a pore network simulator to compute single and two-phase flow properties [26]. The latter technique is very efficient computationally and can be used to simulate larger volumes [27]. However, the older models [22, 34] used empirical models and geometry simplifications to compute the node to node conductivities which is a critical parameter in petrophysical properties computations. In this work, we take the best of both approaches. First, a single-phase DNS simulation is performed on the rock image and coupled with a pore network extraction. This results in a pore network with conductivities measured on the original geometry [25]. Subsequently, PNM simulations are used to perform two-phase flow simulations using TOTAL's quasi-static pore-scale network simulator DynaPNM [27]. The film flow physics in oil and mixed-wet scenarios have been revisited compared to the models used by most of the authors [28, 34] that can have a major impact on relative permeability. Furthermore, DynaPNM has been parallelized allowing us to simulate large volumes and thus to avoid finite size effects and to get as close as possible to the REV for single and two-phase flow.

In this paper, we describe TOTAL's DRP workflow based on 1) GNM technique to extract a pore network with conductivities computed on the rock image, 2) a network stitching code that allows the extraction of larger networks and 3) TOTAL's fully parallelized inhouse tool DynaPNM that can simulate several million networks with several million pore elements extracted from images as large as 8480*8480*10000 voxels. During the simulation exercise, we perform sensitivity studies that vary the uncertain parameters of the simulations. Thousands of different realizations are used to produce P10, P50 and P90 relative permeability sets. This workflow is then applied to several outcrop and reservoir rocks and allows us to conclude of the state of the art of this technology.

2 Description of the simulation workflow

2.1 Pore network extraction

In contrast to some digital rock physics methods, pore network models do not involve two-phase direct flow simulation in a 3D CT image or a reconstructed digital rock. Instead, it needs a pore network that is extracted from 3D reconstructions. Various algorithms exist to extract the skeleton of the 3D model that carries the essential geometric and topological information of the underlying pore system. In this work, we use a pore network extraction platform called GNextract developed with Imperial College, London, during an 8-year collaboration [25]. GNextract is first used to reconstruct an upscaled version of the 3D segmented image of a rock in the form of a network of pore elements where the

single-phase flow conductances in each pore are derived by solving the Stokes equation in the original geometry using OpenFOAM. Unfortunately, the extraction code needs large amount of memory to extract large images (more than 60 GB of RAM for 1500³ voxels image). Furthermore, although OpenFOAM simulations are parallelized, they are computationally expensive and require a large amount of resources and/or simulation time for large images. Therefore, to overcome these limitations, a stitching process has been developed on networks extracted from overlapped sub-volume of a given image (Figure 1). Figure 1 illustrates the stitching process and shows that the stitched network is formed by a first part conserved from PNM1, a second part conserved from PNM2 and a third part obtained on a transition zone where rules inspired from the ones used by GNextract are defined to choose the elements to conserve --some elements being obtained from PNM1 whilst others from PNM2. In the transition zone, if several pore elements are obtained to describe the same feature, only the largest pore bodies and largest pore throats are kept. This is motivated by the fact that the extraction algorithm computes each element size from the largest inscribed sphere in the porous space. Therefore, the extraction algorithm tends to naturally choose the widest space available for determining element size. If a large extraction is required, several stitching operations are performed thus reducing the memory usage and accelerating the computations.

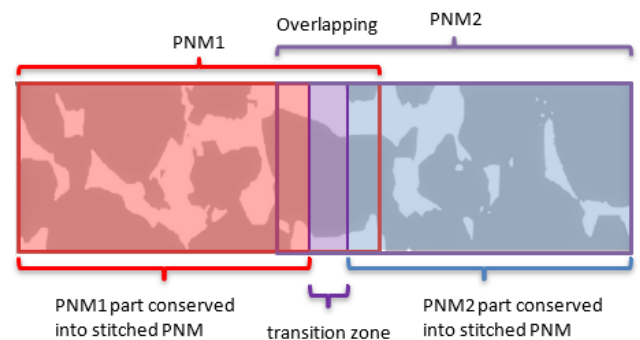


Figure 1 : An illustration of the pore network stitching process

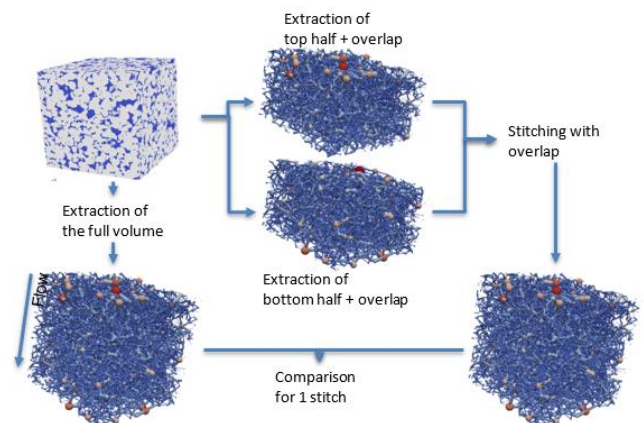


Figure 2: Illustration of the validation of the stitching code

In order to validate the stitching algorithm, we have compared waterflood relative permeability curves from a

reference case in which we extract a pore network from the full image to a stitched pore network from the same image with varying transition length (Figure 2). For the tested rocks (Figure 2), the absolute permeability varied by less than 5% and the waterflood relative permeability in the stitched networks agreed well with the reference network (Figures 4 and 5). In the simulations of Figures 4 and 5, an image 2000x1000x1000 have been used corresponding to network sizes of 10000 nodes and 100000 nodes respectively for rock A and B, An overlap, from 200 to 1600 voxels have been used and constant contact angles were considered (140° for OW and 50° for WW).

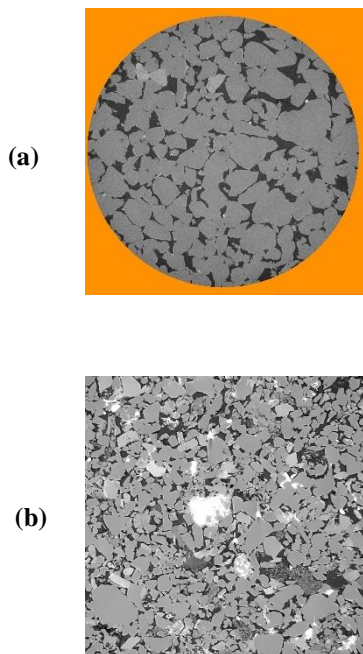


Figure 3 : Micro-CT images of Sandstone Reservoir Rocks used in this paper, clean sandstone that we call Reservoir Sandstone A (a) and Sandstone with clay that we call Reservoir Sandstone B (b)

2.2 Pore network flow simulator

2.2.1 DynaPNM: a parallel pore network simulator

Once a pore network is extracted with the corresponding conductance values from single phase DNS simulation, we go on to perform two-phase flow simulations. These simulations are performed using DynaPNM, TOTAL's inhouse pore network simulator [27], that we use in quasi-static mode as all the cases that we study in this paper are capillary dominated.

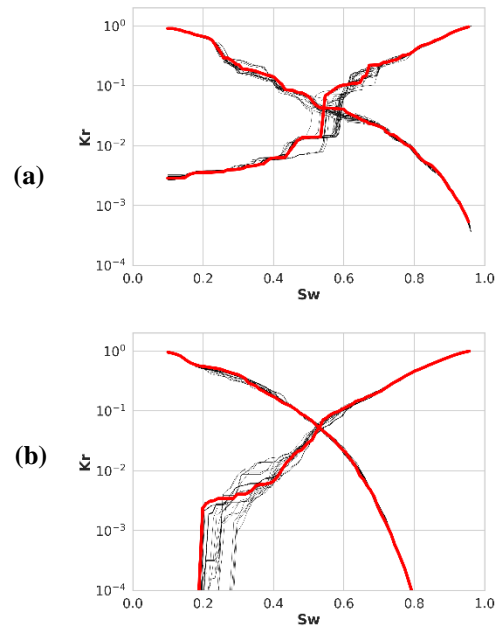


Figure 4 : Comparison of waterflood relative permeability curves of the stitched (black) and reference (red) pore networks for an oil-wet scenario for Reservoir Sandstone A (a) and Reservoir Sandstone B (b)

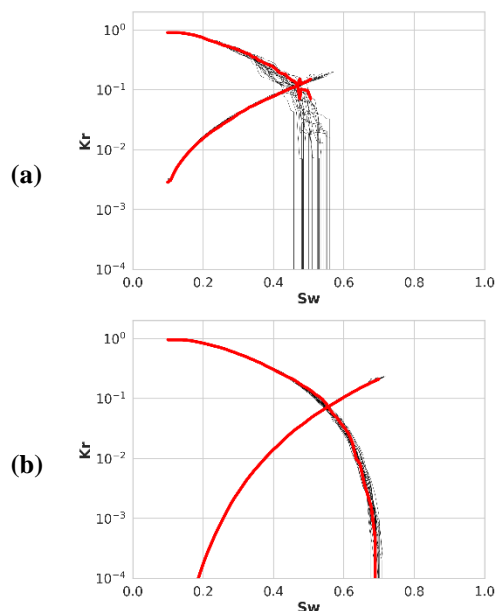


Figure 5 : Comparison of waterflood relative permeability curves of the stitched (black) and reference (red) pore networks for a water-wet scenario for Reservoir Sandstone A (a) and Reservoir Sandstone B (b)

The physical rules implemented in the simulator are broadly similar to the ones used in [22, 34] with the exception of a major change in the film flow model which is presented in the next section. The geometry of the pore network is simplified into an ensemble of pore bodies connected through pore throats during the pore network extraction step. As the invasions are totally controlled by the geometry, there is no need to compute the pressure gradients. The invasion order is determined through the

capillary entry pressure of each element and the trapping is determined through a clustering algorithm. For every relative permeability point computation, the phases are isolated, and a pressure drop is applied to the network. The pressure is then solved, the corresponding production rate is computed, and effective permeability of each phase is determined through Darcy's law.

The network is initially filled with water. A primary drainage is first simulated in order to establish irreducible water saturation, S_{wi} . As the network is assumed water-wet, oil injection follows an invasion percolation regime. Water layers in pore elements with corners make water trapping very difficult and allow to achieve very low S_{wi} values.

Primary drainage is then followed with a waterflood after an aging process where oil filled pore wettability is changed — water filled pores remain water-wet. We note here that we enter receding contact angle distributions in primary drainage and advancing contact angle distributions in waterflood. First, water spontaneously fills the water-wet part of the network through piston like displacement and snap-off. In this phase the smallest pores are filled first, then the next smallest are filled, and so on. The defending oil phase can escape by flowing through oil-filled pores. Once spontaneous imbibition ends, the invading water is over pressured by applying a negative capillary pressure. Now, the largest pore elements are filled first, and oil can escape to the outlet either by flowing through the center of oil filled pores or through oil films. Once all the oil is trapped, the simulation stops.

The simulator has been parallelized to allow the simulation of large systems. First, the domain is decomposed, each processor is allocated memory and performs the computations of a subdomain. Each processor needs also information from the neighboring subdomains and this information is stored by each processor. The pore bodies and throats inside each subdomain of a processor are named local elements while the pore bodies and throats from neighbor subdomains are named ghost elements. Synchronization of the information of the ghost elements is performed after each capillary pressure step or after a maximum change in the network phases saturations. This communication is made using Message Passing Interface library MPI [14]. Furthermore, a parallel clustering algorithm has been implemented in order to determine if the defending phase is trapped and parallel linear solver library [6] is used for permeability and relative permeability computations.

We propose to test the accuracy and the robustness of our parallel pore network simulator for several networks and wettability scenarios. We consider two pore networks, the first is extracted from a Reservoir sandstone that we call Reservoir Sandstone B (320000 pore elements) and from a very heterogenous carbonate network that we call Reservoir Carbonate C (1 million pore elements). Subsequently, we perform waterflood simulations for oil-wet and water-wet wettability scenarios for sequential and distributed computations. Finally, we compare the relative permeability curves obtained from distributed

computations to the reference relative permeability obtained from sequential simulations.

Figure 6 and Figure 7 show that the relative permeability curves obtained from distributed computations were in good agreement with the reference sequential simulation for both networks and for the considered wettability scenarios. However, we point out that the parallelization introduces a small discrepancy with the sequential runs close to S_{or} for the water-wet cases. This is expected as S_{or} is controlled by the trapping in this case and a small perturbation of the filling order induced by the parallelization would impact the S_{or} . For the oil-wet case, there was a good agreement in the S_{or} between the sequential and parallel runs, as for this wettability scenario, the S_{or} is mainly controlled by the collapse of oil layers which is directly linked to the P_c value. In the formulation of our parallel algorithm, we took cautious care to have the same P_c in all the parallel process and thus we could achieve a good agreement in S_{or} for this case. Nevertheless, we observe a small discrepancy in the K_{rw} for low water saturations in the parallel runs compared to the reference run. This could be explained by the fact that, waterflood in an oil-wet rock is a physical drainage process, leading to an invasion percolation waterflood regime. It is well known that invasion percolation is an unstable invasion process where the injected fluid goes into the pore elements with the lowest capillary entry pressure and unlike imbibition processes where the water front is stabilized with cooperative pore filling, a capillary fingering flow regime is obtained. This flow regime creates a fast increase of the water relative permeability once water finger reaches the outlet. A small perturbation of the filling order caused by the temporary decoupling of the computations during the parallelization can lead to discrepancy we observe in K_{rw} .

Although a small discrepancy was observed between the sequential and parallel runs, a very good agreement was observed in the presented cases. We highlight that the presented validation cases are not the simplest for the parallelization as the networks were relatively small (comparing to the ones used in the paper) and were divided into relatively small domains (down to 7800 elements per CPU). In this work, we will use larger subnetworks for each CPU to have more efficient parallelization and to keep higher accuracy of the results.

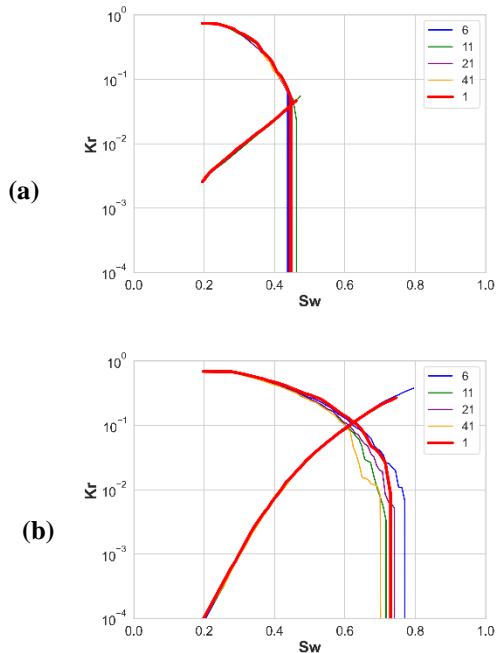


Figure 6: Comparison between waterflood k_r for a WW case with a varying number of CPUs for Reservoir Carbonate C (a) and Reservoir Sandstone B (b)

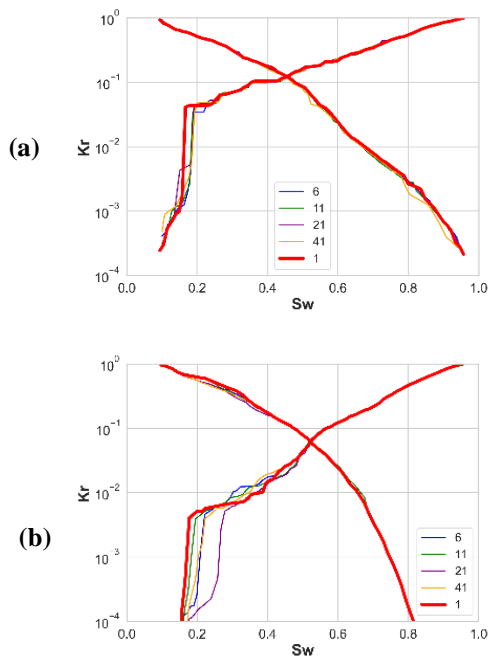


Figure 7 Comparison between several waterflood k_r for a OW case with a varying number of CPUs for Reservoir Carbonate C (a) and Reservoir Sandstone B (b)

2.2.2 Change of film flow hypothesis

Wettability is a key parameter in two-phase flow in porous media. Therefore, it is critical that any pore scale simulation technique can reproduce, at least qualitatively, the trends of the effects of a wettability change on relative permeability. Craig [8] presented the key features of strongly oil-wet and strongly water-wet relative permeability curves and their typical shapes. He showed that water relative permeability is higher in the strongly

oil-wet case compared to the strongly water-wet case. Moreover, he exposed that oil relative permeability in the oil-wet case is lower than that in the water-wet case. We would like to emphasize here that these are rules of thumbs for extreme wettability conditions. Several SCAL subsequent studies have agreed with these rules [18, 19, 21, 23] and the same qualitative behavior was observed between extreme wettability conditions. However, the PNM literature showed otherwise, and the behavior of the oil-wet water relative permeability curves was very different from the behavior and shape of the SCAL curves. In fact, in several modelling studies in the literature [1, 7, 36], the relative permeability of water in oil-wet scenarios was seen to stay very low until high water saturations. This is not consistent with experimental SCAL studies of relative permeability in strongly oil-wet scenarios [18] and it can cause a counter-intuitive trend leading to having relative permeability of water in strongly oil-wet scenario lower than the one in water-wet case [7, 36] which is inconsistent with Craig's rules and the experimental studies that have confirmed them.

McDougall and Sorbie [20] studied the impact of wettability on the relative permeability and their simulations were consistent with Craig's rule. They have seen that strongly oil-wet water relative permeability curves were higher than strongly water-wet ones. They have also observed that the opposite behaviour occurs for oil relative permeability. Unlike the previously cited PNM models McDougall and Sorbie [20] did not use the sandwiched layer model [15, 22, 34], they used instead a simpler pore network bonds model statistically generated with simplified layer physics. Besides, they started their simulations with no initial water in their network.

We propose that the inconsistency is caused by a historical modelling artefact in most PNM models which led to studies that showed the counter-intuitive behavior in k_{rw} in oil-wet systems.

Most of the models in the literature use the sandwiched oil layers model in which water layers remain in the corners in oil-wet pores after aging. This means that the water from S_{wi} is connected to the inlet through these layers which allows invasions starting from the S_{wi} . These invasions would increase the water saturation in the system during a waterflood without increasing the connectivity of the water between inlet and outlet thus resulting in very low water relative permeability curves until water saturations of 70% -80% (not observed experimentally). However, these layers have very small conductivity and are not able to transport large quantities of water.

This issue has been fixed in DynaPNM by disabling the connections of the water through the films in oil-wet pores and throats. This change in the layer modelling hypothesis had a large impact on water relative permeability in oil wet simulations (as we can see in the example of Figure 8). The water relative permeability increases very early in waterflood.

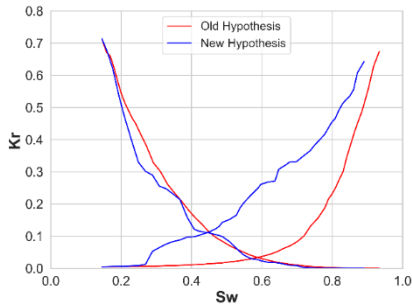


Figure 8 : Comparison between waterflood relative permeability curves for an oil-wet simulation on Reservoir Sandstone A network using the old (red) films connectivity hypothesis and the new one (blue)

2.2.3- Statistical uncertainty workflow

Sorbie and Skauge [32] have explained that several input parameters of pore network simulation are uncertain and presented the wettability assignment step as the most complex and least validated stage of the DRP workflow. There are other uncertain parameters of the DRP such as the amount of clay and the network used in the simulation (i.e. for some rocks, selected networks from different locations could give different simulation results). These uncertainties have been used by some researchers in the past in order to “tune” the simulation results to SCAL relative permeability curves. However, if one wants to be predictive, s/he should not know the result a priori and this makes choosing the uncertain parameters tricky. Therefore, we have developed a statistical uncertainty workflow in which we vary the uncertain pore network simulation parameters (wettability distribution, contact angle spatial location, clay volume, pore network ...). First, thousands of DynaPNM input files are generated in an experimental design phase using WSP method [31]. Subsequently, flow simulations are run on TOTAL’s supercomputer PANGAEA. This is followed by a simulation ranking exercise based on the oil production after a given amount of water injected corresponding to each Kr curve and allows us to define three scenarios:

- P10: an optimistic scenario in which only 10% of the simulations produce more than this case
- P50: a median scenario in which 50% of simulations produce more than this case
- P90: a pessimistic scenario in which 90% of the simulations produce more than this case

2.2.4- Contact angles in the simulations

Contact angle is a key input for PNM simulation as it controls the capillary entry pressures in the network. Several measurement techniques to characterize contact angles exist. Contact angle measurements from Micro-CT images of multiphase flow experiment has been very attractive recently. However, as these measurements use the 3 phase contact line for the computations, they are very sensitive to the image resolution and insufficient image resolution leads to contact angle values close to 90 degrees with very large standard deviation [33]. Furthermore, automated contact angle measurements, take into consideration the pinned menisci which are

different from the contact angle input needed by a PNM simulator. Therefore, we propose in this paper a different methodology to define the contact angle input. We use qualitative information about wettability to determine possible contact angle distributions to be used. This information feeds our uncertainty analysis approach described previously and therefore the simulation produces an envelope of relative permeability curves. Unfortunately, this can lead to large envelopes of relative permeability especially in Mixed-Wet scenarios where the contact angle distribution and the spatial assignment of contact angles can have an important impact on the results. In order to decrease this uncertainty and to constrain our wettability input further, we propose to perform a fast microplug scale DRP experiment in which we reach the residual oil saturation state. The Micro-CT image at Sor is then used to constrain the simulation wettability input by removing all the realizations/wettability inputs that are not in agreement with the Sor measured from the image. As it is well documented that Sor is correlated to wettability input [37], we think that this experiment helps us to obtain less uncertain simulation results. In the future, we plan to use additional information from the fast microplug scale experiment in order to constrain even further our PNM model.

Recent observations [11] have shown that wettability is correlated in space, and the pores having similar wettabilities are likely to be close. Furthermore, the same study has provided indications that contact angle is rather distributed following two distributions in aged samples. Therefore, we consider a fractional wettability model having two contact angle distributions with spatial correlation in our mixed-wet simulations.

3- Results

3.1. Wettability impact on relative permeability

Having built the DRP workflow, we proceed to its validation. As a first test, we would like to test if the PNM simulations agree with the widely used Craig’s rules of thumbs [8]. As mentioned earlier in the paper, unlike the SCAL literature, the PNM literature provides different trends and we think that it is the result of a historical modelling artefact. We run strongly water-wet and strongly oil-wet simulations on several networks. We report in Figure 9 and Figure 10 two examples of our results for Reservoir Sandstone A and Reservoir Sandstone B. We notice that our simulations reproduce well the Craig’s rule of thumb. Water relative permeability was higher in the strongly oil-wet simulation compared to the strongly water-wet one. Moreover, oil relative permeability was lower in the oil-wet case compared to the water-wet simulation.

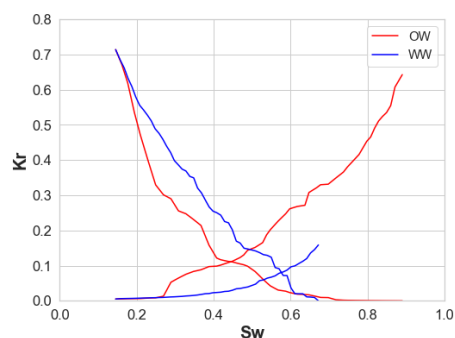


Figure 9 : Comparison between waterflood k_r of strongly water-wet with constant contact angle equal to 50° (blue) and strongly oil-wet with constant contact angle equal to 150° (red) simulations on Reservoir Sandstone A pore network

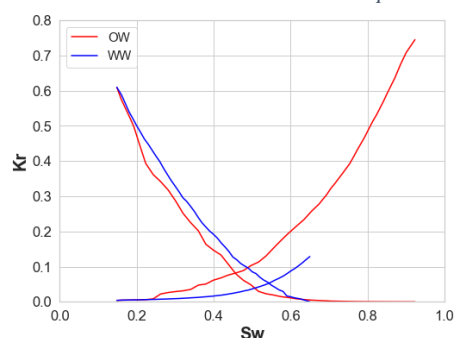


Figure 10 : Comparison between waterflood k_r of strongly WW with constant contact angle equal to 50° (blue) and strongly OW with constant contact angle equal to 150° (red) simulations on Reservoir Sandstone B pore network

3.2. Validation of DRP workflow against microplug experiments

In the last years, new techniques to perform steady-state relative permeability experiments at microplug scale have been developed [5, 12, 13, 16] allowing K_r measurements simultaneously with imaging of the fluids. These datasets are very suitable to validate pore scale simulators as they enable the simulation of the same volume used in the experiment. Furthermore, this data is rich and helps understand the limitations of the DRP simulation in case of discrepancy. We simulate three microplug simulations in this section in order to validate the physics in our simulator. In the three datasets, only a 1 cm long section was scanned at a resolution a priori acceptable for PNM simulations. Therefore, we propose to perform the simulations on this section and compare the simulation results to relative permeability curves estimated using DNS from the experiment multiphase images (called ‘experimental’ K_r in this section). Although the computed relative permeabilities would be limited by the image resolution, they allow us to compare simulated and ‘experimental’ K_r curves from the exact same volume and prevent discrepancies caused by the heterogeneity of the samples and/or by differences in the aspect ratios between the experiment and the simulated system.

To estimate the ‘experimental’ relative permeability curves from the multiphase flow images, we first segment the images to identify the voxels filled with oil, water and grain. This step has some uncertainty as a segmentation is

biased by user decisions. Then, a pressure gradient is applied between the inlet and outlet for each phase separately, and single phase OpenFOAM simulations are performed. The computed flow rate obtained for each phase is then used to compute the effective permeability of each phase using Darcy’s law and finally relative permeability curves are obtained by dividing the effective permeabilities by the absolute permeability. When the raw images of the experiments are available, we perform an uncertainty analysis on the segmentation to have an idea about the ‘experimental’ uncertainty.

Wettability is a key input for a PNM simulation and as discussed previously we use qualitative wettability information from the experiment as a first input to our experimental design usually resulting in large envelope of relative permeability curves especially for mixed-wet scenarios. Then, we constrain this input by only selecting the realisations that agree with the S_{or} of the steady-state experiments.

The first dataset that we consider is Reservoir Sandstone rock A without aging. The microplug experiment showed water-wet (WW) behavior characteristics [13]. Therefore, we have used the wettability input in Table 1. In our experimental design, 10000 realizations have been generated and simulated (with varying the seeds numbers, the parameters of the contact angle distributions as described in table 1 and wettability spatial correlation parameters). Next, only the realizations in agreement with S_{or} (difference less than 5%) have been kept. Finally, the results have been ranked at 10 PV injected and, P10, P50 and P90 scenarios were established. Figure 11 shows that the simulated relative permeabilities agree well with the experimental curves. We point out that the experimental S_{wi} depends on the segmentation of the experimental images. As we performed an experimental uncertainty analysis that takes into account the various segmentations, we could find a range of S_{wi} values. For simplicity, we only considered S_{wi} in the simulation (as an input parameter) from the base case experimental images segmentation.

Table 1 : Waterflood wettability parameters used in simulations of WW Reservoir Sandstone A

	Value/Range
WF advancing contact angle distribution	Normal distribution
WF advancing contact angle standard deviation	1° - 10°
Mean advancing WF contact angle	50° - 80°

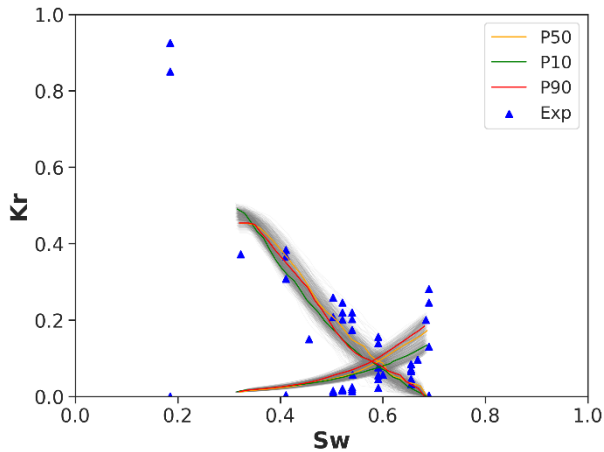


Figure 11: Comparison between simulated and 'experimental' (computed from experimental images at several fw) relative permeability curves for WW Reservoir Sandstone A

Then, we simulate a second dataset of Reservoir Sandstone A with aging. The microplug experiment showed mixed-wet (MW) behavior characteristics [13]. We have then used the simulation workflow described above and the wettability input of Table 2. Figure 12 shows that the simulated oil relative permeability is within the experimental envelope. The water relative permeability is in good agreement with the experimental curve for low and medium saturation values but is slightly higher close to Sor.

Table 2 : Waterflood wettability parameters used in simulations of MW Reservoir Sandstone A

	Value/Range
WF advancing contact angle distribution	Normal distribution
WF dist1, advancing contact angle standard deviation	1°-10°
Mean advancing WF dist1 contact angle	100°-130°
WF dist 2 advancing contact angle distribution	normal
WF dist2, advancing contact angle standard deviation	5°- 20°
Mean advancing WF dist2 contact angle	91°-100°
Fraction of distribution 2	0.35-0.75
Correlation length	3-5

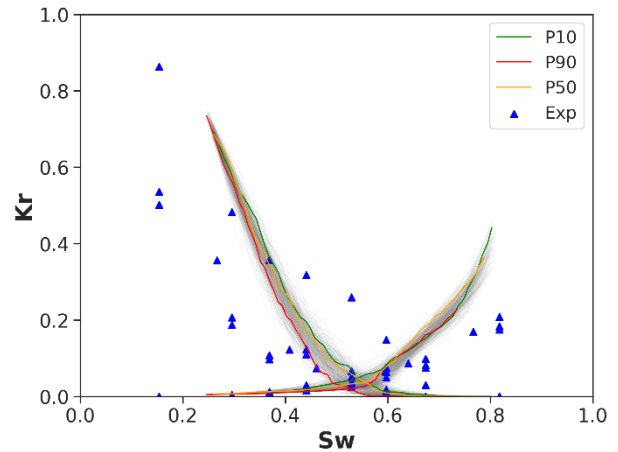


Figure 12: Comparison between simulated and 'experimental' (computed from experimental images at several fw) relative permeability curves for MW Reservoir Sandstone A

Finally, we simulate a dataset of Bentheimer with aging. The microplug experiment showed mixed-wet behavior characteristics [17]. We have then used the simulation workflow described above and the wettability input of Table 3. Figure 13 shows that the simulated water relative permeability is in good agreement with the experiment. The simulated oil relative permeability is however slightly higher than the experimental values. Unfortunately, we didn't have access to the grey scale images of this experiment and therefore could not establish the experimental uncertainty for this dataset. Overall, the agreement was satisfactory between the three datasets and our simulation results.

Table 3 : Waterflood wettability parameters used in simulations of MW Bentheimer

	Value/Range
WF advancing contact angle distribution	Normal distribution
WF dist1, advancing contact angle standard deviation	5°-20°
Mean advancing WF dist1 contact angle	110°-140°
WF dist 2 advancing contact angle distribution	normal
WF dist2, advancing contact angle standard deviation	5°- 10°
Mean advancing WF dist2 contact angle	75°-100°
Fraction of distribution 2	0.5-0.65
Correlation length	4-6

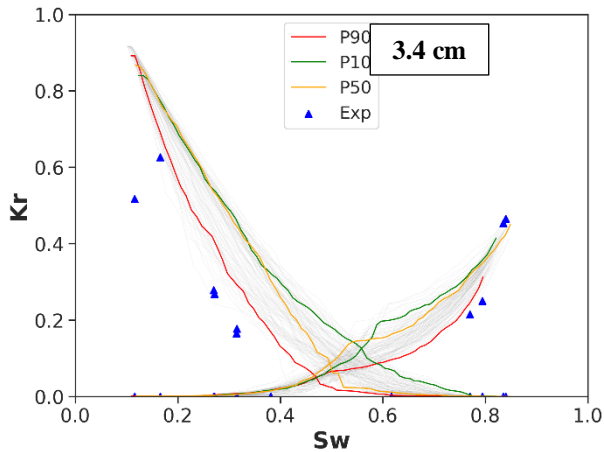


Figure 13: Comparison between simulated and 'experimental' (computed from experimental images at several fw) relative permeability curves for MW Bentheimer

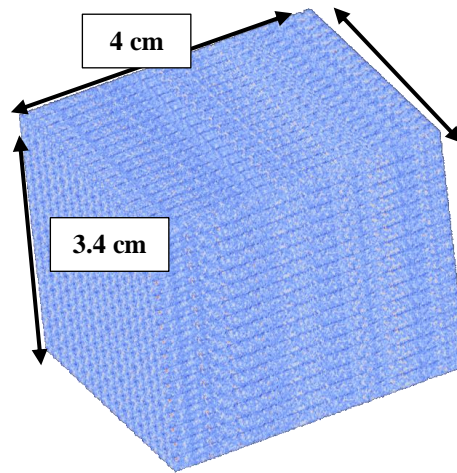


Figure 15: Bentheimer pore network obtained from lateral multiplication of network of Figure 14. This network represents an image of 8480*8480*10000 voxels

3.3. Large scale simulations

We present in this section an example of large-scale simulations on Bentheimer. We start from an image of Bentheimer (560*560*10000) acquired at 4 microns resolution. We extract a pore network from this image from 13 extractions stitched together. This results in a pore network with 242k elements (Figure 14). Although this network is not small, our PNM simulator can handle much larger volumes. Therefore, we perform several PNM duplications by periodicity in the lateral direction in order to achieve large volumes. The original and duplicated networks are linked together via newly generated throats with Delaunay triangulation algorithm [9]. After 16 duplications in each lateral direction, we obtain a pore network having 63 million elements, representing an image of 8480*8480*10000 voxels and representing a physical volume of 46 cm³ which is a typical size of plugs used in MICP measurements.

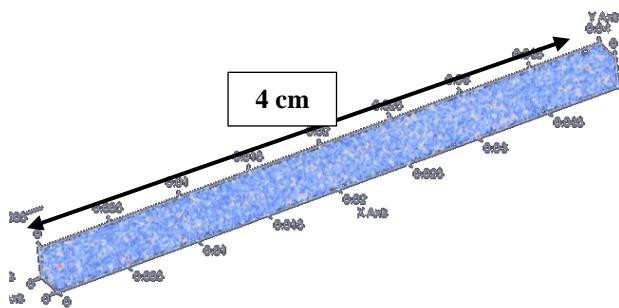


Figure 14: Bentheimer pore network obtained by 13 stitched extractions from 560*560*10000 voxels image

The parallelization of our flow simulator resulted in faster computations and made large networks simulations possible. For instance, simulating a primary drainage, followed by waterflood with Kr computations on the large Bentheimer network (Figure 15) took 6.5 hours with 81 CPUs. This simulation was two orders of magnitude faster than a sequential simulation on the same network. Figure 16 shows the simulation time evolution by varying number of CPUs used. We see that the simulation time decreases very fast with more CPUs to reach an optimal speed-up for 81 cores. Then, it stabilizes and starts increasing meaning that the number of pore elements in each core domain becomes too small to take advantage of the parallelization.

These are, to our knowledge, the largest PNM simulations (in terms of number of pore elements) ever reported in the literature. We think that we can even simulate larger networks as we did not reach yet the limits of our PNM simulator.

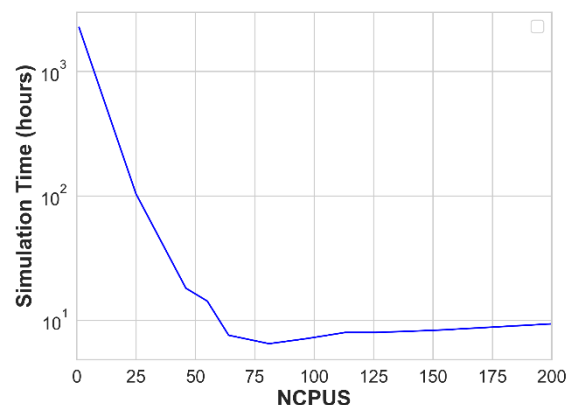


Figure 16: Simulation time on 21 million pore bodies network (representing 46cm³ volume) as a function of the number of CPUS

Being able to simulate large volumes enables us to investigate the impact of image size used in DRP on the dispersion of the results. We crop several networks from a large Bentheimer network obtained as described above.

Subsequently, we simulate primary drainage and waterflood on several realizations of each cropped pore network. Figure 17, Figure 18 and Figure 19 show that the larger the image/network the smaller the variability. This reduction of the dispersion is both due to the reduction of the finite size effect as the number of elements in the network increases and by the fact that more heterogeneity is taken into account in the larger pore networks being closer to REV. However, it is difficult to speak about REV for this case as we are limited by the information available from the image.

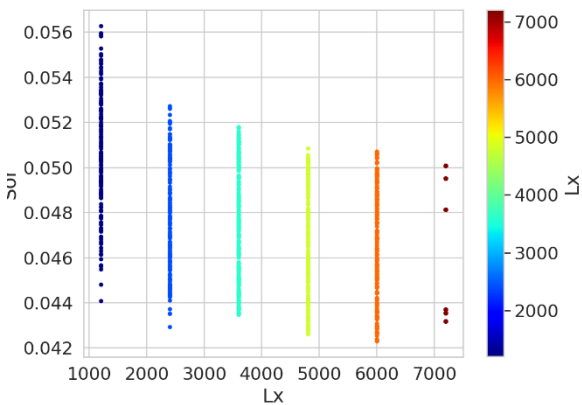


Figure 17: Evolution of the Sor dispersion with varying size of Bentheimer cubic image for an oil-wet system

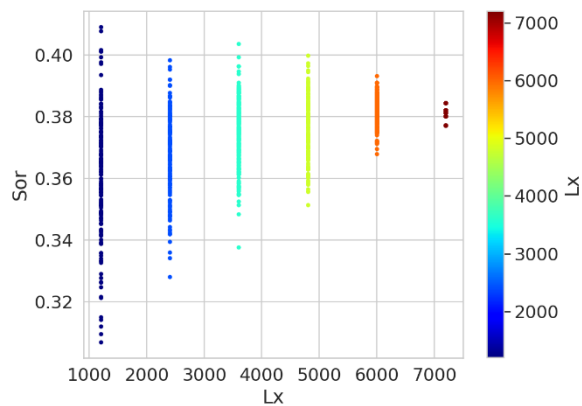


Figure 18: Evolution of the Sor dispersion with varying size of Bentheimer cubic image for a water-wet system

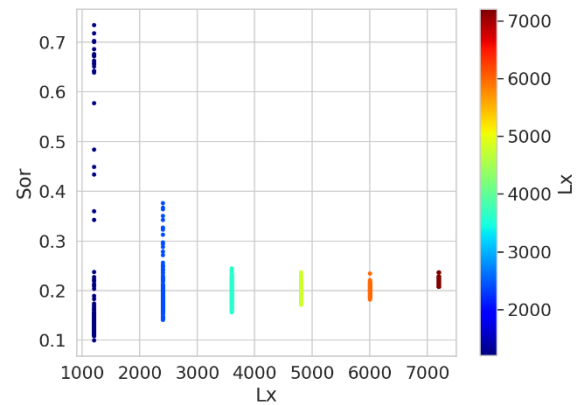


Figure 19 : Evolution of the Sor dispersion with varying size of Bentheimer cubic image for a mixed-wet system

3.4. Validation of DRP workflow against SCAL experiment

Having validated our PNM simulations against microplug experiments, we perform a comparison against a SCAL experiment performed on Reservoir Sandstone B. We acquired an image of size 1300*1300*6358 voxels at 1.5 microns resolution and extracted a pore network having 1.7 million pore elements. To avoid adding bias to our simulations, we propose to use the same aspect ratio as the experiment (equal to 5), and we avoid making network duplications along the flow direction. As our image has the same aspect ratio as the experiment, the largest network that we could use is the network extracted from the full image. First, we check if we reach reasonable dispersion using this network. The full sample image is equivalent to a 2200³ image and we observe that for OW and WW the Sor value had stabilized and that the dispersion became reasonable.

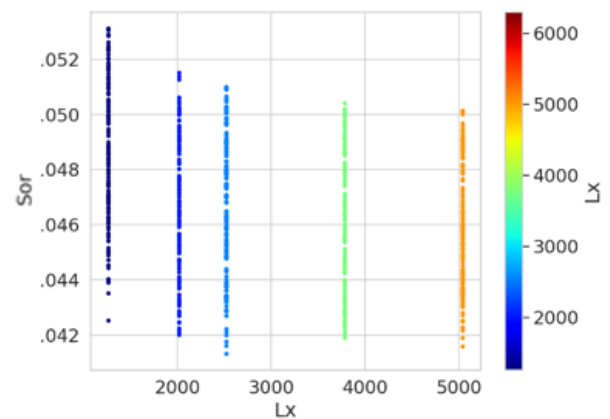


Figure 20 : Evolution of the Sor dispersion with varying size of Reservoir Sandstone B cubic image for an oil-wet system

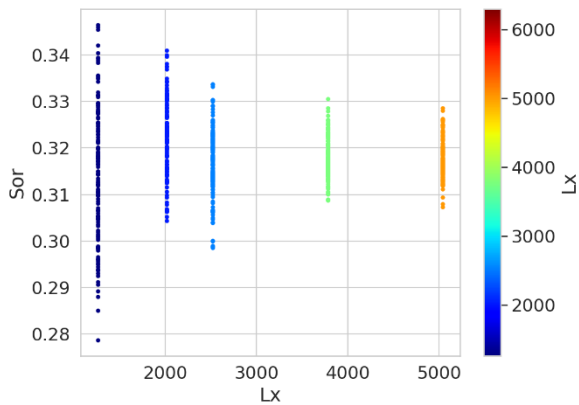


Figure 21 : Evolution of the Sor dispersion with varying size of Reservoir Sandstone B cubic image for a water-wet system

The SCAL experiment has shown water-wet or mixed-wet with large water-wet characteristics. In fact, the oil production was fast and the Sor was high. Therefore, this qualitative information has been used in the simulation. An experimental design was used to generate 1996 realizations. These were run using DynaPNM, the simulated relative permeability curves were ranked at 10 PV injected and, P10, P50 and P90 scenarios were subsequently established. We did not have a microplug experiment for this dataset, therefore we did not use the Sor image to discard some realizations and we report here all the simulated 1996 realizations. Figure 22 shows that the simulated relative permeabilities is in good agreement with the experimental Kr curve. Furthermore, Figure 23 shows that the simulated Sor was close to the experimental residual oil saturation. This gives us confidence of the robustness of our simulation workflow. Although, the agreement was good between the simulations and experiment for this sample without using Sor image of a fast experiment to constrain the wettability input in the simulation, we do not think that this result is guaranteed and we believe that for different cases – especially for mixed-wet cases with more oil-wet fraction, that an experimental input is needed to keep the uncertainty of the PNM simulations reasonable.

Table 4 : Wettability parameters used in the simulation of the SCAL experiment performed on Reservoir Sandstone B

	Value/Range
WF advancing contact angle distribution	Normal distribution
WF dist1, advancing contact angle standard deviation	4°-8°
Mean advancing WF dist1 contact angle	100°-120°
WF dist 2 advancing contact angle distribution	normal
WF dist2, advancing contact angle standard deviation	4°- 8°
Mean advancing WF dist2 contact angle	40°-75°
Fraction of distribution 2	0.65-0.99
Correlation length	1-6

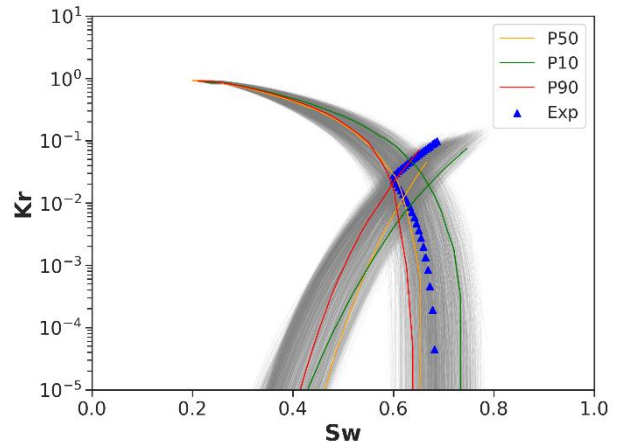


Figure 22 : Comparison between simulated and SCAL experimental relative permeability curves for Reservoir Sandstone B

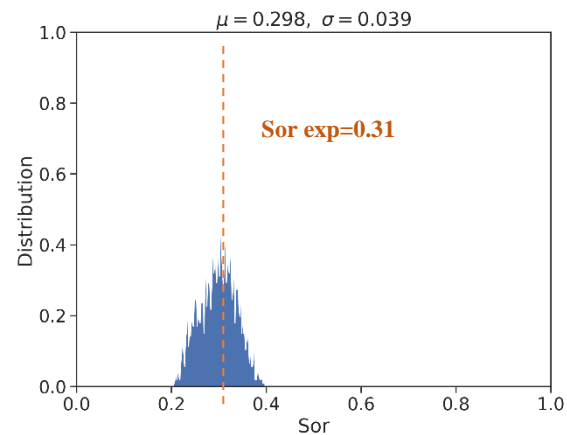


Figure 23: Comparison between simulated (blue) and experimental (orange) Sor value for Reservoir Sandstone B

4- Conclusions

In this paper, we have presented TOTAL’s DRP workflow for multiphase flow simulation and relative permeability estimation. First, an upscaled version of the segmented image was built in the form of a pore network with single phase Direct Numerical Simulation performed to compute the conductivities of the pores. This allows us to get the accuracy of DNS and the computational efficiency of PNM. The network extraction was then completed by a stitching algorithm that allows the extraction of larger volumes and overcome the memory limitations of the extraction code. This network feeds our in-house pore network simulator DynaPNM. The parallelization of DynaPNM unlocked the simulations on networks with tens of million pore elements in few hours and made possible the simulation of plug scale volumes (with few microns resolution). These simulations are to our knowledge the largest PNM simulations (in terms of number of pore elements) ever reported in the literature.

We have made a change in the way to model water films in oil-wet pores to correct a historical modeling artefact in

PNM which is seen to have a very large impact on simulation accuracy in oil-wet and mixed-wet scenarios.

After this change, we show that our simulation workflow reproduced the relative permeability trends with respect to changes of wettability that are consistent with the well-known Craig's rule. Subsequently, we have validated our simulations against three relative permeability experiments performed on microplugs and against a SCAL dataset. The agreement was satisfactory for all cases; however, more validation work is required to test further the robustness of the workflow for more rocks and wettability configurations.

For the future, we plan to constrain further our PNM simulations in order to reduce the uncertainty and dispersion in our results. We would also like to have more heterogeneity information in our simulations by using larger rock images.

Acknowledgements

The authors would like to thank TOTAL management for the authorization to publish this work. Dr. Franck Nono, Régis Brugidou and Dr. Maria Repina are acknowledged for acquiring and processing some of the images used in this work. We would like to thank Dr Branko Bijeljic, Dr Ali Raeini and Prof. Martin Blunt for the technical discussions and providing some experimental data used in this study.

References

- Al-Futaisi, A., Patzek, T.W.: Secondary imbibition in NAPL-invaded mixed-wet sediments. *Journal of contaminant hydrology* **74**(1-4), 61–81 (2004)
- Alhammadi, A.M., AlRatrou, A., Singh, K., Bijeljic, B., Blunt, M.J.: In situ characterization of mixed-wettability in a reservoir rock at subsurface conditions. *Scientific Reports* **7**(1), 1–9 (2017)
- AlRatrou, A., Raeini, A.Q., Bijeljic, B., Blunt, M.J.: Automatic measurement of contact angle in pore-space images. *Advances in Water Resources* **109**, 158–169 (2017). doi: 10.1016/j.advwatres.2017.07.018
- Andrew, M., Bijeljic, B., Blunt, M.J.: Pore-scale contact angle measurements at reservoir conditions using X-ray microtomography. *Advances in Water Resources* **68**, 24–31 (2014)
- Bagudu, U., McDougall, S.R., Mackay, E.J.: Pore-to-Core-Scale Network Modelling of CO₂ migration in Porous Media. *Transport in Porous Media* **110**(1), 41–79 (2015). doi: 10.1007/s11242-015-0556-z
- Balay, S., Abhyankar, S., Adams, M., Brown, J., Brune, P., Buschelman, K., Dalcin, L., Dener, A., Eijkhout, V., Gropp, W.: PETSc users manual (2019)
- Bondino, I., Hamon, G., Kallel, W., Kac, D.: Relative Permeabilities From Simulation in 3D Rock Models and Equivalent Pore Networks: Critical Review and Way Forward. *SPWLA-2012-v53n6a2* **54**(06), 538–546 (2013)
- Craig, F.F.: The reservoir engineering aspects of waterflooding, vol. 3. HL Doherty Memorial Fund of AIME New York (1971)
- Delaunay, B.: Sur la sphere vide. *Izv. Akad. Nauk SSSR, Otdelenie Matematicheskii i Estestvennyka Nauk* **7**(793-800), 1–2 (1934)
- Dong, H., Blunt, M.J.: Pore-network extraction from micro-computerized-tomography images. *Physical review E* **80**(3), 36307 (2009)
- Foroughi, S., Bijeljic, B., Lin, Q., Raeini, A.Q., Blunt, M.J.: Pore-by-pore modeling, analysis, and prediction of two-phase flow in mixed-wet rocks. *Phys. Rev. E* **102**(2), 23302 (2020). doi: 10.1103/PhysRevE.102.023302
- Gao, Y., Lin, Q., Bijeljic, B., Blunt, M.J.: X-ray Microtomography of Intermittency in Multiphase Flow at Steady State Using a Differential Imaging Method. *Water Resour. Res.* **53**(12), 10274–10292 (2017). doi: 10.1002/2017WR021736
- Gao, Y., Raeini, A.Q., Selem, A.M., Bondino, I., Blunt, M.J., Bijeljic, B.: Pore-scale imaging with measurement of relative permeability and capillary pressure on the same reservoir sandstone sample under water-wet and mixed-wet conditions. *Advances in Water Resources* **146**, 103786 (2020). doi: 10.1016/j.advwatres.2020.103786
- Gropp, W., Gropp, W.D., Lusk, E., Lusk, Argonne Distinguished Fellow Emeritus Ewing, Skjellum, A.: Using MPI: portable parallel programming with the message-passing interface, vol. 1. MIT press (1999)
- Kovscek, A.R., Wong, H., Radke, C.J.: A pore-level scenario for the development of mixed wettability in oil reservoirs. *AIChE Journal* **39**(6), 1072–1085 (1993)
- Lin, Q., Bijeljic, B., Pini, R., Blunt, M.J., Krevor, S.: Imaging and Measurement of Pore-Scale Interfacial Curvature to Determine Capillary Pressure Simultaneously With Relative Permeability. *Water Resour. Res.* **54**(9), 7046–7060 (2018). doi: 10.1029/2018WR023214
- Lin, Q., Bijeljic, B., Berg, S., Pini, R., Blunt, M.J., Krevor, S.: Minimal surfaces in porous media: Pore-scale imaging of multiphase flow in an altered-wettability Bentheimer sandstone. *Physical review E* **99**(6), 63105 (2019)
- Masalmeh, S.K. (ed.): The Effect of Wettability on Saturation Functions and Impact on Carbonate Reservoirs in the Middle East. Society of Petroleum Engineers (2002)
- Masle, M., Youssef, S., Deschamps, H., Vizika, O.: In-Situ Investigation of Aging Protocol Effect on Relative Permeability Measurements Using High-Throughput Experimentation Methods. *SPWLA-2012-v53n6a2* **60**(04), 514–524 (2019)
- McDougall, S.R., Sorbie, K.S.: The Impact of Wettability on Waterflooding: Pore-Scale Simulation. *SPE-25271-PA* **10**(03), 208–213 (1995). doi: 10.2118/25271-PA
- Morrow, N.R., Cram, P.J., McCaffery, F.G.: Displacement studies in dolomite with wettability control by octanoic acid. *Society of Petroleum Engineers Journal* **13**(04), 221–232 (1973)
- Oren, P.-E., Bakke, S., Arntzen, O.J.: Extending predictive capabilities to network models. *SPE journal* **3**(04), 324–336 (1998)

23. Owens, W.W., Archer, D.: The effect of rock wettability on oil-water relative permeability relationships. *Journal of Petroleum Technology* **23**(07), 873–878 (1971)
24. Raeini, A.Q., Blunt, M.J., Bijeljic, B.: Modelling two-phase flow in porous media at the pore scale using the volume-of-fluid method. *Journal of Computational Physics* **231**(17), 5653–5668 (2012). doi: 10.1016/j.jcp.2012.04.011
25. Raeini, A.Q., Bijeljic, B., Blunt, M.J.: Generalized network modeling of capillary-dominated two-phase flow. *Physical review. E* **97**(2-1), 23308 (2018). doi: 10.1103/PhysRevE.97.023308
26. Raeini, A.Q., Yang, J., Bondino, I., Bultreys, T., Blunt, M.J., Bijeljic, B.: Validating the Generalized Pore Network Model Using Micro-CT Images of Two-Phase Flow. *Transport in Porous Media* **130**(2), 405–424 (2019). doi: 10.1007/s11242-019-01317-8
27. Regaieg, M., Moncorgé, A.: Adaptive dynamic/quasi-static pore network model for efficient multiphase flow simulation. *Computational Geosciences* **21**(4), 795–806 (2017)
28. Ryazanov, A.V., van Dijke, M.I.J., Sorbie, K.S. (eds.): *Pore-network prediction of residual oil saturation based on oil layer drainage in mixed-wet systems*. Society of Petroleum Engineers (2010)
29. Saxena, N., Hofmann, R., Alpak, F.O., Dietderich, J., Hunter, S., Day-Stirrat, R.J.: Effect of image segmentation & voxel size on micro-CT computed effective transport & elastic properties. *Marine and Petroleum Geology* **86**, 972–990 (2017)
30. Scanziani, A., Singh, K., Blunt, M.J., Guadagnini, A.: Automatic method for estimation of in situ effective contact angle from X-ray micro tomography images of two-phase flow in porous media. *Journal of colloid and interface science* **496**, 51–59 (2017). doi: 10.1016/j.jcis.2017.02.005
31. Sergeant, M.: *Contribution de la Méthodologie de la Recherche Expérimentale à l'élaboration de matrices uniformes: Application aux effets de solvants et de substituants*. Aix-Marseille 3 (1989)
32. Sorbie, K.S., Skauge, A.: Can Network Modeling Predict Two-Phase Flow Functions? SPWLA-2012-v53n6a2 **53**(06), 401–409 (2012)
33. Sun, C., McClure, J.E., Mostaghimi, P., Herring, A.L., Meisenheimer, D.E., Wildenschild, D., Berg, S., Armstrong, R.T.: Characterization of wetting using topological principles. *Journal of colloid and interface science* **578**, 106–115 (2020)
34. Valvatne, P.H., Blunt, M.J.: Predictive pore-scale modeling of two-phase flow in mixed wet media. *Water Resour. Res.* **40**(7) (2004)
35. Yang, J.: *Multi-scale simulation of multiphase multi-component flow in porous media using the Lattice Boltzmann Method* (2013)
36. Zhao, X., Blunt, M.J., Yao, J.: Pore-scale modeling: Effects of wettability on waterflood oil recovery. *JOURNAL OF PETROLEUM SCIENCE AND ENGINEERING* **71**, 169–178 (2010). doi: 10.1016/j.petrol.2010.01.011
37. Zhou, X., Morrow, N.R., Ma, S.: Interrelationship of wettability, initial water saturation, aging time, and oil recovery by spontaneous imbibition and waterflooding. *SPE journal* **5**(02), 199–207 (2000)

Calcite-functionalized micromodels for pore-scale investigations of CO₂ storage security

Malin Haugen^{1,*}, Benyamine Benali¹, Tore Føyen^{1,2}, Wen Song³, Martin A. Fernø¹, and Bergit Brattekkås¹

¹Department of Physics and Technology, University of Bergen, Norway

²SINTEF Industry, Norway

³Hildebrand Department of Petroleum and Geosystems Engineering, University of Texas at Austin, USA

Abstract. Carbon capture and subsequent storage (CCS) is identified as a necessity to achieve climate commitments. Permanent storage of carbon dioxide (CO₂) in subsurface saline aquifers or depleted oil and gas reservoirs is feasible, but large-scale implementation of such storage has so far been slow. Although sandstone formations are currently most viable for CO₂ sequestration, carbonates play an important role in widespread implementation of CCS; both due to the world-wide abundance of saline aquifers in carbonate formations, and as candidates for CO₂-EOR with combined storage. Acidification of formation brine during CO₂ injection cause carbonate dissolution and development of reactive flow patterns. Using calcite-functionalization of micromodels we experimentally investigate fundamental pore-scale reactive transport dynamics relevant for carbonate CO₂ storage security. Calcite-functionalized, two-dimensional and silicon-based, pore scale micromodels were used. Calcite precipitation was microbially induced from the bacteria *Sporosarcina pasteurii* and calcite grains were formed *in-situ*. This paper details an improved procedure for achieving controlled calcite precipitation in the pore space and characterizes the precipitation/mineralization process. The experimental setup featured a temperature-controlled micromodel holder attached to an automatic scanning stage. A high-resolution microscope enabled full-model (22x27 mm) image capture at resolution of 1.1 μm/pixel within 82 seconds. An in-house developed image-analysis python script was used to quantify porosity alterations due to calcite precipitation. The calcite-functionalized micromodels were found to replicate natural carbonate pore geometry and chemistry, and thus may be used to quantify calcite dissolution and reactive flow at the pore-scale.

1 Introduction

Commitments to reach climate goals require us to reduce greenhouse gas concentrations in the atmosphere. Carbon capture, utilization, and storage (CCUS) is identified to play a critical role in achieving these goals. In the Clean Technology Scenario presented by IEA, CCUS is the third-largest contributor (13%) to the cumulative emission reduction until 2060 [1]. Among other, CO₂ can be stored in deep saline aquifers within sandstone or carbonate formations. However, two of the possible risk aspects related to CO₂ storage is the potential for leakage to the surface and, for carbonate formations, dissolution of the reactive calcite rock minerals. The storage potential in carbonate reservoirs is large, but the reactive transport and mechanisms must be accounted for.

Biom mineralization is the formation of minerals by living organisms. Microbial induced calcite precipitation (MICP) has been researched in conjunction with different engineering applications, for instance within construction engineering to seal fracture or strengthen concrete [2], for enhanced oil recovery [3, 4], to constrain contaminated groundwater [5], for cementation of unconsolidated porous media [6], and for CO₂ sequestration by reduction of permeability in fractured rock to potential seal leakage paths in the near well area and/or in the cap-rock [7-9].

Precipitation of calcium carbonate (CaCO₃) is controlled by four key factors: (1) concentration of calcium (Ca²⁺) from the cementation solution, (2) concentration of dissolved inorganic carbon as produced by ureolysis, see equation 1-5 in section 2.2, (3) pH value, and (4) availability of nucleation sites [10]. CaCO₃ precipitation is dependent on presence of sufficient

calcium and carbonate ions to ensure that the ion activity product exceed the solubility product, making the system oversaturated and precipitation of calcium carbonate is likely. Microbial metabolic activity influence key factor no. 2 and 3, and also no. 4 by function as nucleation site [2]. Calcium carbonate is a common element found in many rocks, such as chalk and marble, it is also the main component in shells, pearls, and corals. CaCO₃ can crystallize in different polymorphs, seen as minerals in the nature. This includes calcite, vaterite and aragonite, with calcite as the most stable, and two hydrated polymorphs in addition to several amorphous phases (ACC) [11]. Vaterite is the least thermodynamically stable polymorph and transforms rapidly to calcite or aragonite in aqueous solutions. According to Ostwald's rule of stages, metastable polymorphs are first formed and then transform into thermodynamically more stable polymorphs [12]. For high supersaturation values it is reported that calcite is initially precipitated as the hydrous form of ACC (tens to hundreds of nanometer) which are subsequently transformed into spherical vaterite and later calcite, while lower supersaturation values lead to direct calcite precipitation [13, 14].

A bacteria often used for studying of MICP in the laboratory is the soil bacteria *Sporosarcina pasteurii* [3, 15-18]. In this research this bacteria have also been utilized, with the goal to build upon work by Song et al. 2018 [18] and present an improved procedure to functionalize the pore space in a micromodel with CaCO₃ and enable recording of continuous full-model images. A micromodel is a device with a porous pattern from a representative rock matrix etched into a silicon wafer

* Corresponding author: malin.haugen@uib.no

before an optical transparent glass plate is bonded on top. It has four fluid flow ports, one in each corner, with an open fracture connecting two pairs of flow ports (Fig.). This device enable direct study of microscale interactions between fluids and rocks. By functionalizing micromodels with an existing pore-network made of silica grains, it is possible to both precipitate and dissolve CaCO_3 minerals and still re-use the micromodel afterwards. This starting point is therefore of great interest during study of fundamental pore-level reactive transport dynamics that determine CO_2 storage security in carbonate formations. MICP in micromodels have also been studied by Wang [19, 20], where, among other, the effect of bacterial cells was studied as well as evolution of shape and size of the CaCO_3 precipitates during the MICP process. In this paper we are adding quantification of change in porosity due to CaCO_3 precipitation and pressure development throughout experiments.

The experimental set-up was designed to facilitate flow experiments at pressures between 0-120 bars and temperatures between 25-40 °C. Because of the dependency on the biological process, it is important to regulate the temperature to adjust the growth rate of the bacteria. Further, the tubing and valves included in the set-up provide a low, constant, dead volume. The possibility of independent injection and production from each of the four ports in the micromodel, combined with injection of bacterial solution through a loop with constant volume provide excellent experimental conditions. The result is a permeable porous model with carbonate grains distributed throughout the whole pore volume.

By utilizing an in-house built program, we can calculate change in porosity, and among other, identify area of representative elementary volume. The utilized microscope has an automatic scanning stage and a fluorescence module, which enable us to capture the complete porous network (22x27 mm) with resolution of 1.1 $\mu\text{m}/\text{pixel}$. This paper starts with an overview of the micromodel and bacteria utilized to functionalize the micromodel with calcium carbonate. Then, the experimental set-up and equipment is described, followed by the experimental procedures. Results in the form of images, porosity development due to in-situ CaCO_3 precipitation and relevance to CO_2 sequestration are presented, before concluding remarks.

2 Materials and methods

2.1 Micromodel

Direct study of microscale interactions between fluids and rocks at elevated reservoir temperature and pressure were enabled by microfluidic devices, further referred to as micromodels. The micromodels consist of two parts, an optical transparent borosilicate glass plate bonded on top of a silicon wafer with etched pattern of a representative porous rock matrix. The state-of-the-art etching method provides a two-dimensional porous system with representative pore-scale geometry with vertical grain walls, sharp edges, and a hydrophilic surface.

The porous network is based on thin sections from natural sandstone, a rock type widely used in laboratory flow experiments for enhanced oil recovery and/or CO_2

storage. Dead-end and isolated pores in the thin section were modified in the micromodel to enable flow across the whole pattern, resulting in higher micromodel porosity and permeability compared to the natural sandstone sample. A unique porous network (6.74 x 2.50 mm) was extracted from the thin section and etched in the silicon wafer with a constant depth of 30 μm . The unique pore pattern was repeated 36 times (4 x 9), resulting in a total porous network which is 27.0 x 22.5 mm large (Fig. 1). The grains are discontinuous and irregularly shaped, providing flow tortuosity. In each corner, a port through the silicon wafer can connect the pore network to external fluid flow tubes. Two open channels between ports improve flow communication and sweep of the pore space. Further details about design and production procedures can be found in [21] and [22].

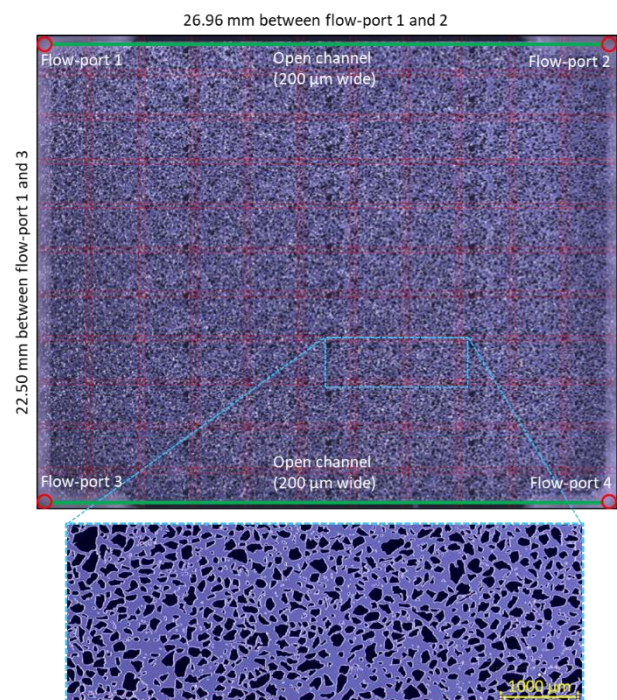


Fig. 1. Full-model image of a micromodel including dimensions. The four flow-ports and the two open-channel fractures between two pairs of ports are highlighted. A pattern generated from thin sections of natural sandstone is repeated 36 times to create the micromodel porous network. A zoom-in of the repeated pattern is highlighted in blue. The full-model image is generated from 121 individual images automatically captured by the microscope software with 10% overlap (shown in red dotted lines), stitched together to one image.

Micromodel properties are listed in Table 1, as previously reported by Benali et.al (2021) [23]. Stitched full-model images were analyzed to determine grain size distribution, pore throat length distribution (defined as the shortest pore space distance between two neighboring grains) and porosity. Porosity was quantified to 0.61 based on amount of pore space to the total area (grains + pore space) and the total micromodel pore volume (PV) was 11.1 μL . Fig. 2 shows the distribution of grains and pore throat length in the micromodel. Average grain size is calculated to 6 464 μm^2 and average pore throat length is 41 μm , with the shortest pore throat being 0.7 μm with square or rectangular cross-section.

Table 1. Micromodel properties

Parameter	Value
Width	27.0 mm
Length	21.4 mm
Depth	30 μm
Porosity	0.61
Pore volume	11.1 μL
Permeability	2.97 D
Repetition of pattern	36
Grain size	0.5 - 78 366 μm^2
Pore throat length	0.7 - 194 μm

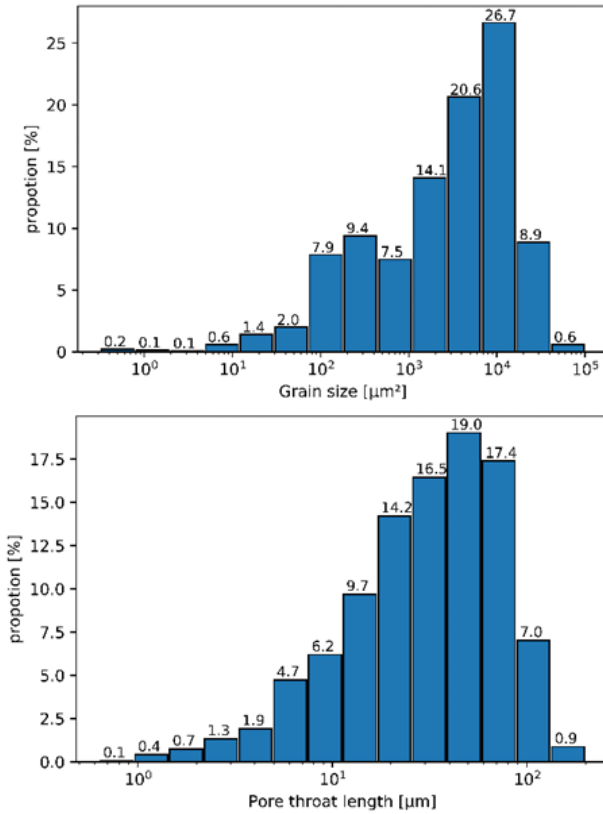


Fig. 2. Distribution of grain size (top) and pore throat length (bottom) in one of the 36 pore network repetitions which make up the micromodel.

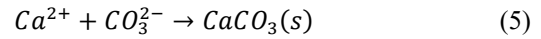
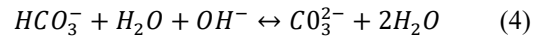
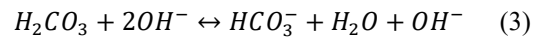
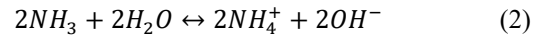
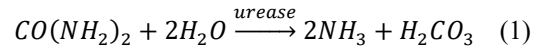
The work presented here describes the experimental set-up and method to functionalize micromodels with calcium carbonate grains utilizing bacteria. This enables experimental investigations of fundamental pore-scale reactive transport dynamics in carbonate rocks.

2.2 *Sporosarcina pasteurii* bacteria

To functionalize micromodels with calcium carbonate for pore-scale investigations of CO_2 storage security, microbially induced calcite precipitation (MICP) by urea hydrolysis have been utilized. The bacteria *Sporosarcina pasteurii*, formerly *Bacillus pasteurii*, (Miquel 1889) DSM33 [24] are urease positive [25] and has a known ability to enable calcite precipitation [15] and growth on solid surfaces [2, 3]. The bacterial cells are gram positive,

motile and rod shaped with size in the range of 0.5-1.2 x 1.3-4.0 μm [25]. This is an aerobic bacteria with optimum growth temperature and pH of 30 $^\circ\text{C}$ and 9, respectively [25].

The MICP process has been studied by several researchers and the following equations (Eq.1-5) have typically been used to describe this process [2, 7, 17, 26]. The bacteria hydrolyze urea ($\text{CO}(\text{NH}_2)_2$) into ammonia (NH_3) and carbonic acid (H_2CO_3), see Eq.1. In solution this leads to production of (OH^-) and accumulation of ammonium (NH_4^+). As a result of increasing (OH^-) concentration, the pH in the microenvironment is increasing (Eq. 2 and 3), and subsequently causes carbonic acid to be converted to bicarbonate (HCO_3^-) and further to carbonate ions (CO_3^{2-}) (Eq.4). When calcium ions (Ca^{2+}) are added to the solution, the increasing pH also leads to precipitation of calcium carbonate (CaCO_3) [3, 7] when the solution is supersaturated with calcium- and carbonate- ions (Eq.5). Precipitation of calcium carbonate can occur in the bulk phase, or on the bacteria cell wall because it is negatively charged and will therefore attract the positive charged calcium ions [2, 16]. If the bacterium is covered in calcium carbonate the cell will die as nutrient transfer is prevented [2, 26].



Details about preparing of bacteria and fluids, and procedure for functionalization of micromodels are described in section 2.4.

2.3 Experimental set-up

A schematic of the experimental set-up for *in situ* visualization of calcite-functionalized micromodels is presented in Fig. 3. The system also contains equipment to inject CO_2 or CO_2 -saturated fluids for pore-scale investigations of CO_2 storage security at elevated reservoir pressure and temperature (see section 3.3). To facilitate injection of these fluids, the set-up is designed with all tubes and equipment (except autoclave-valves) in materials which are chemical compatible with these fluids. Polyether ether ketone (PEEK) has been found to resist all the chemicals and fluids used in this work and is therefore the main material used in this design.

On the inlet side of the micromodel, a high precision plunger pump (Quizix 5000-2.5K) is operated in independent mode and used for injection of water and CO_2 . There is also an option to inject CO_2 into an in-house PEEK accumulator (30 ml) for CO_2 -saturated fluids. As mentioned in section 2.1, the smallest pore throat in the micromodel is calculated to be 0.7 μm . To avoid injection of unwanted particles, like dust, that clogs up the micromodel, all fluids were filtered prior to use and flow

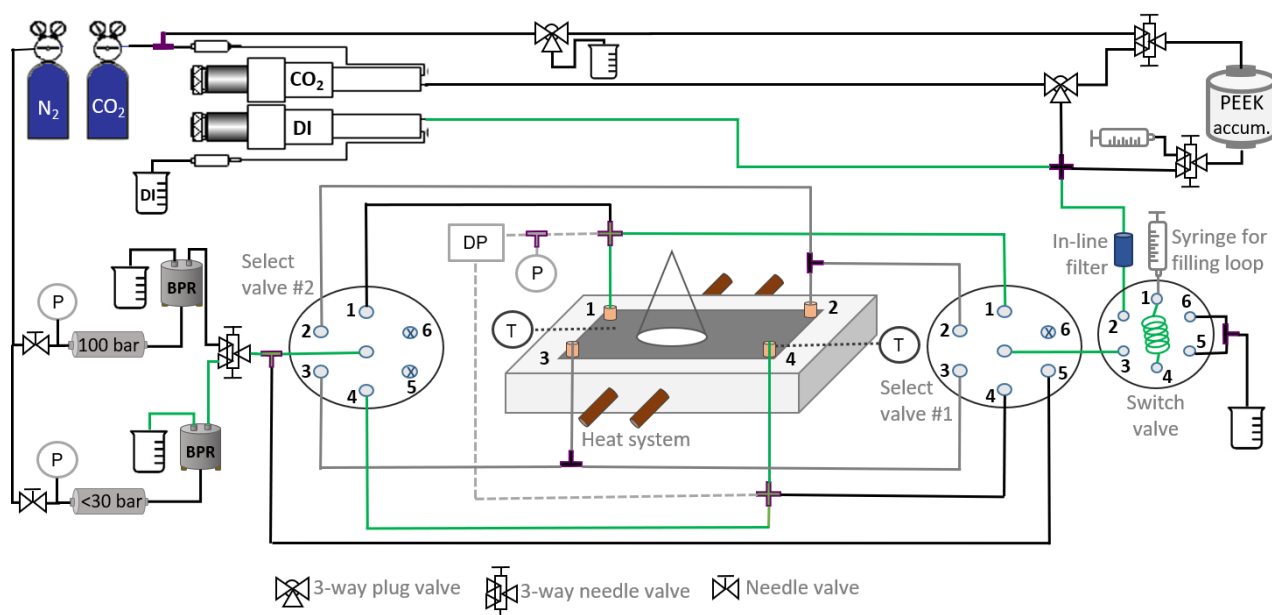


Fig. 3. Schematic of the experimental set-up for calcite-functionalization of micromodels. During injection of bacterial- or cementation solution, tubing marked in green were open/connected. Fluids were injected into a 1.0 ml loop in the switch valve and chased by DI from a pump. The micromodel was placed directly under a microscope, enabling in-situ visualization of CaCO₃ precipitation in the pore space. All tubing and tee/cross (purple) are in PEEK from IDEX.

through a 0.5 μm inline filter assembly (IDEX, A-431) prior to entering the micromodel.

The low pore volume (11.1 μL) makes it important to have a constant system dead-volume to ensure that fluids enter the micromodel when anticipated. This is achieved by utilizing two 6-ports select valves (IDEX, MXP7970-000), one at inlet and one at the outlet. When valves #1 and #2 are connected to the fluid-flow-ports (Fig. 3) it is possible to designate injection and production ports with a single mouse-click. When changing injection fluid, both select valves were set to position 5 for the fluids to bypass the micromodel until pressure stabilized. During calcite generation experiments small amounts of different fluids will be injected into the model at various times. To facilitate variable fluid injection without air entering the tubes, a two-position switch valve (IDEX, 9725) is included in the design. The switch valve has two positions: load and inject. At “load” position, fluids from the pump flow into port 2, via port 3 and to Select Valve #1. A coiled tube (referred to as “loop”, see Fig 3) with a constant volume could then be filled with e.g. bacteria-solution using a luer-lock syringe. At “inject” position, flow from

the pump is rooted through the loop and into Select Valve #1. Other valves used in the set-up are Autoclave valves as described in Fig. 3.

The system is pressurized by two back pressure regulators (Equilibar), where one is kept at 100 bars for high pressure experiments, and one at lower pressure depending on experimental design. The pressure differential between inlet and outlet is logged with differential pressure transmitter (APLISENS PRE-28 SMART) with a measuring range of 0-2.5 bar and a static pressure limit of 250 bar. In addition, absolute pressure transmitter (ESI), with range from 0-250 bar, is connected to flow port 1.

The micromodel-holder in the middle of Fig. 3 is designed and machined in-house from PEEK material. It consists of four drilled holes, made with a 10-32 coned drill, which is aligned with the fluid-flow-ports underneath the micromodel, two Omega temperature probes close to port number 1 and 4, and tracks for two 1/8-inch copper tubing for heating of the micromodel by circulation of warm water. Fluid flow tubes are connected to the micromodel-holder by finger tight fittings 10-32

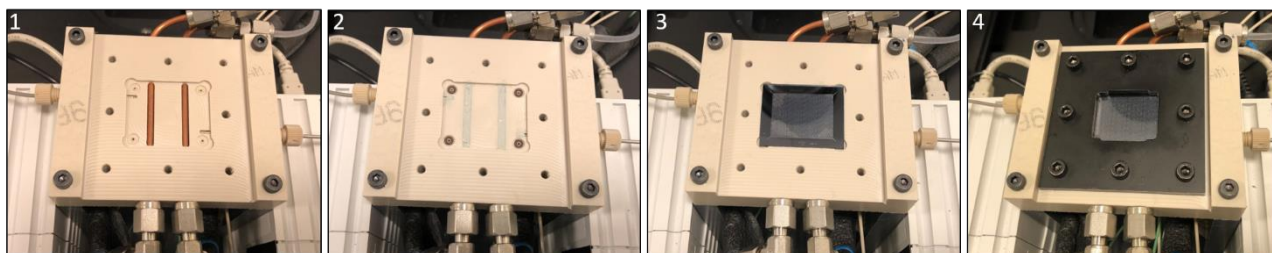


Fig. 4. Image sequence showing steps for mounting micromodel in holder. Left to right: The first image shows only the holder with machined groove for the micromodel, O-rings around the four fluid-flow-ports, two temperature gauges and copper tubing for the heating system. In the second image, the O-rings are in place and thermal paste are covering the temperature gauges and copper tubing to ensure optimal heat transfer. In the third image, the micromodel is in place and in the fourth image the black-painted aluminum plate is placed on-top of the micromodel and tightened with 0.20 Nm force. When everything is in place, the system can be pressurized to 150 bar.

coned (IDEX, F-120X) screwed directly into the four drilled holes in the PEEK holder. Mounting of micromodel in the holder are shown in detail in Fig. 4.

As indicated by the cone in Fig. 3, the micromodel-holder is placed directly underneath a microscope to enable *in situ* visualization of calcite generation and subsequent investigation of CO₂ storage in carbonate formations. The microscope is a Zeiss, Axio Zoom.V16 Microscope including a Fluorescence module. It has an automatic scanning-stage which enables high-resolution imaging of the entire micromodel within 82 seconds (with the diffuser S light source) and automatic stitching of the images to a full-model image. When generating images with both diffuser S light source and one fluorescent (FL) light channel for each tile, a full-model image is acquired within 293 seconds.

2.4 Experimental procedure

2.4.1 Preparation of fluids

Bacterial growth medium and cementation solution (reactant) were prepared as described by [18]:

Bacterial growth medium: 47g of brain heart infusion broth (BHI Broth, 53286 Sigma-Aldrich) was mixed with 900 ml of deionized (DI) water, obtained from Milli-DI synthesis system including 0.2 µm filter (172-5109, Merck). Then the solution was sterilized in 15 minutes at 121 °C in an autoclave before cooled to ~30 °C. Next, a concentrated urea solution was added to make a 2 wt. % urea broth. This was achieved by mixing 20g of urea into 100 mL of DI water. Before injecting this urea solution into the growth medium, it was filtered through a 0.2 µm syringe filter (514-0061, VWR). The finished growth medium (BHI+U) was also filtered through the syringe filter prior to adding bacteria.

Reactant was prepared by mixing urea (urea, U5378, Sigma-Aldrich) and calcium chloride (calcium chloride dehydrate, 31306, Sigma-Aldrich) in DI water. As for the growth medium, the reactant was filtered through a 0.2 µm syringe filter prior to use to minimize the risk of small particles entering the micro-model.

2.4.2 Cultivation of bacteria

Bacterium *Sporosarcina pasteurii* DSM 33 [24] were received freeze-dried from DSMZ GmbH supplier and cultivated as follows: First the pellet was removed from the sealed glass and added to 0.5 ml growth medium where it was allowed to rehydrate for 30 minutes. Second, 0.2 ml of the bacterial solution was moved to a centrifuge tube containing 10 ml growth medium and placed in a heating cabinet at 30 °C for 24 hours. Growth was detected after 24 hours, but the procedure was repeated one more time by adding 0.2 ml of the bacterial solution into a new centrifuge tube with 10 ml growth medium and stored in 30 °C for another 24 hours. After 24 hours, sufficient bacterial growth was observed, and the bacterial solution was ready to be used. Every 7 days, 0.2 ml of bacterial solution is moved to a new centrifuge tube containing 10 ml growth medium to prevent death of bacteria. In case bacteria die, an inventory of glycerol stock was prepared by adding 0.2 ml of bacterial solution

and 0.2 ml of 30 % glycerol into 6 pendlorf microtubes for long term storage at -80 °C.

2.4.3 Calcite-functionalization of micromodels

The experimental set-up (Fig. 3) is designed to withstand pressure up to 150 bar, but the MICP process was performed at atmospheric pressure or slightly elevated pressure conditions (25 bars). The latter based on experience of when all CO₂ generated from the bacterial metabolism during settling time is completely dissolved in aqueous phase, to mitigate gas-filled pores that influence fluid flow. As the MICP process is developing to be utilized in more extreme environment [27], studying this process at elevated pressures is relevant. Several factors impact the precipitation of calcium carbonate during the MICP process and variables can be adjusted depending on the goal. Details about the experimental procedure used to generate calcium carbonate in a micromodel are explained below.

1. Initial conditions.

The micromodel is initially filled with deionized water (DI). DI is miscibly displaced by bacterial growth medium before 20 µl (2 PV) bacterial solution is injected at 6 µl/min (flow port 3 as inlet and 2 as outlet). 2 PV bacteria solution is consistent with results by Wang et.al (2018) [19], who have reported that bacterial suspension was homogeneously distributed in a microfluidic chip after 1.25 PV injected.

2. Bacterial growth in pore space.

Tubing used for bacterial solution are flushed with sterile bacterial growth medium before the micromodel is shut in. This enables time for bacteria to grow, settle and attach to the pore walls.

3. Prepare for injection of cementation solution.

Cementation solution is loaded in the loop of the switch valve and injected through the bypass next to flow port 1 (with both select-valves at position 1). When the bypass is filled with cementation solution, flow is routed at 1 µl/min to flow-port 1 in the micromodel, and flow port 2 is used as outlet.

4. Cementation solution into micromodel.

After the dead-volume from bypass to flow-port 1 has been injected, the outlet flow-port is changed from 2 to 4. *In situ* growth of calcium carbonate is visualized using a high-resolution microscope with automatic scanning stage, enabling full-model images of 1.1 µm/pixel within 82 seconds or 293 seconds if one FL channel is included.

2.5 Quantification of porosity

Changes in porosity from CaCO₃ precipitation were quantified from image analysis (using an in-house python script) on sub-sections during time-lapse imaging, and in the entire pattern for the last time step, see section 3.

Two different light sources (diffuser S and FL) were available for in-situ imaging of the micromodel, each with its own method for calculating the area of precipitated CaCO₃ minerals. With the diffuser S light source, calcium carbonate minerals appear white and can be quantified with simple segmentation. The white reflection edge around each silica grain were omitted from the areal

calculations by subtracting the initial image (experiment A). When both light sources were utilized, two approaches were developed, depending on when the FL tracer was injected: 1) displace the aqueous phase with a FL tracer after the MICP process. In the FL light image, the CaCO₃ minerals then appear as shades from green to black, where black minerals were interpreted as occupying the whole height in the micromodel; 2) include a FL tracer in the cementation solution during the MICP process. Calcite minerals then appear orange with the diffuser S light source (Fig.6, B.1). If the FL tracer is replaced with aqueous phase after the MICP process, only CaCO₃ minerals are visible in the FL light image. By combining threshold diffuser S and FL images, the result contains the area of all precipitated CaCO₃ (Experiment B).

Porosity changes over time can be studied by dividing the full-model images into sub-sections (experiment A). This is achieved by adding the total silica grain area to the calcium carbonate area for each timestep, then normalizing against initial white areas related to reflections around silica grains and bacterial aggregation or potential biofilm. With this approach we mitigate areas related to white reflections which otherwise would impact the porosity as the software/script identify all white colors as porosity. The final fraction of calcite minerals in the pore space was calculated as total calcite grains area divided by the total area of each image, both in the sub-sections and the full-model image. Some calcite grains (part of a whole grain) appear transparent and were not detected by the software. Hence, the calculated calcite fraction is expected to be lower than the real fraction.

3 Results and discussion

3.1 Experimental conditions

Two experiments, with the same bacterial culture and procedure, constitute the experimental results in this study. The pore space bacterial settling times were different between the two experiments (Table 2), but the initially high pH and bacterial movement observed indicated that they were in the active phase of the bacterial growth curve, performing ureolysis, see section 2.2. The procedure to generate calcite in the micromodel is

presented in section 2.4. All experimental conditions for the two experiments are listed in Table 2.

Table 2. Properties of bacterial- and cementation solution of experiments included in this paper.

Experiment	A	B
Properties of bacterial solution		
OD600	~0.6 *	~0.6 *
Initial pH	~ 9.2 *	~ 9.2 *
PV injected	2	2
Injection rate [μ l/min]	6	6
Growth time in micromodel [h]	7	21
Temperature [$^{\circ}$ C]	31	30
Pressure [bar]	25	atm
Properties of cementation solution		
Urea [M]	1	0.5
CaCl ₂ [M]	1	0.5
Injected [μ l]	244.2	221.8
PV injected	22.0	20.0
Injection rate [μ l/min]	1	1
Temperature [$^{\circ}$ C]	31	30
Initial pressure [bar]	25	atm
Pressure when pump stopped [bar]	50	10
FL included	No	Yes

* Based on measurements on three bacterial solutions made with the same procedure/volumes

During cementation solution injection (experiment A) the injection and differential pressure across the micromodel increased rapidly after 4.2 PV injected (Fig. 5), possibly related to large amount of calcium carbonate precipitated. The PV injected increased linearly until the injection pump reached 50 bars (after 22.0 PV injected) due to blockage of the outlet tubing. Continued calcium carbonate growth was observed after injection stopped, reducing the porosity of the pore space (detailed later). For experiment B, the observed pressure behavior was similar.

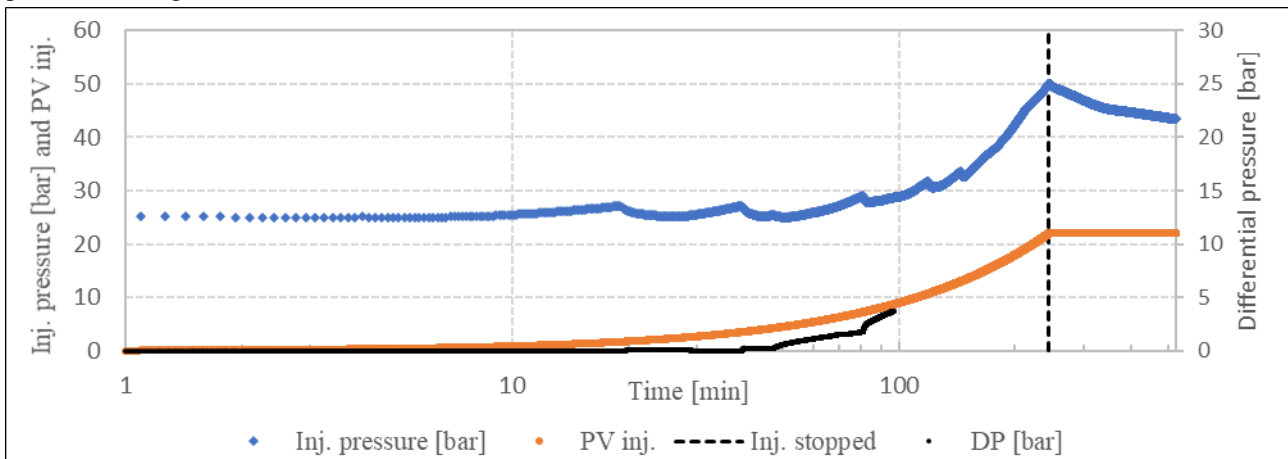


Fig. 5. Injection pressure (blue, left y-axis), differential pressure (black, right y-axis) and pore volumes injected (orange, left y-axis) during injection of cementation solution in experiment A. Injection stopped when the injection pressure reached 50 bars, indicated with vertical dashed line; measurements of differential pressure stopped at 3.7 bars because of limitation in measuring range. Calcite precipitation occurred both during injection and in a period afterwards.

3.2 Calcite precipitation

3.2.1 Single pore

The calcium carbonate grains have a variety of shapes, ranging from square/cubic, spherical to irregular (Fig. 6). Calcite grains precipitated both close to pore walls and in the pore center, and in some cases calcite grains encapsulated silica grains. The *in-situ* development of calcium carbonate through the MICP process was further studied utilizing a fluorescence module that revealed color differences between minerals. Black calcite grains were interpreted as filling the entire height in the pores space (30 μm) and block flow. The internal structure of other minerals was visible in the FL image, in contrast to images generated with diffuser S. Hence, combining FL and diffuser S images has a large potential in characterizing the development of calcite minerals.

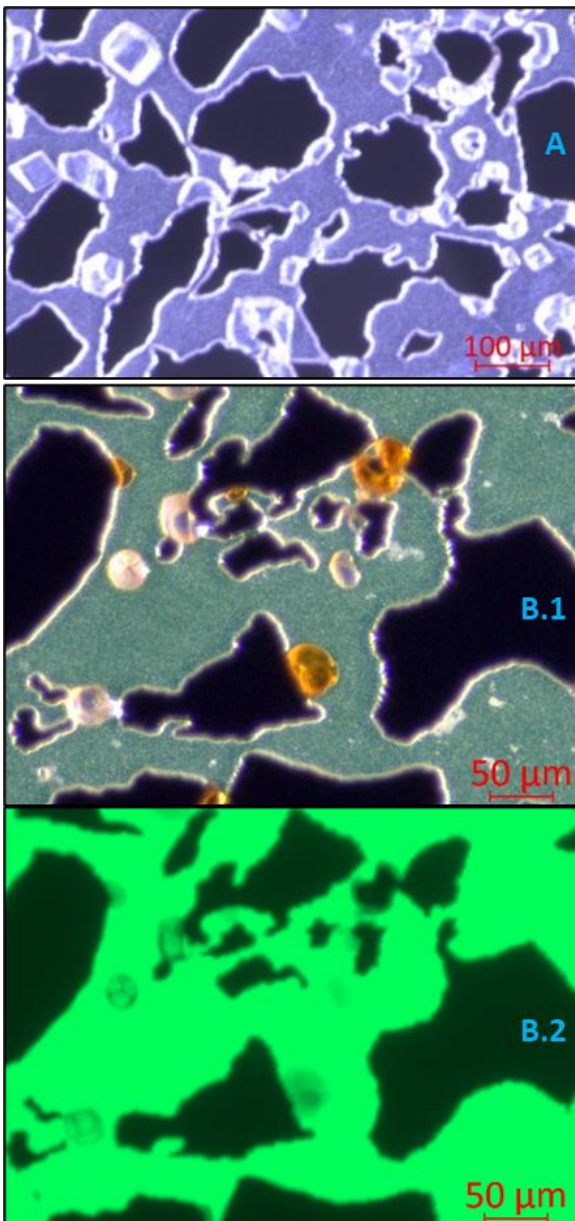


Fig. 6. Top image (A) show example of grains from experiment A, while bottom two (B) show image from experiment B generated with diffuser S light source in B.1 and with fluorescence light source in B.2.

3.2.2 Sweep/areal

The *Sporosarcina pasteurii* bacteria perform urease when settling in the micromodel, prior to injection of cementation solution. During this process, the pH is increasing and subsequently leads to carbonate ions being present in the pore space fluids. When calcium ions are added to the micromodel, calcium carbonate precipitate when the solution is supersaturated with these ions. To study the development of calcium carbonate in more detail the micromodel is divided in three subsets (Fig. 7). The change in porosity due to calcium carbonate precipitation (Fig. 8) was calculated using segmented images (described in section 2.5). The fraction of calcium carbonate (area of CaCO_3 / area of image) is summarized in Table 3. The procedure was compared with manual measurement (using a functionality in the Zeiss software) of the total calcium carbonate grain area divided by total area in the final image (at 520 minutes) in subset 1.

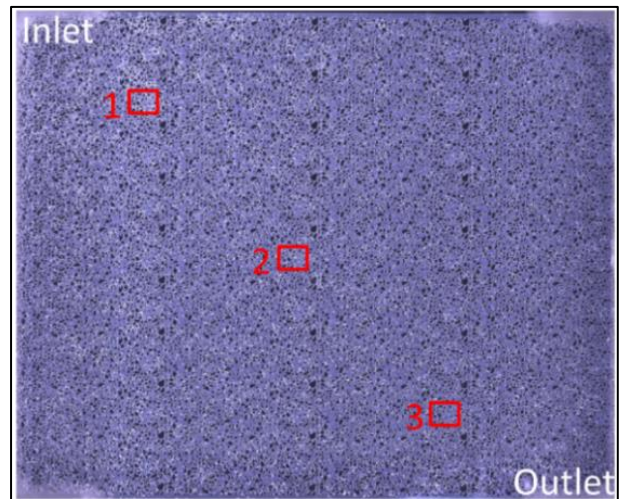


Fig. 7. Full-model image at the end of experiment A (520 min), including subset 1, 2 and 3.

Table 3. Summary of CaCO_3 fractions for experiment A.

Method	Area	CaCO_3 fraction
Polygons in Zeiss	Subset 1	0.15
Python script	Subset 1	0.13
Python script	Subset 2	0.04
Python script	Subset 3	0.02
Python script	Full-model	0.04

The development of calcium carbonate in subset 1 is detailed in Fig. 9. Coinciding with cementation solution entering the inlet-flow-port, a small white irregularly-shaped CaCO_3 precipitate ($< 30 \mu\text{m}^2$) formed close to inlet and reached subset 1 after 1.4 min (0.1 PV injected). The initial porosity reduction (Fig. 8) for subset 1 relates to these irregularly-shaped CaCO_3 precipitates, also seen in the image at 5 minutes in Fig. 9. The amount of CaCO_3 precipitates were relatively constant until 19.3 min of injection (1.7 PV injected), when a small number of additional larger ($\sim 60\text{-}100 \mu\text{m}^2$) irregularly-shaped CaCO_3 precipitates formed. Some of the irregularly-

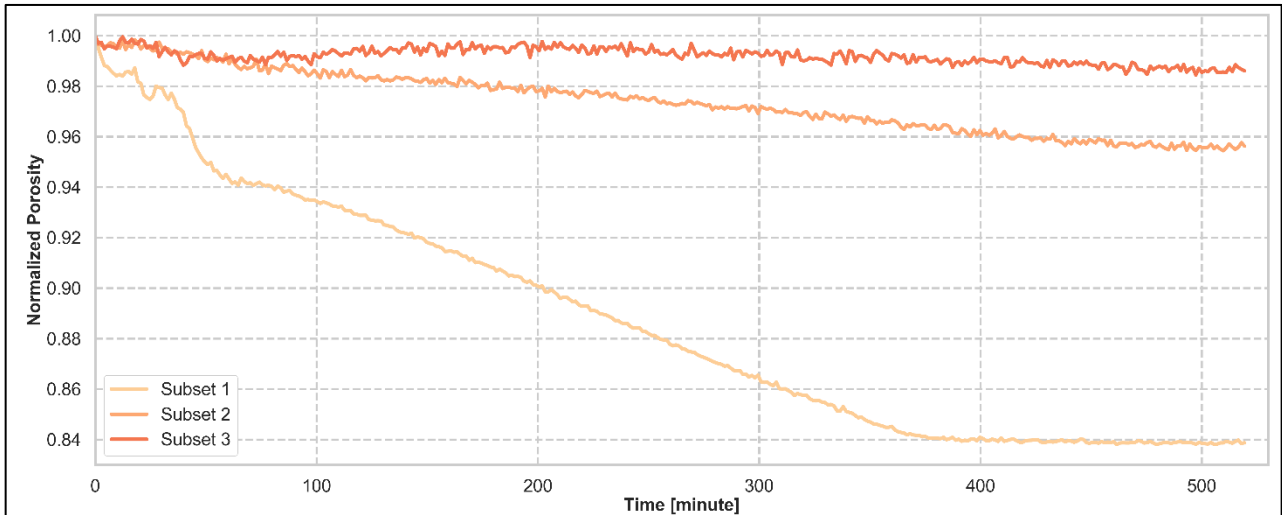


Fig. 8. Development of normalized porosity ($\Phi/\Phi_{initial}$) in each of the three subsets in experiment A. Porosity (Φ) in each timestep was calculated as: $\Phi = 1 - (areal_{silica\ grains} + areal_{CaCO_3})/total\ area$.

shaped $CaCO_3$ precipitates continued to grow at apparently random places in the pore space, located

mainly in the middle/right side in the field of view where the pores were largest. These precipitates dissolved as

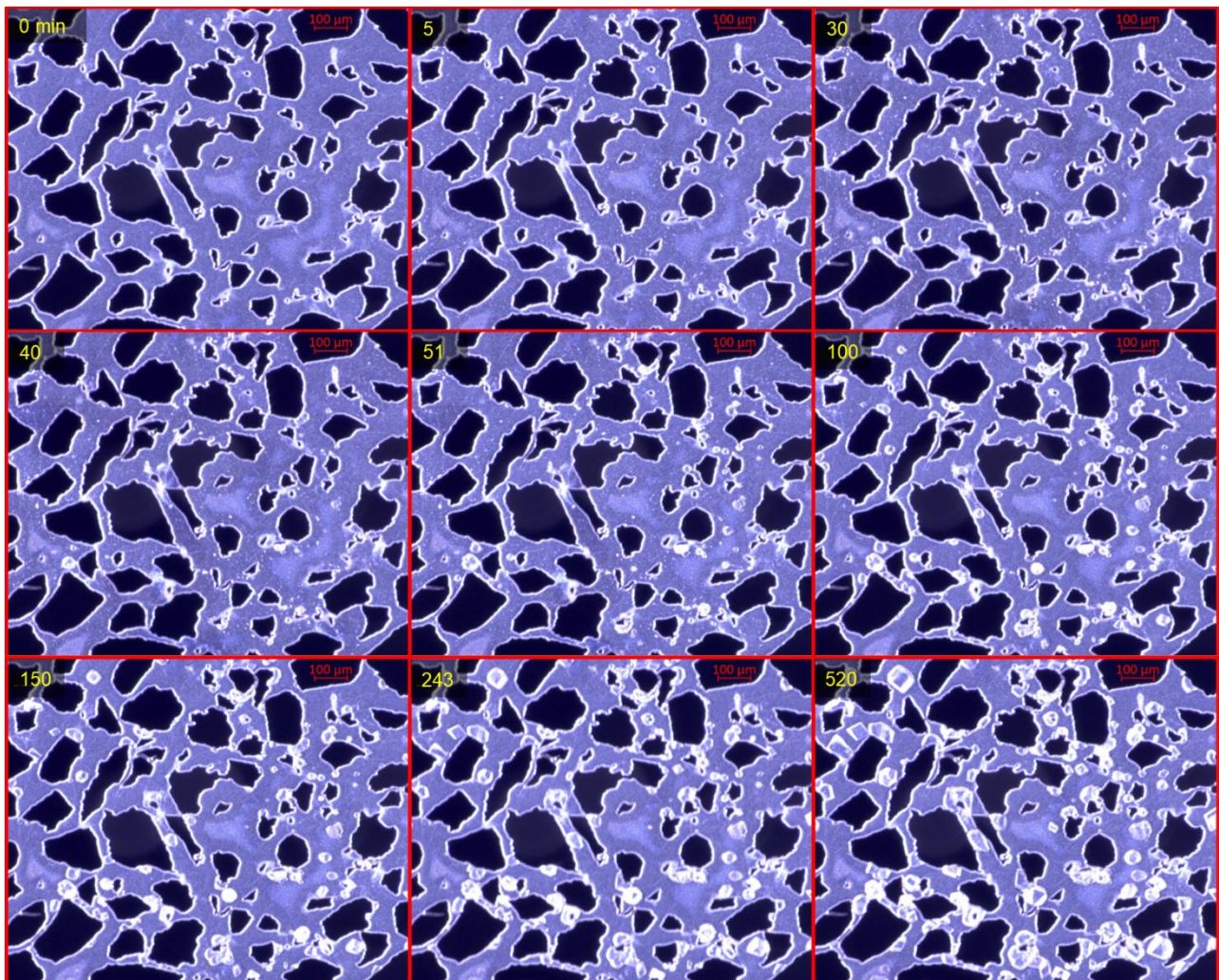


Fig. 9. Calcium carbonate precipitation in subset 1 of experiment A (Fig. 7) at different timesteps. Yellow number represent minutes from cementation solution entering the micromodel from the top left corner. This equal to PV injected until the pump stopped after 244 minutes.

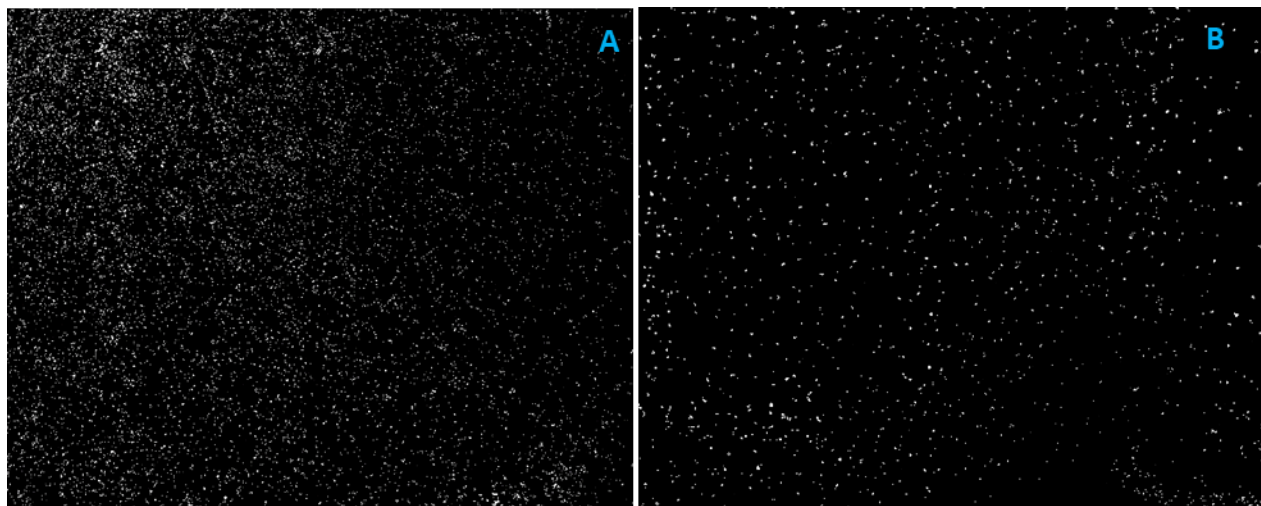


Fig. 10. Segmented images showing grains of calcium carbonate after experiment A to the left and experiment B to the right. For experiment A, the injection is at top left and outlet is bottom right, for experiment B it is opposite, with inlet at bottom right corner and outlet at top left. Width and height of both images are 24.9 mm and 19.9 mm respectively.

larger CaCO_3 crystals (spherical or rhombohedral) formed. These observations are consistent with findings from Wang et al. (2019) [20], reporting irregularly-shaped CaCO_3 dissolving in a circular trend with increasing radius outwards from the growing crystals. They further assumed that the rhombohedral crystals were calcite, spherical crystals were vaterite, and irregularly-shaped precipitates were amorphous CaCO_3 precipitates [20].

For the first 81 minutes, precipitating grains were predominantly spherical and/or irregularly shaped (not square or cubical). These continue to grow, but additional grains forming from this time were mainly square or cubical, with a larger area compared with the spherical grains. This change in grain precipitation coincided with a steeper slope in the differential pressure (Fig. 5). After 244 minutes the cementation solution injection stopped (22.0 PV injected), but the calcite minerals continued to grow until 378 min. Final CaCO_3 fraction in subset 1 was 0.13 (Python script) or 0.15 (manual polygons drawn around all calcite minerals in the Zeiss software), confirming that the Python script could satisfactorily capture porosity reduction.

Many parameters influence the precipitation of calcium carbonate, and concentration of calcium chloride in the cementation solution is one of them. Compared to experiment A, the concentrations of calcium chloride and urea were reduced by 50% in experiment B. From the literature it is expected that lower concentration enables the cementation solution to spread out better in the pore space because the reaction is slowed down. Even though the final CaCO_3 fraction in subset 1 (experiment A) was 0.13, the full-model fraction was only 0.04. This indicates an uneven distribution of the carbonate minerals throughout the micromodel, and it is also visible in left section of Fig. 10. In experiment B the full-model CaCO_3 fraction was calculated to 0.006, it appears to be more evenly distributed, as seen in Fig. 10.

3.2.3 Multiphase

A product of bacterial respiration and urea hydrolysis is CO_2 . The dissolved CO_2 forms carbonic acid ($\text{H}_2\text{O} + \text{CO}_2$) and precipitates as a part of calcite (see eq 1-5), but also functions as a buffer where it slows down the increasing pH as ammonia is produced by the urease [15]. At atmospheric pressure conditions some of the CO_2 develop into bubbles occupying relatively large areas in the pore volume. Because of the low injection rate, these bubbles impacted saturation distribution in the micromodel (Fig. 11). As the permeability was reduced from precipitation of CaCO_3 , the pore-pressure increased, and the bubble area reduced. Once a bubble was removed by dissolution in the aqueous phase, CaCO_3 precipitated in the area previously occupied by a bubble. It is expected that the change in pore-pressure, and hence CO_2 solubility, has an impact on the local pH value. This should be further studied by adding a pH sensitive FL tracer to the system.

3.3 Relevance to CO_2 sequestration

CO_2 sequestration in carbonate formations causes acidification of the brine and subsequent carbonate dissolution and development of reactive flow patterns. CO_2 is also a reaction product from the dissolution of calcium carbonate. Depending on the solubility and saturation of CO_2 in the pore fluid, it will go into solution or become bubbles that can eventually form a free gas phase. Song et al. 2018 presented the phenomena with a gas phase shielding carbonate minerals from dissolution as “grain engulfment” [18]. The functionalized micromodel in Experiment A was pressurized to 100 bars before CO_2 saturated HCl was injected. Fig. 12 shows CO_2 bubbles generated around CaCO_3 minerals during pore-level dissolution. Experiments with full model images of this dynamic reactive flow are ongoing.

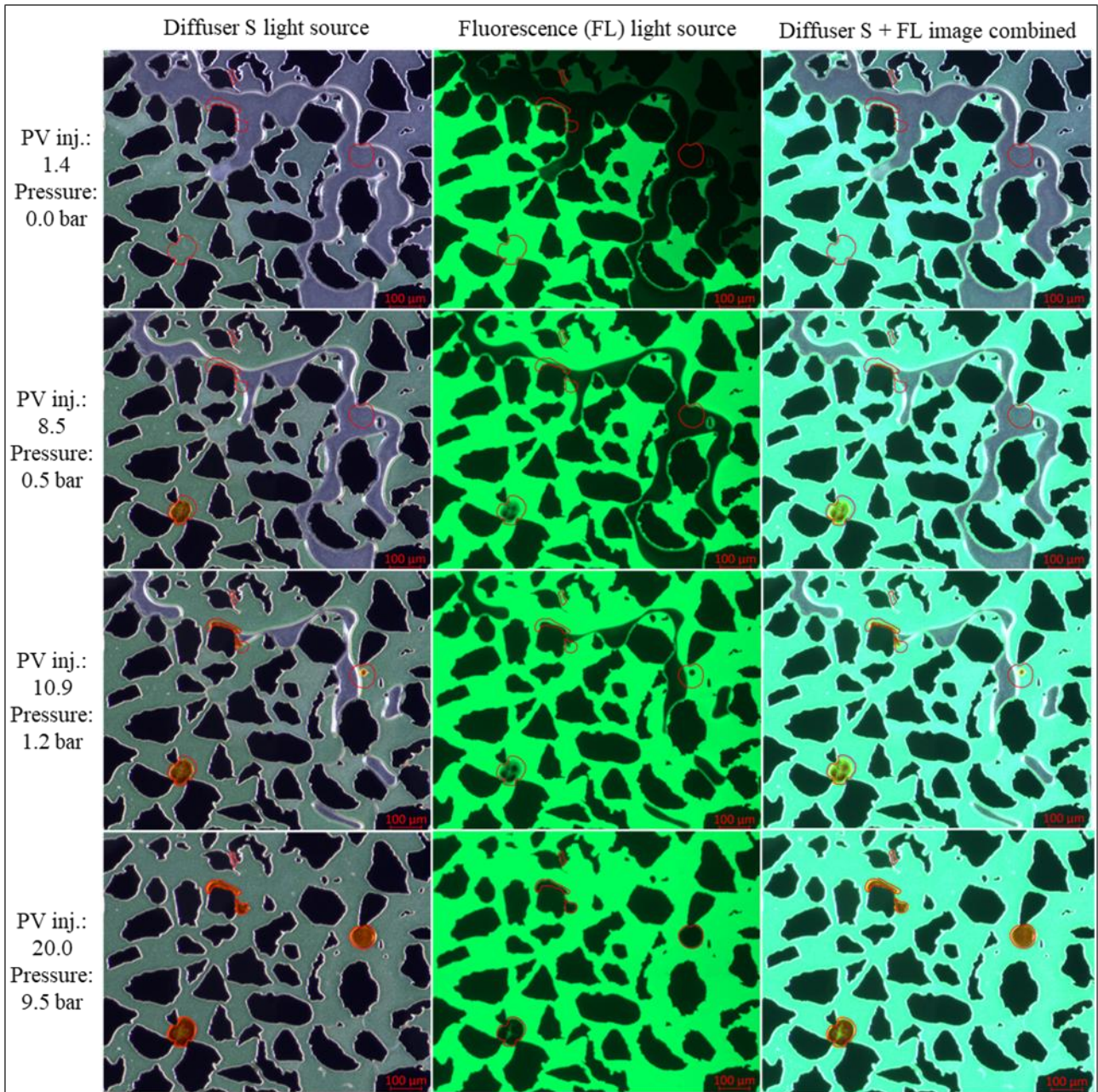


Fig. 111. Image sequence of calcium carbonate precipitation in a subset of experiment B. Pore volume injected is from cementation solution entering the micromodel in the bottom right corner (outside this field of view). Time step from top to bottom row of images are 15 min, 95 min, 122 min and 242 min, respectively. Pump stopped at 222 min (20 PV inj.). Red polygons are drawn in the Zeiss program based on image at 242 min.

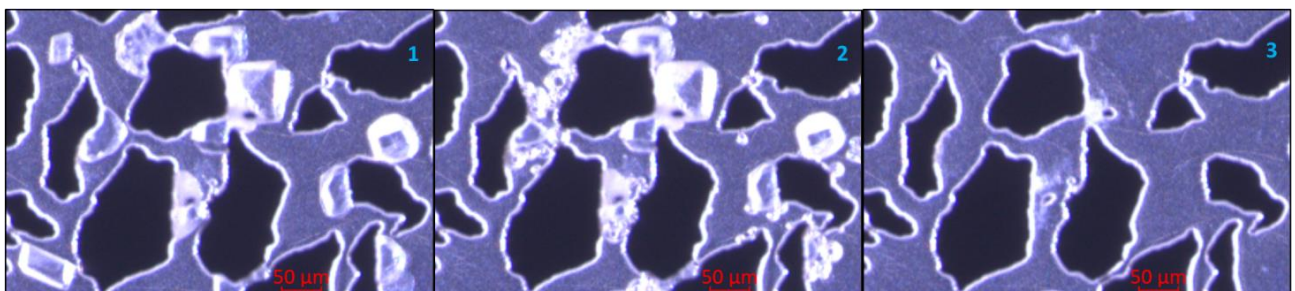


Fig. 12. Image sequence of CaCO_3 dissolution due to injection of CO_2 saturated HCl into a micromodel at 100 bars. Image no. 1 is from the functionalized micromodel in Experiment A, no.2 show CO_2 bubbles as the minerals dissolve and no.3 is after all the minerals have been dissolved.

4 Conclusions

Calcite-functionalization of micromodels was investigated to enable experimental investigation of fundamental pore-scale reactive transport dynamics; eventually determining carbonate CO₂ storage security. The system is very sensitive for external factors, and small procedural changes may result in large variations in results. Throughout this study we have demonstrated that bacteria are still active at 25 bar pore-pressure, and precipitation of calcium carbonate minerals occur at elevated pressures. To obtain the best conditions for segmenting of images, it is optimal to have the system under pressure and thereby limit gas-bubbles caused by the metabolism of bacteria.

This experimental set-up and methodology provide a unique method for studying the MICP process, where quantification of full-model calcite porosity development over time are demonstrated. This work also demonstrate that a micromodel can be functionalized with calcium carbonate minerals within a few days. Full-model images and elevated pressures provide the opportunity to support several research opportunities and investigations of fundamental pore-scale reactive transport dynamics:

- Carbon sequestration and dissolution of calcium carbonate
- Water weakening of chalk
- Injection rate dependency
- pH dependency using a pH sensitive FL tracer

MICP is a complex, biochemical process, and future work is planned to include a pH sensitive fluorescence tracer to improve understanding in how pH is changed throughout the different steps and how it influences the precipitation process. This focus aligns with future opportunities presented by Tang et. al (2020) [27] and would build upon work done by Zehner et.al (2020) [28] by introducing the FL tracer in a micromodel with representative pore scale geometry.

During injection of cementation solution a significant proportion of the bacteria are flushed out, as have also been reported previously [19]. This could lead to preliminary clogging of outlet tube and thereby limit amount of Ca²⁺ injected into the pore space. Future work is therefore planned with increased diameter of the outlet tube, expecting to increase calcite fraction in experiment equal to B.

Nomenclature and abbreviations

CCS	Carbon, capture and storage
CO ₂	Carbon dioxide
MICP	Microbially induced calcite precipitation
BHI	Brain Heart Infusion
BHI+U	Brain Heart Infusion including urea
DI	Deionized water
OD600	Optical density measured at a wavelength of 600 nm
PEEK	Polyether ether ketone

CaCO ₃	Calcium carbonate
CO(NH ₂) ₂	Urea
CaCl ₂	Calcium chloride
NH ₃	Ammonia
NH ₄ ⁺	Ammonium
H ₂ CO ₃	Carbonic acid
HCO ₃ ⁻	Bicarbonate
CO ₃ ²⁻	Carbonate ions
Ca ²⁺	Calcium ions
FL	Fluorescent
Φ	Porosity
HCl	Hydrochloric acid
H ₂ O	Water

This work was supported by Norwegian Research Council under project 280341. The authors thank Dhanasekaran Sivakumaran for assistance in cultivating bacteria, and Tove Skogmo Folkestad and Sonja Ljostveit for autoclaving the bacterial growth medium at Haukeland University Hospital.

References

1. IEA, *The Role of CO₂ Storage*. (2019).
2. W. De Muynck, N. De Belie, and W. Verstraete, *Microbial carbonate precipitation in construction materials: A review*, *Ecological Engineering*, **36**(2): p. 118-136 (2010)
3. F.G. Ferris, et al., *Bacteriogenic Mineral Plugging*, *Journal of Canadian Petroleum Technology*, **36**(09): p. 5 (1996)
4. J. Wu, et al., *Microbially induced calcium carbonate precipitation driven by ureolysis to enhance oil recovery*, *RSC Advances*, **7**(59): p. 37382-37391 (2017)
5. Y. Fujita, et al., *Evaluating the Potential of Native Ureolytic Microbes To Remediate a 90Sr Contaminated Environment*, *Environmental Science & Technology*, **44**(19): p. 7652-7658. (2010)
6. F.D. Meyer, et al., *Microbiologically-Induced Soil Stabilization: Application of *Sporosarcina pasteurii* for Fugitive Dust Control*, *Geo-Frontiers*, Vol. 2011, p.4002-4011 (2011)
7. A.C. Mitchell, et al., *Microbially Enhanced Carbon Capture and Storage by Mineral-Trapping and Solubility-Trapping*, *Environmental Science & Technology*, **44**(13): p. 5270-5276 (2010)
8. A. Phillips, et al., *Potential CO₂ Leakage Reduction through Biofilm-Induced Calcium Carbonate Precipitation*, *Environmental Science & Technology*, **47**: p. 142-149 (2013)
9. A.B. Cunningham, et al., *Microbially enhanced geologic containment of sequestered*

- supercritical CO₂*, Energy Procedia, **1**(1): p. 3245-3252 (2009)
10. F. Hammes, and W. Verstraete*, *Key roles of pH and calcium metabolism in microbial carbonate precipitation*. Reviews in Environmental Science and Biotechnology, **1**(1): p. 3-7 (2002)
 11. B. Krajewska, *Urease-aided calcium carbonate mineralization for engineering applications: A review*. Journal of Advanced Research, **13**: p. 59-67 (2018)
 12. J.W. Mullin, *Crystallization*, 4th ed., Oxford: Butterworth-Heinemann (2001)
 13. W. Zhang, et al., *In Situ Real-Time Study on Dynamics of Microbially Induced Calcium Carbonate Precipitation at a Single-Cell Level*, Environmental Science & Technology, **52**(16): p. 9266-9276 (2018)
 14. L.A. Van Paassen, *Biogrout, ground improvement by microbial induced carbonate precipitation*, in TU Delft, Applied Sciences, TU Delft: The Netherlands (2009)
 15. S. Stocks-Fischer, J.K. Galinat, and S.S. Bang, *Microbiological precipitation of CaCO₃*. Soil Biology and Biochemistry, **31**(11): p. 1563-1571 (1999)
 16. G.E. Mountassir, et al., *Hydrodynamic coupling in microbially mediated fracture mineralization: Formation of self-organized groundwater flow channels*, Water Resources Research, **50**(1): p. 1-16 (2014)
 17. C. Wu, et al., *Microbially induced calcite precipitation along a circular flow channel under a constant flow condition*, Acta Geotechnica, **14**(3): p. 673-683 (2019)
 18. W. Song, et al., *Mechanisms of Multiphase Reactive Flow using Biogenically Calcite-Functionalized Micromodels*, Lab on a Chip, **18**, (2018)
 19. Y. Wang, et al., *A microfluidic chip and its use in characterising the particle-scale behaviour of Microbial-Induced Carbonate Precipitation (MICP)*, Géotechnique, **69** (2018)
 20. Y. Wang, et al., *Microscale Visualization of Microbial-Induced Calcium Carbonate Precipitation Processes*, Journal of Geotechnical and Geoenvironmental Engineering, **145**: p. 04019045 (2019)
 21. M. Buchgraber, et al., *Creation of a dual-porosity micromodel for pore-level visualization of multiphase flow*, Journal of Petroleum Science and Engineering, **86-87**: p. 27-38 (2012)
 22. M. Buchgraber, A.R. Kavscek, and L.M. Castanier, *A Study of Microscale Gas Trapping Using Etched Silicon Micromodels*, Transport in Porous Media, **95**(3): p. 647-668 (2012)
 23. B. Benali, et al. [Preprint] *Pore-scale Bubble Population Dynamics of CO₂-Foam at Reservoir Pressure*. <https://essoar.org> (2021)
 24. J.H. Yoon, et al., *Sporosarcina aquimarina sp. nov., a bacterium isolated from seawater in Korea, and transfer of Bacillus globisporus (Larkin and Stokes 1967), Bacillus psychrophilus (Nakamura 1984) and Bacillus pasteurii (Chester 1898) to the genus Sporosarcina as Sporosarcina globispora comb. nov., Sporosarcina psychrophila comb. nov. and Sporosarcina pasteurii comb. nov., and emended description of th.* International Journal of Systematic and Evolutionary Microbiology, **51**(3): p. 1079-1086 (2001)
 25. P. De Vos, G.M. Garrity, and D.H. Bergey, *Bergey's manual of systematic bacteriology: Vol. 3 : The Firmicutes*. 2nd ed. Vol. 3., New York: Springer (2009)
 26. M.S. Reddy, *Biomining of calcium carbonates and their engineered applications: a review*, Frontiers in Microbiology, **4**(314) (2013)
 27. C.-S. Tang, et al., *Factors affecting the performance of microbial-induced carbonate precipitation (MICP) treated soil: a review*. Environmental Earth Sciences, **79**(5): p. 94 (2020)
 28. J. Zehner, et al., *Microbial-induced calcium carbonate precipitation: an experimental toolbox for in situ and real time investigation of micro-scale pH evolution*, RSC Advances, **10**(35): p. 20485-20493 (2020)

The Problem of Stability of Gas-Condensate Mixture at Pore-Scale: The Study by Density Functional Hydrodynamics

Oleg Dinariev¹, Nikolay Evseev^{1,*}, and Denis Klemin²

¹ Schlumberger, Schlumberger Moscow Research, 16A/3, Leningradskoe shosse, Moscow 125171, Russia

² Schlumberger, Schlumberger Reservoir Labs, 6350 West Sam Houston Pkwy N, Houston, TX 77041, Houston, USA

Abstract. The method of the density functional hydrodynamics (DFH) is used to model compositional gas-condensate systems in natural cores at pore-scale. In previous publications, it has been demonstrated by the authors that DFH covers many diverse multiphase pore-scale phenomena, including fluid transport in RCA and SCAL measurements and complex EOR processes. The pore-scale modeling of multiphase flow scenarios is performed by means of the direct hydrodynamic (DHD) simulator, which is a numerical implementation of the DFH. In the present work, we consider the problem of pore-scale numerical modeling of three-phase system: residual water, hydrocarbon gas and hydrocarbon liquid with phase transitions between the two latter phases. Such situations happen in case of gas-condensate or volatile oil deposits, in oil deposits with gas caps or in EOR methods with gas injection. The corresponding field development modeling by the conventional reservoir simulators rely on phase permeabilities and capillary pressures, which are provided by laboratory core analysis experiments. But the problem with gas-liquid hydrocarbon mixtures is that in laboratory procedures it may be difficult or even impossible to achieve full thermodynamic equilibrium between phases as it must be under the reservoir conditions of the initial reservoir state. However, reaching the said equilibrium is quite possible in numerical simulation. In this work, the gas-liquid mixture, after being injected into core sample, would slowly undergo the rearrangement of the phases and chemical components in pores converging to the minimum of the Helmholtz energy functional. This process is adequately described by DFH with consequent impact on phase permeabilities and capillary pressure. We give pore-scale numerical examples of the described phenomena in a micro-CT porous rock model for a realistic gas-condensate mixture with quantitative characterization of phase transition kinetic effects.

1 Introduction

Core analysis methods based on using digital rock models (DRMs) gradually become more and more accepted as a complimentary tool to traditional lab core analysis. Although not free from its own difficulties, digital rock approaches can help to obtain data and reduce uncertainties in cases where traditional lab-based core analysis becomes especially challenging to perform, e.g., poorly consolidated cores, low permeable cores, complex fluids like live oils and gas-condensates. Currently there are known many alternative methods used for numerical simulation of dynamic processes on DRMs and we refer the reader to reviews in [1-5]. The modeling method developed by the authors is called density functional hydrodynamics (DFH).

In previous publications it has been demonstrated that various multiphase compositional problems can be modeled in the frame of the density functional hydrodynamics (DFH) [7-17], including practical digital rock applications [18-26]. In the present work we discuss the pore-scale modeling of gas-condensate mixtures in digital rock models obtained by X-ray microCT. The

following are specific features of this class of problems:

a) the thermodynamic properties of hydrocarbon mixtures are related to the multicomponent nature of such mixtures, so it is important to retain in the modeling the influence of different components; b) gas and liquid phases undergo chemical component exchange, which can be slow in comparison to the transport processes observed at the laboratory scale. The latter problem can affect the applicability of laboratory results to the gas-condensate reservoir modeling. Namely in the reservoir far from the production and injection wells the transport processes in pores are sufficiently slow, so the gas-condensate mixture at any moment can be close to the minimum of the Helmholtz energy functional, while under laboratory protocols the state of the mixture can be in some metastable state far from the true equilibrium state. In order to demonstrate this problem, we perform the simulation of transport of gas-condensate mixtures in two different scenarios: a) in accordance with laboratory protocols; b) using equilibrium gas-condensate states as initial input for the computations of phase permeabilities and capillary pressures. The results highlight the possible difference between two approaches, which in our

* Corresponding author: nevseev@slb.com

opinion proves the unique value of digital rock analysis in this class of problems.

The summation over repeated indices is implied everywhere. The indices $a, b, c = 1, 2, 3$ are related to Cartesian coordinates x^a , the indices $i, j, k = 1, \dots, M$ are related to chemical components in the fluid mixture. We consider isothermal processes, so the temperature is assumed to be fixed, and dependence of certain variables on temperature is omitted. We use short symbols for partial derivatives: $\partial_a = \partial / \partial x^a$ and $\partial_t = \partial / \partial t$, where t is time.

2 Theoretical concepts and equations

2.1 Reminder of density functional hydrodynamics

Here we provide the reminder of some of the basic concepts of DFH, which are necessary for the modeling of gas-condensate mixtures. A detailed exposition of the DFH can be found in [7-10].

We consider continuum mechanics description of a mixture of M chemical components present inside a spatial region D with overall volume V_D . The region contains N_{iD} molecules of each type. To avoid large numbers, the quantities N_{iD} are measured in moles. In case of homogeneous and static mixture we define chemical component molar densities by $n_i = N_{iD} / V_D$. If the mixture is inhomogeneous and possibly evolving, one can define n_i as a dynamic variable at time t and spatial point x^a by establishing a small volume limit, such as $n_i = n_i(t, x^a) = \lim_{V_D \rightarrow 0} (N_{iD} / V_D)$. Like elsewhere

in continuum mechanics, the small volume limit is understood as the convergent procedure with V_D being small, but still large in comparison to the molecular volume. The molar densities n_i can be used to calculate

overall molar density $n = \sum_j^M n_j$ and molar concentrations $c_i = n_i / n$.

By counting the flow rate of molecules through a small area inside the mixture, one can define the component flux $I_{ia} = I_{ia}(t, x^b)$. The component fluxes are used to calculate the mass flux $I_a = m_i I_{ia}$, where m_i is the molar mass of the i^{th} component. By introducing mass density $\rho = m_i n_i$ it is possible to define mass velocity $v_a = \rho^{-1} I_a$. Component flux I_{ia} can be represented as a combination of transport term $n_i v_a$ and diffusion flux Q_{ia} : $I_{ia} = n_i v_a + Q_{ia}$.

By definition diffusion flux does not influence net mass transfer, i.e., $m_i Q_{ia} = 0$. We assume the existence of the Helmholtz energy functional

$$F_D = F_D[n_i] = \int_D \omega dV + \int_{\partial D} f_* dA, \quad (1)$$

$$\omega = f(n_i) + 2^{-1} v_{ij}(n_k) \partial_a n_i \partial_a n_j, \quad (2)$$

where ∂D is the boundary surface of the region D (when the region is finite), $f = f(n_i)$ is the bulk Helmholtz energy density of homogeneous mixture, v_{ij} is the positive-definite symmetric matrix, and $f_* = f_*(n_i)$ is the surface Helmholtz energy density, which is not equal to zero if ∂D is a contact surface with some immobile solid. It is convenient to recollect certain thermodynamic equations involving Helmholtz energy (here and below κ_i is the chemical potential of the i^{th} component, p is the hydrostatic pressure):

$$f = \kappa_i n_i - p, \quad df = \kappa_i dn_i, \quad dp = n_i d\kappa_i. \quad (3)$$

The model in Eqs. (1) and (2) is adequate for description of many important phenomena involving multiphase multicomponent mixtures. Up to now, it was successfully used to simulate multiphase multicomponent phenomena with or without phase transitions, surfactants, and mixtures with solid phases such as gas hydrates or solid particles [3-11].

The multiphase compositional transport in case of isothermal flow of fluids with Newtonian rheology is governed by the following equations written in a form of conservation laws for chemical components and momentum

$$\partial_t n_i + \partial_a (n_i v_a + Q_{ia}) = 0, \quad (4)$$

$$\partial_t (\rho v_a) + \partial_b (\rho v_a v_b - p_{ab}) = 0, \quad (5)$$

together with the relations

$$p_{ab} = \sigma_{ab} + \tau_{ab}, \quad (6)$$

$$\sigma_{ab} = (\omega - \Phi_i n_i) \delta_{ab} - v_{ij} \partial_a n_i \partial_b n_j, \quad (7)$$

$$\tau_{ab} = \eta_v \delta_{ab} \partial_c v_c + \eta_s (\partial_a v_b + \partial_b v_a - \frac{2}{3} \delta_{ab} \partial_c v_c), \quad (8)$$

$$Q_{ia} = -D_{ij} \partial_a \Phi_j, \quad (9)$$

$$\Phi_i = \kappa_i + 2^{-1} \frac{\partial v_{jk}}{\partial n_i} \partial_a n_j \partial_a n_k - \partial_a (v_{ij} \partial_a n_j), \quad (10)$$

and subject to the boundary conditions

$$v_a = 0, \quad (11)$$

$$l^a Q_{ia} = 0, \quad (12)$$

$$\frac{\partial f^*}{\partial n_i} - l^a v_{ij} \partial_a n_j = 0, \quad (13)$$

where p_{ab} is the stress tensor, σ_{ab} is the static stress tensor, τ_{ab} is the viscous stress tensor, Φ_i is the generalized chemical potential of the i^{th} mixture component, η_v and η_s are nonnegative bulk and shear viscosity coefficients, respectively, D_{ij} is the nonnegative definite symmetric matrix subject to $D_{ij} m_j = 0$, l^a is the internal normal unit vector at the boundary surface ∂D , and δ_{ab} is the Kronecker symbol.

In static equilibrium state (whether it is one-phase or multiphase) the generalized chemical potentials are constant all over the region D

$$\Phi_i = \lambda_i = \text{const}, \quad (14)$$

Since there exists the identity $\partial_b \sigma_{ab} = -n_i \partial_a \Phi_i$, the thermodynamic equilibrium conditions (14) provide the mechanical equilibrium conditions $\partial_b \sigma_{ab} = 0$. In case of two-phase one-dimensional static equilibrium distribution of components $n_i = n_i(x^1)$ (phases A and B, like gas and condensate or condensate and water), when $\lim_{x^1 \rightarrow -\infty} n_i = n_{iA}$ and $\lim_{x^1 \rightarrow +\infty} n_i = n_{iB}$, one can use Eq. (7) to derive the expression for interfacial tension (IFT), which helps to tune the matrix v_{ij} to experimental IFT data

$$\gamma_{AB} = \int_{-\infty}^{+\infty} (\sigma_{22} - \sigma_{11}) dx^1 = \int_{-\infty}^{+\infty} v_{ij} \partial_1 n_i \partial_1 n_j dx^1. \quad (15)$$

If both phases A and B are in contact with solid surface and $|f_*(n_{iA}) - f_*(n_{iB})| < \gamma_{AB}$ then the wetting angle θ is determined by Young equation $\cos \theta = (f_*(n_{iA}) - f_*(n_{iB})) / \gamma_{AB}$. If $|f_*(n_{iA}) - f_*(n_{iB})| \geq \gamma_{AB}$, the phase with lower surface Helmholtz energy density will form a layer in contact with solid surface.

2.2 Modeling of gas-condensate mixtures by density functional hydrodynamics

Our aim is to apply DFH for the numerical modeling of gas-condensate mixtures inside of the pore system of natural rock sample using 3D microCT X-ray models of the rock microstructure. Previously we have demonstrated how the DFH method can be used to

model condensate banking [15] though in less rigorous mixture composition formulation than the one proposed in this work.

Here we use a Cartesian grid with cubic cells in one-to-one correspondence with 3D voxels of segmented microCT images. The numerical realization of DFH equations is described in previous publications [10, 13]. Here we discuss specific numerical features associated with gas-condensate modeling problem.

First, it is necessary to specify the bulk Helmholtz energy density $f = f(n_i)$, which represents bulk mixture thermodynamics including the phase behavior. Currently it is widely accepted, that the thermodynamic behavior of hydrocarbon mixtures is adequately described by Peng-Robinson equation of state (PR EOS) [27], so it is natural to rely on the corresponding analytic expression of Helmholtz energy. The main computational problem with gas-condensate mixtures is that the large number M of chemical components leads to prohibitively large computational time. The way to remedy this problem is to perform computations in terms of smaller number of pseudocomponents, which are artificially constructed from the initial set of chemical components. In our case the transition from the true components to pseudocomponents (lumping) must be compatible with the DFH equations (4)-(13). Now we shall describe the mathematical procedure, which helps to reduce the number of effective components.

Let us consider linear transformation of molar densities with some invertible matrix Λ_α^i (here and below index $\alpha = 1, \dots, M$, and the summation is assumed over the repeated indices) as follows

$$n'_\alpha = \Lambda_\alpha^i n_i. \quad (16)$$

We define an auxiliary vector g_α with all components equal to 1. Since the matrix Λ_α^i is invertible there exists the inverse matrix Ω_i^α such that $n_i = \Omega_i^\alpha n'_\alpha$. We assume that the matrix Λ_α^i satisfies the following additional condition

$$g_\alpha \Lambda_\alpha^i = g_i. \quad (17)$$

This condition means that the new overall molar density $n' = g_\alpha n'_\alpha$ coincides with the old one n . Therefore, there exists the linear relation between the new and the old concentrations, as follows

$$c'_\alpha = n'_\alpha / n' = \Lambda_\alpha^i c_i, \quad (18)$$

with the normalizing condition for concentrations $\sum_{\alpha=1}^M c'_\alpha = 1$. The transformation (16) can be applied to the DFH equations (4)-(13). The mass velocity v_a and mass density $\rho = m_i n_i = m'_\alpha n'_\alpha$ are not transformed given we transform molar masses $m'_\alpha = \Omega_i^\alpha m_i$. The

representation of the DFH problem (4)-(13) in new variables is evidently equivalent to the old representation, and any solution in terms of n'_α, v_α can be used to compute solution in terms of n_α, v_α . So far, the transformation (16) is purely formal and has no physical sense, but it can help to reduce the number of effective components. Indeed, let us consider the phase transitions in the narrow pressure range, when the mixture with overall composition c_{i0} is decomposed into gas and liquid (condensate) with respective compositions c_{ig}, c_{il} . In terms of new concentrations the mixture $c'_{\alpha 0}$ is decomposed into phases with compositions $c'_{\alpha g}, c'_{\alpha l}$. Imagine, that three specific concentrations $c'_{M0}, c'_{Mg}, c'_{Ml}$ coincide or are very close to each other

$$c'_{M0} \approx c'_{Mg} \approx c'_{Ml}. \quad (19)$$

In this case the hydrodynamic processes for the considered mixture, i.e., phase transitions, convective transport, and mixing, negligibly change the quantities (19). Then one can assume that there is a fixed quantity c'_M , and the set of unknown variables is reduced to $n'_\alpha, v_\alpha (\alpha=1, \dots, M-1)$ with corresponding reduction in system of Eqs. (4). If there are similar situations with other concentrations c'_α , the number of effective component densities n'_α can be reduced even further. The problem is to find the matrix Λ^i_α , which provides as many approximations like (19) as possible. Here is the mathematical procedure for the construction of this matrix.

In digital rock transport problems, the variations of pressure are small because of the small size of microCT rock models, so the matrix Λ^i_α is constructed for certain fixed pressure. At the same time variations of local composition can be significant, so we consider variations in the range

$$|c_i - c_{i0}| \leq h c_{i0} \quad (20)$$

with fixed positive parameter h . Note that the concentration vector c_i belongs to the hyperplane $\sum_{i=1}^M c_i = 1$ in M -dimensional space with restrictions $c_i \geq 0$. We shall use the notation $d\mu(c_i)$ for the respective Lebesgue measure at this hyperplane and W_h for the corresponding volume of subset C_h of concentrations (20). Using PR EOS for any vector c_i we can calculate corresponding gas and condensate concentrations $c_{jg}(c_i), c_{jl}(c_i)$. If by chance we have one-phase system, we put both compositions equal to c_i . Let us define by induction the sequence of

vectors $e^i_\alpha (i=1, \dots, M-1)$ in accordance to the following conditions for the subsequent vector e^i_m : a) $g_i e^i_m = 0$; b) $e^i_m e^n_i = 0 (n=1, \dots, m-1)$; c) $e^i_m e^i_m = 1$; d) e^i_m provides the minimum of the following error function

$$J_{M-m} = \left(W_h^{-1} \int_{C_h} d\mu(c_i) \sum_{n=1}^m (e^n_j(c_{jg}(c_i) - c_{jl}(c_i)))^2 \right)^{1/2} \quad (21)$$

Minimization problem for the error function (21) is solved numerically. Using this solution, which is dependent on parameter h , it is possible to define the matrix Λ^i_α as follows

$$\Lambda^i_\alpha = e^i_{M-\alpha+1} (\alpha=2, \dots, M), \quad \Lambda^i_1 = g_i - \sum_{m=1}^{M-1} e^i_m. \quad (22)$$

Now if we assume $c'_\alpha = c'_{\alpha 0} = \text{const} (\alpha = m+1, \dots, M)$, the DFH problem is reduced to the variables $n'_\alpha, v_\alpha (\alpha=1, \dots, m)$, while the parameters n'_α can be interpreted as new effective pseudocomponent densities. The cumulative error of this approximation is characterized by the function J_m . The analysis of this function can help to determine the best minimum number m , when the error is still sufficiently small.

Thus, we described a new lumping technique that is consistent with the DFH. The technique is purely mathematical and can be classified as a space reduction approach.

In this work, we chose the definition of Λ^i_α with $h=1$. After defining the new pseudocomponents, it is necessary to calculate the PR EOS Helmholtz energy function in terms of these new variables. To achieve further reduction in computational time, we approximated this function with Padé-like rational approximation, which is used in numerical solution of the DFH equations. Besides being a thermodynamic description of bulk fluid, this final version of the Helmholtz energy function is used to fit the matrix ν_{ij} to experimental IFT data.

It is necessary to express the surface Helmholtz energy density f_* and transport coefficients D_{ij} through the new variables. We use a linear approximation for f_* , which is compatible with Young's equation as it has been discussed in Section 2.1 (see also [16]). It is necessary to note that in digital rock problems the surface Helmholtz energy function f_* must also compensate the difference between actual specific surface and smaller specific surface in microCT rock models. The transport matrix D_{ij} is initially specified using known data on diffusion [28] and then it

is transformed in accordance with Eq. (16) using the relation $D'_{\alpha\beta} = \Lambda_{\alpha}^i \Lambda_{\beta}^j D_{ij}$.

3 Numerical results

In interpretation of the numerical results for final static states it is necessary to remember that in accordance with equilibrium conditions (14) the chemical potentials for gas and liquid are equal and constant everywhere except for interfacial regions and regions in vicinity of the rock surface:

$$\kappa_{ig} = \kappa_{il} = const \quad (23)$$

Among other things this means that the composition of gas phase is the same everywhere where the conditions (23) take place, and the same statement is true for liquid phase. But variations of composition in grid cells, which cover the interfacial regions or are adjacent to the rock surface are permissible.

In this work, we studied a rich gas-condensate system corresponding to a gas-condensate field in southern Russia. The reservoir pressure is 50.6 MPa and temperature is 82 C. The dew point is at 48.7 MPa. A somewhat simplified composition of the reservoir gas, i.e., above dew point, is listed in Table 1.

Table 1. Initial reservoir gas composition.

Mixture component	Molar fraction
CO2	0.0061
N2	0.0015
C1	0.702
C2	0.083
C3	0.033
iC4	0.0085
nC4	0.0079
iC5	0.019
nC5	0.011
C6	0.015
C7+	0.113

We begin by applying the space reduction technique described in Sec. 2.2 to the 11-component reservoir mixture listed in Table. 1. The calculated numerical values of the criterion J_m of Eq. (21) are presented at Fig. 1. One can see that if maximum relative error at $h=1$ (that is at 100% deviation from the original mixture composition) is set to be 5%, then the reasonable choice is $m=4$, because for $m<4$ the error grows rather drastically and goes well above 5%.

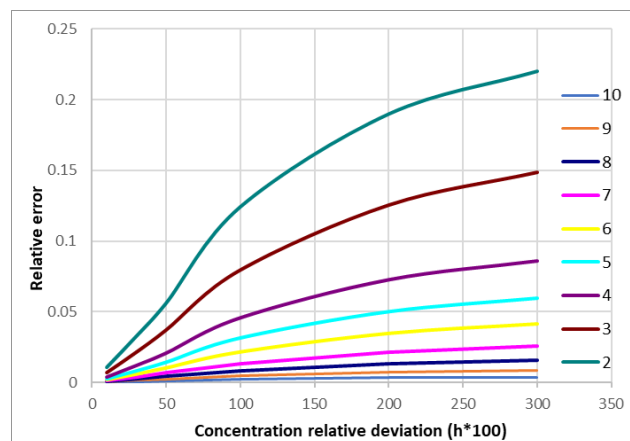


Fig. 1. Relative approximation error measured by the J_m criterion versus maximum deviation from the original mixture composition measured in h . The different lines correspond to specified number of pseudocomponents.

Thus, we settle for a 4-pseudocomponent space that will be used in numerical simulation of gas-condensate flow on a digital rock model.

A core sample used in this work is a low-permeable, but relatively well sorted carbonate rock. The sample was X-ray scanned at 0.82 $\mu\text{m}/\text{voxel}$ spatial resolution. Image segmentation was based on an extended version of the Indicator Kriging approach [29]. An example of a 2D cross-section of the sample as well as a 3D view of the DRM used for numerical simulation are shown in Fig. 2. The porosity of the DRM is 0.175 and permeability is 1.8 mD. The DRM resolved porosity is somewhat lower than the 8 mm diameter core plug measured porosity, which is 0.225. The core plug measured permeability is 2.5 mD. This is a rather typical situation, especially in low-permeable rocks, when a considerable portion of porosity appears below the X-ray microCT resolution. For such cases, we have developed a multiscale workflow based on resolving a core plug at a range of different resolutions and using high-resolution models for determining effective properties that are then used in a combined multiscale low-resolution model [17]. That workflow is fully compatible with the compositional gas-condensate modeling in the frame of the space reduction approach, but we do not use it in the present work to avoid unnecessary complication and blurring the focus of this paper.

As the first step in numerical simulation on the DRM, we have modeled initial saturation of the reservoir gas and connate water (Fig. 3) by solving a full thermodynamic equilibrium problem (global minimum of Helmholtz free energy) following the methodology described in [25]. Spatial distribution of wettability was established by surface Helmholtz energy density field (f_*) with correlated stochastic noise representing expected natural variability in rock surface properties. The connate water saturation is $S_w=0.18$. According to the mixed-wet nature of the core connate water is primarily accumulated within small pores.

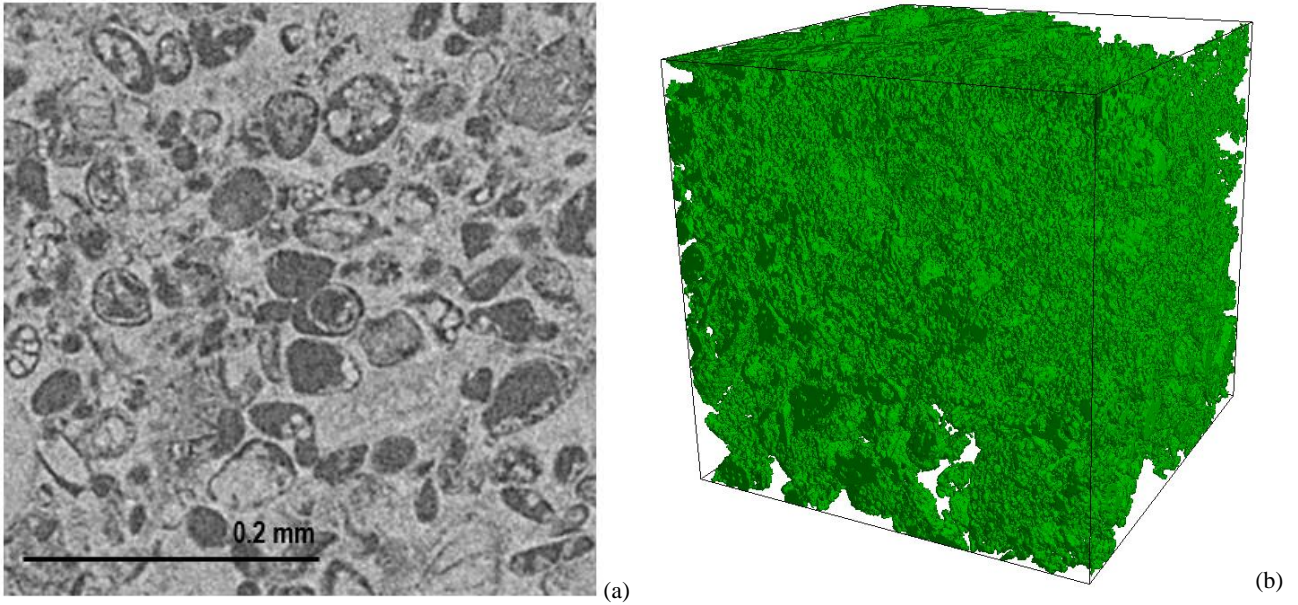


Fig. 2. (a) Micro-CT grayscale cross-section of the carbonate core sample at 0.82 μm resolution, (b) 3D view of the segmented pore space of a cubic DRM with dimensions 500^3 at 0.82 μm resolution.

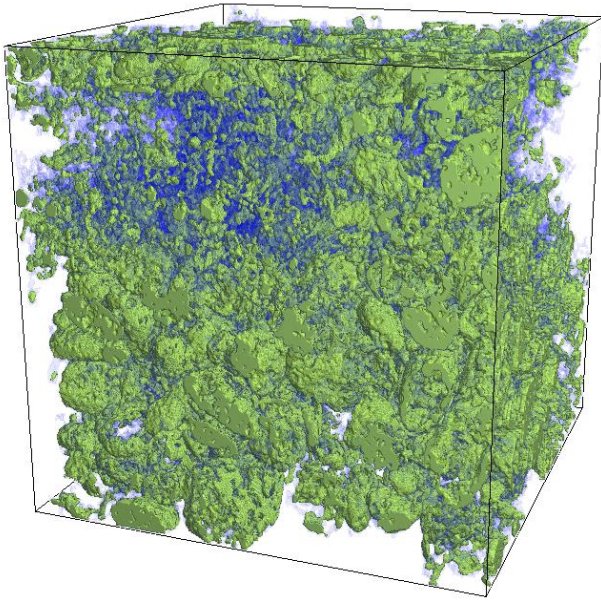


Fig. 3. 3D view of the distribution of the reservoir gas shown in green and connate water shown in semitransparent blue within the pore space of the DRM.

As the next step of numerical simulation, we have evaluated gas-condensate relative permeabilities at connate water. In order to obtain different condensate saturations, the simulations were conducted at different pressures below dew point. Also, two cases distinct in the simulation workflow have been modeled.

In **Case 1**, gas-condensate mixture corresponding to selected pressure below dew point was flowing through the DRM until stabilization of phases saturations within the model and then gas-condensate phase permeabilities were evaluated for each saturation point similarly to how we usually do this in case of immiscible phases [23]. In **Case 2**, after stabilization of phases saturation, we have waited until thermodynamic equilibrium takes place and pseudocomponents

redistribute to minimize global Helmholtz free energy. In each case, the injection was arranged at a constant rate corresponding to a low capillary number flow. The mixture was injected at the bottom side of the model and arriving fluids were removed at the top side to sustain constant overall pressure. The simulations were carried out using the following parameters (inferred for the considered deposit at 42 MPa): $\eta_{sc} = 0.92 \text{ mPa}\cdot\text{s}$, $\eta_{sg} = 0.037 \text{ mPa}\cdot\text{s}$, $\gamma_{cg} = 0.0012 \text{ N/m}$, $\gamma_{cw} = 0.02 \text{ N/m}$, $\gamma_{gw} = 0.05 \text{ N/m}$, where η_{sc}, η_{sg} are the condensate and gas viscosities, and $\gamma_{cg}, \gamma_{cw}, \gamma_{gw}$ are the condensate-gas, condensate-water, and gas-water interfacial tensions, respectively.

Some examples of phases saturation and pseudocomponent distributions obtained during simulations are presented in Figs. 4 through 7. Fig. 4 compares gas, condensate and connate water saturations in Cases 1 and 2 obtained after injection of gas-condensate mixture at 42 MPa pressure. Although the distributions are generally similar, there are visible differences in details. Fig. 6 compares distributions of pseudocomponents that correspond to the saturations from Fig. 4. Similarly, Fig. 5 and 7 show distribution of phases and pseudocomponents, respectively, for lower value of pressure equal to 33 MPa.

As can be seen from the pictures, the heavy pseudocomponents (shown in red and yellow colors in Figs. 6 and 7) tend to group closer to connate water and occupy smaller pores, while bigger pores are mostly occupied by the lighter pseudocomponents (shown in green and aqua colors in Figs. 6 and 7). This is the consequence of the fact that condensate, which is dominated by heavy pseudocomponents, has lower interfacial tension with water than gas that is mostly formed by light pseudocomponents. The said details are seen clearer from the 2D cross-sections in Figs. 6 and 7.

* Corresponding author: nevseev@slb.com

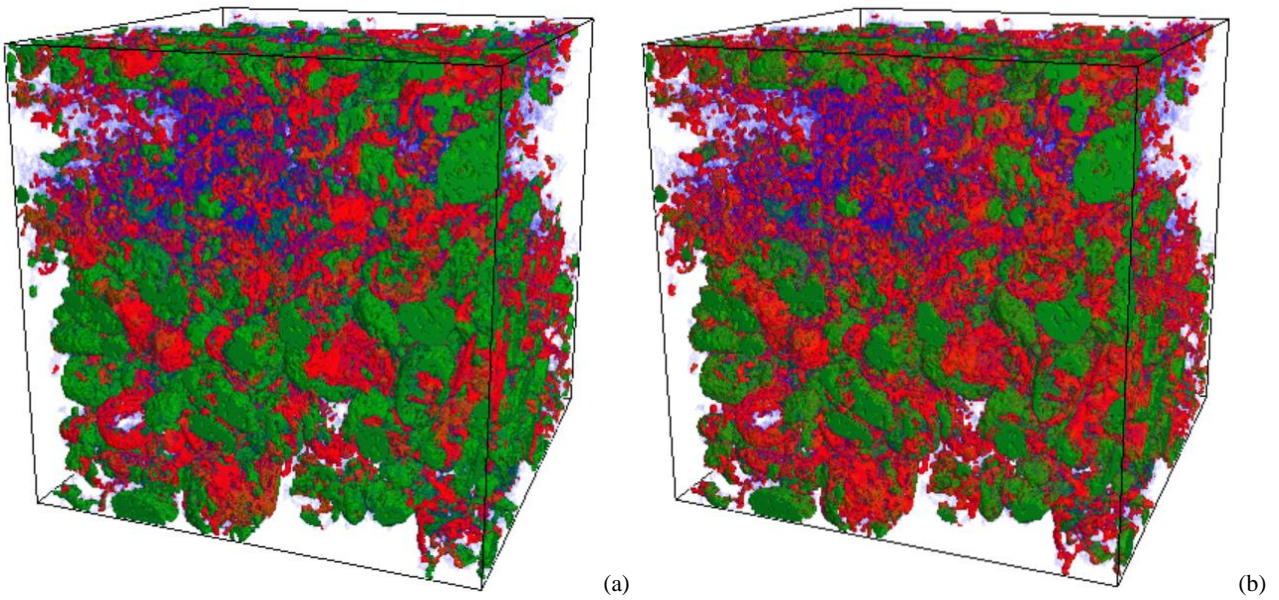


Fig. 4. 3D view of phases saturation within DRM pore space in (a) Case 1, (b) Case 2 at 42 MPa. Condensate is shown in red, gas is shown in green, and connate water is shown in semitransparent blue.

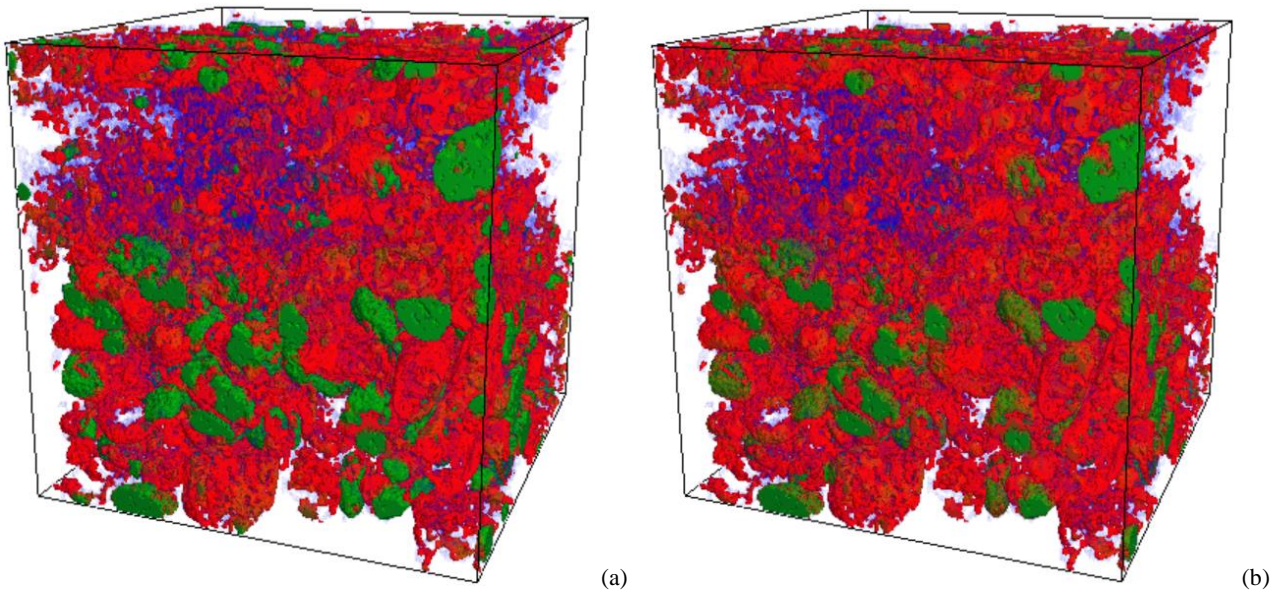


Fig. 5. 3D view of phases saturation within DRM pore space in (a) Case 1, (b) Case 2 at 33 MPa. Condensate is shown in red, gas is shown in green, and connate water is shown in semitransparent blue.

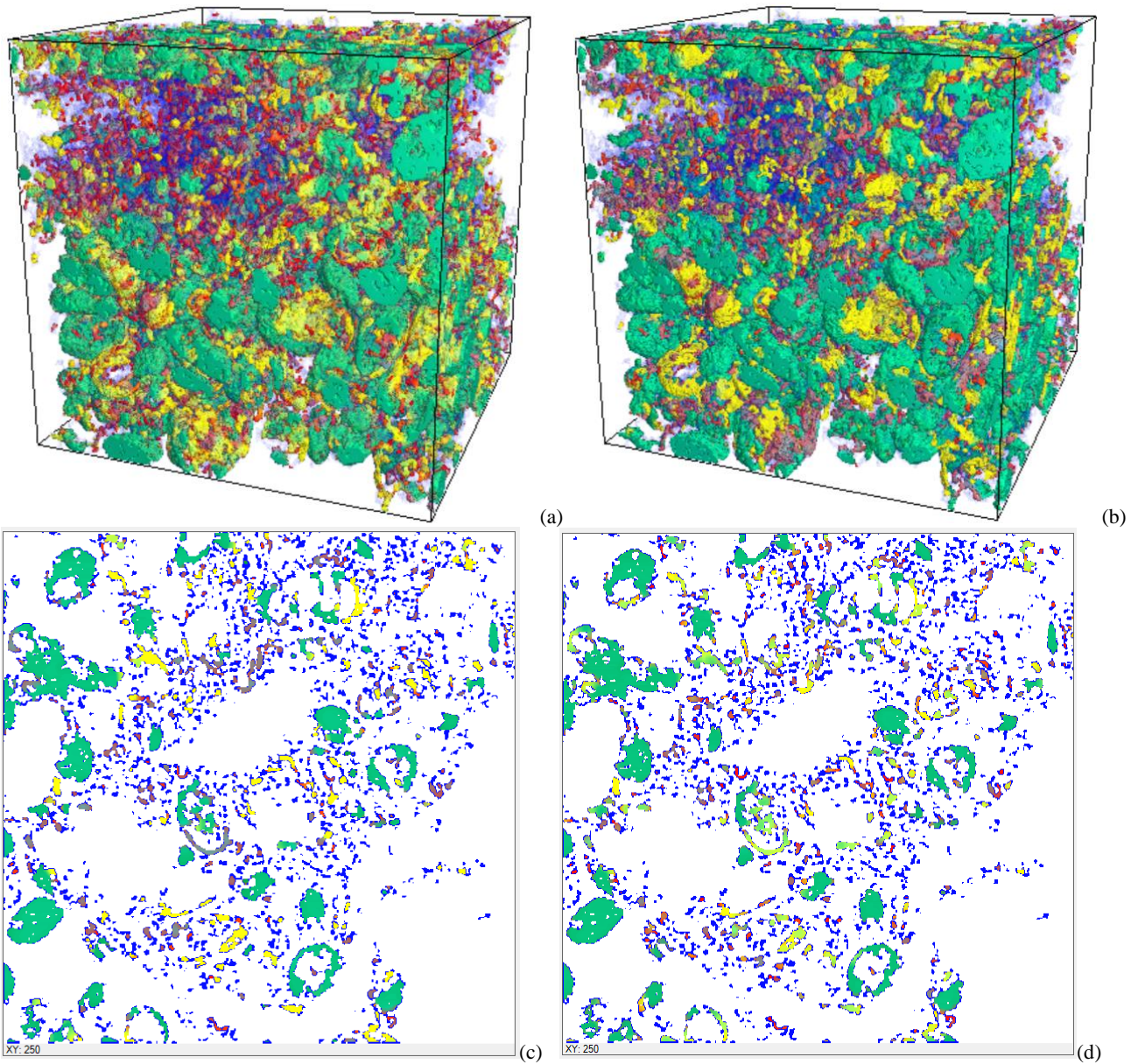


Fig. 6. 3D view of the distribution of pseudocomponents within DRM pore space in (a) Case 1, (b) Case 2 at 42 MPa. The same distributions within 2D cross-sections in (c) Case 1, (d) Case (2). The 4 hydrocarbon pseudocomponents are shown in red (1st), yellow (2nd), green (3^d), aqua (4th), and intermediate colors indicate mixture of these; connate water is shown in blue.

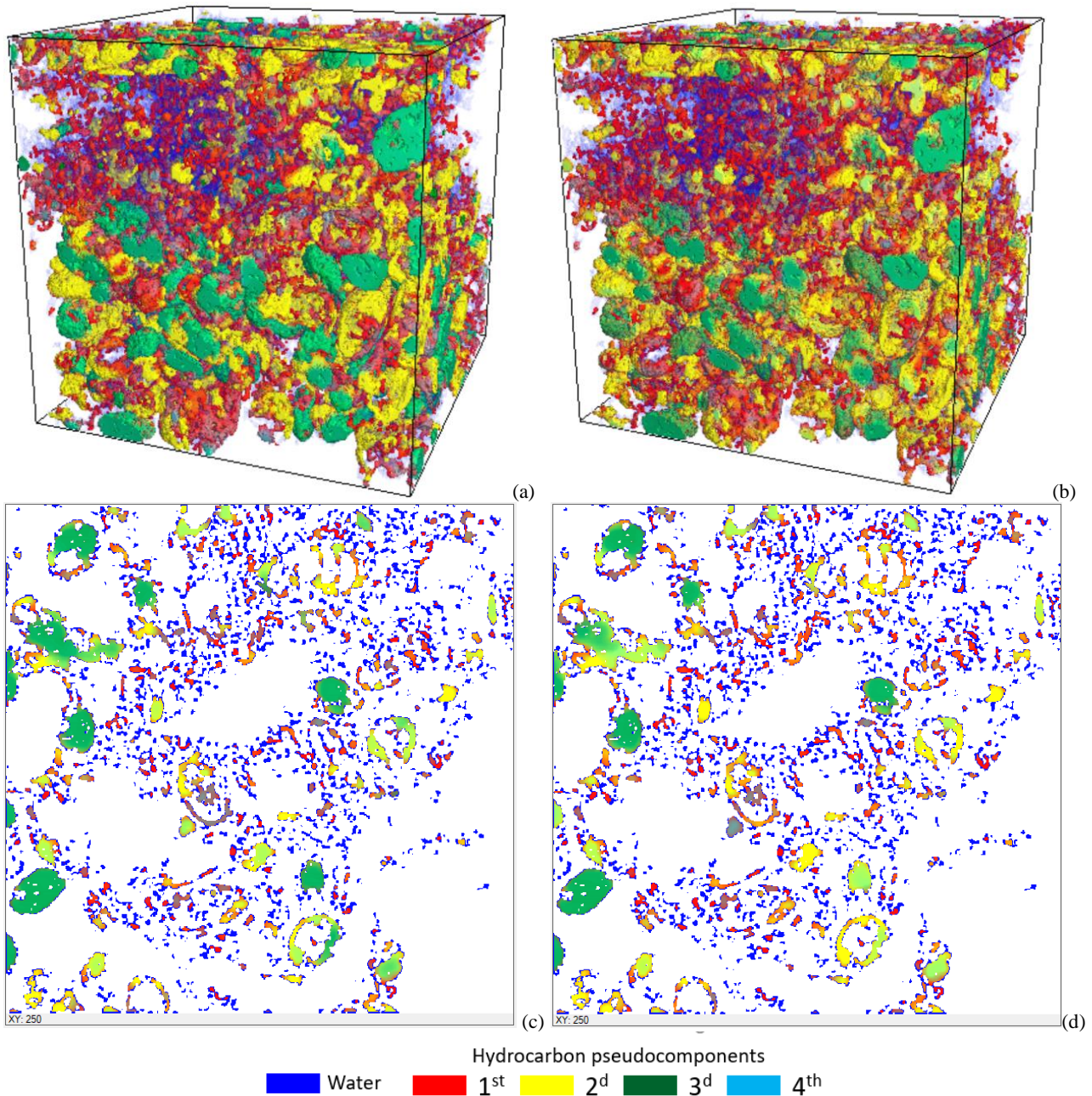


Fig. 7. 3D view of the distribution of pseudocomponents within DRM pore space in (a) Case 1, (b) Case 2 at 33 MPa. The same distributions within 2D cross-sections in (c) Case 1, (d) Case (2). The 4 hydrocarbon pseudocomponents are shown in red (1st), yellow (2nd), green (3^d), aqua (4th), and intermediate colors indicate mixture of these; connate water is shown in blue.

During the flow gas-condensate mixture is not necessarily in equilibrium state everywhere (here it is worth stressing that the DFH equations are compositional and allow for non-equilibrium flows; thermodynamic equilibrium is produced as a result of global minimization of the Helmholtz free energy and the minimization process is coupled with the transport phenomena). Therefore, it is necessary to establish definition of phases for arbitrary mixture composition [10, 12]. This is done by the bulk Helmholtz energy analysis, which has minima corresponding to the equilibrium phases. If mixture composition appears within convex part of the Helmholtz energy around a phase then this composition corresponds to this phase. If,

however, the composition appears outside any convex regions then such composition is unstable and does not belong to any of the phases.

A comparison between gas-condensate relative permeabilities is presented in Fig. 8. The gas and condensate saturations have been normalized relative to the total volume occupied by the hydrocarbon phases (connate water was excluded). It is noticeable that in Case 2 the two-phase mobility region is somewhat narrower than in Case 1. For example, condensate mobility threshold, S_{c0} , is equal to 0.28 in Case 2, while in Case 1 it is 0.23. This is explained by the fact that after fluid injection to saturation stabilization, the non-wetting phase tends to form a cluster connecting the

injection side of the model with the opposite side. But after further stabilization towards thermodynamic equilibrium that cluster can deform, become less connecting, or can even break entirely. It is only because of low interfacial tension between gas and condensate that the difference in relative permeabilities between Cases 1 and 2 appeared to be rather modest; it might have been far greater have the phases had bigger IFT.

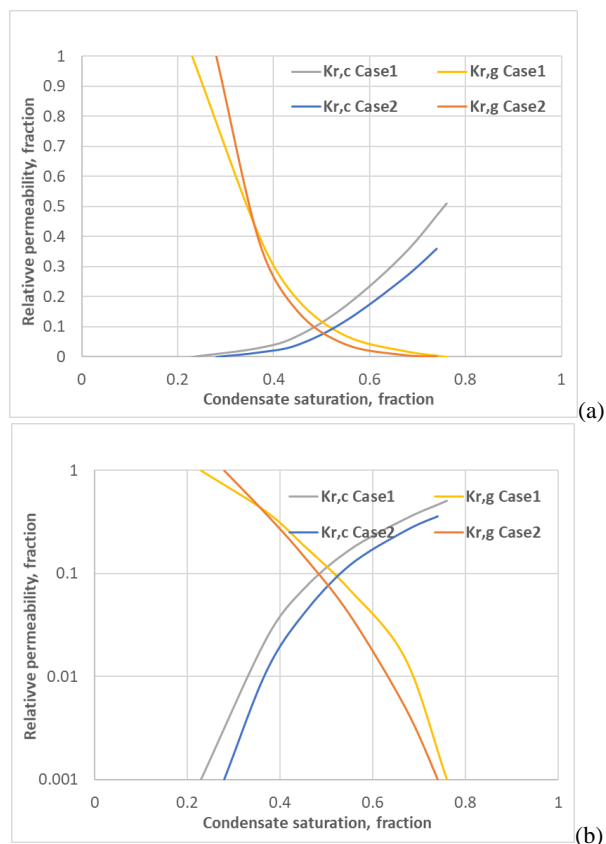


Fig. 8. Comparison between steady-state gas-condensate relative permeabilities calculated in Cases 1 and 2; (a) linear scale, (b) logarithmic scale.

4 Conclusion

In this work, we developed a compositional mixture lumping technique that is fully compatible with the DFH. This new lumping technique is a purely mathematical procedure that can be classified as a space reduction approach. As a result of its application, a pseudocomponent molar density space is built that has fewer dimensions than the space of the original molar densities. However, the inverse transformation exists that allow to reconstruct the original components from the new pseudocomponents. The error of such transformation can be estimated beforehand and can be used to select the optimal number of pseudocomponents.

Starting from an 11-component gas-condensate system we have arrived to a 4-pseudocomponent reduced system yielding maximum error of 5% within a subspace specified by a 100% deviation from the original mixture composition. Using this reduced system, we have conducted digital rock simulations by the DFH and

obtained gas-condensate relative permeabilities. The simulations have been carried out in two different statements – a classical one similar to a standard laboratory protocol, and a new one attempting to mimic thermodynamic equilibrium conditions that can form over prolonged periods of time. It was observed that the second statement provides somewhat poorer overall mobility of phases as compared to the classical formulation disregarding thermodynamic equilibrium.

We thank Schlumberger for permission to publish this work. We also recognize helpful comments from the reviewers that enabled us to improve exposition of the material.

References

1. Blunt, M.J., *Multiphase Flow in Permeable Media: A PoreScale Perspective*, (Cambridge University Press, Cambridge, 2017). ISBN 978-1-107-09346-1
2. C.F. Berg, O. Lopez, H. Berland, *J. Petrol. Sci. Eng.* **157**, 131 (2017)
3. T. Bultreys, W. De Boever, V. Cnudde, *Earth Sci. Rev.*, **155**, 93 (2016)
4. M.J. Blunt, B. Bijeljic, H. Dong, O. Gharbi, S. Iglauer, P. Mostaghimi, A. Paluszny, C. Pentland, *Adv. Water Resour.* **51**, 197 (2013)
5. V. Joekar-Niasar, M.I.J. van Dijke, S.M. Hassanizadeh, *Transp. Porous Med.* **94**, 461 (2012)
6. P. Meakin, A.M. Tartakovsky, *Rev. Geophys.*, **47**, RG3002 (2009)
7. O. Dinariev, *J. Appl. Math. Mech.* **59**, 745 (1995)
8. O. Dinariev, *J. Appl. Math. Mech.* **62**, 397 (1998)
9. A. Demianov, O. Dinariev, N. Evseev, *Can. J. Chem. Eng.*, **89**, 206 (2011)
10. A.Yu. Demianov, O.Yu. Dinariev, N.V. Evseev, *Introduction to the density functional method in hydrodynamics* (Fizmatlit, Moscow, 2014). ISBN 978-5-9221-1539-1
11. D. Koroteev, O. Dinariev, N. Evseev, D. Klemin, A. Nadeev, S. Safonov, O. Gurpinar, S. Berg, C. van Kruijsdijk, R. Armstrong, M. T. Myers, L. Hathon, H. de Jong, *Petrophysics* **55**, 294 (2014).
12. R.T. Armstrong, N. Evseev, D. Koroteev, S. Berg, *Adv. Water Resour.*, **77**, 57 (2015)
13. R.T. Armstrong, S. Berg, O. Dinariev, N. Evseev, D. Klemin, D. Koroteev, S. Safonov, *Transp. Porous Med.*, **112**, 577 (2016)
14. N. Evseev, O. Dinariev, M. Hürlimann, S. Safonov, *Petrophysics*, **56**, 32 (2015)
15. O. Dinariev, N. Evseev, *Computat. Geosci.*, **20**, 835 (2016)
16. O. Dinariev, N. Evseev, *Phys. Rev.*, **E95**, 063307 (2017)
17. O. Dinariev O., N. Evseev N. and D. Klemin D. *E3S Web of Conferences*, 146, 01001 (2020)

18. A. Shandrygin, V. Shelepov, R. Ramazanov, N. Andrianov, D. Klemin, A. Nadeev, Yakimchuk, SPE-176629-MS (2015)
19. A. Shandrygin, V. Shelepov, R. Ramazanov, N. Andrianov, D. Klemin, A. Nadeev, S. Safonov, I. Yakimchuk, SPE-182037-MS (2016)
20. S.I. Geetan, R.M. MacDonald, D. Klemin, 2461115-MS URTeC Conference Paper (2016)
21. S.I. Geetan, R.M. MacDonald, D. Klemin, 2671283-MS URTeC Conference Paper (2017)
22. R.M. MacDonald, S.I. Geetan, D. Klemin, B. Hill, 2902911-MS URTeC Conference Paper (2018)
23. I. Yakimchuk, N. Evseev, D. Korobkov, I. Varfolomeev, O. Dinariev, V. Khan, D. Koroteev, D. Orlov, E. Muravleva, B. Belozеров, V. Krutko, SPE-196928-MS (2019)
24. D. Klemin, A. Serebryanskaya, O. Savelev, S. Melnikov, SPE-198610-MS (2019)
25. I. Yakimchuk, N. Evseev, D. Korobkov, O. Dinariev, O. Ridzel, V. Khan, V. Semkov, A. Zhonin, D. Kravets, SPE-202015 (2020)
26. I. Yakimchuk, N. Evseev, D. Korobkov, O. Ridzel, V. Pletneva, M. Yaryshev, I. Ilyasov, N. Glushchenko, A. Orlov, SPE-202013 (2020)
27. D.Y. Peng, D.B. Robinson, Ind. Eng. Chem. Fundam. **15** 59–64 (1976)
28. R.C. Reid, J.M. Prausnitz, B.E. Poling, *The Properties of Gases and Liquids* (Mc-Graw Hill, New York, 1987).
29. I. Varfolomeev, I. Yakimchuk, I. Safonov, Computers, **8**(4), 72 (2019).

In-situ characterization of capillary pressure during three-phase flow in porous media

Ahmed Zankoor^{1,*}, Mahdi Khishvand¹, Bradley McCaskill¹, and Mohammad Piri¹

¹ Center of Innovation for Flow through Porous Media, Department of Petroleum Engineering, University of Wyoming, Laramie, WY, USA.

Abstract. We characterize the pore-scale fluid distributions, phase connectivity, and local capillary pressures during three-phase flow in a water-wet Berea sandstone sample. In this investigation, we use a set of x-ray microtomography images acquired during three-phase core-flooding experiments conducted on a miniature core sample. We use several image analysis techniques to analyze the pore-scale fluid occupancy maps and use this information to develop several insights related to pore occupancy, oil and gas cluster distribution, and interfacial curvature during the gas injection process. The results of our investigation show that the large-, intermediate-, and small-sized pores are mostly occupied with gas, oil, and brine, respectively, which is consistent with the wetting order of the fluids (i.e., gas, oil, and brine are the nonwetting, intermediate wetting, and wetting phases, respectively). In addition, the connectivity analysis reveals that a significant amount of the gas phase was in the form of disconnected ganglia separated from the connected invading cluster. The presence of these trapped nonwetting phase clusters during the drainage process is presumably attributed to Roof snap-off and Haines jump events, as well as the anti-ripening phenomenon. Moreover, the average local oil-water capillary pressures are found to be greater than the gas-oil counterparts. This observation is then related to the relative location of the interfaces in the pore space and the threshold capillary pressures at which the various displacement events take place.

1. Introduction

Simultaneous flow of gas, oil, and aqueous phases in natural porous media are encountered in various areas of science and engineering, such as enhanced oil recovery processes and CO₂ sequestration in depleted oil reservoirs. The flow behavior in these systems is more complicated than two-phase flow conditions [1, 2] and is controlled by numerous factors including, but not limited to, wettability, interfacial forces between each fluid pairing, and the saturation history.

Previously, many studies have been dedicated to investigating the macro- and micro-scale behavior of three-phase flow systems. While the macro-scale studies in this field have mostly focused on three-phase relative permeability and oil recovery as functions of the key parameters (e.g., spreading coefficient, wettability, and saturation history) [3, 4], the initial micro-scale research attempts, mostly conducted using micromodels [5, 6, 7, 8], have been directed toward presenting detailed descriptions of the pore-scale displacement mechanisms and fluid distribution in the pore space. The information generated during these experimental works has then been used in developing pore-network models to predict fluid occupancy, relative permeability, and capillary pressure in natural rock samples and under various three-phase flow scenarios [9, 10].

The insights provided by the micro-scale studies have been frequently used to enrich the pore-scale physics and improve the predictive capabilities of the pore-scale models. In recent years, the advent of x-ray microtomography imaging and integration of these systems with core-flooding

apparatuses has opened a new window of opportunity to directly observe the multi-phase flow phenomena in natural rock samples and further advance the understanding of such flow behavior on a pore-by-pore basis. Additionally, the advancement of image-based analysis has allowed for better characterization of such phenomena on quantitative basis [11, 12, 13]. Several researchers have used these tools to conduct pore-scale studies for three-phase systems. For instance, Iglauer et al. [14, 15] have examined the impact of secondary and tertiary gas injection processes on the residual oil and gas trapping in water- and mixed-wet sandstones. The micro-CT imaging technique has also been used to investigate the interrelationship of pore-scale fluid configuration, in-situ wettability, and displacement mechanisms in water-wet sandstone [16], oil-wet carbonates [17], and fractured porous media [18]. The research studies in this field have recently been extended to other subjects, including the gas-oil miscibility [19], the dynamics of three-phase flow [20], and CO₂ storage in oil fields [21].

The efforts mentioned above have provided valuable insights into the micro-scale behavior of three-phase systems. Nonetheless, there have always existed some uncertainties in describing the pore-scale displacement mechanisms for three-phase flow due to the limited tools available for image analysis and the complexities associated while performing the flow experiments in natural core samples. In this study, we use improved methodologies to more accurately quantify the multi-phase flow parameters and shed more light on the pore-scale subtleties of a secondary gas injection experiment conducted in a miniature core sample. Specifically, we investigate the gas trapping behavior during a steady-state gas injection (drainage) process and highlight the possible pore-scale displacement mechanisms behind this. Moreover, we characterize the interfacial curvature and the respective in-

* Corresponding author: azankoor@uwyo.edu

situ capillary pressure to examine the pore-scale displacement mechanisms and the conditions for the formation of oil layers. The results of this study are of high importance for future pore-scale experimental and modeling research.

2. Experiments and data acquisition

In this study, we analyzed the micro-CT images obtained during a three-phase flow experiment in a water-wet Berea sandstone sample [16]. The diameter, length, porosity, and permeability of the sample were 81 mm, 4.47 mm, 0.186, and 584.46 mD, respectively. A synthetic brine solution, decalin, and nitrogen gas were used as, respectively, the wetting, intermediate-wetting, and nonwetting phases in this rock-fluid system. The three phases were brought into equilibrium at the experimental conditions (i.e., 5.52 MPa and 20° C) before injection into the rock sample to minimize mass exchange between the phases during the flow processes. The equilibrium spreading coefficient of the oil phase was measured to be -5.04 mN/m, which implies that the oil phase had non-spreading behavior. The experiment was conducted using a core-flooding apparatus integrated with a high-resolution micro-CT scanner. As shown in Figure (1), the core sample was first fully saturated with brine and then subjected to a drainage process using the oil phase to establish a target initial water saturation. The experiment was then followed by a secondary gas injection process through simultaneous injection of all three fluid phases, and the system was allowed to reach stable conditions. At this point, the region of interest was imaged at a resolution of 1.5 μm to generate grayscale images of the fluid occupancy in the pore space. More details about the fluids and experimental apparatus and procedure can be found elsewhere [16].

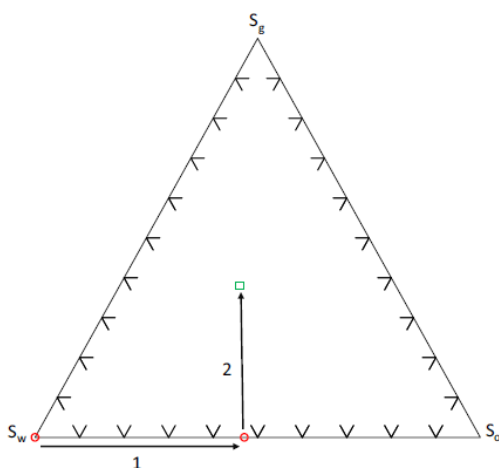


Fig.1. Three-phase saturation path of the core-flooding experiment.

3. Image analysis

The raw grayscale images acquired during the core-flooding experiment were processed using the Avizo software [16]. The images were first filtered using the non-local means filter to improve the signal-to-noise ratio, combined with the corresponding pore map, and subsequently segmented using the interactive thresholding method to generate the pore-scale fluid occupancy maps, i.e., images with unique labels assigned to the gas, oil, aqueous, and solid phases. We then analyzed these images using specific techniques, as mentioned in later sections, to obtain pore-by-pore fluid occupancy data, investigate the volume, connectivity, and morphology of the oil and gas clusters, and characterize the in-situ capillary pressures.

3.1. Pore-by-pore fluid occupancy

Pore-scale fluid occupancy maps can be used to calculate the saturation of each phase in various ranges of pore sizes. Previously, Scanziani et al. [22] proposed a technique to superimpose spheres with specific sizes – representing the pore elements [23]– on the wet images. The dominant phase in each pore is then assigned to the corresponding sphere, and the results are aggregated to calculate the saturation of each phase in various pore-size ranges. In this study, however, we employed a different technique that uses images of the separated pores instead of the spheres extracted using the maximal ball technique. The separated pores were generated using a specific module in the Avizo software that computed the watershed lines of the pore map to identify the local dilations and constrictions in the pore space. The image of the separated pores and the pore-scale fluid occupancy map were then used as input to an in-house MATLAB code, which superimposed the two images and quantified the pore-by-pore fluid occupancy (i.e., volume/saturation of each phase in the pores). The input images were partitioned into sub-volumes, and the computations were performed on multiple CPU cores to account for the large size of the data. Finally, the results were recombined for the entire image. This methodology is assumed to be more accurate since it preserves the pore space geometry, and hence the fluids occupying pore corners and crevices are included in the pore occupancy calculations. An example of the segmented wet image and the separated pore map are shown in Figure (2).

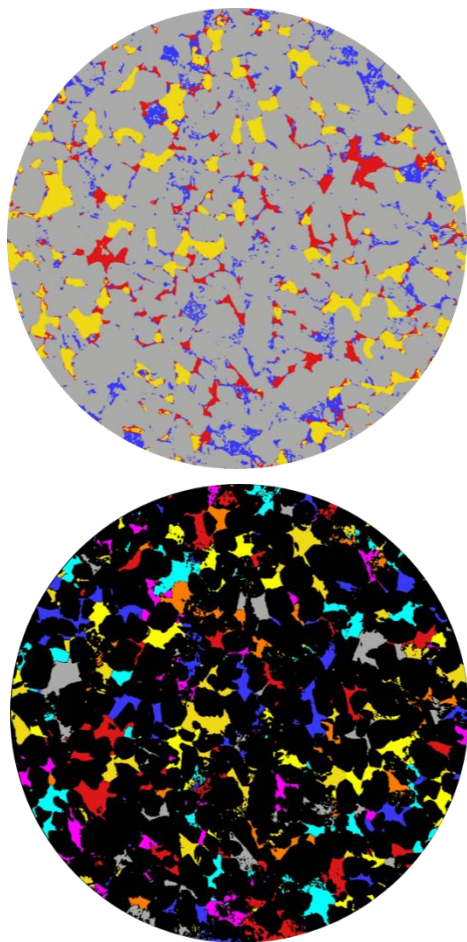


Fig.2. Two dimensional cross-sectional views of (top) the segmented wet image during the gas injection process, and (bottom) the separated pore map with different labels assigned to the individual pore elements.

3.2. Oil and gas cluster analysis

Each of the fluid phases in the pore space is formed of numerous connected and disconnected clusters of various sizes that can reside in the center of a single pore or span over several pore elements. The study of the connectivity and morphology of these clusters allows one to gain better insights into the multiphase phenomena within the pore space. To conduct this type of analysis, we generated separate images of the oil and gas phases and analyzed each set to identify the size of the individual clusters forming that phase. We also computed the Euler number for each phase, a measure of the connectivity, given by the formula: $\chi = \beta_0 - \beta_1 + \beta_2$, where β_0 is the number of disconnected objects, β_1 is the number of loops and β_2 is the number of holes. Furthermore, these data sets were used to quantify the contribution of clusters with various sizes to the total volume of the respective phase and investigated the relationship between the surface area (A) and volume (V) of the oil or gas globules. In addition, we computed the Euler characteristic for the oil and gas phases, which is indicative of the fluid's connectivity [24].

3.3. In-situ capillary pressure characterization

We also characterized the in-situ capillary pressure using the interfacial curvature analysis method described by Zankoor et al. [18]. To this end, we first extracted the free interfaces between each pair of fluids (i.e., oil-water, gas-oil, and gas-water) from the segmented images using the Marching cubes algorithm. The extracted meshes were then smoothed to reduce the impact of discretization on curvature analysis using an implicit fairing method [25, 26]. Afterward, the local curvature values were computed at each point (vertex) on each interface, and a representative average value was found to estimate the local capillary pressure between each fluid pair using the Young-Laplace equation:

$$P_{C_{ij}} = \sigma_{ij}K_T \quad (1)$$

where $P_{C_{ij}}$ is the capillary pressure in Pa, σ_{ij} is the interfacial tension between phases i and j in N/m, and K_T is the average total curvature of the interface in m^{-1} (i.e., summation of the principal curvatures). To obtain an average value of the total curvature, we use arithmetic averaging of the per-vertex curvatures. An alternative approach is to use an area-weighted average, where each per-vertex curvature value is given a weight based on the area of the surrounding mesh elements, which, however, requires further investigation which is beyond the scope of the current study. It should be noted that the vertices at the peripheral rings of the fluid-fluid interfaces (i.e., in contact with the solid surfaces) were excluded from the curvature analysis since these regions introduced significant uncertainties to the measurements. Further details regarding the methodology used for the extraction and smoothing of the fluid-fluid interfaces and the sensitivity analysis on the parameters used in the analysis can be found elsewhere [18].

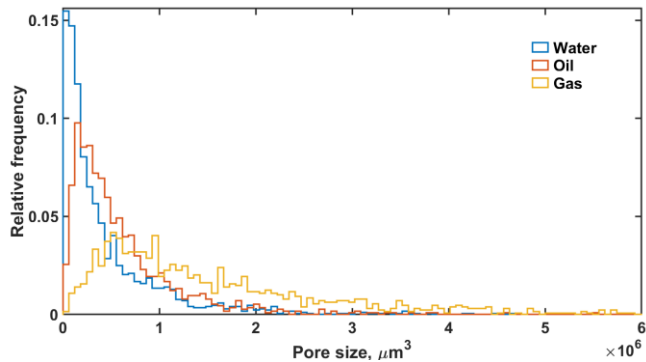
4. Results and discussion

4.1. Pore-by-pore fluid occupancy

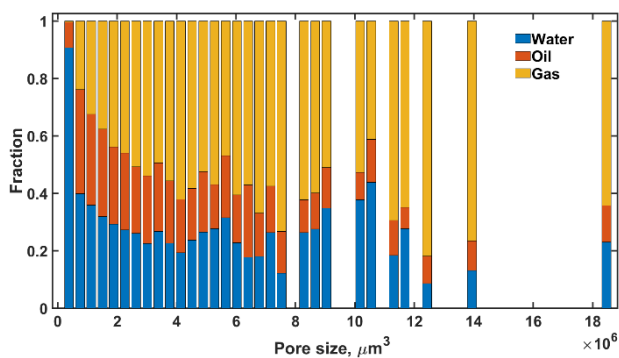
We used the method discussed in section (3.1) to generate the following pore occupancy data from the segmented wet images of the gas injection process:

- (i) Size distribution of pore elements that are mostly saturated with gas, oil, or water phases (see Figure 3.a). To this end, we first categorize the pores into three groups based on the dominant occupying fluid (i.e., gas-, oil-, or water-filled) and then generate the pore size distribution for each of these groups.
- (ii) Fluid saturation in pores with different sizes (see Figure 3.b).
- (iii) The ratio of cumulative fluid volume to the total volume (i.e., cumulative saturation) for each phase as a function of pore size (see Figure 3.c).

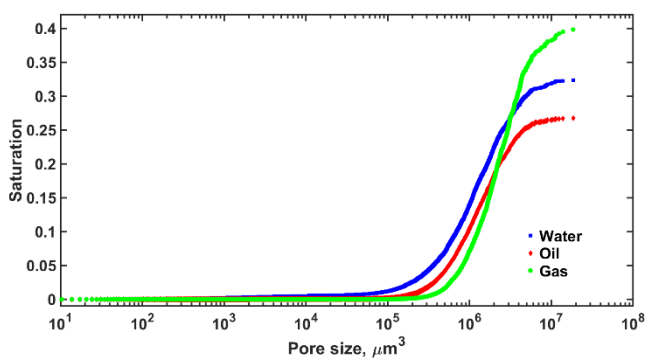
Figure 3.a illustrates that each of the three phases occupied a wide range of pore sizes. Nevertheless, it is observed that most of the water-filled elements are of the smallest pores (smaller than $4.0 \text{ E}+05 \mu\text{m}^3$), while the distribution of the oil- and gas-filled pores shift toward more intermediate- and large-size pores, respectively. This pore occupancy preference agrees with the wettability order of this rock-fluid system, with water, oil, and gas being the most wetting, intermediate wetting, and nonwetting phases, respectively [27].



(a)



(b)



(c)

Fig. 3. Pore-scale fluid occupancy data during the secondary gas injection process: (a) the size distribution of pores mostly occupied by each phase; (b) fluid saturation in various pore-size ranges; and (c) the cumulative saturation of each phase as a function of the pore size.

Likewise, Figure 3.b shows that water saturation is steadily higher than the oil and gas saturation in the smallest pore elements. This behavior occurred because the threshold capillary pressures for gas-to-water or oil-to-water displacement were the highest in the smallest pores, and hence the oil and gas phases had a smaller chance to invade those pore elements. In the intermediate-size ranges, however, a significant portion of the pore space is occupied by each of the three phases while declining trends for water and oil saturations are observed as the pore size increased.

This observation is expected since it was more favorable for the gas (the most nonwetting) phase to invade the large pores. It is worth mentioning that the rise in water saturation in some of the intermediate-size pores (i.e., the range of $8.0 \text{ E}+06 - 1.2 \text{ E}+07 \mu\text{m}^3$) might be attributed to that the invading phases (oil and gas) did not have access to the entrance of all pore elements in this range especially at areas with high clay content. As a result, some of the pores stayed water-filled during the drainage processes and contributed to the observed water saturation.

The observed saturation trend versus pore size is also reflected in Figure 3.c. This figure indicates that the water saturation built up earlier than the other phases (i.e., in smaller pores), whereas the gas saturation was increased significantly only when the contribution from the largest pores was added to the cumulative saturation. As seen, the final water, oil, and gas saturations in the FOV reached 0.32, 0.26, and 0.40, respectively.

4.2 Oil and gas cluster analysis

As mentioned previously, the oil and gas clusters after the gas injection process were separated, and their size and distributions were investigated. Figure 4 shows the overall distribution of these clusters for each of the fluid phases. This figure demonstrates that the water and oil phases were well connected (the connected blue clusters) over the FOV, whereas for the gas phase, a significant number of globules with considerable sizes were disconnected and could be potentially trapped in the pore space. The connectivity of these clusters was further studied by quantifying the contribution of gas/oil clusters with various sizes to the total volume of gas/oil in the FOV. As shown in Figure 5, the disconnected gas globules formed approximately 40% of the total gas saturation. It should be noted that some of these clusters might be incorrectly considered disconnected. For instance, some of these clusters were truncated at the borders of the FOV and might be connected outside of it. Further analysis of the images revealed that the Euler numbers for the gas and oil phases were 3747 and 2442, respectively. These numbers indicate that the gas phase contained a larger number of separated objects compared to the oil phase, and considering the volume contribution mentioned previously, one can conclude that the oil phase has better connectivity.

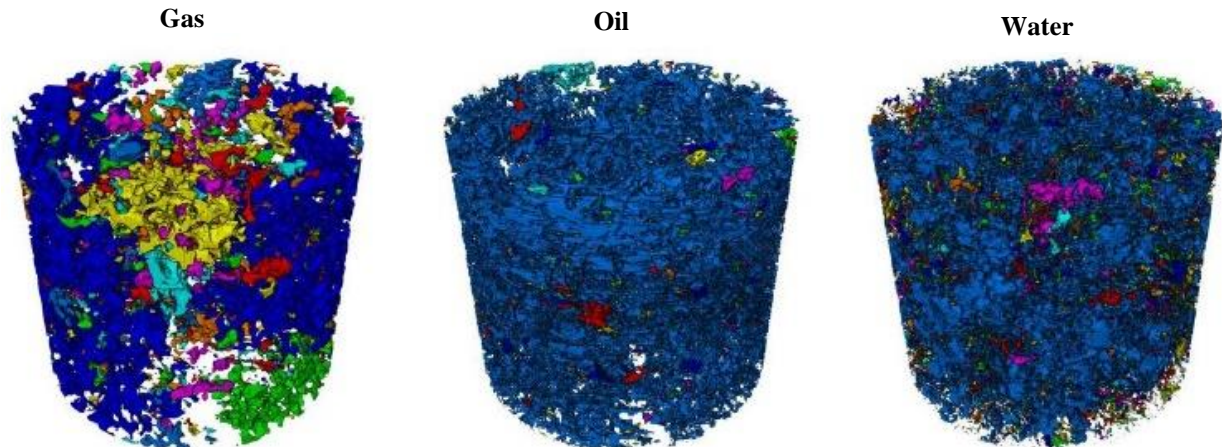


Fig. 4. Three-dimensional visualization of the (from left to right) gas, oil, and water clusters after the gas injection process. The blue clusters are connected from the bottom to the top of FOV, whereas the other colors represent disconnected clusters.

These observations are particularly interesting since (i) the continuous flow of gas was maintained during this process, and hence, one would expect to observe a well-connected network of gas clusters from the inlet to the outlet of the FOV, and (ii) the gas injection was a drainage event during which the trapping of the invading phase was less favorable compared to an imbibition process. Trapping of the most nonwetting phase during the secondary gas injection process can be explained based on some pore-scale displacement events such as Haines jump [28, 29, 20, 11] and Roof snap-off [30, 31]. During a drainage process, the pressure of the invading phase gradually builds up at the pore restrictions. Once the capillary pressure exceeds the threshold capillary pressure of a neighboring pore element, the nonwetting phase invades into that pore with an abrupt movement (jump) of the fluid interface and a transient pressure response. The pore-filling event causes the fluid to be withdrawn from high-pressure locations to supply the invasion front in the low-pressure regions. As a result, and especially in three-phase systems, some clusters may be disconnected from the bulk of the invading phase and be hydraulically trapped in the pore space. Moreover, when the gas phase moves from a pore restriction (i.e., throat) to a pore body, the local capillary pressure can fluctuate significantly. This process may lead to swelling of the wetting phase layer and trigger local Roof snap-off events at the restriction that can trap the gas phase. In addition to Haines jump and Roof snap-off, it is also hypothesized that double or multiple displacement chains (e.g., gas-to-oil-to-gas) [6, 9], and the ripening/anti-ripening phenomena [32] [33] could also contribute to the configuration of the gas phase in the porous medium. During the anti-ripening phenomenon, the gas phase occupying natural porous media may diffuse from large clusters into smaller ones, unlike in bulk mediums, since the former can be at higher local capillary pressures due to the confinements of the pore space.

Figures 5 and 6 also indicate that the disconnected oil clusters were significantly smaller than the connected cluster

and contributed only 5% to the total oil saturation. The oil phase in this study was non-spreading in the presence of gas and water phases, and hence it was expected to form lenses between the water and gas clusters if a certain gas-oil capillary pressure could have been established in the system. This threshold value, however, had presumably not been reached in this case. Furthermore, the continuous injection of the oil phase during the second gas injection process is also believed to help maintain the connectivity of the oil phase.

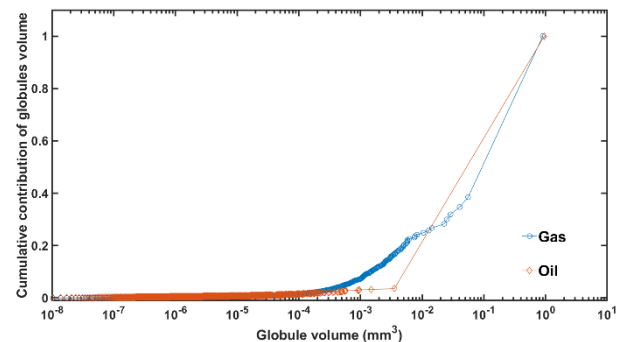


Fig. 5. The cumulative contribution of gas/oil ganglia with various sizes to the total gas/oil volume.

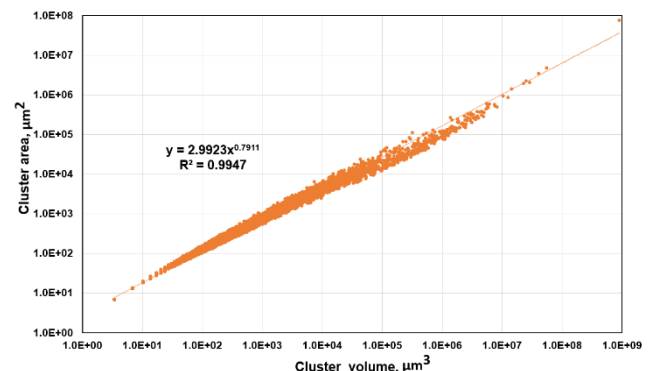


Fig. 6. The surface area versus volume of the gas clusters during the secondary gas injection experiment.

We have also investigated the morphology of the gas ganglia by quantifying the relationship between the volume and surface area of these objects. These parameters can be related through a power-law correlation of $A \propto V^b$ [34]. The correlation exponent b is equal to 0.66 for a perfect sphere and increases as the morphologies of the ganglia become more tortuous or elongated. The result of such a comparison for the gas clusters in this study is shown in Figure 5. The power-law exponent for the gas phase was found – using the least-squares method – to be 0.79, which was consistent with the values reported in literature studies [15].

4.3 In-situ capillary pressure

To quantify the in-situ capillary pressure using the methodology described in section 3.3, we partitioned the segmented image into 18 sub-volumes with equal sizes of $620 \times 620 \times 850$ voxels. For each sub-volume, the interfacial curvature of the gas-oil and oil-water interfaces were estimated, and the representative average values were used to calculate the respective capillary pressures [11]. The results are presented in Figure 7. The computed capillary pressures for each pair of fluids show some degrees of variation across the FOV. This variation is more significant for the gas-oil capillary pressures which is probably attributed to the fact that a significant portion of the gas phase existed in the form of disconnected globules, as discussed in section 4.2., which may have possessed different local capillary pressures [35].

The average oil-water capillary pressures were always greater than the gas-oil values, even though this is not the case for the average oil-water interfacial curvatures. This is attributed to the locations of the interfaces, as shown in Figure 8, which demonstrate that the oil-to-water displacements mostly took place at narrower capillary elements compared to the gas-to-oil events. Furthermore, the oil-water IFT is significantly higher than the gas-oil IFT ($\sigma_{ow} = 45.16 \text{ mN/m} > \sigma_{go} = 26.61 \text{ mN/m}$), while the receding contact angle is lower in the case of gas-oil interfaces [16] (which raises their curvatures). The combined effect of these three factors is that the threshold capillary pressures of the oil-to-water events would have presumably been higher than the gas-to-oil events.

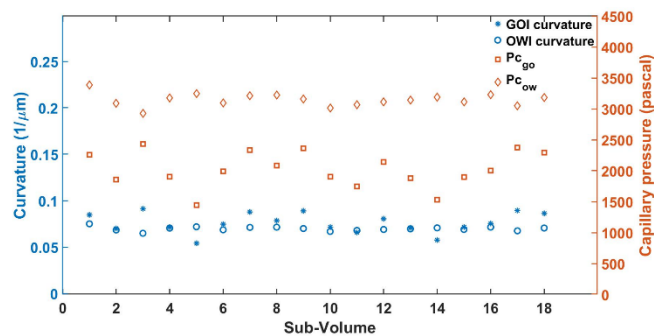


Fig. 7. The average interfacial curvature and the respective capillary pressures in the twenty-four sub-volumes.

In other words, the gas-to-oil displacement would take place at lower capillary pressures (i.e., $P_g - P_o$) and in larger pores compared to the water-to-oil displacements.

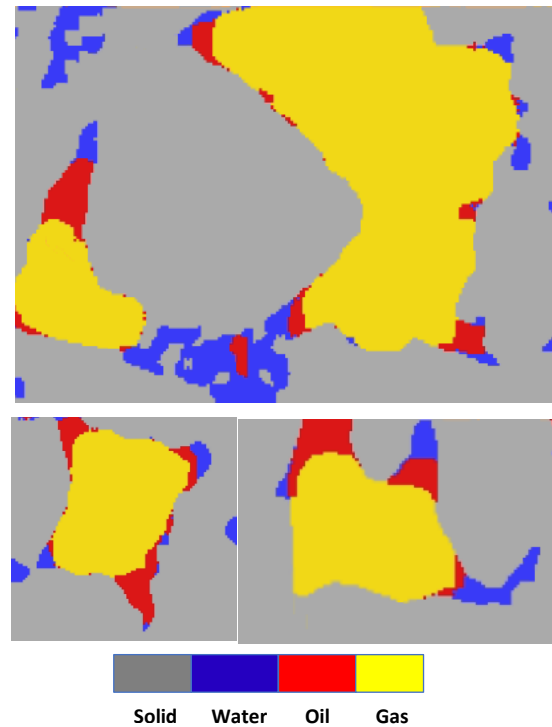


Fig. 8. Examples of three-phase interfaces during the secondary gas injection process (rock, water, oil, and gas are shown in grey, blue, red, and yellow respectively).

4. Conclusions

We characterize the pore-scale flow behavior during a steady-state gas injection process, where the three phases were injected simultaneously into a miniature Berea sandstone core sample. We used specific techniques to obtain pore-by-pore fluid occupancy data, analyze oil and gas clusters, and characterize the in-situ capillary pressure. In agreement with the wettability order of the system, the gas, oil, and water phases mostly occupied the largest, intermediate, and smallest pore elements of the system, respectively. Interestingly, we observed a significant amount of the invading gas phase trapped in the form of disconnected globules during this drainage process. The presence of these disconnected clusters was attributed to special displacement events such as the Haines jump and Roof snap-off. Moreover, the gas diffusion due to the anti-ripening phenomenon was also believed to contribute to the trapping of the gas phase. Finally, the oil-water local capillary pressures were found to be higher than the gas-oil ones. This observation was attributed to the fact that the oil-to-water displacement took place in smaller pore elements in which higher threshold capillary pressures need to be overcome.

We gratefully acknowledge the financial support of Thermo Fisher Scientific, Hess Corporation, and the University of Wyoming.

References

- [1] A. Mohamed, M. Khishvand and M. Piri, "A pore-scale experimental investigation of process-dependent capillary desaturation," *Adv. in Water Res.*, vol. 144, 2020.
- [2] Y. Gong and M. Piri, "Pore-to-Core Upscaling of Solute Transport Under Steady-State Two-Phase Flow Conditions Using Dynamic Pore Network Modeling Approach," *Transp. Porous Med.*, vol. 135, 2020.
- [3] O. Vizika and J. M. Lombard, "Wettability and spreading: Two key parameters in oil recovery with three-phase gravity drainage," *SPE Reservoir Eng.*, vol. 11, 1996.
- [4] A. H. Alizadeh and M. Piri, "Three-phase flow in porous media: A review of experimental studies on relative permeability," *Reviews of Geophysics*, vol. 52, 2014.
- [5] P. Øren, J. Billiotte and W. Pinczewski, "Mobilization of Waterflood Residual Oil by Gas Injection for Water-Wet Conditions," *SPE Formation Eval.*, vol. 7, 1992.
- [6] P. Øren and W. Pinczewski, "Fluid Distribution and Pore-Scale Displacement Mechanisms in Drainage Dominated Three-Phase Flow," *Trans. in Porous Med.*, vol. 20, 1995.
- [7] A. Keller, M. Blunt and A. Roberts, "Micromodel Observation of the Role of Oil Layers in Three-Phase Flow," *Trans. in Porous Med.*, vol. 26, 1997.
- [8] M. Sohrabi, D. Tehrani, A. Danesh and G. Henderson, "Visualization of Oil Recovery by Water-Alternating-Gas Injection Using High-Pressure Micromodels," *SPE J.*, vol. 9, 2004.
- [9] M. van Dijke and K. Sorbie, "Pore-scale modelling of three-phase flow in mixed-wet porous media: multiple displacement chains," *J. of Pet. Sci. and Eng.*, vol. 39, 2003.
- [10] M. Piri and M. J. Blunt, "Three-dimensional mixed-wet random pore-scale network modeling of two- and three-phase flow in porous media. I. Model description," *Phys. Rev. E*, vol. 71, 2005.
- [11] A. Zankoor, M. Khishvand, A. Mohamed, R. Wang and M. Piri, "In-situ capillary pressure and wettability in natural porous media: Multi-scale experimentation and automated characterization using x-ray images," *Journal of Colloid and Interface Science*, 2021.
- [12] R. T. Armstrong, C. Sun and et al., "Multiscale Characterization of Wettability in Porous Media," *Transport in Porous Media*, 2021.
- [13] R. T. Armstrong, M. L. Porter and D. Wildenschild, "Linking pore-scale interfacial curvature to column-scale capillary pressure," *Advances in Water Resources*, vol. 46, 2012.
- [14] S. Iglauer, A. Paluszny and M. Blunt, "Simultaneous oil recovery and residual gas storage: A pore-level analysis using in situ X-ray micro-tomography," *Fuel*, vol. 103, 2013.
- [15] S. Iglauer, T. Rahman, M. Sarmadivaleh, A. Al-Hinai, M. A. Fernø and M. Lebedev, "Influence of Wettability on Residual Gas Trapping and Enhanced Oil Recovery in Three-Phase Flow: A Pore-Scale Analysis by Use of Microcomputed Tomography," *SPE J.*, vol. 21, 2016.
- [16] M. Khishvand, A. Alizadeh and M. Piri, "In-situ characterization of wettability and pore-scale displacements during two- and three-phase flow in natural porous media," *Adv. in Water Res.*, 2016.
- [17] Z. Qin, M. Arshadi and M. Piri, "Micro-scale experimental investigations of multiphase flow in oil-wet carbonates. I. In situ wettability and low-salinity waterflooding," *Fuel*, vol. 257, 2019.
- [18] M. J. Sabti, A. H. Alizadeh and M. Piri, "In-situ investigation of the impact of spreading on matrix-fracture interactions during three-phase flow in fractured porous media," *Adv. in Water Res.*, vol. 131, 2019.

- [19] A. Alhosani, A. Scanziani, Q. Lin, Z. Pan, B. Bijeljic and M. J. Blunt, "In situ pore-scale analysis of oil recovery during three-phase near-miscible CO₂ injection in a water-wet carbonate rock," *Adv. in Water Res.*, vol. 134, 2019.
- [20] A. Alhosani, A. Scanziani, Q. Lin, A. Selem, Z. Pan, M. J. Blunt and B. Bijeljic, "Three-phase flow displacement dynamics and Haines jumps in a hydrophobic porous medium," *The Royal Society*, 2020.
- [21] A. Scanziani, K. Singh, H. Menke, B. Bijeljic and M. J. Blunt, "Dynamics of enhanced gas trapping applied to CO₂ storage in the presence of oil using synchrotron X-ray micro tomography," *Applied Energy*, vol. 259, 2020.
- [22] A. Scanziani, K. Singh, T. Bultreys, B. Bijeljic and M. J. Blunt, "In situ characterization of immiscible three-phase flow at the pore scale for a water-wet carbonate rock," *Adv. in Water Res.*, vol. 121, 2018.
- [23] A. Q. Raeini, B. Bijeljic and M. J. Blunt, "Generalized network modeling: Network extraction as a coarse-scale discretization of the void space of porous media," *Phys. Rev. E*, vol. 96, 2017.
- [24] J. E. McClure, R. T. Armstrong, M. A. Berrill, S. Schlüter, S. Berg, W. G. Gray and C. T. Miller, "Geometric state function for two-fluid flow in porous media," *Phys. Rev. Fluids*, vol. 3, 2018.
- [25] M. Desbrun, M. Meyer, P. Schröder and A. H. Barr, "Implicit Fairing of Irregular Meshes Using Diffusion and Curvature Flow," *ACM Press/Addison-Wesley Publishing Co.*, 1999.
- [26] D. Kroon, "Smooth Triangulated Mesh," *Matlab central file exchange*, 2021.
- [27] A. Alhosani, B. Bijeljic and M. J. Blunt, "Pore-Scale Imaging and Analysis of Wettability Order, Trapping and Displacement in Three-Phase Flow in Porous Media with Various Wettabilities," *Transport in Porous Media*, 2021.
- [28] W. Haines, "Studies in the physical properties of soil. V. The hysteresis effect in capillary properties, and the modes of moisture distribution associated therewith.," *The J. of Agric. Sci.*, vol. 20, 1930.
- [29] S. Berg and e. al., "Real-time 3D imaging of Haines jumps in porous media flow," *Proc. Natl. Acad. Sci.*, vol. 110, 2013.
- [30] J. Roof, "Snap-off of oil droplets in water-wet pores," *Soc. Petrol. Eng. J.*, vol. 10, 1970.
- [31] A. Kavscek, G.-Q. Tang and C. Radke, "Verification of Roof snap off as a foam-generation mechanism in porous media at steady state," *Colloids and Surfaces A: Phys. and Eng. Aspects*, vol. 302, 2007.
- [32] K. Xu, R. Bonnecaze and M. Balhoff, "Egalitarianism among Bubbles in Porous Media: An Ostwald Ripening Derived Anticoarsening Phenomenon," *Phys. Rev. Lett.*, vol. 119, 2017.
- [33] S. Berg, Y. Gao and e. al., "Determination of Critical Gas Saturation by Micro-CT," *Petrophysics*, vol. 61, 2020.
- [34] C. J. Landry, Z. T. Karpyn and M. Piri, "Pore-scale analysis of trapped immiscible fluid structures and fluid interfacial areas in oil-wet and water-wet bead packs," *Geofluids*, vol. 11, 2011.
- [35] M. Andrew, B. Bijeljic and M. J. Blunt, "Pore-by-pore capillary pressure measurements using X-ray microtomography at reservoir conditions: Curvature, snap-off, and remobilization of residual CO₂," *Water Resources Research*, vol. 50, 2014.

Study of relative permeability curves for a CO₂-brine system at reservoir conditions in carbonates

Jorge Tovar^{1,*}, Tatiana Berna¹, Tálisson Borges¹, Janeth Vidal², Rafael Valladares de Almeida³, Gabriel Soares Bassani³, and Erika Koroishi².

¹University of Campinas - UNICAMP, Faculty of Mechanical Engineering, Rua Mendeleev 200, Campinas, SP, Brazil

²Center for Petroleum Studies - CEPETRO, Miscible Methods of Recovery Laboratory - LMMR, Rua Cora Coralina 350, Campinas, SP, Brazil

³Repsol Sinopec Brasil S.A, Research and Development Department, Praia de Botafogo 300, Rio de Janeiro, RJ, Brazil

Abstract. This work presents an experimental study to determine unsteady-state drainage and imbibition relative permeability curves by coreflooding in a two-phase system: equilibrated carbonated brine (ECB) and supercritical CO₂ (scCO₂), using Brazilian Pre-salt carbonate rocks under reservoir conditions (8,500 psi and 70°C). Saturation changes in the rock were monitored by computed tomography (CT) and mass balance. As analytic methods to build relative permeability curve such as Johnson, Bossler and Neuman (JBN) are not valid due to the confirmed presence of fingering, relative permeability curves were defined using the Corey model and Corey exponents found in literature related to this work. Results showed a slow increase of CO₂ relative permeability and a rapid decrease of ECB relative permeability during the first part of the drainage. Also, at the end of the drainage a residual ECB saturation of 27% was achieved. Furthermore, during the imbibition, the hysteresis effect was observed on the ECB relative permeability curve as a result of the CO₂ trapped (19.5%). In addition, evidence that the ECB is not strongly wetting the rock in the presence of CO₂ is presented. Finally, the Land trapping parameter was calculated along the composite core.

1 Introduction

The high CO₂ concentration of produced field gas in Brazilian Pre-Salt reservoirs (10 to 45%) brings essential technological challenges for the applicability of CO₂. For example, the separation of this gas is necessary before transferring to onshore facilities, because the transportation of high CO₂ content gas is not feasible due to its corrosive effects in transport facilities [1]. Nowadays, CO₂ separation equipment is expensive, high energy-consumer, and takes up a significant area of the floating production storage and offloading vessel (FPSO) [1]. On the other hand, flaring could be the most straightforward and cheapest option to dispose this gas. Nevertheless, regulations to control this practice are more rigid every time [2]. For the reasons explained above, it is necessary to find ways to use or store CO₂ to avoid negative impacts on the environment and damage to facilities.

Otherwise, the growing energy demand worldwide in the context of a low-carbon energy transition encourages CO₂ utilization for Enhanced Oil Recovery (EOR) solutions, which improves oil productivity while safely disposing of a gas that would contribute to global warming. As a consequence, CO₂-WAG (Water Alternating Gas) has been applied in Brazilian offshore

oilfields to improve recovery rates and mitigate the environmental impact that venting CO₂ would bring [3].

The alternating injection of water and gas was conceived to compensate the counter tendencies of gas rising upward and water falling downward inside the reservoir by dividing the continuous slug of gas into smaller slugs by alternating water banks [4]. On the other hand, injecting water with miscible gas reduces the instability of the gas/oil displacement, improving the overall sweep efficiency [5].

Consequently, CO₂-WAG projects are sensitive to fluid-rock and fluid-fluid interactions, beyond the characterization of the rock and fluids themselves [5]. Hence, relative permeability curves and their associated parameters are the most relevant petrophysical relations for EOR processes [6]. That is why understanding the physics behind which CO₂ and water displacing oil in the porous medium is of utmost importance for the success of any miscible CO₂-WAG injection [7]. Though there have been attempts to calculate relative permeabilities on theoretical grounds, by far, the most common source of k_r curves has been experimental measurements [6]. Therefore, coreflood experiments have to be designed efficiently to provide relevant information about the complex two and three-phase flow mechanism. The

* Corresponding author: jorgeatovar@hotmail.com

experimental measurements must be accurate and representative of the system as they are key reservoir parameters such as trapped gas saturation, relative permeability curves and hysteresis effects [7].

Some studies present a valuable data set for the evaluation and simulation of CO₂ injection [8, 9]. These works carried out in carbonates and other rocks from oil reservoirs at in situ conditions, showed interesting results such as a relation between residual saturations and heterogeneity of the rock. They also showed a most favorable mobility ratio when brine displaced CO₂ and observed a change in the pore structure of carbonate rocks due to mineral reactions (dissolution and precipitation) that possibly affects the relative permeability displacement behavior of CO₂ and brine.

This work proposes an experimental study of unsteady-state relative permeability curves carried out in a Brazilian Pre-Salt reservoir rock sample at reservoir conditions (8500 psi and 70°C). The study involved both drainage and imbibition tests using equilibrated carbonated brine and scCO₂. In Situ Saturation Monitoring (ISSM) by CT and mass balance were used to trace the saturation evolution during the displacements. Finally, relative permeability curves were determined using the Corey model [10], and the Land trapping coefficient [11] was calculated along the length of the rock sample. Also, a robust experimental setup was commissioned for two- phase unsteady-state relative permeability curves testing.

2 Materials

2.1 Core samples

The reservoir carbonate rock samples were obtained from the oil zone of a Brazilian Pre-salt province field located in the Santos Basin, and its likely oil wet preference has been proven by the operator. In the experiment, a composite core of five short cores was used. An X-ray image of the composite core is shown in Figure 1. The composite core was arranged according to the dolomite content of each sample. Thus, the core samples were ordered from higher to lower dolomite content from injection to production; aiming to preserve the condition of the samples throughout the tests using CO₂ and carbonated brine. The average mineral content and the petrophysical measurements of the composite core are shown in Tables 1 and 2, respectively. The mineral composition of the rocks was provided by the company that provided the samples. Absolute gas permeability and effective porosity were measured using a gas permeameter (CoreLab Ultraperm-500) and a gas porosimeter (CoreLab Ultrapore-300), respectively. Figure 2 shows the initial porosity distribution profile obtained from N₂ and deionized water CT scans. A high degree of heterogeneity in porosity is noted since values obtained vary from 0.09 to 0.24. It should be noted that before the measurements, the samples were cleaned by Soxhlet extraction using toluene and methanol as

recommended by Torsaeter and Abtahi [12]. Even though the wettability of the cores may be turned back to strong water wet preference, this process was needed since the use of the porosimeter and permeameter from initial measurements requires the samples in dry conditions.

Figure 1. X-ray image of the composite core.

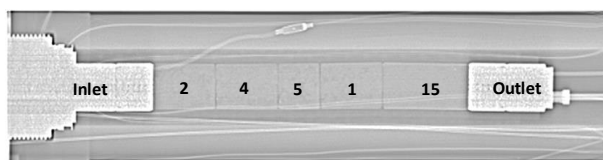


Figure 2. Initial porosity distribution profile

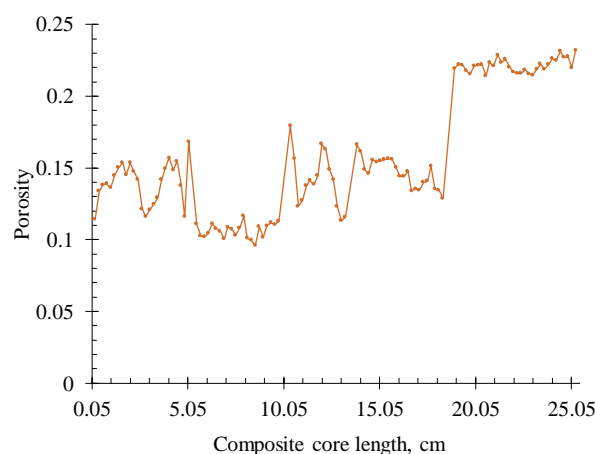


Table 1. Mineral content of the composite core.

Clay, %	Calcite, %	Dolomite, %	Others, %
2.72	57.19	31.94	8.15

Table 2. Petrophysics measurements of the composite core.

Length, cm	Diameter, cm	Permeability, mD	Porosity, %	Pore Volume, cm ³
25.28	3.78	182	15.72	44.71

2.2 Fluids

Two distinct fluids were used during the experimental work: supercritical CO₂ and equilibrated carbonated brine, both at reservoir conditions (8500 psi and 70°C).

2.2.1 Supercritical CO₂

Under laboratory conditions, CO₂ is found as a gas. Using a high-pressure compressor, CO₂ is transferred to the accumulators used in the test and pressurized until 4000 psi. Then, assisted by a positive displacement pump, the

fluid is raised to reservoir pressure. Table 3 presents some properties of CO₂ at reservoir conditions.

Table 3. CO₂ properties at reservoir conditions [13]

Pressure, psi	8500
Temperature, °C	70
Density, g/cm³	0.936
Viscosity, cp	0.103
Z factor	0.966

2.2.2 Equilibrated Carbonated Brine

Using a geochemical software, the injection of carbonated water in the carbonate rock saturated with seawater at reservoir conditions was simulated. The result of the simulation leads to the composition of the equilibrated carbonated brine. The objective of equilibrating the carbonated brine aimed two objectives: firstly, to avoid the mass transfer between the CO₂ and the carbonated brine while executing the test. Secondly, to control severe dissolution effects on the carbonate composite core. The ECB was prepared and fully saturated with CO₂ following a methodology proposed by Nuñez *et al.* [14]. Table 4 shows the equilibrated brine composition that was saturated with 45 cm³ of CO₂ at lab conditions, then heated throughout a band heater until 70°C and pressurized using a positive displacement pump until 8500 psi. The viscosity of the ECB at reservoir conditions is 0.58 cp, as established by Rocha *et al.* [15].

Table 4. Equilibrated brine composition

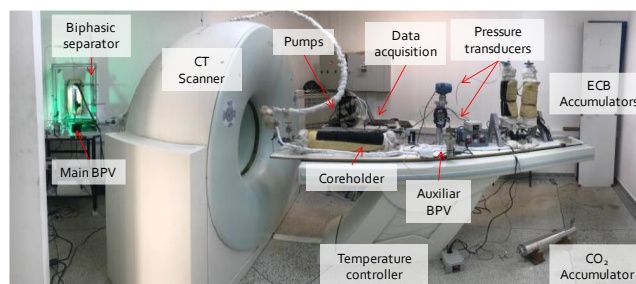
Compound	Concentration, g/L
KCl	0.9490
MgCl ₂ .6H ₂ O	16.9717
SrCl ₂ .6H ₂ O	0.0272
CaCl ₂ .2H ₂ O	7.3213
NaCl	18.5128
Na ₂ SO ₄	0.0587
NaHCO ₃	9.0083
Na ₂ CO ₃	0.0029
TDS	42.0230

2.3 Experimental setup

A robust experimental setup was designed and commissioned to perform unsteady-state relative permeability tests. The whole experimental setup was

installed on and around a medical CT scanner Siemens Somatom Spirit (Figure 3).

Figure 3. Experimental setup



The experimental setup was divided into four major systems:

- 1) Injection system: composed of three Quizix Q5000 precision metering pumps used to displace fluids at a continuous flow rate and to execute the overburden pressure (1000 psi above the working pressure). Also, accumulators for fluids storage and injection.
- 2) Core sample confining system: composed by a special coreholder for relative permeability tests. The coreholder is made of aluminum designed for X-ray tomography. It includes a mixer that is a device made to avoid the gravity segregation effect while displacing fluids. Previous to the placing of the composite core into the coreholder, the samples were individually cemented (to fill surface irregularities) and stacked. Then, the composite core was wrapped with Teflon tape, aluminum foil, a heat shrinking film and then inserted into a nitrile rubber sleeve to avoid fluid leakage. Once the composite core was located inside the coreholder, a vacuum process of 24 hours was done to take out the air present in the porous medium. It was observed severe swelling effects in the Viton O-rings located both in the coreholder and accumulators that is why nitrile O-rings were used for the test. Also, there was presence of corrosion in the Teflon made packing seals of valves.
- 3) Production system: composed by a biphasic visual separator that allowed monitoring the produced fluid volume during the test at reservoir conditions (high pressure and high temperature). Also, a set of 2 (one principal and the other one auxiliary) back pressure valves (BPV) to ensure the execution of the test at 8500 psi.
- 4) Control and monitoring system: composed by differential and absolute pressure transducers, temperature controllers, a camera installed in the biphasic separator, and a laptop for data recording.

All the setup equipment (coreholder, accumulators, biphasic separator, and lines) were coated with band

heaters connected to temperature controllers to keep test temperature constant at 70°C.

3. Experimental procedures

3.1 Attenuation coefficient characterization

Once the fluids needed for the test were prepared, each attenuation coefficient (CT number) was determined. This procedure was executed by scanning with X-ray tomography, a hollow aluminum cylinder (Figure 4) filled with the fluid to study; the cylinder was located inside a coreholder at desired temperature and pressure conditions. The results of the attenuation coefficient with the temperature and pressure conditions are shown in Table 5.

Consecutively, the composite core was sequentially saturated with each fluid and brought to the conditions of Table 5. Then, CT scans were made along the saturated composite core to characterize the attenuation coefficient of 2 mm spaced slices. The CT values of the fluids and saturated composite were performed to obtain the parameters needed for in situ saturation calculation. The procedure is further explained in item 4.1.

Figure 4. Cylinder for fluids attenuation characterization



Table 5. Attenuation coefficients of fluids

Fluid	Temperature, °C	Pressure, psi	CT Number, HU
Nitrogen	70	500	-739
scCO ₂	70	8500	31
Deionized water	70	8500	174
ECB	70	8500	200

3.2 Drainage test

Firstly, as the composite core was saturated with ECB at reservoir conditions (8500 psi and 70°C), the absolute permeability was determined while flowing it by

changing the flow rate from 1 to 3cm³/min and monitoring the pressure drop until equilibrium was reached. This absolute permeability, k , was established as the base permeability for further calculations of relative permeability.

The drainage was performed by displacing the ECB from the porous medium by injecting scCO₂ under reservoir conditions at a constant flow rate of 1 cm³/min. This rate was chosen after reviewing the work of Vidal Vargas *et al.* [16], considering that lower rates would stimulate dissolution effects by increasing contact time, and higher rates could lead to damages inside the porous medium. The pressure drop and the produced ECB volume were monitored during the whole test. Also, CT scans were acquired for in situ saturation monitoring. CT scan parameters used were 130 kV and 80 mA. It is important to say that during the execution of the drainage test, an oscillation in pressure drop occurred caused by the severe volume expansion of scCO₂ when it decompressed rapidly from high (8500 psi) to atmospheric pressure, which ended up freezing and blocking the BPV for some seconds.

At the end of the drainage, the flow rate was increased to 1.5 cm³/min in order to reach the residual ECB saturation. Then, as no more ECB was produced, the flow rate was pushed back to 1 cm³/min until equilibrium was reached, and the effective permeability of scCO₂, k_{CO_2} , at residual ECB saturation was determined.

3.3 Imbibition test

Once the drainage was finished, the biphasic separator was adjusted to measure produced scCO₂. The imbibition was executed at reservoir conditions by injecting ECB at a flow rate of 1 cm³/min. The criterion to choose the rate was the same used in the drainage test. During this process, the scCO₂ present in the porous medium at the end of the drainage was displaced up to residual or trapped scCO₂ saturation, S_{CO_2i} . Before finishing the imbibition test, the flow rate was increased to 2 cm³/min in order to reach the residual scCO₂ saturation, S_{CO_2r} . Then, as no more scCO₂ was produced, the flow rate was decreased to 1 cm³/min and, the effective ECB permeability, k_{ECB} , was determined.

At some time of the imbibition test (before 1 PV of ECB injected), the injection pressure exceeded the maximum allowable working pressure of the biphasic separator (10000 psi), most likely by the freezing effect in the BPV. Thus, the flow was re-addressed through the separator by-pass. Hence, the monitoring of produced CO₂ volume was lost, and it was only possible to keep tracing the saturation via CT scan.

At the end of the imbibition cycle, flow through cleaning injection was performed. It consisted in flooding the composite core with deionized water for 24 hours at reservoir conditions. Also, a CT scan of the fully deionized water saturated composite core was taken, in

order to obtain the required parameter for final porosity determination. However, the flow of deionized water could induce some changes in the porous medium. Then, the system was depressurized, and nitrogen flowed at 70°C and 500 psi. Concluding this stage, a final CT scan of the composite core saturated with nitrogen was taken. It was not possible to perform post-test porosity and permeability measurements due to the unavailability of the samples (they were required immediately for another research).

4. Results

4.1 Saturation evolution

As outlined above, the evolution of saturation was monitored by both mass balance and CT scan, except for the imbibition test, which was traced by CT scan only almost the whole test.

Equations (1) and (2) were used to determine the fluids saturation by mass balance for the drainage test.

$$S_1 = 1 - \frac{Vol_{1P}}{PV} \quad (1)$$

$$1 = S_1 + S_2 \quad (2)$$

Where,

S_1 , Average displaced phase saturation
 S_2 , Average displacing phase saturation
 Vol_{1P} , Produced volume of the displaced phase
 PV , Pore volume

A MatLab™ routine, developed by Vargas [17], was used to process the CT scan images. The CT numbers obtained after that processing were then used in equations (3) and (4) to trace the saturation changes for each slice of the composite core during the experiment.

$$S_W = \frac{CT_R - CT_{NW}}{CT_W - CT_{NW}} \quad (3)$$

$$1 = S_W + S_{NW} \quad (4)$$

Where,

S_W , Wetting phase saturation
 S_{NW} , Non wetting phase saturation
 CT_R , Attenuation coefficient of the composite core saturated with biphasic saturation at a time of interest
 CT_W , Attenuation coefficient of the composite core completely saturated with the wetting phase
 CT_{NW} , Attenuation coefficient of the composite core completely saturated with the non-wetting phase.

4.1.1 Drainage test saturation evolution

Figure 5 shows the produced volume of ECB as a function of the injected volume of scCO₂. The curve displays an approximately linear behavior increase until 30 cm³ of scCO₂ injected (red dot). The curve presents a change in its inclination caused by the beginning of biphasic flow at the end of the composite core. This turning point is the breakthrough [18]. From here, the produced volume of scCO₂ increases, and the produced volume of ECB gradually drops until a residual volume of ECB (higher than the ECB irreducible volume, as the plateau was not accomplished according to Figure 5) is achieved inside the sample.

Figure 5. Produced ECB

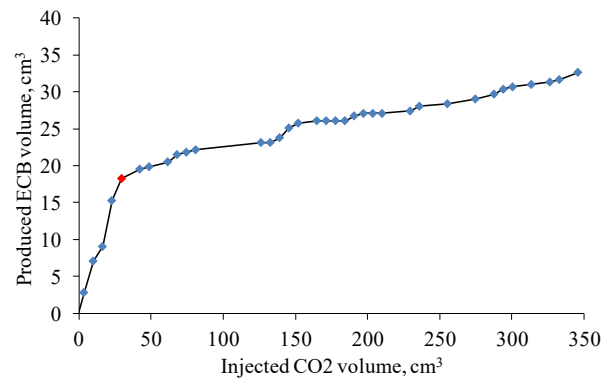
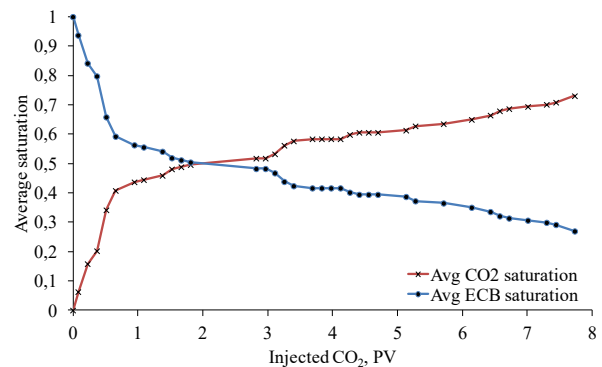


Figure 6 shows the evolution of scCO₂, and ECB average saturation (determined by mass balance) as a function of the pore volumes of scCO₂ injected during the drainage test. The graph depicts a rapid increase of scCO₂ saturation as a decrease in ECB saturation until approximately 0.6 PV of scCO₂ injected. Then, both curves perform an alteration on its inclination; this changing point represents the breakthrough as well. Also, on this Figure, it is possible to find that the breakthrough happened at an approximately ECB saturation of 0.6, and after almost 8 PV of CO₂ injected, a residual ECB saturation of 0.27 was achieved, which indicates that the ECB irreducible saturation will be less than 0.27.

Figure 6. Saturation evolution by mass balance



As part of the mass balance analysis, Figure 7, which is a zoom of the beginning of Figure 5, shows that the

volume of ECB produced from the beginning up to the breakthrough does not correspond to a linear behavior of 45° (depicted by the dashed line). This behavior, as explained by Rosa *et al.* [18], would correspond to an evidence of viscous fingering that occurred during the drainage test as a result of the unfavorable mobility ratio of scCO₂ displacing ECB ($M = 5.01$). As scCO₂ is more mobile than water in the porous medium, the injected scCO₂ tends to bypass water developing a less efficient displacement. Also, it could have been a consequence of having the composite core in a horizontal position, what could have promoted gravity segregation of fluids. The CT scanner used in this work is not adjusted for vertical scanning of the composite core, which would have been desirable in this case to minimize gravity segregation and viscous fingering. In addition, there could have been presence of mass transfer between the phases, since during the test the pressure of the system was occasionally higher than the equilibrium pressure of the two fluids (8500 psi). On the other hand, the compressibility of CO₂ at test conditions was determined (0.0001176 psi⁻¹) and could be negligible once there were not significant pressure changes.

Figure 7. Produced ECB during the first PV of CO₂ injected

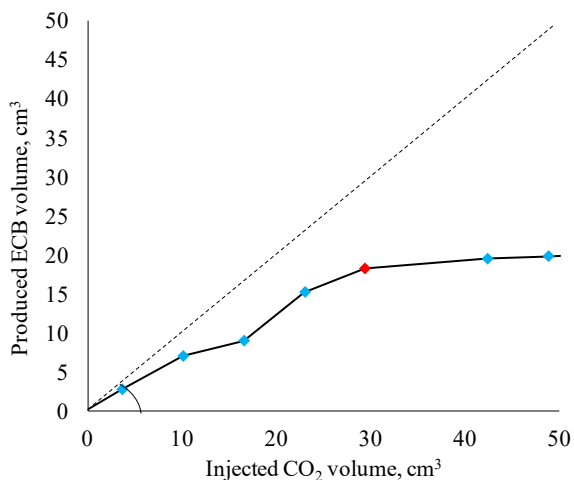


Figure 8 shows a comparison between the average scCO₂ saturations obtained by mass balance and computed tomography. On the chart, it is possible to see the proximity of saturation values from the measurements taken at an approximately same time (pore volumes of injected CO₂), e.g., the values of saturation taken at 1.6, 2.9, and 3.7 PV of scCO₂ injected among others. This proximity allows confirming the correspondence between the two saturation evolution monitoring methods used in this study, as well as the validation of the saturation values. However, there are some other values of saturations provided by CT that do not correspond to the ones of mass balance taken approximately at the same time, e.g., 0, 2, 6, and 8.2 PV of scCO₂ injected. One reason for such differences is the loss of capillary continuity between the core samples at each face to face junction. This, was verified by comparing one of the X-ray images of the composite core with the saturation distribution profiles obtained from each CT scan. This

analogy allowed identifying that at every face to face joining position existed gaps that match with distortions of the saturation values tendency (even negative saturation values). The correlation between the two mentioned elements is presented in Figure 9. The upper part corresponds to the composite core X-ray image, and the gaps existing at each face to face junction are correlated to a saturation distortion on two saturation profiles downwards following the dashed lines. Also, errors associated to the measurement techniques and equipment might have contributed to the distortions in saturation. It is important to note that only saturation values between 0 and 1 were used to calculate the average saturation. Negative and values greater than 1 are presented in Figure 9 to depict the effect of loss of capillary continuity. On the other hand, the capillary end effect is less pronounced than the effects observed in water wet cores showed by Huang and Honarpour [19]. Hence, it might be assumed that the composite core of this study does not have a strong water preference, at least in the presence of scCO₂.

Figure 8. Saturation evolution by mass balance Vs computed tomography

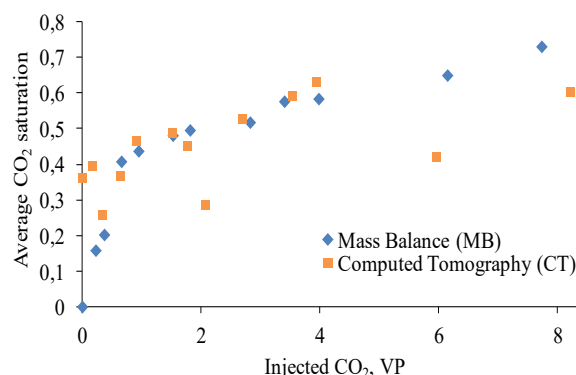
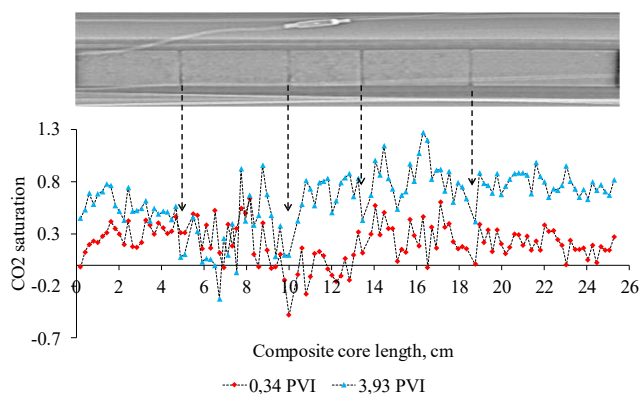


Figure 9. Correlation between composite core X ray image and drainage saturation profiles



4.1.2 Imbibition test saturation evolution

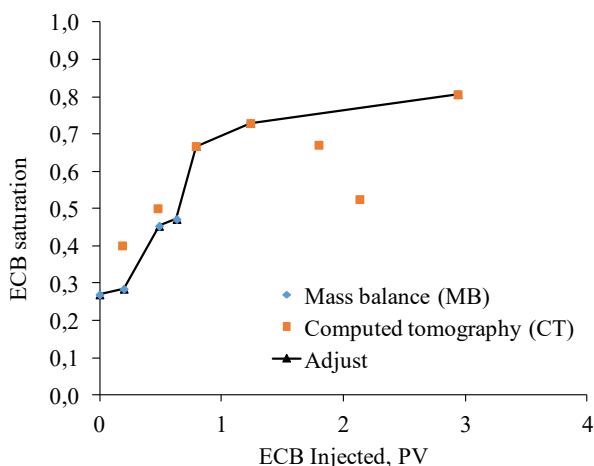
As previously said, it was not possible to monitor the saturation evolution of the entire imbibition test by the mass balance due to the demand for bypassing the biphasic separator because of the pressure increase above

its working pressure. Hence, from that point, the saturation was traced by CT only.

Thus, to compose a complete imbibition saturation curve, the first values of ECB saturation obtained by mass balance were integrated with those taken from CT. Figure 10 presents the result of that integration. The saturation curve of the imbibition is represented by the black curve named “adjust”, which starts at an average value of ECB saturation of 0.23 (residual value of ECB in the drainage). Thus, the curve continues through the saturation values obtained by mass balance until approximately 0.6 PV of ECB injected. From there, the values obtained by CT were used until the end of the imbibition, some values of saturation taken by CT (those close to 2 PV of ECB injected) were not taken into account for the curve, as they do not make physical sense in the saturation field.

Moreover, the adjusted curve presented a shifting point in the inclination at the approximate value of 0.8 PV of ECB injected. This point corresponds to the breakthrough of the ECB. In this case the displacement process occurred at a more favorable mobility ratio ($M = 0.1$), and as stated by Fanchi [20] the ECB displacing CO₂ is a more efficient displacement. Also, Figure 10 shows low post breakthrough scCO₂ recovery. This could imply that the sample is not strongly water wet in presence of scCO₂ which would be wetting the sample surfaces to certain extent and not behaving like a non-wetting gas.

Figure 10. Saturation evolution by mass balance plus computed tomography

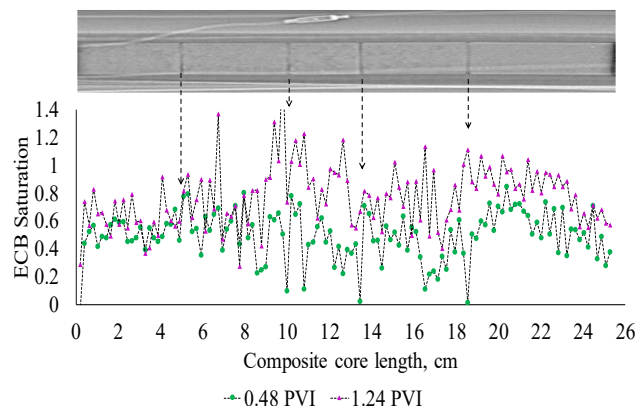


At the end of the imbibition, a trapped scCO₂ saturation value of approximately 0.195 was obtained, which means that a significant pore volume of the porous medium was able to be filled again with ECB (almost 0.8 of saturation).

Figure 11 shows the composite core X-ray image and two saturation distribution profiles obtained by CT scan at different times (0.19 and 0.48 PVI of ECB). In this chart, it is possible to correlate the gaps between each face to face junction of the core samples with the saturation profiles along the composite core. Here the saturation

distributions profiles were also affected by the loss of capillary continuity, but less drastically than in the drainage test probably because of the improvement of the displacement efficiency or the water wet preference of the rock.

Figure 11. Correlation between composite core X ray image and imbibition saturation profiles



4.2 Relative permeability curves

At the beginning of the study, it had been planned to use the JBN method to determine the relative permeability curves. However, there were some experimental conditions such as unstable displacement (presence of viscous fingering) and not constant flow rate or pressure drop while executing the displacements; that disallowed the use of that methodology.

As previously said, no theoretical expression exists for the relative permeability function. However, when analytical expressions are needed, it is possible to use the following exponential form called Corey model [6]:

$$k_{r1} = k_{r1}^o \left(\frac{S_1 - S_{1r}}{1 - S_{1r} - S_{2r}} \right)^{n_1} \quad (5)$$

$$k_{r2} = k_{r2}^o \left(\frac{1 - S_1 - S_{2r}}{1 - S_{1r} - S_{2r}} \right)^{n_2} \quad (6)$$

Where,

- k_{r1} , displacing phase relative permeability
- k_{r2} , displaced phase relative permeability
- k_{r1}^o , displacing phase relative permeability end point
- k_{r2}^o , displaced phase relative permeability end point
- S_1 , saturation of the displacing phase
- S_{1r} , connate saturation of the displacing phase
- S_{2r} , residual saturation of the displaced phase
- n_1 , displacing phase Corey exponent
- n_2 , displaced phase Corey exponent

Table 6 shows a summary of the results of residual saturations and the relative permeability endpoints determined from the drainage and imbibition tests. The absolute permeability measured with ECB at the

beginning of the drainage test was taken as the base permeability, relative permeability endpoints were determined using Darcy's law, and the residual saturations were taken from the measurements of average saturation from mass balance and CT for drainage and imbibition respectively. Also, Table 7 presents the Corey exponents, n_1 and n_2 , that were used in the model. These coefficients are not directly related to the mineralogy or properties of the rock used in this work. However, they were extracted from a research work realized in carbonates at reservoir conditions as well [9].

Table 6. Results summary

Stage	Pressure drop, atm	Permeability, mD	Relative permeability
ECB @ 100%	0.10	209.7	1
CO ₂ @ S_{ECBr} , 27%	0.02	187.6	0.89
ECB @ S_{CO_2r} , 19.5%	0.21	99.3	0.47

Table 7. Corey exponents

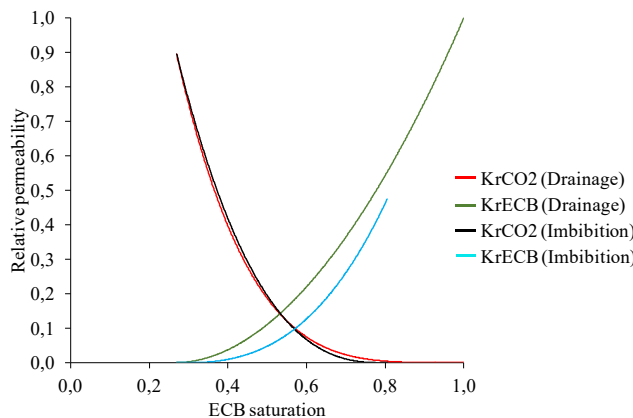
Process	n_1	n_2
Drainage	1.91	4.14
Imbibition	2.92	2.74

Where,

n_1 , displacing phase Corey exponent
 n_2 , displaced phase Corey exponent

Consequently, using the values of saturation obtained during the test and the data of Tables 6 and 7, equations (5) and (6) were applied to construct the drainage and imbibition relative permeability curves (Figure 12).

Figure 12. Relative permeability curves



First of all, relative permeability is a rock fluid property that has a strong dependency on the saturation of the phases present in the porous medium. However, the relationship between relative permeabilities of these phases and their saturations are also a function of rock properties (pore size distribution, for example) and wettability [6,20]. As it is well known for gas-liquid systems, the wettability in this case would have a preference for the ECB. However, the value of S_{ECBi} reached at the end of the drainage (less than 0.27) could be an indication of weak wetting preference to ECB; since a rock with a stronger wetting preference would have reached a higher S_{ECBi} .

Also, it is vital to take into account that the cleaning process performed in the core samples may have not changed severely the wettability of the carbonate samples. In contrast to the results showed by Austad *et al.* [22].

Besides that, other features that can be observed in Figure 12 are the critical gas saturation, and the behavior of ECB and scCO₂ relative permeability curves. The critical gas saturation, that is, the value at which the nonwetting phase becomes mobile, is located at an approximate value of scCO₂ saturation of 0.20. According to Amyx *et al.* [21], this saturation value may vary between 0.10 and 0.30 of nonwetting saturation in carbonates. The relative permeability curves behavior could be some indicator of the distribution of the fluid within the porous medium [21]. There is a rapid decline in the ECB relative permeability for small increases in scCO₂ saturation, which would indicate that the larger pores or longer flow paths are occupied first by the scCO₂. Also, as little scCO₂ volume has been injected into the porous medium after the critical gas saturation, there is a rapid rise in scCO₂ relative permeability for small increases of this phase saturation, this would confirm that above the critical gas saturation, the average pore size saturated with the ECB becomes successively smaller, which means that the scCO₂ would occupy larger pores within the porous medium.

In addition, the trapped scCO₂ saturation at the end of the imbibition test achieved a value of 0.19, close to the average saturation of 0.23 reported by Bennion and Bachu [9]. This study and the one presented by Bennion and Bachu showed low values of porosity (0.15 and 0.12 respectively). This direct relationship between trapped gas saturation and porosity differs from the result obtained by Jerauld [23] in water wet samples, which shows higher values of gas trapped saturation for similar values of porosity. The divergence in porosity and trapped gas in this study may be an evidence that the ECB is not strongly wetting the sample and would indicate that the scCO₂ had certain wetting tendency that prevents it from being capillary trapped like a non-wetting fluid.

On the other hand, the hysteresis effect was confirmed in the relative permeability curve of the ECB. This effect could be associated with the scCO₂ trapping by the ECB within the porous medium during the imbibition process, which decreases the conductivity offered to the ECB.

However, the scCO₂ relative permeability curve does not present a significant change; this probably caused by the slippage effect of supercritical scCO₂. To better depict the hysteresis effect, the Land's trapping parameter, *C*, was determined along the composite core by using Equation (7).

$$C = \frac{1}{S_{CO_2i}} - \frac{1}{S_{CO_2c}} \quad (7)$$

Where,

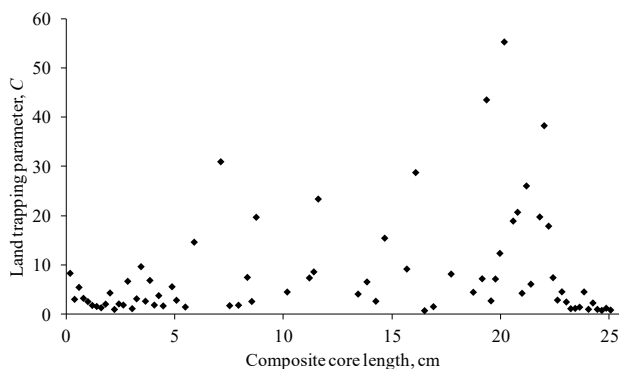
C, Land trapping parameter

*S*_{CO₂i}, Residual or trapped scCO₂ saturation (at the end of the imbibition process)

*S*_{CO₂c}, Initial or connate scCO₂ saturation (at the beginning of the imbibition process)

Figure 13 shows the Land trapping parameter for each CT scan slice taken from the composite core. According to the Land formulation, the lower the parameter, the higher the trapped gas saturation. Then, in line with Figure 13, the last 6 cm of the porous medium shows a lower trapping saturation tendency, contrary to the observed in the beginning (first 5 cm) of the composite core, which shows a higher trapping tendency according to the Land parameter. If the land trapping parameter is compared with the porosity of the composite core in Figure 2, it is possible to find a correlation showing that a higher CO₂ saturation stayed in the zone of lower porosity (beginning of the composite core) and a lower CO₂ saturation stayed in the zone of higher saturation (final end of the composite core).

Figure 13. Land trapping parameter



5. Conclusions

This work presents a novel literature example of relative permeability using scCO₂, given that was carried out at real reservoir conditions in Brazilian Pre-salt carbonate rock samples while similar studies are realized using outcrop rocks at laboratory conditions.

It was confirmed the presence of viscous fingering of scCO₂ using a produced volume graph analysis. The fingering effect was probably instigated by executing the test in horizontal position. It was observed a more favorable mobility ratio of the imbibition process than in

the one of the drainage, caused by the increase of viscosity of the displacing phase. Also, the low post breakthrough scCO₂ recovery and the low trapped scCO₂ at the end of the imbibition might be an evidence that the ECB is not strongly wetting the samples in presence of scCO₂. In addition, the loss of capillary continuity could be evidenced by correlating an X-ray CT image of the composite core and saturation profile distributions, this phenomenon affected some saturation measurements. In addition, there could have been presence of mass transfer between the phases altering the produced volumes in the separator.

It is valid to say that the final saturation reached in each displacement corresponds to a residual saturation instead of an irreducible saturation.

As the JBN methodology was not possible to be applied in this work, Corey coefficients corresponding to rocks from other similar study were used. Hence, the shape of the relative permeability curves determined in this work, could not represent accurately the behavior of the relative permeability.

It could be drawn that despite the cleaning process of the carbonate core samples using toluene and methanol, the wettability of those rocks did not achieve an entirely turn from oil-wet to water-wet.

The hysteresis effect was evidenced on ECB relative permeability curve. However, the scCO₂ curve did not present a significant change. The Land trapping parameter was determined all along the composited core allowing detecting the potentials zones of scCO₂ trapping in the porous medium.

It is recommended not to use Viton O-rings for the coreholder and accumulators in order to avoid severe swelling of the seals. For better performance it is recommended to use nitrile O-rings. Also, it is strongly suggested to ensure the heating of the back-pressure valve located at the production outlet to avoid freezing by scCO₂ expansion. In addition, to avoid leaks trough valves, it is indicated to change its standard Teflon made packing seal for packing seals made of PEEK (Polyether Ether Ketone).

The authors acknowledge Repsol Sinopec Brazil S.A, and the Brazilian National Petroleum, Natural Gas and Biofuels Agency (ANP) for the financial support. Also, the University of Campinas (UNICAMP), the Center for Petroleum Studies (CEPETRO) and the Laboratory of Miscible Methods of Recovery (LMMR) for intellectual and technical support.

6. References

1. E. de Almeida, L. Colomer, W. Vitto, L. Nunes, F. Botelho, F. Costa, L. Waeger. *Gás do Pré-sal: oportunidades, desafios e perspectivas* (IBP – UFRJ, Rio de Janeiro, 2017)
2. Agencia Nacional de Petróleo, Gás e Biocombustíveis. Resolução N° 806, de 17 de Janeiro

- de 2020 (Diario oficial da união, seção 1, ISSN 1677-7042, 2020)
3. H. Rodriguez, E. Mackay, D. Arnold, D. Silva. Optimization of CO₂-WAG and calcite scale management in pre-salt carbonate reservoirs. Offshore technology conference, Brazil (2019)
 4. B. Caudle, A. Dyes. Petroleum Transactions, AIME. v 213, p. 281-283 (1958)
 5. P. Laboissière, R. Santos, O. Trevisan. Carbonate petrophysical properties: computed tomography (CT) for experimental WAG design under reservoir conditions. Offshore technology conference, Brazil (2013)
 6. L. Lake. *Enhanced oil recovery* (Prentice Hall, ISBN 0-13-281601-6, New Jersey, 1989)
 7. S. Duchene, G. Puyou, P. Cordelier, J. Hy-Billiot, G. Hamon. Efficient experimental data acquisition for miscible CO₂-WAG injection corefloods in carbonate. SPE improved oil recovery symposium, Tulsa, 2014
 8. B. Bennion, S. Bachu. SPE Reservoir evaluation engineering J. i. **June**, p. 487-496 (2008)
 9. B. Bennion, S. Bachu. Drainage and imbibition CO₂/brine relative permeability curves at reservoir conditions for carbonate formations. SPE ATCE, Florence (2010)
 10. A. T. Corey. Prod. Monthly. 19 (1), 38. Nov (1954)
 11. C. Land. AIME Transactions. v. 243, p. 149-156 (1968)
 12. O. Torsæter, M. Abtahi. *Experimental reservoir engineering laboratory work book* (NTNU, Trondheim, 2000)
 13. Peace software. Calculation of thermodynamic state variables of carbon dioxide. 2019. Access in: https://www.peacesoftware.de/einigewerte/co2_e.html
 14. R. Nuñez, R. Vaz, E. Koroishi, J. Vargas, O. Vidal. Investigation of dissolution effects on dolomite porous media under carbonated water injection CWI. SPE Abu Dhabi international petroleum exhibition and conference, Abu Dhabi (2017)
 15. E. Rocha, O. Vidal, E. Koroishi, J. Vargas, L. de Oliveira. Materials science fórum. v. 965, p. 69-77 (2019)
 16. J. A. Vidal Vargas, E. Y. Yasuda, E. T. Koroishi, O. V. Trevisan. Applied Geochemistry 113 (2020) 104502
 17. J. Vargas. *Determinação dos parâmetros de convecção- dispersão- transferência de massa em meio poroso usando tomografia computadorizada* (PhD. Thesis, Universidade Estadual de Campinas, Brazil, 2015)
 18. A. Rosa, R. Carvalho, J. Xavier. *Engenharia de reservatórios de petróleo* (E Interciência Ltda, Rio de Janeiro, 2006)
 19. D. Huang, M. Honarpour. Journal of Petroleum Science and Engineering. 19 (1998) 103-117
 20. J. Fanchi. *Integrated reservoir asset management* (E Gulf Professional Publishing, Burlington, 2010)
 21. J. Amyx, D. Bass, R. Whiting. *Petroleum reservoir engineering* (E McGraw Hill Inc, New York, 1988)
 22. T. Austad, S. Strand, T. Puntervold, R. Ravari. New method to clean carbonate reservoir cores by seawater. International symposium of the society of core analysts, Abu Dhabi, 2008
 23. G. Jerauld. SPE Reservoir Engineering, 12(01), p. 66-73 (1997)

Comparing predicted 2D and 3D anisotropic properties from micro CT derived digital rock physics with experimentally measured anisotropy

David K. Potter^{1*}, Liam L. Belisle¹, Allyson L. Shewchuk¹, Brendan C. Snow^{1,2}, Aiden Zhu³, and Shaun Zhang³

¹Department of Physics, University of Alberta, Edmonton, Alberta, T6G 2E1, Canada

²Current address: CNOOC Petroleum North America ULC, Calgary, Alberta, T2G 1A6, Canada

³DigiM Solution LLC, Burlington, MA 01803, USA

Abstract. This study compared anisotropic parameters predicted from microcomputed tomography (μ CT) derived digital rock physics with experimentally measured anisotropy on the same core plug. Full 3D anisotropy comparisons have not been made previously on a single core plug sample, as far as we are aware, since most experimental methods require several core plug samples cut in different orientations to determine 3D anisotropy. A cloud-based image analysis platform (DigiM I2S) was used to process the μ CT scans, with supervised machine learning tools and petrophysics simulations, to produce a digital 3D reconstruction and predict various 3D anisotropic parameters (permeability, electrical conductivity, and acoustic velocity). The results were directly compared with experimentally measured 3D anisotropy of magnetic susceptibility (AMS), anisotropy of magnetic remanence (AMR), and anisotropy of acoustic velocity. A key result was that the orientations of the principal anisotropy axes for the bulk rock components were similar to those of the fine grained ferrimagnetic components. The results were also consistent with the observed petrofabric, giving confidence in the digital rock physics predictions and the rapid 3D experimental measurements, and showed potential for estimating 3D anisotropy of one parameter from measurements or predictions from another parameter on a single core plug (e.g., estimating principal anisotropy axes of permeability, acoustic velocities or electrical conductivity via rapid, non-destructive magnetic anisotropy measurements).

1 Introduction

The major goal of this study is to compare two and three dimensional (2D and 3D) anisotropy parameters from microcomputed tomography (μ CT) digital rock physics predictions with experimentally measured anisotropy on the same single core plug. A key factor is the recognition that the digital rock physics methods of Zhang et al. [1, 2] and the magnetic methods of Potter [3] both utilize second order tensors to characterize 3D anisotropic properties of core plugs, thereby allowing direct comparisons between the different methods. Such comparisons have not been made before on a single core plug sample, as far as we know, because most experimental techniques for determining the full 3D anisotropy require several core plug samples cut in different orientations. For example, 3D permeability anisotropy ideally requires 9 plugs cut in different orientations, since the permeability is measured in 1D along the axis of each core plug. In contrast, the magnetic methods of Potter [3] generate the full 3D anisotropy from a single core plug, allowing direct comparison with the 3D digital rock physics parameter predictions on the same sample. The magnetic methods utilized anisotropy of magnetic susceptibility (AMS), which is rapid and represents the combined anisotropy of all the mineral components in the sample, and anisotropy

of magnetic remanence (AMR), which reflects the anisotropy of only the fine grained remanence carrying mineral components (generally ferrimagnetic minerals such as magnetite, Fe_3O_4). These different methods allowed us to directly compare the anisotropies of different mineral components and grain size fractions.

A cloud-based image analysis platform (DigiM I2S) was used to conduct image processing of μ CT scans of the plug. Supervised machine learning tools and petrophysics simulations were used to predict anisotropies of permeability, electrical conductivity, and s-wave velocity from the μ CT scans. The results were compared with experimentally measured AMS, AMR, and s-wave velocity anisotropy.

2 Sample description

The sample used in this study was part of the VOLC-B (“volcanic” B) group of outcrop igneous rock samples [4] from the Flin Flon Belt of the Trans-Hudson Orogeny in eastern Saskatchewan. These rocks have been studied due to the economic potential of their mineral deposits. **Figure 1** shows the sample with the arbitrary reference X, Y and Z axes indicated. Analysis [4] suggested that this group of rock samples was composed of 22.5% quartz, 61.2% plagioclase, 8.3% biotite, and 1.9% opaque minerals (the remaining 6.1%

* Corresponding author: dkpotter@ualberta.ca

being porosity and/or some other small unidentified minerals). The cylindrical plug sample used for the present study, VOLC-B-X2, had a mass of 27.46 g and a density of 2.635g/cm³. The sample was initially thought to be quasi-isotropic [4] from some preliminary acoustic analysis. However, the current study will demonstrate that the sample is clearly anisotropic. We specifically chose this sample as it had a visible petrofabric that could be compared with the quantitative anisotropy methods. Whilst this is not a typical reservoir rock, it represents a good sample to test all the different methods, since some techniques may not produce sufficient signal in certain sedimentary rocks.

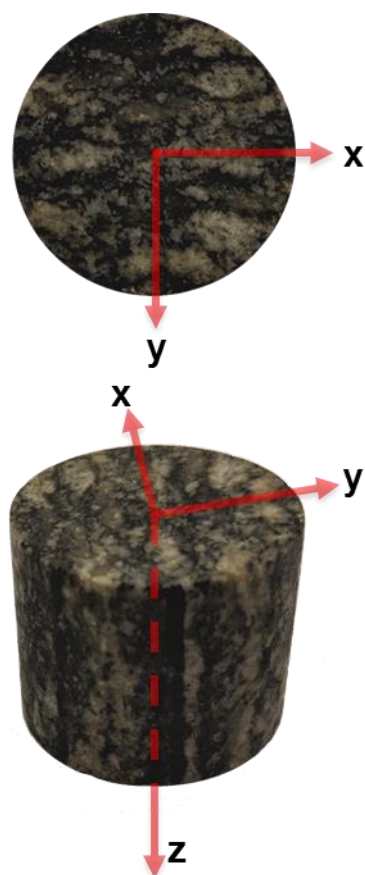


Fig. 1. Images of core plug sample VOLC-B-X2 showing the orientations of the arbitrary orthogonal reference axes X, Y and Z. **Top:** top view of the sample showing the XY plane (the directions of the arrows indicate the positive X and Y directions, and positive Z is into the page). The diameter of the circular XY plane is 25 mm. **Bottom:** side view of the sample showing the positive directions of all 3 orthogonal axes. The orientations of the axes in terms of declination (Dec.) and inclination (Inc.) are as follows: X has Dec. 0° and Inc. 0°, Y has Dec. 90° and Inc. 0°, and Z has Dec. 0° and Inc. 90°.

3 Methods

3.1 Micro CT imaging and digital rock physics predictions of anisotropic properties

Microcomputed tomography (μ CT) imaging with a voxel resolution of 10.7 μ m was used to create a series

of digital images in order to build up a comprehensive 3D representation of the core plug sample, and to distinguish its main components. After some quality control, where a few low quality images were removed, the final dataset consisted of 1,500 good quality images taken in the XY plane along the Z axis. These were used to produce a 3D reconstruction at 10.7 μ m voxel resolution of the majority of the sample. The numerical domain for the reconstruction and the subsequent modelling was a cubic volume 18 mm x 18 mm x 18 mm. The image contrast and saturation were enhanced in order to help accentuate fine details. The density of a mineral phase in the μ CT images was represented by the contrast; a higher contrast indicated a higher density (a lighter grayscale shade in the initial images, which was later replaced by different colours). Image segmentation was conducted to create four different main components within each image, using a machine learning supervised random forest classifying algorithm [5]. The image segmentation module was first trained on a representative sample image taken from the middle of the dataset to distinguish the four main components found in the anisotropic rock: quartz, plagioclase, biotite and porosity. Then, using this training set, the image segmentation module classified every voxel in the dataset under one of the four components. Given its high density, voxels with the highest image contrast were considered biotite. Likewise, given its low density, voxels with the lowest image contrast (darkest grayscale) represented the porosity. The fluid in the pores was assumed to be air, though there is the possibility that some fluid inclusions may be present. Voxels representing the lighter intermediate shade were considered plagioclase, and voxels representing the darker intermediate shade were considered quartz, since labradorite plagioclase has a higher density than quartz. Since there was no immediate way to differentiate the small amount of opaque minerals from the other mineral components in the μ CT images (the resolution was not high enough to identify some of these micron sized grains), we assumed only plagioclase, quartz, biotite and porosity in the μ CT images. These formed the four components of the anisotropic rock classifier. Our magnetic measurements suggested that at least one of the opaque minerals likely comprised ferrimagnetic magnetite or titanomagnetite. For this study, it was assumed that the identified minerals exhibited no compositional variations within the anisotropic rock.

A cloud-based image analysis platform (DigiM I2S) was then used to predict the principal anisotropy axes of the 3D digitally reconstructed core plug sample for various physical parameters (permeability, electrical conductivity and s-wave velocity) by running different software modules on the segmented datasets. For the permeability module, the segmented dataset was loaded in and porosity was chosen as the “active” material. The module seeks to represent the pores as a finite volume mesh. Stoke’s and Darcy’s equations are then solved for the constructed complex pore network. The simulations virtually push fresh water through this network with a pressure difference of 30,000 Pa [1], producing a 9 component (3 diagonal components and 6 off-diagonal

components) permeability second order tensor [1, 2], from which full 3D anisotropy is calculated giving the magnitudes and orientations of the 3 principal anisotropy axes (maximum, intermediate and minimum).

The electrical conductivity module solves Laplace's equations on a multi-component sample with each component assigned an electrical conductivity value as follows [6]: Biotite: 2.5 mSm⁻¹, Plagioclase: 0.01 mSm⁻¹, Quartz: 0.0 mSm⁻¹, Porosity: 0.0 mSm⁻¹ (note that whilst quartz has an extremely small, non-zero, electrical conductivity, the software had a tolerance threshold which meant quartz had to be assigned a zero value). The electrical conductivity module presently only predicts values along individual axes, so we predicted values along the X, Y and Z reference axes (i.e., in three orthogonal orientations) to obtain an estimate of the 3D anisotropy. This process can, if necessary, be repeated in 3 different orthogonal axes to improve the estimate.

The electrical conductivity module was also adapted to predict s-wave velocity values along the X, Y and Z reference axes. S-wave velocities were assigned as follows [7]: Biotite: 1,360 ms⁻¹, Plagioclase: 3,728 ms⁻¹, Quartz: 4,200 ms⁻¹, Porosity: 0 ms⁻¹.

3.2. Magnetic anisotropy

3.2.1 Anisotropy of Magnetic Remanence (AMR)

AMR methods measure the anisotropy of just the remanence carrying minerals (generally fine particles of ferrimagnetic minerals such as magnetite, or canted antiferromagnetic particles such as hematite), and thus quantify the anisotropy of part of the small fraction of "opaque" minerals. This can be important since such minerals can influence the permeability anisotropy [3, 8]. Two methods were used: (i) anisotropy of isothermal remanent magnetization (AIRM), and (ii) anisotropy of gyroremanent magnetization (AGRM). We firstly chose AIRM primarily because the technique produces 9 components representing a second order tensor [3, 9, 10] that was similar to that used to predict permeability anisotropy from μ CT images [1, 2] described earlier. This meant that for the first time the 3D permeability anisotropy predicted from μ CT images could be directly compared with experimental measurements of AIRM on an identical single core plug. Also, AIRM measurements can be made at room temperature to avoid any chemical changes, and they give a large signal compared to other AMR techniques. The sample was first tumble AF demagnetized and then placed in a Molspin pulse magnetizer, which applied a short (100ms) direct field (DF) in a specific orientation. This imparted an IRM, which was measured in a spinner magnetometer, giving 3 components of magnetization. The DF was applied successively along the X, Y, and Z axes and the IRM measured each time, giving a total of 9 components of magnetization as follows:

<u>DF Axis</u>	<u>Measured Remanence</u>	
X	M_{1x} M_{1y} M_{1z}	
Y	M_{2x} M_{2y} M_{2z}	(1)
Z	M_{3x} M_{3y} M_{3z}	

Between each measurement the sample was tumble AF demagnetized. A typical AIRM determination from the 3 magnetization and 3 demagnetization steps takes around 20-30 minutes. The 9 components of magnetization represented a second order tensor from which the magnitude and orientation of the 3 principal anisotropy axes could be calculated [3, 9, 10]. The AIRM measurements were made at two different DF values, 60mT and 20mT, in order to quantify the anisotropy of different particle size fractions. The higher field preferentially affects the small (generally submicron) stable single domain (SSD) ferrimagnetic particles, whilst the lower field preferentially affects the slightly larger (generally up to a few tens of microns) multidomain (MD) ferrimagnetic particles.

AGRM is another AMR method and is produced when an anisotropic distribution of SSD ferro- or ferrimagnetic particles are subjected to an AF with the sample static [10, 11, 12]. It is not theoretically produced in MD particles and so can exclusively quantify the anisotropy of the SSD particles. GRM is produced perpendicular to both the AF axis and the maximum alignment orientation of the particles. This method applies an AF to the static sample at various orientations in 3 orthogonal planes. This was achieved using an AF demagnetizer coil housed within a mumetal shield. The latter shielded the sample from the Earth's field. The sample was subjected to an AF of 60 mT at increments of 15° within a 180° range (from $\theta = -90^\circ$ to 90°) in a particular plane (**Figure 2**). After the AF application, the sample was removed from the AF coil and the GRM components (x, y and z) were measured in a spinner magnetometer. Prior to each AF application the sample was tumble AF demagnetized at 80 mT and the remaining remanence measured, and subtracted from the subsequent GRM measurement. The demagnetizing field was higher than the AF used to impart the GRM in order to remove as much remanence as possible prior to each GRM production step. Thirteen pairs of magnetized and demagnetized values were obtained in the 3 orthogonal planes (XY, YZ, and ZX) giving a total of 39 measurements of GRM. The first axis letter of each plane has an orientation of $\theta = 0^\circ$ and the second axis letter of the plane has an orientation of $\theta = 90^\circ$ (e.g., for the XY plane the X axis is oriented at $\theta = 0^\circ$ and the Y axis is oriented at $\theta = 90^\circ$). The GRM method is extremely sensitive, but quite time consuming, taking a few hours to perform. It is effectively the remanence equivalent of the anisotropy of magnetic susceptibility (AMS) delineator (see the AMS section below), since it measures the differences in anisotropy of the SSD ferro- or ferrimagnetic particles in a particular plane. The magnitude of the GRM is proportional to the anisotropy of the SSD particles in the perpendicular plane [12]. The GRM method does not give the magnitudes of the principal anisotropy axes, since there is no "bulk" value (unlike AMS) to add to the differences. Therefore this method does not produce an anisotropy ellipsoid (unlike the AMS and AIRM methods), but instead the results from each plane can be fit using a standard least-squares algorithm to determine the order (i.e., max, int, and min.) and orientations of the principal anisotropy axes [10].

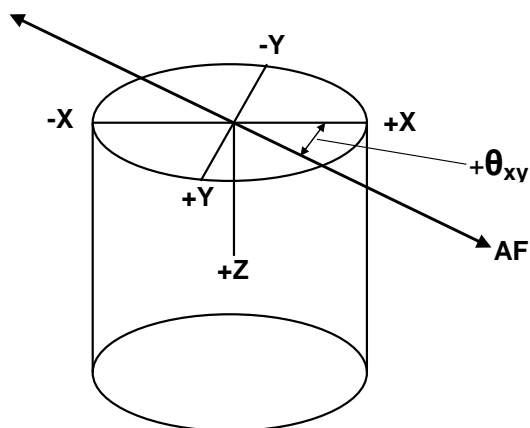


Fig. 2. An example showing the orientation of the AF axis with respect to the sample reference axes during determination of AGRM. The example shows the AF axis at an angle $+\theta_{xy}$ in the XY plane of the sample. This produces a GRM in the Z axis if the sample contains anisotropically distributed SSD ferrimagnetic particles in the XY plane.

3.2.2 Anisotropy of Magnetic Susceptibility (AMS)

This method was quickest to conduct and produced a full 3D anisotropy ellipsoid, and so could be compared exactly with the predicted 3D permeability anisotropy from the μ CT imaging and the 3D anisotropy from the AMR methods (AIRM and AGRM). The sample was first demagnetized by tumbling in an alternating field (AF). It was then placed in a Molspin anisotropy delineator, where the sample was rotated successively in the XY, YZ, and ZX planes in a weak magnetic field (500 μ T), and the difference in magnetic susceptibility in each plane was measured. The rotations allow the weak field to interrogate all possible orientations in each of the 3 orthogonal planes, and the whole process only takes about 1 minute. A bulk magnetic susceptibility measurement was then added to each of these magnetic susceptibility differences in order to produce the magnitudes and orientations of the 3 principal AMS axes. The bulk measurement was taken separately in a Molspin susceptibility bridge by first measuring the background and then the sample magnetic susceptibility in the Z axis. These bulk measurements take less than about 5 s. The AMS represents the sum total of the anisotropies of all the components in the sample. It can be dominated by small amounts of fine-grained remanence carrying particles (such as ferrimagnetic magnetite, Fe_3O_4), which contribute to the “opaque” minerals as mentioned earlier. If these particles are predominantly stable single-domain (SSD) then the maximum magnetic susceptibility will be perpendicular to the long axes of the particles [9, 13], but if they are slightly larger and multidomain (MD) then the maximum magnetic susceptibility will be along the long axes of the particles [9, 13]. Therefore AMS alone may not unambiguously indicate the orientation of these particles (without knowing the domain state). However, a combination of AMS and AMR methods allows one to

uniquely determine the predominant domain state and the correct orientation of the particles [9, 13].

3.3. Anisotropy of shear-wave velocity (ASWV)

Parallel planar transducers, placed on the two flat circular faces of the cylindrical core plug sample, can only measure the p-wave velocity along the cylinder axis (i.e., in 1D along the Z axis) and thus cannot measure 3D anisotropy. However, 2D measurements of s-wave anisotropy were possible in the XY plane. Two parallel planar piezoelectric transducers were attached to aluminium endcaps (calibrated for the extra travel time of the signal through them) and copper electrodes by conductive silver epoxy. The endcaps were placed on the flat end faces (in the XY plane) of the sample, and good coupling was achieved via a thin film of molasses. The frequency of the signal was 1 MHz. While the overall wave train propagated along the Z axis, the s-waves had a transverse motion in the perpendicular XY plane. By rotating the sample in the XY plane with respect to the transducers, using the method described in [14], it was possible to detect s-wave anisotropy in the XY plane. An s-wave was first propagated with the sample at a particular orientation in the XY plane, and the arrival time was recorded manually. Then the sample was rotated through 22.5° in the XY plane and an s-wave was again recorded, and the process repeated every 22.5° as the XY plane was rotated about 360° . The s-wave velocities were determined at each orientation to create a 2D plot of the s-wave velocity anisotropy in the XY plane. The results could be compared to the AGRM in the XY plane, the s-wave predictions from the μ CT imaging, and the other anisotropy data.

4 Results and discussion

4.1. Digital 3D reconstruction from the μ CT images

Figure 3 shows representative digital reconstructions in the 3 orthogonal XY, YZ and ZX planes derived from the μ CT images. One can clearly see that the petrofabric is oriented more towards the X axis in the XY plane, and more towards the Z axis in the YZ plane, whilst the preferred orientation in the ZX plane is less obvious. This indicates that the bulk minerals are aligned more along the X and Z axes than the Y axis, and that the anisotropy in the ZX plane is lower than in the XY and YZ planes. These observations will be shown to correlate with the quantitative anisotropy results for the different parameters detailed later. Another interesting observation is that almost all the modeled porosity appears to be in the quartz, though there may be additional micro porosity that was below the resolution of the μ CT images.

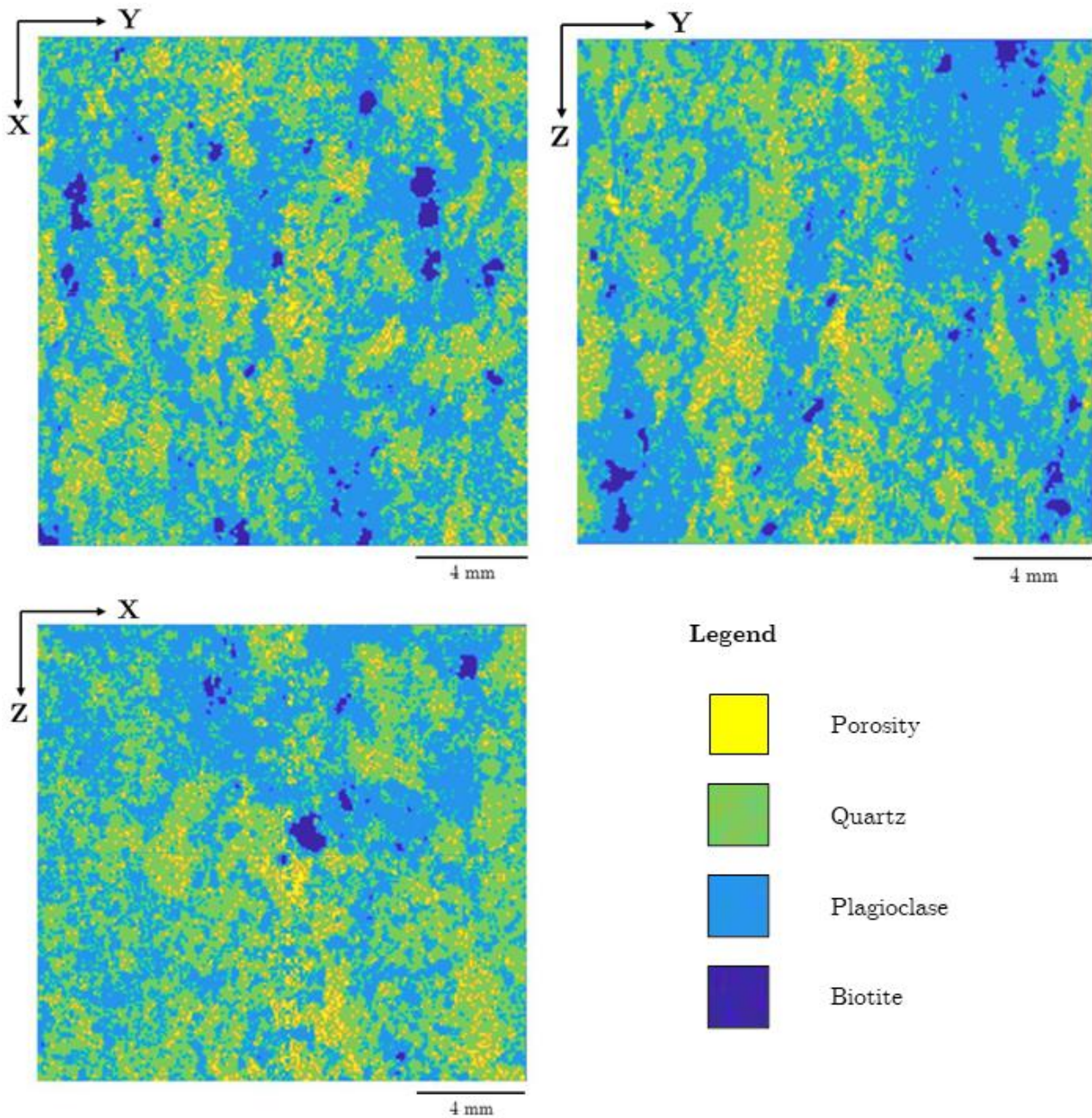


Fig. 3. Digital reconstructions in the 3 orthogonal XY, YZ and ZX planes derived from the μ CT images. The 2D orientations of the sample axes are shown in each image. The density contrasts from the μ CT images were used to classify 4 main components as shown. The digital reconstructions used the following filters: Gaussian blur, difference of Gaussians, Hessian and Sobel. In the XY plane the minerals are generally more aligned along the X axis, whilst in the YZ plane they are generally more aligned along the Z axis. In the ZX plane the alignments are less pronounced. These observations are consistent with the petrofabric alignments described earlier from the whole plug images shown in **Figure 1**. An interesting observation is that virtually all the predicted porosity (that which can be resolved in these reconstructions) appears to reside in the quartz. There may be additional porosity at a smaller scale that was below the resolution of the initial μ CT images.

4.2. Comparisons of 3D anisotropies from μ CT imaging predictions and experimental measurements

Table 1 compares the full 3D anisotropy results for the permeability anisotropy predicted from the μ CT imaging with the experimentally measured AIRM at 20 mT and 60 mT. Both these methods use an identical 9 component second order tensor scheme to calculate the anisotropy, and so can be directly compared on a single core plug for the first time (as far as we are aware). The results from each method gave quite similar orientations for the 3 principal anisotropy axes, which were relatively close to the X, Y and Z reference axes of the sample, and showed that in terms of magnitudes $Z > X > Y$. Some differences in the orientations of the principal anisotropy axes between the two methods may be due to the permeability being related to the orientation of the quartz grains, where most of the predicted porosity resides, whereas the AIRM represents the alignments of the small remanence carrying particles. Also, since the permeability values are quite low, any small variation in the off-diagonal terms will affect the overall orientations. The normalized magnitudes of the two AIRM determinations were quite similar, with the anisotropy at 20 mT being slightly larger than that at 60 mT. This may be partly due to the non-linear acquisition of IRM with applied field strength (which accentuates the anisotropy at lower fields), and/or the shape of the larger MD particles may be more elongate, and/or the MD particles may be slightly more aligned than the SSD particles. The normalized magnitudes of the permeability anisotropy show that the permeability is slightly more anisotropic than the AIRM, though the maximum normalized value is quite similar to that of the AIRM.

Table 1 shows that the orientations of the AMS principal axes are also very similar to the orientations of the AIRM and permeability principal axes. The normalized magnitudes of the AMS axes are quite similar to those of the AIRM axes, though they indicate that the AMS is slightly smaller than the AIRM. This can be explained by SSD and MD particles being aligned in the same orientation (which the 60 mT and 20 mT AIRM results respectively demonstrate), since the magnetic susceptibility of SSD particles is a minimum in the alignment axis, whereas for MD particles it is a maximum in the alignment direction [9, 13]. Therefore the AMS of the two sets of particles partially cancels out resulting in lower AMS than AIRM.

The results for this sample suggest that the data from any one of the parameters (AIRM, AMS or permeability anisotropy) could potentially be used to predict the orientations of the principal anisotropy axes of any of the other parameters. In particular, AMS and AIRM could potentially provide rapid, non-destructive indications of the orientations of the principal permeability axes on a single core plug, something that would otherwise be very time consuming to measure experimentally since it would require permeability to be determined by several core plugs cut in different directions (ideally 9 plugs, each measuring the permeability in 1D).

Table 1 also indicates how the SSD ferrimagnetic particles are aligned from the anisotropy of GRM

(AGRM) results (in terms of maximum, intermediate and minimum) in relation to the reference X, Y and Z axes of the sample. Since the sample acquires a GRM then the SSD particles are very likely to be magnetite or titanomagnetite (since hematite does not acquire GRM). Whilst this method does not give magnitudes for the principal axes (as detailed in the Methods section), it does indicate the maximum and minimum axes and their orientations in each of the 3 orthogonal planes measured. **Figure 4** shows the GRM values (open data symbols with uncertainty bars) acquired along the Z, X and Y axes following application of an AF of 60 mT in the XY, YZ and ZX planes respectively (GRM is acquired along an axis perpendicular to the plane in which the AF is applied). Least squares best fit curves were drawn for each plane of measurements and demonstrated that the GRM largely followed a $\sin(2\theta)$ shape in each case in accordance with GRM theory [11], where θ was the orientation of the applied AF as shown in **Figure 2**. The solid symbol on the best fit curve in each plane in **Figure 4** indicates the maximum GRM on that curve. According to GRM theory [11] the predominant alignment orientation of the ferrimagnetic SSD particles in each plane is 45° from the maximum GRM on the positive slope part of the best fit curves. The GRM results indicate that in the XY plane the predominant alignment of the SSD particles is close to the X direction (actually at $\theta = 11.7^\circ$ where X is at $\theta = 0.0^\circ$), and in the YZ plane the predominant alignment of these particles is close to the Z direction (actually at $\theta = 82.1^\circ$ where Z is at $\theta = 90.0^\circ$). Therefore the SSD particles are aligned more in the X and the Z axes than in the Y axis. The maximum GRM is also greater in the YZ plane than in the XY plane, which shows that the SSD particles are preferentially more aligned along the Z axis than the X axis. The maximum GRM in the ZX plane occurs at a negative value of θ , which is also consistent with the SSD particles being more aligned along Z than X. The GRM values in the ZX plane are small indicating that there is less of a difference between the Z and X axes than between either of these axes and the Y axis. Thus the AGRM indicates $Z > X > Y$, which is consistent with the predicted permeability anisotropy, and the measured AIRM and AMS results.

Also shown in **Table 1** are the predicted anisotropy results for electrical conductivity and s-wave velocity derived from the μ CT images. Whilst these techniques presently do not give the full 3D anisotropy ellipsoid (as detailed in the Methods section) they nonetheless give the predicted values in the 3 orthogonal axes X, Y and Z, which is a reasonable approximation to the 3D anisotropy. Each of these methods also show that in terms of magnitudes $Z > X > Y$, which is consistent with all the other anisotropy results even though the normalized magnitudes differ somewhat.

The combined results in **Table 1** show that the anisotropy of the major mineral components (from the μ CT predicted anisotropies of permeability, electrical conductivity, s-wave velocity, and the observed petrofabric in **Figures 1** and **3**) has a very similar orientation to the fine-grained ferrimagnetic particles (from the AIRM, AGRM and AMS results).

Table 1. The principal 3D anisotropy axes of sample VOLB X2 from different digital rock physics μ CT imaging predictions and experimental measurements. For the permeability anisotropy, AIRM and AMS the full 3D anisotropies were determined. The AGRM measurements in each plane (see text and **Figure 4**) allowed determination of the max., int. and min. axes. The electrical conductivity and s-wave velocity predictions were made along each of the 3 orthogonal X, Y and Z axes without the off-diagonal components. Units for the magnitudes are as follows: permeability (mD); AIRM (10^{-6} A m^3kg^{-1}); AMS (10^{-8} m^3kg^{-1}); electrical conductivity (mSm^{-1}) s-wave velocity (ms^{-1}). Magnitudes are not applicable (N/A) for the AGRM as explained in the text. The orientations of the principal anisotropy axes are generally relatively close to the sample axes, where X has Dec. (declination) 0° and Inc. (inclination) 0° , Y has Dec. 90° and Inc. 0° , and Z has Dec. 0° and Inc. 90° . Note that Dec. 0° is the same as Dec. 360° .

ANISOTROPY METHOD	9-Component Tensor $\begin{bmatrix} xx & xy & xz \\ yx & yy & yz \\ zx & zy & zz \end{bmatrix}$	Principal Anisotropy Axes				
		Magnitudes	Normalised magnitudes	Dec. ($^\circ$)	Inc. ($^\circ$)	
Permeability anisotropy from μ CT	$\begin{bmatrix} 1.367 & -0.011 & 0.015 \\ -0.009 & 0.289 & 0.052 \\ 0.016 & 0.021 & 1.387 \end{bmatrix}$	Max.	1.40	0.46	3.1	62.4
		Int.	1.36	0.45	358.4	-27.5
		Min.	0.29	0.09	89.4	-1.9
AIRM at 20mT	$\begin{bmatrix} 35645 & 3765 & -132 \\ 209 & 18984 & 1752 \\ 2675 & 7931 & 42218 \end{bmatrix}$	Max.	43428	0.45	43.5	73.5
		Int.	35470	0.37	3.3	-12.8
		Min.	17950	0.18	95.6	-10.3
AIRM at 60mT	$\begin{bmatrix} 71810 & -3082 & -438 \\ 5719 & 50343 & 4274 \\ 3403 & 5206 & 83277 \end{bmatrix}$	Max.	84167	0.41	47.0	78.8
		Int.	71643	0.35	1.8	-8.0
		Min.	49620	0.24	92.9	-7.9
AMS	N/A	Max.	2721	0.39	52.3	75.0
		Int.	2478	0.36	8.3	-10.9
		Min.	1698	0.25	100.2	-10.2
AGRM	N/A	Max. (Z)	N/A	N/A	N/A	N/A
		Int. (X)	N/A	N/A	N/A	N/A
		Min. (Y)	N/A	N/A	N/A	N/A
Electrical conductivity anisotropy from μ CT	N/A	Max. (Z)	3.670	0.54	0.0	90.0
		Int. (X)	2.194	0.32	0.0	0.0
		Min. (Y)	0.966	0.14	90.0	0.0
S-wave velocity anisotropy from μ CT	N/A	Max. (Z)	3610	0.336	0.0	90.0
		Int. (X)	3576	0.333	0.0	0.0
		Min. (Y)	3546	0.330	90.0	0.0

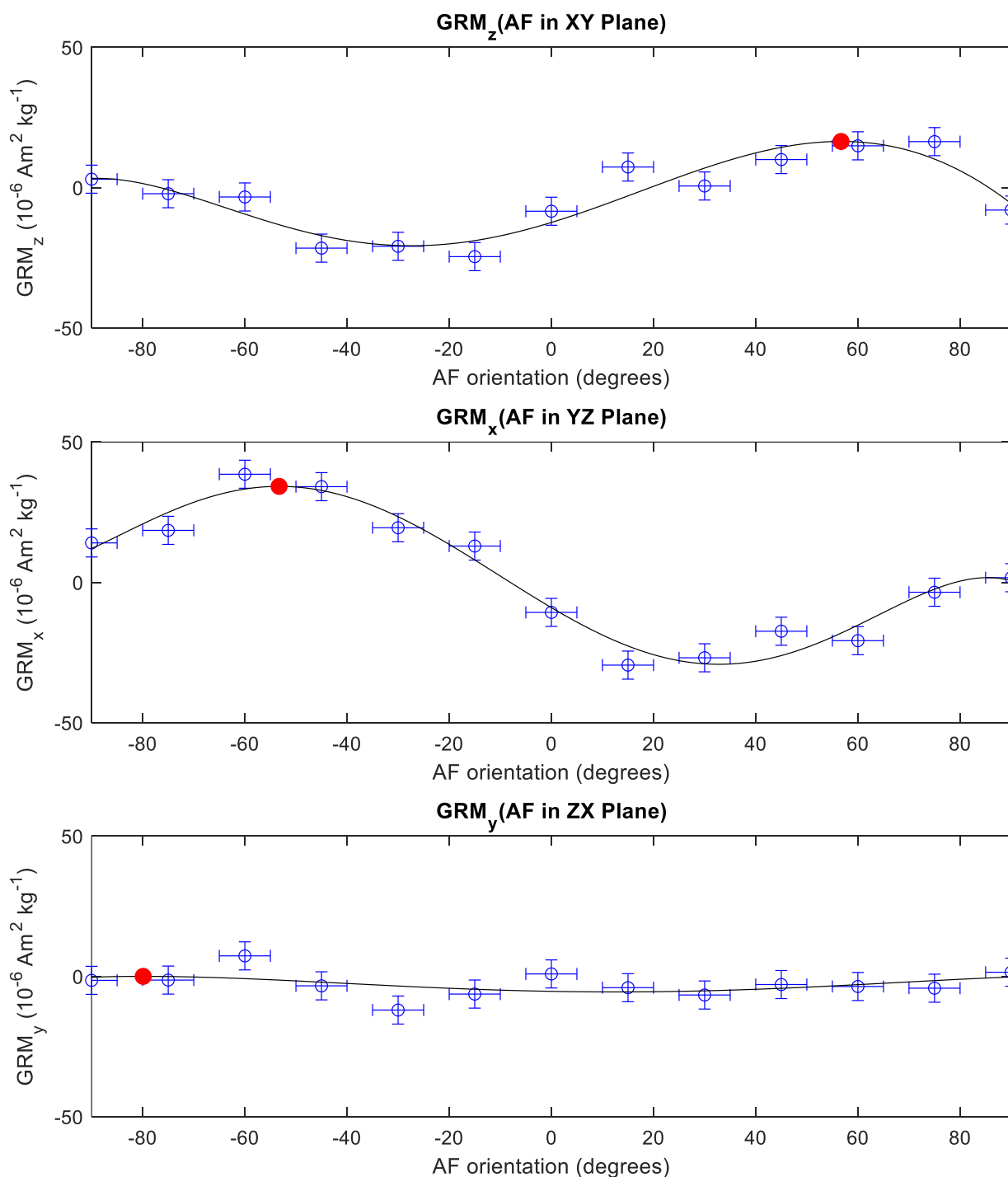


Fig. 4. Components of GRM as a function of AF orientation (θ) in the 3 orthogonal planes. The first axis letter of the plane has an orientation of $\theta = 0^\circ$ and the second axis letter of the plane has an orientation of $\theta = 90^\circ$ (e.g., for the XY plane the X axis is oriented at $\theta = 0^\circ$ and the Y axis is oriented at $\theta = 90^\circ$). The smooth curves are the best fit $\sin(2\theta)$ curves to the experimental data points. The solid circular point on each plane's best fit curve represents the maximum GRM on that curve. **Top:** The z-components of GRM for orientations of the AF axis in the XY plane. From GRM theory [11] a positive GRM for positive angles of θ means that $X > Y$ in this plane. The GRM results indicate that the predominant alignment of the SSD ferrimagnetic particles in this plane is at $\theta = 11.7^\circ$ (45° away from the maximum GRM where the GRM is zero according to GRM theory [11]). **Middle:** The x-components of GRM for orientations of the AF axis in the YZ plane. A positive GRM for negative angles of θ means that $Z > Y$ in this plane. The predominant alignment of the ferrimagnetic particles in this plane is at $\theta = 82.1^\circ$. **Bottom:** The y-components of GRM for orientations of the AF axis in the ZX plane. The slightly more positive GRM (on average) for negative angles of θ means that $Z > X$ in this plane. However, the difference between the Z and X axes is quite small. Compared to the uncertainties shown it is difficult to estimate the predominant alignment of the ferrimagnetic particles in this plane.

4.3. Anisotropies in the XY plane: comparison of μ CT predictions and experimental measurements from 2D and 3D results

Since we were able to measure the s-wave velocity anisotropy and the AGRM in the XY plane, it is useful to directly compare these results with the μ CT predicted anisotropies of s-wave velocity, permeability and electrical conductivity in the XY plane, as well as the measured AIRM and AMS. **Figure 5** shows the 2D s-wave velocity results (diamond symbols) in the XY plane from [14] and the solid line represents a subsequent best fit curve that we added using a least squares fitting method. This curve forms a “figure of 8” pattern, demonstrating anisotropy in the XY plane. If the sample had been isotropic in the XY plane then the results would have formed a circle. On the best fit line the declination of the maximum s-wave velocity axis was at 12.6° (i.e., close to the X axis at 0° or 360°) with a magnitude of 3,033 ms⁻¹ (upper circular point). The minimum s-wave velocity axis was at 103.1° (i.e., close to the Y axis at 90° or 270°) with a magnitude of 2,976 ms⁻¹ (lower circular point). The s-wave results did not form a perfectly symmetrical “figure of 8”, possibly due to slight differences in the coupling of the transducers to the sample during each experimental measurement.

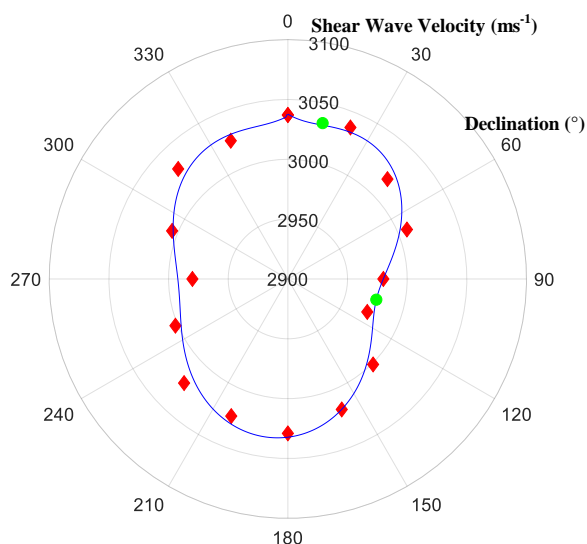


Fig. 5. Shear wave velocities for sample VOLC-B-X2 modified from [10]. The radius axis is the shear wave velocity in ms⁻¹ and the circumferential axis is the declination in degrees. The diamonds represent the data points measured by Snow [14]. Measurements were taken by rotating the sample at 22.5° intervals in the XY plane between planar transducers. The solid “figure of 8” line is a least squares best fit of the diamonds, and the two circular points on the best fit line are the maximum and minimum points of the best fit line.

Table 2 shows that the predicted s-wave velocity anisotropy from the μ CT imaging was consistent with the X axis velocity higher at 3,576 ms⁻¹ than the Y axis velocity of 3,546 ms⁻¹. The measured velocities are lower than the predicted values, possibly due to small micro fractures in the sample below the resolution of our

μ CT images. Any extra porosity is not included in the estimations from our images, which would make our predicted s-wave velocities higher than the measured values. Our digital reconstructions from the μ CT images suggested only 3.4% porosity, but the data of [4] suggested up to 6.1% porosity (though this value may be lower if small amounts of unidentified minerals are present) in the VOLC-B rocks that included our sample.

Table 2. The maximum and minimum principal anisotropy axes in the XY plane from several different methods (digital rock physics predictions and experimental measurements). The 2D determinations all have zero inclinations (0.0 ° Inc.) since only the 2D XY plane was considered. The 3D determinations show the two principal axes nearest to the XY plane for comparison from full 3D determinations. Axes listed “Max. (X)” and “Min. (Y)” for some of the predictions mean determinations were only made along those axes. Units for the magnitudes are as follows: s-wave velocity (ms⁻¹); permeability (mD); AMS (10⁻⁸ m³kg⁻¹); AIRM (10⁻⁶A m³kg⁻¹); electrical conductivity (mSm⁻¹). Magnitudes are not applicable (N/A) for the AGRM as explained in the Methods section in the text.

Method in XY plane	Axis and magnitude	Dec. (°)	Inc. (°)
S-wave velocity (2D measurements)	Max. 3,033	12.6°	0.0°
	Min. 2,976	103.1°	0.0°
S-wave velocity via μ CT imaging (3D predictions)	Max. (X) 3,576	0.0°	0.0°
	Min. (Y) 3,546	90.0°	0.0°
AGRM (2D measurements)	Max. (mag. N/A)	11.7°	0.0°
	Min. (mag. N/A)	101.7°	0.0°
Permeability via μ CT imaging (3D predictions)	Max. 1.36	358.4°	-27.5°
	Min. 0.29	89.4°	-1.9°
AMS (3D measurements)	Max. 2,478	8.3°	-10.9°
	Min. 1,698	100.2°	-10.2°
AIRM at 60mT (3D measurements)	Max. 71,643	1.8°	-8.0°
	Min. 49,620	92.9°	-7.9°
AIRM at 20mT (3D measurements)	Max. 35,470	3.3°	-12.8°
	Min. 17,950	95.6°	-10.3°
Elect. Conductivity via μ CT imaging (3D predictions)	Max. (X) 2.194	0.0°	0.0°
	Min. (Y) 0.966	90.0°	0.0°

Table 2 shows that the orientations of the maximum and minimum principal anisotropy axes from the experimentally measured s-wave anisotropy results (declinations 12.6° and 103.1°) are almost identical to those of the AGRM results (declinations 11.7° and 101.7°). The s-wave results show that the overall rock anisotropy of the main rock forming minerals (plagioclase and quartz) in the XY plane therefore has quite a similar orientation to that of the small fraction of SSD ferrimagnetic particles from the AGRM results.

A comparison of all the anisotropy results for the XY plane in **Table 2** shows that the declinations and inclinations of the maximum and minimum principal axes are quite similar for all the methods. For the results based on 2D data the inclinations are nominally 0.0° since no information in the third dimension is included. For the results based on 3D methods we give the maximum and minimum principal axes (which were very close to the XY plane) based on the full 3D data, and so these determinations include small inclinations in most cases. The results demonstrate that the orientations of the fine SSD and MD ferrimagnetic particles (from the AGRM, AIRM and AMS results) are quite similar to those of the main rock forming minerals plagioclase and quartz (from the measured and predicted s-wave velocity anisotropy, the predicted electrical conductivity as well as the visible petrofabric in **Figures 1** and **3**). Whilst there is a close correspondence between the orientation results for the different methods for this sample, it may not always be the case for other core samples and rock types. The advantage of performing all the different methods described here is that it allows one to determine the anisotropy of the different components (minerals and pore network) and, in the case of the ferrimagnetic fraction, different particle size fractions (SSD versus MD).

5 Discussion

A main aim of this paper was to highlight that the digital rock physics predictions and certain experimental anisotropy techniques (AMS and AIRM) both utilize an identical second order tensor approach, thus allowing direct comparisons of the full 3D anisotropy from the different methods on exactly the same cylindrical core plug. The igneous sample we chose also allowed us to compare many different anisotropy techniques on the same plug, and relate the results to the observed petrofabric. We recognize that the methodology and assumptions employed in the digital physics permeability module are more applicable to sedimentary rocks. Nevertheless we demonstrated that the digital physics predicted principal permeability axes corresponded quite well (in terms of orientations and normalised magnitudes) to the AIRM, AMS and other anisotropy results. This suggests that the digital rock physics predictions do have some physical meaning in this case. Whether the permeability anisotropy results are realistic for our igneous sample is open for discussion. It is not currently possible (with present technology) to measure the full 3D permeability

anisotropy on a single cylindrical core plug in order to verify our predictions. Experimental verification would require plugs cut in several directions as mentioned earlier, but this would be extremely time consuming, expensive and requires that the rock be homogeneously anisotropic in the interval where all the plugs are cut.

The next stage in our research will be to compare digital rock physics anisotropy predictions with the experimental techniques on some sedimentary rock samples, particularly since the digital rock physics permeability anisotropy module methodology, assumptions and predictions are likely to be more realistic for sedimentary rocks. However, the same verification issues will persist, due to currently not being able to measure the full 3D permeability anisotropy on a single cylindrical plug.

Note that for cubic samples anisotropic measurements of certain parameters (such as permeability or acoustic properties using parallel planar transducers) can only potentially be made in 3 orthogonal directions (e.g., in the X, Y and Z axes). Those directions will not necessarily correspond to the 3 principal anisotropy axes, and thus such measurements will not yield the true principal anisotropy axes unless the 3 orthogonal measurements happen to be exactly coincident with the 3 principal anisotropy axes.

6 Conclusions

1. Full 3D anisotropy comparisons between μ CT image derived rock physics predictions and experimental measurements are reported on exactly the same single core plug sample for the first time (as far as we are aware). Full 3D anisotropy comparisons were made between μ CT predicted permeability and measured AIRM and AMS. For μ CT predicted s-wave velocity and electrical conductivity anisotropies the determinations were possible along the 3 orthogonal X, Y and Z sample axes, rather than the full 3D anisotropy (i.e., they didn't include off-diagonal components), but nonetheless were consistent with the permeability anisotropy, AIRM and AMS results. The AGRM also gave consistent orientations, as well as the same order of the principal anisotropy axes (max., int. and min) for the SSD ferrimagnetic particles, but this method does not give the absolute magnitudes of those axes. The results from each method were consistent by giving generally closely related orientations for the 3 principal anisotropy axes, and every method indicated that with respect to the sample reference axes $Z > X > Y$. The results were consistent with the observable petrofabric seen in the core plug images and the μ CT images.
2. The 3D principal anisotropy axis orientations of the bulk rock components (via the digital rock predicted anisotropies of permeability and electrical conductivity, as well as both the predicted and measured s-wave velocity anisotropy) were similar to those of the fine-grained ferrimagnetic components (via AIRM, AGRM and AMS).

3. In terms of direct comparisons in the XY plane, the orientations of the maximum (close to the X axis) and minimum (close to the Y axis) anisotropy axes were similar for the measured s-wave velocities, AGRM, AIRM, AMS and predicted permeability. The μ CT predicted s-wave velocities and electrical conductivities also gave $X > Y$, even though the module for these two determinations only considered the X and Y orientations.
4. The results from our sample suggested the potential for estimating the full 3D anisotropy of any one of the parameters from measurements or predictions from any one of the other parameters on single core plugs (e.g., estimating anisotropies of permeability, acoustic velocities or electrical conductivity via rapid, non-destructive magnetic anisotropy measurements).
5. The links between μ CT derived anisotropy predictions, experimental anisotropy measurements, and observable petrofabric help to provide validation and confidence in the digital rock physics predictions and the experimental measurement techniques.
6. The different methods used in this study allow the anisotropy of different components (e.g., minerals, pore network via permeability anisotropy, and ferrimagnetic grain size fractions via AIRM) and petrophysical properties to be quantified.
7. Differences in the normalized magnitudes of the principal axes from each method may ultimately be related to specific mineral components or properties, which in turn may relate to particular rock types. This study represents a first step towards elucidating such relationships. Moreover, differences in the magnitudes and orientations of the anisotropies of the various mineral components and/or properties will likely be linked to natural processes, such as flow directions (such as the recent work by [15] estimating paleo-wind directions by combining μ CT imaging and AMS), deformation etc.

D. K. P. thanks the Natural Sciences and Engineering Research Council of Canada (NSERC) for a Discovery Grant. Matthias Halisch and Mohammed Ameen are thanked for their constructive review comments, which helped improve the manuscript.

7 List of abbreviations

AF	Alternating Field
AGRM	Anisotropy of GRM
AIRM	Anisotropy of IRM
AMS	Anisotropy of Magnetic Susceptibility
AMR	Anisotropy of Magnetic Remanence
ASWV	Anisotropy of Shear Wave Velocity
CT	Computer Tomography
Dec.	Declination angle
DF	Direct Field
GRM	Gyromanent Magnetization

Inc.	Inclination angle
IRM	Isothermal Remanent Magnetization
MD	Multidomain
SSD	Stable Single Domain
X, Y, Z	X, Y and Z reference axes of the sample
XY etc	XY plane of the sample
x, y, z	x, y and z components of remanence

8 References

1. S. Zhang, R. E. Klimentidis and P. Barthelemy. Micron to millimetre upscaling of shale rock properties based on 3D imaging and modelling. *Proceedings of the Society of Core Analysts*, 27-30 August, Aberdeen, UK. Paper SCA2012-20 (2012).
2. S. Zhang, A. Byrnes and J. Howard. Property upscaling in porosity systems with under-resolved features using image-based rock physics. *SPE/AAPG/SEG Unconventional Resources Technology (URTEC) Conference*, 22-24 July, Denver, Colorado, USA. DOI: <https://doi.org/10.15530/urtec-2019-416> (2019).
3. D. K. Potter. Novel techniques to rapidly determine the magnetic anisotropy of reservoir rocks and shales, and comparisons with permeability and acoustic anisotropies. *Proceedings of the 2011 International Symposium of the Society of Core Analysts*, 18-21 September 2011, Austin, Texas, USA. Paper SCA2011-031 (2011).
4. P. Y. Cholach, J. B. Molyneux and D. R. Schmitt. Flin Flon belt seismic anisotropy: elastic symmetry, heterogeneity, and shear-wave splitting. *Canadian Journal of Earth Sciences*, **42**, 533-554 (2005).
5. S. Zhang, A. P. Byrnes, J. Jankovic and J. Neilly. Management, analysis, and simulation of micrographs with cloud computing. *Microscopy Today*, **27** (2), 26-33 (2019).
6. W. M. Telford, L. P. Geldart, R. E. Sheriff and D. A. Keys. *Applied Geophysics (2nd Edition)*. New York, NY: Cambridge University Press, pp. 770 (1990).
7. O. L. Anderson and R. C. Liebermann. Sound velocities in rocks and minerals. *VESIAC State-of-the-Art Report (Accession Number: AD0804865)*, pp.182 (1966).
8. A. Ali, S. Abdalah and D. K. Potter. Quantifying the role of grain lining hematite cement in controlling permeability in a relatively tight gas sandstone reservoir from the North Sea. *SPE Reservoir Evaluation and Engineering*, **15**, Issue 6, 618-623 (2012).
9. A. Stephenson, S. Sadikun and D. K. Potter. A theoretical and experimental comparison of the anisotropies of magnetic susceptibility and remanence in rocks and minerals. *Geophysical Journal of the Royal Astronomical Society*, **84**, 185-200 (1986).
10. D. K. Potter. A comparison of anisotropy of magnetic remanence methods – a user's guide for application to paleomagnetism and magnetic fabric studies. In *"Magnetic Fabric: Methods and*

Applications.” Martin-Hernandez, F., Luneburg, C. M., Aubourg, C. and Jackson, M. (eds.), Geological Society, London, Special Publications, **238**, 21-35 (2004).

11. A. Stephenson. Gyroremanent magnetization in anisotropic magnetic material. *Nature*, **284**, 49-51 (1980).
12. A. Stephenson and D. K. Potter. Gyroremanent magnetizations in dilute anisotropic dispersions of gamma ferric oxide particles from magnetic recording tape. *IEEE Transactions on Magnetism*, **MAG-23**, 3820-3830 (1987).
13. D. K. Potter and A. Stephenson. Single-domain particles in rocks and magnetic fabric analysis. *Geophysical Research Letters*, **15**, 1097-1100 (1988).
14. B. C. Snow. Nanoparticle magnetic characterization and comparison of rock anisotropy methods. MSc thesis, University of Alberta, pp. 95 (2018).
15. M. Halisch, C. Zeeden and C. Rolf. Towards image based assessment and characterization of cyclic paleo-wind and flow fields. *European Geoscience Union Assembly*, 4-8 May, 2020, Vienna, Austria (2020).

Dissolution behaviour in carbonate reservoirs during WAG injection: A preliminary experimental study

Mohamed Khather¹, Matthew Myers², Ali Saeedi¹, and Ausama Giwelli^{2*}

¹Department of Petroleum Engineering, Curtin University, Kensington, WA, 6151, Australia

²CSIRO Energy, Kensington, WA, 6151, Australia

Abstract. In this study, a core flooding experiment using a water-alternating-gas (WAG) injection was conducted to evaluate its impact on the petrophysical properties of an initially oil-saturated heterogeneous carbonate core sample. Carbon dioxide (CO₂) and synthetic formation brine were injected (0.5 pore volume CO₂ alternating with 0.5 pore volume brine) alternately following establishment of waterflooding residual oil saturation under reservoir conditions. Gas porosity, gas permeability, NMR (nuclear magnetic resonance) T₂ measurements, and X-ray CT scanning were conducted pre- and post-core flooding. The results show that CO₂-WAG injection resulted in substantial additional oil recovery (~30 %) under the applied experimental conditions. The results also show an increase in the permeability of the tested sample from 1.5 to 16 mD, which could be attributed to mineral dissolution. X-ray CT imaging shows signs of excessive mineral dissolution and formation of wormhole structures. It is believed that dissolution within the tested core plug caused the WAG fluids to follow the newly wormhole (causing them to enlarge further), and consequently bypassing many parts of the sample. Therefore, despite a significant increase in oil recovery, a large amount of oil is still left behind.

1 Introduction

With a pressing need to address climate change, carbon dioxide (CO₂) sequestration in hydrocarbon reservoirs (either depleted or producing) is increasingly being considered for many reasons including its large storage capacity (i.e. scalability) compared to other emissions mitigation strategies. Furthermore, initially, the cost of carbon capture and storage (CCS) could be offset by the added value of enhanced hydrocarbon recovery which is a by-product of storing CO₂ in producing reservoirs. Carbonate reservoirs represent about fifty percent of producing oil and gas reservoirs around the world [1]. However, CO₂ injection into carbonate reservoirs for storage/enhanced oil recovery (EOR) is more challenging due to their extreme heterogeneous nature (compared to comparable sandstone reservoirs) and dominant composition of highly reactive minerals (i.e. calcite and dolomite which are readily reactive with carbonated brine) in their rock formations. With the presence of highly reactive minerals in their composition, carbonate rocks may undergo appreciable alterations to their properties to a much larger extent compared with sandstone [2-4]. A combination of mineral dissolution, mineral precipitation, mechanical/physical compaction and asphaltene precipitation during CO₂-EOR injection scheme have been identified as the dominant mechanisms that occur [5-10].

Water-alternating-gas (WAG) injection as an EOR technique was introduced to improve macroscopic sweep efficiency in gas injection processes [11]. Furthermore, this technique is often more economical by lowering the gas volume required to be injected into the reservoir [12]. Each CO₂-EOR method (e.g. continuous CO₂ injection, carbonated water injection, water-alternating CO₂ injection, and cyclic CO₂ injection) has its own merits and disadvantage [13, 14].

Majority of the WAG research studies have focused on the field applications, pilot tests, coreflooding experiments, and simulation studies [15-18]. For instance, Caudle et al [15]

and Kulkarni et al [16] have demonstrated that a high recovery of up to 90% could be achieved during coreflooding experiments. Also, WAG technique has been successfully applied in the North Sea fields such as Gullfaks, Stafjord, South Brae, Snorre, and Oseberg Ost [19].

In this study, we aim to evaluate the impact of CO₂-WAG on the internal pore structure of a carbonate reservoir core sample using nuclear magnetic resonance (NMR) and X-ray CT analysis. The objective is to determine whether the negative effects from CO₂-brine induced processes are reduced relative to other CO₂ injection processes while maintaining effective additional oil recovery. Crude oil and formation brine were used in the coreflooding experiment. Gas permeability, gas porosity, NMR-T₂ analysis and X-ray CT scan techniques were utilised to characterise the selected core sample before and after coreflooding test.

2 Material and Testing Method

A coreflooding experiment was conducted on a typical sample collected from a Middle East carbonate reservoir. Dry gas permeability and porosity were 1.5 mD and 12.7%, respectively. The plug consisted (as measured by power X-ray) of calcite (82.2%), dolomite (13.1%), quartz (0.5%), halite (0.6%), albite (1%) and Ankerite (2.2%). The core plug was cleaned prior to measurement and it had a length and diameter of 63 mm and 35.5 mm, respectively (see Fig. 1).

Nuclear magnetic resonance (NMR) T₂ measurements at ambient condition were conducted on a brine saturated core sample, using Oxford-GIT Instruments Geospec 2 Plus Analyzer. Furthermore, X-ray CT imaging was used to evaluate mineral heterogeneity inside the core sample, as well as core-scale/macroscopic changes to some extent pore-scale features (e.g. wormhole formation) due to the flooding procedure. In this study, all X-ray CT scans (pre- and post-test) were performed at room temperature and atmospheric pressure using an X-ray energy beam of 140 kV and current of 1500 mA. A helical acquisition mode (pitch at 350 μm)

* Corresponding author: Ausama.giwelli@csiro.au

was used to enable the reconstruction of 3D X-ray images with a voxel size of about $110 \mu\text{m} \times 110 \mu\text{m} \times 400 \mu\text{m}$ (512×512 pixels).



Fig. 1. Reservoir core sample used in this study.

Brine composition and test conditions were representative of reservoir conditions from which the core was acquired. The experiment was carried with a pore pressure of 14 MPa, temperature of 65 °C and overburden pressure of 27 MPa. Synthetic formation brine composition used in this experiment is shown in Table 1 and is based on the data available for the selected field. Crude oil used in the experiment was also obtained from the same field in the Middle East. The crude oil has a 38° API gravity and chemical compositions as presented in Table 2. Also, asphaltene content measurement (ASTM D6560) was conducted, and the result shows the crude has 0.075 wt% asphaltene composition.

Table 1. Concentration of major ions used to prepare the synthetic brine.

Major ions	mg/L
Na ⁺	11870
K ⁺	259
Ca ²⁺	2368
Mg ²⁺	452
Cl ⁻	24046

Table 2. Composition of the crude oil used in this study.

Component	Mol %	Component	Mol %
C2	0.21	C18	2.687
C3	1.155	C19	1.983
iC4	0.543	C20	1.995
nC4	2.64	C21	1.768
iC5	1.773	C22	1.566
nC5	3.467	C23	1.375
C6	6.253	C24	1.214
C7	7.056	C25	1.056
C8	8.211	C26	0.984
C9	7.563	C27	0.876
C10	7.12	C28	0.834
C11	5.835	C29	0.784
C12	4.953	C30	0.687
C13	4.587	C31	0.625
C14	4.025	C32	0.579

C15	3.984	C33	0.493
C16	3.16	C34	0.461
C17	3.258	C35	0.426

2.1 Core flooding experimental procedure

Flooding with synthetic formation brine was conducted until residual oil saturation was established; this was followed by water alternating gas (CO₂-WAG) flooding using, the above mentioned, synthetic formation brine and pure CO₂. The following steps were taken in a chronological order:

1. Load the cleaned core sample into the core-holder. The core sample was wrapped into a composite sleeve consisting of a layer of FEP heat shrink, a layer of aluminium foil and a conventional Viton rubber sleeve before being inserted into a standard biaxial core-holder. More information about this step can be found in [3, 20],
2. A low overburden pressure was applied slowly on the sample to eject any trapped air. A vacuum pump was then connected to the core-holder for about 12 hours,
3. The core sample was then aged/saturated for 4 weeks in crude oil, shown in Table 2, under reservoir conditions,
4. The core holder was then connected to the flooding system, shown in Fig. 2, and synthetic brine injection started at a low flow rate while monitoring the pore pressure. The flow rate was then adjusted to 0.5 mL/min throughout the experiment. Brine injection continued until no more oil was produced, indicating establishment of residual oil saturation. Produced liquid was collected in small graduated tubes to keep track of the oil recovery profile against time accurately.
5. After 24 hours under reservoir conditions, CO₂-WAG (pure CO₂ and synthetic brine) injection was then started at a 1:1 ratio, half pore volume CO₂ alternating with half pore volume brine (for a total of ten cycles were used). At the end of this stage, WAG produced no further crude oil, allowing the injected fluids a relatively long time to interact with the rock sample and promote alteration to its petrophysical properties (if any),
6. At the completion of the experiment, the confining and pore pressures were released gradually, and the core sample was removed, cleaned as per [21], and then dried in the oven at 60°C. Post-test characterisation (NMR, gas porosity, permeability, and medical X-ray CT scan) were then carried out.

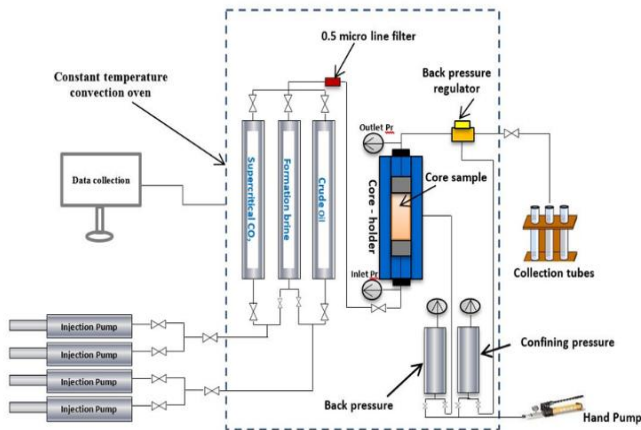


Fig. 2. Schematic diagram of core flooding apparatus used in this study [20].

3 Results and Discussion

Fig. 3 shows oil recovery factor (RF%) obtained throughout the experiment. The RF is defined as the recoverable amount of oil that initially placed inside the core plug. As stated above, the core sample was aged in crude oil under reservoir condition and then flooded by the synthetic formation brine to displace oil. Afterward, CO₂-WAG cycles, total of 10 cycles, was injected. An early water breakthrough was observed at about ~0.17 PV during brine injection/flooding corresponding to 24 % oil recovery (see Fig. 3). At the end of the brine flooding (~1.2 PV), more oil was produced resulting in approximately 40 % recovery. It should be mentioned that no bump flow was performed during this stage.

The low recovery result obtained during brine injection agrees with [22]. The probable cause appears to be as a result of the complex internal pore structure of the rock sample, and/or wettability effects as most carbonate reservoirs are classified as oil wet [23]. The oil recovery during CO₂-WAG was improved to about 51 % at ~5 PV and then increasing to 71 % at ~6 PV. The result revealed that more oil was able to produce during CO₂-WAG process, but did not eventually attain any higher recovery (Fig. 3). Unfortunately, upstream pressure transducer had a technical issue during the experiment and thus, we decided not to show the differential pressure.

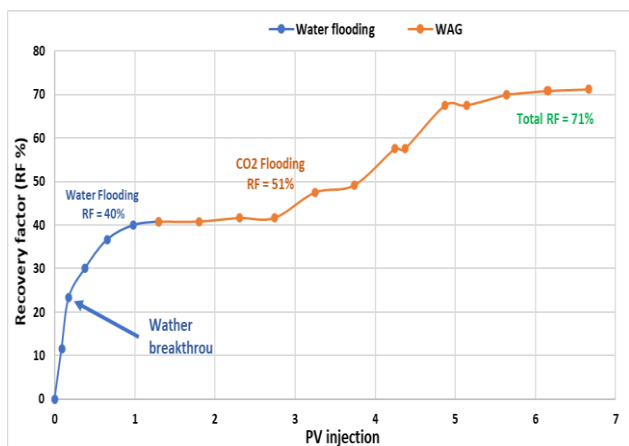


Fig. 3. Oil recovery percentage versus injected pore volume for both brine and CO₂-WAG stages.

Gas permeability results (pre- vs post-flood) showed significant increase (from 1.5 to 16 mD). Such a change can be attributed to the effect of the mineral dissolution mechanism (a wormhole formation) during CO₂-WAG injection. This hypothesis was supported by core effluents analyses, which was collected during the WAG flooding (see Table 3). Geochemistry result shows the concentration of calcium in the first cycle was higher than the base brine composition, which indicates an increase in dissolution. However, as more WAG cycles were injected, the concentration decreased throughout the experiment. In other words, the dissolution of calcium from the calcite dominate core plug mainly occurred in the first few cycles (<5 cycles). Then, the contact/reactivity with the Ca²⁺ in the mineral solid phase is reduced and as a result, less Ca²⁺ was mobilised. On the other hand, magnesium was present in the effluent but at small concentrations and there was, almost, no dissolution throughout the experiment. Gas porosity, on the other hand, shows a slight decrease of about ~ 5% reduction (12.7 to 12.1%). Such observation may have been caused by compaction mechanism (exacerbated by mineral dissolution physically weakening the core sample) caused by the overburden pressure applied during the experiment [10].

CT imaging was used to qualitatively analyse possible spatial changes of the CT attenuation profile/bulk density (within the CT scan resolution > 0.1 mm) along the plug length (as shown in Figure 4). Also a direct threshold segmentation of the CT histogram was used to visualise low density areas (pores) in 3D images (Figure 5) to illustrate possible simultaneous mechanisms (e.g. dissolution, precipitation and/or both), which might occur during the experiment. As mention above, x-ray CT images were generated before and after flooding at ambient conditions, and the sample was cleaned and dried in oven. The CT profile (Fig. 4) along the sample length shows a slight decrease in CT values in comparison with pre-flood state. The value difference between the pre-and post-WAG is small and within the error bar sensitivity of the machine at ± 5 HU. However, 3D x-ray images support mineral dissolution at the inlet face of the plug (a light green colour in Fig. 5), which has led to wormhole that visible in the images. The reaction extend almost to the entire length of the core sample.

We also calculated Peclet (P_e) and Damkohler (D_a) numbers of the dissolution and deposition process [24-29]. The Peclet number is the ratio of convection speed to characteristic diffusive velocity, while the Damkohler number is the ratio of the reaction to the mass transport rate. These dimensionless numbers provide a useful means of combining the physical and chemical processes that control dissolution and deformation regimes (e.g., [24, 27]). The Peclet and Damkohler numbers were estimated as $P_e = v/LD$ and $D_a = A_r k_r L / \phi v C_{eq}$; where v is the interstitial velocity, L is the characteristic length, D is the molecular diffusion coefficient (8×10^{-10} m/sec), A_r is the reactive surface area, k_r is the reaction rate coefficient (1×10^{-4} cf. [30]), ϕ is the porosity and C_{eq} is the average calcium concentration. At the

core length, the tested sample yield high P_e and D_a values characteristic of 5.22×10^3 and 7.26×10^3 , respectively.

The P_e number is $\gg 1$, indicating that the advective transport is dominant over diffusion at the core scale. The fact that $D_a \gg 1$ also suggests an extensive dissolution occurred at the beginning of the flow system [31]. Based on P_e - D_a diagram [26], it could be concluded that the tendency of reaction is dominant wormhole regimes (i.e., permeability increases greatly due to the dissolution process). This result is consistent with the XCT images shown in Fig. 5.

Although, there was a 30% increase in oil production during CO₂-WAG cycles, we believe the dissolution patterns, wormhole in this case, has negatively influenced the total amount of oil that could be recovered from the tested sample (with substantial amounts of oil remaining unrecovered). Apparently, the wormhole has created a preferential flow path for the injected fluids (CO₂ and brine) to bypass parts/islands of the oil inside the pores under the experiment conditions. Brine-CO₂ had a sufficient time to interact at different locations (flowline, inside the rock sample) during WAG, which resulted in accelerated mineral dissolution.

Asphaltene precipitation and to some extent mineral precipitation were expected to occur during the CO₂-WAG cycles. However, it seems that the effects of these precipitation mechanisms on permeability have been masked and suppressed by more dominant mineral dissolution (and wormhole formation).

Table 3. Calcium and magnesium concentration in the core effluents collected during WAG injection.

WAG Cycle number	Brine effluent concentration	
	calcium (Ca ²⁺) mg/L	magnesium (Mg ²⁺) mg/L
1	2500	250
5	2100	210
8	2000	190
10	2000	200

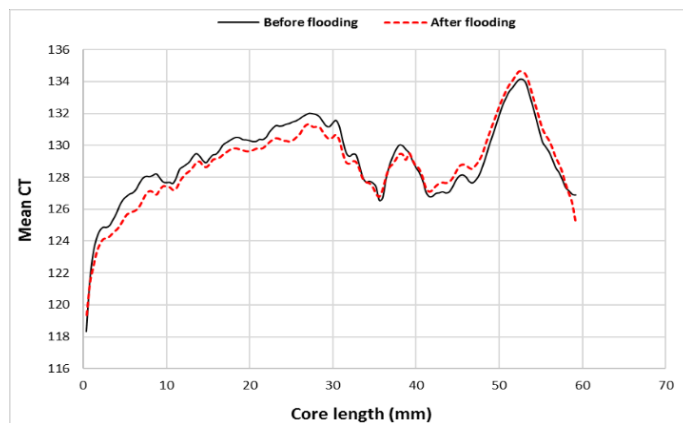


Fig. 4. CT number distribution along the sample length before and after WAG injection. The CT values show signs of dissolution in the first half of the sample, then turns to precipitation toward the end of the sample.

Fig. 6 shows the cumulative and incremental NMR-T₂ spectra of pre- and post-test measurements. The NMR-T₂ relaxation time was used to calculate the connected porosity filled by brine and demonstrate (qualitatively) the pore size distribution. The result shows a shift towards smaller values, meaning that the pore sizes/porosity became smaller and a slight shift in its pore size distribution towards smaller pore sizes (i.e., a reduction in the T₂ relaxation times). However, the NMR-T₂ distribution only examines pore space that is filled with water. This is consistent with gas porosity reduction (~5%) discussed above. Liteanu et al [10] showed CO₂ injection can increase mechanical compaction in carbonate by 7 orders of magnitude. However, in order to clarify how the mechanical strength changes during the experiment, we intend to implement fibre optic sensing technique [32, 33] to measure sample deformation. The NMR-T₂ distribution was not able show larger pores (Figure 6) corresponding to the wormholes, evident in the x-ray CT imaging. This is because water cannot be held inside the pore during ambient NMR-T₂ measurement, as the wormhole created an easy flow path for water to get out of the sample while NMR-T₂ measurement is conducted. Similar behaviour was observed in [34].

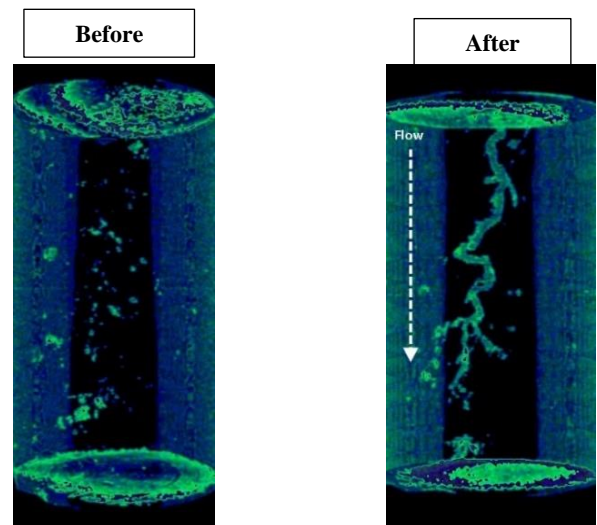


Fig. 5. 3D x-ray CT images for the tested core sample before and after flooding. The images show some low-density areas (corresponding to a light green colour) occurred due to the creation of wormholes along the length of the sample because of dissolution of carbonate minerals.

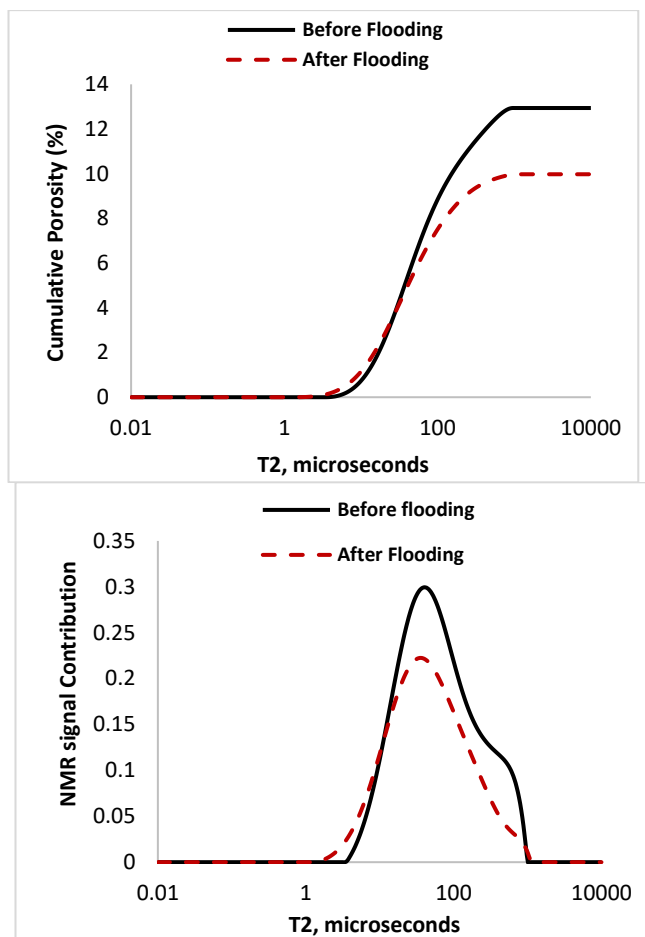


Fig. 6. Change in the cumulative porosity (top) and incremental NMR-T₂ distribution (bottom) of the tested sample, before and after flooding. NMR T₂ distribution shifted slightly to the left, indicating that the sample's pore sizes have become smaller after flooding.

4 Conclusions

While this study has only used one core sample, it is expected that within the context of this study that CO₂-WAG injection into carbonate rocks would improve sweep efficiency, to some extent, and it would also lead to minerals dissolution. In this particular case, fluid-rock interaction was significant and has eventually created wormhole formation across the entire length of the sample. With a high permeability channelling exists along the core sample, large amount of oil that is trapped in lower permeability portions of the rock was not recovered. All of these considerations have significant implications in terms of deployment in the field. Thus, we suggest more experimental studies should be considered to investigate the combined mechanisms to maximise oil recovery factor. Further research should be done to examine the effect of CO₂-WAG injection with the aid of other chemical additives such as surfactants, polymers, nanoparticles into the carbonate reservoirs.

References

- [1] SJ Mazzullo. Overview of porosity evolution in carbonate reservoirs. *Kansas Geological Society Bulletin*, **79**, 20-8 (2004)
- [2] M Seyyedi, HKB Mahmud, M Verrall, A Giwelli, L Esteban, M Ghasemiziarani, B Clennell. Pore structure changes occur during CO₂ injection into carbonate reservoirs. *Sci Rep*, **10**, 3624 (2020)
- [3] A Giwelli, MZ Kashim, MB Clennell, L Esteban, RRP Noble, C White, S Vialle, M Ghasemiziarani, M Myers, S. Md Shah Salwani. *CO₂-brine injectivity tests in high CO₂ content carbonate field, Sarawak basin, offshore East Malaysia*. In proceedings of: The 2018 International Symposium of the Society of Core Analysts, Trondheim, Norway, (2018)
- [4] M. Khather, A. Saeedi, R. Rezaee, R.R.P. Noble, D. Gray. Experimental investigation of changes in petrophysical properties during CO₂ injection into dolomite-rich rocks. *International Journal of Greenhouse Gas Control*, **59**, 74-90 (2017)
- [5] P. Mahzari, AP. Jones, EH. Oelkers. An integrated evaluation of enhanced oil recovery and geochemical processes for carbonated water injection in carbonate rocks. *J Petrol Sci Eng*, **181**, (2019)
- [6] ME. Amin, AY. Zekri, R. Almehaideb, H. Al-Attar. *Optimization of CO₂ WAG processes in a selected carbonate reservoir-An experimental Approach. SPE-161782-MS*. In proceedings of: Abu Dhabi International Petroleum Conference and Exhibition, Abu Dhabi, UAE, (2012)
- [7] M. Motealleh, R. Kharrat, A. Hashemi. An Experimental investigation of water-alternating-CO₂ coreflooding in a carbonate oil reservoir in different initial core conditions. *Energy Sources, Part A: Recovery Utilization and Environmental Effects*, **35**, 1187-96 (2013)
- [8] IM. Mohamed, J. He, HA. Nasr-El-Din. Experimental analysis of CO₂ injection on permeability of vuggy carbonate aquifers. *J Energ Resour-Asme*, **135**, (2013)
- [9] AY. Zekri, SA. Shedid, RA. Almehaideb. Experimental investigations of variations in petrophysical rock properties due to carbon dioxide flooding in oil heterogeneous low permeability carbonate reservoirs. *J Pet Explor Prod Te*, **3**, 265-77 (2013)
- [10] E. Liteanu, CJ. Spiers, CJ. Peach, AN. Obdam. *Effect of CO₂ injection on compaction of carbonate rocks*. In proceedings of: American Geophysical Union, Fall Meeting 2006, (2006)
- [11] S Touray. *Effect of water alternating gas injection on ultimate oil recovery*. Masters of Engineering, Petroleum Engineering, Dalhousie University, (2013)
- [12] G.J. Pariani, K.A. McColloch, S.L. Warden, D.R. Edens. An approach to optimize economics in a West Texas CO₂ flood. *J Pet Technol (SPE-22022-PA)*, **44**, 984-1025 (1992)
- [13] D.M. Malcolm, S.M. Frailey, A.S. Lawal. *New approach to CO₂ flood: Soak alternating gas (SPE-70023-MS)*. In proceedings of: The SPE Permian Basin Oil and Gas Recovery Conference, Midland, Texas, (2001)
- [14] Xg. Xu and A. Saeedi. Evaluation and optimization study on a hybrid EOR technique named as chemical-alternating-foam floods. *Oil Gas Sci Technol Rev IFP Energies nouvelles*, **72**, (2017)

- [15] BH. Caudle and AB. Dyes. Improving miscible displacement by gas-water injection. *T Am I Min Met Eng*, **213**, 281-4 (1958)
- [16] MM. Kulkarni and DN. Rao. Experimental investigation of miscible and immiscible Water-Alternating-Gas (WAG) process performance. *J Petrol Sci Eng*, **48**, 1-20 (2005)
- [17] JR. Christensen, EH. Stenby, A. Skauge. Review of WAG field experience. *Spe Reserv Eval Eng*, **4**, 97-106 (2001)
- [18] E. Fernandez Righi, J. Royo, P. Gentil, R. Castelo, A. Del Monte, S. Bosco. *Experimental study of tertiary immiscible WAG injection. SPE-89360-MS*. In proceedings of: The SPE/DOE Symposium on Improved Oil Recovery, Tulsa, Oklahoma, (2004)
- [19] S. Afzali, N. Rezaei, S. Zendehboudi. A comprehensive review on enhanced oil recovery by Water Alternating Gas (WAG) injection. *Fuel*, **227**, 218-46 (2018)
- [20] M. Khather, A. Saeedi, R. Rezaee, R.R.P. Noble. Experimental evaluation of carbonated brine-limestone interactions under reservoir conditions-emphasis on the effect of core scale heterogeneities. *International Journal of Greenhouse Gas Control*, **68**, 128-45 (2018)
- [21] C McPhee, J Reed, I Zubizarreta. *Core Analysis: A Best Practice Guide*. Elsevier (2015)
- [22] M. Khather, A. Saeedi, M.B. Myers, M. Verrall. An experimental study for carbonate reservoirs on the impact of CO₂-EOR on petrophysics and oil recovery. *Fuel*, **235**, 1019-38 (2019)
- [23] L.E. Treiber and W.W. Owens. A laboratory evaluation of the wettability of fifty oil-producing reservoirs (SPE-3526-PA). *SPE Journal*, **12**, 531-40 (1972)
- [24] CN Fredd and HS Fogler. Influence of transport and reaction on wormhole formation in porous media. *AIChE Journal*, **44**, 1933-49 (1998)
- [25] CN Fredd and HS Fogler. Optimum conditions for wormhole formation in carbonate porous media: Influence of transport and reaction. *SPE Journal*, **4**, 196-205 (1999)
- [26] F Golfier, C Zarcone, B Bazin, R Lenormand, D Lasseux, M Quintard. On the ability of a Darcy-scale model to capture wormhole formation during the dissolution of a porous medium. *J Fluid Mech*, **457**, 213-54 (2002)
- [27] ML Hoefner and HS Fogler. Pore evolution and channel formation during flow and reaction in porous media. *AIChE Journal* **34(1)**, (1998)
- [28] S Vialle, J Dvorkin, G Mavko. Implications of pore microgeometry heterogeneity for the movement and chemical reactivity of CO₂ in carbonates. *Geophysics*, **78**, L69-L86 (2013)
- [29] S Vialle, S Contraires, B Zinzner, JB Clavaud, K Mahiouz, P Zuddas, M Zamora. Percolation of CO₂-rich fluids in a limestone sample: Evolution of hydraulic, electrical, chemical, and structural properties. *J Geophys Res-Sol Ea*, **119**, 2828-47 (2014)
- [30] RS Arvidson, IE Ertan, JE Amonette, A Lutge. Variation in calcite dissolution rates: A fundamental problem? *Geochimica Et Cosmochimica Acta*, **67**, 1623-34 (2003)
- [31] CI Steefel and K Maher. Fluid-rock interaction: A reactive transport approach. *Rev Mineral Geochem*, **70**, 485-532 (2009)
- [32] Y. Kovalyshen, Banks S., A. Giwelli. *Measurement of rock strain using Fiber Bragg Grating sensors*. In proceedings of: The 52nd US Rock Mechanics/Geomechanics Symposium, Seattle, Washington, USA, (2018)
- [33] B. da Silva Falcão, L. Esteban, A. Giwelli, Y. Kovalyshen, S. Banks, A. Al-Yaseri, A. Keshavarz, S. Iglauer. *Monitoring fluid migration using in-situ nuclear magnetic resonance core flooding system integrated with fiber optic sensors: A proof of concept*. In proceedings of: The 35th International Symposium of the Society of Core Analysts (SCA Annual Symposium), Online Event, (2021)
- [34] M. Khather, A. Saeedi, MB. Myers, A. Giwelli. Effects of CO₂-saturated brine on the injectivity and integrity of Chalk reservoirs. *Transport Porous Med*, **135**, 735-51 (2020)

Improved fracture segmentation from unwrapped drill-core images using an innovative two-stage segmentation approach

Fatimah Alzubaidi¹, Harikrishnan Nalinakumar¹, Stuart R. Clark¹, Jan Erik Lie², Peyman Mostaghimi¹, and Ryan T. Armstrong^{1,*}

¹School of Minerals and Energy Resources Engineering, University of New South Wales, Sydney, Australia.

²Lundin Energy Norway AS, Lysaker, Norway.

Abstract. Recent advances in drill-core scanning provide high-quality unwrapped core images that require similarly advanced methods for processing the produced images and extracting important information in an automatic and reliable manner. Unwrapped core images provide a detailed view of fractures that can be segmented and characterized in terms of depth, dip angle, dip direction, aperture, and roughness. Despite the availability of advanced machine learning techniques for instance segmentation, obtaining accurate segmentation of the fractures from high-resolution images is challenging. For Mask Region-based Convolutional Neural Network (Mask R-CNN), a common instance segmentation model, the capacity of the segmentation branch is limited which, in turn, limits the segmentation quality of large objects especially those with fine details, such as the fractures. We propose a two-stage segmentation approach using Mask R-CNN to improve fracture segmentation. We use two CNN models: the first model processes full-size unwrapped core images to detect and segment fractures; the second model performs a more detailed segmentation by processing smaller regions of the images that include the fractures detected by the first model. We investigate using the standard Mask R-CNN architecture and a new architecture of Mask R-CNN with a Point-based Rendering (PointRend) neural network module. The method is evaluated on ~47 m of core and results in an increase in the average intersection-over-union by 0.25 from the baseline (one-stage segmentation with standard Mask R-CNN).

1 Introduction

Unwrapped core images are two-dimensional representations of the core surface. The images are taken by scanning the core in a 360° mode, i.e., by rotating the core and capturing the surface from different angles [1–3]. Modern core scanners provide high-resolution unwrapped core images with resolution up to 40 pixel/mm and can scan approximately three meters of core in 1 minute [2]. The images provide a detailed view of the core surface and the structural features, such as fractures.

Fractures appearing in unwrapped core images are involved in a variety of fracture analysis practices [4, 5]. The fractures, especially those with high dips, are used as matching features during core re-orientation by correlating them with the fractures from borehole image logs, allowing for a low-cost and indirect core orientation method [1]. Moreover, integrating unwrapped core images and borehole image logs (acoustic or resistivity images) are necessary for accurate fracture characterization [3].

In recent work [6], fractures from high-resolution unwrapped core images were used to automatically estimate the degree of fracture roughness and mismatches between fracture edges. The authors computed the joint roughness coefficient (JRC) for each fracture based on statistical estimators.

The mismatch was based on the standard deviation of fracture apertures and the correlation between fracture profiles. They validated the results according to a standard scale of the JRC [7]. The study, however, used pre-digitized fractures that were traced manually to obtain fracture profiles.

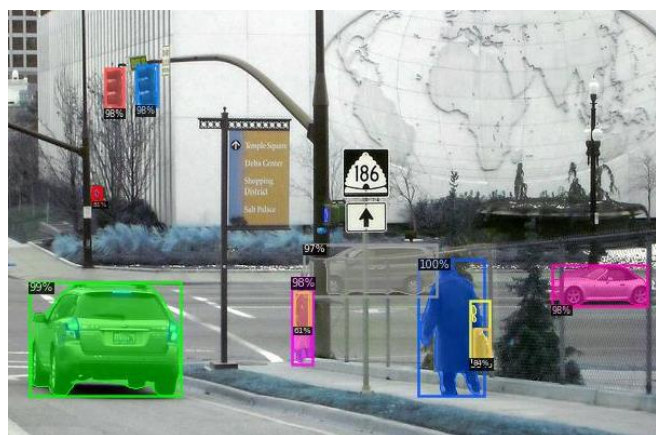
Developing automated and accurate fracture segmentation from unwrapped images can significantly facilitate the characterization process. Accurate and reliable fracture segmentation can be particularly beneficial for detailed fracture analyses, such as estimating fracture roughness or aperture sizes. Such segmentation approaches have not been developed yet due to there being limited research in this area. Previous work [7, 8] used classic image processing algorithms to identify fractures from core tray images, which provided only a limited view of the fracture surface compared to unwrapped images. In addition, several methods have been established to detect fractures from borehole image logs, which range from using edge detection and image processing algorithms to using machine learning (ML) based methods [9–12] with variable results. Thus, more research is needed to explore the feasibility of developing automated and accurate fracture segmentation from unwrapped core images.

Modern ML approaches can provide high-quality image analysis including instance or semantic segmentation [14, 15]. Instance segmentation is distinctly different from the more commonly used semantic segmentation in digital core analysis. With semantic segmentation objects of the same

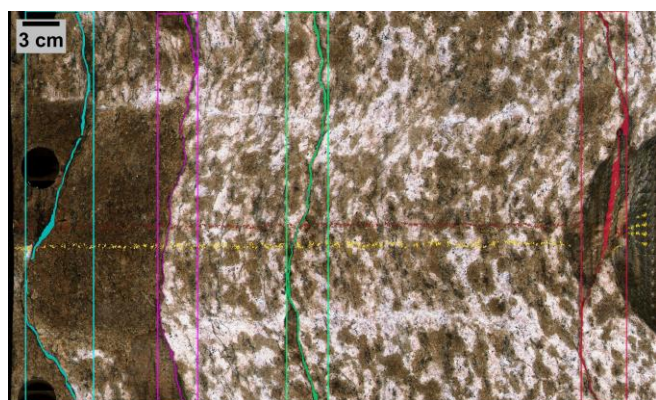
* Corresponding author: ryan.armstrong@unsw.edu.au

category are segmented as a single object while for instance segmentation objects are detected separately. An example application for instance segmentation, using the Mask Region-based Convolutional Neural Network (Mask R-CNN), is provided in Figure 1a where features in a street-level image are identified and segmented. Such technologies are an important step towards the operation of autonomous vehicles. So, can this technology be translated to core analysis applications? The aim would be to develop an instance segmentation algorithm that identifies important core structural features. The focus of our work is displayed in Figure 1b where Mask R-CNN is applied to core images for fracture identification. With this technology fractures could be segmented and characterized on a per fracture basis in an automated way. The efficacy of the method for core analysis, however, remains to be tested.

The accuracy of object segmentation by ML models depends on the size of the object compared to the resolution of the output raw mask, which is usually limited by computational and memory requirements (e.g. [14]). In high-resolution core images, the fractures appear as large objects that span the entire width of the image, but their apertures are finer features that require high-resolution images. The segmentation of such features is directly affected by the trade-off between field-of-view (computational and memory requirements) versus image resolution. We propose that the segmentation of fractures from high-resolution core images can be enhanced using a two-stage segmentation method.



(a)



(b)

Fig. 1. Original application of Mask R-CNN for natural image from COCO test dataset [15] in (a), and the application of the model for fracture segmentation from unwrapped core images in (b), showing

result from two-stage segmentation using Mask R-CNN + PointRend.

Two-stage segmentation has been applied in various applications where there are multi-scale features present in an image. [16] developed a two-stage segmentation framework using two 3D U-Nets to enhance segmentation of organs from computed tomography images. The first U-Net segments the whole image and the second U-Net segments a small part of the image that includes the organ of interest detected by the first model. A similar approach was used by [17] to refine segmentation of ultrasound breast images, which resulted in an improved average Dice score, a segmentation metric [18], of up to 14% approximately. Alternatively, [19] introduced a Point-based Rendering (PointRend) module to produce high-resolution masks from semantic segmentation and instance segmentation models with only a minor increase in the memory requirement.

Herein, we evaluated the standard Mask R-CNN and Mask R-CNN with the PointRend module (Mask R-CNN + PointRend) in a two-stage segmentation approach. The first stage detects full-size fractures in the input image. The second stage provides finer segmentation by processing small regions of the image that include detected fractures. We train the models with images from two boreholes and evaluated the method on new data including images from new boreholes. The results are evaluated using the intersection-over-union (IoU) between manual and predicted segmentation of fractures in new core images.

2 Data and methodology

This section is divided into two sub-sections. Section 2.1 provides a description of the unwrapped core images used in our work and the preparation of the datasets for training and testing the segmentation models. Section 2.2 introduces the proposed two-stage procedure, the tested architectures of the instance segmentation models, the training process of the models, and the evaluation metrics used.

2.1 Data preparation

The core images were obtained from four boreholes located at the Norwegian Barents Sea and North Sea. The boreholes were 7220/6-1, 7220/11-3 16/2-17 B, and 16/2-18 S. The images were acquired from Lundin Energy [20].

Boreholes 7220/6-1 and 7220/11-3 are located on the Loppa High in the Barents Sea whereas boreholes 16/2-17 B and 16/2-18 S are from Johan Sverdrup field and are located on the Utsira High in the North Sea. Core intervals and net lengths of the images used in our work from each borehole are summarised in Table 1. The sections from boreholes 7220/6-1 and 7220/11-3 were from the Ørn formation that is dominated by carbonate rock while the sections from 16/2-17 B and 16/2-18 S were taken from the Asgard formation composes mainly of claystones, marlstones, and limestone, and from the basement group that comprises highly fractured granite [21].

Table 1. Details of the core images from each borehole, showing images resolution, depth intervals and the net lengths of the core used in the study.

Borehole	Image resolution (pixels/mm)	Core images interval (m)	Net core length (m)
7220/6-1	2.6	1149.00–1203.00	52.88
7220/11-3	9.0	1852.20–1944.00	47.19
16/2-17 B	9.0	2130.70–2140.37	5.40
16/2-18 S	9.0	2130.70–2140.37	8.21

The training and validation images were selected from two boreholes as detailed in Table 2, with an initial number of 100 images that included 204 fractures. We used data augmentation to expand this number to 1200 images that were divided into 1000 images for training and 200 images for validation. The augmentation included blurring, altering the brightness and contrast, and horizontal and vertical flipping.

For evaluating the method, the test images were selected from the four boreholes (two blocks) to include the images from boreholes 16/2-17 B and 16/2-18 S obtained from new regions and formations. The test dataset included a total of 72 images that have 160 fractures (Table 2).

Table 2. Number and core length of training, validation, and test images prior to data augmentation.

Borehole	Training & validation		Test	
	Number	Length (m)	Number	Length (m)
7220/6-1	35	33.33	17	13.86
7220/11-3	65	33.60	30	19.28
16/2-17 B	—	—	11	5.39
16/2-18 S	—	—	14	8.21
Total	100	66.93	72	46.74

Fractures in the training, validation and test images were manually labelled using the Supervisely annotation online tool [22]. The images were 811–2905 pixels high and 356–8980 pixels wide with resolution of 2.6–9 pixels/mm as shown in Table 1. To build the model for the second stage of segmentation, we created three smaller images from each fracture in the training and validation datasets following a similar procedure as explained in Section 2.2.1. The resulting images were 144–1057 pixels high and 74–3457 pixels wide.

Before inputting the images into the models during each stage of segmentation, the images were resized to the default size of Mask R-CNN (discussed in Section 2.2.3). After resizing, the full-size images (i.e., the inputs of the first segmentation stage) had an average resolution of 2.1 pixels/mm while the small images (i.e., the inputs of the second segmentation stage) had a higher average resolution of 11.2 pixels/mm.

2.2 Methodology

2.2.1 Two-stage approach

The overall procedure involved using two instance segmentation models, as displayed in Figure 2. Model-A received a full-size image and output a mask for each fracture, like the ordinary implementation of an instance segmentation model. Model-B was then used to segment small regions of the image to enhance the masks produced by model-A.

As demonstrated in Figure 2, three regions were cropped from each fracture and segmented by model-B. The cropping included an overlapping ratio of 5% of the fracture height. We also tested dividing the fracture into four regions instead of three, but it did not provide further improvement from the three-region division.

Next, the resulting high-resolution masks by model-B at each location of the fracture replaced the original mask from model-A at that location. In some cases, model-B yielded more than one mask for a single image when it included parts of nearby fractures. To decide on the correct mask for such images, we used the mask with the highest IoU with the primary mask from model-A at the corresponding location, as shown in Figure 3. See Section 2.2.4 for the definition of IoU.

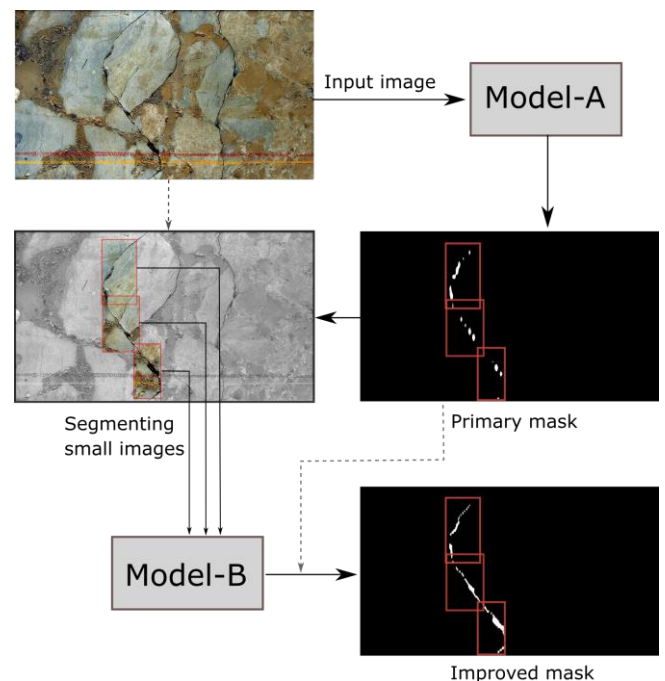


Fig. 2. Workflow of the two-stage segmentation method using two instance segmentation models (for clarity only a single continuous fracture segment is shown). Solid lines show the main flow and dashed lines show additional transitions.

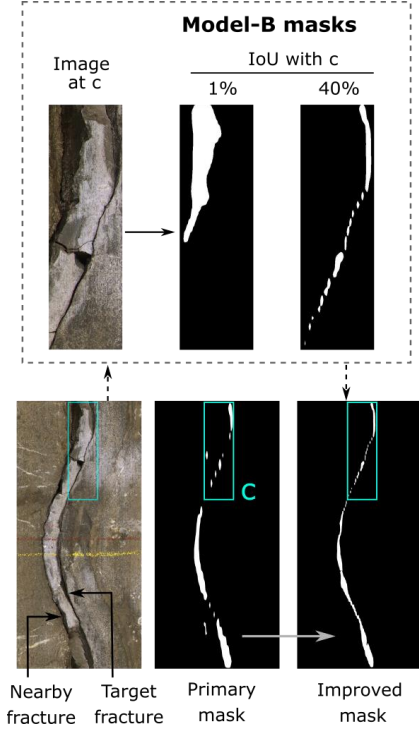


Fig. 3. Process of updating primary masks from model-A showing a case of multiple outputs by model-B. The mask with the highest IoU (40%) was selected to update region C in the primary mask instead of the mask with 1% IoU that belongs to a nearby fracture.

2.2.2 Experimented architectures of Mask R-CNN

To define the architecture of model-A and model-B, we evaluated two recognized instance segmentation architectures: (1) standard Mask R-CNN and (2) Mask R-CNN + PointRender.

The main components of the Mask R-CNN architecture are the region proposal network (RPN), a deep CNN for feature extraction (backbone), the RoIAlign layer, followed by the branches for bounding box detection, classification, and mask segmentation [14].

The purpose of the RPN is to propose candidate object regions, i.e., anchors, in the input image of different sizes and height-to-width ratios. The RoIAlign layer crops features extracted by the backbone of the proposed regions and resizes them to a uniform shape, e.g., 7×7 or 14×14 pixels². Then the detection and classification branches yield a classification score and bounding box coordinates for each region of interest (RoI). In parallel, the segmentation branch outputs a binary mask for each RoI.

A common architecture of Mask R-CNN includes a backbone with a feature pyramid network (FPN) [23] like what was used in this study. In this architecture, the segmentation branch receives RoIs of 14×14 pixels² and yields 28×28 pixels² masks. The branch consists of four convolutional layers, a deconvolutional layer, and an output layer.

Due to the small size of the output masks, segmentation of large objects has limited accuracy and fine details at the

object boundaries are usually not segmented properly. However, increasing the capacity of the segmentation branch would require significantly more computational time and memory. Therefore, an alternative method is required.

The PointRender module was developed by [19] to refine the segmented masks generated by instance segmentation models, such as Mask R-CNN, with a minor increase in the memory requirement. In Mask R-CNN, PointRender can increase the resolution of the output masks to 224×224 pixels² with nearly 30 times less memory and computational time than what would be required by the original segmentation branch to yield the same resolution. The module predicts higher-resolution masks from both lower-resolution masks as well as features of selected points from the masks by sampling points of low uncertainty. The pixel-wise prediction is performed by a multi-layer perceptron [19].

In Mask R-CNN + PointRender, the mask head predicts 7×7 pixels² for each RoI then the PointRender module refines the prediction to 224×224 pixels² through multiple iterations of point sampling and mask resolution enhancement. The mask resolution in each iteration is 7^2 , 28^2 , 56^2 , 112^2 , and 224^2 pixels², respectively. An illustration of the mask refinement process is provided in Figure A1 of Appendix A.

For both standard Mask R-CNN and Mask R-CNN + PointRender, we used ResNet-50-FPN as the backbone. We also added height-to-width ratios of 4:1 and 6:1 to the original ratios of 2:1, 1:1, and 1:2 that define the RPN anchors in model-A to match the shapes of the fractures. The rest of the architectures were left as the defaults used in [15, 19].

2.2.3 Training implementation

We used the Mask R-CNN and Mask R-CNN + PointRender implementations from Detectron2 [24]. We started the training with pretrained models on Microsoft COCO images [25]. The input images were resized to the default size of Mask R-CNN to have a maximum of 1333 pixels on the large edge [24]. We trained the models for 30,000 iterations using a batch size of 2 and 4 images for model-A and model-B, respectively using an NVIDIA GeForce RTX 2080 Ti GPU with 11GB of memory. We defined an initial learning rate of 0.01 and this rate was halved every 10,000 iterations. All other training parameters were like the default values used in Detectron2 [24].

The training loss converged as shown in Figure 4, and the precision of the segmented validation images converged as shown in Figure 5. The details of these results are discussed in Section 3. The segmentation loss was calculated as the average binary cross-entropy loss [14]. The precision was calculated using Eq. 1, where true positives are determined by a specific IoU threshold between the objects segmented by the model and the true objects. Commonly, an average precision is calculated at different IoU thresholds (0.5–0.95).

$$Precision = \frac{true\ positives}{true\ positives + false\ positives} \cdot (1)$$

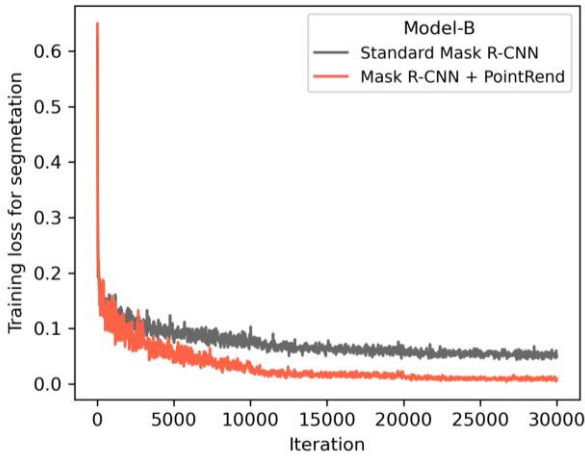
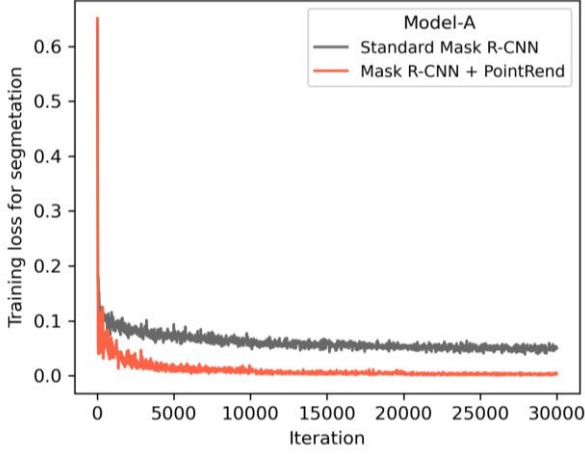


Fig. 4. Training loss for mask segmentation using standard Mask R-CNN and Mask R-CNN + PointRend architectures for model-A (top) and model-B (bottom).

2.2.4 Evaluation of the two-stage method

We evaluated the fracture segmentation using the two-stage method and the PointRend module both statistically and visually. We used IoU to compare the ground truth and predicted segmentation. The IoU between two objects is defined as the ratio of the overlap area between the objects to the total area of both objects. IoU is defined in Eq. 2 where $objectA$ and $objectB$ can be ground truth and predicted masks, respectively. IoU ranges from 0 (no match) to 1 (a perfect match); for the fractures that appear in the core images as detailed thin objects, IoUs around 0.5 can indicate good predictions, as shown in Section 3.

$$IoU = \frac{objectA \cap objectB}{objectA \cup objectB}. \quad (2)$$

We evaluated the effect of mask improvement on the accuracy of fracture aperture calculation, for a group of eight sample fractures (discussed in Section 3.2). Fracture aperture was calculated from the binary masks segmented manually and by the model, following the procedure in Appendix A. To evaluate aperture calculations by the model, we computed the

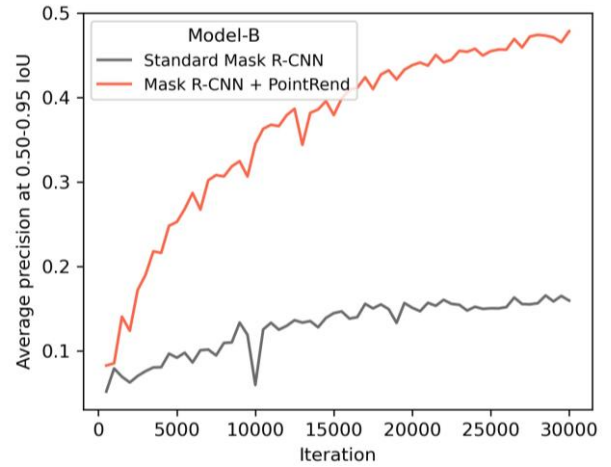
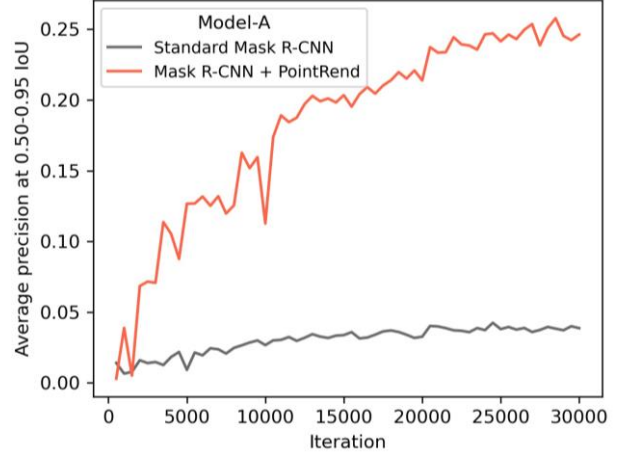


Fig. 5. Validation statistics during training of standard Mask R-CNN and Mask R-CNN + PointRend, for model-A (top) and model-B (bottom).

absolute error as the difference between aperture measurements from ground truth and predicted masks.

We also assessed the quality of the segmentation through visual inspection, including comparing the one-stage and two-stage segmentations as well as comparing standard Mask R-CNN and Mask R-CNN + PointRend segmentations.

3 Results and discussion

The training and validation statistics of segmentation in Figure 4 and 5 demonstrate the following.

- (1) Mask R-CNN + PointRend had lower training loss and significantly higher validation precision than standard Mask R-CNN in both model-A and model-B, suggesting that the PointRend module can enhance fracture segmentation by Mask R-CNN.
- (2) Model-B had more accurate segmentation than model-A as the segmentation precision increased from 4% for the full-size images (model-A) to 16% for the small images (model-B) in standard Mask R-CNN, and from 25% to 48% in Mask R-CNN + PointRend.

The results after integrating model-A and model-B in the two-stage method from the 72 test images (Table 2) are discussed in the next sections.

3.1 Results from IoU calculation

Based on the calculation of IoU between predicted and ground truth fractures in the test images, the two-stage method showed improvement in the segmentation from the one-stage method by both the standard Mask R-CNN and Mask R-CNN + PointRend models. The IoUs increased on average by 0.14 and up to 0.34 using standard Mask R-CNN, and on average by 0.11 and up to 0.27 using Mask R-CNN + PointRend, as shown in Table 3 and Figure 6. The segmentation of the test images from block 7220, which was used in the models training, was better than that of the images from block 16; however, the latter showed slightly more improvement by the two-stage method (Table 3). As demonstrated in Figure 6, the distributions of the IoU obtained by the two-stage method shifted towards the right side of the X-axis, i.e., higher IoUs.

Table 3. Comparison between the average IoU of 160 fractures in the test images from blocks 7220 and 16 (see Table 2), using the one-stage and the two-stage method.

Architecture	Block	One-stage method	Two-stage method
Standard Mask R-CNN	7220	0.34	0.47
	16	0.18	0.33
Mask R-CNN + PointRend	7220	0.47	0.56
	16	0.34	0.45

The method provided a significant increase in the percentage of fractures segmented with IoU greater than 0.5. The percentage increased from 7% in the one-stage method to 31% in the two-stage method using standard Mask R-CNN (Figure 6, top). Similarly with using Mask R-CNN + PointRend, the percentage of fractures with IoU > 0.5 almost doubled by the two-stage method, increasing from 33% to 62% (Figure 6, bottom).

Standard Mask R-CNN gained more improvement from the second stage of segmentation than Mask R-CNN + PointRend as the standard architecture provided poor segmentation of the full-size images in the first stage, due to its limited mask resolution, compared with Mask R-CNN + PointRend.

Overall, the best segmentation, in terms of the IoU, was obtained by the two-stage segmentation using Mask R-CNN + PointRend. It resulted in a greater than 0.5 average IoU for 160 fractures with 62% of the IoUs greater than this average. This represented a 0.25 increase in the IoU from the baseline of the one-stage segmentation using standard Mask R-CNN.

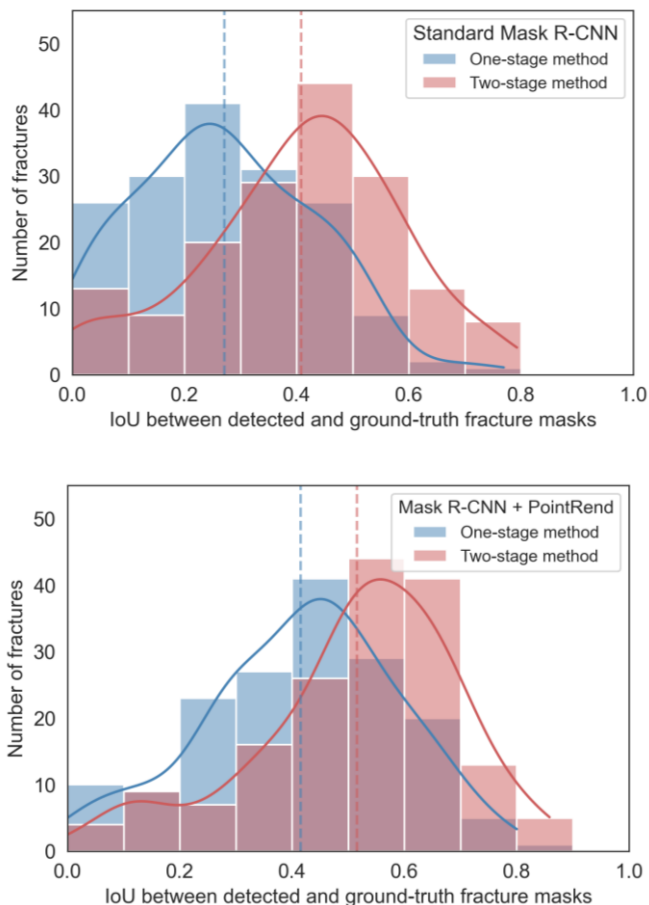


Fig. 6. Improvement in IoUs gained by the two-stage method for 160 fractures in the test images. Dashed lines show average values for each distribution. The distribution after the second stage of segmentation (in red) shifted to the right and the average IoU increased from 0.27 to 0.41 using standard Mask R-CNN (top) and from 0.41 to 0.52 using Mask R-CNN + PointRend in (bottom).

3.2 Improvement in aperture calculation

We evaluated the potential increase in the accuracy of the fracture aperture calculation that resulted from the enhanced segmentation by the two-stage method using both tested architectures. We focused on a group of eight fractures as shown in Table 4.

The third and fourth columns in Table 4 list absolute errors of aperture calculation based on the one-stage and two-stage segmentation, respectively. The errors were the average values of roughly 60 aperture measurements for each fracture (more details in Appendix A). The absolute error decreased by 0.46 mm (i.e., 46%) on average for the eight samples by using the two-stage method. Note that the image resolution of the samples was 2.6–9 pixels/mm. The absolute error decreased by 0.52 mm (i.e., 41%) and 0.40 mm (i.e., 50%) for the samples of standard Mask R-CNN and Mask R-CNN + PointRend, respectively. The results also showed that IoUs > 0.5 yielded an average aperture error of 0.61 mm compared to 0.93 mm from IoUs < 0.5.

Sample 3 showed a significant reduction in the error of 0.74 mm (i.e., 56%) following an increase in the IoU from 0.51 to 0.74. A detail demonstration for 63 aperture

measurements of Sample 3 is provided in Figure 7, indicating the improvement in each measurement using the two-stage standard Mask R-CNN. The mismatch between the ground-truth and estimated apertures have noticeably decreased in the improved segmentation (Figure 7, bottom) compared to the mismatch in the initial segmentation (Figure 7, top).

Thus, it can be concluded that enhancing fracture segmentation using the proposed two-stage segmentation approach can result in a substantial increase in the accuracy of aperture calculation.

Table 4. Absolute error for fracture aperture calculation for eight samples, showing the reduction in error after the second stage of segmentation (column 4) compared to initial results in column 3.

Absolute error (mm)			
	Sample	One-stage method	Two-stage method
Standard Mask R-CNN	1	0.68	0.46
	2	1.81	0.93
	3	1.31	0.57
	4	0.86	0.64
Mask R-CNN with PointRend	5	0.68	0.26
	6	0.8	0.4
	7	0.87	0.4
	8	0.81	0.52

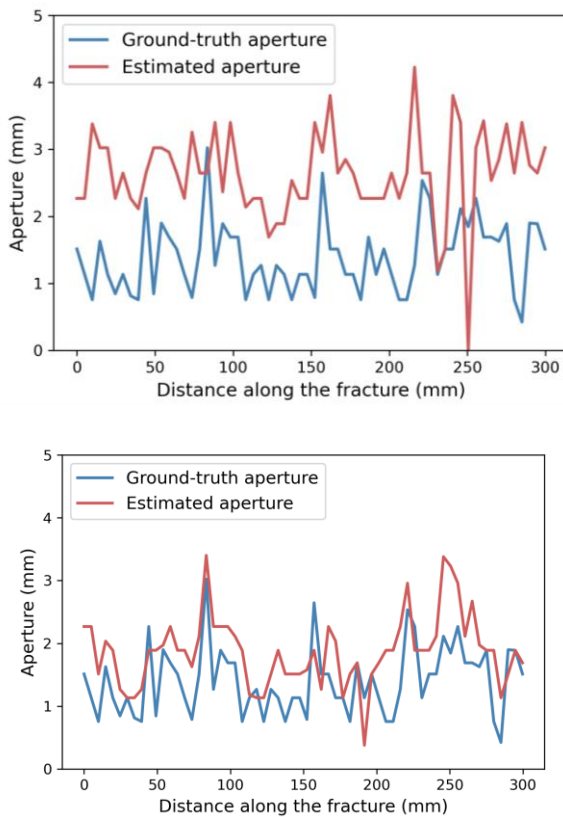


Fig. 7. Improvement in aperture accuracy for Sample 3 in Table 4 from calculation based on initial mask (top) to enhanced mask after a second segmentation (bottom), using standard Mask R-CNN.

3.3 Visual inspection results

Visual inspection of the predicted fracture masks proved that the two-stage method provided more accurate fracture segmentation than the one-stage method using both Mask R-CNN architectures. The proposed method showed visual improvement in the segmentation accuracy of fractures in the test images. The fracture masks can be observed in Figure 8. For standard Mask R-CNN (Figure 8a), enhancement in the fracture segmentation can be noticed in the mask obtained from the second stage of segmentation with a 0.38 IoU compared to the initial mask with a 0.15 IoU. Similarly, for Mask R-CNN + PointRend (Figure 8b), the two-stage method yielded a more detailed segmentation for the fracture than that provided by the one-stage method, as indicated by the IoU increasing from 0.40 to 0.68

From the visual comparison of the results from both architectures, we observed that Mask R-CNN + PointRend segmented the fractures more accurately than the standard Mask R-CNN, in particular for fine fractures, such as the fracture shown in Figure 9. This observation agreed with the IoU-based evaluation, which indicated that Mask R-CNN + PointRend offered more accurate fracture segmentation, i.e., higher IoUs than the standard Mask R-CNN. We attribute this to the mask refinement process by the PointRend module as introduced in Section 2.2.2 and Figure A1 of Appendix A.

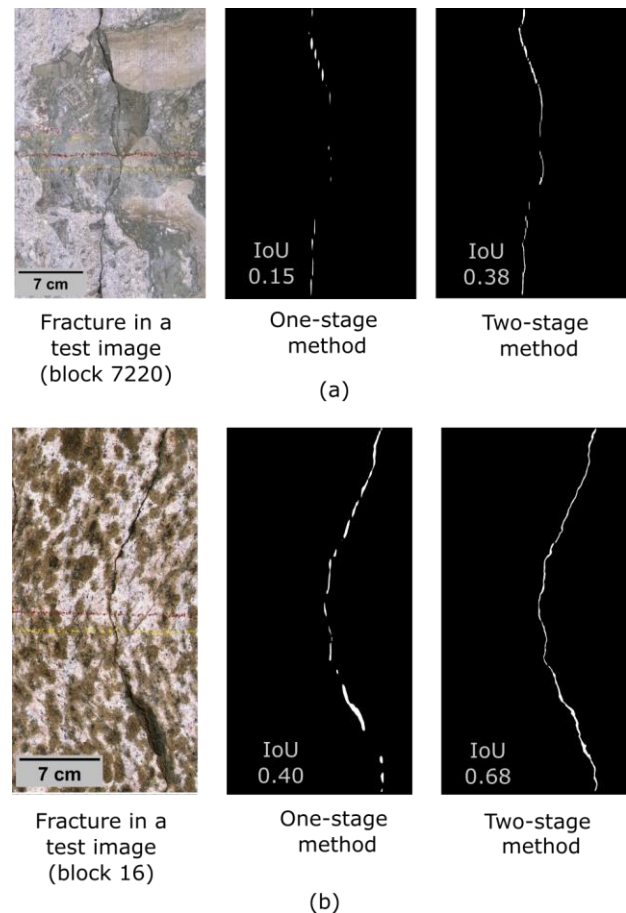


Fig. 8. Visualization of fracture masks enhancement by the two-stage segmentation using (a) standard Mask R-CNN and (b) Mask R-CNN + PointRend.

Although Mask R-CNN + PointRend showed noticeably better segmentation when evaluated both quantitatively and qualitatively than the standard architecture, it introduced an issue when segmenting adjacent or overlapped fractures. In some cases, Mask R-CNN + PointRend failed to distinguish between the main fracture and other fractures present within the detected region. A prime example is shown in Figure 10. We found that this problem, on the other hand, appeared much less often in the results from standard Mask R-CNN.

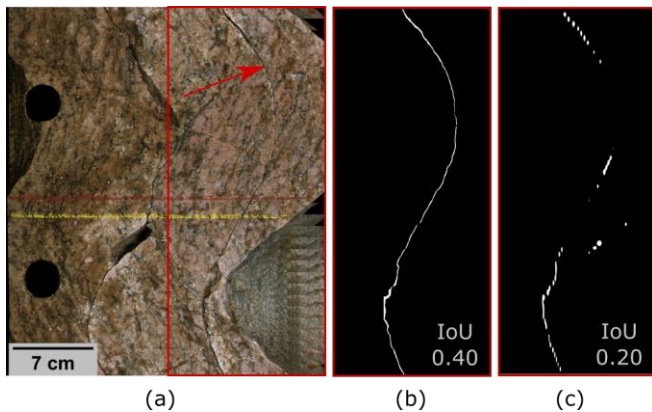


Fig. 9. Fine fracture in test image from block 16 (a) segmented more accurately by Mask R-CNN + PointRend (b) than standard Mask R-CNN (c).

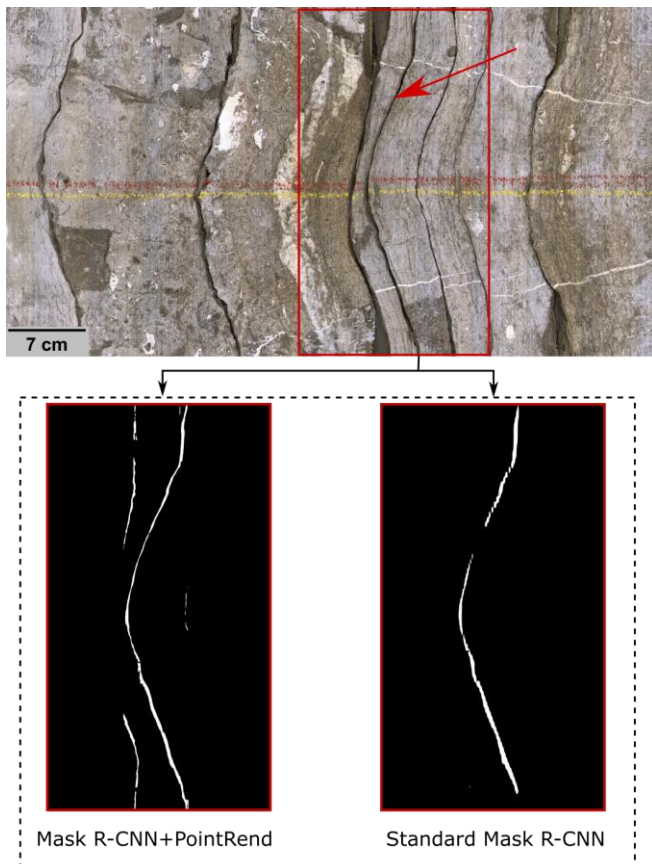


Fig. 10. Visualization of Mask R-CNN + PointRend problem in segmenting adjacent fractures compared to correct segmentation by standard Mask R-CNN.

Overall, the visual evaluation of the results confirmed that the second stage of segmentation improved the results significantly for both architectures. It also demonstrated that Mask R-CNN + PointRend did not always provide better fracture segmentation than standard Mask R-CNN as it was sensitive to the complexity level of the fractures and the presence of adjacent or overlapped fractures.

4 Conclusion

We proposed a two-stage segmentation method to improve fracture segmentation from unwrapped core images and enable detailed fracture characterization. The method relied on using two instance segmentation models that segmented the image at different scales. We tested two architectures of Mask R-CNN with and without the PointRend module.

Fracture segmentation results from the test images were assessed quantitatively and qualitatively. Quantitative analysis showed that the two-stage segmentation can increase the IoU by up to 0.34 and 0.27 using standard Mask R-CNN and Mask R-CNN + PointRend, respectively. Enhancing fracture segmentation can potentially obtain a 46% increase in the accuracy of aperture calculation. The quantitative analysis was confirmed by visual evaluation of the results that demonstrated an improvement in the fracture segmentation, which was noticeable for both tested architectures.

The comparison between standard Mask R-CNN and Mask R-CNN + PointRend demonstrated that the latter provided more accurate and detailed segmentation than the former, but it was affected by overlapping and neighboring fractures.

Instance segmentation is a powerful tool for the identification and characterization of image features where its utility has been readily realized for various applications. For core analysis, instance segmentation provides a platform for the identification of core features. While the current study is limited to fracture identification, future works can build on this platform to provide a spate of tools for the automated analysis of core images. Overall, we envisage a “Digital Geologist” machine learning platform based on deep learning and convolutional neural networks.

Acknowledgment

The authors thank Lundin Energy for providing the unwrapped core images.

List of abbreviations

Mask R-CNN	Mask region-based convolutional neural network
PointRend	Point-based rendering
JRC	Joint roughness coefficient
ML	Machine Learning
Mask R-CNN + PointRend	Mask R-CNN with the PointRend module

IoU	Intersection-over-union
RPN	Region proposal network
FPN	Feature pyramid network
RoI	Region of interest

References

1. T. S. Paulsen, R. D. Jarrard, and T. J. Wilson, “A simple method for orienting drill core by correlating features in whole-core scans and oriented borehole-wall imagery” *J. Struct. Geol.*, **24**, 8, 1233–1238 (2002), doi: 10.1016/S0191-8141(01)00133-X.
2. S. Tiwari *et al.*, “High resolution core scan facility at BGRL-MoES, Karad, India” *J. Geol. Soc. India*, **90**, 6, 795–797 (2017), doi: 10.1007/s12594-017-0793-6.
3. R. Schepers, G. Rafat, C. Gelbke, and B. Lehmann, “Application of borehole logging, core imaging and tomography to geotechnical exploration” *Int. J. Rock Mech. Min. Sci.*, **38**, 6, 867–876 (2001), doi: 10.1016/S1365-1609(01)00052-1.
4. M. M. Al-Fahmi, S. I. Ozkaya, and J. A. Cartwright, “FracRough—Computer program to calculate fracture roughness from reservoir rock core” *Appl. Comput. Geosci.*, **9**, p. 100045 (2021), doi: 10.1016/j.acags.2020.100045.
5. M. Chakraborty and S. Mukherjee, “Structural geological interpretations from unrolled images of drill cores” *Mar. Pet. Geol.*, **115**, p. 104241 (2020), doi: 10.1016/j.marpetgeo.2020.104241.
6. M. M. Al-Fahmi, S. I. Ozkaya, and J. A. Cartwright, “FracRough—Computer program to calculate fracture roughness from reservoir rock core” *Appl. Comput. Geosci.*, **9**, p. 100045 (2021), doi: 10.1016/j.acags.2020.100045.
7. N. Barton and V. Choubey, “The Shear Strength of Rock Joints in Theory and Practice” *Rock Mech.*, **10**, 1–54 (1977).
8. F. Lemy, J. Hadjigeorgiou, P. Côté, and X. Maldague, “Image analysis of drill core” *Inst. Min. Metall. Trans. Sect. A Min. Technol.*, **110** (2001), doi: 10.1179/mnt.2001.110.3.172.
9. H. Ozturk and I. T. Saricam, “Core Segmentation and Fracture Path Detection Using Shadows” *J. Image Graph.*, **6**, 1, 69–73 (2018), doi: 10.18178/joig.6.1.69-73.
10. A. Xavier, C. E. Guerra, and A. Andrade, “Fracture analysis in borehole acoustic images using mathematical morphology” *J. Geophys. Eng.*, **12**, 3, 492–501 (2015), doi: 10.1088/1742-2132/12/3/492.
11. D. Wedge, E. J. Holden, M. Dentith, and N. Spadaccini, “Fast and objective detection and analysis of structures in downhole images” *J. Appl. Geophys.*, **144**, 157–172 (2017), doi: 10.1016/j.jappgeo.2017.07.004.
12. R. A. Q. Cruz, D. C. Cacau, R. M. dos Santos, E. J. Ribeiro Pereira, F. R. Leta, and E. Gonzalez Clua, “Improving Accuracy of Automatic Fracture Detection in Borehole Images with Deep Learning and GPUs” in *2017 30th SIBGRAPI Conference on Graphics, Patterns and Images (SIBGRAPI)*, 345–350 (2017), doi: 10.1109/SIBGRAPI.2017.52.
13. L. O. Dias *et al.*, “Automatic detection of fractures and breakouts patterns in acoustic borehole image logs using fast-region convolutional neural networks” *J. Pet. Sci. Eng.*, **191**, p. 107099 (2020), doi: 10.1016/j.petrol.2020.107099.
14. K. He, G. Gkioxari, P. Dollar, and R. Girshick, “Mask R-CNN” in *2017 IEEE International Conference on Computer Vision*, 2961–2969 (2017), doi: 10.1109/ICCV.2017.322.
15. “COCO - Common Objects in Context.” [Online]. Available: <https://cocodataset.org/>. [Accessed: 1-May-2021].
16. Y. Wang, L. Zhao, M. Wang, and Z. Song, “Organ at Risk Segmentation in Head and Neck CT Images Using a Two-Stage Segmentation Framework Based on 3D U-Net” *IEEE Access*, **7**, 144591–144602 (2019), doi: 10.1109/ACCESS.2019.2944958.
17. M. Amiri, R. Brooks, B. Behboodi, and H. Rivaz, “Two-stage ultrasound image segmentation using U-Net and test time augmentation” *Int. J. Comput. Assist. Radiol. Surg.*, **15**, 6, 981–988 (2020), doi: 10.1007/s11548-020-02158-3.
18. N. J. Tustison and G. C. James, “Introducing Dice, Jaccard, and Other Label Overlap Measures To ITK” (2009).
19. A. Kirillov, Y. Wu, K. He, and R. Girshick, “PointRend: Image segmentation as rendering” in *Computer Vision and Pattern Recognition (CVPR)*, 9799–9808 (2020).
20. “Lundin Energy.” [Online]. Available: <https://www.lundin-energy.com/>. [Accessed: 14-Oct-2020].
21. NPD, “FactPages from the Norwegian Petroleum Directorate.” [Online]. Available: <https://factpages.npd.no/>. [Accessed: 26-Apr-2021].
22. “Supervise.ly.” [Online]. Available: <https://supervise.ly/>. [Accessed: 20-Oct-2020].
23. T.-Y. Lin, P. Dollár, R. Girshick, K. He, B. Hariharan, and S. Belongie, “Feature Pyramid Networks for Object Detection” in *Proceedings of the IEEE Conference on Computer Vision and Pattern Recognition*, 2117–2125 (2017).
24. Y. Wu, A. Kirillov, F. Massa, W.-Y. Lo, and R. Girshick, “Detectron2” (2019).
25. T. Y. Lin *et al.*, “Microsoft COCO: Common objects in context” in *European Conference on Computer Vision*, **8693 LNCS**, PART 5, 740–755 (2014), doi: 10.1007/978-3-319-10602-1_48.

Appendix A

1. PointRend module

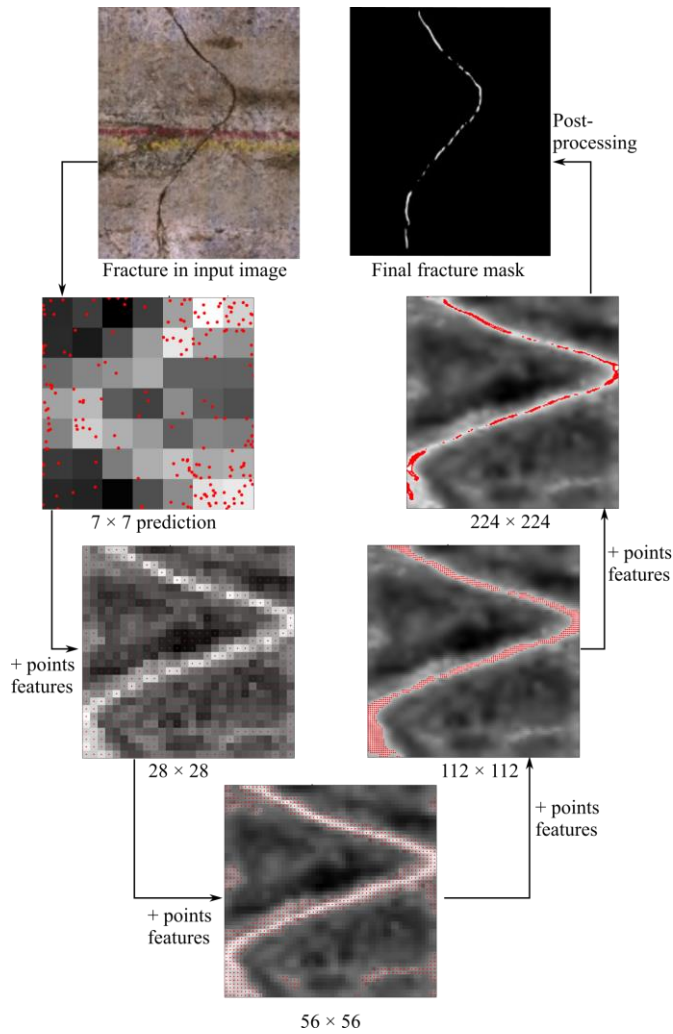


Fig. A1. Mask refinement in PointRend module—incorporated in Mask R-CNN’s segmentation branch— through multiple iterations. Red dots represent the selected uncertain points. At each iteration, a low-resolution mask and points features from the CNN were used to predict a higher resolution mask. The visualization of the intermediate masks was based on [24].

2. Fracture aperture calculation

Fracture aperture was calculated from the binary masks produced by the models or by manual segmentation.

For each fracture, the aperture was measured at over 60 locations by moving a small window along the fracture with a vertical step of 5 mm as shown in Figure A2, then we implemented the following steps at each location:

- Extracting fracture points from fracture skeleton at that location.
- Finding the line of best fit to the extracted points.
- Finding a line perpendicular to the best-fit line.
- Calculate fracture aperture in pixels, represented by the white pixels along the perpendicular line.
- Converting the measurement from pixels to mm using the scale of the unwrapped core image.

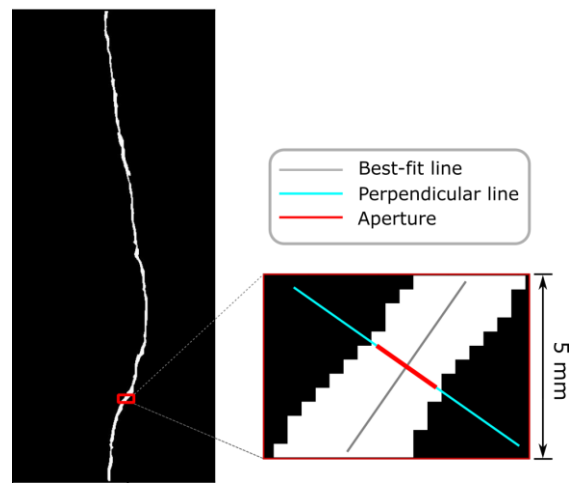


Fig. A2. Demonstration of fracture aperture calculation from a binary mask, showing the process at the highlighted location.

Monitoring fluid migration using in-situ nuclear magnetic resonance core flooding system integrated with fiber optic sensors: A proof of concept

Bruno da Silva Falcão^{1,2,*}, Lionel Esteban², Ausama Giwelli², Yevhen Kovalyshen², Stephen Banks², Ahmed Al-Yaseri^{1,3}, Alireza Keshavarz¹, and Stefan Iglauer¹

¹School of Engineering, Edith Cowan University, Joondalup, WA 6027, Australia

²CSIRO Energy Business Unit, Kensington, WA 6151, Australia

³Currently at School of Engineering, Curtin University, Kensington, WA 6151, Australia

Abstract. In-situ nuclear magnetic resonance (NMR) core flooding system has enabled researchers to monitor several rock properties such as porosity, pore size distribution, and fluid saturation along the tested samples with high resolutions and under reservoir conditions. However, spatially resolved rock strength/mechanical property alteration coupled to fluid migration/substitution remains poorly characterized. To this end, Fiber Bragg Grating (FBG) multiplex sensors were integrated with NMR core flooding system to monitor rock strength changes, or generally speaking, to observe hydro-mechanical-chemical coupling mechanisms during core flooding tests. In this study, we present a novel approach on how to conduct core flooding experiments, while simultaneously monitoring NMR and FBG strain response of the tested limestone plug. The NMR cell was modified to integrate FBG technology without impeding the NMR signal and core flooding high pressure/temperature capacity. A high spatial resolution optical fiber was attached onto the sample radial surface. The results show the successful association of NMR and FBG sensors to track any change at each stage of brine injection. The FBG is capable of measuring the rock strain variations induced by rock-fluid interactions during brine injection, allowing it to capture the fluid front location along with the sample and at a faster rate than the NMR.

1 Introduction

Nuclear magnetic resonance (NMR) core flooding system became an important tool for reservoir rock characterizations [1-3]. It enables the evaluation of several rock properties such as porosity, pore size distribution, and fluid saturation to name a few with high resolution and under reservoir conditions [4-6].

Likewise, the evaluation of rock mechanical properties also plays an important role in reservoir characterization, especially for risk assessment and economic production sustainability. Measuring rock strength changes is essential under reservoir conditions, even more when the rock experiences potential mineralogy alteration during fluids displacements, which can lead to rock deformations, faults reactivation, reservoir leakage pathways [7], and the like. Conventionally, rock strain deformations are measured by linear variable differential transformers (LVDTs) and electrical resistance strain gauges (ESG) [8-10]. However, those conventional sensors are incompatible with the NMR core flooding system as the small confining space and the magnet in-place of the NMR probe prohibit the insertion of such metallic sensors.

Optical fibers were introduced in the 1960s with the sole purpose of transmitting light, which later had a positive impact on telecommunication systems. However, due to the change in the transmitted light properties by the nearby environment, optical fibers were considered a good option for sensing applications [11]. Fiber optic sensors (FOS) have been applied in a vast variety of industries from aerospace [12], medicine [13], civil engineering [14] to petroleum [15]. FOS can be classified into two main categories: distributed

and discrete. Distributed FOS is based on Raman, Rayleigh, or Brillouin scattering mechanisms and measure changes all along the fiber's length. Discrete FOS, however, such as fiber Bragg grating and Fabry-Perot, provide information at specific locations [14, 16]. Fiber Bragg Grating (FBG) sensors can be multiplexed enabling them to measure changes at different locations using a single fiber being considered as a quasi-distributed sensor [14].

FBG sensor is a very promising deformation measurement tool acting as an alternative to the conventional sensors [8-10, 17] with less sensors-sample setup time, more efficient, and cost-effective. It is capable of measuring strain, temperature, pressure, among other parameters. FBG sensors also offer the advantages of being small size, flexible, low weight, high sensitivity, not affected by electromagnetic interference, resistant to corrosion and water, resilient to high-pressures and high-temperatures, and multiplexing capability [8, 10].

In recent years, the application of FBG sensors to monitor rock strain changes in real-time at laboratory scale has expanded and it seems to be a good alternative to LVDTs or ESG but it is still in the exploration stage. Sun et al. [8] proposed the use of multichannel FBG sensor arrays to monitor rock strain. The authors measured both radial and axial strains on the lateral area of a sandstone sample undergoing a uniaxial loading. Sun et al. [9] also employed multichannel FBG sensors to detect strain responses caused by water and CO₂ gas injection during core flooding experiments through a low permeability sandstone. Kovalyshen et al. [10] reported the applicability of FBG sensors to measure strain variations of a limestone sample

* Corresponding author: bruno.falcao@msn.com

under confining pressure. Zhang et al. [17] tracked the CO₂/brine displacement front in a rock sample composed of both reservoir and caprock formations. The fluid displacement was monitored by measuring the strain using the distributed fiber optic strain sensing (DFOSS) technique. X-ray computed tomography imaging was used to estimate the fluid saturation.

In this paper, we present a novel approach on how to conduct core flooding experiments associating NMR core flooding system with FBG sensing technology. To our knowledge, this is the first NMR core flooding experiment that is capable of measuring rock strain deformations at reservoir conditions. An optical fiber with 8 FBG sensors was radially placed around the rock sample surface to monitor the rock strain deformations induced by brine injection while under reservoir pressure condition. The NMR core analyzer was used to monitor the fluid displacement and saturation along the sample throughout the experiment.

2 Material and methods

2.1 Principle of FBG sensing

A Fiber Bragg Grating (FBG) sensor is an optical deflector or filter of specific wavelength responses. Its functioning relies on the optical fiber core's refractive index being periodically altered by UV light. When a light source is emitted into the FBG sensor, it reflects part of the energy in a limited wavelength band around its peak wavelength and transmits all other wavelengths. The reflected wavelength is known as Bragg wavelength λ_B and it is defined by Equation (1) [8-10, 18, 19].

$$\lambda_B = 2n_{eff}\Lambda \quad (1)$$

where n_{eff} is the FBG core's effective refraction index and Λ is the grating spacing. Modifications on n_{eff} or Λ values, or even a combination of both, will represent any changes that occur in the physical properties such as strain and temperature [8-10, 18, 19].

The shift in the Bragg wavelength caused by changes in the strain and temperature is given by Equation (2).

$$\Delta\lambda_B = 2 \left(\Lambda \frac{\partial n_{eff}}{\partial l} + n_{eff} \frac{\partial \Lambda}{\partial l} \right) \Delta l + 2 \left(\Lambda \frac{\partial n_{eff}}{\partial T} + n_{eff} \frac{\partial \Lambda}{\partial T} \right) \Delta T \quad (2)$$

The first term in Equation (2) represents the change in the Bragg wavelength due to the strain effect, while the second term describes the effect of temperature [18, 19].

For the FBG used in this study, the wavelength sensitivity coefficient related to strain and temperature at room conditions, according to the manufacturer, are 0.776 pm/ $\mu\epsilon$, 8.53 pm/ $^{\circ}\text{C}$, and 0.0023 pm/ $^{\circ}\text{C}$. The optical fiber was manufactured by FBGS (FBGS Technologies GmbH), with 125 μm cladding diameter and Ormocer coating. Each single optical fiber has 8 FBG sensors of low bend loss and every sensor is 8 mm long. The eight gratings cover an extent of

315 mm ranging from 1530 to 1565 nm wavelength, with a difference of 5 nm between the gratings to avoid overlap.

2.2 Nuclear magnet resonance (NMR)

When an external magnetic field is applied, protons ¹H (abundant in reservoir fluids) behave like spinning magnets due to their magnetic moment and angular momentum [4, 6]. Rotational proton procession produces signals that decay with time also known as proton relaxation that can be measured by a Nuclear Magnetic Resonance spectrometer (NMR) [4, 6].

The NMR signal decay $\mathbf{M}(t)$ is described by Equations (3)–(5) from two mechanisms: NMR signal can be measured along the applied magnetic field corresponding to proton polarization or longitudinal relaxation T_1 ; while the proton decay post-polarization and then tipped transversally to the magnetic field corresponds to the transversal relaxation T_2 [4, 20, 21].

$$M_x(t) = [M_x(0) \cos(\omega t) - M_y(0) \sin(\omega t)] e^{(-t/T_2)} \quad (3)$$

$$M_y(t) = [M_x(0) \sin(\omega t) + M_y(0) \cos(\omega t)] e^{(-t/T_2)} \quad (4)$$

$$M_z(t) = M_{eq} + [M_z(0) - M_{eq}] e^{(-t/T_1)} \quad (5)$$

Generally speaking, on very porous rock materials, T_1 is sensitive to the environment and fluids interactions while T_2 is more sensitive to surface relaxation and diffusion mechanisms. With negligible fluids interactions, both T_1 and T_2 provide pore size distribution information, though T_1 measurement is more time consuming than T_2 [6].

A 2.37 MHz Geospec2 NMR core analyzer and a P5 overburden NMR probe from Oxford Instruments were used to obtain the brine saturation profile along the sample.

2.3 Sample preparation and characterization

A Savonnières limestone core (Fig. 1), a heterogeneous rock composed of 99% of calcite [22-24], was used in this study and cut along the bedding plane. The yellow dashed lines in Fig. 1 highlight a centimeter-thick bedding composed of high-density/low porosity structure that pervades the middle of the sample. This tight bedding is better illustrated in Fig. 2, which shows a 3D volume rendering from X-ray CT images viewed in two angles color-labeled by density intensity from single threshold method on the X-ray CT attenuation histogram where magenta color corresponds to a highly porous area while yellow color marks much denser and tighter material. The images illustrate that the tight bedding is actually composed of alternating thin-sub layers of high- and low-density materials with some thin dense layers propagating toward one side of the sample. The plug can then be divided into three structural areas along the sample from left to right in Fig. 2: (1) 1.5 cm thick highly porous layer, (2) 1.5 cm thick tight layer, and (3) < 1 cm thin highly porous layer. Table 1 shows the location of the sensors on the sample with respect to the described structural layers: (i) sensors facing the section with the highest void fraction with sensors

1, 4, 5, and 7; (ii) sensors facing the section with the lowest void fraction with sensors 3 and 6; (iii) sensors located perpendicular to the beddings with sensors 2 and 8. The dimension of the tested plug is shown in Fig. 1. The sample was initially dried at 60 °C under air vacuum for 24 hours before attaching FBG wire and then place the assembly in the NMR core flooding system. Further details about the rock properties can be found in the open literature [22, 23, 25].

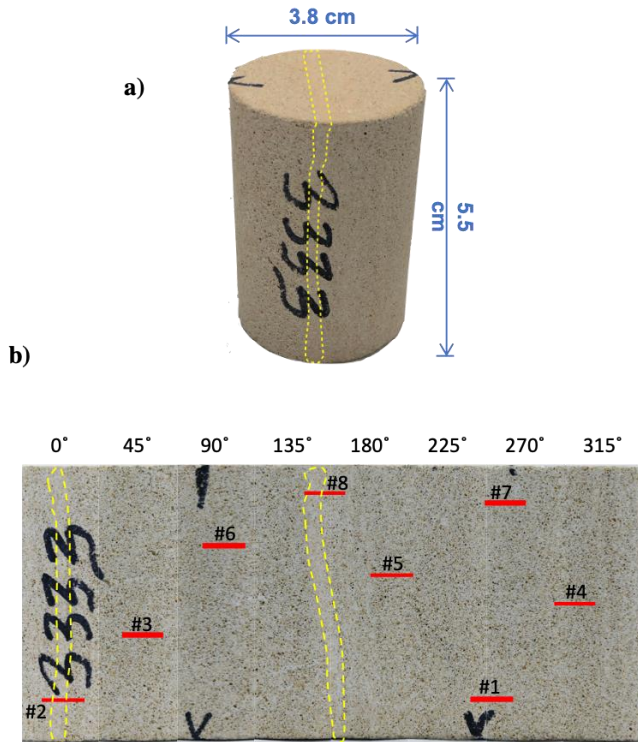


Fig. 1. (a) Savonnières limestone sample used in this experiment. (b) Position of FBG sensors on the sample after unwrapping the plug surface. The dashed yellow area indicates the position of a bedding of higher density/lower porosity.

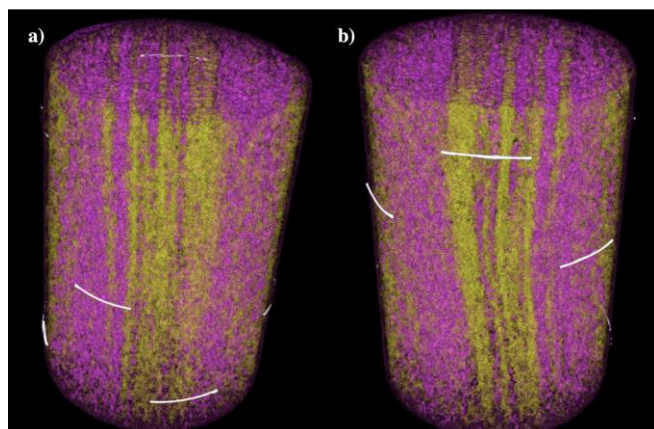


Fig. 2. 3D volume rendering from X-ray CT images of Savonnières limestone sample. The color magenta represents the pores of the rock sample, the yellow represents the existing beddings of higher density in the middle of the sample, and the white (enhanced) indicates the sensors' location. (a) Front view of the sample showing the sensors 3, 2, 4, and 1 at the bottom (from right to left). (b) back view of the sample showing the sensors 5, 8, and 6 (from right to left).

Table 1. Position of the FBG sensors related to the void fractions and beddings.

Category	Sensor	Description
(i)	1, 4, 5, 7	Facing the section with the highest void fraction.
(ii)	3, 6	Facing the section with the lowest void fraction.
(iii)	2, 8	Perpendicular to the beddings.

The optical fiber was spirally attached onto the sample surface using Loctite Super Glue All Plastics and cured for 24 h. This glue adequately couples the optical fiber with the rock surface, without modifying the rock stiffness properties [10]. The position of the sensors is shown in Fig. 1 and Table 2. For the core flooding test, the FBG wire was inserted through the pore fluid line using a modified end-platen, specifically designed for this experiment. A feedthrough component was used to prevent any leakage while the system was pressurized. After the curing process, the whole assembly was covered by a Teflon heat shrink jacket and a Viton sleeve and then placed inside the NMR P5 probe.

The optical fiber was connected to a FAZT I4 optical interrogator (FAZ Technology) through an LC/APC connector at the lead-in. The optical interrogator is capable of detecting wavelengths ranging from 1529 to 1568.2 nm, which limits the total number of sensors to eight due to the 5 nm grating difference.

Table 2. Position of FBG sensors: the distance was measured from the bottom of the sample to the center of the FBG sensor.

Sensor	Distance (mm)
1	7.8
2	8.2
3	20.9
4	26.9
5	32.6
6	38.1
7	46.7
8	48.4

2.4 Testing procedure

The P5 probe assembly was inserted into the NMR spectrometer and a constant hydrostatic confining pressure of 1000 psi was applied at a rate of 50 psi/min using Fluorinert as confining fluid. After stabilization of the confining

pressure, doped brine with 5 g/L NiCl₂ was continuously injected at 0.1 cc/min from the bottom of the sample.

During the imbibition/saturation stage, the outlet of the system was open to the atmosphere such as the FBG sensors can accurately and slowly track the brine front by recording the changes in the strain values. A 200 psi backpressure was then applied, to monitor the effect of pore pressure change on the FBG sensors during brine injection at 0.1 cc/min.

Fig. 3 shows the confining and pore pressure data during the entire experiment. Section I refers to the brine injection while the outlet was open to the atmosphere. Section II represents the period during which the injection was stopped to connect the backpressure regulator. Section III shows the pore pressure behavior after the backpressure was activated and set at 200 psi.

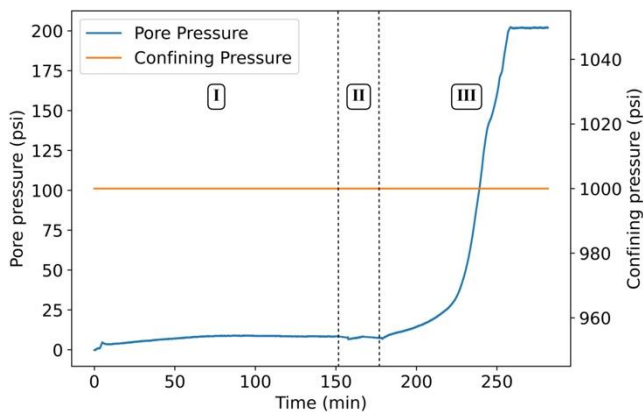


Fig. 3. Pore pressure and confining pressure monitoring with time during imbibition exercise on Savonnières sample under 1000 psi confining pressure: I – brine injection at 0.1 cc/min while outlet was open to the atmosphere; II – injection stopped to connect the backpressure; III – backpressure activated and set to 200 psi.

Three Teledyne ISCO syringe pumps were used to control the confining pressure, pore pressure, and backpressure. All pressure values were recorded using in-house LabView code. The entire experiment was performed at a constant temperature of 22 °C in order to avoid any temperature interference on the strain measurement. To obtain that the NMR system is connected to external chiller throughout the experiment.

2.5 Data acquisition and processing

During the experiment, all the measured NMR data were collected and computed automatically via Green Imaging Technologies software [26, 27]. Water content profile along the sample used the following settings:

- Recycle delay: 3750 ms
- Tau: 500 μ s
- Gradient duration: 300 μ s
- Filter width: 125 kHz
- Resolution: 64

A data acquisition system, using LabView, was designed to continually log the data from the syringe pumps every second. The optical interrogator systems enable the streaming of the data over an ethernet connection. The FBG data acquisition and graphical display software ran on a PC via an

ethernet connection (0.1 Gbit/s) at a sampling rate of 1000 Hz. An in-house algorithm was developed to process the raw data and generate all the relevant figures.

3 Results and discussion

3.1 Confining pressure and strain

In the first stage of the experiment, the objective was to analyze the relationship between confining pressure and rock strain changes in dry state. Initially, the confining pressure was increased from 20 psi to 1000 psi at a rate of 50 psi/min as shown in Fig. 4. After the confining pressure reached 1000 psi, it was temporarily decreased to 885 psi (after ~ 22 min) and kept constant for a few minutes. FBG strain changes caused by the increase in the confining pressure are shown in Fig. 5, which demonstrates the good agreement between the changes in the confining pressure and the rock strain responses. Fig. 5 highlights some different sensor behaviors while the confining pressure increases or decreases. Though most of the sensor responses can be explained from the structural heterogeneities observed in Fig. 1 and Fig. 2, sensors 2 and 3 showed similar responses to the changes in the confining pressure while being within distinct structural areas (Fig. 1). This was also observed for sensors 5 and 8. As depicted in Fig. 6, the strain values of all sensors decreased with the increase in the confining pressure. As a result, the temporary changes in the confining pressure demonstrated the fast and accurate response of the FBG sensors. The final strain values at a constant confining pressure of 1000 psi ranged from -250 to -350 μ ε.

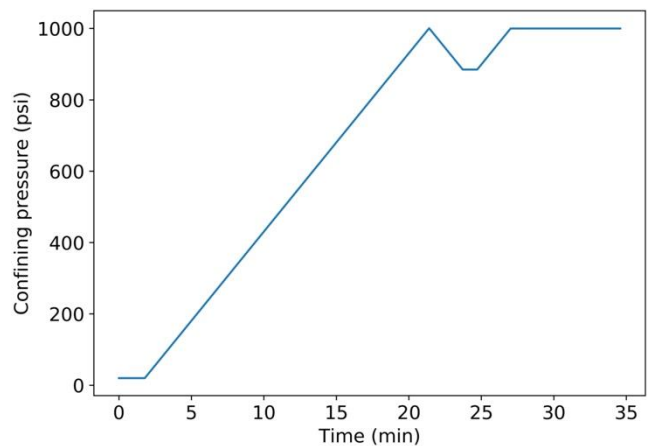


Fig. 4. Confining pressure profile prior to the brine injection.

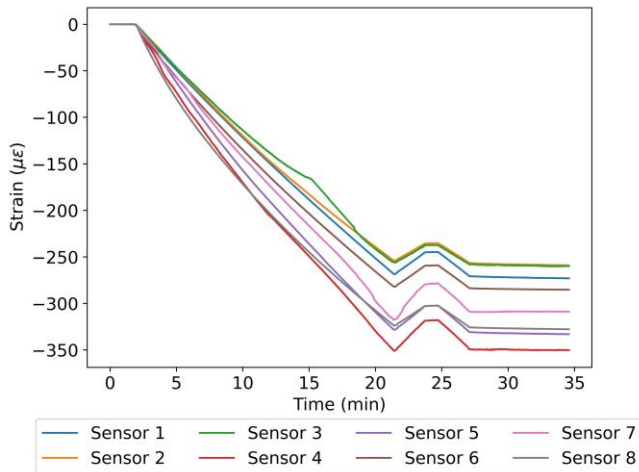


Fig. 5. Corresponding strain changes on the dry rock during the confining pressure build-up, measured by FBG sensors.

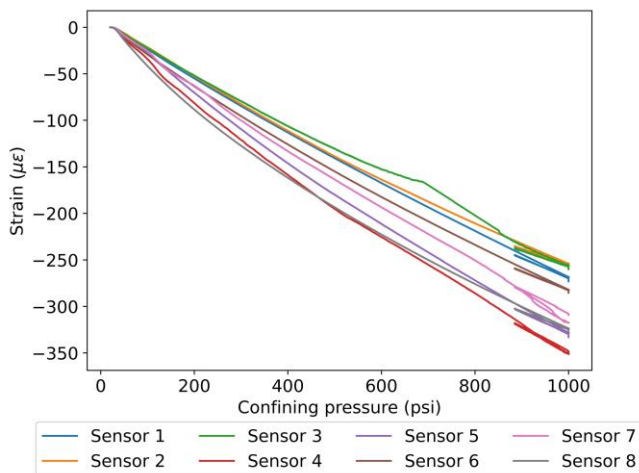


Fig. 6. Measurements of strain at varying confining pressures for each sensor, measured during the build-up of the confining pressure on dry rock.

3.2 Brine front monitoring

In order to monitor the fluid migration with FBG sensors, we kept the outlet pore line opens to the atmosphere, section I in Fig. 3. This brine injection continues until breakthrough occurred, once the brine came out of the sample. Pore pressure was as low as 9 psi, at a 0.1 cc/min brine flow rate.

Fig. 7 illustrates that the FBG sensors effectively monitored the brine front during the injection process. It is possible to identify the location of the brine front in the rock sample at a specific time by monitoring the rock strain changes. The strain changes corresponded well to the fluid migration, and all sensors exhibited an increase in the strain when the fluid reached the sensor location. The differential strain kept increasing to values between 2 and 3 $\mu\epsilon$, until the brine breakthrough.

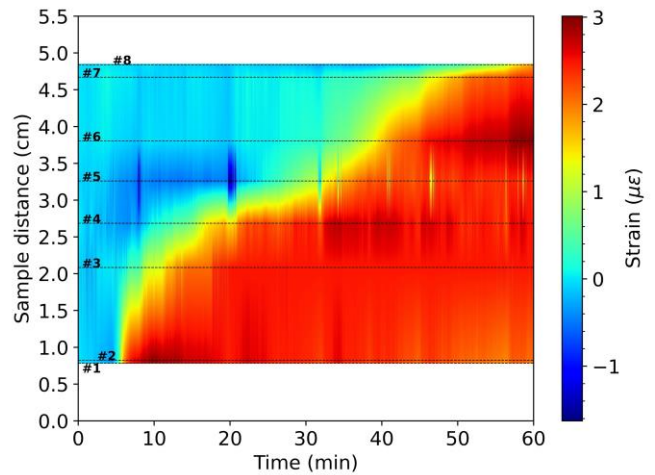


Fig. 7. Mapping of the strain changes throughout the sample until the brine breakthrough. The locations of the sensors are labeled on the figure in dashed lines. Note that the differential strain data were linearly interpolated between the sensors. Information about strain changes before sensor 1 and after sensor 8 is unavailable.

The saturation profiles measured by NMR are shown in Fig. 8. The NMR saturation profile provides information about the migration of the fluid front and the corresponding volume distribution of the fluid within the sample. The results from both FBG and NMR are in good agreement. For instance, it can be estimated that the brine front reached sensor 4 after approximately 10 minutes. However, while the FBG interrogator was recording 1000 points/second, the NMR core analyzer took approximately 2 minutes to acquire each saturation profile measurement. Therefore, the combination of FBG sensors with NMR analysis allows a more accurate time tracking of the fluid front migration during core flooding experiments. It is worth mention that after about 60 mins of injection, the sample did not show uniform saturation distribution. This could be due to air bubble at the top of the sample not fully removed yet or permeability impediment during imbibition.

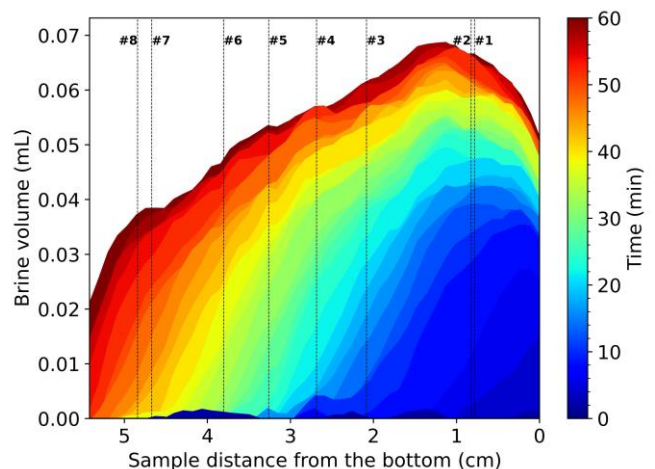


Fig. 8. NMR saturation profiles along the length of the sample.

3.3 Pore pressure effect

After the brine breakthrough occurred, a backpressure regulator was applied. A backpressure regulator at 200 psi was used with the purpose to analyze the effect of the pore pressure on the FBG sensors. After the activation of the backpressure, the pore pressure started to increase, while keeping brine injected at 0.1 cc/min, as shown in Fig. 3 (section III).

Fig. 9 shows the FBG strain changes from each sensor during the entire experiment. Comparing sections I and III in Fig. 9, it is observed that the increase in the pore pressure caused higher changes in the strain values. While the strain changes in section I were between 2 and 3 $\mu\epsilon$, the strain changes increased to values between 30 and 50 $\mu\epsilon$ at the end of section III. This change can be explained by Fig. 10, which shows that an increase in the pore pressure causes an increase in the strain measurements of all sensors.

According to Fig. 9 and Fig. 10, each sensor shows a different strain behavior while the pore pressure is increased, mainly due to rock heterogeneity and internal pore structure (see Fig. 1 and Fig. 2). For instance, sensors 4 and 5, glued on the permeable region of the rock, see Table 1, showed the highest strain value/deformation among the sensors. On the other hand, sensors 2 and 3, glued on/near the bedding area, see Table 1, shows the least strain value. This is a clear indication that all the FBG sensors were very sensitive to detect the internal pore fluid distribution of the sample. As pore pressure is gradually increased inside the rock, brine navigating its way through more permeable section, the pore pressure distribution is not uniform anymore, and accordingly, the net overburden pressure acting on the sample surface is not uniform. It is worth noting that, we anticipated sensor 8 would behave similarly to sensor 2 (see Table 1), but surprisingly the sensor 8 showed a higher deformation. This could be due to test platen effects that caused more damage around the sensor area.

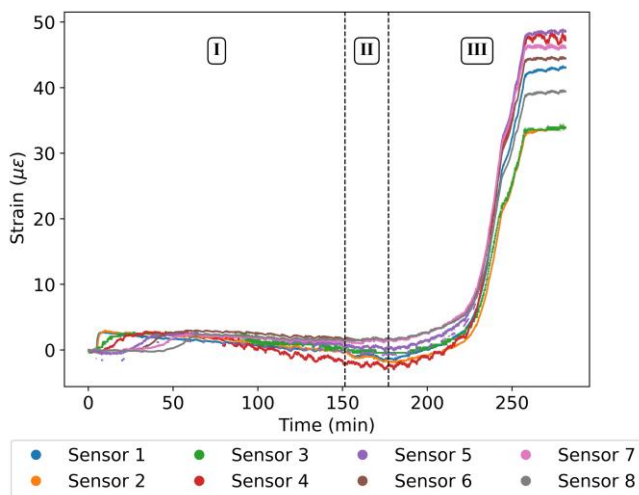


Fig. 9. Strain changes, measured by FBG sensors, during the entire experiment: I – brine injection at 0.1 cc/min while the outlet section was open to the atmosphere; II – injection paused to connect the backpressure; III – backpressure activated and set to 200 psi.

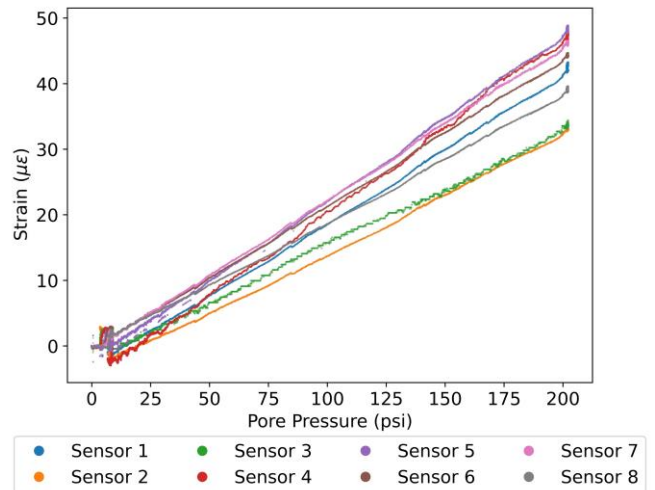


Fig. 10. Differential strain measurements at varying pore pressures for each sensor, measured during the pore pressure build-up.

4 Conclusion

In this study, a new method is presented to perform NMR core flooding experiments associated with fiber optic sensing technology. FBG array of 8 sensors were employed to monitor rock strain induced by the brine injection. We demonstrated that the FBG sensors responded quickly and accurately to the changes in the confining pressure, pore pressure and also were able to track the fluid migration through the Savonnières sample. In addition, we showed that the response of the FBG sensors was related to the sample's structure. Sensors facing the high void fraction sector of the sample were more sensitive to both confining and pore pressure changes than the sensors facing the lower void fraction sector (i.e. denser material).

Prior to brine injection, the confining pressure was increased to 1000 psi and kept constant throughout the experiment stages. The FBG measured changes in the rock strain with high accuracy caused by the increase in the confining pressure, showing an inversely proportional behavior. During the first stage of the brine injection, the outlet was kept open to the atmosphere to capture the fluid front migration. The FBG sensors demonstrated the capability of monitoring the fluid front migration, determining its location along the sample, at a faster rate and higher resolution than the NMR system. After the brine breakthrough, a backpressure regulator was activated to analyze the effect of pore pressure build-up on the FBG strain measurements.

In summary, this pilot experiment proves to be useful to monitor rock strain changes during NMR core flooding stages. Future studies are planned to assess the behavior of different rock types, injection fluids, including CO₂.

The first author acknowledges Edith Cowan University's financial support. We also acknowledge the financial support provided by CSIRO Energy Business Unit through a Strategic Research Fund.

References

1. M. Li, D. Xiao, M. Shakerian, A. Afrough, F. Goora, F. Marica, L. Romero-Zerón, and B. Balcom, International Symposium of the Society of Core Analysts, Snowmass, Colorado, 21-26 (2016)
2. T. Hiller, G. Hoder, A. Amann-Hildenbrand, N. Klitzsch, and N. Schleifer, E3S Web of Conferences, 03005 (2020)
3. S. Hua, Y. Li, and Q. Di, E3S Web of Conferences, (2020)
4. G. R. Coates, L. Xiao, and M. G. Prammer, *NMR logging: principles and applications* (Haliburton Energy Services Houston, 1999)
5. J. Mitchell, T. C. Chandrasekera, D. J. Holland, L. F. Gladden, and E. J. Fordham, Phys. Rep., **526**, 165-225 (2013)
6. C. McPhee, J. Reed, and I. Zubizarreta, *Core analysis: a best practice guide* (Elsevier, 2015)
7. J. Rutqvist, and C.-F. Tsang, Environ. Geol., **42**, 296-305 (2002)
8. Y. Sun, Q. Li, D. Yang, C. Fan, and A. Sun, Eng. Geol., **213**, 1-10 (2016)
9. Y. Sun, Q. Li, and C. Fan, Int. J. Greenh. Gas Control., **60**, 186-198 (2017)
10. Y. Kovalyshen, S. Banks, and A. Giwelli, 52nd US Rock Mechanics/Geomechanics Symposium, (2018)
11. X. Qiao, Z. Shao, W. Bao, and Q. Rong, Sensors (Basel), **17**, (2017)
12. P. F. Díaz-Maroto, A. Fernández-López, J. García-Alonso, M. Iglesias, and A. Güemes, Thin-Walled Struct., **132**, 375-384 (2018)
13. J. Heijmans, L. Cheng, and F. Wieringa, 4th European Conference of the International Federation for Medical and Biological Engineering, 2330-2334 (2009)
14. H.-N. Li, D.-S. Li, and G.-B. Song, Eng. Struct., **26**, 1647-1657 (2004)
15. C. S. Baldwin, Fiber Optic Sensors and Applications XII, 94800D (2015)
16. B. Glisic, and Y. Yao, Struct. Health Monit., **11**, 696-711 (2012)
17. Y. Zhang, Z. Xue, H. Park, J. Q. Shi, T. Kiyama, X. Lei, Y. Sun, and Y. Liang, Water Resour. Res., **55**, 856-867 (2019)
18. L. Grattan, and B. Meggitt, *Optical fiber sensor technology: advanced applications-Bragg gratings and distributed sensors* (Springer Science & Business Media, 2013)
19. C. E. Campanella, A. Cuccovillo, C. Campanella, A. Yurt, and V. M. N. Passaro, Sensors (Basel), **18**, (2018)
20. I. B. Trindade, and R. O. Louro: 'Introduction to biomolecular nuclear magnetic resonance and metals': 'Practical Approaches to Biological Inorganic Chemistry' (2020), pp. 155-199
21. P. R. Connolly, J. Sarout, J. Dautriat, E. F. May, and M. L. Johns, Petrophysics-The SPWLA Journal of Formation Evaluation and Reservoir Description, **61**, 151-161 (2020)
22. M. Seyyedi, H. K. B. Mahmud, M. Verrall, A. Giwelli, L. Esteban, M. Ghasemiziarani, and B. Clennell, Sci Rep, **10**, 3624 (2020)
23. A. Raza, R. Gholami, and M. Sarmadivaleh, AAPG Bull., **103**, 83-96 (2020)
24. Y. Zhang, M. Lebedev, M. Sarmadivaleh, A. Barifcani, and S. Iglauer, SPE asia pacific oil & gas conference and exhibition, (2016)
25. M. Lebedev, M. E. J. Wilson, and V. Mikhaltsevitch, Geophys. Prospect., **62**, 1253-1265 (2014)
26. Geo-Spec 2-53 User Manual, Version 1.8, Oxford Instruments
27. GIT Systems and LithoMetrix User Manual, Revision 1.9, Green Imaging Technologies

Core cleaning and wettability restoration – selecting appropriate method

Raheleh Farokhpoor^{1*}, *Lars Sundal*¹, *Anne Skjærstein*¹, *Albert Hebing*², *Xiangmin Zhang*², and *Lucian Pirlea*²

1. Lundin-Energy, Norway, 2. PanTerra Geoconsultants, The Netherlands

Abstract. The core cleaning approaches aim to remove native crude oil, mud filtrates and evaporated salts which leads to strongly water-wet cores. In the standard core cleaning method, the solvent(s) injection continues until no more oil is observed in effluent. This is generally confirmed by visual examination, rather than by analyzing the composition of effluent, simply because it is expensive.

In this work, we selected two preserved rock sections from an oil reservoir in North Sea. 1.5-inch diameter core plugs were cleaned by two different flush cleaning programs (so-called Program-1 and 2). In Program-1, samples were flushed first with 75% toluene + 25% methanol and then followed by alternate of toluene-chloroform-methanol until the samples were deemed cleaned from visual examination. In Program-2, samples were flushed by alternating toluene-tetrahydrofuran-chloroform for 8 cycles. Oil effluents from Program-2 were collected for composition GC analyses.

The efficiencies of two flush cleaning programs were compared by measuring the wettability of the samples by combined Amott-USBM wettability method. The USBM index shows after cleaning program-2 are more water wet. Samples were then aged in crude oil at reservoir conditions for 4 weeks. Drainage and imbibition capillary pressure using centrifuge and porous plate and the end-point liquid permeabilities were then measured on restored samples. End-point properties after aging process, showed wettability being restored to intermediate water-wet as is expected from field production history.

This study shows that standard cleaning does not fully clean these samples. Meanwhile, the elaborate Program-2 is often impractical, takes too long, is expensive and limited by laboratory capacity.

1. Introduction

Not every feature in core is geological! No matter how careful the attempt to collect and preserve core is, it can be affected by the process of collection, like drilling induced fractures, discoloration by drilling fluids and cutting marks.

A big challenge in SCAL analysis is restoring wettability of core material to a representative reservoir wettability. Wettability determines fluid distribution and fluid flow of wetting and non-wetting phases and is greatly affected by wettability restoration protocol. A standard protocol consists of cleaning the samples to a strong water-wet state, establishing representative initial water saturation and then, aging the samples with dead crude oil at reservoir conditions [1], [2]. The last step is believed to reproduce the core wettability to a representative reservoir state. Inadequate cleaning at the first step may result in a

weak water-wet state and disrupt the final wettability state of the core.

The motivation of this present work comes from an earlier extensive SCAL study on preserved core samples from a sandstone reservoir in the Norwegian Continental Shelf (NCS). Large variations in fluid flow properties from different types of experiments was observed. Experiments included steady-state relative permeability, imbibition capillary pressure from centrifuge and porous plate and combined Amott-USBM wettability tests. These contradictory results led us to re-examine the wettability restoration procedure and ultimately the cleaning program. Cleaning is often performed using solvent in Soxhlet extraction or flushing in a core holder at controlled temperature. A typical solvent system used is combination of toluene and methanol, or chloroform or azeotropic solvents mixture to increase efficiency. But we

* Corresponding author: raheleh.farokhpoor@lundin-energy.com

question if this approach works equally efficient for all types of conventional oil.

In this study, the typical cleaning protocol is compared with a more effective program which tends to remove any trace of hydrocarbon in the cores and it was inspired by a relevant study performed on sandstone cores from North Sea field [3]. This was followed by compositional analysis of effluents after each cleaning cycles. Afterwards, wettability of the clean samples was determined by Amott-USBM method to undermine the effectiveness of the two programs. Later, the most water-wet samples were aged by dead crude oil at reservoir conditions. And then, imbibition capillary pressure, endpoint saturation and relative permeabilities were measured and compared with not-aged samples.

2. Core material

Two preserved core materials (10 cm in diameter and 20 cm in length), from oil and waters zones, were selected for this study. X-ray CT is used to visualize the internal structure of whole core pieces and plugs and are shown in Figure 1. Heterogeneities, fractures, mud invasion and other factors that affect the local density will show up on a CT-image. The 35mm diameter core plug samples are drilled parallel to apparent bedding with a synthetic formation water (SFW). From preserved samples (PS), a

subsample was taken for petrographic analysis (Thin section, SEM and XRD Whole Rock and Clay Fraction) and high pressure mercury injection (MICP) on cleaned and dry samples.

The samples are characterized as fine- to medium-grained subarkoses mainly containing quartz grains with abundant K-Feldspar grains. Primary porosity is moderately interconnected and authigenic illite locally fills intergranular pores. Clusters of kaolinite and mixed layer illite-smectite was also observed, see Figure 2. Whole rock and clay characterization was done by XRD analysis on end-trims and are given in Table 1. From MICP experiments, fairly similar pore throat size distribution was derived for both samples. As it can be observed in Figure 3, pore throat size is predominately unimodal with mean hydraulic radius of 11-15 μm .

Final check was to make sure the preserved cores were not damaged by drilling mud which is water-based mud in this case. A large thin section (10 x 4 cm) from a whole core was taken with the short side parallel to the core axis and the long axis parallel to bedding. High resolution images (Figure 4) shows mud particles are only present in thin layers at the outermost edges of the core and have not invaded the core deeper than 3 or 4 layers of sand-sized grains. Therefore, it was concluded the inner part of the core is unaffected by mud particle.



Figure 1: Photo of core section and CT scans of preserved samples (PS).

Table 1: XRD analysis of whole rock and clay fraction composition

Sample	Whole Rock Composition (%BW)							Clay Fraction (%BW)			
	Quartz	Orthoclase	Kaolinite/ Chlorite	Halite	Illite	Dolomite	Ankerite	Illite	Illite/ Smectite	Kaolinite	Chlorite
PS 1	60	32	4	tr	1	-	2	20	12	54	14

PS 2	62	28	6	1	2	1	-	10	2	88	-
------	----	----	---	---	---	---	---	----	---	----	---

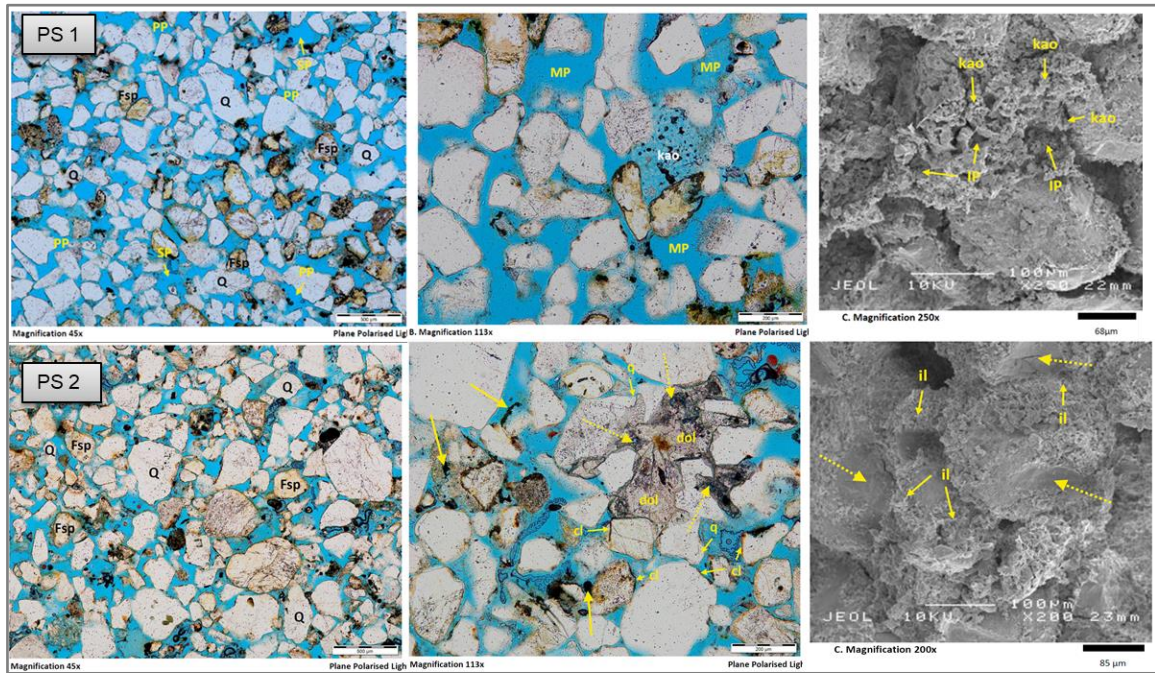


Figure 2: Images of thin section plates and SEM analysis (to the right). Grain dissolution resulted in mouldic pores (MP) and oversized pores and some places is filled by deformed kaolinite (kao) or patches of dolomite cement (dol). Grain surfaces exhibit continuous coatings illite and illite-smectite (il). Q: quartz, Fsp: feldspar, Cl: chlorite, IP: Intercrystalline pores, SP: secondary porosity.

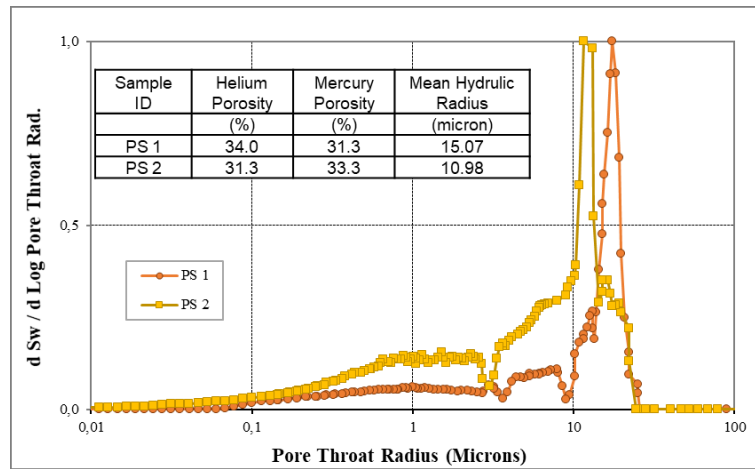


Figure 3: Pore throat size distribution from MICP experiment.

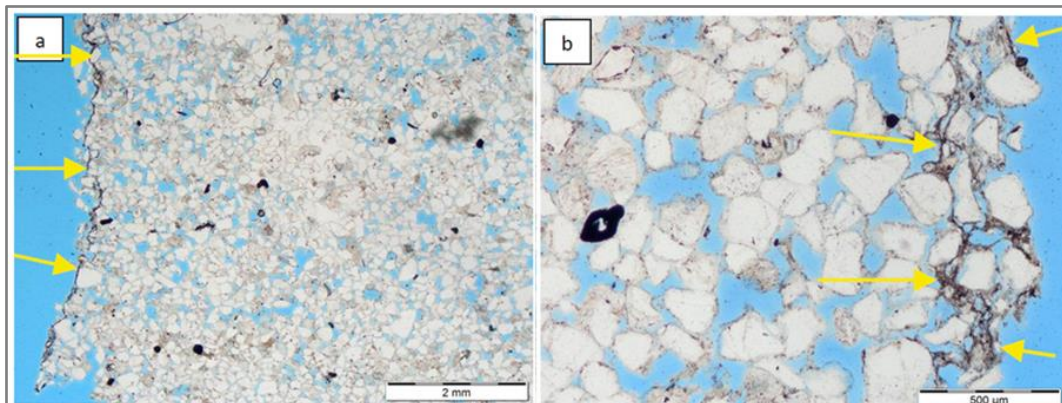


Figure 4: Thin section photomicrographs illustrating the occurrence of mud in the core sample.

3. Core cleaning

In this section the comparative cleaning results of 4 core plug samples are described. Cleaning Program-1 is a standard protocol and cleaning Program-2, is the more elaborate (aggressive) cleaning method. The flush cleaning in both Program-1 and 2 were performed at 60 °C and 20 bars confining pressure with the flow rate of 0.3 ml/min. The individual sample was jacked in a Viton sleeve and loaded into hydrostatic core holder. At controlled temperature, solvent was injected via an automated flushing cleaning system equipped with three KNAUER pumps. Program-1 and 2 are described below:

Program 1:

1. Started with low rate (0.5 ml/min) flush cleaning of mixture of 75% toluene and 25% methanol.
2. Then followed by alternate injection of toluene-chloroform-methanol until effluent was clear.
3. For each sample about 251 ml (~16 pore volumes) solvent was flushed through the sample
4. Absolute permeability to methanol in both directions was measured before samples were sent to hot oven drying and is given in Table 2.

Program 2:

1. The plugs first were flushed with two pore volumes (PV) of toluene to remove the bulk oil.
2. Flushing by 2 PV of tetrahydrofuran (THF) to remove remaining oil and water and effluent was collected (see Figure 5).
3. The oil composition in effluent was measured up to C₄₂₊ utilizing a high-resolution capillary gas chromatography (GC) and an FID detector.

4. Plugs were then flushed by 2 PV of chloroform to desorb THF in step 2.
5. Steps 1 to 4 were repeated for 8 cycles (~ 42 PV) and effluent after each THF flooding (a total of 8 effluents) were analyzed by GC.
6. At the end, plugs were flushed by methanol to remove polar solvents, salts and water.
7. Absolute permeability to methanol in both directions was measured before samples were sent to hot oven drying.

Table 2: petrophysical properties of core plugs

Sample Number	Helium Porosity %	Klinkenberg Permeability (mD)	Methanol Permeability (mD)	
			Forward	backward
2 - PS 1	32.9	1644	1143	1117
4 - PS1	32.3	1374	1137	958.8
9 - PS2	31.3	1373	1102	967.4
10 - PS2	31.0	1122	632.2	600.0

During cleaning Program-2, each subsequent cleaning cycle (methanol/THF/chloroform) removed more oil. The remaining oil fractions became heavier with each flushing, as the molecular weight of crude changed from 225 g/mol at first cycle to 550 g/mol at cycle 8 (see Figure 6), which corresponds to fractions heavier than C₄₂. This is explained by the fact that the relatively light fractions are flushed first and the residual oil composition shifting towards a higher C number. This can be also noticed in the shapes of the chromatograms in Figure 7, where there is a clear reduction in lighter fraction and a shifting of the whole spectrum towards the heavy end (after the retention time of 50 on the graph).

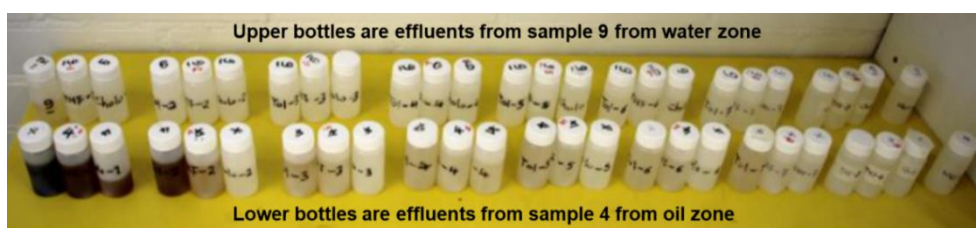


Figure 5: Effluents collected from core plugs after cleaning Program-2. Stack of three bottles representing different cycles.

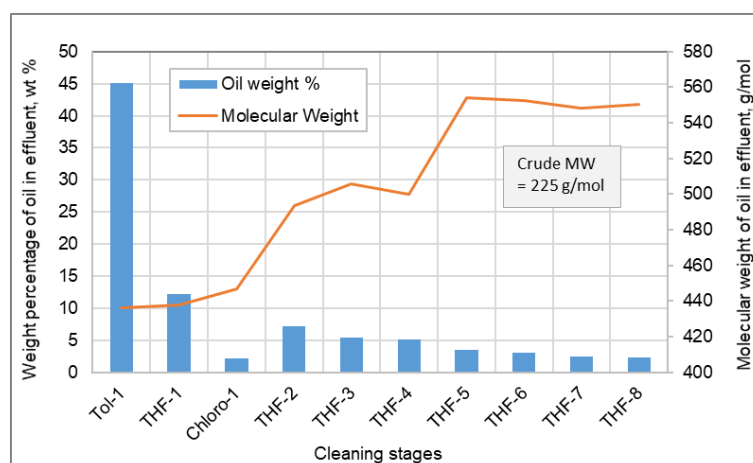


Figure 6: Evolution of oil fraction wt % and molecular weight of oil fraction during the cleaning stages.

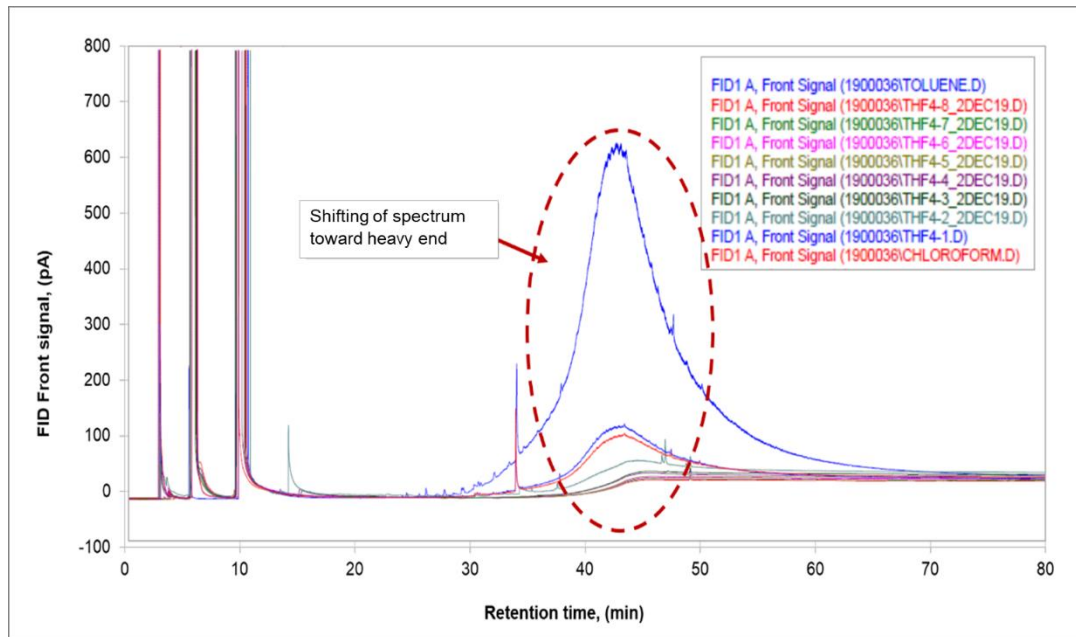


Figure 7: FID front signal over time showing overlapped chromatograms of effluents. First peak is for THF, second for Chloroform and third for toluene. The last peaks are for oil heavy component as it is shifted toward longer retention time from first effluent to eighth effluent.

4. Wettability analysis on clean cores

Two cleaned samples from each of the two different cleaning programs were used for combined Amott and USBM wettability analyses [4], [5], [6], [7]. The aim was to compare the effect of cleaning methods on wettability.

The clean and dry samples were first fully saturated with synthetic formation brine. Each sample was first placed in an Amott cell for two weeks filled with mineral oil. The target water saturations (~20-25%) was achieved by a centrifuge oil-brine drainage process. The samples were then placed in glass Amott cells filled with synthetic formation brine and spontaneous imbibition of brine was monitored before the samples were loaded into the centrifuge for forced imbibition. After establishment of S_{or} , the samples were loaded into Amott cells where spontaneous and forced imbibition of oil was measured.

Based on the same experimental data, two types of wettability indices are calculated, the USBM wettability index (W) and Amott-Harvey Index and are listed in Table 3. All four samples are water-wet based on wettability index. It was observed that water was much easier to spontaneously imbibe into samples than Soltrol oil. This is a direct indication that water is the wetting fluid. Although the Amott-Harvey index does not show much difference in wettability of the four samples, the USBM index seems to show that sample 4 and 9, cleaned by program-2, are more water wet compared to sample 2 and 10, cleaned by Program-1.

Table 3: The Amott-Harvey and USBM indexes after combined Amott-USBM Wettability test at ambient conditions

Sample Number	Amott- Harvey Index	USBM Index	Cleaning Program
2-PS 1	0.54	0.29	Program-1
4-PS 1	0.47	0.75	Program-2
9-PS 2	0.52	0.52	Program-2
10-PS 2	0.57	0.18	Program-1

Effective permeability for oil at irreducible water saturation (S_{wi}) and for water at residual oil saturation (S_{or}) were also measured. The core was mounted in a core holder with 20 bar net overburden pressure, measurements were performed at room temperature with four different flow rates. The results are summarized in Table 4. The oil permeability at irreducible water saturation ($K_o @ S_{wi}$) is close to the Klinkenberg permeability and significantly higher than water permeability at residual oil saturation ($K_w @ S_{or}$). These end-points also support that the samples are water-wet and are consistent with combined Amott-USBM wettability test.

Table 4: The end-point oil and water saturations and permeabilities

End Point data from Amott-USBM					
Sample Number	S_{wi} (frac)	$K_w @ S_{or}$ (mD)	S_{or} (frac)	$K_o @ S_{wi}$ (mD)	S_{wi} (frac)
2-PS 1	0.200	83.6	0.298	1116	0.217
4-PS 1	0.200	359.3	0.194	1131	0.236
9-PS 2	0.250	85.6	0.296	1135	0.289
10-PS 2	0.250	130.6	0.255	921.7	0.284

5. Capillary pressure and endpoint permeability after wettability restoration

For further investigation, four more core plugs were selected from the two preserved samples and then they were flush cleaned by Program-2. The clean and dry samples were first fully saturated with synthetic formation brine. The samples were spun in centrifuge to bring to the initial (target) water saturation (S_{wi}) by injecting crude oil. Samples were then aged in crude dead oil at reservoir conditions (80 °C and 190 bars) for 4 weeks. Properties of formation water and reservoir oil are given in Table 5. Afterwards, the crude oil in the sample was replaced first by decaline and then by Soltrol oil. Flooding the core plugs by decaline is to avoid any chemical reaction between crude oil and Soltrol. The oil permeability at initial water saturation (S_{wi}) was measured by the end of the flushing by Soltrol oil. Oil-brine drainage and imbibition capillary pressures were then measured by two different methods, multi-speed centrifuge and porous plate.

Table 5: Reservoir fluid properties

Parameter	Unit	Value
Viscosity of reservoir oil	cp	0.52
Density of stock tank oil	kg/Sm ³	855
Density of reservoir oil	kg/Sm ³	700
Density of formation water	kg/Sm ³	1050

5.1 Capillary pressure by centrifuge:

After measurement of $K_O @ S_{wi}$, the samples were weighed and loaded into an ultracentrifuge in (brine) imbibition mode. The volume of displaced oil was monitored on consecutive days at each capillary pressure to ensure samples had reached stable saturations. The samples were stored for few days to allow the fluid to redistribute across the sample before measuring effective permeability for water at residual oil saturation ($K_W @ S_{or}$).

The samples were loaded again into an ultracentrifuge in a drainage mode where brine was displaced by mineral oil (secondary drainage process). End-face fluid saturation at each capillary pressure step was modelled with Hassler-Brunner method. Capillary pressure at the final stage of centrifuge and corresponding bound numbers for imbibition and drainage are given in Table 6. Afterwards, the effective permeability for oil at irreducible water saturation ($K_O @ S_{wi}$) was measured. The results are presented in Table 7 and Figure 8.

Table 6: Capillary pressure and corresponding bound number used at the last stage of multi-speed centrifuge

Sample Number	Imbibition		Secondary Drainage	
	End-Pc (Pci)	Bound No. [-]	End-Pc (Pci)	Bound No. [-]
8 - PS 1	-62.6	-2.4E-04	50.3	1.9E-04
14 - PS 2	-62.7	-5.5E-04	50.4	4.4E-04

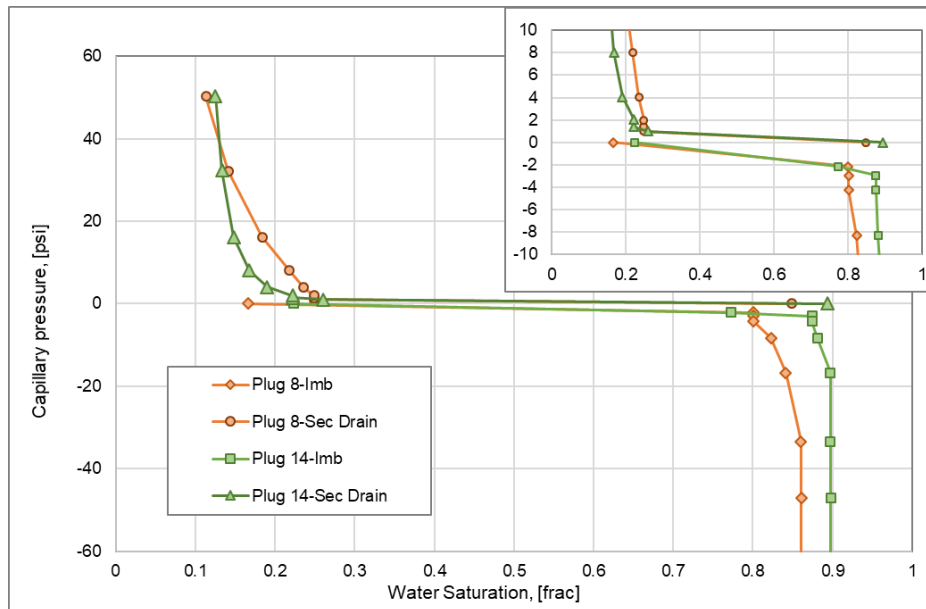


Figure 8: Oil-brine imbibition and secondary drainage capillary pressure measured by centrifuge on aged samples.

Table 7: Endpoint saturation and permeabilities after multi-speed centrifuge test

Routine Analysis			Primary Drainage		Imbibition		Secondary Drainage	
Sample Number	Porosity (%)	Klink Perm (mD)	S_{wi} (ave) (%Vp)	$K_O @ S_{wi}$ (mD)	S_{or} (ave) (%Vp)	$K_W @ S_{or}$ (mD)	S_{wi} (ave) (% Vp)	$K_O @ S_{wi}$ (mD)
8 - PS 1	33.1	1264	0.166	717.3	0.152	586.4	0.163	841.1
14 - PS 2	33.4	2875	0.223	1505	0.106	2065	0.146	2179

5.2 Capillary pressure by Porous Plate:

The other two samples were utilized in Pc-RI experiments where capillary pressure was determined by the porous plate method. Samples saturated with Soltrol at S_{wi} , were mounted in core holders with a net overburden pressure of 115 bar. SFW at different pressure stages was injected from bottom. The top-end of the core is in capillary contact with an oil-wet membrane (porous plate) and it is only permeable to oil under pressure differentials less than the pore entry pressure of the membrane. Multi-step imbibition capillary at different saturations was calculated, and then porous plate was removed and water permeability at residual oil saturation ($K_w @ S_{or}$) was measured. Afterwards, porous plate was replaced by a

water-wet ceramic plate and Soltrol was injected to the core. Once equilibrium was achieved (this took few weeks), the pressure is increased, and the process repeated until a full curve of secondary drainage capillary pressure and resistivity index was obtained. Oil permeability at irreducible water saturation ($K_o @ S_{wi}$) was then measured and is given in Table 8.

Imbibition and secondary drainage capillary pressure curves is shown in Figure 9. Despite differences in petrophysical properties of sister plugs, for similar capillary pressure, generally lower residual oil saturation (after imbibition) and irreducible water saturation (after secondary drainage) was achieved by centrifuge experiment (see Table 7 and Table 8).

Table 8: Endpoint saturations and permeabilities after imbibition and secondary drainage porous plate test

Routine Analysis			Primary Drainage	Imbibition		Secondary Drainage	
Sample	Porosity	Klink Perm	S_{wi} (ave)	S_{or} (ave)	$K_w @ S_{or}$	S_{wi} (ave)	$K_o @ S_{wi}$
Number	(%)	(mD)	(%Vp)	(%Vp)	(mD)	(% Vp)	(mD)
7 - PS 1	34.1	2002	0.232	0.201	330.7	0.248	431.4
13 - PS 2	34.1	1045	0.242	0.209	350.1	0.180	1079

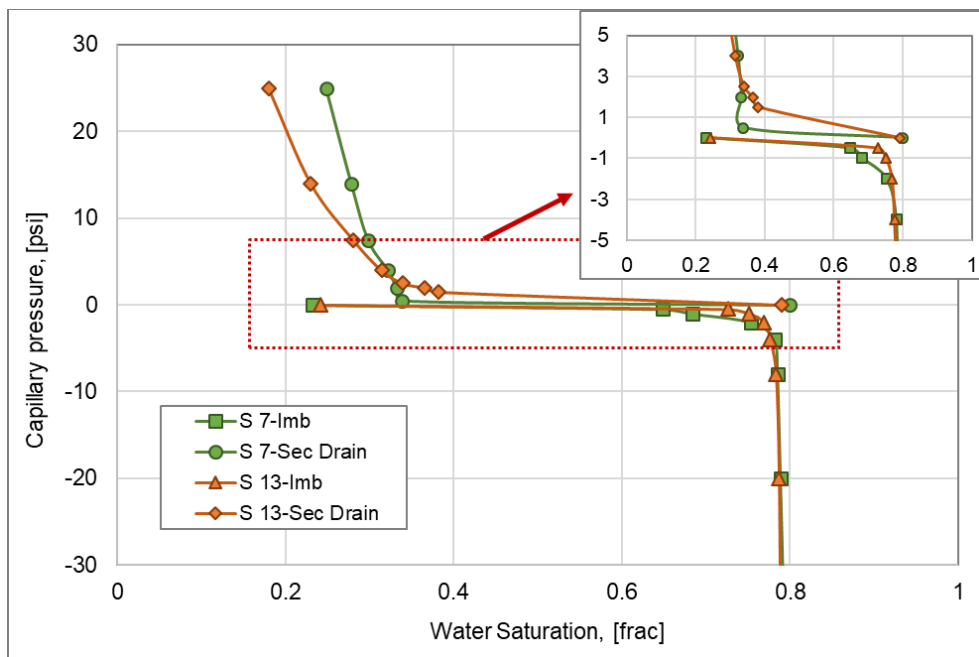


Figure 9: Oil-brine imbibition and secondary drainage capillary pressure measured by porous plate on aged samples.

6. Discussion

Four core samples (two sister plugs) were flushed-cleaned by two different cleaning methods; standard method (Program-1) and more aggressive method (Program-2). After cleaning, wettability was confirmed with combined Amott-USBM method as water-wet. The Amott-Harvey index showed similar wettability for the four samples, while the USBM index exhibit samples cleaned by

Program-2 are more water wet compared to sample cleaned by Program-1.

For further investigation, 4 more core samples (two sister plugs) from similar preserved sample were flushed cleaned by Program-2. Then, the core samples were aged with crude oil at reservoir conditions to restore the in-situ wettability. Afterwards, to examine the core wettability state in terms of fluid flow, oil-brine imbibition and secondary drainage capillary pressure and end-point saturations and relative permeabilities were measured

with two different approaches; multi-speed centrifuge and porous plate.

Imbibition capillary pressure measured on aged and not aged samples from preserved sample 1 and 2 are compared in Figure 10 and Figure 11. Oil-brine imbibition capillary pressure was measured using centrifuge on plugs 2 and 4 from PS 1 and plugs 9 and 10 from PS 2, right after cleaning and without aging process. The plugs are strongly water-wet (as shown earlier in Table 3) and it explained the large increase in water saturation by spontaneous water imbibition. On the other hand, for plugs 7 and 8 from PS 1 and plugs 13 and 14 from PS 2 which are aged, almost no spontaneous water imbibition was observed. The wettability of these plugs is quantified as intermediate water-wet, although less than 1 psi capillary pressure was required to make a large shift in water saturation.

Considering the PS 1 is from oil zone and PS 2 is from water zone, hence the original wettability for these preserved samples was significantly different.

Meanwhile, the cleaning and aging process has resulted in similar wettability behavior for both samples as it is shown in Figure 10 and Figure 11. Therefore, we believe the current rock wettability is entirely dependent on crude oil properties and interaction between rock and fluid. Since the aging time (4-weeks) is not comparable with geological time that porous media were exposed to oil, the current wettability might be underestimated toward oil-wet system.

End-point properties including residual oil saturation (S_{or}) and water permeability ($K_{rw} @ S_{or}$) at the end of water-flooding for aged and not-aged samples are compared Table 9 and Figure 12. For not-aged samples, $K_{rw} @ S_{or}$ do not correlate with cleaning programs. Low $K_{rw} @ S_{or}$ is simply due to strong water-wet system and it varies with core structures. For aged samples, residual oil saturation at the end of water flooding is lower and subsequently water relative permeability is higher reflecting big shift in end-points properties as wettability changes towards intermediate water-wet system.

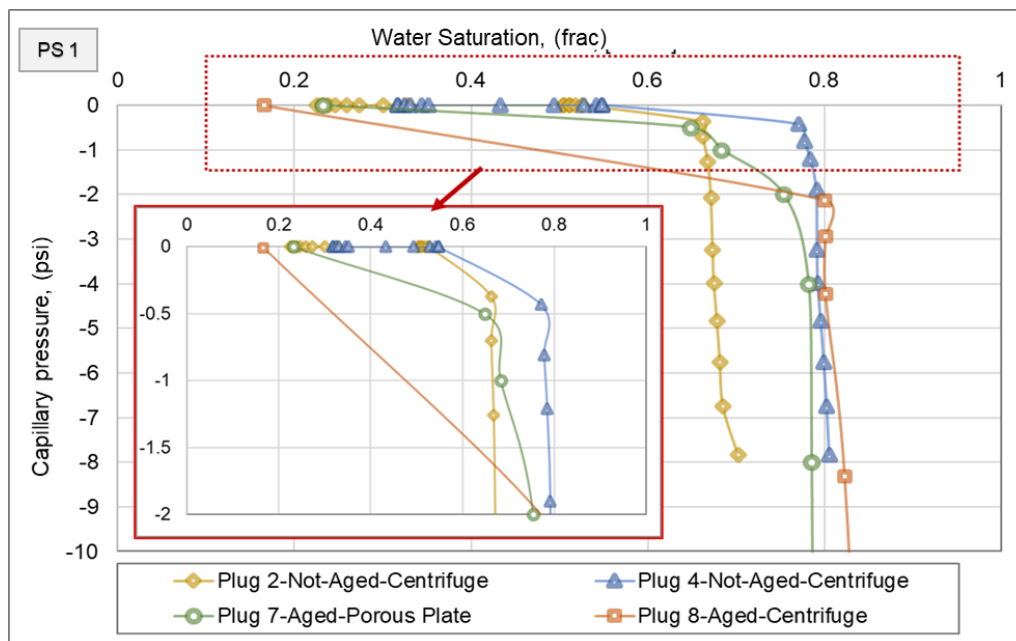


Figure 10: Oil-brine imbibition capillary pressure on sister-plugs from PS 1. Plug 2 (yellow line) is after cleaning program 1, plug 4 (blue triangle) is after cleaning program 2. Plugs 7 (green circle) and plug 8 (orange square) are after cleaning program 2 and aging.

Table 9: initial and residual oil saturation and water relative permeability at end of water flooding

Sample No.	Aging [-]	Cleaning Program	He Poro. (% of Vb)	Klink Perm (mD)	S_{oi} (frac)	S_{or} (frac)	$K_{rw} @ S_{or}$ (frac)
2-PS 1	✗	Program 1	32.9	1644	0.800	0.298	0.07
4-PS 1	✗	Program 2	32.3	1374	0.800	0.194	0.32
7-PS 1	✓	Program 2	34.1	2002	0.768	0.201	0.77
8-PS 1	✓	Program 2	33.1	1264	0.834	0.152	1.00
9-PS 2	✗	Program 2	31.3	1373	0.750	0.296	0.08
10-PS 2	✗	Program 1	31.0	1122	0.750	0.255	0.14
13-PS 2	✓	Program 2	34.1	1045	0.758	0.209	0.32
14-PS 2	✓	Program 2	33.4	2875	0.777	0.106	0.95

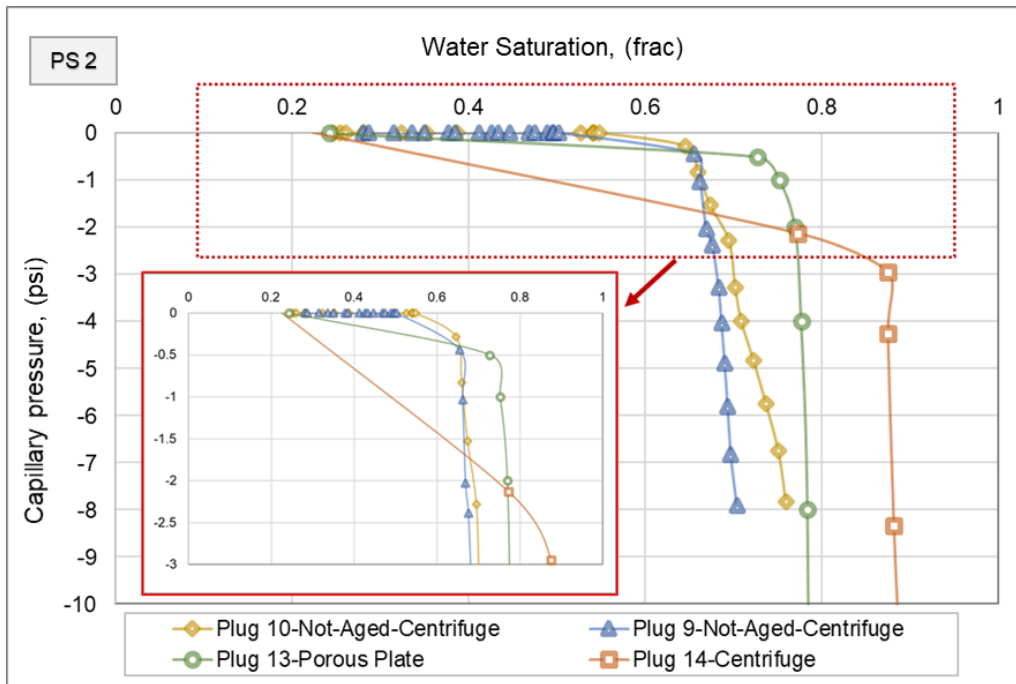


Figure 11: Oil-brine imbibition capillary pressure on sister-plugs from PS 2. Plug 10 (yellow line) is after cleaning program 1, plug 9 (blue triangle) is after cleaning program 2. Plug 13 (green circle) and plug 14 (orange square) are after cleaning program 2 and aging.

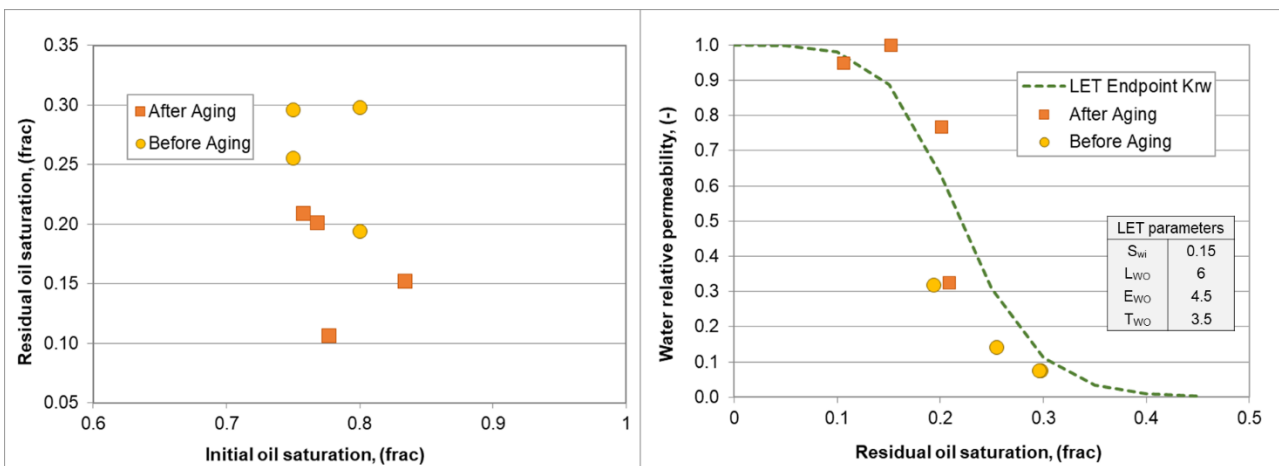


Figure 12: Residual oil saturation and water relative permeability at end of water flooding on aged and not aged samples.

7. Conclusion

In the presented work, effect of two cleaning approaches is studied in detail. Core plugs from two preserved samples with similar petrography and petrophysical properties, but one from oil zone and the other from water zone, were flush cleaned by two programs; Program-1 and Program-2. Gas chromatography analysis on effluents produced from the core plugs showed the presence of heavy hydrocarbon (fractions heavier than C₄₂) even after more than 40 PV solvent injection.

Wettability of the core plugs were then tested using combined Amott-USBM wettability method. The Amott-Harvey index does not show much different in wettability of the samples. But, the USBM index

showed plugs cleaned by the Program-2 are more water-wet compared to those cleaned by Program-1. Spontaneous water imbibition and endpoint properties on clean samples before aging reflects the strong water-wet behavior but did not correlate with cleaning programs. Afterwards, two more plugs from each preserved sample were drilled and cleaned by program-2 and then aged at reservoir conditions. Oil-brine imbibition capillary pressure, endpoint saturation and relative permeability were measured by centrifuge and porous plate. Almost no spontaneous water imbibition was observed on these plugs and endpoint properties were greatly shifted towards intermediate water-wet system. Although the original wettability of the samples was not the same (one from oil zone and the other from water zone), the core treatment procedure resulted in almost similar water-oil flow properties.

Based on our observations, cleaning Program-2 removed more oil, especially heavy hydrocarbons, from the core than typical cleaning protocol so called Program-1. On the other hand, the elaborate Program-2 is often impractical, takes too long, is expensive and limited by laboratory capacity. We believe proper cleaning approach is specific to certain rock and fluid and should be derived separately for an oil field. An effective cleaning method can simply be confirmed by performing gas chromatography compositional analysis of the final effluent at the end of core cleaning.

Acknowledgements

This study is a part of ongoing SCAL (special core analysis) project on core plugs from an exploration well from Edvard Grieg oil field. Therefore, the authors would like to thank Lundin-Energy Norway and our partners, Wintershall Dea Norge and OMV Norge, for funding this project and for allowing to publish these data. We would also give special thanks to PanTerra Geoconsultants for performing the experiments and providing excellent advices.

References

- [1] C. McPhee, J. Reed and I. Zubizarreta, *Core Analysis: a Best Practice Guide*, Amsterdam: Elsevier, 2015.
- [2] E. Donaldson, R. Thomas and P. Lorenz, "Wettability Determination and Its Effect on Recovery Efficiency," **no. 13-20, 1969**.
- [3] G. Hirasaki, J. Rohan, S. Dubey and H. Niko, "Wettability Evaluation During Restored-State Core Analysis," in SPE Annual Technical Conference and Exhibition, New Orleans, Louisiana, 1990.
- [4] E. Amott, "Observations Relating to the Wettability of Porous Rock," **Vols. 216, (156-162)**, 1956.
- [5] W. Anderson, "Wettability literature survey - Part 2: Wettability measurement," **vol. 38:12**, 1986.
- [6] W. Anderson, "Wettability Literature Survey - Part 4: Effects of Wettability on Capillary Pressure," **no. 1283-1300**, 1987.
- [7] W. Anderson, "Wettability Literature Survey - Part 5: Effects of Wettability on Relative Permeability," **no. 1453-1468**, 1987.

Initial Wettability in Carbonates by Advanced Core Analyses: «A Step Closer to Representative Reservoir Wettability»

Iván D. Piñerez Torrijos^{1,2}, Tina Puntervold^{1,2}, Skule Strand^{1,2}, Paul Hopkins¹, Panagiotis Aslanidis^{1,2},

¹University of Stavanger, 4036 Stavanger, Norway

²The National IOR Centre of Norway

Abstract. The cleaning and core restoration strategy proposed in this work has successfully reproduced core scale wettability under spontaneous imbibition (SI) processes in Chalk, high reproducibility of ultimate oil recovery and recovery profiles in between restorations was reported; differences were rather low and ranged from 1.5 to 3.6 %OOIP in 4 different systems. Stevns Klint (SK) outcrop chalk with a high calcium carbonate content was used in this work. The cleaning procedure consisted of a mild cleaning process using kerosene and heptane, with minimized solvent injection. During the core restoration procedure after building up initial water saturation, S_{wi} , oil saturation was performed by limiting the amount of crude oil exposure to $(1-S_{wi})$ pore volume (PV). A comparison at low temperature, 23 °C, between a harsh solvent cleaning method with toluene and methanol and the mild cleaning process by kerosene and heptane was carried out; the results showed that the mild cleaning solvents preserved a larger fraction of polar organic components (POC) adsorbed on the carbonate surfaces during the first restorations process, validating the mild cleaning process as more suitable for preservation of adsorbed POC on carbonate surfaces. Despite the excellent performance of the mild cleaning solvents, they also removed a small fraction of adsorbed POC, making slightly water-wet the mineral surfaces. Thus, even mild organic solvents at low temperature still affect wettability by solvating adsorbed POC. Changes in wettability were assessed by SI and chromatographic wettability (CWT) tests.

1 Introduction

Reliable estimation of in-situ reservoir wettability continues to be an elusive objective despite long-termed efforts and integration of cutting edge technologies for this purpose [1-4].

Integrating wettability measurements in reservoir engineering studies is a critical task because this single parameter has a tremendous impact on recovery factors, reserves estimation and profitability of commercial projects. Low accuracy in wettability assessments can produce erratic results that can lead to underestimation or overestimation of recoverable reserves [2].

As long as the desired goal of in-situ wettability measurements is not reached, Special Core Analyses (SCAL) will continue to serve as the standard practice to quantify reservoir wettability [5, 6]. However, its precision, reproducibility and repeatability stand out as weak points for the current accepted SCAL practices.

Reservoir core sampling is a complex work-routine that aims to preserve wettability. Wettability can be highly affected by drilling fluids, especially the ones bearing surfactants, or by fluids with different pH values

than that of the formation [7, 8]. Such routines also aim to reduce native fluids loss associated to pressure and temperature changes during extraction and sampling. Such changes can potentially induce asphaltene precipitation, loss of light ends of hydrocarbons and fluid redistribution within the porous media; thus, altering core wettability.

Peal packaging is carried out to minimize contamination before sample arrival to the laboratory for routine and special core analyses. Then, typical samples of 3.8 cm of diameter are drilled from sealed peals and the samples are subjected to a core cleaning procedure. During core cleaning the solvents and fluids used can change the composition and concentration of polar organic material initially adsorbed onto the rock surface, leading to substantial changes in wettability [7-9]. The accepted protocol has the objective of shifting the wettability of the core to a strongly water-wet state to later recreate reservoir wettability. This work offers a critical stance specially on the standard procedure, with special focus on the choice of inducing a strongly water-wet state,

* Corresponding author: ivan.d.pinereztorrijos@uis.no

while suggesting an alternative solution to the challenging task of assessing reservoir wettability.

It is well known that several critical parameters assessed in SCAL analyses are wettability dependent. Core restoration begins with core solvent cleaning and it is followed by the establishment of initial fluid saturations, i.e., water and oil.

During SCAL analyses, data related to fluid-flow characterization is collected as fluids saturation is changed, this data includes, resistivity, capillary pressure and pressure drops. From here on, the “*data*” is further processed to be assembled into reservoir simulations through relative permeability curves. Thus, core cleaning and core restoration protocols are of great importance because they have a major impact on the evaluation of field development plans, hydrocarbon productions forecasts, and economic analyses associated to hydrocarbon production.

Core cleaning and core restoration programs that can closely reproduce the native reservoir wettability can contribute to reduce uncertainty in the reservoir characterization value-chain.

Wettability controls fluid distribution on pore surfaces, giving rise to complex fluid-flow recovery processes, and the study of this phenomena has been a primary objective for understanding oil recovery processes. During waterflooding operations, capillarity plays major role in such processes, and this becomes more significant for reservoirs or reservoir zones with greater heterogeneity.

A brief description of the steps taken to restore a core are summarized as follows, (1) solvent cleaning aiming to render the cores to a completely water-wet state, (2) establishment of formation water saturation, (3) introduction of crude oil until reaching residual water saturation (S_w), (4) Maturation or aging process at reservoir temperature.

Combinations of cleaning solvents had been reported to be more adequate than cleaning process engaging single solvents [10]. Up to date, typical core cleaning units are based on high and low temperature cleaning by Soxhlet extraction [11], constant or total immersion, and solvent flooding [6].

Solvent cleaning methods are meant to efficiently remove hydrocarbons from the porous network but at the same time minimizing any possible damage onto the present minerals. Currently, the standard cleaning pair is toluene and methanol but many other options are available; simple examples are hexane, cyclohexane, kerosene, acetone, chloroform, ethylene chloride and tetrachloroethylene among others [6]. The use of different solvents can lead to different restored wettability states [12]. Thus, a correct solvent selection is crucial if preserved core samples are required to be restored to a representative reservoir wettability.

Furthermore, weaknesses of standard core restorations are coming to light [13]. Classical core cleaning methods have as objective to remove mud filtrates [14], precipitated salts and native crude oil to achieve a water-wet state.

However, by taking away the initially adsorbed polar organic components (POC) that dictate reservoir wettability with strong organic solvents, the wettability state to evaluate is simply destroyed. Then, restoring initial core wettability in the laboratory becomes an impractical and difficult task. This is mainly due to the fact that the sampled reservoir crude oil used in core restoration processes might be different in its chemical composition from the oil that initially wetted the reservoir during the first oil migration [15]. Furthermore, the oil chemical composition may have changed during geological time due to adsorption and decomposition processes [16, 17].

Other important aspect of core restoration to consider is oil saturation. The presence of crude oil will expose mineral surfaces to surface active POC. Recent investigations had shown that POC adsorption takes place rapidly as crude oil enters in contact with porous media surfaces; it has also been shown that increased oil volumes reduce the degree of water-wetness of the restored cores [18-23].

The weaknesses of core restoration protocols can promote unrepresentative wetting states in restored carbonate cores, giving rise to scattered wetting states in SCAL experiments.

Acidic and basic material in the crude oil can be quantified by the acid number (AN) and base number (BN), both having the unit mgKOH/g oil. In carbonates, the acidic POC (AN) represent the most relevant wetting parameter [24-30].

In the acidic fraction, carboxylic groups (R-COOH) appear to have a large surface activity, they are found in both resins and asphaltenes. On the other hand, basic POC have less impact on the carbonates wettability [31]. POC get adsorbed onto water-wet outcrop chalk surfaces in crude oil flooding processes, one consequence of this is that the water wetness will decrease [18]; In addition to this, increasing acid number of crude oil appears to reduce the degree in water-wetness [25]. The negatively charged carboxylic groups, R-COO⁻, adsorb strongly onto the positively charged calcite surfaces at slightly alkaline conditions, for this reason, it is challenging to remove all the POC from the carbonate surfaces by using different organic solvent combinations [32-34].

This paper discusses the implications of: (1) correct solvent selection for cleaning mixed wet carbonate cores, and (2) core restoration processes that aim to preserve wettability and reproduce the wetting state of a carbonate system at core scale. For the first topic a comparison between the harsh solvent cleaning combination of toluene and methanol and our proposed mild cleaning with kerosene and heptane is carried out.

In the first section the wetting states of the cores were measured by spontaneous imbibition and chromatographic wettability tests. The results were discussed in terms of the ability of the organic solvents to remove polar organic components adsorbed onto the carbonate surfaces of the cleaning fluids. It is important to know that POC adsorption has a direct impact on surface wettability, the solvents sets compared were toluene-methanol against kerosene-heptane.

In the second part of this work, the crude oil exposure of the restored cores was optimized to achieve wettability reproduction in carbonates at core scale.

The combination of both correct cleaning and a correct understanding of restoration processes facilitated achieving the goal of wettability reproduction at core scale. The proposed cleaning and restoration strategy can potentially be applied in core material with similar mineralogical characteristics, the outcrop material is made of high purity calcite (CaCO₃), the chemical interactions that dictate wettability in this crude oil-brine-rock system (COBR), are heavily controlled by the nature of the mineral phases present, and previous studies on chalk have proved that surface reactivity and wettability can be extended to limestone reservoir cores [12, 34-41].

2 Experimental

A brief description of the materials used is found below, it covers, the outcrop core material used, the synthetic brines, crude oils, model oil and solvents used.

2.1 Materials

2.1.1 Core material

Outcrop chalk from a quarry at Stevns Klint (SK) was used in this work. SK chalk is made up of pure biogenic calcite >98 wt.%, with a minimum silicate traces compared to other types of chalk [42-45]. The presence of natural chalk impurities as quartz or clays can impact on the chemical properties of the material, i.e. surface reactivity and mechanical properties [46-53]. Average porosity values are in the range of 41 to 50 %, and permeabilities varied from 1 to 5 md.

The material is well recognize as an excellent analogue to the North Sea Chalk reservoirs [48, 54], and its high reproducibility of results in laboratory tests have consolidate it as an outstanding material for parametric studies [18, 35, 54, 55]. Its biogenic origin is reflected on its structure, which is largely formed by of coccoliths fragments, **Figure 1**.

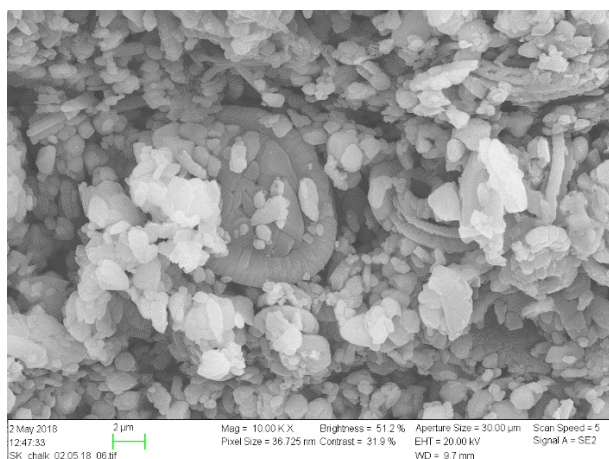


Figure 1. Image of outcrop chalk retrieved from the Stevns Klint quarry. SEM magnification 10000 X.

Mercury capillary injection pressure (MICP) tests were obtained from a representative sample; Stratum laboratories carried out the tests. Pore size distribution is shown in **Figure 2**; average pore size belongs to the micro-pore region (0.1-0.5 μm).

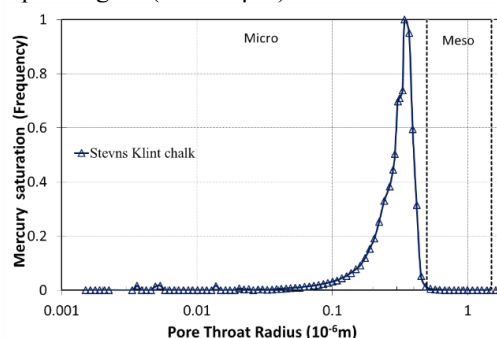


Figure 2. Pore size distribution in SK outcrop chalk.

The cores were retrieved from two blocks and were cleaned and restored as suggested by Puntervold et al [56]. They were initially cleaned with 5 pore volumes (PV) of de-ionized (DI) water to remove dissolvable salts, e.g., calcium sulphate salts that can affect initial core wettability [56]. Subsequently, all cores were dried at 90 °C until achieving constant weight. The main core properties are displayed in **Table 1**.

Table 1. Physical core properties of the SK outcrop material.

Core	Block 1			Block 2					
	B11	B12	B13	B24	B25	B26	B27	B28	B29
L (cm)	6.17	6.17	5.91	6.94	6.94	6.92	7.00	7.00	7.04
Ø(cm)	3.70	3.70	3.75	3.80	3.80	3.82	3.80	3.80	3.79
PV (ml)	30.8	26.5	27.3	38.3	39.9	37.7	37.3	38.8	38.5
Φ, %	46	41	42	49	50	48	47	48	49
K(md)	2.0	1.4	1.3	2.5	1.0	0.8	1.6	2.0	1.2

2.1.2 Brines

All brines were synthetically prepared from reagent grade chemicals purchased from Merck laboratories. Formation water (FW) composition is based on a North Sea chalk reservoir formation water. SW0T and SW½T were used in the chromatographic wettability experiments (CW) [35], these tests are performed at room temperature to minimize wettability alteration induced by sulphate on carbonate surfaces. Compositions are presented in **Table 2**.

Table 2. Brine properties and compositions.

Brines Ions	FW mM	SW0T mM	SW½T mM
Na ⁺	997	460	427
K ⁺	5	10	22
Li ⁺	0	0	12
Ca ²⁺	29	13	13
Mg ²⁺	8	45	45
Cl ⁻	1066	583	538
HCO ₃ ⁻	9	2	2
SO ₄ ²⁻	0	0	12
SCN ⁻	0	0	12
Ionic strength	1.112	0.643	0.644
TDS g/l	62.83	33.39	33.39

2.1.3 Crude oil

A crude oil stock solution was prepared by mixing reservoir crude oil and heptane in a volume ratio of 60/40, respectively; the reservoir crude oil had a low asphaltene content and no asphaltene precipitation was observed. The prepared model oil was filtered using a 5 μ m Millipore filter, its acid number (AN) and base number (BN) were quantified and the results shown that the AN was 1.8 mgKOH/g and the BN was 0.74 mgKOH/g. A fraction of the stock solution was treated with silica gel (10 wt. %) to remove polar organic components, this step was repeated after 4 days. The silica treated oil had an AN and BN of ~0 and 0.03 mgKOH/g, respectively. Three crude oils were prepared by mixing the model and treated oil with the objective of achieving the targeted AN and BN; Oil A, Oil B and Oil C, their crude oil properties are presented in **Table 3**.

Table 3. Chemical and physical crude oil properties

Crude Oil	AN mgKOH/g	BN mgKOH/g	μ at 25°C cP	ρ @ 25°C g/cm ³	Used in cores
Oil A	0.34	0.24	3.25	0.808	B11, B22
Oil B	0.36	0.30	2.52	0.807	B24, B25, B29
Oil C	0.50	0.23	2.36	0.807	B26, B27

The AN and BN quantification was carried out by potentiometric titration, using modified version of the ASTM 664 and ASTM 2898 [57]. The methods reproducibility is better than ± 0.02 mgKOH/g for both AN and BN analyses.

2.2 Analyses

2.2.1 Ion chromatography analyses SDR

A Dionex IC 3000 was used to analyze brine effluent samples. External standards were used for quantification of ionic concentrations.

2.3 Methods

2.3.1 Organic solvents for core cleaning

Two sets of organic solvents were used, a mild cleaning consisting of kerosene/heptane and the standard harsh cleaning with toluene/methanol. Kerosene and heptane have low aromaticity and reduced solvation power of larger oil components. On the other hand, toluene is known for being a strong solvent for heavy oil components and methanol acts as a solvent for both crude oil components and water.

The objective of using the mild core cleaning approach is to remove the residual oil in the core without inducing significant desorption of the adsorbed POC onto the rock surface, since they are the components establishing the original wetting of the core [58]. All solvents were reagent grade and purchased from Merck.

2.3.2 Core preparation

Initial core preparation

All chalk cores were initially flooded with 5 PV of distilled water (DI) with the objective of removing easily dissolvable salts. The presence of sulfate was qualitatively evaluated at the end of this cleaning stage to avoid wettability alteration of the carbonate surface by this ion. The cores were dried to constant bulk weight at 90 °C in an oven.

Core restoration

Initial water saturation, was established with FW at (S_{wi})=0.1, by using the desiccator technique [59]. After reaching the target weight, all cores were stored in a closed container for a minimum time of 72 hours to obtain a uniform distribution of ions within the porous media.

Crude oil saturations were carried out by putting the cores at $S_{wi} = 0.1$, in a Hassler core holder with a confining pressure of 20 bars and 10 bars of backpressure. A short vacuum was performed on the system to avoid trapped gas into the system. Then, the water-wet cores in the first restoration were oil flooded at the temperature of 50 °C and at an injection rate of 0.1 ml/min, 2.5 PVs were injected from both directions, this step helped to establish an initial wettability induced by crude oil adsorption.

With the objective of optimizing the restoration procedure and reproducing wettability, in the second restorations the crude oil exposure, was limited to (1- S_{wi}) PV of crude oil after establishing $S_{wi} = 0.1$.

Core aging was carried out for 2 weeks at the temperature of 50 °C. The cores were placed on marble balls in a closed aging cell containing crude oil, they were wrapped in Teflon tape to avoid adsorption of unrepresentative POC on the core surfaces [25]. The static aging process was chosen over dynamic aging to avoid additional crude oil exposure, which increases POC adsorption affecting wettability [18, 58].

2.3.3 Core cleaning

The cores flooded with crude oil were cleaned in a second restoration using two different of organic solvents. Mild cleaning uses kerosene and heptane, and the standard harsh cleaning uses toluene and methanol. The solvent cleaning process was initiated at S_{or} , i.e., at high water saturation to avoid transport of polar components to non-representative water-wet spots.

The cores from block 1 B11 and B12 were cleaned with 30 PV of solvents. B11 was mildly cleaned with 5 PV of low kerosene and 5 PV of heptane in three cycles. Core B12, was cleaned in the same way as core B11, but with toluene and methanol.

Cores from block 2 were only mildly cleaned by using 10 PV of kerosene and 5 PV of heptane, with a total amount of 15 PV of solvents injected.

To remove the last injected solvent and easily dissolvable salts; 5 PV of distilled water (DI) were flooded in each core. Then, the cores were dried to constant weight at 90°C to evaporate water and solvents.

2.3.4 Oil recovery by Spontaneous Imbibition (SI)

Spontaneous imbibition (SI) was the method chosen for oil recovery tests. The tests were carried out in glass Amott cells at 50 °C; FW was the imbibing fluid to avoid wettability alteration. Oil recovery was expressed as percentage of original oil in place (%OOIP), the values were logged against time until the recovery plateau was reached, the volumetric measurements had a precision of ± 0.05 ml. For water-wet outcrop the SI tests were carried out at 23 °C with distilled water as imbibing fluid and heptane as the organic phase.

2.3.5 Chromatographic wettability test (CW)

The chromatographic wettability tests (CW) was used as an additional way of measuring wettability, the test was

developed by Strand and co-workers [35], In this test, the cores are mounted into a Hassler core holder with a confining and back pressure of 20 and 10 bars, respectively. The test is performed at room temperature to hinder sulphate reactivity. An injection rate of 0.2 ml/min is used in the tests. A brine termed, SW0T, is injected until reaching residual oil saturation, S_{orw} . Then, a brine containing the non-reactive tracer, SCN^- , and sulphate, SO_4^{2-} is flooded, this brine is described as SW $^{1/2}$ T. Effluent samples are collected with an autosampler to be later analyzed by ion chromatography.

The CW test evaluates the water-wet surface area in the core sample by chromatographic separation of the non-adsorbing tracer, SCN^- , and the adsorbing sulphate ion. Then, the area in between the two elution curves is quantified, A_w , this area is proportional to the water-wet surface area of a carbonate core sample. Its reproducibility is $\sim 5\%$ [35]. A strongly water-wet reference core is used as main reference, in this core the area, (A_{ww}) was calculated to be, $A_{ww} = 0.251$. The CW tests provide a wettability index termed, I_{CW} . The index describes the water-wet fraction of a chalk surface, and is quantified with the following Eq.1:

$$I_{CW} = \frac{A_w}{A_{ww}} \quad (1)$$

An index of $I_{CW} = 0$, represents a completely oil-wet surface area, whereas a, $I_{CW} = 1$ corresponds to a strongly water-wet surface area.

2.3.6 Wettability by spontaneous imbibition (SI)

Spontaneous imbibition (SI) is used to evaluate the active presence of capillary forces [60]. Description of the wetting state of the core comes from ultimate recovery and oil production profiles. An advantage of SI experiments is that they can be carried out at reservoir temperatures, reducing uncertainties associated to physical fluid properties, COBR interactions and core wettability.

When a SI test recovery from a strongly water-wet reference core is available, SI_{WWC} , in units of (%OOIP), a simplified wettability index, I_{W-SI} , can be calculated as expressed in Eq.2:

$$I_{W-SI} = \frac{SI_C}{SI_{WWC}} \quad (2)$$

Where, SI_C is the oil recovery (%OOIP) from the tested core. As I_{W-SI} approaches 1 the core is categorized as strongly water-wet, and 0 for a fractional/neutral wet core [61].

3 Results and discussion

This work studies the effect of core cleaning and core restoration on carbonates core wettability. It pretends to show how different core cleaning systems may impact on core wettability. Outcrop chalk from SK is used for this purpose [54]. The outcrop chalk has also been reported to show similar behavior as reservoir limestone regarding wettability and wettability alteration processes [38, 62].

This experimental study has two main sections, the first one evaluates the effect of solvent cleaning on chalk

samples, the second one, proposes an optimized restoration method to reproduce wettability at core scale in chalk cores under spontaneous imbibition processes.

3.1 Impact of solvent selection on wettability

Two solvent cleaning methods are compared in this study: a mild cleaning procedure with kerosene-heptane against the classical harsh cleaning with toluene-methanol. Wettability was measured by SI and CW tests to quantify the cleaning effect on previously crude oil-wetted chalk cores. The effect on a second core restoration process was also tested.

3.1.1 Water-wet outcrop chalk

Initial wettability of a strongly water-wet outcrop chalk core was measured by SI; the chromatographic separation was also measured in a CW test. A strongly water-wet reference core retrieved from block 2 was termed B28. Initial water saturation, $S_{wi} = 0.1$, heptane was used in the SI test as oil phase. A CW test was carried out on a 100% water saturated core. The SI and CW results are presented in Fig. 3.

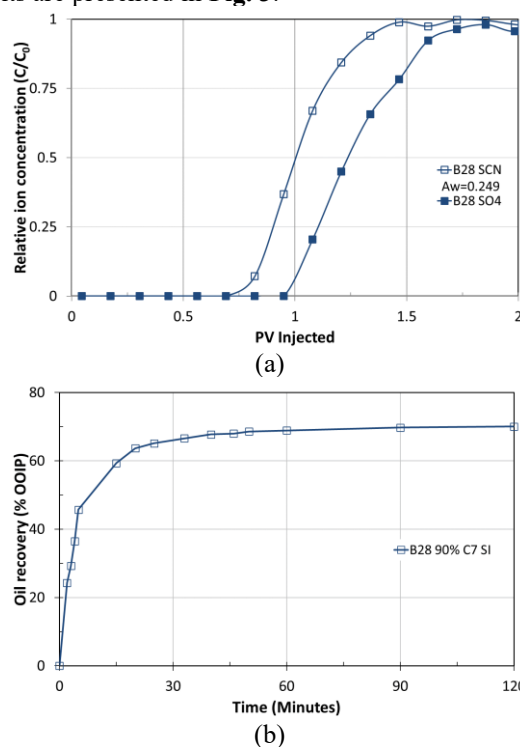


Figure 3. Wettability of water-wet core B28 (a) SI test carried out at 23°C using DI water as FW. Core B28 with $S_{wi} = 0.1$ and heptane (b) CW test on the 100 % water saturated B28 core.

Strongly water-wet behavior is confirmed by both wettability tests. SI tests showed strong positive capillary forces for core B28, the recovery plateau of 70 %OOIP was reached after 1 hour, as seen in Fig. 3a. The CW test resulted in an area between the tracer and sulphate curves of $A_{ww} = 0.249$, Fig. 3b, this correspond to a chromatographic index, $I_{CW} = 1$.

Parallel SI and CW tests were carried out in the strongly water wet core B13, this core was retrieved from block 1. The SI test performed in B13 was done with 100% heptane saturation, the experiment showed evidence of highly active capillary forces, a 75 %OOIP of oil was recovered in less than 30 minutes, validating the strongly

water-wet behavior. The test showed an area of $A_{ww}=0.251$, in line with a strongly water-wet case of block 2. Both results are used in respective wettability indexes calculations. Notice that initial water saturation was different in the cores from the different blocks, this had a consequence in the ultimate oil recovery observed for similar systems. The results are presented in **Tables 4-5**.

3.1.2 Initial wetting conditions by crude oil exposure

The cores B11 and B12 retrieved from block 1, were restored with $S_{wi} = 0.1$ and crude oil flooded with 5PV of Oil A, prior aging. SI tests were performed at 50 °C using formation water (FW) as imbibing fluid. The oil recovery plateau for cores B11 and B12 were achieved after 8 to 10 days, ultimate oil recoveries were 8 and 10 %OOIP, respectively; validating the chalk material reproducibility.

Chromatographic wettability tests were performed after the spontaneous imbibition tests to evaluate the water-wet fraction of the cores surface area. The water-wet surface areas were similar, $A_w = 0.118$ for B11 and $A_w = 0.124$ for B12. Therefore, the water-wet fraction of the surface area, **Eq.1**, was $I_{CW} = (0.118/0.251) = 0.47$ for core B11, and $I_{CW} = (0.124/0.251) = 0.49$ for core B12. The values point to a fractional/neutral wettability for the CW test [35].

By using the modified water index I_{W-SI} (**Eq.2**), the core B11 had a water index of 0.10 and 0.13 for core B12. Both cores were flooded with 5 PV of crude Oil A. Both the CW tests and the SI test results confirm similar cores wetting states.

3.1.3 Mild cleaning kerosene/heptane vs. harsh and conventional toluene/methanol cleaning.

After confirming core wettability in the previous step, both cores were solvent cleaned before undergoing a new core restoration procedure. Each core was subjected to a different solvent cleaning method. Core B11 was cleaned by injecting 5 PV of kerosene (K) and 5 PV of heptane (C₇/H), this process was executed in 3 cycles. Core B12, was cleaned in the same fashion but this time using toluene (T) and methanol (M). After completing the core cleaning stage new SI and CW tests were performed on both cores.

The mildly cleaned core, B11 increased its water-wet fraction to $I_{CW} = (0.150/0.251) = 0.60$, and the harshly cleaned core B12 increased its water wet fraction to $I_{CW} = (0.165/0.251) = 0.66$. Therefore, both solvents removed POC components from the chalk surface. However, the mildly cleaned core cleaning increased its I_{CW} by 13%, whereas the harshly cleaned core increased its I_{CW} by a 17%.

From the CW tests, it was found that after the lengthy solvent flooding, 40% and 34% of the rock surfaces were covered by oil components, hindering SO_4^{2-} ions reactivity towards the carbonate surface. The consequence was that completely water-wet carbonate surfaces in both cases were not obtained.

After the tests, active capillary forces were investigated by SI tests. The cores were flooded with 5 PV of DI water to remove the CW test brines. The cores were then dried, and vacuum-saturated with heptane

without any prior initial water saturation. The SI tests were run at 23 °C with DI as imbibing fluid.

The mildly cleaned core achieved an ultimate recovery of 27 %OOIP. Thus, capillary forces in B11 core had increased after mild cleaning, showing to some extent a more water-wet state. The CW test also showed a slight increase in the water-wet surface area.

The harsh cleaning resulted in a more efficient removal of POC from the chalk surface. With a recovery plateau of 62 %OOIP reached in 5 hours, a very water-wet behavior was displayed [60]. This occurred even though 34% of the rock surface was covered with adsorbed organic material.

The spontaneous imbibition water index, I_{W-SI} , for the mildly cleaned core B11 increased to 0.36, and for the harshly cleaned core B12 the index raised to 0.82, showing major changes in positive capillary forces after the harsh cleaning with toluene and methanol.

From the experimental results it seems that the process of activation or deactivation of capillary forces is not only associated to the water-wet area of the core or by the covered areas with crude oil POCs. From the results it can be deduced that the superficial distribution of the adsorbed POC is crucial. This means that adsorption-desorption processes of POC in pore throats will have a greater influence on the activation-deactivation of capillary forces than when the process occurs onto its pore bodies. In other words, the fluid connectivity from water-wet and oil-wet spots is different due to the different cleaning processes, being B11 less even in terms of water-wet spots in comparison to B12.

SI tests confirmed that extensive toluene-methanol injection removes POC at specific places affecting capillary forces. The consequence of this, is that increased imbibition rates and ultimate oil recovery are achieved, in despite of observing minimum changes in the water-wet surface area quantified by the CW test.

The mild kerosene-heptane core cleaning appears to preserve more adsorbed POC, thus, preserving the initial wettability in a greater degree than the harsh cleaning with toluene and methanol.

3.1.4 Cleaning effect on a second core restoration

The different cleaning methods effects on wettability were compared on a second restoration. The cores B11 and B12 were equally restored for comparison purposes, initial water saturation was established at $S_{wi} = 0.1$ and 5 PV Oil A were flooded in the cores before aging. SI tests at 50 °C were performed using FW as imbibing brine.

The observed crude oil recoveries by SI, were 3 and 12 %OOIP respectively, compared to 8 and 10 %OOIP after the first restoration. The mildly cleaned core behaved this time less water wet than the harshly cleaned core B12. SI water indexes, I_{W-SI} , reduced for core B11 from 0.10 to 0.04 and increased for core B12 from 0.13 to 0.16.

Thus, further crude oil POC adsorption on a mixed wet core appears to reduce its original water-wetness degree. Effects on crude oil exposure and had been previously reported on carbonates [23, 58, 63].

On the other hand, the harshly cleaned core B12 and equally restored, behaved more water wet than core B11,

with a water index, $I_{w-SI} = 0.16$ in comparison to 0.04 for core B11.

In summary, the amount of crude oil exposure and polar components being adsorbed on the carbonate surfaces can significantly affect core wettability in a restoration procedure.

The results suggest that the harsh cleaning with toluene and methanol will remove in a greater extent POC from carbonate mineral surfaces, inducing a significant change in the original wettability towards the water-wet region.

However, it is of high importance to know that the sampled crude oil used in core restoration can be completely different from the one that originally wetted the reservoir as stated by Puntervold (2008).

Thereby, to improve the efficiency of a core restoration protocol to get closer to a representative reservoir wettability it is required to preserve on the mineral surfaces as much as possible of the originally adsorbed crude oil POC. Furthermore, reducing the amount of oil exposed in the restoration process can avoid reducing changing wettability towards a less water-wet state. A general summary of the experimental data is presented below in **Tables 4 and 5**.

Table 4. SI results

Core	Solvent	SI		
		SI-R1 (%OOIP)	SI _{C7-AS*} (%OOIP)	SI-R2 (%OOIP)
B11	K/H	8	27	3
B12	T/M	10	62	12
B13	-	75	-	-

*AS - After-solvent cleaning

Table 5. CW test results summary

Core	Solvent	CW			
		A _w -R1	I _{CW} -R1	A _w -AS*	I _{CW} -AS*
B11	K/H	0.118	0.47	0.150	0.60
B12	T/M	0.124	0.49	0.165	0.66
B13	-	0.251	1	-	-

3.2 Reproducing initial core wettability in mildly cleaned cores

The next section aims to optimize the most important restoration parameters to preserve core wettability. From the previous section it can be concluded that the mild cleaning was more efficient in retaining original POC components on the rock surfaces, and that limiting the amount of kerosene heptane flooded to a minimum injection volume can contribute to preservation of the initial wettability. Another important point is that crude oil should not be flooded extensively, otherwise wettability will also be changed.

For these reasons the proposal for improving the restoration protocol, includes a mild cleaning process with kerosene and heptane. The experimental evidence indicates that by using the mild cleaning method, a minimum amount of oil injected is then required to complete a satisfactory restoration process. As early mentioned, the crude oil available for restoration can significantly differ in composition from the initial oil responsible for generating the original reservoir

wettability. Thus, preserving original POC adsorbed is crucial for achieving a more representative core wettability.

3.2.1 Establishing initial wettability

Four chalk cores were restored with the same procedure, the first two cores were exposed to oil B and the other two to Oil C. The two first chalk cores, B24 and B25, were restored at $S_{wi} = 0.1$ with FW, and flooded with 5 PV of Oil B prior aging. Their initial wettability was quantified by SI at 50 °C, FW was used as imbibing fluid. A CW test was carried out afterwards to verify crude oil adsorption. The oil recovery tests results are shown in **Fig. 4**.

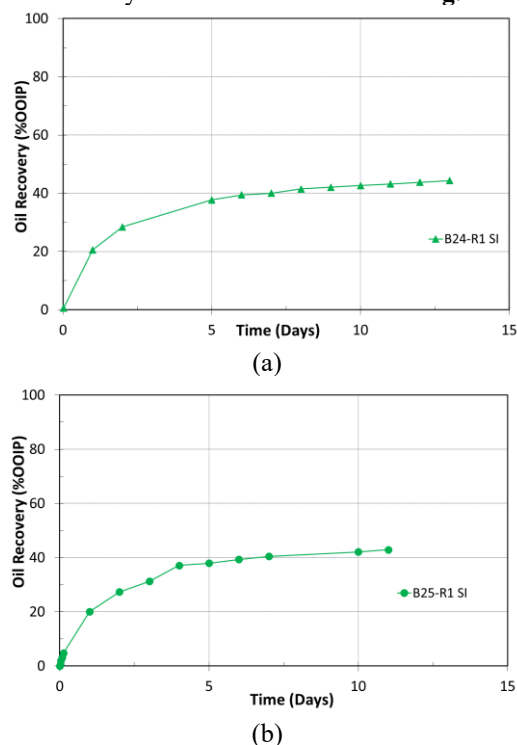


Figure 4. Initial core wetting measured by SI at 50 °C using FW as imbibing fluid (a) Core B24 and (b) core B25. Cores restored with $S_{wi} = 0.1$ (FW) and 5 PV of Oil B prior aging.

Ultimate oil recovery for the core plugs B24 and B25 was reached after 7 to 10 days, with 44 and 43 %OOIP, respectively. Confirming the high reproducibility of the initial core wettability and restoration protocol. The results of the CW tests showed different chromatographic separation areas, $A_w = 0.230$ and $A_w = 0.188$ for B24 and B25 respectively, **Fig. 5**. Please note that both areas were lower than strongly water wet measured areas, $A_{ww} = 0.249$, the results confirm a water-wet surface reduction after oil exposure.

The cores, B26 and B27, were equally restored. However, Oil C with AN=0.50 and BN=0.23 mgKOH/g was used. A higher AN number is meant to reduce the initial core wettability, as reported by Standnes and Austad [25].

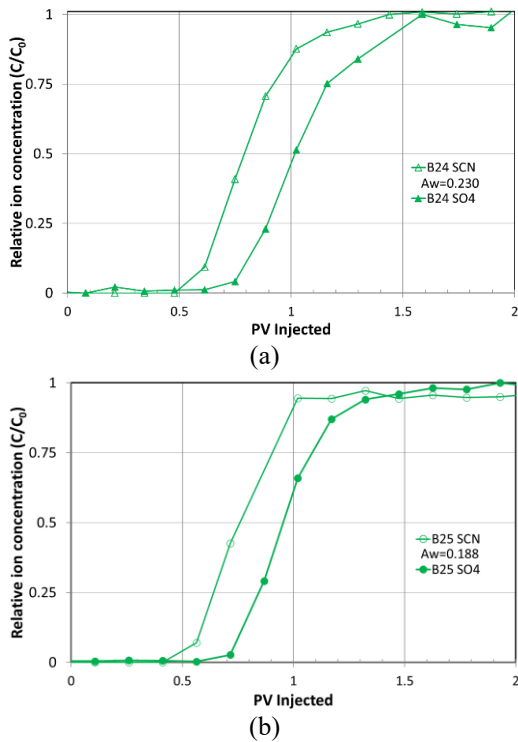


Figure 5. Chromatographic wettability tests (a) Core B24 and (b) core B25. Ultimate recoveries of 25 and 37 (%OOIP) were reached for cores B26 and B27, respectively, **Fig. 6(a-b)**. In this case, core wettabilities were slightly different, even though a general less water-wet state was observed in comparison with the cores that were exposed to Oil B with lower AN, this is in line with the experimental expectations.

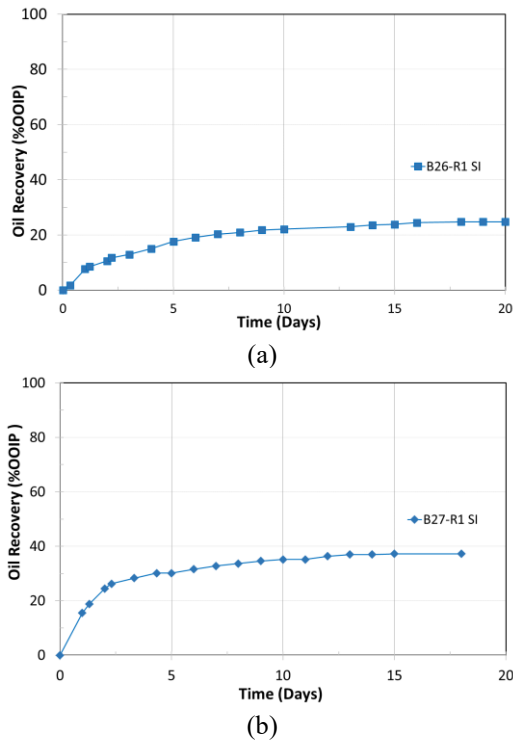


Figure 6. Initial wettability by SI at 50 °C using FW as imbibing fluid. (a) Core B26 and (b) core B27. Cores restored with $S_{wi} = 0.1$ FW and exposed to 5 PV Oil C before aging.

The CW tests showed similar chromatographic separation areas. The measured areas were, $A_w = 0.203$ and $A_w = 0.205$ for B26 and B27, respectively. The quantified water-wet fractions areas were 0.81 and 0.82, which is classified as a water-wet state. The slightly different behavior in cores B26 and B27 can be possible attributed to heterogeneity associated to the core plugs structure, i.e. microfractures or slightly different porous media structure.

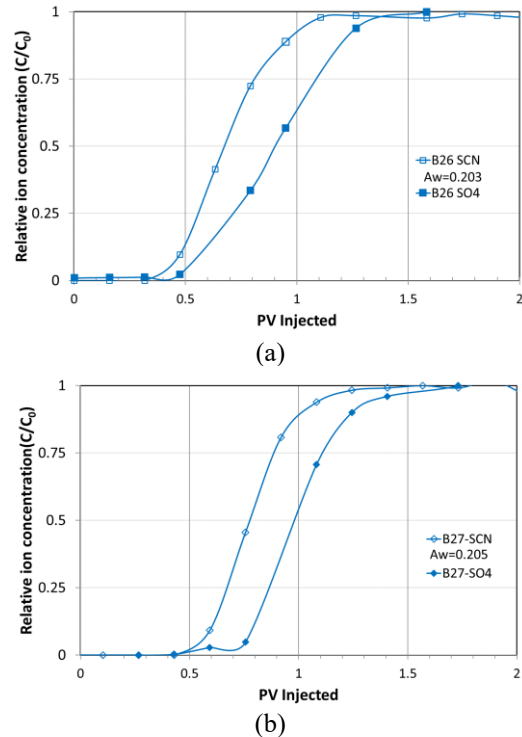


Figure 7. CW tests (a) Core B26 and (b) core B27. All 4 cores exposed oil B or C for 5 PV altered their wettability to a fractional wet state. However, in the cores saturated with oil C differences were observed, these differences can be attributed to pore distribution, microfractures or variation in rock mineralogy and surface reactivity from core to core. In summary, the cores flooded with Oil C with higher AN, were less water-wet than the cores flooded with Oil B.

3.2.2 Optimized core restoration for wettability reproduction at core scale for chalk cores

Mild cleaning preserved more of the adsorbed POC on the mineral surface. Furthermore, the harsh toluene-methanol cleaning has a higher solvation power to remove POC, even at room temperature, the harsh cleaning method removes original polar components from the surface very effectively. As these adsorbed components dictate the original core wetting, one can assume that valuable information is lost by using this method.

In addition, the amount of crude oil injected in the second restoration process had an significant effect on wettability, as reported by Hopkins et al [13].

Taking into account these facts, our proposal to improve the restoration process in chalk cores is based on the following simple assumptions: (1) Mild cleaning is more suitable to preserve wettability, (2) Minimization of the mild solvent floods can help to preserve more

adsorbed POC on the carbonate mineral surfaces, (3) If the POC are preserved during cleaning, a minimum amount of crude oil should be required for an optimum core restoration.

To test these ideas, the four initially restored outcrop cores from block 2 (B24-B27) were subjected to the following second restoration procedure (R2):

1. The cores will undergo a mild solvent cleaning with kerosene and heptane. A limited amount of kerosene (10PV) is injected; in the same way only 5 PV of heptane are used. This step is followed by 5 PV of distilled water to evacuate the resident solvents, then the cores are dried until achieving constant weight.
2. Establishment of initial water saturation, in this case, $S_{wi} = 0.1$, with FW by using the desiccator technique.
3. Once initial water saturation is established, the core is vacuum-saturated at $S_{wi} = 0.1$, with $(1 - S_{wi})$ PV of the same crude oil used in the prior restoration.
4. The core is aged at the test temperature for 2 weeks.
5. Spontaneous imbibition test is carried out with FW in the same temperature conditions as before (50 °C).

The spontaneous imbibition results of the first and second restoration using the mild cleaning with limited solvent injection and minimum crude oil exposure are presented in **Fig. 8**.

The oil recovery displayed in the SI tests, showed minimum differences between the first and second restoration with the proposed cleaning and restoration method, ΔSI , ranged between + 1.5 to + 3.6 %OOIP. The water-wetness degree was measured using the wettability water index based on spontaneous imbibition, I_{W-SI} , **Eq. 2**.

Cores B24 and B25 saturated with Oil B were quite similar, with a 44.4 % for B24 and 42.9 %OOIP for B25. Both resulted in similar water indexes, I_{W-SI} , of 0.63 and 0.61 respectively. After the optimized cleaning and restoration procedures, for both cores the oil recovery slightly increased and the water indexes, I_{W-SI} , obtained were of 0.68 and 0.67 respectively.

For the cores exposed to Oil C, ultimate recoveries were 24.7 for B26 and 37.2 %OOIP for B27. Such differences were attributed to porous media heterogeneity. Despite the differences observed, the second restorations (R2) reproduced closely the initial wetting before cleaning, confirming that the strategy of cleaning and restoration for chalk cores is relatively effective. Core B26 slightly increased its water index by SI, I_{W-SI} , from 0.35 to 0.40, whereas core B27 water index, I_{W-SI} , had a minor drop from 0.53 to 0.51.

To validate the idea that suggests that an increased oil exposure reduces the cores water-wetness. A core was exposed to 5 PV of Oil B instead of 0.9 PV or $(1 - S_{wi})$ PV during the second restoration after a mild cleaning process with 10 PV of kerosene and 5 PV of heptane.

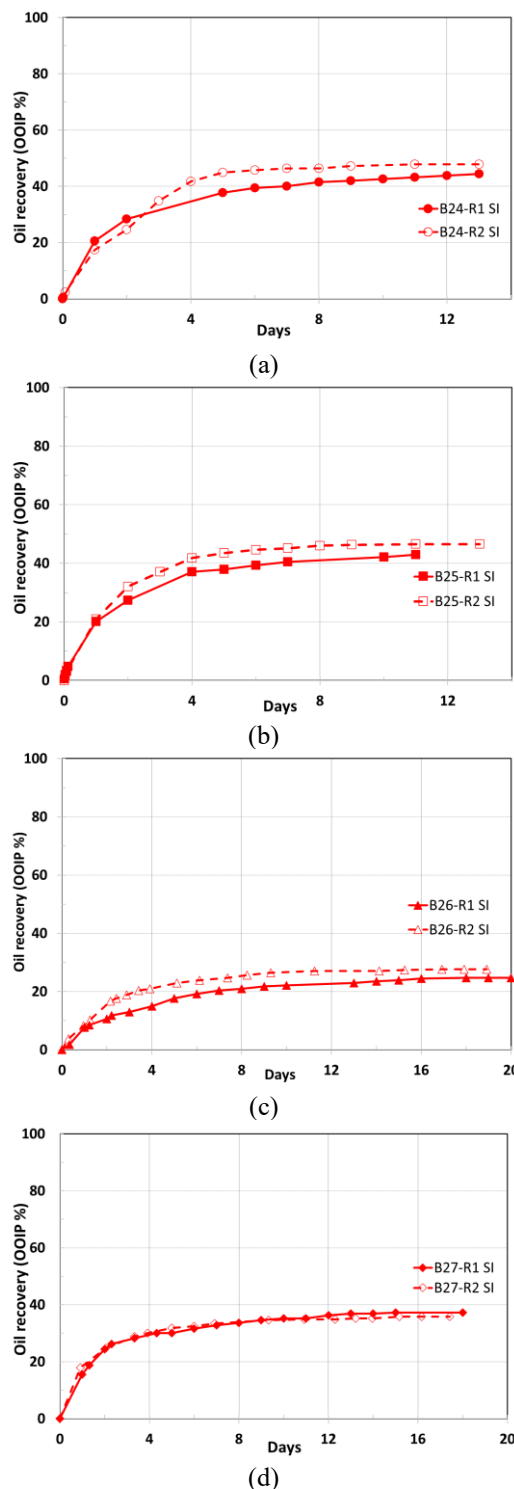


Figure 8. Oil recovery experiments by SI, $T_{tests} = 50$ °C after initial restoration (R1) and a second restoration (R2) after optimized cleaning and restoration process. Cores restored with $S_{wi} = 0.1$. (a) Core B24 and (b) Core B25 exposed to Oil B (AN = 0.36 mgKOH/g). (c) Core B26 and (d) Core B27 exposed to Oil C (AN = 0.5 mgKOH/g).

Thus, the cleaning and restoration processes were equal to the rest of the cores. In **Fig. 9**, oil recovery by SI tests after R1 and R2 were compared. SI from the initially restored core (R1) gave a recovery of 41.5 %OOIP, which was similar to the recoveries observed from cores B24 and

B25 in their first restoration. Cores B24, B25 and B29 were saturated with Oil B.

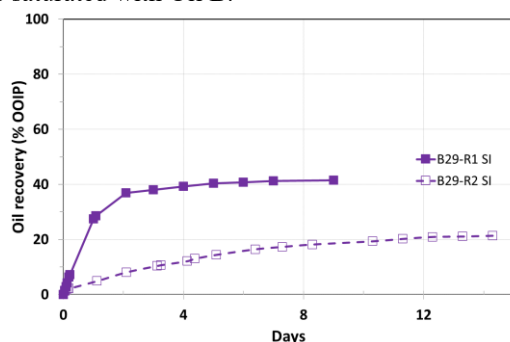


Figure 9. SI tests performed at 50 °C after the initial restoration (R1) and the second restoration (R2) of core B29. During R1 the core was exposed to 5 PV Oil B with AN = 0.36 mgKOH/g. After mild cleaning the core was exposed to another 5 PV of Oil B in R2.

After the mild cleaning with kerosene and heptane, core B29 was restored in a second restoration (R2) with $S_{wi} = 10\%$, and 5 PV of Oil B. Ultimate oil recovery was reduced to 21.0 %OOIP after the second restoration. This represents a significant reduction of 20.5% OOIP, the result confirms a significant drop in the water-wetness of the core due to the increased exposure to Oil B in the second restoration. The water wetting index by SI, I_{W-SI} , dropped from 0.59 to 0.30. The results confirmed the results obtained by Hopkins et al [13].

A summary of SI and CW data before and after mild core cleaning is presented in **Tables 6-7**.

Table 6. Data summary after initial (R1)

Core	SI_{R1} %OOIP	I_{W-SI}	I_{CW-R1}
B24	44.4	0.63	0.92
B25	42.9	0.61	0.75
B26	24.7	0.35	0.81
B27	37.2	0.53	0.82
B28	70.0	1.0	1.0
B29	41.5	0.59	-

Table 7. Data summary after second core restorations (R2) and changes in recovery and wettability in relation to (R1).

Core	SI_{R2} %OOIP	I_{W-SI}	ΔSI %OOIP	ΔI_{W-SI}
B24	47.8	0.68	+ 3.5	+ 0.05
B25	46.6	0.67	+ 3.6	+ 0.05
B26	27.7	0.40	+ 3.0	+ 0.04
B27	35.8	0.51	+ 1.5	+ 0.02
B28	-	-	-	-
B29	21.0	0.30	- 20.5	- 0.29

4 Conclusion

This study compared the effect of two solvent cleaning methods on initially water wet chalk cores exposed to crude oil. The solvent systems studied were harsh cleaning with toluene and methanol, and a mild cleaning method with kerosene and heptane. The effects on wettability were measured by spontaneous imbibition and chromatographic wettability tests.

Oil recovery and capillary forces increased after cleaning the chalk cores with both systems. The harsh cleaning method resulted in higher ultimate oil recoveries than the mild cleaning. Thus, the toluene and methanol system appeared to have a greater solvation effect on the adsorbed POC on the chalk mineral surfaces.

The results suggested that the distribution of adsorbed POC on mineral surfaces is crucial in the activation or deactivation of capillary forces. Apparently, POC adsorbed at pore throats will have a greater impact on wettability than POC adsorbed onto pore bodies. Increased oil recovery together with highly efficient positive capillary forces were observed, even though minor changes were observed in the water-wet fraction measured by the CW tests. The combination of both spontaneous imbibition tests and chromatographic wettability experiments was crucial for this observation.

An injection of 5 PV of crude oil into a mildly cleaned core, showed reduced ultimate oil recovery compared to the first restoration. This effect did not allow the desired wettability reproduction to occur.

Reproduction of initial wettability after mild cleaning was successfully achieved by injecting $(1-S_{wi})$ PV of crude oil by vacuum-saturation. SI tests at 50 °C resulted in an adequate match between the oil production profiles before and after using the optimized cleaning and restoration procedure. Differences of +1.5 - 3.6% OOIP were observed.

Minimizing solvent injection by kerosene and heptane reduced POC desorption from mineral surfaces that established the initial core wettability. In consequence the crude oil required to restore and reproduce the chalk cores wettability was reduced to $(1-S_{wi})$ PV.

The suggested cleaning and restoration procedure could potentially help to get closer to reservoir wettability in carbonate cores with similar mineralogy as chalk. The method can have a positive impact for wettability dependent SCAL analyses, which is critical for reservoir characterization studies.

Acknowledgements

The authors acknowledge the University of Stavanger, the Research Council of Norway, the Erasmus+ student exchange program, the students Hae Sol Yang, and Magnus Sundby Kinn for their experimental input. BP and the industry partners of the National IOR Centre of Norway, ConocoPhillips Skandinavia AS, Aker BP ASA, Vår Energi AS, Equinor ASA, Neptune Energy Norge AS, Lundin Norway AS, Halliburton AS, Schlumberger Norge AS, and Wintershall DEA for financial support.

Nomenclature

- AN Acid Number, mg KOH/g
- ASTM American Society for Testing and Materials
- A_w Water-wet surface area of a core sample, from chromatographic test
- A_{ww} Water-wet surface area of a completely water-wet reference core sample
- BN Base number, mg KOH/g
- C/Co Relative concentration of ion in effluent fractions
- C_7 Heptane
- DI Deionized water
- FW Formation water
- H Heptane
- I_{CW} The fraction of water-wet surface area of a core sample
- K Kerosene

▪ L	Core length
▪ M	Methanol
▪ mM	milli-Molar (10 mol ⁻³ /L)
▪ OOIP	Original oil in place
▪ PV	Pore volume, mL
▪ R-COO ⁻	Carboxylate
▪ SCAL	Special core analysis
▪ SK	Stevens Klint
▪ S _{orw}	Residual oil saturation after waterflood
▪ S _{wi}	Initial water saturation, % PV
▪ SW0T	Sea water without thiocyanate tracer and sulphate
▪ SW½T	Seawater that contains thiocyanate tracer and sulphate
▪ T	Toluene
▪ TDS	Total Dissolved Salt, mg/L
▪ Φ	Core Porosity
▪ Ø	Diameter
▪ ρ _{sat}	Density of saturation fluid, g/cm ³
▪ μ	Dynamic viscosity, mPa.s

References

- Khishvand, M., A.H. Alizadeh, and M. Piri, In-situ characterization of wettability and pore-scale displacements during two- and three-phase flow in natural porous media. *Advances in Water Resources*, (2016). **97**: p. 279-298.
- Cockcroft, P.J., D.R. Guise, and I.D. Waworuntu, *The Effect of Wettability on Estimation of Reserves*, in *SPE Asia-Pacific Conference*. (1989), Society of Petroleum Engineers: Sydney, Australia. p. 10.
- Alhammadi, A.M., et al., *In situ Wettability Measurement in a Carbonate Reservoir Rock at High Temperature and Pressure*, in *Abu Dhabi International Petroleum Exhibition & Conference*. (2017), Society of Petroleum Engineers: Abu Dhabi, UAE. p. 13.
- Al-Hilali, M.M., et al., *A Novel Evaluation of In-Situ Wettability in IRAQI Oil Fields; Case Studies*, in *SPE Russian Petroleum Technology Conference and Exhibition*. (2016), Society of Petroleum Engineers: Moscow, Russia. p. 14.
- Maas, J., et al., *Advanced Core Measurements "Best Practices" for Low Reservoir Quality Chalk*, in *JCR-7 LRQC Best Practices Manual 1st Edition*, SCA, Editor. (2014).
- McPhee, C., J. Reed, and I. Zubizarreta, *Core analysis: a best practice guide*. *Developments in Petroleum Science* ed. J. Cubitt. **Vol. 64**. (2015), Amsterdam, Netherlands: Elsevier.
- Anderson, W.G., *Wettability literature survey- part 1: rock/oil/brine interactions and the effects of core handling on wettability*. *Journal of Petroleum Technology*, (1986). **38**(10): p. 1125-1144.
- Wendell, D.J., W.G. Anderson, and J.D. Meyers, *Restored-State Core Analysis for the Hutton Reservoir*. *SPE Formation Evaluation*, (1987). **2**(04): p. 509-517.
- Soltani, P., et al., *Quantitative Monitoring of Cleaning Time and Wettability Alteration of Carbonate Rocks During Soxhlet Cleaning*. *SPE Reservoir Evaluation & Engineering*, (2019). **22**(04): p. 1334-1345.
- Cuiec, L.E., *Restoration of the natural state of core samples - SPE 5634*, in *The 50th annual fall meeting of the Society of Petroleum Engineers of AIME*. (1975): Dallas, TX, USA.
- Kovalev, K., et al., *Aged Carbonate Cores Wettability Verification*, in *SPE Russian Petroleum Technology Conference and Exhibition*. (2016), Society of Petroleum Engineers: Moscow, Russia. p. 18.
- Shariatpanahi, S.F., et al., *Wettability restoration of limestone cores using core material from the aqueous zone*. *Petroleum Science and Technology*, (2012). **30**(1-9).
- Hopkins, P.A., et al., *Crude Oil Quantity and Its Effect on Chalk Surface Wetting*. *Energy & Fuels*, (2017). **31**(5): p. 4663-4669.
- Fjelde, I., A.V. Omekeh, and M. Wethrus Minde. *Removal of mud components from reservoir sandstone rocks*. in *Symposium of the Society of Core Analysts held in St. John's Newfoundland and Labrador, Canada*. (2015). St. Jhon's Newfoundland and Labrador, Canada.: SCA.
- Puntervold, T., *Waterflooding of carbonate reservoirs - EOR by wettability alteration*. (2008), University of Stavanger, Norway. ISBN 978-82-7644-347-9: PhD Thesis.
- Shimoyama, A. and W.D. Johns, *Formation of alkanes from fatty acids in the presence of CaCO₃*. *Geochimica et Cosmochimica Acta*, (1972). **36**(1): p. 87-91.
- Shimoyama, A. and W.D. Johns, *Catalytic Conversion of Fatty Acids to Petroleum-like Paraffins and their Maturation*. *Nature Physical Science*, (1971). **232**(33): p. 140-144.
- Hopkins, P., et al., *Adsorption of acidic crude oil components onto outcrop chalk at different wetting conditions during both dynamic adsorption and aging processes*. *Energy & Fuels*, (2016). **30**(9): p. 7229-7235.
- Guo, H., et al., *Review of capillary number in chemical enhanced oil Recovery*, in *Paper SPE 175172 presented at the 2015 Oil and Gas Show and Conference*, SPE, Editor. (2015), Society of Petroleum Engineers: Mishref, Kuwait.
- Abeyinghe, K.P., I. Fjelde, and A. Lohne, *Dependency of remaining oil saturation on wettability and capillary number in Paper SPE-160883 presented at the 2012 SPE Technical symposium and Exhibition*. (2012), Society of Petroleum Engineers: Al-Khobar, Saudi Arabia.
- Fulcher, R.A., Jr., T. Ertekin, and C.D. Stahl, *Effect of capillary number and its constituents on two-phase relative permeability curves*. *Journal of Petroleum Technology*, (1985). **37**(2): p. 249-260.
- Mjos, J.E.S., et al., *Effect of Initial Wetting on Smart Water Potential in Carbonates*, in *Paper presented at the 2018 SPE EOR Conference at Oil and Gas West Asia*. (2018), Society of Petroleum Engineers: Muscat, Oman. p. 13.
- Klewiah, I., et al., *Adsorption of Crude Oil Polar Components onto Silica-Rich Chalk and its Impact on Wetting*, in *SPE Norway One Day Seminar*. (2019), Society of Petroleum Engineers: Bergen, Norway. p. 15.
- Zhang, P. and T. Austad, *The relative effects of acid number and temperature on chalk wettability*, in *Paper SPE 92999 presented at the SPE International Symposium on Oilfield Chemistry*. (2005), Society of Petroleum Engineers (SPE), Richardson, TX 75083-3836, United States: Houston, TX, USA. p. 185-191.
- Standnes, D.C. and T. Austad, *Wettability alteration in chalk. 1. Preparation of core material and oil properties*. *Journal of Petroleum Science and Engineering*, (2000). **28**(3): p. 111-121.
- Madsen, L. and I. Lind, *Adsorption of Carboxylic Acids on Reservoir Minerals From Organic and Aqueous Phase*. *SPE Reservoir Evaluation & Engineering*, (1998). **1**(01): p. 47-51.
- Graue, A., B.G. Viksund, and B.A. Baldwin, *Reproducible Wettability Alteration of Low-Permeable Outcrop Chalk*. *SPE Reservoir Evaluation & Engineering*, (1999). **2**(02): p. 134-140.
- Standal, S., et al., *Effect of polar organic components on wettability as studied by adsorption and contact angles*. *Journal of Petroleum Science and Engineering*, (1999). **24**(2): p. 131-144.
- Madsen, L., et al., *Adsorption of polar aromatic hydrocarbons on synthetic calcite*. *Organic Geochemistry*, (1996). **24**(12): p. 1151-1155.
- Karoussi, O., et al., *AFM study of calcite surface exposed to stearic and heptanoic acids*. *Colloids and Surfaces A: Physicochemical and Engineering Aspects*, (2008). **325**(3): p. 107-114.
- Puntervold, T., S. Strand, and T. Austad, *Water flooding of carbonate reservoirs: effects of a model base and natural crude oil bases on chalk wettability*. *Energy & Fuels*, (2007). **21**(3): p. 1606-1616.
- Masalmeh, S.K. and X.D. Jing, *Improved characterisation and modelling of carbonate reservoirs for predicting waterflood performance*, in *Paper IPTC 11722 presented at the International Petroleum Technology Conference*. (2007): Dubai U.A.E.
- Agbalaka, C.C., et al., *Coreflooding studies to evaluate the impact of salinity and wettability on oil recovery efficiency*. *Transport in Porous Media*, (2009). **76**(1): p. 77-94.
- Austad, T., et al., *New method to clean carbonate reservoir cores by seawater*, in *Paper SCA2008-15 presented at the International Symposium of the Society of Core Analysts*. (2008): Abu Dhabi, U.A.E.
- Strand, S., D.C. Standnes, and T. Austad, *New wettability test for chalk based on chromatographic separation of SCN⁻ and SO₄²⁻*. *Journal of Petroleum Science and Engineering*, (2006). **52**: p. 187-197.

36. Austad, T., et al., *Seawater as IOR Fluid in Fractured Chalk*, in *SPE International Symposium on Oilfield Chemistry*. (2005), Society of Petroleum Engineers: The Woodlands, Texas. p. 10.
37. Austad, T., et al., *Seawater in Chalk: An EOR and Compaction Fluid*. SPE Reservoir Evaluation & Engineering, (2008). **11**(04): p. 648-654.
38. Ravari, R.R., *Water-Based EOR in Limestone by Smart Water*, in *Institute of Petroleum Engineering*. (2011), University of Stavanger, Norway: Stavanger, Norway.
39. Song, J., et al., *Effect of salinity, Mg²⁺ and SO₄²⁻ on "smart water"-induced carbonate wettability alteration in a model oil system*. Journal of Colloid and Interface Science, (2020). **563**: p. 145-155.
40. Al-Shalabi, E.W. and K. Sepehrnoori, *A comprehensive review of low salinity/engineered water injections and their applications in sandstone and carbonate rocks*. Journal of Petroleum Science and Engineering, (2016). **139**: p. 137-161.
41. Tetteh, J.T., et al., *Surface Reactivity Analysis of the Crude Oil–Brine–Limestone Interface for a Comprehensive Understanding of the Low-Salinity Waterflooding Mechanism*. Energy & Fuels, (2020). **34**(3): p. 2739-2756.
42. Bertolino, S.A.R., et al. *Mineralogy, geochemistry and isotope geochemistry to reveal fluid flow process in flooded chalk under long term test conditions for EOR purposes*. in *XV International Clay Conference, Brasil*. (2013).
43. Fabricius, I.L. and M.K. Borre, *Stylolites, porosity, depositional texture, and silicates in chalk facies sediments. Ontong Java Plateau–Gorm and Tyra fields, North Sea*. Sedimentology, (2007). **54**(1): p. 183-205.
44. Hjuler, M.L. and I.L. Fabricius, *Engineering properties of chalk related to diagenetic variations of Upper Cretaceous onshore and offshore chalk in the North Sea area*. Journal of Petroleum Science and Engineering, (2009). **68**(3): p. 151-170.
45. Skovbjerg, L.L., et al., *Nano sized clay detected on chalk particle surfaces*. Geochimica et Cosmochimica Acta, (2012). **99**: p. 57-70.
46. Andersen, P.Ø., et al., *Comparative Study of Five Outcrop Chalks Flooded at Reservoir Conditions: Chemo-mechanical Behaviour and Profiles of Compositional Alteration*. Transport in Porous Media, (2018). **121**(1): p. 135-181.
47. Megawati, M., M.V. Madland, and A. Hiorth, *Mechanical and physical behavior of high-porosity chalks exposed to chemical perturbation*. Journal of Petroleum Science and Engineering, (2015). **133**: p. 313-327.
48. Røgen, B. and I.L. Fabricius, *Influence of clay and silica on permeability and capillary entry pressure of chalk reservoirs in the North Sea*. Petroleum Geoscience, (2002). **8**(3): p. 287-293.
49. Fernø, M.A., et al., *Use of Sulfate for Water Based Enhanced Oil Recovery during Spontaneous Imbibition in Chalk*. Energy & Fuels, (2011). **25**(4): p. 1697-1706.
50. Strand, S., et al., *Wettability of chalk: impact of silica, clay content and mechanical properties*. Petroleum Geoscience, (2007). **13**(1): p. 69-80.
51. Skovbjerg, L.L., et al., *Preferential Adsorption of Hydrocarbons to Nanometer-Sized Clay on Chalk Particle Surfaces*. Energy & Fuels, (2013). **27**(7): p. 3642-3652.
52. Andersson, M.P., et al., *Infrared Spectroscopy and Density Functional Theory Investigation of Calcite, Chalk, and Coccoliths—Do We Observe the Mineral Surface?* The Journal of Physical Chemistry A, (2014). **118**(45): p. 10720-10729.
53. Bovet, N., et al., *Interaction of alcohols with the calcite surface*. Physical Chemistry Chemical Physics, (2015). **17**(5): p. 3490-3496.
54. Frykman, P., *Spatial variability in petrophysical properties in Upper Maastrichtian chalk outcrops at Stevns Klint, Denmark*. Marine and Petroleum Geology, (2001). **18**(10): p. 1041-1062.
55. Fathi, S.J., T. Austad, and S. Strand, *Effect of water-extractable carboxylic acids in crude oil on wettability in carbonates*. Energy & Fuels, (2011). **25**(6): p. 2587-2592.
56. Puntervold, T., S. Strand, and T. Austad, *New method to prepare outcrop chalk cores for wettability and oil recovery studies at low initial water saturation*. Energy & Fuels (2007). **21**(6): p. 3425-3430.
57. Fan, T. and J. Buckley, *Acid number measurements revisited - SPE 99884*. SPE Journal, (2007). **12**(4).
58. Hopkins, P., T. Puntervold, and S. Strand, *Preserving initial core wettability during core restoration of carbonate cores*, in *The International Symposium of the Society of Core Analysts*. (2015): St. John's Newfoundland and Labrador, Canada.
59. Springer, N., U. Korsbech, and H.K. Aage, *Resistivity index measurement without the porous plate: A desaturation technique based on evaporation produces uniform water saturation profiles and more reliable results for tight North Sea chalk*, in *Paper presented at the International Symposium of the Society of Core Analysts* (2003): Pau, France.
60. Anderson, W., *Wettability literature survey- part 2: wettability measurement*. Journal of Petroleum Technology, (1986). **38**(11): p. 1246-1262.
61. Schlumberger *Wettability Oilfield Review: The defining series*, (2016).
62. Austad, T., et al., *Low salinity EOR effects in limestone reservoir cores containing anhydrite: a discussion of the chemical mechanism*. Energy & Fuels, (2015). **29**(11): p. 6903-6911.
63. Konstantinopoulos, M., et al., *Effect of Mineralogy on Initial Wettability and Oil Recovery from Silica-containing Chalk*. (2019). **2019**(1): p. 1-5.

Wireless acquisition for Resistivity Index in Centrifuge – WiRI: A new method to estimate Archie’s Law Parameters

Quentin Danielczick^{1*}, Pierre Faurissoux², and Benjamin Nicot²

¹SeaOwl Energy Service, on behalf of TOTAL S.A Editorial Department, 64000 Pau, France

²TOTAL S.A, CSTJF – Experimentation Interpretation Synthesis Department, 64000 Pau, France

Abstract. During the last decades, computing power, digital techniques and instrumentation have been drastically improved. In the petrophysical field, these technological advances help to improve data quality, reduce costs and experimental time. Water saturation determination is key for the knowledge of hydrocarbon in place. It is often estimated from resistivity measurements using Archie’s equations. Archie’s parameter “n” is calibrated from laboratory measurements. The conventional method, known as Porous Plate technique, is based on resistivity measurements on samples with uniform saturation profiles. This method is time consuming. In a previous paper we proposed a faster method: “Ultra-Fast PcRI” (based on the combination of three techniques: centrifugation, Nuclear Magnetic Resonance Imaging (NMR) and resistivity profiling). This allows the use of a non-uniform profile along a sample to determine the n exponent faster, however it increases the amount of sample handling. Here we present a low-cost and low-handling method to obtain capillary pressure curves and saturation exponent using onboard resistivity measurements in operating centrifuge with wireless communication. The centrifuge is used to generate a saturation profile in the sample. During the rotation, resistivity profile is measured with an “in house” developed multi-electrode equipment and recorded wirelessly. The produced volume is recorded with a camera. Finally, a numerical inversion is applied on the Archie’s equation to obtain the n exponent. This method is applied together with the GIT (Green Imaging Technologies) patented capillary pressure method and therefore provide capillary pressure and resistivity index values in parallel. The numerical treatment needed has been tested and validated on synthetic saturation profiles. Also, it has been successfully tested on outcrop and reservoir samples in gas-water drainage process.

1 Introduction

“Mr Archie’s paper suggests an experimental attack for expanding and improving the interpretation technique of electrical well logging. Any contribution of this nature that increases its effectiveness is of great value to the petroleum industry.” This sentence, pronounced by S. W. Wilcox is written in the discussion section of the famous paper of Gustavus Archie, Electrical Resistivity Log as an Aid in determining Some Reservoir Characteristics [1].

The objective of the proposed method is to contribute to speed-up the evaluation of the Archie’s parameters “m” and “n” in laboratory. These two parameters are required to convert resistivity measurements into saturations and thus, to evaluate hydrocarbon in place. Cementation exponent “m” is easily measured in laboratory by measuring rock resistivity at 100 % brine saturation. Obtaining the saturation exponent “n” consists in plotting the resistivity index (RI) versus water saturation (S_w). Exponent n is the slope of this log-log curve. Historically, the Porous Plate (PP) technique, which assumes a

homogeneous saturation profile along the samples, allows the recording of the resistivity-saturation couple one by one. However, the experimental duration for the achievement of the capillary equilibrium is substantial.

Solutions to accelerate the determination of the n exponent have been proposed by Fleury [2-3], Bona *et al.* [4] and more recently by Faurissoux *et al.* [5]. Our experiences with the latest showed great results, however one of the drawbacks of any imaging-based method is still on: the amount of laboratory handling.

In order to deal with this specific problem, the present paper proposes a low handling and fast method to determine both capillary pressure curve and saturation exponent. This method is intended to be a complementary tool to the existing measurements (such as centrifuge) or to provide a fast n determination (for early log interpretation). Assuming the validity of Archie’s law and the homogeneity of analysed rocks, the entire process takes between few hours and few days in gas-water drainage, from loading rock samples into the centrifuge

* Corresponding author: quentin.danielczick@total.com

up to determining the n exponent and the P_c curve. The WiRI (Wireless Resistivity Index) method consists in acquiring a resistivity profile along a sample during centrifugation and transmitting the data wirelessly to the acquisition system (outside the centrifuge) for real time data treatment.

2 Equipment and procedure set-up

2.1 General description

Experiments were conducted using tailor made equipment coupled with a Beckman J6 centrifuge system. The centrifuge rotor can accommodate up to 4 buckets. The rock samples are loaded into core-holders and inserted into the buckets, as shown in Fig. 1.

The core-holders (adapted to 45 mm length and 30 mm diameter samples) are operating at ambient pressure and temperature. To minimize creep and deformation in the centrifuge, the technology combines a cylinder of Polyether Ether Ketone (PEEK) and a cylinder of stainless steel. Each core holder contains current injection and potential electrodes at the top and bottom of the sample, plus 8 radial electrodes (2 mm thick with 3 mm insulated space between the electrodes). The cylinder in PEEK (in contact with the sample) supports the electrodes and acts as an insulator between them. The stainless-steel cylinder is placed around the peek to perform an axial stress and a mechanical radial clamping to ensure good contact between the sample and the electrodes. This device measures 9 impedances at 1kHz frequency to acquire a resistivity profile along the sample. The 4 contacts resistivity method presented by Garrouch and Sharma [6] is implemented.

All the electrodes are wired to a multiplexer and an antenna located on the rotor (Fig.1). In order to perform a measurement, both power and communication are needed. In this case, the difficulty is the transmission of power and information between rotor and stator. Durand and Lenormand [7] proposed a rotating contact solution. In this work this is achieved with a wireless 5 volts induction system and RFID Reader. This system delivers power to the antenna and allows communication at the same time.

During the experiment, the produced effluents are collected in a tube. A centrifuge camera is used to measure the production volume (V_{prod}) over time. Home-made software (designed with VeePro© software) monitors the wireless impedance and the production.

Note that further developments are ongoing to perform tests at high pressure and temperature.

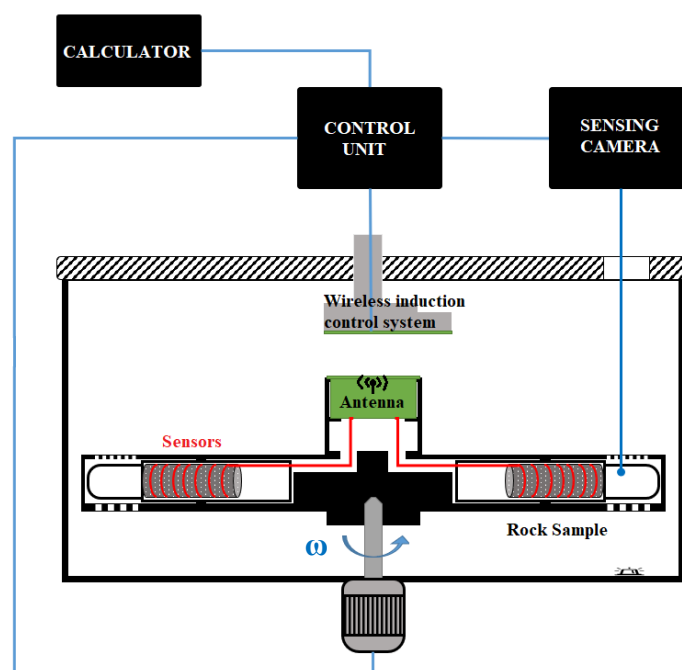


Fig. 1. Wireless Resistivity measurements embedded in centrifuge.

2.2 Rock samples and fluids

Two sample, one Estailades plug and one sandstone reservoir core of 30 mm diameter and 45 mm length are used for the WiRI experiments. In order to characterize the samples, a Conventional Core Analysis program coupled with Nuclear Magnetic Resonance (NMR) imaging was conducted. The Estailades sample was analyzed in a dry and fully saturated (80 g/l NaCl brine) states and the reservoir rock plug was analysed in a fully saturated state (13g/l Formation Water (FW)). Table 1 summarizes the basic properties of the two samples and NMR results are presented in Fig.2.

The study was done on both monomodal and bimodal pore size distribution, respectively for the reservoir rock and the Estailades one, as shown in Fig 2.a with the T2 relaxation time distribution. In addition, a fully saturated NMR profile was performed in order to validate qualitatively the homogeneity of the porosity along the samples (Fig 2.b).

Table 1. Base properties of the analysed samples (20 °C)

Sample	Porosity	Grain Density	K_{klink} perm
Estailades E1	25.7%	1.89 g/cc	200 mD
Reservoir Rock	19.5 %	2.66 g/cc	180 mD

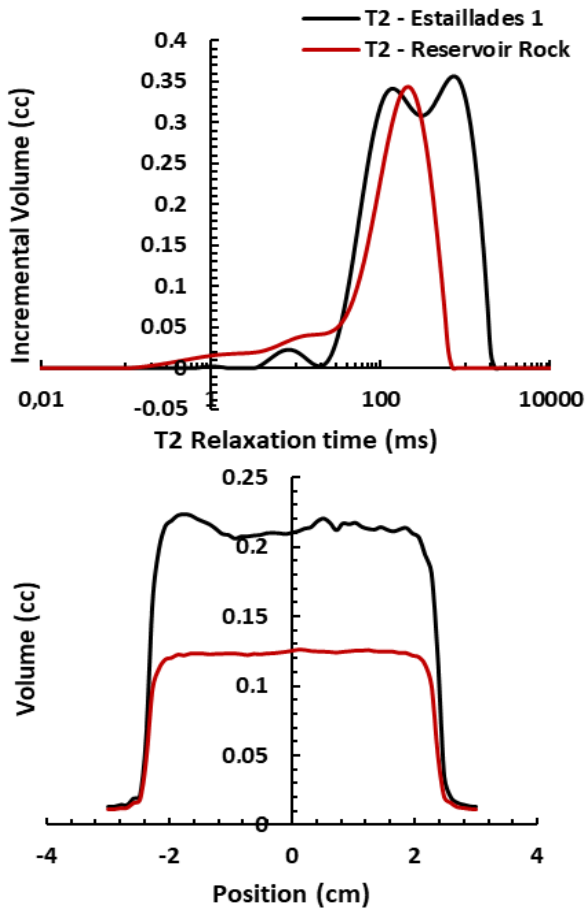


Fig. 2. a- T2 relaxation time b- NMR Volume profile @Sw=100% for Estailades outcrop in black and reservoir rock in red.

Note that in this study, only gas water drainage cycle has been performed. Table 2 summarizes properties of used fluids.

Table 2. Base fluid properties (20 °C)

Sample	Viscosity (cP)	Density (g/cc)
Gas (air)	0.018	0.001
Brine for E1	1.450	1.052
Brine for Reservoir core	1.080	1.007

2.3 Procedure

The experimental protocol for WiRI measurements is presented below. It is important to notice that step 1 to 5 represent conventional characterization, whereas specific WiRI steps begin on step 6.

Sample characterization:

- 1) Clean the core by sequence of toluene and iso-propanol injections; Drying by nitrogen flushing, followed by heating in the oven at 80°C.
- 2) Measure gas permeability and Helium porosity (ϕ).
- 3) Saturate with synthetic brine ($S_w = 100\%$) and determine pore volume (V_p) from weight difference between saturated and dry mass divided by brine density.

Fully saturated properties:

- 4) Determine brine resistivity (R_w) at 20°C.
- 5) Mount the core in the multi-electrode device, and measure resistivity at $S_w=100\%$ (R_0). Verify the resistivity homogeneity. R_0 must have the same value (or at least close ones) for each slice (between pair of electrodes). Resistivity heterogeneity and possible outcomes are discussed in the discussion section.

Determination of primary drainage Capillary Pressure and Resistivity Index (PCRI) curves:

- 6) Spin the core in the centrifuge in drainage mode to enforce a capillary pressure (P_c). V_{prod} will reach a plateau. The process can take several hours up to few days (depending on the permeability of the rock sample and the fluids used for drainage). After the stabilization, the P_c profile induced by centrifuge is calculated using the equation in the Fig.3.

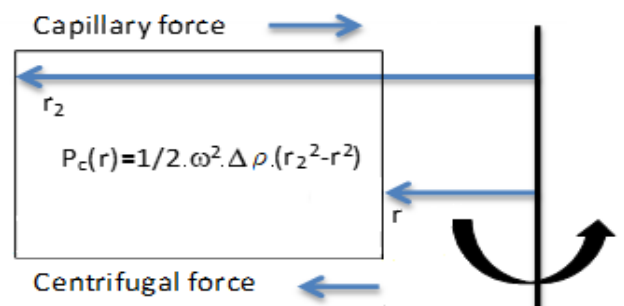


Fig. 3. Capillary Pressure equation for drainage in centrifuge with ω the angular frequency, $\Delta \rho$ the difference between the densities of the fluids, r_2 the maximum radius and r the radius where P_c is calculated. This Figure was introduced by Faurissoux et al. [5]

7) Obtain production volume by the camera and record it across the drainage process. A representation is given on Fig.4 with crosses representing the “end point production” for each step.

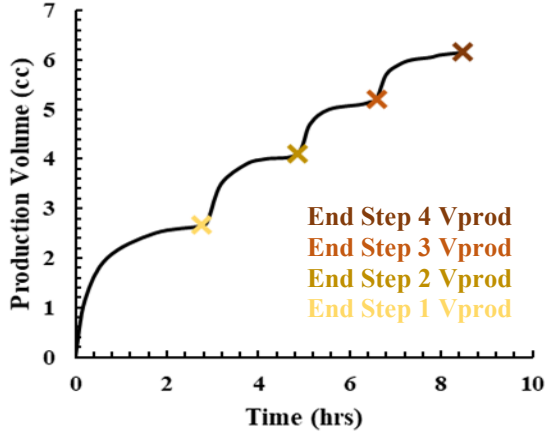


Fig. 4. Schematic representation of Production volume curve.

8) Acquire the resistivity profile (R_t) corresponding to the V_{prod} by the wireless technology. Fig.5 represents multiple R_t profiles measured with the multiple sensors along the sample. The profile resolution is electrode-spacing dependent.

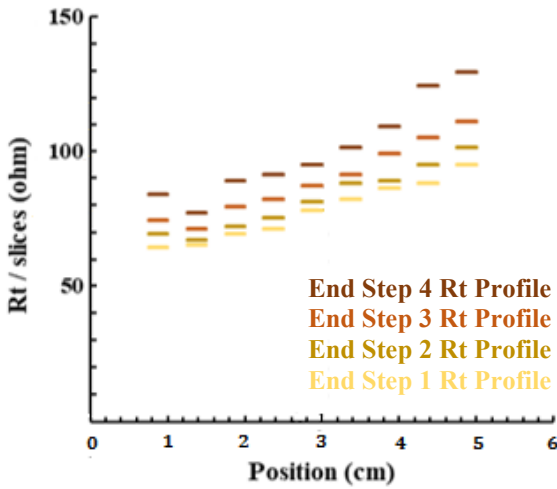


Fig. 5. Schematic representation of Multi-electrode device resistivity measurements in centrifuge.

9) Loop step 6 for next centrifuge speed (and next P_c profile) and iterate to populate multiple end V_{prod} and multiple R_t profiles.

10) Convert Resistivity measurements into Resistivity Indexes (RI) with eq.1

$$RI = \frac{R_t}{R_0} \quad (1)$$

11) Use an optimization process to solve an inverse problem that consists on determining the n exponent only with RI in eq.1 and end V_{prod} of each centrifuge step.

2.4 Optimization problem

In this case, two assumptions are necessary in order to perform the optimization: the sample should be homogenous and must follow the Archie’s Law (eq.2).

$$R_t = \frac{a R_w}{\phi^m S_w^n} \quad (2)$$

Whereas R_w , ϕ and cementation exponent m are determined with conventional methods, the saturation exponent “n” and the S_w profile are determined at the same time by an optimization process and multiple local R_t measurements along the sample.

At each equilibrium stage, water production, “End Step V_{prod} ” (crosses Fig4) is subtracted from V_p (the pore volume) to determine water volumes (V_w) still in place in the samples with eq.3.

$$V_w = V_p - V_{prod} \quad (3)$$

For each centrifuge step, noted j, Archie’s Law is used to build an estimator (eq.4) of the conductive fluid (water) volume inside the rock. This estimator (noted \widehat{V}_w) is dependent on the saturation exponent n and Resistivity Index measured between each slice i. In the eq.4 below, N_{slices} is the number of RI slices (determined by the number of electrodes on the device).

$$\widehat{V}_w(n) = \frac{V_p}{N_{slices}} * \sum_{i=1}^{N_{slices}} \left(\frac{1}{RI_i^n} \right) \quad (4)$$

1) Parameter: Saturation exponent n

The optimization problem consists in finding the n exponent that best fits the measurements. Optimization begins by the initialization of a presumed saturation exponent n.

2) Optimization problem: monodirectional (there is only one parameter (n) to solve this problem). The problem is described by minimising the objective function O – eq. 5

$$O = \sum_{j=1}^{N_{Steps}} [V_{wj} - (\widehat{V}_w(n))]^2 \quad (5)$$

Determining the least squares between our estimator and the measured value is a conventional method to find a solution (it is called identification problem). N_{Steps} represents the number of centrifuge speed steps used to obtain V_{wj} measurements.

3) Optimization interval: $(0; +\infty]$

The formulation of the problem was chosen to define the n exponent as strictly positive.

4) Available methods: derivative free methods or direct methods.

To find the minimum of the objective function, methods based on the calculation of the gradient (derivative methods) or based on direct search methods (such as the bisection method) are used. In both cases, the principle is the evaluation of the objective function for a first “initial guess” of the n value (for example “ $n=2$ ”) and repeat function or gradient evaluations until the minimum is found. Many algorithms to estimate Archie-Parameters as Core Archie-Parameters Estimation – CAPE Model [8] have been developed to minimize the difference between a model and laboratory or well measurements. They could be coupled with our new resistivity acquisition method.

In this work, the Nelder-Mead simplex algorithm described by Lagarias et al. [9] (direct search method) is used to find the minimum of the objective function O . Fig.6 shows the shape of the objective function. An initial guess with a saturation exponent n according to petrophysics will converge to the solution due to absence of local minimums and the quasi-convex behaviour of the function.

In the event of not finding a solution, a meta-heuristic algorithm or hybrid optimization model [10] can be implemented to escape from a “non-convex” part of the function. In the various tests performed, this situation has not been faced.

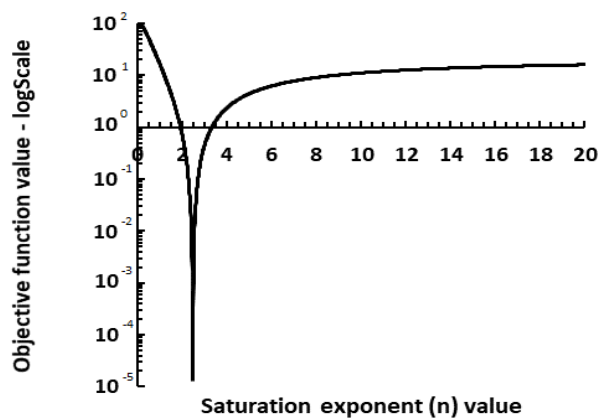


Fig. 6. Objective function shape.

3 Results and Discussion

In order to validate the WiRI method, a two-step approach has been followed. The first step, explained in section 3.1, is a validation of the numerical optimization process. The second one (3.2 – 3.3) presents the results of an entire WiRI measurement process versus a reference method: the PP method. For the PP experiments, most of the advices to maximize data quality from F. Pairoys [11] have been followed.

3.1 WiRI Inversion on UFPCRI Data

Before acquiring WiRI data, the testing of the WiRI inversion is advisable using data coming from the UFPCRI method. Data was acquired on an outcrop sample (25 p.u – 78 mD) in oil water drainage mode.

For the UFPCRI study, Faurissoux *et al.* [5], performed multi-electrode measurements on samples. After each centrifuge step, the sample was removed from the centrifuge for resistivity profile (Keysight E4980A precision LCR meter at 1 V and 1KHz.) and NMR saturation profile measurements.

At each centrifuge speed, the UFPCRI generates a dataset containing:

1. Resistivity profile along the sample
2. Volume produced in the centrifuge
3. NMR saturation profiles

As the WiRI method requires only resistivity profiles and produced volumes at each centrifuge speed, an UFPCRI dataset is used to test the WiRI inversion as first assessment

The first speed of rotation was not correctly chosen (1500 rotation per minutes) and caused more produced volume than desired (i.e. the first data point of S_w is low).

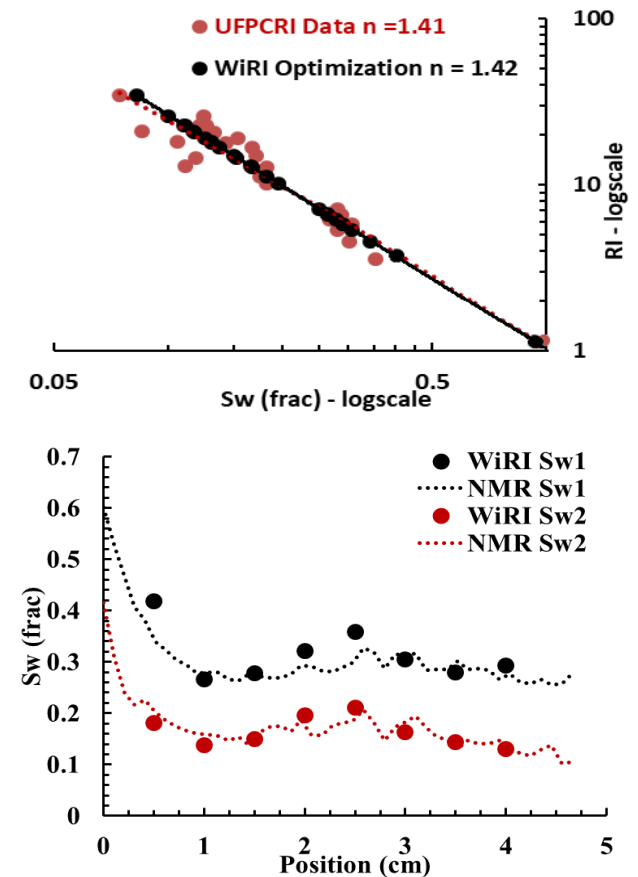


Fig. 7. Comparison between the WiRI and UFPCRI method applied to the same dataset. a- RI/Sw logscale graph for determination of exponent n b- Saturation profiles NMR versus reconstructed profiles with WiRI inversion.

Fig.7.a shows the saturation exponent determined from UFPCRI versus the saturation exponent from WiRI inversion with same RI and V_{prod} . In this case, the WiRI inversion gives an n exponent close to the UFPCRI. With the WiRI method, a single n value is found to fit the entire dataset. As a result, the RI-Sw log-log curve obtained with WiRI is a straight line

WiRI resistivity profiles can be converted into saturation profiles once the optimum n is found. Fig.7.b presents a comparison between the NMR profiles post UFPCRI and WiRI tests, for two different speeds. WiRI saturation profiles have a lower resolution but enable the non-uniform profiles reconstruction along a sample with good consistency with NMR Imaging.

Therefore, the optimization algorithm is considered as accurate.

3.2 WiRI vs PP

The validation of the entire protocol was done as follows: For the Estailades outcrop, the conventionnal Porous Plate technique was performed on the sample at ambient conditions in gas water drainage mode. Then, an entire sequence of WiRI was conducted on the same sample (after cleaning, drying and resaturating it with the same brine).

Comparisons between the results obtained with the two methods are shown in Fig.8 and 9. For the WiRI experiment, P_c curve was reconstructed with the method proposed by Green et al. [12] and the S_w calculated from the inversion. The main difference between these two experiments is the time required for obtaining the results: 42 days with PP technique versus 28 hours (including handling) with our new method.

The observations are:

- 1) IR/S_w log-log curves are very close as well as the n exponent.
- 2) P_c/S_w shows good consistency (PP was aborted too early due to a failure of the control system).
- 3) WiRI experiment was quick to set up and the results were interpreted in a short time.

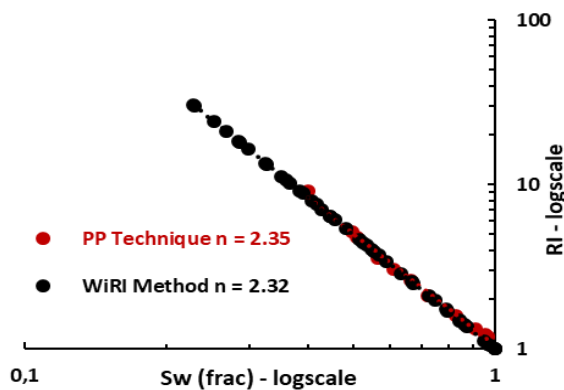


Fig. 8. Resistivity Index Vs Saturation (logscale) comparison between PP experiment and WiRI.

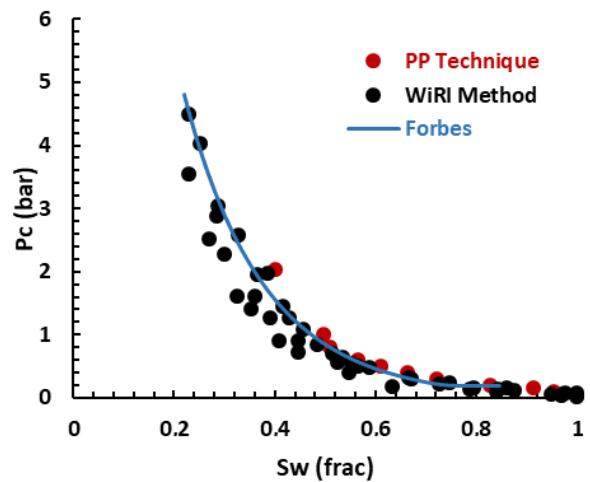


Fig. 9. P_c/S_w curve corresponding to PP technique, WiRI and Forbes curve from Cydar© simulation with centrifuge data.

3.3 WiRI on real case – Reservoir Core

The WiRI method was applied on twin reservoir sandstone samples, so extracted from the same core and at the same depth. Full core CT scan enabled the selection of an homogeneous zone to extract the samples. Both plugs were cleaned, dried and saturated with formation water. For the first plug, (38 mm diameter and 25 mm length) the PP technique was performed. For the second plug (30mm diameter and 45 mm length) the complete WiRI sequence was accomplished. The results of the two gas-water drainage experiments are shown in Fig.10 and 11.

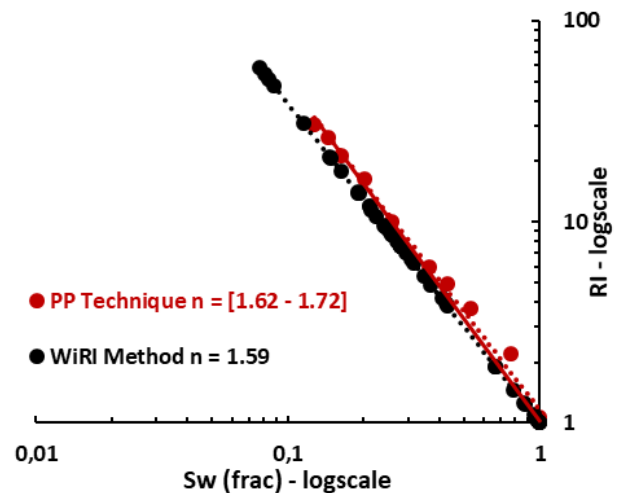


Fig. 10. Resistivity Index vs Saturation (logscale) comparison between PP and WiRI for a reservoir sandstone sample.

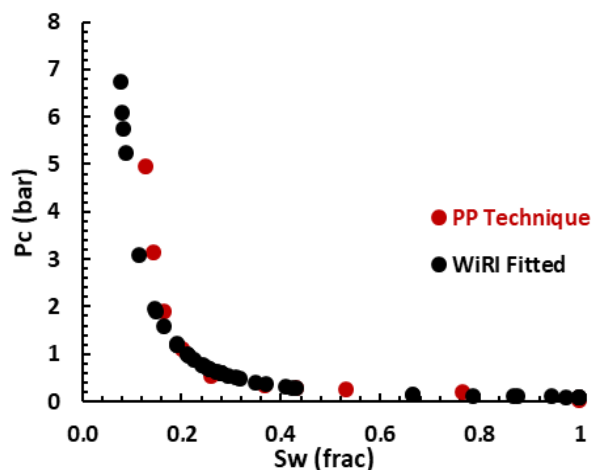


Fig. 11. P_c/S_w curve corresponding to PP technique and WiRI method on reservoir sample.

In Fig.10, the Porous Plate technique gave results subject to interpretation. First, the curvature of RI at high S_w may well be explained by a moving shock front [13]. Second, PP data is subject to measurement uncertainties. Consequently, the n exponent obtained with the PP technique was found to be between 1.62 (red dotted line) and 1.72 (red continuous line). With WiRI, $n = 1.59$. This new method shows expected results, i.e. a determination of n value close to the reference method with a reduced duration and handling. The coherence with the reference method is extended to the capillary pressure curve.

The total duration of the WiRI experimental cycle was 53 hours, compared to the 118 days of experimental duration for the PP method.

These results demonstrate that WiRI provides resistivity and capillary pressure data in the same timeframe as log interpretation. This new tool is designed to provide a quick and simple measurement and data-set. It can be used in the following ways:

- 1) Provide quick additional measurements in centrifuge.
- 2) Use the data acquired to complete a reference method (or to get an idea of the curves trends before starting a long reference method).
- 3) Automate acquisition, interpretation and Archie's parameter determination.

3.4 Electrode spacing – measurements uncertainties

In a centrifuge, the capillary pressure gradient induces a non-uniform saturation profile along the samples. Unfortunately, resistivity measurements are discrete and do not allow representing this continuous profile. It is then obvious that the higher the resistivity resolution, more correct will be the inversion.

- 1) Sensitivity to electrode spacing at zero noise

In this section, a WiRI acquisition is simulated for one hundred thousand samples (with different petrophysical characteristics).

Simulations with different S_w profiles, porosities and n exponents have been performed without noise in the produced water volumes and the R_t values. Each simulation contains the WiRI optimization algorithm presented in section 2.4 for different electrode spacing to determine the n exponent. The Mean Absolute Percentage Error (MAPE) between n_a , the actual fixed n value, and n_f , the forecast value given by the optimization, is evaluated by eq.6 for different electrode spacings. Results are plotted against the electrode spacing on Fig.12. The red point represents the electrode spacing used for our WiRI method.

$$MAPE = 100 * \frac{1}{N_{Sim}} * \sum_{i=1}^{N_{Sim}} \left| \frac{n_a - n_f}{n_a} \right| \quad (6)$$

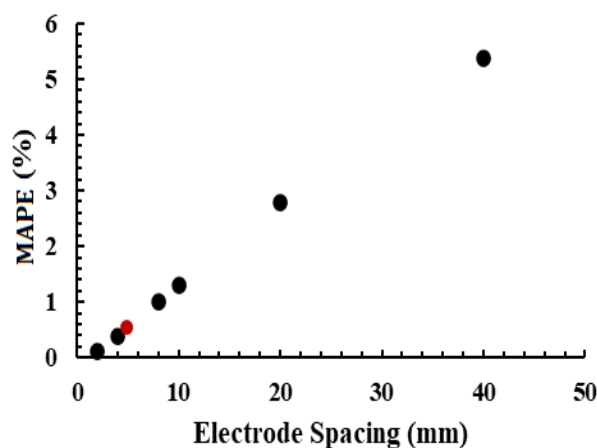


Fig. 12. Impact of the R_t profile resolution on the saturation exponent mean error (evaluation done on 100 000 synthetic profiles). The red point represents the electrode spacing used for our WiRI method.

MAPE decreases linearly with electrode spacing. Below 8 mm spacing, the mean error is less than 1 % of the fixed n value. With our tailor-made technology (detailed in section 2.1), our measurement system ensures that it will not add a measurement error due to spacing greater than 1%.

- 2) Noise impact on measurements and inversion

In this section, one hundred thousand WiRI acquisitions are simulated on the same sample.

In order to evaluate the impact of measurement uncertainties, simulations have been performed with the introduction of a $\pm 5\%$ relative error on R_t and V_w (the measured values in the process). Impact of the electrode spacing, and the number of centrifuge steps are then analysed in Fig.13 with MAPE evaluation and Relative Standard Deviation (RSD or %RSD) defined in eq.7 with \bar{n}_f the mean value of the forecasted n exponents.

$$\%RSD = \frac{100}{\bar{n}_f} * \sqrt{\frac{\sum_{i=1}^{N_{Sim}} (n_f - \bar{n}_f)^2}{N_{Sim} - 1}} \quad (7)$$

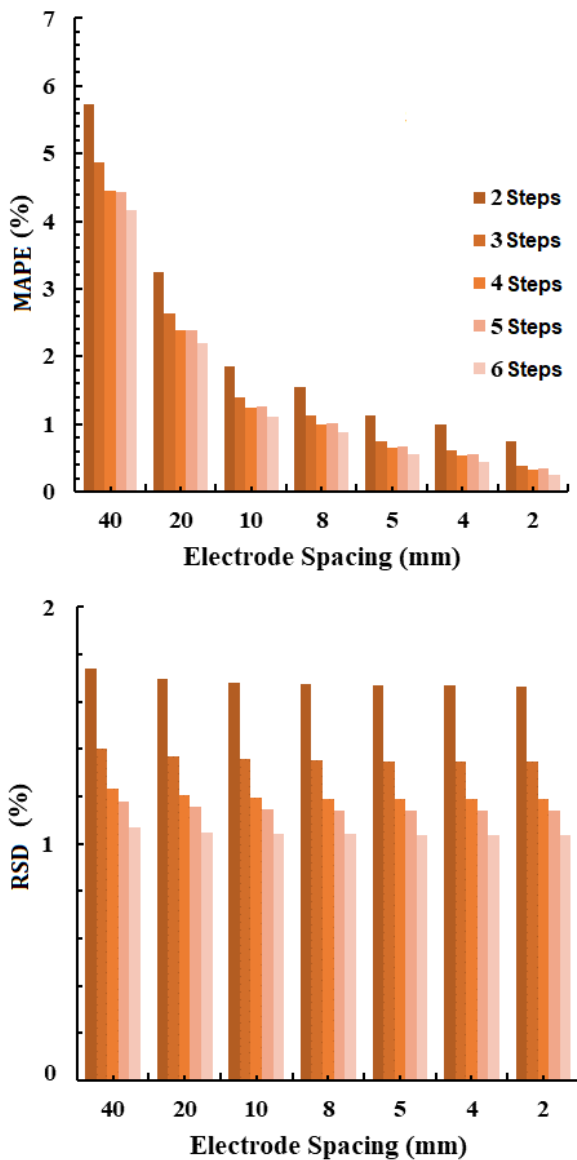


Fig. 13. Impact of centrifuge steps and electrode spacing on optimization process with synthetic data **a-** MAPE (%) evaluation for multiple electrode spacings and multiple speed steps **b-** The corresponding %RSD

As expected, Fig.13. shows that decreasing the electrode spacing improve the MAPE while increasing the number of centrifuge steps improve the %RSD. The lower the electrode spacing the higher the accuracy. The higher the number of centrifuge steps the higher the precision.

Results from this numerical investigation have been considered during our experiments. Electrode spacing is 5 mm and number of centrifuge steps is high enough to minimize standard deviation (between 4 and 6 for each experiment).

3.5 Heterogeneity - Discussion

The WiRI method has two very strong assumptions:

- A uniform porosity profile along the axis of the cylindrical plug

If the sample has heterogeneous pore distribution, it can be early identified qualitatively in the process using NMR, Resistivity profile (R0 profile) at Sw=100% or quantitatively from X-CT [14]. Big differences of R₀ between each slice is a first clue of porosity heterogeneity. In this case, another method will probably be more suitable.

- A uniform Archie n exponent profile along the axis of the cylindrical plug

The presented WiRI process has an objective function for the entire sample, therefore a single value of n is found. However, it is possible to define an objective function for each slice, therefore allowing the determination of n for each slice. Varying values of n in different resistivity slices could give a clue of n exponent heterogeneity. Work is currently ongoing to develop this approach.

Despite the drawbacks above reported, the total duration of WiRI method is so reduced compared to other methods that it is still interesting to finish the process even if heterogeneity is detected. Results could give a first trend or idea of the behaviour of the resistivity with saturation variation, helping the design of more conventional measurements such as PP.

CONCLUSION

The technique presented here is based on wireless transmission of resistivity data during a centrifuge test. For the first time, an experimental method (WiRI) allows the determination of the capillary pressure curve and the saturation exponent n during a multistep centrifuge process. This technique combines the method proposed by Green *et al.* [12] to derive capillary pressure with a novel approach to provide resistivity index wirelessly. WiRI has the advantage of avoiding the porous plate drawbacks (loss of capillary contact, long equilibrium time, risk of leaks) and avoiding extensive handling and interpretation time by the use of numerical optimization.

Numerous simulations have been done to determine and ensure the best experimental conditions for this technique. The obtained results showed good consistency for both outcrops and reservoir core with a satisfying n value determination and P_c curve.

To summarize, the proposed method:

- Simplifies the acquisition and the processing of RI measurements with wireless technology and optimization method.

- Allows the acquisition of additional measurements during centrifuge.
- Is able to deliver fast measurements and interpretation of the PCRI data.

Further work is ongoing to:

- Allow high pressure and temperature experiments.
- Adapt the system for different sample scales.
- Improve the detection and the treatment of heterogeneities during the centrifugation.

ACKNOWLEDGEMENTS

The authors thank Rachel Jorand, Fabrice Pairoys, Regis Brugidou, Ghislain Pujol, Ata Nepesov, Laurent Rochereau and Victor De Oliveira Fernandes for fruitful discussions and technical assistance.

REFERENCES

- [1] Archie, G.E. "The Electrical Resistivity Log as an Aid in Determining Some Reservoir Characteristics." *Trans* 146: 54–62, (1942)
- [2] M. Fleury, "FRIM: A Fast Resistivity Index Measurement Method," in SCA, paper 29, (1998)
- [3] M. Fleury, "Advances in resistivity measurements using the FRIM method at reservoir conditions. Application to carbonates" in SCA, paper 31, (2003)
- [4] N. Bona, E. Rossi and B. Bam, "Ultrafast Determination of Archie and Indonesia m&n Exponents for Electric log Interpretation: a Tight Gas Example," IPTC-17446-MS, (2014)
- [5] P. Faurissoux, A. Colombain, G. Pujol, O. Fraute, B. Nicot, "Ultra Fast Capillary Pressure and Resistivity Index measurements (UFPCRI) combining Centrifugation, NMR Imaging, and resistivity Profiling" in SCA, paper 2, (2017)
- [6] A. Garrouch and M. Sharma, "Techniques for the Measurement of Electrical Properties of Cores in the Frequency Range 10Hz to 10MHz," in SCA, paper 11, (1992)
- [7] C. Durand, R. Lenormand, "Resistivity measurements while centrifuging" in SCA, paper 15, (1997)
- [8] R.E. Maute, SPE, W.D. Lyle, SPE, and Eve S. Sprunt, SPE, Mobil R&D Corp, "Improved Data-Analysis

Method Determines Archie Parameters from Core Data", in SPE-19399-PA, (1992)

[9] Lagarias, J. C., J. A. Reeds, M. H. Wright, and P. E. Wright, "Convergence Properties of the Nelder-Mead Simplex Method in Low Dimensions", in *SIAM Journal of Optimization*, Vol. 9, Number 1, pp. 112–147, (1998)

[10] Jianjun Liu, Honglei Xu, Guoning Wu, and Kok Lay Teo, "A New Hybrid Optimization Algorithm for the Estimation of Archie Parameters", in book - *Optimization Methods, Theory and Application* pp 137-154 Chapter 7, (1998)

[11] F. Pairoys, "Rock Electrical Properties from Porous Plate and Resistivity Experiments: Tips to Maximize Data Quality", in SCA, paper 38, (2018)

[12] D. Green, J. Dick, J. Gardner, B. Balcom and B. Zhou, "Comparison Study of Capillary Pressure Curves Obtained Using Traditional Centrifuge and Magnetic Resonance Imaging Techniques," in SCA, paper 30, (2007)

[13] Jos G. Maas, Niko van der Post, Krijn H. van der Gyp, John G.C. Coenen and Wim J. Looyestijn, "Resistivity Index Measurements Under Weak Capillary Forces", in SCA, paper 18, (2000)

[14] J. G. Maas, N. Springer, A. Hebing, "Defining a sample heterogeneity cut-off value to obtain representative Special Core analysis (SCAL) measurements, in SCA, paper 24, (2019)

Comparing Centrifuge, Steady-State and Semi-Dynamic Methods for Relative Permeability and Capillary Pressure Determination: New Insights

Fabrice Pairoys¹, Cyril Caubit¹, Micah Alexander², and Javier Ramos²

¹TOTAL CSTJF, Pau, France

²Schlumberger Reservoir Laboratories, Houston, United States

Abstract. Relative permeability and capillary pressure are essential parameters for understanding multiphase flow in porous media and scenarios of production in oil or gas reservoirs. There are several experimental methods for determining the relative permeability curves: unsteady-state (USS), steady-state (SS), and semi-dynamic (SD) methods. Each method has advantages and weaknesses. Although the USS approach leads to fast data results, the interpretation neglects the capillary pressure effects and provides a limited amount of data points obtained after breakthrough. The SS method is time consuming but enables covering a wider range of saturation with data points if the test is well designed. The SD method may be more time consuming than the SS method but provides both relative permeability to the injected phase and capillary pressure. The relative permeability to the produced phase is then determined by numerical means. The main objective of this study was to compare the water-oil relative permeability curves obtained from the steady-state and semi-dynamic methods performed at reservoir conditions with live fluids. Carbonate core plugs of same rock type and same properties were selected for this experimental program. The samples were brought to the same irreducible water saturation at a constant brine-oil capillary pressure using a centrifuge before being dynamically aged with live oil. In addition to monitoring the average saturation using material balance (MB), a linear X-ray scanner was used for in-situ saturation monitoring (ISSM) along the core samples. The oil relative permeability from the SD method was simulated with fixed water relative permeability and capillary pressure by history-matching the oil production and the differential pressure signal. Two additional centrifuge tests on twin plug were performed in order to measure imbibition capillary pressure and oil relative permeability at pseudo-reservoir conditions. This comparative study shows that the SD method provides similar capillary pressure and oil relative permeability curves to those obtained by centrifuge methods. Even if all Kr curves are in an acceptable envelop, some differences are observed between SD and SS Kr curves: several investigative leads are given to explain this discrepancy. It is also shown that a better saturation method needs to be implemented, especially when dealing with heterogeneous rocks. While a more robust ISSM method is being tested at TOTAL, the results presented in this paper are very encouraging.

1 Introduction

Relative permeability and capillary pressure are important petrophysical parameters for interpreting fluid flow in reservoirs and for calibrating appropriate reservoir simulation models. They are obtained in the laboratory, separately in most of the cases. The only method able to dynamically measure both parameters on a same test is the semi-dynamic method. This method was first implemented by [1]. By recirculating the produced fluid at constant pressure at the outlet of rock sample, the capillary pressure P_c at the core inlet is directly equal to the differential pressure dP , assuming the outlet capillary pressure is nil. The injected fluid relative permeability $K_{r_{inj}}$ can be obtained from the slope of the injected fluid rate Q_i plotted against the inlet P_c (or dP). The inlet injected phase analytical saturation given by [1] has a

similar form to that of Welge equation. With this method, relationships for relative permeability of the injected phase and capillary pressure are obtained.

Using the semi-dynamic approach, [2] developed a method to provide both positive and negative P_c for drainage and imbibition cycles at ambient conditions, using an ultrasonic method for monitoring the local saturation. Later, the same method was validated and used by [3] to build an integrated petrophysical tool able to determine full P_c curves, resistivity index and end-point relative permeability at reservoir conditions. [4] used the technique for measuring full P_c curves with live fluids at reservoir conditions. Relative permeabilities were derived by history matching of the transient pressures and saturation profiles acquired by X-ray attenuation method. [5] studied the variability in P_c curves due to local heterogeneity using the semi-dynamic method with x-ray

* Corresponding author: fabrice.pairoys@total.com

in situ saturation monitoring. [6] and [7] used the method at reservoir conditions with x-ray saturation monitoring for estimating oil recovery from transition zones. More recently, [8] developed a full petrophysical rock characterization workflow similar to [3] but included the full relative permeability curve, the produced phase relative permeability being derived from the electrical properties or using history match process. Few other studies can be found in the literature, there is not one comparing the semi-dynamic capillary pressure P_c and relative permeability K_r to those obtained from the standard methods, centrifuge and steady-state methods. The aim of the study is to compare data results from all these methods, performed at true reservoir conditions with live fluids (except for centrifuge tests). A 1D linear x-ray scanner was used to monitor the saturation profiles obtained at capillary equilibrium. It is shown that a more robust in situ saturation monitoring method is required to avoid erroneous interpretation, especially for heterogeneous rocks.

2 Background

The steady-state method is well known and accepted in the industry for determining relative permeability, it is not really the case for the semi-dynamic method despite being investigated since the '90s. A description of the method is found in [1]. The main idea is to recirculate the produced fluid at constant pressure at the outlet of the rock while injecting the displacing fluid at several constant rates at the inlet until steady-state condition (no more variation of saturation and differential pressure). In the following, consider an imbibition cycle, water displacing oil.

The method allows obtaining the relative permeability of the injected water phase, K_{rw} , the analytical water saturation, S_w , and the capillary pressure, P_c , at the inlet of the core. It is a unique way of determining both K_r and P_c during a single coreflooding test.

A set of pressure drops, final average saturations and flow rates are required inputs for the method which consists of three steps:

- 1- The capillary pressure at the inlet simply equals the pressure drop (with oil gradient pressure and outlet P_c equal to 0):

$$P_c = dP = P_i(\text{inlet}) - P_o(\text{outlet}) \quad (1)$$

- 2- The relative permeability of water at the inlet of the sample is calculated using Darcy's law:

$$K_{rw} = \frac{\mu_w L}{k_{eo}(S_{wi})A} \frac{dQ_w}{dP_c} \quad (2)$$

The relative permeability to oil K_{ro} , with fixed relative permeability to water and capillary pressure, is then determined by numerical simulation and history match of the oil production volume, V_o , and differential pressure dP

- 3- The oil saturation at the inlet is calculated by differentiating the product of steady-state water Darcy velocity and average oil saturation, leading to the following simplified equation:

$$S_o = \langle S_o \rangle + Q_w \frac{d\langle S_o \rangle}{dQ_w} \quad (3)$$

and

$$S_w = 1 - S_o = 1 - \left(\langle S_o \rangle + Q_w \frac{d\langle S_o \rangle}{dQ_w} \right) \quad (4)$$

Equation 4 can be substituted with a direct measurement of the inlet saturation using in situ saturation monitoring such as x-ray method.

3 Rocks and Fluids

In this study, a tight carbonate rock was selected. Several core plugs were extracted from a same whole core to perform composite stack coreflooding experiments, semi-dynamic and steady-state tests, and also centrifuge tests, with the aim of comparing the methods for K_r and P_c characterization. The core plug selection was based on the degree of heterogeneity of the samples, using CT scan images. All fractured core plugs were discarded.

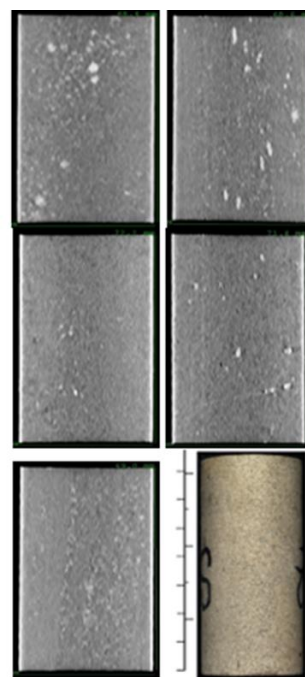


Fig. 1. CT scan images of samples S1/S2 (SDM), S3/S4 (SS), S5 (Centrifuge) and 1 core plug photography of sample S1

There were no miscible tracer tests programmed in this study. However, it is highly recommended to perform these tests to discard the rocks with too high longitudinal heterogeneity (especially for the unsteady-state experiments) but also to compare the degree of heterogeneity from one rock to another one.

XRD was performed on the end-trims to confirm the selected core plugs had the same mineralogy. The clay-free samples represent limestones composed of 90-95% calcite with traces of anhydrite, potassium feldspar and quartz. Before measuring the porosity and permeability, the core plugs were batch-cleaned in Soxhlet using a chloroform/methanol azeotropic mixture and then dried in a convection oven at 116°C. The routine properties were measured at 2000 psi of net confining stress (NCS), representative of the NCS applied during the coreflooding

and centrifuge tests. Table 1 proves that the samples have similar properties.

Table 1. Routine core properties

Plug Id	Test Type	He ϕ (%)	Kg (mD)	Kw (mD)
S1	SD	12.7	1.35	0.75
S2	SD	12.1	1.25	0.51
S3	SS	15.6	2.09	0.92
S4	SS	14.7	1.21	0.63
S5	Pc centri	16.1	1.78	0.66

The core plugs were individually saturated with a 220 kppm synthetic formation brine before being desaturated with dead oil. A recombined oil was also prepared to replace the dead oil before performing the coreflooding experiments with live fluids. Fluid properties at various experimental conditions are listed in Table 2:

Table 2. Fluid properties

	Pp (psig)	T (°C)	ρ_w (g/cc)	ρ_o (g/cc)	μ_w (cP)	μ_o (cP)
SD&SS	3000	100	x	x	0.48	3.17
Centrifuge	0	70	1.12	0.85	0.66	5.45

Both brine and oil were filtered through a 0.1 μ m filter to limit potential plugging issues during the tests (based on MICP pore throat size distribution).

Figure 2 shows pore throat radius going down to 0.05 μ m, highlighting the necessity of the 0.1 μ m fluid filtering process. The distribution looks unimodal but spread along the pore throat radius range. All selected samples have similar pore throat size distributions.

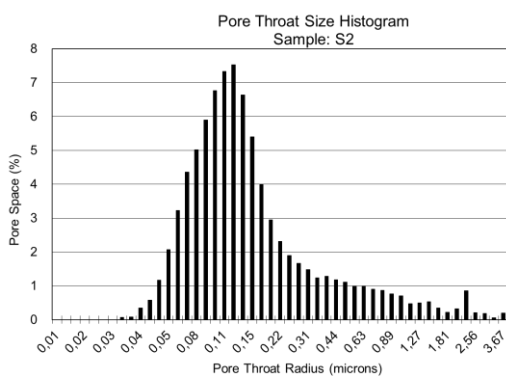


Fig. 2. MICP pore throat size distribution

Figure 3 represents an example of thin section (TS) and Scanning Electron Microscopy (SEM) images from S1 end-trims, confirming a certain degree of heterogeneity.

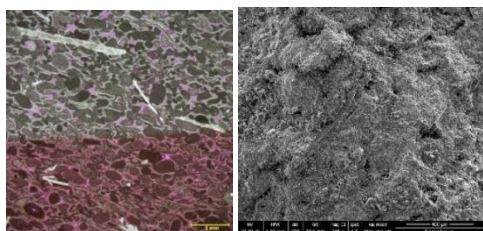


Fig. 3. TS and SEM images

4 Experimental Setups, Conditions and Methodology

The same coreflooding system was used to perform the SD and SS tests (Figure 4):

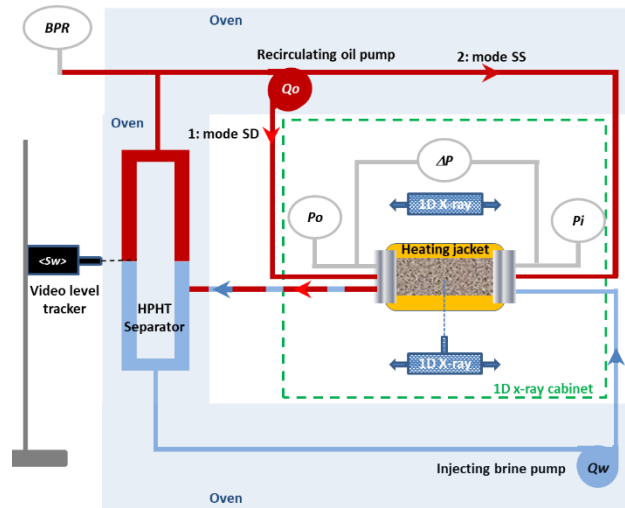


Fig. 4. Schematic of the HPHT coreflooding system

The coreflooding system is composed of a triple-pump system per phase -brine and oil- for injection and recirculation (mode 1 for SD method, mode 2 for SS method), an x-ray transparent core holder with heating jacket in x-ray protective cabinet, a 1D linear x-ray system for measuring saturation profiles, one High Pressure High Temperature (HPHT) video level tracker for material balance monitoring, three differential pressure sensors of different ranges with automatic switches, two -inlet and outlet- pressure transducers, a back pressure regulator with single pump pore pressure control, and one single pump controlling the confining pressure. All measurements are automatically recorded during the tests.

A centrifuge with ability to perform the tests under confining pressure was used to determine multispeed centrifuge Pc and single-step Kro tests. Note it is not possible to perform live oil experiments in a centrifuge (no pore pressure, limited temperature). In the centrifuge tests, NCS of 2000 psi was applied (Table 2).

After the 100% brine saturation under vacuum and applied hydrostatic pressure of 5000 psi, the samples were centrifuged at a constant capillary pressure Pc with dead oil up to irreducible water saturation Swi. To reduce the capillary end-effects, they were flipped to flatten the saturation profile during a second centrifuge step. The samples were then loaded in the x-ray transparent core holders (two composite stacks of two samples) and brought to the reservoir conditions (100 °C of temperature, 3000 psi of pore pressure Pp and 5000 psi of confining pressure Pconf. Samples with the lowest permeability were placed at the outlet of each composite stack. Stack 1 was composed of samples S1 and S2 for the SD test. Stack 2 was composed of samples S3 and S4 for the SS test. Sample S5 was loaded in a Hassler core holder and dynamically aged with dead oil for four weeks. S5 was then measured for effective permeability to oil at

irreducible water saturation, then loaded in a centrifuge core holder for the forced imbibition cycle (without spontaneous imbibition). After cleaning and measuring porosity and permeability properties to ensure the rock was not altered during the centrifuge multistep test and cleaning, the same sample was later aged again and tested for single-step centrifuge desaturation in order to calculate the relative permeability to oil.

Four weeks of dynamic aging was performed to restore the rock wettability. As for S5, the effective oil permeability K_{eo} at S_{wi} on the two stacks (stack 1 for SD and stack 2 for SS tests) was measured prior water flooding.

Table 3. Initial conditions

Test Type	Sample Id	Oil Type	K_{eo} (mD)	S_{wi} (frac.)	X- S_{wi} (frac.)
SD	S1/S2	Live	0.387	0.223	0.224
SS	S3/S4	Live	0.385	0.193	0.188
Centri Pc	S5	Dead	0.216	0.197	x
Centri Kro	S5	Dead	0.196	0.203	x

The design of the SD and SS Kr coreflooding tests and multistep Pc and single-step Kro centrifuge tests was performed using the core analysis software CYDAR, using a first guess of Kr/Pc anticipating a slightly water-wet behaviour based on previous works.

5 Experimental Results

SD results on S1/S2:

Figure 5 represents the differential pressure and the oil production versus time acquired during the SD experiment:

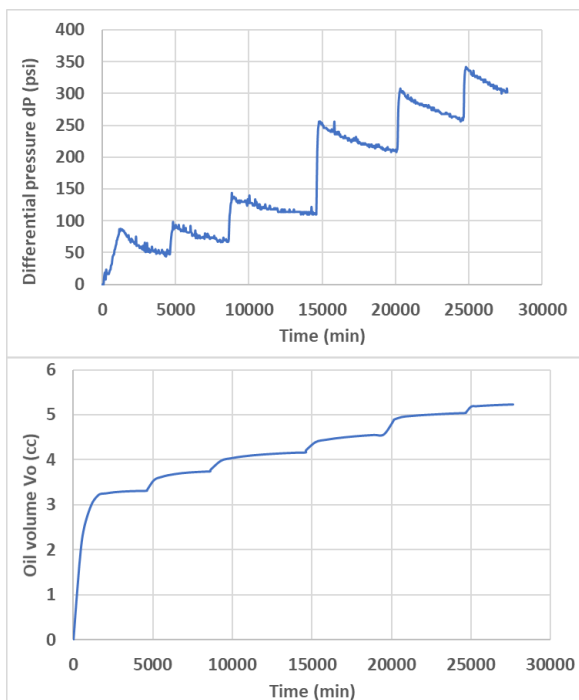


Fig. 5. dP and produced V_o versus time during the SD waterflood

The stabilization criteria were difficult to reach: if the stabilization criterion for oil production (<0.5% PV change in 24hr) was obtained, the dP stabilization was not fully satisfying, leading to a potential slight shift of the resulting Pc curve. Concerning the saturation profiles, the applied stabilization criterion was 10 overlapping and consecutive scans. This criterion was satisfied.

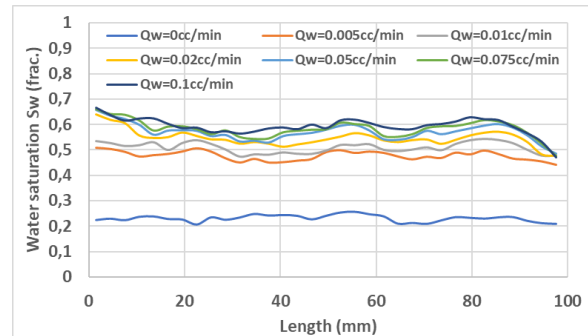


Fig. 6. Saturation profiles at equilibrium

To reduce the error on the counting, a minimum of 10,000 counts was successfully targeted, leading to less than 1% error on the number of transmitted photons (calculation via Poisson's law): it was achieved by applying a counting time per point of 5 seconds, at the specific applied energy.

The experimental design and specification limitations did not allow to obtain saturation profiles well spread on the full saturation range (Figure 6). The average of the water saturation profiles $\langle S_{w,x-ray} \rangle$ obtained from x-ray attenuation technique and average water saturation $\langle S_{w,sep} \rangle$ obtained from material balance using the separator at each stabilized step were found to be very close (<3 saturation units, s.u.), as shown on Figure 7:

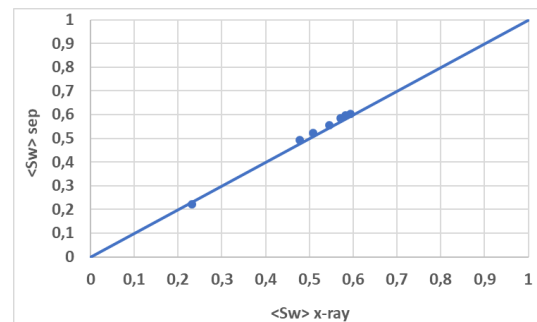


Fig. 7. Comparison between separator $\langle S_w \rangle$ and x-ray $\langle S_w \rangle$ during the SD waterflood

Figure 7 shows the robustness of both methods to acquire averaged saturations. On the other hand, higher discrepancy was observed between the analytical inlet local S_w calculation using Equation 4 and inlet local S_w value from the linear 1D x-ray method:

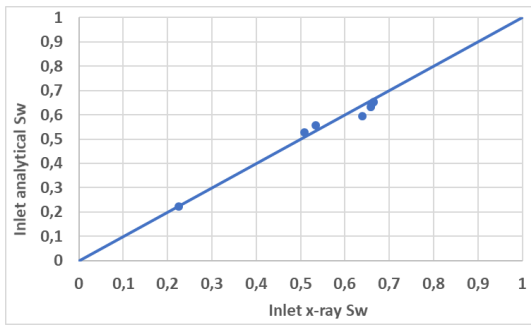


Fig. 8. Comparison between inlet local x-ray and analytical saturations at each equilibrium step

Although the comparative result looks acceptable, a single point of x-ray measurement does not allow to accurately capture the local saturation at the inlet section due to the degree of heterogeneity, the difference going up to 5 s.u. It is highly recommended for future tests to acquire more points on the full inlet section, requiring at least a 2D x-ray acquisition.

Nevertheless, the saturation profiles can help validate the numerical simulations and provide qualitative information on the rock wettability state.

Figure 9 represents the SD relative permeability curves on Cartesian and semi-log scale:

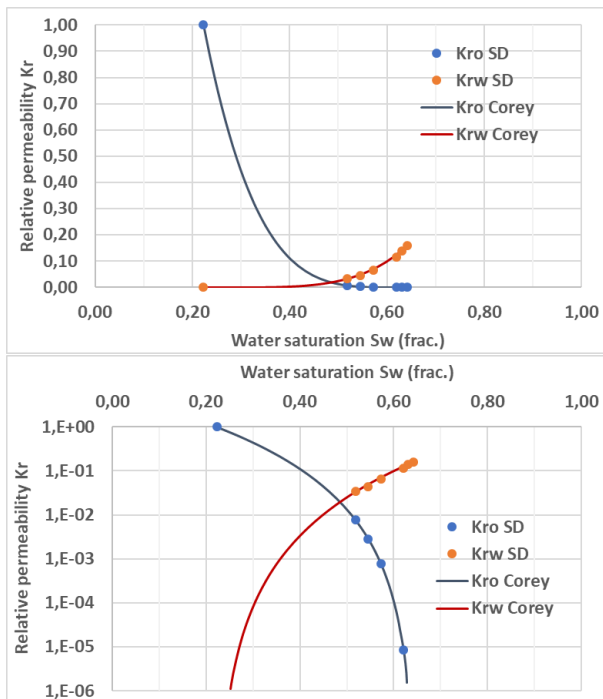


Fig. 9. SD Kr curves (Cartesian and semi-log plots)

Krw was directly obtained using Equation 2 while Kro was obtained by history matching oil production and differential pressure. The Sw values in Figure 9 are the ones analytically calculated using Equation 4, with $\langle S_o \rangle$ calculated using the produced oil volume from the separator. In the simulations, Pc was also entered using measured data points, fitted with a log(beta) function allowing positioning of the saturation Sw at Pc=0: this fitting function was optimized during the history-matching process.

The experimental program could not fully satisfy the CYDAR design due to too low water rate required to obtain Kr data points well spread over the saturation range, as shown in Figure 9. The minimum water rate applied during the test was 0.005 cc/min (lowest limit), the maximum rate was 0.1 cc/min (due to dP limitation).

To best fit the Kr data points, a Corey model was used. The values of the water and oil Corey exponents are:

$$\begin{aligned} N_w &= 4.5 \\ N_o &= 4.0 \\ K_{rw \text{ Max}} &= 0.16 \\ S_{wi} &= 0.224 \\ S_{or} &= 0.346 \end{aligned}$$

The capillary pressure curve was directly obtained from the differential pressure values at each equilibrium, as explained in the background section. Figure 10 represents the measured differential pressure or capillary pressure versus Sw, with the fitting log(Beta) function used for the numerical simulations.

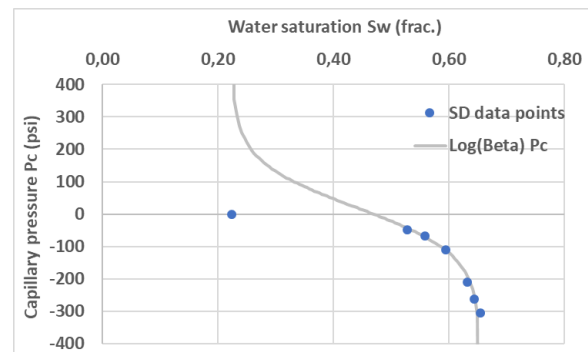


Fig. 10. SD Pc data points and optimized fitted Pc curve using a log(Beta) function

Unfortunately, the positive part of the Pc curve was not acquired for this project. A first attempt of fitting function going from Pc=0 at Swi value and passing through all data points using a single hyperbola function did not allow to match the oil production and differential pressure well. A log(Beta) function was used to fit the measured data points and to successfully history match the oil production and differential pressure. The data point at Pc=0 can be at a value of Sw varying from Swi to Sor. The saturation profiles were used to provide an estimation of this value (Sw=0.47 at Pc=0). The results of the numerical simulations and history matching are presented later.

The log(Beta) function is a 3 input-parameter function [Po, β, Sw(Pc=0)] in CYDAR, as defined in Equation 5:

$$P_c = c P_m \ln \left(\frac{1 - S_w^{*B}}{S_w^{*B}} \right) - b \quad (5)$$

With Pm a pressure coefficient to control the magnitude of the Pc curve, Sw* the reduced saturation ($S_w^* = [S_w - S_{wi}] / [1 - S_{wi} - S_{or}]$), B coefficient to control the asymmetry of the function, b, a function dependent on the water saturation at Pc=0, and c parameter calculated as a function of β to impose a slope equal to Po at the middle of the Pc curve ($S_w^* = 0.5$). In the following simulations, the parameters Po and β were kept constant for both SD and SS numerical simulations: only the value of Sw(Pc=0)

was changed, according to the observation on the saturation profiles of the SD and SS tests.

Table 4. Parameters of the log(Beta) Pc function

Tests	Po (bars)	β	Sw(Pc=0)
SD	20	1	0.47
SS	20	1	0.57

SS results on S3/S4:

Figure 11 represents both dP and produced Vo versus time:

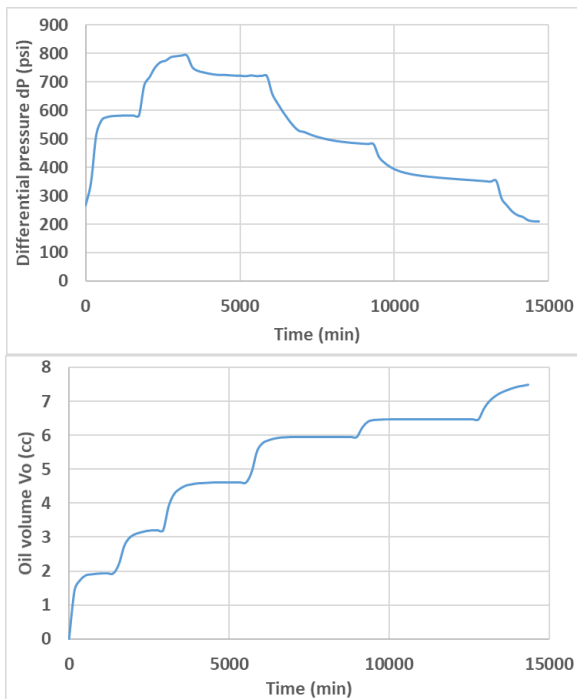


Fig. 11. dP and produced Vo versus time during the SS waterflood

For this test, the stabilization criteria were all obtained.

Concerning the saturation monitoring (Figure 12), the saturation profiles were noisier than the ones from the SD test: despite the choice of similar or “twin” samples and same experimental protocol, rocks may have different degree of heterogeneity.

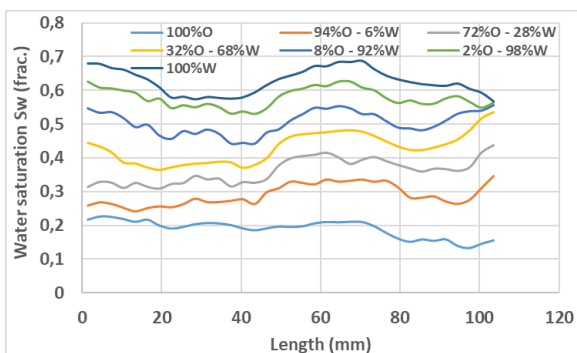


Fig. 12. Saturation profiles at equilibrium

Test parameters were well designed, with data points well spread over the saturation range. The outlet Sw seems to converge towards a value of 0.57. this information helps in choosing the imbibition log(beta) Pc curve for further numerical simulations.

Again, the comparison between the average water saturation $\langle Sw \rangle$ obtained by material balance and by averaging the x-ray profiles is acceptable, with less than 3 s.u. difference (Figure 13):

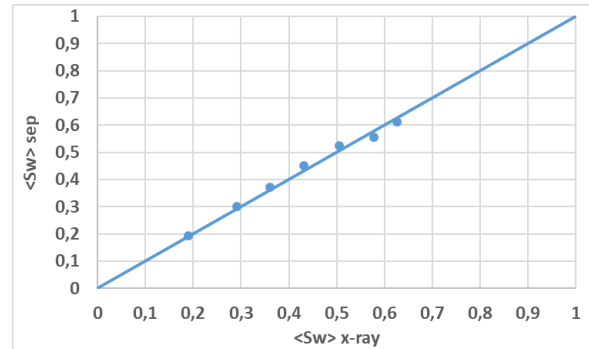


Fig. 13. Comparison between $\langle Sw_{sep} \rangle$ and $\langle Sw_{x-ray} \rangle$ during the SS waterflood

Figure 14 represents the non-interpreted SS relative permeability curves on Cartesian and semi-log scale:

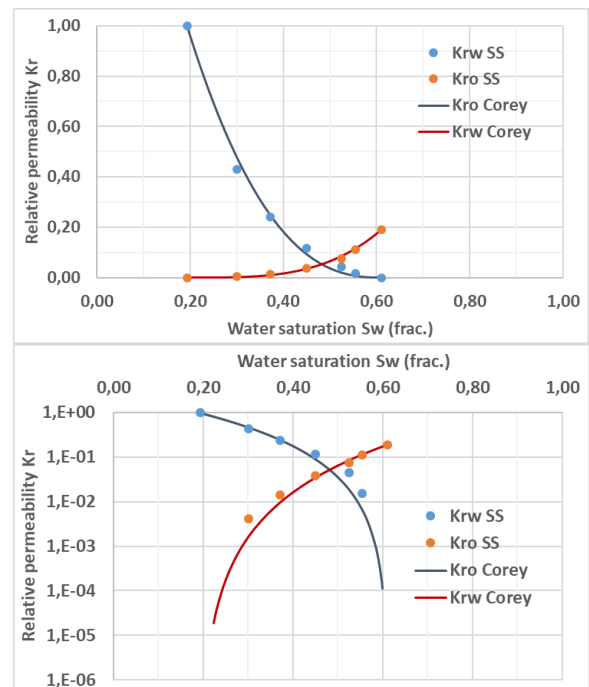


Fig. 14. SS Kr curves (Cartesian and semi-log plots)

The saturation Sw points are those calculated by material balance. Similar curve is obtained by using the average saturation profiles. As for the SD test, a Corey model was used to best fit the data points. The values of the water and oil Corey exponents are:

- Nw=3.5
- No=2.5
- Krw Max=0.191
- Swi=0.193
- Sor=0.389

Pc centrifuge results on S5:

A forced imbibition multistep centrifuge test was performed to measure the capillary pressure P_c of sample S5. Unfortunately, there was no spontaneous imbibition performed before starting the forced imbibition. This step would have been interesting to compare with the value of $SD S_w$ at $P_c=0$.

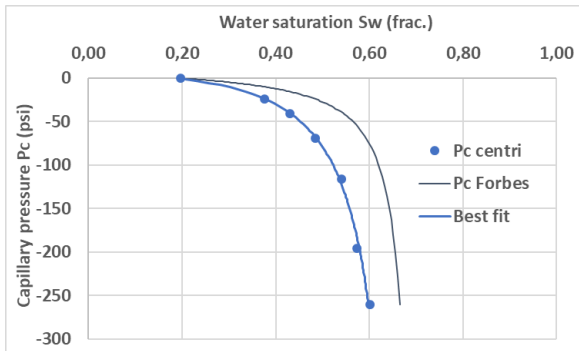


Fig. 15. Capillary pressure P_c (experimental and local Forbes P_c)

A modified hyperbolic function was first used to fit the experimental data points before calculating the local inlet saturation using Forbes' approach.

The same sample S5 was cleaned, brine-saturated, brought to S_{wi} and run for single-step centrifuge (10000rpm) with dead oil to determine K_{ro} . Note that intermediate porosity and permeability measurements were performed to ensure good sample integrity.

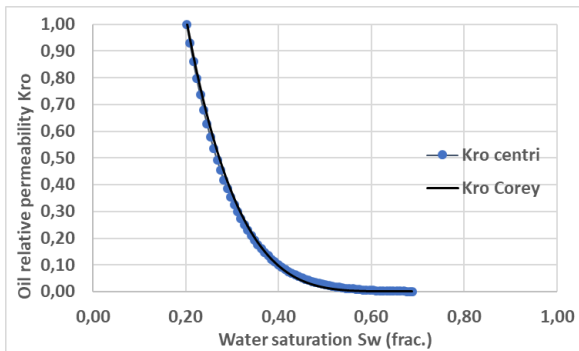


Fig. 16. Relative permeability to oil K_{ro} from single-step centrifuge

Collected data were analysed using techniques published in [9] and [10], taking into account the correction for ramp up, capillary hold up, and mobility effects. The resulting oil relative permeability was then fitted with a Corey model. The No exponent was found to be equal to 4.0.

Interpretation: Simulations and History Matching

SD Method:

The results of the history-match process on the semi-dynamic waterflood are shown in Figure 17:

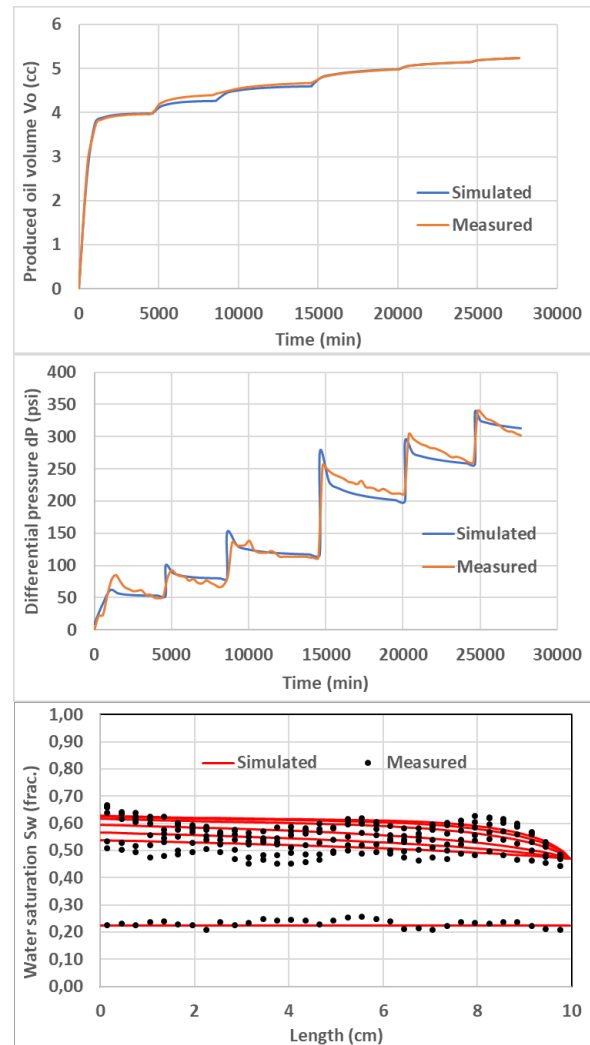


Fig. 17. Comparisons between measured properties and numerical simulations for the SD waterflood

Figure 17 represents the results of the produced oil V_o , differential pressure and saturation profiles history matches by tuning the K_{ro} parameter during the simulations. As a matter of fact, local and inlet K_{rw} and P_c are directly determined during the experiment. P_c parameters from $\log(\beta)$ function were also tuned to fit the experimental data points and to find an optimal value of $S_w(P_c=0)$ for improving the history-match results.

The history match appears acceptable for production V_o and differential pressure, but it is less obvious for the saturation profiles. This is mainly the result of the 1D x-ray limitation and the degree of heterogeneity rock. As explained before, using one single point of x-ray acquisition through the diameter at the core inlet does not represent the average water saturation through the inlet corresponding section.

In order to better history-match the production and differential pressure, a modified Corey or L.E.T. function may have been preferred. But in the frame of comparing the SD and SS methods, keeping consistency/coherence and limiting the number of matching parameters, it was decided to keep a Corey model for K_r and provide the best match possible. The resulting Corey parameters were:

Nw=4.5
 No=4.0
 Krw Max=0.16
 Swi=0.224
 Sor=0.346

SS Method:

In the SS simulations, the SD local Pc was taken as first guess input, preserving the same parameter values discussed earlier but with the value of Sw(Pc=0) adjusted by using saturation profile observations.

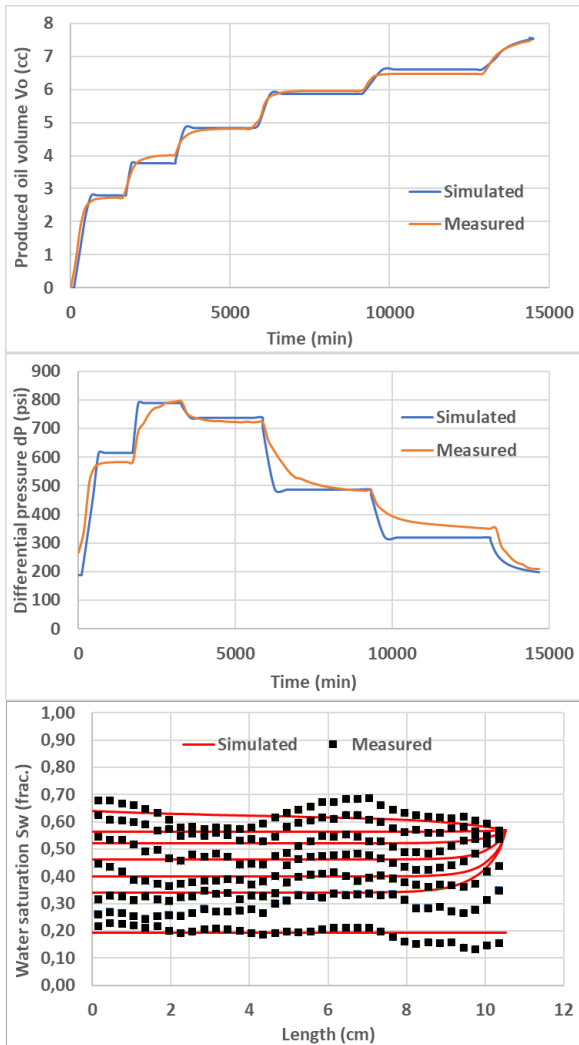


Fig. 18. Comparisons between measured properties and numerical simulations for the SS waterflood

As for the SD numerical simulations and history-match, it was difficult to improve the quality of the production and differential pressure history-match results using a simple Corey model. As explained before, even if better results may have been obtained using a modified Corey or L.E.T. function, it was decided to keep consistency/coherence and to limit the number of matching parameters by using a simple Corey model for Kr. The resulting Corey parameters were:

Nw: 3.5
 No: 3.0
 Krw Max=0.220
 Swi=0.193

Sor=0.330

Figure 19 represents both uninterpreted and interpreted SS Kr and Pc curves:

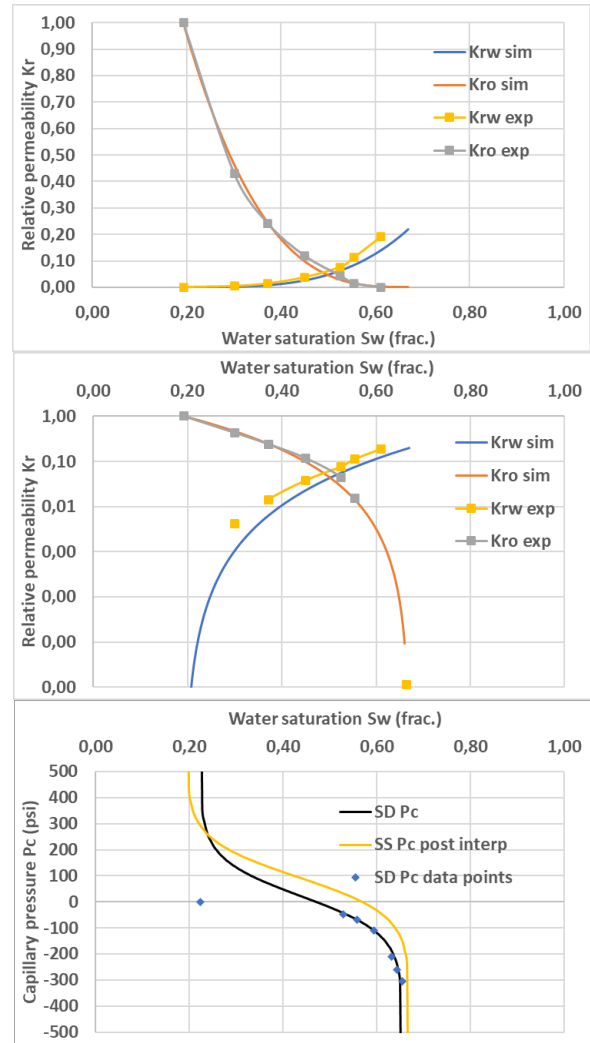


Fig. 19. Pre- and post-interpretation Kr and Pc curves for the SS waterflood

Note that Forbes Pc curves as shown in Figure 15 were tested for the two SD and SS waterfloods. An acceptable history-match of dP and Vo were obtained using newly interpreted Kr curves. The observations were:

- The newly interpreted Kr curves were found to be very close to the Kr curves obtained with log(Beta) Pc
- The Forbes Pc function does not mimic the outlet Sw, as shown in saturation profiles in Figure 16 and Figure 17 where a log(Beta) Pc function was used with an appropriate value of Sw(Pc=0).

Centrifuge Pc Simulation and History-Matching:

The local centrifuge capillary pressure was obtained using the Forbes' approach (Figure 15). The Kr curve was built with a Corey model, with No equal to 4, as for the single-step test. A first guess of water Corey exponent Nw equal to 2 and Krw Max of 0.2 were tested before running the history-match optimization. The best history match was finally obtained with the below Kr and Pc curves:

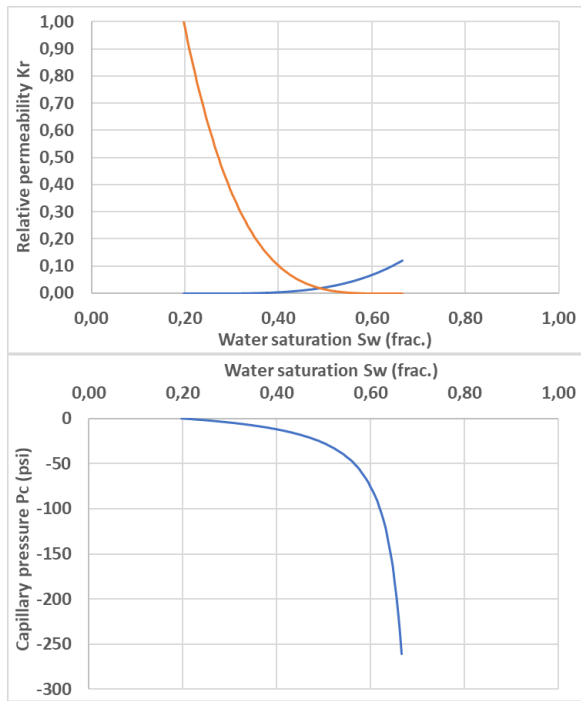


Fig. 20. Interpreted Kr curve for the Pc multistep test with the associated Forbes' Pc curve

Nw=3.8
 No=4.0
 Krw Max=0.12
 Swi=0.197
 Sor=0.334

The quality of the history-match is presented in Figure 21:

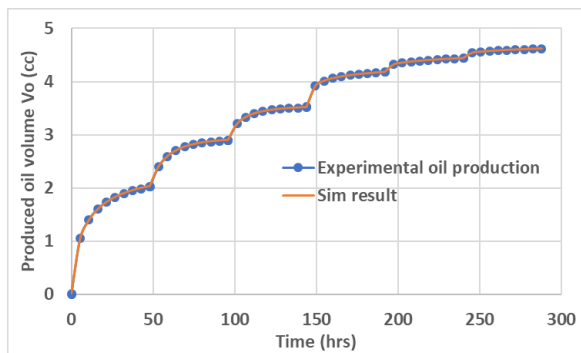


Fig. 21. Interpreted Kr curve for the Pc multistep test with the associated Forbes' Pc curve

Centrifuge Kro Simulation and History-Match:

An history-match of the single-step centrifuge oil production was performed. The Kro was taken as calculated via Hirasaki's method (Figure 16). The same Forbes Pc curve as is in Figure 15 was used as input. An initial Krw guess with Corey exponent Nw equal to 4 was attempted first. Krw Max, Sor and Nw were then tuned for the history-match. Considering the Pc and Kro parameters are well determined, the resulting Kr and Pc curves are shown in Figure 22:

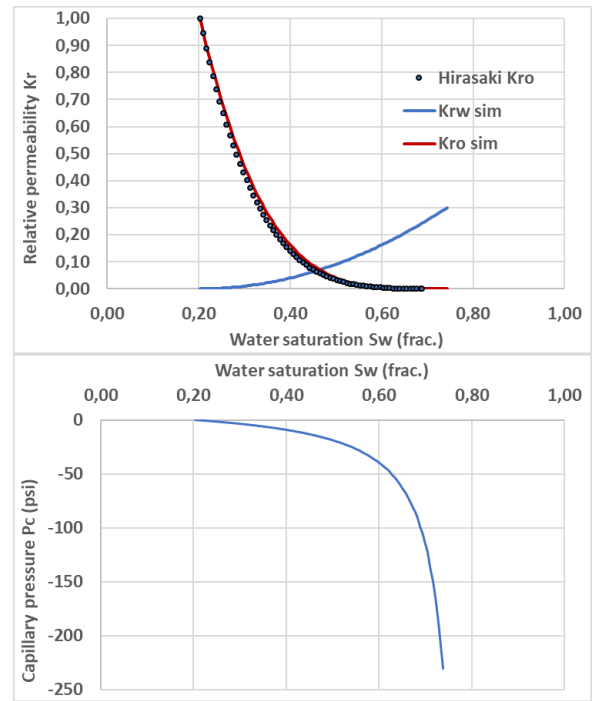


Fig. 22. Optimized Kr curve for single-step centrifuge with fixed Forbes Pc

To history-match the oil production Vo, a Corey coefficient of 2 was taken for Nw.

Nw=2
 No=4
 Krw Max=0.30
 Swi=0.203
 Sor=0.257

The resulting history-match is shown in Figure 23:

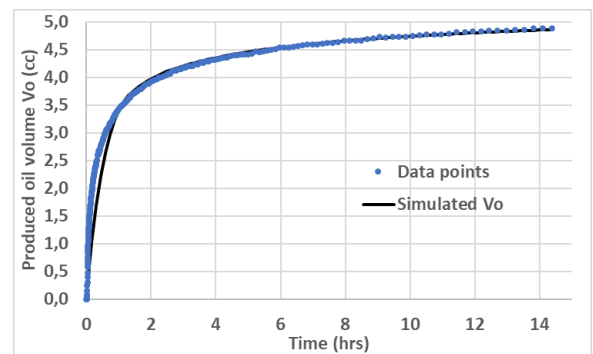


Fig. 23. Measured and simulated Vo for the single-step Kr centrifuge test

It is difficult to history-match the early oil production well, probably because no spontaneous displacement was performed before the forced imbibition cycle.

Kr and Pc Comparisons

Kr Comparison:

For comparing the petrophysical parameters Kr and Pc from different experiments but on the same rock type, it is generally recommended to plot the results using the same value of Swi (the averaged value) and preserving the recovery information. In this study, the Swi values were

found to be very close. It was decided to directly compare the results without rescaling them to a same value of Swi.

Reminder: for the SD and SS tests, the material balance method was preferred to the x-ray method to interpret the data.

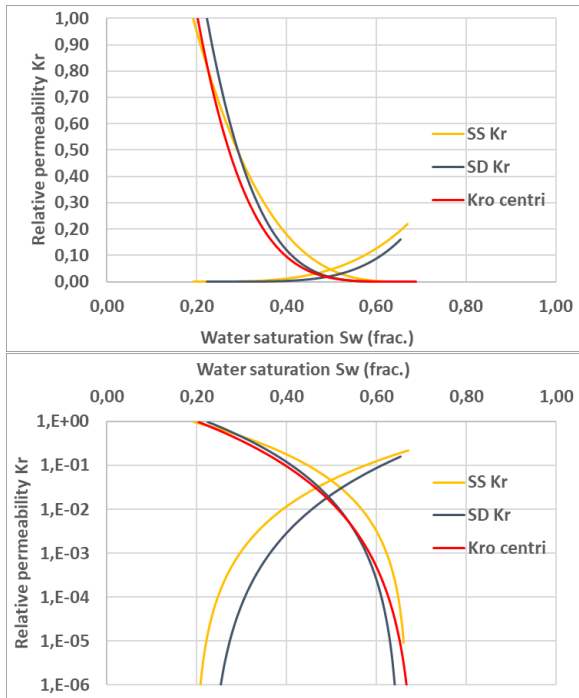


Fig. 24. Comparison of SD, SS and centrifuge relative permeability curves

Figure 24 shows that centrifuge and SD Kro curves overlap nicely while SS and SD Kr curves on the Cartesian plot look quite similar. But the semi-log graph better highlights the differences. All can see that SS Kr shows higher oil and water mobility at same saturation compared to the SD. It may be due to the heterogeneity or wettability differences. Fraction flow curve helps in comparing the SD and SS Kr curves:

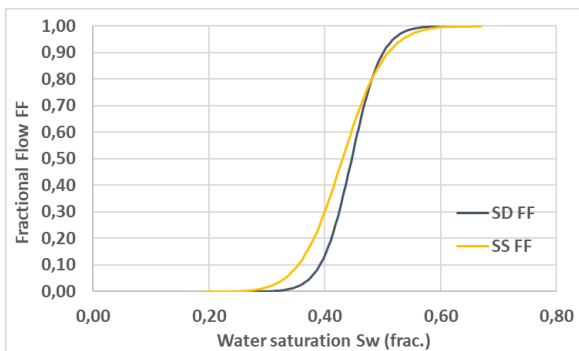


Fig. 25. Comparison of relative permeability ratios

Figure 25 shows that the SD case is more optimistic from Swi to Sw~50% while SS case is more optimistic from Sw~50% to residual oil saturation Sor. The difference can be explained by the difference in degree of heterogeneity, the lack of equilibrium during the SD test, as shown on the dP signal in Figure 17, possible effect of the capillary contact between the samples. Wettability difference may also explain the difference despite the tests were run at

same conditions, with same fluids, at same Swi and with initial uniform fluid distribution for both stacks.

The Kr Corey exponents and saturation ranges are not so different as presented in Table 5:

Table 5. Final Kr Corey parameters and saturation range

Test	Krw Max	Swi frac.	Sor frac.	Nw	No
SD	0.16	0.223	0.346	4.5	4.0
SS	0.22	0.193	0.330	3.5	3.0
Pc centri	0.12	0.197	0.334	3.8	4.0
Kr centri	0.30	0.203	0.257	2.0	4.0

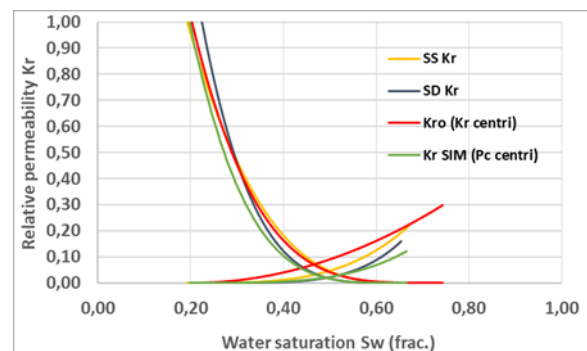
Wettability could have also explained the Kr difference, but the parameters in Table 5 highlight an intermediate-wet state of the rocks (typically with $3 < Nw < 5$ and $3 < No < 6$), also confirmed by the positions of the Kr cross-points.

Even if it is not observed on the saturation profiles (Figure 6 and Figure 12), a poor capillary contact could lead to non-uniform fluid distribution and so, lead to a difference in flow behaviour. The use of composite stack may not be a good way to perform the waterflooding tests.

Finally, the use of Pc curve for the SS optimization process/history-match, fixed with same SD Pc parameters may also explain the discrepancy. If porous plate or centrifuge Pc could have been individually performed on the composite core plugs prior the SS test, an averaging process (J-function...) would have been necessary to build an averaged Pc curve, introducing again an uncertainty.

It is concluded that having both Kr and Pc measured during similar test on a non-composite stack (to avoid capillary contact issue), is the most acceptable way of avoiding erroneous interpretation.

Even if it is not an objective of the study, the SD and SS Kr curves were compared to the interpreted Kr curves from the single and multistep centrifuge tests:



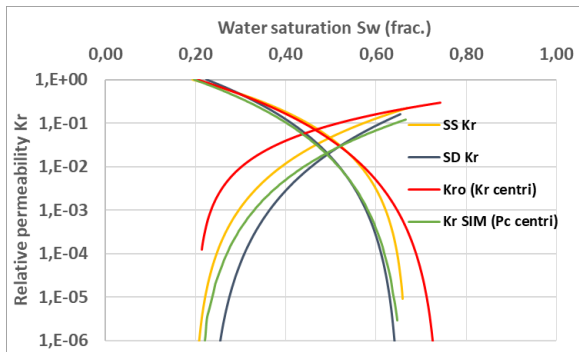


Fig. 26. All interpreted Kr curves from coreflooding and centrifuge tests

The Kr curves obtained from the different methods are not so different, except the one from the single-step Kr centrifuge test, probably due to the small amount of signal/data to be history-matched and re-use of the multistep Pc sample after cleaning it again, restored wettability being maybe different. Other curves are in the same range of saturation, close Kr cross-points, close Krw Max and close Kr curvatures, showing a certain consistency in the obtained results. In reservoir engineering, it is not unusual to observe such Kr envelops when dealing with a same rock type.

Pc Comparison:

Both the local Pc from centrifuge obtained using the Forbes approach and local Pc directly obtained from SD method are plotted together:

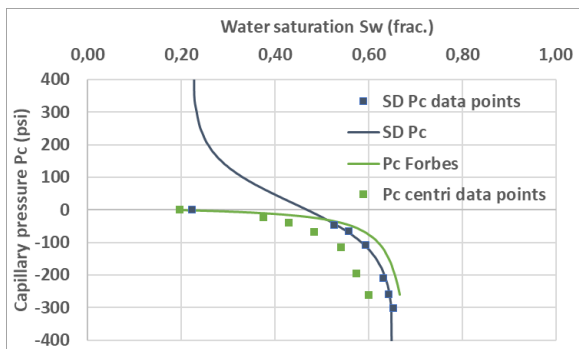


Fig. 27. SD and SS capillary pressure Pc curves

Despite using oil at different conditions (dead oil for centrifuge – live oil for SD), Figure 27 shows an acceptable similarity between the SD and Forbes Pc curves. It is very encouraging to notice that the SD method provides similar local Pc to the Forbes method using centrifuge. Again, the SD Sw was analytically calculated and not obtained using the 1D x-ray method. Also, note that there was no spontaneous imbibition performed before running the forced centrifuge and SD imbibition tests. It could have helped in validating the SD Pc, especially the Sw value at Pc=0.

Figure 28 shows all measured and interpreted Pc curves. The interpreted negative Pc parts are all close together, proving a certain consistency of the results and adequate interpretation workflow. The positive part of the Pc curve was unfortunately not measured. It could have been done using the semi-dynamic method.

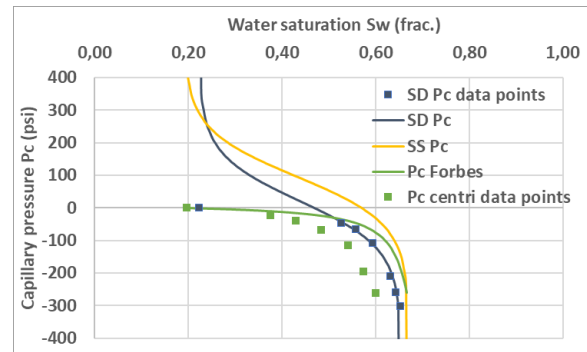


Fig. 28. Capillary pressure Pc curves

Based on the capillary pressure curves, it is observed that the SS stack behaves as a more water-wet rock than the SD stack, which is consistent with the observation on the fractional flow (Figure 25). Further investigations must be done to better understand the potential wettability change during the forced imbibition using different methods.

6 Conclusions

In this study, several methods for measuring relative permeability and capillary pressure were tested in order to compare the data results and validate the SD method as a unique experiment able to provide both petrophysical parameters during a same test, on same core, with live fluids at real reservoir conditions. It was concluded that:

- The SD Pc data points were found to be similar to the local analytical Forbes Pc obtained during the multistep centrifuge, despite aging and testing with two different oils (dead versus live). The interpreted SD Pc curve using the log(Beta) function passing through the data points is also forced to pass on the true value of Sw(Pc=0) observed on the saturation profiles. Unfortunately, neither the positive part of SD Pc nor the spontaneous imbibition displacement prior centrifuge test were acquired in this study
- The SD Kr was quite different from the SS one. Assuming that the wettability was identical in both tests, the difference may be explained by the rock heterogeneity. The interpreted SS Kr curve was obtained using SD Pc curve (and using centrifuge Pc curve, not presented here), while SD Kr and Pc curves are directly measured during the same test on same composite stack. This is a real advantage to avoid erroneous interpretation
- The simulated SD Kro was consistent with centrifuge Kro. This observation is very encouraging, validating the workflow for the SD history-matching process
- Large rocks should be preferred to composite stacks to avoid potential capillary contact issue
- The quality of the simulated and interpreted Kr curves from the centrifuge tests (multistep and single step) are more questionable because they are based on oil production history match only

If the results of the study are building confidence in the semi-dynamic approach to determine both relative permeability and capillary pressure, some experimental improvements are still required:

- 2D or even 3D x-ray method should be preferred to the 1D or analytical means to measure the inlet water saturation, especially for heterogeneous rocks. A new x-ray setup is being tested in TOTAL [11]. This system allows having enough contrast between water and oil without additional dopants, reducing the risk of a wettability change during the waterfloods
- Pc curve, including the positive part, must be measured with the SD method to determine the full Pc and to better quantify the value of Sw(Pc=0). This can easily be done with the current SD setup, by reducing the oil flow rate and recirculating water at the outlet before injecting water
- The conclusions of this study would need to be confirmed by performing more tests and ensuring the repeatability of the observed results
- Wettability alteration, from the initial restoration while recirculating oil at the core outlet during the semi-dynamic test or while co-injecting oil during the steady-state test, both in a closed loop, requires more attention and investigation
- Finally, a large project for multiple history-matching process is ongoing at TOTAL with the aim of finding Kr and Pc curves via simultaneous assisted history-match on data collected from several experiments [12]

The authors would like to thank TOTAL and Schlumberger for permission to publish this work.

Nomenclature

A: section area, in cm^2
B:
CT: Computed Tomography
dP: differential pressure, in psi
HPHT: High Pressure High Temperature
ISSM: in situ saturation monitoring
Kg: apparent gas permeability, in mD
Kw: water permeability, in mD
Keo: oil relative permeability, in mD
Kr: relative permeability
Krw: relative permeability to water
Kro: relative permeability to oil
Krw Max: maximum water relative permeability
MB: Material Balance
MICP: mercury injection capillary pressure
NCS: net confining stress, in psi
Nw: water Corey exponent
No: oil Corey exponent
Pc: capillary pressure, in psi
Pp: pore pressure, in psi
Pconf: confining pressure, in psi
Pi: inlet pressure, in psi

Po: outlet pressure, in psi
Qw: water flow rate, in cc/min
Qo: oil flow rate, in cc/min
ROS: Remaining Oil Saturation
SD: Semi-Dynamic method
SS: Steady-State method
SEM: Scanning Electron Microscopy
So: oil saturation, in v/v or %
Sor: residual oil saturation, in v/v or %
<So>: average of oil saturation, in v/v or %
Sw: water saturation, in v/v or %
Swi: irreducible water saturation, in v/v or %
<Sw>: average of water saturation, in v/v or %
<Sw_{sep}>: average of water saturation using separator, in v/v or %
<Sw_{x-ray}>: average of water saturation using x-ray attenuation method, in v/v or %
*S**: normalized water saturation, in v/v or %
T°C: temperature, in °C
TS: Thin Section
USS: Unsteady-State method
Vo: produced oil volume
XRD: X-Ray Diffraction
X-Swi: irreducible water saturation measured with x-ray attenuation method, in v/v or %

φ_{He}: helium porosity, in v/v or %
ρ_w: water density, in g/cc
ρ_o: oil density, in g/cc
μ_w: water viscosity, in cP
μ_o: oil viscosity, in cP

References

1. T.S. Ramakrishnan, A. Cappiello, Chem. Eng. Sci., **46** (1991)
2. R. Lenormand, A. Eisenzimmer, Society of Core Analysts, SCA1993-22 (1993)
3. R. Lenormand, P. Schmitz, Society of Core Analysts, SCA1997-17 (1997)
4. J-M. Lombard, P. Egermann, R. Lenormand, Society of Core Analysts, SCA2002-09 (2002)
5. J-M. Lombard *et al.*, Society of Core Analysts, SCA2004-32 (2004)
6. D.R. Maloney, Society of Core Analysts, SCA2006-05 (2006)
7. M.C. Spearing *et al.*, ADIPEC, SPE-171892 (2014)
8. F. Pairoys, Society of Core Analysts, SCA2014-05 (2014)
9. G.J. Hirasaki *et al.*, SPE Reservoir Engineering, SPE-25290 (1992)
10. G.J. Hirasaki *et al.*, SPE Advanced Technology Series, **3**, SPE-24879 (1995)
11. G. Puyou *et al.*, Society of Core Analysts, SCA2017-37 (2017)
12. A.E. Sylte, Society of Core Analysts, SCA2004-17 (2004)

Physical origin of pressure- and saturation fluctuations in steady-state core floods

Steffen Berg^{1,*}, Hilbert van der Linde¹, Niels Brussee¹, Maja Rücker^{2,3}, Harm Dijk⁴, Evren Unsal¹, Tibi G. Sorop¹, and Matthias Appel¹

¹Shell Global Solutions International B.V., Grasweg 31, 1031 HW Amsterdam, The Netherlands

²Department of Mechanical Engineering, Technical University Eindhoven, De Rondon 70, 5612 AP Eindhoven, The Netherlands

³Department of Chemical Engineering Imperial College London, United Kingdom

⁴Shell Global Solutions International B.V., Lange Kleiweg 40, Rijswijk, 2288 GK, Netherlands

Abstract. Relative permeability is traditionally obtained in core flooding experiments during which water and oil phases are co-injected, using either using simplified analytical methods or by inverse modelling (history matching) including assisted/automated methods. However, in many steady-state (fractional flow) core flooding experiments significant fluctuations in pressure and saturation are observed, which can lead to increased uncertainty ranges of relative permeability and may even persuade experimentalists to dismiss the experiment altogether. Here we provide a more detailed insight into fluctuations and show that they may not always be related to instrumental artefacts such as produced by back pressure regulators, but rather have a physical origin. Over the past decade we have learned that pore scale displacement events such as Haines jumps and snap-off can lead to small pressure pulses. Moreover, recent synchrotron-beamline based fast micro-CT experiments clearly show that collective displacements on a millimeter-sized scale of the oil cluster may lead to pressure- and saturation fluctuations on similar magnitude as typically observed in classical SCAL steady-state experiments on samples of several centimeters length and diameter. Furthermore, when monitoring pressure and saturation on a centimeter length scale we sometimes observe, depending on wettability and other parameters, periodic fluctuations which are accompanied by travelling waves in the saturation profiles. While the origin of such fluctuations are likely pore-scale events one would expect that on a Darcy-scale, such fluctuations of pore scale origin would average and decay very quickly. However, a more detailed analysis shows that such Darcy-scale solutions for traveling waves leading to fluctuations in pressure and saturation are permissible by fractional flow theory. The adequate interpretation of such phenomena requires consideration of both drainage and imbibition relative permeability bounding curves and respective hysteresis models. A potential physical reason is that travelling waves can have higher total mobility than a flat saturation profile.

1 Introduction

For most subsurface applications such as dynamic modelling in reservoir engineering, multiphase flow in porous rock is described with the multiphase extension of Darcy's law. That is a continuum formulation where the phase fluxes are linearly related to the respective pressure gradients. While very effective from a practical perspective, one of the consequences of this phenomenological extension is that the flow parameters such as relative permeability and capillary pressure need to be determined experimentally or more recently with Digital Rock methods. Relative permeability is typically determined in core flooding experiments where in particular the steady-state method is preferred because of a number of reasons [1, 2]. As illustrated in Figure 1, in steady-state core flooding experiments the relative permeability is determined from the average pressure-drop at the end of each fractional flow step.

However, in many steady-state experiments, depending on a range of factors, sometimes very "large" pressure

* Corresponding author: steffen.berg@shell.com

fluctuations are observed [3-7] which can be significantly larger than instrumental noise e.g. from pressure transducers.

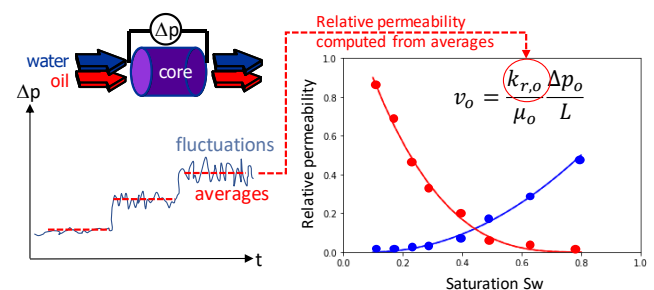


Figure 1. Steady-state core flooding experiments: water and oil phases are co-injected at varying fractional flow f_w . Relative permeability is determined from the average pressure drops at each f_w while the raw data often shows sometimes significant fluctuations in pressure drop and saturation.

In the past, in special core analysis (SCAL) programs large fluctuations in pressure drop or saturation [3-11] have been

interpreted as experimental artefacts as they can be potentially also caused by e.g. back pressure regulators, which has led in many cases to the dismissal of the data set. Pressure fluctuations have been also observed in many pore-scale experiments [8-24]. In [9] the connection between pressure and saturation fluctuations in Darcy-scale experiments and pore scale displacement events and respective flow regimes such as ganglion dynamics [25-27] and intermittency [14-18] has been made. Individual pore filling events and associated capillary fluctuations are expected to average out at the Darcy scale (i.e. when averaged over hundreds to thousands of pores) at least for stationary processes and not lead to a significant saturation. However, that is not what is experimentally observed [3-11]. In a range of independent experiments, with different setups, by different groups, significant saturation fluctuations were observed which exceed the level of individual pore filling events by orders of magnitude. That raises the question about the underlying cause of pressure and saturation fluctuations at the Darcy scale, i.e. whether they reflect the movement of large oil clusters in a ganglion dynamics flow regime [26, 27], or if there is actually another reason why we sometimes observe significant pressure fluctuations.

In this work we address this question by analyzing a steady-state fractional flow experiment in significantly more detail than normally done in the interpretation of steady-state experiments. The experiment has been designed to suppress all known experimental artefacts that could cause fluctuations i.e. no back-pressure controller is involved but fluids are re-circulated, pulse-free injection pumps with zero-dead volume switching pumps are used and monitored for continuous injection, the fluid pair chosen cannot form emulsions, etc.

We show that large pressure and saturation fluctuations are associated with travelling saturation waves consisting of sequences of drainage and imbibition. The main conclusion is that Darcy scale saturation fluctuations can be reconciled with fractional flow solutions for a hysteretic drainage and imbibition relative permeability pair.

There are several consequences for the interpretation and application of relative permeability observed from such an experiment ranging from the insight that e.g. drainage relative permeability may involve elements of imbibition and vice versa and obtained relative permeability is in fact on a scanning curve. There are also potential consequences whether in presence of significant fluctuations the 2-phase Darcy equations correctly represent the dissipation of energy.

2 Methods and Materials

2.1 Flow experiment

Steady-state core flooding experiments are performed in an experimental setup illustrated in **Figure 2** which is similar to the ones used routinely for relative permeability SCAL measurements [28,3,4]. Water and oil phases are co-injected with pulse-free Quizzix pumps (Chandler, Metek) equipped with with zero-dead volume switching valves for smooth and pulse-free continuous flow (Vindum Engineering) at fractional flow

$$f_w = \frac{q_w}{q_w + q_o} \quad (1)$$

where q_w and q_o are the volumetric rate of water and oil phase, respectively.

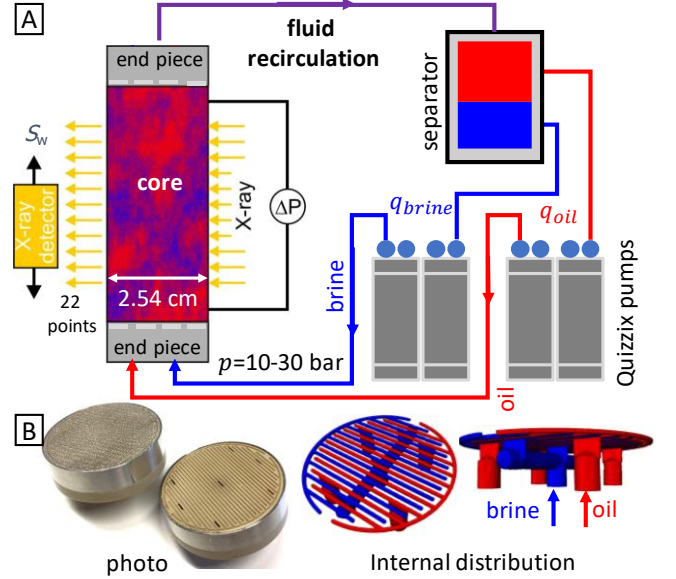


Figure 2. (A) Steady-state core flooding experimental setup where water and oil phases are co-injected at varying fractional flow f_w with 2 dual-piston Quizzix pumps that operate with zero-dead volume switching valves for smooth and pulse-free continuous flow. Typically, fluids are re-circulated (after separation) without any back-pressure controller to accommodate for large number of injected pore volumes. Saturation is monitored in-situ with a linear X-ray system. (B) Photo of the end piece (with and without the metal mesh) and internal distribution network providing a continuous injection of oil and brine across the end face of the core.

Water saturation S_w is determined by in-situ X-ray monitoring using a linear X-ray scanner at 22 positions along the core (using an X-ray transparent core holder) at time intervals of 8 min 30s. Saturation from X-ray was consistent with an Amott spontaneous imbibition test. Electrical conductivity along the core is recorded at the same time interval. Pressure drop Δp along the core and the central section, outside of capillary end-effects [29], is monitored at a time interval of 1 min. The flow rate is kept constant at $q_w + q_o = 3 \text{ ml/min}$ corresponding to a capillary number of 10^{-5} which is still below the onset of capillary de-saturation. More details are given in [30,28].

Experiments started with primary drainage at $S_w = 1$ injecting at $f_w = 1.0$ (brine only) which is stepwise reduced to $f_w = 0.0$ (oil only), followed by imbibition starting at $f_w = 0.0$ which is systematically increased to $f_w = 1.0$. At each f_w step pressure-drop Δp , saturation S_w and electrical conductivity are monitored. The steady state is experimentally achieved when Δp and S_w are stable (vary by less than 1%) and relative permeability $k_{r,\alpha}$ is then computed (at each f_w) using the two-phase Darcy equation

$$q_\alpha = -\frac{k_{r,\alpha}}{\mu_\alpha} AK \frac{\Delta p_\alpha}{L} \quad (2)$$

where K is the (absolute) permeability of the rock, L the length and A the cross-sectional area of the cylindrical rock sample, μ_α the viscosity of phase $\alpha = o, w$ (oil, water).

2.2 Rock, Fluids

A cylindrical sample of Fontainebleau sandstone [31,32] with diameter $d=2.54$ cm and length $L=4.45$ cm was used. It has a porosity of $\phi=0.13$ and permeability $K=539$ mD. Prior to the experiment the sample was cleaned by Soxhlet extraction (chloroform-methanol) The sample remained strongly water-wet after the Soxhlet extraction. The fluids were n-decane with a density of 731.9 kg/m³ and a viscosity of 0.933 mPas, and NaCl brine doped with 5% CsCl, with a density of 1037 kg/m³ and viscosity of 0.992 mPas. The interfacial tension was approximately 40 mN/m.

3 Results

3.1 Raw data of fractional flow experiments

In **Figure 3** the pressure drop Δp of a primary drainage experiment conducted on the Fontainebleau sandstone rock is displayed for the first two cycles (out of 5). The sample had been cleaned in-between with isopropanol inside the core holder without removing the sample. Both experiments show in a repeatable way a lesser degree of fluctuations at high fractional flows and the end of drainage while at intermediate fractional flows between $0.75 \geq f_w \geq 0.1$ significant pressure fluctuations are observed. The imbibition data and further cycles (not shown) reproduce the pattern in a conceptually similar manner.

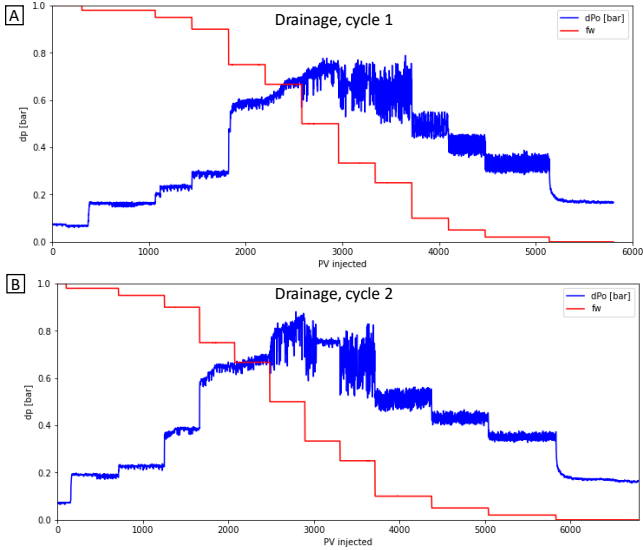


Figure 3. Pressure drop Δp and fractional flow f_w of a primary drainage steady-state experiment for cycle 1 (A) and cycle 2 (B) on the same sample (in total, 5 cycles were performed).

In **Figure 5** the raw data of the cycle 1 drainage experiment is displayed in more detail. **Figure 5A** shows the overview of pressure drop Δp , saturation S_w and electrical conductivity as a function of time and injected PV are shown. For selected fractional flows f_w in (B-G) the pressure-drop Δp and saturation S_w are shown with subtracted baseline which provides a more focused visualization of the associated fluctuations. Respective histograms and Fourier spectra of the fluctuations are shown in panels (B-G) in the middle and left.

For fractional flows $f_w > 0.75$ and $f_w = 0.0$ the histograms of the pressure and saturation fluctuations are Gaussian as shown in **Figure 4** and the fluctuation magnitude is more of the order of instrumental noise.

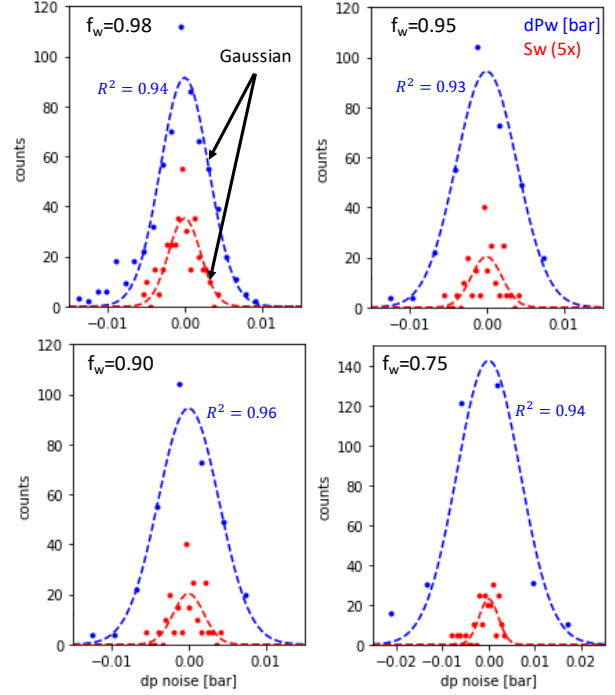


Figure 4. Histograms for Δp and S_w fluctuations (S_w fluctuations are magnified by a factor of 5 for better visibility) from **Figure 5** for $1.0 \geq f_w \geq 0.75$ following a Gaussian behavior (dotted lines are fits with Gaussian).

For $0.67 \geq f_w \geq 0.02$ the fluctuation amplitude is significantly larger than for the other f_w and the histograms are not Gaussian anymore. In many cases the histogram is actually bi-modal (**Figure 5E,F**) and respective pressure and saturation fluctuations are periodic in time with notable peaks in the Fourier spectrum representing the frequency of the periodicity in time. That clearly suggests that the pressure and saturation fluctuations for $0.67 \geq f_w \geq 0.02$ do not represent instrumental noise but have a different cause.

3.2 Separating fluctuations from noise and energy scale

In **Figure 6** pressure and saturation fluctuations are separated from instrumental noise. From the noise statistics for $f_w > 0.75$ where noise amplitudes are consistent with instrumental noise and histograms are Gaussian a noise floor is estimated which is proportional to the respective mean $\overline{\Delta p}$ and $\overline{S_w}$. Pressure fluctuations of up to $\delta \Delta p = 50$ mbar are clearly above the thermal noise level. Already for a single pore-filling event the associated pressure-volume work

$$\Delta W_{\text{pressure-volume}} = p_c \Delta V \quad (3)$$

is $\Delta W \approx 4.5 \cdot 10^{-10}$ J with $\Delta V \approx 1.1 \cdot 10^{-13}$ m³ for a spherical pore of $60 \mu\text{m}$ diameter and a capillary pressure $p_c = 2\sigma/r \approx 0.04$ bar (for a pore throat of $d = 2r = 25 \mu\text{m}$).

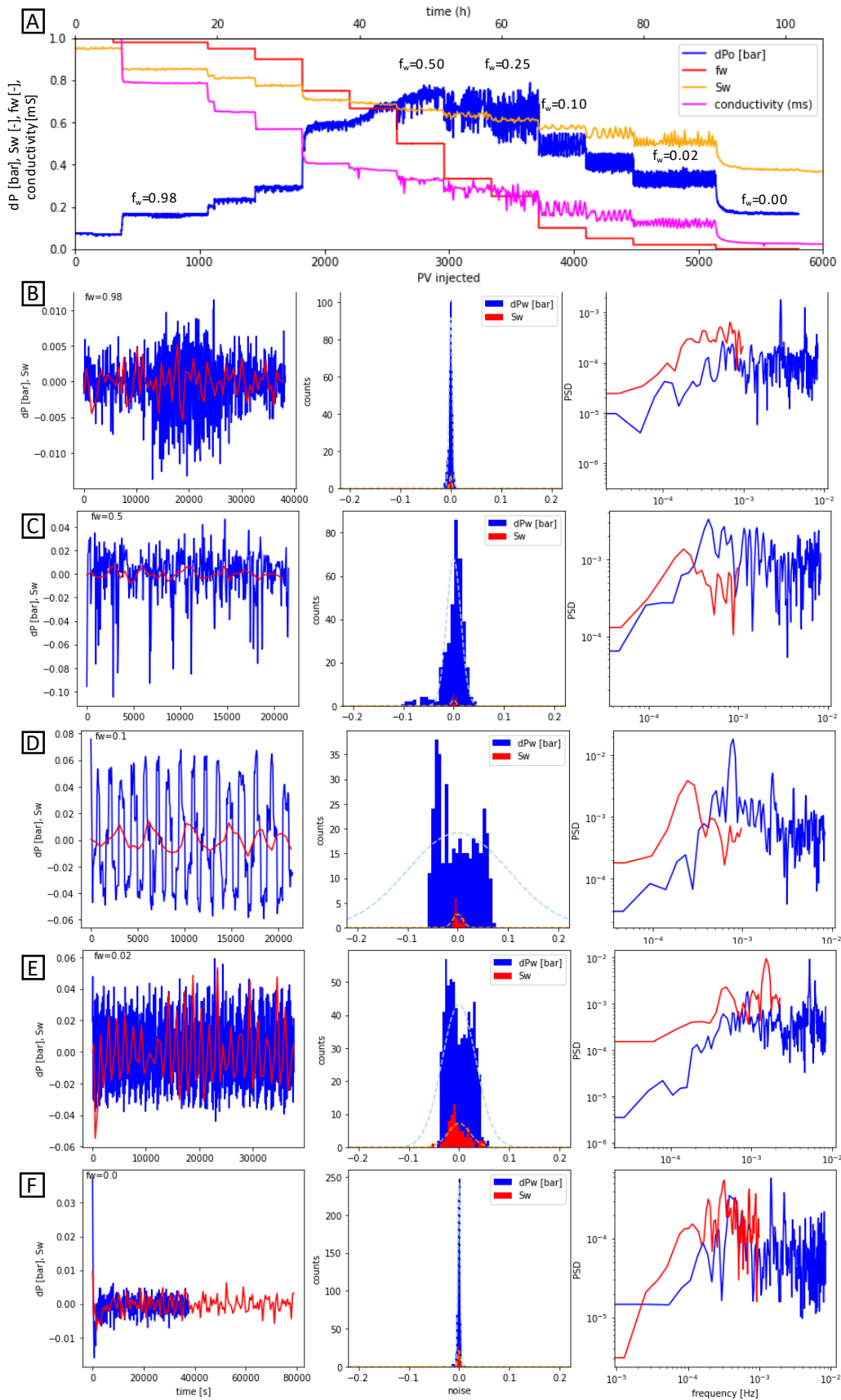


Figure 5. Raw data of the drainage experiment (A) showing pressure drop Δp , saturation S_w and electrical conductivity as a function of time and injected PV. For a number of selected fractional flow f_w (B-G) Δp and S_w are shown with subtracted baseline which provides a clearer focus on the fluctuations (left), the respective histograms for Δp and S_w (middle) and Fourier spectrum (right) of the fluctuations.

Expressed in units of $k_B T \Delta W = 1.1 \cdot 10^{11} k_B T$ meaning that pressure fluctuations associated with single pore filling events (Haines jumps) are many orders of magnitude larger than the thermal energy scale. Just as a comparison, pressure-volume work related viscous dissipation from connected pathway flow is of the same order of magnitude as the thermal energy scale.

The saturation fluctuations which can range up to $\delta S_w = \pm 5\%$, however, are much larger than individual pore filling events. For Fontainebleau sandstone with typical pores of volume $V_{pore, single} = 1.1 \cdot 10^{-7} \text{ cm}^3$, 5% fluctuation of saturation for a total pore volume of $V_{pore, tot} = 2.85 \text{ cm}^3$ means that a very large number of individual pores are involved.

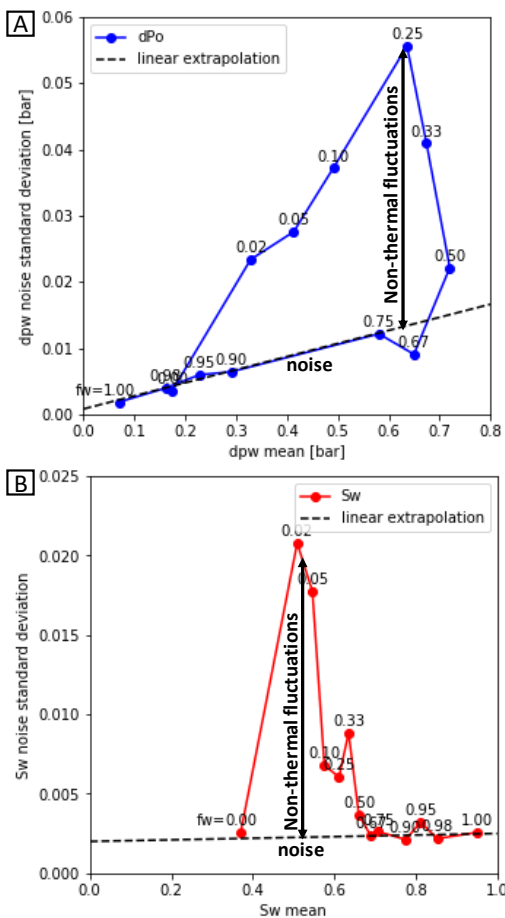


Figure 6. Fluctuations can be separated from instrumental noise by considering the relationship between mean and standard deviation for each f_w . Respective figures for Δp (A) and S_w (B) show a clear deviation from the linear trend for noise (established for $f_w \geq 0.67$) in the range of fractional flows $0.67 > f_w \geq 0.02$. For e.g. $f_w = 0.67$ the fluctuation amplitude is about 3 times larger than the instrumental noise.

3.3 Averaging pressure and saturation raw data

In **Figure 7A** we see that the saturation fluctuations do not follow exactly the same trend as the pressure fluctuations. That can be caused by the different sampling rates of pressure (1 min) and saturation (8min30s) in comparison with the frequency of the fluctuations (**Figure 5B-G**). When averaging or under-sampling the periodic structure of

fluctuations can disappear, and fluctuations become Gaussian. That can potentially explain why in **Figure 7** the saturations do not follow exactly the same trend as pressure. It also clearly shows what happens when raw data is averaged or only reported as average to make it “look nicer” because that can hide underlying physics.

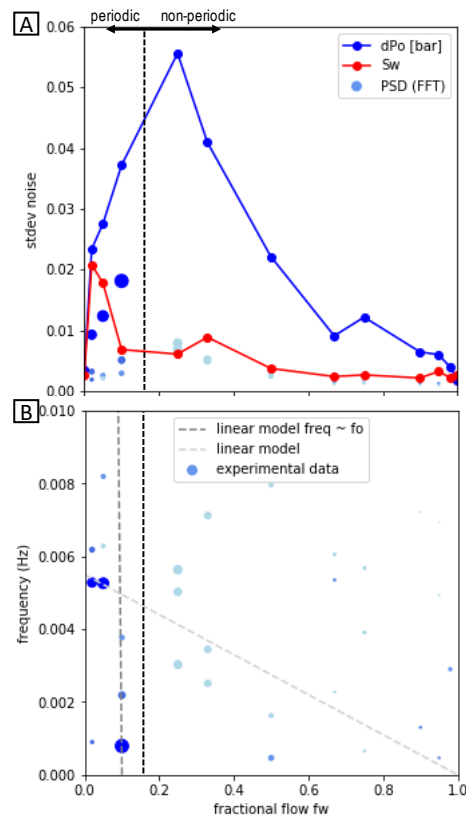


Figure 7. Fluctuation standard deviation as a function of fractional flow (A) shows a systematic trend. Due to the much lower sampling rates it is possible that saturation fluctuations are missed. From the dominant peaks in the Fourier spectrum the fluctuations can be separated into period and non-periodic fractions. The first three dominant peaks in the Fourier transform of the time signal (**Figure 5B-G**, third column) do not scale linearly with injection fractional flow f_w (linear trends - dashed grey lines - do not represent relevant fraction of dominant peaks) (B).

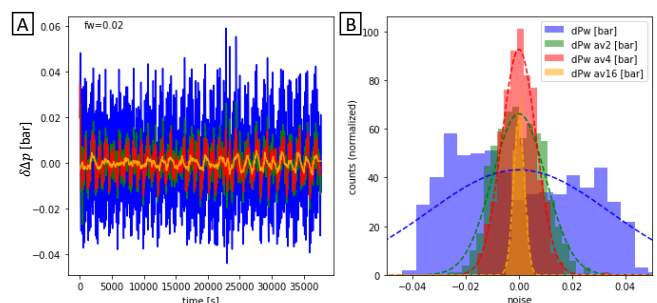


Figure 8. Averaging or under-sampling pressure fluctuations $\delta \Delta p$ (here applying a rolling average over 2, 4 and 16 subsequent samples for $f_w = 0.02$) can hide periodic fluctuations and transform histograms from bimodal to Gaussian (dotted lines) which is ultimately a consequence of the central limit theorem.

3.4 Relative Permeability

From averaged Δp and fluxes the relative permeability can be obtained using the 2-phase Darcy equation (2) but capillary pressure needs to be taken into account e.g. by inverse modelling [1-5,28,29]. In **Figure 9** the relative permeability for all 5 drainage and imbibition cycles are displayed. The 5 cycles superimpose very well with only very little scatter suggesting that the repeatability of the experiment is given. In addition, we show the fractional flow curves (C,F) for the first drainage and imbibition cycle.

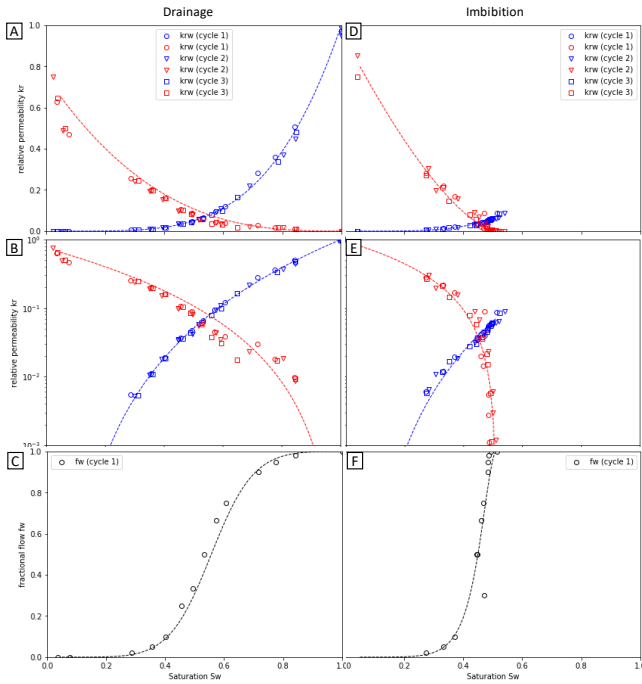


Figure 9. Relative permeability $k_r(S_w)$ for all 5 cycles on a linear (A,D) and logarithmic (B,E) scale, for drainage (A,B) and imbibition (D,E). The dotted line represents a fit with a Corey function. Results for all 5 cycles are very well reproducible. Respective fractional flow curves $f_w(S_w)$ are shown in C,F.

3.5 Travelling Saturation waves

In **Figure 7** the pressure and saturation fluctuations are not only separated from noise but also divided into a mainly periodic and non-periodic fraction. By focusing on the dominant peaks in the Fourier transform of the time signal i.e. power spectral density (PSD) in third column in **Figure 5B-G** we can see **Figure 7A** that the amplitude of the first 3 peaks of $\delta\Delta p$ follows a very similar trend with f_w as the standard deviation. However, as shown in **Figure 7B** the dominant fluctuation frequencies do not linearly scale with fractional flow f_w . That is also an important insight as it rules out simple experimental artefacts such as back pressure regulators or a capillary instability at the injection or outflow [36-38] because these would show a frequency proportional to fractional flow.

The observation that pressure and saturation data time series show systematic but non-linear trends with f_w in general e.g. fluctuations beyond noise level are encountered reproducibly only for $0.67 \geq f_w \geq 0.02$ and highly periodic fluctuations only for $0.20 \geq f_w \geq 0.02$ raises the question

even more about the physical origin. When inspecting the saturation profiles $S_w(x)$ for $f_w = 0.10$ and $f_w = 0.05$ where the most periodic fluctuation behavior is observed the saturation profiles $S_w(x, t)$ represented in a space-time contour plot in **Figure 10** show travelling saturation from inlet to outlet in a periodic fashion during the core flooding experiment, even at “steady-state”.

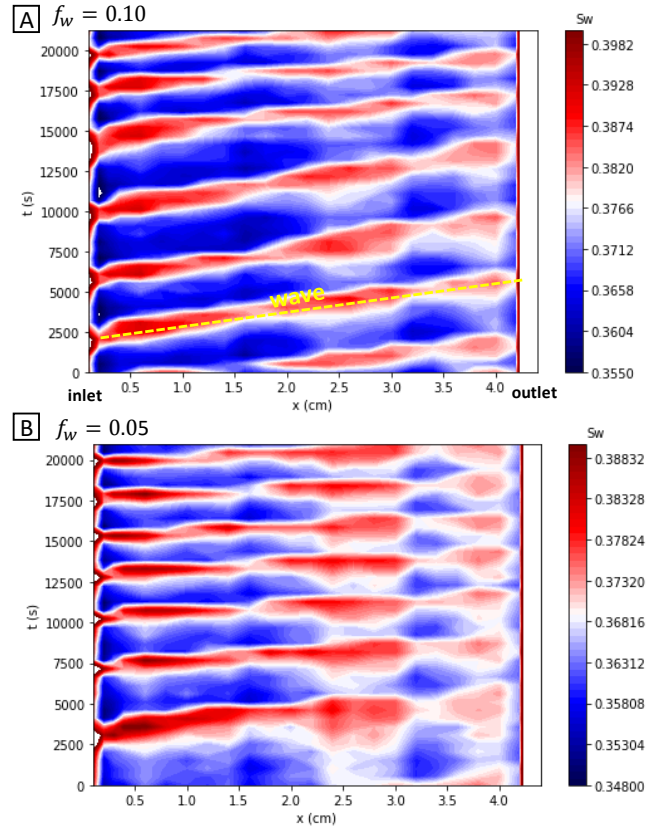


Figure 10. Space-time plot for the saturation $S_w(x, t)$ for $f_w = 0.10$ (A) and $f_w = 0.05$ (B). Travelling saturation waves are visible which travel at nearly constant velocity from inlet to outlet in a periodic manner.

3.6 Fractional flow solution

Saturation profiles consist of a water peak that travels at largely constant velocity from inlet to outlet with an amplitude $\delta S_w \approx 0.04$ consistent with saturation fluctuations in e.g. **Figure 5F**. As already pointed out previously, that saturation change is significant and involves a very large number of individual pores. This suggests that travelling saturation waves are a Darcy scale phenomenon.

Fractional flow theory based travelling wave solutions have been reported in the literature [33,34]. The question is whether that is indeed the situation in our experiment. The validation involves 2 steps: a fractional flow construction for the saturation S_w for the maximum and minimum saturation in the traveling wave solution from **Figure 10**, show for two specific fractional flows at specific times in **Figure 11**.

Starting point for a respective analysis is a hysteresis fractional flow model as shown in **Figure 12** where both drainage and imbibition $f_w(S_w)$ are considered since the moving saturation peak represents water displacing oil

(imbibition) at the leading edge and oil displacing water (drainage) at the trailing edge.

For constructing the fractional flow solution we start with a line from the origin to intersection with the drainage $f_w(S_w)$ at injection fractional flow $f_{w,inj}$ as shown in **Figure 12** [35].

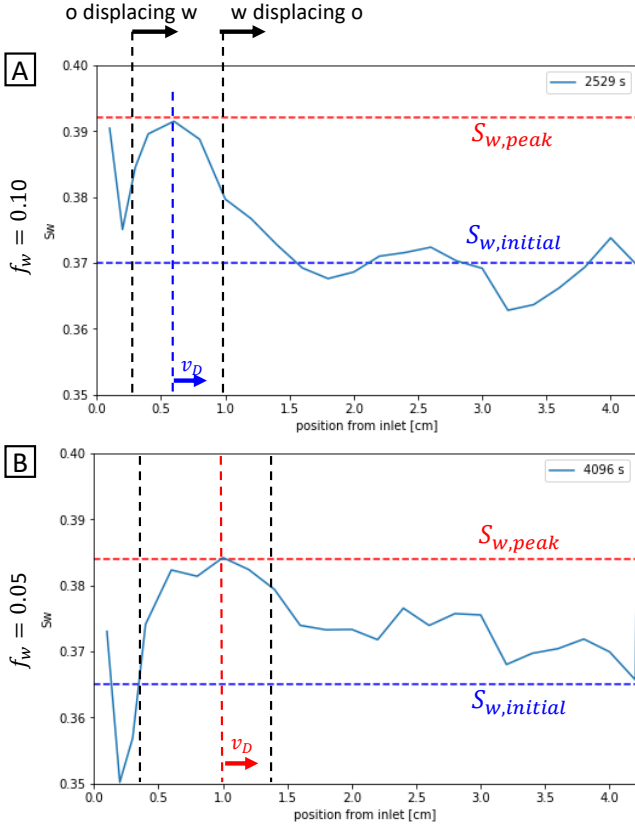


Figure 11. Saturation profiles $S_w(x)$ at a specific time t for $f_w = 0.10$ (A) and $f_w = 0.05$ (B). From an initial water saturation $S_{w,initial}$ a saturation peak $S_{w,peak}$ is observed which moves forward through water displacing oil at the leading edge (imbibition). At the trailing edge, oil displaces water (drainage). In principle both edges can move at different velocities, but the width of the peak in space is less than a capillary dispersion zone [29] and therefore we only operate with an average velocity v_D at which the peak moves and refer to it as an overall drainage process at which the peak is pushed forward by the injected oil fraction.

The fractional flow shock front solution is constructed from imbibition fractional flow $f_{w,im}$ at initial water saturation $S_{w,initial}$ to the intersection of the line (4) and the imbibition $f_{w,im}(S_w)$.

In **Figure 13** this fractional flow construction is applied to the cases for $f_{w,inj} = 0.15$ and $f_{w,inj} = 0.10$. While for $f_{w,inj} = 0.15$ we see a behavior conceptually similar as in the cartoon in **Figure 12** i.e. that the shock front saturation S_w^* which would represent the saturation peak of the travelling wave from **Figure 10** and **Figure 11** is larger than the initial saturation $S_w^* > S_{w,initial}$. However, for fractional flow $f_{w,inj} = 0.10$ we see that $S_w^* < S_{w,initial}$ meaning that there is an inflection point for a fractional flow somewhere $0.07 < f_w^* < 0.12$. For injections above the inflection point $f_{w,inj} > f_w^*$ the shock front saturation increases over the initial saturation i.e. represents an imbibition process, and for

$f_{w,inj} < f_w^*$ the shock front saturation decreases i.e. is a drainage process.

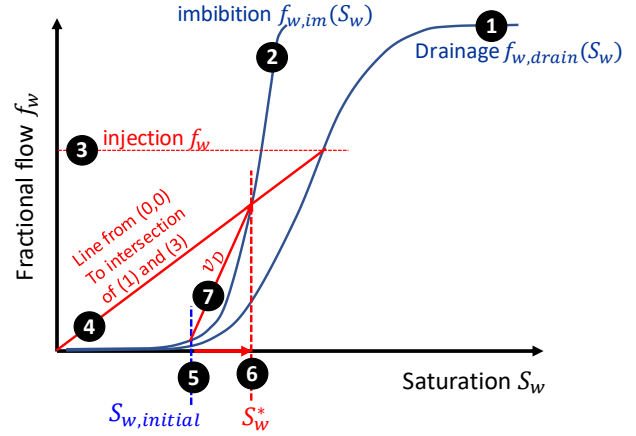


Figure 12. Schematic description of the fractional flow solution for the traveling wave: starting with drainage (1) and imbibition (2) $f_w(S_w)$ curves, a line (4) is drawn from the origin to the intersection (3) of the injection fractional flow $f_{w,inj}$ and the drainage $f_{w,drain}(S_w)$ curve (1). The fractional flow shock front solution (7) is constructed from the imbibition f_w at initial saturation $S_{w,initial}$ (5) to the intersection of line (4) with the imbibition $f_{w,im}(S_w^*)$ at shock front saturation S_w^* (6).

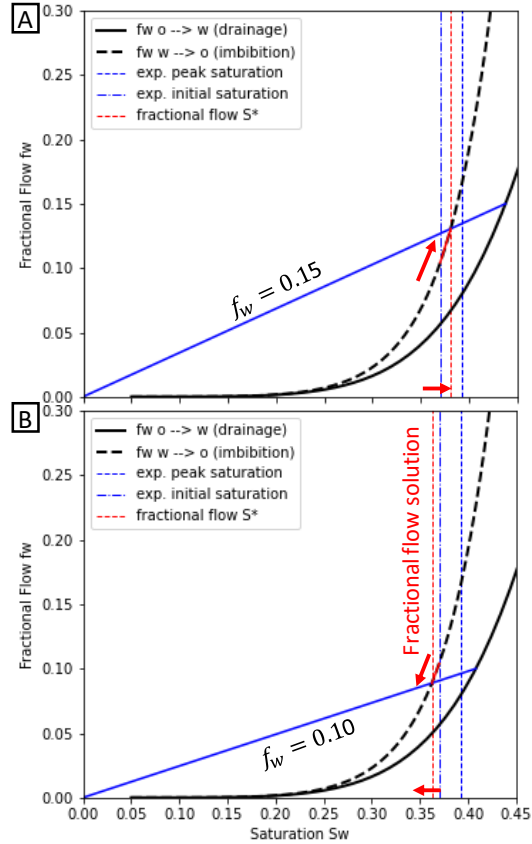


Figure 13. Fractional flow solution for injection at $f_{w,inj} = 0.15$ (A) and $f_{w,inj} = 0.10$ (B) considering the hysteresis fractional flow model from **Figure 12** but with the drainage and imbibition fractional flow curves of the Fontainebleau experiment (**Figure 9**).

Given the limited experimental accuracy and uncertainties with which the initial saturation $S_{w,initial}$ can be determined (see **Figure 11**) which also impacts the fractional flow solution it is very well possible that the $f_{w,inj} = 0.10$ step is still above the inflection point while $f_{w,inj} = 0.05$ would be clearly below the inflection point. From the space-time plot $S_w(x, t)$ in **Figure 10** it is difficult to see any conceptual difference above and below the inflection point f_w^* . Only the slope of the waves in the space-time domain is different which suggest a different propagation speed. However, in the saturation profiles shown in **Figure 11B** we see that for the trailing front the saturation falls below the initial saturation which could indicate that water is pushing oil, i.e. has more of an imbibition character.

3.7 Velocity of the traveling waves

In the next step we compare the propagation velocity of the saturation peak with the prediction from fractional flow theory for the velocity v_D at which saturation S_w propagates

$$v_D|_{S_w} = \frac{x_D}{t_D}|_{S_w} = \frac{df_w}{dS_w}|_{S_w} \quad (4)$$

where $x_D = x/L$ is the dimensionless distance (L is the length of the core) and $t_D = PV_{injected}/PV$ the dimensionless time expressed in terms of the fraction of injected pore volumes to the pore volume of the core PV .

In the experiment, for $f_{w,inj} = 0.10$ we find $v = 0.76 \text{ mm/min}$ which corresponds to a dimensionless velocity $v_D = 0.6$. For $f_{w,inj} = 0.05$ the wave velocity v is between 1.7 and 2.1 mm/min which corresponds to dimensionless velocity $v_D = 2.1 - 2.6$. In **Figure 14** v_D from the two experiments is compared with the fractional flow prediction from eq. 4.

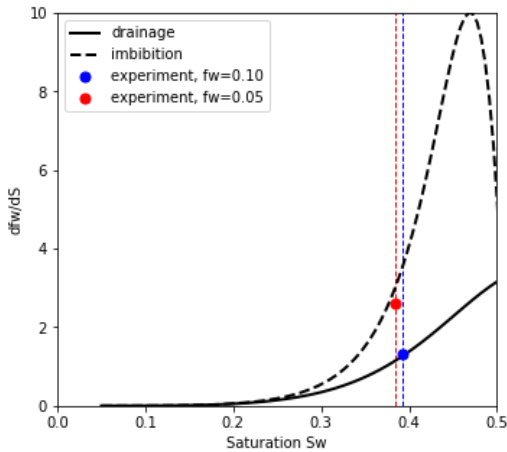


Figure 14. Dimensionless velocity v_D of the propagating saturation peak from **Figure 9** and comparison with the fractional flow prediction where $v_D = df_w/dS_w$ (eq. 4). For injection $f_{w,inj} = 0.10$ we find a behavior compatible with the drainage df_w/dS_w while for $f_{w,inj} = 0.05$ v_D is compatible with imbibition. That is somewhat consistent with the observation of the inflection point somewhere $0.07 < f_w^* < 0.12$ observed in **Figure 13**.

We find that for $f_{w,inj} = 0.10$ the experimental v_D is compatible with a **drainage** behavior consistent with the

fractional flow construction above the inflection point i.e. from **Figure 13A**. As already pointed out, even though **Figure 13B** suggests that $f_{w,inj} = 0.10$ is below the inflection point f_w^* , because of the experimental uncertainty it is very well possible that it is actually above the inflection point. v_D being consistent with drainage df_w/dS_w also suggests that overall the velocity of the saturation peak is dominated by the trailing edge.

for $f_{w,inj} = 0.05$ the experimental v_D is compatible with an **imbibition** behavior. That is consistent with the observation that $f_{w,inj} = 0.05$ is clearly below the inflection point f_w^* .

3.8 Physical interpretation of travelling waves

From **Figure 10** it is clear that saturation fluctuations are caused travelling saturation waves. They are also likely the cause of pressure fluctuations as per fractional flow theory, pressure and saturation response are coupled. The observation of different pressure and saturation frequency and amplitudes from **Figure 6** and **Figure 7** can be potentially attributed to the different sampling rates and the associated impact of under-sampling as shown in **Figure 8**.

The remaining question is why we observe travelling waves first place. The traditional expectation is that when a steady-state is reached, saturation is constant in time and space (except for capillary end-effects [29]).

A possible reason for the presence of travelling saturation waves is that for the specific flow conditions, the solution of the governing fractional flow equations are unstable against perturbations such as pore scale displacements, Haines jumps etc. The effects of such instabilities could be shown mathematically by using for instance linear stability analysis.

However, moving banks that are initialized via respective initial conditions do not explain why during constant fractional flow injection the moving saturation banks appear, i.e. why a homogeneous saturation solution becomes unstable against perturbations. In order to prove that, a linear stability analysis of the governing equations e.g. in [33,34] would be required, which would involve a significant level of complexity. Given the degree of uncertainty and assumptions involved it is not clear whether such an analysis can be successful.

Here we follow a different approach and argue more from a physical side why nature would prefer a travelling wave solution over constant saturation. Starting point is the question whether travelling waves would transport more flux than fractional flow at constant saturation. The assessment of that question will be based on the flux $\lambda_\alpha = k_{r,\alpha}/\mu_\alpha$ of phase α . We have to honor the flux boundary condition i.e. injecting water and oil phases at f_w . Therefore, we weigh the mobility of water with f_w and oil with $(1 - f_w)$. For a flat saturation profile we obtain

$$\lambda_{tot}^{flat} = f_w \frac{k_{r,w}^{drain}}{\mu_w} + (1 - f_w) \frac{k_{r,o}^{drain}}{\mu_o} \quad (5)$$

In order to estimate the total mobility of a travelling saturation wave we treat it as a moving water bank with length $l_w = 0.1 - 0.2$ (i.e. having a length of 10-20% of the total saturation profile, see **Figure 10** and **Figure 11**) and a

saturation height of $\delta S_w = \pm 0.01$ and $\delta S_w = \pm 0.02$. The total mobility of the travelling bank is then

$$\lambda_{tot}^{bank} = l_w \lambda^{water\ bank} + (1 - l_w) \lambda^{oil\ bank} \quad (6)$$

In **Figure 15** we plot the ratio of λ_{bank}^{tot} from eq. 6 over the total mobility of the flat saturation profile λ_{tot}^{flat} from eq. (5), i.e. $\lambda_{bank}^{tot}/\lambda_{tot}^{flat}$. For $\lambda_{bank}^{tot}/\lambda_{tot}^{flat} < 1$ the flat saturation profile has the higher total mobility. But for $\lambda_{bank}^{tot}/\lambda_{tot}^{flat} > 1$ the travelling wave has the total higher mobility. We can see from **Figure 15** that this is the case for saturations $S_w < 0.4 - 0.5$ or $f_w < 0.4$ which is consistent with the general observation

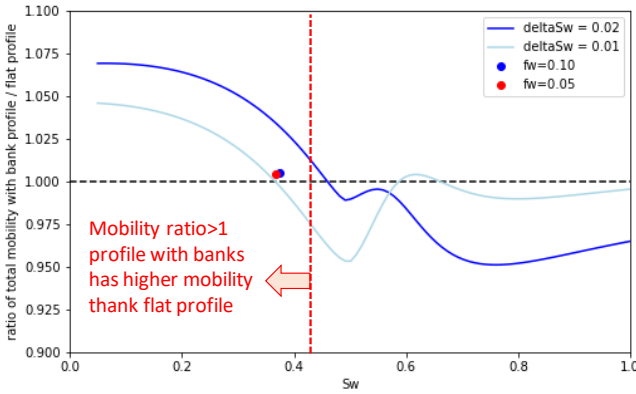


Figure 15. Ratio of the total flux of the travelling saturation waves (“banks”) and the total flux of a flat saturation profile. We see that – depending on the saturation wave amplitudes δS_w – the total mobility of the traveling wave solution is higher than for a homogenous saturation profile, meaning that for the same pressure drop more total flux is transported than for a homogenous saturation profile. For a saturation wave amplitude $\delta S_w = \pm 0.01$ that occurs for $S_w < 0.39$ and for $\delta S_w = \pm 0.02$ for $S_w < 0.45$. That is roughly consistent with the experimentally observed onset of fluctuations beyond the noise level from $S_w < 0.4 - 0.5$ or $f_w < 0.4 - 0.6$.

That means that travelling waves can transport at the same pressure drop more flux than a homogeneous saturation profile, i.e. it is energetically more favorable than transport at a flat saturation profile. Note that this is just a rough approximation and does not replace a more rigorous stability analysis which is subject to future work.

4 Influence of Wettability

In an unrelated study (but with the same experimental setup) we demonstrate the influence of wettability conditions on the magnitude of the pressure and saturation fluctuations. For that study, three cylindrical samples (5 cm length and 3.8 cm diameter) of Bentheimer rock ($\phi = 0.25$, $K = 2.6 D$, twin-samples taken from the same block specifically selected for homogeneity) were aged with 3 different crude oils (properties listed in **Table 1**) following largely the desaturation (using a centrifuge) and ageing protocol (40 days) outlined in [41] (but without pre-drilling small sub-samples because these are Darcy scale experiments). The flow experiment was conducted with decalin instead of crude oil.

The raw data for first imbibition experiment for the 3 samples is shown in **Figure 16A**. Based on an extensive analysis of the 3 different crude oils using gas chromatography and cyclotron resonance mass spectrometry methods which allows to distinguish chemical species to the level of functional groups extending significantly beyond TAN, TBN and SARA analysis, the potential for wettability alteration is highest for crude oil 3 followed by crude 2 and the least for crude 1. This is confirmed by the trend of residual oil saturation, $S_{o,r}$ and the water endpoint relative permeability $k_{r,w}(S_{o,r})$ displayed in **Figure 16B**.

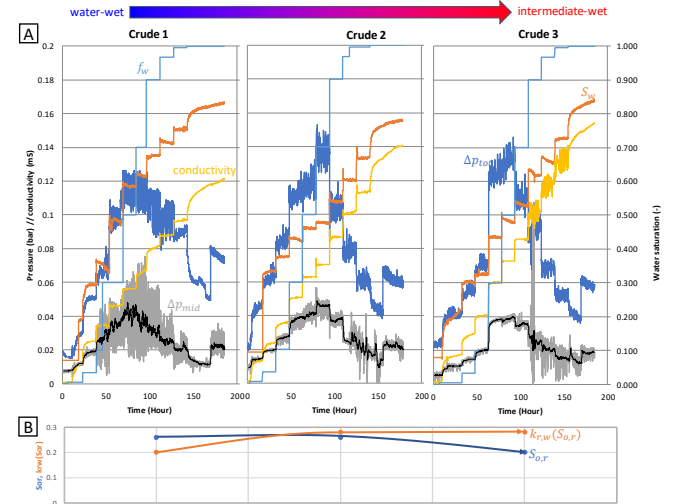


Figure 16. Raw data for 3 steady-state core floods in Bentheimer rock aged with 3 different crude oils (A) resulting in 3 different wettability conditions from more water-wet to more intermediate-wet, consistent magnitude of residual oil saturation, $S_{o,r}$ and water relative permeability endpoint, $k_{r,w}(S_{o,r})$ (B). The magnitude of pressure and saturation fluctuations systematically decreases from water-wet to intermediate-wet conditions.

Table 1. Properties of crude 1, 2 and 3.

Crude	Density	Visc.	TAN	TBN	Sat	Aro	Res
	kg/m ³	mPas	mg KOH/g	mg /kg	wt-%	wt-%	wt-%
1	934.7	88.43	1.37	320	37	48	14
2	833.9	4.87	0.07	83.9	58	37	4
3	859.2	9.47	0.09	271	44	44	10

The pressure and saturation fluctuations shown in **Figure 16A** follow a systematic trend with wettability where the fluctuations are largest for water-wet conditions and lowest for intermediate- to mixed-wet conditions. This observation confirms that the fluctuations are not an artefact because except for the wettability no other condition was changed and the same setup was used with practically identical rock samples. It rather confirms that the effect is systematically affected by wettability conditions. In an independent set of pore-level experiments conducted with smaller twin-samples

from the same block of Bentheimer rock following the preparation protocol in [41] similar trends i.e. strong fluctuations in the water-wet case [10] and much less fluctuations in the intermediate-wet (aged) case [11] were observed. This confirms, on the one hand, the independent reproducibility of the effect, and on the other hand, links the Darcy-scale observation to pore scale flow regimes. Already a previous study performed in Ketton limestone showed that in mixed-wet rock the flow regimes are systematically different due to enhanced ganglion dynamics [27]. The study by Lin et al. [11] provided the insight of increased connectivity in mixed-wet conditions due to bi-continuous interfaces. Increased connectivity implies less pore scale displacement events together with an overall lower capillary pressure magnitude resulting in lower magnitude of pressure fluctuations. At the same time the different wettability will also impact relative permeability and consequentially the fractional flow curves. A detailed analysis similar to that presented in section (3) would be required to fully understand how that impacts the travelling saturation wave instability.

5 Summary & Conclusions

The raw data of a steady-state (drainage) core flooding experiment in water-wet Fontainebleau sandstone rock shows reproducibly pressure, saturation and electrical conductivity fluctuations in a systematic manner in terms of fractional flow and saturation range but also wettability (for imbibition experiments where rock has been aged with crude). The experimental setup has been designed to rule out common experimental artefacts such as back pressure regulators or complex fluid behavior. Artefacts from e.g. the injection instability (effects in the end-piece and capillary entry pressure for oil) can be also largely ruled out because the effect would be present for all fractional flows and would scale with oil injection rate but that is not what is experimentally observed. In a very recent experiment using the same concepts and in particular the same end pieces as shown in **Figure 2B** the fluid distribution inside the end piece was imaged, observing continuous injection for both oil and water phases. While water injection occurred mainly in the center (and re-distributed in the first few layers of pores) the oil phase is distributed over the whole end face of the core, i.e. no signature of slug-like injection has been observed.

By systematically analyzing the raw data, fluctuations can be separated from instrumental noise suggesting that fluctuations mainly occur in the fractional flow range of $0.67 \geq f_w \geq 0.02$. The saturation space time $S_w(x, t)$ analysis reveals that the underlying reason of saturation (and pressure) fluctuations are travelling saturation waves, which can be reconciled with fractional flow theory. There is also an intuitive physical explanation for traveling saturation waves as a rough estimate reveals that travelling waves transport more flux at the same pressure drop than for flat saturation profiles which occurs roughly in the same fractional flow and saturation range where non-noise fluctuations are observed in the experiment.

That clearly demonstrates that the observation of strong pressure and/or saturation fluctuations in steady-state experiments are not necessarily experimental artefacts or noise but can have a physical origin. This also means that

observation of such strong fluctuations can no longer be a reason for dismissing the experiment as invalid. It rather means that we need to update our interpretation methodology for such experiments and this work provides respective guidance.

There are a range of potential consequences which we need to be aware. Travelling saturation waves involve hysteresis because the leading front of a propagating water saturation peak represents an imbibition process while the trailing front is a drainage process. Therefore, construction of the fractional flow solution involves both drainage and imbibition fractional flow curves. That also means that the resulting relative permeability curve measured in such steady-state experiments is not a pure drainage or imbibition bounding curve anymore but rather a scanning curve. Given the complexity of hysteresis models, previous work [34] pointed out that solutions of such models are inherently non-unique. That would explain why interpretation workflows of relative permeability core floods by inverse modelling [1,2] show even with the most flexible relative permeability model still residuals which are non-Gaussian.

The second level of consequences are more conceptual and relate to the transition from pore- to Darcy scale. While we speculate that pore scale events provide a trigger for pressure and saturation fluctuations, it is clear that based on volumetric assessment the saturation change associated with fluctuations involve hundreds to thousands of pores, i.e. are not a pore scale phenomenon anymore. Without a valid fractional flow solution, pore scale fluctuations would eventually average out at REV scale. Only because a valid fractional flow solution exists, they are still visible on the centimeter scale. The length of the moving saturation bank of a few mm is approximately in the same range as the size of the biggest possible oil clusters [39] just before getting mobilized by viscous forces [40] and also approximately the length of a capillary dispersion zone [29]. Therefore, the travelling saturation waves represent the transition from pore to Darcy scale. We have never looked at the transition from pore to Darcy scale in this way which means that it deserves also a more detailed investigation in the future.

Diederik van Batenburg, John van Wunnik and Jasper de Reus are acknowledged for helpful discussions about the fractional flow analysis.

References

1. Berg, S., Unsal, E., Dijk, H., Non-Uniqueness and Uncertainty Quantification of Relative Permeability Measurements by Inverse Modelling, *Computers and Geotechnics* 132, 103964, 2021.
2. Berg, S., Unsal, E., Dijk, H., Sensitivity and uncertainty analysis for parameterization of multi phase flow models, *Transport in Porous Media*, *in press*, 2021, DOI: 10.1007/s11242-021-01576-4.
3. Masalmeh, S. K., Sorop, T. G., Suijkerbuijk, B.M.J.M., Vermolen, E.C.M., Douma, S., van der Linde, H. A. and Pieterse, S.G.J. (2014), *Low Salinity Flooding: Experimental Evaluation and Numerical Interpretation*, IPTC 17558, presented at the International Petroleum

- Technology Conference, Doha, Qatar 19-22 January 2014.
4. Sorop, T. G., Masalmeh, S. K., Suijkerbuijk, B. M. J. M., van der Linde, H. A., Mahani, H., Brussee, N. J., Marcelis, F. A. H. M., and Coorn, A. (2015). Relative permeability measurements to quantify the low salinity flooding effect at field scale. In Abu Dhabi International Petroleum Exhibition and Conference held in Abu Dhabi, UAE, 9-12 November 2015, number SPE-177865-MS.
 5. Wang, Y., Masalmeh, S.K., Obtaining High Quality SCAL Data: Combining different measurement techniques, saturation monitoring, numerical interpretation and continuous monitoring of experimental data, E3S Web of Conferences 89, 02007, 2019. SCA2018.
 6. Clennell, M. B., White, C., Giwelli, A., Myers, M., Esteban, L. Cullingford, M., Richardson, W., Ward, G., Waugh, M., Cole, S., Hunt, A., Bright, P., Improved method for complete gas-brine imbibition relative permeability curves, International Symposium of the Society of Core Analysts held in Pau, France, 26-30 Aug. 2019, paper SCA2019-006.
 7. Alcorn, Z. P., Fredriksen, S. B., Sharma, M., Føyen, T., Wergeland, C., Ferno, M. A., Graue, A., Erslund, G., Core-scale sensitivity study of CO₂ foam injection strategies for mobility control, enhanced oil recovery and CO₂ storage, International Symposium of the Society of Core Analysts held in Pau, France, 26-30 Aug. 2019, paper SCA2019-030.
 8. Primkulov, B. K., Pahlavan, A. A., Fu, X., Zhao, B., MacMinn, C. W., Juanes, R., Signatures of fluid-fluid displacement in porous media: wettability, patterns and pressures, *J. Fluid Mech.* 875, R4, 2019.
 9. Rücker, M., Berg, S., Armstrong, R. T., Georgiadis, A., Ott, H., Simon, L., Enzmann, F., Kersten, M., de With, S., The Fate of Oil Clusters During Fractional Flow: Trajectories in the Saturation-Capillary Number Space, International Symposium of the Society of Core Analysts held in St. John's Newfoundland and Labrador, Canada, 16-21 August, 2015, paper SCA2015-007.
 10. Lin, Q., Bijeljic, B., Pini, R., Blunt, M. J., Krevor, S., Imaging and Measurement of Pore-Scale Interfacial Curvature to Determine Capillary Pressure Simultaneously with Relative Permeability, *Water Resources Research* 54, 7046-7060, 2018.
 11. Lin, Q., Bijeljic, B., Berg, S., Pini, R., Blunt, M. J., Krevor, S. (2019), Minimal surfaces in porous media: Pore-scale imaging of multiphase flow in an altered-wettability Bentheimer Sandstone, *Phys.Rev.E* 99: 063105.
 12. Datta, S. S., Dupin, J.-B., & Weitz, D. A., Fluid breakup during simultaneous two-phase flow through a three-dimensional porous medium. *Physics of Fluids*, 26, 62004, 2014.
 13. Datta, S. S., Ramakrishnan, T. S., & Weitz, D. A., Mobilization of a trapped non-wetting fluid from a three-dimensional porous medium. *Physics of Fluids*, 26, 22002, 2014.
 14. Gao, Y., Lin, Q., Bijeljic, B., Blunt, M. J., X-ray microtomography of intermittency in multiphase flow at steady state using a differential imaging method, 2017.
 15. Gao, Y., Raeini, A. Q., Blunt, M. J., Bijeljic, B., Pore occupancy, relative permeability and flow intermittency measurements using X-ray micro-tomography in a complex carbonate, *Advances in Water Resources* 129, 56-69, 2019.
 16. Gao, Y., Lin, Q., Bijeljic, B., Blunt, M. J., Pore-scale dynamics and the multiphase Darcy law, *Physical Review Fluids* 5 (1), 013801, 2020.
 17. Spurin, C., Bultreys, T., Bijeljic, B., Blunt, M. J., Krevor, S., Intermittent fluid connectivity during two-phase flow in a heterogeneous carbonate rock, *Physical Review E* 100 (4), 043103, 2019.
 18. Spurin, C., Bultreys, T., Rücker, M., Garfi, G., Schlepütz, C. M., Novak, V., Berg, S., Blunt, M. J., Krevor, S., Real-time imaging reveals distinct pore scale dynamics during transient and equilibrium subsurface multiphase flow, *Water Resources Research* 56(12), e2020WR028287, 2020.
 19. Armstrong, R.T., Ott, H., Georgiadis, A., Rücker, M., Schwing, A., Berg, S., Sub-second pore scale displacement processes and relaxation dynamics in multiphase flow, *Water Resources Research* 52(12), 9162–9176, 2014.
 20. Reynolds, C.A., Krevor, S., Characterizing flow behavior for gas injection; relative permeability of CO₂-brine and N₂-water in heterogeneous rocks, *Water Resources Research* 51, 9464-9489, 2015.
 21. Menke, H.P, Gao, Y., Linden, S., Andrew, M.G., Using nano-XRM and high-contrast imaging to inform micro-porosity permeability during Stokes-Brinkman single and two-phase flow simulations on micro-CT images., *Advances in Water Resources* under review 2021 / Earth ArXiv, <https://doi.org/10.31223/osf.io/ubg6p>
 22. Moebius, F., Or, D., Interfacial jumps and pressure bursts during fluid displacement in interacting regular capillaries, *Journal of Colloid and Interface Science* 377, 406-415, 2012.
 23. DiCarlo DA, Cidoncha JIG, Hickey C (2003) Acoustic measurements of pore scale displacements. *Geophys Res Lett* 30(17):1901.
 24. Reynolds, C. A., Menke, H., Andrew, M., Blunt, M. J., & Krevor, S., Dynamic fluid connectivity during steady-state multiphase flow in a sandstone. *Proceedings of the National Academy of Sciences*, 114(31), 8187-8192, 2017.
 25. Winkler, M., Gjennestad, M. Aa., Bedeaux, D., Kjelstrup, S., Cabriolu, R., Hansen, A., Onsager-Symmetry Obeyed in Athermal Mesoscopic Systems: Two-Phase Flow in Porous Media, *Frontiers in Physics* 8:60, 2020.
 26. Rücker, M., Berg, S., Armstrong, R. T., Georgiadis, A., Ott, H., Schwing, A., Neiteler, R., Brussee, N., Makurat, A., Leu, L., Wolf, M., Khan, F., Enzmann, F., Kersten, M., From Connected Pathway Flow to Ganglion

- Dynamics, *Geophysical Research Letters* 42, 3888-3894, 2015.
27. Rücker, M., Bartels, W.-B., Singh, K., Brussee, N., Coorn, A., van der Linde, H., Bonnin, A., Ott, H., Hassanizadeh, S.M., Blunt, M.J., Mahani, H., Georgiadis, A., Berg, S., The Effect of Mixed Wettability on Pore Scale Flow Regimes Based on a Flooding Experiment in Ketton Limestone, *Geophysical Research Letters* 46(6), 3225-3234, 2019.
 28. Kokkedee J.A., Boom W., Frens A.M., Maas J.G., Improved special core analysis: scope for a reduced residual oil saturation, *Proceedings of Society of Core Analysis conference paper 9601*, 1-13, 1996.
 29. Huang, D. D. and Honarpour, M. M., Capillary end effects in coreflood calculations, *Journal of Petroleum Science and Engineering* 19: 103-117, 1998.
 30. Berg, S., Rücker, M., Ott, H., Georgiadis, A., Van der Linde, H., Enzmann, F., Kersten, M., de With, S., Becker, J., Wiegmann, A., Connected pathway relative permeability from pore-scale imaging of imbibition. *Advances in Water Resources*, 90, 24-35, 2016.
 31. Jacquin, C., Correlations between the permeability and the geometric characteristics of the Fontainebleau gres. *Rev. Inst. Fr. Pet.* 19: 921- 937, 1964.
 32. Al Saadi, F., Wolf, K., Kruijsdijk, C. V. Characterization of Fontainebleau sandstone: Quartz overgrowth and its impact on pore-throat framework. *Journal of Petroleum & Environmental Biotechnology*, 7(328), 1-12, 2017.
 33. Plohr, B., Marchesin, D., Bedrikovetsky, P., Krause, P., Modeling hysteresis in porous media flow via relaxation, *Computational Geosciences* 5, 225-256, 2001.
 34. Corli, A., Fan, H., Two-phase flow in porous media with hysteresis, *Journal of Differential Equations* 265, 1156-1190, 2018.
 35. Lake, L. W., *Enhanced Oil Recovery*, Prentice Hall, 1984.
 36. Unsal, E., Mason, G., Morrow, N.R., Ruth, D.W., Co-current and counter-current imbibition in independent tubes of non-axisymmetric geometry, *Journal of colloid and interface science* 306 (1), 105-117, 2007.
 37. Unsal, E., Mason, G., Ruth, D.W., Morrow, N.R., Co- and counter-current spontaneous imbibition into groups of capillary tubes with lateral connections permitting cross-flow, *Journal of colloid and interface science* 315 (1), 200-209, 2007.
 38. Unsal, E., Mason, G., Morrow, N.R., Ruth, D.W., Bubble snap-off and capillary-back pressure during counter-current spontaneous imbibition into model pores, *Langmuir* 25 (6), 3387-3395, 2009.
 39. Georgiadis, A., Berg, S., Maitland, G., Makurat, A., Ott, H., Pore-Scale micro-CT Imaging: Non-Wetting Phase Cluster Size Distribution During Drainage and Imbibition, *Physical Review E* 88(3), 033002, 2013.
 40. Armstrong, R. T., Georgiadis, A., Ott, H., Klemin, D., Berg, S., Pore-scale mobilization of non-wetting phase ganglia and critical capillary number for onset of macroscopic capillary desaturation, *Geophys. Res. Lett.*, 41, 1-6, 2014.
 41. Lin, Q., Bijeljic, B., Krevor, S.C., Blunt, M.J., Rücker, M., Berg, S., Coorn, A., van der Linde, H., Georgiadis, A., Wilson, O.B., A new waterflood initialization protocol for pore-scale multiphase flow experiments, *Petrophysics* 60(02), 264-272, 2019.

In-situ investigation of salt precipitation dynamic induced by gas flow-through drying using simultaneous Neutron and X-ray dual-beam Radiography.

Matthieu Mascle^{*1}, Olivier Lopez², Herve Deschamps¹, Lars Rennan², Nicolas Lenoir^{3,4}, Alessandro Tengattini^{3,4}, Souhail Youssef¹

¹IFP Energies Nouvelles, Rueil-Malmaison, France

²Equinor ASA, Trondheim, Norway

³Univ. Grenoble Alpes, CNRS, Grenoble INP, 3SR, Grenoble, France

⁴Institut Laue-Langevin (ILL), Grenoble, France

Abstract. In this work, a new dual beam monitoring technique is presented to demonstrate its interest to investigate the salt precipitation dynamics induced by gas flow-through drying. It consists of imaging simultaneously a coreflood using both Neutron and X-ray beams. A method to calibrate and process the two signals is presented. It takes advantage of the difference of attenuation pattern between the two beams to quantify the different phase saturations and composition as well as the reduction of porosity caused by salt precipitation. A set of experiments has been conducted at the NeXT-Grenoble beamline of the Institut Laue-Langevin facilities (ILL, France). Experiments were conducted on an homogeneous rock sample of Bentheimer sandstone using dry nitrogen and a 100g/L KBr brine. The two first experiments aimed to calibrate the dual monitoring for the different phases. The last two experiments have been conducted with a brine capillary contact maintained at the gas outlet. Experimental data have given new insight to understand the organization of the three phases (the brine, the gas and the precipitated salt) when a salt bank is formed in the sample. The quantity of salt that accumulates allows to estimate the flow rate of brine pumped through the capillary contact to compensate the brine evaporation in the gas phase. Observations have shown that a reduction of the initial porosity in some sections of the sample by 13-15% was enough to trigger a gas draw-down characterized by the migration of the salt toward the gas inlet. In some conditions (low gas inlet pressure for example), the rise of the water can be fast enough to form a second salt bank higher in the sample. It has been observed that the formation of the second salt bank could spread the precipitated salt in a less damaging configuration for the gas flow, triggering a phase of gas build-up characterized by the withdrawal of the water. These phases of gas draw-down and build-up can alternate until the sample clogging.

* Corresponding author: matthieu.mascle@ifpen.fr

1. Introduction

The injection of a gas phase through a water saturated porous medium can reduce the saturation above the residual water saturation (S_{wi}) reached after a viscous displacement, by evaporation mechanisms. In the presence of brine, this process can induce salt crystallization and precipitation within the porous medium. The salt precipitation has been investigated in many studies, both experimentally [1–3] and numerically [4–6]. These studies aim to understand the physical and chemical interplay between the gas injection, capillary forces and the porous structure. They showed that the drying rate is proportional to the gas velocity and that any dissolved salt in the water can be transported by capillary flows induced by drying and can even accumulate near the injection surface. The permeability can then be reduced by pore clogging. They conclude that all these mechanisms must be included in models to calculate the near wellbore permeability and porosity changes with time, in order to correctly determine the well injectivity. Yet calibrating such a multi-parameter model is not straightforward and requires advanced experimental investigation to properly quantify the key parameters such as local saturation and salt concentration as well as the porosity reduction or precipitated salt quantity [1, 7, 8]

In a previous study [1] a comprehensive experimental investigation of the effect of gas flow in a sandstone sample initially saturated with water or brine using X-ray radiography has been presented. This study has qualitatively shown the impact of brine capillary contact on the accumulation of salt within the sample during dry gas injection. However, following Beer-Lambert law, X-ray intensity is attenuated by all crossed materials. The measured X-ray contrast is therefore sensitive to all material variations including the water saturation and the salt concentration. X-ray monitoring is not capable by itself to de-correlate and quantify the evolution of local water saturation, salt concentration and precipitate salt quantities.

To overcome this limitation, we introduce in this work a new in-situ monitoring instrument named NeXT-Grenoble and located at Institut Laue-Langevin (ILL, France) [9]. It consists in imaging simultaneously, by radiography, a sample using both Neutron and X-ray beams. We take advantage of the difference in attenuation characteristics of Neutron and X-ray [10]. Indeed, while X-ray is mainly sensitive to material electronic density, Neutron will mainly interact with atomic nuclei (if magnetic interaction is excluded). There is no straightforward relation between Neutron attenuation coefficient and the material density, while X-ray attenuation coefficients globally increase with the electronic density. For example, Neutron has a very high scattering cross section for hydrogen while chemical element like Bromine (Br), which considerably attenuates X-ray, will be almost transparent to Neutron. A state-of-the-art equipment designed for in-situ coreflood experimentation was used on NeXT-Grenoble to capture the dynamic of salt precipitation induced by gas flow-through drying. The experiments were conducted using a homogeneous rock sample of Bentheimer sandstone. First, the dry-out is conducted with deionized water to

characterize the dynamic without salt precipitation. The same experiment is repeated with a KBr brine water to evaluate when salt precipitation occurs. Finally, the last experiments are conducted with the KBr brine and a capillary contact maintained at the core outlet. This experiment is repeated with two gas injection scenarios: a high and low gas pressure gradient.

The two first experiments aimed to construct and calibrate a method to compute the different phases from the Neutron and X-ray monitoring. It is then applied to monitor the experiments conducted with the capillary contact. The dual monitoring allowed to separately quantify the dissolved and precipitated salt. The latter can be interpreted in terms of porosity reduction.

2. Materials and methods

2.1 Fluids and sample properties

Experiments have been conducted on a homogeneous Bentheimer sandstone of length and diameter $L = 2.0$ cm and $D = 9.32$ mm. The sample exhibits high porosity and permeability, measured to $\phi = 23\%$ and $K = 1500$ mD. Its pore-volume is measured to $PV = 0.31$ cc. X-ray and Neutron radiographies of the sample are showed in **Fig. 1** when saturated with nitrogen (N_2).

Three different fluids have been used to perform the experiments: dry nitrogen N_2 for the gas phase, deionized water for the first experiment and a 100g/l KBr brine (this salt concentration is referred as C_0). KBr salt was used for its high electronic density, giving a good X-ray contrast with the gas, and its low Neutron attenuation. Experiments are conducted at ambient temperature ($24^\circ\text{C} \pm 1^\circ\text{C}$). KBr solubility in deionized water is estimated to 650g/l for these conditions.

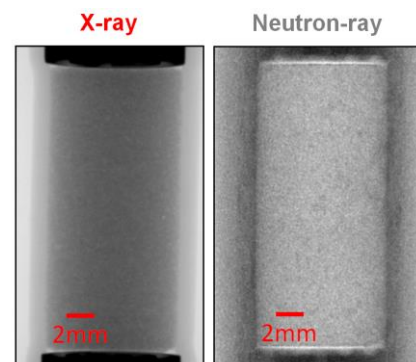


Fig. 1 : X-ray and Neutron-ray radiographies of the Bentheimer rock sample. X-ray and Neutron-ray projections were acquired respectively at a pixel resolution of $40 \mu\text{m}$ and $15 \mu\text{m}$.

2.2 Experimental set-up

The experimental set-up used in this study is shown in **Fig. 2**. Nitrogen is injected from the top at a constant pressure using a downstream pressure regulator. Gas flow rate is monitored using a Coriolis mass flowmeter. Brines (either deionized water or KBr brine) are injected using an Isco-pump. The confining pressure is set to 10bars using deuterated water to be less attenuating to Neutrons compared to normal water, and a 1mm thick perfluoro-

elastomer (FFKM) sleeve. All tubing are connected to a Hassler type cell. The main imaged components of the cell are presented in **Fig. 3**. The cell was designed to bear more than 15bars while being transparent to X-ray and Neutrons. The cell body is composed of a 2mm thick Teflon cylinder, to mitigate both Neutron activation and attenuation. The cell is equipped from each side with three connections (inlet, outlet and static line for the pressure transducer). The inlet/outlet pressures and differential pressure (ΔP) is measured using a Keller differential pressure sensor. A data acquisition system was used to monitor the pressure, mass flow and temperature. Finally, the set-up was installed in dedicated radiography facility equipment for in-situ saturation monitoring.

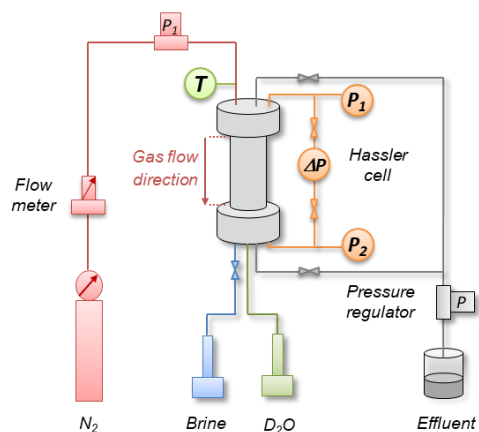


Fig. 2. Overview of the experimental set-up.

For all dry-out tests, the sample is set vertically, with the gas injected from the top of the plug and the water from the bottom. The capillary contact (for the experiments 3 and 4) is maintained by sweeping the bottom of the plug. For the 2D plots, the core axis is normalized as follow: $x = 0$ refers to the bottom, $x = L$ refers to the top.

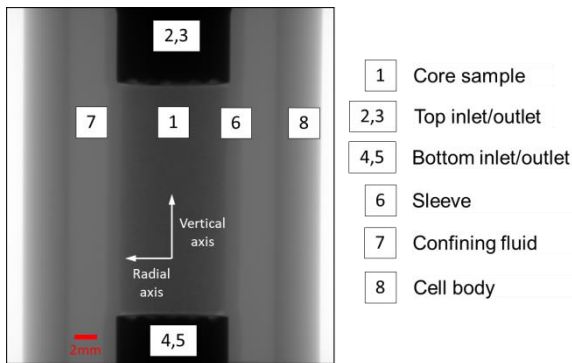


Fig. 3: X-ray Radiography showing the Hassler injection cell.

2.3 Experimental procedure

The four dry-out experiments are conducted using the same injection procedure:

- 1- Saturating the sample with the brine by injecting from the bottom inlet and opening the top outlet (the bottom outlet and top inlet are closed). To ensure a full saturation, a back pressure of 7bars is imposed after water breakthrough to compress and produce the trapped gas.
- 2- Opening the bottom outlet and top inlet and closing the top outlet. The water injection is maintained for allowing a sweeping of the bottom face of the sample.
- 3- After lowering the pore pressure to the atmosphere, the gas is injected at a constant pressure.
- 4- The sample is finally cleaned by injecting deionized water and increasing the back pressure until the reference X-ray attenuation is reached.

2.4 Dual beam in-situ monitoring

Dynamic in-situ monitoring is performed using the NeXT-Grenoble station recently designed at ILL [9]. It is composed of the dual Neutron and X-ray beams, simultaneously monitoring the sample from a different angle (see illustration Fig. 4). A nuclear reactor supplies several experimental stations with neutron flux (hot, thermal or cold neutrons). The NeXT station (used here) is supplied by a flux of up to $1.4 \text{ E}10 \text{ n/cm}^2/\text{s}$ of cold neutrons. A medium resolution detector allows the neutron imaging. It is composed of a scintillator, a mirror and camera plus optics, X-rays are generated using a sealed source generator (Hamamatsu L12161-07 X-ray microfocus generator) X-ray are monitored using a VarexScan® detector, equipped with a Cesium Iodide scintillator.

The main advantage of the dual beam is to benefit from different beam attenuation patterns [5, 9]. As hydrogen's neutron attenuation coefficient is very high compared to other materials used here, the Neutron contrast is mainly

sensitive to the water saturation. X-ray contrast however is sensitive to both water saturation and salt content.

The main parameters for radiography acquisitions are: X-ray pixel resolution of $40 \mu\text{m}$; Neutron pixel resolution of $15 \mu\text{m}$; acquisition time of 8s for both beams. Using this configuration, the resulting X-ray attenuation map appears to be noisier than the Neutron one. The 2D Neutron and X-ray projections are pre-processed in order to allow further quantitative computations. First, the Neutron projections are down-scaled by a factor of $0.375 (=15 \mu\text{m}/40 \mu\text{m})$ to match the X-ray projection pixel resolution. Then, the Neutron and the X-ray projections are registered to have the two sets of projections spatially aligned. It shall be reminded that the two beams are hitting the core sample from a different angle (see Fig. 4), the sample is not rotated during the monitoring. Therefore the two sets of projections are not showing the same 2D view of the core (especially in the radial direction). This effect is mitigated when considering the mean value (2D projection averaged on the whole sample range) or the vertical profile (2D projection averaged in the radial direction). Finally, the natural logarithm is applied to all projections.

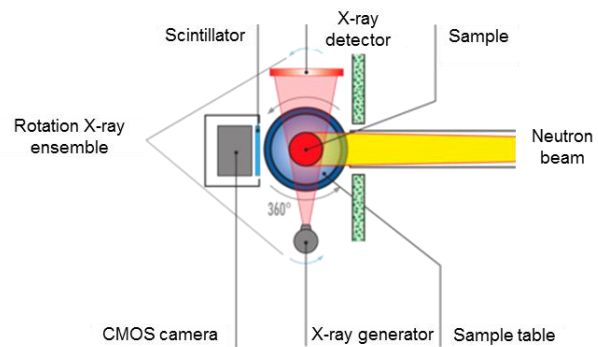


Fig. 4: Schematized top view of the NeXT dual beam lines (modified from [9]).

For both beams, the relation between intensity attenuation and the materials crossed can be expressed using the Beer-Lambert law [11]. For a multi-component system, it can be written as (1):

$$I(t) = I_0 e^{-\sum \mu_i x_i} \quad (1)$$

Where $I(t)$ and I_0 respectively refer to the transmitted and incident ray intensity, μ_i and x_i are respectively the material i attenuation coefficient and linear path of material i crossed by the beam. The summation operation \sum applies for all material crossed between the source and the detector, including all the cell components, the rock sample and the fluids saturating the rock. All constant quantities can be gathered and lumped in the incident ray intensity. In these experiments, three material paths are changing through time namely deionized water, nitrogen and salt. For all computations, the following simplifying hypothesis are made: (i) The KBr salt has the same attenuation coefficient when at solid or dissolved state and (ii) X-ray attenuation is linear to the salt quantity. With these hypotheses, the intensity attenuation $I(t)$ can be expressed for both beams as follow (2):

$$I(t) = I'_0 e^{-\sum \mu_{H_2O} x_{H_2O} + \mu_{KBr} x_{KBr} + \mu_{N_2} x_{N_2}} \quad (2)$$

$$\text{with } I'_0 = I_0 e^{-\alpha}$$

Where α account for the set-up constant contribution to the beam attenuation. The conservation of the total length path X of material crossed allows to write equation 3:

$$x_{H_2O} + x_{N_2} + x_{KBr} = X \quad (3)$$

As the natural logarithm is applied on all projections during the pre-processing, equation 2 become:

$$\log[I(t)] = \log[I'_0] - \sum_{N_2, H_2O, KBr} \mu_i x_i \quad (4)$$

Equation 4 needs to be calibrated for both beams to characterize the attenuation coefficients of all materials. It can be easily conducted for μ_{H_2O} and μ_{N_2} by saturating the sample with deionized water and nitrogen. However, the salt coefficient μ_{KBr} cannot be directly measured using its pure phase (solid salt), but its contribution on the Neutron and X-ray intensities attenuations can be estimated using a mixture: the 100g/L KBr brine (referred as the C_0 brine). This solution allows to calibrate the attenuations for a pore volume filled with 31mg of KBr salt ($C_0 * PV$) and the remaining space by deionized water ($\mu_{C_0} * X = x_{KBr} * \mu_{KBr} + \mu_{H_2O} * x_{H_2O}$, with $x_{KBr} + x_{H_2O} = X$). Its comparison with the Neutron and X-ray values recorded with the deionized water will allow to determine the contribution of the salt alone.

The calibration of both beams is conducted with the following injection sequence:

- 1- The sample is initially dried and saturated with N_2 .
- 2- It is saturated with deionized water (see details in section 2.3)
- 3- It is then saturated with the C_0 brine using miscible displacement.
- 4- Nitrogen is injected in the brine. Only the first steps are recorded during the viscous drainage, before the water evaporation starts, changing the brine concentration.

The mean Neutron and X-ray intensities monitored during the calibration are displayed in **Fig. 5**. The two signals variations are normalized between the dry state (N_2 saturated, reached at the end of step 1) and saturated with the C_0 brine (C_0 saturated, reached at the end of step 3). Equation 4 can be written for both beams for these two chosen references, giving respectively:

$$\log[I(N_2)] = \log[I'_0] - \mu_{N_2} X \quad (\text{when } N_2 \text{ saturated})$$

$$\log[I(KBr)] = \log[I'_0] - \mu_{C_0} X \quad (\text{when } C_0 \text{ saturated})$$

With the normalization, equation 4 becomes:

$$\frac{\log[I(t)] - \log[I(C_0)]}{\log[I(N_2)] - \log[I(C_0)]} = \frac{\mu_{C_0} X - \sum_{N_2, H_2O, KBr} \mu_i x_i}{X(\mu_{C_0} - \mu_{N_2})} \quad (5)$$

All projections (Neutron and X-ray) are processed with the operations described by equation 5. The values obtained after this processing are no longer intensities. They neither express a saturation, as the sample saturation evolves between more than two phases. They are referred in the rest of the text as the X-ray and the Neutron-ray values. In this system of normalization, the X-ray and the Neutron-Ray values are both set to 0 when the sample is saturated with C_0 brine ($x_{C_0} = X$); and to 1 when it is dry ($x_{N_2} = X$). The question that remains is how these values behave when the brine salinity is changed (lower or higher salinities).

The normalization described above is used for all next graphical representations. The cross-plot (**Fig. 5**) shows the Neutron and X-ray values for our three references phases: the nitrogen, the deionized water and the C_0 brine. Their coordinates (in this system of normalization) are given on the plot. All the points between these poles are recorded during the phase replacement. They show a perfect linear evolution from pole to pole. The positions of the poles confirm that the Neutron attenuation is mainly sensitive to water (because of the hydrogen). However, there is a small variation between deionized water and C_0 brine: C_0 brine attenuates slightly less the Neutron than the deionized water. It might be explained by an effect of dilution of the water molecules by the ionic species dissolved in the brine. For the X-ray, both the salt and the water attenuate the beam: the attenuation measured between the N_2 phase and the C_0 phase is caused at 36% by the water molecules and at 64% by the dissolved salt.

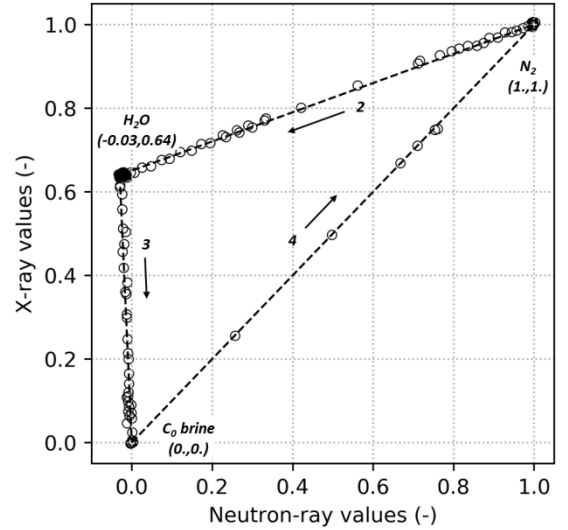


Fig. 5: Scatter plot of X-ray and Neutron-ray values during the calibration experiment. Arrows indicate the injection sequences described in the text. X-ray and Neutron-ray values are obtained with equation 5.

These poles and vectors that connect them draw a two axes plot that enables to compute the gas saturation S_g , the salt quantity m_{KBr} and the brine concentration C_{KBr} from the Neutron and X-ray values. These axes are drawn in **Fig. 6**. The green axis expresses the gas saturation, the blue axis expresses the salt quantity (1 unit = 31mg, the quantity of salt contained in one PV of C_0 brine). The grey diagonals give the brine concentration, in C_0 unit. An example is given in **Fig. 6** with a Neutron and X-ray measurement (see the

red marker) that records the saturation process, half-way through, of the dry sample with a 50g/L KBr brine ($C_0/2$ brine). The marker projection on the saturation axis gives the gas saturation: $S_g = 0.5$; its projection on the salt axis give the quantity of salt: $\frac{1}{4} * 31\text{mg} = 0.8\text{mg}$; and the grey diagonal the marker fall on gives the brine concentration: $C_0/2$.

The previous calculus strictly applies only when all the salt is dissolved in the brine phase. A correction is made when salt precipitates. Its effect on X-ray attenuation is considered to be the same, following the hypothesis made above, but its effect on the Neutron attenuation is different. When the salt is dissolved in the brine phase, it alters the density of water molecules and causes the reduction of attenuation described above. When the salt is in solid state, a third phase is formed. It still attenuates the X-ray, but no longer alters the brine phase (and no longer affect the Neutron-ray). The volume it occupies is computed using a salt density of 2.16g/cc. The reduction of porosity caused by the salt precipitation could then be estimated using equation 6.

$$\phi = \frac{m_{KBr}^{solid}}{\rho_{KBr} * PV} \quad (6)$$

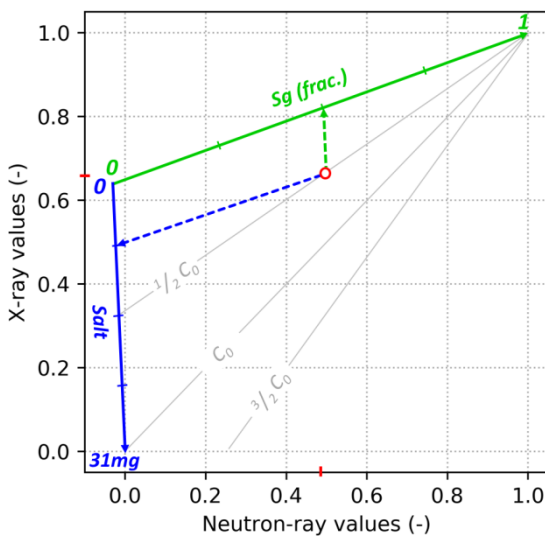


Fig. 6: Illustration of gas saturation, salt quantity and brine concentration computations from a Neutron and X-ray measurements (red marker). Explanations are given in the text.

3 Results and discussion

The four tests are presented and interpreted successively. They have been conducted one after the other, in the same acquisition sequence, without interrupting the X-ray and Neutron beams. As mentioned in the introduction, the two first tests aimed to calibrate the dual beam monitoring method.

3.1 Dry-out with the deionized water

Deionized water is used for this preliminary experiment. In these conditions, the Neutron and X-ray beams are expected to show the same trend when normalized between the dry

and the saturated states. The Neutron and X-ray attenuations are plotted in **Fig. 7** with the mass flow rate. The protocol described in section 2.3 is applied: the sample is saturated with the water from $t = 0$ to $t = 14\text{min}$. The gas injection starts at $t = 14\text{min}$, the gas inlet pressure is set to 0.55bars. The 1D vertical profiles recorded during the dry-out (from $t = 14\text{min}$ to $t = 28\text{min}$) are displayed in **Fig. 8**.

The gas saturation during the dry-out shows the variation steps already described in previous works [1, 3]. We observe a viscous gas drainage to S_{wi} (until $t = 17\text{min}$) followed by the evaporation of the remaining trapped brine. The S_{wi} value can be estimated at 20% from these plots. In **Fig. 8**, a front is observed during the evaporation with only a small production of water ahead of the front (the gas saturation plateau ahead of the front increase from 72% to 82% during the front advancement). Different mechanisms can explain this production ahead of the front (drainage, evaporation or a small capillary back flow), and will be discussed later. Globally, the evaporation process is quick enough to prevent the capillary forces to re-distribute the water in the sample.

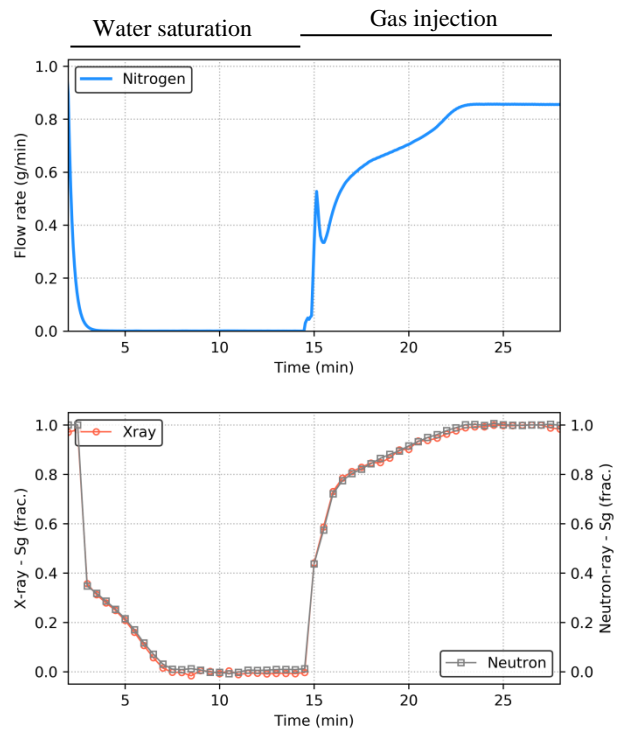


Fig. 7 : Dry-out with deionized water. X-ray and Neutron beams are normalized between dry state and saturated with deionized water.

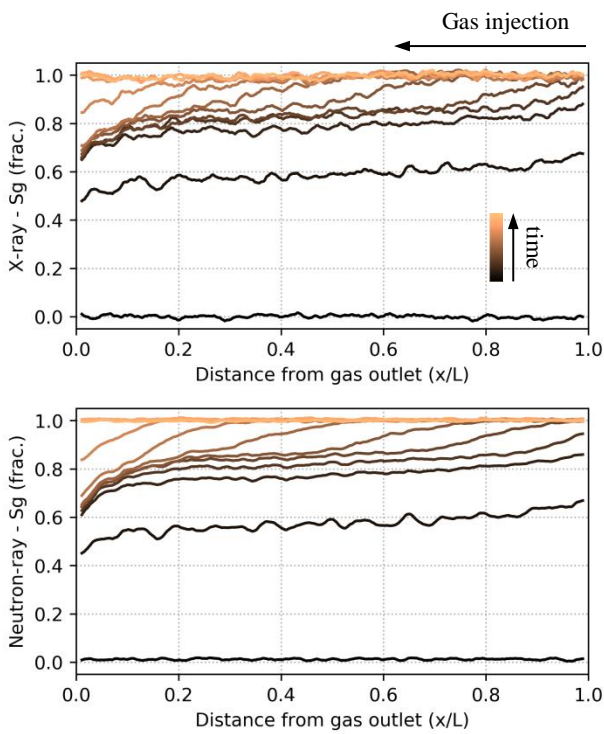


Fig. 8: X-ray and Neutron-ray profiles during the dry-out with deionized water (from $t = 14$ min to $t = 28$ min). X-ray and Neutron beams are normalized between dry state and saturated with deionized water. Gas is injected from the right.

3.2 Dry-out with the KBr brine

The previous experiment is reproduced with the deionized water replaced by the 100g/L KBr brine. The same gas inlet pressure of 0.55bars is set. The Neutron and X-ray attenuations are plotted in **Fig. 9**. In this experiment, the two attenuation curves are not superimposed due to the addition of salt. The quantity of salt and the gas saturation are computed in blue and green using the method detailed in section 2.4. The deionized water replacement by the KBr brine is recorded from $t = 45$ min to $t = 65$ min. The gas injection starts at $t = 66$ min. Pollutions with deionized water occur between $t = 55$ min to $t = 65$ min.

The salt mass curve shows an increase from 0 to 1unit during the replacement of deionized water by the KBr brine. Here, 1unit is defined as 31mg, the quantity of salt contained in a PV of C_o brine. This normalization allows to read the fraction of the initial quantity of salt that remained trapped in the sample during the dry-out. The dry-out dynamic is similar to the previous experiment, exhibiting the same steps: (1) the viscous drainage during which the salt is produced with the water and (2) the water evaporation during which salt is left in the sample. The second step is detected when the Neutron and X-ray attenuations divert. The quantity of salt left in the core at the end of the dry-out allows to quantify the contribution of the two production mechanisms (drainage and evaporation) to the water production. Here, we observe that 20% of the initial salt remain in the sample at the end of the experiment (cf. blue curve on **Fig. 9**). This is in agreement with the S_{wi} value that was estimated at the end of the drainage with deionized water.

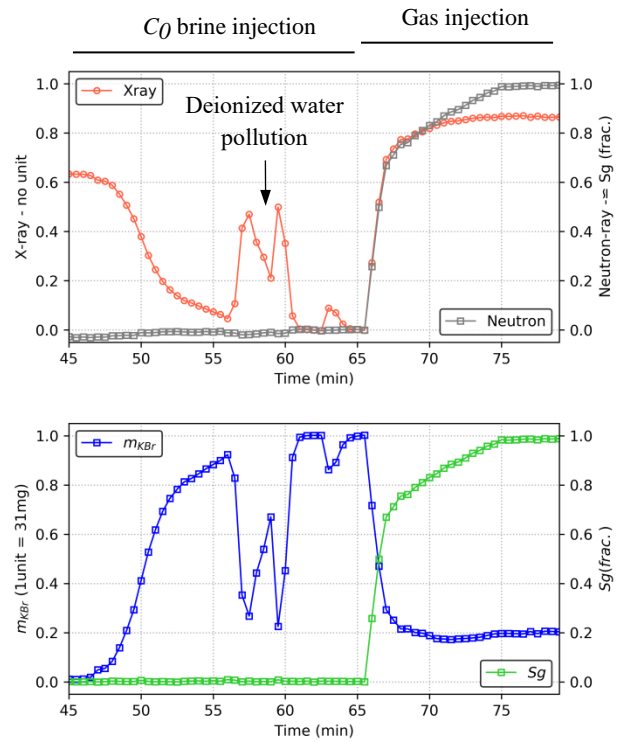


Fig. 9: Dry-out with the 100g/L KBr brine. At $t = 45$ min, the sample is saturated with deionized water before being replaced by the KBr brine.

The 2D projections recorded at the end of the dry-out are given in **Fig. 10**. They clearly show a small horizontal salt bank on the X-ray projection, close to the gas outlet. The salt distribution profiles recorded at S_{wi} (dissolved in the brine) and at the end of the dry-out (precipitated in the sample) are compared in **Fig. 11**. The dissolved salt distribution shows that the capillary end-effect locally increases the quantity of salt. The edges of the sample (1 mm from each side) are cropped during the data processing. It hides the extent of the end-effect and the dissolved salt it contains. The precipitated salt curve shows a salt deposition all along the core, with an accumulation close to the outlet. It is partly explained by the initial dissolved salt distribution at S_{wi} and probably also by a small redistribution of the salt contained in the capillary end-effect. However, if we exclude the capillary end-effect zone, the two curves show a perfect superposition, suggesting no water reorganization during the evaporation. The water production that was observed ahead of the front during the first experiment shall therefore be explained by early evaporation. All others production mechanisms (drainage or capillary back flow) would have redistributed the salt.

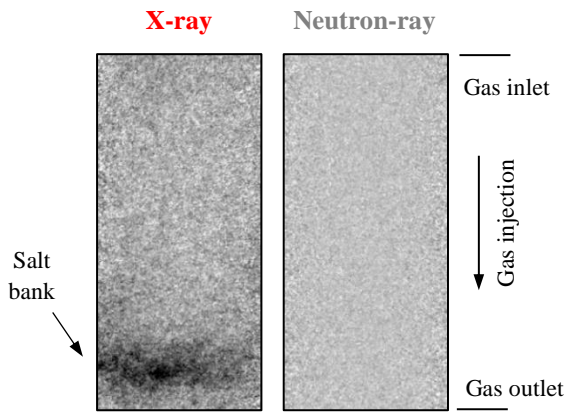


Fig. 10: 2D projections at the end of the dry-out (no capillary contact), when initially saturated with the KBr brine. On the X-ray projection, darker shades suggest salt bank position. The Neutron-ray projection shows a flat profile confirming that the sample is dry.

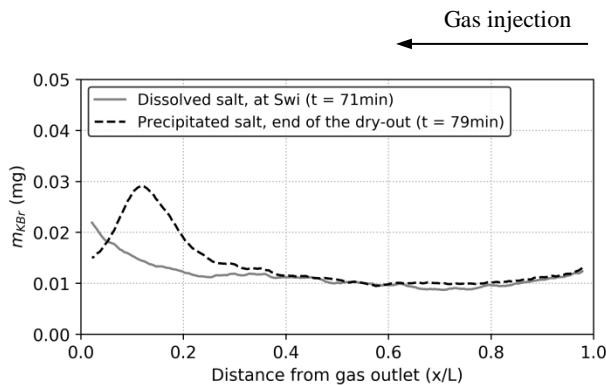


Fig. 11: Salt distribution, dissolved in the brine at S_{wi} (plain curve) and precipitated at the end of the dry-out (dashed curve).

3.3 Dry-out with capillary contact

The dry-out with the KBr brine is reproduced with a capillary contact maintained at the gas outlet using the bottom inlet and outlet lines (see **Fig. 3**). A recent work [1] has suggested that the capillary contact acts as a salt pump, allowing to accumulate more salt in the sample than initially dissolved. The underlying mechanism is believed to be a competition between evaporation and capillary forces [3]. The effect of the gas flow rate on this equilibrium is studied: the experiment is conducted twice with the inlet pressure set to 0.55bars and 0.35bars. These two configurations are referred to high and low pressure gradient dry-out, respectively.

3.3.1 High pressure gradient

For this dry-out experiment the inlet gas pressure is set to 0.55 bars. The gas is injected in the sample initially saturated with the 100g/L KBr brine. The gas flow rate during the dry-out is given in **Fig. 12**, with the gas saturation in green and the computed salt quantity in blue.

The initial steps of the dry-out exhibit a similar behavior as previously seen (i.e. a drainage step followed by the evaporation steps). The S_{wi} value can be estimated to 20%, from the minimum salt quantity trapped after the

drainage ($t = 95\text{min}$, blue curve). After that, the quantity of salt is multiplied by 4, from 0.2 units to 0.8 units (corresponding to 25mg). This demonstrates a substantial salt accumulation in the sample, while only gas is injected through it. During this salt accumulation sequence, we observe a strong decrease of the gas flow rate. This is easily explained by a reduction of the initial sample permeability as salt precipitates in the porous-space [1, 2]. The reduction of porosity caused by salt deposition will be estimated using the Neutron and X-ray profiles.

2D projections recorded before the salt starts to accumulate are shown in **Fig. 13**. They show a comparable small salt bank formed close to the gas outlet, as observed when no capillary contact was maintained (**Fig. 10**). However, in this experiment, the Neutron projection clearly shows that the bottom of the sample remains partially saturated with water. This behavior is obviously due to the imposed capillary contact boundary condition.

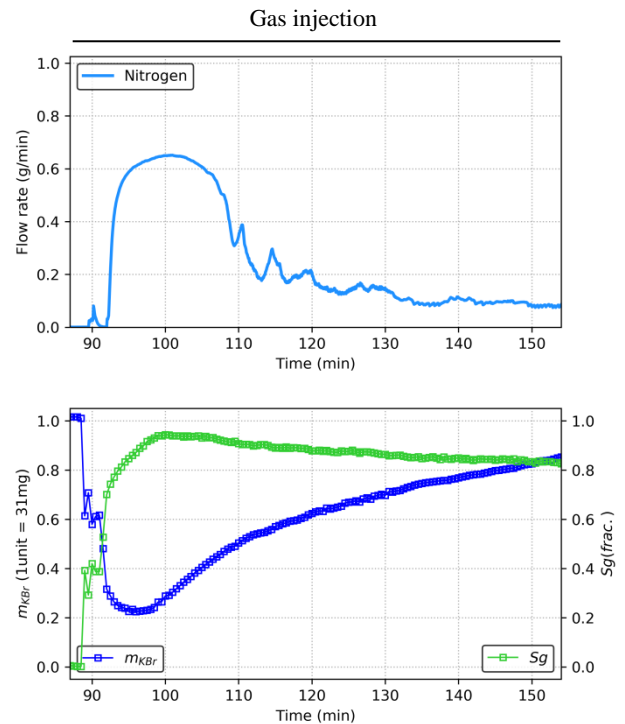


Fig. 12 : Dry-out with the 100g/L KBr brine and a capillary contact maintained at the gas outlet (high pressure gradient case).

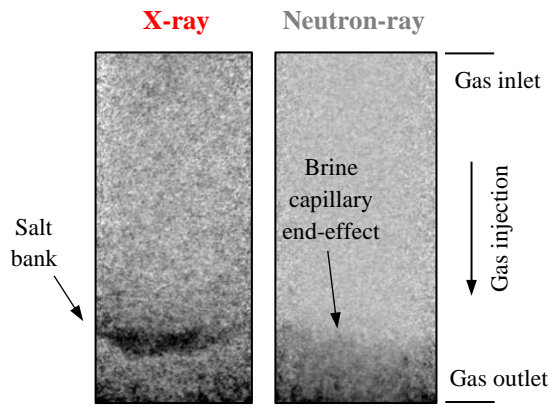


Fig. 13: 2D projections at the end of the dry-out (before the salt accumulation $t = 95\text{min}$), when initially saturated with the KBr brine (dry-out with a capillary contact). On the X-ray projection, darker shades suggest salt bank position. On the Neutron-ray projection, darker shades suggest higher water saturations.

The evolution of the initial small bank during the dry-out is shown in **Fig. 14**. The 2D projections show a rise of both the salt bank and the water front in the sample. The evolution visible on the X-ray projections suggests an evolution in two steps: first the salt bank is getting quickly wider and thicker while staying at same height, and secondly, from $t = 107\text{ min}$, it starts migrating upward in the core while slowly getting wider. During the first step, salt accumulation results in substantial gas flow rate reduction (almost 50%). Afterward, we observe a stick and slip like behavior of water and salt rises.

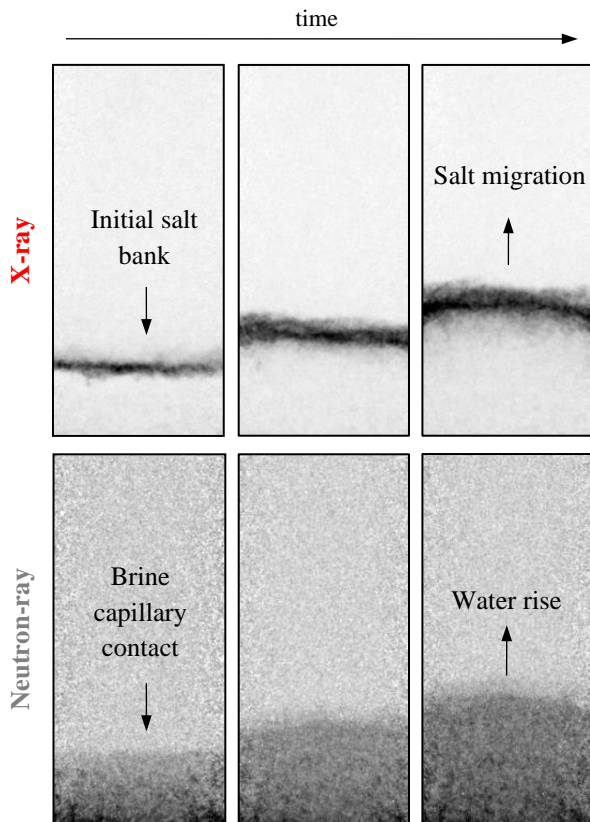


Fig. 14: 2D projections during the salt accumulation, taken at 100 min, 120 min and 140 min from left to right. Gas is injected from the top. On the X-ray projections, darker shades suggest salt bank

position. On the Neutron-ray projections, darker shades suggest higher water saturations.

The brine saturation S_w , the brine concentration C_{KBr} and the precipitated salt m^{solid}_{KBr} profiles are given in **Fig. 15** for different time steps during the salt accumulation. The profiles give meaningful insight to understand the mechanism of salt accumulation and rising. In this work, we consider that salt precipitates instantaneously once the solubility limit of $6.5 \cdot C_0$ is reached excluding any supersaturation condition. Actually, the salt only precipitates when two conditions are met: $S_w > 0$ and $C_{KBr} = 6.5 \cdot C_0$. The brine saturation and the KBr concentration profiles show that the capillary contact maintained almost constant boundary conditions at the gas outlet which prevents salt precipitation at the outlet. The brine concentration, however, quickly rises to its limit of solubility ($6.5 \cdot C_0$) at few mm from the gas inlet, where salt starts to precipitate. The brine saturation profiles show that the sample is completely dry behind the salt bank. A residual value can be read on these curves, around 2%. It can be attributed to the X-ray and Neutron-ray signals calibration. The precipitated salt curves clearly show the salt bank migration toward the gas inlet and its thickening during its displacement. Following the previous remarks, the salt migration can be explained by the water front displacement that carries more salt and allows salt to precipitate higher in the sample.

The reduction of porosity is computed from the precipitated salt curves (cf. equation 6) and it is directly proportional to the precipitated salt quantity. The apparent migration of the salt starts when the local porosity is reduced by up to approximately 13-15% in some section of the sample. At the end of the experiment (at $t = 155\text{min}$), some sections of the sample show a reduction of the pore space by up to 20%. This relatively moderate porosity reduction induces an average flow rate reduction by almost a ratio of 6 (cf. maximum to minimum ratio of flow rate in **Fig. 12**). This observation supports the hypothesis of a preferential salt precipitation along the pore wall plugging by the throats between pores.

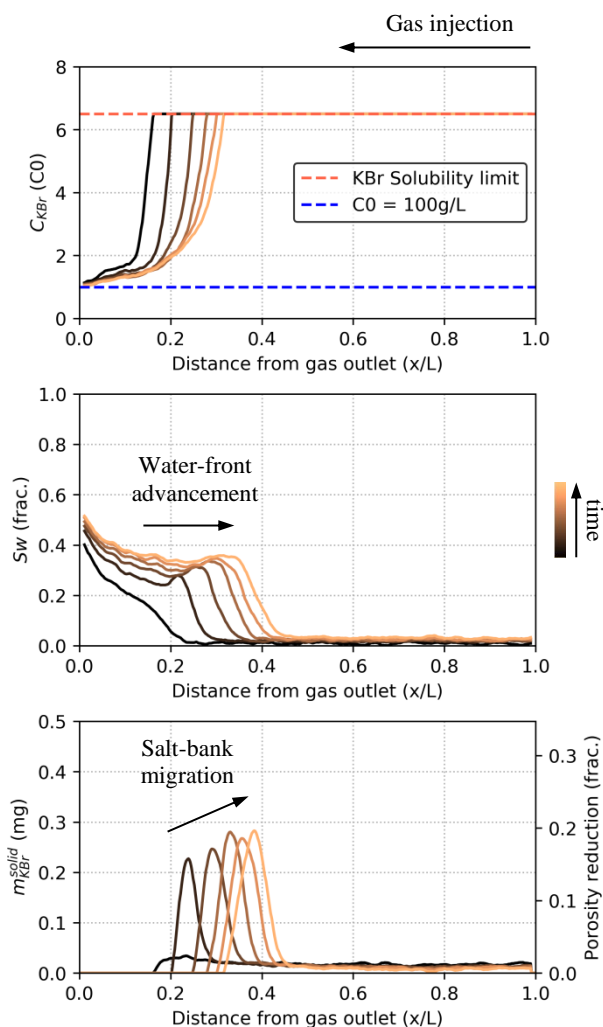


Fig. 15: Brine concentration C_{KBR} , brine saturation S_w and precipitated salt profiles m_{KBR}^{solid} profiles computed during the salt accumulation. The reduction of porosity is estimated from the m_{KBR}^{solid} curves. Profiles are computed regularly from $t = 100$ min to $t = 150$ min.

These different curves are plotted for a single time step on the same plot in **Fig. 16**. It shows the relation between the salt bank and the brine phase. The section where salt precipitates is saturated by both the gas and the brine. The presence of these two phases is actually required to allow the precipitation. The salt bank doesn't act as a barrier for the brine. It is in constant rise in the sample by capillary forces, but the height reached by the front is limited by its evaporation. If deionized water had been used, the height reached would have quickly stabilized. Here, the evaporation is causing salt to precipitate. As it accumulates in the pore-space, the porosity is reduced and the gas flow rate decreases (**Fig. 12**), changing the equilibrium between capillary forces and evaporation speed. The decrease of the gas flow rate allows the water to imbibe higher in the sample. Salt precipitates ahead the previous bank while its rear back is dissolved by under-saturated brine.

The curves plotted in **Fig. 16** show the equilibrium of the different phases for specific injection conditions. The brine phase is not breaking-through the sample, suggesting flowing conditions close to null. From $t = 100$ min to $t = 150$ min, the water saturation is increased by 9% by capillary rise, corresponding to an average flow rate of $33\mu\text{l/h}$. Yet, this flow rate is not high enough to explain the rate of salt

accumulation in the sample. Indeed, the brine is constantly evaporating in the gas, and it is compensated by an additional brine pumping through the capillary contact. This additional contribution is estimated using the salt mass curve to an average of $190\mu\text{l/h}$ between $t = 95$ min to $t = 150$ min. It is twice more important during the early stages of the dry-out. Despite the brine saturation profiles being close to static, the brine flow rate is far from being null. It explains how the rear back of the salt bank is quickly dissolved while the brine slowly rises.

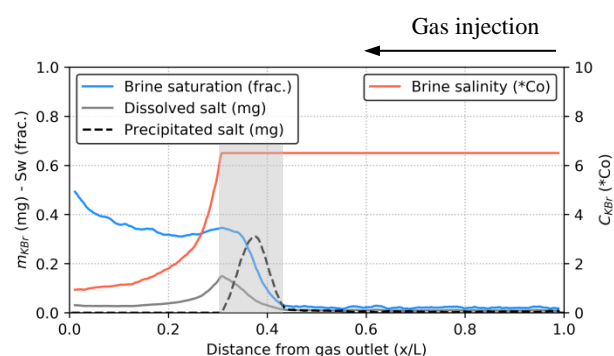


Fig. 16: Salt repartition in the different phases during the dry-out with capillary contact ($t = 150$ min). The gray area shows where the conditions for salt precipitation are met.

3.3.2 Low pressure gradient

For the second dry-out experiment with capillary contact, the inlet gas pressure is set to 0.35bars. The gas is injected in the sample initially saturated with the 100g/L KBr brine. The gas flow rate during the dry-out are given in **Fig. 17**, with the gas saturation in green and the salt quantity in blue.

The early phases of the dry-out are again comparable to what has been reported previously. The initial salt bank is formed at halfway-up the sample, higher than in the previous experiment. This is consistent with the lower inlet pressure allowing the capillary forces and the brine evaporation to equilibrate higher in the sample.

The next steps of the dry-out demonstrate a completely different behavior than previously observed, with the gas flow rate showing alternating phases of draw-down and build-up (see phases referred as 1 and 2 in **Fig. 17**). The gas saturation is correlated to these variations: the higher the gas flow rate, the higher the gas saturation. During the draw-down phases, the gas flow rate is reduced by 10 times its initial value (from 0.25g/min to 0.025g/min), while the total quantity of salt in the sample is increasing monotonously. The quantity of salt dissolved in the brine and the quantity of salt precipitated in the sample are also displayed in **Fig. 17** in red and black respectively. These two curves demonstrate the same alternating cycles of build-up and draw-down, yet inversely correlated. Indeed, during a gas draw-down, the quantity of precipitated salt decreases while the quantity of dissolved salt in the brine phase increases, and conversely during a gas build-up. These curves suggest the phases of gas draw-down and build-up are controlled by cycles of salt precipitation and salt dissolution.

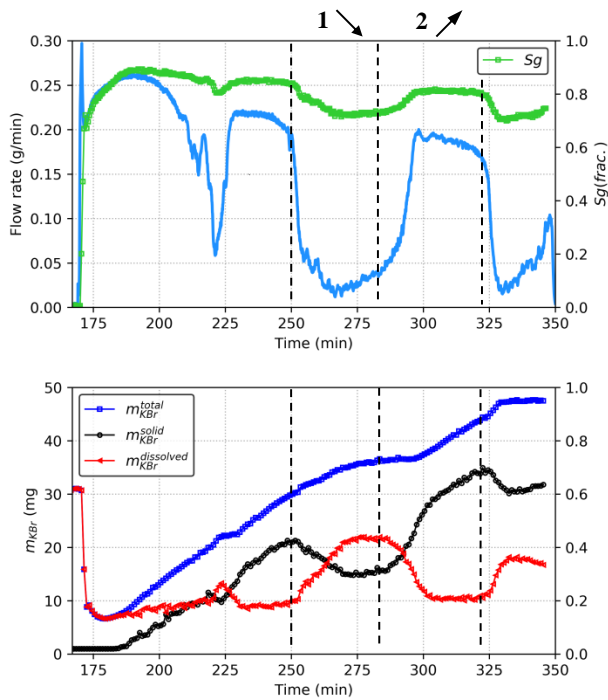


Fig. 17: Dry-out with the 100g/L KBr brine and a capillary contact maintained at the gas outlet (low pressure gradient case). The two sections noted 1 and 2 shows a cycle of gas draw-down and gas build-up.

The 2D X-ray projections recorded during draw-down and build-up phases are given respectively in **Fig. 18** and **Fig. 20**. The corresponding precipitated salt profiles computed for different time steps are given in **Fig. 19** and **Fig. 21**, for the draw-down and the build-up respectively.

As seen earlier, the gas draw-down is initiated by a strong reduction of the porosity in a limited section of the core. For the draw-down described here, the porosity is reduced by up to 30% (see **Fig. 19**). This allows first the brine to rise in the sample while dissolving the rear back of the salt bank and then the salt to precipitate higher in the sample. These steps are clearly visible on the 2D X-ray projections (**Fig. 18**). The quantity of salt dissolved is balanced by the quantity of salt that precipitates. The total quantity of salt is still showing an increase due to the rise of the water in the sample, pumping additional dissolved salt through the capillary contact. The major difference with the previous dry-out experiment is that a second salt bank is formed while a unique one was observed previously. This difference is crucial as it triggers the gas build-up cycle: the formation of a second salt bank globally spreads the salt in a less damaging configuration for the permeability. This is well understandable in **Fig. 19**: the maximum of porosity reduction falls from 30% to 20% during the formation of the second bank. The gas flow rate quickly increases following this, initiating the gas build-up.

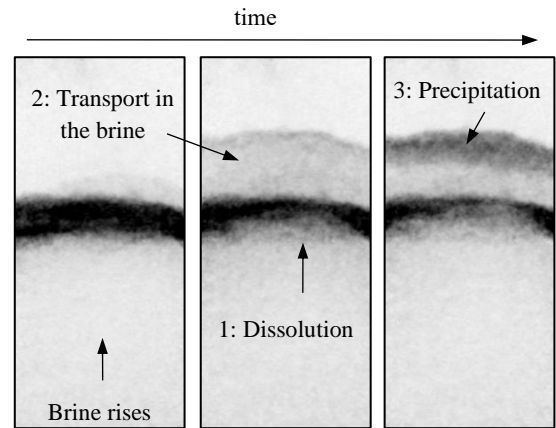


Fig. 18: 2D X-ray projections during a gas draw-down (see cycle 1 in **Fig. 17**), taken at 250 min, 265 min and 280 min from left to right. Gas is injected from the top. On the X-ray projections, darker shades suggest salt bank position.

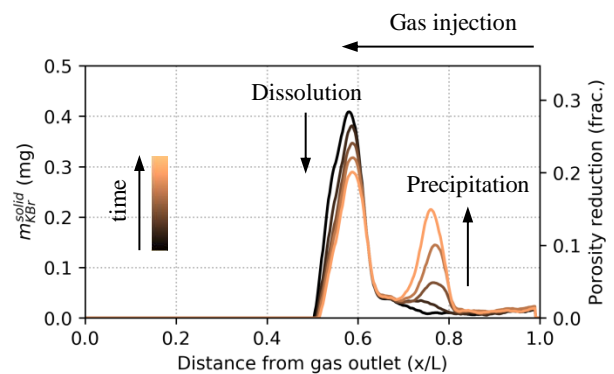


Fig. 19: Precipitated salt profiles during a gas draw-down (see cycle 1 in **Fig. 17**).

During the gas build-up, the water withdrawn from the sample, and no salt dissolution is observed. As a matter of fact, the newly formed salt bank is left ahead of the water-front, where the sample is dry and only salt precipitation is observed during this phase. This is clearly visible on the salt profiles in **Fig. 21** and on the 2D projections given in **Fig. 20**. It is during these phases of gas build-up that the quantity of salt in the sample increases the most. The porosity is strongly reduced again during this step and consequently triggers the next gas draw-down phase.

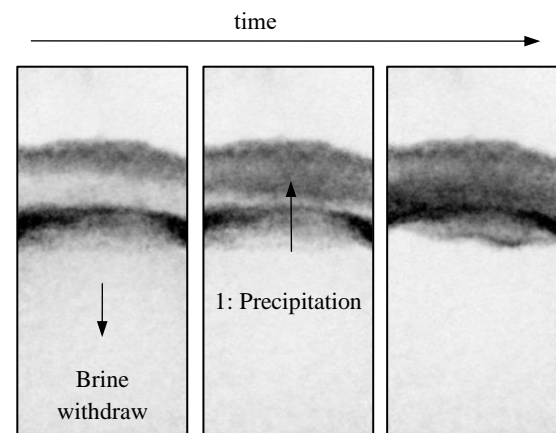


Fig. 20: 2D X-ray projections during a gas build-up (see cycle 2 in **Fig. 17**), taken at 280 min, 300 min and 320 min from left to right. Gas is injected from the top. On the X-ray projections, darker shades suggest salt bank position.

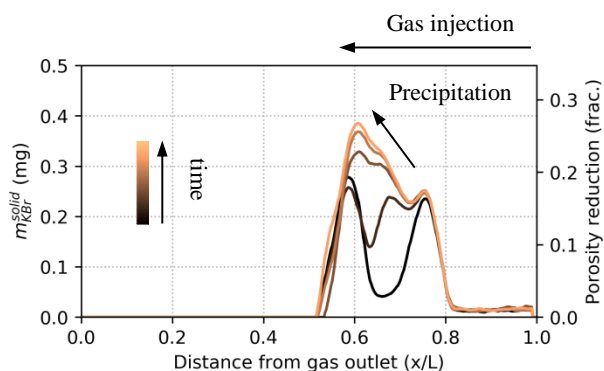


Fig. 21: Precipitated salt profiles during a gas build-up (see cycle 2 in Fig. 17).

4. Conclusion

The dual beams monitoring technique has demonstrated a real contribution to study the salt precipitation dynamic induced by gas flow-through drying. The difference of attenuation pattern between the Neutron and the X-ray beams is used to de-correlate beam attenuations caused by the water and the salt. A method to calibrate and process the two signals has been presented, allowing to separately quantify the different phase saturations and brine salinity as well as the reduction of porosity caused by the salt deposition. This information is crucial to better calibrate numerical models and particularly the permeability reduction with salt precipitation.

Results of four dry-out experiments monitored with this method are presented here. The two first experiments mostly aimed to calibrate the dual monitoring for the different phases. The last two experiments have been conducted with a brine capillary contact maintained at the gas outlet. Experimental data have given new insight to understand the organization of the three phases (the brine, the gas and the precipitated salt) when a salt bank is formed in the sample. The quantity of salt that accumulates allows to estimate the flow rate of brine pumped through the capillary contact to compensate for the brine evaporation in the gas phase. The observations have shown that a reduction of the initial porosity in some section of the sample by 13-15% was enough to trigger a gas draw-down, characterized by the migration of the salt toward the gas inlet. The rise of the salt bank involves three steps: salt dissolution, salt transport in the brine phase and salt precipitation where the water front stabilizes. In some conditions (low gas pressure gradient for example), the rise of the water can be fast enough to form a second salt bank higher in the sample. It has been observed that the formation of the second salt bank could spread the precipitated salt in a less damaging configuration for the gas flow, triggering a phase of gas build-up characterized by the withdrawal of the water. These phases of gas draw-down and build-up can alternate until the sample clogging.

Future works can include:

- The construction of a permeability reduction curve as a function of the porosity reduction.
- The evaluation of the thermodynamic aspect of the drying, especially the water vapor concentrations.

Acknowledgments

NeXT-Grenoble project was supported by the French National Research Agency in the framework of the "Investissements d'avenir" program (ANR-15-IDEX-02). DOI of the neutron data: 10.5291/ILL-DATA.UGA-77.

References

- [1] O. Lopez *et al.*, "Permeability alteration by salt precipitation: Numerical and experimental investigation using X-Ray Radiography," *E3S Web Conf.*, vol. 146, A, p. 3001, 2020, doi: 10.1051/e3sconf/202014603001.
- [2] Y. Peysson, B. Bazin, C. Magnier, E. Kohler, and S. Youssef, "Permeability alteration due to salt precipitation driven by drying in the context of CO₂ injection," *Energy Procedia*, vol. 4, pp. 4387–4394, 2011, doi: 10.1016/j.egypro.2011.02.391.
- [3] Y. Peysson, L. André, and M. Azaroual, "Well injectivity during CO₂ storage operations in deep saline aquifers—Part 1: Experimental investigation of drying effects, salt precipitation and capillary forces," *International Journal of Greenhouse Gas Control*, vol. 22, pp. 291–300, 2014, doi: 10.1016/j.ijggc.2013.10.031.
- [4] L. André, Y. Peysson, and M. Azaroual, "Well injectivity during CO₂ storage operations in deep saline aquifers – Part 2: Numerical simulations of drying, salt deposit mechanisms and role of capillary forces," *International Journal of Greenhouse Gas Control*, vol. 22, pp. 301–312, 2014, doi: 10.1016/j.ijggc.2013.10.030.
- [5] T. Giorgis, M. Carpita, and A. Battistelli, "2D modeling of salt precipitation during the injection of dry CO₂ in a depleted gas reservoir," *Energy Conversion and Management*, vol. 48, no. 6, pp. 1816–1826, 2007, doi: 10.1016/j.enconman.2007.01.012.
- [6] J. Mahadevan, M. M. Sharma, and Y. C. Yortsos, "Flow-through drying of porous media," *AIChE J.*, vol. 52, no. 7, pp. 2367–2380, 2006, doi: 10.1002/aic.10859.
- [7] J. Mahadevan, M. M. Sharma, and Y. C. Yortsos, "Water removal from porous media by gas injection: Experiments and simulation," *Transport in Porous Media*, vol. 66, no. 3, pp. 287–309, 2007, doi: 10.1007/s11242-006-0030-z.
- [8] D. Le, H. Hoang, and J. Mahadevan, "Impact of Capillary-Driven Liquid Films on Salt Crystallization," *Transport in Porous Media*, vol. 80, no. 2, p. 229, 2009, doi: 10.1007/s11242-009-9353-x.
- [9] A. Tengattini *et al.*, "NeXT-Grenoble, the Neutron and X-ray tomograph in Grenoble," *Nuclear Instruments and Methods in Physics Research Section A: Accelerators, Spectrometers, Detectors and Associated Equipment*, vol. 968, p. 163939, 2020, doi: 10.1016/j.nima.2020.163939.
- [10] Florian Grünauer, "Design, optimization, and implementation of the new neutron radiography facility at FRM-II," 2005. [Online]. Available: <https://pdfs.semanticscholar.org/041f/fe1ef9477759f231bd46224240ef152141d7.pdf>

- [11] P. Rinard, "Neutron interactions with matter," *Passive Nondestructive Assay of Nuclear Materials*, pp. 375–377, 1991.

Material balance and mixing behavior during emulsification of crude oil by using micro-X-ray tomography

Mostafa Borji, Ahmad Kharrat and Holger Ott*

Department Petroleum Engineering, Montanuniversität Leoben, 8700 Leoben, Austria

Abstract. The emulsification of water and crude oil is typically examined and optimized in test tubes by optical means, i.e., rated outside the porous medium. We examine the rather complex case of crude oil emulsification by alkaline solutions, and follow the question, whether or not those phase behavior experiments are representative for emulsification under the typically laminar flow conditions in porous media. Instead of a qualitative optical evaluation, we use X-ray attenuation coefficients in μ CT to establish the material balance during emulsification in the test tubes. We show that in such cases the optical inspection can lead to a considerable misinterpretation of the phase behavior. Using X-ray attenuation makes those experiments quantitative and comparable to μ CT-based core flood experiments, where phase mixing occurs in porous media flow. Using X-ray attenuation, we conclusively show that even in the complex case of in-situ saponification by alkaline flooding, (a) emulsification in test tubes and in porous media flow is comparable, and (b) that a minimum emulsion volume with balanced compositions leads to optimal oil recovery in micro-CT-based and conventional core flooding.

1 Introduction

Recovery factors from conventional oil reservoirs using conventional methods reach an average of 35% [1], implying a high remaining potential even after secondary water flooding. Enhanced oil recovery (EOR) methods are developed to target unrecovered trapped and bypassed hydrocarbons and reduce the remaining oil saturation in the reservoirs [2, 3].

Alkaline flooding is one of the economically most attractive chemical EOR methods [4, 5, 6] reported to be an efficient technique for recovering oils containing high amounts of acidic components [7, 8]. In this process, a high pH solution is injected into the reservoir. Upon contact, the alkaline solution undergoes an in-situ saponification reaction with the acidic crude components generating natural surfactants at the oil-water interfaces. These surfactants may lower the interfacial tension (IFT) to a degree that leads to the formation of emulsion phases. By lowering the IFT, capillary trapped oil may be mobilized by substantially increasing the capillary number [3, 9]. Whether the reservoir is a target for alkaline floods or not depends on the total acid number (TAN), which is a measure of the concentration of acidic and thus saponifiable components in the crude oil; the number is defined as the milligrams of potassium hydroxide required to neutralize on gram of crude oil [1]. Candidate fields should have a TAN of 0.5 or higher. [1]. If a high TAN is given, the injection water composition is typically designed by a combination of phase behavior tests and core flood experiments.

The phase behavior is typically tested by bringing crude oil into contact with water of different compositions. The alkali agents, their concentration, and the salinity of the solution are typically varied to optimize the water for injection. Such tests are performed in test tubes and are evaluated visually and qualitatively. This is often

sufficient, e.g. for surfactant flooding if the phase behavior is following the Winsor sequence. But this may not be the case for emulsification as result of in-situ saponification of crude. This may have its origin in the wide variety of molecular properties of in-situ surfactants compared to the rather narrow specs of synthetic surfactants in surfactant flooding. It turned out that the interpretation of complex phase behavior may require more sophisticated analytical methods [7, 8]. Even with a quantitative assessment, it may not be easy to find a valid criterion for optimal conditions from phase behavior experiments alone. Then core flood experiment must ultimately lead to the decision.

In this paper, we study the effect of alkaline solutions on emulsification and the displacement of high-TAN crude oil from the Vienna basin. Emulsion formation is evaluated in conventional phase behavior experiments but using the linear mass attenuation coefficient of micro-X-ray computed tomography (μ CT) for quantifying the phase compositions and mixing behavior of crude oil and water. The predictive strength and the representativeness of such ex-situ experiments were investigated by the comparison of the results to flooding experiments and imaging emulsion phases under laminar flow conditions. Flooding experiments were performed in μ CT-based mini-core floods, and recovery, average phase composition and spatial phase distributions were assessed.

2 Materials and Methods

Fluids: The crude oil sample was derived from the 16 TH reservoir of the Matzen oil field located in Austria. The sample was characterized by viscosity, $\mu = 80$ cP at 20°C, density, $\rho = 0.87$ kg/m³ at 20°C, and a high total acid number (TAN) between 1.5 [10] and 1.78 mg KOH/g

* Corresponding author: holger.ott@unileoben.ac.at

[11] which makes it a suitable candidate for EOR by alkaline flooding. Detailed field data and the oil composition are reported in several publications [12, 13, 14]. In Order to increase the X-ray contrast to the aqueous phase, 7 wt% Iododecane with 98% purity (Sigma Aldrich) was added; the influence of X-ray doping agents was investigated in a separate study [15] and was minimized.

As injection water, alkaline solutions were prepared by adding sodium carbonate (Na_2CO_3) powder (Sigma Aldrich) as alkali agent in deionized (DI) water, and stirring the solution for ten hours by using a magnetic stirrer. The pH of the solutions was measured using an electronic pH meter and is reported in [7, 16].

Phase Behavior Experiments: Phase behavior tests were carried out by contacting the alkalic solutions with the crude oil in 15 ml glass tubes from Carl ROTH. To minimize any interaction between the fluids prior to the mixing step, we first filled the test tubes with 5 ml of aqueous solution from bottom to top and then added 5 ml of oil. The filling process was done using a high-precision syringe pump (CHEMYX Fusion 200) to guarantee the volumes are equal, and the water-oil ratio is kept at 1. The samples were sealed and then mixed in a rotator (Fisher) for 24 hours at 25 rpm and subsequently put vertically at rest at ambient conditions. To monitor the changes over time, in addition to taking high-quality optical pictures with a NIKON D5600 camera, we performed fast X-ray scans with an in-house μCT scanner (PROCON X-Ray GmbH – CT ALPHA) every 24 hours for three weeks. For the test tube experiments, the scanner was operated at 66 kV and 150 μA with a resolution of 53 μm .

Porous Medium: The flooding experiments were performed in a cylindrical mini-plug with 5 mm diameter and 15 mm length, drilled from a Robuglass® sintered glass filter, representing a 3D porous medium. Such samples were used in earlier studies [17, 18, 19], and are characterized by a high porosity of $\phi = 0.35$ and a high permeability of $K = 22 \pm 2$ D. Pore diameters were reported to be in the range of 40-100 μm , and the total pore volume (PV) was determined to 107 mm^3 . This porous medium was chosen for mainly three reasons: (a) the pore space is well resolvable in μCT , (b) it supports laminar flow conditions, and (c), it is made out of borosilicate glass, which is the same material as the test tubes are made of, used for characterizing the phase behavior.

Flooding Experiments: The sample was embedded in a Viton rubber sleeve placed in an X-ray transparent carbon-fiber-epoxy-bases core holder. To mitigate the adverse effects of the rubber sleeve wetting conditions, the sample was wrapped in a single layer of aluminum foil. The core holder was mounted to the sample-manipulation stage of the μCT scanner. High precision VP-series pumps from Vindum Engineering, Inc. were used to inject the fluids and provide the confinement

pressure. Three-way high-pressure valves (Swagelok) and PEEK tubes were used as connections and flow lines between the pump, core holder, and the outlet vessel with a sealed cap in which the effluent was collected. For preparation and pre-saturation purposes, a vacuum pump was installed on the downstream side of the flow loop. The oil was then injected under vacuum conditions by means of a Chemyx Fusion 200 syringe pump with a Hamilton gas-tight glass syringe. The experiments were finally carried out in a vertical flooding geometry at ambient pressure and temperature conditions as the phase behavior tests were performed.

3 Quantitative Evaluation of Phase Behavior

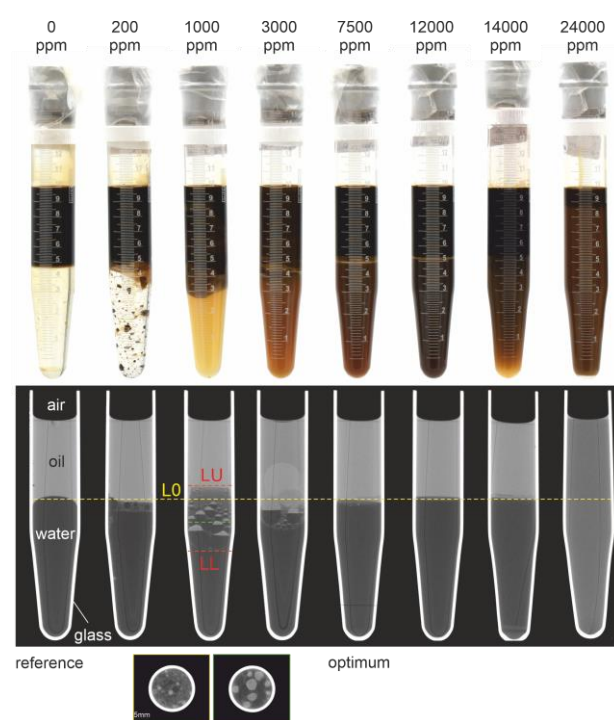


Figure 1: Upper row: optical images of the phase after contacting crude oil with aqueous phases of different Na_2CO_3 concentrations in test tubes. The images are recorded two weeks after mixing at rest. Lower row: μCT scans of the same samples. The yellow line (LO) indicates the oil water contact line of the reference system. For quantitative evaluation, the contact line has been volumetrically corrected for the meniscus. The red lines (upper level LU and lower level LL) represent the extend of the mixing zone as discussed in the text.

To study the type and degree of emulsification, classical phase behavior tests were carried out by contacting the crude oil with aqueous solutions of different Na_2CO_3 concentrations, $C_{\text{Na}_2\text{CO}_3}$. The top row of Figure 1 shows optical images of the phase behavior tests after two weeks of rest. As reported in various studies [20, 21, 11], the mixtures does not follow the conventional Winsor [22] sequence, and a clear trend with $C_{\text{Na}_2\text{CO}_3}$ was not observed. At low concentrations (i.e., below 3000 ppm), the aqueous phase is still transparent and optically distinguishable from the swollen oil phase. At higher concentrations, the alkaline solutions become darker and more difficult to differentiate from the oil phase. Above a concentration of 3000 ppm, the phases appear optically mixed indicating strong emulsification. Having a closer

look, a narrow strip of a “third phase” is detectable at 7500 and 12000 ppm $c_{\text{Na}_2\text{CO}_3}$, which disappears at higher concentrations. This phase is rather difficult to be detected by eye, but already indicates, that phases may still be separated despite the homogeneous coloring. But in general, the tests do not give a clear hint, why an optimum displacement efficiency is found at 7500 ppm of Na_2CO_3 [10] – this concentration appears as rather arbitrary with respect to the optically evaluated phase behavior.

Such phase behavior experiments typically ignore that the slightest contamination of water by crude oil may lead to a deep coloring. Therefore, in a next step, we use micro-X-ray tomography for imaging the test tubes. We do this for two reasons: firstly, with the high resolution of the 3D imaging method, we are able to detect interfaces and structures like droplets with sizes above the physical resolution of the image. Secondly, the X-ray absorption contrast directly scales with the fluid density. Therefore, it is possible to quantitatively determine the degree of mixing, which is not possible in the visible spectrum of wavelength.

In the second row of Figure 1, the associated μCT scans are shown. The gray scale directly indicates the density of the fluid phases; the gray values range in between the pure aqueous phase (dark phase, high density) and the pure oil phase (light phase, low density) of the left images (0 ppm), where no mixing is observed and expected – this case is used as reference defining the maximum and minimum gray level. All the other test tubes show a certain degree of mixing, respectively emulsification. The overall result surprises; despite the rather homogeneously appearing coloring in the optical images above 3000 ppm, the X-ray images indicate clearly separated phases up to the 14000-ppm case. Just at the highest concentration, a homogeneous emulsion phase is observed. Furthermore, between 200 and 3000 ppm, heterogeneous phases can be detected in between the aqueous and the oleic phase. The qualitative observations in detail:

- 0 ppm: The meniscus at the oil-water interface indicates that the glass is rather wetted by oil, which is different than what was previously observed for the oil sample of the 8 TH Matzen field [7, 16].
- 200 ppm: A narrow third phase is formed at the oil-water interface, containing dark bubbles of different sizes that may be described as a loose water in oil emulsion.
- 1000 to 3000 ppm: A considerable volume of a third heterogeneous phase is observed at the oil-water contact (OWC). Oil and water bubbles of various sizes (smaller at the top and become larger towards the bottom) were observed.
- 7500 ppm: The oil-water interface becomes flat (no preferential wetting and/or neglectable IFT). A narrow area with a different gray value is observed at the OWC, indicating the formation of a third phase. This middle phase appears as homogeneous.
- 12000 and 14000 ppm: No meniscus at the OWC is observed. The original OWC level is slightly moved upwards indicating swelling of the aqueous phase.
- 24000 ppm: Oil and water seem to be mixed to a high degree forming an isotropic phase similar to a Winsor type IV system. This phase is stable, with no

significant changes in time neither optically nor in the X-ray images.

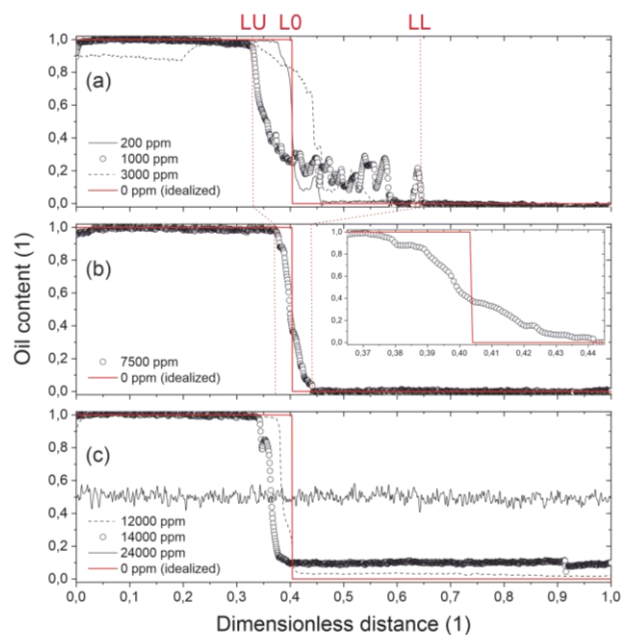


Figure 2 : Oil content as function of distance obtained from the grayscale μCT images as shown in Figure 1. (a) profiles for Na_2CO_3 concentration below, (b) at and (c) above optimum concentration. The data are compared to the reference measurement with 0 ppm Na_2CO_3 . The optimum concentration is a result of the present study. The interval LU to LL refers to the mixing zone for selected cases and LO to the oil-water contact line of the reference case (compare Figure 1).

As already discussed, using X-ray attenuation as analytical method allows a quantitative data interpretation with respect to the material balance. The mixing zone is reflected in the gray scale variation of the resulting phases and the level of the OWC, respectively the boundary levels of an additional occurring phase (UL and LL). Both properties are in the following discussed on basis of vertical density profiles along the central axis of the test tubes as shown in Figure 2.

To make these profiles comparable, the X-ray images were first aligned and the gray values of the fluids averaged over the cross-section. The gray scale was adjusted based on the gray values of glass and air, with X-ray mass-attenuation coefficients that can reliably be considered as constant during the experiment. This led to a consistent scale for all experiments independent of the phase behavior inside the tubes. The gray values of the pure fluid phases were identified from the reference case using deionized water (0 ppm), for which no fluid mixing was observed and expected. Emulsions or in general mixed phases show an intermediate gray value, linearly scaling with the volumetric fluid fractions. This is a result of the volumetric superposition of the mass absorption coefficients in each image voxel. We normalize the gray scale such that the pure oil phase is set to 1 and pure water to 0, directly reflecting the oil content. We ignore the slight variation of the aqueous phase with the alkaline concentration, and we corrected for the slightly varying influence of the test tube material due to its conical shape.

The data are plotted against the dimensionless distance, with 0 being the air-oil contact and 1 the bottom of the test tube.

Changes of the OWC line are described relative to the reference case (L0); the sharp gray value change across the interface (see Figure 1) confirms a good contrast and no detectable mixing of the two fluids. However, the oil-water contact can be misinterpreted due to the interface curvature, which is visible in the X-ray image. The curvature leads to an incorrect interface location in a central line profile, or to an artificial smearing of the interface due to cross-sectional averaging. Therefore, we calculated the volumetric center of the interface, which is given as the red reference level (L0) in the panels of Figure 2. Details on data handling is given in [15].

Concentration dependence: The normalized line profiles for different Na_2CO_3 concentrations in comparison to the base case are shown in Figure 2. Phase (emulsion) boundaries are determined by the first and last points at which the individual profiles deviate from the reference case (0 ppm), given as red lines in panel (a) and (b), for selected cases. The deviation can be with respect to the position of the OWC, or with respect to the gray level of the reference phases. The 200-ppm case shows a rather small deviation from the base case at the interface, essentially indicating the formation of a lower third phase with a low oil content ($\sim 20\%$). The profile is as well influenced by a single water bubble in the oil phase. The 1000 ppm profile shows a wide mixing interval with significant fluctuations in the aqueous domain, representing the heterogeneous phase with large oil and water bubbles – a loose emulsion phase; two cross-sections of these structures are shown at the initial OWC and in the lower phase as indicated in the image. At 3000 ppm, even larger scale structures appear. These structures are stable in time, and lead to the rather odd profile in Figure 2 (a). At 7500 ppm, the total emulsion is significantly smaller in volume than in the aforementioned cases, and the phases become smooth without macroscopic bubbles. Optically, the emulsion phase appears as a narrow stripe at the oil-water contact at the exact height of the volumetrically corrected interface of the reference system, which is comparable to the conventional definition of the optimum condition, a Winsor type III emulsion. Referring to literature and the next section, this system results in the highest recovery factor.

As the Na_2CO_3 concentration increases (12000 and 14000 ppm), the water phase is homogeneously swelling, which is reflected in a rise of the contact line, and in a density decrease, respectively increase of the oil content in the aqueous phase. At even higher alkaline concentrations (above 19000 ppm), the mixing behavior changes significantly. The entire test tube content turns into a stable homogeneous emulsion phase comparable to the Winsor type IV system with an exact average density.

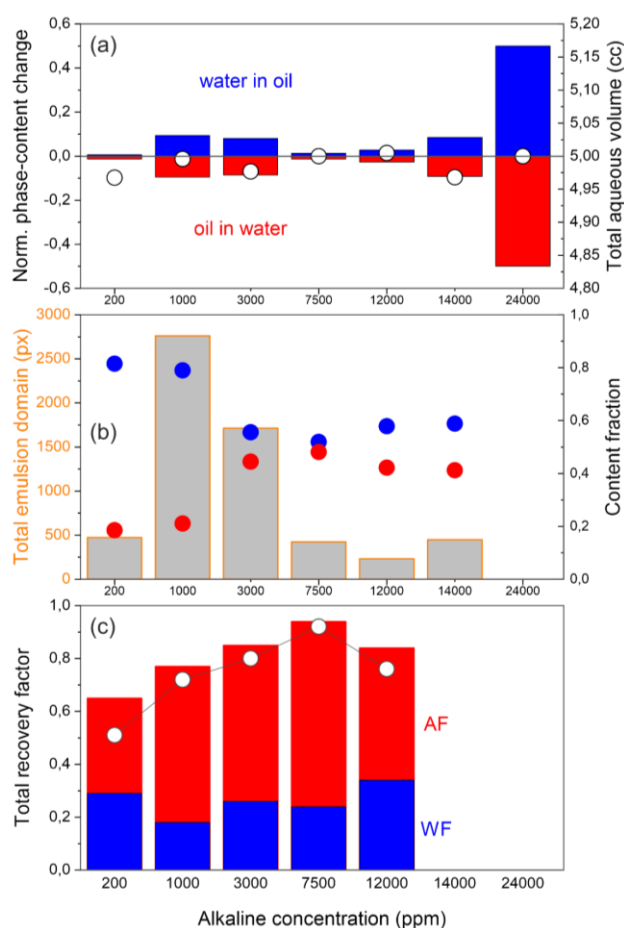


Figure 3 : (a) mutual participating volume of water in oil (blue bars and positive) and oil in water (red bars and negative). The total detected aqueous phase volume in the test tube (initially 5 cc). (b) The total emulsion volume (gray chart bars) and the fraction of water (blue) and oil (red) in the emulsion phase. (c) Recovery factors from the mini-core flood experiments derived from μCT scans. The total recovery factor is split in the contributions of water (blue) and alkaline (red) flooding (cumulative). The incremental tertiary recovery is given by the white circles.

Figure 3 (a) and (b) summarize these results. The data clearly show that at the optimum concentration of 7500 ppm, the mutual solubilization is well balanced and confined to the original OWC. For the other cases, the content fraction – the average fraction of water and oil in the emulsion phase – is rather on the water side, i.e., the emulsion phase is dominated by water.

4 Phase Mixing and Distribution in the Pore Space

The key question to be answered is whether or not the phase behavior in the classical test tube experiments is representative for porous media flow. This is not a trivial question, because the mixing regimes are entirely different; while in porous media flow the flow, respectively mixing regime is laminar, in test tube experiments, mixing is turbulent and the phases are finally observed in equilibrium at rest. To answer this question, we perform mini-core flood experiments including saturation monitoring by in-situ μCT scanning. In all

experiments, secondary water floods at an initial saturation state of $S_o = 1$ were performed, followed by tertiary floods with water of different Na_2CO_3 concentrations. To make the situations comparable, we use the exact same fluids, thermodynamic conditions and solid material (borosilicate) in both type of experiments. We use also the same analytical method – X-ray attenuation – for the evaluation of the resulting phases. However, before we discuss the phase behavior, we discuss the achieved recovery factors in order to identify, respectively verify the optimum alkalinity on basis of the displacement efficiency.

Recovery factor: For calculating the recovery factors, the individual fluid phases were firstly segmented and the volume fractions of oil and water were calculated. We applied two-phase segmentation by thresholding, and therefore, emulsion phases are not explicitly considered. This was not possible for the 24000-ppm case, in which the emulsion phase dominates the end of the tertiary flood. Figure 3 (c) shows the total recovery factor defined as the displaced oil (at initial saturation $S_o = 1$) and split in to the effect of water flooding (blue contribution to the bars) and alkaline flooding (red). The incremental tertiary recovery factor refers to the displaced oil by alkaline flooding with reference to the remaining oil after secondary water flooding. The secondary recovery ranges between 0.18 and 0.34 with an average of 0.26 and a standard deviation of 0.06. The incremental tertiary recovery is with 0.51 lowest at 200 ppm, but monotonically improves with alkaline concentration until reaching its maximum of 0.89 at 7500 ppm. From the recovery factor as well as from the phase behavior, we interpret 7500 ppm as the optimum alkaline concentration, which agrees with earlier conventional core flood experiments [10]. Due to the complexity of the 24000-ppm case, which will be discussed later, the respective recovery results are not included in the diagram.

Average phase saturations: As has been shown in the previous section, the water and oil phases have different X-ray attenuation coefficients and are therefore distinguishable in μCT scanning. This is reflected in the volume-averaged histogram of the μCT scans as shown in Figure 4. The phases are identified by their position on the grayscale axis, while their volumetric contributions (phase saturations) are given by their frequency (the number of μCT voxels in the gray scale interval). Emulsions are mixtures and must appear at intermediate gray values.

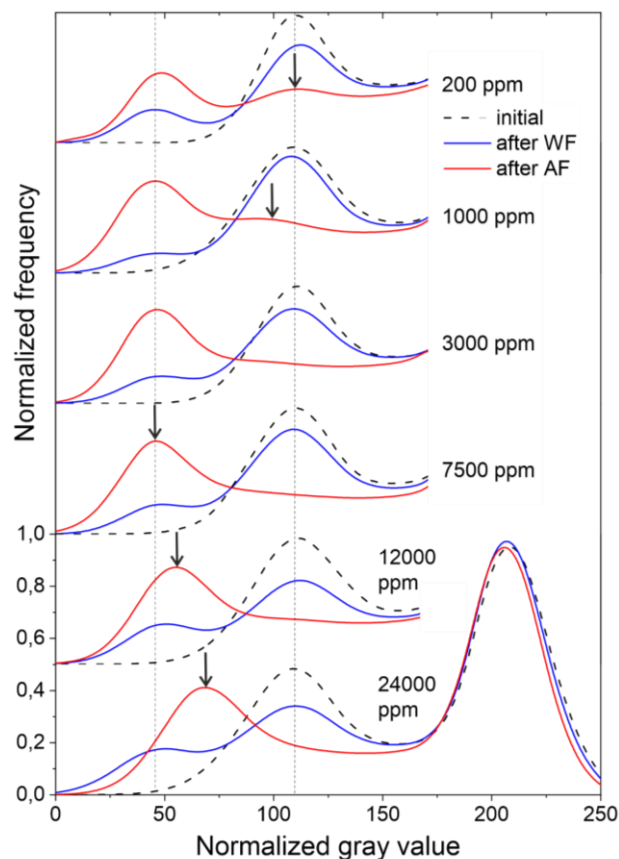


Figure 4 : μCT gray-value histograms of flooding experiments with varying alkaline concentrations. The states before and after water flooding and after the subsequent alkaline floods are shown as black-dashed, blue, and red lines, respectively. The peak on the right correspond to the solid grains; middle peaks represent the crude, and left peaks are related to the water/aqueous phase. Vertical dashed show the original peak positions. The arrows indicate shifts referring to phase mixing.

Figure 4 presents the μCT histograms of the performed flooding experiments. The histograms were taken from the entire scanned field of view, before and after waterflooding and after subsequent alkaline flooding.

The initial-state histograms show a bimodal distribution; the right, dominant peak (at ~ 210) corresponds to the solid material and the second and weaker peak (at $110\sim$) to the oil phase initially occupying the pore space. The contribution of the solid phase shows a reasonably constant contribution since the solid phase doesn't change throughout the experimental series.

During waterflooding, a fraction of the oil became immiscibly displaced by the injected water. The presence of water in the system was detected by the emergence of a new peak at gray levels lower than that of the doped oil. The water peak intensity is directly proportional to the water saturation and complimentary related to the oil peak intensity. A comparison between the oil peaks before and after the waterflooding shows a decrease in height that indicates oil displacement, and no significant shift in their gray values, pointing out that there is no compositional change of phases during immiscible displacements on a scale smaller than a voxel size.

Subsequent alkaline floods result in further oil displacement, i.e., a further reduction in oil saturation

(except for the 24000-ppm case that will be discussed separately). This is reflected in an increasing water peak on expense of the oil-peak intensity. Contrary to the waterflooding scenarios, oil and water peaks after alkaline flooding show lateral shifts that are attributed to phase density changes caused by solubilization of the respective other fluid phase. An increase in the aqueous-phase oil content (i.e., oil-in-water emulsions) causes the water peak to shift towards higher gray values, and with increasing water content in the oil phase (i.e., water-in-oil emulsions), the oil peak laterally shifts towards lower gray values. The vertical lines in Figure 4 indicates the water and oil peak positions, and the arrows mixing-related shifts. Case-by-case, the following can be stated:

- 200 ppm: There is additional displacement by alkaline flooding, but no significant peak shift is detected, i.e., in the sensitivity of the measurement, there is no emulsion phase forming.
- 1000 and 3000 ppm: There is more additional recovery than in the 200-ppm case as indicated in the peak intensities. A lateral shift in the of the peak positions suggests the formation water-in-oil emulsion. For 3000 ppm, the oil peak nearly disappeared.
- 7500 ppm: The water peak shows no lateral shift, and there is no clearly detectable oil peak since the oil saturation was significantly reduced. Emulsion phases are undetectable.
- 12000 ppm: The aqueous-phase peak shows a slight shift indicating that oil was solubilized in water. The oil peak intensity is strongly reduced, but detectable.
- 24000 ppm: The histogram becomes bimodal after alkaline flooding. The peak position of the left peak shows a maximum at a gray value representing an average phase density in between oil and water. The bimodality suggests a Winsor type IV emulsion system as observed in the test tube experiments. The peak position is more on the water side, which is explained by the already displaced oil volume; there is more water than oil in the system. Interestingly, the emulsion phase remained in the system with a high peak intensity, even after 25 PV of alkaline flooding. It seems that the formed emulsion phase remains stationary in the pore space, without displacement by further alkaline-water injection.

3D phase distributions: More advanced fluid-phase segmentations were performed using *ilastik*, a machine learning image segmentation tool, in order to study the spatial phase distribution, with focus on emulsion phases. Contrary to the water and oil phases, emulsion phases were nor characterized by a dedicated and separable grayscale, but rather appeared as volumes of gradually changing gray levels. Identification and segmentation of emulsion phase were carried out by utilizing histograms and grayscale shifts. For those cases with well separated aqueous- and oil-phase peaks, the images were segmented twice: a) using the water and oil mean values identified from respective waterfloods and b) with respect to the oil-aqueous phase boundary gray level obtained from tertiary floods. The difference of the images using both

segmentation methods result in an estimation of the emulsion phase contribution.

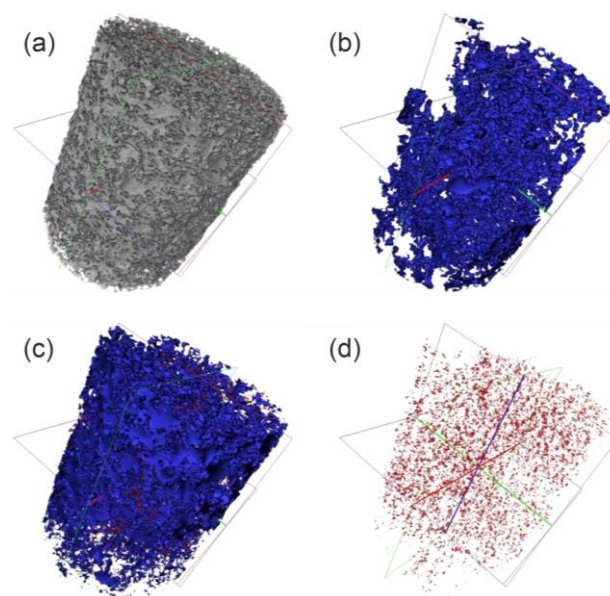


Figure 5 : Three-dimensional visualization of the field of view of the 200-ppm- Na_2CO_3 flooding experiment. (a): pore space, (b): water saturation after water flooding, (c): water saturation and generated emulsion phase (red) after alkaline flooding, and (d): the extracted emulsion phase.

Figure 5 shows the 3-D visualization of the 200-ppm flooding experiment's field of view. The pore space was derived from the initial scans at $S_o = 1$ and is shown in (a). The water-invaded pore space after water flooding is shown in (b). The water saturation of 28% corresponds to the recovery of oil from this volume. Subsequent alkaline injection resulted in a further decrease in oil saturation and in-situ formation of emulsions as shown in (c). In Figure 5 (d), only the emulsion phase is shown, which exists as small isolated clusters spread through the imaged domain.

Figure 6 shows a sub-volume with a detailed phase distribution of the 24000-ppm experiment. The extracted pore space is shown in (a) and (b). The water-phase distribution after secondary water flooding is shown in (c); 36% of the oil was displaced in this process. After alkaline flooding, the histograms indicated a single emulsion phase in the volume without separate aqueous and oil peaks present. After *ilastik* segmentation, we indeed found a dominance of a homogeneous emulsion phase (Figure 6 (d) and (e)). However, also a pure oil phase was detected, with a saturation of 9% and in the form of small clusters (dark gray phase in Figure 6 (f)). No separate aqueous phase was observed, which is quite surprising, because the images were taken under (alkaline) water injection.

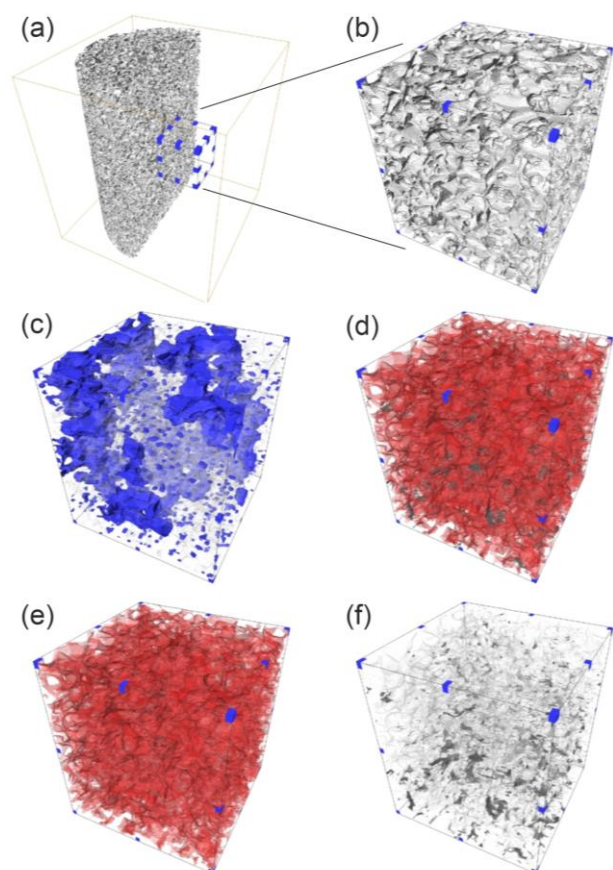


Figure 6 : 24000-ppm flooding experiment: (a) and (b): pore space of extracted sub-volume. (c): immiscible displaced oil (blue) after waterflood. (d): significant emulsion (red) formation and remaining oil (gray) after alkaline flooding. (e) and (f): extracted emulsion phase (red) and remaining oil clusters (gray) after Na_2CO_3 injection.

5 Summary and Conclusions

We investigated the concentration dependence of sodium carbonate on crude oil emulsification. The target scenario is alkaline flooding of a field in the Vienna Basin from which the oil sample was taken. We targeted both, emulsification under turbulent mixing conditions in test tubes and under laminar conditions in porous media flow. We do this in order to investigate whether or not those phase behavior experiments are representative for displacement conditions.

During screening it turned out that the optically evaluated phase behavior was not in alignment with the results of flooding experiments; a complex phase behavior was observed with no link to the optimum sodium carbonate concentrations of 7500 ppm observed in classical core flood experiments and in micro-core flooding, which coincided. The resulting question was about the value of ex-situ phase behavior experiments. This seemed to be a problem especially for alkaline flooding, which is a consequence of the naturally wide variation of the molecular properties of acidic crude components; the resulting variety of generated surfactants may not lead to a Winsor type of phase behavior as expected from synthetic surfactants with rather narrow molecular specifications. The issue of the comparability of experiments was solved in this study by using X-ray μCT

to quantitatively analyze both type of experiments. From the present study, we are able to make the following statements:

1. Classical phase behavior tests may be misleading if visually evaluated.
2. An evaluation using X-ray attenuation of fluids by comparison is objective and can be made quantitative in terms of exact phase compositions.
3. Observations under laminar flow conditions in porous media are comparable with the phase behavior tests under rather turbulent mixing conditions in test tubes. Discrepancies between them can be understood in terms of a changing oil-water ratio by the displacement process and the limited spatial resolution of μCT scanning.
4. As for classical surfactant flooding, in alkaline flooding the optimum condition goes along with well-balanced and interface-confined emulsification in test tube experiments. Otherwise it does not follow the classical Winsor picture. The confinement to the interface leads to an undetectable emulsion phase in μCT -based core flooding.

Ongoing investigations – an outlook: As previously shown in 2D microfluidics [7, 16], a statistical analysis of the oil-phase topology delivers robust results on chemical injection-water optimization. With the presented 3D data set and additionally performed 2D-microfluidic experiments on the same fluid system (not presented here), we can show (preliminary data) that the previously found 2D topological fingerprint is reproduced in 3D. Especially Lorenz plots on the cluster-volume statistics are robust indicators for EOR performance. This is far from trivial, since the observed cluster volumes in 3D μCT and 2D microfluidics are quite different on an absolute basis. With the present study, we are certain that the combination of microfluidics and classical phase-behavior experiments with X-ray monitoring provides conclusive results on chemical screening. Both proposed methods can be performed in high throughput and are therefore suitable EOR screening methods.

Acknowledgements

The work has partly been performed in the frame of the EmulPore project funded by The Austrian Research Promotion Agency (FFG), with the OMV Exploration & Production GmbH as project partner. The authors would like to acknowledge Pit Arnold, Rene Ritter for their experimental support, and Dr. Torsten Clemens for valuable discussions.

References

- [1] L. W. Lake, *Fundamentals of enhanced oil recovery*, 2nd ed., Richardson Texas: Society of Petroleum Engineers, 2014.
- [2] V. Alvarado and E. Manrique, "Enhanced oil recovery: an update review," *Energies*, 2010.

- [3] J. J. Sheng, *Modern chemical enhanced oil recovery: theory and practice*, Burlington: Elsevier Inc., 2011.
- [4] C. E. Cooke, R. E. Williams and P. A. Kolodzie, "Oil recovery by alkaline waterflooding," *Journal of Petroleum Technology*, 1974.
- [5] J. J. Sheng, *Enhanced oil recovery field case studies*, Amsterdam: Gulf Professional Publishing, 2013.
- [6] M. Tang, G. Zhang, J. Ge, P. Jiang, Q. Liu, H. Pei and L. Chen, "Investigation into the mechanisms of heavy oil recovery by novel alkaline flooding," *Colloids and Surfaces A: Physicochemical and Engineering Aspects*, 2013.
- [7] H. Ott, A. Kharrat, M. Borji and P. Arnold, "Fluid-phase topology of complex displacements in porous media," *Physical Review Research*, 2020.
- [8] Y. She, C. Zhang, M. A. Mahardika, A. Patmonoaji, Y. Hu, S. Matsushita and T. Suekane, "Pore-scale study of in-situ surfactant flooding with strong oil emulsification in sandstone based on X-ray microtomography," *Journal of Industrial and Engineering Chemistry*, 2021.
- [9] D. W. Green and G. P. Willhite, *Enhanced oil recovery*, 2nd ed., Society of Petroleum Engineers, 2018.
- [10] B. Schumi, T. Clemens, J. Wegner, L. Ganzer, A. Kaiser, R. E. Hincapie and V. Leitenmueller, "Alkali/Cosolvent/Polymer Flooding of High-TAN Oil: Using Phase Experiments, Micromodels, and Corefloods for Injection-Agent Selection," *Society of Petroleum Engineers*, 1 May 2020.
- [11] D. Magzymov, T. Clemens, B. Schumi and R. T. Johns, "Experimental Analysis of Alkali-Brine-Alcohol Phase Behavior with High Acid Number Crude Oil," 2020.
- [12] S. Poellitzer, M. Gruenwalder, G. Kienberger and T. Clemens, "How to Optimise Oil Recovery after almost 60 Years of Production from the Matzen Field, Austria.," 2008.
- [13] M. Lüftenegger, R. Kadnar, C. Puls and T. Clemens, "Operational Challenges and Monitoring of a Polymer Pilot, Matzen Field, Austria," 2015.
- [14] B. J. 2. Rupprecht, "Hydrocarbon Generation and Alteration in the Vienna Basin," PhD Thesis, Leoben, 2017.
- [15] M. Borji, *Phase behavior and pore-scale study of complex alkali-based EOR processes*, Leoben: Montanuniversität, 2021.
- [16] H. Ott, A. Kharrat, M. Borji, T. Clemens and P. Arnold, "Screening of EOR potential on the pore scale by statistical and topological means," *International Symposium of the Society of Core Analysts*, 2019.
- [17] A. Georgiadis, S. Berg, G. Maitland and H. Ott, "Pore-Scale Micro-CT Imaging: Cluster Size Distribution During Drainage and Imbibition," *Energy Procedia*, pp. 521-526, 2012.
- [18] A. Georgiadis, S. Berg, A. Makurat, G. Maitland and H. Ott, "Pore-Scale Micro-Computed-Tomography Imaging: Non-Wetting Phase Cluster Size Distribution During Drainage and Imbibition," *Physical Review E*, 2013.
- [19] S. Berg, R. Armstrong, H. Ott, A. Georgiadis, S. Klapp, A. Schwing, R. Neiteler, N. Brussee, A. Makurat, L. Leu, F. Enzmann, J. O. Schwarz, M. Wolf, F. Khan, M. Kersten, S. Irvine and M. Stampanoni, "Multiphase Flow in Porous Rock Imaged Under Dynamic Flow Conditions with Fast X-Ray Computed Microtomography," *Petrophysics*, pp. 304-312, 2014.
- [20] A. R. Sagi, M. C. Puerto, Y. Bian, M. C. A., H. G. J., M. Salehi and J. T. Kwan, "Laboratory Studies for Surfactant Flood in Low-Temperature, Low-Salinity Fractured Carbonate Reservoir," in *Society of Petroleum Engineers*, 2013.
- [21] J. Wegner and L. Ganzer, "Rock-on-a-Chip Devices for High p, T Conditions and Wettability Control for the Screening of EOR Chemicals," in *Society of Petroleum Engineers*, 2017.
- [22] P. A. Winsor, "Hydrotrophy, solubilization and related emulsification processes," *Transactions of the Faraday Society*, 1948.

SmartWater synergy with surfactant and polymer: A microscale investigation at crude oil-water interface

Subhash Ayirala^{1*}, Abdulkareem AlSofi¹, Zuoli Li², Rubia Mariath², Zhenghe Xu², and Ali Yousef¹

¹EXPEC Advanced Research Centre, Saudi Aramco, Dhahran-31311, Saudi Arabia

² Department of Chemical and Materials Engineering, University of Alberta, Edmonton, Alberta T6G 1H9, Canada

Abstract. Different microscale interactions of surfactant, polymer, and surfactant-polymer with SmartWater, at crude oil/water interface, were studied by using interfacial shear rheometer, and Langmuir trough at both ambient and elevated temperatures. The reservoir crude oil is used and high salinity water (HSW) is selected as the base-line to provide representative comparisons SmartWater. An amphoteric surfactant (1,000 ppm) and sulfonated polyacrylamide polymer (500 ppm) are chosen for this experimental investigation. Interfacial shear rheology results showed that viscoelasticity of interface is reduced with SmartWater in comparison to HSW. Such decrease in viscoelasticity is quite evident with the reductions observed in both viscous and elastic modulus data. Polymer either alone or together with surfactant resulted in relatively lower elasticity for SmartWater when compared to HSW. Interfacial pressures with polymer remained almost the same as brines, however they decreased with SmartWater. Surfactant significantly reduced the interface pressures and these reductions in interface pressures were greater with SmartWater when compared to HSW. The interface compression energies were reduced by approximately two orders of magnitude with surfactant. SmartWater also showed better efficacy to lower the interface compression energies over HSW in the presence of surfactant. These consistent findings obtained from interface viscoelasticity, interface pressures and compression energies demonstrated the favorable microscale interactions of surfactant and polymer chemicals with SmartWater to result in the formation of less rigid films at crude oil-water interface. Such softer interfacial films can easily be destabilized to improve oil phase connectivity and mobilize incremental oil in chemical enhanced oil recovery (EOR) processes.

1 Introduction

In the past few years, the potential synergy between SmartWater flooding and chemical Enhanced Oil Recovery (EOR) has attracted significant attention. Several laboratory studies have demonstrated the potential value of combining the two EOR methods. Early studies focused on the potential synergy between SmartWater and polymer flooding (Ayirala et al., 2010; Torrijos et al., 2018; AlSofi et al., 2018; AlSofi et al., 2019). Later studies focused on SmartWater or low-salinity water synergy with surfactant and surfactant-polymer flooding (Wang et al., 2018; Ayirala et al., 2019; Moradi et al., 2019; Eslahati et al., 2020; Veiskarami et al., 2020; Al-Murayri et al., 2021).

All these reported studies focused on macroscopic scale observations and relied heavily on macroscopic experiments. Displacement experiments – core imbibition in Eslahati et al. (2020), and corefloods in most of the remaining – formed the major component of previous studies. Such displacement results were complemented by measurements such as polymer rheology (Ayirala et al., 2010; AlSofi et al., 2019), surface-potential (AlSofi et al., 2019; Ayirala et al., 2019), interfacial tension (AlSofi et al., 2019; Ayirala et al., 2019; Moradi et al., 2019; Eslahati et al., 2020), contact angle (AlSofi et al., 2019; Ayirala et al., 2019; Moradi et al., 2019; Eslahati et al., 2020; Veiskarami et al., 2020), and phase behavior (Ayirala et al., 2019; Veiskarami et al., 2020; Al-Murayri et al., 2021). Also these studies have attempted to explain the underlying microscopic mechanisms of the observed synergism through the results obtained from macroscopic to core scale experiments. For example, AlSofi et al. (2018) noted that many of the observed effects of SmartWater on polymer injectivity and transport can be

attributed to polymer coil expansion in the lower-salinity SmartWater.

So clearly, besides some limited hypothetical attempts, little attention has been given to uncovering the underlying synergistic micro-scale mechanisms in play. Therefore, in this work, we study the potential synergies between SmartWater and chemical EOR (surfactant, polymer, and surfactant-polymer) at the microscale. The study scope includes a thorough primary suite of interfacial measurements (interfacial shear rheometry and Langmuir trough) together with a complementary comprehensive characterization of fluids (both brines and chemical solutions). These interfacial experiments characterize crude oil/water interfaces – obtained with the different brines and chemical solutions – in terms of interface viscoelasticity, interface pressure, and interface compression energies. The main objectives of this study are: (1) use the interfacial results to uncover some of the potential micro-scale synergies between SmartWater and chemical EOR, and (2) discuss the applicability of these findings in terms of macro-scale implications and more specifically oil mobilization.

2 Experimental Materials and Methods

2.1 Materials

Brines: different salts such as magnesium chloride, calcium chloride hydrate, anhydrous sodium sulfate, sodium chloride, and sodium bicarbonate were used to prepare two different synthetic-brine solutions using the deionized (DI) water. These salt compounds are obtained from Fisher Scientific, and all were American Chemical Society (ACS) grade certified. The thermos Scientific NanoPure™ system was used to produce DI water with a resistivity of 18.2

* Corresponding author: nethajisubhash.ayirala@aramco.com

MΩ·cm at 25°C. The salinity of two different synthetic brines used in experiments are shown in Table 1.

Table 1. Synthetic brine compositions used.

Ions	High Salinity Water (HSW) (ppm)	SmartWater (SW) (ppm)
Na ⁺	18,300	1,824
Ca ²⁺	650	65
Mg ²⁺	2,110	211
SO ₄ ²⁻	4,290	429
Cl ⁻	32,200	3,220
HCO ₃ ⁻	120	12
TDS	57,670	5,761

Chemicals: A high molecular weight sulfonated polyacrylamide polymer is used. This polymer (P) had a molecular weight of 12 million Dalton with a sulfonation degree of 25 mol%. The surfactant used is amphoteric, which is betaine-type with an active content of 50%. Both these surfactant (S) and polymer (P) chemicals are chosen, since they were reported to be tolerant to high salinity and high temperature conditions (Han et al., 2014; Jouenne, 2020; Wang et al., 2015).

Water conditions: amphoteric surfactant, and/or sulfonated polyacrylamide polymer were added to HSW and SW brines, respectively to prepare the polymer in brine, surfactant in brine, and polymer plus surfactant in brine solutions. Together with the baseline of HSW and SW, all the water conditions tested in the current study are listed in Table 2.

Table 2. Different water conditions used in experiments.

Base case runs (2)	HSW, SW
Surfactant runs (2)	HSW+1000 ppm S SW+1000 ppm S
Polymer runs (2)	HSW+500 ppm P SW+ 500 ppm P
Surfactant-polymer runs (2)	HSW+1000 ppm S + 500 ppm P SW+ 1000 ppm S + 500 ppm P

2.2 Viscosity of polymer solutions

The viscosities of polymer in brine solutions were measured with a rheometer (AR-G2 Rheometer, TA Instruments) supported by TRIOS software (TA Instruments), using the 60 mm plate method with shear rate increasing from 1 s⁻¹ to 100 s⁻¹. Rheometer was well calibrated before using it for viscosity measurements. Freshly prepared polymers solutions were kept at room temperature and used within 12 hours after preparation. A thermostat water bath was used to keep temperature constant at either 23°C or 70°C during the measurements.

2.3 Geochemical analysis of crude oil

SARA analysis. SARA analysis was done with crude oil samples to determine the fraction amount of saturates, aromatics, resins and asphaltenes in the sample by following the ASTM D2007-03 test procedure. The test, designed depending on the polarizability and polarity of each fraction, took about 8 days. Asphaltenes are not soluble in heptane and can be precipitated out from the crude oil by adding heptane. Aromatics were adsorbed with silica gel and resins were adsorbed with clays. Saturates cannot be adsorbed by these solids and were flushed off the column with heptane.

Total acid number (TAN) and Total base number (TBN). The TAN measurement followed ASTM D664 protocol, while TBN measurement is done using ASTM D4739 protocol. Both analyses were done by Maxxam Analytics Edmonton.

Density and viscosity. The viscosity of crude oil was measured with a digital density meter (Model DDM 2910, Rudolph Research Analytical). Crude oil was introduced into the cell and kept inside for 5 minutes to stabilize at 23°C and 70°C, respectively. Viscosity values were read after stabilization and the density values were given by the density meter based on the viscosity values.

2.4 Shear rheology

The viscoelastic properties (G', elastic and G'', viscous) of the crude oil-water (different brine compositions, surfactant and/or polymer) interfacial layers were determined using an AR-G2 stress-controlled rheometer (TA Instruments, New Castle, DE, USA) equipped with a double-wall ring (DWR) geometry, which is made of Pt/Ir. The radius of the DWR is 35 mm and its square-edged cross section helps to pin it on the water-oil interface, as shown in Figure 1a. The ring was flamed before each experiment to remove all the organic contaminants. A Delrin trough with a circular channel as the sample holder was attached to a Peltier plate for temperature control, as shown in Figure 1b.

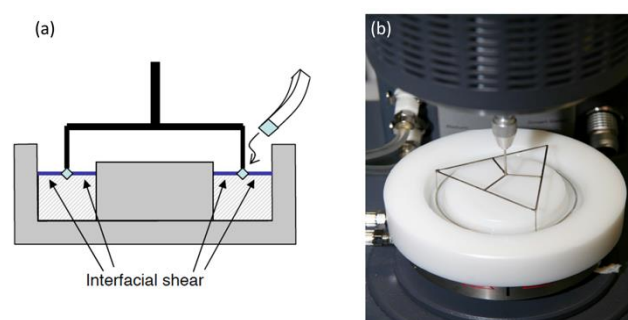


Fig. 1. (a) Illustration of the DWR configuration, and (b) the setup on the AR-G2 rheometer.

Pipetted into the sample holder was firstly 19.2 mL aqueous solution as the bottom phase or sub-phase. After positioning the ring at the air-aqueous solution interface, 15 mL of crude oil was slowly pipetted onto the top of the aqueous phase. Finally, a Teflon cap was placed over the sample to prevent solvent evaporation. To study the effect of aging on viscoelastic properties of interfacial layers, time sweeps were conducted at an angular frequency of 0.3 Hz and

with a 0.8% strain amplitude for 7 hrs. The measurements were conducted at $70 \pm 0.1^\circ\text{C}$.

2.5 Langmuir trough

The compressional behavior of interfacial films at the dectol/water (different brine compositions, surfactant and/or polymer) interface was characterized by interfacial pressure-area (π -A) isotherm obtained through a Langmuir trough. The experiments were conducted using a computer-controlled KSV trough (Biolin Scientific, Espoo, Finland) whose area is 250 cm^2 . A paper Wilhelmy plate sensor (Biolin Scientific; product identification, KN 0005) was used to detect the interfacial pressure (π) which represents the change in the interfacial tension (IFT) due to the presence of interfacial material relative to the clean interface (IFT_0), and is given by

$$\pi = IFT_0 - IFT \quad (1)$$

Prior to each measurement the trough was carefully cleaned with toluene, acetone, and Milli-Q water respectively. As shown in Figure 2, the lower part of the trough was filled with 120 mL of Milli-Q water solutions as the subphase. The trough was considered clean when the pressure isotherm at the air-DI water interface has a pressure reading of within $\pm 0.1\text{ mN/m}$ with the water phase being compressed from 250 cm^2 to 25 cm^2 . The barriers were then fully expanded, and the balance was zeroed at clean air-water interface. 100 mL of dectol (volume of decane: toluene=50:50) was then added to the top of DI water as the top phase. 23 μL of 20 wt% crude oil in toluene solution was then injected into top dectol phase using a Hamilton gastight syringe. After equilibrating the film for 1 hour, the system was compressed at 10 mm/min to obtain the isotherms. DI water was replaced by brine solutions with/without polymer and/or surfactants to study the effect of polymer and surfactants on the compressional behavior of oil/water interface.

23 μL 20% toluene-diluted crude oil

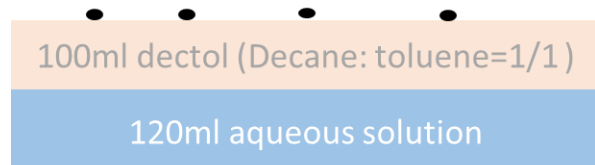


Fig. 2. Illustration showing the addition of water and oil phases in the trough for Langmuir trough measurements.

3 Results and Discussion

3.1 Characterization of brine solutions and crude oil

Brine/polymer solutions. The viscosity of both brine and polymer solutions measured as a function of temperature at 23°C and 70°C are shown in Figure 3 (a) and 3 (b), respectively. As shown in the Figure, the viscosity of polymer solutions decreases with increasing shear rate at both the temperatures while the viscosity of brines is almost constant at different shear rates, indicating that the polymer solutions are non-Newtonian and shear-thinning. The viscosity of all brine and polymer solutions is higher at 23°C than at 70°C .

As expected, higher viscosities were obtained with polymer in SmartWater (SW) at different shear rates in comparison to high salinity water (HSW) at the same temperature. Such result is obvious by considering the well-established favorable effect of lower salinities on viscosifying characteristics of polyacrylamide and sulfonated polyacrylamide polymers (Ayirala et al., 2010; AlSofi et al., 2019). The measured viscosities of HSW, SW, HSW + 500 ppm polymer, and SW + 500 ppm polymer at 6.3 sec^{-1} shear rate and 23°C were found to be 1.0 cP, 0.93 cP, 3.6 cP, and 4.9 cP, respectively. Similarly, the viscosities of these respective solutions at 6.3 sec^{-1} shear rate and 70°C were measured as 0.70 cP, 0.49 cP, 3.2 cP, and 4.2 cP.

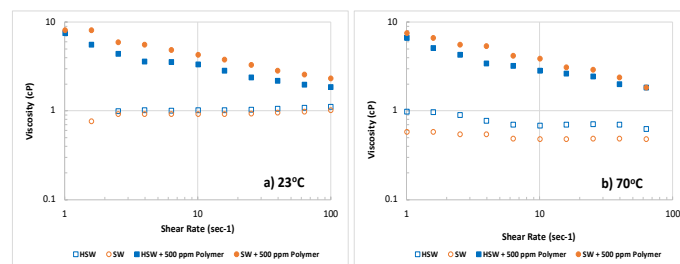


Fig. 2. Viscosity of brine/polymer solutions as function of shear rate at 23°C (a) and 70°C (b).

Crude oil. Total acid number (TAN) and total base number (TBN) of crude oil analyzed by Maxxam Analytics Edmonton are shown in Table 3. As can be seen, the oil is relatively acidic in nature due to the presence of predominantly acidic fractions over basic components.

Table 2. TAN and TBN of crude oil.

Analysis	Crude oil
TAN (mg KOH/g)	0.47
TBN (mg KOH/g)	0.04

Based on the SARA analysis, the crude oil had a much lower content of asphaltenes, while the contents of saturates, aromatics and resins are found to be higher in comparison to asphaltenes (Table 4).

Table 3. SARA analysis results (in wt%) for crude oil.

Parameter	Crude oil
Saturates	50.67%
Aromatics	17.12%
Resins	20.94%
Asphaltenes	1.65%

As can be seen from Table 5, the viscosity of crude oil was lowered significantly as the temperature was increased from room temperature to 70°C . The decreasing of density upon increasing temperature was also quite evident. At room temperature, the viscosity of crude oil was measured to be about 19.2 cP, while the viscosity decreased to 2.3 cP at 70°C .

Table 4. Density and viscosity of crude oil.

Property	Crude oil (23°C)	Crude oil (70°C)
Density (gm/cc)	0.87	0.84
Viscosity (cP)	19.2	2.3

3.2 Interface viscoelasticity

The elastic (G') and viscous (G'') modulus for crude oil/brine interface obtained with HSW and SW at 70°C are shown in Figure 4. As shown in this figure, the crude oil/brine interface was elastic-dominant ($G' > G''$) from the beginning, and there was no significant increase in moduli of the oil/brine interface even after aging for 7 hours. Such buildup of elasticity for oil-water interface may be caused by the accumulation of asphaltenes at the interface to form a rigid network of asphaltenic structures (Freer et al., 2003). At high temperatures, it is expected that asphaltene molecules would move faster and quickly accumulate at the interface to result in early elastic dominant behavior. Interestingly, the elastic modulus of interface was found to be higher with HSW when compared to SW. But only minor increase in viscous modulus was observed with HSW. The interface viscoelasticity is primarily governed by the competitive adsorption between asphaltene and the non-asphaltenic components of crude oil, such as naphthenic acids (Yarranton et al., 2007; Moradi et al., 2013; Alves et al., 2014). The adsorption of surface-active components at the interface is dominated by asphaltenes when compared to naphthenic acids in HSW (Verruto et al. 2009; Moradi et al. 2013). The asphaltenes adsorb onto the interface, while naphthenic acids remain in the bulk aqueous phase at this high salinity thereby resulting in the formation of a rigid viscoelastic film.

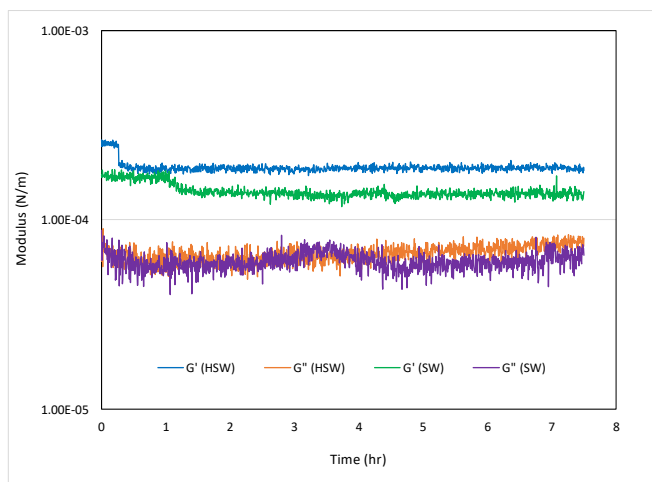


Fig. 4. Viscous and elastic moduli of interface with HSW and SW brine solutions at 70°C.

The viscoelasticity data of the oil/water interface obtained with 1,000 ppm surfactant in both HSW and SW brines at 70°C are presented in Figure 5. As can be seen, surfactant decreased the elastic modulus in HSW but increased the elasticity in SW. However, the addition of surfactant showed no effect on viscous modulus in both HSW and SW brines. The measured viscous and elastic modulus data obtained at crude oil/water interface with HSW+polymer and SW+polymer solutions at 70°C are shown in Figure 6. These results confirmed the impact of polymer on elastic modulus, wherein the elasticity of the interface has been found to be higher with HSW in the presence of polymer. This behavior is contrastingly opposite to that observed with HSW + surfactant solution. However, the viscous modulus almost remained the same for both HSW+polymer and SW+polymer solutions. Figure 7 summarizes the viscous and elastic modulus results obtained with surfactant + polymer in HSW

and SW brines at 70°C. From these results, it is quite evident that both elastic and viscous modulus are higher with HSW in the presence of surfactant + polymer. Such finding intuitively suggests that interface viscoelasticity is mainly dictated by polymer rather than surfactant when both the chemicals are present. This may be due to increased viscosities of aqueous phase caused by polymer, which forms a viscous barrier that would either slow down or prevent the movement of surfactant molecules to the interface.

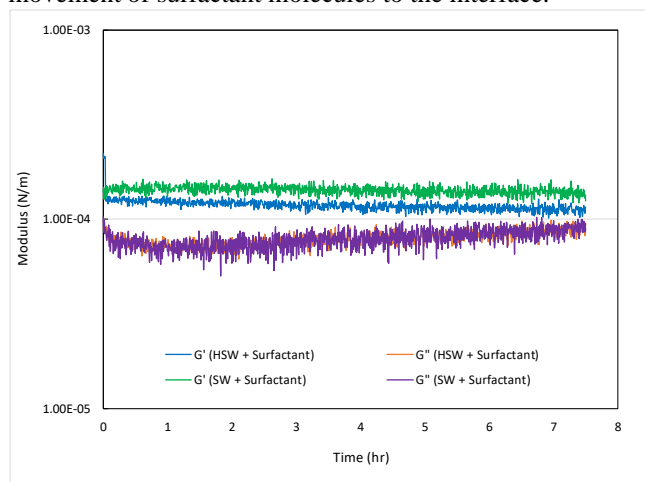


Fig. 5. Viscous and elastic moduli of interface with HSW+surfactant and SW+surfactant solutions at 70°C.

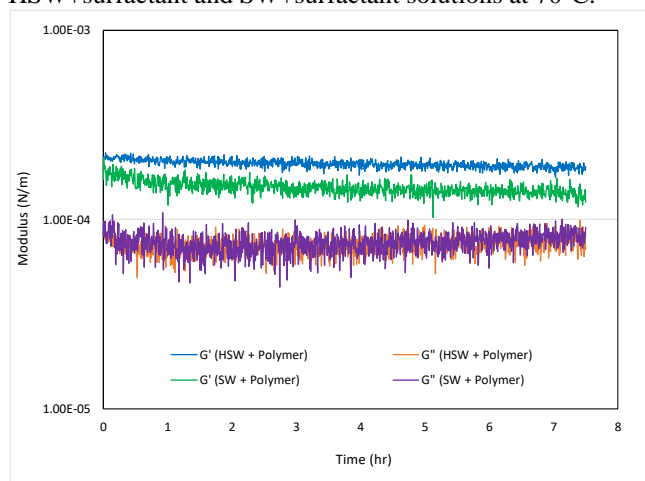


Fig. 6. Viscous and elastic moduli of interface with HSW+polymer and SW+polymer solutions at 70°C.

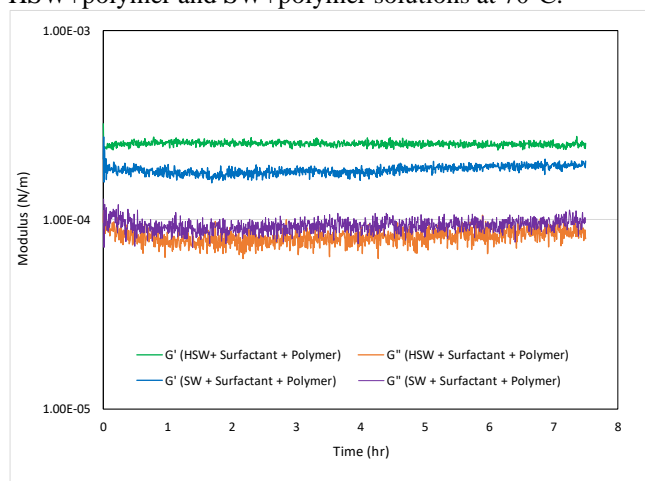


Fig. 7. Viscous and elastic moduli of interface with HSW+surfactant+polymer and SW+surfactant+polymer solutions at 70°C.

Overall, the results described in this section demonstrated the beneficial synergy of SmartWater on interface viscoelasticity either alone or in combination with polymer and surfactant + polymer. The lower salinity of SmartWater can decrease the elasticity of interfacial film to make it less rigid. These less rigid oil-water interfacial films can quickly be destabilized to promote the coalescence between oil droplets. Such faster coalescence of oil droplets would eventually improve oil phase connectivity for easy mobilization of oil in chemical EOR processes.

3.3 Interfacial pressures and compression energies

The effect of brine composition on the interfacial pressure was studied by recording the oil-water interfacial pressure (π) as the oil-brines/DI water interface area was compressed (A) at ambient temperature (23°C). Figure 8 presents the interfacial pressure vs. area isotherms obtained with brine and brine + polymer solutions. As illustrated in Figure 8, the interfacial pressure increases with the compressing of the surface area. Because the compressional viscoelastic moduli are proportional to the ratio between the changes in interfacial pressure and in the compressed area, the slope of the π - A isotherms is an indication of the rigidity of the interfacial layer and steeper isotherms represent more rigid oil-aqueous phase interfacial layers. Obviously, the interfacial film was most rigid in brines, and became less rigid with the addition of polymer. The interfacial pressures are highest with HSW followed by SW, HSW+polymer, and SW+polymer, respectively. These results indicated that rigidity of oil-water interfacial film is decreased by SmartWater and the lowest interfacial pressures obtained with SW+polymer also demonstrate the favorable synergy of SmartWater with polymer to form less rigid films at oil-water interface.

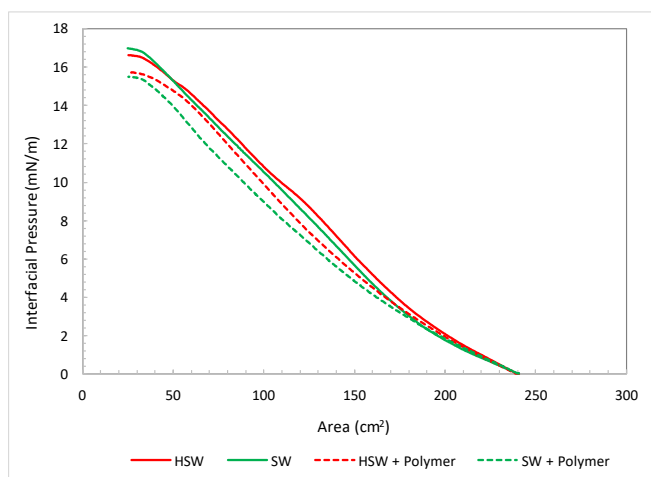


Fig. 8. Effect of brine compositions and polymer on π - A isotherms obtained for interfacial films at the diluted crude oil-brine interfaces at 23°C.

The interfacial pressure vs. area isotherms obtained by the addition of surfactant at different concentrations to HSW and SW brines at 23°C are shown in Figure 9. As can be seen, the interfacial pressures are significantly reduced by the addition of surfactant to both HSW and SW brines. The high efficiency of surfactant in softening the interfacial film was

confirmed even at lower surfactant concentrations of 125 ppm and 10 ppm. It is interesting to note that the interfacial pressure was decreased to lower than 1 mN/m at a much lower surfactant concentration of 10 ppm. Almost two orders of magnitude reduction in interfacial pressure was observed at 1000 ppm surfactant concentration to result in interfacial pressure values lower than 0.1 mN/m. Another important point to be highlighted is that interfacial pressures obtained with SW brine at each surfactant concentration is relatively lower than that obtained with HSW brine. This observation confirms the synergistic effect of SW brine with surfactant to result in lower interfacial pressures and subsequently decrease the rigidity of oil-water interfacial film.

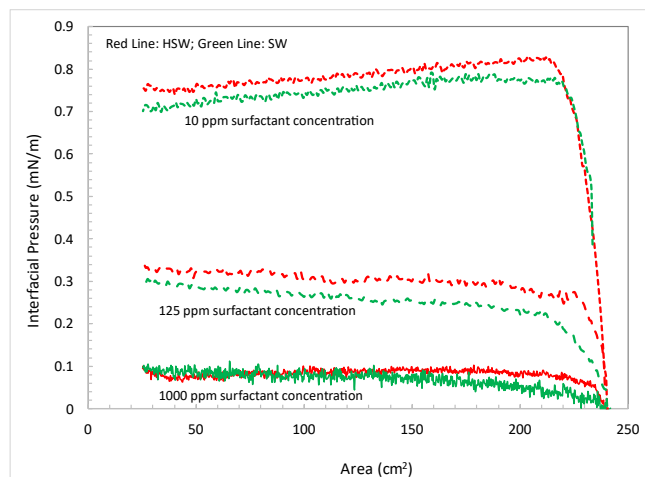


Fig. 9. Effect of surfactant on π - A isotherms obtained for interfacial films at the diluted crude oil-brine interfaces at 23°C.

Figure 10 presents the interface pressure vs. area isotherms obtained with surfactant + polymer in HSW and SW brines at 23°C. Since both of polymer and surfactant can soften the film, it is reasonable to see the lowest interfacial pressure in the brine solution with both of surfactant and polymer due to their combined effect. Similar to those results observed with either polymer or surfactant, SmartWater showed lower interfacial pressures with surfactant + polymer to confirm the favorable synergy even when both the chemicals are present together in the aqueous solution.

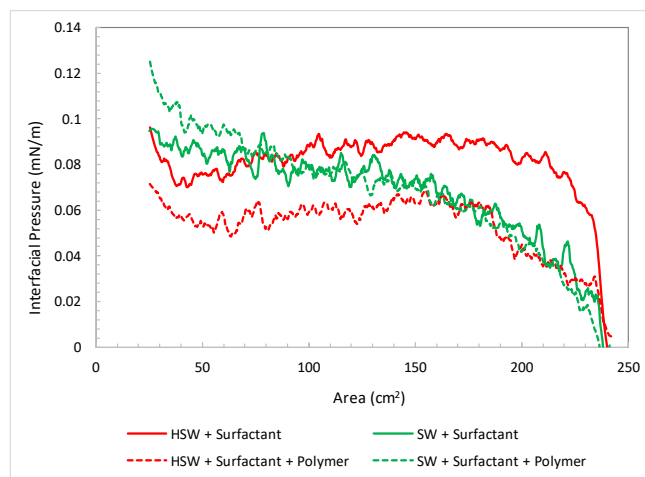


Fig. 10. Effect of surfactant-polymer on π -A isotherms obtained for interfacial films at the diluted crude oil-brine interfaces at 23°C.

The compression energy, calculated by the integration of interfacial pressure from π -A isotherms over the surface area, directly quantifies the film rigidity as it represents the difficulty to compress the interface. As shown in Figure 11, while the compression energy is comparable in HSW and SW brines, it is decreased by the addition of polymer or surfactant, and is lowest with the combination of surfactant and polymer. Surfactant by itself is found to be very effective to soften the interfacial film by significantly lowering the interfacial compression energy by almost two orders of magnitude. SmartWater brine lowered the interface compression energy at all conditions including the brine, brine + polymer, brine + surfactant, brine + surfactant + polymer when compared to the HSW brine. These results showed consistent trends with viscoelasticity and interfacial pressure data discussed earlier to demonstrate very well that SmartWater can synergistically combine with the beneficial effects of surfactant, polymer, surfactant-polymer to result in favorable microscale interactions at oil-water interface. Such favorable interactions can develop less rigid oil-water interfaces, which can easily be destabilized to fasten the coalescence between oil droplets to form larger oil ganglia and quickly form oil bank in chemical EOR processes.

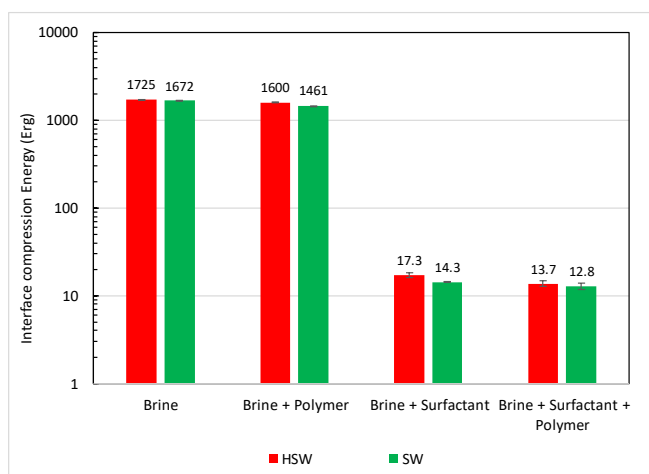


Fig. 11. Compression energy for the diluted crude oil-brines/DI water interface with brine, brine + polymer, brine + surfactant, and brine + surfactant + polymer solutions at 23°C.

3.4 Relationship between interfacial film rigidity and oil mobilization

In surfactant based tertiary chemical EOR processes, the residual oil droplets trapped in pore throats are released by the reductions in capillary forces caused by lowering of oil-water interfacial tension (IFT) at fluid-fluid interface and favorable wettability alteration at rock-fluids interface. The released oil droplets should reconnect with each other to grow into larger oil ganglia and sequential coalescence of these larger ganglia eventually forms a small oil bank. This small oil bank once formed grows bigger and bigger in size as it effectively reconnects additional ganglia in the flow path. The reconnection of oil ganglia mainly occurs through coalescence of oil droplets. The coalescence process happens when the interfacial film between the two oil droplets is

drained to eventually become very thin and rupture, which is directly linked with the rigidity of the interfacial film. As the interfacial film is less rigid, it can be ruptured at a higher critical film thickness to commence the coalescence process and fasten the time required to complete the coalescence between oil droplets.

Even though oil-releasing from rock surface is critical to chemical EOR process, by sole means it is not sufficient to result in efficient oil mobilization. It is most likely possible that without the coalescence of oil droplets after their release from the rock, the droplets will largely remain isolated in the production path. Such isolation can result in further breakup and re-entrapment of oil droplets in pore throats to adversely impact the recovery efficiency. Relatively lower interface viscoelasticities, interfacial pressures, and compression energies observed with SmartWater in comparison to HSW with surfactant, polymer, and surfactant-polymer chemicals indicate the ability of SmartWater to lower the oil-water interfacial film rigidity in chemical EOR. As a result, the use of SmartWater as injection fluid in chemical EOR processes can quickly destabilize the oil-water interfacial film to promote the coalescence between oil droplets and improve the connectivity of oil phase for easy oil mobilization (Figure 12). These favorable effects hasten the formation of oil bank not only to accelerate oil production but also to increase oil recovery in chemical EOR.

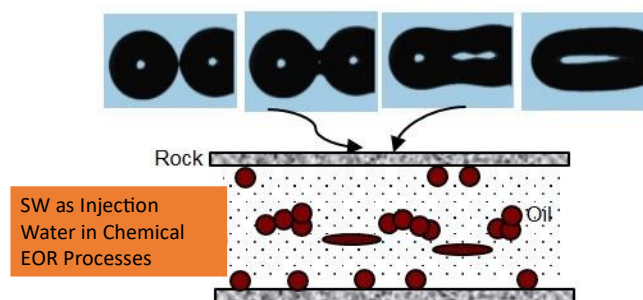


Fig. 12. Schematic representing the enhanced coalescence between oil droplets for improved oil phase connectivity in chemical EOR with SW as injection water.

4 Conclusions

In this experimental investigation, we presented the results obtained from interfacial shear rheology and Langmuir trough measurements to explore the micro-scale synergistic effects of SmartWater with surfactant, polymer, and surfactant-polymer chemicals at crude oil-water interface. The experimental data analyzed include interface viscous and elastic modulus (viscoelasticity), interface pressures and compression energies. The data showed consistent trends to demonstrate the favorable effects of SmartWater to lower the rigidity of oil-water interfacial film in the presence of surfactant, polymer, surfactant-polymer. These favorable effects can promote the coalescence of oil droplets to improve oil phase connectivity and oil mobilization in chemical EOR. The main conclusions are summarized in the following:

- SmartWater reduced both viscous and elastic modulus of the interface when compared to HSW. There was no impact of SmartWater on viscous modulus with surfactant, polymer, and surfactant-polymer. However, the elasticity of interface is lowered by SmartWater in combination with polymer and surfactant-polymer.
- Interfacial pressures were lowered by SmartWater, over HSW, at all water conditions including brine, brine-polymer, brine-surfactant, and brine-surfactant-polymer. Both polymer and surfactant are effective in lowering the interfacial pressure, while surfactant showed the highest efficiency to reduce interfacial pressures by almost two orders of magnitude.
- Interfacial compression energies also confirmed the favorable effect of SmartWater to effectively synergize with surfactant, polymer, surfactant-polymer to increase the easiness to compress the interface. The lowest interface compression energies are obtained with SmartWater in the presence of surfactant and surfactant-polymer.
- These results on viscoelasticity, interfacial pressure, and compression energies agreed very well with each other to demonstrate that SmartWater can synergistically combine with the beneficial effects of surfactant, polymer, surfactant-polymer to result in favorable microscale interactions at oil-water interface.
- Such favorable interactions can develop less rigid oil-water interfaces, which can easily be destabilized to fasten the coalescence between oil droplets to form larger oil ganglia and quickly form oil bank in chemical EOR processes.

References

- Al-Murayri, M.T., Kamal, D.S., Al-Qattan, A., Winoto, W., Li, Z., Britton, C. and Delshad, M., 2021. A practical and economically feasible surfactant EOR strategy: Impact of injection water ions on surfactant utilization. *Journal of Petroleum Science and Engineering* 201:108479.
- AlSofi, A.M., Wang, J. and Kaidar, Z.F., 2018. SmartWater synergy with chemical EOR: Effects on polymer injectivity, retention and acceleration. *Journal of Petroleum Science and Engineering* 166: 274-282.
- AlSofi, A.M., Wang, J., AlBoqmi, A.M., AlOtaibi, M.B., Ayirala, S.C. and AlYousef, A.A., 2019. Smartwater synergy with chemical enhanced oil recovery: Polymer effects on smartwater. *SPE Reservoir Evaluation & Engineering* 22 (01): 61-77.
- Alves, D.R., Carneiro, J.S.A., Oliveira, I.F., Façanha, F., Santos, A.F., Dariva, C., Franceschi, E. and Fortuny, M., 2014. Influence of the salinity on the interfacial properties of a Brazilian crude oil-brine systems, *Fuel* 118: 21-26.
- Ayirala, S.C., Uehara-Nagamine, E., Matzakos, A., Chin, R., Doe, P. and van Den Hoek, P. A designer water process for offshore low salinity and polymer flooding applications. 2010. SPE-129926-MS. SPE Improved Oil Recovery Symposium, Tulsa, Oklahoma, USA.
- Ayirala, S.C., Boqmi, A., Alghamdi, A., and AlSofi, A.M. 2019. Dilute surfactants for wettability alteration and enhanced oil recovery. *Journal of Molecular Liquids* 285: 707-715.
- Eslahati, M., Mehrabianfar, P., Isari, A.A., Bahraminejad, H., Manshad, A.K. and Keshavarz, A., 2020. Experimental investigation of Alfalfa natural surfactant and synergistic effects of Ca²⁺, Mg²⁺, and SO₄²⁻ ions for EOR applications: interfacial tension optimization, wettability alteration and imbibition studies. *Journal of Molecular Liquids* 310: 113123.
- Freer, E.M., T. Svitova, T. and Radke, C.J. 2003. The role of interfacial rheology in reservoir mixed wettability, *Journal of Petroleum Science and Engineering* 39: 137-158.
- Han, M., Fuseni, A., Zahrani, B. and Wang, J. 2014. Laboratory study on polymers for chemical flooding in carbonate reservoirs. SPE-169724-MS. SPE EOR Conference at Oil and Gas West Asia. Muscat, Oman.
- Jouenne, S. 2020. Polymer flooding in high temperature, high salinity conditions: selection of polymer type and polymer chemistry, thermal stability. *Journal of Petroleum Science and Engineering* 195: 107545.
- Moradi, M., Topchiy, E., Lehmann, T.E. and Alvarado, V. 2013. Impact of ionic strength on partitioning of naphthenic acids in water-crude oil systems – determination through high-field NMR spectroscopy, *Fuel* 112: 236-248.
- Moradi, S., Isari, A.A., Bachari, Z. and Mahmoodi, H., 2019. Combination of a new natural surfactant and smart water injection for enhanced oil recovery in carbonate rock: Synergic impacts of active ions and natural surfactant concentration. *Journal of Petroleum Science and Engineering* 176: 1-10.
- Torrijos, I.D.P., Puntervold, T., Strand, S., Austad, T., Bleivik, T.H. and Abdullah, H.I., 2018. An experimental study of the low salinity Smart Water-polymer hybrid EOR effect in sandstone material. *Journal of Petroleum Science and Engineering* 164: 219-229.
- Veiskarami, S., Jafari, A. and Soleymanzadeh, A., 2020. Phase behavior, wettability alteration, and oil recovery of low-salinity surfactant solutions in carbonate reservoirs. *SPE Journal* 25 (04): 1784-1802.
- Verruto, V.J., Le, R.K., and Kilpatrick, P.K. 2009. Adsorption and molecular rearrangement of amphoteric species at oil-water interfaces. *J Phys Chem B.* 113 (42):13788–13799.
- Wang, J., Han, M., Fuseni, A.B. and Cao, D. 2015. Surfactant adsorption in surfactant-polymer floodin in carbonate reservoirs. SPE 172700-MS. SPE Middle East Oil & Gas Show Conference. Manama, Bahrain.
- Wang, J., Ayirala, S.C., AlSofi, A.M. and Yousef, A.A. 2018. SmartWater synergy with surfactant polymer flooding for efficient oil mobilization in carbonates. SPE EOR Conference at Oil and Gas West Asia, Muscat, Oman.
- Yarranton, H.W., Urrutia, P. and Sztukowski, D.M. 2007. Effect of interfacial rheology on model emulsion coalescence. *Journal of Colloid and Interface Science* 310: 253-259.

DarcyShale: An improved GRI method for more reliable measurements on low permeability samples

Roland Lenormand^{1*}, and Sandra Profice²

¹CYDAREX, 31 avenue Gabriel Péri, 92500 Reuil-Malmaison, France

²TOTAL CSTJF, avenue Larribau, 64018 Pau Cedex, France

Abstract. In 1993 Luffel *et al.* proposed the Gas Research Institute (GRI) method for permeability measurement on crushed rock. In 2019, a benchmark analysis of GRI tests (SCA2019-016) revealed that the measured permeabilities were not reliable. The principal conclusion was that the thermal relaxation generated at the beginning of the test completely or partially hid the sample pressure response. In this paper we present an improved GRI method, named DarcyShale. By optimizing the device design, we minimized the experimental thermal effects at short times. We quantified the pressure variations not due to the viscous flow inside the rock with a highly permeable rock whose response should be instantaneous. We studied the impact of different gases and found that nitrogen is preferred to helium or krypton. We also show that mixing a fine powder with the crushed sample improves the quality of the measurement. As a quality control, we systematically checked that the signal amplitude agreed with the theoretical value computed from a porosity value obtained separately.

1 Introduction

In the early 90s, Luffel *et al.* [1] proposed an innovative method for measuring low permeabilities on crushed rocks or packs of drill cuttings, named Gas Research Institute (GRI) method. The test consists in imposing a gas pressure pulse on the particles and recording over time the response due to the gas flow in the pore network. The experimental signal is interpreted using either a numerical model or a simplified analytical solution. A GRI test being nothing more than a pycnometry test, the GRI device classically found in the industry is the pycnometry device sketched in Figure 1.

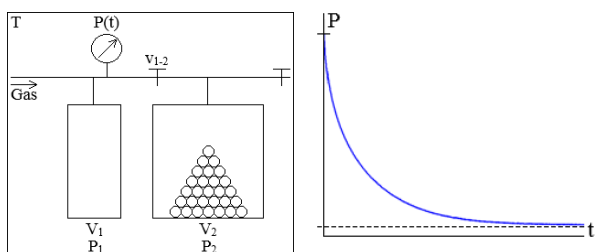


Figure 1 - GRI or pycnometry device and recorded pressure signal as function of time.

The sample is introduced in a chamber of volume V_2 that is connected to a chamber of volume V_1 via a valve v_{1-2} . Initially, the valve v_{1-2} is closed and the pressure in the dead volume of the chamber V_2 is at P_2 , as well as the pressure in the sample pore volume V_p . The test starts with the pressurization of the chamber V_1 at a pressure P_1 higher than the pressure P_2 , P_2 being generally equal to the atmospheric pressure P_{atm} . At time $t=0$, the valve v_{1-2} is opened, and the recording of the pressure transient $P(t)$ is started simultaneously. The device is placed in a

temperature-controlled oven or laboratory to keep its temperature T constant.

The option to work on rock particles is particularly appealing as it enables cost and time saving. Just a few grams of drill cuttings are enough for the test, which drastically reduces the test cost. Besides, the test duration is significantly shortened by both the increase of the medium exchange area with the invading gas and the decrease of the medium characteristic penetration depth [2]. Another argument proposed by Luffel *et al.* to promote the GRI method is the elimination of the coring-induced microfractures while crushing. The authors argue that such microfractures remain open even if the sample is confined and are thus responsible for a bias in the estimated matrix permeability.

As any method, the GRI method has limitations. The fact that a realistic confining pressure cannot be applied on the rock particles is as problematic as the existence of microfractures in a confined sample. Indeed, tight materials are highly sensitive to stress [3]. Moreover, Tinni *et al.* [4] refuted Luffel *et al.* argument that microfractures completely disappear when finely crushing. They detected microfractures in micro-computed tomography images of shale particles having sizes of 3.5 mm and 0.7 mm. From scanning electron microscopy images taken before and after crushing, Profice and Lenormand [5] even proved that crushing can generate microfractures. Crushing has the potential negative effect to damage the pore network [4]. Tinni *et al.* observed, for diverse rocks, that the permeability decreases as the mean particle diameter decreases. The mercury injection tests proved that this trend is not due to the gradual elimination of microfractures but to the modification of the pore throat size distribution.

* Corresponding author: roland.lenormand@cydarex.fr

Anisotropy is an additional factor affecting the estimated permeability. Contrary to tests on core plugs, tests on crushed samples do not give a directional permeability but a mean measurement, the gas penetrating the particles in the three space directions [3]. Simplifying the sample geometry by representing the polydisperse pack of particles by a monodisperse pack of spheres [2, 4, 5] or cylinders [1] possibly induces an error on the permeability [6]. However, as far as we know, quantifying this error has never been addressed rigorously in the current literature. Finally, the recorded pressure response is altered at short times by thermal effects created when opening the valve v1-2 [2, 5]. Sandra *et al.* [5] showed that these effects were one of the major causes explaining the significant dispersion of permeabilities determined for similar samples by different commercial laboratories equipped with GRI devices [7]. The pressure relaxation related to the gas flow and carrying information about the permeability is either partially or entirely hidden by the thermal relaxation.

The real nature of the thermal effects occurring at short times is not perfectly understood in the literature. They are usually qualified as Joule-Thomson effects [8]. A Joule-Thomson adiabatic gas expansion supposes a steady-state gas flow through a rigid and insulated tube obstructed by an obstacle, because of a pressure gradient along the tube [9]. In the case of a GRI test, the cross-section restriction introduced by the valve v1-2 acts as obstacle. However, the gas flow from the pressurized chamber V1 to the dead volume in the chamber V2 is never assimilated to a steady-state gas flow. It is generally assumed to be instantaneous [2, 4, 5]. A classic example of Joule-Thomson expansion is the injection of supercritical CO₂ (high pressure and low temperature) in a depleted reservoir (low pressure and high temperature) [10]. The gas expansion engendered when opening the valve v1-2 resembles more a Joule-Gay Lussac adiabatic gas expansion. This type of expansion involves two rigid and insulated chambers isolated from each other by a valve, one chamber being pressurized and the other one being at a pressure equal to 0 [9]. The gas flow provoked by the valve opening is abrupt, as in a GRI test. The Joule-Thomson and Joule Gay-Lussac expansions are not identical in terms of Thermodynamics. Consequently, the gas temperature variations observed during these two expansions are not identical as well [9]. In a Joule-Gay Lussac expansion, the temperature decreases for most gases. Some exceptions exist. Helium, for instance, is subjected to temperature increase. In a Joule-Thomson expansion, the gas temperature increases or decreases depending on its initial value. The gas gets cooler only when its initial temperature is lower than a threshold temperature, named inversion temperature.

Some authors tried to model the heat exchanges between the gas and its environment during its expansion in a porous medium. Civan [6] started from the simulation work that App *et al.* [11] did to better understand the temperature variations observed at the field scale during oil and gas production tests. He developed an analytical model describing the gas flow under non-isothermal conditions by combining the equation of mass

conservation, Darcy's law, the equation of energy conservation for the gas and the equation of energy conservation for the rock. This model considers the heat exchanges between the gas and the rock which originate from the fact that the gas has a temperature different from the rock temperature. It relates the changes in the gas temperature to energy loss by viscous dissipation and Joule-Thomson effects accompanying the gas expansion inside the rock. Suarez-Rivera *et al.* [12] went further in the modelling process by incorporating in their numerical model the various thermal phenomena taking place over the whole duration of a GRI test: heat exchanges between the gas and the matrix, heat exchanges between the gas and the device walls, heat transfer through the device walls. The authors identified the gas expansion right after valve opening to an adiabatic frictional gas flow through a tube having a constant cross-section. Such a flow is called Fanno flow.

The models applying in non-isothermal conditions are very complex and the true physics they are supposed to rely on is maybe still somewhat unclear. Our strategy regarding the thermal effects consisted in reducing the effects to keep the interpretation simple rather than modelling them.

In this paper we will first describe and discuss results obtained with a standard GRI apparatus that we have built. Then we will describe several improvements. The change of design allows a better determination of the average pressure during the relaxation leading to a more accurate determination. We have tested several gases: nitrogen; helium and krypton. We will discuss why the best results are obtained with nitrogen. We will also show that adding a powder to the crushed sample improves the accuracy of the measurements.

2 Results with the standard GRI method

We have built our own GRI device and analysed several experiments to discuss the limitations and the possible improvements.

2.1 Description of our GRI equipment

The volume V1 is 0.8 cc and volume V2 containing the sample is 8 cc. The maximum working pressure is 10 barg.

We used the pyrophyllite and shale samples described in the 2019 benchmark publication [5]. Porosities are respectively 0.045 and 0.13 frac. and liquid permeabilities around 20 and 10 nD. Crushed samples have a mean diameter of 1.7 mm. We have used both nitrogen and helium since these two gases were used in the benchmark.

For all the experiments described in this paper, permeabilities are determined by history matching of experimental data with the numerical model.

The model used in the interpretative procedure is based on two hypotheses. First, the crushed sample is assumed to be a monodisperse pack of homogeneous and isotropic

spheres. Second, the gas is supposed to follow the Boyle's law, to have a constant viscosity and to propagate in isothermal conditions. The model is a numerical model which considers the gas compressibility. Determining K_L and b values instead of a K_g value is not feasible since the two properties are correlated. As we will show at the end of this paper, the Klinkenberg correction is determined by performing several experiments at different pore pressures.

2.2 Results for L23

Figure 2 shows the recorded pressure for nitrogen and helium with the shale sample L23. The initial pressure in V1 is around 10 bar. After opening the valve, the pressure is around 1.5 bar, as it can be calculated using thermodynamics laws.

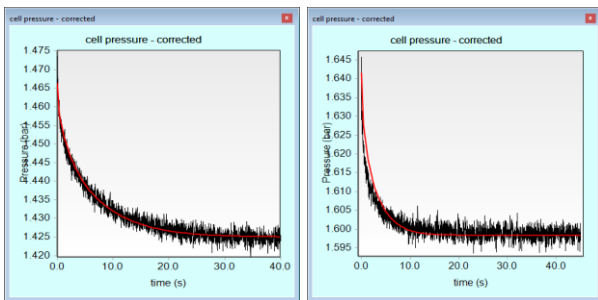


Figure 2 – L23: Recorded signal (black) during the relaxation and interpretation (red): a) with Nitrogen; b) with Helium

The interpreted permeabilities are 93 nD for nitrogen and 134 nD for helium. The difference is due to the Klinkenberg effect: the b coefficient being larger for helium than for nitrogen.

2.3 Results for Pyrophyllite

Figure 3 shows the results for the crushed pyrophyllite sample. The decreasing part of the curve is very short for N_2 (less than 0.5 s) and not visible for He. For N_2 , Figure 4 shows the interpretation with $K_g=500$ nD, the gas permeability measured on plugs.

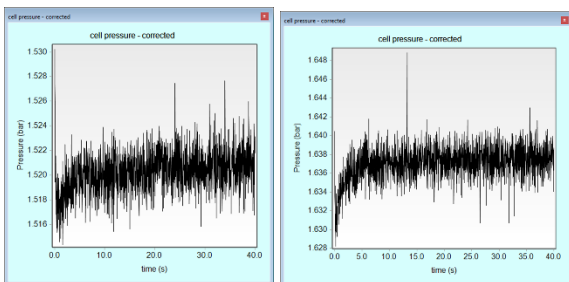


Figure 3 - Recorded signal during the relaxation with pyrophyllite sample: a) with Nitrogen; b) with Helium

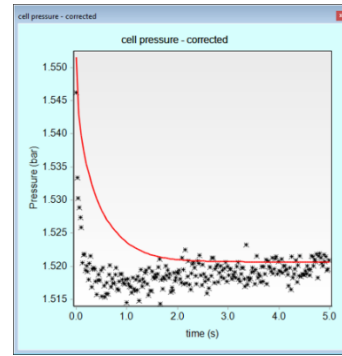


Figure 4 – pyrophyllite sample with N_2 : interpretation with $K_g = 500$ nD (in red)

2.4 Discussion of the results

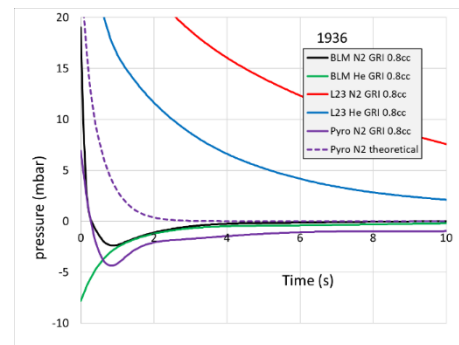
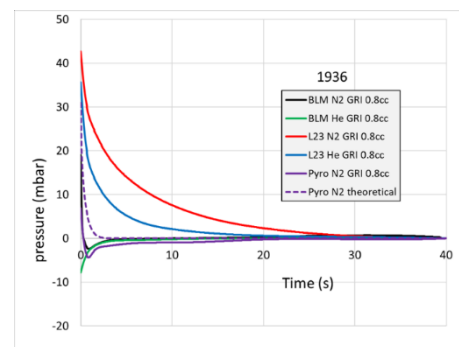


Figure 5 — N_2 and He signals for L23 and pyrophyllite, normalized to the final pressure, and fitted with a spline function. Comparison to the signal recorded with the high permeability sample BLM.

Figure 5 show the signals for the shale L23 and pyrophyllite (N_2) compared to the signal obtained with a highly permeable brick sample (10 mD), called BLM. The signals are fitted with splines and shifted to finish at zero final pressure for all experiments.

With this standard equipment, we have two main problems:

2.4.1 Large variation of pressure in the sample

Figure 2 shows the pressure signal for experiment L23. The amplitude of the signal is around 50 mbar with an average pressure around 1.5 barg. But this measured pressure is the pressure outside the sample. For Klinkenberg correction, we need the average pore

pressure inside the sample. Initially the sample is at atmospheric pressure and the final pressure is 1.5 barg. The average relative pressure is 0.75 barg.

To determine accurately the Klinkenberg correction, we need average pore pressures in a large range of values, and around 10 barg seems a reasonable target. With 10 barg initial pressure, the final pressure is around 1.5 barg. Around 120 barg would be necessary to get a final pressure of 10 barg. Even in this case, the average pore pressure will be 5 barg (since the initial pressure is 0 barg).

The standard GRI method is not adapted for Klinkenberg correction and in the SCA benchmark [5], no company provided a Klinkenberg correction.

2.4.2 Abnormal relaxation at short times

For BLM with 10 mD permeability, the viscous relaxation inside the sample is too fast to be observed on the pressure record (less than 1 ms using numerical simulation). The recorded pressure transient is due to other mechanisms that we will discuss later.

This relaxation has two components: below 1s, decreasing for N₂ and increasing for He, possibly related to Joules-Thomson effect, since the effect is inverse for these two fluids, and after 1s, an increasing effect for both gases. We will assume that this "blank signal" related to the gas behaviour in the volumes and the intergranular space is always present and superimposed to the viscous relaxation in pores for other less permeable samples.

For the shale L23, due to the large porosity and low permeability, the signal due to the viscous flow is much larger than the blank signal, for both N₂ and He, and gas permeability can be accurately determined.

For the pyrophyllite sample with N₂, the dashed line represents the calculated response, assuming the gas permeability measured on the plugs (500 nD). The duration of this signal is comparable to the blank signal and the interpretation is not possible. We also can note that the shape of the signal shows a minimum, as for the blank. This shape of signal was also reported by services companies during the benchmark [5].

Now, we will show how we have solved these two problems by designing a new equipment that we call DarcyShale, by studying the effect of the nature of the gas and by adding a powder to fill the space between the grains of crushed porous material.

3 Improvements of the GRI method

3.1 Improvements of the design of the equipment

In the standard GRI design the volume V1 is small compared to volume V2 where the sample is placed

The advantage is a relaxation signal with a large amplitude since the volume outside the rock is small. The drawback is the limited pressure that can be reached.

The main modification of our equipment is to place the sample under pressure in the vessel V2 and then make a pulse decay by opening the valve on the vessel V1 at lower pressure (atmospheric pressure or vacuum). The pressure sensor measures the pressure in V2. The amplitude of the pulse can be adjusted by choosing the volume V1. With the same equipment as described previously (ratio V1/V2 = 1/10), when sample is initially at 10 barg, the final pressure is around 9 barg.

This configuration has several advantages:

- 1) A small total volume leading to a signal of large amplitude since V1 is small.
- 2) Pressure around 10 bar can be easily obtained, directly with a pressure regulator from a gas cylinder.
- 3) The average pressure is better defined (between 9 and 10 bar in the previous example instead of between 0 and 10 barg in the standard GRI equipment), leading to a better determination of the Klinkenberg coefficient.

Figure 6 shows the DarcyShale response of BLM (10 mD) with initial pressure at 10 bar in red to be compared to the black curve for the GRI at 1.5 barg final pressure. The sign of the blank response is inverted for the two equipment since V2 is under pressure in DarcyShale, but the amplitudes and durations are similar.

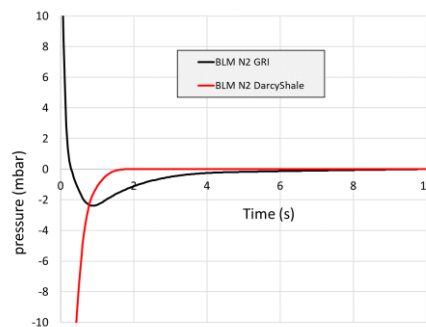


Figure 6 – Comparison of the blank BLM response for GRI and DarcyShale equipments.

To reduce the amplitude of the blank response, we have studied two parameters: the nature of gases and the effect of adding a fine powder between the grains of crushed material.

3.2 Effect of the nature of the gas

For the commercial measurements described in the 2019 SCA benchmark [5], both N₂ and He were used. Here we have studied these two gases. In addition, we also used krypton that has a larger molar mass and should lead to lower apparent permeabilities due to the Klinkenberg effect. For simplicity of interpretation, we have not tested CO₂ that presents Kelvin condensation in small pores. However, this effect may present some interest and should be studied in the future.

The properties of the gases are given in Table 1 (from Air Liquid encyclopedia). We have added the properties of

xenon, but due to its cost, it has not been tested. By comparison with krypton, we do not think it presents an interest.

What is the effect of these gas properties on the experiments?

- Molar mass (and density) influences the inertial effects, the Reynolds number being proportional to the density. But we do not think that inertial effects are significant in our experiments.
- Molar mass also influences the apparent permeability through the coefficient b of the Klinkenberg effect. Using Klinkenberg law:

$$K_G = K_L \left(1 + \frac{b}{P_m} \right),$$

Where K_G is the apparent gas permeability, K_L the corrected (or liquid) permeability and P_m the average absolute pressure in the sample (generally, the arithmetic average between pressures at inlet and outlet of the sample). The expression of b is:

$$b = \frac{4c\mu}{r} \sqrt{\frac{\pi RT}{M}},$$

M is the gas molecular weight, μ the gas viscosity, c is a coefficient close to 1, r is the radius of the capillary tubes used to model the pore network (linked to permeability), T is absolute temperature and R is the universal gas law constant.

- The kinetic diameter is used to define the mean free path, also related to the Klinkenberg effect. This parameter is similar for the different gases.
- Viscosities are directly related to the transient flow, but the values are similar for all the gases.
- Joule-Thomson coefficient is related to the variation of temperature during a pressure drawdown through a porous medium of an orifice. The important point is that the effect is of opposite sign for N₂ and He.
- γ is the adiabatic expansion or compression coefficient. It differs for mono or diatomic gases.
- The specific heat is the amount of thermal energy accumulated per degree and unit of mass in the gas. Note that its value is higher for helium. However, the mass of helium in the vessels is much lower than for the other gases.
- Thermal conductivity characterized the rate of heat exchange through the gases, which is much higher for helium.

Table 1- Main physical properties of the gases at 25°C (from Air Liquid encyclopedia)

	unit	Helium	Nitrogen	Krypton	Xenon
Molar Mass		4	24	84	131
Viscosity	cP	0.0199	0.0178	0.0251	0.0212
compressibility factor		1.0005	0.9998	0.998	0.995
Density	Kg/m ³	0.168	1.15	3.43	5.4
Kinetic diameter	nm	0.260	0.364	0.360	
Thermal conductivity	mW/m.K	155.3	25.8	9.36	5.54
Specific heat	kJ/(kg.K)	5.19	1.04	0.25	0.16
Joule-Thomson coefficient	K/bar	- 0.07	0.23		
γ		1.69	1.4	1.67	1.68

We have tested the 3 gases: N₂, He and Kr on different samples without using additional powder between the grains of crushed porous material.

The non-porous glass beads are used, like BLM, as samples that should not present any relaxation. Figure 7 shows a small relaxation for helium, that increases for N₂ and Kr.

For the shale sample L4 (Figure 8), the amplitude of the signal is low for he, larger for N₂ and Kr. However, the difference with the glass beads is significant and the experiments can be interpreted, at least with N₂ and Kr.

For the pyrophyllite sample (Figure 9), the signal is very similar to the blank response of the glass beads and the experiments cannot be interpreted.

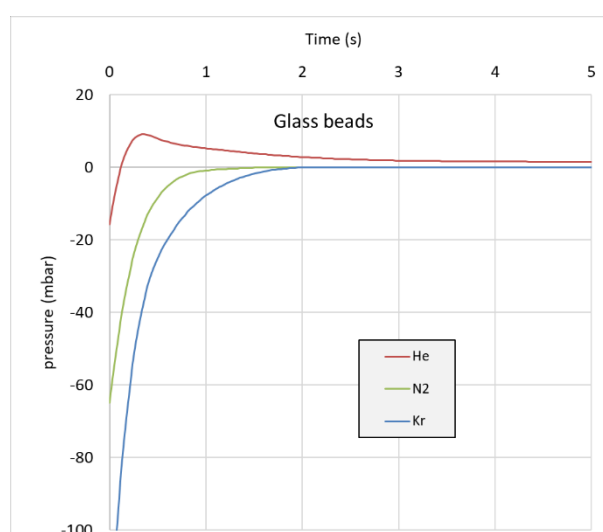


Figure 7 – 2 mm glass beads: Relaxations with the 3 gases.

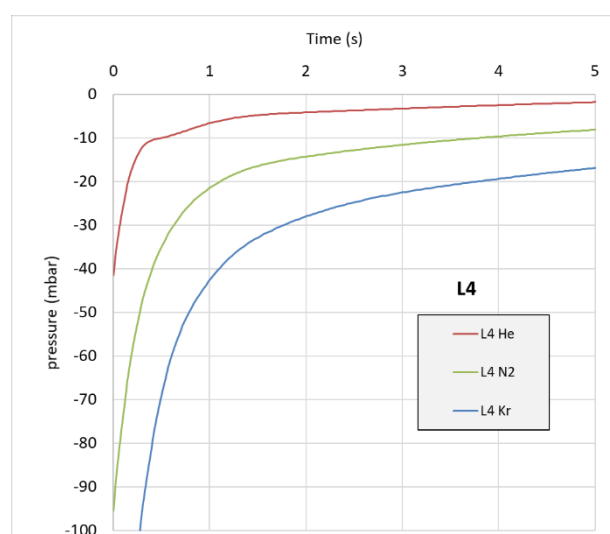


Figure 8 – Shale sample L4: Relaxations with the 3 gases

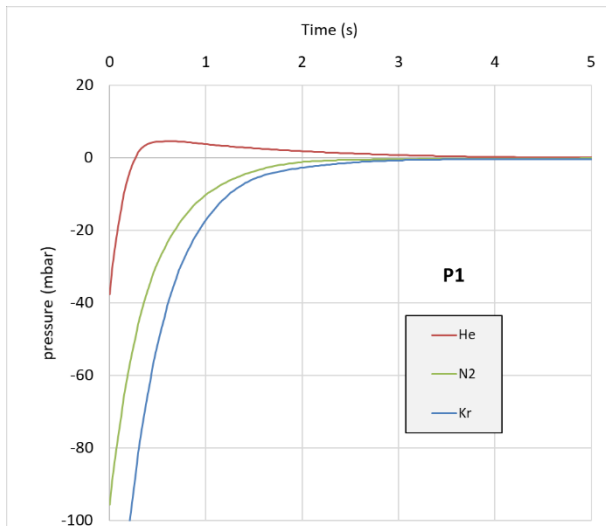


Figure 9 - Pyrophyllite: Relaxations with the 3 gases

As a conclusion, we see that He reduces the signals, both for the blank and for the samples. At the opposite, krypton leads to a large signal, both for the blank and for samples. Obviously, Helium must be discarded, at least for samples with permeabilities in the range of L4 or pyrophyllite. Krypton has no real advantage compared to N₂. We will see other results with adding powder in the next part of this paper that confirms that N₂ is the best gases for this type of measurement.

3.3 Adding powder to improve the pressure response

We will now discuss the effect of adding powder mixed with the grains of crushed rock.

Our first motivation was to reduce the dead volume around the crushed sample to improve the amplitude of the pressure signal. However, we quickly noticed that the effect of adding powder in reducing the blank response was more important than only a volume reduction.

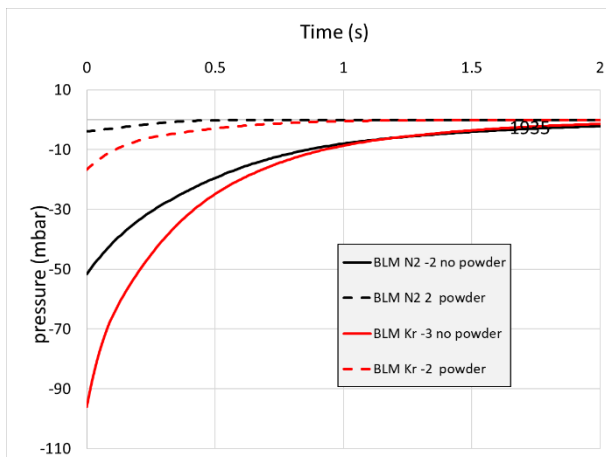


Figure 10 – Blank response of BLM with N₂ and Kr with and without powder.

Figure 10 shows the effect of a diatom earth powder (silica porous material) on the BLM with nitrogen and krypton. The powder has a large impact, reducing by a factor close to 10 the amplitude of the blank signal for

both gases. Figure 11 shows a similar effect with 1 and 2 mm non-porous glass beads with krypton.

For all the experiments with powder, the amplitude of pressure at 1 second is reduced by a factor close to 10.

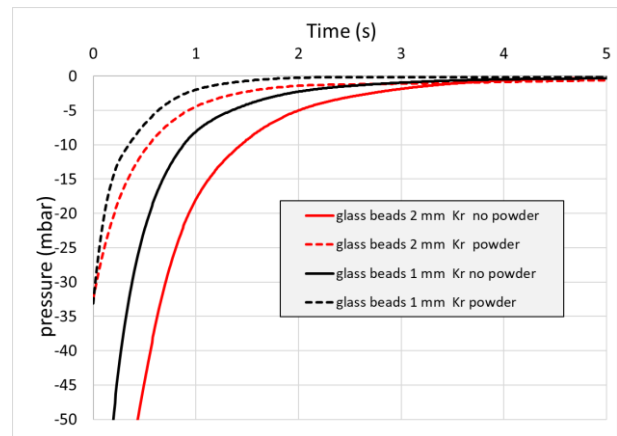


Figure 11 - Response for 1 and 2 mm glass beads with krypton with and without powder.

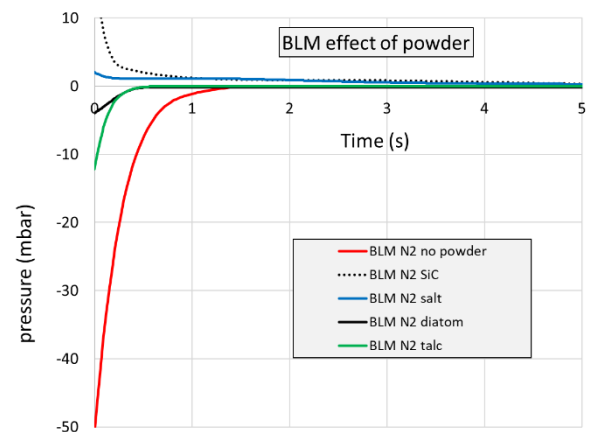


Figure 12 – Effect of the different powders on the pressure response for the BLM sample with N₂.

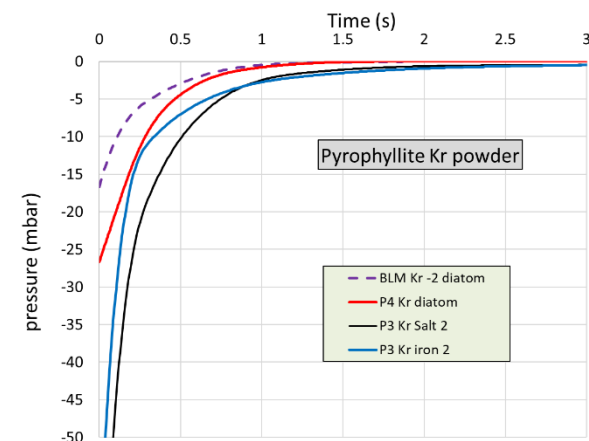


Figure 13 - Effect of the different powders on the pressure response for pyrophyllite with krypton. The dashed black curve is the response of the BLM sample.

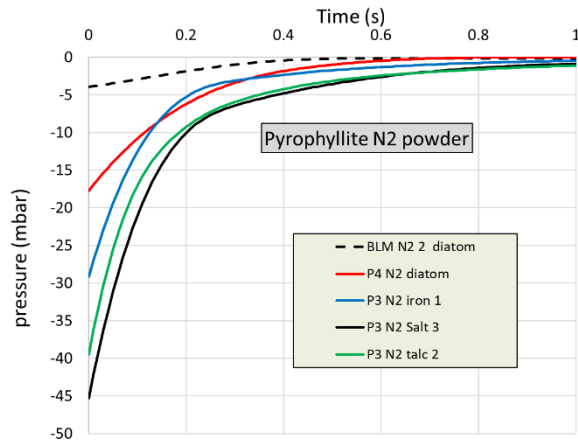


Figure 14 - Effect of the different powders on the pressure response for pyrophyllite with nitrogen. The dashed black curve is the blank response of the BLM sample.

The powder is well packed and fills all the empty space and we do not see any compaction after the experiment. In addition, we have tested the repeatability of the measurements.

We then studied the effect of the nature of the powder on the BLM sample with nitrogen (Figure 12) and pyrophyllite with krypton (Figure 13) and nitrogen (Figure 14).

Iron powder was tested expecting a larger effect for stabilizing the temperature due to its high thermal capacity. The purpose was to switch from an adiabatic toward an isothermal process. But there was no real difference with the other powder. The non-porous powders like SiC are more efficient than diatom earth but are difficult to use since any grain of SiC in a valve can damage the valve. The NaCl salt is efficient but difficult to operate since it does not "flow" easily between the grains of the crushed samples. Our first selection was talc that mixed very well with the sample particles. However, there are some questions about talc safety. We have opted for wheat flour that gives similar results.

Figure 15 shows the comparison between pyrophyllite (P4) and the blank BLM with nitrogen and krypton. As already discussed, the amplitude of the signal is larger and the relaxation time longer for krypton (red). However, the difference between the pyrophyllite signal and BLM is more pronounced for nitrogen (black). Therefore, we have selected nitrogen for the experiments.

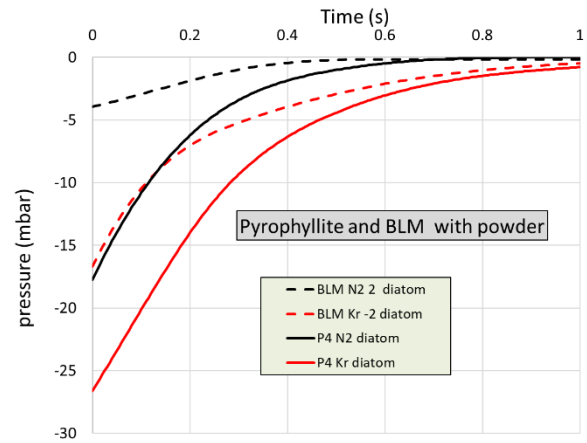


Figure 15 - Pyrophyllite (P4) and BLM with diatom powder: comparison of N₂ and Kr experiments.

4 Results with the improved DarcyShale equipment

With the DarcyShale equipment, we performed experiments with and without powder for pyrophyllite and the shale sample, and at different pressures to derive the Klinkenberg correction for the shale sample.

All the figures present the raw experimental pressure in black, and the numerical simulation in red.

4.1 Results with pyrophyllite (with nitrogen)

Figure 16 shows the result of an experiment without powder. The numerical simulation (in red) is performed using the real porosity of the sample (0.045 frac.). The numerical simulation cannot represent the experiment with the real value of porosity; a porosity 10 times larger is necessary to cover the amplitude of the signal. Without powder, the real signal is hidden by the thermal artifact over 1 second as previously described.

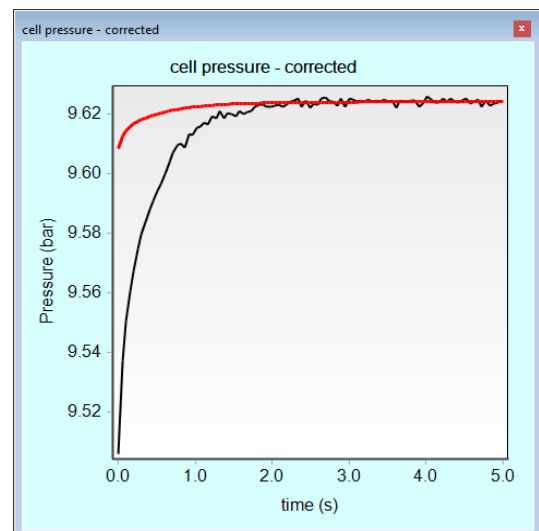


Figure 16 - Sample Pyrophyllite N₂ without powder. Experimental data in black and numerical simulation in red with real porosity of the sample (0.045) and Kg = 100 nD.

With diatom powder (Figure 17), the signal seems noisier, but it is due to the scale of the axis. The numerical simulation can fit the experiment over the entire range of the relaxation using the real porosity.

This point is very important and can be considered as the main criterion for quality control of the experiment. With this criterion, the experiment without powder cannot be qualified.

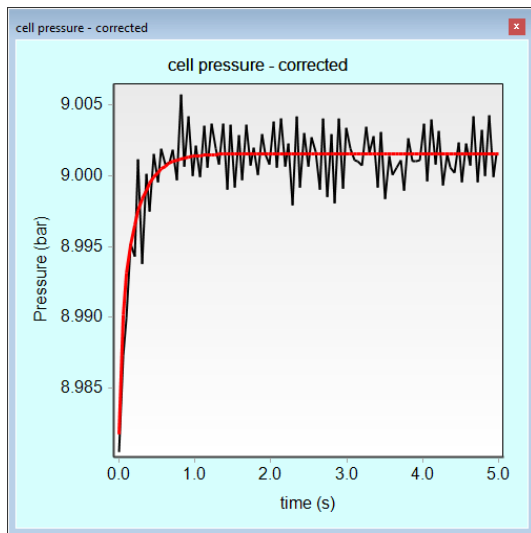


Figure 17 - Sample Pyrophyllite N2 with diatom powder. Experimental data in black and numerical simulation in red with real porosity of the sample (0.045) and $K_g = 250$ nD.

4.2 Results with the shale sample L (with krypton)

The signal is better for shale L since its permeability is lower (longer relaxation time) and porosity higher (higher amplitude of the signal). However, the comparison with and without powder is similar to the pyrophyllite.

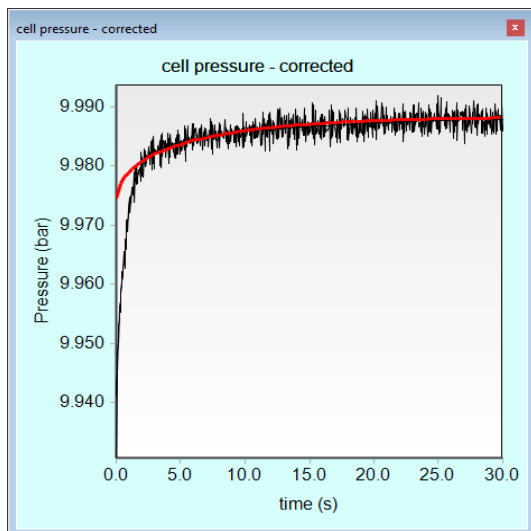


Figure 18 – Sample L4 without powder. Experimental data in black and numerical simulation in red with real porosity of the sample (0.13) and $K_g = 25$ nD.

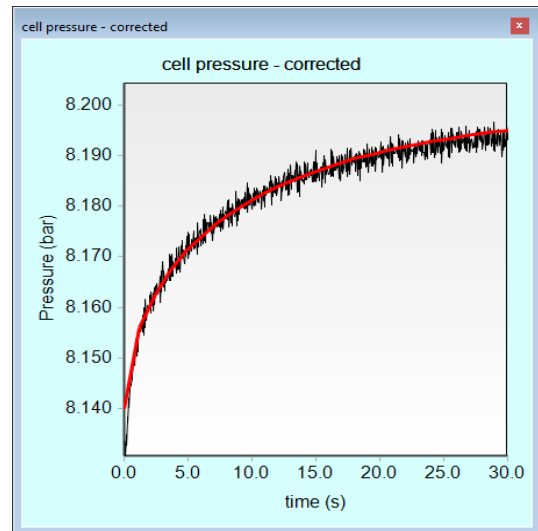


Figure 19 - Sample L4 with diatom powder. Experimental data in black and numerical simulation in red with real porosity of the sample (0.13) and $K_g = 17$ nD.

Without powder (Figure 18), the simulation cannot represent the experiment: the amplitude is too small when using the real porosity of the sample and the result is not acceptable for quality control.

With powder (Figure 19), the agreement is very good between the experiment and the simulation over the entire range of the relaxation using the real porosity of the sample.

Klinkenberg plot for shale sample

Figure 20 shows the results for the shale sample with diatom earth at different pressures to derive the Klinkenberg correction. The results with the three gases used in the study are plotted. The measurements have been checked for quality control as described previously. The pressure P is the average between initial and final pressures in the sample. The lower values in $1/P$ correspond to initial pressure around 10 barg and the highest value to initial pressure around 1.3 barg. Below this pressure, the signal is too noisy to be interpreted.

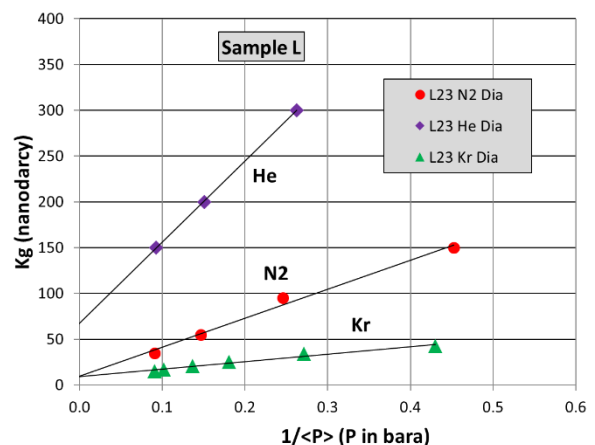


Figure 20 - Klinkenberg plot for L crushed samples with different gases.

For all the gases, the gas permeabilities follow a linear law as function of $1/Pm$ as expected from Klinkenberg theory. For this L sample, with low permeability and high porosity, the results with helium are acceptable. Extrapolated values for $1/Pm=0$ agree for nitrogen and krypton but differ for helium. As already discussed, helium leads to very short relaxation times and is not recommended.

For N_2 and Kr, the extrapolated absolute permeabilities are respectively 9.6 and 9.4 nD and the b coefficients 33 and 8.6 bar. If we take as reference the b value for nitrogen, the theory predicts $b=25$ bar for krypton, higher than the experimental value. We have no explanation for this difference. It cannot be related to a bad flushing of the sample after nitrogen or helium experiment since the b would have been higher. It has been reported that the Klinkenberg correction formulated at the scale of the sample was not valid for transient flow [8]. Further study would need to re-interpret all the experiments with Klinkenberg effects calculated at the grid scale in the numerical simulations. So far, we consider that this difference is within the range of the accuracy of the method.

5 Discussion

We will present a tentative explanation of the role of the powder to reduce the "blank" relaxation at the beginning of the experiment. A proven theory would need additional measurements, high speed record of temperature in the vessels, measurement of powder packing permeability and modelling using non-isothermal flow with thermodynamics effects. This is not in our capacities and not the purpose of this study.

Let us consider Figure 1 with the crushed sample at pressure $P_2=10$ barg in volume V2 and the volume V1 at atmospheric pressure. Gas is nitrogen. After opening the valve, we assume that the volumes are such that the pressures equilibrate at 9 barg.

Now, we must consider the thermal effects. We can consider two extreme cases:

- 1) **Pressure equilibrium:** A very fast change of pressure when opening the valve; no pressure drop in the valve and in the space between the grains of crushed sample (no powder). We assume that there is no thermal exchange between the gas and the container at the opening of the valve. Therefore, the experiment is an adiabatic expansion in V2 (10 to 9 barg) and compression in V1 (0 to 9 barg). The actual physics is more complicated since there is a transfer of gas between the two vessels. Neglecting the transfer of gas, the theoretical calculation leads to a decrease of temperature of 8°C in V2 corresponding to a decrease of pressure of 270 mbar, and an increase of temperature of 280°C in V1. The corresponding increase of pressure for V1 is 9.3 bar. In this process, the equilibrium of pressure is much

faster than the temperature equilibrium. The pressure quickly equilibrates but the temperature needs more time and is function of the heat

- 2) accumulated (mass of gas and heat capacity) and the rate of heat transfer (heat conductivity).

2) **Thermal equilibrium:** if we consider now a very slow process, for instance by connecting the two vessels through a needle valve, the pressures will not be in equilibrium between the two vessels, but the temperatures will equilibrate by thermal conductivity in the gas. However, with such a slow process, it would be impossible to study the transient inside the rock.

Without powder, the process corresponds to the first case of fast pressure equilibrium in the two volumes. During an experiment, we record the pressure in V2, and we observe the decrease of pressure reaching 100 mbar after around 0.1 second., in agreement with the theoretical calculation of 270 mbar at time $t=0$.

Adding powder involves the second case of thermal equilibrium. The powder slows down the pressure exchange and allows the temperature to equilibrate over a few tens of second, fast enough to allow the observation of the transient of pressure by viscous flow in the sample.

The thermal equilibrium is much faster with helium, which presents a low thermal capacity (due to its low mass, even if its thermal capacity is high) and a high thermal conductivity. However, helium has the drawback to decrease the apparent permeability, and therefore reduces the relaxation of the sample due to the Klinkenberg effect. On the other hand, krypton has a much higher thermal capacity and lower thermal conductivity than helium. Thermal equilibrium is much slower. Even if the apparent permeability is lower with krypton, the thermal effect impacts the quality of the measurement.

As already shown, nitrogen, with properties between helium and krypton, gives the best results.

6 Conclusions

We first discussed the limitations of the standard GRI method using an apparatus that we have built:

- Large difference between initial and final pressures in the sample not allowing the Klinkenberg correction.
- Thermal effects at the beginning of experiments that hides the short transient effects due to the viscous flow in the sample.

This paper presents an improved GRI method, named DarcyShale:

- We minimized the experimental artifacts at short times by optimizing the device design, minimizing the dead volumes and the procedure for realizing the pulse decay.

- We studied the impact of the gas nature and highlighted that nitrogen is preferred to helium or krypton.
- We have also shown that mixing a fine powder with the crushed sample improves the quality of the measurement. A tentative explanation was given.
- We quantified the pressure variations due to the residual artifacts with a highly permeable rock whose response should be instantaneous.
- As a quality control, we systematically checked that the signal amplitude agreed with the theoretical value computed from a porosity value obtained separately.

7 Nomenclature

b	bar	Klinkenberg coefficient
c	-	Coefficient close to 1 in b Klinkenberg coefficient
K _G	mD	Gas Permeability
K _L	mD	Klinkenberg corrected permeability
M	g.mol ⁻¹	Molecular weight
P	bar	Pressure
r	m	Radius in the b formula
R	J.mol ⁻¹ .K ⁻¹	Universal gas law constant
t	s	Time
V	cm ³	Volume
μ	cP	Viscosity

8 References

1. D. L. Luffel, C. W. Hopkins and P. D. Shettler, "Matrix permeability measurement of gas productive shales", presented at the SPE Annu. Tech. Conf. and Exhib., Houston, TX, USA, Oct. 3 - 6, 1993, Paper SPE 26633.
2. S. Profice, D. Lasseux, Y. Jannot, N. Jebara and G. Hamon, "Permeability, porosity and Klinkenberg coefficient determination on crushed porous media", presented at the SCA Int. Symp., Austin, TX, USA, Sep. 18 - 21, 2011, Paper SCA2011-32.
3. O. Kwon, A. K. Kronenberg, A. F. Gangi and B. Johnson, "Permeability of Wilcox shale and its effective pressure law", *J. Geophys. Res.-Atmos.*, vol. 106, n° B9, pp. 19,339 - 19,353, Sep. 10, 2001, doi: 10.1029/2001JB000273.
4. A. Tinni, E. Fathi, R. Agarwal, C. Sondergeld, Y. Akkutlu and C. Rai, "Shale permeability measurements on plugs and crushed samples", presented at the SPE Can. Unconventional Resources Conf., Calgary, AB, Canada, Oct. 30 - Nov. 1, 2012, Paper SPE 162235.
5. S. Profice and R. Lenormand, "Low permeability measurement on crushed rock: insights", presented at the SCA Int. Symp., Pau, France, Sep. 26 - 30, 2019, Paper SCA2019-016.
6. F. Civan, "Can gas permeability of fractured shale be determined accurately by testing core plugs, drill cuttings and crushed samples?", presented at the SPE/AAPG/SEG Unconventional Resources Technol. Conf., Austin, TX, USA, Jul. 24 - 26, 2017, Paper URTEC: 2666389.
7. Q. R. Passey, K. M. Bohacs, W. L. Esch, R. Klimentidis and S. Sinah, "From oil-prone source rock to gas-producing shale reservoir - Geologic and petrophysical characterization of unconventional shale-gas reservoirs", presented at the CPS/SPE Int. Oil & Gas Conf. and Exhib., Beijing, China, Jun. 8 - 10, 2010, Paper SPE 131350.
8. R. Lenormand, F. Bauget and G. Ringot, "Permeability measurement on small rock samples", presented at the SCA Int. Symp., Halifax, NS, Canada, Oct. 4 - 7, 2010, Paper SCA2010-A073.
9. J.-P. Qadri. (2008-2009). T4 - Appendice 1 - Détentes de Joule - Bilans énergétique et entropique [Online]. Available : <http://pcsi-unautreregard.over-blog.com/>
10. D. R. Maloney and M. Briceno, "Experimental investigation of cooling effects resulting from injecting high pressure liquid or supercritical CO₂ into a low pressure gas reservoir", presented at the SCA Int. Symp., Abu Dhabi, UAE, Oct. 29 - Nov. 2, 2008, Paper SCA2008-40.
11. J. F. App, "Field cases: nonisothermal behavior due to Joule-Thomson and transient fluid expansion/compression effects", presented at the SPE Annu. Tech. Conf. and Exhib., New Orleans, LA, USA, Oct. 4 - 7, 2009, Paper SPE 124338.
12. R. Suarez-Rivera, M. Chertov, D. Willberg, S. Green and J. Keller, "Understanding permeability measurements in tight shales promotes enhanced determination of reservoir quality", presented at the SPE Can. Unconventional Resources Conf., Calgary, AB, Canada, Oct. 30 - Nov. 1, 2012, Paper SPE 162816.

The KPC-Log: A new method for measuring the permeability of a non-cylindrical tight sample

Sandra Profice^{1,*}, Romain De Loubens¹, Diego Potenzoni², Philippe Chehade³, Benjamin Nicot¹, and Roland Lenormand⁴

¹TOTAL CSTJF, Avenue Larribau, 64018 Pau Cedex, France

²PAN AMERICAN ENERGY, Avenida Leandro Nicéforo Alem 1180 (1001), Argentina Buenos Aires, Argentina

³ENSG, 2 rue du Doyen Marcel Roubault, 54518 Vandœuvre-lès-Nancy, France

⁴CYDAREX, 31 avenue Gabriel Péri, 92500 Rueil-Malmaison, France

Abstract. When shale cores or core plugs are fractured, the most direct solution to characterize permeability consists in crushing the rock and performing a Gas Research Institute (GRI) test. Yet, crushing efficiency is questionable when observing microfractures in some particles. Moreover, the recorded pressure response is short, the particles being small. If the experimental artefacts at early times are substantial, the interpretation provides erroneous results. Lastly, the sample geometry is systematically simplified but the effect generated on the estimated permeability has never been addressed rigorously. This paper focuses on the KPC-Log, an innovative method for measuring permeability (K) on centimetric pieces (P) of core (C). Reliable values of absolute permeability (k_{abs}) and Klinkenberg coefficient (b) are obtained by interpreting improved GRI tests with a numerical model using as input a 3D image of the sample surface. By studying pieces of rock having variable shapes, we highlighted that simplifying the geometry impacts more b than k_{abs} . This means that the error on the apparent permeability (k_{app}) increases when the mean pore pressure decreases. Furthermore, we confirmed that not elongated cuttings or crushed rock particles can be assimilated to uniform spheres. With the emergence of micro-coring bits, the KPC-Log offers a new way to build a log of permeability.

1. Introduction

Characterizing shales can be a real challenge since these rocks are often laminated and hence brittle [1]. They tend to break easily at the interface between two layers. Cores fracture during tripping from the reservoir to the surface and core plugs, during sampling, cleaning or drying. The CT-scans of Figure 1 were acquired on heavily fractured cores from Vaca Muerta shale formation in Argentina.

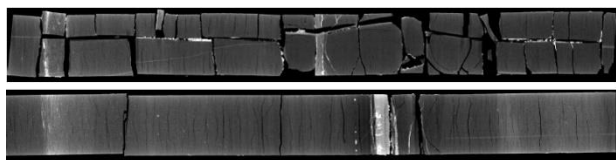


Fig. 1. CT-scans of highly fractured cores from the Argentinian Vaca Muerta shale formation

When dealing with samples having unusual shapes or sizes, the number of methods available in the industry for determining permeability is limited. The most immediate solution would be to crush the sample and perform a Gas Research Institute (GRI) test. Developed in the early 90s by Luffel *et al.* [2] for crushed rocks or drill cuttings, the GRI method consists in exciting the particles with a gas pressure pulse and interpreting the response related to the

gas flow in the pore network to derive the permeability. The test is nothing more than a pycnometry test. Most of the commercial laboratories are currently equipped with the original GRI device, sketched in Figure 2. They tend to prefer particles of a few millimetres while Luffel *et al.* opted for submillimetric particles (0.50 to 0.84 mm).

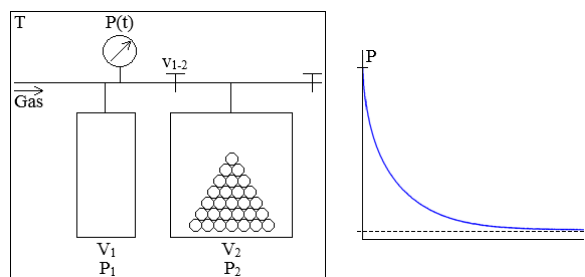


Fig. 2. GRI or pycnometry device and recorded pressure signal

The sample is introduced in a chamber of volume V_2 which is connected to a chamber of volume V_1 by means of a valve v_{1-2} . Initially, the valve v_{1-2} is closed and both the sample pore volume and the dead (or empty) volume in the chamber V_2 are at the pressure P_2 (generally equal to the atmospheric pressure). To start with, the chamber V_1 is pressurized at a pressure P_1 higher than the pressure P_2 . At time $t=0$, the valve v_{1-2} is opened and the recording

* Corresponding author: sandra.profice@total.com

of the pressure transient $P(t)$ is triggered simultaneously. The system is kept at a constant temperature T either by regulating the laboratory temperature or by placing it in a temperature-controlled oven.

Egermann *et al.* [3] proposed in 2003 a variant of the GRI technique, called Darcylog. At the beginning of the test, the chamber containing the rock particles is flushed with helium and filled afterwards with a viscous oil. The oil spontaneously imbibes in the particles, expelling the helium. At residual helium saturation, the oil pressure is gradually increased from atmospheric pressure to 10 bar so that the oil penetrates in the particles by compressing the trapped gas ganglia. The permeability is obtained by interpreting the oil pressure and injected oil volume data recorded over time with a numerical model. Egermann *et al.*'s Darcylog paved the way for two new variants of the GRI method: Carles *et al.*'s Darcygas [4] and Lenormand *et al.*'s Pulse Decay Open Surface (PDOS) [5], invented in 2007 and 2010 respectively. Both techniques rely on a device with only one chamber whose initial volume can be modified in a very short time by moving a piston. The air filling the dead volume surrounding the sample in the chamber is compressed in a Darcygas test to engender a pressure decay and expanded in a PDOS test to produce a pressure build-up. Interpretation is based on a numerical model for both types of test. The Darcylog, Darcygas and PDOS methods were designed to be applicable on either millimetric particles (1 to 5 mm) or a small cylinder with a diameter of 1 cm and a length of 1.5 cm. The Darcygas and the PDOS are dedicated to tight and unconventional rocks. These two methods and the Darcylog, appropriate for tight and conventional rocks, are complementary.

In addition to the PDOS, Lenormand *et al.* presented in 2010 several methods specific to small cylinders only. The authors undertook steady-state and Pulse Decay tests with gas on plugs whose diameters were close to 0.5 cm and lengths close to 1 cm. Each plug was either inserted in a silicone tube or confined in a Hassler microcell. The inlet pressure did not exceed 100 mbar with the silicone tube, to prevent any gas leak between the sample and the tube. Besides, they took a method introduced for cuttings in the late 90s and they adapted it to plugs with diameters of about 1 cm and lengths varying from 0.2 to 0.5 cm. In their method, called Darcypress, the sample is embedded in a resin disc whose faces are polished until the material shows on the surface, so that the gas can flow through it. After preparation, the disc is placed between the plates of a press to be subjected to a vertical stress. Steady-state or Pulse Decay tests can be conducted and interpreted with the standard analytical or numerical models existing for cylinders. The permeabilities measurable by Darcypress vary in a large range, going from 0.1 nD to a few darcies.

Lastly, the literature provides examples of techniques in which a rather big cylinder undergoes a test similar to a GRI test. Plug diameters and lengths range from 2.5 to 5 cm. In canister degassing tests, studied by Cui *et al.* [6] in 2009 and Zhao *et al.* [7] in 2019, the plug degasses at constant temperature, in a canister at lower and constant pressure. Cui *et al.* derived two analytical expressions for

permeability, a first one true at early times and a second one true at late times. The authors used them to interpret the desorbed gas cumulative volume data recorded over time. Zhao *et al.* went further in the modeling process by including anisotropy. The analytical solution, true at any time, enables the computation of horizontal and vertical permeabilities from the gas flow rate data recorded over time. In a paper published 2 years before, Hannon Jr. [8] dealt with anisotropy quantification too by interpretation of data collected during a GRI-type test. His method, the Full-Immersion Pressure-Pulse Decay (FIPPD), relies on the generation of a pressure pulse on the plug surface, by depressurizing a first chamber in the second one holding the sample. The horizontal and vertical permeabilities are obtained by matching the pressure decay simulated from a numerical model with the experimental one. In another version of the FIPPD test, the plug is wrapped in a mesh sleeve before being confined in a core holder. The pulse is emitted at one sample end but the gas flows through its whole surface because of the permeable membrane. The test at the center of the Modified Gas Expansion (MGE) technique, imagined by Peng and Loucks [9] in 2016, is similar, except that the gas invades the medium through its top end only since no mesh sleeve is used. An average permeability is estimated by interpreting the late times of the recorded pressure decay with an analytical solution.

In the majority of the methods previously described, the sample is unconfined [2 -7]. Confining small samples at realistic overburden pressures is not an easy task. This is problematic as low-permeability media are particularly sensitive to stress [10]. Small sample representativity is another important problem. For heterogeneous rocks, the sample size significantly impacts the permeability. When comparing the permeabilities found for a granodiorite by 24 laboratories, David *et al.* [11] noticed that dispersion in the results increased for decreasing plug lengths. Their explanation was that the volumes of the short plugs were potentially below the Elementary Representative Volume (REV), the selected granodiorite having centimetre-sized mineralogical heterogeneities. Permeability variation in Peng and Loucks' work was more related to plug radius variation. The studied rocks were laminated shales. The heterogeneities encompassed in the plugs changed when increasing the radius since sampling was done parallel to bedding. The debate about the place of microfractures in sample representativity and the best manner to deal with a fractured sample is still open in the literature. Luffel *et al.*'s principal argument to defend the GRI method is that microfractures result from coring and thus, must be fully eliminated by rock crushing. Sinha *et al.* [12] were more inclined to keep the plug intact and confine it, given that determining undoubtedly if microfractures are natural or artificial is complicated. Natural microfractures acting as preferential pathways for the gas in the reservoir must be preserved when measuring the permeability. In the case where microfractures are deemed to be artificial, opting for plug confinement is an insufficient solution for Peng and Loucks, these microfractures remaining open even at high confining pressures. Plug crushing is inadequate too for Tinni *et al.* [13] who spotted microfractures in micro-computed tomography images of crushed shale particles

having sizes of 3.5 mm and 0.7 mm. Comisky *et al.* [14] evidenced from mercury injection capillary pressure tests that such microfractures can be crushing-induced and not coring-induced. Profice and Lenormand [15] highlighted it too by analyzing scanning electron microscopy images taken before and after crushing. Several authors attribute another negative effect to rock crushing. Cui *et al.*, Tinni *et al.* and Peng and Loucks proved that the mean particle size decrease leads to a permeability decrease. They did not explain this behavior by a continuous elimination of microfractures. They related it to a gradual damaging of the material pore structure when crushing finer and finer. Cui *et al.* and Peng and Loucks based their reflection on models correlating permeability and pore radius. Tinni *et al.* compared the pore throat size distributions of several samples composed of smaller and smaller particles. Last but not least, crushing makes difficult sample modeling, the particles having variable shapes and sizes distributed in a range depending on the preparation procedure [15]. Though Luffel *et al.* represented the sample as a pack of identical cylinders, most of the authors who focused later on the GRI technique and its derivatives assimilated it to a pack of identical spheres [3 - 6, 9, 13, 15]. The fact that such assumptions can impact the permeability if the true geometry substantially deviates from the simplified one was evoked by Civan [16] but not demonstrated. Suarez-Rivera *et al.* [17] simulated the pressure signal expected from a GRI test for multiple packs of identical particles, the aspect ratio changing from one pack to the other. The simulations revealed that the signal remains close to that corresponding to a pack of spheres while the aspect ratio is low, *i.e.* while the particles are not excessively oblate. To the best of our knowledge, no author has ever deeply examined the errors induced on the estimated properties by the sample geometry simplification.

2. KPC-Log method

TOTAL purchased in 2014 a robot equipped with a laser, which enables the sample surface mapping in 3D and the sample bulk volume computation from the reconstructed surface. The goal was to abandon mercury immersion for bulk volume measurement owing to all problems caused by mercury to health and environment. Very few papers of the petroleum literature refer to this type of device [9], which remains infrequent for bulk volume estimation.



Fig. 3. Laser robot

The sample shape and dimensions must be such that the whole surface can be correctly scanned by the laser. The tiniest samples on which we successfully tested our robot had dimensions hardly reaching a few millimetres. The 3D map of the sample surface is a point cloud image in which any point is located by spatial coordinates. The point cloud is closed by executing a numerical algorithm and the bulk volume is deduced from the 3D envelope.

When facing massive plug breaking during our many studies of cores from Vaca Muerta formation, we had the idea to generate a 3D mesh from the point cloud to make the interpretation of a GRI-type test possible for a piece of rock with a non-geometrical form. Our new technique for determining the permeability of a sample having any shape is named KPC-Log, K referring to “permeability” and PC to “Piece of Core”. It offers an innovative way to build a log of permeability, considering the existence of the Micro-Coring Bit (MCB) which provides centimetric micro-cores while drilling [18]. The MCB was proposed by TOTAL and Diamant Drilling Services in 2008. The photos of Figure 4 show the MCB and one of the micro-cores obtained during the first test done with the MCB in an interbedded shale and sandstone formation.



Fig. 4. MCB and one of the micro-cores collected while drilling an interbedded shale and sandstone formation [18]

Cutting the sample of Figure 4 to give it a cylindrical shape would be perhaps possible but likely tricky. In the photo of Figure 5 can be observed pieces of broken core whose forms depart much from the common geometrical ones: sphere, cylinder and disc. Taking plugs from such irregularly shaped fragments of a few centimetres would be too difficult.



Fig. 5. Pieces from a broken shale core having irregular forms and too small sizes to be plugged

With the KPC-Log method, there is no need to crush the sample anymore when its geometry cannot be easily defined or modified. The potential problem of bias in the permeability related to sample modelling disappears, the sample shape being accurately captured. Coring-induced

microfractures are not eliminated but crushing the piece of rock to destroy them seems to be even less satisfactory than keeping it intact. As mentioned before in Section 1, crushing could produce new microfractures and alter the sample representativity by harming its pore structure. In addition, crushing reduces the interval of permeabilities measurable with a GRI-type test. The pressure response duration decreases when the sample exchange area with the gas around increases and its characteristic penetration depth decreases [15]. Therefore, crushing is particularly detrimental for relatively high-permeability media whose responses are already short without crushing, as the even shorter responses after crushing can be inappropriate for interpretation. Instantaneous responses are obviously not reliable. This is also the case for responses hidden by the pressure relaxation caused by the thermal effects created when opening the valve between the two chambers [15]. In the reference [19], Lenormand and Profice describe an innovative solution to reduce these effects. Furthermore, they formulate recommendations about the device design and the experimental procedure. All these improvements brought to the GRI method optimize the estimation of the absolute (or intrinsic) permeability and the Klinkenberg coefficient from several tests on the crushed sample. The authors called Darcyshale their new GRI-type technique. The KPC-Log encompasses the innovations at the origin of the Darcyshale, in addition to the sample form capture innovation. The impacts on the estimated properties that are still uncontrolled with the KPC-Log are those due to the absence of confining stress, rock anisotropy and rock fracturing.

3. Experimental device

The KPC-Log device, schematically drawn in Figure 6, is a bigger version of the device presented in the reference [19] for the analysis of crushed samples or drill cuttings. These devices are comparable to the pycnometry or GRI device of Figure 1 but the operating procedure followed to use them is different from the standard GRI procedure. The sample, piece of rock or rock particles, is introduced in the chamber V_1 , chamber pressurized at the beginning of the test. This means that both the sample pore volume V_p and the dead volume in the chamber V_1 are initially at an identical pressure P_1 higher than the pressure P_2 in the chamber V_2 , P_2 being equal to the atmospheric pressure. Pressure recording is triggered a few seconds before the time $t=0$ at which the valve $v_{1,2}$ is opened, to capture the pressure P_1 . The system temperature is stabilized at T by regulating the laboratory temperature.

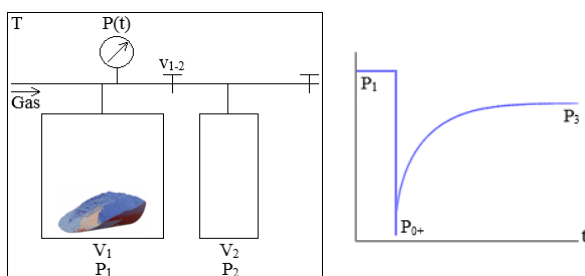


Fig. 6. KPC-Log device and recorded pressure signal

As illustrated through the pressure signal $P(t)$ plotted in Figure 6, the test comprises three successive phases. In the first phase, the chamber V_1 is at pressure balance and the recorded pressure is equal to P_1 . In the second phase starting at $t=0+$ (just after opening the valve $v_{1,2}$), the gas in the dead volume surrounding the sample expands from the chamber V_1 to the chamber V_2 . The pressure decline from P_1 to P_{0+} is assumed to be instantaneous. Moreover, the pressure in the porous medium is supposed to be still equal to P_1 at $t=0+$. In the third phase, the rock expels its gas until the whole system equilibrates at the pressure P_3 . Consequently, the pressure transient interpreted to derive the permeability is a pressure build-up and not a pressure decay as in the majority of the GRI-type methods.

The porosity ϕ can be computed from two equations. Each of them arises from a material balance between two states: initial and final states for Equation (1), initial and transitional states for Equation (2). While initial state and first phase coincide, the transitional state is reached at the end of the second phase and the final state, at the end of the third phase. In the equations below, V_t is the sample bulk volume given by the laser robot.

$$\phi_1 = 1 - \frac{V_1}{V_t} - \frac{(P_2 - P_3)V_2}{(P_1 - P_3)V_t} \quad (1)$$

$$\phi_2 = \frac{(P_{0+} - P_3)(V_t - V_1 - V_2)}{(P_1 - P_3)V_t} \quad (2)$$

The uncertainty on the pressure P_{0+} is high because of the thermal effects altering the pressure build-up at early times. Hence, ϕ is deduced from Equation (1) and P_{0+} is corrected using Equation (2) if required. In the KPC-Log technique, these effects are almost completely eliminated by filling the dead volume of the chamber V_1 as much as possible with calibrated billets and a powder. Among the various powders tested in the reference [19], we selected here talc. The intensity of the residual thermal effects can be assessed by comparing ϕ from Equation (2) to ϕ from Equation (1), *i.e.* ϕ_2 to ϕ_1 . They are negligible when ϕ_2 is consistent with ϕ_1 .

We chose a very small chamber V_2 for our KPC-Log device, to be in line with the device design advised in the reference [19]. When decreasing the expansion chamber capacity, the amplitude of the pressure build-up recorded outside the sample decreases, which can be prejudicial to the signal quality. At the same time, the amplitude of the pressure decay occurring inside the rock decreases. This is beneficial especially when Klinkenberg's method [20] is implemented to characterize the intrinsic permeability and the Klinkenberg coefficient. The need to work with a pressure variation in the porous medium remaining small compared to the mean pressure level is further discussed in Section 4.2. In conclusion, the volume of the chamber V_2 must be fixed by seeking a good compromise between the limitation of the pressure decay inside the sample and the quality of the pressure build-up outside the sample.

4. Interpretation

4.1. Numerical method for k_{app} estimation

4.1.1. 3D mesh

The numerical interpretation of a given KPC-Log test is divided into two phases. In the first phase, a 3D mesh of the whole system is constructed to enable the simulation of the gas flow from inside to outside the rock. The total volume around the sample, dead volume in the chamber V_1 added to the volume of the chamber V_2 , is noted V_{1+2} . In the second phase, the apparent permeability k_{app} in our numerical model is adjusted by means of an optimization process, until matching the experimental pressure signal $P_{exp}(t)$ with the numerical one $P_{num}(t)$.

The whole system is meshed in several steps. To start with, a surface reconstruction algorithm is applied to the point cloud from the laser robot. Several algorithms exist and specific libraries allow easy access to some of them, as Computational Geometry Algorithms Library (CGAL) for example. The algorithm we drew from CGAL relies on Delaunay's 3D triangulation. It creates the point cloud convex envelope via a triangulation based on tetrahedra and eliminates the tetrahedra considered to be out of the porous medium. For information, we do not know if the laser robot uses the same algorithm, as its data processing program was totally developed by the manufacturer. The volume delimited by the envelope is meshed afterwards with regular hexahedra forming a cartesian grid. A mesh involving tetrahedra would be more relevant to faithfully reproduce the surface reconstructed earlier. However, an unstructured mesh is complex to handle for a simulator. Flux computation is seldom robust and accurate with an unstructured mesh and, when it is satisfactory, it is much more time-consuming than with a structured mesh. As a consequence, the structured mesh we build with regular hexahedra makes numerical calculations easier and faster but mars surface reproduction. The discrepancy between the bulk volume V_t' obtained from the cartesian grid and the reference V_t coming from the robot is sometimes not negligible. It can reach a few percents for the coarse grid used in the optimization process. This is the reason why the numerical porosity ϕ' assigned to the grid cells is not the experimental porosity ϕ computed from Equation (1) or Equation (2). Its value, determined from Equation (3), ensures the preservation of the true pore volume. Even if the type of mesh we chose is not ideal for an accurate 3D reconstruction, the results of Section 5 confirm that it is adequate for our application.

$$\phi' = \frac{\phi V_t}{V_t'} \quad (3)$$

The mesh generated for the sample is finally extended to the volume where the pressure build-up occurs. Its value V_{1+2} must be perfectly respected but its geometry has no impact on the simulation, the pressure outside the sample being supposed to be homogeneous. Hexahedra are piled all around the sample to define a parallelepipedic domain of volume V_{1+2}' close to V_{1+2} . The cell size is uniform in the whole grid and the domain edges do not cross or even touch the sample. Besides, the volume V_{1+2}' is corrected

by associating a porosity $\phi_{1+2}' \neq 1$ to the domain. Its value is deduced from Equation (4).

$$\phi_{1+2}' = \frac{V_{1+2}}{V_{1+2}'} \quad (4)$$

The algorithm we wrote for constructing the 3D mesh works for multiple pieces of rock as well. It meshes each piece from the related point cloud and then concatenates the grids by creating around them the grid corresponding to the volume V_{1+2} . Contact between either two pieces or one piece and the domain edges is avoided. The cell size is identical for all pieces and the volume V_{1+2} .

4.1.2. Numerical model

Our model describing the gas flow in the porous medium is based on the mass conservation equation and Darcy's law, given by Equation (5) and Equation (6) respectively.

$$\phi \frac{\partial \rho}{\partial t} + \nabla \cdot (\rho \mathbf{v}) = 0 \quad (5)$$

$$\mathbf{v} = - \frac{k_{app}}{\mu} \nabla P \quad (6)$$

Concerning the notations, \mathbf{v} is the gas velocity, ρ the gas density and μ the gas viscosity. The gas flow is supposed to be isothermal. As a result, ρ depends on P only and μ can be assimilated to a constant, the variation of μ with P being small in our tests. Moreover, the gas we opted for, nitrogen, authorizes the assumption of a perfect gas. We have implicitly made this assumption yet when deriving Equation (1) and Equation (2) from Boyle and Mariotte's law.

The gas flow outside the sample is also governed by Equation (5) and Equation (6) since the volume V_{1+2} acts as a porous medium in the simulation. The permeability in the grid cells of the domain surrounding the sample is very high, in order that the pressure equilibrates instantly in V_{1+2}' at any time. Notably, the permeability in V_{1+2}' is about 10^6 times higher than the rock permeability, in our simulations.

The gas velocity in the grid cells forming the domain edges is equal to 0, the walls of the chambers V_1 and V_2 being impermeable to gas. The simulation is initiated by fixing P to P_1 in the grid cells of the sample and P to P_0 in the grid cells around it.

4.1.3. Optimization process

The optimum k_{app} value is the solution of a minimization problem.

$$k_{app} = \underset{k_L < k_{app}^* < k_U}{\operatorname{argmin}} \left(F(k_{app}^*) \right) \quad (7)$$

The function to be minimized is the objective function F , whose argument k_{app}^* varies in the interval $[k_L - k_U]$.

$$F(k_{app}^*) = \int_0^{t_f} |P_{exp}(t) - P_{num}(t, k_{app}^*)| dt \quad (8)$$

In Equation (8) defining F , t_f is the final time of the test. The integral is estimated numerically for each new k_{app}^* value, *i.e.* at the end of each iteration of the optimization process. Any grid cell around the sample can be selected to obtain the P_{num} values at the end of the simulation time steps. Both P_{exp} and P_{num} are considered to be piecewise linear functions. This means that the computation of any missing pressure value, at an experimental time for P_{num} or at the end of a simulation time step for P_{exp} , is done by linear interpolation. The minimization problem is solved thanks to a classic gradient descent algorithm.

In order to speed up the convergence towards the best k_{app} value, our optimization process works in two times. A first little time-consuming run with a coarse grid gives a rough k_{app} value, noted $k_{app,c}$, acting as initial guess in a second run with a fine grid. In most cases, the number of simulations needed during the second run to find a more accurate k_{app} value, noted $k_{app,f}$, is small owing to the fact that $k_{app,c}$ is close to $k_{app,f}$. Time saving can be substantial since decreasing cell size makes simulation time increase quickly. The coarse grid involves a cell size higher than that of the fine grid by a factor of 2 to 4. In other words, the coarse grid includes 8 to 64 times fewer cells than the fine grid.

4.2. Klinkenberg's method for k_{abs} and b estimation

When gas is injected, the measured permeability is not a property intrinsic to the rock. It depends not only on the material but also on the gas nature and the gas pressure. The frequency at which fluid molecules collide with pore walls is higher for a gas than for a liquid. Consequently, the gas velocity at the pore walls is not equal to 0, which enhances the gas flow in the medium. This phenomenon, known as gas slippage effect, was first described in 1941 by Klinkenberg [20]. The author introduced Equation (9) correlating permeability to gas and permeability to liquid, k_{app} and k_{abs} respectively.

$$k_{app} = k_{abs} \left(1 + \frac{b}{p} \right) \quad (9)$$

The permeability to liquid is considered to be absolute or intrinsic to the rock as it is exclusively controlled by the pore network structure. The permeability to gas is said to be apparent as it does not depend on the material only. It is also influenced by the gas pressure and the gas nature. The gas nature effect is hidden in the corrective factor b , named Klinkenberg coefficient.

Equation (9) is a local equation verified at any point of the sample. For an isothermal, 1D and steady-state gas flow, Equation (9) can be replaced by Equation (10) after integration along the sample [5].

$$\langle k_{app} \rangle = k_{abs} \left(1 + \frac{b}{\langle P \rangle} \right) \quad (10)$$

At the macroscopic scale, the gas flow at the mean pore pressure $\langle P \rangle$ is driven by a mean apparent permeability

$\langle k_{app} \rangle$. Equation (10) is behind the method proposed by Klinkenberg to determine k_{abs} and b from several steady-state tests executed at increasing $\langle P \rangle$. The $\langle k_{app} \rangle$ values resulting from the interpretation of the different tests are plotted against $1/\langle P \rangle$. The properties k_{abs} and b are then deduced from the coefficients of the regression line over the data points. For more simplicity in the notations, the brackets $\langle \rangle$ added around k_{app} to designate the property at macroscopic scale will be subsequently omitted (as in Section 4.1.3).

Inversing numerically the pressure response recorded during a GRI-type test is not appropriate to characterize k_{abs} and b simultaneously. Profice *et al.* [21] proved that these properties are correlated, which means that a good match between the experimental signal and the numerical one is achieved for several pairs (k_{abs} , b). Klinkenberg's method provides reliable k_{abs} and b estimations if $\langle P \rangle$ is properly defined or controlled, as explained below. In the opposite case, it leads to erroneous estimations. All these elements likely justify why k_{app} values are preferentially delivered by commercial laboratories [15].

For a core plug subjected to a steady-state test, $\langle P \rangle$ is the average of the pressures at the inlet and outlet faces. A GRI-type test occurs at unsteady-state from beginning to end. In such a purely transient test, what is $\langle P \rangle$? Total and I2M-TREFLE laboratory focused on this question in a study jointly conducted on the GRI technique [21, 22]. For a monodisperse pack of homogeneous and isotropic spheres undergoing a GRI test at a regulated temperature (refer to Figure 2), Equation (11) predicts the pressure at the surface of the particles over time. In this equation, R is the mean particle radius, C the gas compressibility and γ_i the i^{th} root of Equation (14). The initial-boundary value problem was linearized by supposing that C is constant, to enable the computation of an analytical solution.

$$P(R, t) = \left[\alpha + \sum_{i=1}^{\infty} \beta_i e^{-\frac{\gamma_i^2 k_{app} t}{\phi \mu R^2 C}} \right]^{1/2} \quad (11)$$

$$\alpha = P_2^2 + \frac{P_{0+}^2 - P_2^2}{1 + \frac{3V_p}{V_{1+2}}} \quad (12)$$

$$\beta_i = \frac{(P_{0+}^2 - P_2^2) \sin \gamma_i}{\frac{\gamma_i \cos \gamma_i}{2} + \left(1 + \frac{3V_p}{2V_{1+2}} \right) \sin \gamma_i} \quad (13)$$

$$\tan \gamma_i = \frac{\gamma_i}{1 + \frac{\gamma_i^2 V_{1+2}}{3V_p}} \quad (14)$$

It is interesting to emphasize that the compressibility of a perfect gas is equal to $1/P$. The assumption consisting in assimilating $1/\langle P \rangle$ to C was tested numerically. Several direct simulations of GRI tests were first run for different pressure excitations, with a numerical model considering gas slippage and gas compressibility variation over time. The signal from each direct simulation was then inverted twice. In the first inverse simulation, k_{app} was determined by using the direct simulation model with $b=0$ to ignore

gas slippage. In the following one, C was obtained from Equation (11) and the k_{app} value previously estimated. To finish, k_{app} was plotted against C and the couple (k_{abs}, b) resulting from the linear regression was compared to that acting as input in the direct simulations. With $\langle P \rangle = 1/C$, the errors on k_{abs} and b were small. With $\langle P \rangle = \langle P(R,t) \rangle$, $\langle P(R,t) \rangle$ being the average pressure at the surface of the particles, they were systematically higher.

The reason why C is a good approximation of $1/\langle P \rangle$ is still unclear. However, the common practice consisting in defining $\langle P \rangle$ as $\langle P(R,t) \rangle$ is undeniably wrong and this is obvious when having two things in mind. First, $\langle P \rangle$ is the mean pore pressure in a steady-state test. Second, in a standard GRI test, $\langle P(R,t) \rangle$ cannot be close to $\langle P(0,t) \rangle$, mean pressure at the centre of the particles, since $P(R,t)$ and $P(0,t)$ vary in very different ranges. Generally, $P(R,t)$ decreases from P_{0+} by a few tens of millibars, V_{1+2} being large compared to V_p , whereas $P(0,t)$ increases by a few bars, V_p being initially at atmospheric pressure [15]. As a conclusion, the easiest way to overcome the problem due to $\langle P \rangle$ characterization is to limit the pressure variation inside and outside the particles. In this case, $\langle P \rangle$ can be effectively taken equal to $\langle P(R,t) \rangle$ without affecting k_{abs} and b . The impact on k_{abs} and b of the value given to $\langle P \rangle$ depending on the test design is illustrated in Section 5.2.

5. Experimental results

5.1. Materials

The rock we chose to validate the KPC-Log method was pyrophyllite, which is a low-grade metamorphic outcrop rock. Its name comes from its mineralogical composition including exclusively pyrophyllite minerals. Its absolute permeability does not exceed a few tens of nanodarcies. Besides, its ideal properties make it a good candidate to test methods adapted to low-permeability measurement: high homogeneity, low anisotropy and low sensitivity to mechanical stress and ambient humidity.

We took four plugs from our pyrophyllite block. All of them had a diameter of 23 mm and a length of 25 mm. One plug was sampled in each space direction, numbered from 1 to 3, to orientate and quantify anisotropy. The last plug was taken far from the others to check homogeneity. For each plug, we determined the k_{abs} , b and ϕ properties by Step Decay method [23]. The test consists in emitting several pressure pulses with nitrogen at the plug inlet and inverting the signal recorded at the outlet to estimate the three properties simultaneously. The effective confining pressure was set at 80 barg for the different tests. We did not clean the plugs to prevent rock damage. Drying was unnecessary since pyrophyllite permeability is quite not altered by ambient humidity. The results are presented in Table 1.

Table 1. k_{abs} , b and ϕ values for the pyrophyllite plugs

Plug	Direction	k_{abs} (nD)	b (bara)	ϕ (frac)
1	1	55	31	0.042
2	2	28	31	0.041

3	3	58	30	0.033
4	1	61	29	0.042

The results corroborate that pyrophyllite is homogeneous and slightly anisotropic, the anisotropy ratio being equal to 2. The lowest k_{abs} value is observed in Direction 2 and in the plane perpendicular to that direction, k_{abs} is almost uniform.

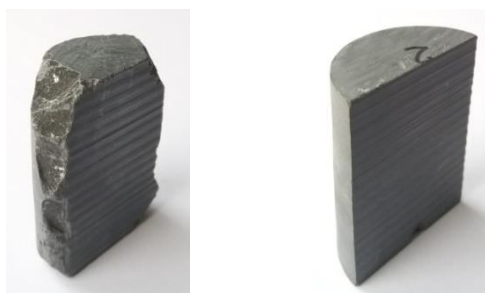
After validation of the technique, we selected a shale rock for an application case. This shale was that we used in the reference [15] to analyze GRI methods available in the industry. Its properties are reported in Table 2. While ϕ was deduced from a simple pycnometry test on a core plug (23*24 mm), k_{abs} and b were measured on different samples and with different methods. Darcypress tests [5] were done on small cylinder-shaped samples (10*5 mm), oriented parallel and perpendicular to bedding to evaluate anisotropy. They were followed by Darcyshale tests [19] on crushed rock (average particle diameter of 1.72 mm). The axial confining pressure was fixed to 100 barg in all Darcypress tests. We did not clean the sample. We only dried them in an oven at 65 °C until mass stabilization to eliminate the mobile liquids which could have generated biases in the measurements. The initial liquid phase was probably not entirely eliminated at 65 °C. However, this is not problematic since our goal was not to find a “true” permeability but to control the consistency of the results coming from various methods.

Table 2. k_{abs} , b and ϕ values for the shale samples

Cylinder - 10*5 mm - // to bedding		Cylinder 23*24 mm
k_{abs} (nD)	b (bara)	
28	18	ϕ (frac)
Cylinder - 10*5 mm - \perp to bedding		0.141
k_{abs} (nD)	b (bara)	
8	28	
Crushed sample - 1.72 mm		
k_{abs} (nD)	b (bara)	
10	33	

5.2. Method validation

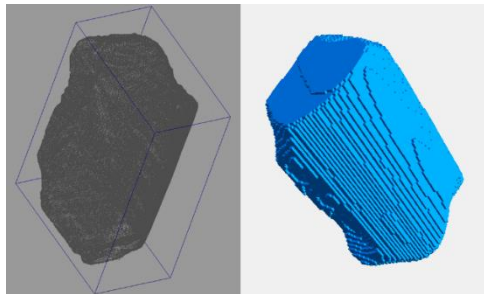
The pyrophyllite samples used to validate the KPC-Log method can be seen in the photos of Figure 7. A cylinder having a diameter of 38 mm and a length of 50 mm was taken in Direction 2 and cut in two half-cylinders with a saw. One half-cylinder was damaged with a hammer and a chisel. Neither the cylinder nor the half-cylinders were cleaned or dried.



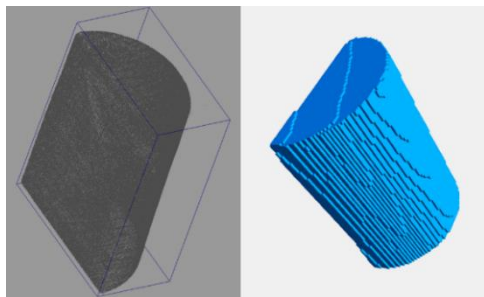
a. Broken half-cylinder b. Intact half-cylinder

Fig. 7. Pyrophyllite half-cylinders

Standard GRI tests (refer to Figure 2) were carried out on the cylinder before cutting it along the longitudinal axis. The pressure P_1 in the chamber V_1 successively reached 4.2 bara, 6.9 bara and 9.9 bara. The chamber V_2 holding the cylinder was initially at atmospheric pressure in each test. KPC-Log tests were first done on the damaged half-cylinder only (refer to Figure 6). To assess the technique repeatability, some of them were reiterated in conditions as similar as possible. Nine tests were performed in total. The pressure P_1 in the chamber V_1 and the medium pore volume V_p ranged from 10.8 bara to 52.8 bara, each test beginning with the chamber V_2 at atmospheric pressure. To validate the code written for multiple pieces of rock, three KPC-Log tests were then undertaken on both half-cylinders put together in the chamber V_1 . The pressure P_1 was set at 26.5 bara, 31.3 bara and 42.4 bara. Each series of GRI or KPC-Log tests was interpreted by applying the whole procedure detailed in Section 4, from the 3D mesh generation to k_{abs} and b characterization. Figure 8 shows, for both half-cylinders, the 3D point cloud coming from the laser robot and the resulting 3D cartesian grid.



a. Broken half-cylinder

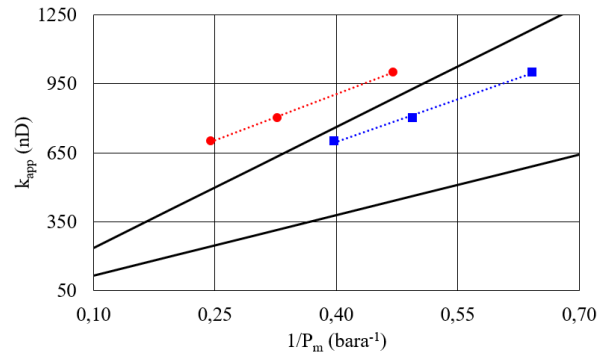


b. Intact half-cylinder

Fig. 8. 3D point clouds and cartesian grids for the pyrophyllite half-cylinders

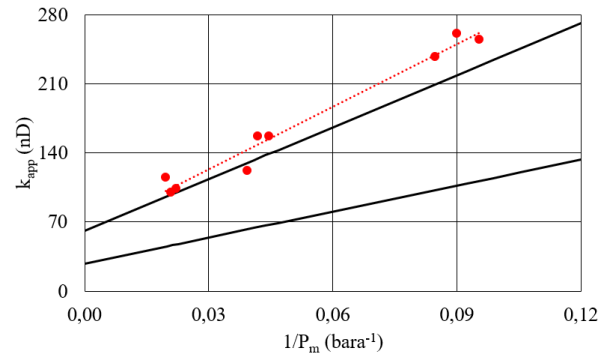
For the cylinder, the linear regression leading to k_{abs} and b was accomplished twice, first with $\langle P \rangle = \langle P(R,t) \rangle$ and second with $\langle P \rangle = \langle P(0,t) \rangle$. The graphs of Figure 9.a, Figure 9.b and Figure 9.c give k_{app} plotted against $1/\langle P \rangle$ for the cylinder, the damaged half-cylinder and both half-cylinders respectively. In all graphs, two lines demarcate the area where the $(1/\langle P \rangle, k_{app})$ points are expected to be located. They were drawn considering Equation (10), *i.e.* Klinkenberg's law, and the data listed in Table 1: k_{abs} and b values in Direction 2 for the lower limit line, mean k_{abs}

and b values in the plane perpendicular to Direction 2 for the upper limit line. In Table 3 are reported the k_{abs} and b values determined from the coefficients of the regression lines plotted in the graphs.



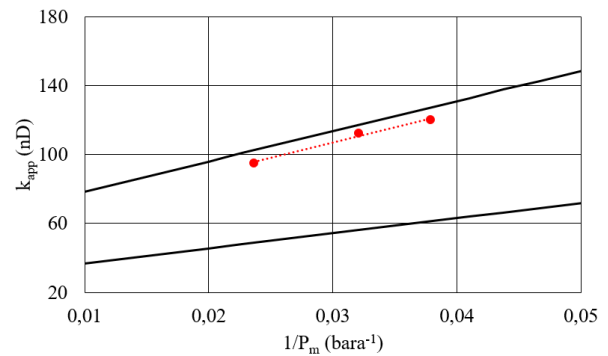
—SD tests - Upper & lower limits ● KPC-Log tests - $\langle P \rangle = \langle P(R,t) \rangle$
 ■ KPC-Log tests - $\langle P \rangle = \langle P(0,t) \rangle$

a. Cylinder



—SD tests - Upper & lower limits ● KPC-Log tests

b. Broken half-cylinder



—SD tests - Upper & lower limits ● KPC-Log tests

c. Broken half-cylinder and intact half-cylinder

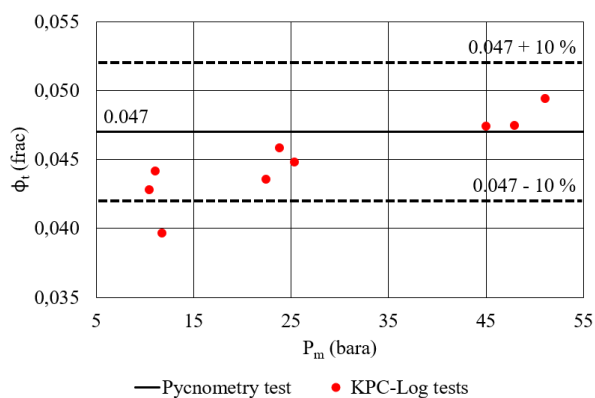
Fig. 9. Graphs of k_{app} plotted against $1/\langle P \rangle$ for the pyrophyllite samples

Table 3. k_{abs} and b values for the pyrophyllite samples

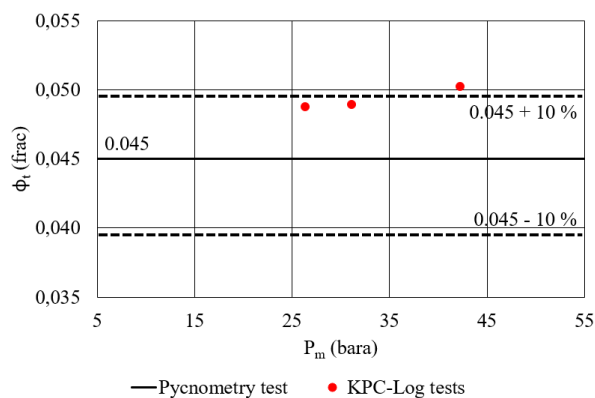
Cylinder			
$\langle P \rangle = \langle P(R,t) \rangle$		$\langle P \rangle = \langle P(0,t) \rangle$	
k_{abs} (nD)	b (bara)	k_{abs} (nD)	b (bara)
368	4	202	6
Broken half-cylinder			
k_{abs} (nD)		b (bara)	
60		35	

Broken half-cylinder and intact half-cylinder	
k_{abs} (nD)	b (bara)
54	33

Each half-cylinder underwent a pycnometry test with Micromeritics' Accupyc II 1340 device, which works as our KPC-Log device except that helium is injected. The goal was to associate a reference porosity, delivered by a device different from the KPC-Log device, to the broken half-cylinder on one hand and the set of half-cylinders on the other hand. This reference is simply ϕ_1 deduced from Equation (1) and the helium pycnometry data. A ϕ_2 value was derived from Equation (2) after each KPC-Log test. The diverse ϕ_2 values are compared to ϕ_1 in the graph of Figure 10.a for the broken half-cylinder and in the graph of Figure 10.b for the set of half-cylinders.



a. Broken half-cylinder



b. Broken half-cylinder and intact half-cylinder

Fig. 10. Graphs comparing the ϕ_2 values to the ϕ_1 value for the pyrophyllite samples

The impact of the pyrophyllite anisotropy on the gas flow was minimized by plugging parallel to Direction 2 the cylinder at the origin of the half-cylinders. The rock properties are indeed virtually homogeneous in the plane perpendicular to Direction 2. For both series of KPC-Log tests, the $(1/\langle P \rangle, k_{app})$ points are well aligned, practically along the upper limit line. This observation is consistent with the fact that the gas propagation is mainly driven by the average properties along Direction 1 and Direction 3, the upper limit line being based on these properties. The errors on k_{abs} and b reach 6 % and 18 % respectively for the broken half-cylinder. They are even more negligible for the set of half-cylinders since, for it, they are equal to

4 % and 8 % respectively. For the series of GRI tests, the line formed by the $(1/\langle P \rangle, k_{app})$ points does not diverge so much from the upper limit line, no matter how $\langle P \rangle$ is defined. Nevertheless, the biases affecting k_{abs} and b are significant in both cases. As an example, in the best case where $\langle P \rangle = \langle P(0,t) \rangle$, k_{abs} is overestimated by a factor of 3.6 while b is underestimated by a factor 5.1. These last results back the fact that $P(0,t)$ variation must be limited during the test in order that accurate k_{abs} and b values can be found. To finish, the good consistency between the ϕ_1 and ϕ_2 values for both media studied with the KPC-Log technique highlights that the talc powder was efficient to reduce the thermal effects at short times.

The pressure signals coming from the tests on the set of half-cylinders were inverted twice, with the KPC-Log code and with Cydar software developed by Cydarex for the interpretation of laboratory petrophysical tests. In this software, we used the module specific to PDOS tests [5] (refer to Section 1), in order to appraise how simplifying the sample geometry impacts k_{abs} and b. We built a basic model in which all volumes characterizing the KPC-Log device (chambers and powder) were divided by 2 and the sample was either a sphere or a cylinder having the mean volume of one half-cylinder. We defined two geometries for the cylinder based on the average dimensions of one half-cylinder, being 1.9 cm for the radius and 5.0 cm for the length. In a first time, the cylinder diameter was fixed to 1.9 cm and its length was computed accordingly. In a second time, the cylinder length was fixed to 5.0 cm and its diameter computed. The k_{abs} and b values delivered by Cydar for the sphere and the cylinders are in Table 4.

Table 4. k_{abs} and b values for the sphere and the cylinders

Sphere - 3.7 cm	
k_{abs} (nD)	b (bara)
44	108
Cylinder - 1.9*9.4 cm	
k_{abs} (nD)	b (bara)
20	111
Cylinder - 2.6*5.0 cm	
k_{abs} (nD)	b (bara)
28	132

The results from the simulations involving the simplified geometries were compared to those from the simulations relying on the true geometry (refer to Table 3). It seems that simplifying the geometry has a more negative effect on b than on k_{abs} . Indeed, while k_{abs} is underestimated by a factor of 1.3 to 2.7, b is overestimated by a factor of 3.6 to 4.4.

5.3. Method application

We prepared a set of thirteen cube-shaped pieces of shale having dimensions of a few millimetres. Their forms and sizes were irregular since they were cut manually, with a simple saw. Our goal was to produce an artificial crushed sample comprising particles which are big enough so that their surfaces can be properly mapped by the laser robot. Some of these particles appear in the photo of Figure 11

and the concatenated 3D meshes of the thirteen particles can be observed in Figure 12.



Fig. 11. Cube-shaped particles of shale



Fig. 12. 3D cartesian grids for the particles of shale

The particles were not cleaned but dried at 65 °C before scanning with the robot. We conducted on them a series of tests with the Darcyshale device. The KPC-Log device was inappropriate because of its chamber V_1 designed for big samples only. The recorded pressure build-ups were interpreted twice, first using Cydar and second using the numerical model working with the true sample geometry. The particles were represented by spheres in Cydar. The (k_{abs}, b) pairs coming from both interpretations are listed in Table 5 and their corresponding $(1/\langle P \rangle, k_{app})$ datasets are compared to those from reference [15] in the graph of Figure 13.

Table 5. k_{abs} and b values for the particles of shale

True sample geometry	
k_{abs} (mD)	b (bara)
25	21
Simplified sample geometry	
k_{abs} (mD)	b (bara)
25	38

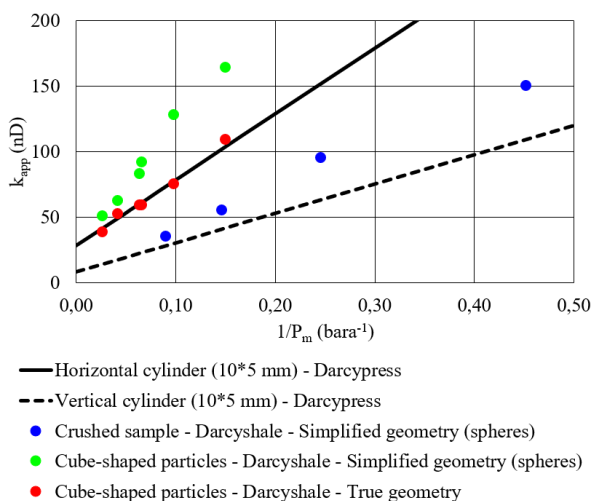


Fig. 13. Graph comparing both $(1/\langle P \rangle, k_{app})$ datasets related to the particles of shale to datasets from the reference [15]

The discrepancy between the k_{abs} values is quite equal to 0 and that between the b values is less than a factor of 2.

As already highlighted in Section 5.2, b is more sensitive than k_{abs} to the geometry. When accurately capturing the shapes of the particles, the $(1/\langle P \rangle, k_{app})$ points are more consistent with those from past experiments described in the reference [15], especially at low pressures where b is meaningful. The influence of the geometry on k_{abs} and b remains yet negligible in this specific case. This suggests that our cube-shaped particles of shale can be reasonably modelled by spheres. As the numerical results detailed in the reference [17], our experimental results confirm that cuttings or crushed rock particles can be supposed to be spherical if they are not excessively elongated.

6. Summary and conclusions

This paper focuses on the KPC-Log method designed for characterizing the properties of a tight sample having any shape, a geometrical one or not. Each test is an improved GRI test resting upon the experimental recommendations formulated in the reference [19] and leading to k_{app} and ϕ values. The recorded signal is a pressure build-up due to gas expansion from inside to outside the porous medium. By pressurizing the material and limiting the surrounding volume, the pressure variation in the pore volume is kept small during the test. This is crucial when estimating k_{abs} and b from a series of tests at increasing pore pressures, by applying Klinkenberg's method. Indeed, $\langle P \rangle$, whose definition is not trivial in a purely unsteady-state test, is correctly approximated by the value of the mean pressure level. This is not true when the pore volume experiences huge pressure variations. Consequently, reliable k_{abs} and b values are found from the coefficients of the regression line over the $(1/\langle P \rangle, k_{app})$ points. The KPC-Log method relies on another key element, namely the introduction of a powder in the dead volume of the chamber containing the sample. The talc used in the tests proved to decrease efficiently the thermal effects occurring at short times. A test is interpreted with a numerical model and a 3D mesh of the system composed of the chambers and the sample. The mesh is created from a 3D point cloud of the sample surface that a robot captures by laser mapping. The code producing the mesh was initially written for one piece of rock. It was extended afterwards for several pieces, each piece having its own point cloud.

We validated our technique on pyrophyllite, an ideal low-permeability material having known properties. We successively used one big half-cylinder and a set of two half-cylinders. Afterwards, we implemented the method on a pack of small cube-shaped particles of shale. From each series of tests were estimated k_{abs} and b values with an accurate reconstruction of the sample and a simplified one as well. The goal was to appraise how k_{abs} and b are affected when the true sample geometry is not respected. The results demonstrated that the error on b arising from geometry simplification systematically exceeds the error on k_{abs} . This means that the error on k_{app} increases when the pressure decreases. Besides, the experimental results from the tests on the small particles of shale corroborated one conclusion drawn from the numerical study detailed in the reference [17]. Modelling cuttings or crushed rock

particles by spheres is adequate if their shapes are not too elongated.

The k_{abs} and b values coming from KPC-Log tests are more accurate than those from standard GRI tests. They are also more representative since crushing can engender microfractures and distort the pore network. Keeping the material intact has for other notable advantage to enlarge the range of measurable permeabilities, the signals being longer owing to the larger distances traveled by the gas. The KPC-Log method offers a new option to build a log of permeability along the well if a MCB is preferred for drilling, given that this tool delivers centimetric pieces of rock at the surface. Moreover, even if the technique was initially developed for unconventional formations, its use could be extended to conventional ones by replacing gas with liquid [3]. Finally, additional improvements would be needed in the future to solve the remaining problems that the KPC-Log technique has still in common with the GRI technique: sample anisotropy, sample fracturing and no sample confinement.

References

1. C. E. Molinares, R. M. Slatt and R. Sierra, "The effects of lamination/bedding on the brittleness for the Woodford shale silica-rich intervals, from the Wyche-1 core-well analysis, Pontotoc County, Oklahoma", presented at the AAPG Annu. Conv. and Exhib., Houston, TX, USA, Apr. 2 - 5, 2017.
2. D. L. Luffel, C. W. Hopkins and P. D. Shettler, "Matrix permeability measurement of gas productive shales", presented at the SPE Annu. Tech. Conf. and Exhib., Houston, TX, USA, Oct. 3 - 6, 1993, Paper SPE 26633.
3. P. Egermann, R. Lenormand, D. Longeron and C. Zarcone, "A fast and direct method of permeability measurement on drill cuttings", *Petrophysics*, vol. 44, n° 4, pp. 243 - 252, Jul. - Aug. 2003, doi: 10.2118/77563-PA.
4. P. Carles, P. Egermann, R. Lenormand and J.-M. Lombard, "Low permeability measurements using steady-state and transient methods", presented at the SCA Int. Symp., Calgary, AB, Canada, Sep. 10 - 12, 2007, Paper SCA2007-07.
5. R. Lenormand, F. Bauget and G. Ringot, "Permeability measurement on small rock samples", presented at the SCA Int. Symp., Halifax, NS, Canada, Oct. 4 - 7, 2010, Paper SCA2010-A073.
6. X. Cui, A. M. M. Bustin and R. M. Bustin, "Measurements of gas permeability and diffusivity of tight reservoir rocks: different approaches and their applications", *Geofluids*, vol. 9, pp. 208 - 223, 2009, doi: 10.1111/j.1468-8123.2009.00244.x.
7. Y. Zhao, C. Wang and J. Bi, "A method for simultaneously determining axial permeability and transverse permeability of tight reservoir cores by canister degassing test", *Energy Sci. Eng.*, vol. 8, n° 4, pp. 1220 - 1230, Apr. 2020, doi: 10.1002/ese3.580.
8. M. J. Hannon Jr., "Fast and reliable estimates of low permeabilities by the Full-Immersion Pressure-Pulse Decay", presented at the SPE/AAPG/SEG Unconventional Resources Technol. Conf., Austin, TX, USA, Jul. 24 - 26, 2017, Paper URTEC: 2669302.
9. S. Peng and B. Loucks, "Permeability measurements in mudrocks using gas-expansion methods on plug and crushed-rock samples", *Mar. Petrol. Geol.*, vol. 73, pp. 299 - 310, May 2016, doi: 10.1016/j.marpetgeo.2016.02.025.
10. O. Kwon, A. K. Kronenberg, A. F. Gangi and B. Johnson, "Permeability of Wilcox shale and its effective pressure law", *J. Geophys. Res.-Atmos.*, vol. 106, n° B9, pp. 19,339 - 19,353, Sep. 10, 2001, doi: 10.1029/2001JB000273.
11. C. David, J. Wassermann and the KG²B team, "KG²B, a collaborative benchmarking exercise for estimating the permeability of the Grimsel granodiorite - Part 1: measurements, pressure dependence and pore-fluid effects", *Geophys. J. Int.*, vol. 215, n° 2, pp. 799 - 824, Nov. 1, 2018, doi: 10.1093/gji/ggy304.
12. S. Sinha, E. M. Braun, Q. R. Passey, S. A. Leonardi, A. C. Wood III, T. Zirkle, J. A. Boros and R. A. Kudva, "Advances in measurement standards and flow properties measurements for tight rocks such as shales", presented at the SPE/EAGE Eur. Unconventional Resources Conf. and Exhib., Vienna, Austria, Mar. 20 - 22, 2012, Paper SPE 152257.
13. A. Tinni, E. Fathi, R. Agarwal, C. Sondergeld, Y. Akkutlu and C. Rai, "Shale permeability measurements on plugs and crushed samples", presented at the SPE Can. Unconventional Resources Conf., Calgary, AB, Canada, Oct. 30 - Nov. 1, 2012, Paper SPE 162235.
14. J. T. Comisky, M. Santiago, B. McCollom, A. Buddhala and K. E. Newsham, "Sample size effects on the application of mercury injection capillary pressure for determining the storage capacity of tight gas and oil shales", presented at the SPE Can. Unconventional Resources Conf., Calgary, AB, Canada, Nov. 15 - 17, 2011, Paper CSUG/SPE 149432.
15. S. Profice and R. Lenormand, "Low permeability measurement on crushed rock: insights", presented at the SCA Int. Symp., Pau, France, Sep. 26 - 30, 2019, Paper SCA2019-016.
16. F. Civan, "Can gas permeability of fractured shale be determined accurately by testing core plugs, drill cuttings and crushed samples?", presented at the SPE/AAPG/SEG Unconventional Resources Technol. Conf., Austin, TX, USA, Jul. 24 - 26, 2017, Paper URTEC: 2666389.
17. R. Suarez-Rivera, M. Chertov, D. Willberg, S. Green and J. Keller, "Understanding permeability measurements in tight shales promotes enhanced determination of reservoir quality", presented at the

SPE Can. Unconventional Resources Conf.,
Calgary, AB, Canada, Oct. 30 - Nov. 1, 2012, Paper
SPE 162816.

18. S. Desmette, B. Deschamps, R. Birch, M. Naegel and P. Essel, “Drilling hard and abrasive rock efficiently or generating quality cuttings? You no longer have to choose...”, presented at the SPE Annu. Tech. Conf. and Exhib., Denver, CO, USA, Sep. 21 - 24, 2008, Paper SPE 116554.
19. R. Lenormand and S. Profice, “Darcyshale: an improved GRI method for more reliable measurements on low-permeability samples”, presented at the SCA Int. Symp., Austin, TX, USA, Sep., 2021, Paper SCA2021-T040.
20. L. J. Klinkenberg, “The permeability of porous media to liquids and gases”, in *Drilling and Production Practice*. New-York, NY, USA: API, 1941, pp. 200 - 213.
21. S. Profice, D. Lasseux, Y. Jannot, N. Jebara and G. Hamon, “Permeability, porosity and Klinkenberg coefficient determination on crushed porous media”, presented at the SCA Int. Symp., Austin, TX, USA, Sep. 18 - 21, 2011, Paper SCA2011-32.
22. S. Profice, “Mesure de propriétés monophasiques de milieux poreux peu perméables par voie instationnaire”, Ph.D. dissertation, I2M - Dept. TREFLE, Bordeaux Univ., Bordeaux, France, 2014.
23. D. Lasseux, Y. Jannot, S. Profice, M. Mallet and G. Hamon, “The “Step Decay”: a new transient method for the simultaneous determination of intrinsic permeability, Klinkenberg coefficient and porosity on very tight rocks”, presented at the SCA Int. Symp., Aberdeen, Scotland, Aug. 27 - 30, 2012, Paper SCA2012-25.

num	Numerical
p	Pore
t	Total
0+	Just after valve opening
1	Chamber 1 - Initial state (IS) Material balance between IS and FS
2	Chamber 2 - Transitional state (TS) Material balance between IS and TS
3	Final state (FS)
1-2	Between Chamber 1 and Chamber 2
1+2	Chamber 1 and Chamber 2 as a whole

Exponents

'	Cartesian grid
---	----------------

Nomenclature

b (Pa)	Klinkenberg coefficient
C (Pa ⁻¹)	Gas compressibility
F	Objective function
k (m ²)	Permeability
P (Pa)	Pressure
R (m)	Mean particle radius
t (s)	Time
T (K)	Temperature
v (- / m.s ⁻¹)	Valve / Darcy gas velocity
V (m ³)	Volume
μ (Pa.s)	Gas viscosity
ρ (kg.m ⁻³)	Gas density
φ (frac)	Porosity
< . >	Mean property

Subscripts

abs	Absolute
app	Apparent
c	Coarse grid
exp	Experimental
f	Final / Fine grid

Of rats and rocks: using pre-clinical PET imaging facilities in core analysis

Bergit Brattækås^{1*}, Martin A. Fernø¹, Malin Haugen¹, Tore Føyen¹, Marianne Steinsbø¹, Arne Graue¹, Njål Brekke², Tom Christian Holm Adamsen², Cecilie Brekke Rygh³ and Heidi Espedal⁴

¹Dept. of Physics and Technology, University of Bergen, Norway

²Center for Nuclear Medicine - PET, Department of Radiology, Haukeland University Hospital, Norway

³Department of Radiology, Haukeland University Hospital, Norway

⁴Molecular Imaging Center, Department of Biomedicine, University of Bergen, Norway

Abstract. Positron emission tomography (PET) is routinely used for medical imaging; a current surge in published geoscientific research utilizing this modality also infer increasing interest for *in-situ* PET imaging in core analysis. Excellent signal to noise ratio coupled with high temporal and spatial resolution suggest that PET might become the new method-of-choice for core analysis. Obstacles related to production, transfer and handling of radioactive fluids and gases must, however, be dealt with for PET to become a widely used core scale imaging technique. This paper describes an ongoing, true multidisciplinary collaboration, where pre-clinical PET imaging facilities are routinely used in core analysis to investigate dynamic fluid flow at high pressure conditions. We detail challenges and opportunities related to porous media research in established pre-clinical laboratory facilities designed for small-animal imaging, and demonstrate the significant potential of PET imaging in core scale analysis in a context related to long-term porous media carbon storage.

Explicit imaging of several fluid phases is possible by PET imaging using a range of readily available radiotracers. Relevant radiotracers to carbon storage in porous media are e.g. the carbon radioisotope ¹¹C and water-soluble tracer ¹⁸F. These are both short-lived tracers (20 - 110 min) and must be used in high doses of radiation, which present challenges related to safe transfer and handling. Although there are several obstacles to conduct advanced core analysis in hospital imaging facilities (some of which are detailed in this paper), significant advantages include trained personnel on-site to operate a local cyclotron, procedures in place to ensure safe and efficient transfer of short-lived radiopharmaceuticals from the cyclotron, and advanced image analysis capabilities available. Cyclotrons are widely available worldwide (currently more than 1200 operating cyclotrons), often located in close proximity to medical and pre-clinical imaging facilities and academic institutions. Similar collaborations may therefore also be possible elsewhere, reducing the need for allocated geophysical PET-scanners and lowering the threshold for routinely using PET imaging in core analysis.

1 Background

1.1 A quick introduction to Positron Emission Tomography imaging

Positron emission tomography (PET) imaging utilizes positron-emitting radionuclides to gain insight into fluid flow and accumulation. These radionuclides are rich in protons and decay by beta plus decay; the spontaneous physical phenomenon where an emitted positron annihilates with an electron and consequently emits a pair of specific energy photons (511 keV) in opposite directions. PET scanners can determine annihilation

events with high spatial and temporal accuracy; by detecting gamma rays (photons) occurring simultaneously on opposite sides of an object. The number, position and size of PET detector elements, as well as the distance between the object and detectors, strongly influence the spatial resolution of PET imaging [1]. PET is established as a diagnostic tool in medicine, where the radioactively labelled “object” is often a human (in clinical imaging) or animal (in pre-clinical research) but has also recently been demonstrated as a highly useful tool for non-medical purposes: flow visualization in porous rocks [2-15]. For practical purposes the beta plus decay is insensitive to pressure and temperature [16]. PET imaging is, hence, a suitable tool to visualize fluid flow and accumulation

* Corresponding author: bergit.brattækås@uib.no

within core plugs placed in confinement vessels under high pressure and temperature conditions; e.g. to investigate porous media CO₂ storage at relevant storage conditions.

PET imaging has several advantages, which in sum renders PET a strong competitor to other imaging methods initially used for diagnostic purposes, e.g. computed tomography (CT) and magnetic resonance imaging (MRI). Advantages include 1) high spatial resolutions, 2) high temporal resolutions (i.e. possibility to investigate fast processes at high flow rates), 3) excellent signal-to-noise ratio (i.e. a small amount of radioactivity is sufficient to produce high-quality images; without altering the properties of the labelled fluid), 4) explicit detection of radioactively labelled fluid only (i.e. fluid flow paths are imaged without the porous medium influencing image quality). For a general introduction to PET imaging in water resources research we recommend Zahasky and Benson (2019) [21].

During core scale imaging by CT and MRI, high spatial resolution may be achieved by decreasing temporal resolution: a trade-off which must be set within each experiment. Micro-CT for example enables micrometer visualization of the pore space, but the time scale for acquiring 3D images is several hours. PET imaging does not suffer from this tradeoff: photon emissions are continuously recorded during imaging, and spatial and temporal resolutions are set during post-processing. 3D images may, hence, be achieved during short time spans (seconds), while maintaining a high spatial resolution. A simple schematic of imaging methods and resolution relations is shown in **Fig. 1**.

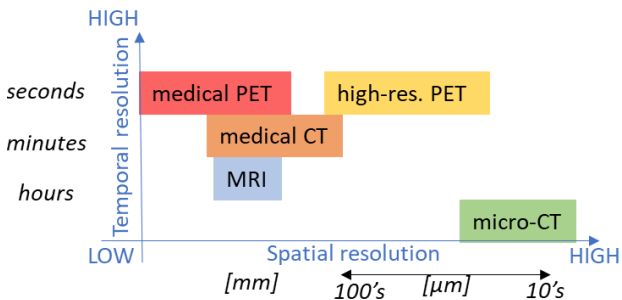


Fig 1. Imaging technologies used for 3D *in-situ* visualization of core material and core floods. Spatial resolution may be high for MRI and CT imaging, although that typically increases the scan time. PET images are post-processed; and maintain high spatial resolution regardless of temporal resolution preferences.

1.2 Existing opportunities

Although some research groups have procured or built their own PET imaging systems (e.g. [17-20]), this is not a realistic solution for the average core analyst. Several necessary specifications and requirements must be fulfilled and a number of challenges (both perceived and real, recently described by Zahasky *et al.* [21]) dealt with to perform core analysis with PET imaging. Most obstacles relate to the production, transportation, safe use and handling of radioisotopes, especially short-lived

radioisotopes, that are often used for geoscientific purposes. These obstacles are manageable, but requires significant funds and space for necessary equipment and personnel. The threshold for PET-imaging utilizing private facilities therefore remains high, and other options may be explored to make PET-imaging available for a broader range of users.

Hospitals world-wide are actively applying PET imaging for diagnostic purposes [22, 23], and clinical PET-scanners have become widespread during the last few decades. Obstacles related to production, transportation and safe handling of radioisotopes have therefore already been handled to routinely perform PET-imaging in hospitals. Clinical scanners are intended for human use, and are normally reserved for patients during operating hours. The time frame available for non-essential flow experiments is therefore limited. Access to operational IT infrastructure connected to clinical scanners is also restricted, to prevent insight into sensitive patient information. Further limitations related to cleanliness (operating potentially messy equipment in a sterile lab) and spatial resolution (limited to 2-5mm, because gantry and detector element sizes are constructed for human use [24]) in sum prevents clinical PET-scanners to be widely utilized in core analysis, although occasional experiments are feasible, and have been reported [2, 25, 26].

Another option also exists within many hospital research facilities: high-resolution PET-scanners used for pre-clinical imaging of small animals. This paper highlights the opportunity in using pre-clinical PET-imaging facilities in core analysis, and describes an ongoing collaboration that has successfully utilized this opportunity. Pre-clinical PET shares the advantages of clinical imaging in terms of radioisotope production, transportation and handling albeit with weight and size limitations not normally encountered using clinical scanners. A higher spatial resolution, however, results from the smaller size (due to decreased distance between scanned object and detector elements, and smaller detector element size, see e.g. Bailey *et al.* [1]), and the high-resolution PET-CT scanner used in this work features voxel sizes of 0.3-0.4 mm. Issues related to experimental duration may be largely overcome and the pre-clinical scanners available for longer continuous time spans, depending on the number and frequency of parallel animal studies.

Table 1 summarizes the obstacles associated with PET imaging in private facilities, and using existing clinical and pre-clinical imaging facilities. The table illustrates that several obstacles are overcome using pre-clinical PET imaging, but some remain; e.g. it may be a challenge using software and settings intended for soft-tissue small animals in studies on sedimentary rocks. Tailor-made software is an advantage reserved for geo-scientifically oriented, private PET-imaging facilities. Additionally, access requirements may vary between facilities; the pre-clinical PET-scanner used in this work is a part of the Molecular Imaging Centre (MIC) (Department of Biomedicine, University of Bergen, Norway) and is

Table 1 : General obstacles in PET-imaging may be overcome within medical imaging facilities- although new obstacles occur. An overview of obstacles for each option (private, clinical or pre-clinical PET-imaging) is shown below.

Obstacles	Present	Partly handled	Handled	
Production of radioisotopes	PET (general)		Pre-clinical PET	Clinical PET
Transportation of radioisotopes	PET (general)		Pre-clinical PET	Clinical PET
Safe handling of radioisotopes	PET (general)		Pre-clinical PET	Clinical PET
Experiment duration	Clinical PET	Pre-clinical PET		PET (general)
Access for personell	Clinical PET	Pre-clinical PET		PET (general)
IT access	Clinical PET	Pre-clinical PET		PET (general)
Software modification	Clinical PET	Pre-clinical PET		PET (general)
Cleanliness	Clinical PET	Pre-clinical PET		PET (general)
Spatial resolution	Clinical PET	PET (general)		Pre-clinical PET
Weight and size of laboratory equipment	Pre-clinical PET	Clinical PET		PET (general)

located at the PET-centre at Haukeland University Hospital.

MIC was started in 2003 and is an open access national (Normolim²) and international/European (Euro-BioImaging³) level, providing access to advanced small animal imaging to the research community. Obstacles related to researcher access have therefore been minor. MIC maintains instrumentation and has highly qualified scientific and technical personnel to facilitate a variety of research (usually in the field of biomedicine). Their experience in interacting across research groups have also made the leap from physiology to flow physics research relatively short. The existence of this operational open core facility is obviously a significant advantage in using pre-clinical PET-imaging for core analysis.

1.3 Availability of pre-clinical PET scanners

The pre-clinical PET-CT scanner used in this work is a nanoScan® PET-CT from Mediso, who is one of the main suppliers of pre-clinical PET scanners in addition to Bruker, MR Solutions and Siemens. Bruker reports 60-70 delivered pre-clinical PET scanners world-wide. Mediso reports 61 operational PET-CT and 30 PET-MRI scanners. MR Solutions do not wish to provide information about the exact number of scanners delivered by their company, but features more than ten customers on their web home page. Siemens no longer produce pre-clinical scanners, but some may still be in operation. Tracers used for animal studies are usually short-lived, and the PET-scanners are therefore often located in close proximity to cyclotrons.

1.4 Availability of cyclotrons

Medical cyclotrons are used to produce isotopes used in diagnostic imaging. More than 1200 cyclotrons exist world-wide, according to the International Atomic Energy Agency (IAEA) [27], and many are localized in close

proximity to research institutions and/or hospitals that are actively applying PET-imaging as a diagnostic tool.

A searchable and detailed overview of cyclotrons may be found at:

<https://nucleus.iaea.org/sites/accelerators/Pages/Cyclotron.aspx>, providing location, affiliation, make and model.

The cyclotron connected to the current research facility is shown in **Fig. 2**.



Fig. 2. World-wide map of cyclotrons from International Atomic Energy Agency (IAEA), with country and city inserts. Modified screenshot from [27].

2 Overcoming the obstacles

We have used the MIC pre-clinical PET-CT scanner since 2013 and have developed a procedure to routinely utilize shared pre-clinical imaging facilities for core analysis.

² Normolim: NORwegian MOLeclar IMaging infrastructure. More information available on normolim.w.uib.no

³ See eurobioimaging.eu for more information

Our experience is described, and attempted generalized, in the following; to highlight the possibilities of similar collaboration elsewhere.

2.1 Production of radioactive tracers

Medical imaging often utilizes short-lived radionuclides, produced at local cyclotrons. Radionuclides are attached to larger molecules before imaging. ¹⁸F (Fluorine-18) e.g. often substitutes the normal hydroxyl group in glucose to make radiotracer ¹⁸F-FDG (Fludeoxyglucose). The accelerated uptake of this glucose analogue by cancer cells enables visualization of cancerous tissue within the human body. ¹⁸F-FDG is also the most used radiotracer in fluid flow visualization for geoscientific purposes [21], due to its miscibility in water coupled with PET sensitivity. Minute amounts of ¹⁸F-FDG is needed to procure accurate, high-quality images, and can be added to water without notably altering its properties. E.g. in the MIC research facility the ¹⁸F-FDG concentration is high; at around 20 GBq in 24 mL of water directly after production. We typically receive <1 mL of this solution to label the desired aqueous solution. A variety of aqueous solutions have so far been labelled by ¹⁸F-FDG, including: brine, polymer solution and surfactant solution. The small volume of tracer compared to the aqueous solution volume ensures that macroscopic fluid properties are unaltered during PET imaging. This is one of the main advantages of PET-imaging compared to e.g. attenuation methods (exemplified by CT), where density contrasts are necessary to capture flow dynamics. ¹⁸F-FDG is routinely produced at the PET-centre (Haukeland University Hospital) to facilitate medical imaging, and trained personnel are available on a daily basis. Daily production of ¹⁸F-FDG for clinical use reduces the need for dedicated ¹⁸F-FDG production for pre-clinical imaging. The half-life of ¹⁸F-FDG is short, at $t_{1/2} = 109$ minutes, and it is delivered in vials as a liquid.

¹¹C (Carbon-11) can be attached to Carbon dioxide (CO₂) to make radiotracer ¹¹CO₂, suitable for explicit visualization of CO₂ flow in porous rocks. ¹¹CO₂ has a half-life of $t_{1/2} = 20$ minutes. The short half-life requires higher doses of radiation to be handled in flow experiments, because the radiation (which will, in turn, produce the PET signal) swiftly decays. The preferred state of radiotracer used for CO₂ flow experiments is gaseous- which also makes transfer more challenging (see Section 2.2).

The challenges related to production of radioisotopes are very well handled by trained personnel at the PET-centre. The end user- in this case core analysts aiming to use PET to visualize fluid flow- should therefore not perceive the production of radiotracers as a large obstacle. Basic understanding of radiation is, however, necessary to accurately design and implement flow experiments.

2.2 Safe transfer of radioactive tracers

Safe transportation of short-lived radiotracers varies with the type and state of radiotracer. This far in our work, ¹⁸F has been used as ¹⁸F-FDG mixed in water, delivered in vials within lead containers. The containers are taken into the imaging lab through a wall hatchway (Fig. 3). ¹⁸F-FDG radioactivity is measured and mixed with aqueous solution within the imaging lab. The obstacles related to transportation of liquid radiotracer at ambient conditions between labs in this facility are minor.

Transfer of gaseous ¹¹CO₂ is more challenging and requires an introduction to the layout of the interconnected labs (Fig. 3). ¹¹CO₂ is produced locally and transferred from the cyclotron through a hot cell (shielded nuclear radiation containment chamber) located at the chemistry lab. A Swagelok nylon tubing is connected to the hot cell in one end to prepare for gas transfer, stretched across the floor and through the wall hatchway to the control room. The other end of the tubing is connected to a receiving single-piston pump located within the PET-CT imaging lab. Two operators are needed for safe transfer: one operator present by the cyclotron, to transfer ¹¹CO₂ to the hot cell and monitor radiation levels within the receiving laboratories, and one operator monitoring and controlling the receiving pump. During gas transfer the radiation levels within both the chemistry and imaging lab are high, and both rooms should be empty. The receiving pump (Fig. 4) should therefore be remote controlled to avoid operator exposure to high levels of radiation.

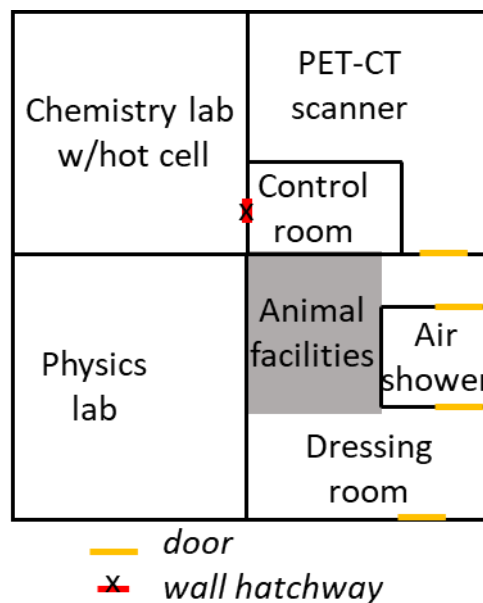


Fig. 3. Schematic layout of relevant labs at MIC/PET-centre.

¹¹CO₂ is sent to the hot cell by the cyclotron operator (normally a physicist or radiochemist employed at the PET-centre) and progresses directly through the tubing and into the pump, which should be empty and set to receive. Depending on CO₂ injection volume, rate, conditions and desired radiation dose, several consecutive

volumes of $^{11}\text{CO}_2$ may be transferred. The system is thereafter flushed by non-radioactive gas (N_2) to displace $^{11}\text{CO}_2$ from the tubing. When laboratory radiation levels have decreased sufficiently, the pump is isolated from the hot cell and connected to the experimental set-up (Fig. 4), by activating a set of valves. We use pressure- and remote-controlled valves for this purpose. Manual valves are also mounted on the pumps as a precaution. The received $^{11}\text{CO}_2$ is mixed and swiftly pressurized to the experimental conditions by transferring pre-pressurized CO_2 from a second pump (Fig. 4). Although obstacles remain and the risk for failure is higher when transferring gas (e.g. gas leakage could force temporary shut-down of several labs, with implications for hospital capacities), safe transfer has repeatedly been demonstrated, which enable visualization experiments of high scientific value (Section 3).

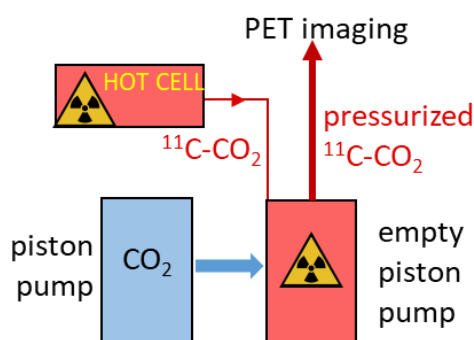


Fig. 4. Safe transfer of radioactive gas using two single-piston pumps. The pumps are connected to each other, the experimental setup and the hot cell via remote controlled valves.

2.3 Safe use and handling of radioactivity

During experimental work with radiotracers the well-known principles of radiation safety apply: ALARA, “as low as reasonably achievable”. The basic protective measures are to increase distance (from the radiation source), decrease time (close to the radiation source) and use proper shielding (between radiation source and personnel). Shielding is important both in terms of health, safety and environmental guidelines for workers (HSE) and to improve image quality, by avoiding radiation from the experimental setup into the PET scanner (increase in background radiation leads to higher level of noise in images). Portable lead walls have been used for shielding towards users in the control room and in adjacent imaging labs. During $^{11}\text{CO}_2$ injection radiation levels are initially high, and shielding walls have also been placed between the experimental setup and the PET-CT scanner, or the CO_2 pumps have been shielded by placing custom made lead rings around the pistons.

An additional important human safety precaution during core analysis with PET is to avoid leakages of radioactive fluids from the experimental setup. Hence; all parts of the setup, especially pumps, valves and line connections

should be checked thoroughly at the experimental conditions before radioactive fluids are introduced. Performing baseline tests with non-radioactive fluids is recommended. At ambient conditions, where radioactively labelled liquid is used at low radiation dose, manual control of pumps and effluent production is possible. ^{18}F -FDG mixed in aqueous solution may be produced into shielded graded cylinders, flasks or beakers where the radiation can decay, and is thereafter discharged according to local regulations. For more complicated experiments, for example injecting radioactive gas at high pressure conditions, installation of remote-controlled computers and pressure control valves is highly recommended. Hence; injection rates, direction of flow and fluid production may be monitored remotely and operator exposure to radiation minimized. Radioactive $^{11}\text{CO}_2$ should not be produced into air, and is collected in a piston accumulator at the production end of the core holder. The lower end of the accumulator is pressurized to the experimental conditions by mineral oil or distilled water, which is produced through a back-pressure regulator as produced effluents accumulate above the piston. After decay, the gas is vented into air. Image acquisitions may be remote controlled from an office outside the preparation room. The PET signal is typically recorded in time spans of 20 min – 2 hours per acquisition, and the signal is post-processed into three-dimensional images. The temporal resolution in each image frame is flexible and set during post-processing.

2.4 Weight and size of laboratory equipment

Safe transfer and use of radioactively labelled fluids for PET imaging is only possible by choosing suitable experimental equipment. Experimental conditions, such as pressure and temperature, and possibilities, such as flow rates and directions, directly relates to the different mechanical parts of an experimental setup, and their inherent limitations. Inevitably: operational limits of equipment often relate to their weight and size.

Clinical scanners are intended for human use, hence the gantry opening diameter is larger and can fit large and heavy equipment. Because the PET detector elements are also larger and positioned further away from the imaged object, the spatial resolution will, however, decrease. High-resolution (pre-clinical) PET scanners tend to have smaller gantry openings, which improves spatial resolution but also limits the possible size of an imaged object. In our case, the size of equipment that can be moved into the PET-scanner (i.e. core and core holder) is limited by 1) the gantry opening diameter (16 cm), 2) the PET field of view (FOV) of $120^{\circ} \times 120^{\circ} \times 97\text{mm}$ in the x,y,z directions, and 3) a mechanical arm which moves the equipment into the FOV and has inherent weight limitations (Fig. 5).

Several experiments have been performed using epoxy-coated cores, where the core circumference is cast in epoxy and the end faces are fitted with POM (polyoxymethylene) end pieces that are attached to nylon

fittings and lines [28-33]. The most influential factors in terms of weight are then the core material and saturating fluids. Use of epoxy allows flexibility in terms of core shape and defined no-flow boundaries, and small cores may be aligned either horizontally or vertically within the

albeit with consequences for the total weight of the equipment.

The mechanical arm moves the core horizontally for positioning within the CT and PET FOV. The core is

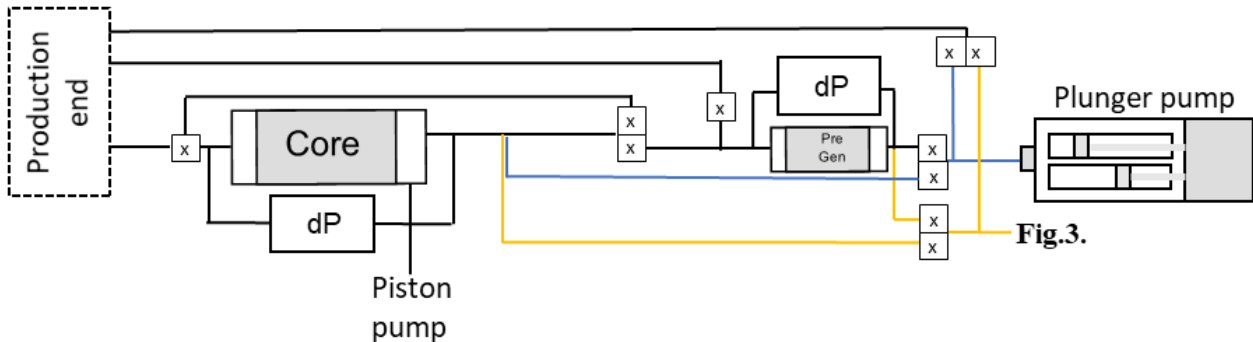


Fig. 6. Example of experimental setup used for PET imaging of CO₂-foam. The setup is very flexible, and can with few adjustments be used for a variety of experiments. «x» marks pressure-control valves and «dP» marks pressure measurements. CO₂ only flows in orange lines and only the aqueous phase in blue lines. The production end varies with radioactively labelled phase, as described in Section 2.3.

scanner. Experimental investigations of subsurface carbon sequestration, however, often require relevant conditions, i.e. higher pressures, and it is necessary to use a core holder and apply overburden pressure to the core.



Fig. 5. A custom-made core holder by RS systems © (Trondheim, Norway) is installed on a mechanical arm for imaging with high-resolution PET.

The core holder is then the single most influential factor in terms of weight, and the pressurizing fluid, fittings, valves, lines, core and saturating fluid will also contribute to the total weight. We use a custom-made, aluminium core holder (Fig. 5) for our setup (©RS systems, Trondheim, Norway). The core holder is attached directly to the mechanical arm, and can fit cores of 1.5'' diameter and 10cm length. The core holder can withstand confinement pressure up to 200Bar. With thicker aluminium walls, higher pressures may be achieved-

always horizontally aligned when using the core holder. Epoxy coated cores rest on plastic animal beds attached to the mechanical arm and can also be oriented at an angle. In the combined Mediso PET-CT, the CT scanner is located further into the scanner, and the PET scanner ring is located closer to the gantry opening. The two modalities are run in sequence and simultaneous images from the two modalities cannot be acquired. The mechanical arm moves the core between modalities and is controlled by the operator through the scanner software. CT is initially acquired to position the core. The mechanical arm thereafter moves the core into the defined position for PET acquisition. Lines connecting the core holder to the experimental setup therefore needs to be flexible and allow for horizontal movement during experiments. We have successfully used both 1/8'' peek and 1/16'' stainless steel lines, due to their low weight, flexibility and ability to withstand high pressures.

Another obstacle in terms of size and weight during pre-clinical imaging is that all equipment must pass through the air shower illustrated in Fig. 3. The purpose of the air shower is to remove animal allergens from researchers going out of the imaging lab. Air showers are proven effective to remove allergens from hair and clothes, to prevent spreading to the surrounding facilities. Because the imaging lab and surrounding facilities were intended for animal studies and users, this procedure must be followed also during core analysis (it is not possible to physically bypass the air shower). We have solved this for our use by mounting all laboratory equipment (pumps, accumulators, core holder, pressure transducers etc) on a portable trolley, that fits within the air shower (width 60cm, length 100cm). The trolley is wheeled into the imaging lab through the air shower before imaging experiments, and is stored in the physics lab (Fig. 3) in between experiments. In lab facilities shared by several research disciplines, compact and easily transportable

experimental setups are necessary, as the time available for imaging may be short (down to few days).

3 Opportunities in CCUS

Permanent storage of CO₂ in deep sedimentary reservoirs is being developed worldwide, to curb atmospheric carbon emissions. Demonstrations of safe storage on the field scale must be supported by experimental data on smaller scales, to fully understand how CO₂ storage influences, and is influenced by, the pore space. PET imaging has significant potential to capture dynamics during CO₂-flow in porous media, both implicitly (labelling the aqueous phase) and explicitly (radioactively labelling the CO₂). This section summarizes the opportunities and demonstrated potential for PET in CCUS (Carbon Capture Utilization and Storage) research. For an overview of previous application of PET imaging in water resources research, we refer to Zahasky *et al.* [21].

An example experimental setup is demonstrated in Fig. 6: the setup is designed to be flexible and can easily be modified for the purpose of the experiment, e.g. to facilitate circulation of fluids at the inlet end face.

3.1 CO₂ storage

In-situ experimental observations of forced CO₂ displacement into porous media is necessary to explain the influence of heterogeneities on CO₂ saturation development and capillary trapping: to accurately predict CO₂-brine migration in carbon sequestration reservoirs. Fernø *et al.* [2] initially demonstrated decoupled PET-CT imaging for CO₂ storage applications. They injected CO₂ into water-saturated sandstone at 90 Bar pressure to measure decoupled saturation information from each method. CO₂ saturation development was determined implicitly by quantifying the decrease in signal from ²²Na-labelled (half-life of 2.6 years) water, using a clinical PET-CT scanner with lower spatial resolution. Exhaustive sensitivity studies comparing PET and CT imaging were performed by Pini *et al.* [7] and Zahasky and Benson [3], applying a previously derived analytical method [6, 34] to extract capillary pressure and relative permeability functions on the sub-core scale. Zahasky and Benson [3] used high-resolution PET imaging to measure single- and multiphase transport properties in heterogeneous sandstone during gas injections: Nitrogen constituted the gas phase and the pressure was approximately 1.4 Bar, i.e. the experimental conditions were less relevant for CCUS, but the data analysis provided a solid foundation for using

PET in further quantification experiments. Zahasky and Benson [35], [36] also used high-resolution PET to investigate CO₂-flow and trapping in heterogeneous sandstone cores at pressures ranging from 1-8 Bar. CO₂ displacement was implicitly imaged by injecting pulses of ¹⁸F-FDG labelled water, or co-injecting water and Nitrogen. PET-imaging was again repeatedly and successfully used to assess flow parameters on the sub-core scale. Brattekkås and Haugen [37] recently demonstrated explicit and dynamic imaging of CO₂ during flow through a low-permeable chalk core at elevated pressure conditions. High-resolution PET imaging was used to visualize CO₂, labelled explicitly by ¹¹C-CO₂ and injected into a chalk core at 50 Bar pressure (Fig. 7). The procedure for CO₂ radiolabelling and injection was similar to the procedure detailed in Section 2; and accurate quantification of spatial phase saturations were achieved during both brine and CO₂ injections, at the [mm] scale. Visualization revealed heterogeneous displacement patterns, as expected during gas-brine displacements at less-than-ideal mobility ratio. The heterogeneities were attributed to a sub-core variation in permeability, which could be determined from PET displacement data at the millimetre scale.

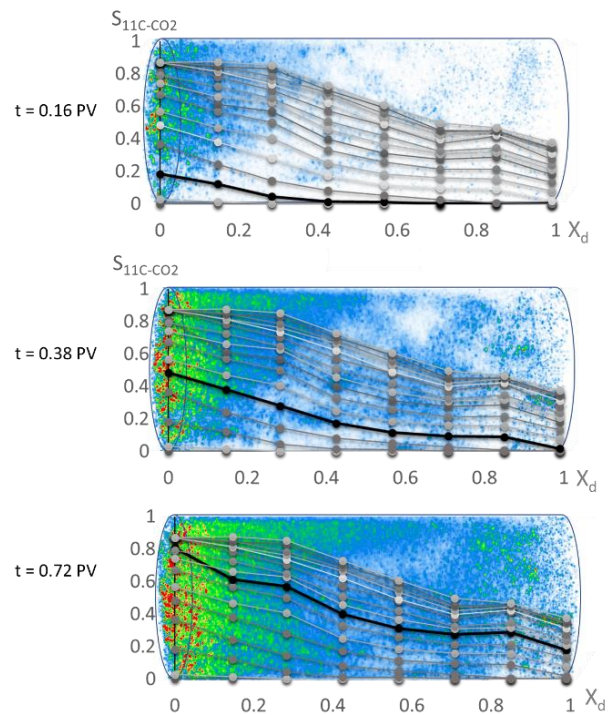


Fig. 7.⁴ Dynamic saturation development during ¹¹C-CO₂ injection into a chalk core, demonstrated by three timesteps. Qualitative 3D images of core saturation are overlaid by quantitative 1D profiles derived from PET. The red colour in 3D images represents the highest PET signal intensity, followed by green and blue. White areas do not contain ¹¹C-CO₂. The variations in the colour map hence indicate large spatial

⁴ A modified version of this figure was first published in *Explicit tracking of CO₂-flow at the core scale using Micro-*

variations in CO₂ saturation. The experiment and results are detailed in [37].

These recent publications illustrate that PET imaging can (and should) be utilized to investigate CO₂-brine displacements at a range of conditions and flow rates, where insight into local saturations and flow patterns allow for accurate determination of flow functions. Few publications are yet available where CO₂ injection is captured with high-resolution PET at high pressure conditions; but may be provided as necessary by broader access to PET imaging technology.

Spontaneous imbibition is another important mechanism during CO₂ sequestration, and may control the redistribution and remobilization of fluids after CO₂ injection. High-resolution PET imaging has in several instances been used to image the imbibing, radioactively labelled, water front [28-30]. The results confirmed that PET is an excellent tool to quantify dynamics during spontaneous imbibition, **Fig. 8**.

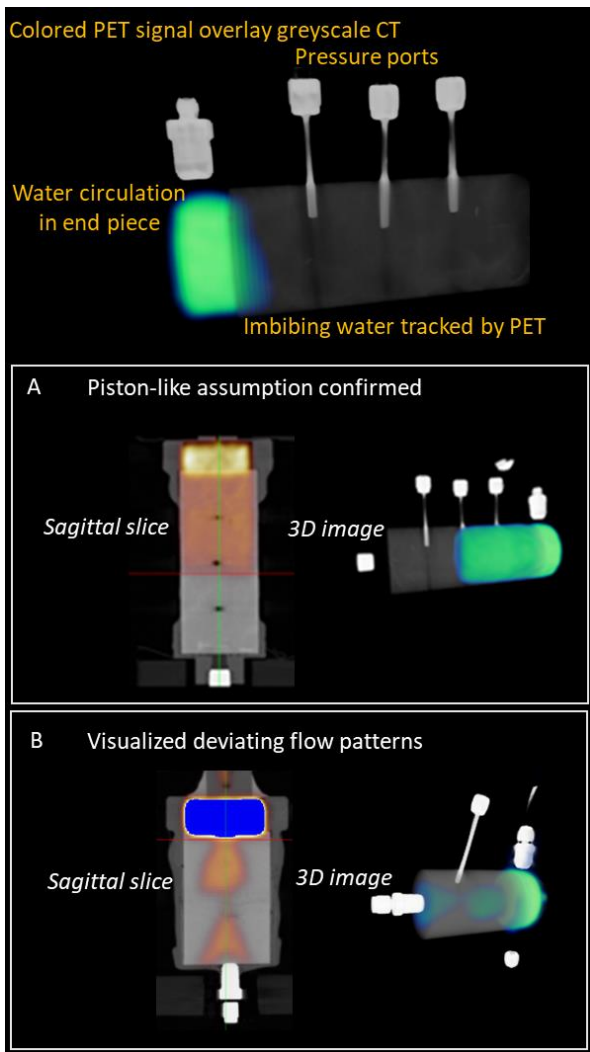


Fig. 8. PET imaging was previously used to confirm piston-like behaviour during spontaneous imbibition [28], and to visualize and explain behaviour deviating from general assumptions [33].

PET imaging can confirm the assumption of piston-like behaviour necessary to extract relative permeability and capillary pressure from spontaneous imbibition data [28], or provide insight to displacement patterns deviating from the general assumptions, where extraction of flow functions would be inaccurate [33]. The referenced works were simple in terms of experimental conditions and equipment: using epoxy-coated cores at ambient conditions. With minor adjustments, however, the high-pressure experimental setup in **Fig. 6**. can be modified for high-pressure spontaneous imbibition at relevant CO₂ storage conditions, applying e.g. the method proposed in Zahasky and Benson [38]. Relevant saturation functions for CCUS can then be extracted from the data set when important assumptions are confirmed by imaging.

3.2 CO₂ utilization (CO₂-EOR)

Combined CO₂ storage and enhanced oil recovery (EOR) can lower the carbon footprint of produced oil, while improving the recovery factor in many reservoirs. PET imaging can provide insight into complex flow systems used for EOR applications; including the flow of complex fluids such as polymers [39], polymer gels [32, 40-42] and foams [10] in heterogeneous and fractured porous media.

Displacement of oil by CO₂ can be imaged by PET similarly to CO₂-brine displacements (**Section 3.1**) using ¹¹C to explicitly label CO₂. Water and CO₂ flow may be explicitly imaged by PET in the same pore network, but each fluid must then be allowed to decay before injection of the other- i.e. only one fluid phase may be imaged at a time. Multimodal imaging by PET-CT [2] or PET-MRI [26] allows for explicit and simultaneous imaging of up to three fluid phases within the same porous medium, with high potential benefits for core scale research.

Foam represents an opportunity to reduce CO₂ mobility, to improve the displacement of oil. Foam is a dispersion of gas separated by liquid lamella, where both foam constituents may often be imaged by PET: aqueous surfactant solution labelled by ¹⁸F-FDG or injected CO₂-foam gas phase labelled by ¹¹CO₂. Brattekkås *et al.* [10] used PET imaging to quantify foam flow in natural fracture networks, where an impermeable matrix ensured fluid flow in the fracture network only. The spatial resolution of PET is too low to facilitate direct observation of foam structure (bubble size etc), but is an efficient tool to establish foam distribution within fractures. PET may also be used to establish improved sweep efficiency within adjacent (permeable) matrix.

Polymer gel is often used for water shutoff purposes, and may also have significant potential in CO₂-EOR applications. Polymer gel reduce fracture conductivity,

without influencing matrix properties; hence, polymer gel placed in fractures improve sweep efficiency by diverting subsequently injected fluids into the matrix. Previous studies showed that the efficiency of polymer gel in EOR is heavily dependent on core wettability, the properties of the fracture-filling gel, and the properties of the chase fluid [43]. CO₂ has several inherent benefits as a chase fluid, such as miscibility with matrix oil. Recent studies demonstrated that PET imaging is an efficient method to establish gel behaviour and matrix sweep during chase floods. Brattekkås *et al.* [32] used PET imaging and ¹⁸F-FDG labelled water to gain insight into dynamics during chase waterflooding of gel-filled fractures. The water injection rate was initially low, and gel rupture was controllably measured: the pattern of gel rupture was found to be heterogeneous within the fracture, and its width could not be derived from global measurements of flow rate and differential pressure. Further, Brattekkås and Seright [31] and Brattekkås and Seright [42] used PET imaging to establish how the rupture channels through gel evolved when the salinity of the injected water-phase was reduced. They proved that gel swelled when contacted by low-salinity water and consequently improved fracture blocking efficiency. The coupled dynamics of gel-swelling with continuous water injection improved matrix displacement in fractured cores. The studies used ¹⁸F-FDG mixed in high-salinity or low-salinity water to explicitly image water flow through the gel-filled fractures and adjacent matrix. The gel was first ruptured using high-salinity water (w/¹⁸F-FDG), which was flushed out or decayed before low-salinity water w/¹⁸F-FDG was imaged. Because of the short half-life of ¹⁸F-FDG, tracing of several water composition was possible within the duration of the experiments; i.e. hours to days. PET imaging was a significant advantage in assessing the behaviour of different water phases within gel-filled fractures: where other imaging methods would require chemical alterations of the water phase(s) or gel (e.g. using D₂O instead of H₂O for MR imaging, or adding sodium iodide for CT imaging) to distinguish the behaviour of the injected phase from gel or previously injected water. The PET signal is not influenced by injected fluids that have decayed, hence the labelled phase is tracked during injection without disturbances from the surroundings.

3.3 CO₂ storage security

PET imaging has significant potential in establishing seal security for CO₂ storage applications. Seal ability to prevent leakage of buoyant CO₂ is important in field scale applications; and demonstration of safe CO₂ storage is crucial to implement widespread CCUS. Fernø *et al.* [25] used a clinical PET-CT scanner to visualize CO₂ flow in tight shale and demonstrated the excellent sensitivity of PET imaging compared to CT in tight, low-porous and -permeable rocks, **Fig. 9**; where a very low volume of ¹¹C-

CO₂ was sufficient for PET quantification of saturation. The uneven fluid displacement within shale, visible by PET, could be tied to structural heterogeneities, visible by CT.

PET imaging could be further used to quantify CO₂ capillary entry pressure in seals by modifying established methods (previously summarized in e.g.

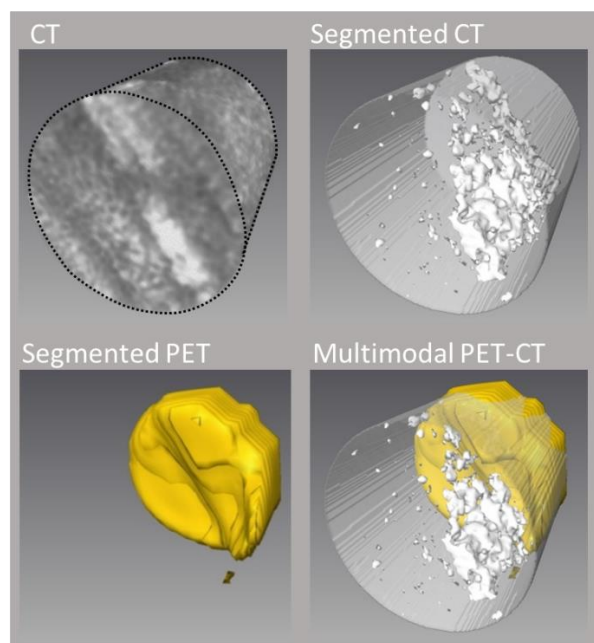


Fig. 9⁵. PET imaging captures the inflow of ¹¹CO₂ in tight shale. The nonuniform displacement front can be tied to structure, visible by CT. For in-depth discussion and results of the experiment showed in the figure we refer to [25].

[44]) for imaging. The established experimental methods (without imaging) applies pressure to CO₂ in contact with the core end face, either stepwise (step-by-step approach) or continuously (continuous injection approach), while pressure and production is monitored and logged. The capillary entry pressure may be calculated from pressure and production data when the cores are assumed to be homogeneous. The same approach may be followed during imaging, applying ¹¹CO₂ pressure at the inlet end face of the core (**Fig. 6**) and monitoring gas entry into the core by PET, and the capillary entry pressure may be extracted by connecting the imaged gas entry to pressure data. The high temporal resolution of PET ensures that the entry pressure is measured at the correct time, and the influence of core heterogeneities is accounted for rather than neglected. Longer-term experiments to assess seal wettability or CO₂ diffusion, which are also important in terms of seal security [45], are more challenging and requires radiotracers with longer half-lives to be assessed by PET.

⁵ A modified version of this figure was first published in *Description of CO₂ EOR and Storage in Tight Shale*

CO₂ storage is most commonly developed in sandstone formations, but carbonates also play an important role in the development and widespread implementation of CCUS: both due to the world-wide abundance of saline aquifers within carbonate formations, and as candidates for CO₂-EOR with combined storage. Acidification of formation brine during CO₂ injection in carbonates may cause dissolution of the rock material and reactive flow patterns are developed that significantly influence fluid flow and, inevitably, carbonate CO₂ storage security. PET imaging enables experimental investigations of reactive transport dynamics at the core scale. Dynamic quantification of dissolution (rate and degree) at the core scale may further support upscaling to larger scales. **Fig. 10** shows preliminary images from an ongoing dissolution study. The CT modality shows structural changes in the core resulting from dissolution. The PET modality shows changes in the preferred fluid flow pattern, consistent with the development of wormholes. Carbonate dissolution and formation of wormholes was previously observed using CT [46, 47]. Multi-modal PET-CT imaging represents a new addition to the experimental portfolio available to study dissolution; by simultaneously connecting the flow of labelled fluids to the structure through which it flows, **Fig. 10**. The unique contribution of PET imaging to dissolution studies is, hence, to non-invasively, dynamically and explicitly study the development of fluid flow patterns. Flow patterns may be tied to minor or major changes in structure by CT scans. CT scans may be performed either dynamic, pre- and/or post- flow experiment imaging. Pre- and post-imaging of micro-CT may than also be applied to visualize structural changes at a much higher spatial resolution.

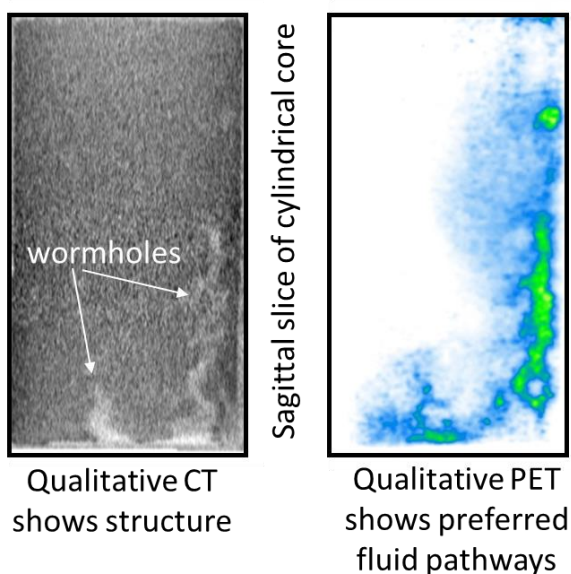


Fig. 10: Dissolution of carbonate during CO₂ or carbonated water injection is often visualized using CT, but PET imaging may be an important contribution. While CT (left) portrays structural changes during dissolution, PET determine dynamic changes in the preferred flow paths within the core.

This work was supported by Norwegian Research Council under project 280341. The authors acknowledge Kristine Fasmer and Kjartan Foldnes for valuable help during radiotracer production and transfer, and PET-imaging. Thank you to Torunn Veien and Olav Parelius Folkvord (UiB MSc students) for providing image data from ongoing dissolution studies. Pre-clinical imaging is routinely performed at the Molecular Imaging Center, Dept. of Biomedicine, University of Bergen. Personnel and equipment associated with the PET-centre at Haukeland University Hospital contributes greatly to the collaboration. The mechanical workshop at the Dept. of Physics and Technology, University of Bergen tailored experimental equipment to our needs, for which the authors are thankful.

References

1. Bailey, D.L., et al., eds. *Positron Emission Tomography*. Basic Sciences. 2005, Springer.
2. Fernø, M.A., et al., *Combined positron emission tomography and computed tomography to visualize and quantify fluid flow in sedimentary rocks*. Water Resources Research, 2015.
3. Zahasky, C. and S.M. Benson, *Micro-positron emission tomography for measuring sub-core scale single and multiphase transport parameters in porous media*. Advances in Water Resources, 2018. **115**: p. 1-16.
4. Krevor, S.C.M., et al., *Capillary heterogeneity trapping of CO₂ in a sandstone rock at reservoir conditions*. Geophysical Research Letters, 2011. **38**(15): p. L15401.
5. Krevor, S.C.M., et al., *Relative permeability and trapping of CO₂ and water in sandstone rocks at reservoir conditions*. Water Resources Research, 2012. **48**(2): p. W02532.
6. Pini, R., S.C.M. Krevor, and S.M. Benson, *Capillary pressure and heterogeneity for the CO₂/water system in sandstone rocks at reservoir conditions*. Advances in Water Resources, 2012. **38**(0): p. 48-59.
7. Pini, R., et al., *Quantifying solute spreading and mixing in reservoir rocks using 3-D PET imaging*. J. Fluid Mech., 2016. **796**: p. 558-589.
8. Brattekkås, B., et al., *New Insight to Wormhole Formation in Polymer Gel during Water Chases*. *Proceedings of the SPE Bergen One Day Seminar*. 2016: Bergen, Norway.
9. Dechsiri, C., et al., *Positron emission tomography applied to fluidization engineering*. Can J Chem Eng, 2005. **83**(1): p. 88-96.
10. Brattekkås, B., et al., *Foam Flow and Mobility Control in Natural Fracture Networks*. Transport in Porous Media, 2020. **131**(1): p. 157-174.
11. Khalili, A., A.J. Basu, and U. Pietrzyk, *Flow visualization in porous media via Positron Emission Tomography*. Phys Fluids, 1998. **10**(4): p. 1031-1033.
12. Kulenkampff, J., et al., *Evaluation of positron-emission-tomography for visualization of migration processes in geomaterials*. Phys Chem Earth, 2008. **33**((14-16)): p. 937-942.
13. Maucec, M., et al., *Imaging of Fluid Mobility in Fractured Cores Using Time-lapse Positron Emission Tomography*, in *SPE Annual Technical Conference and Exhibition*. 2013, Society of Petroleum Engineers: New Orleans, LA, USA.

14. Maguire, R.P., et al., *Positron emission tomography of large rock samples using a multiring PET instrument*. Ieee T Nucl Sci, 1997. **44**(1): p. 26-30.
15. Degueudre, C., et al., *Porosity and pathway determination in crystalline rock by positron emission tomography and neutron radiography*. Earth Planet Sc Lett, 1996. **140**((1-4)): p. 213-225.
16. Emery, G.T., *Perturbation of Nuclear Decay Rates*. Annual Review of Nuclear Science, 1972. **22**(1): p. 165-202.
17. Haugan, A. *A Low-Cost PET System for Use in Flow Experiments of Porous Media*. in *SPE Annual Technical Conference and Exhibition*. 2000. Dallas, Texas.
18. Kulenkampff, J., et al., *Evaluation of positron-emission-tomography for visualisation of migration processes in geomaterials*. Physics and Chemistry of the Earth, 2008. **33**(14-16): p. 937-942.
19. Richter, M., et al., *Positron emission tomography for modelling of geochemical transport processes in clay*. Radiochimica Acta, 2005. **93**: p. 643-651.
20. Gründig, M., et al., *Tomographic radiotracer studies of the spatial distribution of heterogeneous geochemical transport processes*. Applied Geochemistry, 2007. **11**: p. 2334-2343.
21. Zahasky, C., et al., *Positron emission tomography in water resources and subsurface energy resources engineering research*. Advances in Water Resources, 2019. **127**(May 2019): p. 39-52.
22. Rohren, E.M., T.G. Turkington, and R.E. Coleman, *Clinical Applications of PET in Oncology*. Radiology, 2004. **231**(2): p. 305-332.
23. Anand, S.S., H. Singh, and A.K. Dash, *Clinical Applications of PET and PET-CT*. Medical journal, Armed Forces India, 2009. **65**(4): p. 353-358.
24. Bailey, D.L., et al., *Positron Emission Tomography*, ed. M.N. Maisley. 2005: Springer.
25. Fernø, M.A., et al., *Flow visualization of CO₂ in tight shale formations at reservoir conditions*. Geophysical Research Letters, 2015. **42**: p. 7414-7419.
26. Brattekkås, B., et al., *Unlocking multimodal PET-MR synergies for geoscience*. Advances in Water Resources, 2020. **142**: p. 103641.
27. Agency, T.I.A.E. <https://nucleus.iaea.org/sites/accelerators/Pages/Cyclotron.aspx>. 2020.
28. Fernø, M.A., et al., *Quick and Affordable SCAL: Spontaneous Core Analysis*, in *the International Symposium of the Society of Core Analysts*. 2015: St.John's, Newfoundland&Labrador, Canada.
29. Fernø, M.A., et al., *Spontaneous Imbibition Revisited: A New Method to Determine Relative Permeability and Capillary Pressure by Inclusion of the Capillary Backpressure*, in *EAGE 18th European Symposium on Improved Oil Recovery*. 2015: Dresden, Germany.
30. Ruth, D., et al. *Matching Experimental Saturation Profiles by Numerical Simulation of Combined Co-/Counter-Current Spontaneous Imbibition*. in *International Symposium of the Society of Core Analysts*. 2016. Snowmass, CO, USA.
31. Brattekkås, B. and R.S. Seright, *Implications for improved polymer gel conformance control during low-salinity chase-floods in fractured carbonates*. Journal of Petroleum Science and Engineering, 2018. **163**: p. 661-670.
32. Brattekkås, B., et al., *New Insight Into Wormhole Formation in Polymer Gel During Water Chase Floods With Positron Emission Tomography*. SPE Journal, 2017. **22**(01): p. 32-40.
33. Føyen, T.L., M.A. Fernø, and B. Brattekkås, *The Effects of Nonuniform Wettability and Heterogeneity on Induction Time and Onset of Spontaneous Imbibition*. SPE Journal, 2019. **24**(03): p. 1192-1200.
34. Pini, R. and S.M. Benson, *Simultaneous determination of capillary pressure and relative permeability curves from core-flooding experiments with various fluid pairs*. Water resources research, 2013. **49**(6): p. 3516-3530.
35. Zahasky, C. and S.M. Benson. *Phase saturation validation and tracer transport quantification using microPET in a heterogeneous sandstone core*. in *International Symposium of the Society of Core Analysts*. 2016. Snow Mass, Colorado, USA: Society of Core Analysts.
36. Zahasky, C. and S.M. Benson, *Using micro-positron emission tomography to quantify single and multiphase flow in heterogeneous reservoirs*. Energy Procedia, 2017. **114**: p. 5070-5082.
37. Brattekkås, B. and M. Haugen, *Explicit tracking of CO₂-flow at the core scale using micro-Positron Emission Tomography*. Journal of Natural Gas Science and Engineering, 2020. **77**.
38. Zahasky, C. and S.M. Benson, *Spatial and temporal quantification of spontaneous imbibition*. Geophysical Research Letters, 2019.
39. Sandnes, M.F., *Wetting Stability of Aged Limestone in the Presence of HPAM Polymer*, in *Department of Physics and Technology*. 2020, University of Bergen: Bergen Open Research Archive.
40. Brattekkås, B. and M.A. Fernø, *New Insight from Visualization of Mobility Control for Enhanced Oil Recovery Using Polymer Gels and Foams*, in *Chemical Enhanced Oil Recovery (cEOR) - a Practical Overview*, L. Romero-Zèron, Editor. 2016, InTech.
41. Brattekkås, B. and R.S. Seright, *Implications for improved polymer gel conformance control during low-salinity chase-floods in fractured carbonates*. Journal of Petroleum Science and Engineering, 2017.
42. Brattekkås, B. and R. Seright, *The Mechanism for Improved Polymer Gel Blocking During Low-Salinity Waterfloods, Investigated Using Positron Emission Tomography Imaging*. Transport in Porous Media, 2020. **133**(1): p. 119-138.
43. Brattekkås, B., et al., *Fracture Mobility Control by Polymer Gel- Integrated EOR in Fractured, Oil-Wet Carbonate Rocks*, in *EAGE Annual Conference & Exhibition incorporating SPE Europec*. 2013: London, UK.
44. Busch, A. and N. Müller, *Determining CO₂ /brine relative permeability and capillary threshold pressures for reservoir rocks and caprocks: Recommendations for development of standard laboratory protocols*. Energy Procedia, 2011. **4**: p. 6053-6060.
45. Iglauer, S., C.H. Pentland, and A. Busch, *CO₂ wettability of seal and reservoir rocks and the implications for carbon geo-sequestration*. Water Resources Research, 2015. **51**(1): p. 729-774.
46. Menke, H.P., et al., *Dynamic Three-Dimensional Pore-Scale Imaging of Reaction in a Carbonate at Reservoir conditions*. Environmental science & technology, 2015. **49**: p. 4407-4414.

47. Ott, H., et al., *Core-flood experiment for transport of reactive fluids in rocks*. Review of Scientific Instruments, 2012. **83**(8): p. 084501.

Integrated workflow for rotary sidewall cores orientation: best practices and examples from planning to execution

Giorgio Volonté¹, Antonella Bersani¹, Roberto Berto¹, Riccardo Cerri^{1,*} and Fabio Pinelli¹

¹Eni S.p.A., 20097 San Donato Milanese, Italy

Abstract. Over the last five years, the acquisition of rotary sidewall cores has become increasingly important in the O&G business. It is a matter of fact that the current tendency is to prefer them as a replacement to bottom hole cores, essentially for rig time related cost saving. This fact leads to force their use also for those types of characterisation usually reserved to larger size samples so, by consequence, some specific issues associated to their small size and to the lack of knowledge of *in situ* orientation have to be faced. For several applications such as geomechanics (whose experimental analysis require vertical plugs), petrophysics (permeability anisotropy, natural fracture orientation) and sedimentology, the original orientation, or its *a posteriori* identification, is mandatory in order to correctly measure properties relevant for reservoir management and studies. The full orientation of rotary sidewall cores requires to acquire or compute three couples of spatial information: high-side and low-side, wellbore end and formation end, trend and plunge of the samples. A dedicated workflow to *a posteriori* reconstruction of the orientation of large size rotary sidewall cores has been developed by means of the integration of multiple scale imaging techniques: images from logs and sidewall core are integrated through commercial software usually adopted for dip analysis. This approach has been successfully applied to several sidewall cores gathered in different geological environments. Currently, new coring and conveyance technologies allowing a predetermined sidewall cores orientation are emerging, increasing the reliability of the orientation workflow. Therefore, different scenarios of log planning strategy, operational solutions and post-coring analysis can be expected, depending on the confidence in the geological-structural interpretation and on the complexity of the technical environment. In all cases, it is extremely important to plan specific data acquisition and handling operations from wellsite to laboratory; including formalized minimum requirements and dedicated procedures, in order to maximize the quality of the subsequent laboratory analyses.

1 Introduction

The recovery of bottom hole cores (BHC) has always been a significant component of worldwide drilling costs. Over recent years, however, the general trend has become to acquire an increasing number of large size rotary sidewall cores (RSWC) instead, trying to find a balance between reducing costs and ensuring the acquisition of enough material for laboratory analyses. Unfortunately, RSWCs are not currently suitable for several types of characterization usually reserved for larger size samples, since they recover a much lower amount of material than BHCs and their original *in situ* orientation is unknown. The first drawback makes the overall quality of the acquired RSWCs extremely important (in order to maximize the data obtainable from most types of experimental analyses). Moreover, several applications require also the knowledge, or the *a posteriori* identification, of the original orientation of the recovered plug. For example, in petroleum-related experimental geomechanics, this requirement arises from the need to simulate in the laboratory the stress and deformation boundary conditions observable in a reservoir; similarly, the sedimentology can base its studies on oriented thin sections [1]. Furthermore, reservoir characterization often requires oriented permeability measurements [1] or the evaluation of natural fracture distribution also in terms of their spatial orientation [2, 3, 4]. A complete reconstruction of the *in situ* orientation of a RSWC

requires the determination of the following parameters (see Fig. 1 below):

- trend and plunge, which are function of the borehole orientation (hole azimuth and deviation) and of the RSWC azimuth;
- wellbore end and formation end, corresponding to the two opposite sides of the RSWC facing the wellbore and the formation respectively;
- high side and low side, which are the geometrical intersection of the RSWC with the vertical plane.

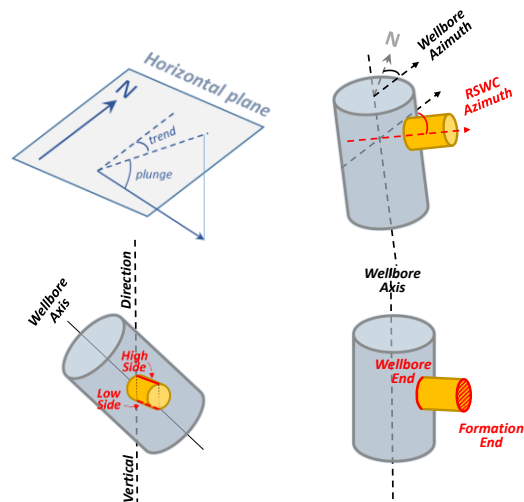


Fig. 1. Reference nomenclature for RSWC goniometry.

* Corresponding author: riccardo.cerri@eni.com

Some of the above parameters, such as the borehole orientation, are generally known or acquired during the operation of coring and logging. The azimuth of the RSWC is not usually recorded during coring operations, unless specific conveyance methods (i.e. tool taxi) are adopted or a dedicated image log is run after coring. Wellbore and formation ends are generally easily identifiable since the most common commercial tools for RSWC acquisition store the samples in the core container with the same side-up (Fig. 2).

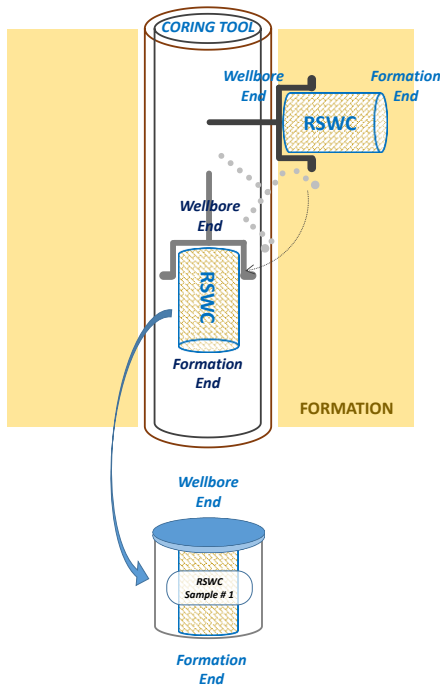


Fig. 2. Recovery of a RSWC.

When RSWC quality is high, this information can also be inferred by inspecting the RSWC: the wellbore end is the borehole wall and it is concave (and usually shows a more polished surface, Fig. 3a), while the formation end can show an indentation generated by the breaking of the RSWC (Fig. 3b) [2, 3].

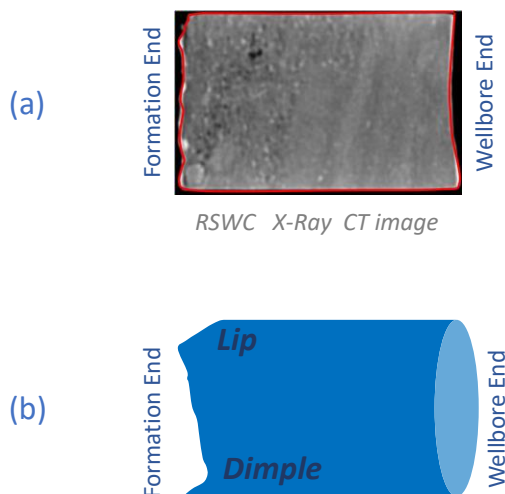


Fig. 3. RSWC characteristics helpful for orientation.

The high/low sides of the RSWC are never recorded during coring. In some cases, where the RSWC quality is particularly good and recovery procedures are known, at least the direction in which the RSWC has been broken by tilting, which corresponds to wellbore axis, can be inferred from the first inspection of the core (lip/dimple in Fig 3b and Fig. 6) [2, 3].

Therefore, to provide an accurate *a posteriori* reconstruction of the parameters describing the *in situ* orientation of RSWCs, a workflow mainly based on laboratory X-Ray CT scans and wellbore log images has been developed by integrating all the available wellsite and laboratory data.

Regardless of the adopted procedure, the *a posteriori* orientation of a RSWC is not a straightforward task and, to maximize the probability of success of this operation, it is extremely important to accurately track all the required data and to preserve the quality of the RSWC along all its lifetime. So, all the recovery, data acquisition and handling operations from wellsite to laboratory have to be specifically planned. In the following paragraphs, the identified minimum operative requirements will be formalized and dedicated procedures will be suggested in order to maximize the accuracy of the orientation process and, by consequence, the quality of the subsequent laboratory analyses. Indeed, orientation is particularly important for some petrophysical properties that strongly depend on the measurement direction (e.g. to validate permeability in anisotropic geological environments).

2 Minimum requirements and procedures for coring

2.1 Job planning and execution

Whenever the orientation of the RSWC is required for the subsequent studies, careful planning of the acquisition operations must be put in place and all relevant information and best practices gathered in a dedicated coring protocol to guarantee the reliability of the dataset required by the orientation procedure. This paragraph dictates the specific requirements that must be followed throughout the coring operations, namely: a) purpose of core acquisition and formation characteristics, b) selection of core samples, c) log acquisition and correlation plan, d) rotary sidewall coring operational procedures, e) wellsite handling of core samples.

a) The objectives of the acquisition must clearly state that the core orientation is requested based on the core analysis purposes. Furthermore, the lithological and sedimentological formation characteristics significant to the acquisition have to be highlighted. The Uniaxial Compressive Strength (UCS) computation from sonic Δt (using the appropriate algorithm calibrated on nearby wells or analogues) has to be provided in order to properly plan the operations.

b) The criteria for selecting number and depth of the sampling points must be defined taking into account the expected quality in terms of size and shape, always in connection with the requirements for the laboratory analyses. The sequence and priority of sampling points

have to be considered; extra cores must be planned when targeting thin beds or bed boundaries, since depth accuracy issues are emphasized.

c) The log suite suggested to support the orientation of the RSWC would better include two image log runs, before and after the coring operation.

- The image log acquired before coring is aimed at defining the formation texture and structure; therefore high resolution image tools are needed where complex and not homogeneous geological environments are expected in order to correctly plan the RSWC coring points; a full coverage image log is not mandatory. The complete logging suite will also allow basic lithological and petrophysical characterization.

- The image log run after coring has the main target to define the correct depth of sampling points and, moreover, the azimuth of the RSWC. Thus, a full coverage view of the borehole wall is needed, since it ensures the location of the holes left by cutting the RSWC. High resolution image logs are not necessary, provided that the quality is enough to clearly identify the coring points.

The two previous targets can be reached by combining image logging while drilling (LWD) and/or wireline (WL) in the safest and most cost effective ways:

- Image log acquisition before the RSWC performed in LWD mode, using either low resolution (e.g. density azimuthal imaging) or high resolution (e.g. resistivity) tools depending on the geological environment complexity; then a WL image acquisition after coring, even with low resolution tools (e.g. ultrasonic).

- WL image log acquisition before and after coring, choosing high resolution tools for the first run when the geology is complex and low resolution otherwise.

- Regardless of whether the image log acquisition before coring is planned in LWD or WL mode, it can be provided in LWD mode after coring if a wiper trip is needed.

d) Depending on the available tool, dedicated coring and breaking procedures to maximize the RSWC recovery and quality must be selected on the based on the formation characteristics and the well environment (mud type, overbalance, solids content etc.). Recommendations must be detailed and strictly followed for approaching each station, by reducing the speed and according to the well depth, to minimize both the cable stretch and creep; finally, a dedicated tripping out procedure must be pursued according to the formation petrophysical and lithological characteristics and well environment conditions.

e) All wellsite surface procedures are aimed at minimizing damage during handling and shipping to the laboratories. Particular care is needed to preserve the RSWC order of collection within the container and its formation end/wellbore end orientation. The documentation must include for future reference a close-up picture of each core in the container before its removal (Fig. 4) This is crucial when no core separators are used due to tool design and/or well deviation [5].

Care is recommended when wiping off the samples and packing them in the transportable jars with the wellbore end facing up. Additional wrapping of the sample is

required with plastic or aluminium foil on which red and black parallel lines should be marked to preserve the correct sequence and top/bottom ends of the samples (red on the left, facing the core from wellbore end towards formation end) (Fig. 5). Shock adsorbing materials to stabilize the RSWC inside the containers are always suggested to preserve the sample integrity.

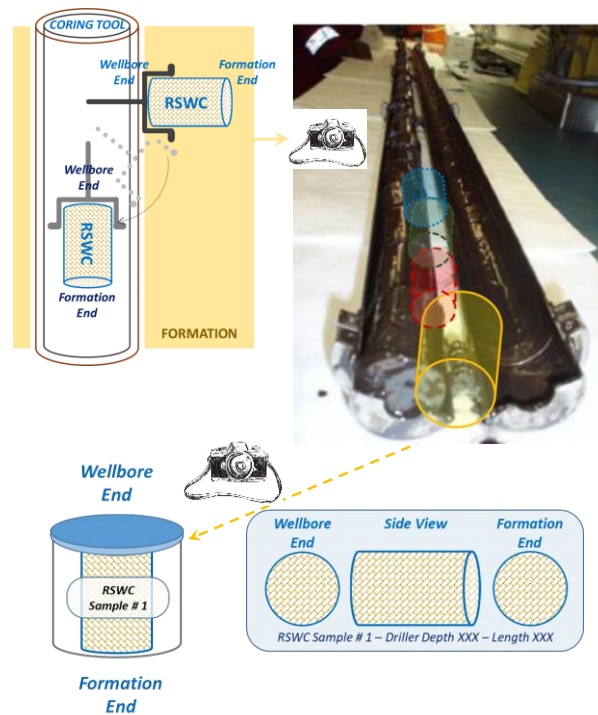


Fig. 4. Suggested pictures to be acquired on site.

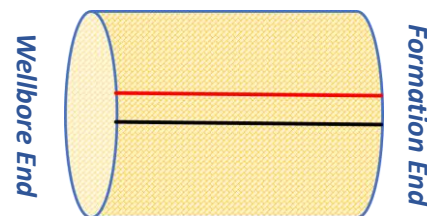


Fig. 5. Marking of RSWC packing to track formation/wellbore ends.

2.2 Laboratory processing of samples

The procedures to be observed when receiving and handling sidewall cores are analogous to those adopted for bottom hole cores: it is mandatory to treat them with great care in order to avoid mechanical shock; to protect them from extreme temperatures, humidity and dehydration and to limit as much as possible the use of fresh water to

clean them. Labelling and marking require even greater attention. In fact, it is extremely important to preserve the proper sequence and core orientation ensuring that individual samples are not out of order or turned upside down.

More in detail, specific actions have to be performed in terms of: a) wellsite data retrieval; b) visual inspection of the core and RSWC labelling and marking; c) RSWC photos; d) X-Ray CT scan.

a) Generally speaking, all the coring-related well site data should be retrieved. In particular, the following cannot be neglected: coring parameters (weight on bit, rate of penetration, coring time, etc.); sample description, included its quality (intact, fractured, broken, crumbled, etc.); effective length and diameter of each recovered sample; trace of the wellbore/formation ends of the sample, according to the established conventions (see Fig. 5).

b) It is mandatory to preserve the correct sequence of the samples and their orientation, properly labelling and marking each RSWC. This implies the validation of the collected field data through a visual inspection of the core and, when possible, the data integration through the determination of the direction in which each RSWC has been broken by tilting, which corresponds to wellbore axis (Fig. 6).

The red and black parallel lines drawn at wellsite on the external surface of the wrapping must be transferred onto the RSWC sample. Moreover, to provide a further reference for the subsequent operations, it is recommended to draw the double line along the upper side with respect to the determined tilting direction, if previously identified.

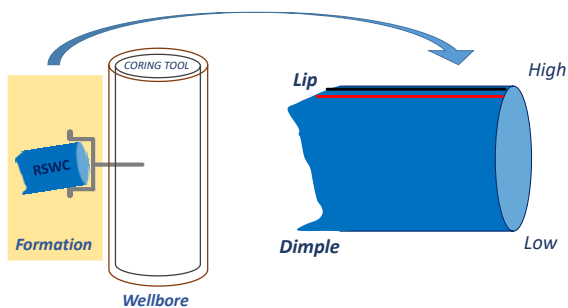


Fig. 6. Marking of RSWC to track the identified formation and wellbore ends

c) A complete set of RSWC photos (Fig. 7) should be acquired. Wellbore end, formation end and side views must be photographed, taking care to correctly mark the references. A comparison with the wellsite photos is also recommended to confirm the RSWC ends identification (see Fig. 4).

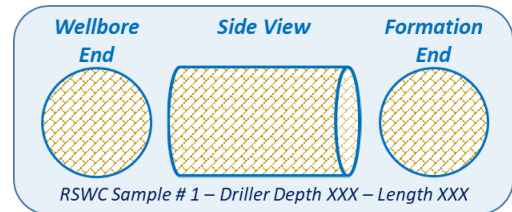


Fig. 7. Suggested views for RSWC photos at the laboratory.

d) A 3D X-Ray Computed Tomography of the sidewall core must be acquired at the maximum feasible resolution (the typical resolution of a medical CT scanner, 250 μm , is assumed satisfactory in most of the cases) A 2D 360° unrolled image must be extracted from the acquired volume, by following the maximum possible circumference, compatibly with the surface roughness. This picture is the main input for the goniometry procedure described in section 3. Moreover, it is mandatory that the position of the starting point of the unrolled images be recorded and recoverable on the sample. This starting point position (left border of the 2D image) should be measured as the angle from the line representing the side corresponding to the tilting direction, if its estimate has been possible. A corresponding reference notch or sign must be created on the RSWC.

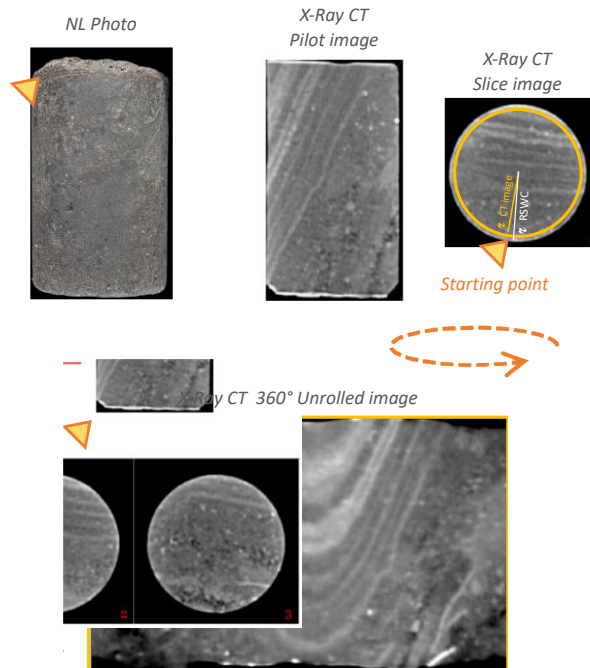


Fig. 8. RSWC Imaging.

3 The sidewall core goniometry procedure

The proposed “Eni SideWall Core Goniometry” (e-SWCG) procedure has been developed in order to provide an exhaustive methodology for the *a posteriori* reconstruction of the original *in situ* orientation of RSWCs. As described in Fig. 1, the determination of three main variables is required: wellbore/formation ends, RSWC azimuth and high/low sides.

The e-SWCG workflow is based on the identification of geological features (layering, fractures, stylolites, etc.) that are recognizable both at the laboratory scale on the X-Ray CT image of a RSWC and at the well scale on the image logs. Since these two scales are very different, to properly apply this procedure, the analysed large size RSWC must honor a diameter as close as possible to the nominal one (1.5”) and a minimum length around 1.5”. By consequence, lithologies without features detectable at both image scales of resolution or smaller diameter RSWC are not suitable for this approach.

The workflow starts with the 3D X-Ray CT acquisition of the analysed RSWC. Then, a 360° unrolled image is extracted from the volume; this unrolled “sampling” must be obtained at the maximum possible radius able to avoid the external surface roughness (Fig. 9).

The unrolled X-Ray CT image is converted into a digital borehole image format, uploaded onto an image analysis software platform and treated in the same way as an image log with its own deviation coordinates: inclination and azimuth. The top of the unrolled image is assumed to be coincident with the wellbore end of the RSWC.

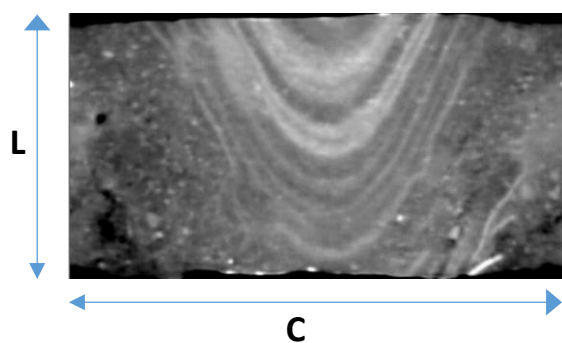


Fig. 9. Unrolled X-Ray CT image of a RSWC, where L is the length and C is the circumference. The actual image diameter is 1.34” (see field case of paragraph 4.2).

Since the commercial software platforms for log analysis usually manage the data loading according to the borehole depth and the sidewall core is oriented at 90° with respect to the well axial direction, the unrolled image has to be loaded assuming the following rules to preserve its correct aspect ratio:

- Top: Core wireline depth – 0.5L;
- Bottom: Core wireline depth + 0.5L;

where L is the length of the RSWC.

Bedding planes, fractures or other geological features must be identified and manually interpreted on both RSWC and log images.

The geological feature visible on the image log is oriented by picking the sinusoid and the corresponding tadpole will be generated (see 4th track on Fig. 11).

This tadpole, which represents a plane specifically oriented in space (true dip), has to be replicated on the RSWC image. The amplitude and offset (apparent dip) of the sinusoid drawn on the core image depend on the three unknown orientation variables.

To obtain the original orientation of the RSWC, the three variables must be tuned until the geological feature visible on the RSWC image matches exactly the sinusoid. The final orientation is best achieved step by step with a trial and error procedure. If the orientation variables are all unknown, it is suggested to start the procedure from the four base cases shown on Fig. 10 and then fine tuning the variables starting from the case that provides the best match.

The e-SWCG procedure allows the unique determination of the vertical direction along the RSWC, which is an essential input for the subsequent studies. On the other hand, an ambiguity of 180° persists on azimuth and high/low sides: in fact, two opposite choices of azimuth and wellbore/formation end of the RSWC can both honor the image log evidence. This ambiguity can be removed, as previously outlined, by providing additional information through one of the following actions:

- by observing the azimuth on an image log acquired after the coring, or
- by adopting coring tools allowing the user to define in advance the azimuth, or
- by identifying the high side from the RSWC topology, but only in vertical wells; or
- by recognizing the wellbore end by inspecting the physical RSWC, the RSWC pictures or the RSWC CT Scan images.

Once the match is achieved on the images, the final step consists of physically orienting the sample. The obtained inclination of the unrolled image coincides with the true inclination of the RSWC and the lateral shift (expressed as angle) of the unrolled image corresponds to the rotation to be applied to the RSWC initially positioned with the reference line up. This information should be provided to core analysts in order to reproduce the true orientation of the RSWC in laboratory before going ahead with analysis.

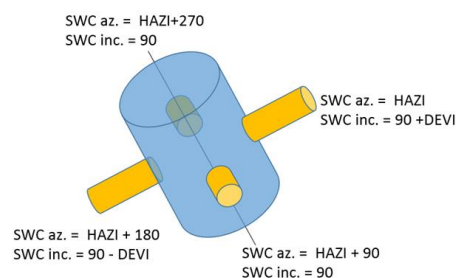


Fig. 10. Possible orientations of a RSWC with respect to a deviated well: blue cylinder represents the borehole and the 4 orange cylinders represent the RSWC in 4 base cases of the

possible orientations: 2 cases on the plane of the borehole direction and another 2 orthogonal to the previous ones.

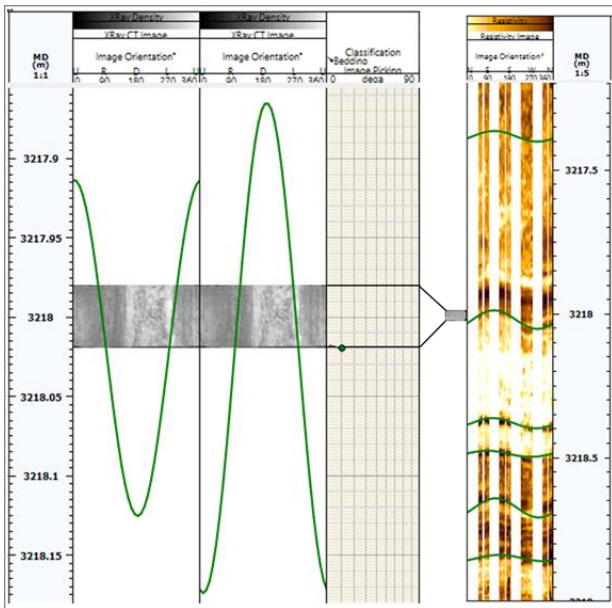


Fig. 11. Green sinusoids represent the bed boundary picked on the image log but show different attitudes because the orientation of the RSWC images are offset by 90° from each other.

4 Case histories

The two field applications of the e-SWCG procedure presented in this section are related to wells that are very different in terms of lithology, borehole environment and, more importantly, *a priori* knowledge of the RSWC orientation. In the first case, all the variables were unknown, while in the second the RSWC azimuth was predefined using a specific conveyance method (tool taxi). Both case histories successfully provided the correct parameters to orient the physical rock samples.

4.1 Carbonate reservoir

The first case is related to a sub-vertical deepwater well crossing Cretaceous to Miocene carbonate shelf and reef build-ups. WL resistivity images at very high vertical resolution were acquired in a 12.25" borehole with water based mud (Fig. 13). On the RSWC, a lamination pattern is visible at low angle with respect to the core axis (Fig. 14). On the image logs, many bed boundaries are well recognisable at the surrounding depth of the SWC, the sequence being well laminated and the borehole imaging at very high resolution (Fig. 13). The bed boundary closest to the RSWC depth has an attitude of 10° dipping toward W. The exercise of orientation of this RSWC is to match the lamination of the RSWC with the sinusoid from the image log interpretation.



Fig. 12. Side view in white light photo of carbonate RSWC (wellbore end on the right side).

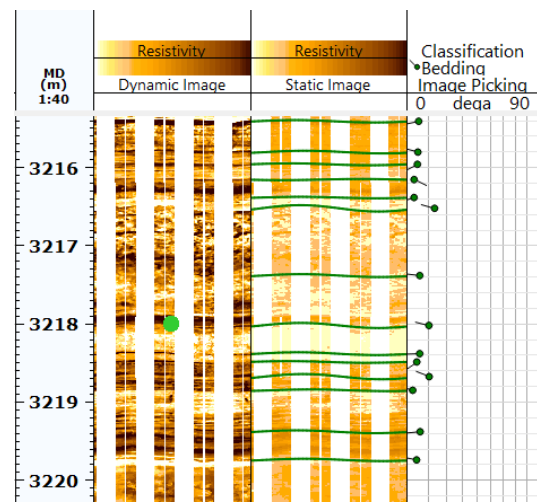


Fig. 13. Image logs and picking in the interval surrounding the carbonate RSWC.

For this RSWC, all three orientation variables, defined in paragraph 1, are unknown because the RSWC azimuth was neither measured nor imposed *a priori*. For this reason, the search for the match was started by trying the 4 RSWC azimuths corresponding to the 4 base cases of Fig.10 and selecting the case with the closest match. Then, the one in which the best-fitting feature has an orientation as close as possible to the sinusoid was selected. To improve the match quality, fine tuning was also performed by applying a further rotation of 25° to the RSWC image and the final match was obtained (Fig. 14).

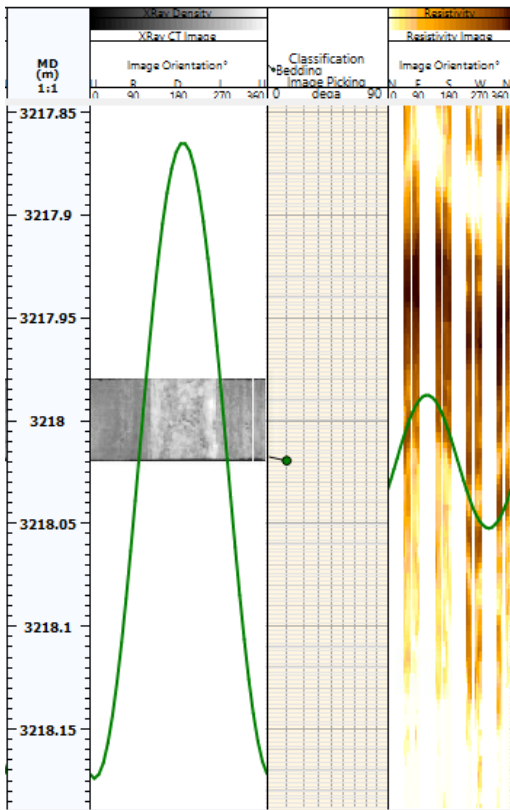


Fig. 14. Final match of carbonate sample.

4.2 Clastic reservoir with conveyance tool

The second case was an offshore 40 slanted well drilled through a Pliocene deltaic to turbiditic siliciclastic sequence where several RSWCs were cut inside the sandstones. The 12.25" phase in the reservoir section was drilled using oil based mud and the available image log was Density LWD with low vertical resolution. One of the RSWCs was taken in a portion of rock where laminations are well visible at the image log scale. On visual inspection, the core sample is apparently homogeneous without sedimentary laminae (Fig. 15), whereas the X-Ray CT shows that it is actually well laminated, with the layering displaying a high angle with respect to the RSWC axis (Fig. 9). Fig. 16 shows the LWD density image including the bedding interpretation. At the RSWC depth, the bedding inclination is between 10° to 20°, dipping toward NNW.



Fig. 15. Side view in white light photo of siliciclastic RSWC (wellbore end on the left side).

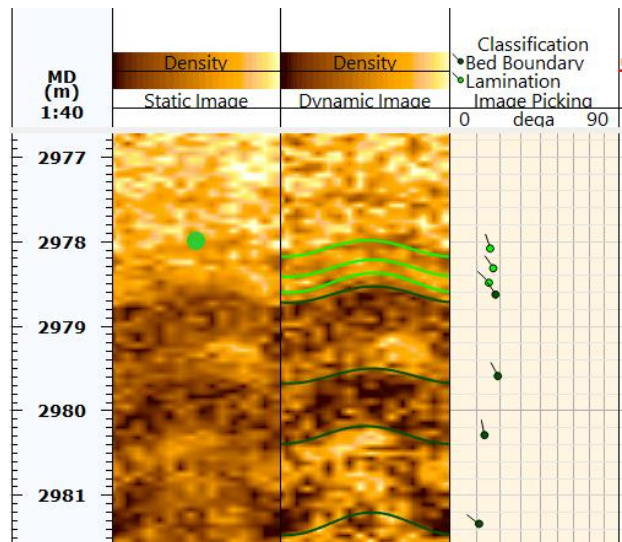


Fig. 16. Image logs and picking in the interval surrounding the siliciclastic RSWC.

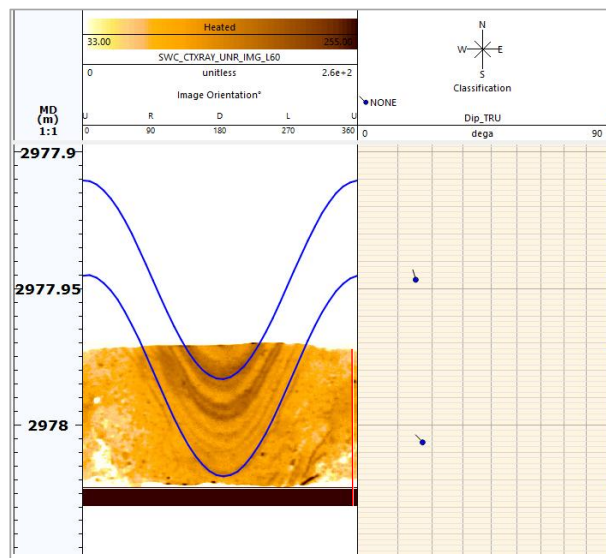


Fig. 17. Final match of clastic sample.

The RSWC azimuth and inclination are known because the coring tool was run with the tool taxi and the RSWC was taken in the lower side of the borehole. The wellbore end information was preserved during the wellsite recovery from the core barrel. The only unknown variables are the high and low sides of the RSWC. The match between sinusoids and laminations was achieved by choosing the right angular offset of the RSWC, which means a 10° lateral shift on the RSWC image. The position of the reference line can be used to orient the real sample (Fig. 17).

5 Conclusions

The original *in situ* orientation of RSWC is a fundamental input for obtaining reliable results from geological studies

and for the proper execution of experimental analyses. The e-SWCG procedure presented in this paper can deliver a complete *a posteriori* goniometry of the RSWC, provided that an appropriate core and log acquisition program has been planned, as well as correct handling operations at wellsite in order to obtain and accurately track all the data needed for the orientation procedure. Moreover, the overall quality of the acquired RSWC is extremely important to maximize the data that can be recovered through experimental analyses and studies from an inherently more limited amount of material with respect to BHC. The presented case studies highlight the possibility of applying the orientation procedure in different geological contexts. Particularly, the case history on carbonates shows the reliability of the procedure even with limited data. On the other hand, the example related to a clastic reservoir emphasizes the advantages of using coring tools providing greater control on RSWC positioning.

The authors gratefully thank Eni S.p.A. for the authorization to publish this work, and colleagues Mauro Rossi for his valuable collaboration in X-Ray CT image acquisition/processing and Anna Maria Lyne for the manuscript review.

This paper is dedicated to the memory of our dear colleague and friend Sandro Atzei, who recently passed away.

References

1. D.K.T. Hansen, M.B. Enderlin, "Petrophysical significance of oriented sidewall cores for improved reservoir characterization", in Worthington, P.P., and Longeron, D., eds., *Advances in core evaluation II - reservoir appraisal*, p. 135-144 (Gordon and Breach Science Publishers, 1991)
2. B. A. Hardage, E. Doherty, S.E. Laubach, F. T. Hentz, "Secondary Natural Gas Recovery in the Appalachian Basin: Application of Advanced Technologies in a Field Demonstration Site, Henderson Dome, Western Pennsylvania", PhD Thesis Bureau of Economic Geology The University of Texas at Austin Austin, TX (1998).
3. S.E. Laubach, E. Doherty, "Oriented Drilled Sidewall Cores for Natural Fracture Evaluation", *SPE Annual Technical Conference and Exhibition*, (SPE56801, 1999).
4. J.F.W. Gale, L.A Gomez, "Late opening-mode fractures in karst-brecciated dolostones of the Lower Ordovician Ellenburger Group, west Texas: Recognition, characterization, and implications for fluid flow", *AAPG Bulletin*, **91**, 7, p. 1005-1023 (2007).
5. V. Torlov, C. Bonavides, A. Belowi, "Data Driven Assessment of Rotary Sidewall Coring Performance", *SPE Annual Technical Conference and Exhibition*, (SPE187107-MS, 2017).

Rock Image Enhancement Using Super-Resolution Neural Networks

Bo Gong* and Paul Duke

Chevron, 1500 Louisiana St, Houston, TX 77002, USA

Abstract. Pore-scale rock properties can be estimated from core images through image-based calculation or numerical simulation. However, accuracy of the estimation is directly limited by the resolution of the applied imaging technique, leading to uncertainties in interpretations. Imaging at an extremely high resolution can be time-consuming and expensive, and hence is usually done on selected samples, but the imaged area or volume is often not large enough to represent the formation heterogeneity. The method presented in this work helps resolve the trade-off between image scale and resolution in heterogeneous rocks. By training and applying a super-resolution convolutional neural network, pore-scale details can be effectively learned and reconstructed using relatively low-resolution images acquired in large rock volumes. Backscattered electron microscopy images and microCT images were acquired at multiple resolutions, and used for training and testing the models. Results showed that a properly trained model could increase image resolution by up to eight times, even when the training images appeared to be significantly different from the test images. Compared to bicubic interpolation techniques, the presented method resulted in more realistic visualization, as it better preserved the sharp edges of pore spaces.

1 Introduction

Rock imaging techniques, like X-ray computed tomography (CT), microtomography (microCT), scanning electron microscopy (SEM), and confocal microscopy, allow earth scientists to visualize and analyze rock samples in extremely fine detail. The ability to characterize micrometer- and nanometer-scale features, such as pore size, grain surface roughness, and mineral composition, is critical for understanding fluid flow behaviors in subsurface reservoirs, which in turn impacts reservoir production forecast and development decisions. With digital rock physics techniques, numerical simulations can be conducted on 2D or 3D images to study static and dynamic properties of the imaged rock systems.

Typically, the physical size of rock samples being imaged is directly linked to the resolution of the image: higher-resolution images are usually acquired on samples with smaller sizes, as they are relatively more expensive and time-consuming to acquire on large samples. Lower-resolution data (coarser images) are more available on larger volumes, which may be more statistically representative for the properties of interest, but accuracy of the resulted interpretations could be compromised because of the loss of fine details.

In heterogeneous rocks with complex pore systems, properties estimated with any image-processing-based methods could be especially sensitive to the image resolution. An example is demonstrated in **Fig. 1**. A backscattered scanning electron microscopy (BSEM) image of a carbonate rock sample was down-sampled by 2 times (2x), 4 times (4x), 8 times (8x) and 16 times (16x).

The original image has a resolution of 1 μm per pixel. The reduction of image quality by down-sampling can be seen from the comparison of **Fig. 1(a)** and **Fig. 1(b)**, where a section of the original (1x) image and the 16x down-sampled image are shown.

Pore size distribution was estimated on the original and all four down-sampled images using the maximum inscribed sphere method (modified for 2D images) described in [1]. As shown in **Fig. 1(c)**, pore size distribution is strongly impacted by the reduced resolution. The pore sizes estimated from the 8x and 16x down-sampled images failed to maintain the bi-modal distribution seen on the original image, whereas the 4x down-sampled image showed a shifted left peak, because small pores close to or below the degraded resolution were clustered into larger, artificial “pores”. This exercise suggests that even the same rock sample imaged at different resolutions could result in very different interpretations on pore space geometries, introducing high uncertainties into reservoir quality prediction. This effect was further discussed in [2] and [3].

Numerous methods have been explored in the past to improve the perceptual image quality [4]. Standard interpolation methods can reduce the pixelation effect on the low-resolution images, but they do not preserve high-frequency features very well and result in blurry images. Statistical methods like [5] and [6] aim to improve the preservation of sharp details, but often rely on image priors like gradient profiles and total variation, the extraction of which may be time-consuming.

To help resolve the trade-off between image scale and resolution in heterogeneous rocks, we present a new workflow to digitally enhance image resolution with a

* Corresponding author: bo.gong@chevron.com

minimal amount of acquisition. By training and applying a super-resolution convolutional neural network, high-resolution images can be reconstructed from low-resolution images, while preserving details like pore throats and angular corners of pore spaces. We first apply the method to synthetically generated low-resolution BSEM images, and then test it on manually acquired BSEM and microCT images. Besides using the traditional metric, means squared error (MSE), to compare the pixel-by-pixel similarity of the predicted and the target images [7], we also calculate pore size distribution to demonstrate the impact of the enhancement on petrophysical interpretations.

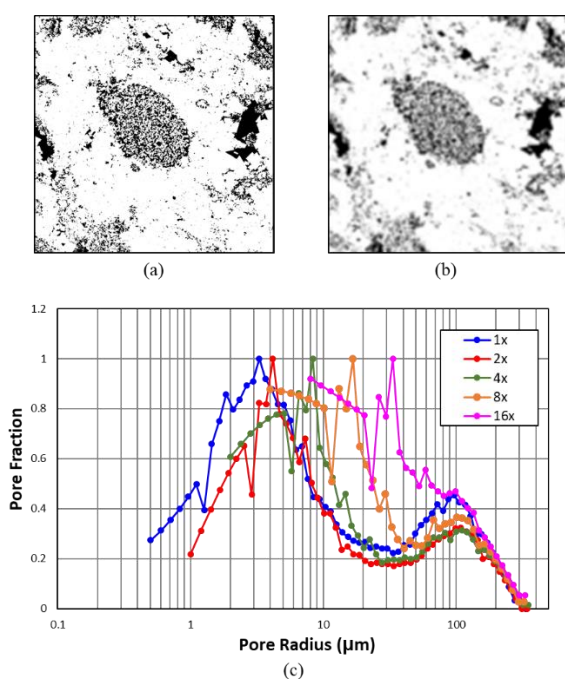


Fig. 1. Pore size distribution estimated from images of different resolutions show very different characteristics. (a) A section of the original image (1x); (b) The same section of the original image down-sampled by 16 times (16x). (c) Pore size distribution computed from the original image and four down-sampled images. Microporosity (left peak) is no longer captured on 8x and 16x images.

2 Image super-resolution using deep learning

Super-resolution refers to the process of reconstructing a high-resolution image based on one or more low-resolution images [4]. The objective is to recover details that have been lost during data compression, transmission, or low-resolution acquisition. Due to the non-unique nature of the problem, multiple solutions exist for the same low-resolution image. Therefore, the reconstruction requires the guidance of certain a-priori knowledge, which could be obtained either through feature extraction beforehand, or through example-based learning. Deep learning algorithms have made automatic learning possible, so a trained model could approximate the mapping from low-resolution images to high-resolution with minimal user intervention.

Convolutional neural network (CNN) is a type of deep-learning algorithms that are commonly used for image recognition and classification. Designed to handle 2D data, CNNs can effectively optimize the mapping from input images to output images by changing the weights between different layers of nodes (“filters”), based on the tasks they are trained on. Super-Resolution Convolutional Neural Network (SRCNN) [8] was specifically designed for image restoration using the basic architecture of CNNs. With low-resolution images paired with the corresponding high-resolution images, the model could learn the non-linear relationship between inputs and targets, and establish the rules to enrich image quality without creating anything inconsistent with the context. Information in the high-resolution images helps constrain the reconstructed rock texture, so that the enhanced images resemble the sampled rock facies. Different variants of SRCNN models were applied to synthetically down-sampled microCT images in [9], which showed high enhancement accuracy at a scale factor of 4.

U-Net is a CNN model type originally developed for medical image segmentation [10]. One challenge with plain CNNs is that certain information gets lost as it goes deeper into the network, e.g., the spatial relationship among different edges and corners is not maintained, so it may encounter issues with feature localization. Such problems are overcome in U-Net through the use of shortcut connections between corresponding layers, preserving spatial information as much as possible. As a result, U-Net is capable of delivering good performance with a relatively small training data set. This is especially beneficial for core image analysis, where data acquisition is usually costly. [11] shows that U-Net can be modified for image super-resolution with better performance than a simpler SRCNN.

In this study, we experimented with both SRCNN and U-Net for core image enhancement and compared their performances.

3 Super resolution on synthetically generated low-resolution images

3.1 Data preparation

We first used synthetically generated images to explore the enhancement limit, since arbitrary resolutions can be created for the training data.

Two BSEM images of a carbonate rock, S-01 and S-02, were selected for building and evaluating the models, as shown in **Fig. 2**. Each image has $32,768 \times 32,768$ pixels, with a resolution of $0.25 \mu\text{m}$. We used only S-01 to create the training set, and reserved S-02 as a blind test image.

S-01 was first down-sampled, or coarsened, to lower-resolution images. Four levels of low-resolution images (2x, 4x, 8x and 16x) were created as input images of the training data. Each low-resolution image was then up-sampled to create a blurred image which matches the number of pixels with the original high-resolution image using bicubic interpolation. Because of the large size of the BSEM images, the blurred images and the original image were sectioned into sub-images, each having

128×128 pixels. This process and the resulted sub-images are illustrated in **Fig. 3** and **Fig. 4**. Each level yielded 65,536 sub-images.

3.2 Model training and results

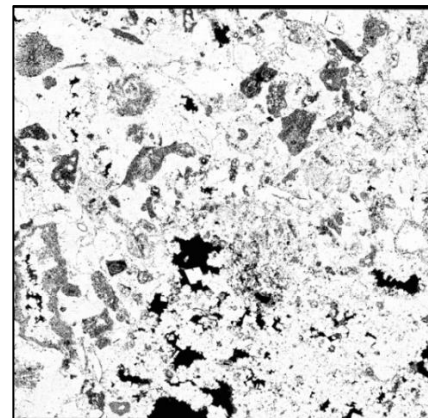
Two approaches were taken with the SRCNN method. In the first scenario, we built separate, fit-for-purpose models to enhance specific resolutions. Each model was exclusively trained on images of a certain resolution. Those models were then tested on the corresponding low-resolution images they were designed for. In the second scenario, a single model was trained with all levels of input images, this is referred to as the “mixed model”. In practice, a mixed model would be more desirable than separate models, because it offers flexibility in the resolution of input images. This is essential when images are acquired in different batches or stages, and the resolutions are inconsistent. With a mixed model, one does not need to train a new network each time when new images of a different resolution become available.

Considering the practicality and efficiency of the mixed-model approach, we trained two mixed models, one with SRCNN, the other with U-Net. The MSEs of the reconstructed images for the different models are plotted in **Fig. 5**. A bicubic baseline was also included for reference. With the architecture of SRCNN, although the separate models performed slightly better than the mixed models on each level, the latter produced promising results, with a much higher accuracy than bicubic interpolation. The U-Net mixed models outperformed the SRCNN separate models on all levels except for 2x, where they produced similar results.

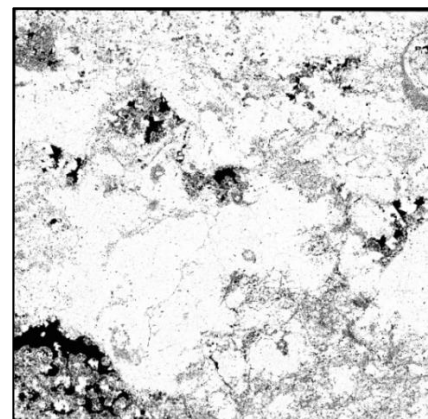
The advantage of the U-Net mixed model can also be seen in **Fig. 6**, where the 16x enhanced images from both mixed models are shown. Even though many of the details are lost beyond the recovery limit because of the high scale factor, the U-Net model seems to have better preserved the edges of the pore spaces than the SRCNN model (see features in the red boxes).

With the U-Net mixed model, we investigated the limit for image recovery with CNNs. **Fig. 7** shows the enhancement results of the U-Net mixed model from different levels of down-sampled images. For the 2x and 4x enhancement, the reconstructed images are very close to the original, with little details missing. On the 8x enhanced image, some small pores start to disappear (red

boxes) or cluster with nearby pore spaces (blue boxes), but most of the edges and corners of larger pore spaces are still well preserved. On the 16x enhanced image, pore spaces are further rounded, and the microporosity seen on the original image is visibly lost. An 8x enhancement appears to be the limit of reliable resolution recovery with CNNs, based on visual assessment. Beyond that level, small features like pore throats and angular pore spaces are smoothed out to an unacceptable degree, which would lead to biased interpretations.



(a)



(b)

Fig. 2. Two visually different BSEM images were selected for building and evaluating the models. (a) S-01, image used to create the training set; (b) S-02, image reserved for out-of-sample testing.

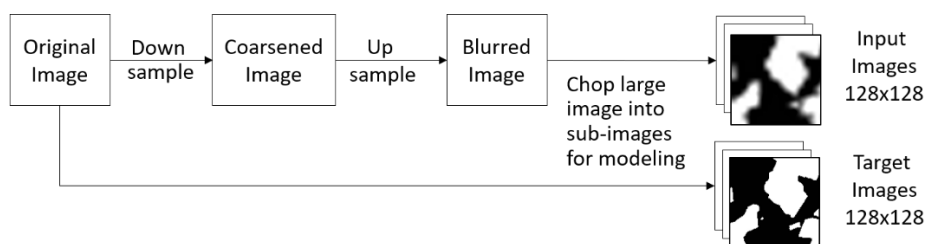


Fig. 3. Creating input and target images for the training set by degrading the original image.

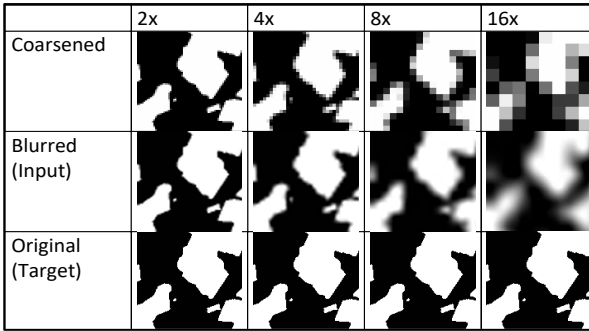


Fig. 4. Sub-images (128×128 pixels) created for model training.

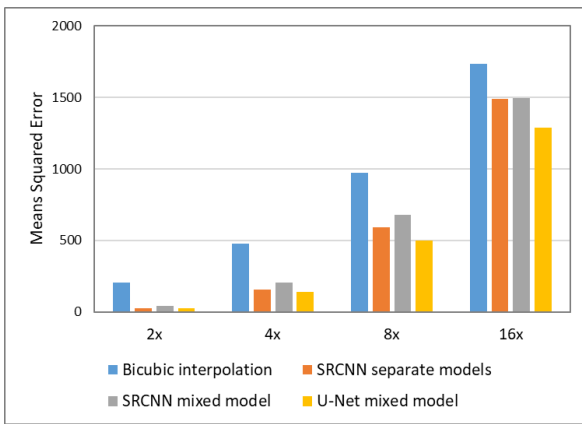


Fig. 5. Mean squared error (MSE) of enhanced images from different models, implemented on test image S-02.

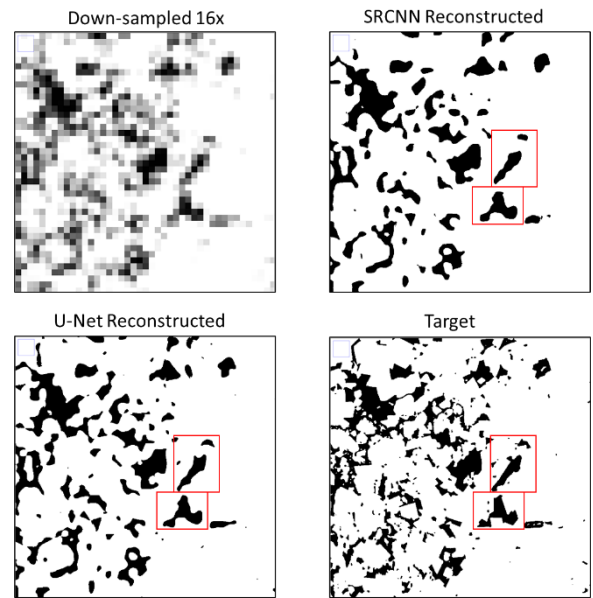


Fig. 6. Comparison of images enhanced with SRCNN and U-Net mixed models.

Besides the perceptual image quality, it is also important to examine the impact of the enhancement on the properties derived from the images, because the ultimate goal for core image enhancement is not pixel-by-pixel recreation, but the maximum preservation of the rock properties of interest. As an example of petrophysical properties, pore size distribution was calculated to evaluate the effectiveness of the feature reconstruction, using the method described in [1]. The results are plotted in (a)8.

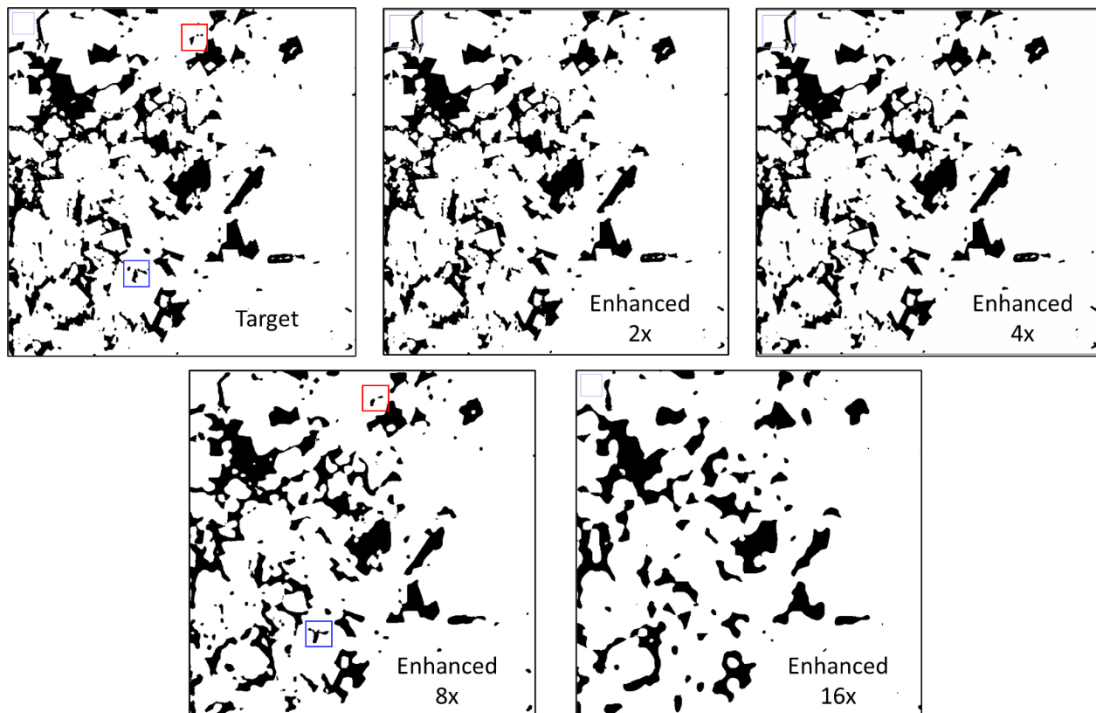


Fig. 7. A 170 μm × 170 μm section of target image, with the same area of four enhanced images at 2x, 4x, 8x and 16x. The enhanced images were reconstructed from down-sampled images with a U-Net mixed model.

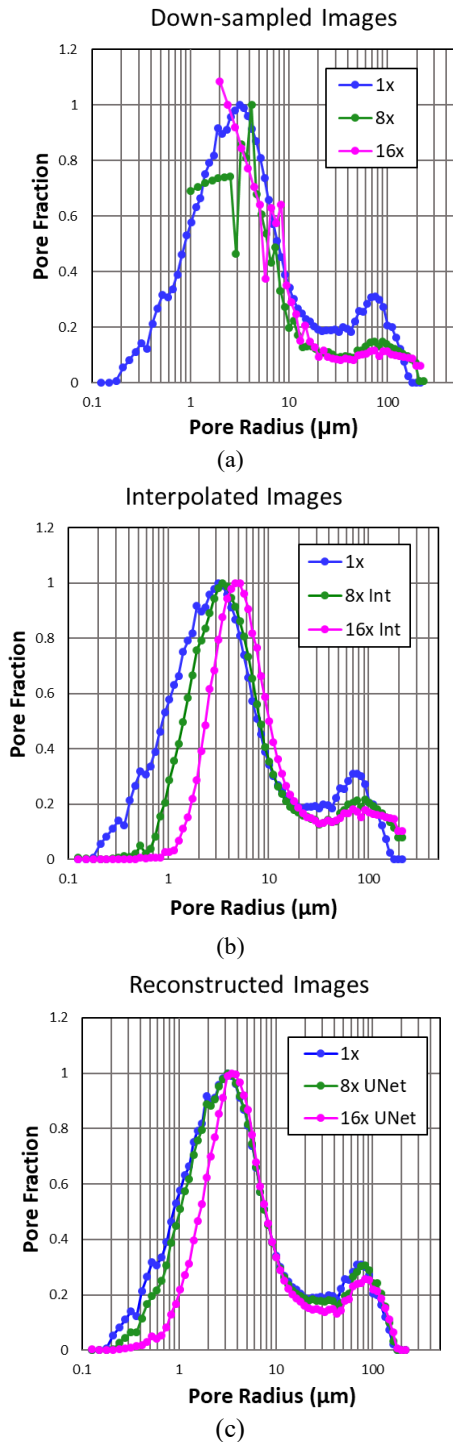


Fig. 8. Comparison of pore size distribution calculated with down-sampled, interpolated, and U-Net reconstructed images, compared with the original (1x). (a) Images down-sampled by 8x and 16x, and segmented by thresholding. (b) Images down-sampled by 8x and 16x, and interpolated to match the original image size. (c) Images down-sampled by 8x and 16x, and reconstructed with the U-Net mixed model.

(a) shows the pore size distributions calculated on two down-sampled images (8x and 16x), compared with the original (1x). Impacted by the image degradation, not only a large amount of the microporosity (left peak) was missing on the down-sampled images, but the secondary porosity (right peak) was also smoothed out due to the

resolution reduction. (b) shows the results calculated from images that were first down-sampled by 8x and 16x, and then interpolated to match the original image size. The 8x interpolated image recovered the location of the left peak, but failed to capture a large portion of the pores smaller than 2 μm (radius smaller than 1 μm). A larger amount of microporosity is lost on the 16x interpolated image. Moreover, the location of the left peak is shifted to the right, with the peak radius almost doubled. Both the 8x and 16x interpolated images resolved the right peak better than the down-sampled images, but a smoothed-out effect can still be seen.

In contrast, the U-Net reconstructed images showed a better performance, as shown in Fig. 8). The 8x enhanced image preserved the bi-modal pore size distribution very well, with only a small difference on the pores that have radius less than 1 μm. This indicates that the statistical impact on pore sizes is insignificant. The 16x enhanced image did not fully recover the left peak, but its location is almost identical to the original. Both the 8x and the 16x enhanced images produced the right peak with a good resolution.

For core image interpreters, it is essential to determine what level of recovery is truly necessary, since different applications call for different precisions. In this example, if it is known that pores smaller than 2 μm play a critical role in the studied rock, the 8x enhancement would be preferable to the 16x. However, if a task only requires the identification of the local maxima, a 16x enhancement would be sufficient. These varying criteria to judge the enhancement performance distinguish the image super-resolution applications in digital rock physics from some of the other fields, which may have lower tolerance for errors.

4 Super resolution on manually acquired low-resolution images

4.1 Application on BSEM images

We then tested the workflow with BSEM images manually acquired at different levels.

Two levels of BSEM images were acquired on multiple carbonate rock samples, with one resolution roughly 5 times as high as the other. For each low-resolution image, a high-resolution image was positioned in its centre for the ease of registration, as shown in Fig. 9. Consequently, the high-resolution images covered a much smaller area of the rock samples. Because of the limitation of the imaging speed, it would not be practical to scan the entire surface of the cores at the high resolution.

Images of the two resolutions were then registered with an internally developed software. The low-resolution images were trimmed to match the areas covered by the high-resolution patches. Once aligned, each image was divided into sub-images with 128x128 pixels, and pairs of low-resolution/high-resolution sub-images were used as training data, containing 86,400 examples. Images from different rock samples outside of the training data were reserved as a testing dataset of the same size.

* Corresponding author: bo.gong@chevron.com

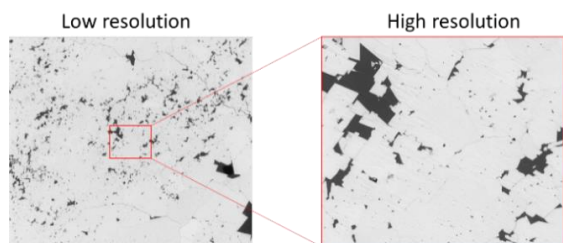


Fig. 9. BSEM images acquired at two resolutions of roughly 5 times difference. The high-resolution image was acquired in the central section of the low-resolution image.

A new U-Net-based model was trained and applied to enhance the low-resolution BSEM images. An example of the results is shown in **Fig. 10**. The enhancement effectively sharpened the edges of the pore spaces, and preserved small pores and pore throats well. A reduction in noise was also seen as a by-product of the enhancement. The White grain boundaries seen on the high-resolution images were not captured by the enhancement, likely due to their low color contrast compared with the background.

Fig. 6 shows the pore size distribution calculated on an image before and after a 5x enhancement. A bi-modal distribution can be clearly seen from the reconstructed image, but was not captured by the low-resolution image due to the resolution limit. The existence of the microporosity peak was further confirmed by mercury injection capillary pressure (MICP) data, measured on the same rock sample (**Fig. 12**).

This exercise confirms that the presented workflow not only applies to synthetically generated low-resolution/high-resolution image pairs, but can also be trained with images actually acquired at two different resolutions.

4.2 Application on microCT images

The same workflow was trained with and applied to microCT images on a slice-by-slice basis. Two levels of

images were acquired on the same rock sample at 22.5 μm per voxel and 6.6 μm per voxel. The training was done in a similar manner to the BSEM super-resolution model, with low-resolution and high-resolution images registered and paired. The training dataset contains about 135,000 samples, and the testing dataset has about 20,000. All the sub-images are 128x128 pixels.

The enhancement results are shown in **Fig. 8**. Compared with the high-resolution image, many details were recovered from the low-resolution image. Noise level was also suppressed during the enhancement.

5 Conclusion

Super-resolution convolutional neural networks provide a low-cost solution to increase the accuracy of image-based rock property evaluation with a minimal amount of high-resolution image acquisition. With images digitally enhanced on samples of larger sizes, interpretations would be more representative of the rock heterogeneity, which helps resolve the incompatibility between imaging resolution and scale.

With synthetically generated images, we demonstrated that U-Net based models are more suitable for the super-resolution task than traditional SRCNNs. One could train a single mixed model with images of multiple resolutions instead of multiple fit-for-purpose models, since the sacrifice in performance is insignificant.

Results have shown that pore structures can be well preserved for images coarsened by up to 8x, whereas local maxima of the pore size distribution could be correctly identified from a 16x enhancement. We also confirmed that the presented workflow is equally applicable to training data consisting exclusively of manually acquired images, including BSEM and microCT images. The enhanced image quality could be beneficial for any following digital rock workflows, leading to more reliable observations of pore-scale rock properties and less uncertainties in rock texture analysis.

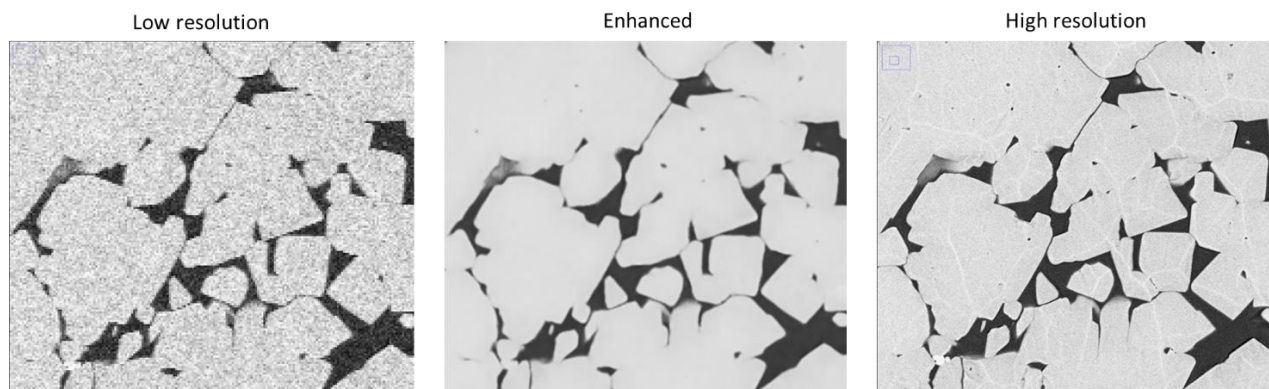


Fig. 5. Comparison of an enhanced image (middle) with manually acquired low-resolution and high-resolution BSEM images.

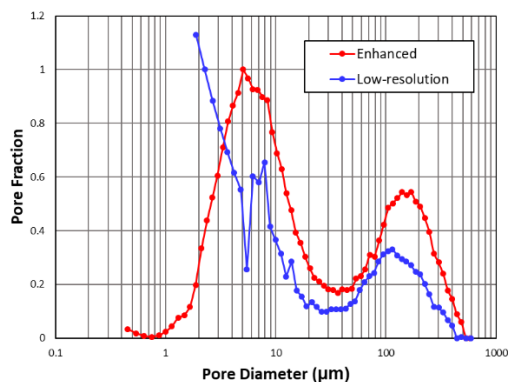


Fig. 6. Pore size distribution of a low-resolution image and its enhanced image. The enhanced image exhibited a bi-modal distribution.

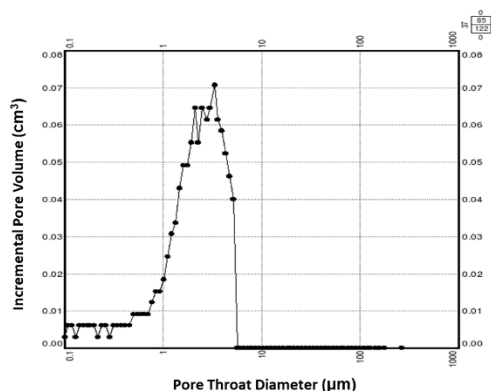


Fig. 7. Mercury injection capillary pressure (MICP) data confirms the presence of the microporosity revealed from enhanced image.

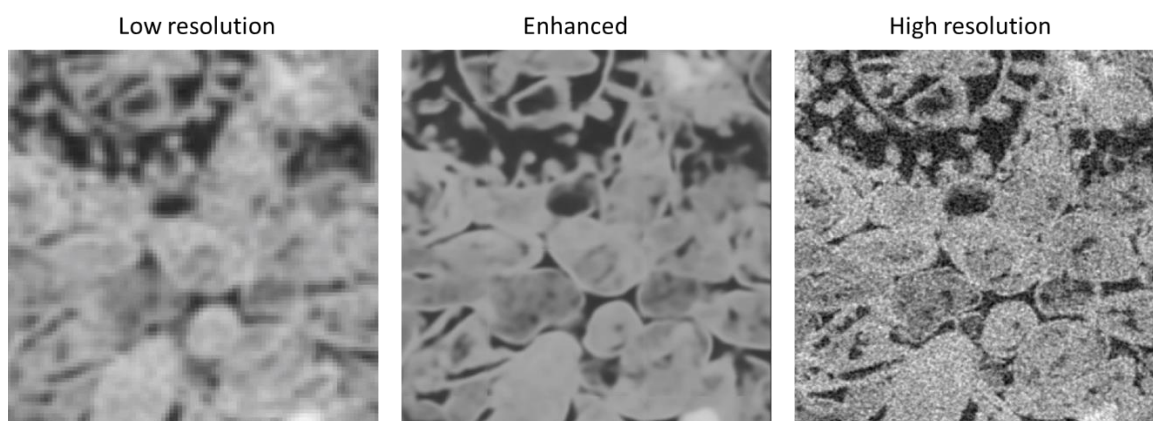


Fig. 8. Comparison of an enhanced image (middle) with manually acquired low-resolution and high-resolution microCT images.

References

1. D. Silin, & T. Patzek, Pore space morphology analysis using maximal inscribed spheres. *Physica A: Statistical Mechanics and its Applications*, **371**, 336-360 (2006)
2. Y. Bazaikin, B. Gurevich, S. Iglauer, T. Khachkova, D. Kolyukhin, M. Lebedev, . . . G. Reshetova, Effect of CT image size and resolution on the accuracy of rock property estimates. *Journal of Geophysical Research: Solid Earth*, **122**(5), 3635-3647 (2017)
3. N. Alyafei, A. Q. Raeini, A. Paluszny, & M. J. Blunt, A Sensitivity Study of the Effect of Image Resolution on Predicted Petrophysical Properties. *Transport in Porous Media*, **110**(1), 157-169 (2015)
4. W. Yang, X. Zhang, Y. Tian, W. Wang, & J. Xue, Deep Learning for Single Image Super-Resolution: A Brief Review. *arXiv:1808.03344 [cs.CV]* (2019)
5. A. Marquina, & S. Osher, Image super-resolution by tv-regularization and bregman iteration. *J. Sci. Comput.*, **37**(3), 367-382 (2008)
6. J. Sun, Z. Xu, & H. Shum. Image super-resolution using gradient profile prior. *2008 IEEE Computer Society Conference on Computer Vision and Pattern Recognition* (2008)
7. Z. Wang, A. C. Bovik, H. R. Sheikh & E. P. Simoncelli. Image quality assessment: from error visibility to structural similarity. *IEEE Transactions on Image Processing*, **13**(4), 600-612 (2004)
8. C. Dong, C. C. Loy, K. He, & X. Tang, Image Super-Resolution Using Deep Convolutional Networks. *arXiv:1501.00092 [cs.CV]* (2015)
9. Y. D. Wang, R. T. Armstrong, & P. Mostaghimi, Enhancing Resolution of Digital Rock Images with Super Resolution Convolutional Neural Networks. *Journal of Petroleum Science and Engineering*, **182**, 106261 (2019)
10. O. Ronneberger, P. Fischer, & T. Brox, U-Net: Convolutional Networks for Biomedical Image Segmentation. *arXiv:1505.04597v1 [cs.CV]* (2015)
11. Z. Lu, & Y. Chen, Single Image Super Resolution based on a Modified U-net with Mixed Gradient Loss. *arXiv:1911.09428 [eess.IV]* (2019)

Evolution of electrical resistivity and NMR during early-stage maturation of an organic-rich chalk

Eva G. Vinegar^{1,*}, *Yoav O. Rosenberg*², *Scott V. Nguyen*³, *Larry W. Lake*¹, and *Harold J. Vinegar*⁴

¹The University of Texas at Austin

²Geological Survey of Israel

³17TeraWatts

⁴Vinegar Technologies, LLC

Abstract. This paper studies the changes in the electrical resistivity of an organic-rich source rock chalk containing a Type-II kerogen during early-stage maturation of the kerogen. As bitumen is generated during maturation, the chalk changes from water wet to a complex mixed-wet pore system, with the micritic pore space remaining water wet while the bitumen expelled into the macro pores converts some pores to oil wet. This mixed-wet system results in non-Archie electrical behavior with pronounced curvature of the $I-S_w$ curve. We find that this curvature is well fit by connectivity theory. The connectivity theory parameters are determined both on native state core and from artificial laboratory pyrolysis which generates bitumen. NMR is used to distinguish the brine in micritic, water-wet pore spaces from that in the intergranular, mixed-wet pore spaces, from which the observed connectivity parameters may be independently estimated. Comparison between electrical resistivity and dielectric logs show that the connectivity parameters match the laboratory results over more than 300 m calcareous section.

Introduction

The Late Cretaceous Ghareb-Mishash formation in Israel provides a unique opportunity to study the evolution of electrical resistivity and NMR responses to organic maturation in a source rock chalk. This chalk has an extremely high TOC up to 15 wt%. In the coastal plain containing the Shefela basin, the organic-rich chalk has experienced shallow burial and the kerogen is immature. In contrast, in the Golan basin in northern Israel, the same Ghareb-Mishash formation has been buried much deeper and experienced a higher geothermal gradient, leading to a higher level of kerogen maturation to bitumen. Using core and log data from both basins, we have been able to follow the change in the electrical resistivity and NMR responses from immature to early-stage organic maturation.

The early-stage mature, kerogen-rich Late Cretaceous formation in the Golan basin is characterized by large amounts of bitumen and light hydrocarbons which affect the connectivity of the fluids within the rock and thus the electrical resistivity and NMR responses. Increasing burial of these organic-rich chalks affects connectivity by compaction (reduction in porosity) and by organic maturation of the kerogen (hydrocarbon generation and wettability changes).

Electrical resistivity, dielectric and NMR data are used to aid the interpretation of petrophysical properties of reservoir rocks, such as porosity, pore size, fluid type, fluid saturation, tortuosity, and permeability [1, 2].

Improvements to the models and interpretations used to evaluate the petrophysical properties have been ongoing with the development of unconventional resource plays. For example, extremely high values of electrical resistivity are common in mixed-wet micritic calcites and are difficult to model using Archie's resistivity model which is applicable to conventional reservoir rocks. Cementation and saturation exponents are about 2 for conventional rocks, but often vary significantly for vuggy rocks, shaly sands, and mixed or oil-wet systems. Furthermore, the Archie exponents selected may not fit well for a range of water saturations. Several resistivity models have been developed to better fit the electrical resistivity in different types of rock systems, but few fit the curvature of the resistivity index with water saturation [3-6]. A more general form of Archie's resistivity model based on connectivity theory provides a more consistent fit with relatively few parameters [5,6].

In agreement with connectivity theory, the electrical resistivity in the Ghareb-Mishash formations shows a sharp increase in $I-S_w$ curvature for early-stage thermal maturation. The change from Archie-type behavior in the Shefela basin to $I-S_w$ curvature in the Golan basin is due to the generation and expulsion of bitumen from the kerogen, which blocks many of the pore throats in the dual-porosity system and creates mixed wet or oil-wet surfaces in the larger, intergranular pore spaces.

* Corresponding author: evavinegar@gmail.com

We first present a brief review of connectivity theory. We then show how the resistivity index changes from Archie-type behavior to non-Archie behavior once the organic-rich chalk is artificially matured. We show how bitumen saturation increases with depth and maturation in the Ghareb basin. As bitumen is generated during maturation, the chalk changes from water wet to a complex mixed-wet pore system, with the micritic pore space remaining water wet while the bitumen expelled into the macro pores converts some pores to oil wet. This mixed-wet system results in non-Archie electrical behavior with pronounced curvature of the I-S_w. We show that this curvature is well fit by connectivity theory. The connectivity theory parameters are then determined on native state core and found to match those found during artificial laboratory pyrolysis. NMR is used to distinguish the brine in micritic, water-wet pore spaces from that in the intergranular, mixed-wet pore spaces, from which the observed connectivity parameters may be independently estimated. Finally, we compare electrical resistivity and dielectric logs and show that the connectivity parameters match the laboratory results over a 350 m calcareous section.

Electrical resistivity and connectivity theory

The petroleum industry has long used Archie's equation [7] to estimate the hydrocarbon saturation of reservoirs using resistivity and porosity logs. Archie's equation is:

$$R_t = \frac{R_w}{\phi^m S_w^n} \quad (1)$$

where R_t is the total resistivity of the rock, R_w is the resistivity of the brine, ϕ is the porosity, S_w is the water saturation, m is the cementation exponent, and n is the saturation exponent.

The sensitivity of oil reserve estimates to the value of these exponents has been critical for reservoir evaluation and project decisions. For many reservoirs, m is about 2, but can be much higher for vuggy rocks. n is usually about 2 in clean, water-wet sandstones, less than 2 in shaly sands, and much more than 2 in mixed-wet and oil-wet systems. Heterogeneous systems further make it difficult to fit these exponents to a dataset.

Deviation from the Archie straight line values on a resistivity index versus water saturation log-log plot is a common issue in assessing many reservoir rocks. The Archie saturation exponent needed to match data on this plot changes significantly with water saturation [6, 8]. Several methods were developed to represent the saturation in non-Archie rocks. Montaron [5,6] proposed a more generalized version of Archie's equation based on percolation theory:

$$R_t = R_w \left[\frac{1-P_c}{P-P_c} \right]^\mu \quad (2)$$

where R_t is the electrical resistivity of the system, R_w is the electrical resistivity of the conductive portion, P is the probability that a portion of the rock will be conductive (water volume fraction), P_c is the percolation threshold (Montaron calls P_c a water connectivity correction index, χ_w), and μ is the conductivity exponent (~ 2). The water

volume fraction is the water saturation times the porosity of the rock, $S_w \phi$, giving:

$$R_t = R_w \left[\frac{1-\chi_w}{S_w \phi - \chi_w} \right]^\mu \quad (3)$$

This connectivity equation elegantly accounts for the curvature of the resistivity index with saturation in some systems. We note that when the percolation threshold is 0, the connectivity equation reduces to Archie's equation if $m=n$. Montaron further derived this connectivity equation for a variety of cases using a modified CRIM mixing law [9,10]. We find this particularly applicable to the organic-rich Ghareb-Mishash chalk.

As described in Vinegar et al. [11], **Fig. 1** shows a core sample from the Shefela containing immature organic matter that was artificially matured and its resistivity index versus brine saturation. T_{max} is 421°C for the post-pyrolysis sample and the porosity is 50 pu. The blue circles represent measurements taken post-pyrolysis (dry pyrolysis), and the red circles represent measurements taken pre-pyrolysis. An Archie equation fits the pre-pyrolysis data with a saturation exponent $n=1.93$. The model based on connectivity theory fits the post-pyrolysis data with $\chi_w = 0.03$ and $\mu = 2$. The results show curvature beginning to develop at lower values of water saturation.

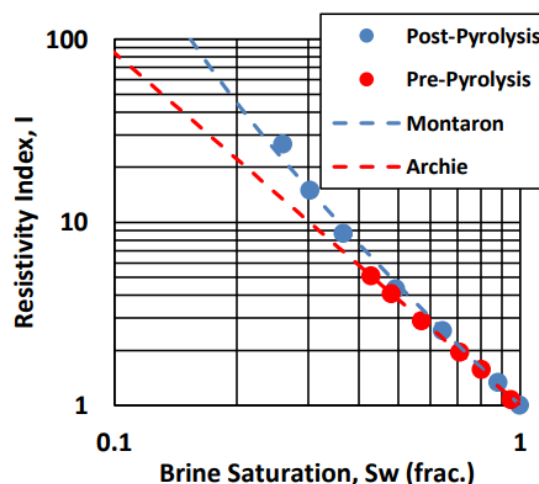


Fig. 1: Resistivity index versus brine saturation for an immature core sample from the Shefela basin pre- and post-pyrolysis [11].

We can show the deviation of the electrical resistivity from Archie's equation using connectivity theory [6]. The water connectivity correction index primarily controls the curvature of the resistivity index versus water saturation plot. There are two main contributors to the water connectivity correction index: one due to the micritic pore space and one due to the oil-wet pore space.

The water-filled pores of the micritic space are highly connected, and the conductivity exponent of micritic grains is often taken to be 1.5 as a result (as Montaron points out, 1.5 is the conductivity exponent for

a packing of spherical grains). If the micritic space contributes to the electrical resistivity, then the electrical resistivity would be slightly less resistive than if one were to consider only larger, intergranular pore spaces. A non-organic, water-wet carbonate containing a dual micro and meso-macropore system would consist of three phases: micritic grains, water in the intergranular pore space, and solid grains. The micritic grains are treated as an independent unit with its micropores Montaron [5,6] derived the equation for the water connectivity correction index for a rock containing micritic grains:

$$\chi_w = x_m (\phi_m - \phi_m^{\mu_m/\mu}) \quad (4)$$

where χ_w is the water connectivity correction index, x_m is the volume fraction of the rock containing micritic grains, ϕ_m is the porosity of the micritic portion of the rock, μ_m is the conductivity exponent of the micritic portion of the rock, and μ is the conductivity exponent of the intergranular portion of the rock.

Assuming that x_m is around 0.25, μ_m is 1.5, and μ is 2, χ_w can be strongly negative, as shown in **Fig. 2a**. Negative values of χ_w suggest that compared to Archie, the resistivity index would be much smaller, especially with decreasing water saturation. If the system is fully water-saturated, however, in many cases the resistivity index will be close to that predicted by Archie.

If we neglect the micritic space and consider a system where the larger pore spaces are mixed-wet, with some water-wet pores and some oil-wet pores, then the water connectivity correction index as derived by Montaron [6] is:

$$\chi_w = x_o S_{co} \phi_M \quad (5)$$

where x_o is the fraction of pores that are oil-wet, S_{co} is the critical oil saturation at which the conductive fluids no longer percolate, and ϕ_M is the porosity of the macro pores. χ_w is positive and grows linearly.

In the early-stage mature case, where the bitumen has partially blocked the pore throats of the micritic space, $\chi_w = x_o S_{co} \phi_M$ is positive and the resistivity index compared to Archie is higher, especially with decreasing water saturation.

For the case in which there are oil-wet spaces and there is connectivity between the brine in the micritic space and that in the larger pore spaces, χ_w is the sum of the two terms:

$$\chi_w = x_m \left(\phi_m - \phi_m^{\frac{\mu_m}{\mu}} \right) + x_o S_{co} \phi_M \quad (6)$$

where the first term is negative, and the second term is positive.

Fig. 2a shows the behavior of χ_w with x_m and ϕ_m due to the micritic grains. Over a large range of porosities inside the micritic portion of the rock, χ_w does not vary significantly, particularly if the bulk volume fraction of micritic grains is low. **Fig. 2b** shows the behavior of χ_w due to the oil-wet pore spaces. With burial and compaction, the porosity of the oil-wet pore spaces decreases, but the oil-wet fraction of the intergranular pore spaces increases. These factors keep χ_w more stable along the length of the organic-rich portion of the well.

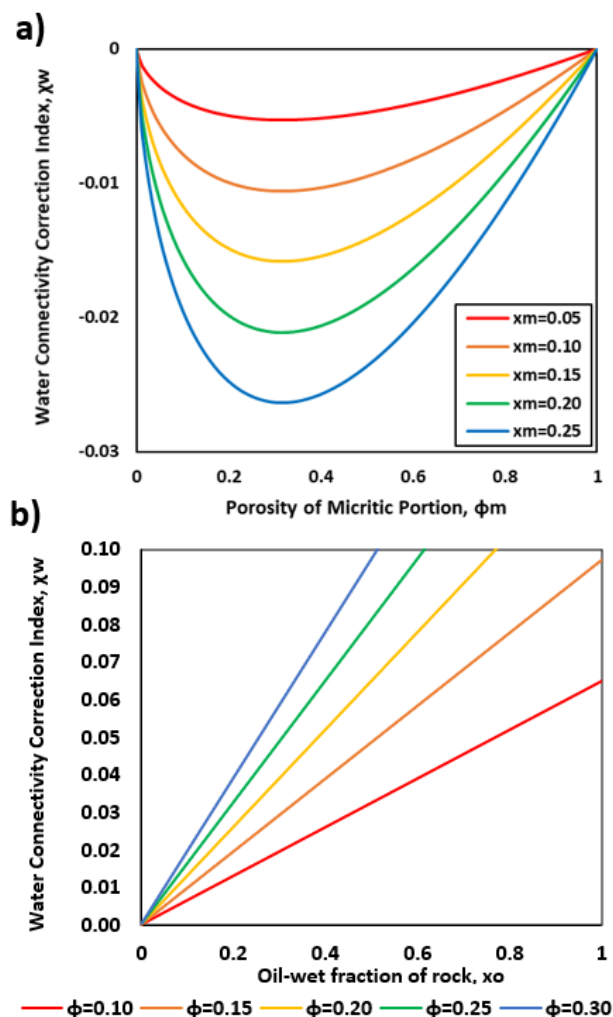


Fig. 2: a) χ_w for a micritic portion of the rock in which μ_m is 1.5 and μ is 2 in equation (4). b) χ_w for a rock with oil-wet pore spaces in which S_{co} is 0.65 in equation (5). ϕ is the porosity of the macro pore space.

Creating Oil-Wet Spaces with Bitumen Generation

The immature organic-rich chalk from the Shefela basin is water wet. In contrast, the early-stage mature kerogen from the Golan basin has generated bitumen and light hydrocarbons, and thus created oil-wet surfaces. These oil-wet surfaces induce the curvature in the resistivity index. Furthermore, the distribution of the organic matter in the rock cause much of the micritic water-wet pore spaces to be blocked by bitumen.

The SEM images in **Fig. 3** from Vinegar et al. [11] show the distribution of the pore spaces and organic matter. The upper right image is the base SEM image. The circular coccoliths and larger calcite grains are shown in the upper right image in green (calcium mapping using SEM-EDS). The lower left image shows the kerogenous organic matter dispersed between the larger calcite grains. Sulfur mapping was used to identify the organic matter because Type II-s kerogen (S/C ratio above 0.04) is dominant in this rock [12]. The lower right image shows

the pore spaces, organic matter, and calcite. The co-deposition of organic matter and calcite minerals allow for bitumen generation to enter the macropore system and block many of the entrances to the micritic pore space. This observation is in agreement with the change in NMR diffusional coupling from strong to weak as the kerogen generates bitumen [2,11].

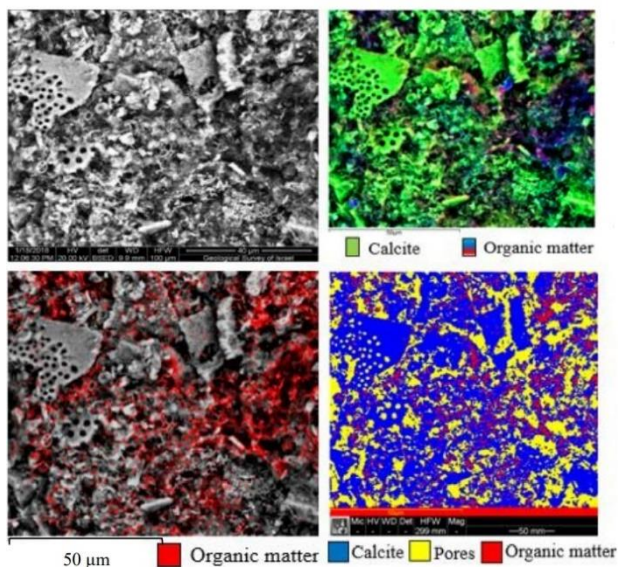


Fig. 3: SEM (upper left) and SEM-EDS images showing calcite, organic matter, and pores for the organic-rich chalk [11].

An immature, organic-rich Ghareb rock was artificially matured in a semi-open pyrolysis reactor gradient experiment [13]. The sample was evaluated in a Vinci Technologies Rock-Eval 6 analyzer to determine T_{max} and hydrocarbon content with TOC. Bitumen was obtained from cuttings using a Soxhlet extractor (Vinci Technologies) with dichloromethane and methanol solvent (9:1 V/V). The bitumen and light hydrocarbon content with T_{max} and corresponding windows of hydrocarbon generation are shown in **Fig. 4**. Bitumen generation begins at a T_{max} value of about 417°C. The variation of bitumen saturation with T_{max} for cuttings from the NESS 2 well is shown in **Fig. 5**. Bitumen saturation increases significantly through a T_{max} value of about 436°C.

Fig. 6 shows the bitumen saturation with depth for the NESS 2 well in the Golan basin. There is significant bitumen saturation over the 350 meters. This is quite different from the immature organic-rich rock from the Shefela basin, where there is no bitumen saturation. The porosity decreases from the upper to lower portion of the well.

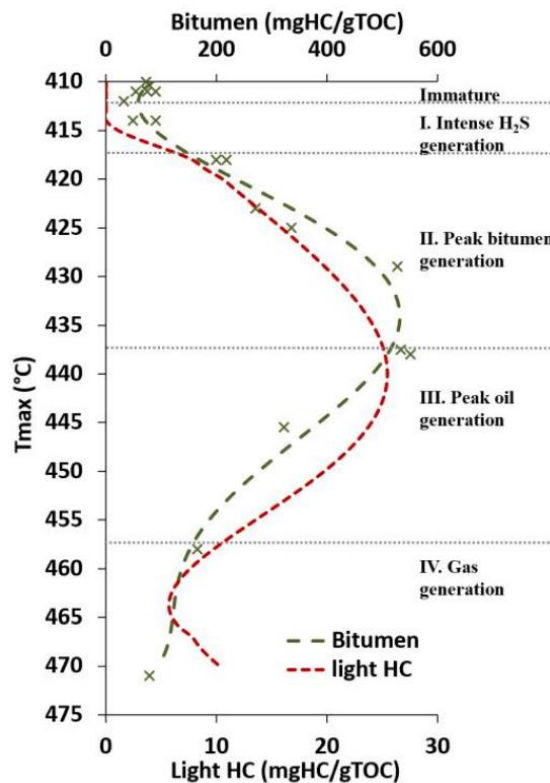


Fig 4: Bitumen and light hydrocarbon generation versus T_{max} of an artificially matured organic-rich Ghareb sample from the Shefela basin. The immature stage, hydrogen sulfide, bitumen, oil, and gas windows are marked by the dotted lines [11,13].

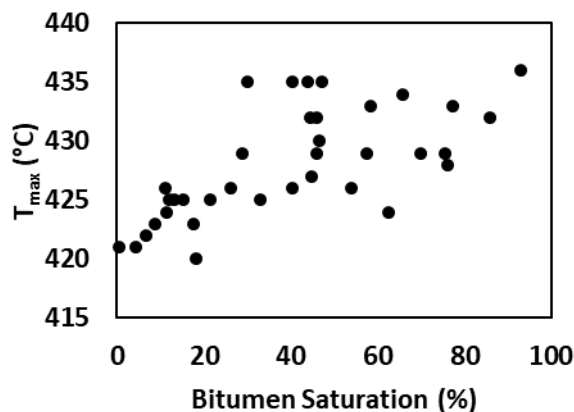


Fig. 5: Bitumen saturation versus maturity indicator T_{max} for the NESS 2 well.

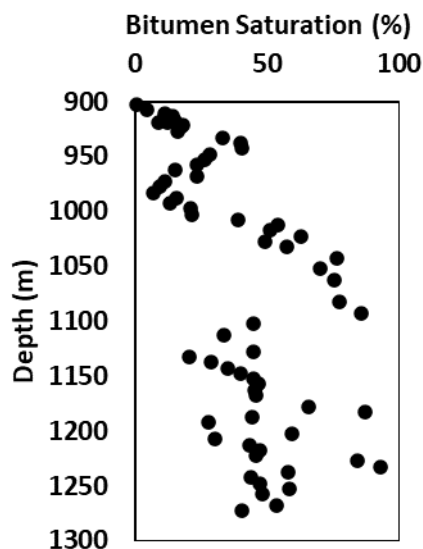


Fig. 6: Bitumen saturation with depth for the NESS 2 well.

χ_w using NMR core data

We consider the components used for the connectivity theory-based resistivity model in the immature and early-stage mature cases. In the immature stage, the organic-rich chalk contains mostly calcite, immature kerogen, and water in both the macropores and micropores. During early-stage maturation, the kerogen generates bitumen and lighter hydrocarbons. Once bitumen is expelled into the macropores, some of the macropore space becomes oil wet. We assume that the micropores remain water-wet and contain only water as demonstrated by D2O diffusion eliminating the entire H2O signal from the micropores. The macropore system is mixed-wet, and for the purposes of our model, we assume that the water is in water-wet macropores, while the light hydrocarbons are in oil-wet pores. Our electrical resistivity model therefore has three classes of pores: water-wet micritic pores, water-wet macropores, and oil-wet macropores.

One method of estimating the values of χ_w is by using NMR T_2 distributions for “as received” core and fully saturated with brine. Downhole, the light hydrocarbons (NGLs) are in the oil-wet pores but the NGLs blow out of the core on the trip to the surface. This provides a method for separating the volume of water-wet and oil-wet macropores.

The laboratory NMR analysis was performed at Rice University as detailed in Chen et al. [2]. An Oxford Instruments GeoSpec2 rock-core analyzer was used with a Larmor frequency of 2.3 MHz to match that of the MREX logging tool.

Fig. 7 shows the T_2 distribution of an early-stage mature Ghareb sample from 920m in the NESS 2 well [2,11]. The region with the shortest T_2 values, depicted in the A region of the spectrum (3 ms and shorter), responds to part of the bitumen. Kerogen has relaxation times which are too short to be detected by this NMR

spectrometer. Bitumen also has values which are short, but a fraction may be detected if the viscosity is low enough. Region B, which includes T_2 values between 3 and 32 ms, is the response due to the water-wet micritic calcite. The signal with the longer relaxation time in region C (T_2 greater than 32 ms) responds to the fluids in the macro pore space. The separation of the T_2 distribution for water into regions B and C, corresponding to the micritic and macropores, is a result of weak diffusive coupling due to bitumen blocking [11]. The water molecules no longer diffuse easily between the two spaces because bitumen is blocking many of the pore throats. Downhole, region C contains some connate water in the macropore space as well as methane and condensates.

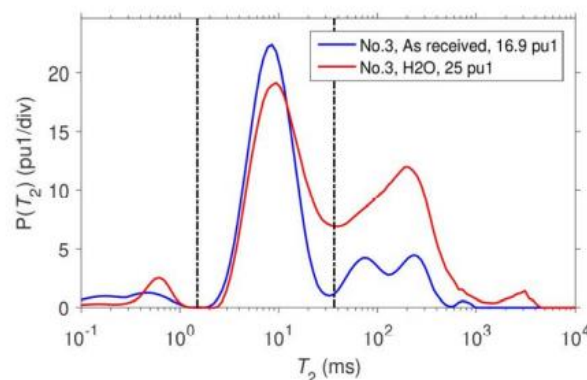


Fig. 7: NMR T_2 distribution of a core sample from the NESS 2 well at 920m, as-received and after saturating with brine [2,11].

The light hydrocarbons in this core is taken to be the difference between the porosity in the “as received” core and the porosity when fully brine saturated. The micritic porosity is about 12 pu and the macro porosity of the as received core is about 4.9 pu. When saturated with brine, the macro porosity is 13 pu. The oil-wet macro porosity is taken to be the difference between the brine-saturated total porosity and the “as received” total porosity, or 8.1 pu. The fraction of the oil-wet macropore space is $8.1\text{pu}/13\text{pu} = 0.62$. The bulk volume micritic portion of the rock is 25%, which implies that the porosity of the micritic portion is 48%. S_{co} is about 0.65 [6]. Using $\mu_m = 1.5$ and $\mu = 2$, the value of χ_w is about 0.028. This value is in agreement with the 0.03 fit to the resistivity index dataset in Fig. 1.

χ_w measured from core

The electrical resistivity profile of the organic-rich chalk at these maturity levels shows a significant increase compared to the immature case—more than would be expected for an Archie-type rock because of curvature. Table 1 shows the Dean-Stark core data for a set of samples from the NESS 5 well in the Golan basin. Fig. 8a shows the fit of the Dean-Stark core data to the Archie resistivity model. The fit for the Archie model is best when $m=4$ and $n=3.5$; however, the brine resistivity is very low: 0.03 ohm-m. Fig. 8b shows the fit of the Dean-

Stark core data to the connectivity theory-based resistivity model. The fit when $\chi_w=0.03$ and $\mu=2$ gives a brine resistivity of 1.2 ohm-m, which is the measured brine resistivity in the Upper Ghareb. **Fig. 9** shows the excellent fit between the electrical resistivity using the connectivity theory-based model ($\chi_w = 0.03, \mu = 2, R_w = 1.2$ ohm-m) with the Dean Stark core data shown in **Table 1** versus the NESS 5 resistivity well log in the Golan basin.

Table 1: Dean-Stark core data and resistivity log values for the NESS 5 well from 1050-1056m

Depth (m)	Phi	S _w	Rt (Ω-m)
1050.7	0.13	0.16	8370
1050.9	0.12	0.31	13544
1051.2	0.14	0.35	7510
1051.4	0.15	0.31	5545
1051.8	0.13	0.38	2935
1052.1	0.14	0.38	2023
1052.4	0.17	0.35	2023
1052.7	0.16	0.47	787
1052.8	0.17	0.53	473
1054.4	0.18	0.69	79
1054.8	0.20	0.73	103
1055.2	0.18	0.75	140
1055.4	0.18	0.70	167
1055.7	0.16	0.69	137
1055.9	0.15	0.66	129

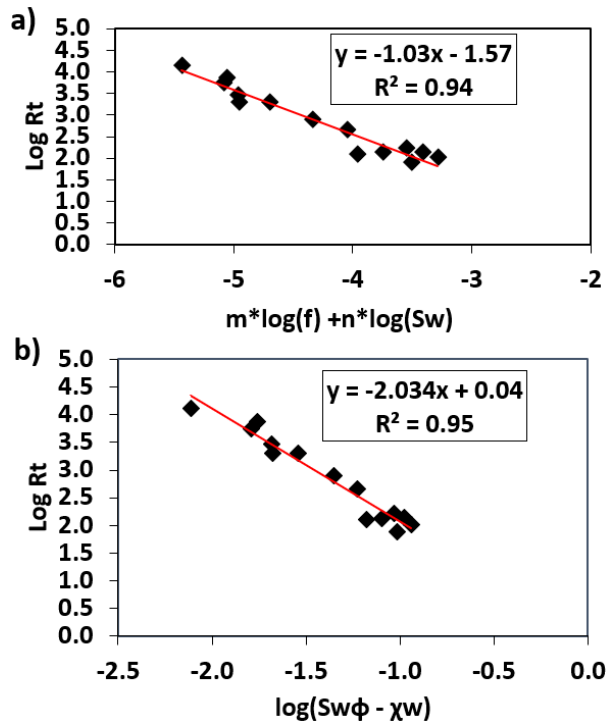


Fig. 8: a) Regression to fit Archie parameters for the NESS 5 well from 1050-1056m. $m=4$ and $n=3.5$ fit this dataset, but R_w is only 0.03 ohm-m. b) Regression to fit connectivity theory parameters for the NESS 5 well from 1050-1056m. $\chi_w = 0.03$ and $\mu = 2$ gives $R_w=1.2$ ohm-m.

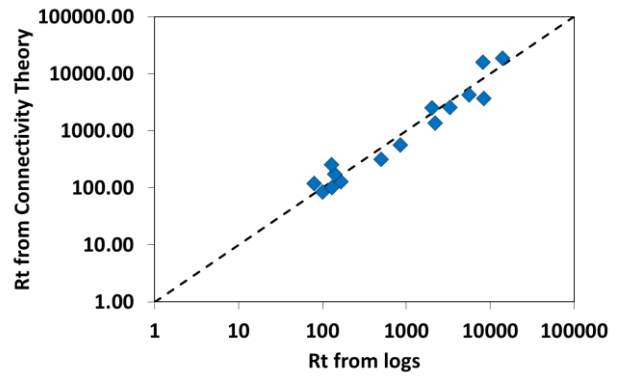


Fig. 9: Resistivity from NESS 5 well log from 1050-1056m versus resistivity calculated using the connectivity theory model, with $\chi_w = 0.03$ and $\mu = 2$.

Comparison between dielectric and resistivity log using connectivity theory

The $S_w\phi$ term in the connectivity theory-based resistivity model (Eq. 3) is directly measured with the dielectric log. One advantage of using the dielectric log in this model is that it is not necessary to use two separate logs to determine ϕ and S_w independently.

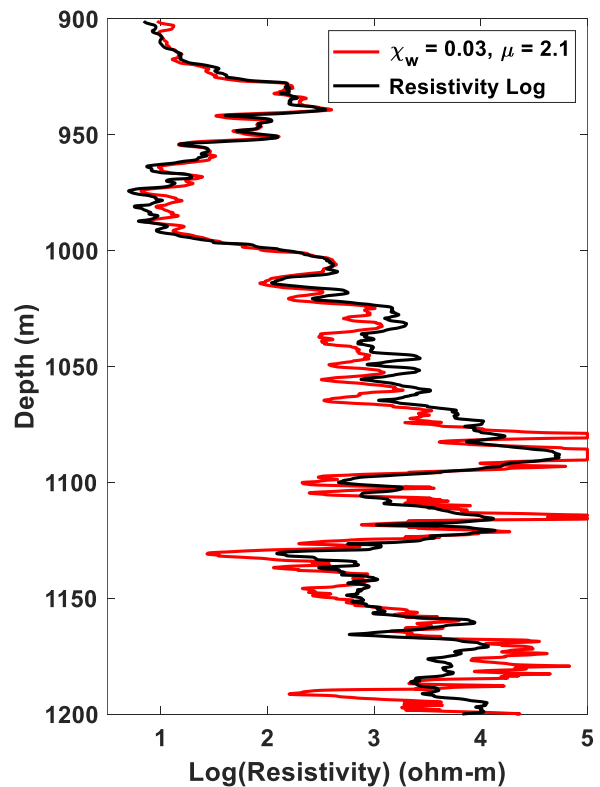


Fig. 10: Resistivity log from the NESS 2 well overlaid with the connectivity theory resistivity calculated from Eq. 3 using the dielectric log for $S_w\phi, \chi_w = 0.03$, and $\mu = 2.1$.

The NESS 2 resistivity log was overlaid with the connectivity model (Eq. 3) using the dielectric log for ϕS_w , $\chi_w = 0.03$, and $\mu = 2.1$ in **Fig. 10**. The brine resistivity R_w is 0.3 ohm-m which matches the R_w using Archie's equation in the organic-free carbonate at the top of the Ghareb. We note there is excellent agreement for over 300 meters of organic-rich rock with resistivity values ranging from less than 10 to over 10,000 ohm-m and porosities from 10 to 35 pu.

Conclusions

1. The amount of bitumen in macropores increases with organic maturity, leading to a mixed wet pore system with water-wet micritic pores and some oil-wet and some water-wet macropores.
2. The change in wettability causes a curvature in the I-S_w relation, resulting in a non-Archie behavior. NMR measurements on core shows the micritic pores stay water-wet even with a high bitumen saturation.
3. Comparing immature and post-pyrolysis resistivity, the change to non-Archie behavior occurs at T_{max} ~ 420°C, where the bitumen saturation increases rapidly. A connectivity model using $\mu = 2$ and $\chi_w = 0.03$ matches the post-pyrolysis data.
4. Dean Stark core data in NESS 5 shows the connectivity theory-based resistivity model provides a good fit to the I-S_w curvature with the same value of connectivity parameter ($\chi_w = 0.03$).
5. The value of χ_w can be explained using NMR T₂ relaxation data on "as received" and fully brine-saturated core.
6. Comparing the resistivity and dielectric logs in NESS 2, and using the value of $\chi_w = 0.03$ previously measured, we obtain an excellent match over a large calcareous section of ~300 m, covering an extremely wide range in resistivity and porosity.

Acknowledgements

We thank Weidong Li and Mohammad Chohan from Baker Hughes, George Hirasaki, Philip Singer, Zeliang Chen, and Xinglin Wang from Rice University, Itay Resnick from the Geological Survey of Israel for their contributions to this paper.

Symbols and Abbreviations

NMR = Nuclear Magnetic Resonance
 R_t = electrical resistivity of the saturated rock
 R_w = electrical resistivity of the brine
 ϕ = porosity
 S_w = brine saturation

m = cementation exponent
 n = saturation exponent
 P = probability that a site will be conductive
 P_c = pseudo-percolation threshold
 χ_w = water connectivity correction index
 μ = conductivity exponent
 μ_m = conductivity exponent of the micritic portion of the rock
 x_m = bulk volume fraction of rock that contains micritic grains
 ϕ_m = porosity of the micritic portion of the rock
 x_o = fraction of macro pores that are oil-wet
 S_{co} = critical oil saturation at which conductive fluids no longer percolate
 ϕ_M = porosity of the macro pores
 T_{max} = temperature of peak S2 response during programmed Rock-Eval pyrolysis
 TOC = total organic carbon

References

1. R.L. Kleinberg, W.E. Kenyon, P.P. Mitra, *Journal of Magnetic Resonance, Series A* **108**, 206-214 (1994)
2. Z. Chen, P.M. Singer, X. Wang, H.J. Vinegar, S.V. Nguyen, G.J. Hirasaki, *Petrophysics* **60**, 771-797 (2019)
3. D. Kennedy, *Petrophysics* **48**, 335-361 (2007)
4. A.P. Garcia, Z. Heidari, A. Rostami, *Petrophysics* **58**, 454-469 (2017)
5. B. Montaron, *15th SPE Middle East Oil & Gas Show and Conference* (2007)
6. B. Montaron, *Petrophysics* **50**, 102-115 (2009)
7. G.E. Archie, *SPE 942054-G, Transactions, AIME* **146**, 54-62 (1942).
8. W.G. Anderson, *SPE 13932* (1986)
9. J. Birchak, L. Gardner, J. Hipp, J. Victor, *IEEE Proceedings* **62**, 93-98 (1974)
10. J.G. Berryman, *Mixture Theories for Rock Properties, Rock Physics and Phase Relations- A Handbook of Physical Constants*, 205-228 (1995)
11. E.G. Vinegar, Y.O. Rosenberg, I. Resnick, Y. Gordin, P.M. Singer, X. Wang, Z. Chen, S.V. Nguyen, W. Li, T. Bradley, G.J. Hirasaki, L.W. Lake, S. Feinstein, Y. H. Hatzor, H.J. Vinegar, *SPWLA 61st Annual Logging Symposium* (2020)
12. I. Kutuzov, M.Sc. Thesis. Ben-Gurion of the Negev, Be'er Sheva, Israel (2017)
13. Y. O. Rosenberg, I. J. Resnick, H. J. Vinegar, S. Feinstein, Y. Bartov, *Marine and Petroleum Geology* (2020)

Study of Bakken and Three Forks Formations using NMR Core Analysis

Mohamed M. Awad^{1,3,4,*}, Philip M. Singer¹, Z. Harry Xie², Maura Puerto¹, Hui pu³, and George Hirasaki¹

¹Rice University, Department of Chemical and Biomolecular Engineering, Houston, TX, USA 77005

²Core Laboratories, Houston, TX, USA 77040

³University of North Dakota, Petroleum Engineering Department, Grand Forks, ND, USA 58202

⁴Egyptian Petroleum Research Institute, Production Department, Cairo, Egypt 11727

Abstract. NMR has proven to be a valuable tool in the petrophysical analysis of unconventional plays such as shale-gas and tight-oil formations. In this study, we use NMR T_1 - T_2 measurements at 2.3 MHz and 22 MHz to provide key insights into the wettability, presence of bitumen, surface-relaxation mechanism, and internal gradient effects in cores from the Bakken and Three Forks formations. We determine the NMR wettability index of the Bakken and Three Forks formations by comparing the NMR response of octane saturated and formation-brine saturated cores (without cleaning the cores prior to saturation). The results indicate that the Upper Bakken cores are strongly oil-wet, the Middle Bakken cores are water-wet to intermediate-wet, and the Three Forks cores are strongly water-wet. In the case of the Upper Bakken cores, the presence of bitumen is detected at 22 MHz where a short echo-spacing is possible. We used the temperature dependence (25 °C to 100 °C) of T_2 at 2.3 MHz to determine the origin of the NMR surface-relaxation mechanism in the saturated nanometer-sized pores. The results indicate that NMR surface relaxation in the Upper Bakken is dominated by enhanced ^1H - ^1H dipole-dipole relaxation, while in the Three Forks it is dominated by paramagnetic surface relaxation. In the case of the Middle Bakken, NMR surface relaxation for the octane saturated cores is dominated by enhanced ^1H - ^1H dipole-dipole relaxation with surface water film, while for brine saturated cores it is dominated by paramagnetic surface relaxation. Finally, we vary the echo-spacing of the T_2 measurement to check for internal gradient effects, which (if present) would complicate the interpretation of wettability and surface-relaxation mechanism from T_2 . While no internal gradients were found at 2.3 MHz, we find strong internal gradient effects in the specific case of octane-saturated cores in the Middle Bakken and Three Forks at 22 MHz.

1 Background

Unconventional reservoirs are any reservoir that requires utilizing special recovery operations outside the conventional recovery operations. According to the U.S. Geological Survey in 2013, the Bakken reservoir is considered one of the world largest unconventional resources with approximately 7.4 billion barrels estimated recoverable oil [1] with an API gravity of 42°. The Bakken formation was deposited from the Late Devonian to Early Mississippian age. The new Bakken wells have high decline rate from the initial production rate, sometimes as high as 85% per year, this high decline rate is because of the complex nature of the Bakken formation, and the formation porosity ranges from 4 ⇔ 8 pu (porosity units) with low permeability 0.001 ⇔ 0.01 mD.

There are three members in the Bakken formation, the Upper Bakken and Lower Bakken are organic shale, separated by dolomitic siltstone and sandstone called Middle Bakken [2]. The Bakken formation lies above the Three Forks and below the Lodgepole limestone. The Upper Bakken and Lower Bakken are organic-rich and the hydrocarbon source rocks with total organic carbon (TOC) content range from 12 ⇔ 36 wt% [3, 4]. The Middle Bakken lithology is highly variable, where it includes interbedded siltstone, sandstone, siliceous limestone, limestone, and sandy dolomite. The dominant lithology of the Middle Bakken in most of the Williston basin is calcareous, dolomitic, or argillaceous siltstone [5]. The upper layer of the Three Forks is located under the Lower Bakken, and consists of a well-sorted very fine-grained layer of Sanish sand. Laminations of illite-rich clay with dolomitized limestone is the main composition

* Mohamed M. Awad: mohamed.awad91990@yahoo.com, mmmohame@cougarnet.uh.edu

of the Three Forks. The TOC of Middle Bakken and Three Forks formations ranges from 0.1 ⇔ 0.3 wt% [4].

NMR core-analysis is a powerful technique for characterizing unconventional plays such as shale-gas and tight-oil formations. Previous NMR studies have provided unique information such as bitumen and kerogen content, wettability, pore-size distribution, movable vs. bound fluid, and water vs. hydrocarbon saturation [6, 7, 8, 9, 10, 11, 12, 13, 14, 15]. For instance it was previously shown in the Barnett shale that $(T_1/T_2)_o \approx 4$ for oil-saturated cores was larger than $(T_1/T_2)_w \approx 2$ for water-saturated cores [6]. It was also previously shown for conventional cores that $(T_1/T_2)_o \approx 4$ for oil-wet cores was larger than $(T_1/T_2)_o \approx 1$ for water-wet cores [16].

In this report, we build on previously reported techniques and show how NMR core-analysis can give a wealth of information about wettability and the presence of bitumen in the Bakken formation. We also show how the NMR surface relaxation mechanism and presence of internal gradients can be determined using a combination of frequency and temperature dependence of the NMR response.

2 Experimental Work

All core samples tested in this study are from one well. The core samples were 2.54 cm (1") diameter, not preserved and left to equilibrate with the core-lab moisture. All the cores are twin cores. The twin cores consisted of one ≈ 4.8 cm (1.89") in length, and the other is ≈ 3.1 cm (1.22") in length. Both ends of all core samples tested in any of the experiments were trimmed with an electrical saw to eliminate the effect of the inverted drilling mud (oil-based mud) used in the coring process.

The formation brine was prepared with the same salinity (309,612 ppm) and composition as the formation brine in the well analysis reports in the well files. The sodium bicarbonate and sodium sulfate were replaced with sodium chloride with the same ionic strength to prevent precipitation. No precipitation was observed in the collected brine samples from the wells because all the salts were in equilibrium with the reservoir rock.

For the as-received twin cores tested in this study, one was saturated with Bakken formation brine and the other was saturated with octane as a model oil. In order to preserve wettability, the cores were not cleaned prior to saturation. All core samples in this study were saturated using the same method. The saturation setup consisted of vacuum pump, two vacuum gauges, saturation cell, pressure gauge, hand pump for saturation fluid, and saturation fluid tank. The cores were saturated with CO₂ after the vacuum to replace any air inside the pores with CO₂. Since CO₂ is more soluble in both brine and oil, this leads to the highest possible saturation [17].

Figure 1 shows the flowchart of the experiments work flow. Specifically, the core samples were exposed to vacuum for 1 ⇔ 1.5 hours (-29.5 in-Hg), then saturated

with CO₂ for 4 hours at one atmospheric pressure, again exposed to vacuum for 1 ⇔ 1.5 hours (-29.5 in-Hg) followed by saturation with CO₂ for 4 hours, then exposed to vacuum (-29.5 in-Hg) again for 1 ⇔ 1.5 hour, and finally saturated with either formation brine or octane at 2,000 psi using a hand pump. During the saturation process, the pressure was monitored in order to maintain the pressure at 2,000 psi by hand pump. The saturation process lasted for approximately 4 days, one day for vacuuming and CO₂ saturations, and 3 days for pressurizing the cell at 2,000 psi. The saturation process was stopped when no pressure change was noticed for one day.

NMR T_1 - T_2 measurements of the as-received, octane-saturated and brine-saturated cores were acquired at 30 °C with a Larmor frequency of 2.3 MHz, and an echo spacing (t_E) of $t_E = 0.2$ ms and 0.4 ms, using a GeoSpec2 by Oxford Instruments, located at Rice University. T_1 - T_2 measurements of the saturated cores were then acquired at 22 MHz with $t_E = 0.06$ ms and 0.2 ms at CoreLab using a custom-built instrument.

Since the NMR hydrogen index (HI) of the fluids in the as-received cores are unknown, all the NMR porosities are reported assuming $HI = 1$, which we report in units of "pu1". In other words, "pu1" is short for porosity units (i.e. percent of bulk volume) assuming $HI = 1$. The change in fluid filled porosity after saturation was also measured by the change in weight of the core samples after saturation, which agreed well with the NMR porosity change after saturation.

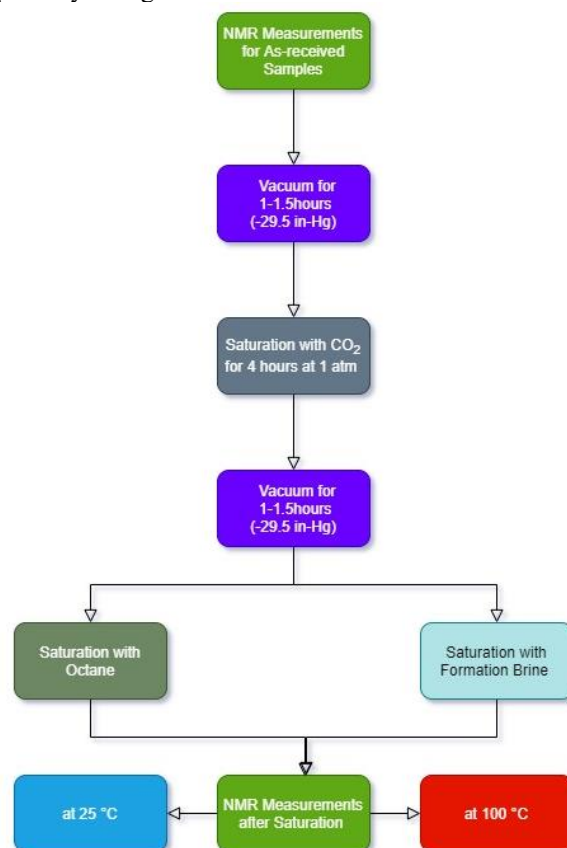


Fig. 1 Flowchart of the Experiments Workflow

NMR T_2 measurements at ambient (25 °C) and elevated temperature (100 °C) were then acquired at 2.3 MHz with $t_E = 0.2$ ms, using a Temco core-holder for 1” cores. The core holder was sealed with the core inside, and then heated in an oven to 105 °C. After 2 hours heating in the oven, the core holder was quickly inserted into the GeoSpec2. A thermocouple connected to the sample space indicated a drop from 102 °C to 98 °C during the 4 minute-long T_2 measurement. Repeatability of the measurement indicated no fluid loss. The empty Temco core-holder indicated ≈ 2 pu1 of background signal. The magnetization decay (i.e. the echo train) of the background signal was subtracted from the saturated core signal before inverting for the T_2 distribution.

3 Theory

The measured T_1 and T_2 relaxation times are composed of the following components:

$$\frac{1}{T_1} = \frac{1}{T_{1B}} + \frac{1}{T_{1S}}, \quad (1)$$

$$\frac{1}{T_2} = \frac{1}{T_{2B}} + \frac{1}{T_{2S}} + \frac{1}{T_{2D}}. \quad (2)$$

$T_{1B,2B} (\propto T/\eta)$ are the bulk-fluid relaxation times. $T_{1S,2S}$ are the surface-relaxation times, which are defined by the following expressions in the “fast-diffusion regime”:

$$\frac{1}{T_{1S,2S,W}} = \rho_{1,2,W} \frac{S}{S_W V} \quad \& \quad \frac{1}{T_{1S,2S,O}} = \rho_{1,2,O} \frac{S}{S_O V} \quad (3)$$

S_W and S_O are the saturation for water and oil, respectively, in the empty pores of the as-received cores. The saturation of the total pore volume is not known since the saturation of the as-received cores is not known. S/V is the surface to pore-volume where $S/V = 6/d$ for spherical pores of diameter d . $\rho_{1,2,W}$ ($\rho_{1,2,O}$) are the surface-relaxivities for water and oil, respectively, which depend on wettability but do not depend on saturation. We use $T_{1S,2S} = T_{1,2}$ throughout given that bulk-fluid relaxation is negligible (i.e. $T_{1B,2B} \gg T_{1S,2S}$) in the present case. We used Eq. (3) to determine the surface relaxivity ratios $\rho_{1,W}/\rho_{1,O}$ and $\rho_{2,W}/\rho_{2,O}$ from the $T_{1,2,W,O}$ distributions peaks (i.e. modes) shown in Figure 2 at 2.3 MHz, and the measured values of S_W and S_O . The only exception is for $T_{1,2,W}$ in the Upper Bakken where the log-mean, is used instead of the peak in the region above $T_{2,W} > 1$ ms to avoid the as-received signal $T_{2,AS} \approx 0.2$ ms.

We find a large contrast in $\rho_{1,W}/\rho_{1,O}$ between the Upper Bakken, the Middle Bakken and the Three Forks, where $\rho_{1,W}/\rho_{1,O} \gg 1$ indicates strongly water-wet conditions, and $\rho_{1,W}/\rho_{1,O} \ll 1$ indicates strongly oil-wet conditions (similarly for $\rho_{2,W}/\rho_{2,O}$). We also report NMR wettability indices $I_{W,1,2}$ which range from $I_{W,1,2} = +1 \Leftrightarrow -1$ as such [16]:

$$I_{W,1} = \frac{\rho_{1,W}/\rho_{1,O} - 1}{\rho_{1,W}/\rho_{1,O} + 1} \quad \& \quad I_{W,2} = \frac{\rho_{2,W}/\rho_{2,O} - 1}{\rho_{2,W}/\rho_{2,O} + 1}. \quad (4)$$

We assume that there is no difference between the intrinsic water and oil relaxivities (i.e. $\rho_{\text{ratio}} = 1$) [16] given that we are using a pure alkane (octane) rather than a crude-oil. We also assume there is no diffusive coupling between the saturating fluids and the as-received fluids.

In nanometer-confined pores, surface relaxation originates from (1) enhanced ^1H - ^1H dipole-dipole relaxation, where the enhancement is due to hindered rotational and translational motion of the fluid at the surface [7, 18], and/or (2) paramagnetic surface-relaxation induced by 2D diffusion of the fluid in the proximity of a paramagnetic site at the surface [9]. In the case of enhanced ^1H - ^1H dipole-dipole relaxation, $T_{1,2,W,O}$ are expected to increase with increasing temperature since the fluid’s correlation time or residence time at the surface decreases with increasing temperature [19, 20]. In the case of paramagnetic surface-relaxation, the absence of any observable temperature dependence in $T_{1,2,W,O}$ is attributed to the lack of temperature dependence in the electron relaxation time [20]. In this report, we therefore use the observation of an increase in $T_{2,W,O}$ with temperature as a sign of enhanced ^1H - ^1H dipole-dipole relaxation, and constant $T_{2,W,O}$ with temperature as a sign of paramagnetic surface-relaxation.

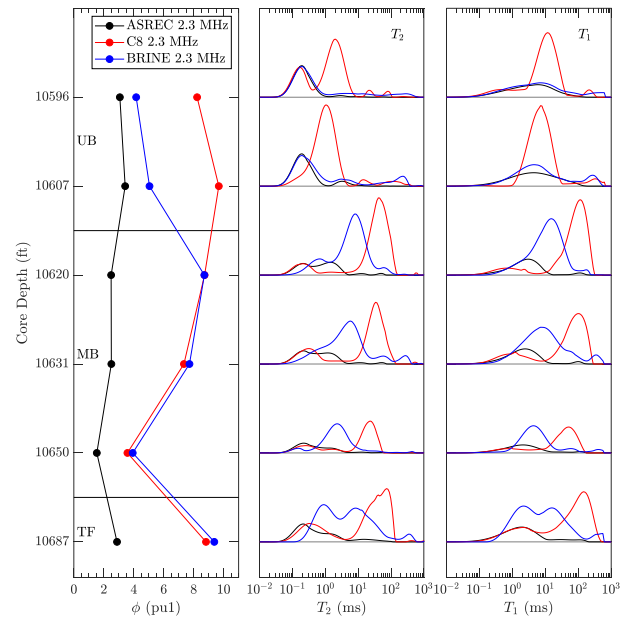


Fig. 2 Porosity, T_2 , and T_1 at 2.3 MHz ($t_E = 0.2$ ms) at 30 °C for as-received (black), octane-saturated (red) and brine-saturated (blue) cores, across the Upper Bakken, Middle Bakken, and Three Forks.

For fluids under nano-confinement, an increase in $T_{1,W,O}$ with increasing frequency can occur from both relaxation mechanisms. In the case of enhanced ^1H - ^1H dipole-dipole relaxation, an increase in $T_{1,O}$ with

frequency was previously observed in polymer-heptane mixes, where the viscous polymer acts like a kerogen surface for heptane [21]. In the case of paramagnetic surface-relaxation, the frequency dependence in $T_{1,W,O}$ can be explained by 2D diffusion of the fluid in the proximity of a paramagnetic site [9]. We note that the observed frequency dependence in $T_{1,W,O}$ is much weaker than predicted by the traditional Bloembergen-Purcell-Pound model for bulk fluids in the slow-motion regime.

T_{2D} is the relaxation time from diffusion in internal gradients, where higher magnetic fields B_0 (i.e. higher NMR frequencies, $\omega_0 = \gamma B_0$) or longer t_E (echo-spacing) result in shorter T_{2D} , assuming the “free diffusion” or “short-time regime” [22]:

$$\frac{1}{T_{2D}} = \frac{1}{12} (\gamma G t_E)^2 D \quad \text{where} \quad G \approx \Delta\chi B_0 / d. \quad (5)$$

G is the approximate strength of the internal gradient in a pore of size d . $\Delta\chi$ is the magnetic susceptibility contrast between fluid and matrix, or between fluid and fluid for oil-water emulsions (for instance). γ is the gyro-magnetic ratio, and D is the diffusion coefficient of the fluid in the pore. In cases where internal gradients are present, caution must be taken when interpreting wettability or pore-size from T_2 . The lack of t_E dependence on T_2 at 2.3 MHz indicates no internal gradient effects at 2.3 MHz. However, at 22 MHz we observe a decrease in T_2 with increasing t_E for certain cases, which indicates internal gradients for those cases.

4 Wettability

For the Upper Bakken, the total NMR porosity, T_2 , and T_1 distributions at 2.3 MHz are shown in Figure 2, for as-received, octane-saturated and brine-saturated cores. The as-received data indicate ≈ 3 pu1 at short $T_{2,AR} \approx 0.18$ ms and large $(T_1/T_2)_{AR} \approx 14$, which is most likely from bitumen [23]. Even though the same saturation process and pressure was used for octane and brine saturation, the NMR data indicate that the octane saturation (≈ 6 pu1, $S_O = 1$) is much higher than the brine saturation (≈ 2 pu1, $S_W = 0.24$) of the twin cores, in agreement with the weight change of the core after saturation. This indicates that the Upper Bakken is resistant to brine saturation of oil-wet nano-pores. More specifically, brine saturation at 2,000 psi was insufficient to overcome capillary forces in oil-wet pores of size $d < 10$ nm. Using Eq. (3) we find that $\rho_{1,2,W}/\rho_{1,2,O} \approx 0.026$ (defined as the log-mean of $\rho_{1,W}/\rho_{1,O}$ and $\rho_{2,W}/\rho_{2,O}$ in Figure 3(a)). Using Eq. (4) we find that $I_W \approx -0.94$ (defined as mean of $I_{W,1}$ and $I_{W,2}$ in Figure 3(b)), indicating that the Upper Bakken is strongly oil-wet.

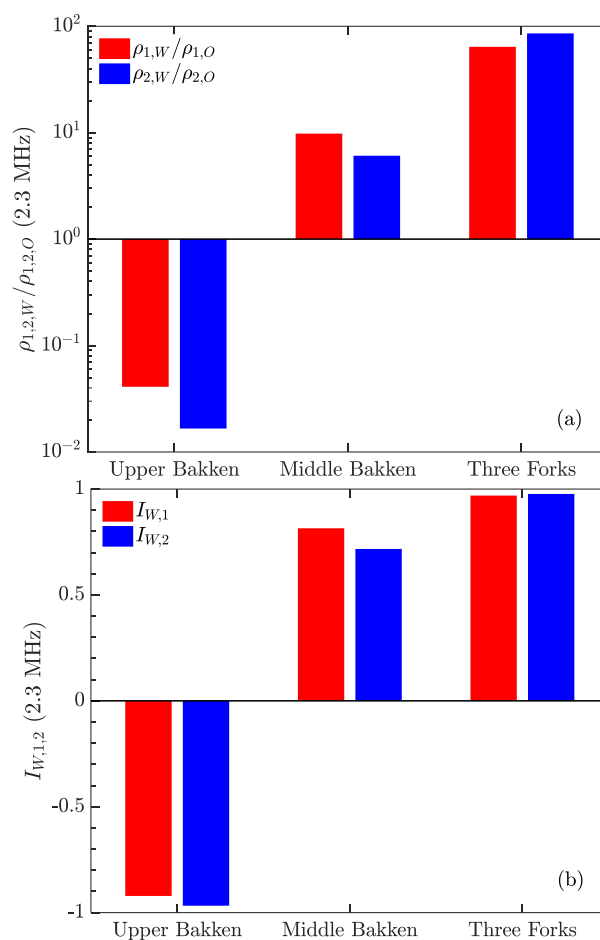


Fig. 3 (a) Ratio of surface relaxivities $\rho_{1,W}/\rho_{1,O}$ and $\rho_{2,W}/\rho_{2,O}$ and (b) NMR wettability indices $I_{1,W}$ and $I_{2,W}$ for the Upper Bakken, Middle Bakken, and Three Forks, all at 2.3 MHz.

For the Middle Bakken, the as-received data indicate ≈ 3 pu1 at short $T_{2,AR} \approx 0.6$ ms and moderate $(T_1/T_2)_{AR} \approx 3.2$, which is most likely from clay-bound water [7]. The pore volume saturated in both the octane and brine saturations in the twin cores was approximately the same (≈ 6 pu1) according to NMR, in agreement with the weight change of the core after saturation. We find that $\rho_{1,2,W}/\rho_{1,2,O} \approx 7.7$ and $I_W \approx +0.77$, indicating water-wet to intermediate-wet conditions.

The Three-Forks as-received is similar to the Middle Bakken. The Three Forks saturated cores show $\rho_{1,2,W}/\rho_{1,2,O} \approx 74$ and $I_W \approx +0.97$, indicating strongly water-wet conditions.

5 Frequency Dependence and Presence of Bitumen

For the Upper Bakken, Figure 4 shows an example of the T_1 - T_2 maps for the octane saturated and brine saturated core samples using 2.3 MHz ($t_E = 0.2$ ms) and 22 MHz ($t_E = 0.06$ ms), at 30 °C. In the octane saturated core samples, $T_{1,O}$ increased by a factor of ≈ 6 with increasing frequency. In both octane and brine saturated core samples, there was also an additional ≈ 6 pu1 observed at

short T_2 as a result of the shorter t_E used for 22 MHz compared to 2.3 MHz. The additional signal at $T_2 < 0.1$ ms at 22 MHz shows a large $T_1/T_2 \approx 100$, and is therefore attributed to bitumen (Yang et al. 2012). Given the short $T_2 < 0.1$ ms, there is most likely more bitumen signal which is not detectable even at $t_E = 0.06$ ms.

frequency indicates strong internal gradients at 22 MHz. In both octane and brine saturated core samples, there was an additional ≈ 2 pu1 at short $T_2 < 0.1$ ms and $T_1/T_2 \approx 10$, which is most likely from hydroxyls in the clay-bound water signal [8].

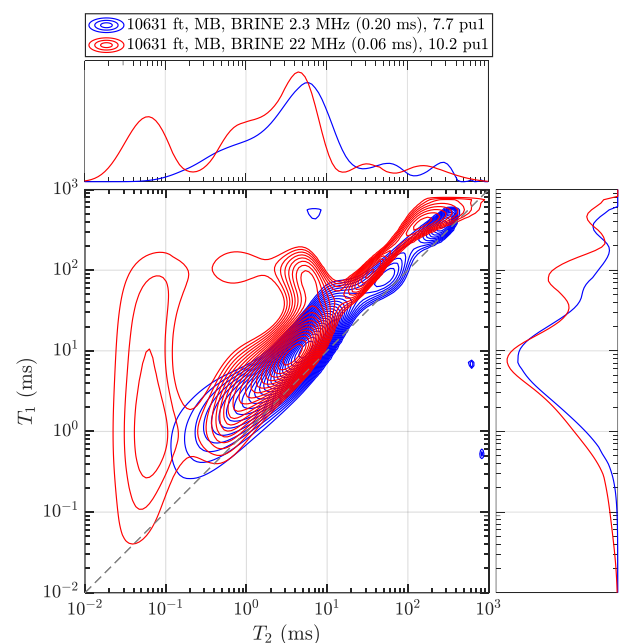
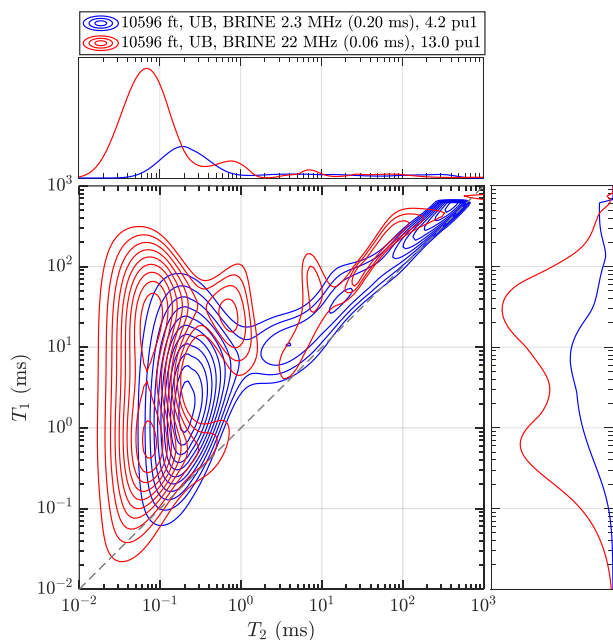
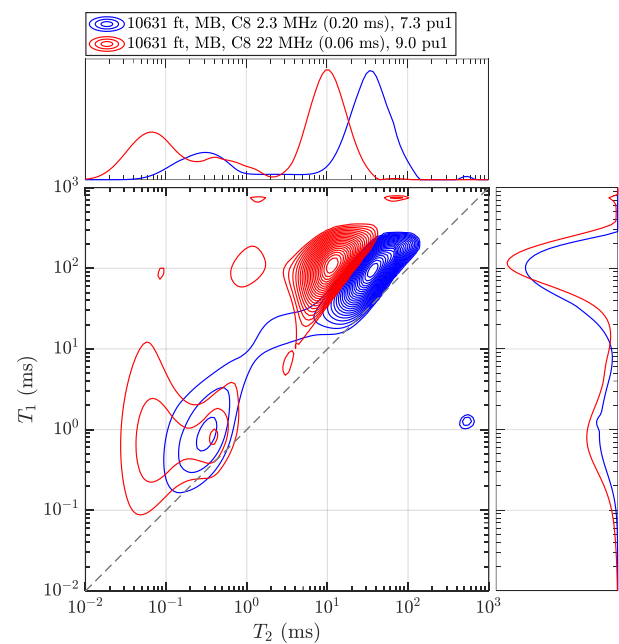
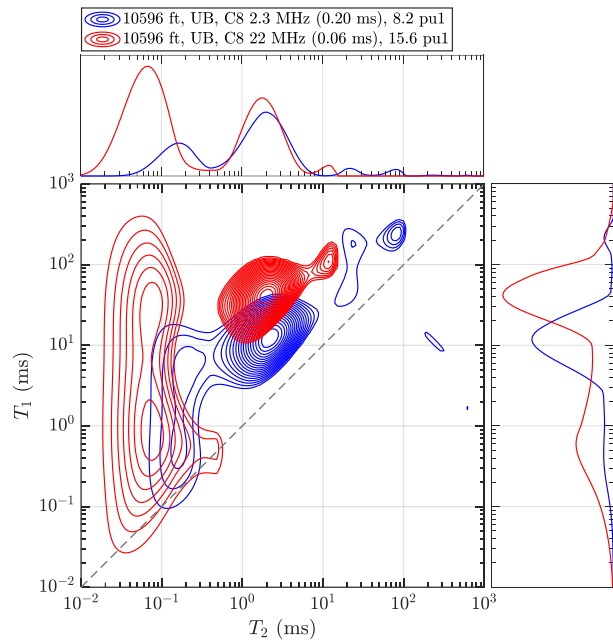


Fig. 4 T_1 - T_2 maps at 2.3 MHz (blue, $t_E = 0.2$ ms) and 22 MHz (red, $t_E = 0.06$ ms) at 30 °C, for octane-saturated (upper) and brine-saturated (bottom) core in the Upper Bakken.

Fig. 5 T_1 - T_2 maps at 2.3 MHz (blue, $t_E = 0.2$ ms) and 22 MHz (red, $t_E = 0.06$ ms) at 30 °C, for octane-saturated (upper) and brine-saturated (bottom) core in the Middle Bakken.

For the Middle Bakken and Three Forks, Figures 5 and 6 show examples of the T_1 - T_2 maps for the octane saturated and brine saturated core samples using 2.3 MHz ($t_E = 0.2$ ms) and 22 MHz ($t_E = 0.06$ ms), at 30 °C. For both saturating fluids, there was only a minor increase in $T_{1,W,O}$ with increasing frequency. In the case of octane saturated cores, the decrease in $T_{2,O}$ with increasing

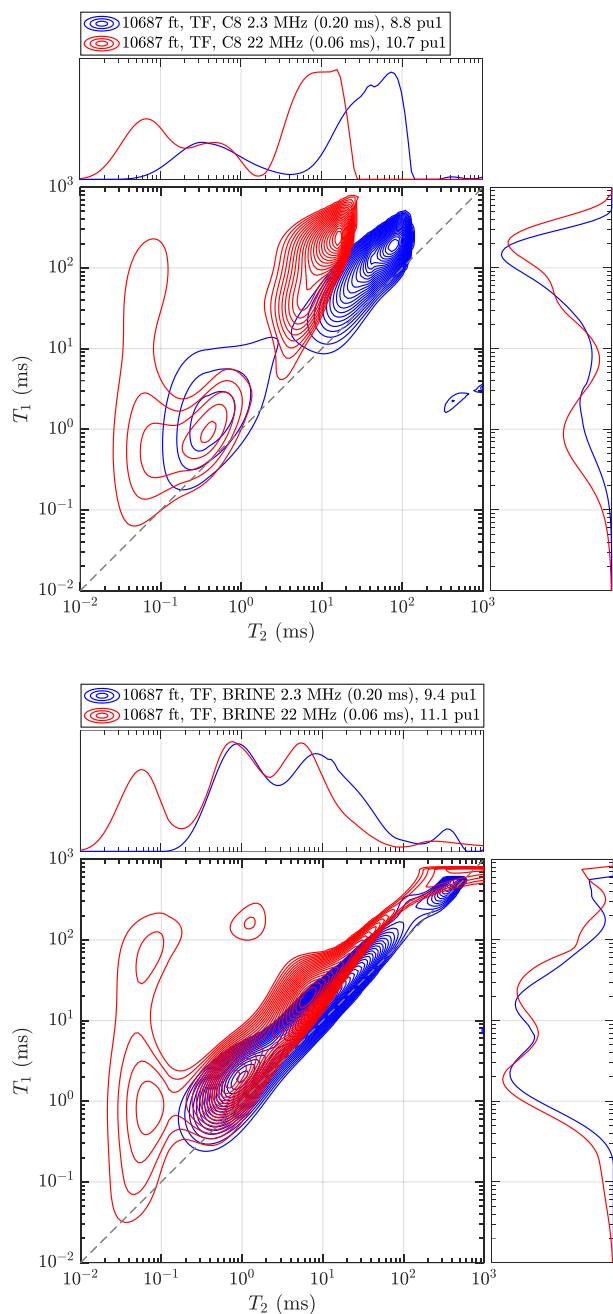


Fig. 6 T_1 - T_2 maps at 2.3 MHz (blue, $t_E = 0.2$ ms) and 22 MHz (red, $t_E = 0.06$ ms) at 30 °C, for octane-saturated (upper) and brine-saturated (bottom) core in the Three Forks.

6 Surface Relaxation Mechanism

Figure 7 (middle) shows the T_2 distribution for octane-saturated cores measured with 2.3 MHz at 25 °C and 100 °C with $t_E = 0.2$ ms. The surface relaxivity $T_{2,o}$ increases by a factor of ≈ 3 with increasing temperature in the Upper Bakken, indicating enhanced ^1H - ^1H dipole-dipole relaxation with the oil-wet nano-pores. $T_{2,o}$ increases by a factor of ≈ 2 with increasing temperature in the Middle Bakken core samples, indicating enhanced ^1H - ^1H dipole-dipole relaxation with the surface water film. These temperature effects are consistent with findings for oil in shale [10]. In the case of the Three Forks, there is no

change in $T_{2,o}$ with the increase of temperature, indicating paramagnetic surface-relaxation.

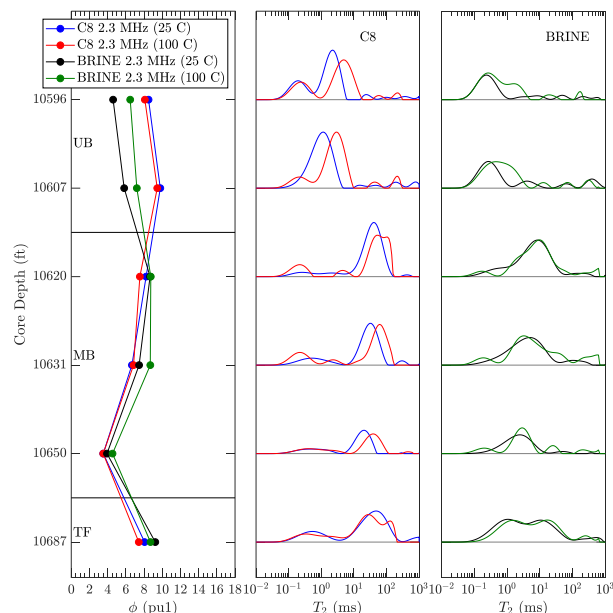


Fig. 7 Porosity and T_2 at 2.3 MHz ($t_E = 0.2$ ms) for octane-saturated cores at 25 °C (blue) and 100 °C (red), and brine-saturated cores at 25 °C (black) and 100 °C (green), across the Upper Bakken, Middle Bakken, and Three Forks.

Figure 7 (right) shows the T_2 distribution for brine-saturated cores. The Upper Bakken core samples show an increase of ≈ 2 pu1 with increasing temperature. This is attributed to a decrease in bitumen viscosity with temperature, which results in more observable NMR signal at $t_E = 0.2$ ms. Meanwhile, $T_{2,W}$ is roughly constant in both the Middle Bakken and Three Forks, indicating paramagnetic surface-relaxation.

Our data indicate that an increase in $T_{2,W,0}$ with increasing temperature correlates with an increase in $T_{1,W,0}$ with increasing frequency, which is expected for enhanced ^1H - ^1H dipole-dipole relaxation [21]. Our data also indicate that a constant $T_{2,W,0}$ with increasing temperature correlates with a constant $T_{1,W,0}$ with increasing frequency, which is expected for paramagnetic surface relaxation [20]; a different interpretation for the frequency dependence is given by Nicot *et al.* 2016 [9].

7 Internal Gradients

While we have already indicated the presence of internal gradients in T_2 at 22 MHz for octane-saturated cores by comparing 2.3 MHz to 22 MHz in Figures 4,5, and 6. Another (more common way) to test for internal gradients in T_2 is to increase t_E . Figure 8 shows how increasing t_E has minimal effect at 2.3 MHz, while it has a large effect at 22 MHz in the case of octane-saturated cores. In the case of brine-saturated cores (not shown), increasing t_E has minimal effects at both 2.3 MHz and 22 MHz. The difference in internal gradients between octane and brine saturated cores at 22 MHz is a result of the difference in magnetic susceptibility contrast between the fluid and the

matrix. In the case of brine-saturated cores, the magnetic susceptibility of brine is closer to that of the matrix. For octane-saturated cores, the magnetic susceptibility of octane is significantly different to that of the matrix.

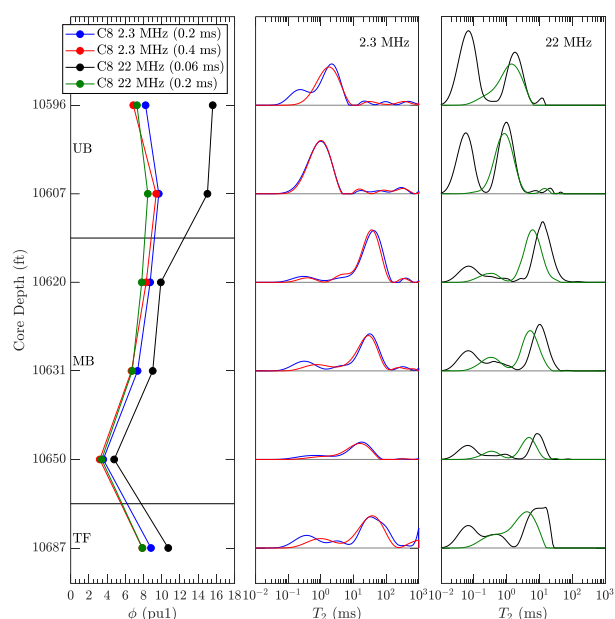


Fig. 8 Porosity and T_2 for octane-saturated cores at 30 °C, at 2.3 MHz with $t_E = 0.2$ ms (blue) and $t_E = 0.4$ ms (red), and at 22 MHz with $t_E = 0.06$ ms (green) and $t_E = 0.2$ ms (black) across the Upper Bakken, Middle Bakken, and Three Forks.

8 Conclusions

The accurate identification of the rock wettability is very crucial for improving the oil recovery using fluid injection. Previous NMR studies performed on the Bakken were focused on porosity, pore size distributions, fluid typing, the identification of the bitumen and bound water signals [24, 25, 26, 27, 28]. Previous research on native-state and post cleaning Bakken/Three Forks cores, concluded dual wettability where the small pores are water wet and the larger pores are oil wet, and the clay is oil wet [28].

In this paper, NMR measurements have shown that the Upper Bakken cores are strongly oil-wet, while the Middle Bakken cores are water-wet to intermediate-wet, and the Three Forks cores are strongly water-wet. We were able to detect the presence of bitumen in the Upper Bakken cores at 22 MHz where a short echo-spacing is possible. We investigated the origin of the NMR surface-relaxation mechanism in the saturated nanometer-sized pores by studying the temperature dependence (25 °C to 100 °C) of T_2 at 2.3 MHz. The results indicate that NMR surface relaxation in the Upper Bakken is dominated by enhanced ^1H - ^1H dipole-dipole relaxation, while in the Three Forks it is dominated by paramagnetic surface relaxation. On the other hand, the octane saturated Middle Bakken cores is dominated by enhanced ^1H - ^1H dipole-dipole relaxation with surface water film, while for brine saturated cores it is dominated by paramagnetic surface relaxation.

We checked for the presence of the internal gradient by varying the echo-spacing of the T_2 measurement. While no internal gradients were found at 2.3 MHz, we found strong internal gradient effects in the case of octane-saturated cores in the Middle Bakken and Three Forks at 22 MHz. These results suggest that the echo-spacing dependence on T_2 should be investigated on a routine basis in unconventional shale (particularly at 22 MHz), where it is often assumed that internal gradients are negligible.

Our findings are also summarized in the table below. We have shown how NMR core-analysis can give a wealth of information in the Bakken formation including wettability, presence of bitumen, surface relaxation mechanism, and presence of internal gradients. In order to preserve the wettability of the cores, our methodology *does not* involve core cleaning. Our methodology also highlights the advantages of measuring the cores at both 2.3 MHz and 22 MHz.

	Octane saturated	Brine saturated
Upper Bakken	<ul style="list-style-type: none"> Strongly oil-wet ($I_W \approx -0.94$) ^1H-^1H dipole-dipole relaxation with organic surface Presence of bitumen 	<ul style="list-style-type: none"> Strongly oil-wet ($I_W \approx -0.94$) Resistant to brine saturation ($S_W \approx 0.24$) Presence of bitumen
Middle Bakken	<ul style="list-style-type: none"> Water-wet ($I_W \approx +0.77$) ^1H-^1H dipole-dipole relaxation with surface water film Strong internal gradients at 22 MHz 	<ul style="list-style-type: none"> Water-wet ($I_W \approx +0.77$) Paramagnetic surface relaxation with minerals
Three Forks	<ul style="list-style-type: none"> Strongly water-wet ($I_W \approx +0.97$) Paramagnetic surface relaxation with minerals Strong internal gradients at 22 MHz 	<ul style="list-style-type: none"> Strongly water-wet ($I_W \approx +0.97$) Paramagnetic surface relaxation with minerals

We thank the Wilson M. Laird Core and Sample Library for providing the core samples used in this study. We also thank Zeliang Chen and Xinglin Wang for useful discussions.

References

- H. Pu, Y. Li, "CO₂ EOR Mechanisms in Bakken Shale Oil Reservoirs" *Carbon Management Technology Conference*, SPE-439769-MS (2015)
- North Dakota Geological Survey, "Overview of the Petroleum Geology of the North Dakota Williston Basin." *North Dakota Industrial Council* (1986) <https://www.dmr.nd.gov/ndgs/Resources/>
- T. Tran, P.D. Sinurat, B.A. Wattenbarger, "Production Characteristics of the Bakken Shale Oil." *SPE Annual Technical Conference and Exhibition*. SPE-145684-MS (2011)
- L.C. Price, "Origins and Characteristics of the Basin-Centered Continuous-Reservoir Unconventional Oil-Resource Base of the Bakken Source System, Williston Basin: EERC" *EERC Website*. (1999) <http://www.undeerc.org/News-Publications/Leigh-Price-Paper/Default.aspx>
- R.L. Webster, "Petroleum Source Rocks and Stratigraphy of the Bakken Formation in North Dakota." *Hydrocarbon Source Rocks of the Greater Rocky Mountain Region*, AAPG Bulletin (1984), **68** (7): 953
- A.E. Ozen, R.F. Sigal, "*T*₁/*T*₂ NMR Surface Relaxation Ratio for Hydrocarbons and Brines in Contact with Mature Organic-Shale Reservoir Rocks" *Petrophysics* **54** (1), 11-19 (2013)
- P.M. Singer, Z. Chen, G.J. Hirasaki, "Fluid Typing and Pore Size in Organic Shale Using 2D NMR in Saturated Kerogen." *Petrophysics*, **57** (6): 604–19 (2016)
- M. Fleury, M. Romero-Sarmiento, "Characterization of Shales Using *T*₁-*T*₂ NMR Maps" *Journal of Petroleum Science and Engineering* **137**: 55–62 (2016)
- B. Nicot, N. Vorapalawut, B. Rousseau, L.F. Madariaga, G. Hamon, J. Korb, "Estimating Saturations in Organic Shales Using 2D NMR" *Petrophysics*, **57** (1): 19–29 (2016)
- Z.H. Xie, Z. Gan, "Investigation of Physical Properties of Hydrocarbons in Unconventional Mudstone using Two-dimensional NMR Relaxometry" *SPWLA 60th Annual Logging Symposium*, SPWLA (2019)
- D. Kausik, D. Freed, K. Fellah, L. Feng, Y. Ling, G. Simpson, "Frequency and Temperature Dependence of 2D NMR *T*₁-*T*₂ Maps of Shale" *Petrophysics* **60** (1), 37-49 (2019)
- Z. Chen, P.M. Singer, X. Wang, H.J. Vinegar, S.V. Nguyen, G.J., Hirasaki, "NMR Evaluation of Light Hydrocarbon Composition, Pore Size, and Tortuosity in Organic-Rich Chalks" *Petrophysics* **60** (6), 771-797 (2019)
- I. Sulucarnain, C.H. Sondergeld, C.S. Rai, "An NMR study of shale wettability and effective surface relaxivity" SPE Canadian Unconventional Resources Conference (2012)
- R.F. Sigal, E. Odusina, "Laboratory NMR Measurements on Methane Saturated Barnett Shale Samples" *Petrophysics* **52** (1), 32-49 (2011)
- I. Gupta, C. Rai, C. Sondergeld, "Study Impact of Sample Treatment and Insitu Fluids on Shale Wettability Measurements using NMR" *Journal of Petroleum Science and Engineering* **176**, 352-361 (2019)
- A. Valori, B. Nicot, "A Review of 60 years of NMR Wettability" SCA-17 (2018)
- "Recommended Practices for Core Analysis." *American Petroleum Institute* (1998) <http://w3.energistics.org/RP40/rp40.pdf>
- K.E. Washburn, "Relaxation Mechanisms and Shales." *Concepts in Magnetic Resonance Part A* **40**: 39–65 (2012)
- C. Straley, "A Mechanism for the Temperature Dependence of the Surface Relaxation Rate." SCA-27 (2002)
- I. Foley, S.A. Farooqui, R.L. Kleinberg, "Effect of Paramagnetic Ions on NMR Relaxation of Fluids at Solid Surfaces." *JMR* **123** (1): 95–104 (1996)
- P.M. Singer, Z. Chen, L.B. Alemany, G.J. Hirasaki, K. Zhu, Z.H. Xie, T.D. Vo, "Interpretation of NMR Relaxation in Bitumen and Organic Shale Using Polymer-Heptane Mixes." *Energy & Fuels* **32**, 1534-1549 (2018)
- M.D. Hurlimann, "Effective Gradients in Porous Media Due to susceptibility Differences" *Journal of Magnetic Resonance* **131**, 232-240 (1998)
- Z. Yang, G.J. Hirasaki, M. Appel, D.A. Reed, "Viscosity Evaluation for NMR Well Logging of Live Heavy Oils" *Petrophysics*, **53** (1), 22–39 (2012)
- O.S. Tomomewo, H. Jabbari, N. Badrouchi, C. Onwumelu, M. Mann, "Characterization of the Bakken Formation using NMR and SEM Techniques" *ARMA*, 19-1875 (2019)
- C. Onwumelu, O. Kolawole, I. Bouchakour, O. Tomomewo, A. Adeyilola, "Effective Correlation between Petrophysical Characterization of Magnetic Resonance Imaging Log and Nuclear Magnetic Resonance Core Data" *ARMA/DGS/SEG International Geomechanics Symposium*, 20-001 (2020)
- C. Onwumelu, S. Nordeng, A. Adeyilola, "Rock Characterization Using Nuclear Magnetic Resonance and Scanning Electron Microscope: A Laboratory Study of Bakken Formation" *SEG International Exposition and 89th Annual Meeting*, 3354-3358 (2019)
- R. Kausik, K. Fellah, L. Feng, G. Simpson, "High- and Low-Field NMR Relaxometry and Diffusometry of the Bakken Petroleum System" *Petrophysics*, **58** (4), 341–351 (2017)

28. G. Simpson, N.S. Fishman, S. Hari-Roy, "New Nuclear Magnetic Resonance Log T2 Cut-off Interpret Parameters for the Unconventional Tight Oil of the Bakken Petroleum System Using 2-D NMR Core Laboratory Measurements on Native state and Post-Cleaned Core Samples" *SPWLA 59th Annual Logging Symposium* (2018)

Effect of specimen size and shape on the mechanical properties measured on plugs subsampled from sidewall cores

Giorgio Volonté^{1,*}, Jørn Stenebraten², and Euripides Papamichos²

¹Eni S.p.A., 20097 San Donato Milanese, Italy

²SINTEF Industry, NO-7465 Trondheim, Norway

Abstract. For several disciplines, the increasing acquisition of rotary sidewall cores (RSWC) in the oil and gas industry gives the opportunity for more extensive experimental rock characterization but, on the other hand, the limited amount of recovered material, their shape and orientation are not optimal for geomechanical experiments in the triaxial cell. These drawbacks can be overcome by performing experiments on properly shaped and oriented small diameter plugs subsampled from the RSWCs. These plugs are smaller than conventional ones, so the effects of both specimen shape (i.e., length over diameter L/D ratio) and size (i.e., diameter) on strength, stiffness (i.e., Young's modulus), and dilation (i.e., Poisson's ratio) must be carefully considered. In this work, an experimental study on specimen shape and size effects on rock mechanical properties has been tailored to materials and testing conditions generally encountered in petroleum related geomechanics. Triaxial compression experiments at three confining pressures have been performed on outcrop analogues of typical reservoir rock lithologies, i.e., two sandstones and two limestones, and within a range of shapes and sizes relevant for specimens prepared from RSWCs with emphasis on 10 mm diameter specimens. The strength, stiffness and dilation results were analysed and compared with relevant data and relations available in the literature. Then, analytical equations, useful for the practice of geomechanical experimental studies on RSWCs, have been derived to correlate mechanical properties measured on specimens of any shape or size to the ones obtainable on reference specimens.

1 Introduction

Several wellbore and field scale problems in the Oil & Gas industry require dedicated geomechanical experimental characterization that is usually performed on material acquired from 3" to 4" diameter bottom hole cores (BHCs). However, in the recent years, industry is increasingly promoting the partial replacement of bottom hole cores with 1 1/2" diameter rotary sidewall cores (RSWC) since the cost of their acquisition is lower. It should be noticed that RSWCs provide an opportunity to several disciplines to acquire data already from exploratory wells or from non-reservoir facies with a limited additional expense. But, on the other hand, geomechanical testing, e.g. triaxial compression tests, requires the use of multiple plugs sampled at the same depth interval and properly oriented with respect to bedding or in situ stresses. These requirements, easily satisfied by conventional plugs sampled on BHCs, requires that RSWCs are subsampled to plugs whose dimensions are smaller than conventional ones.

Since measured mechanical properties are affected by specimen shape (i.e., length over diameter L/D ratio) and size (i.e., diameter D), in this work an experimental study on their effect on the strength, stiffness (i.e., Young's modulus), and dilation (i.e., Poisson's ratio) of the rock has been tailored to materials and testing conditions generally encountered in petroleum related geomechanics. In the literature several experimental studies investigate these effects and especially the effects on the unconfined compressive strength (UCS) (e.g., [1] and references within). However, most of them are based on larger samples or on lithology not common in the Oil & Gas industry. A summary of these experimental evidence is presented in the following paragraphs.

1.1 Effect of specimen size and shape on strength

Generally, the compressive strength of the rock increases with decreasing L/D ratio especially for values lower than 2.5. The reasons for this increase may be related to the impediment of the development of an inclined shear band for failure in short specimens. For such specimens the inclination of the failure plane (shear band) is such that it meets the loading platens and thus it cannot develop freely, while in more slender specimens it meets the side of the specimen and can form a kinematically possible failure mechanism. Another reason is the confinement due to friction at the loading platens which is more dominant in shorter specimens and provides lateral support to the specimen. It should be anyway highlighted that, for small samples, these boundary conditions may dominate the failure, not the intrinsic failure mechanisms. Experimental data for granite specimens presented in [2] are an example of such behaviour. Figure 1 plots various correlations, based on experimental results, that have been proposed in the literature [1,3,4,5] to describe the shape effect on strength. The ASTM suggested equation for the correction of measured strength is also shown [6]. Regarding the size effect, a decrease in strength is observed with increasing specimen size since, statistically, with larger specimens there is a larger probability to include critical flaws in the sample that may lead to specimen failure. Moreover, the strength of a specimen increases as the ratio of specimen size to internal length of the rock, e.g. grain size, decreases. This behaviour has been highlighted by the experimental results reported in [7] and described, e.g., by the following equation proposed in [8]:

$$\frac{UCS}{UCS_{D_{ref}}} = \left(\frac{D_{ref}}{D}\right)^k \quad (1)$$

* Corresponding author: giorgio.volonte@eni.com

where D_{ref} is the diameter of the reference specimen and k a parameter equal to 0.18 for D_{ref} equal to 50 mm.

However, in [9] it is suggested that the relation presented in [8] is rather valid for hard rocks whereas for carbonates and sandstones a peak strength is observed between 38-54 mm diameter specimens as shown in Figure 2 where the strength decreases in either side of the peak.

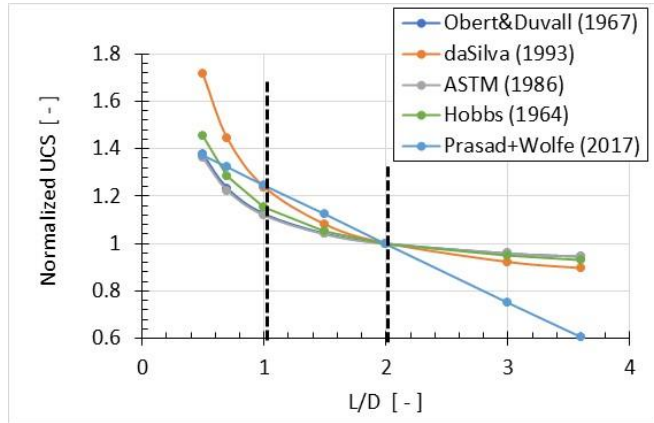


Fig. 1. UCS relations with L/D proposed by various investigators. The UCS is normalized with the UCS for L/D = 2. The dotted lines indicate the range of L/D ratios investigated in this study.

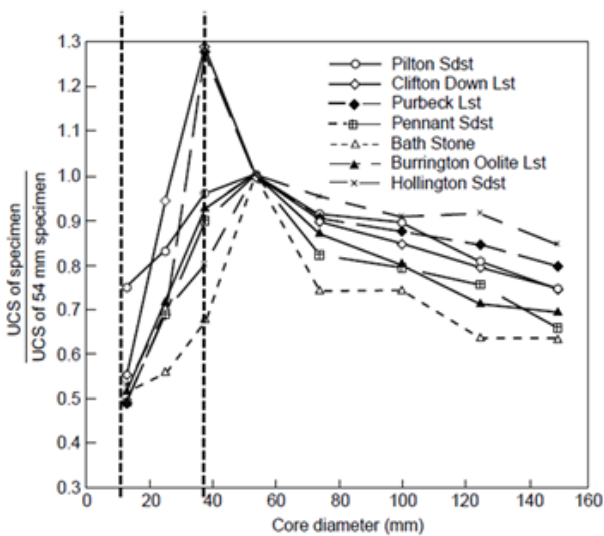


Fig. 2. UCS of seven sedimentary rocks measured on samples of eight different diameter [9]. Values are normalized with respect to the strength of the 54 mm diameter sample of the corresponding rock type. The dotted lines indicate the range of diameters investigated in this study.

1.2 Effect of specimen size and shape on stiffness

Although the effect of shape and size on stiffness has not been studied as extensively as that on strength, most of the data in the literature indicate that it is relatively small or that there is a significant scatter in the observations. In [10] it is shown that the stiffness modulus is practically independent of the shape. However, both an increase and a decrease of stiffness with increasing L/D ratio have been reported in [11] for kersantite rock and in [12] for Berea sandstone, respectively. In [13] a small, if any, increase in stiffness with increasing

L/D in a granite is highlighted. Reference [14] also reports an increase in stiffness with increasing L/D ratio in Red Wildmoor sandstone, but this increase was attributed to the bedding error in the contact between the specimen and the loading platens.

Similarly, the size does not seem to have a large effect on the stiffness of the rock. In [7] and [13] a small effect of the size of granite specimens on stiffness is reported. Reference [13] presents a small increase in stiffness, while [15] reports a larger increase with increasing diameter in limestones. All the experimental results presented are for diameters in the range of 45 – 900 mm, which are larger than the diameters analysed in this study which were in the range of 10-38 mm.

1.3 Effect of specimen size and shape on dilation

The effect of shape and size on dilation, i.e. on the tangent Poisson's ratio ν_{50} , has been studied even less than that on stiffness. In [10], from the few available data, a decrease of Poisson's ratio with increasing L/D ratio for granitic rocks is reported. Reference [12] shows a decrease, no effect or increase of Poisson's ratio with increasing L/D for Berea sandstone with no clear effect of the confining stress. In [13] a small, if any, effect on Poisson's ratio is shown for a granite. Similarly, the size does not seem to have a consistent effect on the Poisson's ratio. In [13] variable effects of the size of granite specimens on Poisson's ratio is seen.

2 Experimental program

The effect of the specimen shape and size on the triaxial compressive strength (TCS), tangent Young's modulus E_{50} and tangent Poisson's ratio ν_{50} at 50% the peak deviatoric stress was studied experimentally through conventional triaxial compression (CTC) tests at 0.5, 10 and 30 MPa confining stresses. Tests on two sandstones, Carbon Tan (CT) and Saltwash North (SWN), and two limestones, Indiana (IND) and Burlington (BURL), were performed. Table 1 lists the shape and size combinations that were studied experimentally by listing the typical number of tests that were performed. The repetition of tests performed with L/D = 2 specimens allowed to verify the repeatability of the experiments. Some dispersion of the results has been anyway observed (as shown in terms of standard deviation in the plots of the subsequent sections), especially for SWN and IND due to their more accentuated heterogeneity, but this scatter does not hide the observable trends when present. In the cases where tests were repeated also for different L/D ratios, similar repeatability was confirmed.

Table 1. Test matrix for the shape (L/D) and size (D) effect on the triaxial compressive strength, the tangent stiffness modulus E_{50} , and the tangent Poisson's ratio ν_{50} . The table lists the typical number of tests performed for each lithology.

L/D	D [mm]		
	10	25	38
1	1	-	-
1.5	1	-	-
2	3	3	3

Experiments were performed on oven dried specimens (60°C for 2 days). Samples were cored with a rotary core barrel and the end-surfaces were flattened with a surface grinder. The samples were mounted between steel end-pistons and surrounded with a Fluorinated Ethylene Propylene (FEP) heat shrink sleeve. A thin Teflon sheet was placed on each sample-end to reduce end-friction between the sample and end-pistons. Axial deformation was measured with three Linear Variable Differential Transformers (LVDTs), oriented in one plane, 120° apart. Radial deformation was measured with two pairs of strain-gaged cantilevers oriented orthogonally to each other and measuring the diametrical deformation at mid-height of the sample.

The testing was performed in a hydraulic servo-controlled load frame with digital feedback control and data acquisition. Confining pressure was ramped at 36 MPa/h and an axial strain rate of 1E-05 s⁻¹ was used for the shearing segment.

The shape effect was studied on 10 mm diameter specimens with L/D equal to 1, 1.5 and 2, while the size effect was studied on specimens with L/D equal to 2 and diameters 10, 25 and 38 mm (Figure 3).



Fig. 3. Photographs showing the size range of tested samples.

3 Data analysis

The results of the experimental campaign were analysed to derive useful expressions for practical applications that correlate the mechanical properties measured on small specimen retrieved from RSWCs with those that would have been obtained through conventional plugs. For this purpose, a series of elaborations have been performed to reduce, as much as possible, the effect of specimen variability and, subsequently, to highlight or rule out eventual lithology dependent behaviours.

A measure of inherent sample variability can be the oven-dry bulk density of the specimens, since samples with higher density are expected to have a higher strength and stiffness. Indeed, some rocks in the present study showed a systematic difference in mechanical properties for a specific shape and size, that were prepared from blocks of rock with lower or higher density than the remaining samples. This resulted in an apparent lower or higher strength/stiffness, respectively. This effect is especially evident in the Carbon Tan samples whose data showed that the D = 25 mm specimens had systematically lower density and, thus, lower strength and stiffness (Figure 4a).

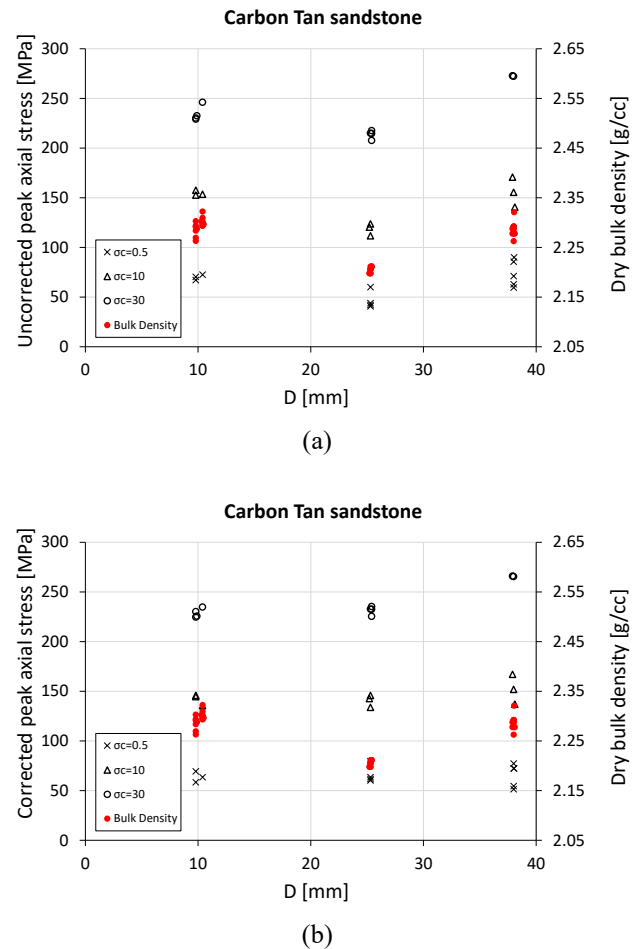


Fig. 4. Carbon Tan sandstone. Oven dried density and TCS before (a) and after (b) density correction.

Since this specimen variability influences the size and shape effects, correction correlations were considered necessary for Carbon Tan, Saltwash North, and Indiana. They were derived through the procedure described in the Appendix. An example of the corrected results is reported in Figure 4b for the strength of Carbon Tan sandstone: corrected data are slightly less sparse while trends are more evident and independent of the specimen density. This procedure was not applied to Burlington limestone which showed similar densities between all the samples.

To allow the comparison and the integration of data referring to different lithologies, all the corrected strength, moduli and Poisson's ratio values measured in the experiments at given confining pressure were averaged and normalized with respect to the corresponding average values obtained by testing reference dimension specimens. The reference dimensions have been assumed equal to 10 mm diameter with L/D = 2 for the study of shape effect and 38 mm diameter with L/D = 2 for the analysis of size effect.

Finally, all normalized values of strength, moduli and Poisson's ratio at given confining pressure were averaged across all rocks and integrated to derive correlations with size and shape independent of lithology. The data from the three confining stresses were not combined because the confining stress may play a role in the scale effect as suggested in the literature.

The outcomes of these analyses are described in the following sections where the obtained correlations with size and shape are reported.

4 Triaxial compressive strength

4.1 Shape effect

The values of normalized compressive strength in Figure 5 show some variability within each lithology at the various confining stresses. In some cases, the strength is higher at lower L/D ratios but in most it is lower. No clear difference can be identified between the four rocks. The plot in Figure 6a indicates that the strength of specimens with L/D = 1.5 and 2 are, for all practical purposes, similar. On the other hand, the strength of the specimens with L/D = 1 seems to be between 5% and 24% lower than the one of specimens with L/D = 1.5 and 2. This finding does not agree with similar findings in the literature which suggest an increase of strength with decreasing L/D ratio. In the range of L/D between 1 to 2, the literature suggests an increase of the strength of specimens with L/D = 1 compared to the one of specimens with L/D = 2 by anything between 12% [6] to 25.5% [1]. This difference can be explained by the small size of the specimens with L/D = 1 used in this study compared to the much larger diameters used in the studies in the literature. In this study the diameter is equal to 10 mm, and thus the specimens are 0.79 cm³ cylinders with dimensions 20 or 30 times their grain size. Due to their relatively small size any damage during specimen coring and polishing may have a considerable effect on the strength.

For the practical applications involving 10 mm diameter specimens, we can combine a formula from literature, e.g., the one suggested by ASTM [6], for L/D > 2 with an equation that accounts for the apparent strength decline due to plug damage for L/D < 2. The combined formula is valid only for 10 mm diameter specimens and may be written as:

$$\frac{TCS_{L/D,10}}{TCS_{2,10}} = \begin{cases} 1.007 - e^{-3\frac{L}{D}} & \text{for } \frac{L}{D} \leq 2 \\ 0.88 + \frac{0.24}{\frac{L}{D}} & \text{for } \frac{L}{D} \geq 2 \end{cases} \quad (2)$$

This equation is plotted in Figure 6b together with test data. In this formula and in all the following ones, the first part of the lower index indicates the L/D ratio of the specimen while the second part its diameter in mm. For example, TCS_{2,10} refers to the TCS of a specimen with L/D = 2 and D = 10 mm. Since, in this study, the shape effect has not been tested in other diameters, any of the formulas in the literature can be used for other diameter values, such as e.g., the following ASTM formula [6]:

$$\frac{TCS_{L/D,D}}{TCS_{2,D}} = 0.88 + \frac{0.24}{\frac{L}{D}} \quad \text{for } D \geq 25 \text{ mm} \quad (3)$$

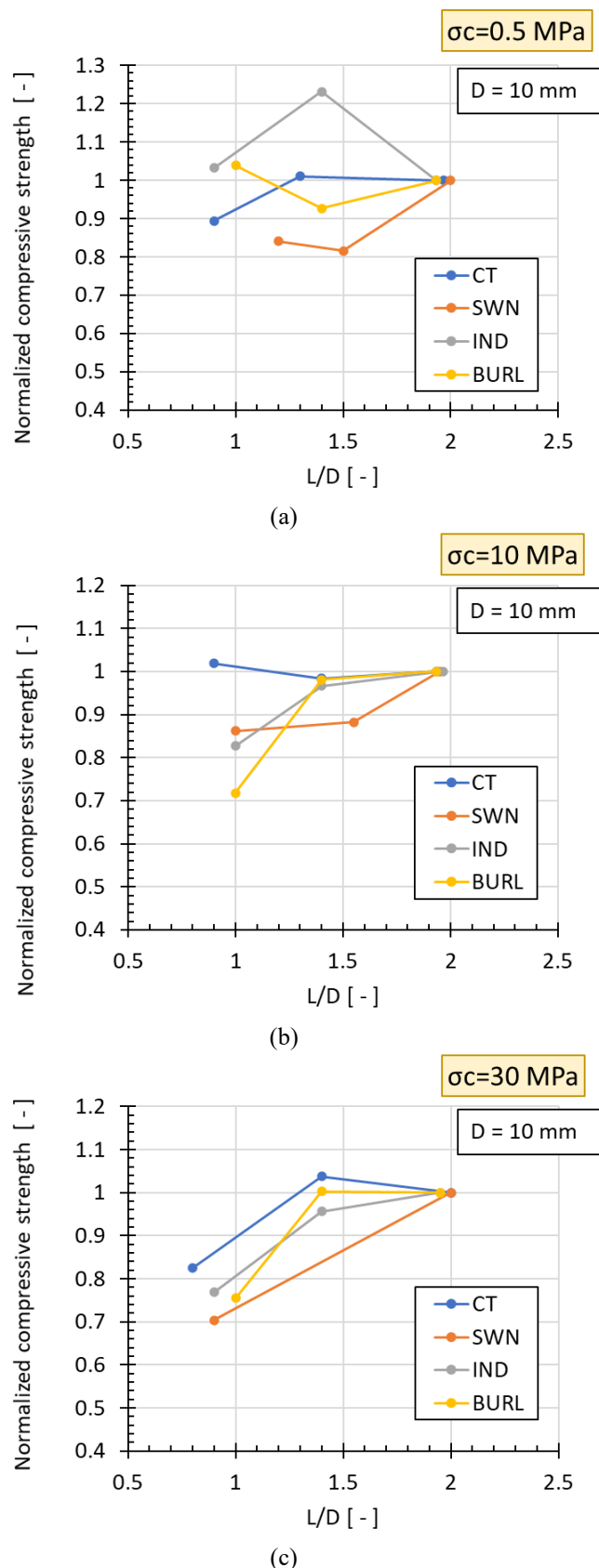
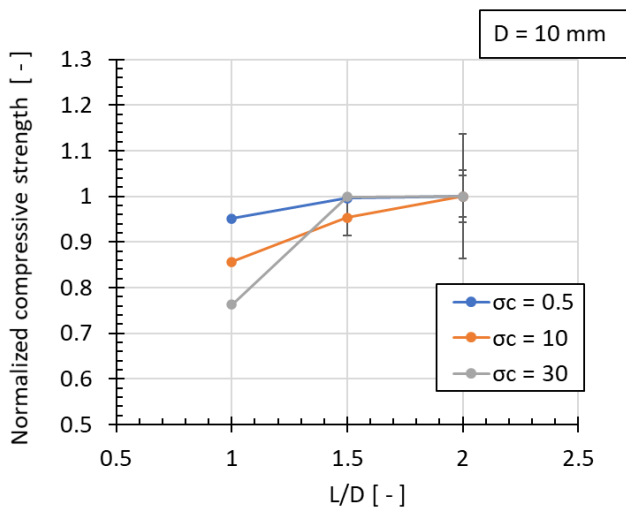
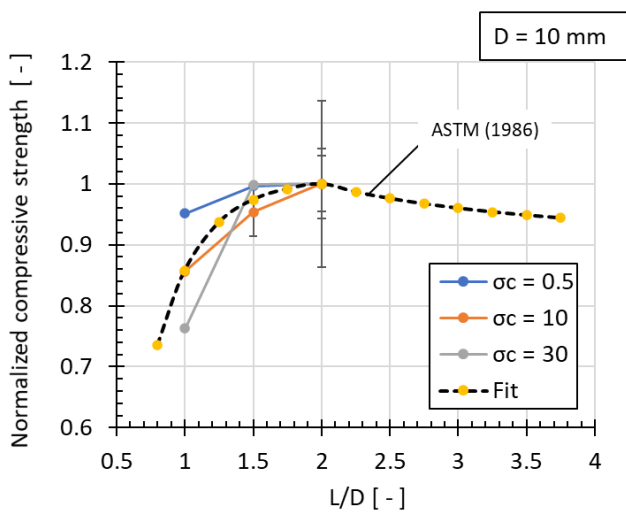


Fig. 5. Normalized TCS of all rocks vs. L/D ratio for confining stress σ_c = (a) 0.5, (b) 10 and (c) 30 MPa. All samples have diameter equal to 10 mm.



(a)



(b)

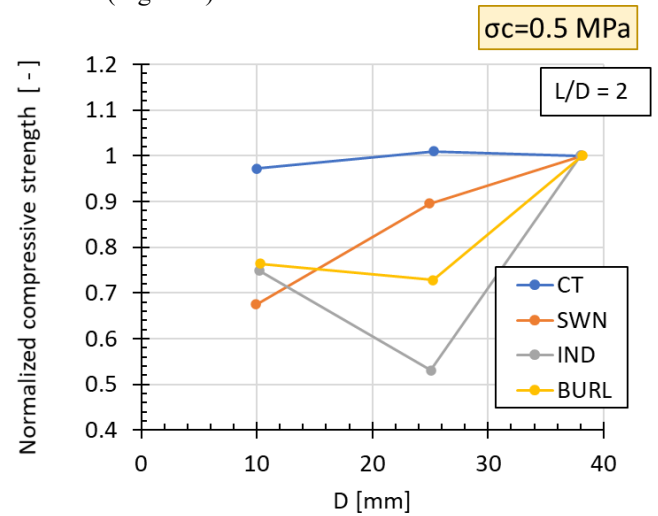
Fig. 6. Average normalized TCS of all rocks vs. L/D ratio for confining stress $\sigma_c = 0.5, 10,$ and 30 MPa. All samples have diameter equal to 10 mm. In (a), data with standard deviation are reported while, in (b), they are superimposed with the Eq. (2) approximation.

4.2 Size effect

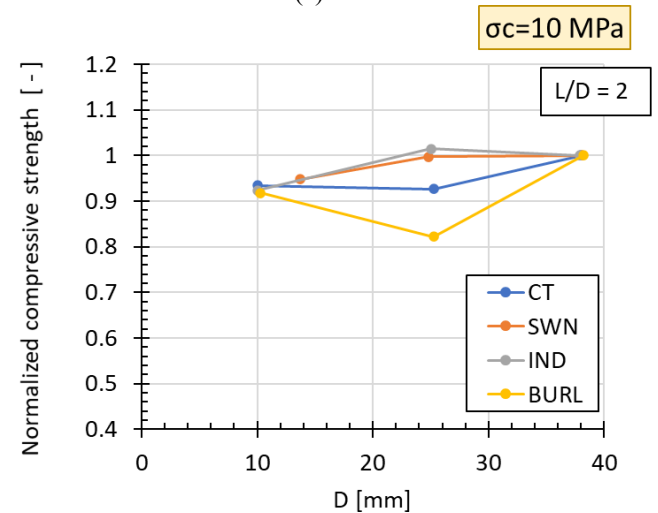
The values of normalized compressive strength in Figure 7 show some variability within each lithology at the various confining stresses. The variability is larger at low confining pressure $\sigma_c = 0.5$ MPa and lower for $\sigma_c = 10$ and 30 MPa. This reduction in variability with increasing confinement has been reported also in the literature, e.g., in [16] where earlier works are summarized saying that confining pressure tends to suppress the size effect on failure strength.

No clear difference is noticeable between the four rocks consistent for all confinement stresses. The plot in Figure 8a indicates that the strength decreases with decreasing size for all confining stresses, but the decrease is larger at low confinement, i.e. ca. 21% decrease, and smaller at higher confinement stresses, i.e. ca. 7-10%. This decrease for small specimen diameters has also been reported in the literature [9,17] where it is suggested that the peak strength occurs for specimens with diameters between 38 and 54 mm. For larger

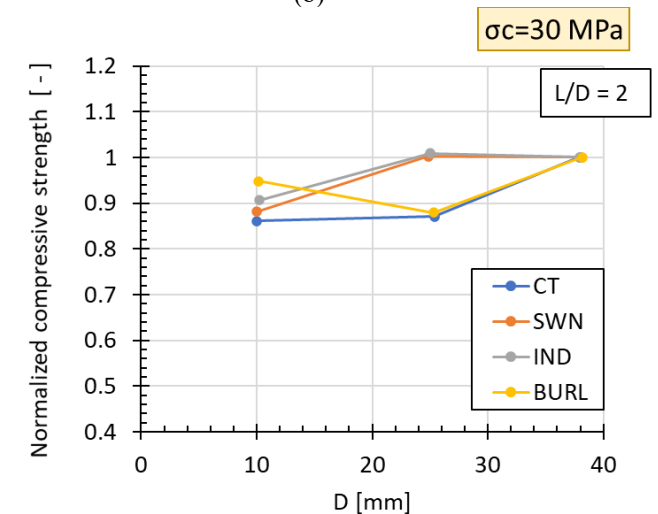
sizes, the strength decreases again according to an exponential law [7,16,8]. The results in this study seem to corroborate the ones reported in [9] for limestones and sandstones (Figure 2).



(a)



(b)



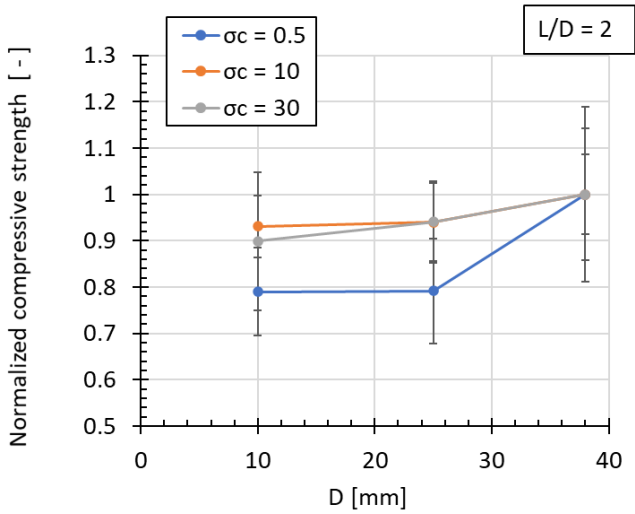
(c)

Fig. 7. Normalized TCS of all rocks vs. diameter for confining stress $\sigma_c =$ (a) $0.5,$ (b) 10 and (c) 30 MPa. All samples have L/D ratio equal to $2.$

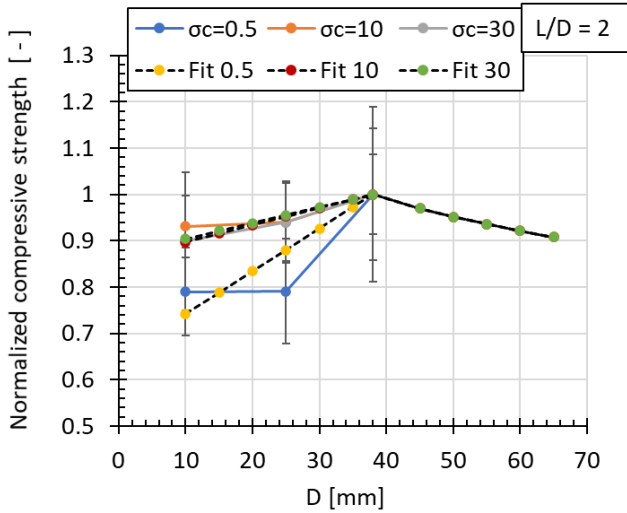
It is thus proposed to combine the exponential decline formula reported in [8] for $D > 38$ mm with a linear formula where strength decreases with decreasing diameter. The linear relationship assumes a confining stress dependent slope to accommodate the effect of confining stress on the strength reduction. The combined formula may be written as:

$$\frac{TCS_{2,D}}{TCS_{2,38}} = \begin{cases} 1 - 0.13 \left(1 + 2e^{-\frac{\sigma_c}{3}}\right) \left(1 - \frac{D}{38}\right) & \text{for } D \leq 38 \\ \left(\frac{D}{38}\right)^{-0.18} & \text{for } D \geq 38 \end{cases} \quad (4)$$

where D is in mm. The approximation to the data using Eq. (4) is plotted in Figure 8b together with test data.



(a)



(b)

Fig. 8. Average normalized strength of all rocks vs. diameter for confining stress $\sigma_c = 0.5, 10,$ and 30 MPa. All samples have L/D ratio equal to 2. In (a), data with standard deviation are reported while, in (b), they are superimposed with the Eq. (4) approximation.

4.3 Combined shape and size effect

Equations (2) or (3) and (4) can be combined to obtain the TCS value of a specimen with arbitrary shape L/D or size D :

$$\frac{TCS_{L/D,D}}{TCS_{2,38}} = \begin{cases} \left(0.88 + \frac{0.24}{L/D}\right) \left(\frac{D}{38}\right)^{-0.18} & \text{for } D \geq 38 \\ \left(0.88 + \frac{0.24}{L/D}\right) \beta & \text{for } \begin{cases} 20 \leq D < 38 \\ \text{or} \\ D \leq 20, L/D > 2 \end{cases} \\ \left(1.007 - 3e^{-3L/D}\right) \beta & \text{for } D \leq 20, \frac{L}{D} \leq 2 \end{cases} \quad (5a)$$

where

$$\beta = \left[1 - 0.13 \left(1 + 2e^{-\sigma_c/3}\right) \left(1 - \frac{D}{38}\right)\right] \quad (5b)$$

D is in mm and σ_c is in megapascals. It should be noted that Eq. (5) is based on both data derived in this study and data available in the literature. In particular, the relations for $D \geq 38$ mm and for $L/D > 2$ are based on data and expressions from literature.

5 Tangent stiffness modulus

5.1 Shape effect

The values of the normalized stiffness moduli in Figure 9 show some variability within each lithology at the various confining stresses. In some cases, the stiffness is higher at lower L/D ratios but in most it is lower. No clear difference is noticeable between the four rocks. The plot in Figure 10 suggests that the stiffness modulus increases with increasing L/D . The modulus of the $L/D = 1$ specimens is between 27% and 58% lower than the $L/D = 2$ specimens. This difference can be observed also by comparing the stress-strain curves reported in Figure 11 for Saltwash North sandstone. This finding agrees with some results in the literature [11] although other results suggest a stiffness modulus independent of L/D [10], or decreasing with increasing L/D [12], or even both decreasing and increasing with L/D [15]. One of the reasons for the increase of stiffness with increasing L/D ratio is the bedding error associated with the specimen-piston interfaces when the axial strain is calculated from the deformation of the whole specimen [14]. Similarly to what observed for strength, another reason for the lower stiffness modulus of the low L/D ratio specimens is the small size of the specimens with $L/D = 1$, that allows any damage to have a considerable effect in stiffness as well as in strength.

For practical applications involving 10 mm diameter specimens, experimental data can be regressed with a linear function to model the shape dependency of stiffness modulus as:

$$\frac{E_{50,L/D,10}}{E_{50,2,10}} = 0.5 + 0.25 \frac{L}{D} \quad (6)$$

which is also superimposed to test data in Figure 10. It should be highlighted that in this case data are quite sparse, especially for $L/D=1.5$. The shape effect has not been tested

in other diameters in this study and no formula is available in the literature.

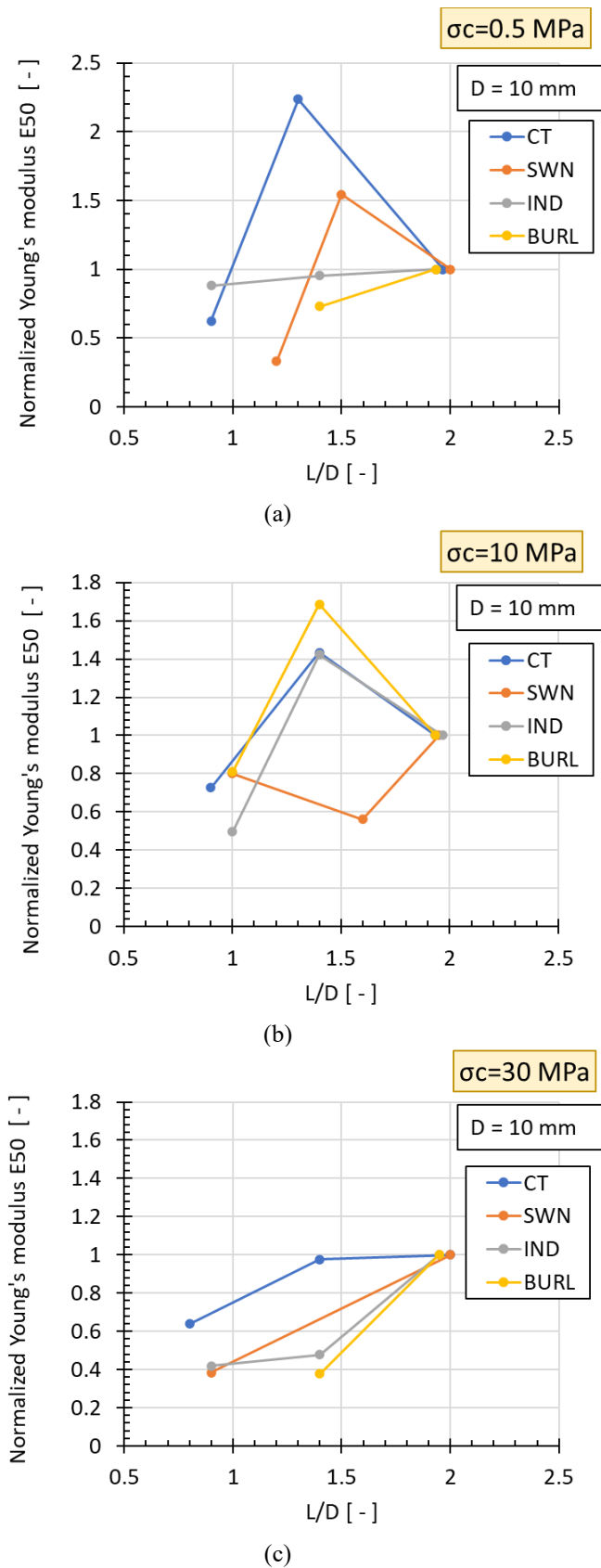


Fig. 9. Normalized E_{50} of all rocks vs. L/D ratio for confining stress $\sigma_c =$ (a) 0.5, (b) 10 and (c) 30 MPa. All samples have diameter equal to 10 mm.

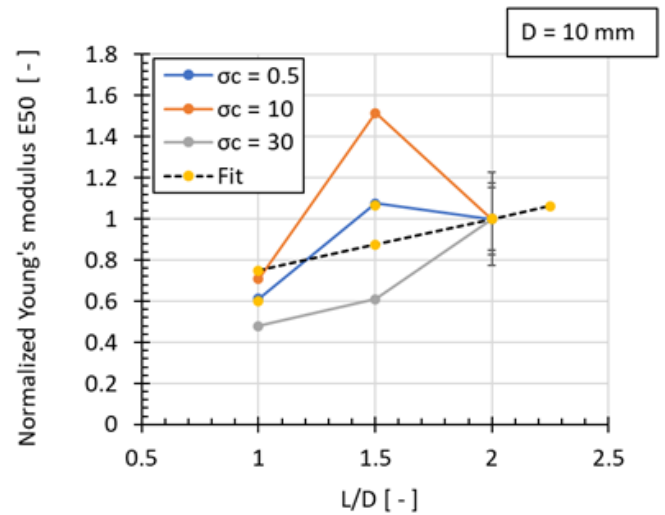


Fig. 10. Average normalized E_{50} of all rocks vs. L/D ratio for confining stress $\sigma_c = 0.5, 10,$ and 30 MPa. All samples have diameter $D = 10$ mm. Standard deviation and approximation of the data with Eq. (6) are also reported.

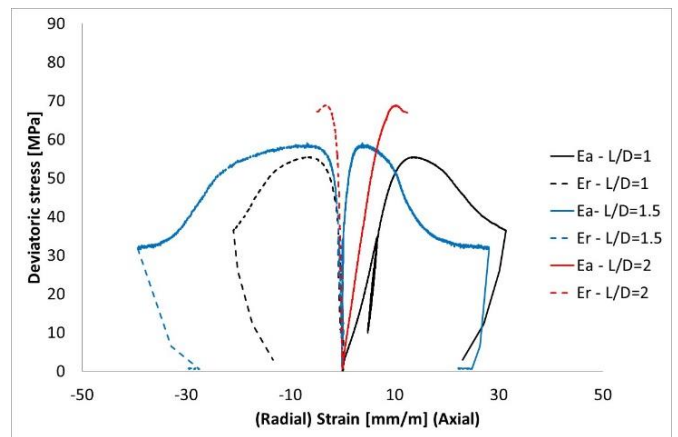
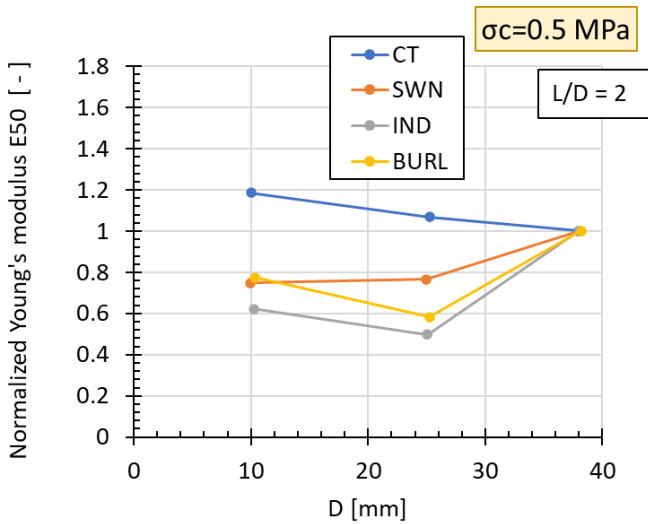


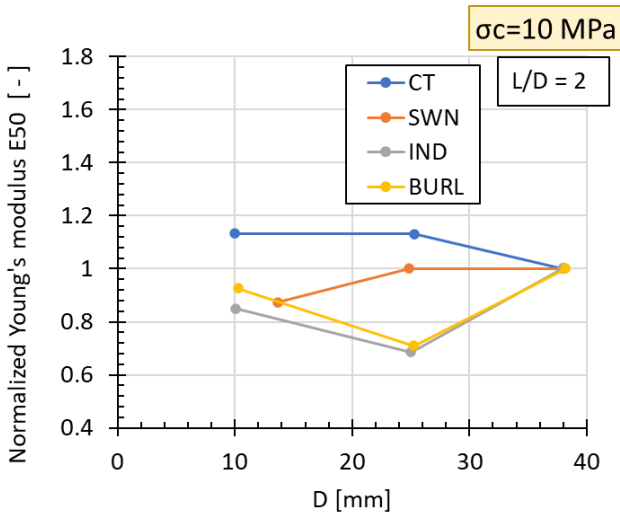
Fig. 11. Example of stress-strain curves for three experiments on Saltwash North sandstone at a confining pressure equal to 10 MPa.

5.2 Size effect

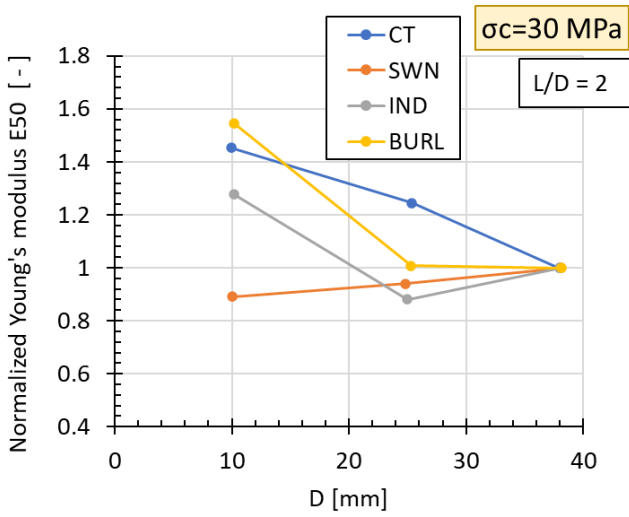
The values of normalized stiffness moduli in Figure 12 show some variability within each lithology at the various confining stresses. No clear difference is noticeable between the four rocks consistent for all confinement stresses (Figure 13). The plot does not demonstrate a clear dependency of the stiffness modulus with the size of specimen. Similar results have also been presented in [2] and [11]. However, in [15] an increase in stiffness with increasing size is shown. This behaviour can be observed also in Fig 14 where an example of stress-strain curves obtained by testing specimens of different sizes is reported for Saltwash North sandstone. According to the data, it is thus proposed to keep the stiffness modulus independent of the size of the specimen.



(a)



(b)



(c)

Fig. 12. Normalized E_{50} of all rocks vs. diameter for confining stress σ_c = (a) 0.5, (b) 10 and (c) 30 MPa. All samples have L/D ratio equal to 2.

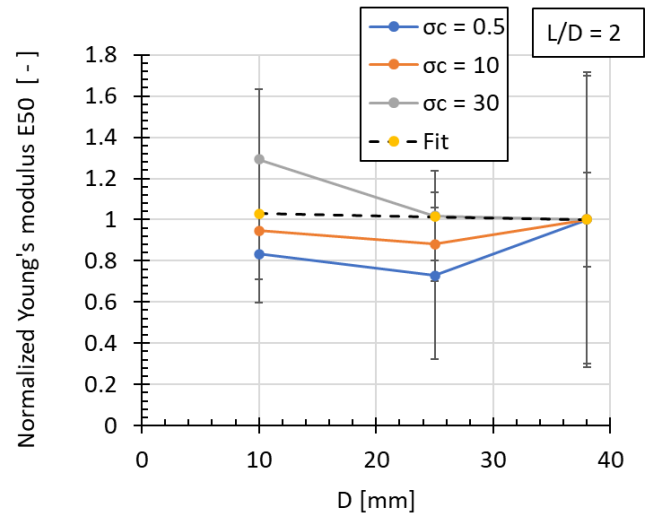


Fig. 13. Average normalized E_{50} of all rocks vs. diameter for confining stress σ_c = 0.5, 10, and 30 MPa. All samples have L/D ratio equal to 2. Standard deviations are also reported.

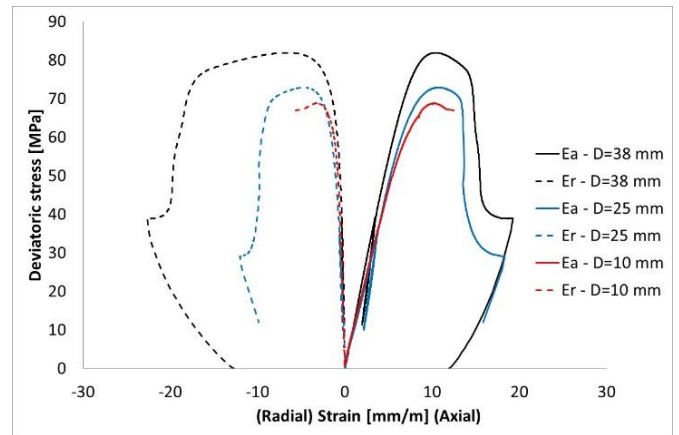


Fig. 14. Example of stress-strain curves for Saltwah North sandstone at 10 MPa.

5.3 Combined shape and size effect

In this study, the stiffness modulus appears independent of the specimen size. Therefore, only the shape effect formula Eq. (6) is necessary to obtain the E_{50} value of a specimen with arbitrary shape or size.

6 Tangent Poisson's ratio

6.1 Shape effect

The values of normalized Poisson's ratio in Figure 15 show some irregular variability within each lithology at the various confining stresses. In some cases, the dilation is higher at lower L/D ratios but in other cases it is lower.

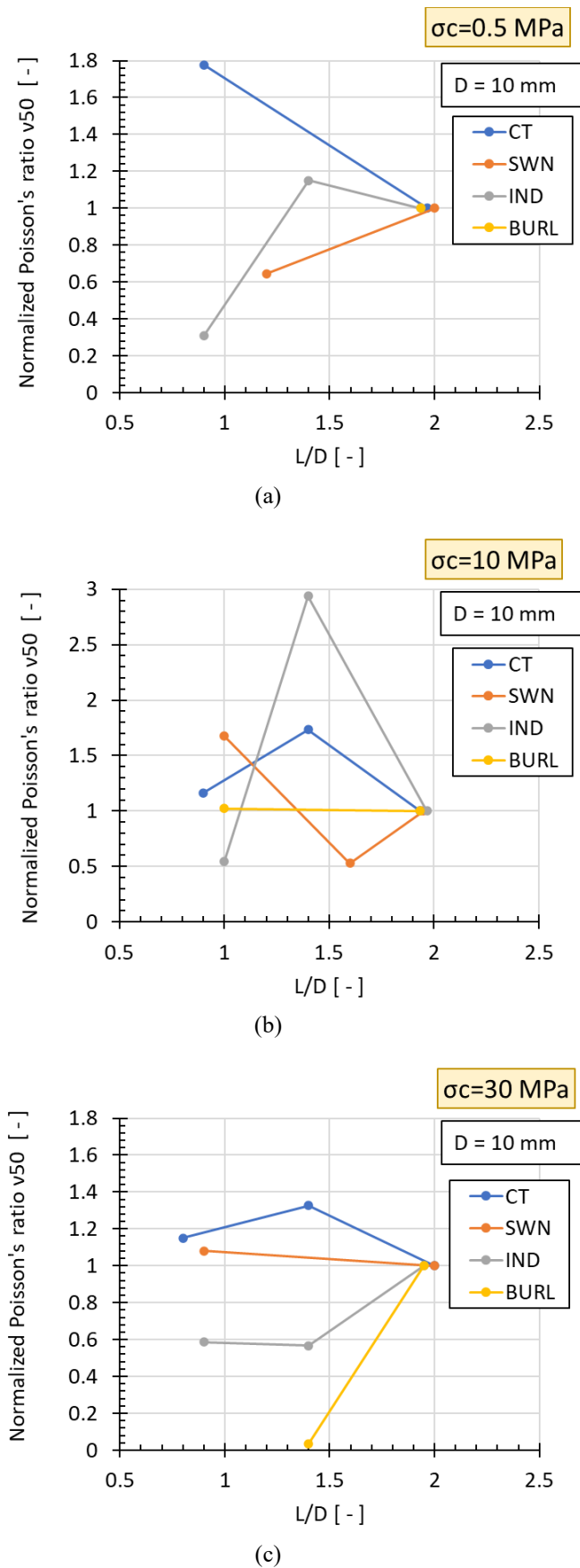


Fig. 15. Normalized v_{50} of all rocks vs. L/D ratio for confining stress $\sigma_c =$ (a) 0.5, (b) 10 and (c) 30 MPa. All samples have diameter equal to 10 mm.

An increase of dilation with increasing L/D ratio may be expected due to the frictional effect in the interfaces between the platens and the specimen which may act as confinement and restrain lateral deformation. For shorter specimens, this effect may be more pronounced because the mid-height of the specimen, where the lateral deformation is measured, is closer to the loading platens. Despite that, experimental data show that Poisson's ratio increases modestly, if any at all, with increasing L/D (Figure 16). So, no correction of dilation measurement as function of L/D ratio is considered needed. It should be anyway highlighted that, as for Young's modulus, results are quite scattered for L/D = 1.5. The shape effect has not been tested in other diameters in this study and no correlation in the literature is available.

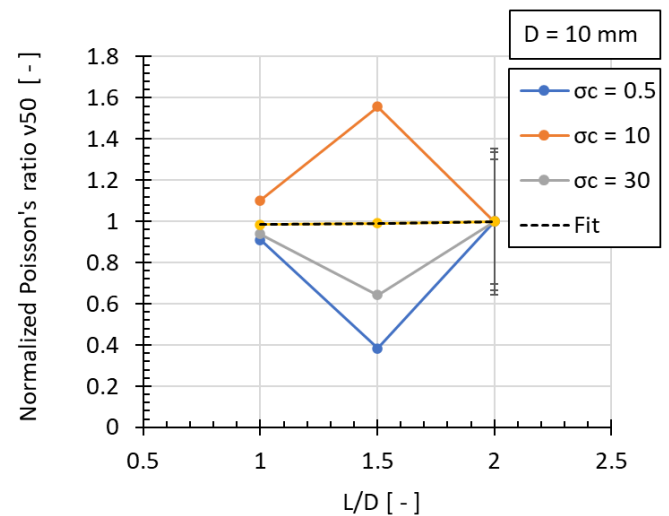


Fig. 16. Average normalized v_{50} of all rocks vs. L/D ratio for confining stress $\sigma_c = 0.5, 10,$ and 30 MPa. All samples have diameter equal to 10 mm Standard deviation is also reported.

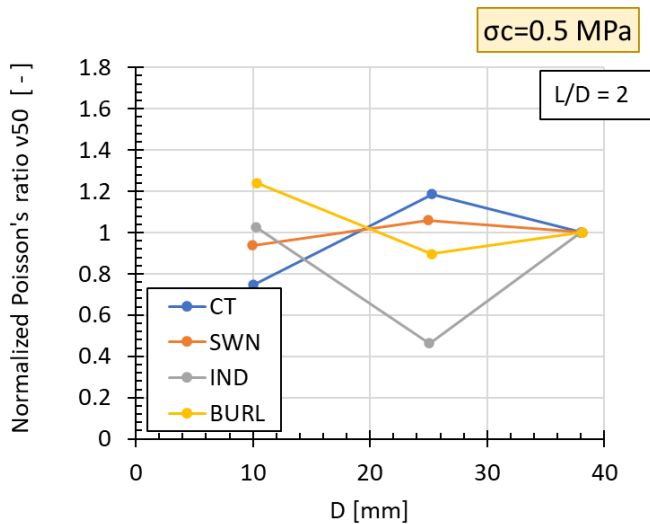
6.2 Size effect

The values of normalized Poisson's ratios in Figure 17 show little variability within each lithology at the various confining stresses, more accentuated at a confining pressure of 30 MPa especially for Indiana and Burlington limestones. Indeed, in these cases, the plot shows a decrease of the Poisson's ratio with increasing diameter which however is mostly influenced by the scatter of experimental results. At other confining stresses, no size effect is observed.

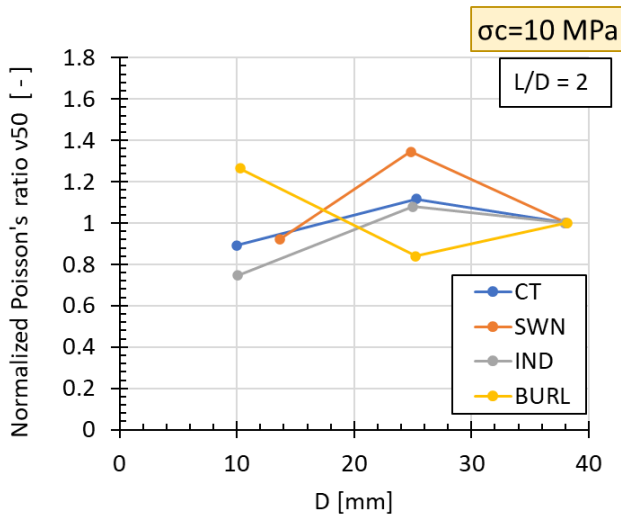
The overall trend of experimental data can be regressed with a linear function (Figure 18) to model the size dependency of Poisson's ratio as:

$$\frac{v_{50_L/D_10}}{v_{50_2_38}} = 1.2 - 0.0054D \quad (7)$$

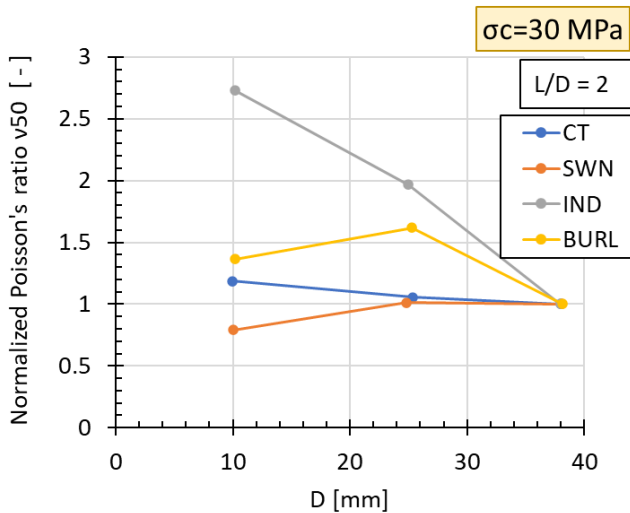
where D is in mm.



(a)



(b)



(c)

Fig. 17. Normalized v_{50} of all rocks vs. Diameter (D) for confining stress $\sigma_c =$ (a) 0.5, (b) 10 and (c) 30 MPa. All samples have L/D ratio equal to 2.

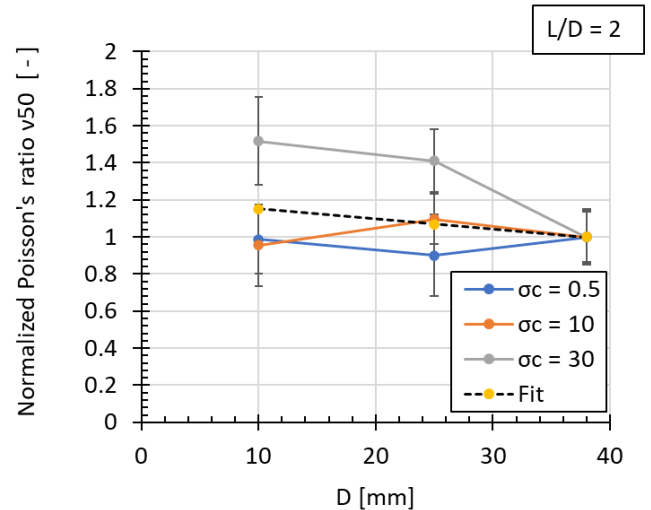


Fig. 18. Average normalized v_{50} of all rocks vs. diameter for confining stress $\sigma_c = 0.5, 10,$ and 30 MPa. All samples have L/D ratio equal to 2. Standard deviation and approximation of the data with Eq. (7) are also reported.

6.3 Combined shape and size effect

In this study, the tangent Poisson's ratio appears independent of the specimen shape. Therefore, only the size effect formula Eq. (7) is necessary to obtain the v_{50} value of a specimen with arbitrary shape or size.

7 Conclusions

In this work, an experimental campaign has been performed to evaluate the effect of specimen size and shape on the mechanical properties measured on the small plugs that can be subsampled from field RSWCs. Indeed, few evidence are available in the literature on small specimens [9] of typical reservoir lithologies [1, 9].

Unlike the literature on larger specimens [1,2,3,4,5], rock strength for 10 mm diameter plugs decreases for decreasing L/D ratios, especially for L/D = 1 where, reasonably, damage during specimen coring and polishing can affect rock behaviour. The dependency of strength on size, instead, is coherent with evidence available in literature for diameters lower than 38-54 mm, where strength increases with size.

Stiffness, instead, is not influenced by the size of the specimen while increases with increasing L/D ratio due to the bedding effect. This problem may be eliminated if strain gauges or other local axial deformation measurements are used for plugs with low L/D ratio.

Dilation is not significantly affected by the shape of the specimen while it slightly decreases for increasing size.

The results of the tests were also quantitatively integrated to propose analytical equations that correlate strength, stiffness and dilation with both size and shape. These correlations will be useful in practical application to correlate the mechanical properties measured on small specimen retrieved from RSWCs with those that would have been measured through conventional plugs.

Previous observations suggest that small diameter specimens can be a useful tool for practical experimental rock characterizations involving RSWCs, but the use of only plugs

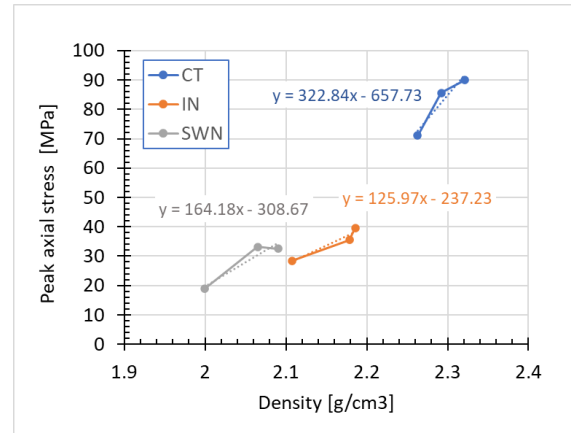
with L/D greater than 1.5, for which the effects of experimental artifacts is negligible, is recommended. This study, based on experiments on dry plugs, was focused on the effects on the mechanical properties measurements of specimen geometry exclusively. Therefore, no saturation dependency was included in the proposed correlations. Anyway, future studies on saturated specimens with different shape and size could be desirable to understand the potential effect of the different allowed drainage paths during the experiments, especially for low permeability rocks.

Appendix. Method for correcting the inherent specimen variability though density measurements.

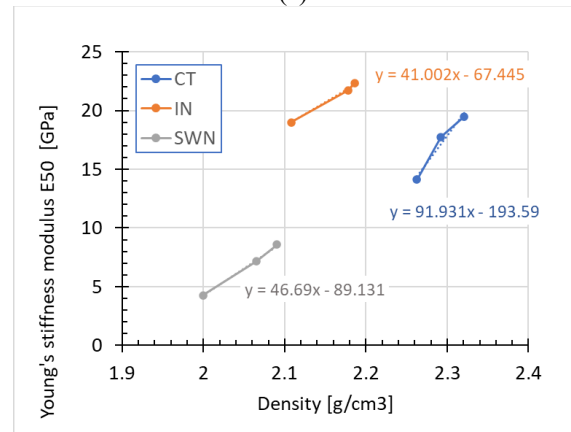
With the final aim of removing, as much as possible, the inherent specimen variability from the strength, stiffness, and dilation measurements, a procedure has been defined to quantify this variability based on dry bulk density measurements. A series of experiments were performed on three specimens for each lithology that were prepared from blocks characterized by different density to measure the variability of mechanical properties related to density variations. Burlington limestone was not tested since all block showed similar densities. All tests were run on specimens with L/D = 2, D = 38 mm, and at confining stress $\sigma_c = 0.5$ MPa. Figure 19 plots peak axial stress, stiffness modulus and Poisson's ratio as functions of dry density together with the linear regression of the data. Due to the limited number of data for each series, the linear approximation has been considered the most suitable: the deviation with respect to measured data is anyway small within the investigated density range, only Poisson's ratio shows higher dispersion. The slopes a_σ , a_E and a_N of the linear approximations for the peak axial stress, the stiffness modulus and the Poisson's ratio respectively were used to define the following relations between the measured mechanical properties and the mechanical properties corresponding to a reference value of density:

$$\begin{aligned} \sigma_{ref} &= \sigma_m + a_\sigma(\rho_{ref} - \rho_m) \\ E_{50ref} &= E_{50m} + a_E(\rho_{ref} - \rho_m) \\ \nu_{50ref} &= \nu_{50m} + a_N(\rho_{ref} - \rho_m) \end{aligned} \quad (8)$$

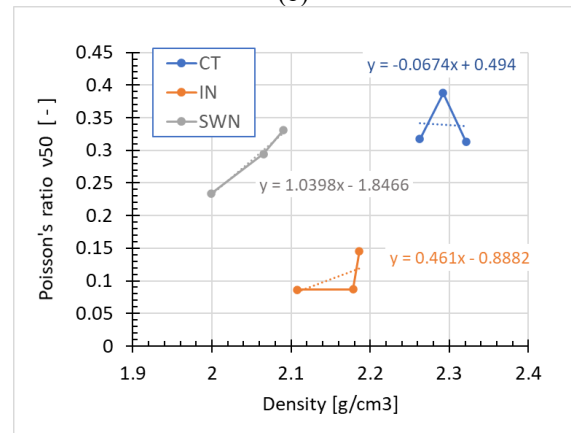
where σ_m , E_{50m} , and ν_{50m} are, respectively, the peak axial stress, the stiffness modulus and the Poisson's ratio of a specimen with density ρ_m , while σ_{ref} , E_{50ref} , and ν_{50ref} are the corresponding values for the reference density. This reference density ρ_{ref} was assumed equal to the average density of all the specimens of a given lithology. The corrected mechanical properties σ_{ref} , E_{50ref} , and ν_{50ref} were then used in the analysis of experimental results to directly compare values corresponding to the same density.



(a)



(b)



(c)

Fig. 19. (a) Peak axial stress, (b) Stiffness modulus E_{50} , and (c) Poisson's ratio ν_{50} vs. density for Carbon Tan (CT), Indiana (IN) and Saltwash North (SWN). The linear approximations to the data are also plotted.

References

1. U. Prasad, C. Wolfe, Formation specific size correction for strength (UCS) on rotary sidewall cores. *51st US Rock Mechanics/Geomechanics Symposium*, San Francisco, CA, ARMA17-534 (2017).

2. K. Mogi, Some precise measurements of fracture strength of rocks under uniform compressive stress. *Rock Mech. Eng. Geol.* IV, 41-55, (1966). *Mechanics of Cohesive-Frictional Materials* 5, 1, 1-40, (2000).
3. L. Obert, W.I. Duvall. Rock mechanics and the design of structures in rock. New York, Wiley, (1967).
4. L.A.A. da Silva, E.C. Sansone, J. Fujii, Shape effects considerations on the uniaxial compressive strength of hard rocks. *ISRM International Symposium EUROCK 93*, 1993-092, Lisbon, Portugal, (1993).
5. D.W. Hobbs, Rock compressive strength. *Colliery Engineering* 41, 287-292, (1964).
6. ASTM, Standard test method of unconfined compressive strength of intact rock core specimens. D 2938: 390–391, (1986).
7. K. Mogi, The influence of the dimensions of specimens on the fracture strength of rocks – Comparison between the strength of rock specimens and that of the Earth's crust. *Bulletin of the Earthquake Research Institute*, 40, 175-185, (1962).
8. E. Hoek, E.T. Brown, Underground excavations in rock. *The Institution of Mining and Metallurgy*, London, Chapman & Hall, (1980).
9. A. B. Hawkins, Aspects of rock strength. *Bulletin of Engineering Geology and the Environment* 57, 17–30, (1998).
10. P. Dirige, J. F. Archibald, The effects of geometry on the uniaxial compressive strength properties of intact rock core specimens. *Golden Rocks 2006, 41st US Symposium on Rock Mechanics*, Golden, CO, ARMA/USRMS 06-1016 (2006).
11. K. Thuro, R.J. Plinningr, S. Zah, Scale effect in rock strength properties, *Eurock 2001: Rock Mechanics a challenge for society*. Espoo, Finland, 169-174, (2001).
12. D. A. Moronkeji, U. Prasad, J. A. Franquet, Size effects on triaxial testing from sidewall cores for petroleum geomechanics. *48th US Rock Mechanics / Geomechanics Symposium.*, Minneapolis, MN, ARMA14-7405, (2014).
13. F. Nunes, V. Cavaleiro, L. Oliveira e Sousa, Scale effect of granitic materials. *45th US Rock Mechanics/Geomechanics Symposium.*, San Francisco, CA, ARMA 11-373, (2011).
14. E. Papamichos, J. Tronvoll, I. Vardoulakis, J. F. Labuz, A. Skjærstein, T. E. Unander, J. Sulem, Constitutive testing of Red Wildmoor sandstone. *17th Symposium on Rock Mechanics*, Snowbird, UT, Paper 5 D6, (1976).
15. A.H.J. Al-Rkaby, Z. M. S. Alafandi. Size effect on the unconfined compressive strength and modulus of elasticity of limestone rock. *Electronic Journal of Geotechnical Engineering* 20, 12, 5143-5149 (2015).
16. A.S. Abou-Sayed, C. E. Brechtel, Experimental investigation of the effects of size on the uniaxial compressive strength of Cedar City quartz diorite. *17th Symposium on Rock Mechanics*, Snowbird, UT, Paper 5 D6, (1976).
17. H. Masoumi, K. J. Douglas, S. Saydam, P. Hagan, Experimental study of size effects of rock on UCS and point load tests. *46th US Rock Mechanics / Geomechanics Symposium.*, Chicago, IL, ARMA 12-215 (2012).

Core restoration and its effect on initial wetting of NCS sandstone reservoir cores

Panagiotis Aslanidis^{1,2*}, Iván D. Piñerez Torrijos^{1,2}, Skule Strand^{1,2} and Tina Puntervold^{1,2}

¹University of Stavanger, 4036 Stavanger, Norway

²The National IOR Centre of Norway

Abstract. During the core cleaning and restoration process several crude oil – brine – rock factors affect the restored core wettability. Different solvents used during cleaning as well as the volume of oil flooded into the core are some of them. It has been observed in previous experiments, that different types of solvents can wash away different amounts of oil, influencing the later adsorption process of crude oil components. Similarly, increased amount of crude oil exposure affects the wettability of the system toward less water-wet state. Preserved reservoir cores from the Norwegian Continental Shelf were cleaned using kerosene and heptane and using toluene and methanol. In this paper, the effect of multiple core cleaning and restoration processes on initial wettability and on the ultimate oil recovery by spontaneous imbibition experiments was investigated. Not only did the two cleaning procedures affect wettability differently, but the experiments also showed that the cleaning method significantly influenced the wettability in the subsequent core restoration of this reservoir core material. For the cores cleaned with kerosene/heptane, cumulative increased crude oil exposure during the core restorations resulted in lower oil recovery by SI, thus the cores appeared less water-wet. The cores cleaned with toluene/methanol, better reproduced the previous wettability. Whether this restored wettability is more representative of the reservoir wettability is still unknown. However, it seemed that 5 pore volumes of crude oil exposure in each core restoration generated a reasonable wettability in these initially preserved reservoir cores.

1. Introduction

Several laboratory core experiments the past decade [1-14] have shown that the ionic composition of the brine injected can alter the wettability and drive more oil to production. In sandstone cores, the extra oil produced during Smart Water injection was accompanied by an increase in the produced water pH [15]. Surface chemistry phenomena like adsorption and desorption of ions on the mineral surfaces could increase the pH of the system leading to a more water-wet surface because of crude oil component desorption [2].

To observe any enhanced oil recovery (EOR) because of wettability alteration during Smart Water or low salinity brine injection, the reservoir needs to be in a mixed-wet state. If the reservoir is already very water-wet the potential for observing any extra oil production by modified water injection, is low. Therefore, the initial wettability of a reservoir and its correct determination is of utmost importance. However, knowing the initial wettability of the reservoir is very challenging because there exists, to date, no direct in-situ wettability measurement tools. Instead, the reservoir wettability is determined based on laboratory special core analysis

(SCAL) work on preserved reservoir material and reservoir log data.

From previous experiments on outcrop chalk cores, it was observed that different types of solvents remove different amounts of oil components from mineral surfaces and salts influencing the wettability, and later oil adsorption process during core restoration [16]. Similarly, increased exposure to crude oil during core restoration affected the wettability of chalk toward less water-wet [17].

In this paper, the effect of the core cleaning processes; by kerosene and n-heptane and by toluene and methanol, on initial wettability and on the ultimate oil recovery from reservoir sandstone cores after core restoration was investigated and compared by spontaneous imbibition (SI) experiments.

* Corresponding author: panagiotis.aslanidis@uis.no

2. Experimental

2.1. Core material

Reservoir core material was retrieved from two seal peels cored from the Varg field on the Norwegian Continental Shelf (NCS). The analysed cores were obtained from the upper sequence (at depths less than 3479.50m) of the 9S well and from the lower sequence (at depths over 3493.75m) of the A5T2 well. More specifically, cores P1 and P3 from the 9S well were located at 3404.83m and

Table 1: Mineralogy of the core material

Mineral	Well	
	9S	A5T2
Illite+Mica [wt%]	15.4	9.5
Kaolinite [wt%]	1.1	1.1
Chlorite/Smectite [wt%]	0.1	0
Chlorite [wt%]	2.4	3.4
Quartz [wt%]	62.3	67.6
K Feldspar [wt%]	4.5	5.6
Plagio-clase [wt%]	8.4	8.7
Calcite [wt%]	0	0.6
Dolomite [wt%]	3.9	2.8
Siderite [wt%]	1.1	0
Pyrite [wt%]	0.8	0.8
Total [wt%]	100	100

3404.88m depth, respectively, whereas the cores P9 and P10 were located at depths of 3528.82m and 3528.87m, respectively. The company operating the Varg field provided the mineralogy of the core material, and the data are given in **Table 1**. The physical properties of the core material are given in **Table 2**. Permeability was measured at S_{or} during the flooding of LS brine in the core cleaning process (described later), and it varied between 2-22 mD in the A5T2 cores and between 5-17 mD in the 9S cores. The pore size distribution of the core material was determined by Stratum Reservoir and the results are shown in **Fig. 1** and **Fig. 2** respectively.

Table 2: Core properties

Core	P1	P9	P2	P10
Well	9S	A5T2	9S	A5T2
Cleaning	Kerosene/Heptane		Toluene/Methanol	
Length (cm)	8.85	8.22	8.18	8.18
Diameter (cm)	3.80	3.80	3.80	3.80
Bulk volume (cm³)	100.4	93.2	92.8	92.8
Dry weight (g)	203.52	179.65	188.47	167.62
Pore volume (ml)	21.27	21.58	21.40	24.97
Porosity (%)	21.2	23.2	23.1	26.9
Permeability (md)	11.3	3.5	10.9	22.4

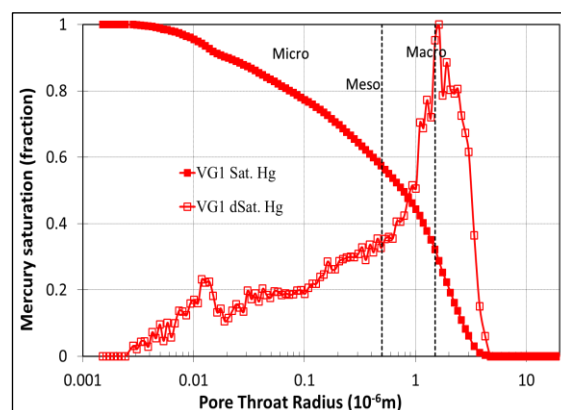


Fig. 1: Pore size distribution for the 9S well.

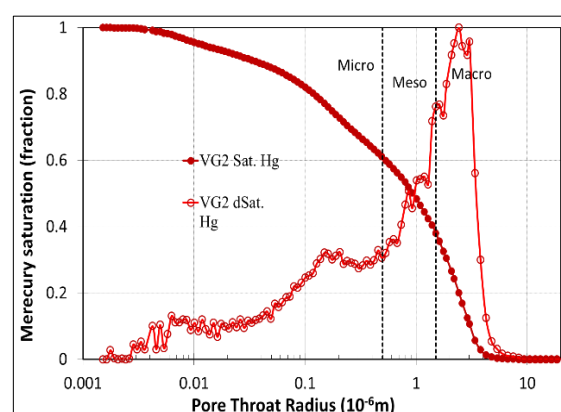


Fig. 2: Pore size distribution for the A5-T2 well.

From the results it is clear that the core material from both wells have heterogeneous pore size distributions, with pore throat radii varying between 0.002 to 4 μm , with a large proportion of meso and micro pores.

During the core restoration procedure described later, the cores P1 and P9 from the 9S and A5T2 wells, respectively, underwent a kerosene/heptane cleaning restoration process, whereas the cores P2 and P10 from the 9S and A5T2 wells, respectively, were restored using a toluene/methanol cleaning restoration process.

2.2. Brines

The brines used for this study were two synthetic brines that were prepared in the laboratory; Varg formation water (FW) with total dissolved solids (TDS) or salinity of 201600 ppm and a low salinity brine (LS) consisting of 1000 ppm NaCl. Fivefold diluted Varg FW (d5FW) was used in the establishment of initial water saturation (S_{wi}) using the desiccator technique (described later). The properties and composition of the brines are given in Error! Reference source not found..

Table 3: Brine properties

Ions	LS	FW	d5FW
[Na ⁺], mM	17.1	2086.0	417.2
[K ⁺], mM	-	51.0	10.2
[Ca ²⁺], mM	-	536.0	107.2
[Mg ²⁺], mM	-	144.0	28.8
[Cl ⁻], mM	17.1	3526.0	705.2
[Ba ²⁺], mM	-	7.0	1.4
[Sr ²⁺], mM	-	8.0	1.6
Density (g/cm ³)	0.999	1.139	1.027
Bulk pH	5.7	5.86	5.75
Viscosity (cP)	0.945	1.45	1.01
TDS (mg/L)	1000	201600	40.3

2.3. Oils

Stock tank reservoir crude oil from the Varg field was used in the oil recovery tests by SI. The crude oil acid number (AN) and base number (BN) were analysed by potentiometric titration according to the procedures described by Fan and Buckley [18], procedures that are modified from the standard methods ASTM664-89 and ASTM2896-88 for acid and base number measurements, respectively. The density of the crude oil was measured at ambient conditions using an Anton Paar densitometer. The viscosity of the crude oil was measured by an MCR 302 rheometer by Anton Paar at 23 and 60 °C. The crude oil properties are presented in **Table 4**.

Table 4: Crude oil properties

Crude Oil	Varg
AN (mgKOH/g)	0.13
BN (mgKOH/g)	1.25
Viscosity at 60°C (cP)	4.3
Viscosity at 23°C (cP)	11.3
Density at 23°C (g/cm ³)	0.845

2.4. Chemicals

During core cleaning, several chemical solvents were used; low aromatic kerosene, n-heptane (hereafter referred to as heptane) having reduced solubility of larger oil components, toluene and methanol. Toluene is a strong solvent that efficiently removes heavy oil components whereas methanol can dissolve oil and water. The above chemicals were purchased from Merck laboratories.

2.5. Core cleaning and restoration

In this work two different cleaning procedures used in the core wettability restoration process were compared. Note that the procedures used are chosen for comparative purposes and are not necessarily examples of what is considered current best practices for core restoration procedures.

2.5.1. Core cleaning

A Hassler core holder was used for all cleaning processes. This equipment consisted of two threaded ends, two pore fluid lines (distributors) and a viton type rubber sleeve. The system was supported by a confining pressure at 10 bars using water or nitrogen as the confining fluid. A back pressure of 4 bars was used to avoid two phase flow and the inlet and outlet pressures were monitored by pressure gauges. Fluids were injected through the system by a piston cell connected to an HPLC pump. All cleaning processes were performed at room temperature (23 °C) and at a rate of 0.1 ml/min.

2.5.2. Core cleaning solvents

Two different core cleaning procedures were used in this comparative study: (1) kerosene/heptane cleaning and (2) toluene/methanol cleaning. The kerosene/heptane core cleaning procedure was developed in-house, while the toluene/methanol cleaning procedure is representative of the standard methods preferred by the industry. The same amounts of solvents were injected in each restoration process using either method.

Kerosene/heptane cleaning

The cores P1 and P9 were first flooded with approximately 10 pore volumes (PV) of kerosene until a clear effluent was obtained. Kerosene flooding was succeeded by the flooding of 5 PV of heptane to displace the kerosene. Finally, the cleaning process was completed by injecting 10 PV of LS brine to displace the heptane and remove easily dissolvable salts.

The aim of this suggested cleaning procedure is to preserve the initial reservoir wettability by only displacing the mobile crude oil during core cleaning, leaving the adsorbed oil components and initial wettability intact, and to replicate the initial wettability in multiple core restorations. Low-aromatic kerosene is used to remove the mobile oil phase and non-polar oil constituents, whereas heptane finally displaces the kerosene fraction. LS brine is injected to displace the FW and any easily dissolvable salts while preventing the clays from swelling.

Toluene/methanol cleaning

This cleaning procedure included the usage of toluene and methanol, injected in two repeated cycles. Firstly, cores P2 and P10 were flooded with 5 PV of toluene followed by 5 PV of methanol. This process was repeated once using the same amount of solvents. Finally, the cleaning process was completed after injecting 10 PV of LS brine. Toluene/methanol cleaning scheme is a well-known, standard cleaning method, which, in contrast to kerosene/heptane cleaning, tends to remove most of the material that contribute to the natural wettability of the rock. Toluene removes the oil phase, including polar organic components, asphaltenes and bitumenic precipitates, while methanol dissolves polar compounds (e.g. resins), water and precipitated salts.

2.5.3. Establishing initial water saturation, S_{wi}

Initial water saturation (S_{wi}) was established using the desiccator procedure described by Springer et al. [19] After the cleaning procedure, the cores were dried at 90 °C, until constant weight. Then they were vacuum-saturated with five times diluted FW (d_5FW). Subsequently, a desiccator was used to gradually dry the cores to a predetermined weight, corresponding to 20% S_{wi} , which was chosen for this study. Finally, the cores were stored for 3 days in order to ensure an even brine distribution inside the core.

2.5.4. Crude Oil Exposure and aging

At S_{wi} , the Varg cores were exposed to a total of 5 PV of Varg crude oil. First the core was shortly vacuumed and saturated with crude oil in the Hassler core holder. Due to the heterogeneity of the porous media, oil flooding from one direction might not be sufficient. Therefore, the cores were flooded from both sides, 2PV in each direction at a rate of 0.1 ml/min. The above process took place at 50 °C to facilitate the oil flooding process. To finish, the cores were placed in aging cells surrounded with Varg oil for 14 days at 60 °C.

2.6. Spontaneous imbibition tests

A spontaneous imbibition (SI) test is a method for evaluating the wettability of a crude oil – brine – rock (COBR) system. The test consists of an Amott [20] cell, which contains a core submerged in oil or water. If the fluid that surrounds the core is the wetting phase of the system, then it will imbibe into the pores of the core displacing the fluid that already exists inside. The imbibition of the fluid is monitored with time, by collecting the displaced fluid in a graded burette. Evaluation of wettability with this method can be done by observing the ultimate recovery of the fluid displaced and the rate of imbibition of the wetting phase.

The aged core, containing crude oil and S_{wi} of 20 %, was placed on top of three marbles inside the Amott imbibition cell and surrounded by the imbibition brine. FW was used to evaluate the wettability of the core without causing any chemical induced wettability alteration during imbibition. The FW is already in chemical equilibrium with the COBR-system. The produced crude oil was collected in a graded burette, and the recovery in %OOIP (oil originally in place), was determined versus time of imbibition. After the SI experiment was terminated the core was again cleaned and restored with initial water and oil and aged in a subsequent restoration process.

3. Results and discussion

The purpose of this study was to evaluate the wettability of the Varg reservoir cores after performing two distinctly different core cleaning methods using toluene/methanol and kerosene/heptane cleaning approaches. Secondly, the

effect of crude oil exposure into the two differently cleaned sandstone rock systems was evaluated.

3.1. Restoration effects on wettability in toluene/methanol cleaned cores

Two reservoir cores, P2 and P10, were cleaned with toluene and methanol, which are the standard cleaning solvents used by the industry to clean reservoir cores in core restoration procedures [16]. Only core flooding was used in the cleaning process, no Soxhlet extraction was performed. Toluene is a good solvent, and the purpose of this cleaning procedure is to efficiently clean the core toward a more water-wet state. Thereafter, the initial water saturation was established, before crude oil exposure (5PV) and aging for 14 days at 60 °C. After completing the aging period, the cores were put for SI with FW brine to evaluate the wettability of the core. By imbibing FW there was no chemical induced wettability alteration taking place as the core was already in equilibrium with its formation brine, used for establishing S_{wi} . The oil recovery by SI curves are shown in Fig. 3 and Fig. 4 for core P2 and P10, respectively. After the first restoration (R1) both cores behaved mixed-wet but clearly on the water wet side as shown by the production profile and quite high ultimate oil recoveries of 27 and 40 %OOIP, respectively. When oil production ceased and the plateau had been reached, the cores underwent a subsequent restoration process involving cleaning, S_{wi} establishment, crude oil exposure and aging according to the same procedures as described above in section 2.5. After new core cleaning/restoration processes additional second (R2) and third (R3) restoration oil recovery tests were performed, and only small differences in recovery were observed.

The *P2 core* produced a total amount of 27%, 33% and 34% OOIP after first, second and third restoration respectively.

The *P10 core* produced a total amount of 40%, 43% and 45% OOIP after first, second and third restoration respectively.

In summary, the toluene/methanol cleaned cores P2 and P10 showed a small change regarding wettability alteration toward slightly more water-wet conditions after each restoration process. This might suggest that toluene and methanol efficiently removed adsorbed organic components before the wettability restoration, and that the increased amount of solvents flooded through the core by time in multiple restorations improved the water wetness of the reservoir cores.

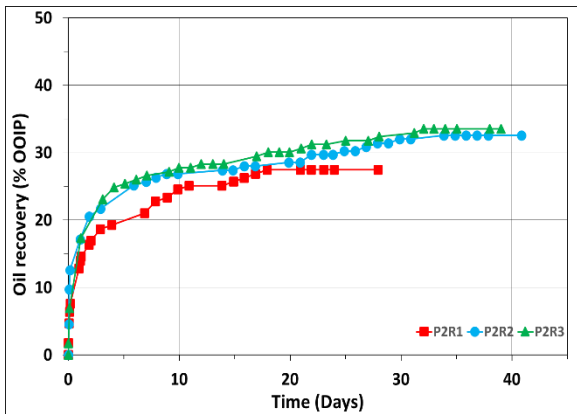


Fig. 3: SI experiments at 60 °C of the toluene/methanol cleaned core P2 with FW as imbibing fluid. R1, R2 and R3 refer to restoration number 1,2 and 3, respectively.

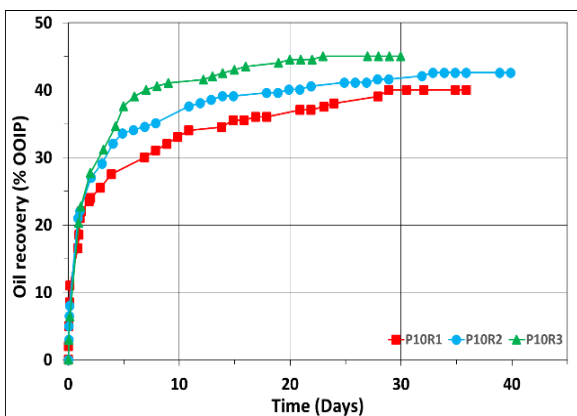


Fig. 4: SI experiments at 60 °C of the toluene/methanol cleaned core P10 with FW as imbibing fluid. R1, R2 and R3 refer to restoration number 1,2 and 3, respectively.

3.2. Restoration effects on wettability in kerosene/heptane cleaned cores

The kerosene/heptane core cleaning procedure is used with the aim of preserving the initial wettability during core cleaning. Core P1 and core P9 were cleaned with kerosene and heptane followed by the same restoration process as that for the toluene/methanol cleaned cores. Thus, the only difference was the core cleaning procedure. After completed aging, the cores were put for SI with FW to evaluate initial wettability.

The oil recovery by SI curves are shown in **Fig. 5** and **Fig. 6**. After the first restoration (R1) both cores behaved mixed-wet, but clearly on the water wet side as shown by the production profile with ultimate oil recoveries of 34 and 43 % OOIP, for P1 and P9 respectively. When oil production ceased and the plateau had been reached, the cores underwent a subsequent restoration process involving cleaning, S_{wi} establishment, crude oil exposure and aging according to the same procedures as described above in section 2.5. After the kerosene/heptane core cleaning and an additional second (R2), third (R3) and fourth (R4) restoration the oil recovery tests were repeated. In contrast to the results observed with toluene/methanol cleaned cores, large restoration effects

were observed, even though the same core treatments were performed in each restoration. The kerosene/heptane cleaned cores P1 and P9 showed significant wettability alteration toward less water-wet state.

The *P1 core* produced a total amount of 34%, 25% and 14% OOIP after the first, third and fourth restoration, respectively, as clearly seen in **Fig. 5**.

The *P9 core* produced a total amount of 44%, 29%, 24% and 17% OOIP after the first, second, third and fourth restorations, respectively, shown in **Fig. 6**.

Since kerosene and heptane cleaning is aimed at preserving wettability in the cores and only desorbing a limited amount of crude oil components from the rock surface, the cumulatively increased oil exposure after every restoration lead to a decrease in water wetness in the core. The kerosene/heptane cleaning procedure is confirmed to not remove all adsorbed crude oil components from the surface during cleaning. These results for reservoir cores are in agreement with similar experiments on outcrop sandstone cores [3]. From these results it can also be found that 5 PV of Varg crude oil exposure is too extensive for reproducing wettability between restorations after kerosene/heptane cleaning. Future studies should focus on finding the optimum amount of Varg crude oil exposure to reproduce wettability in these reservoir cores.

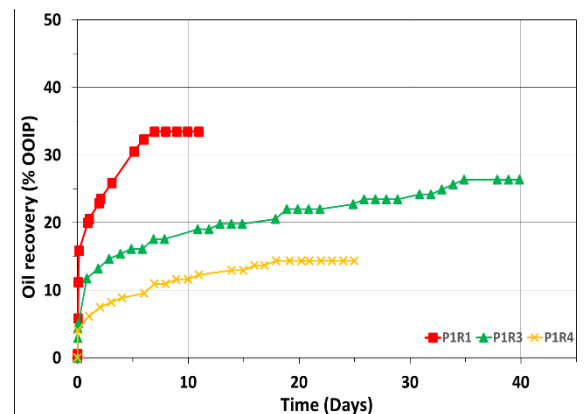


Fig. 5: SI experiments at 60 °C of the kerosene/heptane cleaned core P1 with FW as imbibing fluid. R1, R3 and R4 refer to restoration number 1, 3 and 4, respectively.

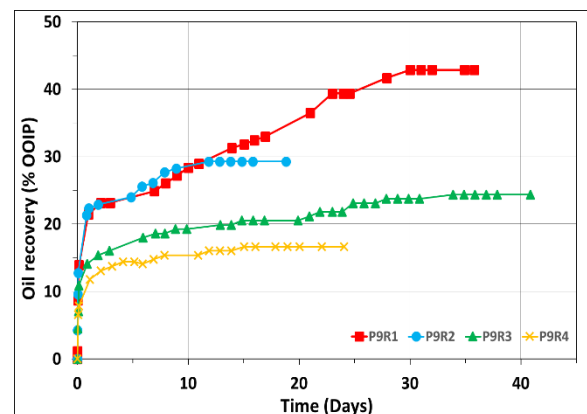


Fig. 6: SI experiments at 60 °C of the kerosene/heptane cleaned core P9 with FW as imbibing fluid. R1, R2, R3 and R4 refer to restoration number 1, 2, 3 and 4 respectively.

3.3. Representative reservoir wettability?

In this paper the effect of cleaning solvents on initial wettability was investigated. All oil recovery results using both cleaning procedures are summarized in **Table 5**.

If the results after toluene/methanol and kerosene/heptane cleaning procedures are compared for each well, it can be seen that the ultimate oil recoveries after R1 are quite similar, although there is a slight tendency of the kerosene/heptane cleaned cores P1 and P9 behaving somewhat more water-wet than their toluene/methanol cleaned sister cores P2 and P10. At this point, it is not clear whether these results are because of core heterogeneity effects, or if they are real core cleaning effects. Reservoir cores are generally more heterogeneous than outcrop cores, thus direct comparisons between sister cores are in some cases difficult. Apart from that it could be that more rigorous cleaning by toluene/methanol allows for a larger extent of adsorption of polar crude oil components than does kerosene/heptane cleaning, which leaves most of the already adsorbed crude oil components on the rock surface, perhaps limiting more oil component adsorption. However, this is speculations, and further studies are needed to understand this observation.

Previous studies on both sandstone and carbonate outcrops have shown that increased amount of crude oil exposure into the core during core restoration decreases water wettability [16], [17]. Therefore, the question is which core cleaning and restoration method better represents the true wettability of the reservoir. What is important to highlight when interpreting these results is that the amount of crude oil exposure was the same and equal to 5 PV in both restoration procedures, thus only small differences in initial wettability should be expected. However, if crude oil exposure increased, then larger deviations from true reservoir wettability should be expected. Therefore, a kerosene/heptane cleaning procedure aiming to preserve initial wettability in reservoir cores is presumed being a better approach. The challenge is knowing how many PV of crude oil should be injected into a toluene/methanol cleaned core to obtain a representative reservoir wettability. By comparing kerosene/heptane and toluene/methanol cleaned core it seems like 5 PV of Varg crude oil injection is reasonable in these Varg reservoir cores.

Table 5: SI summary results

Core	Cleaning system	SI (%OOIP)			
		R1	R2	R3	R4
P1	Kerosene/Heptane	34	-*	25	14
P9		43	29	24	17
P2	Toluene/Methanol	27	33	34	-
P10		40	43	45	-

*Spontaneous imbibition experiment failed

4. Concluding remarks

The effect of two different cleaning systems on the wettability of sandstone reservoir cores retrieved from the NCS were examined in this study. Kerosene/heptane and toluene/methanol cleaning were used during the experimental procedures. Kerosene/heptane cleaning is aimed at preserving wettability during the core restoration procedure, while the toluene/methanol cleaning is aimed at cleaning the core to water-wet conditions followed by crude oil component adsorption during the core wettability restoration.

Multiple restorations under kerosene/heptane cleaning conditions showed significant alteration of the wettability toward less water-wet state because of successive adsorption of organic polar components onto the sandstone surface after each restoration process. Preservation of polar organic components and thus preservation of the initial wettability of the system is an indication that kerosene/heptane cleaning solvents do not significantly interfere with the natural wettability of the system.

On the other hand, the toluene/methanol cleaning approach showed opposite results, where the cores seemed to become slightly more water-wet after multiple restorations. This observation indicates that the usage of stronger cleaning solvents removes crude oil wetting compounds that are responsible for the initial wettability of the rock, and that increased cleaning solvent volumes improve water wetness.

Based on the results obtained in this study, it seems that toluene/methanol cleaned Varg reservoir cores followed by 5 PV Varg crude oil exposure generated a wettability similar to that of the kerosene/heptane cleaned Varg cores. It must, however, be noted that the amount of crude oil exposure is of extreme importance, because increased exposure as demonstrated by the kerosene/heptane cleaning restoration effect, has dramatic impact on wettability also in toluene/kerosene cleaned cores.

References

1. Z. Aghaeifar, S. Strand, T. Puntervold, T. Austad, and F. M. Sajjad, "Smart Water injection strategies for optimized EOR in a high temperature offshore oil reservoir," *Journal of Petroleum Science and Engineering*, vol. **165**, pp. 743-751, 2018/06 (2018), doi: 10.1016/j.petrol.2018.02.021.
2. T. Austad, A. Rezaeidoust, and T. Puntervold, "Chemical Mechanism of Low Salinity Water Flooding in Sandstone Reservoirs," presented at the SPE Improved Oil Recovery Symposium, Tulsa, Oklahoma, USA, 2010/1/1/, (2010). [Online]. Available: <https://doi.org/10.2118/129767-MS>.
3. A. Mamonov, M. A. I. Khan, T. Puntervold, and S. Strand, "Optimized Alkalinity for EOR Purposes in Sandstone Reservoirs," presented at the SPE Asia Pacific Oil and Gas Conference and Exhibition, Brisbane, Australia, 2018/10/19/, (2018). [Online]. Available: <https://doi.org/10.2118/192015-MS>.

4. A. Mamonov, O. A. Kvandal, S. Strand, and T. Puntervold, "Adsorption of Polar Organic Components onto Sandstone Rock Minerals and Its Effect on Wettability and Enhanced Oil Recovery Potential by Smart Water," *Energy & Fuels*, vol. **33**, no. 7, pp. 5954-5960, 2019/07/18 (2019), doi: 10.1021/acs.energyfuels.9b00101.
5. J. E. S. Mjos, S. Strand, T. Puntervold, and H. Gaybaliyev, "Effect of Initial Wetting on Smart Water Potential in Carbonates," presented at the SPE EOR Conference at Oil and Gas West Asia, Muscat, Oman, 2018/3/26/, (2018). [Online]. Available: <https://doi.org/10.2118/190414-MS>.
6. I. Piñerez Torrijos, T. Puntervold, S. Strand, and A. Rezaeidoust, "Optimizing the Low Salinity Water for EOR Effects in Sandstone Reservoirs - Composition vs Salinity." (2016).
7. I. D. Piñerez Torrijos, T. Puntervold, S. Strand, T. Austad, V. V. Tran, and K. Olsen, "Impact of temperature on the low salinity EOR effect for sandstone cores containing reactive plagioclase," *Journal of Petroleum Science and Engineering*, vol. **156**, pp. 102-109, 2017/07/01/ (2017), doi: <https://doi.org/10.1016/j.petrol.2017.05.014>.
8. A. Rezaeidoust, T. Puntervold, and T. Austad, "A Discussion of the Low-Salinity EOR Potential for a North Sea Sandstone Field," presented at the SPE Annual Technical Conference and Exhibition, Florence, Italy, 2010/1/1/, (2010). [Online]. Available: <https://doi.org/10.2118/134459-MS>.
9. A. RezaeiDoust, T. Puntervold, and T. Austad, "Chemical Verification of the EOR Mechanism by Using Low Saline/Smart Water in Sandstone," *Energy & Fuels*, vol. **25**, no. 5, pp. 2151-2162, 2011/05/19 (2011), doi: 10.1021/ef200215y.
10. A. RezaeiDoust, T. Puntervold, S. Strand, and T. Austad, "Smart Water as Wettability Modifier in Carbonate and Sandstone: A Discussion of Similarities/Differences in the Chemical Mechanisms," *Energy & Fuels*, vol. **23**, no. 9, pp. 4479-4485, 2009/09/17 (2009), doi: 10.1021/ef900185q.
11. R. Farajzadeh, H. Guo, J. van Winden, and J. Bruining, "Cation Exchange in the Presence of Oil in Porous Media," *ACS Earth and Space Chemistry*, vol. **1**, no. 2, pp. 101-112, 2017/04/20 (2017), doi: 10.1021/acsearthspacechem.6b00015.
12. A. Lager, K. J. Webb, and C. J. J. Black, "Impact of Brine Chemistry on Oil Recovery," (2007), doi: <https://doi.org/10.3997/2214-4609-pdb.24.A24>.
13. D. J. Ligthelm, J. Gronsveld, J. Hofman, N. Brussee, F. Marcelis, and H. van der Linde, "Novel Waterflooding Strategy By Manipulation Of Injection Brine Composition," presented at the EUROPEC/EAGE Conference and Exhibition, Amsterdam, The Netherlands, 2009/1/1/, (2009). [Online]. Available: <https://doi.org/10.2118/119835-MS>.
14. G. Q. Tang and N. R. Morrow, "Salinity, Temperature, Oil Composition, and Oil Recovery by Waterflooding," SPE-36680-PA, vol. **12**, no. 04, pp. 269-276, 1997/11/1/ (1997), doi: 10.2118/36680-PA.
15. I. D. Piñerez T, T. Austad, S. Strand, T. Puntervold, S. Wrobel, and G. Hamon, "Linking Low Salinity EOR Effects in Sandstone to pH, Mineral Properties and Water Composition," presented at the SPE Improved Oil Recovery Conference, Tulsa, Oklahoma, USA, 2016/4/11/, (2016). [Online]. Available: <https://doi.org/10.2118/179625-MS>.
16. I. Klewiah, I. D. Piñerez Torrijos, S. Strand, T. Puntervold, and M. Konstantinopoulos, "Adsorption of Crude Oil Polar Components onto Silica-Rich Chalk and its Impact on Wetting," presented at the SPE Norway One Day Seminar, Bergen, Norway, 2019/5/13/, (2019). [Online]. Available: <https://doi.org/10.2118/195603-MS>.
17. I. Piñerez et al., "Core wettability reproduction: A new solvent cleaning and core restoration strategy for chalk cores," *Journal of Petroleum Science and Engineering*, vol. **195**, p. 107654, 2020/12/01/ (2020), doi: <https://doi.org/10.1016/j.petrol.2020.107654>.
18. T. Fan and J. S. Buckley, "Acid Number Measurements Revisited," *SPE Journal*, vol. **12**, no. 04, pp. 496-500, 2007/12/1/ (2007), doi: 10.2118/99884-PA.
19. N. Springer, U. C. C. Korsbech, and H. K. Aage, "Resistivity Index Measurement without the Porous Plate," (in eng), Proceedings International Symposium of the Society of Core Analysts, pp. 459-470, 2003.
20. E. Amott, "Observations Relating to the Wettability of Porous Rock," *Transactions of the AIME*, vol. **216**, no. 01, pp. 156-162, 1959/12/1/ (1959), doi: 10.2118/1167-G.

Micromechanics Digital Rock: Parameterization of Consolidation Level using a Grain Contact Model

Zhuang Sun*, Rafael Salazar-Tio, Andrew Fager, and Bernd Crouse

Dassault Systèmes, 343 Sansome St San Francisco, CA, USA

Abstract. The mechanical behaviour of sedimentary rocks is conditioned by the interactions at the grain-grain contacts. We present a micromechanics digital rock workflow based on a cohesive contact model and introduce a general parameterization that can capture two extreme contact behaviours: free grains and fixed grains, as well as any intermediate degree of grain consolidation. With this parametric cohesive contact model, we can simulate a wide range of sedimentary rocks, from unconsolidated to well-consolidated rocks. We present a benchmark study on several samples and compare with laboratory-measured elastic moduli to calibrate its degree of consolidation. Simulations that do not include the grain contact modelling, tend to overestimate the elastic moduli, which manifests the significance of this contribution to capture well the grain contact behaviour. To demonstrate the impact of properly capturing the degree of consolidation on the rock strength and failure pattern, we present results for numerical uniaxial compression testing. This workflow provides physics-based solution to complex grain contact behaviour, which complements laboratory core analysis, and can be useful to reveal underlying grain-scale processes governing rock mechanical behaviour.

1 Introduction

Digital rock applications have rapidly emerged over the past decades based on X-ray micro-tomography (micro-CT) imaging technology that allows capturing pore-scale three-dimensional (3D) structures of reservoir rocks at the micrometer scale, and virtually simulating the flow of fluids under different production conditions [1–9]. However, digital rock simulation of rock mechanical properties has been considered challenging given the intrinsic limitation of micro-CT images to capture the degree of consolidation between grains in rocks, due to the limit in imaging resolution and also because micro-CT is typically obtained at ambient conditions and does not capture the actual net confining stress (NCS) pore geometry [10–15].

Different levels of consolidation, compaction, recrystallization, and diagenesis in general, can produce a wide range of grain contact behaviours in sedimentary rocks, from loosely consolidated sand packs to completely fused grains that form a single solid structure [16]. Numerical methods in the literature typically use a single solid frame formed by the mineral grains, generally overestimating the simulated rock stiffness as compared to experimental measurements [2,10,17–19]. Some ideas have been discussed to assign different properties to contact regions and grain regions [20–22]. However, a commonality among these approaches is that grain relocation is not allowed, which limits the grain-grain contact behaviour of real rocks as well as rock failure significant deformation.

We recently introduced a micromechanics digital rock workflow based on finite element modelling of grain structures obtained from micro-CT images [23]. Some unique features of this workflow include, a robust grain-grain

segmentation method, a conformal grain-grain contact meshing algorithm, and grain relocation capabilities, instead of modelling a solid framework as a whole. We are able to simulate linear elastic moduli comparable with experimental values, as well as being able to simulate significant compaction found at in-situ conditions, which are difficult to capture using micro-CT imaging at ambient conditions.

Here we present an extension of that work, based on a cohesive contact model and we introduce a general parameterization that can capture both extreme contact behaviours: free grains and fixed grains, as well as an intermediate degree of grain consolidation. The proposed workflow intends to solve problems including: (1) model properly variable grain-grain consolidation to correctly simulate mechanical rock properties, (2) being able to recover the correct NCS pore geometry to simulate all petrophysical properties under the correct in-situ conditions, (3) allow grain relocation capabilities, including failure test simulations. This paper is structured as follows. First, we describe the parametric cohesive contact model to simulate a wide range of sedimentary rocks, from unconsolidated to well-consolidated rocks. Second, we show a benchmark study on sandstone samples and compare with laboratory-measured elastic moduli to calibrate its degree of consolidation. Finally, we perform numerically uniaxial compression tests to demonstrate the impact of properly capturing the degree of consolidation on the rock strength and failure pattern.

2 Methodology

A micro-CT 3D voxelized image is needed as an input to identify individual grains and a connected pore geometry of

* Corresponding author: zhuang.sun@3ds.com

rock. The limitations of micro-CT images for properly capturing a micro-mechanics rock model are related to the insufficient contrast for the identification of different mineral grains, and for the identification of grain-grain contacts between same mineral grains. Identification of grain mineralogy and contacts can be improved by complementing 3D micro-CT imaging with 2D higher resolution and mineralogy imaging such as scanning electron microscopy (SEM) and energy dispersive x-ray spectroscopy (EDS). In order to setup a finite element (FE) micro-mechanics rock model from micro-CT data, two critical pre-processing steps are required: (1) grain-grain segmentation, and (2) conformal meshing of grain contacts. We have described these steps in detail in [23], but for the sake of completeness we include here a brief description.

For the grain-grain segmentation we start from a direct binary thresholding on the micro-CT that classifies voxels as pore or solid. After this, we want to reclassify the solid voxels with an integer index that represents at which grain it belongs. For this purpose we use a class of algorithms refer as watershed methods used for separating touching objects in binary images [24]. This algorithm computes first a distance transform 3D image, where for each solid voxel, the value of the Euclidean distance to the nearest pore/solid interface is recorded. If this is considered as a topographic depth map, the deeper parts of the image are the center of the objects. A watershed classification considers each solid voxel by the center to which it will roll down when following this inverted distance transform topographic map. In the final grain segmented 3D image each grain voxel has the value of the corresponding grain index, while pore voxels are labelled as 0.

In order to achieve an initial static solution for the segmented grains, it is of great importance to create a conformal mesh at the grain-grain contacts. A conformal mesh indicates that there is neither separation nor overclosure between any two grains of contact. The labeled voxelized 3D image is transformed into an unstructured mesh representation, where elements of the same grain are suitable for FE simulation and the elements at each side of a contact between grains conform to each other perfectly, without voids or overlaps in the contact boundary [23]. We generate the meshing for all the grains together, while maintaining the indices representing segmented grains, which results in a conformal mesh at the grain-grain contact. We can choose to have two separate surfaces or one combined interface for the conformal mesh, which corresponds to two case scenarios of free or fixed grain-grain contacts.

Finally, the meshed model is input into the finite element solver with prescribed strains/stress boundary conditions and grain-grain contact models [25,26]. A general parametrization of the cohesive contact model is used to capture contact behaviors of different levels of grain consolidation including two extreme scenarios: free grains, where only friction is modeled between grains, and fixed grains, where grains are completely fused. In terms of the FE simulations, the free grain contacts introduce duplicate nodes and elements that allows grain relocation whereas the fixed grain contacts model the solid framework as a whole.

2.1. Cohesive contact model

The concept of “bonded grains” has been widely adopted in discrete element method (DEM), which simulates each individual grain as a discrete rigid body [27–29]. Similarly, the FE simulations can simulate the bonded grain interface based on the cohesive contact model, with or without the possibility of damage and failure of the bond (Figure 1a). The cohesive constitutive laws include the linear elastic traction-separation model, damage initiation criterion, and damage evolution laws, which allow a precise description of the contact behavior. This work does not explicitly model the cement volume. Some processes, such as mineral segmentation, cement material property characterization, and grain meshing for cement phase, need to be developed to understand the effect of cement relative volume. We present an overview of the contact model, more details can be found in the FE solver documentation [26,30].

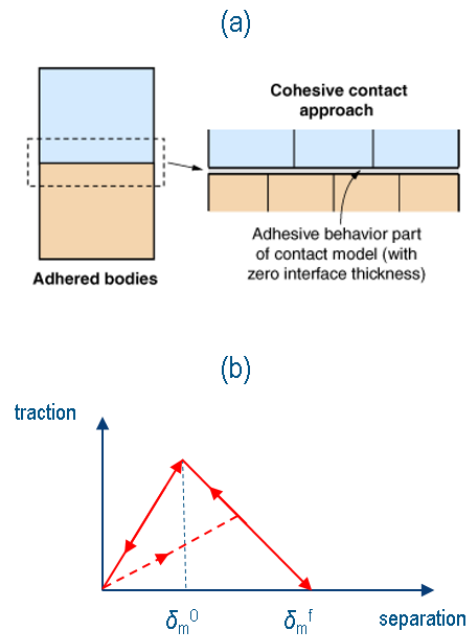


Fig. 1. (a) Schematic of cohesive contact behaviour [26]. (b) Typical traction-separation response.

The model assumes the traction-separation behavior initially linear elastic followed by the damage initiation and evolution. The elastic matrix K relates the normal and shear stresses to the normal and shear separations:

$$\begin{bmatrix} t_R \\ t_S \end{bmatrix} = \begin{bmatrix} K_{RR} & 0 \\ 0 & K_{SS} \end{bmatrix} \begin{bmatrix} \delta_R \\ \delta_S \end{bmatrix} \quad (1)$$

where t_R and t_S represent the traction stress components in normal and shear directions, δ_R and δ_S represent the corresponding separations. Normal compressive stress follows the usual contact behavior. The damage modeling consists of a damage initiation criterion and a damage evolution law. Damage initiation begins when the separations satisfy the specified initiation criteria:

$$\max \left\{ \frac{\delta_R}{\delta_R^0}, \frac{\delta_S}{\delta_S^0} \right\} = 1 \quad (2)$$

where δ_R^0 and δ_S^0 are critical separations in normal and shear directions. Note that purely compressive stress (negative

value) does not result in damage. The damage evolution law describes the degradation rate of the contact stiffness once the damage initiation starts. The contact stresses follow:

$$t_R = (1 - D)\bar{t}_R \quad (3)$$

$$t_S = (1 - D)\bar{t}_S \quad (4)$$

where D is the damage variable, \bar{t}_R and \bar{t}_S are contact stresses predicted by the elastic behavior (Eq. (1)) without damage. The damage variable D changes from 0 to 1 as the damage initiates and evolves and can be specified as a linear function of the effective separation δ_m . δ_m^f and δ_m^0 are the effective separation at complete failure and damage initiation, respectively. δ_m^{\max} refers to the maximum value of the effective separation attained during the loading history. Figure 1b shows a typical traction-separation response for the cohesive contact model. Unloading subsequent to damage initiation is assumed to follow the history traction-separation path. Therefore, the cohesive contacts remain elastic until a bond failure occurs.

$$D = \frac{\delta_m^f(\delta_m^{\max} - \delta_m^0)}{\delta_m^{\max}(\delta_m^f - \delta_m^0)} \quad (5)$$

$$\delta_m = \sqrt{\delta_R^2 + 2\delta_S^2} \quad (6)$$

2.2 General parameterization

We describe in more detail the proposed new general parameterization of cohesive contact model that can capture both extreme contact behaviors: free grains and fixed grains, as well as any intermediate degree of grain consolidation.

The parameters of the contact model include the stiffness K_{RR} and K_{SS} for the linear elastic behavior, the critical separation δ_R^0 and δ_S^0 , and the effective separation at complete failure δ_m^f for the damage behavior. In order to simplify the representation, we assume $K_{RR} = K_{SS} = K$, $\delta_R^0 = \delta_S^0 = \delta^0$, $\delta_m^f = 2.5 \times \delta_m^0$ to reduce the number of parameters. The stiffness K needs to be pre-determined and can be automatically computed such that the cohesive contact model of a very large δ^0 can reproduce the mechanical behavior of a solid framework with no grain contacts involved (i.e. fixed grain-grain contacts). Therefore, the cohesive contact model has only one adjustable parameter, the critical separation δ^0 , which can be recast into a parametric relationship that represents the consolidation level as a function of a new parameter C .

We propose the following relationship between the critical separation δ^0 and the consolidation level, new parameter C , as follows:

$$\delta^0 = \Delta x \frac{C}{1-C} \quad (7)$$

where Δx is a characteristic length for the granular system (with the same unit of δ^0), C is dimensionless and can change from 0 to 1 with an increasing level of consolidation. Eq. (7) indicates that $\delta^0 = \infty$ when $C = 1$ and $\delta^0 = 0$ when $C = 0$, representing two extreme scenarios of fixed and free grain-grain contacts. Figure 2 shows the traction-separation responses of various consolidation levels. A characteristic length is a global variable that can be estimated for instance

from the grain size distribution, or grain-grain contact area distribution, as extracted from the 3D image itself.

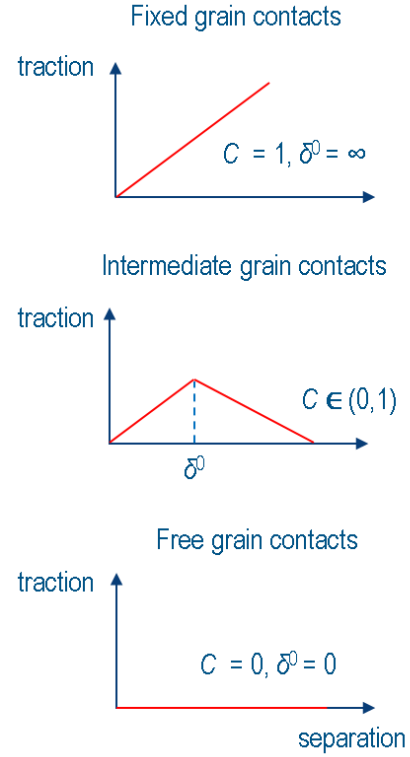


Fig. 2. Traction-separation responses of various consolidation levels (quantified by parameter C).

This single model can capture contact behaviors for different levels of grain consolidation. With this parametric cohesive contact model, we can simulate a wide range of sedimentary rocks, from unconsolidated (free grain contacts) to intermediate-consolidated rocks to well-consolidated rocks (fixed grain contacts).

2.3 Model validation

In order to validate this proposed simplification, first we test the parametric cohesive contact model through a simple scenario of three-grain packing. The grains are extracted from a micro-CT image of Fontainebleau sandstone model [31]. Figure 3a shows the grain mesh used in the FE simulation.

We fix the bottom of the packing and apply either a tensile or compressive stress on the top, i.e. tensile or compressive testing. The characteristic length Δx is assumed as $0.5 \mu\text{m}$. Figure 3b shows the tensile testing results from simulations of the cohesive contact model with different consolidation levels C , and fixed and free grain contacts (no cohesive contacts applied). The results indicate that the parametric cohesive contact model can reproduce the fixed and free grain contact behaviors when $C = 1$ and $C = 0$, respectively. When $C = 0$, the grains will be readily separated by the tensile stress. When $C = 1$, the three grains behave as a solid framework with no grain separation. When $C = 0.5$, the tensile force shows an increase followed by a decrease due to the damage initiates, similar to Figure 2.

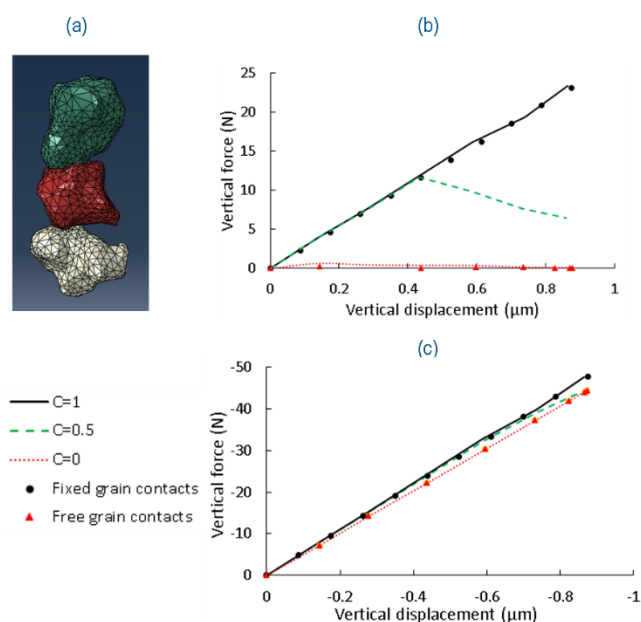


Fig. 3. (a) Grain mesh of a three-grain packing. Grains are differentiated by colors. Force-displacement results of (b) tensile testing, and (c) compressive testing. Parametric cohesive contact model can reproduce the fixed and free grain contact behaviors by changing the consolidation level C .

Figure 3c shows the simulation results of compressive testing. The compressive forces are with negative values to indicate the compaction. The parametric cohesive contact model can reproduce the fixed and free grain contact behaviors when $C = 1$ and $C = 0$, respectively. When $C = 0.5$, the force-displacement curve exhibits a transition from fixed grain contacts to free grain contacts because only two bonded contacts exist in the packing. The collective force-displacement behavior of a larger number of bonds appears to become linear as shown in the following section.

3 Results and discussion

We apply this new parametric cohesive contact model to three rock sample models including a sphere packing, a Grosmont Carbonate and a Fontainebleau Sandstone, each of it exhibiting different grain-grain contact behaviour. We measure the static elastic modulus by modelling the deformation of rock sample, rather than the dynamic elastic modulus (e.g. acoustic velocities). The dynamic elastic modulus is typically higher than the static modulus, and the values diverge significantly in rocks with a low elastic modulus [32,33]. We also present simulation results of a failure test on the Fontainebleau Sandstone model to demonstrate the impact of properly capturing the degree of consolidation on the rock strength and failure pattern.

3.1 Free grain contacts

A sphere packing is a very good example of free grain-grain contact behavior, where grain contacts are introduced duplicate nodes and elements that allows grain relocation. Sain (2010) generated the micro-CT image of a sphere packing (as shown in Figure 4a) and obtained its bulk and shear modulus as 1.17 GPa and 1.22 GPa through granular

dynamic simulations [34]. The granular dynamic simulations can yield very similar elastic moduli as laboratory experiments on glass beads packs, dry Ottawa sands and dry Galveston sand [34–36]. Andr a et al. (2013) compared their numerical simulations directly based on image voxels (i.e. only allowing fixed grain-grain contacts) with the granular dynamic simulations and found a significant deviation [2]. On the contrary, our micromechanical finite element model allows grain relocation (i.e. free grain-grain contacts) therefore resulting in a very close modulus as the reference data in [34].

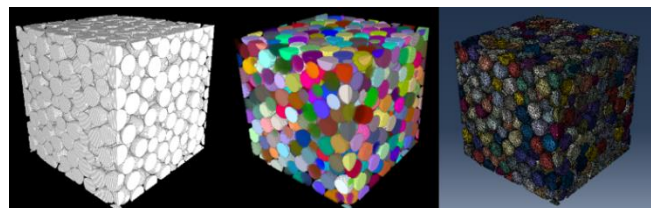


Fig. 4. From left to right: the original binary micro-CT image of sphere packing, segmented grains indicated by different colors, grain mesh for the FE solver.

Using this sphere pack model we demonstrate that the parametric cohesive contact model can mimic the free grain contacts. Following reference [2,23], we use a material property of quartz for the sphere packing: density is 2.65 g/cm³, bulk modulus is 37.0 GPa, and shear modulus is 44.0 GPa. Table 1 summarizes the specifications for the sphere pack model.

Table 1. Specifications of the sphere packing.

Rock type	Sphere packing
Sample size (voxels)	398x319x398
Voxel size (μm)	14
Porosity	34.3%
Number of nodes	693,635
Number of elements	3,306,874

The parametric cohesive contact model has two parameters: the consolidation level C and the stiffness K . The consolidation level C is equal to 0 for free grain contacts. The stiffness K is calibrated to reproduce the mechanical behavior of fixed grain contacts. We perform hydrostatic compression test to measure the bulk modulus and shear test to measure the shear modulus. Table 2 summarizes the results. The parametric cohesive contact model with $C = 0$ yields very similar moduli as the free grain contacts from our previous work [23]. The results are not expected to be identical considering that the numerical simulations are based on different contact mechanisms.

Table 2. Bulk and shear moduli of sphere packing.

	Bulk modulus (GPa)	Shear modulus (GPa)
Cohesive contact model with $C = 0$	1.29	1.57
Free grain contacts	1.34	1.62
Difference	3.7%	3.1%

3.2 Fixed grain contacts

The Grosmont Carbonate was deposited around 380 million years ago in the late Devonian period in an open shallow limestone marine shelf environment [37]. The formation is composed of limestone and dolomite with minor amount of siltstone and shale. Grosmont Carbonate is a good example of fixed grain-grain contact behaviour, given the fact that Carbonates are typically recrystallized due to diagenetic processes. Therefore, all the grains behave as one solid framework. In this section, we perform the grain segmentation to demonstrate that cohesive contacts can mimic the behaviour of fixed grain contacts when $C = 1$. Please note that watershed grain segmentation is typically not applicable to complex carbonate structure. Such a segmentation is intended for validating the numerical asymptotic behaviour of the parametric cohesive contact model, but not necessarily indicates a real grain contact behaviour.

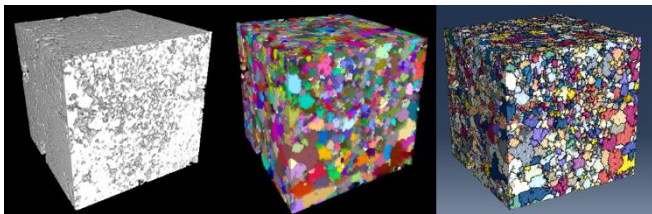


Fig. 5. From left to right: the original binary micro-CT image of Grosmont Carbonate, segmented grains indicated by different colors, grain mesh for the FE solver (only exterior edges are shown for better visualization).

Table 3 summarizes the specifications for the Grosmont Carbonate model. Following reference [22], we use a material property of 50% calcite and 50% dolomite for the Grosmont Carbonate: density is 2.79 g/cm^3 , bulk modulus is 81.6 GPa, and shear modulus is 36.7 GPa. The consolidation level C is equal to 1 for fixed grain contacts and the stiffness K is the calibrated parameter. Table 4 shows the comparative results with our previous simulation for this model, and show that the parametric cohesive contact model with $C = 1$ gives very similar elastic moduli as the fixed grain contacts.

Table 3. Specifications of the Grosmont Carbonate.

Rock type	Grosmont Carbonate
Sample size (voxels)	400x400x400
Voxel size (μm)	2.02
Porosity	24.7%
Number of nodes	11,416,848
Number of elements	50,105,905

Table 4. Bulk and shear moduli of Grosmont Carbonate.

	Bulk modulus (GPa)	Shear modulus (GPa)
Cohesive contact model with $C = 1$	23.8	13.6
Fixed grain contacts	24.0	13.4
Difference	0.8%	1.5%

3.3 Various consolidation levels

Many sedimentary rock samples may exhibit different levels of consolidation as sediments are compacted and cemented under various geomechanical and geochemical conditions. In this section we focus on an intermediate consolidated rock, a Fontainebleau Sandstone.

For illustration purposes, we firstly apply the parametric cohesive contact model to a Fontainebleau model [31,38], with a relatively small volume of $100 \times 100 \times 100$ voxels, and voxel size of $7.3 \mu\text{m}$. Figure 6 shows the binary voxelized image, segmented grains, and conformal grain mesh used in the FE solver. Following reference [22], the material properties assigned are for quartz as in the sphere packing case.

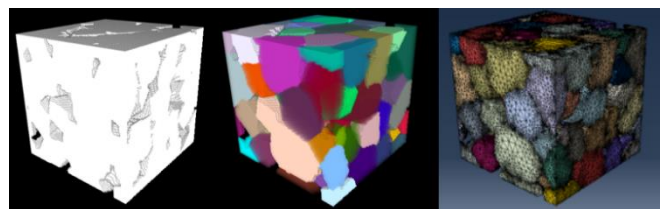


Fig. 6. From left to right: the original binary micro-CT image of Fontainebleau model, segmented grains indicated by different colors, and grain mesh for the FE solver.

We perform uniaxial strain tests on this Fontainebleau model, which requires an incremental strain in the vertical direction and zero strains in the horizontal directions [23]. Figure 7a shows stress-strain behaviours of various consolidation level C . When $C = 0$ and $C = 1$, the cohesive contact model can reproduce the moduli of free and fixed grain contacts, respectively. The modulus shows an increase as the consolidation level C increases. Figure 7b shows the normalized modulus as a function of the consolidation level. The modulus tends to become asymptotic approaching to the

two ends. We find that the data can be fitted well by a logistic function:

$$f(x) = \frac{1}{1+e^{-k(x-x_0)}} \quad (7)$$

where the fitted parameters k and x_0 are 10.0 and 0.5, respectively. The purpose of using a fitting function is to minimize the number of simulations needed to create a complete contact model valid for all range of consolidation levels $0 \leq C \leq 1$ behavior. We found that we only need to run two more simulations apart from the two end-member simulations ($C = 0$ and $C = 1$) to completely capture the effect of consolidation level.

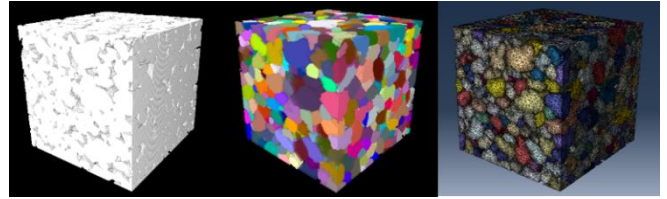


Fig. 8. From left to right: the original binary micro-CT image of Fontainebleau sandstone, segmented grains, and grain mesh.

We perform a hydrostatic compression test to measure the bulk modulus. Figure 9a shows the stress-strain behaviours for various consolidation levels C . The parametric cohesive contact model can reproduce the moduli of fixed and free grain contacts when $C = 1$ and $C = 0$, respectively. Two intermediate consolidation levels result in a modulus in between. The parameters k and x_0 of our logistic fitting function are 15.9 and 0.5, respectively.

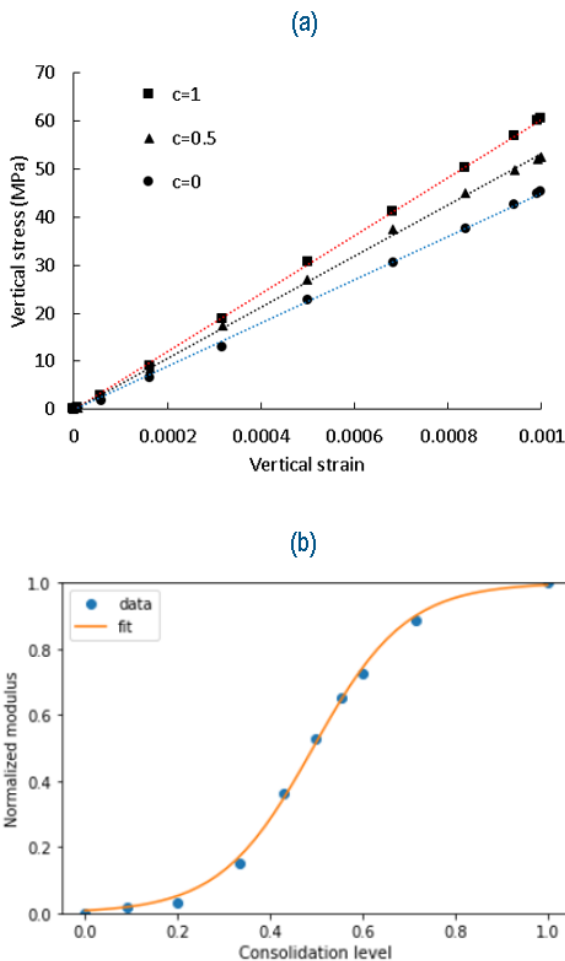


Fig. 7. (a) Stress-strain response for various consolidation levels C . (b) Normalized modulus as a function of consolidation level. The result can be fitted by a logistic function.

With the knowledge obtained from simulations on the small Fontainebleau model, we further apply the parametric cohesive contact model to a larger Fontainebleau Sandstone micro-CT model of $288 \times 288 \times 300$ voxels [2]. The voxel size is $7.5 \mu\text{m}$. The sample porosity is 14.7%. The material properties are assigned as quartz. Figure 8 shows the voxelized image, segmented grains, and conformal grain mesh.

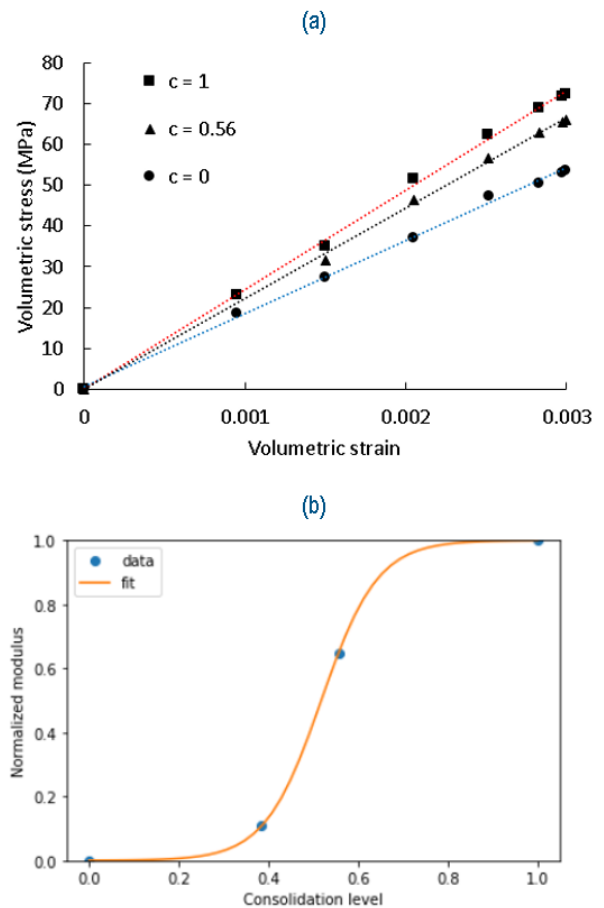


Fig. 9. (a) Stress-strain response for various consolidation levels C . (b) Normalized modulus as a function of consolidation level. The result can be fitted by a logistic function.

The experimentally measured bulk modulus is ~ 22.2 GPa, which corresponds to a consolidation level C of 0.56 based on the simulation results in Figure 9 [2]. We further perform a shear test to measure the shear modulus when $C = 0.56$. We obtain a shear modulus of 24.9 GPa, which is also close to the laboratory-measured shear modulus. Therefore, this method can be used to estimate the contact consolidation level by finding the C value so that the experiments match with simulations on a corresponding micro-CT image. The

model also allows the users to select the consolidation level as an input parameter based on their knowledge of diagenesis history of sedimentary rock samples. Some ideas have been discussed about relating the consolidation level with the relative size of the grain-grain contact areas relative to the grain sizes. Small relative contact areas should correspond to lower consolidation levels, while larger relative contact areas should correspond to higher consolidation levels. A systematic study with a representative population of rock types and consolidation levels using the new parametric cohesive contact model should provide some validation of this idea.

Table 5. Bulk and shear moduli of Fontainebleau Sandstone.

	Bulk modulus (GPa)	Shear modulus (GPa)
Experimental result	22.2	23.5
Numerical result ($C = 0.56$)	22.2	24.9
Difference	0.0%	5.9%

3.4 Failure test

The rock failure behaviour manifests the significance to capture well the consolidation level. Uniaxial compression tests are widely used to determine the uniaxial compressive strength (UCS) and deformability of rock samples [39,40]. The testing sample is loaded in the axial direction with no confinement in the radial directions. The ratio of height/diameter of the samples is typically between 2 and 3 [41]. A ratio smaller than 2 will result in high uniaxial compressive strength [42].

In this section, we perform uniaxial compression tests on a cylindrical volume from the Fontainebleau model used in the previous section, at various consolidation levels C . All the other model parameters remain invariant. The sample has a height of 500 voxels and a diameter of 250 voxels. The voxel size is 7.3 μm . Figure 10 shows the voxelized image of segmented grains and the corresponding grain mesh used in the FE simulations of uniaxial compression test.

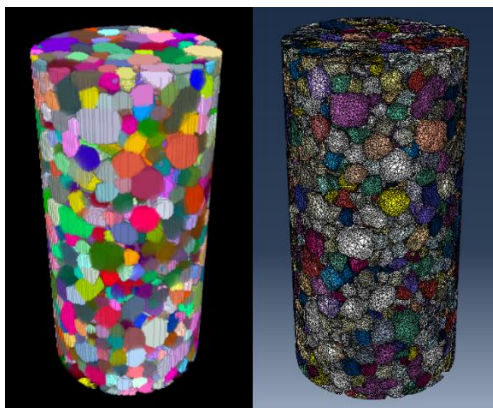


Fig. 10. (Left) Voxelized image of segmented grains. (Right) Grain meshing for FE simulation of failure test.

Figure 11 shows the evolution of vertical displacement field as the sample is being compressed in the vertical direction ($C = 0.2$). The Fontainebleau sample is initially intact and finally ruptures with a shear band. Figure 12 shows the vertical stress as a function of vertical strain for various consolidation levels C . When $C = 1$, the grains are fused together and the sample behaves elastic with an infinite strength. When $C = 0$, the grains are unconsolidated and the sample fails when the vertical stress reaches the uniaxial compressive strength, with friction as the only remaining force. An intermediate C will result in stress-strain curves in between the two end-member scenarios. When C is relatively small (e.g. $C = 0.2$), the stress-strain curve is very close to the result of $C = 0$ due to the asymptotic nature of Eq. (7), and shown in Figures 7b and 9b. The simulation results show that the rock failure behaviour is conditioned by the consolidation level, which is parameterized into the cohesive contact model in this work.

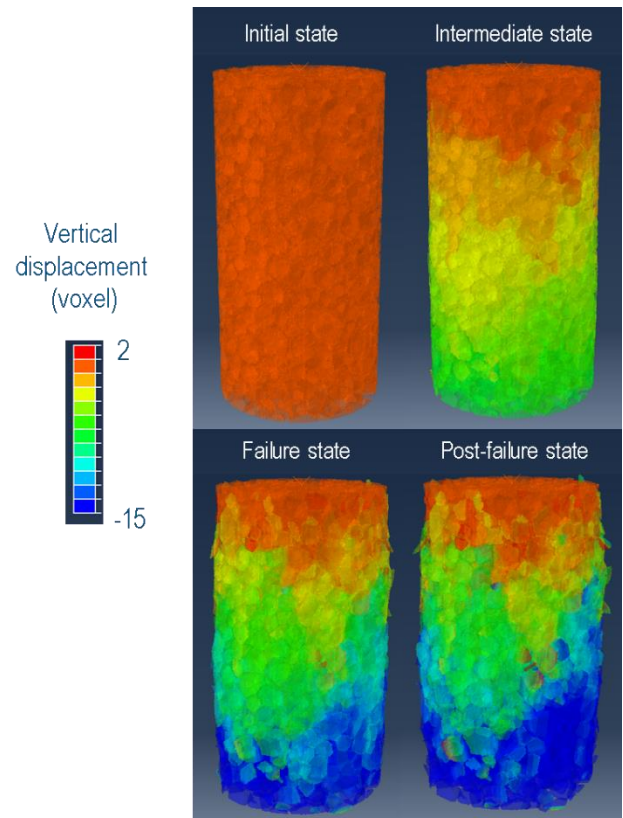


Fig. 11. Evolution of vertical displacement field as the Fontainebleau model is compressed in the vertical direction. The grains are shown semi-transparent for a better visualization. The sample ruptures with a shear band at the failure state.

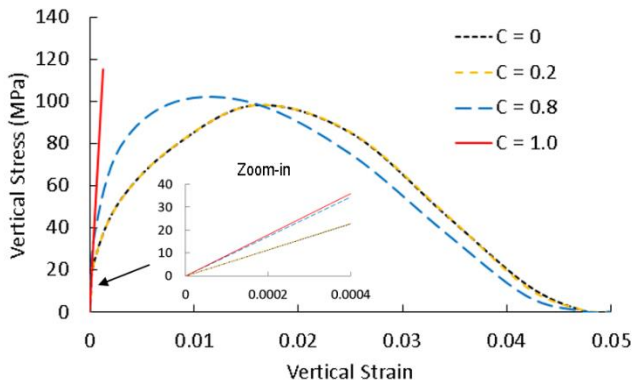


Fig. 12. Vertical stress as a function of vertical strain for various consolidation levels C . A larger C results in a larger uniaxial strength and elastic modulus.

Table 6 summarizes the Young's modulus and uniaxial compressive strength based on the results shown in Figure 12. A larger consolidation level parameter C will result in a larger Young's modulus and uniaxial compressive strength. Han (1987) experimentally measured the Young's modulus of several Fontainebleau sandstones and the results range from 36 to 79 GPa [43]. Baud et al. (2014) experimentally measured the uniaxial compressive strength of several Fontainebleau sandstones and the results were from 44 to 122 MPa [44]. Our numerical simulations for this particular Fontainebleau model yield reasonable values of Young's modulus and uniaxial compressive strength compared to these reference experimental data.

In addition to the consolidation level, the contact friction is another critical parameter to the rock failure process. We adopt the Coulomb friction model which relates the maximum allowable frictional stress across a grain contact to the contact pressure between the grains. The critical frictional stress at which sliding of the contacts starts is proportional to the product of friction coefficient and contact pressure. We assume a friction coefficient of 0.2 throughout this study. Besides, we find that (1) the elastic-plastic transition is smooth compared to many real loading scenarios, and (2) the post-peak behaviour is less catastrophic than real failures. This may be a result of the fact that the current meshing process is not ideal and introduces non-smooth contact boundaries that can add friction to grain contacts. The future work will be improving the grain meshing process to allow smooth contact boundaries that facilitate relative large-strain grain relocation.

Table 6. Bulk and shear moduli of Fontainebleau Sandstone.

	Young's modulus (GPa)	Uniaxial compressive strength (MPa)
$C = 0$	57.0	98.2
$C = 0.2$	57.4	98.3
$C = 0.8$	86.1	102.6
$C = 1.0$	89.8	infinity

4 Concluding remarks

In this paper, we extend our previous micromechanics workflow described in [23] to a parametric cohesive contact model. The presented workflow can capture both extreme contact behaviors: free grains and fixed grains, as well as any intermediate degree of grain consolidation. We present a benchmark study on several samples and compare with laboratory-measured elastic moduli to estimate its degree of consolidation. Simulations that do not include the grain contact modeling, tend to overestimate the elastic moduli, which manifests the significance of our contribution to capture well the grain contact behavior. To demonstrate the impact of properly capturing the degree of consolidation on the rock strength and failure pattern, we present results for numerical uniaxial compression testing consistent with measured results. This workflow provides a physics-based solution to the complex grain-grain contact behavior, which complements laboratory core analysis, and can be useful to reveal underlying grain-scale processes governing rock mechanical behavior. The importance of a more complete microscopic understanding of core-scale mechanical properties is ultimately reflected in the quality of the inputs that we use for our up-scaled geomechanics models, as well as enabling a more comprehensive framework for digital rock simulated petrophysical properties at different NCS conditions.

5 Nomenclature

Notation

K = stiffness
 t = traction stress
 δ = separation in normal direction
 D = damage variable
 C = consolidation level
 Δx = characteristic length
 k, x_0 = fitting parameters for logistic function

Subscripts

R = normal direction
 S = shear direction
 m = effective property

Superscripts

f = failure condition
 0 = critical condition
 max = maximum value

Acknowledgments

We would like to acknowledge the support of Dassault Systèmes to allow the publication of this work.

References

- [1] H. Andrä, N. Combaret, J. Dvorkin, E. Glatt, J. Han, M. Kabel, Y. Keehm, F. Krzikalla, M. Lee, and C. Madonna, *Digital Rock Physics Benchmarks—Part I: Imaging and Segmentation*, *Comput. Geosci.* **50**, 25 (2013).

- [2] H. Andrä, N. Combaret, J. Dvorkin, E. Glatt, J. Han, M. Kabel, Y. Keehm, F. Krzikalla, M. Lee, and C. Madonna, *Digital Rock Physics Benchmarks—Part II: Computing Effective Properties*, *Comput. Geosci.* **50**, 33 (2013).
- [3] R. Xu, B. Crouse, D. M. Freed, A. Fager, G. R. Jerauld, N. Lane, and Q. Sheng, *Continuous vs Discontinuous Capillary Desaturation and Implications for IOR/EOR*, in *Paper SCA2018-066 Presented at the International Symposium of the Society of Core Analysts Held in Trondheim, Norway* (2018).
- [4] B. Crouse, D. M. Freed, N. Koliha, G. Balasubramanian, R. Satti, D. Bale, and S. Zuklic, *A Lattice-Boltzmann Based Method Applied to Digital Rock Characterization of Perforation Tunnel Damage*, in *Paper SCA2016-058 Presented at the International Symposium of the Society of Core Analysts Held in Snow Mass, Colorado, USA* (2016).
- [5] M. J. Blunt, *Flow in Porous Media—Pore-Network Models and Multiphase Flow*, *Curr. Opin. Colloid Interface Sci.* **6**, 197 (2001).
- [6] J. Dvorkin, M. Armbruster, C. Baldwin, Q. Fang, N. Derzhi, C. Gomez, B. Nur, and A. Nur, *The Future of Rock Physics: Computational Methods vs. Lab Testing*, *First Break* **26**, (2008).
- [7] C. H. Arns, M. A. Knackstedt, M. V. Pinczewski, and W. B. Lindquist, *Accurate Estimation of Transport Properties from Microtomographic Images*, *Geophys. Res. Lett.* **28**, 3361 (2001).
- [8] M. Andrew, H. Menke, M. J. Blunt, and B. Bijeljic, *The Imaging of Dynamic Multiphase Fluid Flow Using Synchrotron-Based X-Ray Microtomography at Reservoir Conditions*, *Transp. Porous Media* **110**, 1 (2015).
- [9] A. K. Turner, F. H. Kim, D. Penumadu, and E. B. Herbold, *Meso-Scale Framework for Modeling Granular Material Using Computed Tomography*, *Comput. Geotech.* **76**, 140 (2016).
- [10] C. H. Arns, M. A. Knackstedt, W. V. Pinczewski, and E. J. Garboczi, *Computation of Linear Elastic Properties from Microtomographic Images: Methodology and Agreement between Theory and Experiment*, *Geophysics* **67**, 1396 (2002).
- [11] T. W. J. De Geus, J. Vondřejc, J. Zeman, R. H. J. Peerlings, and M. G. D. Geers, *Finite Strain FFT-Based Non-Linear Solvers Made Simple*, *Comput. Methods Appl. Mech. Eng.* **318**, 412 (2017).
- [12] M. M. Hossain, J. Arns, Z. Liang, Z. Chen, and C. H. Arns, *Humidity Effects on Effective Elastic Properties of Rock: An Integrated Experimental and Numerical Study*, *J. Geophys. Res. Solid Earth* **124**, 7771 (2019).
- [13] M. A. Knackstedt, C. H. Arns, and W. V. Pinczewski, *Velocity-Porosity Relationships, I: Accurate Velocity Model for Clean Consolidated Sandstones*, *Geophysics* **68**, 1822 (2003).
- [14] B. Crouse, S. Gill, J. Bautista, G. Balasubramanian, and D. Freed, *Digital Prediction of Porosity and Permeability Variation of Unconsolidated Sands Caused by Over-Burden Pressure*, in *NAFEMS World Congress* (2019).
- [15] A. B. Andhumoudine, X. Nie, Q. Zhou, J. Yu, O. I. Kane, L. Jin, and R. R. Djaroun, *Investigation of Coal Elastic Properties Based on Digital Core Technology and Finite Element Method*, *Adv. Geo-Energy Res.* **5**, 53 (2021).
- [16] S. Boggs Jr, *Principles of Sedimentology and Stratigraphy* (Pearson Education, 2014).
- [17] E. J. Garboczi and J. G. Berryman, *Elastic Moduli of a Material Containing Composite Inclusions: Effective Medium Theory and Finite Element Computations*, *Mech. Mater.* **33**, 455 (2001).
- [18] S. Meille and E. J. Garboczi, *Linear Elastic Properties of 2D and 3D Models of Porous Materials Made from Elongated Objects*, *Model. Simul. Mater. Sci. Eng.* **9**, 371 (2001).
- [19] E. H. Saenger, *Numerical Methods to Determine Effective Elastic Properties*, *Int. J. Eng. Sci.* **46**, 598 (2008).
- [20] C. H. Arns, M. Madadi, A. P. Sheppard, and M. A. Knackstedt, *Linear Elastic Properties of Granular Rocks Derived from X-Ray-CT Images*, in *SEG Technical Program Expanded Abstracts 2007* (Society of Exploration Geophysicists, 2007), pp. 1711–1715.
- [21] N. Saxena, R. Hofmann, A. Hows, E. H. Saenger, L. Duranti, J. Stefani, A. Wiegmann, A. Kerimov, and M. Kabel, *Rock Compressibility from Microcomputed Tomography Images: Controls on Digital Rock Simulations*, *Geophysics* **84**, WA127 (2019).
- [22] J. Fredrich, N. Lane, and J. Toms, *Image-Based Direct Numerical Simulation of Petrophysical Properties under Simulated Stress and Strain Conditions*, U.S. Patent 9,348,056 (24 May 2016).
- [23] Z. Sun, R. Salazar-Tio, L. Duranti, B. Crouse, A. Fager, and G. Balasubramanian, *Prediction of Rock Elastic Moduli Based on a Micromechanical Finite Element Model*, *Comput. Geotech.* **135**, 104149 (2021).
- [24] D. Legland, I. Arganda-Carreras, and P. Andrey, *MorphoLibJ: Integrated Library and Plugins for Mathematical Morphology with ImageJ*, *Bioinformatics* **32**, 3532 (2016).
- [25] S. Qin, R. McLendon, V. Oancea, and A. M. Beese, *Micromechanics of Multiaxial Plasticity of DP600: Experiments and Microstructural Deformation Modeling*, *Mater. Sci. Eng. A* **721**, 168 (2018).
- [26] Abaqus, *Abaqus 6.10 Online Documentation*, Abaqus User Subroutines Ref. Man. (2010).
- [27] M. Obermayr, K. Dressler, C. Vrettos, and P. Eberhard, *A Bonded-Particle Model for Cemented Sand*, *Comput. Geotech.* **49**, 299 (2013).
- [28] D. O. Potyondy and P. A. Cundall, *A Bonded-Particle Model for Rock*, *Int. J. Rock Mech. Min. Sci.* **41**,

- 1329 (2004).
- [29] Z. Sun, D. N. Espinoza, and M. T. Balhoff, *Discrete Element Modeling of Indentation Tests to Investigate Mechanisms of CO₂-Related Chemo-Mechanical Rock Alteration*, *J. Geophys. Res. Solid Earth* **121**, 7867 (2016).
- [30] H. Harkness, G. Ang, P. Vijalapura, and D. Cojocar, *Contact Stress Accuracy with Robust and Broadly Applicable Implicit Contact Algorithm*, in *NWC (Nafems World Congress)* (2011).
- [31] F. D. E. Latief, B. Biswal, U. Fauzi, and R. Hilfer, *Continuum Reconstruction of the Pore Scale Microstructure for Fontainebleau Sandstone*, *Phys. A Stat. Mech. Its Appl.* **389**, 1607 (2010).
- [32] V. Brotons, R. Tomás, S. Ivorra, A. Grediaga, J. Martínez-Martínez, D. Benavente, and M. Gómez-Heras, *Improved Correlation between the Static and Dynamic Elastic Modulus of Different Types of Rocks*, *Mater. Struct.* **49**, 3021 (2016).
- [33] J. M. Ide, *Comparison of Statically and Dynamically Determined Young's Modulus of Rocks*, *Proc. Natl. Acad. Sci. U. S. A.* **22**, 81 (1936).
- [34] R. Sain, *Numerical Simulation of Pore-Scale Heterogeneity and Its Effects on Elastic, Electrical and Transport Properties* (Stanford University, 2010).
- [35] S. N. Domenico, *Elastic Properties of Unconsolidated Porous Sand Reservoirs*, *Geophysics* **42**, 1339 (1977).
- [36] M. A. Zimmer, *Seismic Velocities in Unconsolidated Sands: Measurements of Pressure, Sorting, and Compaction Effects* (Stanford University, 2004).
- [37] B. E. Buschkuehle, F. J. Hein, and M. Grobe, *An Overview of the Geology of the Upper Devonian Grosmont Carbonate Bitumen Deposit, Northern Alberta, Canada*, *Nat. Resour. Res.* **16**, 3 (2007).
- [38] R. Hilfer and T. Zauner, *High-Precision Synthetic Computed Tomography of Reconstructed Porous Media*, *Phys. Rev. E* **84**, 62301 (2011).
- [39] C. E. Fairhurst and J. A. Hudson, *Draft ISRM Suggested Method for the Complete Stress-Strain Curve for Intact Rock in Uniaxial Compression*, *Int. J. Rock Mech. Min. Sci.* **36**, 279 (1999).
- [40] Z. T. Bieniawski and M. J. Bernede, *Suggested Methods for Determining the Uniaxial Compressive Strength and Deformability of Rock Materials: Part I. Suggested Method for Determining Deformability of Rock Materials in Uniaxial Compression*, in *International Journal of Rock Mechanics and Mining Sciences & Geomechanics Abstracts*, Vol. 16 (Elsevier, 1979), pp. 138–140.
- [41] E. Tuncay and N. Hasancebi, *The Effect of Length to Diameter Ratio of Test Specimens on the Uniaxial Compressive Strength of Rock*, *Bull. Eng. Geol. Environ.* **68**, 491 (2009).
- [42] A. B. Hawkins, *Aspects of Rock Strength*, *Bull. Eng. Geol. Environ.* **57**, 17 (1998).
- [43] D.-H. Han, *Effects of Porosity and Clay Content on Acoustic Properties of Sandstones and Unconsolidated Sediments*, Stanford Univ., CA (USA), 1987.
- [44] P. Baud, T. Wong, and W. Zhu, *Effects of Porosity and Crack Density on the Compressive Strength of Rocks*, *Int. J. Rock Mech. Min. Sci.* **67**, 202 (2014).

Integration of core-scale logging, dual-energy computed tomographic imaging and geochemical and mineralogical analysis of a composite core

Helene Velcin^{1,2*}, *Jeremie Dautriat*², *Lionel Esteban*², *Mark D. Lindsay*¹, *Annette D. George*¹, *Thomas Richard*³, *Adam Ramage*²

¹The University of Western Australia, School of Earth Sciences, WA 6009, Australia

²CSIRO Energy, Australian Resources Research Centre, Kensington, Western Australia 6076

³Epslog SA, 69 Jean Street, Hamilton Hill, 6163 WA, Australia

Abstract. Determining reservoir properties is challenging because it requires integration of data collected at different scales, from wireline measurements to sample powders analysed in laboratory. Low spatial resolution of well-log data (usually collected at ~50 mm intervals at best) and plug intervals (every 0.25–0.3 m) generates gaps between data points that may lead to over- or underestimate reservoir properties. The objective of this study is to measure different petrophysical properties, directly at the drill core-scale, to reduce the laboratory plug characterisation, as well as the gap between data points. Eleven different sandstones, three different limestones and a piece of granite were used to create a composite core of 10 cm in diameter and 84 cm long. The sandstones are homogeneous with distinct petrophysical properties from each other and were selected as appropriate analogues for oil and gas reservoirs. Sections of these sandstones, cut at different angles, were assembled to simulate realistic core heterogeneities with different: (i) rock types (texture, porosity and mineralogical variations), (ii) interface orientations between sandstones and (iii) fracture distribution. This study presents the integration of measurements obtained at different scales with core-scale logging techniques and dual energy (DE) method from X-ray imaging, supported with X-ray diffraction analysis and laboratory measurements to determine rock type, mineralogical composition, density and porosity variation along the composite core. These datasets may then be integrated with wireline log data (e.g. depth correction, porosity quality check, density and mineralogy log derivations) to facilitate selection of representative plug samples for more advanced analysis. The combination of 1D properties measured with core-scale logging techniques, and the 3D data obtained with the X-ray imaging technique, have the potential to generate 3D properties in future studies.

1 Introduction

Evaluation of the distribution of mineralogical, petrophysical and geomechanical properties of subsurface rocks is fundamental for geological modelling and reservoir production estimation. A large part of the data used to constrain 3D reservoir models originates from downhole wireline logging tools and core characterisation, by means of collecting data across multiple scale from indirect and direct measurements. Wireline logging gathers physical properties such as density, resistivity and gamma ray used for rock typing (distribution of clay content and permeable layers), depositional environment interpretation, well to well correlation, porosity distribution estimation, and prediction of hydrocarbon content [1, 2]. However, the data collected are only an indication/estimation of the reservoir properties because they are determined from indirect measurements. Moreover, they can be

discontinuous, caused by tool malfunction; and the depth of measurements, estimated from the tool speed, must be corrected as well as the effect of the mud filtration [3, 4, 5]. In order to calibrate, correct and validate these well log data and interpretation, it may be necessary to physically sample the core for further laboratory evaluation.

Laboratory data can be collected at different scales on the core. At meter scale, the X-ray medical CT scanner is commonly used as a non-destructive method to measure the density of the material and quickly identify the degree of sedimentological/stratigraphic heterogeneity and/or potential core damage. From the collected 3D images, a sampling strategy can be defined for further laboratory measurements to better constrain and calibrate well logs and reservoir model [6]. After plugging the core material, samples are then used to perform direct measurements of critical reservoir properties such as porosity, permeability and capillary pressure. Petrographical and mineralogical analyses are conducted on thin sections and powders.

* Corresponding author: Helene.Velcin@csiro.au

These local measurements remain difficult to upscale as uncertainties remain as to the representativeness of the tested material of a given facies at well or reservoir scales. In addition, temperature, pressure and fluid present at depth may affect the bulk rock properties such as porosity and permeability [1]. Uncertainties regarding representativeness of the laboratory dataset needs to be taken into account in assessing the reliability of 3D geological models and evaluation of the reservoir [7, 3, 8].

X-ray computed tomography (XCT) scanning is the only non-destructive technique able to image bulk density at high resolution ($\sim 100\mu\text{m}^3$) of whole cores in 3D [9]. In addition, recent developments on dual-energy XCT acquisition have proven able to provide bulk density and effective atomic numbers maps that can be used to calculate porosity and mineralogy variation along the core. The different methods used in this study include XCT, HyLogger-3, Multi-sensor core logger (MSCL-S), and Scratch test. These generate measurements, in a semi-automated manner, of mineralogical composition, bulk density, magnetic susceptibility, chemical elements, P and S-wave velocities, and rock strength. Most of these instruments produce continuous images of the core surface, and the MSCL-S permits the acquisition of ultraviolet (UV) fluorescence images. In this paper, we applied and integrated these methods on a composite core composed of homogeneous sandstones and limestones, pre-characterised in the laboratory. The use of a composite core is important to develop, test and validate the workflow presented here for future application to real core materials, and also for discussion of the limitations and uncertainties related to each technique.

2 Integrated workflow

The proposed approach for core-scale characterisation involves the following key steps summarised in Figure 1:

1. Creation of an “artificial” core, referred as composite core, using different homogeneous and well-described rock materials, with contrasting rock properties, distinct grain size or distinct mineralogy;

2. Petrophysical properties and mineralogical composition are determined in the laboratory on companion samples extracted from the same component materials;

3. Collection of petrophysical, physical, geomechanical, geochemical and petrographic data, along the core using different logging instruments such as the HyLogger-3, Multi-sensor Core Logger and the scratch test. All these techniques: (i) are non- or micro destructive; (ii) produce profiles (well log-like dataset) of rock properties along the core in a semi-automatic fashion and; (iii) acquire data at relatively high spatial resolution (every cm);

4. Dual-Energy XCT scan of the composite core and interpretation of logs and 3D maps of density and effective atomic numbers;

5. Combination of this technique with HyLogger and/or X-Ray Diffraction (XRD) data to convert density

3D maps into mineral composition (quantitative analysis) that can be used to recalculate grain density and porosity along the core (profile/3D maps).

5. Calibration and validation of the profile data against the dataset acquired from point 2 on companion samples.

Core preparation and operation and functionality of instruments are reported in the following sub-sections.

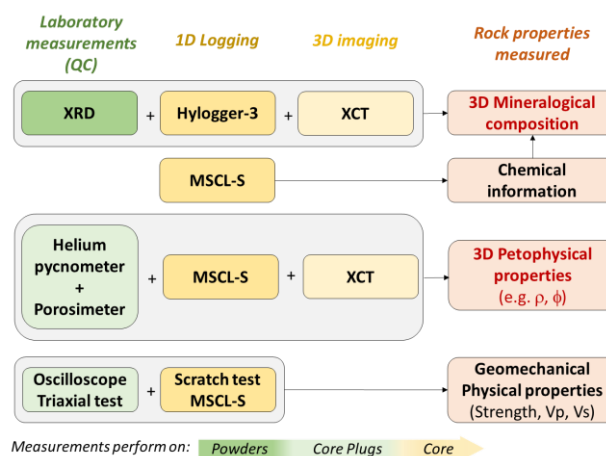


Fig. 1. Illustration of the integrated workflow and techniques used in this study to collect the rock properties of interest for core characterisation and our aim to ultimately create 3D models of these properties. Direct measurements are performed at core scale and validated using laboratory measurements performed on the analogue companion samples.

2.1 Core preparation and preliminary laboratory characterisation

To test the workflow, the composite core was composed of alternating rock materials extracted from blocks available in CSIRO’s core library. This approach allows use of companion samples for petrophysical and mineralogical characterisation. The composite core was created by cutting and assembling 18 pieces of cored material of 10cm in diameter. The selected rocks cover a large range of properties similar to actual petroleum reservoirs and are recognised as international reference materials. A total of 15 different materials were considered, covering mainly siliciclastic materials (including Berea, Nugget, Bentheimer, Crab Orchard, Idaho, Scioto, Colton, Carbon Tan, Castlegate, Kentucky and Boise sandstones, mostly extracted from deltaic deposits), a few calcareous materials (including Lueder, Mont Gambier and Savonnieres limestones) and a granite section at the base of the core (Figure A1). The total length of the synthetic core is 0.84 m. Some of the interfaces between material pieces were cut obliquely to the core axis to simulate tilted fractures and discontinuities, which were locally filled with clay (glaze). The different rocks used and their properties (porosity, permeability and uniaxial compressive strength) reported from the literature and the rock suppliers are listed in Figure A1 [10, 11, 12].

Petrophysical and mineralogical characterisation were performed on cylindrical samples (of 38 mm in diameter and ~80 mm in length) and powders extracted from each considered material block, respectively. Cylindrical samples and powders were dried for 48 hours at 105°C prior to testing. Bulk density (ρ_{bulk}) of the companion samples and grain density (ρ_{grain}), measured on powder sample with the Accupyc II 1340 helium pycnometer, were used to derive the total porosity (Φ). Compressional wave velocity (V_p) and shear wave velocity (V_s) were also measured on these plugs along the core length at ambient conditions. The mineralogical composition of the samples was determined by X-ray diffraction (XRD) and reported in Table A1.

2.2 1D properties logging

2.2.1 Petrophysical and chemical characterisation

Petrophysical properties were measured along the core every centimetre using a Multi-sensor core logger (MSCL-S), developed by Geotek accommodating cores up to 1.5 m long. The MSCL-S enables continuous and non-destructive logging of the core surface. The equipment available at CSIRO can be used for the following measurements (see further details in [13, 14]:

- *Gamma density* measures the bulk density profile based on gamma attenuation on approximately 5 mm with a low activity Cs-137 gamma ray source
- *Magnetic susceptibility* represents the type and amount of magnetic minerals in the sample. Data are collected with a point sensor of 10 mm diameter measuring approximately 1000 mm³ of the rock material at the core surface.
- *Primary wave travel times* are measured between two stainless steel ultrasonic transducers of 25 mm diameter placed on each side of the core. The thickness of the core, as determined by the P-wave travel path, is estimated at each measurement point using a contactless laser. The first P-wave arrival time is picked automatically and knowing the distance between both transducers, the P-waves velocity (V_p) can be computed.
- *A high performance X-Ray Fluorescence (XRF)* core scanner used for XRF spectroscopy on 100 mm² at the surface of the core and can analyse a large range of elements from Mg to U.

The cores were also imaged using the Geoscan V colour line-scan camera that captures visible and UV light sources. The core images are recorded at the same depth as other data measured and then useful for core description to locate the different facies.

2.2.2 Geomechanical/physical logs

The equipment developed by Epslog was used in this study to measure the rock strength, V_p and V_s profile along the core. This transportable bench test is able to perform measurements on cores from 20 mm up to 0.15 m in diameter and from 20 mm up to 1 m long. A

Polycrystalline Diamond Compact (PDC) cutter ~10 mm wide is used to scratch the core surface along its length while measuring the force/strength, amplitude and orientation on the blade. The movement/speed of the PDC along the core (~ few mm/s) and the cut depth (between 0.1 and 2 mm, depending on lithology) are both controlled and kept constant during the test. The blade is equipped with three strain gauge sets mounted along three axes recording the force applied. It is shown in the literature that the pure cutting force is directly correlated with Uniaxial Compressive Strength (UCS) values [15, 16, 17, 18]. A four-centimetre sensor equipped with an ultrasonic emitter of 50 kHz and a receiver, is measuring both V_p and V_s along the surface of the core. Due to the geometry of the core as assembled, and the discontinuities between each lithology, axial measurements were available on limited core sections only. To overcome this limitation, V_p and V_s were also measured manually perpendicular to the core axis.

2.2.3 Mineralogical logging

Mineralogical composition of the core was assessed using the HyLogger-3 at CSIRO, Perth. This equipment uses hyperspectral reflectance to identify a large range of minerals using three different spectrometers covering spectra from visible-near-infrared (VNIR), between 400 nm and 1000 nm, to shortwave-infrared (SWIR), from 1000 nm to 2500 nm, and to thermal infrared (TIR), from 6000 to 14,500 nm [19,20]. VNIR measures iron oxides, rare earth element minerals and SWIR measures mainly minerals such as hydrous silicate, carbonate and sulphate minerals. TIR is used to characterise anhydrous silicates such as quartz, feldspar, garnet, pyroxene, olivine, and hydrous silicate, sulphate and carbonate minerals [20, 21]. The sensor has a footprint of 12x8 mm that can record a 1D spectral profile at the core surface along the core axis. The measurements are acquired automatically every 4 mm with an overlap while the table is moving at 48 mm/s, which records twelve simultaneous spectra per second. The data were processed using "The Spectral Geologist" software (TSG®).

2.3 3D XCT imaging – Dual energy

The petroleum industry largely uses XCT technologies to describe core and study their properties. There are two methods of XCT imaging acquisition. The most common is XCT single energy for routine core characterisation. The core is scanned in preserved or unpreserved condition to visualise its internal structure (bedding, macro porosity/cavities, fossil content, bioturbation, or core damage such as fractures, drilling fluid invasion etc.) and compute the bulk density profile. The second and more rarely used XCT acquisition method relies on the use of dual energy (DE-XCT) which scans the same material under high and low power energy. In DE, two different physical effects are predominant [22]: At high energy (> 100 kV), the Compton scattering effect is dominant and sensitive to density of material whereas at low energy (< 100 kV), the photoelectric absorption effect is dominant

and sensitive to atomic number of the component material. This technique has been developed for medical application and is widely used for fluid flow visualisation studies. However, limited research has been published on the use of this technique for core-scale characterisation [23, 24, 25, 26, 27]. By combining these two physical effects, XCT attenuation images can be inverted into density (ρ_{bulk}) and effective atomic number (Z_{eff}) images [22, 23]. In this study, a new image segmentation method combining HyLogger-3/XRD data and DE-XCT images was also developed to improve the mineralogical and porosity quantification along the core in 3D.

A medical XCT scanner, Siemens SOMATOM definition AS, was used at CSIRO, Perth, on the composite core, with a helical acquisition (0.35 mm pitch and slice thickness of 0.6 mm) every 0.1 mm slice spacing under 80 kV and 140 kV (i.e. dual energy). DE-XCT was used to compute bulk density (ρ_b) and atomic number (Z_{eff}) following the method described by Wellington and Vinegar^[22] (1987) and refined by Siddiqui and Khamees^[23] (2004). The density and Z_{eff} derived from DE-XCT acquisition was calibrated using four standard samples, quartz, teflon, water and air. These standards were scanned before and after DE-XCT acquisition on the composite core to check for any potential drift of the scanner settings during scanning. Both standard samples and composite core XCT images were reconstructed using a sharp reconstruction kernel algorithm (H60s from Siemens) that has the advantage of enhancing the high spatial frequency information on images and correct beam hardening effect around the core, at the cost of degrading the signal-to-noise ratio on the XCT images. However, such noise can be drastically reduced using a Non-Local mean (NLM) filter.

The following workflow describes the different steps in DE-XCT image processing applied to the standard samples and core composite to retrieve its ρ_{bulk} , Z_{eff} and mineralogical composition profiles along the core axis.

1. Standard samples and composite core DE-XCT images (80kV and 140kV) were opened on Avizo© (Thermofisher).
2. A Non-Local Mean filter was applied to all the data to reduce noise.
3. The mean XCT attenuation values from each standard sample acquired at 80kV and 140kV before and after composite core XCT acquisition were extracted.
4. An inversion code, following the methodology described by Siddiqui and Khamees^[23] (2004), and calibrated from standard samples in point 3, converted the composite core DE-XCT images into ρ_{bulk} images set and Z_{eff} images set.
5. The mean ρ_{bulk} , mean Z_{eff} and within each image set was calculated on Avizo© to generate their profiles along the core axis.
6. A median filter was applied to each Z_{eff} image to reduce the noise created by the inversion code.
7. Z_{eff} images were segmented and converted into mineral phases, guided by the mineralogical

qualitative and quantitative analysis provided by the HyLogger-3 and XRD data respectively.

8. A porosity profile was computed from the bulk density and grain density derived from the mineral composition (point 7) and compared with porosity measured on the companion plug samples in the laboratory.

3 Results and discussion

3.1 Physical properties and chemical analysis (MSCL-S)

Figure 2a shows the results obtained with the MSCL-S with (a) the physical properties measured (ρ_{bulk} , V_p and magnetic susceptibility per unit volume K) compared to the measurements performed in laboratory. An excellent correlation is observed for the ρ_{bulk} collected in laboratory and the MSCL-S profile. As regards the V_p , the MSCL-S data are discontinuous due to the nature of the core. The magnetic susceptibility profile displays significant variation, especially for the Colton sandstone with a magnetic susceptibility greater than 20×10^{-5} SI, but also Idaho, Scioto, Kentucky and Boise sandstones with magnetic susceptibility values between 5×10^{-5} and 10×10^{-5} SI. Higher susceptibility values are associated with a lower quartz content and higher hematite and or mica/illite content.

An example of some elemental results obtained with the XRF MSCL-S sensor are reported in Figure 2b and c. Major elements Si, Ca, Fe and Al indicate the different composite core lithology. Siliciclastic rock types have a Si concentration higher than 0.5×10^6 ppm. Glazed sections can be dissociated from the siliciclastic rock types if Fe and Al concentrations are higher than 4×10^4 ppm and higher or equal to 2×10^5 ppm respectively. Finally, calcareous rock types are easily identifiable with Si concentrations lower than 0.5×10^6 ppm and Ca concentrations greater than 2.5×10^5 ppm. The K log can be used to discriminate sandstone rich in K feldspar, or potassic clays such as illite. Natural light and UV images of the whole core were obtained by rotating the core manually and stacking the obtained images. The UV light images enable identification of calcareous facies in the core. Calcite in these rock types fluoresces orange in Lueder and Savonnieres limestones, whereas calcite in Mt. Gambier limestone fluoresces white. It is known that calcite can fluoresce in different colours depending on mineral impurities^[28] such as metal cations (e.g. Mn) and/or rare earth elements (e.g. Y) present in the fluid during precipitation or diagenetic alteration of the minerals and/or cements.

In the case of non-composite cores, XRF analysis gives valuable information not only in terms of facies determination, but also on the presence of specific minerals that can affect the permeability such as clays or different cements.

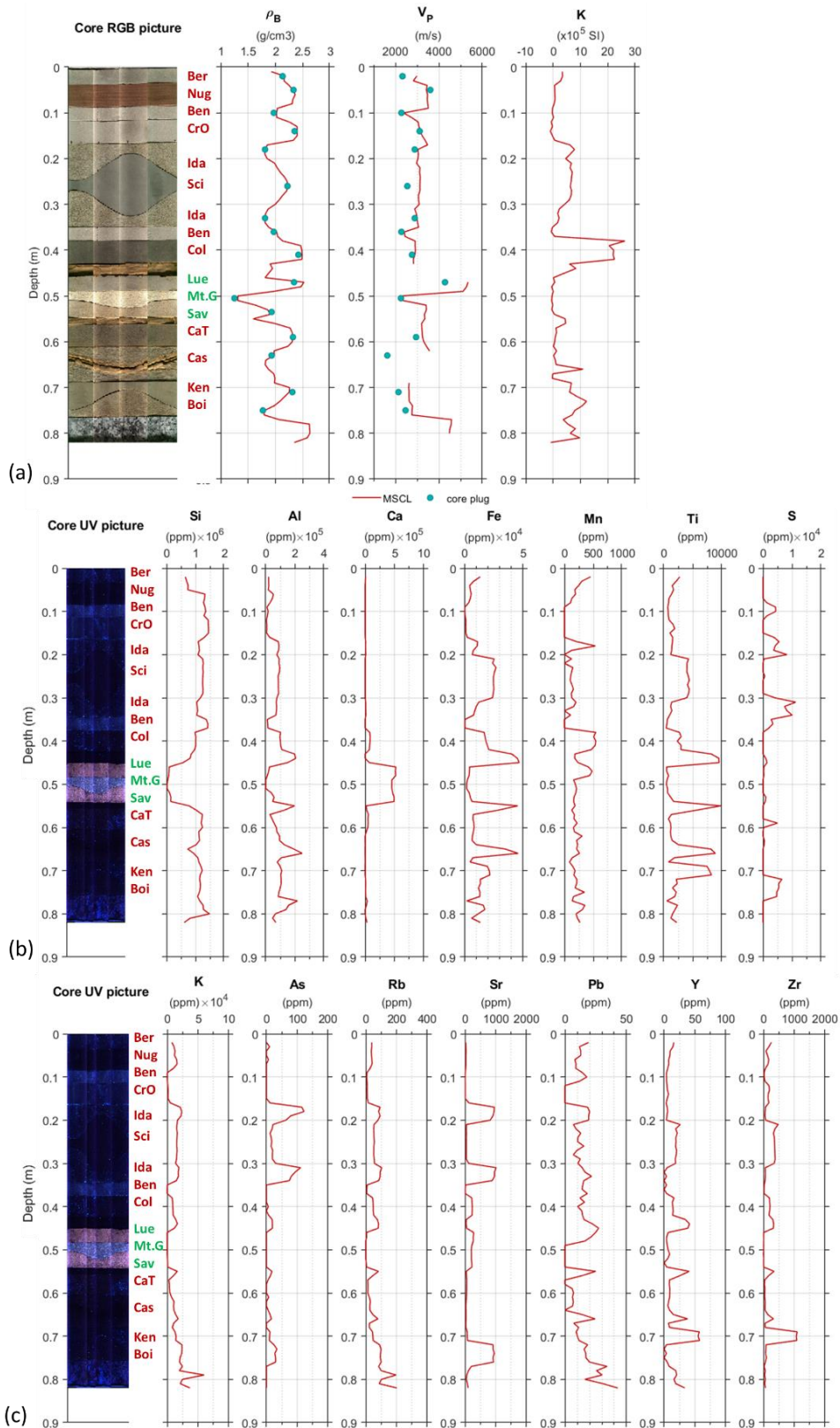


Fig. 2. Images, physical properties, and chemical analysis acquired with the MSCL-S. Image of the composite core acquired under natural and UV light. (a) Different physical property profiles measured along the core with ρ_{bulk} the gamma bulk density, V_p the P-waves and K the magnetic susceptibility. The laboratory measurements performed on the companion samples and powders for the bulk density and the V_p measurements are reported on the corresponding profiles (green filled circles). (b) and (c) Major and trace elements measured with the XRF sensor along the core.

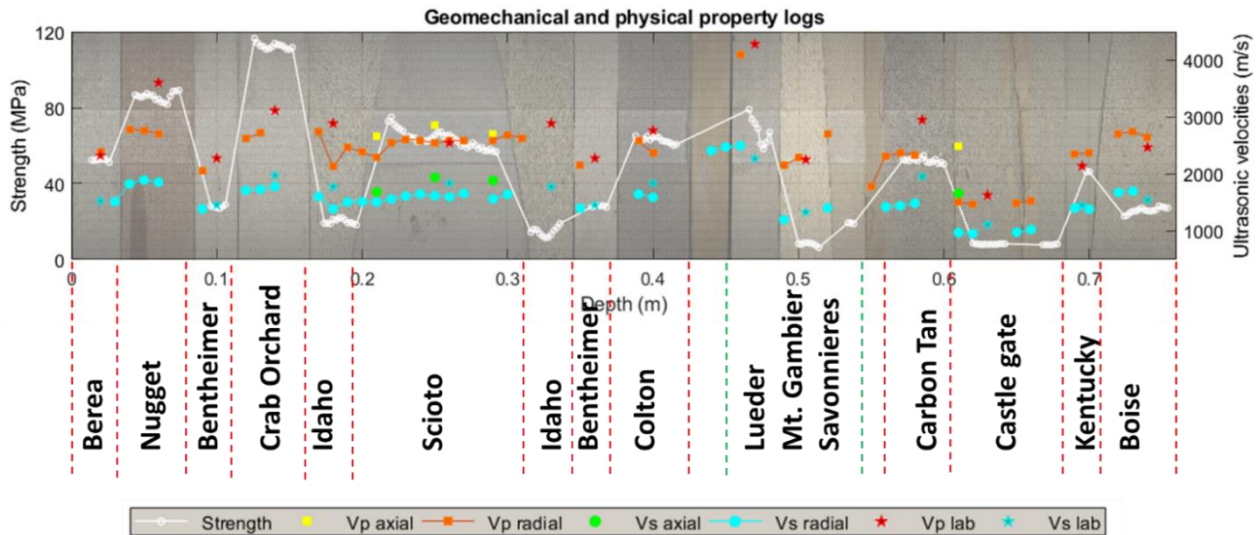


Fig. 3. Summary of the geomechanical and physical measurements generated by Epslog on the composite core using the scratch test and Vp -Vs sensors. In white high-resolution scratch test measurements (every 2mm); Vp (squares) and Vs (discs) were acquired in axial (yellow and green) and radial direction (orange and cyan) every 1 cm when the data acquisition was possible. Vp and Vs measurements performed on the companion samples are also reported in this figure (red and blue stars for Vp and Vs respectively).

3.2 Geomechanical and ultrasonic properties (Scratch test)

Figure 3 illustrates the strength, Vp and Vs data that were collected along the core with the scratch test. The strength data reported on the graph were collected every 2 mm whereas the Vp and Vs data were collected every 1 cm. Epslog's equipment measures ultrasonic velocities at the core sub-surface with a single sensor equipped with an emitter and a receiver. Note that the Vp, Vs and strength data were not measured on the granite base and glaze since these lithologies could not be analysed under the current equipment configuration.

The Vp and Vs data collected with the Epslog equipment (orange and cyan filled circles on the Figure 3) present the same trend as the data collected in laboratory (red and cyan stars), varying between 4250 and 1600 m/s for the Vp and between 2500 and 1000 m/s for the Vs. The strength (white circles) measured with the Scratch test gives a direct measurement of the UCS along the core. The UCS values obtained vary between ~9 and 120 MPa and are in accordance with the UCS data found in the literature or provided by the rock blocks suppliers (Figure A1, [10, 11, 12]).

UCS and elastic modulus are two critical parameters for determining mechanical properties of the rock, essential for well bore stability or reservoir subsidence studies. The scratch test has the unique advantage of providing continuous UCS profiles in a micro-destructive and cost-effective manner, avoiding the plug drilling process commonly undertaken for laboratory UCS measurements. It also provides ultrasonic velocity profiles along the core enabling the calculation of dynamic elastic moduli by combining these profiles and the density profile obtained with the MSCL-S (Medical XCT-scanner) equipment.

3.3 Mineralogical composition – qualitative analysis (HyLogger-3).

Figure 4 provides a comparative analysis of the XRD results introduced in the previous section and the HyLogger-3 measurements recorded in two orthogonal directions. The TSA library was used to process the data and the non-geological spectra were excluded from the dataset. The results obtained with the HyLogger-3 are consistent with the XRD data. The carbonate section has been well identified using the HyLogger-3. Silica/quartz, chlorite, sulfate, smectite and kaolin minerals in the sandstones were all recognized at their expected locations. However, note that kaolin was identified in the HyLogger-3 data in CrabOrchard but not via XRD. HyLogger-3 results indicate the presence of white micas where micas/illite was identified with the XRD analysis. The glazed sections are easily recognizable with the TIR spectrometer and are composed mostly of kaolinite with Na-feldspar and quartz. Na and K-Feldspar were only identified in the Idaho, Boise, and Kentucky sandstones where they represent more than 15% of the rock composition according to the XRD analysis. They were not detected in the other sandstones with a lower feldspar percentage. The Hylogger-3 results appear to be reliable, especially for rock type identification, although some caution is needed in terms of mineralogical identification. A complementary method such as XRD or scanning electron microscopy should be used for a quality check of the data and thus improving the reliability of this method.

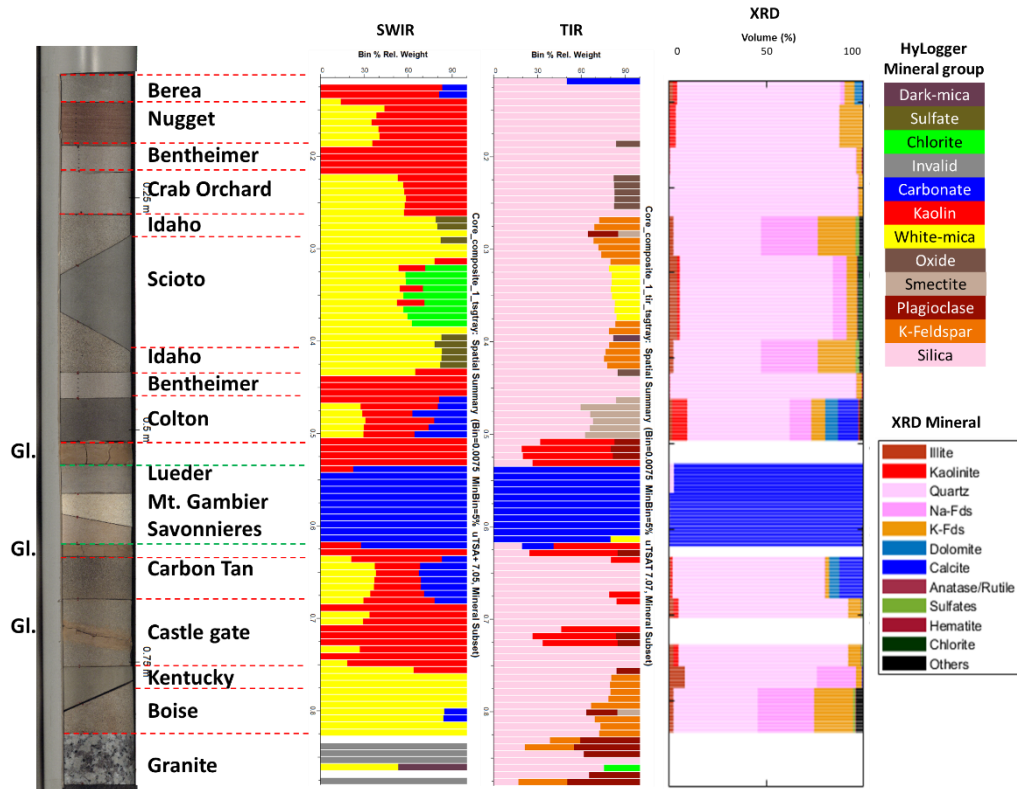


Fig. 4. Mineralogical qualitative analysis performed with the HyLogger-3 with TIR and SWIR spectrometer. The measurements were performed at the surface of the core. At the right end of the figure, the core-scale propagation of XRD results which are summarised in the Table A1 for comparison purpose with the HyLogger. Note that the granite base and the glaze sections were not analysed (corresponding to the four blank sections on the bar chart).

3.4 Petrophysical, physical properties and mineralogical composition 3D imaging (DE XCT)

The composite core picture, its 140kV post-filtered XCT image and the two properties ρ_b and Z_{eff} , derived from DE-XCT images on the composite core, are presented in map form, colour coded by intensity, as well as the mean profile (black line on Figure 5). These profiles clearly highlight the different rock types and their contacts along with some local heterogeneity.

Five different rock types are identified from Z_{eff} data and supported by HyLogger-3 mineralogy data (Figure 5 – Z_{eff} map): (i) sandstones composed mainly of quartz (in blue); (ii) sandstones rich in feldspars (in green); (iii) sandstone and glaze rich in calcite (green/yellow) which can be differentiated using the HyLogger-3 and/or MSCL-S data; (iv) limestone (in pink); (v) granite where the minerals are larger than the pixel size and characterized by very high bulk density.

For each rock type, ρ_{bulk} fluctuations are primarily related to fluctuation of porosities from one material to another. Porosity calculation is also dependent on the minerals present in each rock and requires a segmentation of each mineral, to compute the grain density, as described below. Both ρ_{bulk} and Z_{eff} maps are affected by area of high porosity in between each piece of rock composing the core. As highlighted on the profiles Figure 5, those discontinuities induce most of the time lower values of Z_{eff} , which is expected since the air Z_{eff} is 7.52^[23]. However, on both sides of the glazed sections

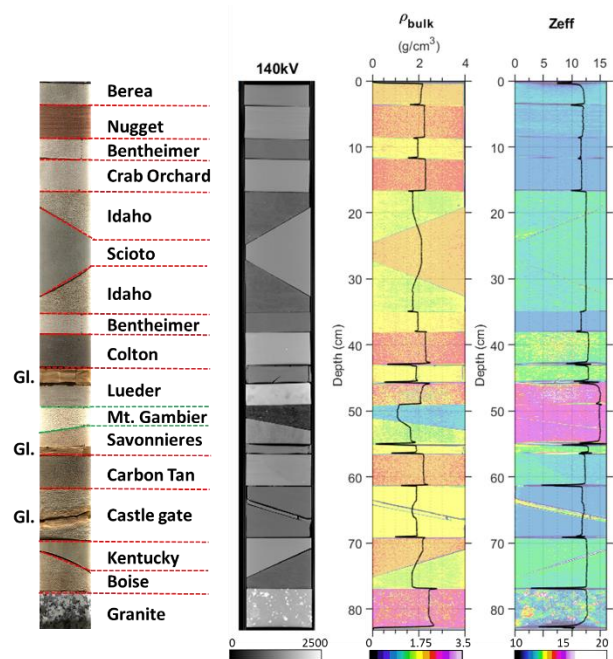


Fig. 5. Composite core image and rock types location (Gl. Sections correspond to the glaze), DE-XCT image and data from the composite core: from left to right: filtered raw XCT image acquired at 140kV; bulk density and Z_{eff} images colour labelled by intensity (their mean profiles is added in black line).

where the space between each piece is wider, artefacts with anomalously high Z_{eff} values are observable (Figure 5).

Note that such artefacts are not expected in the case of natural core that do not have such contrasting density values if undamaged.

Further to rock type identification, we proposed a segmentation of the Z_{eff} maps to quantify the mineralogical content along the core axis. This segmentation was calibrated and validated with HyLogger-3 and XRD data, respectively. Knowing the mineralogical composition of the core determined by HyLogger-3 and XRD, and by assuming that the minerals are “pure”, their corresponding/respective chemical formula was used to compute the Z_{eff} of each mineral constituting the composite core as follow:

$$Z_{eff} = \left(\sum f_i Z_i^n \right)^{\frac{1}{n}}, \quad (1)$$

with Z_i the atomic number of the i -th element and f_i the fraction of atoms of the i -th element in the mineral [23].

From XRD and HyLogger-3 data, the following minerals were considered for Z_{eff} segmentation: illite, kaolinite, Na-feldspar, quartz, K-feldspar, dolomite, calcite, rutile, anatase, natrojarosite and hematite. Their chemical formula and computed Z_{eff} from Eq.1 are summarized in Table 1.

Table 1. Minerals used for the composite core segmentation and their corresponding ρ_{grain} and calculated Z_{eff} from Eq. 1.

Mineral	Chemical Formula	Z_{eff}	ρ_{grain}
Illite	$KAl_3Si_3O_{10}(OH)_4$	9.6058	2.80
Kaolinite	$Al_2Si_2O_5(OH)_4$	11.1622	2.60
Na-Feldspar	$Na(AlSi_3O_8)$	11.5534	2.61
Quartz	SiO_2	11.7842	2.65
K-Feldspar	$KAlSi_3O_8$	13.3895	2.53
Dolomite	$CaMg(CO_3)_2$	13.7438	2.87
Calcite	$CaCO_3$	15.7100	2.71
Rutile	TiO_2	19.0006	4.20
Natrojarosite	$NaFe_3(SO_4)_2(OH)_6$	19.5642	3.09
Hematite	Fe_2O_3	23.4417	5.30

Figure 6 reports the results of two segmentation approaches to interpret the Z_{eff} maps, namely Thresholding #1 and Thresholding #2. The mineral segmentation (Thresholding #1: Figure 6) from Z_{eff} was achieved by defining Z_{eff} range for each identified mineral from HyLogger/XRD data. The computed Z_{eff} from Table 1 were first sorted in ascending intensity. For each mineral i , the threshold is centred on the Z_{eff} value and range from the mean value of the preceding ($i-1$) and considered mineral i , to the mean value of the following ($i+1$) and considered mineral i , as:

$$\frac{Z_{eff(i-1)} + Z_{eff(i)}}{2} < threshold(i) < \frac{Z_{eff(i+1)} + Z_{eff(i)}}{2}, \quad (2)$$

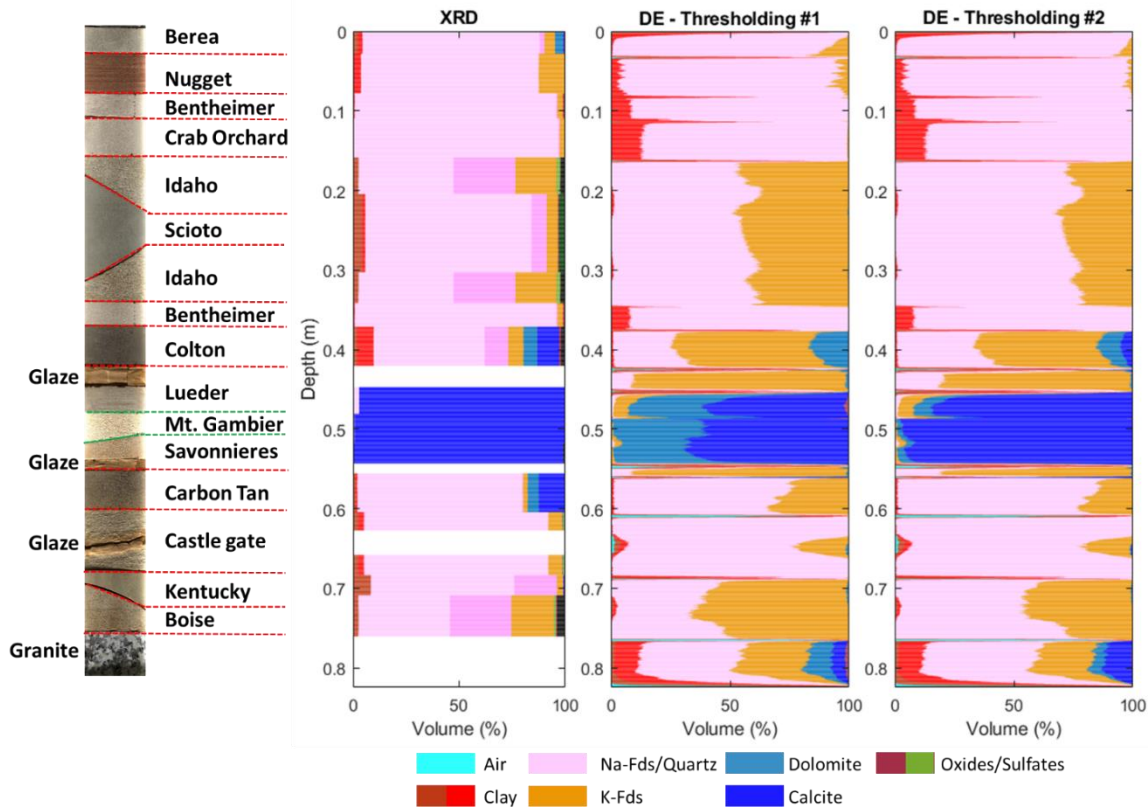


Fig. 6 Mineral composition along the composite core from XRD and DE-XCT. XRD analysis on a single sample extracted from each rock types of the composite core. DE-XCT mineralogy was computed from two threshold methods: (i) Basic mineral Z_{eff} boundaries and (ii) Improved Z_{eff} boundaries.

Due to their low contrast in Z_{eff} , Na-feldspar and quartz were segmented as a single mineral phase. The derived volume of each mineral in the different sandstones and limestones from Thresholding#1 was compared with XRD analyses (Figure 6). Overall, the result of the segmentation#1 is well correlated with the XRD data. However, some discrepancies remain observed, in terms of over- or under-estimation of some mineral phases. Kaolinite is overestimated in the vicinity of rock pieces edges, around the discontinuities described above, where only air or minerals such as quartz and feldspar are expected.

- Kaolinite is concentrated in some samples where it was measured with the HyLogger-3 but not with the XRD method.
- K-feldspar is overestimated in most sandstones such as Idaho, Scioto, Colton, Carbon Tan, Kentucky and Boise sandstones.
- Carbonate is also segmented and overestimated on both side of the glazed sections where anomalously high mean Z_{eff} values are observed. Calcite is underestimated in Colton, Carbon Tan sandstones and the limestone sections, where it is substituted by higher content in dolomite and/or K-Feldspar.

In order to improve the results of the Thresholding#1, a second segmentation was undertaken (Thresholding #2: Figure 6). The Z_{eff} mineral ranges were adjusted manually and calibrated against the XRD results. K-feldspar contribution is then successfully updated for the coarse sandstones Boise and Idaho but remains slightly overestimated in Scioto, Colton, Kentucky and

CarbonTan sandstones. All these sandstones are composed of fine grains, and are relatively tight with porosity values below 20%, low permeability (<5mD according to laboratory measurements), quartz content <80% and a high content in Fe and Ti for Scioto, Colton and Kentucky Sandstones (Table A1, Figure A1). The mineralogical diversity, the fine grain size and the resolution of the XCT scanner make difficult the segmentation of the different mineralogical phases, as the attenuation measured at the voxel size will more likely correspond to a mineral mixture than a single phase. The dolomite contribution remains unresolved in CarbonTan sandstone but was successfully improved in Colton sandstone, Lueder, Mt Gambier and Savonnières limestone sections. The remaining dolomite and K-Feldspar observed in the Lueder limestone may reflect a mixture of calcite and quartz. Note also that the segmentation used in this work is suitable for pure minerals having the chemical formula described in Table 1. However, in the case of chemical substitution or impurities in these minerals, Z_{eff} can be slightly different to those calculated from equation (2) and reported in Table 1. Finally, some remaining noise, after filtering, can also alter the quality of the segmentation and affect the resulting mineralogical content.

In conclusion, the combination of DE-XCT and HyLogger-3 scanning (quality checked with a few XRD points) appears to be a powerful method to determine the mineral composition and porosity changes along the core at high resolution and in 3D.

The porosity profiles, computed from the bulk density and grain density retrieved from mineralogical

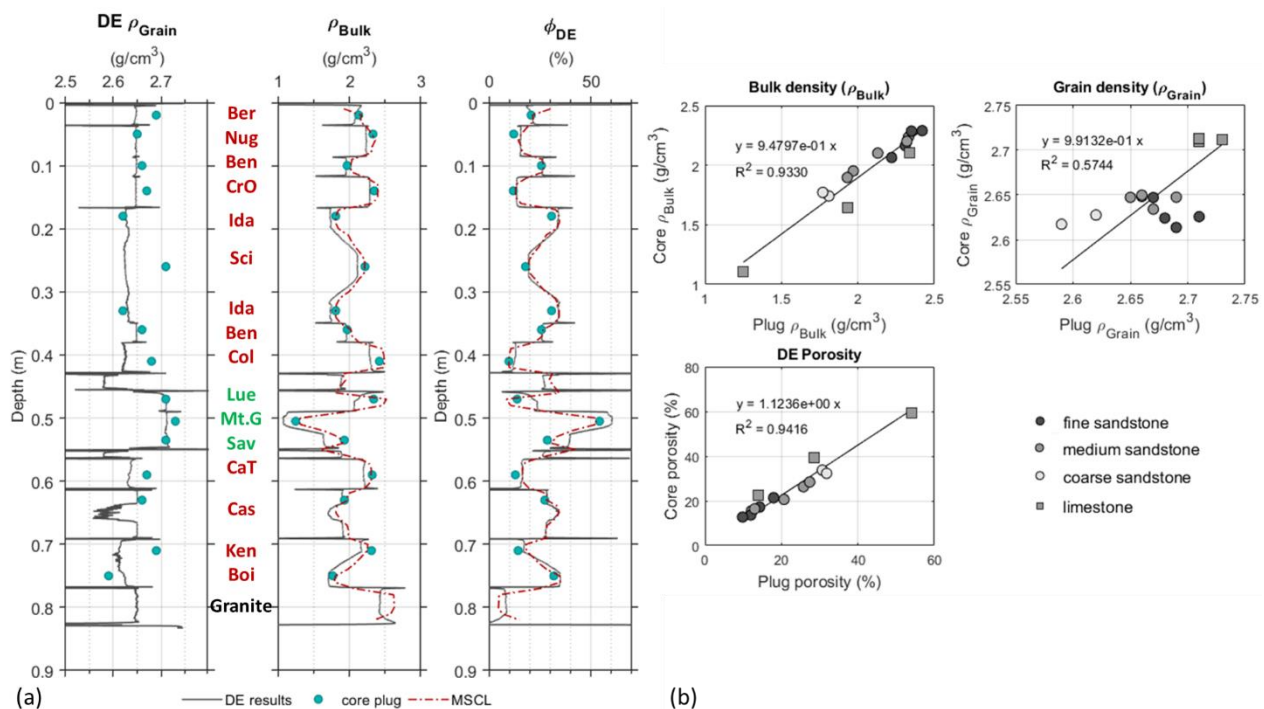


Fig. 7. (a) ρ_{grain} , ρ_{bulk} logs obtained with the DE methods using the second threshold and ρ_{bulk} measured with the gamma source on the MSCL-S are also reported on this plot for comparison purpose. Φ_{DE} calculated using both of the DE density and Φ_{DE} calculated using the DE ρ_{grain} and the gamma ρ_{bulk} . On each log are reported the measurements conducted in laboratory on the companion samples. (b) ρ_{bulk} , ρ_{grain} , and ϕ measured and calculated with the DE vs the measurements performed in laboratory on the companion samples.

composition along the composite core, is compared with porosity values inferred from different techniques (Figure 7). First, the bulk density derived from DE-XCT method is consistent with the bulk density measured with the MSCL-S gamma-density sensor, as well as those measured on companion samples in laboratory (green filled circles on Figure A5a, Figure A5b) with an excellent correlation factor. Grain density remains underestimated in Scioto, Colton, Kentucky and CarbonTan sandstone due to their characteristics described previously which impact the mineralogy segmentation (Figure 7a). Despite those grain density inconsistency values in tight samples, the porosity derived from DE-XCT is consistent with the laboratory porosity data with a coefficient of determination of 0.94 between the two datasets (Figure 7a, b).

4 Conclusion

Multiple datasets of petrophysical, geochemical, physical and mechanical properties and mineralogical composition of core extracted from exploration wells is essential for core characterisation, property interpretation and prediction of reservoir character. In this study, laboratory analyses were undertaken on plug samples to validate our workflow and methods. It has been shown that data acquired using different bench logging tools, in a non-destructive manner, matched conventional laboratory data. A full geochemical analysis was performed with the XRF sensor on the MSCL-S, supporting the mineralogical characterisation generated with the HyLogger-3 and the dual energy method. DE XCT imaging can be used to accurately determine the varying rock types of the composite core.

We demonstrate the relevance of DE-XCT scanning and core logging integration for : (i) rock typing, by capturing the proportion of minerals in each interval if the segmentation of the images is supported and constrained by HyLogger-3 or complementary local data such as XRD; (ii) bulk density and porosity calculation, (iii) collection of rock mechanical and acoustic velocities properties along the core. XCT scanning offers a unique opportunity to retrieve these properties along the core in 3D with a resolution of few 100s of micrometre. Future potential of this work is to build-up 3D models of the petrophysical, physical and mechanical properties by integrating 1D profiles and 3D models obtained using the different methods presented in this paper.

Acknowledgements

CSIRO Deep Earth Imaging Future Sciences Platform (DEI FSP) funded this research and provided a postgraduate scholarship, and UWA provided an international fees scholarship for HV. Dr Belinda Godel (CSIRO) is thanked for providing important advice to this project. Dr Ian Lau (CSIRO) is thanked for his help with HyLogger-3 data acquisition. This research utilized the X-ray medical CT, Hylogger-3 and Multi-sensor core logger at CSIRO, Kensington, Perth, as well as Epslog's

equipment. ML acknowledges support from MinEx CRC and ARC DECRA DE190100431.

References

1. S., Cannon, *Petrophysics: A Practical Guide*. John Wiley & Sons Incorporated, pp. 224. ISBN 978-1-118-74673-8 (2016)
2. E.J., Peters, *Advanced Petrophysics: Geology, Porosity, Absolute Permeability, Heterogeneity, and Geostatistics*. Vol.1, First Edition. ISBN: 978-1-936909-44-5 (2012).
3. W.R., Moore, Y.Z., Ma, J., Urdea, and T., Bratton, *Uncertainty Analysis in Well-Log and Petrophysical Interpretations*. In Y. Z. Ma and P. R. La Pointe, eds., *Uncertainty analysis and reservoir modelling: AAPG Memoir 96*, p. 17 – 28 (2011).
4. J.D., Walls, and M.B., Carr, *The Use of Fluid Substitution Modeling for Correction of Mud Filtrate Invasion in Sandstone Reservoirs*. SEG Technical Program Expanded Abstracts 2001: pp. 385-387. <https://doi.org/10.1190/1.1816624> (2001).
5. J.D., Walls, J., Dvorkin, M.B., Carr, *Well Logs and Rock Physics in Seismic Reservoir Characterization*. Offshore Technology Conference paper, Houston, Texas, U.S.A. (2004).
6. C., McPhee, J., Reed, I., Zubizarreta, *Core analysis: A best practice guide*. Elsevier, Developments in Petroleum Science 64 (United Kingdom). ISBN: 978-0-444-63533-4, ISSN: 0376-7361 (2015).
7. M.D., Lindsay, L., Ailleres, M.W., Jessell, E.A., de Kemp, P.G., Betts, *Locating and quantifying geological uncertainty in three-dimensional models: Analysis of the Gippsland Basin, southern Australia*. *Tectonophysics* 546-547, pp. 10-27. doi:10.1016/j.tecto.2012.04.007 (2012).
8. Z., Rui, J., Lu, Z., Zhang, R., Guo, K., R., Ling, Zhang, S., Patil, *A Quantitative Oil and Gas Reservoir Evaluation System for Development*, vol. 42. pp. 31–39 (2017).
9. F., Mees, R. Swennen, M., Van Geet, P., Jacobs, *Applications of X-ray computed tomography in the geosciences*. Geological Society, London, Special Publications 2003, v.215;p1-6 (2003)
10. Kocurek Industries INC. <https://kocurekindustries.com/>
11. V., Mikhaltsevitch, M., Lebedev, and B., Gurevich, *Low-frequency laboratory measurements of the acoustic parameters of Savonnières limestone*. SEG Denver 2014 Annual Meeting, 2978-2982. DOI <http://dx.doi.org/10.1190/segam2014-1500.1> (2014).
12. Stone Contact <https://www.stonecontact.com/>
13. GEOTEK, *Documentation for the GEOTEK Multi-Sensor Core Logger (MSCL)*. Available online at: <https://www.geotek.co.uk/wp-content/uploads/2016/04/MSCL-manual-1-Nov-16.pdf> (version Nov 1, 2016)
14. A., Vatandoost, P., Fullagar, and M., Roach, *Automated Multi-Sensor Petrophysical Core Logging*, *Exploration Geophysics*, 39, 181-188 (2008).

15. S., Doshvarpassand, *Investigation into the impacts of rock/cutter interface geometry on drilling response of PDC cutters*. P.h.D. thesis. Curtin University (2017).
16. T., Richard, *Determination of rock strength from cutting tests*. Master of Science thesis. University of Minnesota, Minneapolis, Minnesota, USA (1999)
17. T., Richard, E. Detournay, A. Drescher, P. Nicodeme, D. Fourmaintraux, et al., *The scratch test as a means to measure strength of sedimentary rocks*. In *SPE/ISRM Rock Mechanics in Petroleum Engineering*. Society of Petroleum Engineers (1998)
18. T., Richard, F. Dagrain, E. Poyol, and E. Detournay. *Rock strength determination from scratch tests*. *Engineering Geology* 147, 91_100 (2012).
19. D.W., Coulter, X., Zhou, L.M., Wickert, P.D., Harris, *Advances in Spectral Geology and Remote Sensing: 2008-2017*. In "Proceedings of Exploration 17: Sixth Decennial International Conference on Mineral Exploration", p. 23–50(2017).
20. M. C., Schodlok, L., Whitbourn, J., Huntington, P., Mason, A., Green, M., Berman, D., Coward, P., Connor, W., Wright, M., Jolivet, R., Martinez, *HyLogger-3, a visible to shortwave and thermal infrared reflectance spectrometer system for drill core logging: functional description*, *Australian Journal of Earth Sciences*, 63:8, 929-940 (2016).
21. P., Mason, and J.F., Huntington, *HyLogger 3 components and pre-processing: An overview*. Northern Territory Geological Survey, Technical Note 2012-002 (2012).
22. S., Wellington, and H., Vinegar, *X-ray computerized tomography*. *Journal of Petroleum Technology*, 39(08), 885-898. <https://doi.org/10.2118/16983-PA> (1987).
23. S., Siddiqui, A.A., Khamees, S., Aramco, *Dual-Energy CT-scanning application in rock characterization*. Paper presented at the SPE Annual Technical Conference and Exhibition held in Houston, Texas, U.S.A., 26-29 September (2004).
24. J., Walls, and M., Armbruster, *Shale Reservoir Evaluation Improved by Dual Energy X-Ray CT Imaging*. *Journal of Petroleum Technology*, Vol.64, 28-32 (2012).
25. H., Al-Owihan, M., Al-Wadi, S., Thakur, S., Behbehani, N., Al-Jabari, M., Dernaika, S., Koronfol, *Advanced Rock Characterization by Dual Energy CT Imaging: A Novel Method in Complex Reservoir Evaluation*. 10.2523/IPTC-17625-MS (2014).
26. M.,Dernaika, Y., Naseer Uddin, S., Koronfol, O., Al Jallad, G., Sinclair, Y., Hanamura, K., Horaguchi, *Multi-Scale Rock Analysis for improved characterization of complex carbonates*. SPE-175598-MS, (2015)
27. R. A., Victor, M., Prodanovic, and C., Torres-Verdin, *Monte Carlo approach for estimating density and atomic number from dual-energy computed tomography images of carbonate rocks*. *Journal of Geophysical Research: Solid Earth*, 122, 9804–9824. <https://doi.org/10.1002/2017JB014408> (2017).
28. Geology page, *Florescence: Why Minerals Fluoresce?* (2020)
<http://www.geologypage.com/2020/03/fluorescence-why-minerals-fluoresce.html>

Appendix

Table. A1. Summary of the mineralogical quantitative analysis of the different formation used to create the composite core. These analyses were performed using the XRD technique on rock powders. (Qz.= quartz, Dolo.= dolomite, Natro.= natrojarosite, Hem.=hematite, Smec.=smectite, Chl=chlorite, Micro.=microcline, Orth.=orthoclase).

Sample	Qz.	Calcite	Dolo	Natro.	Mica/ Illite	Hem.	Kaolin	Smec.	Chl.	Albite	Micro.	Orth.	Zeolite	Anatase/ Rutile
	%	%	%	%	%	%	%	%	%	%	%	%	%	%
Berea	83.4	0.4	3.8		2.3	0.4	2.2			2.3	5.0			0.2
Nugget	83.7				0		3.8			0	12.2			
Bentheimer	95.0					1.1	0.8			0.5	2.6			
Crab Orchard	96.8					0.2				0.5	2.5			
Idaho	44.8			1.9	2.6					29.1	8.4	10.9	2.2	
Scioto	78.3				4.5		1.3		2.9	7.1	2.2	3.1		0.4
Colton	52.4	10.3	6.5		2.0	0.8	7.7	2.0		11.1	7.1			
Lueder	2.9	97.1												
Mt. Gambier	0.6	99.4												
Savonniere		99												
CarbonTan	77.7	12.0	5.2		1.2	0.4	0.9			0.4	2.1			
Castlegate	86.8	0.2		0.9	2.6	0.2	2.6				2.6	4.0		
Kentucky	67.6	0.4			8.4					20.0	1.8	1.3		0.5
Boise	43.1			1.1	2.6	0.4				28.9	7.8	12.2	3.9	



Fig. A1. Composite core and description of the analogue sandstones and limestones used to create the core. The porosity, permeability and uniaxial compressive strength (UCS) reported here are the ones provided by the rock suppliers or extracted from the literature [10, 11,12]

Comparison of high resolution probe magnetics, X-ray fluorescence and permeability on core with borehole spectral gamma ray and spontaneous potential in an oil sand well

Toan H. To and David K. Potter*

Department of Physics, University of Alberta, Edmonton, Alberta, T6G 2E1, Canada

Abstract. The purpose of this study was to assess some novel techniques to improve oil sand reservoir characterization. The main focus was on high resolution, non-destructive, low field probe volume magnetic susceptibility measurements on slabbed core sections from an oil sands well in northern Alberta. The results demonstrated that this technique was able to distinguish the main lithologies (clean sands, inclined heterolithic stratification – IHS – beds comprising interbedded sand and clay, and shale) better than traditional borehole logging data such as gamma ray and spontaneous potential. The magnetic data also allowed estimates of a paramagnetic “illite” clay content parameter to be determined. High resolution X-ray fluorescence (XRF) measurements were taken at the same points as the magnetic susceptibility in order to provide supplementary elemental information. The magnetically derived illite contents correlated with the elemental contents of iron, potassium and aluminium (all components of illite) from the XRF. The magnetically derived illite contents also correlated with available fluid permeability measurements, and provided a tool for identifying anomalous mineralogies where the “illite” content exceeded 100%.

1 Introduction

This study primarily details the application of a novel, quantitative, high resolution probe magnetic technique for reservoir characterization of slabbed cores from an oil sands reservoir in Northern Alberta, Canada. The purpose was to produce an additional tool that complements, yet has significant advantages over, other traditional core and log based methods of oil sands reservoir characterization. Some preliminary work was previously reported [1, 2]. In the present study non-contact measurements of X-ray fluorescence (XRF) were also undertaken on the slabbed cores to support the interpretations provided by the magnetic technique. Reservoir characteristics and petrophysical properties are determined by various traditional methods using well logging, core analysis and well production data. Well logging allows in-situ estimation of properties, whereas core analysis allows ground truthing by performing measurements on recovered samples (rock and fluid) from the reservoir. Well production data gives generally large-scale information after a reservoir is in economic production. These traditional methods, however, have certain limitations. For example:

1. Borehole and laboratory core gamma ray techniques can be influenced not only by clay minerals (which often control permeability), but also by uranium in organic matter or small amounts of gamma ray emitting heavy minerals. Borehole gamma ray data

can also be influenced by high gamma ray emitting drilling muds such as potassium chloride (KCl).

2. The spontaneous potential (SP) log is usually used to detect permeable beds based on the difference in salinity between the borehole fluids and the formation fluids, and causes a voltage deflection (generally measured in millivolts) from the shale baseline. However, if the salinities are equal there will be no deflection and the SP log will not be able to pick out the permeable zones in this situation.
3. Certain core analysis techniques are not always applicable in unconsolidated oil sands reservoirs. Often it is not possible to cut core plugs in such unconsolidated oil sands cores. In addition, some measurement techniques on slabbed cores might damage the cores. For example, standard probe permeability measurements require the probe tip to be sealed to the rock surface, and the procedure can lead to the probe tip puncturing and therefore damaging the core, resulting in incorrect permeability values. Other core measurement techniques, such as X-ray diffraction, can be time consuming, costly, and therefore tend to be limited to a small number (and small size) of samples.
4. For oil sands slabbed cores it is often difficult to visually recognize and quantify lithological changes in the cores when they are saturated with black heavy oil or bitumen. This paper will demonstrate how useful the probe magnetic method is in

* Corresponding author: dkpotter@ualberta.ca

identifying lithological changes and quantifying mineralogy in these situations.

- Well production data can be useful for large scale interpretations, but not so useful for small scale high resolution lithological and sedimentological heterogeneities.

In contrast, the novel, quantitative probe magnetic technique and the XRF method used in this study are rapid and non-destructive. These techniques are particularly suitable for unconsolidated oil sands slabbed cores, unlike some other core analysis techniques that can potentially damage the cores as previously mentioned. Moreover, the probe magnetic sensor and recording meter are relatively inexpensive pieces of kit (totalling about \$4,500 US for both items). The main applications of these techniques in this study were to identify the different lithologies and help quantify the mineralogy of the slabbed cores at high resolution, as additional tools to complement existing traditional methods. The oil sands well studied in this paper is located in the northeast region of the Athabasca oil sands near Fort McMurray. It was drilled to the McMurray Formation in the Mannville Group of the Western Canada Sedimentary Basin [3].

2 Core Screening Methods

2.1 Probe magnetic susceptibility

Magnetic susceptibility is usually expressed in terms of magnetic susceptibility per unit volume k as:

$$k = J/H \quad (1)$$

or in terms of magnetic susceptibility per unit mass χ as:

$$\chi = M/H = k/\rho \quad (2)$$

where J is the magnetization per unit volume and determined as the magnetic moment divided by the volume of the material, M is the magnetization per unit mass and determined as the magnetic moment divided by the mass of the material, H is the applied external magnetic field, and ρ is the density of the material. A Bartington MS2E sensor was used to perform high resolution measurements of magnetic susceptibility along the flat surface of the slabbed core. The sensor tip at the end of a ceramic tube (label 1 in **Figure 1 (A)** and label 4 in **Figure 1 (B)**) senses a rectangular surface area of 3.8 mm x 10.5 mm on the sample. This allows high resolution measurements to be made at the lamina scale. The sensor is calibrated to measure true volume magnetic susceptibility (k) when against a flat surface of a sample greater than 10 mm in thickness. Most of the magnetic susceptibility signal is acquired within a penetration depth of up to about 5 mm into the sample. The ceramic tube is mounted on a metal enclosure that houses the electronic circuitry. When the sensor is connected to the MS2 meter via a cable and the power is supplied, a low intensity alternating field (about 80 Am⁻¹ and about 2 kHz in frequency) is generated. This applied field penetrates a few mm into the sample when the tip of the sensor is placed on the flat surface of the slabbed core. A calibration sample comprising magnetite

particles dispersed in resin was used to check that sensor was working correctly.

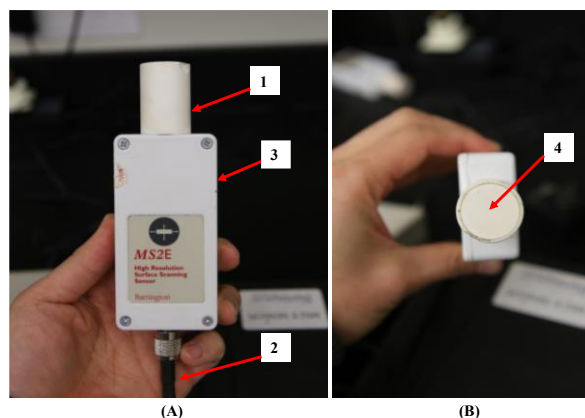


Fig. 1. MS2E probe sensor for surface magnetic susceptibility measurements on slabbed core. **(A)** side view showing: **1** is the probe tip with a ceramic guard and a sensor located at the end of the tube, **2** is the cable connected to the MS2 meter, **3** is a metal enclosure that houses the electronic circuitry, and **(B)** top view **4** shows the cross section of the probe sensor tip that is gently applied to the surface of the slabbed cores.

Following the methodology in Potter et al [4] and Potter [5] each magnetic susceptibility value can be converted to an estimate of mineral content in simple model systems. Assuming that a rock sample is a two-component system of diamagnetic quartz and paramagnetic illite clay and that the contribution of fluids in the pore space in the sample is negligible (most reservoir fluids are diamagnetic [6] and will have little effect on the results), the proportion of each mineral component can then be estimated. The total measured magnetic susceptibility signal per unit volume is:

$$k_T = \{F_I (k_I)\} + \{(1-F_I) (k_Q)\} \quad (3)$$

where k_T is the total susceptibility value measured by the probe magnetic technique, F_I is the illite fraction per unit volume, $(1-F_I)$ is the quartz fraction per unit volume, and k_I and k_Q are the volume magnetic susceptibilities of illite (41×10^5 SI) and quartz (-1.64×10^5 SI), respectively. The illite fraction is then calculated as:

$$F_I = (k_T - k_Q) / (k_I - k_Q) \quad (4)$$

Note that from **Equation (4)** an illite content of around 4% or higher by volume in an illite + quartz mixture means that the net magnetic susceptibility signal of the sample is positive, whilst lower values mean the net signal is negative. Furthermore there are two key advantages of converting the raw magnetic susceptibility signal into a mineral content as follows:

- The mineral contents can be plotted on logarithmic graphs (as long as the values are not zero), whereas raw negative magnetic susceptibility values cannot. This becomes important when correlating the magnetically derived illite content with other parameters such as fluid permeability.
- Any values greater than 100% illite content using **Equation (4)** immediately indicate the presence of a mineral or minerals with higher positive magnetic susceptibility than illite.

2.2 X-ray fluorescence (XRF)

In an XRF measurement, two types of X-rays, Bremsstrahlung X-rays and characteristic X-rays, are involved. Bremsstrahlung X-rays are a continuous high energy spectrum generated by the X-ray source. These Bremsstrahlung X-rays eject electrons from the inner shells of atoms. Then, the vacancies left by the ejected electrons are quickly filled by other electrons dropping down from the outer shells as the atoms attempt to regain stability. During this latter process characteristic X-rays are emitted and received by the analyzer, and their precise energies are associated with the difference between the energy levels of the outer and inner electron shells of the atom. Since the distance between electron shells is different for each element, the energy level of each electron shell and the difference in energy between the shells are also different for each element. The emission of characteristic X-rays is the foundation of an X-ray fluorescence analysis.

In this study elemental contents in the slabbed cores of the oil sands well were quantified by the application of a portable XRF analyzer, the Thermo Scientific Niton XL3t [7], supplied by Elemental Control Limited (Toronto). The analyzer is designed to work either in a laboratory or as a field operation device. The analyzer can be positioned in a customized stand for accurate portable, non-destructive measurements in the laboratory or used as a handheld device in the field. The analyzer contains an X-ray tube that emits radiation only when the shutter is opened, and a detector to detect the characteristic X-rays of the elements in a sample. The radiation of the Bremsstrahlung X-rays is produced by the analyzer and emitted through the measurement window, and the radiation of the characteristic X-rays, which is generated by ejected electrons, also reaches the detector through the window. Therefore, during a measurement the sample should always be in contact with the window.

For sedimentary rock samples, as in this study, the analyzer was used in “Mining Cu/Zn mode” as recommended in the manual [7]. It was calibrated with a reference sample with known values for Fe and K. The instrument operates with four different filters in order to obtain accurate results for a wide range of elements. Each measurement takes a total of 3 minutes, with 45 seconds for each filter beam. In the laboratory, the cores are usually measured in the form of pressed powder, or are cut into small pieces for use with suitable portable stands. However, to measure the slabbed cores in the present study, the device needed to be kept in contact with the surface of the cores during the measurements. The measurement time was too long for one to hold the device by hand during the operation, so we fabricated a customized stand to ensure the accuracy of the results (**Figure 2**). The stand was simply comprised of two legs and a bridge that allowed the height of the analyzer to be suitably adjusted in relation to the surface of the slabbed cores. With the support of the stand, the analyzer was always stable, and therefore the measuring window was always in contact with the surface of the slabbed cores during the measurements. Each XRF measurement

analyzes a small area of 3 mm in diameter on the slabbed core, and a depth of penetration up to a few millimetres (very similar to the magnetic susceptibility probe). The XRF readings were taken in the middle of each corresponding area previously analysed by the magnetic susceptibility probe. The analyzer was connected to a PC with an application that allowed one to control the XRF measurement from a safe distance. This helped to minimize the dose of radiation received by the operator during the measurements.

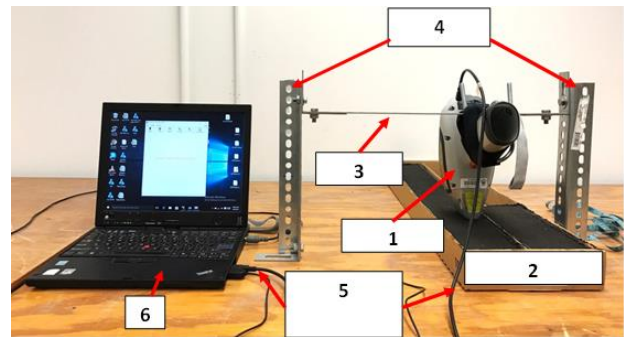


Fig. 2. The set-up for XRF measurements on the oil sands slabbed cores. **1** is the XRF analyzer, **2** is the slabbed core, **3** is the stand, **4** shows the bridge of the stand, **5** is the cable connecting the analyzer and the computer, and **6** is the laptop computer with an application to control the XRF analyzer from a distance.

3 Results and discussion

3.1 Probe magnetic susceptibility on slabbed oil sands core: example illustrating a key advantage of this technique

Figure 3 shows the probe volume magnetic susceptibility profile for a short oil sands slabbed core section saturated with bitumen in the well. Since quartz sand is diamagnetic and bitumen is also expected to be diamagnetic then it's not surprising that all the data points in this example exhibit negative magnetic susceptibility. The probe results show real quantitative variations greater than the measurement uncertainties shown. A major advantage of the quantitative probe magnetic measurements is that they reveal variations that one cannot see from mere visual observations, since the black bitumen obscures any small differences in the mineralogy.

There are a number of possible reasons for the variations in magnetic susceptibility in **Figure 3**. The most likely explanation is due to the presence of small amounts of paramagnetic clay mixed with the sand. Another possibility is the presence of a very small amount of ferrimagnetic particles (such as magnetite). A further possible reason could be slight variations in the porosity and the bitumen saturation within the pore space. The MS2E sensor probe volume magnetic susceptibility measurements are susceptible to variations in porosity (though the effect is likely to be very small).

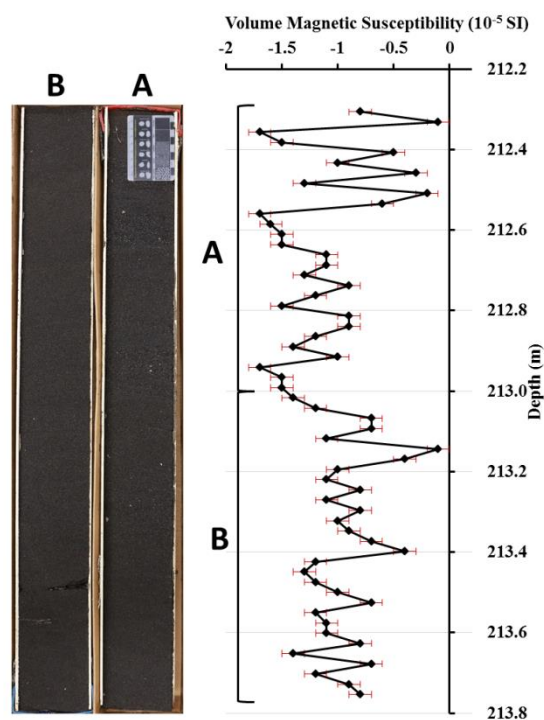


Fig. 3. Typical results of the MS2E probe volume magnetic susceptibilities measured on a short 1.6 m section of oil sands slabbed core saturated with black bitumen in the well. The magnetic probe is able to identify quantitative variations in the core that are extremely difficult to determine from mere visual observations. Uncertainty bars are shown.

3.2 Comparison of probe magnetic results with downhole log data

Figure 4 shows the depth profiles of probe volume magnetic susceptibility on the slabbed core, downhole total gamma ray (GR), and spectral downhole GR in a 68 m interval. **Figure 4** (left hand plot) clearly shows how the probe volume magnetic susceptibility measurements (far left curve) can differentiate the 3 main lithology types in this well. At the top of the profile (depths 149.4–159.1 m) the magnetic susceptibility values are highest and positive, indicating shale. In the middle of the profile (depths 161.7–183.0 m) the magnetic susceptibility values are generally positive and relatively low, which generally means some clay mixed with sand in these oils sands wells, and in this case represents the inclined heterolithic stratification (IHS) beds. At the bottom of the profile (depths 184.9–216.4 m) the magnetic susceptibility is generally negative, indicating clean sand (diamagnetic quartz), which is the best oil sands reservoir interval.

The total GR curve (right hand curve in the left hand plot of **Figure 4**) generally follows the trend of the magnetic susceptibility profile (high GR in the shale, lower GR in the clean sand), however the GR does not distinguish the different lithologies quite as well as the magnetic susceptibility. For example, between depths 162–168 m the total GR signal decreases, suggesting that this may be a clean sand interval. However, the positive magnetic susceptibility values suggest this is actually

part of the interbedded clay and sand IHS beds. The spectral gamma ray signals (right hand plot of **Figure 4**) indicate that the total gamma ray signal is influenced by the thorium content, which drops significantly in the 162–168 m interval. It is not clear at present why the thorium content is lower in this interval. Several lines of evidence support the interpretation of IHS beds from the magnetic susceptibility:

(i) The magnetically derived illite content (far left curve of the left plot in **Figure 5**) shows values of 3–15% in this interval, which is more consistent with the IHS beds. Moreover, the spectral potassium gamma ray (**Figure 4**) follows the trend of the magnetically derived illite content (**Figure 5**). Potassium is a component of illite, and the spectral potassium curve shows no significant decrease in the interval 162–168 m, consistent with this interval being part of the IHS beds.

(ii) The grain size profile (right hand plot of **Figure 5**) clearly illustrates the three main lithologies (shale, IHS beds with interbedded clay and sand, and coarser grained clean sand), which correspond to those in the magnetic susceptibility (**Figure 4**) or magnetically derived illite (**Figure 5**) profiles. In particular, the grain size profile clearly shows the IHS beds extending from 161.7 to 182.2 m and containing a number of thin layers of very fine sands interbedded with thin layers of clay, and not clean sand in the interval 162–168 m as suggested by the total GR.

(iii) The deflection of the spontaneous potential (SP) curve in this interval (right hand curve of the left plot of **Figure 5**) is not larger than in the rest of the IHS bed interval, again supporting the interpretation from the magnetic susceptibility that the 162–168 m interval is part of the IHS beds with higher clay content and lower permeability than the clean sands below depth 184.9 m.

The total GR curve in **Figure 4** is also very variable and quite high in parts of the “clean sand” interval. The magnetic susceptibility is very low (mainly negative values due to diamagnetic quartz) and so picks out the clean sand much more clearly. If one used the total GR log data alone it would be much more difficult to be sure this was a large clean sand interval and one might misinterpret part of this interval as interbedded clay and sand.

The magnetic results clearly pick out a thin bed of an anomalous mineral or minerals with a high magnetic susceptibility (**Figure 4**) corresponding to a magnetically derived illite content greater than 100% (from the simple quartz + illite mixture model of **Equation (4)**) at a depth of about 158 m (**Figure 5**). The total GR, spectral GR and SP curves don’t pick out this thin bed as clearly as the magnetic data does, even though the magnetic data is averaged over the same vertical interval as each wireline log data point averages.

Comparisons between the magnetically derived illite contents and the SP log (**Figure 5**) show correspondences in the two profiles with depth. In particular, one of the lowest illite contents occurs at exactly the same depth (in the clean sand) as the largest deflection of the SP log to the left, both curves suggesting a permeable zone at this depth.

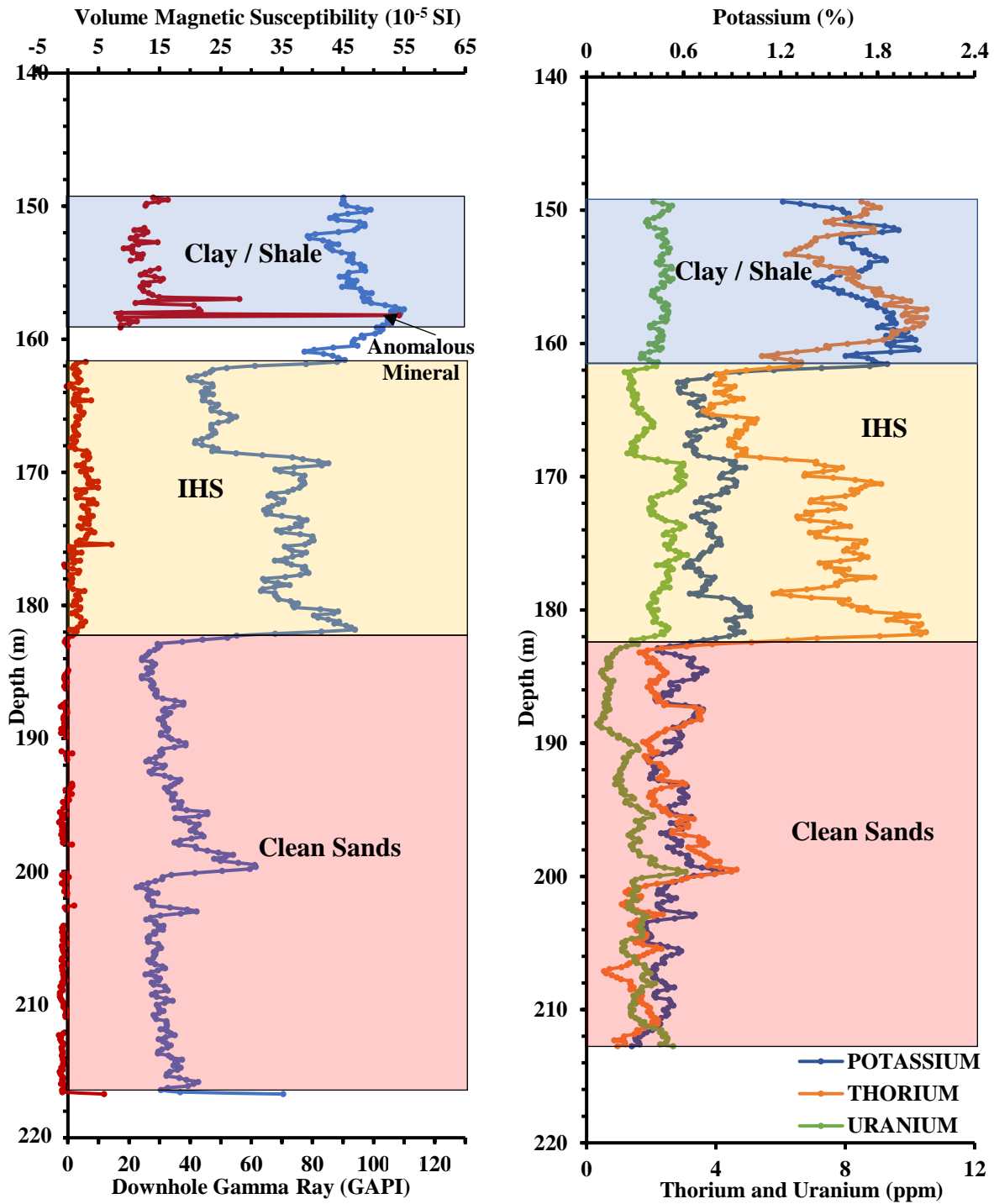


Fig. 4. Comparisons between the magnetic susceptibility results and the downhole gamma ray logs. **Left:** comparison of the vertically averaged, every 0.3048 m (1 ft), probe volume magnetic susceptibility (far left curve) and the total gamma ray log (right curve). **Right:** the spectral gamma ray logs of potassium, thorium and uranium.

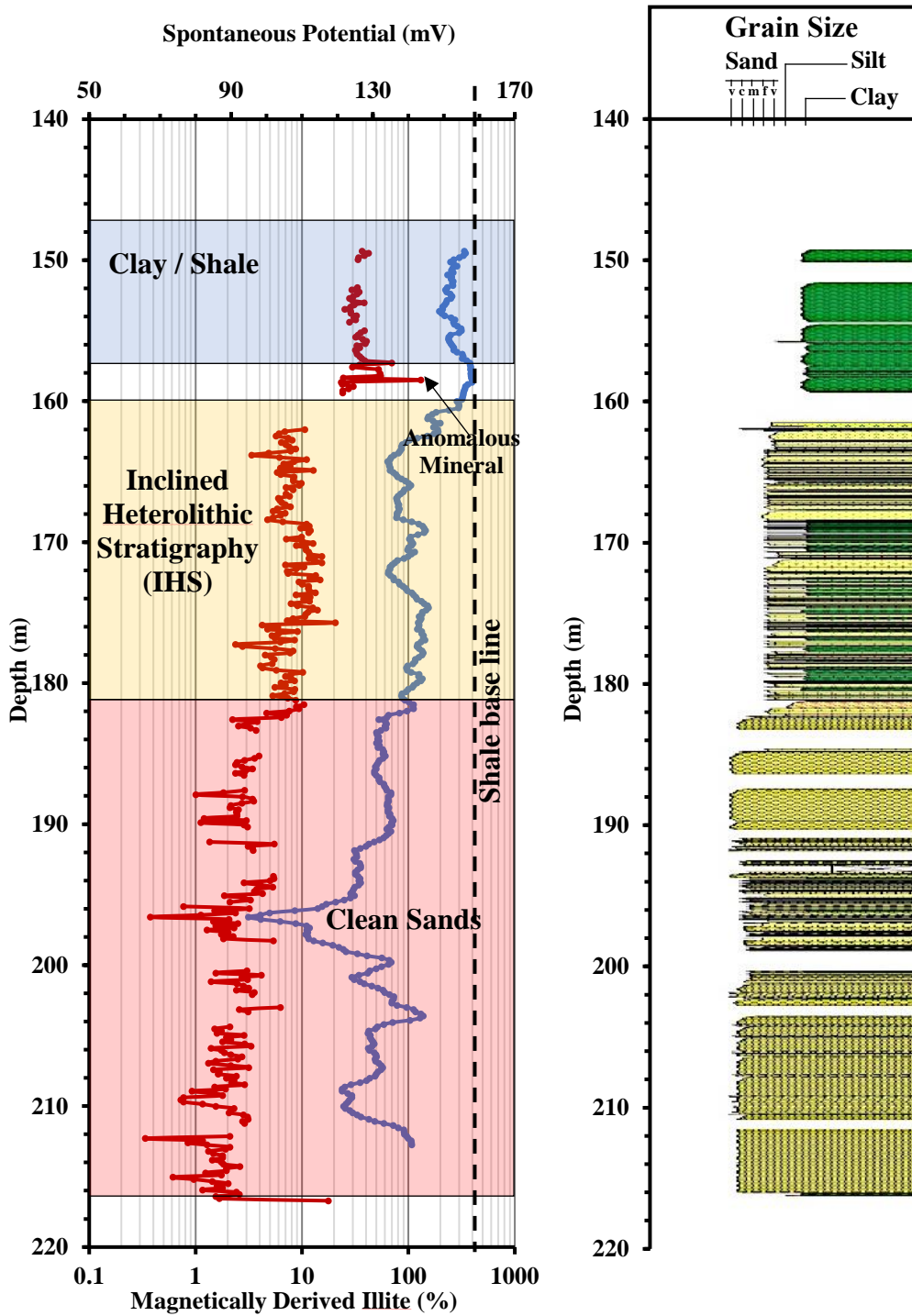


Fig. 5. Left: comparison of the vertically averaged, every 0.3048 m (1 ft), magnetically derived illite contents by volume (far left curve) and the SP log (right curve). Right: the grain size profile, which was determined from the slabbed core manually and displayed using Applecore™ software.

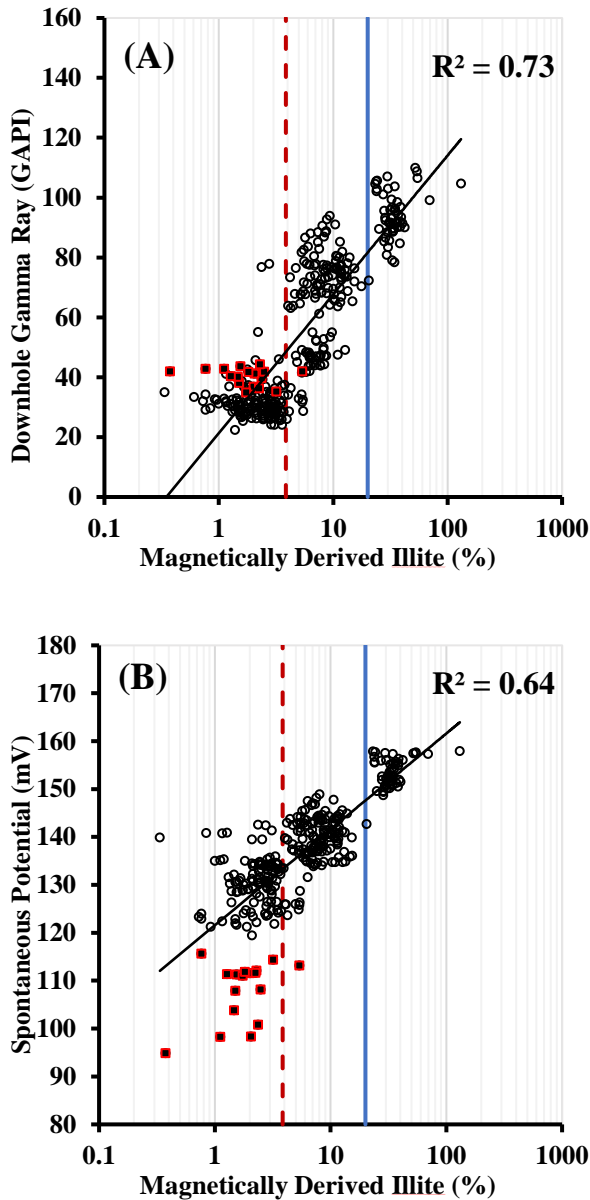


Fig. 6. Crossplots of the vertically averaged, every 0.3048 m (1 ft), magnetically derived illite contents by volume and the (A) total gamma ray log data, and (B) spontaneous potential log data. The dashed vertical line represents 3.85% illite, whilst the solid vertical line represents 20% illite.

3.2 Correlations between magnetically derived illite content, downhole log data and permeability

Figure 6 shows crossplots of magnetically derived illite contents using Equation (4) and the total GR and SP log data, with correlation coefficients of $R^2 = 0.73$ and 0.64 . The coefficients increase to 0.75 and 0.69 if one omits the square data points, which correspond to the largest deflection of the SP curve to the left (lowest SP values), and some of the lowest illite contents. Figure 6 shows that the crossplots have 3 clusters relating to the clean sand, the IHS beds, and the clay/shale. The dashed vertical line at 3.85% and solid line at 20% differentiate the 3 clusters. In general the clean sand is below 3.85%

illite, the IHS beds between 3.85 and 20% illite, and the clay/shale greater than 20% illite.

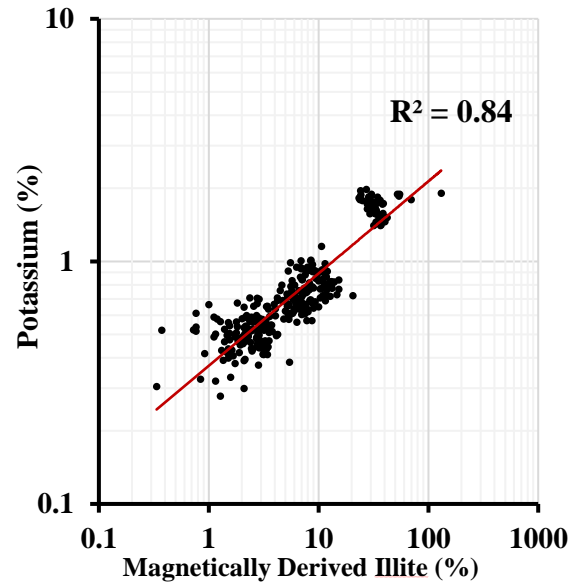


Fig. 7. Crossplot of the vertically averaged, every 0.3048 m (1 ft), magnetically derived illite contents by volume with the spectral potassium downhole gamma ray log data.

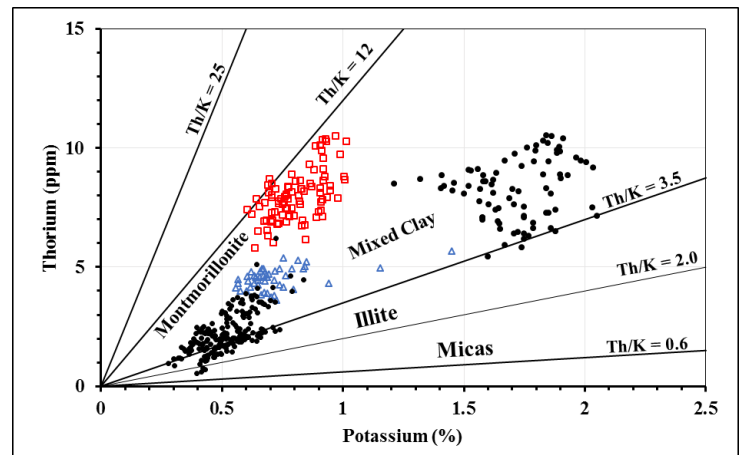


Fig. 8. Spectral gamma ray potassium versus thorium crossplot for this well (plotted on a standard Schlumberger chart CP-19). Upper right solid symbol cluster (19.7% of data points) is shale, and lower left solid symbol cluster (48.2%) is relatively “clean” sand. Open triangle cluster (10.8%) is IHS beds in the interval 161.7-168.4 m. Open square cluster (21.3%) is IHS beds in the interval 168.4-182.2 m.

Figure 7 shows a crossplot of the magnetically derived illite contents against the spectral potassium gamma ray log data. The high regression coefficient $R^2 = 0.80$ is consistent with illite being a key clay mineral in these oil sands. Our simple 2 component quartz + illite model from Equations (3) and (4) assumes that the “illite” includes mixed paramagnetic clays and micas, since “illite” is the only positive magnetic susceptibility component in the equations. Our “illite” content is effectively a catch all “magnetically equivalent illite” parameter and is useful because it correlates with several other key parameters as we show in this paper. The other

mixed clays in general have a range of magnetic susceptibility values quite close to that of illite. The spectral GR log data in **Figure 8** shows that virtually all the data points are within the illite, mixed clay and mica regions. Note that the data in **Figure 8** needs to be treated with some caution, however, since the points can be affected by other minerals present in the samples (e.g., small amounts of gamma ray emitting heavy minerals can shift the points to higher potassium and thorium contents).

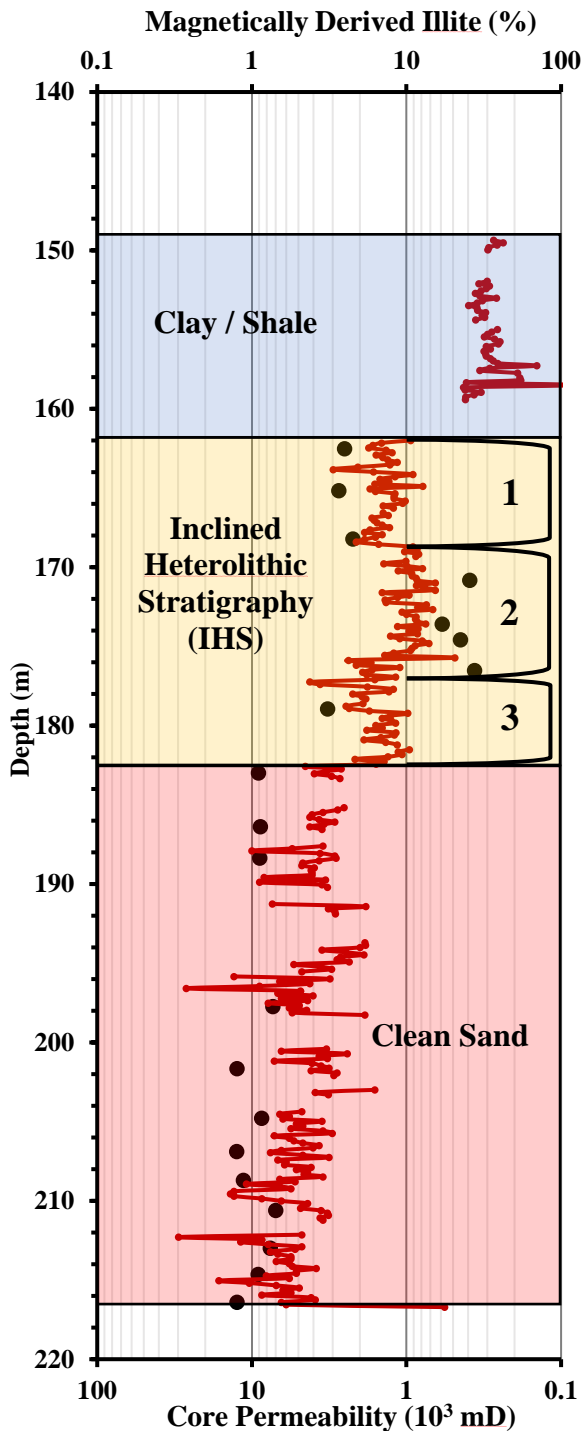


Fig. 9. Profiles with depth comparing the core permeability values (black circles) with the depth-matched magnetically derived illite contents by volume (curve).

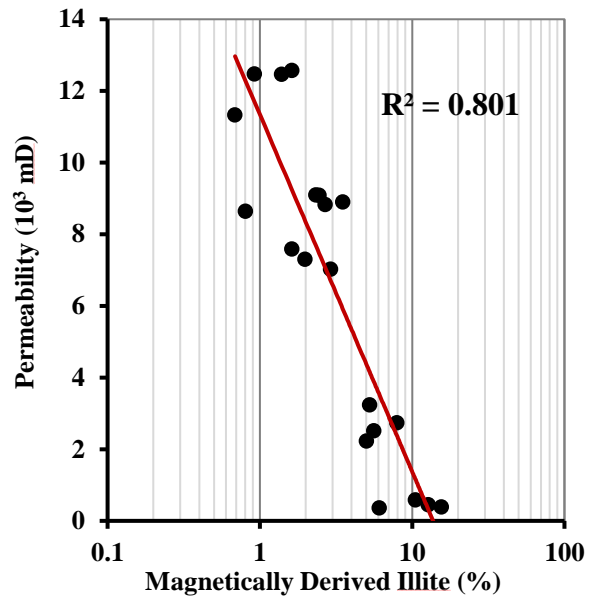


Fig. 10. Crossplot between the core permeability values and the depth-matched magnetically derived illite contents by volume.

Around 20 core air permeability measurements were available between the depths of 162–216 m. **Figure 9** shows the comparisons between the core permeability values and the magnetically derived illite contents with depth. The core permeability results correlate very well with the trend of magnetically derived illite content, but to a lesser extent with the SP curve (**Figure 5**). In the clean sand interval (185–216 m), the high permeability values (from 7.0×10^3 mD to 12.5×10^3 mD) correlate with low illite contents (generally less than 4%) and larger deflections to the left of the SP curve. In the IHS beds (161.7–183 m) the lower permeability values (from 0.4×10^3 mD to 3.2×10^3 mD) correlate with higher illite contents and less of a deflection to the left of the SP curve. However, the magnetically derived illite contents appear to correlate with the core permeability values better than the SP log in these IHS beds. Interval 2 in the IHS beds (**Figure 9**) has the lowest core permeability values which correlate with higher magnetically derived illite contents, while higher core permeabilities in intervals 1 and 3 (**Figure 9**) correlate with lower magnetically derived illite contents. In contrast, the variation of the SP log (**Figure 5**) does not clearly show the differences in permeability between these intervals.

Figure 10 shows a crossplot of the measured core permeability data with the depth-matched magnetically derived illite contents. The plot clearly indicates a strong relationship ($R^2 = 0.801$) between the core permeabilities and the magnetically estimated illite contents. A crossplot between the core permeability and the corresponding depth-matched SP log data (not shown) gives a much lower correlation ($R^2 = 0.42$), supporting our suggestion above that the trend of the magnetically derived illite contents better matches the trend of the core permeability values.

3.3 Correlations between magnetically derived illite contents and elemental contents from X-ray fluorescence

The crossplots of **Figures 11, 12 and 13** clearly show increasing Fe, Al, and K contents with higher magnetically derived illite contents, consistent with these elements being components of illite. The R^2 regression coefficient is 0.62 between the magnetically derived illite contents and both Fe and Al elemental contents, but a bit lower at 0.45 between the magnetic results and K content. In contrast, a crossplot (not shown) between magnetically derived illite contents and Ca contents showed no correlation ($R^2 = 0.03$) as expected as there were virtually no carbonates in the interval studied.

The crossplots also show clusters of data points which represent different lithologies. The clay / shale region is distinguished from the other lithologies with generally more than 20% magnetically derived illite content by volume and 2-7%, 1-2%, and 3-7% of Fe, K and Al respectively. In these crossplots the clean sand and IHS bed data tends to merge into one large cluster, although in general the clean sand has <4% magnetically derived illite content and <0.5%, <1% (most <0.6%) and <1% of Fe, K and Al respectively, whereas the IHS beds generally have around 4-20% magnetically derived illite content and 0.1-1% (mainly above 0.2%) Fe, 0.2-1% K and 0.5-3% Al.

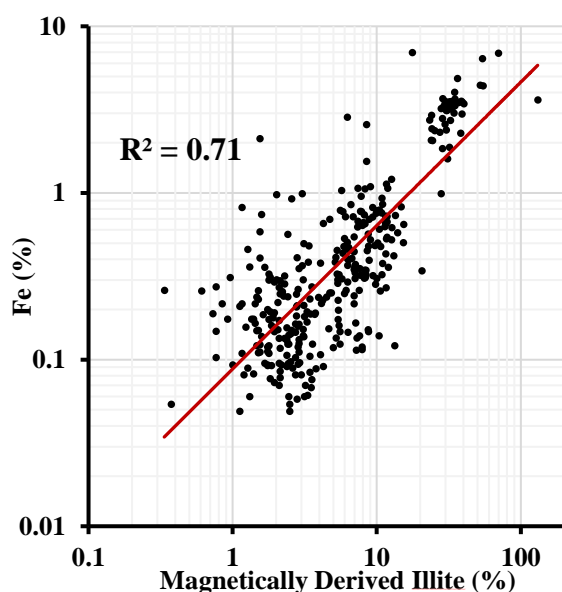


Fig. 11. Crossplot of the magnetically derived illite contents by volume against the Fe contents measured by the XRF technique on the slabbed cores.

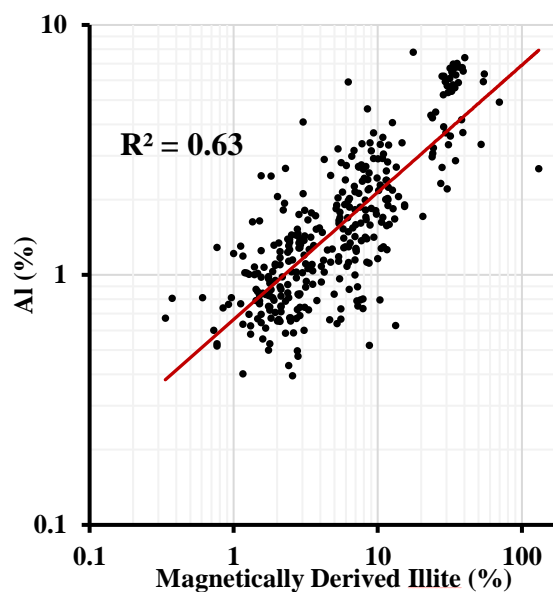


Fig. 12. Crossplot of the magnetically derived illite contents by volume against the Al contents measured by the XRF technique on the slabbed cores.

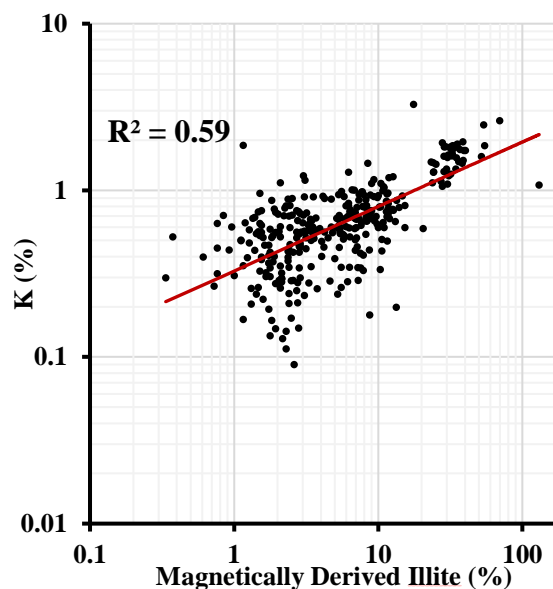


Fig.13. Crossplot of the magnetically derived illite contents by volume against the K contents measured by the XRF technique on the slabbed cores.

The profiles with depth of the elemental contents from the XRF measurements for Fe and K (**Figure 14**) and Al (**Figure 15**) show correspondences with the magnetic susceptibility (**Figure 4**) and the magnetically derived illite contents (**Figure 5** and the right hand curve in the right plot of **Figure 14**). This is consistent with these 3 elements all being components of illite. All 3 elements significantly increase in the more clay rich shale interval at the top of the section.

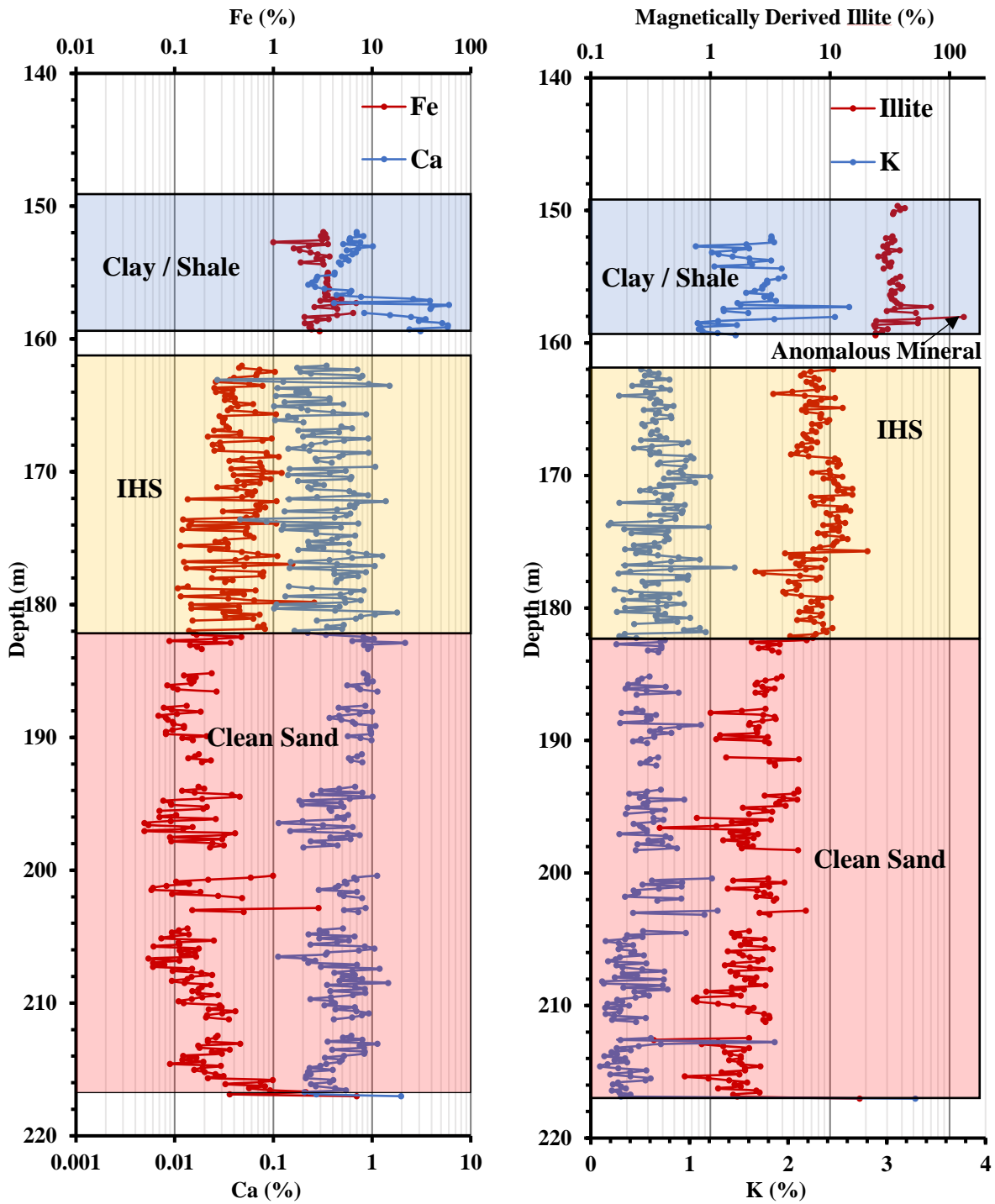


Fig. 14. X-ray fluorescence profiles with depth on the slabbed cores. **Left:** shows the iron (Fe) elemental contents from XRF (left curve), and the calcium (Ca) elemental contents from XRF (right curve). **Right:** shows the potassium (K) elemental contents from XRF (left curve) and for comparison the magnetically derived illite contents by volume (right curve).

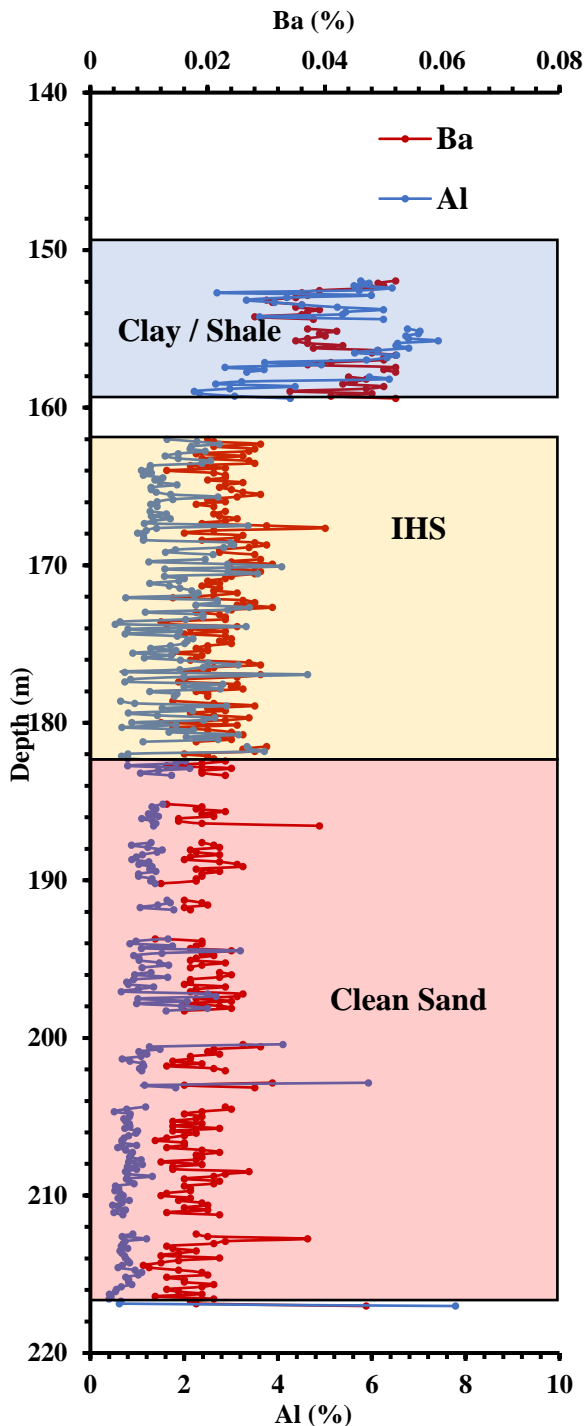


Fig. 15. X-ray fluorescence profiles with depth for the aluminium (Al) (left curve) and barium (Ba) elemental contents (right curve). Al is a component of illite, and Ba can be used to identify naturally cemented barite zones and/or drilling mud invasion.

3.4 Test for small remanence carrying particles

Reservoir samples often contain small particles of remanence carrying minerals [8, 9], such as the ferrimagnetic iron oxide magnetite, Fe_3O_4 , or the canted antiferromagnetic mineral hematite, $\alpha\text{-Fe}_2\text{O}_3$. These minerals have high magnetic susceptibility compared to paramagnetic clay minerals, and thus a small amount of

them can sometimes affect the total susceptibility signal and cause an overestimate of the paramagnetic illite clay content if they are not accounted for. The presence of these remanence carrying particles can be identified from magnetic hysteresis curves by exhibiting loops or kinks at low fields [8, 9]. However, a quicker and simpler method to test for the presence of these particles is to see whether they acquire a magnetic remanence when subjected to a magnetic field. Acquisition of isothermal remanent magnetization (IRM) provides an ideal technique [10], since it is rapid, and produces the largest signal of any magnetic remanence method. A relatively high clay content IHS bed sample was subjected to stepwise direct field (DF) treatment in a Molspin pulse magnetizer. The sample acquired a small IRM, and the shape of the acquisition curve (which was close to saturation at an applied field of 130 mT) indicated that the remanence carrying particles were very likely magnetite. The acquisition curve was similar to 4.4-7.6 μm particle size magnetite [11] and represented an extremely small percentage of the total mass of the sample (0.0007 %). The magnetically derived illite content for this sample is 32.97% if one ignores the effect of this small amount of magnetite, and 30.67% illite if one corrects for the effect of the magnetite. Therefore the magnetite does not have a major effect on the illite determinations for this sample.

4 Conclusions

The following overall conclusions can be drawn:

1. Low field probe volume magnetic susceptibility profiles, which can be generated rapidly and non-destructively on this unconsolidated slabbed core, could clearly distinguish the 3 main lithologies in this oil sands well. Negative and close to zero volume magnetic susceptibility values indicated clean sand intervals, small positive values (generally up to about 5×10^{-5} SI) corresponded to inclined heterolithic stratification (IHS) beds or muddy sands, and higher positive values (generally greater than 10×10^{-5} SI) corresponded to shale. Whilst there were general correspondences between the magnetic results and the downhole log data for total gamma ray (GR) and spontaneous potential (SP), the magnetic results were better at distinguishing the 3 main lithologies.
2. The probe magnetic technique was particularly useful for distinguishing different lithologies, and quantifying variations in mineralogy, in this bitumen saturated core. This is a major advantage of the probe magnetic technique in oil sands core. Visual observations alone are often not able to distinguish the different lithologies or quantify the variations in mineralogy, since the black reservoir hydrocarbons obscure the visual details.
3. The raw probe magnetic susceptibility results were processed using a simple model mineral mixture of quartz + illite to derive illite contents. The

magnetically derived illite content was a useful parameter that distinguished the main lithologies, and exhibited good correlations with the following:

(i) *Total downhole gamma ray (GR) and spectral potassium gamma ray log data.*

(ii) *Downhole spontaneous potential (SP).* Permeable zones were indicated by low values of magnetically derived illite and large deflections to the left by the SP tool. However, the magnitude and direction of the deflection of the SP log depends on the difference in salinity between the formation water and drilling mud filtrate and would not show a deflection at a permeable zone if the salinities of the two fluids are equal. In contrast, the magnetic technique has the advantage that it can potentially identify a permeable zone in this situation regardless of whether the two salinities are equal or not.

(iii) *Fluid permeability.* A strong correlation was observed between the magnetically derived illite contents and core permeability values. The results were significantly better than the correlation between the core permeability and the SP log data.

(iv) *X-ray fluorescence (XRF).* Strong correlations between the magnetically derived illite contents and elemental contents of Fe, K and Al (all components of illite) supported the suggestion that illite was a major paramagnetic clay in the well.

4. The magnetically derived illite contents enabled one to identify thin layers of anomalous minerals, where “illite” contents were greater than 100% from the simple model. The total GR, spectral GR and SP logs did not generally identify these thin layers of anomalous minerals. The raw high resolution magnetic results were averaged over the same vertical interval as each wireline log data point averages, and therefore anomalous mineral identification from magnetic susceptibility was not merely due to resolution differences between the laboratory magnetic probe and the wireline tools.
5. Crossplots of magnetically derived illite content against XRF (elemental contents of Fe, K and Al) identified 3 clusters of points representing the 3 main lithologies (clean sand, IHS beds and shale), thus showing the potential of the combination of magnetic susceptibility and XRF measurements in the laboratory.

Cenovus FCCL Ltd are thanked for access to the slabbed core, downhole log and core permeability data, and a research grant to D. K. P. Matthias Halisch and Stefano Pruno are thanked for their thorough and constructive reviews of the manuscript.

5 List of abbreviations

DF	Direct Field
GR	Gamma Ray
IHS	Inclined Heterolithic Stratification
IRM	Isothermal Remanent Magnetization
SP	Spontaneous Potential
XRF	X-Ray Fluorescence

6 References

1. B. C. Agbo and D. K. Potter. Novel high resolution probe magnetic susceptibility and comparison with wireline gamma ray and grain size in an Albertan oil sand well. *Society of Exploration Geophysicists (SEG) Technical Program Expanded Abstracts 2014*: pp. 2590-2594. DOI: 10.1190/segam2014-1140.1 (2014).
2. T. H. To, D. K. Potter, A. Abiola, and V. T. Ebufegha. Probe magnetics as a rapid, non-destructive screening tool for consolidated and unconsolidated core in conventional and unconventional reservoirs. *Proceedings of the 2018 International Symposium of the Society of Core Analysts, 27-30 August 2018, Trondheim, Norway. Paper SCA 2018-057* (2018).
3. M. J. Ranger and M. K. Gingras, M. K. Geology of the Athabasca oil sands – field guide and overview. *Canadian Society of Petroleum Geologists*, Calgary, pp. 123 (2003).
4. D. K. Potter, P. W. M. Corbett, S. A. Barclay and R. S. Haszeldine, R. S. Quantification of illite content in sedimentary rocks using magnetic susceptibility—a rapid complement or alternative to X-ray diffraction. *Journal of Sedimentary Research, Research Methods Papers Section*, **74** (no. 5), 730-735 (2004).
5. D. K. Potter. Magnetic susceptibility as a rapid, non-destructive technique for improved petrophysical parameter prediction. *Petrophysics*, **48** issue 3), 191-201 (2007).
6. O. P. Ivakhnenko and D. K. Potter. Magnetic susceptibility of petroleum reservoir fluids. *Physics and Chemistry of the Earth*, **29**, 899-907 (2004).
7. B. Backman, K. Lindqvist, K. and E. Hyvönen. Manual for measuring soil samples with the Niton XL3 GOLDD+ XRF-instrument. *Geologian Tutkimuskeskus*, pp. 14 (2016).
8. O. P. Ivakhnenko and D. K. Potter. The use of magnetic hysteresis and remanence measurements for rapidly and non-destructively characterizing reservoir rocks and fluids. *Petrophysics*, **49**, (issue 1), 47-56 (2008).
9. A. Ali and D. K. Potter. Temperature dependence of the magnetic properties of reservoir rocks and minerals and implications for in situ borehole predictions of petrophysical parameters. *Geophysics*, **77** (no.3), 211-221 (2012).
10. D. Heslop, M. J. Dekkers, P. P. Kruiver and I. H. M. van Oorschot. Analysis of isothermal remanent magnetization acquisition curves using the expectation-maximization algorithm. *Geophysical Journal International*, **148** (1), 58-64 (2002).
11. D. K. Potter and A. Stephenson. Field-impressed anisotropies of magnetic susceptibility and remanence in minerals. *Journal of Geophysical Research - Solid Earth*, **95**, 15573-15588 (1990).

Developed emulsification in porous media flow

Ahmad Kharrat¹, Bianca Brandstätter¹, Mostafa Borji¹, Gerhard Fritz-Popovski², Oskar Paris², and Holger Ott^{1,*}

¹ Department Petroleum Engineering, Montanuniversität Leoben, 8700 Leoben, Austria.

² Institut für Physik, Montanuniversität Leoben, 8700 Leoben, Austria.

Abstract. With the use of surfactants, the interfacial tension between oil and water can be lowered to a degree that solubilisation of oil by the injection water leads to a near-miscible displacement. The resulting type of emulsion, however, depends on the way how the two phases contact each other and ultimately on the mixing, respectively flow regime. While mixing can be turbulent in classic test tube experiments, under laminar flow conditions in porous media the miscibility can develop slowly over time, depending on the dispersion mechanisms that facilitate the contact between the phases. The present study investigates this developed miscibility during surfactant flooding. We perform microfluidic experiments with generic oil and surfactant solutions in a wide salt concentration range across optimum displacement conditions. The study shows that in addition to a classic immiscible displacement, oil is increasingly solubilized and transported in a phase with a foam-like texture that develops from a drop-traffic flow. The extend and the stability of those phases depends on the salinity and hence of the efficiency of the surfactant solution.

1 Introduction

Oil and water are usually immiscible. Almost miscible conditions can, however, be facilitated by the addition of surface-active components - surfactants - which can settle on the oil-water interfaces and reduce the interfacial tension between the two liquids [1]. In this way, stable emulsion phases can form. In different scientific areas emulsions, their formation and stability play a decisive role and are investigated [2] [3] [4] [5]. Although our understanding of emulsion formation has improved, important connections are still missing, especially the connection of emulsification under various mixing or flow conditions.

In recent years, pore scale studies on mixing behavior and emulsification appeared [6] [7] [8] [9]. The in-situ formation of microemulsions from generic fluid systems was investigated in T-junctions by variation of the salt content of the aqueous phase [10]. The work was continued by examining emulsification in dead-end pores. It has been found that phase behavior alone is insufficient to predict emulsification under dynamic conditions, and that the flow rate controls emulsification [11]. The influence of the exact pore space geometry was investigated using three different microfluidic pore patterns [12]. The work was repeated, but using a radial flow geometry while focusing on the displacement stability based on the microemulsion type and particle size, which significantly impact the displacement efficiency [13]. The results show that the observed flow regimes follow the equilibrium phase behavior, i.e. that dimensionless scaling parameters based on equilibrium emulsion properties explain the observed displacement patterns.

Generally, emulsion phases can be classified by their particle sizes into macro (loose) and micro (tight) emulsions, which differ by the latter being thermodynamically stable.

Another classification scheme was introduced by Winsor defining three emulsion types: Type I – oil-in-water emulsion, Type II – water-in-oil emulsion, and a Type III [14]. Type III forms a third phase at the interface between oil and water, characterized as microemulsion. Type III is considered as the optimum condition in displacement physics. Especially the optimum has been intensively investigated in the oil and gas industry with regards to enhanced oil recovery (EOR) [15] [16] [17].

However, the situations may be different if surfactants are generated in-situ, like in alkaline flooding. Due to the wide variety of acidic crude-oil components, in-situ saponification of crude by alkaline solutions may lead to surfactants with a wide variety of molecular properties, predominantly characterized by the wide size and property distribution of their lipophilic tails. In such situations, the variation of brine salinity may not lead to clear optimum conditions since molecular properties are too different to match with a global tuning parameter. However, displacements outside the optimum can lead to the formation of complex fluid textures on a pore scale leading to complex displacements [9].

In order to understand displacements outside the optimum, we study a generic oil-water-surfactant system in the over- and under-optimum by tuning injection water salinity in a wide concentration range across the optimum condition. Sub-optimal conditions can also be of interest for surfactant flooding, since salinity variations due to dispersive effects in porous-media flow, likely lead to salinity variations – the system may be locally outside the optimum. In this context, we investigate the spatial and temporal development of emulsion phases in microfluidics by means of optical and quantitative-fluorescence microscopy. We observe the actual mechanisms of oil mobilization and displacement with a particular interest in the question of the comparability of emulsification in classic ex-situ experiments and under flow conditions in porous media.

* Corresponding author: holger.ott@unileoben.ac.at

2 Materials and Methods

2.1. Microfluidic chip – the porous medium

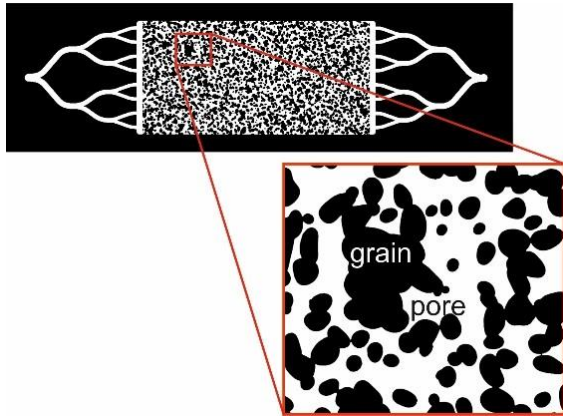


Figure 1 : 2D pore structure etched in glass microfluidic chips. The porous domain is $2 \times 1 \text{ cm}^2$ in size and is contacted on the left and right by channel systems for fluid injection and production resulting in a linear flow geometry.

Experiments were performed with microfluidic chips made from borosilicate glass, representing a 2D porous media. The pattern is characterized by a homogeneous etching depth of $20 \mu\text{m}$ and a lateral definition of pores and pore throats. Porosity and permeability have been determined to $\phi = 0.57$ and $K = 2.5 D$ and total pore volume to $2.3 \mu\text{l}$. The total porous domain is $2 \text{ cm} \times 1 \text{ cm}$ with channel systems at the inlet and outlet for a proper fluid distribution and fluid collection as displayed in Figure 1. The lateral porous structure is rather open and homogeneous with all features larger than the etching depth. This microfluidic pattern has been used in earlier studies [9].

2.2 Fluids

Experiments were performed using decane (Sigma Aldrich, 99% purity) as oil phase. The injection water was based on deionized (DI) water with J13131 as surfactant, 2-Butanol as a cosolvent, and sodium chloride in different concentration as tuning parameter. This surfactant cocktail was used in earlier studies as well [12] [13]. The chemicals are given in Table 1. Since both fluids, water and decane are transparent and optically indistinguishable, contrast agents were added to achieve optical and fluorescence contrast between them. For the optical contrast, the colorant Sudan II was added to the oil phase, which resulted in a brownish color. As fluorescence agent, a fluorescence sodium salt was added to the aqueous phases. The influence of the contrast agents on the IFT and phase behaviour was studied; no significant influence was observed for the given concentrations.

Table 1 : Chemicals used in this study.

Chemical	Concentration	Source
J13131	0.5 wt.%	Shell
2-Butanol	2 wt.%	Sigma Aldrich
NaCl	1 to 5 wt.%	Sigma Aldrich
Fluorescent salt	100 mg/l	Sigma Aldrich
Sudan II	10 mg/l	Sigma Aldrich

The combination of the optical and fluorescence microscopy allowed to separate the phases. In the combined data set, it turned out that the Sudan II does not detectably participate in the emulsion phase, which helped to identify specific features in the observed macro structures. At the same time, the fluorescence salt scales nicely with the amount of oil in aqueous phase, even to very high oil content, but did not participate in the pure oil phase. Therefore, both agents deliver complementary information on the fluid-fluid system.

2.3 Instrumentation

Leica DMi8 microscope with fluorescence filter was used to capture high quality and detailed optical and fluorescence images of porous domain and the fluids therein. The images were acquired from the entire domain by an integrated wide-range automated XY table in combination with a stitching software. The images were recorded with a Leica DMC2900 camera and a pixel size of $1.8 \mu\text{m}$. The temporal resolution of the individual image was given by the acquisition time of 1 ms in optical, and 2 ms for fluorescence microscopy. The overall time resolution was limited by the XY scanning to about 30 s, and 150 s, respectively. In some cases, videos were taken for smaller regions of specific interests.

Fluids were injected with a high precision Chemyx Fusion 200 syringe pump. For each fluid type, a separate syringe was used. On the downstream side, a constant pressure boundary condition was realized by producing fluids into a vessel at atmospheric pressure. For preparation purpose, a vacuum pump was installed on the downstream side to evacuate the micromodel and the flow lines, and for pre-saturation.

2.4 Experimental Procedure

The initial state of all experiments was a fully oil saturated porous domain, i.e., $S_{o,i} = 1$. The flooding experiments were performed at stabilized ambient temperature and ambient pressure with a constant flow rate boundary condition at the inlet, and a constant pressure boundary condition at the outlet. In all shown images, the flooding direction is from left to right. Surfactant solutions were injected for about 60 hours, with an injection rate of 0.002 ml/h (corresponding to a Darcy velocity of ($\sim 1 \text{ ft/day}$)), resulting in ~ 50 pore volumes (PV) injected in total. The experiments were stopped at times where no changes in the remaining oil saturation could be detected.

The images were captured in tiles with a small field of view, covering altogether the total domain after stitching.

The small field of view allows for high spatial resolution to observe emulsification and displacement processes on a sub-pore scale.

After each experiment, the chip was flushed with a sequence of 3 ml water and decane to dissolve the remaining salt, surfactant and dye agents in the system. Afterward, 2 ml of acetone was injected to miscible displace the remaining fluids (mainly water), and in the last stage, a vacuum was applied for at least 4 hours to remove the acetone from the system. All the steps were observed by microscope to ensure the quality of the cleaning procedure.

3 Fluid-Fluid Interactions

The fluid-phase behavior was characterized using various standard methods. The tuning parameter for optimizing phase behavior is typically the salinity, in the present case the NaCl concentration, which we vary between 1 and 5 wt.%.

3.1 Test-tube experiments

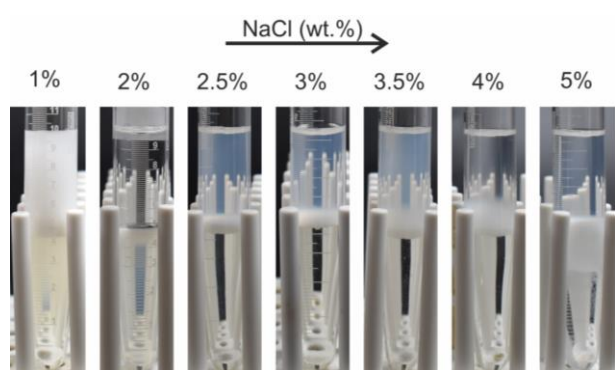


Figure 2: test-tube phase behavior experiments of a decane-surfactant solution system with increasing NaCl concentration.

Oil and surfactant solutions were contacted in glass test tubes with equal volumes of 5 ml of both fluids. To guarantee the quality of the volumes and to minimize the interactions between the fluids prior to the mixing step, we first filled the test tubes with 5 ml of the aqueous from bottom to top and then added 5 ml of oil by using a high-precision syringe pump. The fluids were then mixed by a tube rotator (FisherbrandTM, USA) for 24 hours at 25 rpm. Afterward, the tubes were placed vertically at stabilized ambient temperature to reach its equilibrium gravity-separated phases. Images were taken during and in the final stage of the separation process. The images of the final equilibrium state are shown in Figure 2. The tests were reproduced in repeat experiments.

Since we are interested in displacements outside optimum conditions, the steps in which the NaCl concentration increased are rough and the concentration range is wide. Optimum conditions can be assumed to be in between 2 wt.% and 2.5 wt.% where the upper and lower phase are relatively clear, and the behavior changes from a lower slightly blurred phase to a blurring of the upper phase. The principal behavior has been reproduced with the optical and fluorescence contrast agents in the respective phases.

3.2 Nano structures of emulsion phases

In the phase behavior experiments, milky and transparent phases were observed. A transparent phase may indicate a pure fluids phase. However, microemulsions may be transparent as well, if the particle sizes are smaller than the wave length of light. To further understand the observed phases, some of the phase-behavior experiments were repeated in small-scale tubes (Mark tubes) suitable for small-angle X-ray scattering (SAXS). With SAXS, fluid particle, respectively bubbles of nm size are accessible.

As for the classical phase-behavior experiments discussed above, equal volumes of both phases were dosed in test tubes, the tubes were sealed and mixed by shaking. The mixture was then filled in the mark tubes and sealed. In such small-size tubes, gravity separation is suppressed. As for the classical tests, clear and milky phases are visually observed. In case of 2 wt.% NaCl, a single homogeneous phase is observed as may be expected near the optimum without gravity separation. At all other concentrations, milky and clear phases were observed.

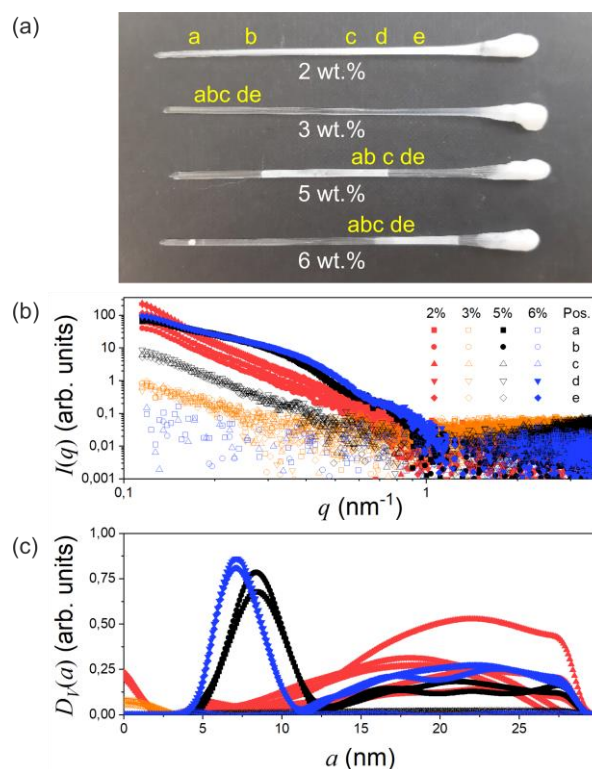


Figure 3 : SAXS measurements to determine micro structures in emulsions. (a) Small-scale test tubes with indicated NaCl concentration and positions at which SAXS measurements were taken. (b) SAXS curves for the concentrations and positions indicated in (a). (c) Size distributions calculated from the scattering curves in (b).

SAXS measurements were performed using a Bruker Horizon-N8 (Bruker-AXS, Germany) equipped with a 1 μ S micro-focus source (INCOATEC, Germany) and a VÅNTEC 500 detector (Bruker-AXS, Germany). Copper K α radiation was used. The samples were moved in an oscillating way along the capillary's axis in order to average a larger sample volume.

Figure 3 shows details of the experiment. The test tubes with the samples and the positions at which measurements were taken are marked in image (a). Scattering curves are shown in panel (b) as function of the wave vector q . Untextured fluids are expected to show a pure q^{-4} behavior while fluid with texture in the sensitivity range up to ~ 30 nm show features like shoulders and deviating slopes in the double logarithmic plot. From these features, a particle size distribution can be calculated. Additionally, pure decane and aqueous solutions have been measured in order to correct for the background in the scattering signal. By background correction, the scattering signal from the emulsion phases can be isolated.

The observations may be split in scattering responses from clear and milky phases; in the accessible particle size range, only the milky phases responded, and the clear phases appear as untextured.

The scattering curves have been transformed into size distributions assuming globular particles (Figure 3 (c)). The distributions show that all observed milky phase contain particles in a wide range of radii above 10 to 15 nm. The size distribution is artificially truncated (sharp drop at ~ 28 nm) by the accessible size range of the measurement, and is likely to continue. The samples with higher NaCl concentrations – 5 and 6 wt.% – show a distinct additional contribution with smaller particle radii peaking in between 7 and 12 nm with a rather narrow distribution.

The measurements show, that observed milky phases may be considered as microemulsions. However, larger scale textures in and above the size of the wave length of light can be assumed, otherwise the phases should appear optically transparent. These sizes are out of sensitivity range of the SAXS measurements. The clear phases, on the other hand, appear as untextured.

4 Displacement Mechanisms at sub- and near-optimal conditions

4.1 Flooding experiments

Displacement experiments were performed in microfluidics to study the displacement efficiency and also the effect of in-situ emulsification. In this study, we focus on the simplest process, which is water injection in an initially oil saturated domain, i.e. surfactant flooding in a secondary recovery mode. Such flooding experiments have been performed for NaCl concentration in between 1 to 5 wt.%, with otherwise leaving the overall composition of the aqueous phase constant. Figure 4 shows a typical flooding sequence for 4wt.% NaCl, i.e., in the over optimum. In the left column of Figure 4, the total flooding domain at different time steps from the water invasion in (a) to the time of breakthrough in (e) is shown. The light-blue phase is the pore space occupied by the invading aqueous solution, while the oil is colored in brown and the solid grains in white.

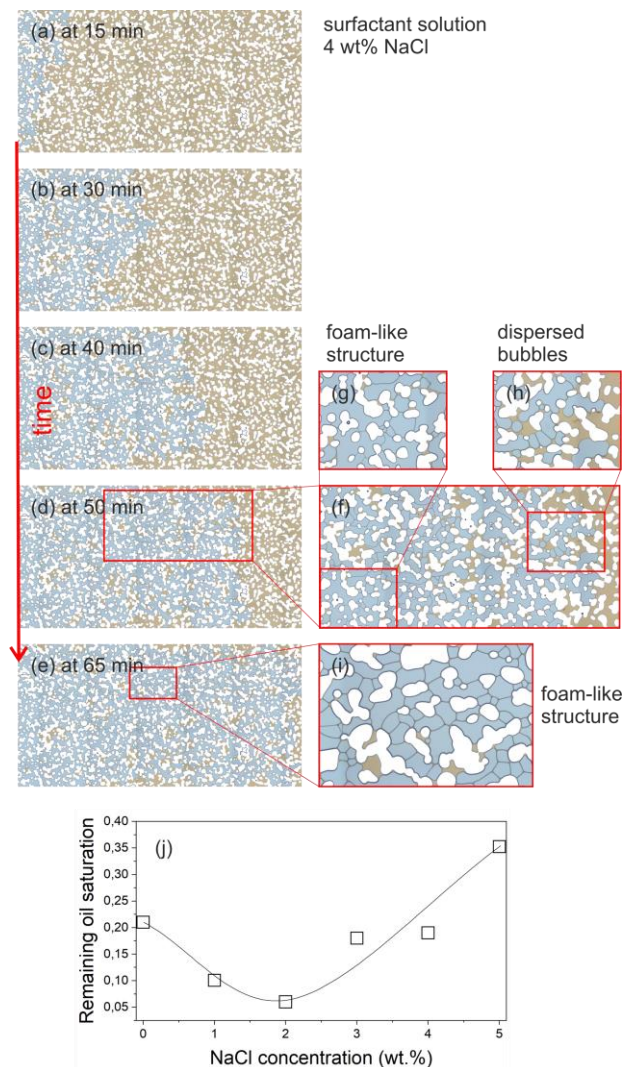


Figure 4 : (a) to (e) time series of an oil displacement process by a surfactant solution with 4 wt.% NaCl – in the over optimum. The phases are colored with white being the grains, blue the injection water, and brown the oil phase. (f) to (h) zoom images into the displacement front show the development from a loose emulsion of dispersed bubbles at the front into a foam-like phase further behind the front. (j) Remaining oil saturation as function of NaCl concentration. The data are taken right after breakthrough for comparability reasons.

Before going into details of displacements and emulsification, it is intuitive to discuss the displacement efficiency. Figure 4 (j) shows the remaining oil saturation right after breakthrough for experiments at different NaCl concentrations. The curve was calculated from the optically taken images considering only the desaturation of the pure oil phase marked by Sudan II as contrast agent (brownish phase in Figure 4). The optical contrast does not allow to detect the oil participating in the aqueous phase, since Sudan II does not participate in the emulsion with a detectable concentration. Defining the remaining oil saturation, respectively the recovery like this, the optimum concentration can be found at 2 wt.% NaCl.

What causes this difference in displacement efficiency and how is this related to emulsification processes in the pore space? The invasion process is similar to a primary drainage process, with the injection water being the non-wetting phase during the invasion. This can be seen from the

contact angles right at the displacement front in Figure 4 (f) and (h). The wetting state is per definition a result of the initial saturation state ($S_{o,i} = 1$) with the solid surfaces being covered with oil, which forces the invading water into a classic drainage process. As illustrated in the same images, the injection water breaks in dispersed droplets and ganglia right at the displacement front leading to drop-traffic and ganglia flow. Right behind the displacement front, the aqueous phase appears disintegrated in droplets as well. There, the drops are very tightly packed and touch each other. However, there are clear boundaries between the droplets and there is no coalescence between them. From an emulsion point of view, dispersed water bubbles may be described as water-in-oil type with a dominant water content. In the dense packed phase, the boundaries between the droplets show similarity to a foam phase, with the boundaries being interpreted as lamella and vertices.

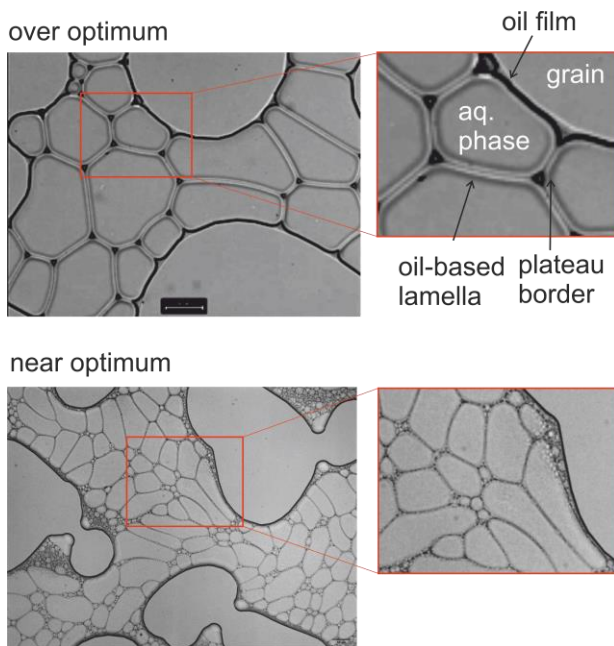


Figure 5 : Details of the foam-like phase in the over optimum (a) and at near-optimum conditions (b) salinity. The phases show all signatures of a foam texture.

In all experiments, sequences of dispersed bubbles/ganglia followed by a foam-like phase and followed by a rather connected, homogeneous aqueous phase can be observed from the front in downstream direction.

But why do we call this emulsion phase “foam like”? Typically, water-oil mixtures are not called foam. However, having a closer look to the emulsion texture, the similarity becomes striking. Figure 5 (a) shows zoom images on the sub-pore scale in the foaming regime at over optimum conditions. This phase shows all signatures of a foam and is as well flowing like a foam phase as illustrated in (supp. mat.) and further below in Figure 8; these textures may be compared to work on foam flooding in microfluidics [18] [19] [20]. In a quasi 2D porous media, planar 2D foam structures were found; water is the internal phase enclosed in oil-based lamella forming

closed compartments. The structure is triggered by the oil wet conditions of the solids, enabling the lamella to attach to the solid grains covered by oil films. The stabilizing function of the oil films becomes visible in the respective video sequence (supp. mat.). As in classical foam phases, vertices are formed connecting three lamellae with the (close to) 120-degree angles (for 2D structures).

At 2 wt.% NaCl, near the optimum, the texture changes and more complex structures can be observed. Due to the reduced IFT, the system is able to generate more interfacial area, resulting in a structure as shown in Figure 5 (b). The bubble-size distribution becomes broader with smaller bubbles at interfaces to the solid and in between the compartments.

4.2 Solubilization in fluorescence microscopy

Fluorescence microscopy provides additional information on the optically observed phase. What has optically been identified as aqueous phase in different droplets, ganglia or compartments, turned out to contain solubilized oil and is therefore an emulsion phase itself, but without optical contrast to the pure aqueous phase; the oil-in-place becomes solubilized by the surfactant solutions.

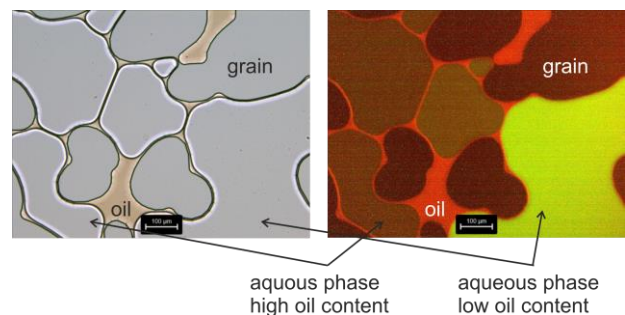


Figure 6: Comparison of the information from optical microscopy (left image) and fluorescence microscopy (right image). The right image was recorded with a long exposure time.

Figure 6 illustrates that each aqueous compartment shows a different response to the fluorescence light, indicating micro emulsions, an optically homogeneous appearing phase, with different compositions, respectively oil content in water.

Figure 7 (a) shows the spatial variation of fluorescence intensity after breakthrough in the near-optimum case with 2 wt.% NaCl in the aqueous phase. The zoom image shows a reverse order of structures with the foam like phase in front of dispersed bubble phase. This is a result of step-wise mobilized remaining oil as will be discussed in the next section. From the textural point of view, the phases become more obvious. Because of the limited participation of the different used contrast agents, the lamella of the foam-like structure can be identified as oil phase, while the interior of the droplets and compartments seem to be aqueous-based, but with different solubilized oil content, depending on their history in moving through the oil saturated porous medium. The intensity of the fluorescent light is a measure of the water content in the

phase, and with this, the phase composition can be identified.

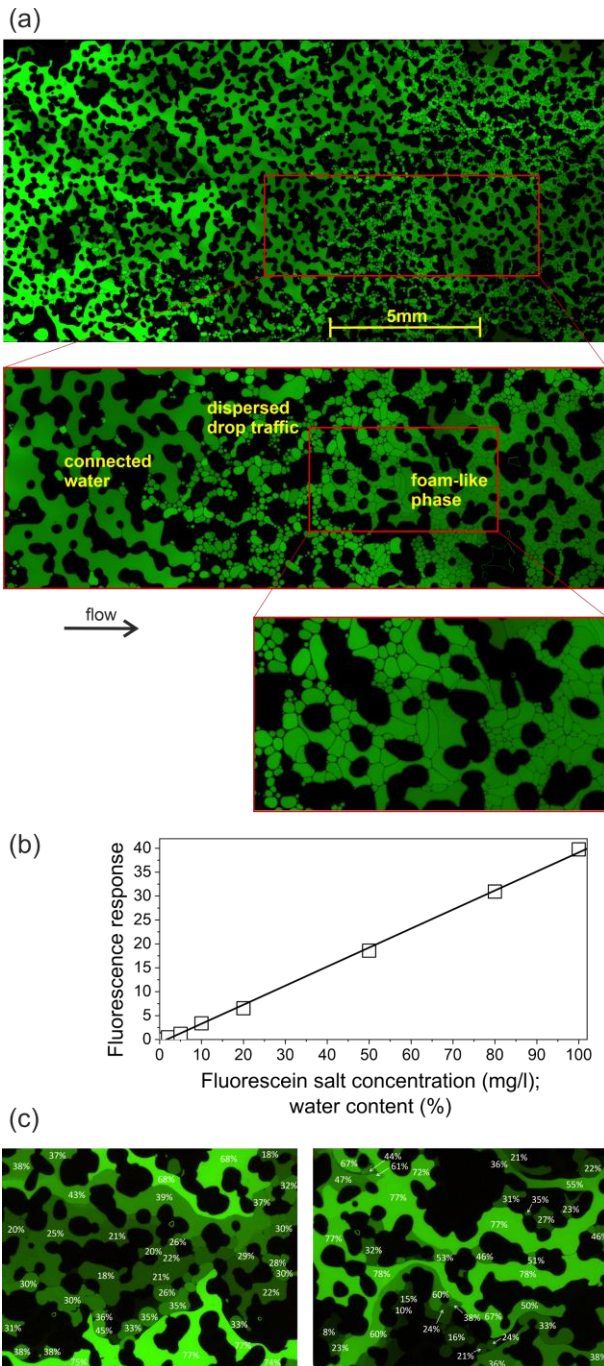


Figure 7 : (a) fluorescence-microscopy images at near-optimum conditions (2 wt.% NaCl). Due to the high contrast, the texture and the sequence is well represented in the images. (b) independently determined calibration curve linking the fluorescence response to the water content. (c) Images from a flooding experiments with 4 wt.% NaCl with a calibrated color scale. The numbers refer to the oil-in-water content: 100% would denote a pure aqueous phase and 0% refer to a pure oil phase.

Figure 7 (b) shows a calibration curve with the fluorescence response as function of the Fluorescein-salt concentration. With the calibration, the oil content can be quantified. The images in (c) and are taken from a 4 wt.%-NaCl experiment and are labelled with the percentage of

water being in the phases. The exact spatial distribution is the first thing that is catching the eye. The individual compartments, representing foam cells or droplets, show a homogeneous intensity with a well-defined fluorescein concentration; each compartment seems to be isolated from the surrounding others maintaining partly the high compositional differences with a well-defined oil content in each compartment. The detected water fractions range from below 20% (above 80% oil) to the pure aqueous phase. This reflects a wide variation of emulsions, that may be labelled as microemulsions, since no structures are optically resolved within the compartments.

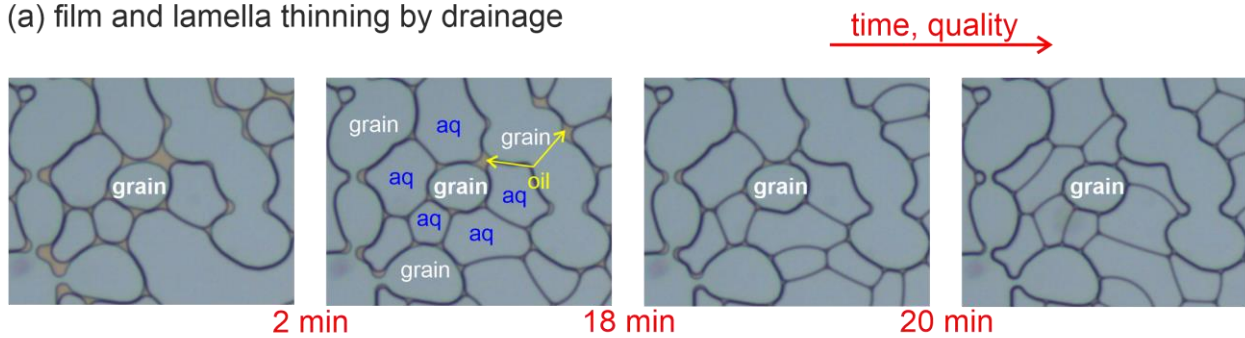
4.3 Interpretation

The observed foam-like structures suggest an interpretation of the observed macro (loose) emulsion phases in terms of foam formation. While foam is typically referred to gas-surfactant solution systems, we observe these structures in surfactant flooding, respectively in oil displacement processes. The structures outside the optimum develop continuously from a ganglion, respectively droplet flow to the foam-like flow. Due to this continuous transition and considering a foaming mechanism, we are able to explain the peculiarities in the drop-traffic flow and macro emulsion structures observed in earlier investigations [9]. Especially the fact that coalescence between adjacent – touching – water droplets is rare, may be related to the nature of the interfaces between those droplets. Our hypothesis is that those droplets already form a low-quality foam. Through time and distance, oil becomes solubilized (and displaced) and foam quality is increasing. The oil phase is then confined in the observed lamella, stabilized by surfactants and the classical competition of electrostatic repulsion at the interfaces and capillary forces in the vertices. The zoom image of Figure 7 (a) illustrates the similarity and the transition between the two types of structures, referring to foam quality as in the classical foam phase.

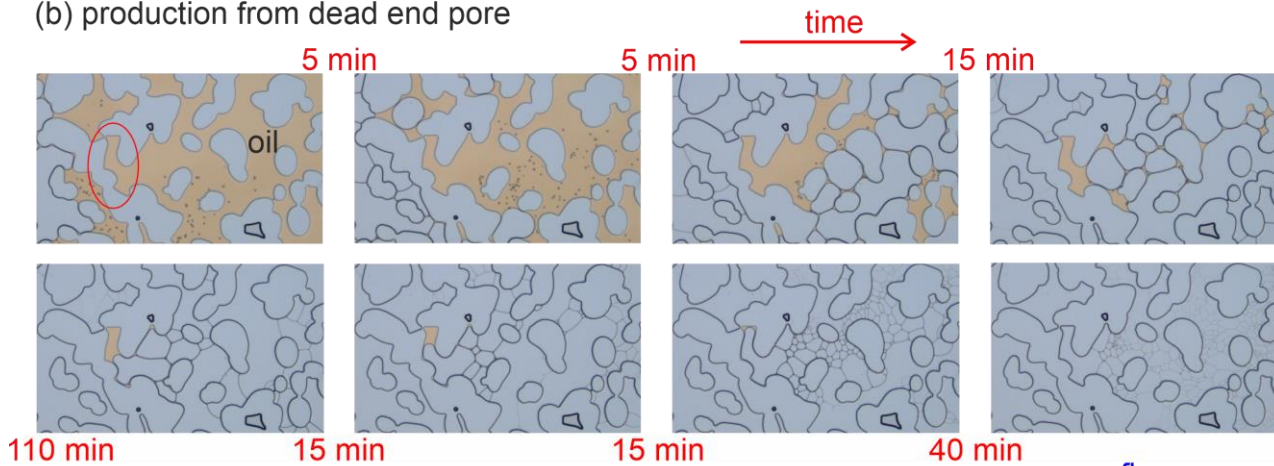
Those structures can be found for all NaCl concentrations, but are especially stable at over- and under-optimum conditions, where we can assume that the surfactant molecules are not efficiently used. This is exactly in analogy to the classical foam formation, where surfactants are needed for lamella stabilization, but as well for the adjustment of capillary suction. Under ultra-low IFT conditions, foam would collapse, because capillarity forces cannot prevent the swelling of the interface layers, respectively the lamella in foam phases. The further away for the optimum the more the displacement is similar to the classical immiscible displacement, with droplets and interfaces being rather confined to the actual displacement front.

Coming closer to optimum conditions at 2 wt.% NaCl, lamella can easily be formed, but are indeed unstable, not for the above given reason of missing capillary forces at ultralow IFT conditions; the oil phase confined in the

(a) film and lamella thinning by drainage



(b) production from dead end pore



(c) displacement in high quality foam

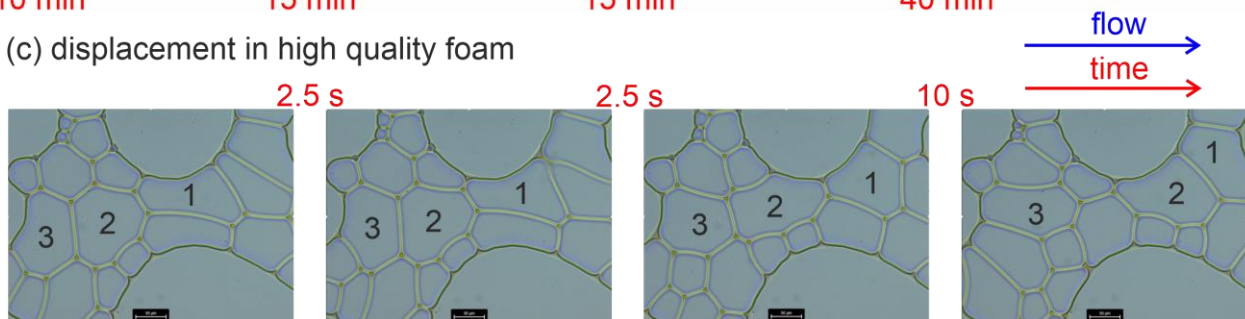


Figure 8 : Oil mobilization mechanisms. (a) Film thinning and drainage process, which leads to a reduction in foam quality. (b) Immiscible displacement and production from a dead-end pore. (c) Oil is transported as foam phase. The lamellae are oil-based and with the compartments, oil is transported as micro emulsion (compare to Figure 7).

lamella becomes progressively solubilized in the “aqueous” phase, which can be detected by the vanishing contrast in between compartments/bubbles and lamella, as seen in Figure 8 (b) and discussed in the following section.

5 Pore scale oil mobilization mechanisms

The foam-like structures consist of aqueous-phase and emulsion compartments of homogenous composition and the surrounding oil phase. Both phases are mobile and carry oil solubilized in water as seen from fluorescence microscopy and in the lamella. The images presented in the previous section show this foam-like phase is (a) displacing initially trapped oil and (b) is increasing its foam quality by displacement. The underlying mechanisms are visualized and explained in the following examples.

5.1 Film thinning and film drainage

The key mechanisms for oil displacement in the foam phase is the ability of the system to drain the oil films

covering the initially oil-wet solid surfaces by forming lamella. This effect is illustrated in Figure 8 (a), referring to the 3 wt.-%-NaCl case in the over-optimum. The image shows a time series from left to right, in which the “foam quality” is increasing, respectively the oil saturation is decreasing. Likely due to injection pressure, the compartments are coming close together, draining the oil phase in between them – the foam quality is increasing. The oil volumes may disappear into newly formed lamella, leading to an increasing compartmentalization and increasing interfacial area. The lamella, vortices, contacts to the solid and oil films became thinner over time forming a high-quality foam with a minimum oil phase forming the boundaries.

As predominantly observable in the videos (supp. mat.), moving lamella often means stretching of those, which requires additional material. This material is supplied from the oil films covering the solid surfaces via the “plateau borders”, which apparently is thinning the oil films.

There is a third mechanism thinning or even removing the oil films. In the course of the displacement, oil films are continuously contacted with injection fluid, continuously solubilizing it. We may say that during the process – especially near optimum conditions – the foam quality is increasing, which coincides with the observation on the larger scale as discussed in the previous section. Ultimately, the oil film may disappear, which may be interpreted as wettability change, since the surfaces are ultimately covered by the aqueous phase. However, solubilization of lamella and films may not play a dominant role in the present case over optimum (Figure 8 (a)) and on the time scale of observation. Solubilization would lead to a vanishing optical contrast between lamella and films with respect to the compartments as discussed in the following.

5.2 Production from dead-end pores

The production from dead-end pores – or maybe in general the production from capillary trapped oil volumes – may be described by a series of mechanisms. This series is illustrated in Figure 8 (b): The dead-end pore described is marked by the red oval in the first image of the time series. The situation refers to the 2 wt.% case. In a first step, a compartment of the aqueous phase is penetrating into the pocket by the injection pressure, displacing the oil from the dead end. This displacement is possible even if the invading phase is “sealing” the dead-end. This is because in the oil wet system the oil is allowed to escape via the oil films covering the solid surfaces. These films are connected via the plateau borders to the lamella and therefore the initially trapped oil can be transported and transformed to new lamella forming a foam-like phase. The oil displacement happens finally in the form of the oil-based foam. This mechanism has been observed for all systems outside and near the optimum salinity. The major difference between sub-optimal and optimal conditions is that near optimum, the foam phase, respectively the lamellae are progressively solubilized on their way through the porous medium forming a single-phase fluid, which is nicely illustrated in the last to images of the time series and the respective videos at optimum conditions (supp. mat.). Outside optimum, the lamellae are generally more stable. This solubilization is most efficient near the optimum, leading to the highest ultimate recovery factor.

5.3 Oil displacement in high quality foam

The time evolution of the high-quality foam phase is shown in Figure 8 (c). Even if the pattern is qualitatively not changing, the individual compartments transport solubilized oil, and oil is transported by moving lamella. The images, again, shows a time series and three of the compartments are marked for tracking them. On the way through the image series, lamella, vertices and plateau borders continuously disappear and are created. This may best be seen in the respective video in the supplementary material (supp. mat.).

6 Summary and Conclusions

In the present paper we investigate the phase behavior and the development of emulsion phases during surfactant flooding. For this, we make use of the high spatial and temporal resolution of microfluidics and we use complementary contrast agents of optical and fluorescence microscopy in order to highlight the oil solubilized in the invaded phase and the remaining oil phase, separately.

The surfactant flooding experiments were carried out for different NaCl concentrations in order to tune the phase behavior across an optimum as examined in classical phase behavior experiments and by the remaining oil saturation from the displacement experiments.

During the flooding, emulsion phases with substantially different textures developed in time and space. A sequence of loose droplets/ganglia at the flood front developed into a foam-like phase. Comparing the texture to classical foam flooding experiments in literature, this sequence may be described as a foam phase with varying foam quality.

By combining optical with fluorescence microscopy, oil displacement mechanisms could be identified and described. A central role plays the drainage, respectively the thinning of oil-films and lamellae during displacement, which leads to the quality increase and to oil transportation. Flow in thin films have also been identified as mechanism to successively drain oil trapped in dead end pores. On top of the displacement of the pure oil phase, oil is transported solubilized in the injection water, which is compartmentalized in the foam structure. By using fluorescence microscopy, the solubilized oil content could be quantified.

The major qualitative difference between near-optimum and sub-optimum conditions is the degree to which oil is solubilized. Near optimum, lamellae and films progressively disappear on their way through the porous medium making a transition to a single phase. Further away from the optimum, the foam-like phase is rather confined to the region close to the flood front and for the highest investigated salinity in the over optimum, only some interfaces were observed.

Acknowledgements

The work has been performed in the frame of the EmulPore project funded by The Austrian Research Promotion Agency (FFG), with the OMV Exploration & Production GmbH as project partner. The authors would like to acknowledge Rene Ritter for experimental support, and Dr. Torsten Clemens for valuable discussions.

Supporting Material

Videos as supporting material are provided under: <https://oc.unileoben.ac.at/index.php/s/N4bCc0NEhnW9D6h>

References

- [1] L. W. Lake, R. T. Johns, W. R. Rossen and G. A. Pope, *Fundamentals of Enhanced Oil Recovery*, SPE, 2014.
- [2] M. Lawrence and G. D. Rees, "Microemulsion-based media as novel drug delivery systems," *Advanced Drug Delivery Reviews*, vol. 45, no. 1, pp. 89-121, 2006.
- [3] D. J. McClements, "Crystals and crystallization in oil-in-water emulsions: Implications for emulsion-based delivery systems," *Advances in Colloid and Interface Science*, vol. 174, pp. 1-30, 2012.
- [4] L. Sagalowicz and M. E. Lese, "Delivery systems for liquid food products," *Current Opinion in Colloid & Interface Science*, vol. 15, no. 1-2, pp. 61-72, 2010.
- [5] A. Bera, "Microemulsions: a novel approach to enhanced oil recovery: a review," <https://link.springer.com/journal/13202>, 2015.
- [6] I. B. Ivanov and P. A. Kralchevsky, "Stability of emulsions under equilibrium and dynamic conditions," *Colloids and Surfaces A: Physicochemical and Engineering Aspects*, vol. 128, no. 1-3, pp. 155-175, 1997.
- [7] E. Unsal, S. Oedai and J. v. Wunnik, "Microemulsion Formation and its Effects on in Situ Rheology During ASP Corefloods: Scouting Study," *SPE*, 2016.
- [8] M. Tagavifar, K. Xu, S. H. Jang, M. T. Balhoff and G. A. Pope, "Spontaneous and Flow-Driven Interfacial Phase Change: Dynamics of Microemulsion Formation at the Pore Scale," *Langmuir*, 2017.
- [9] H. Ott, A. Kharrat, M. Borji and P. Arnold, "Fluid-phase topology of complex displacements in porous media," *Phys. Rev. Research*, 2020.
- [10] E. Unsal, M. Broens and R. T. Armstrong, "Pore Scale Dynamics of Microemulsion Formation," *Langmuir*, 2016.
- [11] M. Broens and E. Unsal, "Emulsification kinetics during quasi-miscible flow in dead-end pores," *Advances in Water Resources*, 2018.
- [12] Y. Alzahid, P. Mostaghimi, M. Ebrahimi Warkiani, V. Joekar-Niasar, N. Karadimitriou and R. T. Armstrong, "Alkaline Surfactant Polymer Flooding: What Happens at the Pore Scale?," *SPE*, 2017.
- [13] Y. A. Alzahid, P. Mostaghimi, S. D. Walsh and R. T. Armstrong, "Flow regimes during surfactant flooding: The influence of phase behaviour," *Fuel*, 2019.
- [14] P. A. Winsor, "Hydrotropy, solubilisation and related emulsification processes," *Trans. Faraday Soc*, 1948.
- [15] R. N. Healy, R. L. Reed and J. Clarence W. Carpenter, "A Laboratory Study of Microemulsion Flooding," *SPE*, 1975.
- [16] G. Willhite, D. Green, D. Okoye and M. Looney, "A Study of Oil Displacement by Microemulsion Systems Mechanisms and Phase Behavior," *SPE*, 1980.
- [17] D. Levitt, A. Jackson, C. Heinson, L. N. Britton, T. Malik, V. Dwarakanath and G. A. Pope, "Identification and Evaluation of High-Performance EOR Surfactants," *SPE Res Eval & Eng*, 2009.
- [18] N. Quennouz, M. Ryba, J.-F. Argillier, B. Herzhaft, Y. Peysson and N. Pannacci, "Microfluidic Study of Foams Flow for Enhanced Oil Recovery," *Oil & Gas Science and Technology*, 2014.
- [19] C. Yeates, S. Youssef and E. Lorenceau, "New insights of foam flow dynamics in a high-complexity 2D micromodel," *Colloids and Surfaces A*, 2019.
- [20] L. Labarre and D. Vigolo, "Microfluidics approach to investigate foam hysteretic behaviour," *Microfluidics and Nanofluidics*, 2019.

Tortuosity and Cementation Exponent as Variables related to Heterogeneity and the Impact on S_w Calculations in Tambaredjo Field of Suriname

Aima Mijland¹, Elias R. Acosta², and Mitchel Pinas³

¹Staatsolie Maatschappij Suriname N.V., Functional Subsurface Support Division / Petrophysics Department, Paramaribo, Suriname

²Dunia Technology Solutions assigned to Staatsolie Maatschappij Suriname N.V., Functional Subsurface Support Division / Petrophysics Department, Paramaribo, Suriname

³Independent Consultant (former FSS / Petrophysics Department trainee), Paramaribo, Suriname

Abstract. The objective of this research was to propose an alternative method regarding the determination of tortuosity (a) and cementation exponent (m) by finding the best correlation between these parameters and a heterogeneity index using the available core data. Estimate log curves of these parameters and analyze the impact on S_w calculations in the Tambaredjo field.

Core data was used to obtain a relationship between grain and pore size distribution. For grain size distribution, Folk, Moment and Trask indices for sorting were used and plotted against several heterogeneity indices (HI), reservoir properties and pore throat size (PTS) representing pore size distribution. After filtering low regression correlations and non-logical trends, clay volume (V_{cl}), shale volume (V_{sh}), and Basic Petrophysical Property Index (BPPI) were defined as best matches. Equations for each were applied to log data and were evaluated. The ones based on BPPI were selected based on the criteria of depth variations and inverse proportionality between a and m .

Water saturation (S_w) calculations using Indonesian (Poupon & Leveaux) was updated incorporating a and m as variables (log curves), comparing it with S_w from core data and previous calculations using fixed average values ($a=1$ & $m=1.66$) from core data. Results show that using a and m as variable parameters improves previous calculations of S_w from 42 to 37% average and delivers a better fit compared to core data.

Even though many studies have been conducted related to a and m determination and their impact on water saturation calculations, still it is a common practice to use average values over a whole field, regardless of heterogeneity considerations. This study proposes a method to include formation heterogeneity in a and m determination, allowing for a more reliable water saturation determination as demonstrated in the Tambaredjo field of Suriname.

1 Introduction

Analysis of petrophysical data of a reservoir is determining the information that facilitate on defining the Stock Tank Oil Initially in Place (STOIP). Water saturation (S_w) calculated from open-hole resistivity measurements is a primary input for STOIP estimation. S_w determination is a critical and complex petrophysical calculation, as each S_w equations consist of several parameters, with each having their own uncertainty in their determination.

A correct estimation of Archie's parameters (tortuosity (a) and cementation factor (m)) within a specific reservoir is important as there are considerable variations in texture and pore type, hence these parameters become more sensitive to pore pattern distribution and lithofacies properties [1].

Schon [2] described that the parameters m and a , can be related to the pore geometry (texture) of the rock. Hamada, et al. [1], Attia [3] and Tiab and Donaldson [4] examined the effect of petrophysical rock properties on the lithology factor a and used the tortuosity factor to improve water saturation calculations and regression fitting [5].

During a Reservoir Characterization Study (RCS) of the TAM Central study area [6] S_w calculations were estimated using the Indonesian [7] equation (Equation 1).

$$S_w = \sqrt[n]{\left[\left(\frac{V_{cl}^2 - V_{cl}}{R_{cl}}\right)^{1/2} + \left(\frac{\phi_e^m}{a \times R_w}\right)^{1/2}\right]^2} \times R_t \quad (1)$$

Where: S_w = water saturation (v/v); V_{cl} = clay volume (v/v); R_{cl} = clay resistivity (ohm.m); ϕ_e = effective porosity (v/v); R_w = formation water resistivity (ohm.m); R_t = true formation resistivity (ohm.m); m = cementation factor (dimensionless); a = tortuosity factor (dimensionless) and n = saturation exponent (dimensionless).

* Corresponding author: eacosta@staatsolie.com

The calculated S_w values appear not to agree with initial production performances, hence resulting in very low estimated STOIIP and perhaps very high oil recovery. This did not match observed reserves nor expected primary oil recovery.

Correct estimation of the Archie [8] parameters (a and m) has always been challenging. They are functions of the changes in pore geometry, tortuosity of the pores, formation pressure and clay content. They are inputs of the Indonesian equation (Equation 1) and both are affected by formation lithology. The variable input values of these parameters do impact S_w calculation in a considerable amount if translated to STOIIP estimates as concluded by Lang in 1972 [9]. Therefore, accurate determination of these parameters is required, which is the aim of this study.

In standard formation evaluation, Archie's parameters are usually held constant. Knowing this, the change in lithology per location is not considered when these parameter values are used as constants in a heterogeneous reservoir.

Heterogeneous formations vary in sizes, shapes and distribution of grains and pores. Selecting the correct heterogeneity index related to a and m values from core data should lead to better representation of changes in formation lithology. Choosing an appropriate index is critical and should be done with caution.

The values of a and m will be different depending on the approach (free regression fitting or forced regression fitting). As perceived, reservoir samples differ in rock quality, which indicates variation differences in rock quality per well. The heterogeneity distributed over the

Tambaredjo field results in different pairs of a and m for each well. These parameters vary widely and change continuously for each sample due to the changes in lithology depending on the depth [10].

2 Tambaredjo Field (study area)

The study area is the Tambaredjo Central Area (TCA), that is part of the Tambaredjo producing field. This field is in the marshy coastal area of Suriname in the district of Saramacca, about 45 km west of the capital city Paramaribo (Fig. 1).

TCA (Fig. 1) is composed of 4 sub-areas: Area I, Area II, Area III and Extended Petro Boundary. Methodology and findings from this study will be extrapolated or applied to other areas of Tambaredjo field and other fields (Tambaredjo North West and Calcutta), adapting these to the features of the mentioned areas or fields.

Heavy oil production from TCA comes from unconsolidated sands, the so-called T-sands, at average depth of 900 to 1,400 ft. The T-sands are of Paleocene age and of fluvial-estuarine to coastal marine of origin and consists of angular, medium to coarse drained unconsolidated sands with intercalated clays and lignites. The reservoir is sealed by locally continuous clays that overlap the Cretaceous surface in the South [6].

The sands are deposited on a well cemented erosional Cretaceous basement, during an overall transgressive period, as multilateral and vertically stacked sand bodies. Fig. 2 illustrates the geological conceptual model of the T sand reservoirs of the T unit in the TAM field [6].

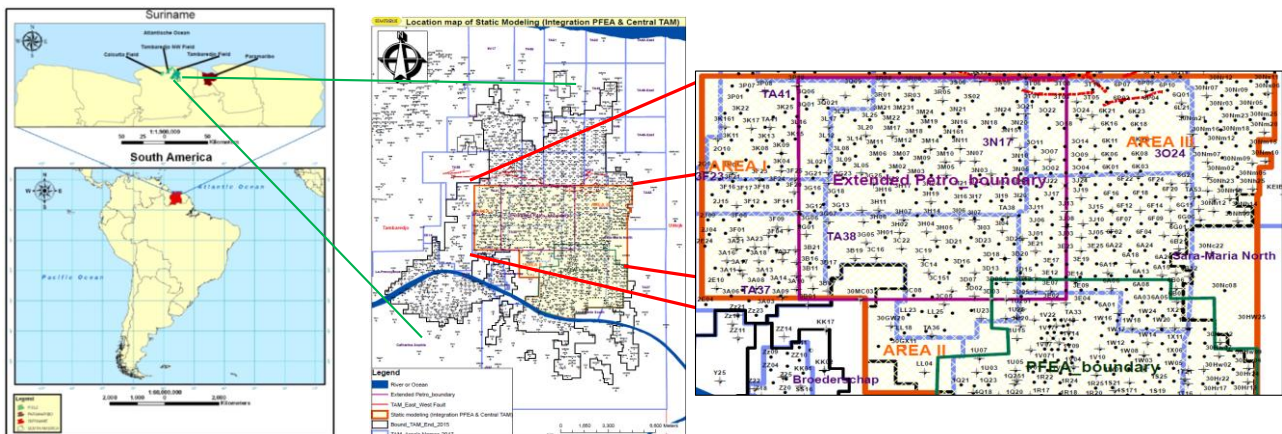


Fig. 1. Location map of Staatsolie oilfields (left) and of the TCA (Area I, II, III and Extended Petro Boundary) [6].

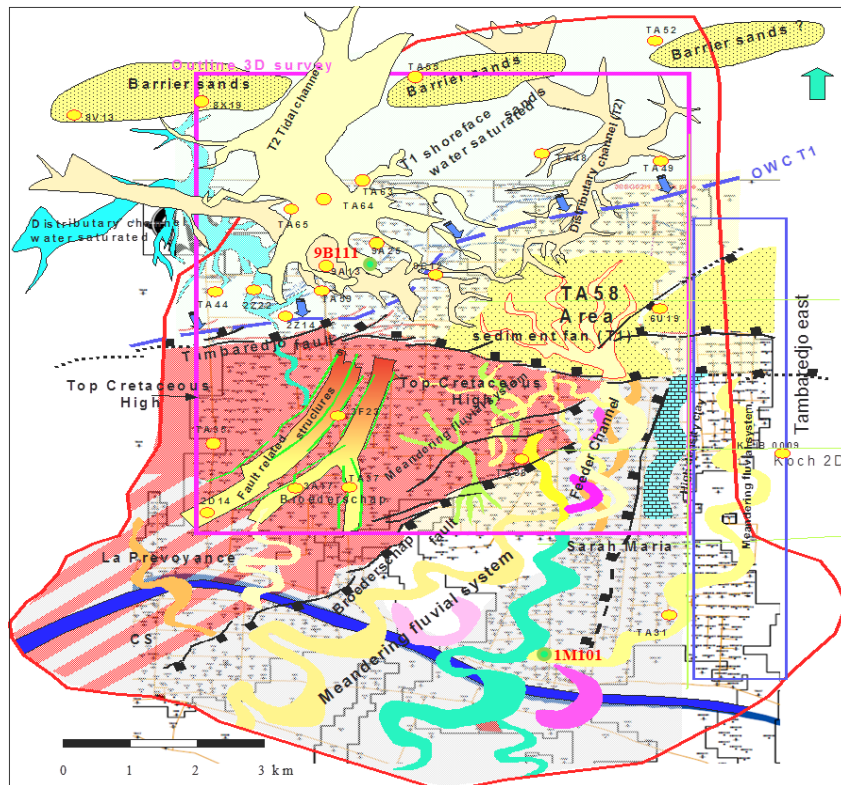


Fig. 2. Geological concept of the depositional environment of the Tambaredjo field [11].

3 Previous studies

Appendix A summarizes previous studies done regarding the determination of tortuosity (a) and cementation factor (m). This summary was one of the key facts that led the authors to search for a practical method to estimate a and m as variables related to heterogeneity.

As presented in this table (Appendix A), a and m vary with lithology and geological facies.

Pinas and Acosta [10] demonstrated the impact of varying a and m on S_w in the Tambaredjo field. The differences found was $\pm 11.89\%$ when using maximum and minimum core values for a and m .

4 Methodology

Fig. 3 summarizes the activities done for determining tortuosity (a) and cementation factor (m) as variables for TAM Central Area (TCA).

Items 2 and 3 of the workflow are explained in this section and preliminary results are presented. Items 4 and 5 are explained in the Results Analysis section.

4.1 Data gathering, validation and preliminary calculations

4.1.1 Core data

Clay volume (V_{cl}) from X-Ray Diffraction (XRD) data from 2 wells (9B111 and 1M101) was used to calibrate log derived V_{cl} .

Special Core Analysis (SCAL) data from 2 wells (9B111 and 1M101) consisting of: formation factor (F_a), cementation exponent (m), air permeability (K_a) and porosity. This data was used to calibrate the indexes, comparing core derived indices to log derived indices.

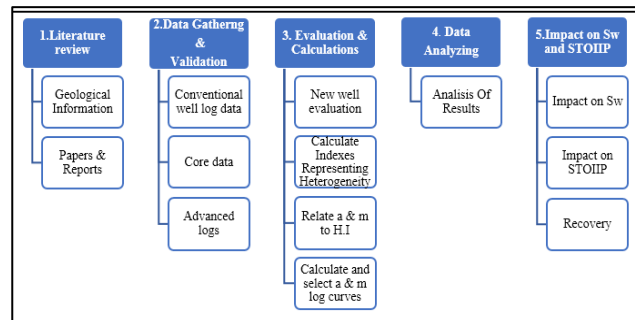


Fig. 3. Workflow for determining S_w Equation.

Permeability corrected (Klinkenberg) and porosity from conventional plug analysis data of 7 wells (I211, 9B08, 6P22, 3D19RE, 3Z24, 9B111, 1M101), were used as input to calculate the indexes representing heterogeneity.

LPSA (Laser Particle Size Analysis) data of 7 wells (I211, 9B08, 6P22, 3D19RE, 3Z24, 9B111, 1M101) consisting of: clay volume, silt volume, permeability, porosity and Folk, Moment and Trask indexes for sorting. The data was reported and named according to the depth at which each sample was taken.

4.1.2 Conventional logs

Well log data (532 wells) consisting of gamma ray logs, neutron logs, density logs and resistivity logs.

- Log data of 500 wells that were evaluated within the TCA were used for water saturation (S_w) estimation.
- 30 additional wells located North of TCA were evaluated during this study. The log data was used to calibrate the S_w , as these wells have an Oil Water Contact (OWC), meaning that S_w should be close to 100% in these water zones.
- Log data of the 2 cored wells (9B111 and 1M101) within TCA were used to calibrate the a and m curves. Both wells were already evaluated, and the well log data was directly used.

4.2 Heterogeneity Indexes calculation

An approach towards determining a and m as variables is by finding an index that represents the formation's heterogeneity. The following table (Table 1) summarizes the indexes used: heterogeneity index (HI, input parameters and Pore Throat Size (PTS).

Table 1. Heterogeneity indexes (HI).

Index	Equation	Reference	Features
BPPI (Basic Petrophysical Property Index)	$BPPI = \frac{\phi_e}{1 - \phi_t} \times (1 - V_{sh})$	Angel [12]	Ratio of volume of fluids in the interconnected pore space to the volume of solid rock
NRI (Net Reservoir Index)	$NRI = \frac{\phi_t \times V_{sh}}{1 - \phi_t} \times \phi_e$		Relationship between BPPI and PHIE.
Rock Texture	$Rock\ Texture = \frac{\phi^3}{1 - \phi^2}$	Kozeny [13] and Carman [14]	Term from the Kozeny-Carmen Equation used for pressure drop in porous medium
RQI (Roc Quality Index)	$RQI = 0.0314 \frac{k^{0.5}}{\phi}$	Jude and Mehmet [15]	Hydraulic flow unit used for flow unit's identification
PHIZ (Pore Grain volume Ratio)	$Phiz = \frac{\phi}{1 - \phi}$	Amaefule and Altunbay [16]	The ratio of pore volume to grain volume
FZI (Flow Zone Indicator)	$FZI = \frac{RQI}{Phiz}$		Fluid flow in a porous medium, based on modified Kozeny-Carmen Equation

Table 2 lists the used input parameters, which are basically modification features used in several S_w equations (e.g. Indonesian [7], Modified Indonesian [17], Simandoux [18], Modified Simandoux [19], Acosta and Rosales [20]) based on the clay and shale deposition.

Table 2. Reservoir Properties related to heterogeneity.

Input Parameters	
V_{cl}	V_{sh}
$1 - V_{cl}$	$1 - V_{sh}$
$1 - V_{cl}^2$	$1 - V_{sh}^2$
$1 - V_{cl}/2$	$1 - V_{sh}/2$
$1 + V_{cl}/2$	$1 + V_{sh}/2$

Calculations of the PTS were also included in this study, this was done using the R55 formula recommended for rock type classifications for TCA (Table 4).

Table 3. R55 formula used for PTS determination [21].

Index	Equation	Reference	Features
PTS	$Log\ R55 = 0,948 + 0,632 \times Log\ K - 1,426\ Log\ \phi$	Kolodzie [22] and Pittman [23]	R55 is the corresponding pore throat radius (PTS) at 55% of mercury saturation. Recommended for TCA.

From Laser Particle Size Analysis (LPSA) data, distribution statistics is used to obtain indexes for grain sorting. Folk, Moment and Trask are the 3 statistical methods used for delivering sorting indexes [24].

LPSA indexes were plotted against those of Table 1, Table 2 and Table 3 to obtain a relationship between grain distribution and formation heterogeneity (index of the rock quality regarding heterogeneity). A total of 115 correlation cross plots were made [25]. Table 4 groups the indexes according to the terms they represent.

Table 4. Index grouping according to grain size and pore size [25].

Representing	
Grain Distribution (y-axis)	Heterogeneity (x-axis)
Sorting Indexes	HI Indices
	Input parameters
	PTS

Fig. 4 shows the calculated BPPI (red dots) using core data for well 9B111.

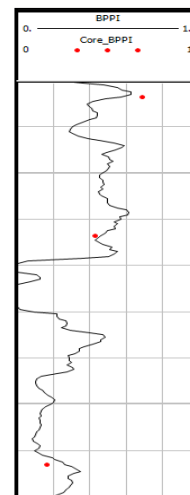


Fig. 4. Example of calibration of log calculated to core calculated BPPI on well 9B111

4.3 Tortuosity and cementation exponent relationships with Heterogeneity Index

m is determined for each plug sample analyzed assuming $a = 1$ from equation (2).

$$F = \frac{a}{\phi^m} \quad (2)$$

Where: F = formation factor (dimensionless); ϕ = porosity (v/v); m = cementation factor (dimensionless); a = tortuosity factor (dimensionless)

In this research the semi-forced regression fitting was introduced to obtain different a values for each core sample with electrical properties. Application of this statistical processing technique for sample groups, resulted in a and m values for each group by adding 1 extra (1.1) coordinate to the dataset (Fig. 5).

Rearranging equation (2) delivers an equation for obtaining the tortuosity factor:

$$a = F \times \phi^m \quad (3)$$

Where: F = formation factor (dimensionless); ϕ = porosity (v/v); m = cementation factor (dimensionless); a = tortuosity factor from regression line (dimensionless)

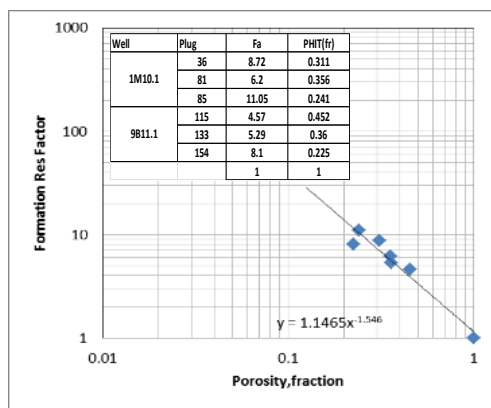


Fig. 5. Semi forced regression fitting cross plot (well 1M101 and 9B111).

Separate F - ϕ cross plots were made using data of well 1M101 and 9B111. Values for the m were obtained by applying both the free regression [5] and semi-forced regression approach, delivering 4 values for m (Fig. 6 and Fig. 7).

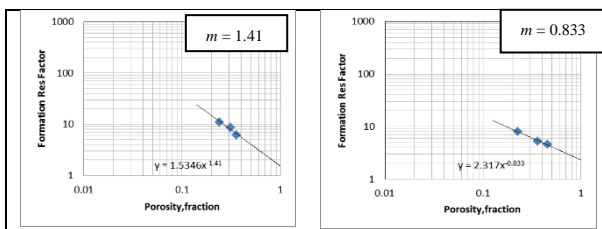


Fig. 6. Free regression fitting crossplot for well 1M101 (left graph) and 9B111 (right graph).

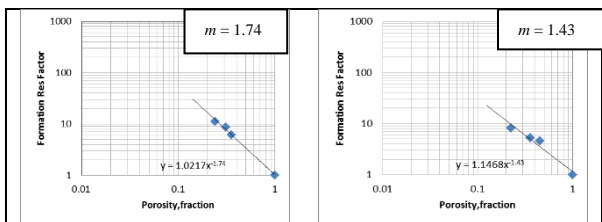


Fig. 7. Semi-forced regression fitting crossplot for well 1M101 (left graph) and 9B111 (right graph).

Using equation (3) and the four obtained values (Fig. 6 and Fig. 7), the m values for the tortuosity factor were back calculated. The usage of the cementation factor

value depends on the well and the approach used for obtaining it. The free tortuosity factor refers to the a calculated using m from the free regression [5] approach and the semi-forced tortuosity factor refers to the a calculated using m from the semi-forced tortuosity factor (Table 5).

Table 5. Core m , free regression and semi-forced calculated a , reservoir properties and HI for core plug samples.

Well	Sample	m	Regression		V_{cl} (v/v)	V_{sh} (v/v)	BPPI
			Free	Semi-forced			
1M101	36	1.85	1.68	1.143	0.124	0.277	0.29
	81	1.77	1.45	1.028	0.094	0.276	0.36
	85	1.69	1.49	0.929	0.104	0.294	0.2
9B111	115	1.91	2.36	1.468	0.034	0.129	0.69
	133	1.63	2.26	1.227	0.041	0.199	0.43
	154	1.4	2.34	0.96	0.131	0.373	0.16

From left to right: Column 1: Well name; Column 2: Plug sample number; Column 3: Cementation factor from core; Column 4: tortuosity factor using free regression approach; Column 5: Tortuosity factor using semi-forced regression approach. Column 6: Clay volume from core data or calibrated log data; Column 7: Shale volume from core or calibrated log data; Column 8: Basic petrophysical property index calculated using core data or calibrated log data

Correlation cross plots were made by plotting data of Table 5 (a and m vs. V_{cl} , V_{sh} and BPPI) [25] where each m and a , were plotted as a function of V_{cl} , V_{sh} and BPPI (which were considered the preliminary selections based on the criteria of $R^2 > 0.75$ and logical trend (matching lithology)).

4.4 Selection of tortuosity and cementation factor log curves

The analysis of the preliminary results plotted as log curves [25] led to some questions. The determination of a and m maybe should be estimated by pair as they should be inverse proportional according to the free and semi-forced regression crossplots. None of the sets of curves created could totally fulfill the criteria even though some were showing very good match with core data. Considering this and that because of the unconsolidated nature of the reservoir, samples in good rock quality intervals could not be retrieved, a different approach was needed.

Using the R55 formula (Table 3) for PTS calculation and the classification ranges (Table 6), the core samples were classified by rock type numbers (Table 7). Rock type 0 is the best possible rock quality and rock type 5 is the worst.

Table 6. Rock type classification ranges [26].

Rock Type	PTR [microns]
RT0	PTR > 30
RT1	20 < PTR < 30
RT2	14 < PTR < 20
RT3	8 < PTR < 14
RT4	3 < PTR < 8
RT5	PTR < 3

Rock type classification according to the pore throat radius

Table 7. Core samples and their rock type number

Well	Plug	Rock Type
1M10.1	36	RT4
	81	RT3
	85	RT4
9B11.1	115	RT4
	133	RT5
	154	RT5

Core samples classified by rock type

Table 7 reveals, that the data set available is limited to rock type 3, 4 and 5, which is mainly silty-shaly sand. This data set does not accommodate for good quality reservoir sand (RT0). It was also noted that the data set neither covered shale nor clay. In other words, the full spectrum of rock types was not possible to use to estimate a and m for all the types present in the reservoir.

Compiling the data set to accommodate rock quality ranges from RT0 to shale:

1. For RT0, *a* and *m* values from literature, proposed for unconsolidated sands (Humble formula) were used (Table 8). The BPPI was estimated using average inputs for clean sands ($V_{sh} < 5\%$).
2. For RT4 and RT5, the *a* and *m* values were obtained by F- ϕ cross plots (Fig. 8). The V_{sh} and V_{cl} values are averages from available core data and were used for BPPI calculations including \emptyset .
3. For shale, the *a* and *m* values were extrapolated using the trend equations for the parameters representing V_{sh} , V_{cl} and BPPI. BPPI was estimated using known values for shale.

Table 8. Data set for final *a* and *m* equations

	Free regression Fitting				
	Vsh	Vcl	BPPI	<i>m</i> (plot)	<i>a</i> (plot)
RT0 (Literature)	0.025	0.013	0.784	2.15	0.62
RT4	0.203	0.066	0.470	1.68	1.17
RT5	0.334	0.092	0.263	1.23	1.56
shale		0.85	0.02	0.99	2.35
	0.95			1.11	1.93

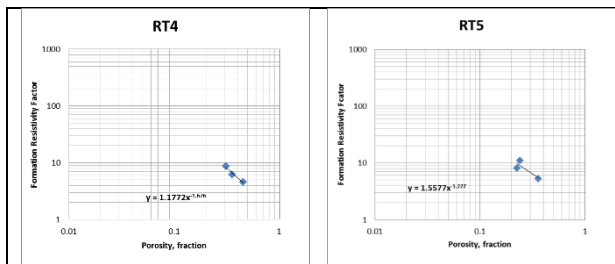


Fig. 8. F- ϕ cross plots for RT4 and RT 5.

Porosity versus Formation resistivity factor cross plots using data of the samples classified as RT 4 and RT5

Plotting the data of Table 8 (Figs. 9, 10 and 11), equations for *a* and *m* were obtained. Each parameter was plotted as a function of V_{sh} , V_{cl} and BPPI.

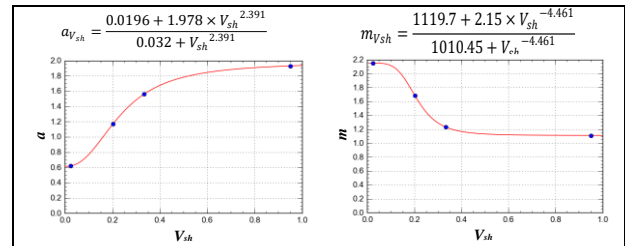


Fig. 9 Crossplots of *a* and *m* as functions of V_{sh} .

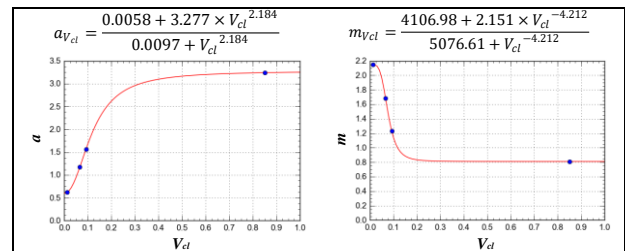


Fig. 10. Crossplots for *a* and *m* as functions of V_{cl} .

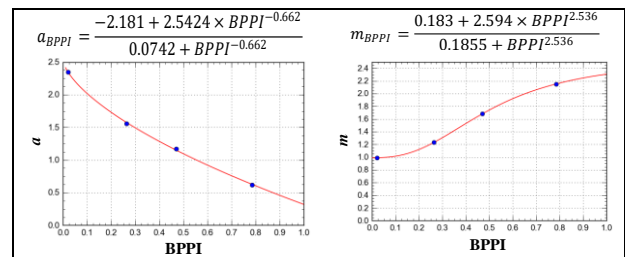


Fig. 11 Crossplots for *a* and *m* as functions of BPPI.

The log curves for *a* and *m* were created for each well (e.g. 1M101 Fig. 12: tracks on the right). The *a* from core is indicated by the red dots and the *m* from core is indicated with the black dots.

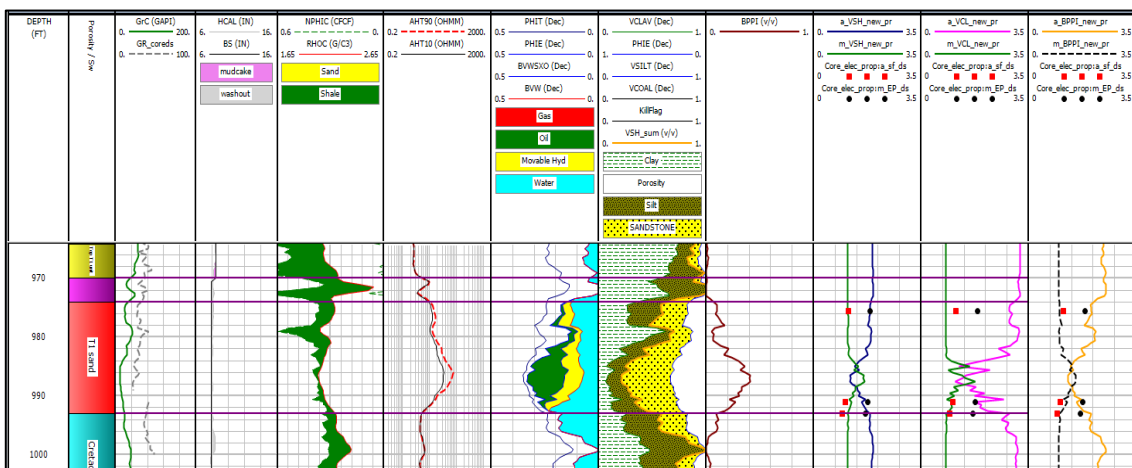


Fig. 12. Petrophysical evaluation with imported *a* and *m* curves (before adjustments) for well 1M101.

From left to right: Track 1: Depth reference; Track 2: Formation tops zonation; Track 3: Gamma ray; Track 4: Caliper and Bit size; Track 5: Neutron & Density; Track 6: Resistivity curves; Track 7: Porosity calculations; Track 8: Lithology composite; Track 9: Basic Petrophysical Property Index; Track 10: *a* & *m* as a function of V_{sh} (red squares: core tortuosity and black circle: core cementation factor); Track 11: *a* & *m* as a function of V_{cl} (red squares: core tortuosity and black circle: core cementation factor); Track 12: *a* & *m* as a function of BPPI (red squares: core tortuosity and black circle: core cementation factor)

5. Results analysis

In this section the results of the approach to determine a and m as variable parameters are presented and discussed, establishing S_w calculations using a and m log curves that depend on reservoir heterogeneity.

5.1 Indexes representing formation heterogeneity

Out of the 115 correlation cross plots made [25], three indexes were selected based on the criteria of $R^2 > 0.75$ and logical trend line. These are:

- V_{cl} with $R^2 = 0.829$ (Fig. 9)
- V_{sh} with $R^2 = 0.849$ (Fig. 10)
- BPPI with $R^2 = 0.936$ (Fig. 11)

Even though V_{sh} and V_{cl} are not really indexes, they do express in a certain form the reservoirs heterogeneity. These and BPPI show good correlations between grain distribution and heterogeneity.

5.1.1 Final selection and adjustments for the curves

Adjustments were made to the correlations (Figs. 9, 10 and 11) to match core data. Adjustments required for well 1M101 (Fig. 13) to match the core data, were not the same adjustments required for well 9B111 (Fig. 14).

An analysis was done exploring to explain these two sets of adjustments. The locations of both wells (9B111 and 1M101) were reflected to a geological concept of the depositional environment of the Tambaredjo field, showing clearly that both wells are in 2 different depositional environments (Fig. 2). Well, 1M101 was drilled in a meandering fluvial system, while 9B111 is in a deltaic system. Depositional facies for each system are very different and this explains the necessity of different adjustments to match core data for each well. Before taking the final decision of which correlation set of curves to select, it was obvious that these would need to be applied by areas according to the well location. In other words, wells in Tambaredjo Central should use

correlation set for a and m curves with adjustments made for well 1M101 and wells in Tambaredjo North should use correlation set for a and m curves with adjustments made for well 9B111.

The correlation set curves were selected using the following criteria:

- a and m curves must be variable within the depth, avoiding straight vertical lines in the reservoir.
- Values of a must be inversely proportional to the values of m , when one increases in value, the other should decrease in value (according to the free regression crossplot approach).

The ultimate selection of a and m curves are the ones representing BPPI (Equations (6) and (7) for well 1M101; and Equations (8) and (9) for well 9B111) (further referred to as variable a and m), highlighted with red rectangle box in Fig. 13 and Fig. 14 (Track 11). S_w was then calculated using the field average of $a = 1$ and $m = 1.66$ (further referred to as average a and m) and compared to S_w calculated using variable a and m . The green triangle represents S_{wir} from core data.

$$a_{BPPI} = \frac{-2.181 + 2.242 \times BPPI^{-0.662}}{0.0742 + BPPI^{-0.662}} - 0.55 \quad (6)$$

$$m_{BPPI} = \frac{0.183 + 2.594 \times BPPI^{1.836}}{0.1855 + BPPI^{1.836}} + 0.4 \quad (7)$$

$$a_{BPPI} = \frac{-2.181 + 2.242 \times BPPI^{-0.662}}{0.0742 + BPPI^{-0.662}} - 0.05 \quad (8)$$

$$m_{BPPI} = \frac{0.183 + 2.594 \times BPPI^{1.836}}{0.1855 + BPPI^{1.836}} - 0.15 \quad (9)$$

Where: a_{BPPI} = Tortuosity as function of BPPI (dimensionless); m_{BPPI} = Cementation Factor as function of BPPI (dimensionless); BPPI = Basic Petrophysics Properties Index

For both wells (Track 15 in Fig. 13 and Fig. 14) the continuous curve is the calculated S_w using average a and m and the dotted curve is S_w calculated using variable a and m , showing a slight decrease in S_w in the reservoir zones (T1 and T2 sands).

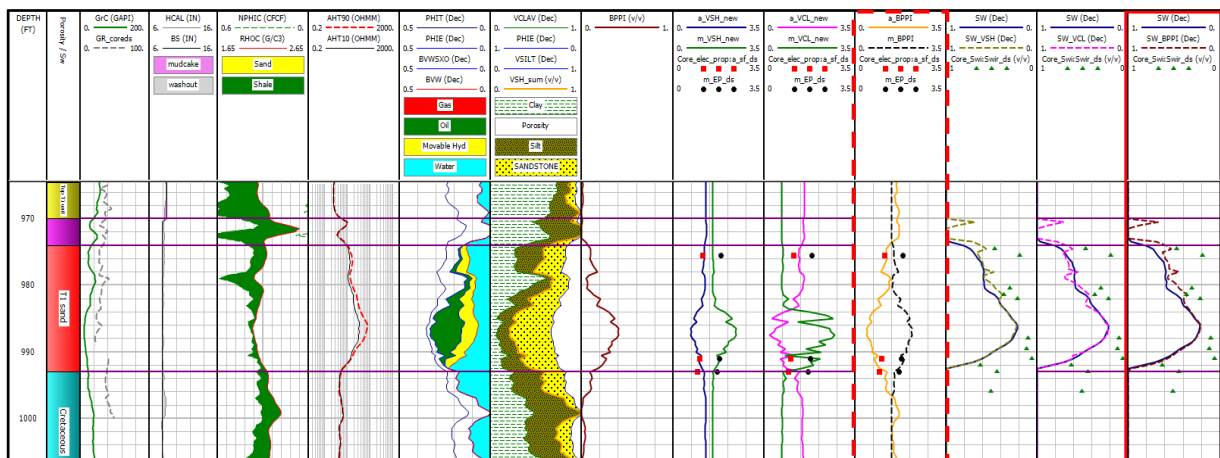


Fig. 13. Petrophysical evaluation with ultimate a & m curves adjustments for well 1M101.

From left to right: Tracks 1 to 12 as per Figure 12; Track 13: S_w using fixed a & m values compared to S_w using a & m from V_{sh} and S_{wir} from relative permeability analysis (green triangles); Track 14: S_w using fixed a & m values compared to S_w using a & m from V_{cl} and S_{wir} from relative permeability analysis (green triangles); Track 15: S_w using fixed a & m values compared to S_w using a & m from BPPI and S_{wir} from relative permeability analysis (green triangles).

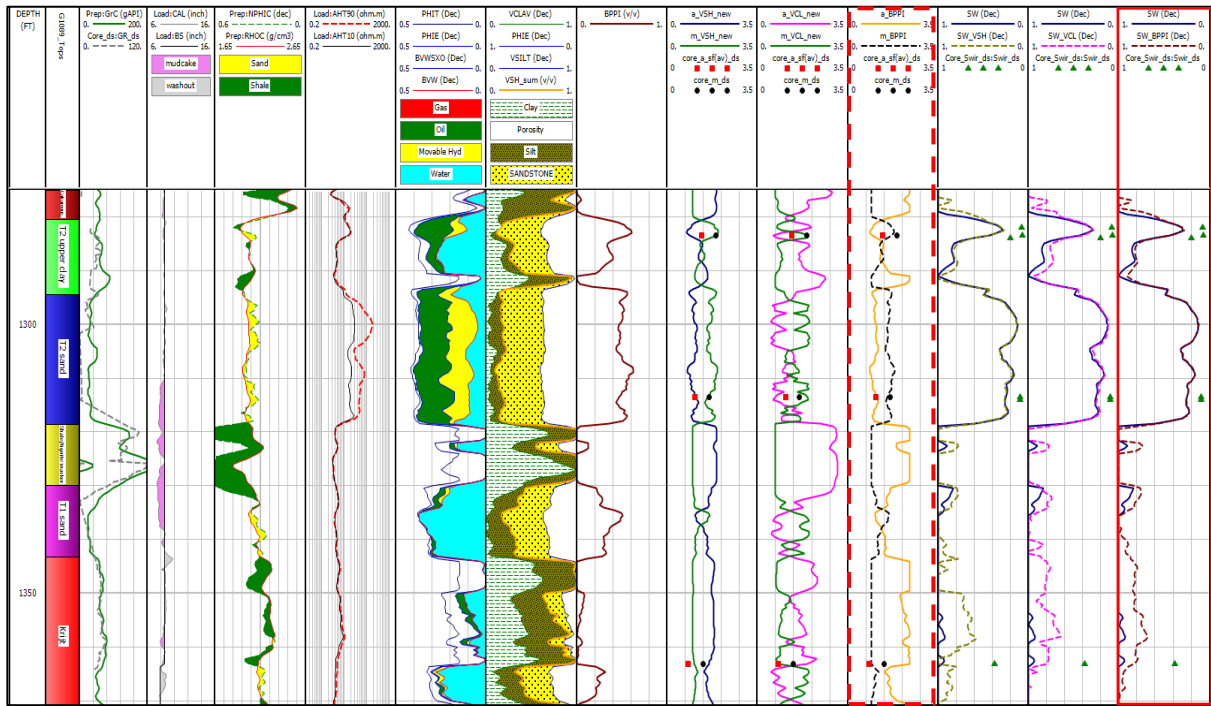


Fig. 14. Petrophysical evaluation with ultimate a & m curves adjustments for well 9B111.

From left to right: Tracks 1 to 12 as per Figure 12; Track 13: S_w using fixed a & m values compared to S_w using a & m from V_{sh} and S_{wir} from relative permeability analysis (green triangles); Track 14: S_w using fixed a & m values compared to S_w using a & m from V_{cl} and S_{wir} from relative permeability analysis (green triangles); Track 15: S_w using fixed a & m values compared to S_w using a & m from BPPI and S_{wir} from relative permeability analysis (green triangles)

Some wells were selected randomly for discussion. S_w was calculated, using both average and variable a and m values.

Well 3E141 (Fig. 15) is located South West in Area III and was evaluated using well 1M101 variable a and m adjustments. Displayed in track 7 is the lithology volumetrics (sand, silt, clay and porosity) for the T-unit reservoirs. In this well, the T1 sand is the cleanest sand according to the maximum clay volume of 0.2%. The S_w curves in track 10 show a reduction of 6.8% in the T1 sand, 4.4% in T2 sand and 0.4% in T3 sand. As observed,

the calculated S_w using average a and m values, is mostly overestimated in the T1 sand which is the cleanest sand.

Well 3Z24 (Fig. 16) is located North outside of Area III and was evaluated using well 9B111 variable a and m adjustments. Displayed in track 7 is the lithology volumetrics (sand, silt, clay and porosity) for the T-unit reservoirs. The S_w curves in track 10 show an average reduction of 3.1% in the T1 sand, 4.1% in T2 sand and 5.3% in T3 sand.

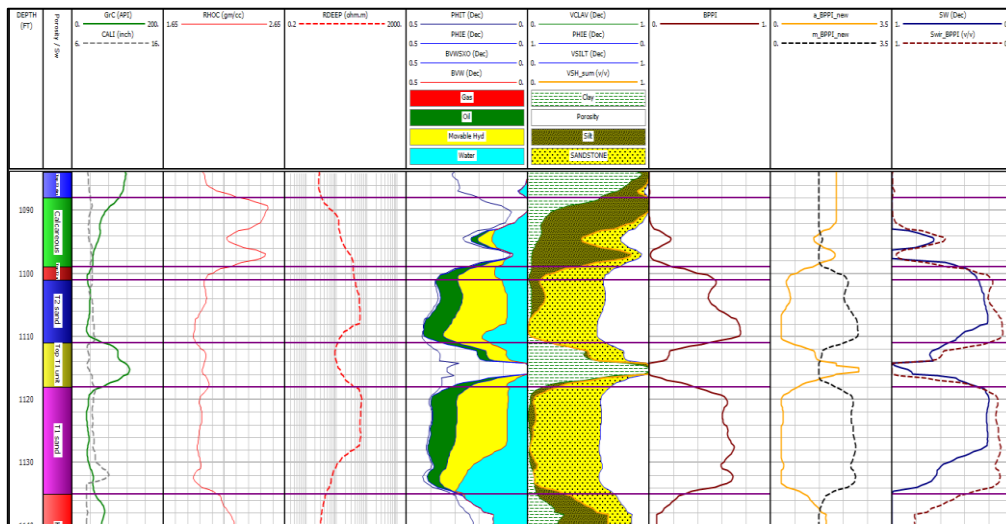


Fig. 15. Petrophysical evaluation of well 3E14.1 located in Area III and using well 1M101 parameter adjustments.

From left to right: Track 1: Depth reference; Track 2: Formation tops zonation; Track 3: Gamma Ray & Caliper; Track 4: Neutron & Density; Track 5: Resistivity curves; Track 6: Porosity calculations; Track 7: Lithology composite; Track 8: Basic Petrophysical Property Index; Track 9: a & m as a function of BPPI; Track 10: S_w using fixed a & m values compared to S_w using a & m from BPPI.

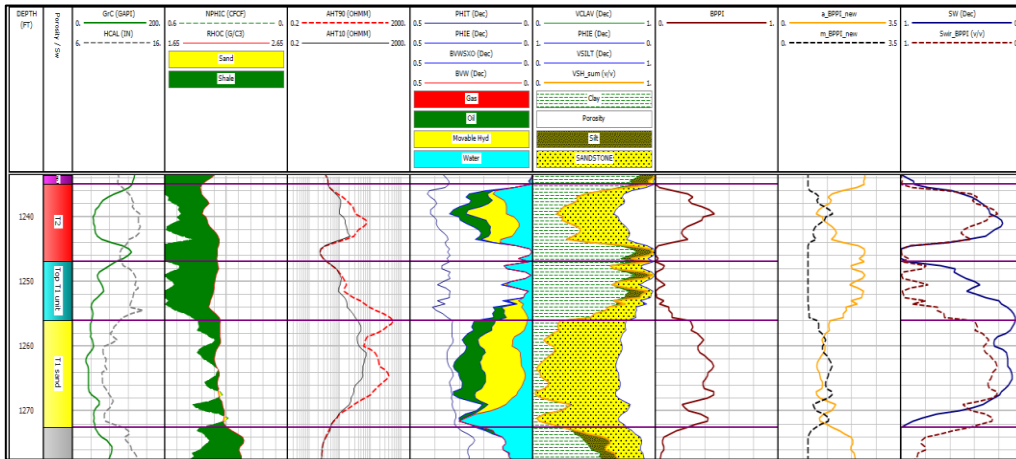


Fig. 16. Petrophysical evaluation of well 3Z24.1 located in Area III and using well 9B111 parameter adjustments.

From left to right: Track 1: Depth reference; Track 2: Formation tops zonation; Track 3: Gamma ray; Track 4: Neutron & Density; Track 5: Resistivity curves; Track 6: Porosity calculations; Track 7: Lithology composite; Track 8: Basic Petrophysical Property Index; Track 9: a & m as a function of BPPI; Track 10: S_w using fixed a & m values compared to S_w using a & m from BPPI.

5.2 Impact on water saturation

Water saturation for the T-unit was calculated and analyzed using histograms (Figs. 17, 18 and 19). Discriminators ($V_{cl} \leq 50\%$ and $R_t \geq 10$ ohm.m) were applied to analyze the impact of the variable a & m in S_w only in the reservoir intervals. Following histograms for Area III are discussed. All other areas histograms can be found in the Appendix (B, C and D).

The T1 histograms (Fig. 17) comparison for calculated S_w show a mean decrease of 6.96% when S_w is calculated using variable a and m , instead of the average a and m values.

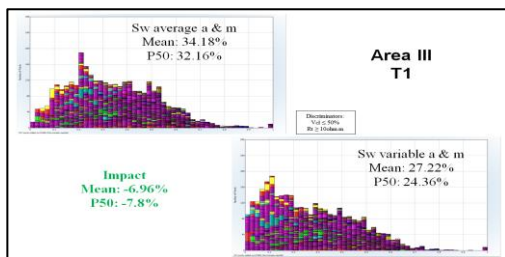


Fig. 17. S_w histogram comparison of the T1 sand (Area III)

The T2 sand histograms (Fig. 18) comparison for calculated S_w show a mean decrease of 5.66%, when S_w is calculated using variable a and m , instead of the average values.

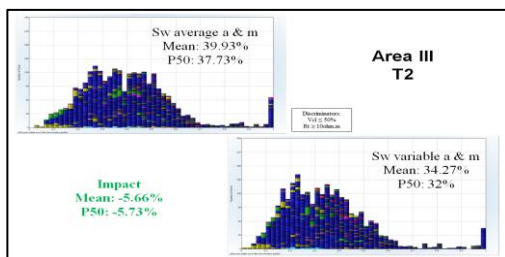


Fig. 18. S_w histogram comparison of the T2 sand Area III.

The T3 sand histograms (Fig. 18) comparison for calculated S_w show a mean decrease of 9.61% when S_w is calculated using variable a and m , instead of the average values.

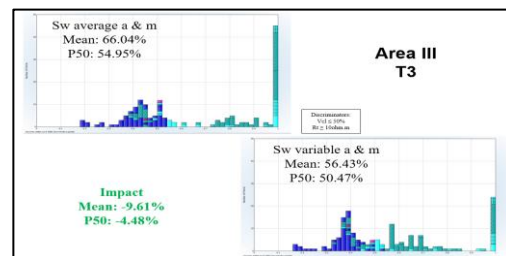


Fig. 19. S_w histogram comparison of the T3 sand (Area III).

S_w estimations for Area III using average a and m values, was mostly overestimated in the T1 sand which is the cleanest reservoir sand within Area III. The more the reservoir was rich in clay, the smaller was the difference in S_w calculations using average and variable a & m values. When comparing T1 versus T2 sands, they differ in reservoir quality. The mean V_{cl} for the T1 is 18% and the ϕ_e is 28% and the mean V_{cl} for the T2 is 28% and the ϕ_e is 25%. Calculated S_w using the variable a & m values is notably corrected in the clean reservoir sands (T1) compared to the more clay rich sands (T2 and T3). T3 histogram comparison shows the highest improvement, and this can be associated to the update of clay endpoints and re-zonation.

It is important to highlight the fact that good reservoir quality intervals (RT0, RT1, RT2) (Table 7) will have their S_w calculations improved as previous average values ($a=1$ & $m=1.66$) were related to rock types classified as RT3, RT4 and RT5, which are mainly shaly sandstones to shale rocks.

A summary of analyzed statistical data from the T1, T2 and T3 sands for all the 4 areas from TCA are presented in Table 9. Average decrease in S_w is from 42% to 37% with improvements varying from 6 to 20%.

Table 9. Summary of S_w histogram comparison for all Areas (TCA) using fixed and variable a and m .

Sw Models	Area I			Area II			Area III			Extended Petro.		
	Sw(%)			Sw(%)			Sw(%)			Sw(%)		
	T1	T2	T3	T1	T2	T3	T1	T2	T3	T1	T2	T3
Indonesian/a:1.18 & m:1.66/Rw:1.18 @ 67°F	33.9	34.8	43.0	43.9	31.6	53.9	34.2	39.9	66.0	39.3	36.0	46.3
Indonesian/a & m: variable /Rw: 1.18 @ 67°F	31.0	31.7	39.5	41.3	29.4	48.7	27.2	34.3	56.4	33.6	29.5	41.7
Difference (%)	-2.8	-3.2	-3.5	-2.6	-2.2	-5.2	-7.0	-5.7	-9.6	-5.7	-6.5	-4.6
Improvement (%)	-8.3	-9.1	-8.1	-5.9	-7.0	-9.7	-20.4	-14.2	-14.6	-14.4	-18.0	-10.0

5.3 Impact on Stock Tank Oil Initially In Place

Since the commercial purpose is to know the current reserves volume, before going to production, determining accurate water saturation for a reservoir is vital. S_w is used to calculate the oil saturation ($S_o = 1 - S_w$), which is the real quantity of interest. STOIP estimations were made for all studied areas (Area I, Area II, Area III & Extended Petro.) using the S_w calculated with fixed average a and m values and compared to estimations using S_w calculated with variable a and m (Table 10). Estimates were done only for T1 and T2 sands, as previous estimates for Static Model update, Material Balance and Simulation only involve these reservoirs.

Table 10. STOIP estimations for the T-unit sands from all TCA areas using variable a & m .

Area	Reservoir	Updated Sw using variable a & m				
		Net Volume	Pore volume	Sw	So (1-Sw)	STOIP
		MM ft3	MM RBls	v/v	v/v	MMBls
I	T2 Sand	572.81	32.93	0.317	0.683	22.18
	T1 Sand	173.82	9.71	0.31	0.69	6.61
II	T2 Sand	430.92	23.71	0.294	0.706	16.51
	T1 Sand	281.14	15.07	0.413	0.587	8.72
III	T2 Sand	1638.17	86.54	0.343	0.657	56.07
	T1 Sand	1215.35	67.45	0.272	0.728	48.43
Ext. Petro	T2 Sand	1988.86	109.75	0.295	0.705	76.31
	T1 Sand	1073.78	60.91	0.336	0.664	39.89
		7375	406	0.323	0.678	274.71

From left to right: Column 1: Study area analyzed; Column 2: Reservoir analyzed; Column 3: Net volume (in millions of cubic feet); Column 4: Pore volume (in millions of reservoir barrels); Column 5: Average water saturation using average variable a & m values; Column 6: Average oil saturation using variable a & m ; Column 7: Stock tank oil initially in place using variable a & m

Table 11 shows how STOIP estimations are in comparison with the actual recovery of TAM Central. Ambastha [27] and Lyons, et al. [28] refer to the following ranges regarding primary oil production for heavy oil: 5 to 10% and 7 to 13% respectively. 13.7% found is comparable with Lyon’s range but out of Ambastha’s.

Table 11. STOIP estimations comparison and actual recovery for T1 and T2 sands of TCA

Model	Average S_w (%)	STOIP (MMbbls)	Actual recovery (%)*
Static update	66	175	21.5
Material Balance	----	195	19.3
Simulation	----	209	18.0
Static update including S_w	36.7	252	14.9
Variable a & m	32.3	275	13.7

*estimated with 37.62 MMbbls (October 2018)

Conclusions

- The Basic Petrophysics Property Index (BPPI) appears to be the most suitable Heterogeneity Index (HI) for estimating tortuosity (a) and cementation factor (m) as variable parameters based on core data and the inverse proportionality of these.
- It was found that depositional environment is an important feature to consider when relating a & m to heterogeneity as different set of adjustments were applied to the two core data set during calibration (well 1M101 in a fluvial system and 9B111 in a deltaic system).
- When formation heterogeneity is reflected in variable a and m , water saturation (S_w) improves in average from 41.9% to 38%. Considering only the T1 and T2 reservoirs intervals, STOIP estimation in terms of actual recovery (using 37.62 MMbbls as of October 2018) represents 13.7%, which is now matching better the expected primary recovery.
- Despite of the low quantity of core data regarding electrical properties, properly relating these to reservoir heterogeneity allows improvements in S_w with higher impact in good quality reservoir rock (better properties), as now the variable a & m are not a value related to regular to poor quality rock (current core data average), only samples tested due to unconsolidation of the formation.

The authors would like to acknowledge F. Graanoogst (Petrophysics Specialist), P. Naigi (Sr. Petrophysicist), J. Oedietram (Sr. Petrophysicist), R. Ramdajal (G&G Teamleader), B. Nandlal (Functional Subsurface Support Division Manager) for their comments and encouragement during this project.

References

- 1 G. M. Hamada, A. Almajed, T. Okasha, and A. Algateh, Uncertainty analysis of Archie’s parameters determination techniques in carbonate reservoirs: Journal of Petroleum Exploration and Production Technology, November, pp.1-10 (2012)
- 2 J. H. Schon, Physical properties of Rocks, Elsevier, pp. 273 – 336 (2011)
- 3 A. M. Attia, Effects of petrophysical rock properties on tortuosity factor. Journal of Petroleum Science Engineering, 48 (3-4), pp 185-198 (2005)
- 4 D. Tiab and E. C. Donaldson, Petrophysics: Theory and practice of measuring reservoir rock and fluid transport properties, 3rd ed. Gulf Professional Publishing. Houston, Texas, USA. pp. 976 (2012)
- 5 M. El Sharawy and B. S. Nabawy, Determining the porosity exponent m and lithology factor a for sandstones and their control by overburden pressure: AAPG Bulletin, pp. 1893-1910 (2018)
- 6 E. R. Acosta, A. Mijland and B. Nandlal, Detailed assessment for water saturation equations for determining the proper S_w model for unconsolidated sandstones in Tambaredjo field, Suriname. 22nd ICGPE. July 15-16, 2020 at Copenhagen, Denmark. pp. 371, 372. (2020).

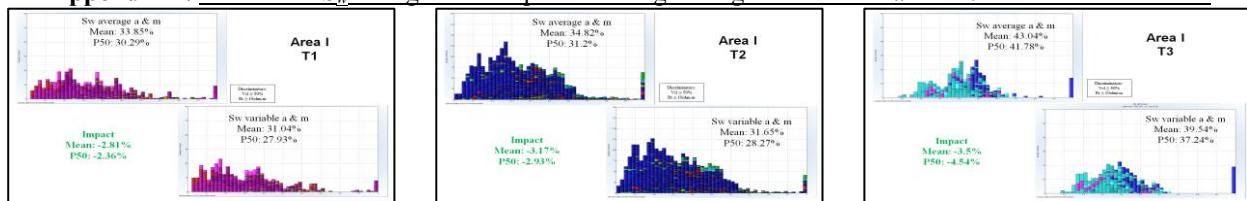
- 7 A. Poupon and J. Leveaux, Evaluation of water saturation in shaly formations. *SPWLA 12th Annual Logging Symposium Transactions* (1971).
- 8 G. E. Archie, The electrical resistivity log as an aid in determining some reservoir characteristics: AIME Transactions, 146, pp. 54-62. (1942)
- 9 E. R. Acosta and E. Rosales Z., Tortuosity and Cementation Factor Parameters: A Review on their Determinations. Researchgate.com (2017)
- 10 M. Pinas and E. R. Acosta, Impact of tortuosity and cementation factor in water saturation calculations in heterogeneous sands of the Tambaredjo Field, Guiana Basin, Suriname. Researchgate.net (2019)
- 11 Staatsolie Maatschappij Suriname N.V., Development Drilling Program 2009 Tambaredjo Field. unpublished (2009)
- 12 F. Angel, Substituting Traditional Cutoff Parameters by a More Practical Novel Methodology for Estimating Net Pay Intervals in Shaly Sands, PDVSA (2018)
- 13 J. Kozeny, Ueber kapillare Leitung des Wassers im Boden. *Sitzungsber Akad. Wiss., Wien*, 136(2a): 271-306. (1927)
- 14 P. C. Carman, Flow of gases through porous media. Butterwoths, London, UK. (1956)
- 15 O. Jude and A. Mehmet, Enhanced Reservoir Description: Using core and log Data to Identify hydraulic (Flow) Units and Predict Permeability in Un-cored Intervals/Wells (1993)
- 16 O. Amaefule and M. Altunbay, SPE Enhanced Reservoir Description: Using Core and Log Data to Identify Hydraulic (Flow) Units and Predict Permeability in Uncored Intervals/Wells, SPE 26436 (1993)
- 17 R. Woodhouse, Athabasca Tar Sands Reservoir Properties Derived from Core and Logs. SPWLA 17th annual Logging Symposium Transactions (1976)
- 18 P. Simandoux, Dielectric measurements on porous media application to the measurement of water saturations: study of the behavior of argillaceous formations: *Revue de l'Institut Francais du Petrole* 18, Supplementary Issue, pp. 193-215 (1963)
- 19 C. Bardon and B. Pied, Formation water saturation in shaly sands: *SPWLA 10th Annual Logging Symposium Transactions*, Paper Z, 19 (1969).
- 20 E. R. Acosta, Petrophysical Model for High Irreducible Water Saturation Reservoirs in Oficina Formation (in Spanish). Master's Thesis. La Universidad del Zulia. Maracaibo, Venezuela (2006) <http://dx.doi.org/10.13140/RG.2.2.22760.47369>
- 21 Baker Hughes Inc., Field optimization using horizontal wells (feasibility study). Dynamic modelling. pp 47-56 unpublished (2015)
- 22 S. Kolodzie, Analysis of pore throat size and use of the Waxman-Smiths Equation to determine OOIP in Spindle Field, Colorado. *SPE 55th Annual Fall Technical Conference*, Paper 9382, pp 10 (1980)
- 23 E. D. Pittman, Relationship of Porosity and Permeability to various Parameters Derived from Mercury Injection-Capillary Pressure Curve for Sandstone. *AAPG Bulletin*, 76 pp 191-8 (1992)
- 24 S. J. Blott and K. Pye, Gradistat: A grain size distribution and statistics package for the analysis of unconsolidated sediments. Surface Processes and Modern Environments Research Group, Department of Geology, Royal Holloway University of London, Egham, Surrey, TW20 0EX, UK, pp. 1237-1248. (2001)
- 25 M. Pinas, Determination of tortuosity (a) and cementation factor (m) as a variable parameter in T-Unit in Tambaredjo Central Field. BSc. Thesis. Anton de Kom Universiteit van Suriname. unpublished (2019)
- 26 J. Jowintinie, R. Ramadajal, A. Redjosentono, J. Oedietram, and E. Acosta, Advanced Facies Rock Typing Approach for 3D Geocellular Static Modeling for Polymer Flooding in the Tambaredjo Oil Field, Suriname. AAPG ICE 2019, Buenos Aires, Argentina, 27 – 30 August (2019)
- 27 A. Ambastha, SPE Reprint Series No. 61. Heavy oil recovery (2008)
- 28 W. Lyons, G. Plisga, and M. Lorenz, Standard Handbook of Petroleum and Natural Gas Engineering (Third Edition), pp. 225-228 (2016)
- 29 M. R. Wyllie and W. D. Rose, Some theoretical considerations related to the quantitative evaluation of the physical characteristics of reservoir rocks from electrical log data. AIME 189, pp. 105-118. (1950)
- 30 W. O. Winsauer, H. M. Shearin, P. H. Masson, and M. Williams, Resistivity of brine saturated sands in relation to pore geometry: *American Association of Petroleum Geologists Bulletin*, v. 36, no. 2, pp. 253-277 (1952)
- 31 J. E. Carothers, A statistical study of the formation relation: *The Log Analyst*, v. 9, p. 13-20. (1968)
- 32 C. R. Porter and J. E. Carothers, Formation factor-porosity relation from well log data: *Soc. Professional Well log Analysts*, 11th Annual Logging Symposium, Trans., Paper D (1970)
- 33 D. K. Sethi, Some considerations about the formation resistivity factor-porosity relationships: *Soc., Professional Well Log Analysts*, 20th Annual Logging Symposium Trans., Paper L (1979)
- 34 G. V. Keller, Electrical properties of rocks and minerals. In: Carmichael, R.S. Ed. *Handbook of Physical Properties of Rocks*, Vol. 1. CRC Press, Boca Raton, FL, pp. 217-293 (1982)
- 35 M. A. Lovell and P. A. Pezard, Electrical properties of basalts from DSDP Hole 504B: a key to the evaluation of pore space morphology, *Geological Applications of Wire line Logs*, Geological Society, London, pp. 339 – 345. (1990)
- 36 R. Ehrlich, E. L. Etris, D. Brumfield, L. P. Yuan, and S. J. Crabtree, Petrography and reservoir physics III — Physical models for permeability and formation factor. *American Association Petroleum Geologists*. 75, pp. 1579-1592. (1991)
- 37 H. S. Salem and G. V. Chilingarian, The cementation factor of Archie's equation for shaly sandstone reservoirs: *Journal of Petroleum Science and Engineering*, March, pp. 83-93 (1999)
- 38 Schlumberger, A review of New Petrophysical Data and Analysis in the Tambaredjo field. (2009) unpublished
- 39 E. Larreal (2015), Petrophysical evaluation Suriname – Guyana Basin April, pp. 39 unpublished (2015)

Appendix

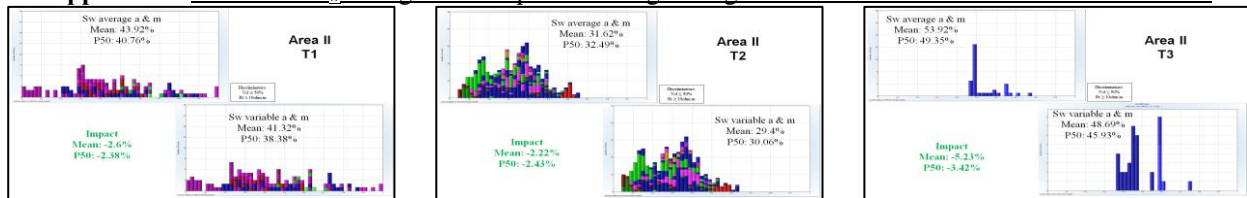
Appendix A. Summary of previous studies regarding a and m determination.

Researcher(s)	Year	Findings	Proposed		Comments
			a	m	
Archie [8]	1942	Values related to consolidation of the sandstone sample	1	2	For clean sands or carbonates
Wyllie and Rose [29]	1950	m shows wide variations from sample to sample, formation to formation, interval to interval in the same medium, and from medium to medium			
Winsauer, <i>et al.</i> [30]	1952	Generalized a from 1 to the term tortuosity factor, so that it could accommodate a variety of sandstone types	0.62	2.15	Also known as Humble. Unconsolidated sandstones
Carothers [31]	1968	Found different values for sands depending on the shalyness and lithologies	1.45	1.54	Average sands (fairly shaly)
			1.65	1.33	Shaly Sands
			1.45	1.70	Calcareous sands
			0.85	2.14	Carbonates
Porter and Carothers [32]	1970	Found new values for other formations	2.45	1.08	Pliocene sands, southern California, USA
Sethi [33]	1979		1.97	1.29	Miocene sands, Texas-Louisiana Gulf Coast, USA
Keller [34]	1982	m is affected by lithology, porosity, pore throat size, degrees of compaction and cementation, and age		$\phi(2.05-\phi)$	
Lovell and Pezard [35]	1990		6.2	1.05	
Ehrlich, <i>et al.</i> [36]	1991	m varies widely and changes continuously due to variations in depositional subfacies			
Salem and Chilingarian [37]	1999	m indicates reduction in pore openings. a has effect on various parameters such as porosity (ϕ), permeability (k), specific surface tension (s) and formation factor (F), hence, its effect on m is significant			
Acosta [20]	2006	S_w values could be overestimated from 6 to 18% when a and m values are different from recommended shaly sand ones	1 to 1.65 depending on V_{sh} ranges	2 to 1.33 depending on V_{sh} ranges	Oficina Formation, Eastern Basin Venezuela
Schlumberger [38]	2009	S_{wir} values are due to the wide variation in m and pore connectivity. An alternate way to estimate m was proposed using microresistivity	1	1.69	Tambaredjo field, Suriname
Schon [2]	2011	a and m , can be related to the pore geometry (texture) of the rock			
Hamada, <i>et al.</i> [1]	2012	a and m become more sensitive to pore pattern distribution and lithofacies properties			
Larreal [39]	2015	m varies from 1.48 to 1.72 within the region		1.6	Guyana Basin core data
Acosta and Rosales [9]	2017	S_w values could be overestimated from 6 to 18% when a and m values are different from recommended shaly sand ones	$0.285 \times \ln(V_{sh}) + 2.069$	$-0.29 \times \ln(V_{sh}) + 0.899$	Oficina Formation, Eastern Basin Venezuela
Pinas and Acosta [10]	2019	Values depend on the approach (free regression fitting or forced regression fitting) Different pair of values for each cored well indicates field heterogeneity influence. Using fixed average values for the entire field will mislead S_w calculations.			Tambaredjo field, Suriname

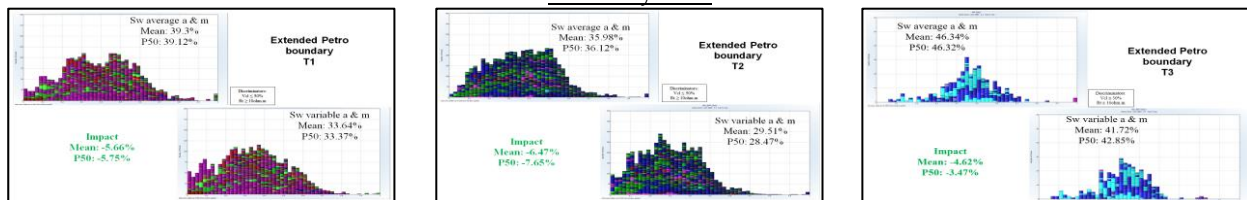
Appendix B. Indonesian S_w histograms comparison using average vs. variable a and m . T-Unit sands. Area I



Appendix C Indonesian S_w histograms comparison using average vs. variable a and m . T-Unit sands. Area II



Appendix D Indonesian S_w histograms comparison using average vs. variable a and m . T-Unit sands. Extended Petro Boundary Area



Data-driven methods to predict recovery factor in Water-Alternating-Gas (WAG) laboratory coreflood experiments

Akpevwe Kelvin Idogun¹, Lesley A. James^{1*}

¹Hibernia EOR Research Group, Department of Process Engineering, Memorial University of Newfoundland, St. John's, NL, Canada, A1B 3X5

Abstract. Water Alternating Gas (WAG) flooding employs the benefits of microscopic and macroscopic sweep efficiency to the Enhanced Oil Recovery (EOR) process. The complexity of the WAG technology remains an impediment to its widespread application, and a good understanding of the physics behind the displacement of oil through the porous medium is imperative for the success of the WAG process. As a result, coreflood studies are an integral subset of full field WAG project assessment, feasibility and approval workflow. These experimental procedures also provide insights into the WAG Incremental Recovery Factor (IRF) as a precursor to field scale reservoir simulation. However, these experiments tend to be tedious, expensive, time-consuming and fraught with uncertainties from domain expertise and other factors. In order to overcome the experimental limitations outlined above, this paper presents a data-driven approach to address the oil recovery performance of the WAG EOR process. Consequently, we apply and evaluate the performance of three deterministic models namely Artificial Neural Network (ANN), Extreme Gradient Boosting (XGBoost), and Random Forest (RF) towards the prediction of (IRF) of the WAG coreflood process using 150 experimental datapoints. The IRF is predicted as a function of 17 independent input variables commonly reported in experimental studies including pressure (MPa), temperature (°F), porosity (%), porous medium (sandstone, carbonate), viscosity (cP), API, brine salinity (ppm), gas type (CO₂, N₂, Flue and Hydrocarbon.), slug size, injection mode (secondary, tertiary), cycle/frequency, WAG ratio, injection sequence (W-A-G, G-A-W), core length, water injection rate (cm³/min), mode (tertiary, secondary) and miscibility (miscible, immiscible). Results show that all three models are capable of predicting WAG IRF with the ANN model exhibiting the best performance with an R² of 0.97, MSE of 15.96, RMSE of 4, MAE of 1.85 and MAPE of 0.07 for the full dataset. Graphical and statistical analysis show that the models can describe the WAG RF with reasonable accuracy compared to the experimental data. For the purpose of explaining interpretability, a sensitivity study was also applied for the determination of the most influential independent parameters affecting the RF of the WAG process at core scale. To the best of our knowledge, this is the first time a data-driven modelling study will be applied to laboratory coreflood studies as a fast and reliable WAG EOR predictive and screening tool.

1 Introduction

Gas injection offers the advantage of microscopic displacement and sweep efficiency through the reduction of the oil viscosity and the increase in capillary number. A variety of gases utilized for EOR have been reported in the literatures namely CO₂, N₂, H₂S and hydrocarbon gas [1]. Gas EOR can be applied through a variety of schemes like the Continuous Gas Injection (CGI) and the Gas Assisted Gravity Drainage (GAGD) processes.

A drawback of Gas EOR is viscous fingering, gravity override and high mobility. However, injecting water alternately with Water Alternating Gas (WAG) flooding helps overcome these drawbacks through improved microscopic and macroscopic efficiency. Early laboratory and field studies reported the efficiency of water in reducing the relative permeability to gas in a porous medium thereby reducing the gas mobility and increasing the viscosities of the fluids in the region of displacement when injected alternately with gas [2–4]. Over the years

* Corresponding author: ljames@mun.ca

WAG has grown to become an efficient technology for the EOR process.

Different WAG injection schemes exist and depending on economic and reservoir/injection fluid

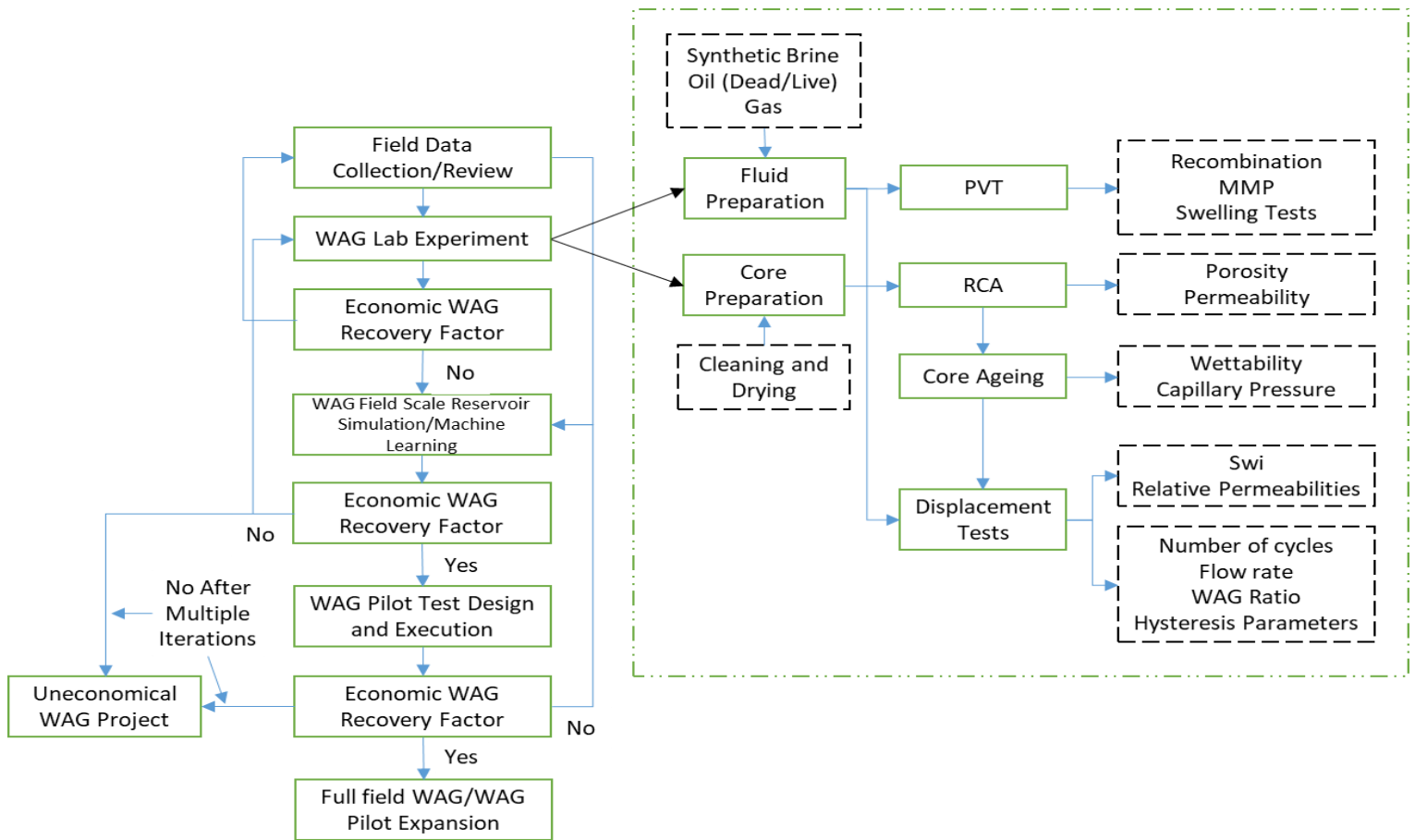


Figure 1: Interplay between workflows for WAG field-scale project approval and WAG laboratory process (Modified from [22], [24])

conditions, they can be classified as miscible or immiscible WAG. Acid gases have been reported to give lower MMP values as compared to other gases utilized for the WAG process, though they have also been reported as corrosive to the well equipment [5]. The most common gas utilized for WAG EOR as reported in literatures is CO₂. Historically, CO₂ WAG was applied for the first time in 1957 at field scale in the North Pembina Cardium formation, Alberta, Canada [6].

Figure 1 shows the interplay between workflows for WAG field-scale project approval and WAG laboratory process. The laboratory process (core and fluid preparation) is an integral part of the WAG field-scale development workflow. These experiments are however expensive, complex, and time-consuming with a high level of variation in the reliability and consistency of experimental data. For instance, it takes weeks to run experiments to determine Minimum Miscibility Pressure (MMP), wettability and irreducible water saturation [7–10]. Also, process failure during coreflooding can lead to loss of reliability and consistency with experimental data. An example is cited in Zhang *et al.* (2010) [11] where

excessive water was injected due to pump failure during an overnight flood thereby resulting in high water/gas injection ratio.

For this reason, it is proposed that Machine Learning (ML) and regression-based methods like Response Surface Methodology (RSM) can help with fast screening and prediction of WAG IRF pending results from laboratory tests. ML, as a subset of Artificial Intelligence (AI), utilizes computer programmed algorithms for pattern recognition in data, for prediction or forecasting, with learning and adaptation being evaluated by the aid of a metric or a loss function [12], [13]. ML models are categorized into supervised learning, unsupervised learning and reinforcement learning, and has been extensively applied in the oil and gas industry [14–18].

Jaber *et al.* reported the application of data-driven models to predict WAG recovery factor based on Design of Experiments [19], [20]. They applied Central Composite Design (CCD) and Box-Behnken Design (BBD) to develop regression models capable of predicting WAG recovery factor from heterogeneous clastic reservoirs with data obtained from different reservoir

simulation runs. In another study, data-driven models were applied to predict field-scale WAG recovery factor from WAG field pilot data [21–23]. To the best of our knowledge, a data-driven ML modelling study has not been applied to laboratory coreflood studies for WAG recovery factor prediction.

The objective of this study is to generate and compare the performance of fast and reliable data-driven models capable of predicting the WAG Incremental Recovery Factor (IRF) from laboratory coreflood experiments as a function of pressure, temperature, porosity, porous media, viscosity, API, brine salinity, gas type (CO₂, N₂, Flue gas etc.), slug size, Injection mode (secondary, tertiary), cycle/frequency, WAG ratio, WAG type/Injection sequence (W-A-G, G-A-W), water injection rate, core length, permeability and miscibility.

2 Methodology

In this study, we apply ML techniques for the prediction of IRF for WAG. The following section briefly describes the methodology utilized for this study.

2.1 Data Collection

The data used in this study were sourced from various literatures on WAG experimental studies [25–43]. The size of the sourced datasets involved 150 datapoints with 80% (120) of the dataset used for training and 20% (30) reserved for training the ML algorithm. The independent variables and input data for the dataset are commonly used experimental data from literatures including pressure (MPa), temperature (°F), API, viscosity (cP), permeability (mD), porosity (%), brine salinity (ppm), water injection rate (cm³/min), gas injection rate (cm³/min), slug size, porous media (sandstone, carbonates), core length (cm), miscibility (miscible, immiscible), cycles, WAG ratio, aqueous phase (synthetic brine, reservoir brine), gas type (CO₂, N₂, flue gas, hydrocarbon gas), cumulative water injected (PV), cumulative gas injected (PV), cumulative fluid injected (PV), WAG Type/injection sequence (G-A-W, W-A-G) and WAG mode (secondary, tertiary); with the dependent variable being the IRF (%). Data imputation was applied to compensate for missing values by selecting carefully from a list of data imputation techniques.

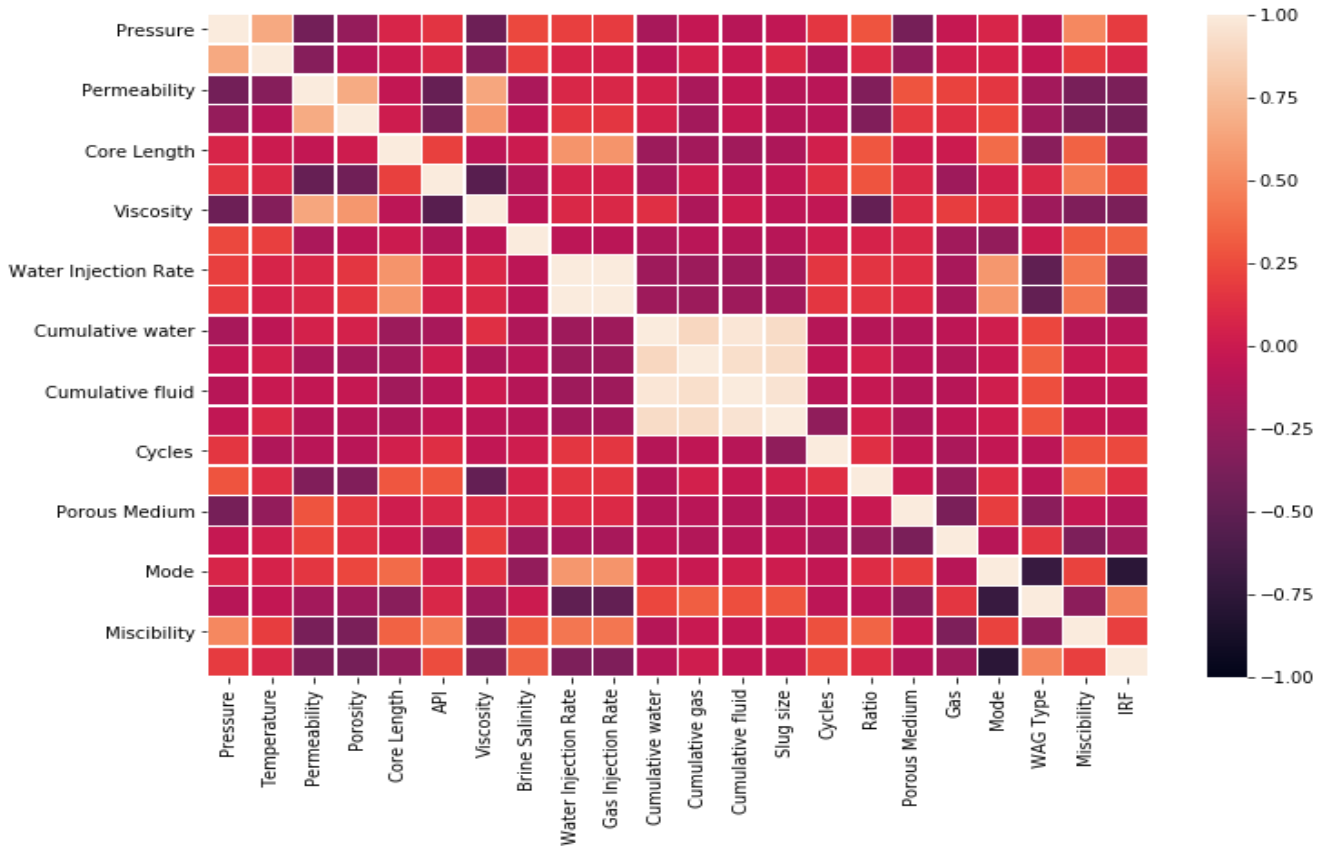


Figure 2: Correlation Matrix for Independent and dependent features of WAG dataset

2.2 Model Evaluation

ML algorithms were evaluated with performance indices to measure their efficiency which is usually indicated with a loss function. The accuracy of the models was evaluated using various statistical techniques including Mean Squared Error (MSE), Root Mean Squared Error (RMSE), Mean Absolute Percentage Error (MAPE), Mean Absolute Error (MAE) and the co-efficient of determination (R^2). The following statistical models for evaluation are defined as follows:

$$MSE = \frac{1}{N} \sum_1^N (IRF_1^{Actual} - IRF_i^{Predicted})^2 \quad (1)$$

$$RMSE = (MSE)^{1/2} \quad (2)$$

$$R^2 = 1 - \frac{\sum_1^N (IRF_i^{Actual} - IRF_i^{Predicted})^2}{\sum_1^N (IRF_{Ave}^{Actual} - IRF_i^{Actual})^2} \quad (3)$$

$$MAPE = \frac{1}{N} \sum_i^N \left| \frac{IRF_i^{Actual} - IRF_i^{Predicted}}{IRF_i^{Actual}} \right| \quad (4)$$

$$MAE = \frac{1}{N} \sum_i^N |IRF_i^{Actual} - IRF_i^{Predicted}| \quad (5)$$

2.3 Feature Selection

We commenced ML modelling by pre-processing collected data and selecting the most important independent variables or features affecting the target variable (IRF). This was achieved with a combination of various statistical techniques, combined with domain knowledge. Independent variables that exhibit collinearity will lead to redundancy in our model. The correlation plot in **Figure 2** shows the correlation between the 21 independent features and the target variable. We observe at a glance that cumulative gas, water and fluid injected have low correlation with the target variable (IRF). It is also pertinent to note that these aforementioned independent variables also show strong correlation and collinearity with each other and the slug size. Collinearity was determined with the Variance Inflation Factor (VIF) given mathematically as:

$$VIF = \frac{1}{1 - R_i^2} \quad (6)$$

Water and gas injection rates also show strong correlation and collinearity as their values are usually closely reported to each other in literatures. Based on the results of the VIF, gas injection rate, cumulative gas, water and fluid injected were dropped as independent variables. We applied domain knowledge in retaining temperature and slug size in the model regardless of their low values of correlation with the target variable as both have been shown in literatures to influence the WAG process [28]. This feature engineering exercise guided the

decision to reduce the size of the independent variables from 21 to 17 for the modelling study.

2.4 Feature Ranking and sensitivity analysis with SHAP (SHapley Additive exPlanations) Plots

The advent of complex models like deep learning and ensemble methods mean that a high accuracy can be achieved for large datasets. However, the trade-off is that these models often lack interpretability. SHAP (SHapley Additive exPlanations) plots help address this challenge by providing a unified framework for prediction interpretation [44].

The sum of all feature contributions for an occurrence is expressed mathematically as:

$$\sum_{i=1}^n \phi_i(\hat{f}) = \sum_{i=1}^n (\beta_i x_i - E(\beta_i X_i)) = (\beta_0 + \sum_{i=1}^n \beta_i x_i) - (\beta_0 + \sum_{i=1}^n \beta_i X_i) = \hat{f}(x) - E(\hat{f}(X)) \quad (7)$$

where ϕ_i is the contribution of the i-th feature on the prediction $\hat{f}(x)$ and $E(\beta_i X_i)$ is the estimate of the mean effect for the i-th feature [45]. The shapely value of a feature is expressed mathematically as:

$$\phi_i = \sum_{S \subseteq \{x_1, \dots, x_n\} \setminus \{x_i\}} \frac{|S|!(n-|S|-1)!}{n!} ((S \cup \{x_i\}) - (S)) \quad (8)$$

where S represents the subset of the features utilized in the model, x represents a vector of the feature values and n represents the number of features.

2.5 WAG Modelling

In this section, we briefly introduce the Machine Learning algorithms applied in this study for the prediction of Recovery Factor (RF) for WAG EOR. The field of Artificial Intelligence (AI) has gained wide popularity in different fields over the years. The application of AI in the oil industry is diverse and transcends different subsets of the oil and gas value chain [46–50]. The application of Machine learning (ML) for the determination of Recovery Factor has been reported in literatures [51–55]. ML is a subset of AI and works based on pattern recognition. Various algorithms are applied to allow computers learn through pattern recognition, to aid prediction and forecasting, whilst optimizing the performance of the model against a standardized metric. The models applied in this study for comparative model performance are briefly described below.

2.5.1 Artificial Neural Networks

Artificial Neural Networks (ANN), also famously known as a universal approximators, can be utilized for supervised learning problems. The simplest ANN structure is called the perceptron which consists of just an

input layer and an output node. Alternatively, multi-layer ANN architecture is composed of an input layer, a hidden layer and an output layer. The ANN is generally represented by the equation below:

$$y = \varphi(w^T x + b) \quad (9)$$

where w represents the weight, b represents the bias and φ represents the activation function. ANN gives the relationship between independent and dependent variable by mimicking the network of neurons present in the human brain to process the non-linear transformation of input data. ANN performance is highly dependent on the scale of the input variables, network structure, data size, activation function and learning rules. The three commonly used activation functions are the hyperbolic function, sigmoid function and the Rectified Linear Unit (ReLU) which is applied when the target variable is continuous [56]. The multi-layer ANN uses an iterative process called backpropagation to reduce the prediction errors until the condition for model accuracy is attained. The optimization techniques for reducing these errors include Stochastic Gradient Descent (SGD), Gradient Descent (GD), Adaptive moment estimation (Adam), Adaptive Gradient (AdaGrad) and Root Mean Square Propagation (RMSProp) [57].

2.5.2 Random Forest

Random Forest algorithm was proposed by Breiman in 2001 [58]. The Random Forest algorithm functions based on the bagging principle and is built on an ensemble of decision trees. Ensemble learning involves the combination of many weak learners to create a strong ensemble capable of high prediction accuracy. Bootstrapping is a statistical technique in which samples from a dataset are drawn with replacement [12]. Bootstrap Aggregation or Bagging reduces the prediction variance by sampling each ensemble model with replacement, to generate predictions which are in turn averagely aggregated to produce the bagged model's prediction [59]. Through bootstrapping, the trees are grown by randomization of the feature subsets (usually controlled by a parameter k) to produce the best nodal split, for the purpose of reducing feature correlation among trees. In the case of classification, prediction is achieved by majority vote while aggregated averaging is used for regression prediction [60].

2.5.3 Extreme Gradient Boosting (XGBoost)

Extreme Gradient Boosting (XGBoost) is a scalable, decision tree-based ensemble machine learning algorithm, introduced by Chen and Guestrin in 2015 [61] and capable of handling classification and regression problems. XGBoost is an improved version of the

Gradient Boosting algorithm proposed by Friedmann [62]. XGBoost differs from the Gradient Boosting algorithm in that the second-order Taylor series expansion is applied to the loss function, thereby leading to faster convergence. Also, the XGBoost algorithm is less prone to over-fitting due to the addition of a regularization term to the loss function. The loss function is given by the following equation:

$$obj^t = \sum_{i=1}^n L(y_i, \hat{y}_i^{(t-1)} + f_t(x_i)) + \Omega(f_t) \quad (10)$$

where L is the loss function and $\Omega(f_t)$ represents regularization parameter which measures the model complexity.

$$\Omega(f_t) = \gamma \cdot T_t + \lambda \frac{1}{2} \sum_{j=1}^T \omega_j^2 \quad (11)$$

where γ is the regularized parameter of the leaf number, λ is the regularized parameter of the leaf weight, T is the number of leaves and ω represents the leaf score. The simplified second-order Taylor series expansion is given below:

$$obj^t = \sum_{i=1}^n \left[L(y_i, \hat{y}_i^{t-1}) + g_i f_t(x_i) + \frac{1}{2} h_i f_t^2(x_i) \right] + \Omega(f_t) \quad (12)$$

$$g_i = \frac{\delta L(y_i, \hat{y}_i^{t-1})}{\delta \hat{y}_i^{t-1}} \quad (13)$$

$$h_i = \frac{\delta^2 L(y_i, \hat{y}_i^{t-1})}{\delta \hat{y}_i^{t-1}} \quad (14)$$

where g_i and h_i are the first and second order derivatives of the loss function, x represents the prediction data and y represents the true response data. Advantages of XGBoost include its ability to handle sparse data as well as faster learning due to parallel and distributed computing.

3 Results and Discussion

Three ML models namely XGBoost, ANN and RF were utilized for predicting Incremental Recovery Factor (IRF) during the WAG process. This section examines the performance of these models using a combination of metrics from statistical analysis as well as parity, prediction and residual plots. A sensitivity analysis is also performed using SHAP plots to determine the most influential selected independent features on the target variable (IRF).

3.1 Comparative Analysis of ML Algorithms

A total of 150 data points were analyzed with three different ML models for WAG IRF prediction. **Figure 3 (a-f)** displays the parity and residual plots for testing, training and full datasets for all three models employed in this study. It can be observed from the parity plots for the test, train and full datasets shown in **Figure 3 (a-c)** that

the ANN model shows the best performance for the test, training and full datasets as more of the datapoints from the ANN model lie on or close to the 45-degree diagonal.

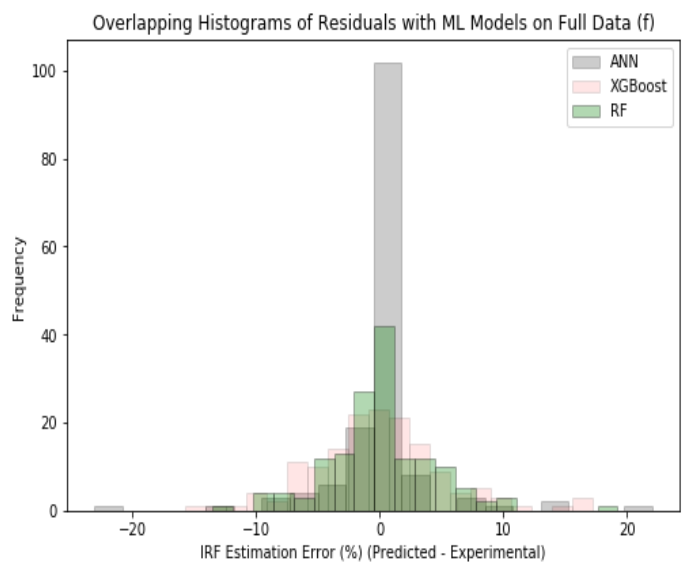
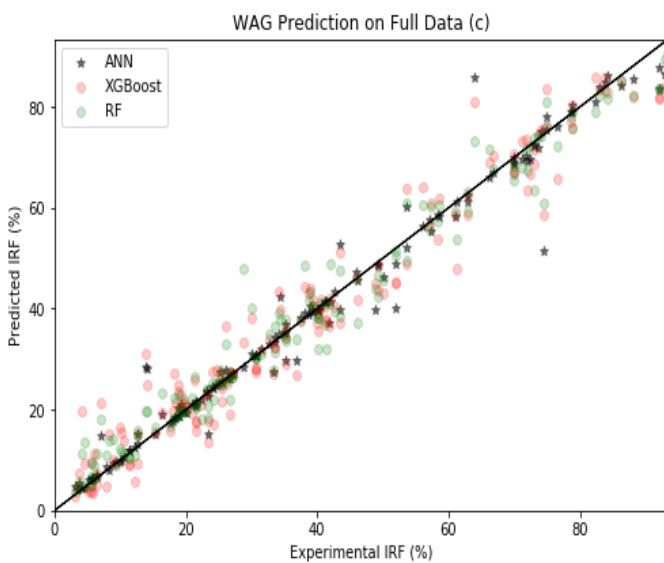
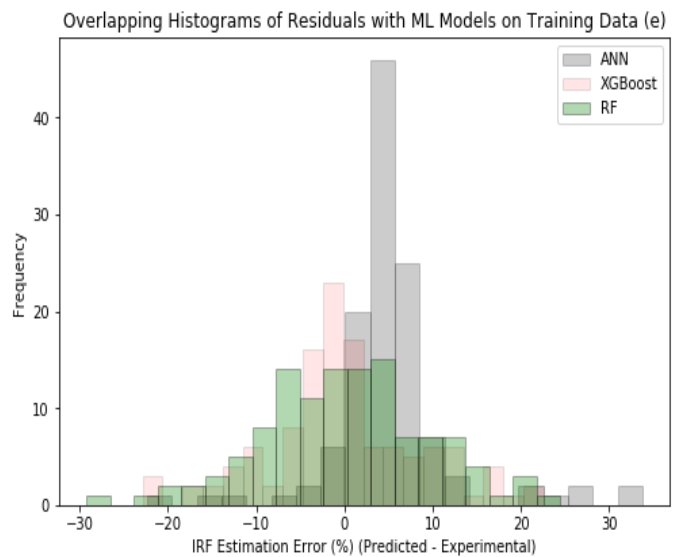
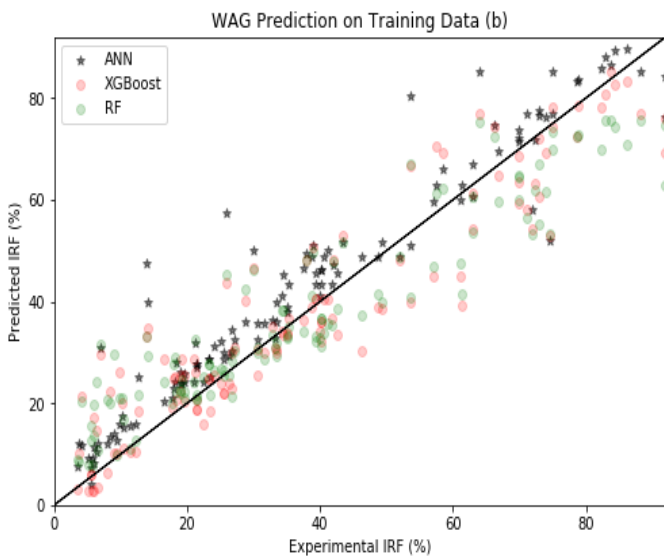
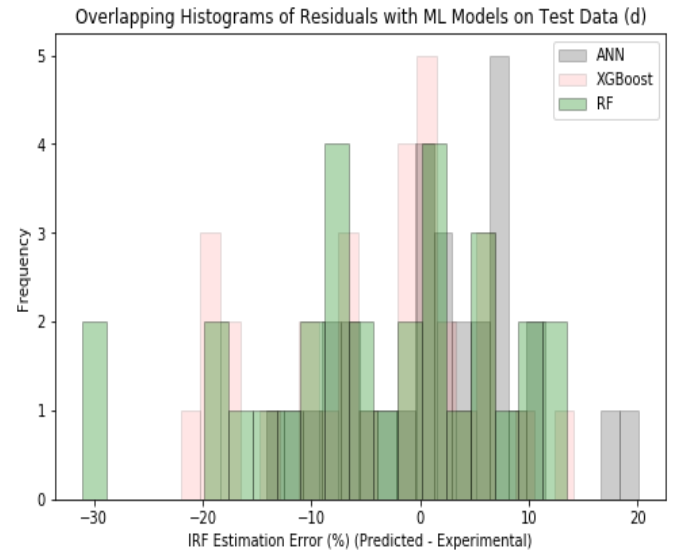
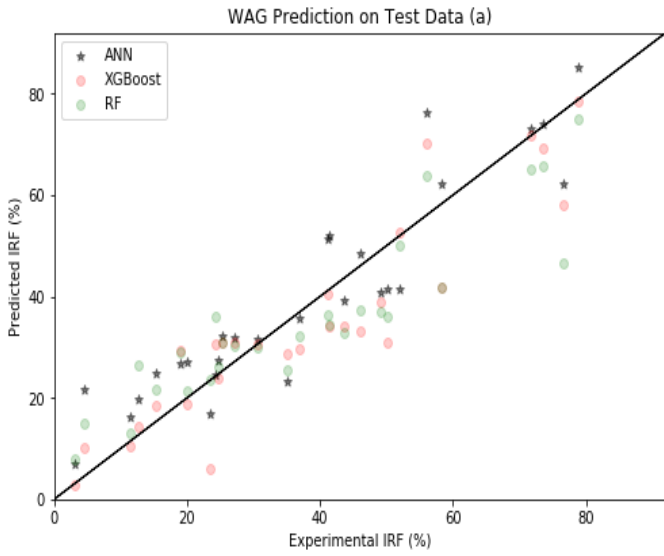


Figure 3: (a-c) Parity plots and residual plots (d-f) for ANN, XGBoost and RF for Test, Training and Full data

The residual error plots as indicated by **Figure 3 (d-f)** show the difference between the predicted and experimental IRF values respectively. **Figure 3 (d-f)** are residual plots for test, training and full datasets. It can be observed that the variance for the ANN model is lower than the variance for the XGBoost and RF models respectively, indicating the superior performance of the ANN model.

The performance of all three models is further validated by their statistical power based upon metrics given in **Table 1**. The statistical metrics for the ANN model are given in bold and can be observed to be better performing than the other two models for test, training and full datasets.

Table 1: Statistical comparative analysis of ML models for Test, Training and Full data

Statistical Estimator	Training Data			Testing Data			Full Data		
	ANN	XGBoost	RF	ANN	XGBoost	RF	ANN	XGBoost	RF
R ²	0.91	0.87	0.85	0.9	0.85	0.79	0.97	0.95	0.97
MSE	58.86	77.07	91.39	66.14	103.19	141.33	15.96	29.75	19.46
RMSE	7.67	8.78	9.56	8.13	10.16	11.89	4	5.45	4.41
MAE	4.66	6.46	7.5	6.54	7.63	9.21	1.85	4.04	3.08
MAPE	0.15	0.32	0.4	0.34	0.22	0.34	0.07	0.2	0.14

3.2 Ranking of Feature Importance and Sensitivity analysis

The influence of the 17 independent variables on the target variable was studied to determine their relative importance on WAG IRF prediction. SHAP plots were utilized for ranking the importance of the features utilized in this study and also giving interpretability to the model. SHAP plots use shapely values for computing the contributions of independent variables for single

predictions for ML models. The seven most influential variables on WAG EOR as indicated from the SHAP plot in **Figure 4** are the mode (secondary or tertiary), number of cycles, miscibility (miscible or immiscible), oil API, gas utilized for the EOR process, reservoir temperature and pressure. The mode being the most influential parameter is in good agreement with a recent study where statistical Design of Experiments (DoE) and Analysis of Variance (ANOVA) were used to rank the main operational WAG parameters [63].

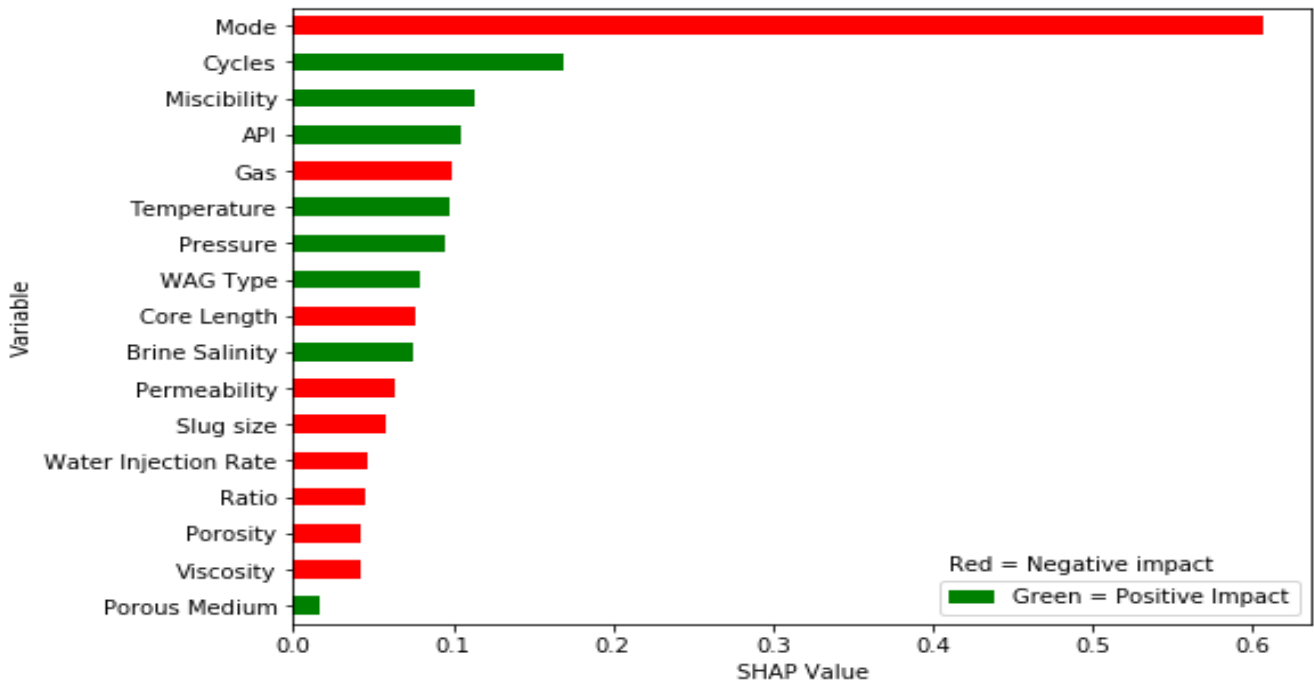


Figure 4: SHAP summary plot showing sensitivity analysis on target variable and variable importance (modified from [64])

The sensitivity plot for the WAG IRF is illustrated in **Figure 4**, showing how the input parameters affect the IRF. Visual observation shows the parameters that positively impact the WAG IRF are represented in green and the parameters that negatively impact the WAG IRF process represented in red. As a result, sensitivity studies indicate that the number of WAG cycles, miscibility, oil API, reservoir temperature and pressure, WAG type or injection scheme, brine salinity and the porous medium positively affect the WAG IRF.

The oil displacement process by water/gas is usually influenced by reservoir permeability and heterogeneities [5]. Permeability contrasts can greatly hinder the WAG process. In a study by *Al-Bayati et al.* [65] and *Xie et al.* [66], the effect of crossflow was investigated and it was observed that the presence of crossflow negatively impacts the RF. In essence, WAG would perform better in a non-communicating reservoir due to the high effect of conformance control. Absolute permeability has also been reported to have a linear relationship with WAG EOR RF [30]. Also, the injection mode (secondary or tertiary) is a critical parameter to be considered during the WAG injection process. WAG in secondary mode has been reported to perform better than WAG in tertiary mode [26], [67]. The higher oil recovery in secondary WAG is attributed to the high initial oil saturation in the reservoir pore matrix which provides a reasonable oil bank for mobilization. For tertiary WAG floods, the lower RF is attributed to water-blocking effect which shields the oil from being contacted by the gas. It is however pertinent to note that the extent of recovery in either mode has been reported to be dependent on the wettability of the system [68].

The type of injection gas used can also negatively impact the WAG process. Carbon Dioxide (CO₂) is the most commonly utilized gas for WAG EOR [6]. Nitrogen (N₂) and Hydrocarbon gas are utilized for their economic benefits, availability and inert nature [69]. However, miscible CO₂ WAG has been reported to give better than recovery than immiscible N₂ WAG [29]. The WAG ratio is defined mathematically as the quotient of the volume of injected water to the volume of injected gas. Optimal value of the WAG ratio reported in literatures is 1:1 [70]. WAG ratios outside this optimum could negatively affect the EOR process.

The effect of core length is an important parameter to consider during the WAG EOR process. Longer cores have been reported as being critical to establishing miscibility during the WAG process for a favourable RF [71], [72]. Furthermore, they are also imperative in examining the effects of gravity segregation [25], [73]. The water and gas injection flow rates during the core flooding procedure should be kept low to ensure stable

floods and is the slowest step in the experimental procedure [38]. The RF has been reported to be affected by the WAG flow rate and is dependent on an optimum value [31]. Slug size is an important parameter that also affects the WAG process and is defined as the volume of water or gas injected per cycle. Optimization of the slug size is imperative as extremely high or low values negatively affect the IRF [36]. The effect of viscosity is observed on the impact of the mobility ratio. Highly viscous oils will lead to unfavourable mobility ratio and poor displacement, thereby leaving a large uncontacted volume of oil [74].

In conclusion, variable importance from SHAP plots indicate that a high oil recovery in terms of IRF is dependent on the represented input parameters. However, the WAG mode, number of cycles, miscibility, oil API, injected gas and reservoir temperature and pressure seem to play a predominant role on oil recovery with regards to IRF.

4 Conclusion

In this study, we proposed three models to predict WAG IRF using machine learning namely; Artificial Neural Networks (ANN), Extreme Gradient Boosting (XGBoost) and Random Forest (RF). The modelling study was initiated with 21 independent features but reduced to a total of 17 using a combination of statistical techniques and domain knowledge. The following conclusions are drawn from analyzing the predicted results and comparing all three ML models:

- 1) ML models can be utilized as predictive and screening tools for the WAG EOR process;
- 2) ANN, XGBoost and RF models are intelligent ML models capable of predicting WAG IRF;
- 3) ANN performs better than XGBoost and Random Forest for WAG IRF prediction;
- 4) Feature ranking and model interpretability with the aid of SHAP plots indicate that the seven most salient features affecting the WAG IRF are the WAG mode, number of cycles, miscibility, API, injected gas and reservoir temperature and pressure.
- 5) Model interpretability, through the use of ML tools like SHAP plots, gives insight into the negative and positive effects of WAG parameters on the IRF.

The authors would like to thank the Hibernia Management and Development Company (HMDC), Chevron Canada Ltd, Petroleum Research Newfoundland and Labrador (PRNL), the Natural Sciences and Engineering Research Council of Canada (NSERC), the Province of Newfoundland and Labrador, and

The 35th International Symposium of the Society of Core Analysts

Mitacs for financial support. We thank our colleagues in the Hibernia EOR Research Group for their technical support.

References

- [1] J. R. Christensen, E. H. Stenby, and A. Skauge, 'Review of WAG Field Experience', *SPE Reserv. Eval. Eng.*, **vol. 4**, no. 02, pp. 97–106, 2001, doi: 10.2118/71203-PA.
- [2] D. M. Beeson and G. D. Ortloff, 'Laboratory Investigation of the Water-Driven Carbon Dioxide Process for Oil Recovery', *J. Pet. Technol.*, **vol. 11**, no. 04, pp. 63–66, 1959, doi: 10.2118/1100-G.
- [3] B. H. Caudle and A. B. Dyes, 'Improving Miscible Displacement by Gas-Water Injection', *Trans. AIME*, **vol. 213**, no. 01, pp. 281–283, 1958, doi: 10.2118/911-G.
- [4] H. D. Holloway, R. A. Fitch, P. A. N. American, P. Corp, F. Midland, and M. Aime, 'Performance of a Miscible Flood with Alternate Gas-Water Displacement', *J. Pet. Technol.*, **vol. 16**, no. 04, pp. 372–376, 1964, doi: 10.2118/626-PA.
- [5] S. Afzali, N. Rezaei, and S. Zendejboudi, 'A comprehensive review on Enhanced Oil Recovery by Water Alternating Gas (WAG) injection', *Fuel*, **vol. 227**, no. February, pp. 218–246, 2018, doi: 10.1016/j.fuel.2018.04.015.
- [6] J. R. Christensen, E. H. Stenby, and A. Skauge, 'Review of WAG field experience', in *Proceedings of the SPE International Petroleum Conference & Exhibition of Mexico*, 1998, pp. 357–370.
- [7] S. M. Fatemi, M. Sohrabi, M. Jamiolahmady, S. Ireland, and G. Robertson, 'Experimental Investigation of Near-Miscible Water-Alternating-Gas WAG Injection Performance in Water-wet and Mixed-wet Systems'. Sep. 06, 2011, doi: 10.2118/145191-MS.
- [8] J. S. Sachdeva, E. A. Sripal, A. Nermon, R. I. Korsnes, M. V. Madland, and L. A. James, 'A Laboratory Scale Approach to Wettability Restoration in Chalk Core Samples', in *International Symposium of the Society of Core Analysts, Trondheim, Norway*, 2018, p. 12.
- [9] E. Sripal and L. A. James, 'Application of an Optimization Method for the Restoration of Core Samples for SCAL Experiments', *Petrophysics - SPWLA J. Form. Eval. Reserv. Descr.*, **vol. 59**, no. 01, pp. 72–81, Feb. 2018.
- [10] M. A. Ahmadi, S. Zendejboudi, and L. A. James, 'A reliable strategy to calculate minimum miscibility pressure of CO₂-oil system in miscible gas flooding processes', *Fuel*, **vol. 208**, pp. 117–126, 2017, doi: 10.1016/j.fuel.2017.06.135.
- [11] Y. P. Zhang, S. G. Sayegh, P. Luo, and S. Huang, 'Experimental Investigation of Immiscible Gas Process Performance for Medium Oil', *J. Can. Pet. Technol.*, **vol. 49**, no. 02, pp. 32–39, Feb. 2010, doi: 10.2118/133203-PA.
- [12] Y. N. Pandey, A. Rastogi, S. Kainkaryam, S. Bhattacharya, and L. Saputelli, *Machine Learning in the Oil and Gas Industry: Including Geosciences, Reservoir Engineering, and Production Engineering with Python*. Apress, 2020.
- [13] H. Belyadi and A. Haghghat, *Machine Learning Guide for Oil and Gas Using Python: A Step-by-Step Breakdown with Data, Algorithms, Codes, and Applications*. Elsevier Science, 2021.
- [14] T. Ertekin and Q. Sun, 'Artificial intelligence applications in reservoir engineering: A status check', *Energies*, **vol. 12**, no. 15. 2019, doi: 10.3390/en12152897.
- [15] M. A. Ahmadi, S. Zendejboudi, and L. A. James, 'Developing a robust proxy model of CO₂ injection: Coupling Box–Behnken design and a connectionist method', *Fuel*, **vol. 215**, pp. 904–914, 2018, doi: <https://doi.org/10.1016/j.fuel.2017.11.030>.
- [16] M. A. Ahmadi and Z. Chen, 'Comparison of machine learning methods for estimating permeability and porosity of oil reservoirs via petro-physical logs', *Petroleum*, **vol. 5**, no. 3, pp. 271–284, 2019, doi: <https://doi.org/10.1016/j.petlm.2018.06.002>.
- [17] H. Vo Thanh, Y. Sugai, and K. Sasaki, 'Application of artificial neural network for predicting the performance of CO₂ enhanced oil recovery and storage in residual oil zones', *Sci. Rep.*, **vol. 10**, no. 1, p. 18204, 2020, doi: 10.1038/s41598-020-73931-2.
- [18] H. H. Alkinani, A. T. Al-Hameedi, S. Dunn-Norman, R. E. Flori, M. T. Alsaba, and A. S. Amer, 'Applications of Artificial Neural Networks in the Petroleum Industry: A Review'. Mar. 18, 2019, doi: 10.2118/195072-MS.
- [19] A. K. Jaber, M. B. Awang, and C. P. Lenn, 'Box- Behnken design for assessment proxy model of miscible CO₂-WAG in heterogeneous clastic reservoir', *J. Nat. Gas Sci. Eng.*, **vol. 40**, pp. 236–248, 2017, doi: <https://doi.org/10.1016/j.jngse.2017.02.020>.
- [20] A. K. Jaber, A. K. Alhuraishawy, I. Ministry, and W. H. AL-Bazzaz, 'A Data-Driven Model for Rapid Evaluation of Miscible CO₂-WAG Flooding in Heterogeneous Clastic Reservoirs', in *SPE Kuwait Oil & Gas Show and Conference*, 2019, p. 14, doi: 10.2118/198013-MS.

- [21] L. Belazreg, S. M. Mahmood, and A. Aulia, 'Novel approach for predicting water alternating gas injection recovery factor', *J. Pet. Explor. Prod. Technol.*, **vol. 9**, no. 4, pp. 2893–2910, 2019, doi: 10.1007/s13202-019-0673-2.
- [22] L. Belazreg and S. M. Mahmood, 'Water alternating gas incremental recovery factor prediction and WAG pilot lessons learned', *J. Pet. Explor. Prod. Technol.*, **vol. 10**, no. 2, pp. 249–269, 2020, doi: 10.1007/s13202-019-0694-x.
- [23] L. Belazreg, S. M. Mahmood, and A. Aulia, 'Random forest algorithm for CO₂ water alternating gas incremental recovery factor prediction', *Int. J. Adv. Sci. Technol.*, **vol. 29**, no. 1, pp. 168–188, 2020.
- [24] Y. C. Itriago, M. Araujo, and J. Molinaris, 'Best Practices for Laboratory Evaluation of Immiscible WAG'. Apr. 14, 2018, doi: 10.2118/190303-MS.
- [25] M. M. Kulkarni, 'Immiscible and Miscible Gas-Oil Displacements in Porous Media', Louisiana State University and Agricultural and Mechanical College, 2003.
- [26] M. M. Kulkarni and D. N. Rao, 'Experimental investigation of miscible and immiscible Water-Alternating-Gas (WAG) process performance', *J. Pet. Sci. Eng.*, **vol. 48**, no. 1, pp. 1–20, 2005, doi: <https://doi.org/10.1016/j.petrol.2005.05.001>.
- [27] S. A. R. Tabatabaei Nezhad, M. Rahimzadeh Mojarad, S. J. Paitakhti Oskouei, J. S. Moghadas, and D. R. Farahmand, 'Experimental Study on Applicability of Water Alternating CO₂ Injection in the Secondary and Tertiary Recovery', *International Oil Conference and Exhibition in Mexico*. Society of Petroleum Engineers, Cancun, Mexico, p. 4, 2006, doi: 10.2118/103988-MS.
- [28] V. Rahimi, M. Bidarigh, and P. Bahrami, 'Experimental Study and Performance Investigation of Miscible Water-Alternating-CO₂ Flooding for Enhancing Oil Recovery in the Sarvak Formation', *Oil Gas Sci. Technol. - Rev. IFP Energies Nouv.*, **vol. 72**, no. 6, 2017, [Online]. Available: <https://doi.org/10.2516/ogst/2017030>.
- [29] A. Ghafoori, K. Shahbazi, A. Darabi, A. Soleymanzadeh, and A. Abedini, 'The Experimental Investigation of Nitrogen and Carbon Dioxide Water-alternating-gas Injection in a Carbonate Reservoir', *Pet. Sci. Technol.*, **vol. 30**, no. 11, pp. 1071–1081, Apr. 2012, doi: 10.1080/10916461003681745.
- [30] A. A. AlQuraishi, A. M. Amao, N. I. Al-Zahrani, M. T. AlQarni, and S. A. AlShamrani, 'Low salinity water and CO₂ miscible flooding in Berea and Bentheimer sandstones', *J. King Saud Univ. - Eng. Sci.*, **vol. 31**, no. 3, pp. 286–295, 2019, doi: 10.1016/j.jksues.2017.04.001.
- [31] M. Jafari, 'Laboratory Study for Water, Gas and WAG Injection in Lab Scale and Core Condition', *Pet. Coal*, **vol. 2**, no. 56, pp. 175–181, 2014.
- [32] B. Moradi, P. Pourafshary, F. Jalali, M. Mohammadi, and M. A. Emadi, 'Experimental study of water-based nanofluid alternating gas injection as a novel enhanced oil-recovery method in oil-wet carbonate reservoirs', *J. Nat. Gas Sci. Eng.*, **vol. 27**, pp. 64–73, 2015, doi: <https://doi.org/10.1016/j.jngse.2015.07.009>.
- [33] S. Mahdavi and L. A. James, 'High pressure and high-temperature study of CO₂ saturated-water injection for improving oil displacement; mechanistic and application study', *Fuel*, **vol. 262**, p. 116442, 2020, doi: <https://doi.org/10.1016/j.fuel.2019.116442>.
- [34] M. Moayedi, 'An Experimental Study on Surfactant-Alternating-Gas Process', Memorial University of Newfoundland, 2015.
- [35] M. Moayedi, L. A. James, and M. Mahmoodi, 'An Experimental Study on Optimization of SAG Process Utilizing Nonionic Surfactants and Sodium Lignosulfonate', in *International Symposium of the Society of Core Analysts, Avignon, France*, 2014, p. 6.
- [36] L. Han, 'Optimum Water-Alternating-Gas (CO₂-WAG) Injection in the Bakken Formation', University of Regina, 2015.
- [37] L. Han and Y. Gu, 'Optimization of Miscible CO₂ Water-Alternating-Gas Injection in the Bakken Formation', *Energy Fuels*, **vol. 28**, no. 11, pp. 6811–6819, 2014, doi: 10.1021/ef501547x.
- [38] M. E. A. Amin, 'Optimization of CO₂ WAG Processes in a Selected Carbonate Reservoir: Laboratory Study', United Arab Emirates University, 2012.
- [39] M. E. Amin, A. Y. Zekri, R. Almehaideb, and H. Al-Attar, 'Optimization of CO₂ WAG processes in a selected carbonate reservoir - An experimental approach', *Soc. Pet. Eng. - Abu Dhabi Int. Pet. Exhib. Conf. 2012, ADIPEC 2012 - Sustain. Energy Growth People, Responsib. Innov.*, **vol. 4**, pp. 2652–2662, 2012.
- [40] S. Touray, 'Effects of Water Alternating Gas Injection on Ultimate Oil Recovery', Dalhousie University, 2013.
- [41] M. Wojnicki, 'Experimental investigations of oil displacement using the WAG method with carbon dioxide', *Nafta-Gaz*, no. 11, pp. 864–870, 2017, doi: 10.18668/NG.2017.11.06.
- [42] M. Wojnicki, J. Lubaś, M. Warnecki, J.

- Kuśnierczyk, and S. Szuflika, 'Experimental Studies of Immiscible High-Nitrogen Natural Gas WAG Injection Efficiency in Mixed-Wet Carbonate Reservoir', *Energies*, **vol. 13**, no. 9, 2020, doi: 10.3390/en13092346.
- [43] S. Pancholi, G. S. Negi, J. R. Agarwal, A. Bera, and M. Shah, 'Experimental and simulation studies for optimization of water-alternating-gas (CO₂) flooding for enhanced oil recovery', *Pet. Res.*, **vol. 5**, no. 3, pp. 227–234, 2020, doi: <https://doi.org/10.1016/j.ptlrs.2020.04.004>.
- [44] S. M. Lundberg and S. Lee, 'A Unified Approach to Interpreting Model Predictions', in *31st Conference on Neural Information Processing Systems (NIPS 2017)*, 2017.
- [45] C. Molnar, *Interpretable Machine Learning. A Guide for Making Black Box Models Explainable*. 2019.
- [46] T. Ertekin and Q. Sun, 'Artificial Intelligence Applications in Reservoir Engineering: A Status Check', *Energies*, **vol. 12**, no. 15, 2019, doi: 10.3390/en12152897.
- [47] E. Mohagheghian, L. A. James, and R. D. Haynes, 'Optimization of hydrocarbon water alternating gas in the Norne field: Application of evolutionary algorithms', *Fuel*, **vol. 223**, no. January, pp. 86–98, 2018, doi: 10.1016/j.fuel.2018.01.138.
- [48] R. K. Pandey, A. K. Dahiya, and A. Mandal, 'Identifying Applications of Machine Learning and Data Analytics Based Approaches for Optimization of Upstream Petroleum Operations', *Energy Technol.*, **vol. 9**, no. 1, p. 2000749, Jan. 2021, doi: <https://doi.org/10.1002/ente.202000749>.
- [49] Y. Cheraghi, S. Kord, and V. Mashayekhizadeh, 'Application of machine learning techniques for selecting the most suitable enhanced oil recovery method; challenges and opportunities', *J. Pet. Sci. Eng.*, **vol. 205**, p. 108761, 2021, doi: <https://doi.org/10.1016/j.petrol.2021.108761>.
- [50] H. Li, H. Yu, N. Cao, H. Tian, and S. Cheng, 'Applications of Artificial Intelligence in Oil and Gas Development', *Arch. Comput. Methods Eng.*, **vol. 28**, no. 3, pp. 937–949, 2021, doi: 10.1007/s11831-020-09402-8.
- [51] I. Makhotin, D. Orlov, D. Koroteev, E. Burnaev, A. Karapetyan, and D. Antonenko, 'Machine Learning for Recovery Factor Estimation of an Oil Reservoir: A Tool for De-Risling at a Hydrocarbon Asset Evaluation', *ArXiv*, 2021, [Online]. Available: <https://arxiv.org/pdf/2010.03408v5.pdf>.
- [52] A. F. Teixeira and A. R. Secchi, 'Machine learning models to support reservoir production optimization', *IFAC-PapersOnLine*, **vol. 52**, no. 1, pp. 498–501, 2019, doi: <https://doi.org/10.1016/j.ifacol.2019.06.111>.
- [53] S. Ghassemzadeh, M. G. Perdomo, and M. Haghighi, 'Application of Deep Learning in Reservoir Simulation', in *Petroleum Geostatistics 2019*, Sep. 2019, **vol. 2019**, no. 1, pp. 1–5, doi: 10.3997/2214-4609.201902252.
- [54] M. Shayan Nasr, H. Shayan Nasr, M. Karimian, and E. Esmaeilnezhad, 'Application of Artificial Intelligence to Predict Enhanced Oil Recovery Using Silica Nanofluids', *Nat. Resour. Res.*, **vol. 30**, no. 3, pp. 2529–2542, 2021, doi: 10.1007/s11053-021-09829-1.
- [55] B. Han and X. Bian, 'A hybrid PSO-SVM-based model for determination of oil recovery factor in the low-permeability reservoir', *Petroleum*, **vol. 4**, no. 1, pp. 43–49, 2018, doi: <https://doi.org/10.1016/j.petlm.2017.06.001>.
- [56] P. Bangert, *Machine Learning and Data Science in the Oil and Gas Industry: Best Practices, Tools, and Case Studies*. Elsevier Science, 2021.
- [57] J. Krohn, G. Beyleveld, and A. Bassens, *Deep Learning Illustrated: A Visual, Interactive Guide to Artificial Intelligence*. Pearson Education, 2019.
- [58] L. Breiman, 'Random Forests', *Mach. Learn.*, **vol. 45**, no. 1, pp. 5–32, 2001, doi: 10.1023/A:1010933404324.
- [59] T. Hastie, R. Tibshirani, and J. Friedman, *The Elements of Statistical Learning: Data Mining, Inference, and Prediction*. Springer New York, 2013.
- [60] M. Kuhn and K. Johnson, *Applied Predictive Modeling*. Springer New York, 2013.
- [61] T. Chen and C. Guestrin, 'XGBoost: A Scalable Tree Boosting System', in *Proceedings of the 22nd ACM SIGKDD International Conference on Knowledge Discovery and Data Mining (KDD '16)*, 2016, pp. 785–794, doi: <https://doi.org/10.1145/2939672.2939785>.
- [62] J. H. Friedman, 'Greedy Function Approximation: A Gradient Boosting Machine', *Ann. Stat.*, **vol. 29**, no. 5, pp. 1189–1232, Jun. 2001, [Online]. Available: <http://www.jstor.org/stable/2699986>.
- [63] T. D. Quach, 'Immiscible WAG Injection: A Core-scale Investigation of Operational Parameters Impacts', Memorial University of Newfoundland, 2020.
- [64] D. Dataman, 'Explain Your Model with the SHAP Values'. 2020, [Online]. Available: <https://github.com/dataman->

git/codes_for_articles/blob/master/Explain_your_model_with_the_SHAP_values_for_article.ipynb.

- [65] D. Al-Bayati, A. Saeedi, M. Myers, C. White, Q. Xie, and B. Clennell, 'Insight investigation of miscible SCCO₂ Water Alternating Gas (WAG) injection performance in heterogeneous sandstone reservoirs', *J. CO₂ Util.*, **vol. 28**, no. October, pp. 255–263, 2018, doi: 10.1016/j.jcou.2018.10.010.
- [66] J. Xie *et al.*, 'Experimental investigation of permeability heterogeneity impact on the miscible alternative injection of formation Brine–Carbon dioxide', *Energy Reports*, **vol. 6**, pp. 2897–2902, 2020, doi: <https://doi.org/10.1016/j.egy.2020.10.012>.
- [67] M. E. Amin, A. Y. Zekri, R. Almehaideb, and H. Al-Attar, 'Optimization of CO₂ WAG Processes in a Selected Carbonate Reservoir-An Experimental Approach'. Nov. 11, 2012, doi: 10.2118/161782-MS.
- [68] D. D. Jackson, G. L. Andrews, and E. L. Claridge, 'Optimum WAG Ratio vs. Rock Wettability in CO₂ Flooding'. Sep. 22, 1985, doi: 10.2118/14303-MS.
- [69] A. H. Alagorni, Z. B. Yaacob, A. H. Nour, and R. B. Junin, 'Effect of water alternating gas (WAG-N₂) after water or gas flooding on crude oil recovery in sandstone reservoirs', *IOP Conf. Ser. Mater. Sci. Eng.*, **vol. 736**, no. 2, 2020, doi: 10.1088/1757-899X/736/2/022015.
- [70] A. Y. Zekri and A. A. Natuh, 'Laboratory Study of the Effects of Miscible WAG Process on Tertiary Oil Recovery', *Abu Dhabi Petroleum Conference*. Society of Petroleum Engineers, Abu Dhabi, p. 12, 1992, doi: 10.2118/24481-MS.
- [71] J. J. Rathmell, F. I. Stalkup, and R. C. Hassinger, 'A Laboratory Investigation of Miscible Displacement by Carbon Dioxide'. Oct. 03, 1971, doi: 10.2118/3483-MS.
- [72] A. Zekri, H. Al-Attar, O. Al-Farisi, R. Almehaideb, and E. G. Lwisa, 'Experimental investigation of the effect of injection water salinity on the displacement efficiency of miscible carbon dioxide WAG flooding in a selected carbonate reservoir', *J. Pet. Explor. Prod. Technol.*, **vol. 5**, no. 4, pp. 363–373, 2015, doi: 10.1007/s13202-015-0155-0.
- [73] A. S. Al-Netaifi, 'Experimental Investigation of CO₂-Miscible Oil Recovery at Different Conditions', King Saud University, 2008.
- [74] N. A. B. M. Anuar, M. H. Yunan, F. Sagala, and A. Katende, 'The Effect of WAG Ratio and Oil Density on Oil Recovery by Immiscible Water Alternating Gas Flooding', *Am. J. Sci. Technol.*, **vol. 4**, no. 5, pp. 80–90, 2017.

Rate-Controlled Mercury Injection Experiments to Characterize Pore Space Geometry of Berea Sandstone

Walid Mohamed Mahmud^{1,*}

¹Department of Petroleum Engineering, Faculty of Engineering, University of Tripoli, Tripoli, Libya

Abstract. Interpretation of the relationship between heterogeneity and the flow in porous media is very important in increasing the recovery factor for an oil or gas reservoir. Capillarity for instance, controls fluids static distribution in a reservoir prior to production and remaining hydrocarbons after production commences. Therefore, capillary pressure data are used by petroleum engineers, geologists, and petrophysicists to evaluate production characteristics of petroleum accumulations. Conventional pressure-controlled mercury porosimetry produces an overall capillary pressure curve and pore throat size distribution data that provide little information about the porous medium structure and pore geometry. The present study provides information on three capillary pressure curves obtained from rate-controlled mercury injection porosimetry; one describes the larger pore spaces or pore bodies of a rock, another describes the smaller pores or pore throats that connect the larger pores, and a final curve which corresponds to the overall capillary pressure curve obtained from the conventional pressure-controlled mercury injection. An experimental constant-rate mercury injection apparatus was constructed that consists of a piston displacement pump, a computer controlled stepper motor drive and a core sample cell designed to minimize dead volume. The apparatus was placed in a glass chamber and subjected to an air bath to maintain a constant temperature of 27° C throughout the experiments. Then constant rate mercury injection experiments were performed on three Berea Sandstone core plugs. Results show that volume-controlled or rate-controlled porosimetry provides considerably more detailed data and information on heterogeneity and the statistical nature of pore space structure than the conventional pressure-controlled porosimetry as pressure fluctuations with time reveal menisci locations in pore bodies and pore throats. Moreover, pore size distributions based on volume-accessed pores and pore radii were obtained from the pressure versus saturation relationship.

1 Introduction

The main principle of capillary pressure measurements by mercury porosimetry is by the incremental increase of pressure while monitoring the increase in mercury saturation being injected into a porous core plug. Pressure-controlled porosimetry method, or the conventional technique, measures the capillary pressure curves in a way that it is possible to obtain one capillary pressure curve from different distributions of pore systems. Yuan and Swanson [1] introduced a pioneering method to Wood's metal porosimetry at which mercury was injected into a core plug at a very slow and constant flow rate. It was possible, through this method, to conceptually partition pore space into pore throats; which they named rison, pore bodies or subison besides the standard capillary pressure curve identical to that obtained from the pressure-controlled mercury porosimetry. Pressure-controlled mercury intrusion method may indirectly measure significantly narrow throats but does not detect larger pores that rate-controlled method detects as it quantitatively separates and characterizes throat and pore size distributions. Therefore, more accurate information can be obtained, from the rate-controlled method, about pore space characterization and micro-pore structure characteristic parameters. Moreover, rate-controlled mercury porosimetry yields information and data on the sizes and volumes of pore bodies or nodes and pore throats or links that can be utilized to calibrate network models that, in turn, used to estimate relative permeability, capillary pressure and residual saturation. Network models may also be used to validate correlated heterogeneity in rocks by comparing measured curves

obtained from rate-controlled mercury injection and those predicted from network models.

Gao et al. [2] used rate-controlled or constant-rate mercury intrusion technique on tight core plugs to determine the size of pore and throat parameters. Zhang et al. [3] utilized rate-controlled mercury injection on tight sandstone core plugs to investigate pore-throat structure characteristics. Smith and Chatzis [4] developed a method of measuring the breakthrough capillary pressure involving a constant-rate injection technique. Zhang et al. [5] analyzed pore-throat structure effect of tight rocks on the seepage and storage capacity employing, among other techniques, rate-controlled mercury injection technique. Zhang et al. [6] performed constant-rate mercury injection experimental measurements in low permeability reservoirs to investigate poor correlation while calculating permeability. Wang et al. [7] recently studied the pore throat structure characteristics of sandy conglomerate and tight sandstone using constant-rate mercury injection along with the conventional constant-pressure mercury injection and micro CT scanning data. It was shown that substantial regions of the rock remain uninvasion at low and moderate non-wetting phase saturations [8]. However, the uninvasion regions then become filled as the non-wetting phase saturation increases indicating that correlated heterogeneity might exist at the core scale. Moreover, visual studies on sandstone pore casts showed correlations between pore body sizes and adjoining pore throats [9]. Therefore, it is important to consider and model spatial and local correlations in network models [10]. Mercury porosimetry was used to study the effect of pore-throat correlations; a widening drainage capillary pressure curves were noticed on correlated networks [11].

Rate-controlled and pressure controlled porosimetries and

* Corresponding author: w.mahmud@uot.edu.ly

scanning electron microscopy were utilized to study pore size distribution of bentonite [12]. The combined use of rate-controlled and pressure-controlled porosimetries was found the best for obtaining the bentonite full-scale pore size distribution while employing each method separately has its limitation.

Yao and Liu [13] compared between the conventional pressure-controlled mercury injection porosimetry, rate-controlled mercury injection porosimetry, micro focus computerized tomography and low-field nuclear magnetic resonance spectral analysis in measuring coals' pore size distribution. Pressure-controlled mercury injection method was found to have limitations such as coal sample destruction, due to high-pressure, and therefrom inaccurate estimations of coal pore size distribution, pore volume and porosity. Rate-controlled mercury injection method, on the other hand, was found effective and provided very detailed pore size distribution information of macropores but insufficient information on pore size distribution of mesopores.

Adams [14] incorporated nuclear magnetic resonance and conducted mercury injection capillary pressure measurements on carbonate and sandstone core plugs to determine large, medium, and small pore sizes, and their associated pore shapes. He calculated mercury injection capillary pressure curves and distributions of pore-throat aperture and compared the results with other techniques. It was possible to discriminate between pores of different genetic origin from one another by using a combination of pore size and pore geometry. Moreover, median pore-throat apertures were found strongly correlated to permeability.

In the present study, rate-controlled mercury porosimetry equipment was built and utilized to characterize pore morphologies by quantitatively dividing pore space into pore bodies and pore throats using Berea sandstone core plugs. Constant-rate mercury injection experiments yielded important structural parameters that includes throat and pore bodies volumes, pores radii distribution, independent pore bodies, throats and total capillary pressure curves. Pore bodies and throats might be orderly or disorderly distributed. Therefore, correlations might exist between the sizes and shapes of throats and pores over extended field-scale porous media or only over a few pores [15]. Data obtained may also be utilized in network modeling studies to identify the nature of spatial and pore throat and pore body correlations and heterogeneity in rocks.

2 Core plugs preparation and properties

Core plugs were sampled from a full diameter Berea sandstone core that has a gas permeability of 1.31 D. Core plugs were cylindrical in shape with similar dimensions and no visual irregular external surfaces. Porosity was measured separately for each core plug using helium gas expansion porosimeter based on the principle of Boyle's Law. A sealed reference chamber in the instrument is filled with helium gas at ambient temperature to a pressure of 100 psig. The core plug is then placed in another sealed chamber, connected to the reference chamber by a two-way valve. This valve when opened allows the gas in the reference chamber to expand into the combined volume of the two chambers. From

Boyle's Law, the volume of the core plug chamber can be calculated when the volume of the reference chamber, the initial pressure and the final pressure are known. The porosity and the grain density were then calculated by determining the bulk volume, and the weight of the core plug. Pore volume of the core plug equals the bulk volume minus the grain volume. Porosity equals the core plug pore volume divided by the bulk volume. Distribution of core plugs porosities ranged from 28.2 to 30.7%. The permeability and porosity values indicate good reservoir rock quality.

3 Experimental equipment and methodology

The experimental equipment is shown schematically in Figure 1. Unlike the conventional mercury intrusion, quasi-static capillary equilibrium injection was achieved by injecting mercury at a very low and constant flow rate of 0.0000002 cc/sec. The experimental equipment consists of a stepper motor drive controlled by computer, a cell of 11 cc capacity to contain core plug designed to minimize dead volume, a piston displacement pump that is vertically mounted to eliminate air trapping. The cell is connected at the top through a vacuum port. Each core plug was preprocessed/placed under vacuum before mercury injection commences and the core plug becomes fully surrounded and submersed in mercury. Vacuum of fifty microns of mercury was applied for eight hours before conducting each experiment. A pressure transducer measures the pressure in the cell that is powered by a twelve-volt battery to minimize signal noise. Pressure transducer's range is from 0 to 100 psi with a resolution of +/- 0.00005 psi. The equipment was put in a glass built chamber, shown in Figure 2, at constant temperature of 27 °C. In order to maintain and control constant temperature throughout the experiments and to eliminate any possible thermal effects on pressure fluctuations, electric fan heater was placed inside the chamber that is visible in Figure 2. Volume measurement resolution was 0.000031 cc equivalent to one shaft encoder count. A program was generated to read the Hewlett Packard voltmeter and to control the stepper motor that drives the mercury injection pump. The outcome of the program is readings of the cumulative mercury injected volume, pressure and time. Pore volume invaded by mercury is then obtained from the cumulative pore volume filled by mercury and the overall pore volume of the core plug.

Figure 3 shows the overall, full scale, capillary pressure versus mercury pore volume injected saturation of the rate-controlled mercury injection experiments of the present work. Figures 4 and 5 show magnified sections of the data collected during the experiment; pore volume injected represents volume of mercury injected divided by ambient helium pore volume. Constant-rate mercury injection enables the division of the overall mercury injection capillary pressure curve into pores and throats mercury injection capillary pressure curves that are utilized to characterize throat and pore size distributions [1]. It is also possible analyzing throats and pores parameters including throats and pores radii distribution and the ratio between

them. Figure 5 shows the capillary pressure fluctuations and response corresponding to filling of interconnected pores. A sudden ‘primary’ drop in capillary pressure as mercury meniscus falls from a narrow pore throat into a wide pore body. Immediately afterwards, the capillary pressure gradually increases as mercury commences filling adjoining interconnected pore throats. This ensembles a drainage displacement at which non-wetting fluid, mercury in the present study, displaces wetting fluid, air, in the pore space of the rock. The instant pore-scale displacement events that occur are also referred to as Haines jumps [16].

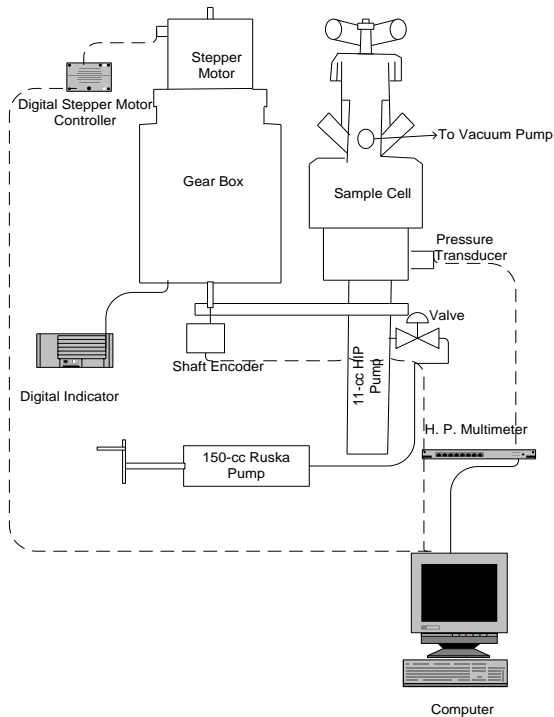


Figure 1: Schematic of experimental equipment.

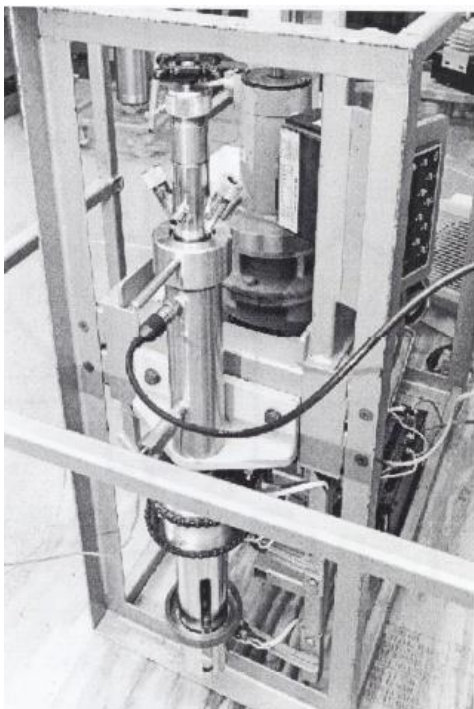


Figure 2: Experimental equipment inside the glass chamber.

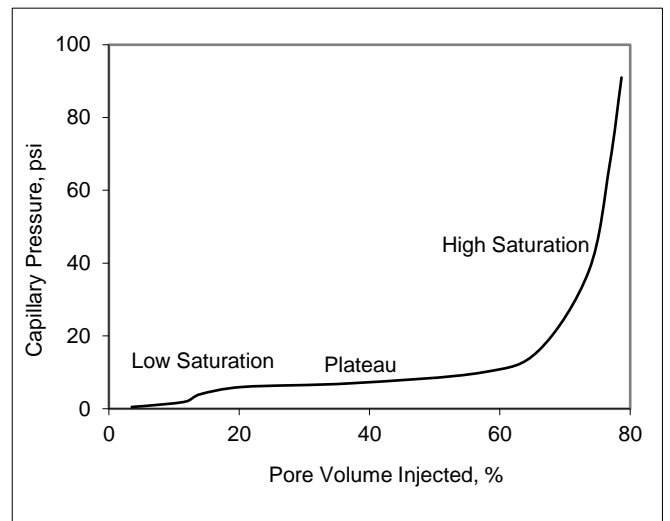


Figure 3: Core plug 3 capillary pressure versus mercury pore volume injected saturation.

The capillary pressure may increase to a level that has already been attained, shown as secondary in Figure 5, then it drops before increasing to a new level shown as tertiary in Figure 5. Mercury volume inserted from the primary capillary pressure drop commences until the tertiary pressure increase is reached equals the pore volume of interconnected pore bodies or system that has a threshold pressure less than or equals the pressure preceding the primary pressure drop. Compressibility tests are recommended for poor consolidated or compressible low permeability reservoir rocks where pores not yet filled by mercury might be compressed with increasing net overburden pressure as function of time. However, these tests are not relevant for the present high permeability and well-cemented Berea sandstone core plugs.

Figure 6 shows the basic principle of constant-rate mercury injection as the injected mercury pressure fluctuates with the porous media pore structure. Thus, detailed information on pore throats and pore bodies can be distinguished on the pressure fluctuations [17].

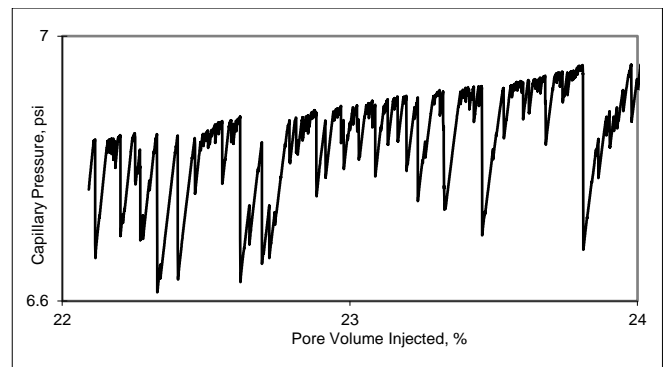


Figure 4: A magnified section shown the capillary pressure versus mercury volume injected divided by the ambient core plug pore volume.

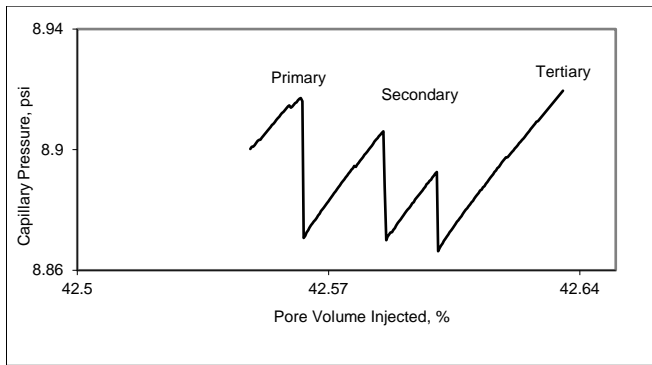


Figure 5: A magnified section from one of the experiments showing primary, secondary and tertiary pressure drops in an interconnected pore system.

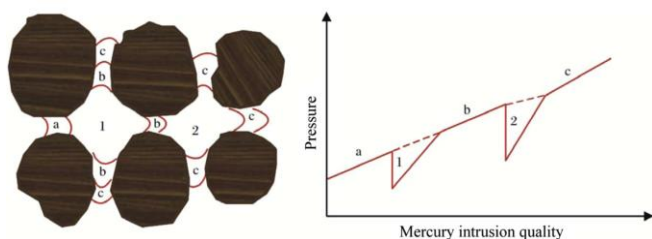


Figure 6: Schematic of the constant rate mercury injection process: a, b and c are throats, 1 and 2 are pores [17].

Laplace's equation is used to determine a pore throat effective entry radius:

$$r = \frac{2 \sigma \cos \theta}{P_c} \quad (1)$$

Where σ is the interfacial tension, θ is the contact angle, P_c is the capillary pressure obtained from the measured pressure-volume trace and r is the effective radius of the pore throat. For the calculation of the effective pore throat radius, the mercury/air contact angle equals 140° and the interfacial tension equals 480 mN/m invariant. These values were considered to be constant during the entire test because of the low rate of mercury injection applied during the experiments. As the capillary pressure increases to previously unattained levels, mercury meniscus advances into uninvaded pore throats. This analysis, therefore, resolves the rock pore space into pore throats and pore bodies, with each throat and pore is characterized by an entry volume and pressure.

Laplace's equation assumes straight capillary tubes, while in principle the rock pore network is model as a bundle of interconnected capillary tubes. Moreover, capillary hysteresis effects are not taken into account using this model. A program was developed to determine the number and volume of pore bodies. Volume of a pore body is determined by:

$$V_{pb} = \Delta P \left(\frac{dV}{dP} \right) \quad (2)$$

Where $\left(\frac{dV}{dP} \right)$ is the rate constant determined from the pressure and time as shown in Figure 7. However, the above

formula was modified to accommodate for the volumes of multiple smaller pores existing within an interconnected pore system. Volume of such system has previously been calculated by separating the pressure-volume fluctuations into compartments [18]. However, this method underestimates the invaded volume in a primary pore and overestimates the invaded volume in subsequent pores within the same system of interconnected pores [19]. Alternatively, multi-pore system was separated by extending the pressure-volume fluctuations vertically to the threshold pressure of the primary pressure drop assuming that the rate constant remains unchanged throughout the pores at a given pressure meaning $(dV/dP)_1 = (dV/dP)_2$ [19]. This might be true in an individual interconnected pore system, however, it was observed in the present study that the rate constant varies from one interconnected pore system to another. Therefore, average rate constant was considered for every individual interconnected pore system. For instance, the difference between rate constants, from one of the experiments, in two neighboring interconnected pore systems was 0.000134 cc/psi . The overall pore systems volume is determined by Equation 3 and as shown in Figure 8:

$$TV_{pb} = \left(\frac{dV}{dP} \right)_1 (\Delta P_{1r_1} + \Delta P_{2r_1} + \dots) \left(\frac{dV}{dP} \right)_2 (\Delta P_{1r_2} + \dots) + \left(\frac{dV}{dP} \right)_i (\Delta P_{1r_i} + \dots) \quad (3)$$

Where TV_{pb} is the total volume of the pore systems in the core plug, $(dV/dP)_1$ is the local rate constant in region number one, and ΔP_{1r_1} is the pressure drop in region one, and so on.

Pore space morphology, rock fluid properties, local pore geometry and topology are factors that determine the distribution and volume of residual oil ganglia in the pore space or in other words pore and core scales heterogeneities [11, 20, 21]. In a drainage displacement, as mercury, being the non-wetting phase is injected into a rock, it preferentially occupies larger pores because of their low entry threshold pressure then it occupies smaller pores and throats. The large pores with low capillarity, therefore, would most likely trap the non-wetting phase in an imbibition displacement while the smaller throats are filled by the wetting phase. ΔV

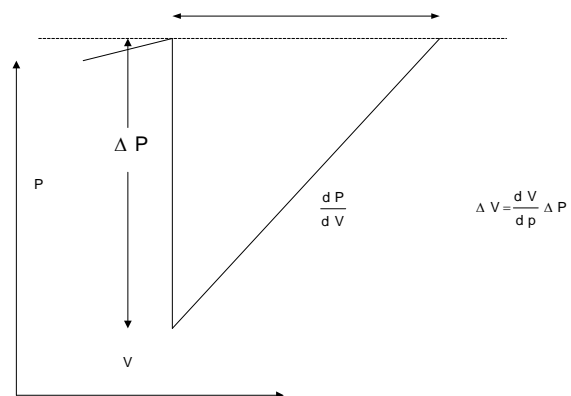


Figure 7: Rate constant determined from pressure and time.

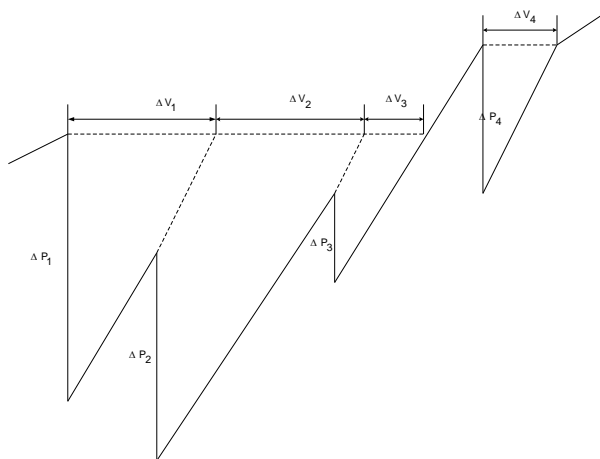


Figure 8: Volume determination of interconnected pore systems.

Because mercury is a strongly non-wetting phase, it can be assumed that snap-off disconnects the continuous filament of mercury and traps it in all pores during reduction of capillary pressure as the experiment is terminated [22].

The cumulative pore bodies' saturation provides good estimates of the residual mercury/air saturation assuming that all mercury is trapped in the pore bodies upon the experiment completion and pressure reduction [18]. Pressure was gradually decreased down to atmospheric pressure of 14.7 psi and sufficient time was given for capillary pressure-mercury saturation equilibrium. Thus, an imbibition cycle displacement takes place as the wetting phase (air) displaces the non-wetting phase (mercury). Therefore, cumulative volume of pores represents the final non-wetting phase saturation S_{nwr} that can be determined by:

$$S_{nwr} = \sum_{i=1}^N \frac{V_{rs}}{V_p} \quad (4)$$

N is the number of pores, V_{rs} is the volume of i pore and V_p is the core plug pore volume. Pore geometry affects the residual non-wetting phase saturation, which is the most important factor for the estimation or reservoir ultimate recovery and in any EOR operation. The value of residual non-wetting phase saturation by mercury entrapment might not be representative of the reservoir residual fluids saturation value. Mainly due to the fact that reservoir fluids wettability behavior is not properly reproduced during the experiment, as both mercury and air are by definition non-wetting phases.

4 Results and discussion

Figures 9 to 11 show the total rate-controlled mercury injection capillary pressure curve along with the individual pores and throats capillary pressure curves. In Figure 9, initial steep increase in capillary pressure due to entry effect where potential surface, irregular and truncated pores are initially filled. Then at mercury saturation of approximately

15.0 to 56.0%, overlapping takes place between total and pores capillary pressure curves. Mercury penetrates and fills large number of interconnected pore bodies as the capillary pressure increases to a threshold displacement pressure of around 2 psi, which renders a plateau in the total and pore capillary pressure curves followed by sharp increase in the capillary pressure with small increase in mercury saturation. There is slight increase in the capillary pressure in the plateau region with significant increase in mercury saturation. The total number of pores, occupied by mercury, for core plug 1 is 24138 occupying volume of 0.2234 cc. The throat capillary pressure curve, on the other hand, gradually increases as mercury is injected into the core plug. By the end of the experiment, the total mercury injection saturations of the pores and throats are 60.4 and 27.5%, respectively. Therefore, higher pores saturation than the throats saturation indicates that pores mostly control the overall displacement. The pores saturation of 60.4% also represents the residual non-wetting phase saturation or the final mercury entrapment saturation as detailed in section 3. Some throats might also trap mercury as the capillary pressure is reduced to atmospheric conditions, however, volume of mercury trapped in some throats is assumed to be negligible.

The pore throats of the well-sorted and highly permeable Berea sandstone rock might have similar sizes to the pore bodies. Moreover, as shown in Figure 4, the highly sensitive pressure transducer employed in the present study detects the smallest pressure fluctuations which indicates that distinguishing between pore throats and pore bodies is considerably arbitrary. Thus, similarly the distinction between pore throat capillary pressure and pore body capillary pressure curves is also considerably arbitrary. This indicates that pore throats still and also control the displacement and have an important portion of the Berea sandstone pore space. For this reason, the distinction between pore throats and pore bodies might be considered arbitrary.

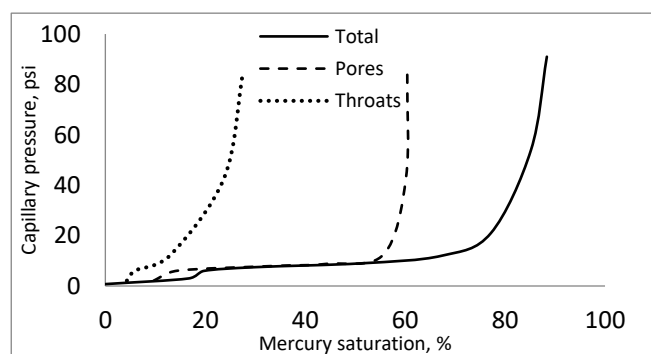


Figure 9: Core plug 1 mercury injection capillary pressure curves of the total, pores and throats.

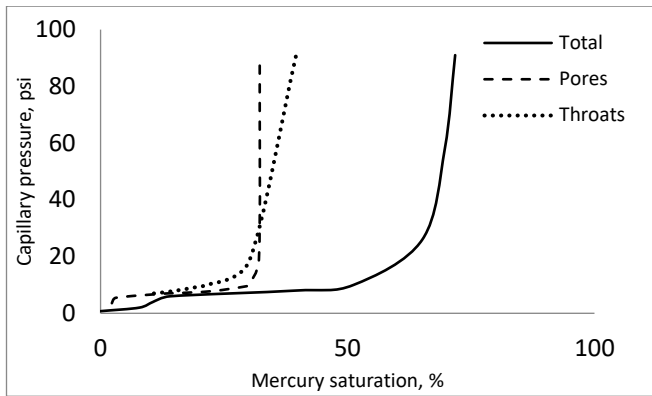


Figure 10: Core plug 2 mercury injection capillary pressure curves of the total, pores and throats.

Core plugs 2 and 3 shown in Figures 10 and 11, respectively have similar threshold displacement pressure of around 14 psi. The throat capillary pressure curves are higher than the pores capillary pressure curves. By the end of the experiment on core plug 2, the total mercury injection saturations of the pores and throats are 32.2 and 39.5%, respectively. The pores saturation of 32.2% also represents the residual mercury saturation.

By the end of the experiment on core plug 3, the total mercury injection saturations of the pores and throats are 32.3 and 46.3%, respectively. The pores saturation of 32.3% also represents the residual mercury saturation. The lower pores saturation than the throats saturation indicates that the throats mainly control the total mercury injection saturations of core plugs 2 and 3.

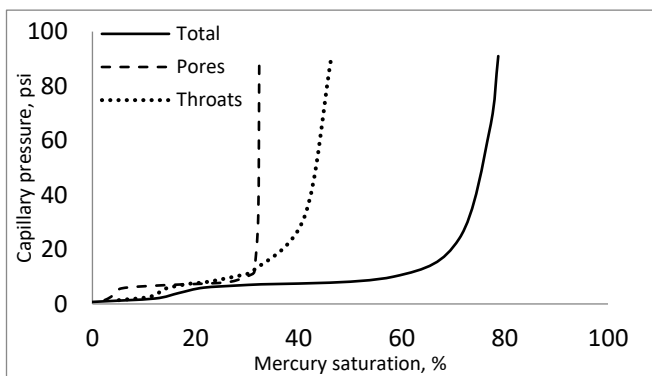


Figure 11: Core plug 3 mercury injection capillary pressure curves of the total, pores and throats.

The total number of pores, occupied by mercury, in core plug 2 is 21980 occupying volume of 0.2083 cc. The total number of pores, occupied by mercury, in core plug 3 is 21537 occupying volume of 0.2095 cc. The threshold displacement pressure of core plugs 2 and 3 is around 7 psi. As the threshold displacement pressure decreases, a lengthy overlap between the pore capillary pressure curve and the total capillary pressure curve exists while the overlap between the throat capillary pressure curve and the total capillary pressure curve is somewhat more evident as the threshold displacement pressure increases. Similar constant-rate mercury injection findings were reported for tight sandstone [3]. Shape of pore and throat capillary pressure

curves variations as well as pore and throat occupancies between core plug 1 and core plugs 2 and 3, despite having the same lithology, textural properties and permeability, indicates that there is a cut-off limit to both spatial and local pore-throat correlations within the full diameter Berea sandstone core. Core plug 1 can be different or more heterogeneous at the pore network scale than core plugs 2 and 3. Thus, correlated heterogeneity at the pore scale may not extend to the sample size. Moreover, short-range correlations or local pore-throat correlations between pore bodies and the adjoining pore throats might not persist throughout the core plug. Therefore, large pore bodies do not necessarily adjoin large pore throats and small pore bodies do not necessarily adjoin small pore throats.

The volume and number distribution curves of the three core plugs are shown in Figure 12. Volume of pores distribution characteristics is similar for the three core plugs. It can be observed that the volume of pores ranges from 1 to more than 200 nL, however, peaking for the three core plugs at approximately 5 nL. In general, as porosity increases, the distribution of the volume of pores widens. This implies that even slightly tighter correlated sandstone may contain fewer pores and more wide and narrow throats.

Pore radius distribution curves of the three core plugs have similar characteristics as shown in Figure 13. Pore radii expand over a wide range from 0.0106 to 644 μm peaking at around 130 μm . Therefore, the pore radii of the Berea sandstone core plugs utilized contain nanopores, micropores and mesopores that are less than 1 μm , from 1 to 62.5 μm and from 62.5 μm to 4 mm, respectively, according to Loucks et al. [23] pore classification. There might be no significant difference between the throat radius and pore radius distribution for large permeability core plugs [6].

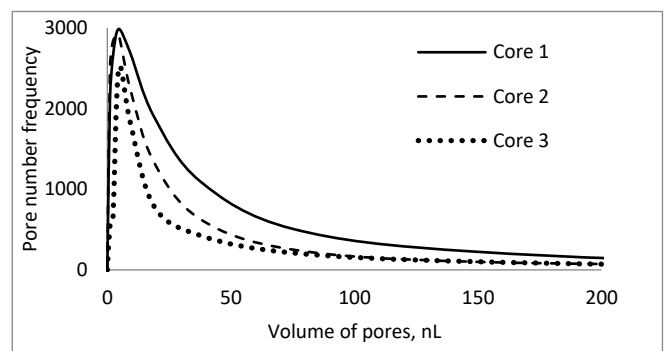


Figure 12: Volume and number distribution of the core plugs.

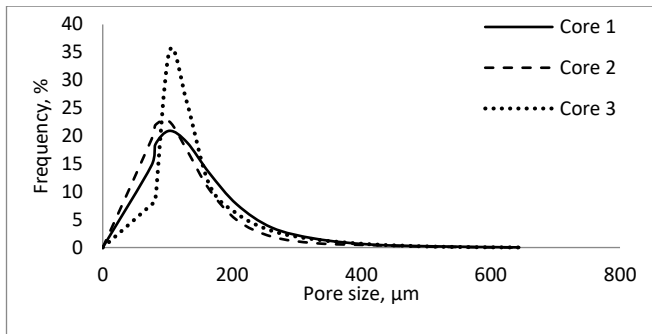


Figure 13: Core plugs pore size distributions.

Figure 3 shows a typical capillary pressure curve obtained from core plug 3 of the rate-controlled mercury injection experiments of the present work. The overall shape of the constant-rate mercury capillary pressure curve is similar to pressure-controlled capillary pressure curve. Equation 1 calculates the radius of a cylindrical capillary tube; however, Berea sandstone and all reservoir rocks have complex pore throats and bodies geometry and structural configurations that are very complex in geometry. Therefore, the calculated values of pore throats represent the effective radii of the pore throats that might not equal their actual dimensions. Figure 3 shows a flat and broad plateau indicating well-sorted correlated Berea sandstone dominated by throats of similar sizes. Previous studies on pore-throat correlated networks revealed that steepness of drainage capillary pressure curves decrease as correlations increase [24, 25].

The maximum pressure achieved during the experiments of the present work is around 91 psi, which was sufficient for mercury to penetrate up to around 88.0% of the pore space. Some of the previous rate-controlled mercury injection experiments underwent maximum mercury injection pressure of 899 psi especially when tight rocks were used [3]. Overall, the significant pressure increase towards the end of the experiments with small increase in mercury saturation indicates that the injected mercury only fills some unfilled small pores and throats as shown in Figure 14. Capillary pressure fluctuations in these pores and throats are very small, even when plotted on magnified scale as in Figure 14, because the relative injection rate relative to the pore volume is very high. As the relative mercury rate becomes high, the resultant capillary pressure curve is similar to that obtained by constant-pressure mercury porosimetry where pores and throats filling times are extremely short for the pressure transducer to detect or resolve.

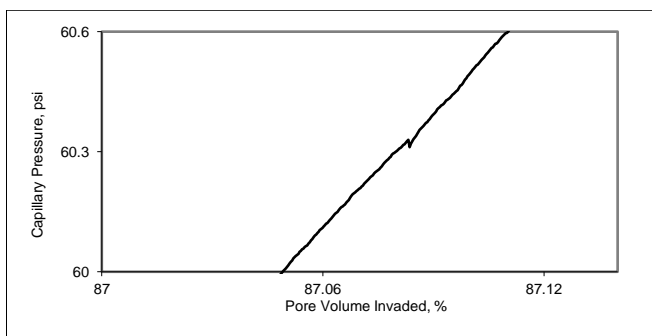


Figure 14: Capillary pressure fluctuations towards the end of the experiment.

Calibrations of the interpretations of the present study with petrographic observations, such as optical and electron microscopy, of the pore types, pore texture, and pore throats was not performed mainly due to health and safety reasons. However, to address the uncertainties concerning the calibration of the interpretation, some previously published data on pore geometry from petrographic observations maybe used. Figure 15 shows a back-scattered electron (BSE) image of petrographic thin section of Berea sandstone [26]; the pore space is black, quartz is medium grey, feldspar is light grey, and clays are dark grey.

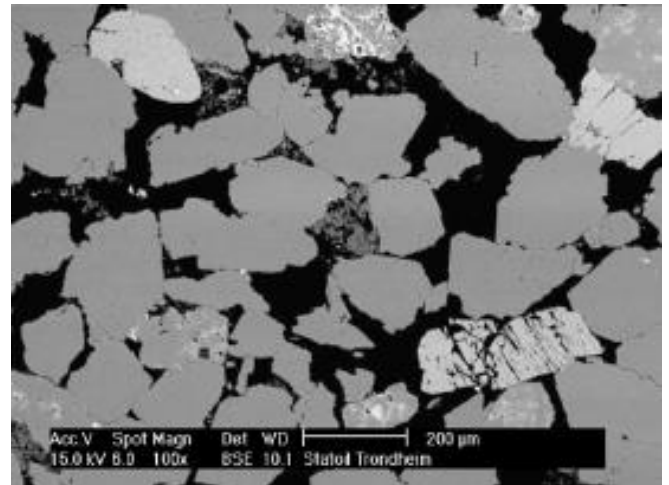


Figure 15: Back-scattered electron image of a thin section of Berea sandstone [26].

Figure 16 shows a scanning electron microscope image of Berea sandstone; clays was found to preferentially coat the quartz grains that resulted in no correlation between the modal mineral composition of the rock and the fraction of surface area made up by the mineral [27].

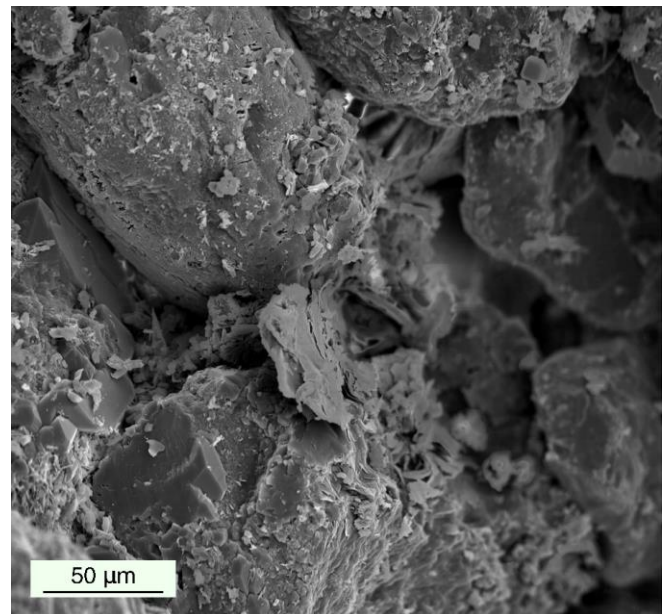


Figure 16: Scanning electron microscope image of Berea sandstone [27].

Figure 17 shows a microtomographic image of Berea sandstone slice [28]. Berea sandstone was characterized by an increase in porosity, resulting in a higher coordination number and characterized by a dense network of numerous smaller throats and pores of radii ~ 1.3 and ~ 2.7 μm , respectively.

Figures 15 and 17 show that Berea sandstone, and all porous rocks, is composed of grains, pore bodies and throats. The pore bodies represent the voids or spaces between the rock mineral grains, and the throats are narrow tubes or channels in the rock that connect all different types of pores. The rate-controlled results of the present study reveal that the pore size ranges from 0.0106 to 644 μm . Figures 15 to 17 of the petrographic microscopic observations show that pore sizes fall within the experimentally determined range. Therefore, rate-controlled mercury experiments can effectively characterize a wide range of Berea sandstone pores. However, the accuracy of these findings can only be ensured when the petrographic microscopic thin sections are performed for the same core plugs subjected to the rate-controlled mercury injection experiments.

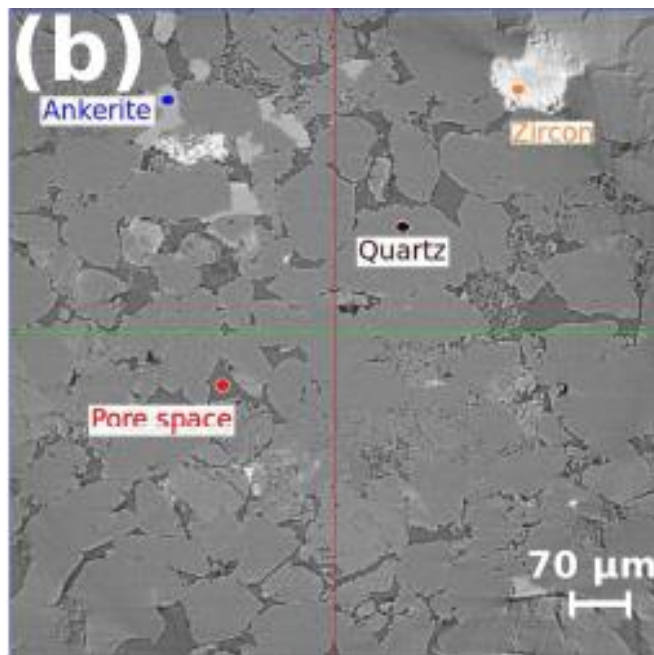


Figure 17: Microtomographic image of Berea sandstone slice [28].

5 Conclusions

Rate-controlled mercury porosimetry equipment was constructed and used to characterize Berea sandstone rock into pore bodies and pore throats. Three capillary pressure curves were obtained; one describes the larger pore spaces or pore bodies of the rock core plug, another describes the smaller pores or pore throats that connect the larger pores, and a final curve which corresponds to the overall capillary pressure curve, similar to that obtained from the conventional pressure-controlled mercury injection. The Berea sandstone used had good physical properties with a porosity ranged from 28.2 to 30.7% and gas permeability of 1.31 D. Information on the statistical nature of the pore structure and

heterogeneity were obtained as pressure fluctuations with time revealed menisci locations of pore bodies and throats.

Pore size distributions based on volume-accessed pores and pore radii were obtained from the pressure versus saturation relationship. The radii of the pores ranged from 0.0106 to 644 μm indicating that pore radius classification included nanopores, micropores and mesopores; however, the majority of pore radii were mesopores. Results matched previously published petrographic observations data on Berea sandstone.

One of the constraints of rate-controlled mercury injection technique is that the experimental pressure is generally low; therefore, maybe limited nanopores' radii threshold entry pressure can be exceeded. Although pore bodies control the porosity, throats also constitute an appreciable portion of the pore space volume. Varying pore and throat capillary pressure curves obtained for the Berea sandstone core plugs indicate complex geometry of the throats and pores systems. Furthermore, the shapes of the total capillary curves indicate that the core plugs' local pore throats and spatial correlations persist and pore distribution can still be heterogeneous within the same core plug. It is important to mention that despite the valuable pore space morphology characteristics and hydrocarbon saturation information that the rate-controlled mercury injection technique provides, it is also financially costly, very slow to conduct and labor intensive compared to the routine conventional pressure-controlled mercury injection techniques. The experimental procedure is also extremely time consuming and data processing is complex.

References

1. H.H. Yuan and B.F. Swanson. *SPE Form. Eval.* **4**, 17-24 (1989).
2. H. Gao, T. Li and L. Yang. *J Petrol Explor Prod Technol.* **6**, 309-318 (2016). <https://doi.org/10.1007/s13202-015-0186-6>
3. W. Zhang, Z. Shi and Y. Tian. *Energy Explor. Exploit.* **38**(6), 2389-2412 (2020). doi: [10.1177/0144598720920729](https://doi.org/10.1177/0144598720920729).
4. J. Smith and I. Chatzis. Canada: N. p., (2004).
5. Y. Zhang, Z. Bao, F. Yang, S. Mao, J. Song, L. Jiang. *Geofluids.* 2018, ID 3403026 (2018). <https://doi.org/10.1155/2018/3403026>
6. C. Zhang, Y. Cheng and C. Zhang. *J. of Geophys. Eng.* **14**, 132-142(2017).
7. Y. Wang, Y. Gao and Z. Fang. *Petrol. Explor. Develop.* **48**(2): 308-322(2021).
8. B.F. Swanson. *J. Pet. Technol.* 10-18(1979).
9. N.C. Wardlaw, N.C. Li and D. Forbes. *Transp Porous Media.* **2**, 597-614(1987).
10. A. Makse, H. Hernan, P.S. Ivanov et al. *Physica A.* **233**, 587-605(1996).
11. C.D. Tsakiroglou and A.C. Payatakes. *J. Colloid Interface Sci.* **2**, 479-494(1991).
12. J. Liu, S. Song, X. Cao, Q. Meng, H. Pu, Y. Wang, J. Liu. *J. Rock Mech. Geotech. Eng.* **12**(2), 403-413(2020).
13. Y. Yao and D. Liu. *Fuel.* **95**, 152-158(2012).

14. A. J. Adams. Doctoral dissertation, Texas A&M University. Texas A&M University, (2005).
15. W.M. Mahmud. *Pet. Sci. Eng.* **2**(1):23-29(2017).
16. W.B. Haines. *J. Agri. Sci.* **20**, 97-116 (1930).
17. H.-Y. Zhu, L.-Z. An and C.-Y. Jiao. *Natural Gas Geoscience.* **26**(7):1316-1322 (2015).
18. H.H. Yuan. *SPE* 19617 (1989).
19. G. Mason. *SPE Form. Eval.* (1991).
20. N.R. Morrow. *J. Can. Pet. Technol.* 35-46(1979).
21. H.K. Christenson, J.N. Israelachvili and R.M. Pashley. *SPE Reserv. Eng.* 155-165(1987).
22. W.M. Mahmud and V.H. Nguyen. *Trans. In Por. Media.* **64**, 279-300(2006).
23. R.G. Loucks, R.M. Reed, S.C. Ruppel, et al. *AAPG Bulletin* **96**(6): 1071–1098 (2012).
24. Y. Li, W.G. Laidlaw and N.C. Wardlaw. *Adv. Colloid Interface Sci.* 26,1-86(1986).
25. M.A. Ioannidis and I. Chatzis. *Water Resour. Res.* **29**, 1777-1785(1993).
26. P-E. Øren and S. Bakke. *J PETROL SCI ENG.* **39**(3-4), 177-199 (2003).
27. P. Lai, K. Moulton and S. Krevor. *Chem. Geol.* **411**, 260-273 (2015).
28. T. Paul-Ross, A-Z. Aizhan, H-M. Saswata. *Front. Earth Sci.* **6** (2018).

Evaluation of a Numerical Solver (interFoam) to Predict Imbibition and Drainage in a Pore-Doublet System

Hosein Derijani¹, Lesley A. James¹, and Ronald D. Haynes²

¹ Hibernia EOR Research Mathematics, Memorial University of Newfoundland, St. John's, NL, Canada A1B 3X5

Abstract. Drainage and imbibition at low to moderate capillary number, are very important phenomena, in which the SCAL data are derived. In this venue, there is an increasing trend to apply computational fluid dynamic models at pore scale to extract the required parameters for multiphase flow study. Before applying these methods, their abilities to capture the real performance of fluids at the pore scale with corresponding capillary numbers should be validated. Moreover, due to the dimensional difference from pore to core scale, rigorous statistical methods are required to successfully extract the corresponding SCAL parameters. Hence for any model, before constructing any SCAL data via digital methods, validation at the pore scale along with the investigation of the possible effect of the dimensional change from pore to core scale are significant priorities. In this study, the performance of interFoam, a solver for immiscible two phase flow from OpenFOAM, at the pore scale is evaluated. An image of the pore doublet system is digitized and meshed with different resolutions to capture the contact angle movement. The average pore diameters are different and the pore diameter pathway varies. The experimental results are extracted from an article, which extensively performed the tests for different imbibition and drainage regime on this pore doublet system. Moreover, a sensitivity analysis on mesh geometry, refinement near boundaries, and contact angle is conducted. The drainage simulation and experimental results in the pore doublet system are in good agreement with each other. As expected, the displacement happens in the larger diameter and bypasses the wetting fluid in the narrow constriction. In imbibition, the displacement first takes place in the smaller constriction and then the wetting phase starts invading the larger diameter pore. From the sensitivity analysis, it is concluded that the instability of the front is mainly related to the slip condition at the walls. Moreover, the spreading of wetting film near the wall is prevalent at very low contact angles. The results show that the solver can predict the flow behavior in imbibition and drainage on the pore doublet system and the results are comparable with the experiments.

1. Introduction

Understanding two-phase flow behavior especially immiscible flow is crucial in different areas of science and industry including the petroleum industry [1]. Multiphase fluid flow through porous media, at the macro scale (core and/or field), is often modeled based on the derivation of relative permeability curves which are extracted from drainage and imbibition experiments. Another approach is to extract the pore structure and apply CFD equations at the pore scale to capture the flow behavior at micro-scale. Typically, in hydrocarbon recovery the scale of fluid velocity is on order of cm/s (ft/day) and the flow regime away from the wellbore and even near the wellbore is in the laminar regime. This article aims to investigate the applicability of CFD modeling on pore scale structures and determine if they can reproduce immiscible flow behavior.

OpenFOAM, a leading, free CFD open-source software owned by OpenFOAM Foundation is being used for this purpose [2]. OpenFOAM (Open-source Field Operation and Manipulation) is an object-oriented C++ framework capable of performing a variety of computational fluid dynamics in continuum mechanics. The solver uses the finite volume discretization method [3]. This software includes solvers for incompressible, compressible flow, and covers multiphase flow modeling. Specifically, the interFoam solver is being used for this study. Deshpande et al. [4] analyzed the two-phase flow behavior at the scale of 10^{-6} - 10^{-3} m under capillary dominant and viscous dominant

regimes. In the capillary dominant regime, they investigated the effect of perturbation at the interface of fluids in a standing column. They found interFoam can produce satisfactory results when spurious currents are controlled. Recent modifications in interFoam include an adaptive interface compression scheme to minimize parasitic current [5]. However, a study is needed to investigate the pore scale behavior of this solver for drainage and imbibition process.

We use the standard interFoam solver from OpenFOAM version 5.0. In this article, first the formulation of the underlying equations and the solution procedure are presented. Afterward, a meshed pore-doublet is used for the CFD experiment to investigate the capability of the solver to predict flow behavior in imbibition and drainage processes. The sensitivity to the contact angle, and the resolution of mesh near the surface are investigated.

2. Methodology

The method that is being used for the solver is presented, mostly adapted from [4]. In two phase flow, the phase fraction $\alpha_i, i = 1, 2$, is the volume of one phase over the total volume of interest:

$$\alpha_i = \int_v \frac{dv_i}{v} \quad i = 1, 2 \quad (1)$$

The mass conservation is given as:

$$\frac{\partial \rho}{\partial t} + \nabla \cdot (\rho U) = 0 \quad (2)$$

The density of fluid (which is a mixture of immiscible phases) is calculated as:

* Corresponding author: ljames@mun.ca

$$\rho = \alpha_1 \rho_1 + \alpha_2 \rho_2 \quad (1)$$

The result of combining equation 1 and 2 yield the phase fraction equation as:

$$\frac{\partial \alpha}{\partial t} + \nabla \cdot (\alpha U) = 0 \quad (2)$$

The above equations along with the momentum equation can be used to obtain the phase fraction and the velocity and pressure fields of interest.

The momentum equation is written as:

$$\frac{\partial(\rho U)}{\partial t} + \nabla \cdot (\rho U U) = -\nabla p + \nabla \cdot (\mu(\nabla U + \nabla U^T)) + \rho g + f_\sigma \quad (3)$$

The last two terms on the RHS of the above equation are forces which are related to the gravitational field and interfacial tension between the two phases. [These equations can be used at the pore scale for continuous flow.](#) The boundary conditions can be modified to account for the slip-flow regime which is prevalent near the surfaces [6].

The interfacial tension is based on the continuous surface force model adapted from [7] and is obtained as:

$$f_\sigma = \sigma \kappa \nabla \cdot \alpha \quad (4)$$

where σ is interfacial tension and κ is the curvature of the interface defined as:

$$\kappa = \nabla \cdot \left(\frac{\nabla \alpha}{|\nabla \alpha|} \right) \quad (5)$$

The above equations are coded in interFoam solver with the aid of the finite volume method. The finite volume formulation is presented below (description based on [8]).

Equation 8 is the general balance equation for any physical property being carried in the fluid.

$$\frac{\partial(\rho \phi)}{\partial t} + \nabla \cdot (\rho U \phi) - \nabla \cdot (\rho \Gamma_\phi \nabla \phi) = S_\phi(\phi) \quad (6)$$

From the LHS of the equation, the first term stands for temporal evolution of property, the second one stands for the convective contribution of property by the fluid and the third one represents the contribution from diffusive distribution of the property. The RHS term represents the contribution of a property from a sink or source within the system.

Integrating over a domain of interest at specified time step yields:

$$\int_{V_p}^{t+\Delta t} \left[\frac{\partial}{\partial t} \int_{V_p} \rho \phi dV + \int_{V_p} \nabla \cdot (\rho U \phi) dV - \int_{V_p} \nabla \cdot (\rho \Gamma_\phi \phi) dV \right] dt = \int_{V_p}^{t+\Delta t} \int_{V_p} S_\phi(\phi) dV dt \quad (7)$$

Every volume integral can be transformed to an integral over faces using Gauss' theorem:

$$\int_{V_p} \nabla \cdot a dV = \int_S a dS \quad (8)$$

A second order equation discretization in time, known as the Crank-Nicolson method is used:

$$\begin{aligned} & \frac{\rho_p \phi_p^n - \rho_p \phi_p^o}{\Delta t} V_p + \frac{1}{2} \Sigma_f F \phi_f^n - \frac{1}{2} (\rho \Gamma_\phi)_f \cdot S \cdot (\nabla \phi_f)^n \\ & + \frac{1}{2} \Sigma_f F \phi_f^o - \frac{1}{2} (\rho \Gamma_\phi)_f \cdot S \cdot (\nabla \phi_f)^o \\ & = S_u V_p + \frac{1}{2} S_p V_p \phi_p^n + \frac{1}{2} S_p V_p \phi_p^o \end{aligned} \quad (9)$$

where the F is the mass flux through the faces:

$$F = S \cdot (\rho U)_f \quad (10)$$

This system of equations on every cell will be simplified to:

$$a_p \phi_p^N + \Sigma_N a_N \phi_N^N = R_p \quad (11)$$

These equations on every cell form a sparse matrix with a_p on diagonal and *the quantities* a_N on the off diagonals:

$$[A][\phi] = [R] \quad (12)$$

The momentum equation is solved by a combination of SIMPLE and PISO methods. The benefit of the combined procedure is the ability to use a larger time step with the Courant Number higher than unity [9].

The procedure for solving the equation is as follows [10]:

1. Initiate variable based on internal initial (previous time step) and boundary conditions.
2. Adjust the time step based on the Courant Number.
3. Use old time volumetric flux to solve the phase fraction equation.
4. Update physical properties; density, viscosity, face densities, unit normal vector, and curvature.
5. Solve the momentum and pressure equations using SIMPLE, PISO, or combined SIMPLE/PSIO methods.
6. Move to the next time step.

3. Results and Discussion

In Hydrocarbon production practice, the fluid velocity is at very low orders, in a way that capillary forces gain their significant role in immiscible fluid movements. Depending on the relative importance of capillary and viscous forces, the microscopic sweep efficiency may differ [11]. Mahmoodi et al. developed a visualization method to capture multiphase fluid displacement in micro-models [12]. Saturation evolution was quantified during EOR process at the pore scale [13-15]. The behavior of imbibition and drainage is visualized experimentally based on viscosity ratio and capillary number by Guo and Aryana [16]. Based on their findings for the specific microfluidic device used to perform the experiments, stable front movement is guaranteed when $\log M < 0$ and $\log Ca > -4$. Here M and Ca are viscosity ratio and capillary number respectively. Raeini et al. [17] used a finite volume method to investigate the controlling mechanisms at pore scale in two-phase flow including the layer flow, snap-off, and the geometry effect on trapping and mobilization of disconnected ganglia. Berg et al. [18] computed the relative permeability curves from pore scale quasi-static method and compared the results with relative permeability obtained from 3-D imaging.

The attempt here is to evaluate the performance of the interFoam solver in the prediction of two-phase immiscible flow at pore scale in drainage and imbibition scheme. A thorough investigation of the problem analytically and experimentally is presented by Chatzis and Dullien [19]. In their work, they used the conventional pore-doublet configuration to visualize the microscopic phenomena at narrow constriction on the scale of mm. As displacement may occur in imbibition or drainage schemes, numerical studies on both imbibition and drainage are performed.

3.1. Pore Doublet Reconstruction for Numerical Study

To reconstruct the 2-D pore doublet configuration for numerical study, the image of pore-doublet is digitized and imported to Gmsh [20] for meshing. The cells are composed of 54230 unstructured hexahedra grids. The overall domain of the pore doublet structure is 6.94 x 3.19 x 0.5 mm in x, y, z directions. Table 1 shows the overall quality of the mesh where results were obtained by checkMesh, an OpenFoam utility for evaluating mesh quality.

Table 1. Mesh Quality used for CFD Study

Avg mesh non-orthogonality	Maximum skewness	Maximum aspect ratio	Maximum cell openness
4.139	0.7876	2.2	2.4e-16

A view of meshed structure and representative cell configuration is presented in Figure 1.

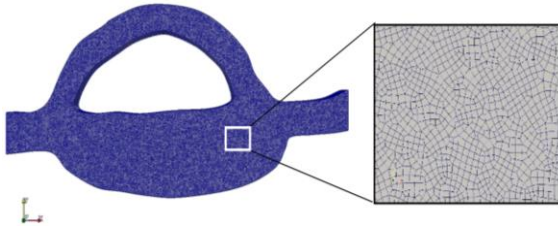


Fig. 1. Pore-Doublet, Left: meshed structure (54,230 cells); Right: zoom view of hexahedral grid mesh

3.2. Imbibition in a Pore-Doublet

The imbibition process is the displacement of the non-wet phase with the wetting phase due to the contribution of only capillary pressure [21]. Generally, for a pore-doublet configuration in either forced or spontaneous imbibition at very low speed when the capillary forces become significant, the wetting phase, first, fill and displace the non-wetting phase at the narrowest pore. Afterward, the process continues to push and displace the non-wet fluid in the larger constriction. The efficiency of the process is reported as 100% and all the non-wet fluid is displaced.

An imbibition experiment performed by Chatzis and Dullien [19] is selected for comparison with numerical results. The imbibition experiment is performed as

displacement of n-decane (colored with an oil-soluble dye), by 2% NaCl brine.

The fluid properties are extracted from the literature and presented in Table 2. [22, 23]. The boundary and initial conditions are shown in Table 3.

Table 2. Physical Properties of the Fluids

Fluid	Density (kg/cm ³)	Dynamic Viscosity (cP)	Interfacial Tension (dyne/cm)
n-Decane	700	8.38	53.2
2% NaCl Brine	1012.5	1.04	

Table 3. Boundary & Initial Conditions in Imbibition Simulation

	Flow rate (cm ³ /sec)	Pressure (MPa)	Water saturation (%)	Contact angle
Initial condition	0	200	0	-
Inlet	1.13e-9	fixed flux pressure	1	-
Outlet	1.13e-9	200	zero gradient	-
Top	No-slip	fixed flux pressure	0	45
Bottom	No-slip	fixed flux pressure	0	45
Wall	No-slip	fixed flux pressure	0	45

3.3. Numerical setup

In OpenFOAM, the numerical set up to build the discretization matrix for equation 14 is specified in a file called fvScheme. Every term in the differential equation can be discretized based on the specified scheme. The summary of discretization schemes is presented in Table 4. The 2-D solution procedure for the linear system is given in fvSolution file. The method of solving alpha, pressure, and speed are those presented in Table 5.

Table 3. Discretization Schemes used for the Set of Equations

Term	Discretization scheme
$\partial/\partial t$	Euler
$\nabla()$	Gauss Linear
$\nabla \cdot (\rho\phi\mathbf{U})$	Gauss Linear Upwind
$\nabla \cdot (\phi\alpha)$	Gauss van Lear
$\nabla \cdot (\alpha(1-\alpha)\phi_r)$	Gauss Linear
$\nabla^2()$	Gauss Linear
interpolation	Linear
normal gradient	corrected

ϕ here stands for the velocity.

Table 4. Solution Method for Alpha, Pressure, and Velocity

Parameter	Solver	Smoother	Pre-conditioner	Tolerance
α	smooth solver	symmetric Gauss-Seidel		1e-8
P	GAMC ^a	Gauss-Seidel	FDIC ^b	1e-5
U	smooth solver	symmetric Gauss-Seidel		1e-5

^a GAMC: Generalized geometric- algebraic multi-grid

^b FDIC: a faster version of the diagonal based incomplete Cholesky preconditioner

Two iterations for the α loop and one iteration for its sub-cycle are selected. The compression parameter for the saturation equation is set to 1 and the PIMPLE method is employed with 3 inner corrections and one outer correction.

Figure 2 shows the visual representation of the experiment extracted from Chatzis and Dullien [19]. The water is white and the n-decane is black. The water imbibes from the right into the pore doublet and first displaces the n-decane in the smaller capillary followed by imbibition into the larger capillary. The results of OpenFOAM modeling are presented in the sequence of plots on the right where water and n-decane are depicted in blue and red, respectively.

As expected from the pore doublet experiment and also observed in the simulation, when the velocity is very low the situation becomes more similar to spontaneous imbibition and capillary force is the main contributing driving force for the system. Consequently, imbibition takes place in the smaller constriction first then displacement occurs in the larger diameter pore. The process continues until 100% displacement of the non-wetting phase by the wetting phase is accomplished, as observed from the experiment (Figure 2). It is evident that the numerical results obtained are similar to the experiment results.

However, it should be mentioned that at higher injection rates, as the viscous forces become comparable to the capillary force, the displacement in the pore with a larger diameter will start even before displacement in the smaller diameter pore is completed. The simulation results at very first stages of the imbibition process are presented in Figure 3. The front advances at both pores, and as the process continues the front in pore with larger diameter stops and it retreats back. Confirmation of the numerical results requires visual experiments to monitor the flow behavior at the early stages of its development.

3.4. Drainage Experiment

At the pore-scale, drainage is defined as the forced displacement of wetting fluid by a non-wetting fluid [21]. It is expected that the invading fluid occupies and pushes the fluid in the pore with a larger radius because the capillary entry pressure is lower compared to a pore with smaller radius [19]. The drainage boundary conditions are shown in

Table 6. All the settings for discretization and solution of equations are the same as the imbibition process which is explained in the imbibition section.

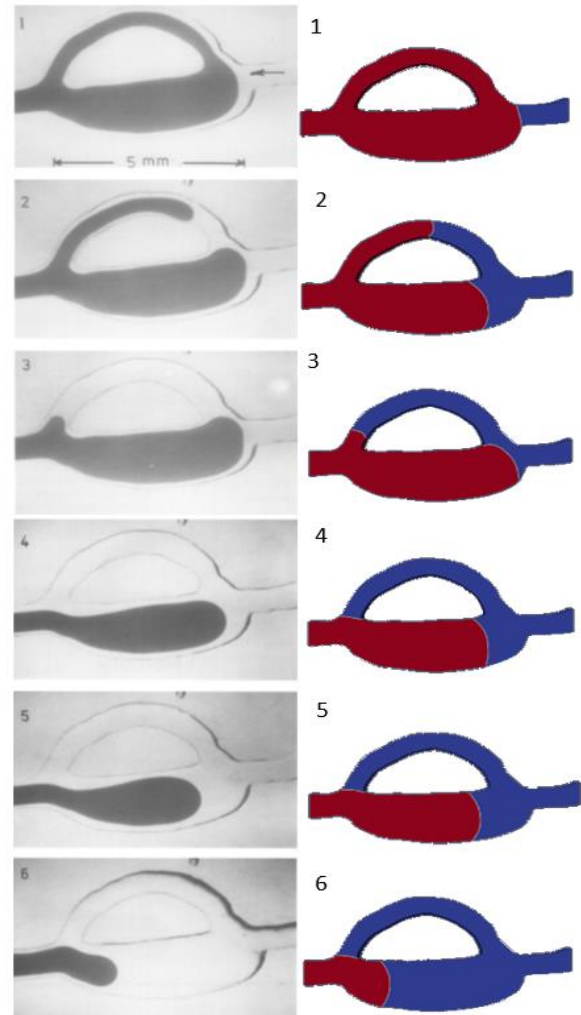


Fig. 1. Imbibition in a Pore-Doublet, with fluid movement from right to left; Left: Experimental; Right: Numerical

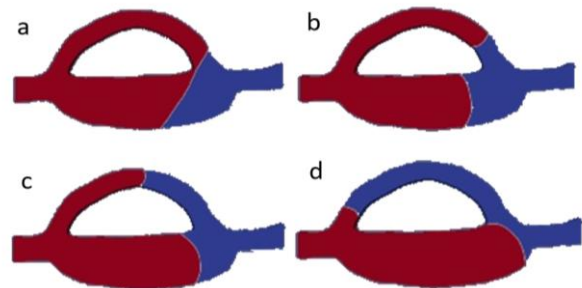


Fig. 2. Simulation results of initial imbibition stages

Table 5. Boundary & Initial Conditions in Drainage Simulation

	Flow rate (cm ³ /sec)	Pressure (MPa)	Water saturation (%)	Contact angle
Initial condition	0	200	0	-
Inlet	1.13e-9	fixed flux pressure	0	-
Outlet	1.13e-9	200	zero gradient	-
Top	No-slip	fixed flux pressure	1	45
Bottom	No-slip	fixed flux pressure	1	45
Wall	No-slip	fixed flux pressure	1	45

The drainage experimental results in the pore-doublet are presented in Figure 4 (left) with n-decane (black), a non-wetting fluid, injected from the left draining the water (white) to the right (downstream) preferentially through the larger diameter capillary. The numerical simulation results are presented on the right.

3.5. Sensitivity Analysis on Wall Boundary Conditions

To evaluate the ability of interFoam to capture the effect of the wetting film, some sensitivity analysis is performed by considering different slip conditions and contact angles. Four cases are compared as shown in the following subsections.

3.5.1. Slip Condition on Walls

In this case, all the parameters and boundary conditions are the same, just slip conditions on walls are active. The slip boundary condition erases the normal component of the variable at the patch and keeps the tangential components untouched. The results do not show any obvious difference with no-slip as boundary conditions.

The movement of the front at the juncture of two pore throats becomes unstable which leads to a snap-off effect. The overall behavior of front movement remains the same as the previous case. Snapshots of the simulation results are shown in Figure 5.

3.5.2. Slip Condition with Dynamic Contact Angle

Here, a dynamic contact angle was set at the boundaries. The advancing and receding dynamic contact angles are set to 45 and 60 degrees respectively. Results do not show any obvious difference compared to previous case, i.e., slip condition on walls.

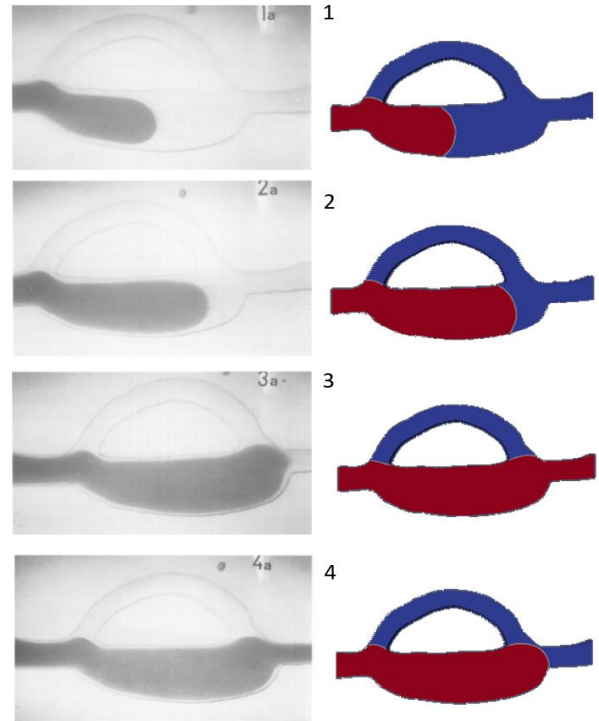


Fig. 3. Pore-Doublet Drainage; Left: Experimental; Right: Numerical



Fig. 4. Unstable drainage displacement from left to right with water (blue) displacing n-decane (red); c) shows backwards imbibition through the small capillary in the pore-doublet

3.5.3. Slip Condition with Low Dynamic Contact Angle

Here, the receding and advancing contact angles are set to 10 and 15 degrees respectively, a spread of wetting film near the walls can be seen. This is expected because, by setting the contact angle as low as 10 degrees, we assumed the walls are strongly water wet. The sequence of front advancement, in this case, is also presented in Figure 6. The advancing fluid (water) starts moving in both pore conduits, but at some point, the front retreats back and stays stagnant in the pore with a larger diameter. At the same time, the front at the pore with small diameter moves and pushes the n-decane out of the pore. The simulation results are comparable to the experiment. Large diameters control imbibition and the wetting fluid imbibes the pore with a smaller diameter first.

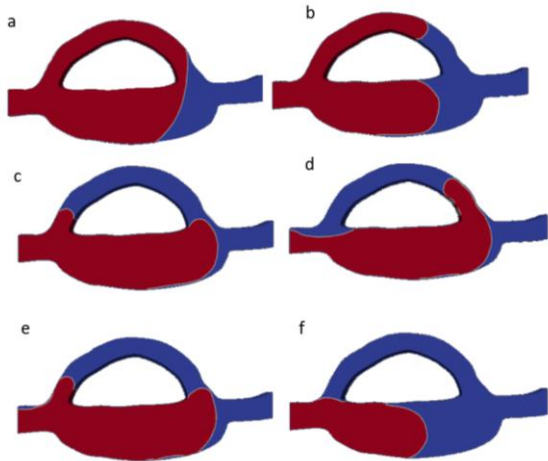


Fig. 5. Advancement of the Imbibition Front in Pore-Doublet with Low Dynamic Contact Angle

3.5.4. Refinement of Mesh at Wall, Dynamic Contact Angle, 3D Flow

Using snappyHexMesh the mesh is refined near the walls to better capture two-phase interface curvature near the wall. Consequently, the number of cells increased to 107891. The properties of cells are shown in Table 7 and a picture of the cells is shown in Figure 7.

Table 6. Mesh Properties Generated for Three Phase Flow with snappyHexMesh

Avg mesh non-orthogonality	Max skewness	Max aspect ratio	Max cell openness
15.75	1.844	108.1	2.18e-16

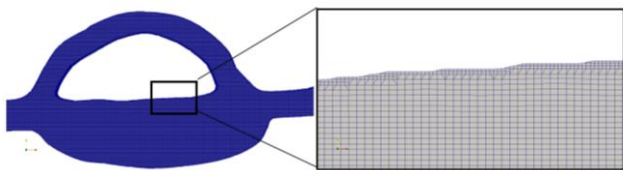


Fig. 6. Representation of Mesh with ParaView Software

The dynamic contact angle with receding and advancing angles of 10 and 15° is being used in the simulation. Three-dimensional flow simulation, despite the huge increase in run time, is being applied. Some snapshots from simulation on interface movement are being represented. The effect of thin-film flow of water that spreads over the wall is evident. As the slip condition is prevalent near the wall and water is being considered as wetting fluid, thin-film extension near the wall is expected. This phenomenon is being predicted by simulation. As demonstrated, interFoam can capture the advancement of film flow near the walls due to the high

wettability of water which is being set at boundaries. Figure 8 shows a thin film of water is being constructed while water imbibes throughout the pore doublet. The results are in agreement with the simulation obtained in case 3.5.3.

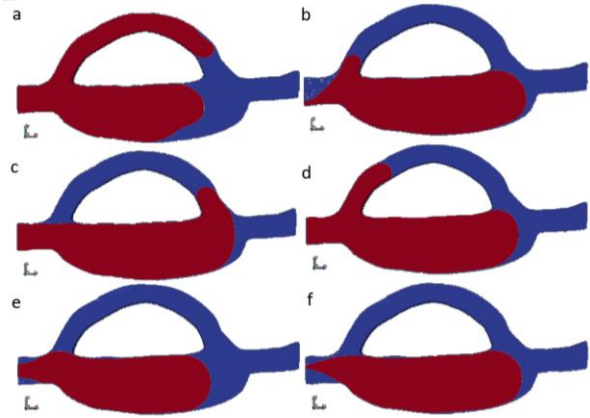


Fig. 7. Spreading of Wetting Film Near the Walls during Imbibition (right to left)

Comparing the results of slip conditions with no-slip conditions at the rock surface, the progression of film flow cannot be captured in no-slip conditions. However, at low to medium wettabilities, these conditions have no preferences in determining the movement of fluid and interface in the pore-doublet system. For strong wettability, applying slip flow is important to predict the creation and evolution of film flow near the rock surface. The effect of film flow due to the geometry of pore interconnection and their tortuosity will be more pronounced even in fluids with weak to medium wettabilities. Hence, applying slip conditions at the rock surface is important to capture the entrapment of non-wet fluids.

4. Conclusions

The interFoam solver for immiscible two phase flow was evaluated by predicting imbibition and drainage in a pore doublet and qualitatively comparing the results to the experiments carried out by Chatzis and Dullien [19]. As expected, the wetting fluid first enters the smaller diameter pore, in imbibition, displacing the non-wetting fluid then continues to the larger diameter pore. The results from the experiments and simulation are, qualitatively, in good agreement with each other. The simulation shows initial displacement in the smaller pore, then front movement in the larger diameter pore due to the competition of viscous and capillary forces. The wetting fluid in the larger diameter pore then retreats to the pore inlet before displacement in the smaller diameter pore continues. These phenomena are analytically explained by Chatzis and Dullien[19].

Drainage results from the simulation and experiment are, qualitatively, in agreement with each other. As

expected, the displacement happens in the larger diameter pore first and bypasses the wetting fluid in the narrow pore.

The sensitivity analysis shows that instability of the front is mainly related to the slip condition at the walls, and spreading of wetting film near the wall is prevalent at very low contact angles or in other words, in advancing fluids with strong wettabilities. Film flow is predicted at low contact angles, as shown in sections 3.5.3 and 3.5.4. Moreover, the effect of film flow especially in fluids with strong wettabilities can be predicted by applying slip conditions at the rock surface.

In this study, the ability of interFoam in prediction of imbibition and drainage for simple pore doublet system is evaluated. Numerical analysis must be conducted on a pore scale system, representative of real porous media for validation in the next step. Overall, the numerical solver can qualitatively predict the drainage and imbibition in a pore doublet system. Other CFD tools can be evaluated compared with each other.

Acknowledgements

The authors would like to thank the Hibernia Management and Development Company (HMDC), Chevron Canada Ltd, Petroleum Research Newfoundland and Labrador (PRNL), the Natural Sciences and Engineering Research Council of Canada (NSERC), the Province of Newfoundland and Labrador, and Mitacs for financial support. We thank our colleagues in the Hibernia EOR Research Group for their technical support.

References

1. S. Pasquier, M. Quintard and Y. Davit, "Modeling Two-Phase Flow of Immiscible Fluids in Porous: Buekley Leverett Theory with Explicit Coupling Terms," *Physical Review Fluids*, vol. **2**, no. 10, (2017).
2. "OpenFOAM," 2019. [Online]. Available: <https://openfoam.org/>.
3. F. Moukalled, L. Mangani, and M. Darwish *The Finite Volume Method in Computational Fluid Dynamics*, Springer, (2016), p. 129.
4. S. S. Deshpande, L. Anumolu and M. F. Trujillo, "Evaluating the Performance of the Two-Phase Flow Solver in InterFoam," *Computational Science and Discovery*, (2012).
5. M. Aboukhader, A. Georgoulas, M. Marengo, M. Gavaises and K. Vogiatzaki, "Simulation of Micro-Flow Dynamics at Low Capillary Numbers Using Adaptive Interface Compression," *Computers and Fluids*, vol. **165**, pp. 13-32, (2018).
6. M. Gad-El-Hak, "The Fluid Mechanics of Microdevices—the Freeman Scholar Lecture," *J. Fluids Eng. Trans. ASME*, vol. **121**, no. 1, pp. 5–33, (1999).
7. J. U. Brackbill, D. B. Kothe and C. Zemach, "A Continuum Method for Modeling Surface Tension," *Computational Physics*, vol. **100**, pp. 335-354, (1992).
8. S. M. Damian, PhD Thesis: An Extended Mixture Model for the Simultaneous Treatment of Short and Long Term Scale, (2013).
9. T. Holzman, Mathematics, Numerics, Derivations and OpenFOAM, (2016).
10. H. Rusche, Computational Fluid Dynamics of Dispersed Two Phase Flow at High Phase Fractions, University of LONDON, (2002).
11. R. Lenormand and E. Touboul, "Numerical Models and Experiments on Immiscible Displacements in Porous Media," *Journal of Fluid Mechanics*, vol. **189**, pp. 165-187, (1988).
12. M. Mahmoodi, L. A. James and T. Johansen, "Automated Advanced Image Processing for Micromodel Flow Experiments: An application Using LabView," *Journal of Petroleum Science and Engineering*, no. **167**, pp. 829-843, (2018).
13. S. Mahdavi and L.A. James, "Micro and Macro Analysis of Carbonated Water Injection (CWI) in Homogeneous and Heterogeneous Porous Media," *Fuel*, vol. **257**, no. June, p. 115916, (2019).
14. P. Nguyen, H. Fadaei, and D. Sinton, "Pore-scale Assessment of Nanoparticle-Stabilized CO₂ Foam for Enhanced Oil Recovery," *Energy and Fuels*, vol. **28**, no. 10, pp. 6221–6227, (2014).
15. H. Khorshidian, L.A. James, and S. D. Butt, "Pore-Level Investigation of the Influence of Wettability and Production Rate on the Recovery of Waterflood Residual Oil with a Gas Assisted Gravity Drainage Process," *Energy and Fuels*, vol. **32**, no. 6, pp. 6438–6451, (2018).
16. F. Guo and S. A. Aryana, "An Experimental Investigation of Flow Regimes in Imbibition and Drainage Using a Microfluidic Platform," *Energies*, vol. **12**, pp. 1-13, April (2019).
17. A. Q. Raeini, B. Bijeljic, and M. J. Blunt, "Numerical Modelling of Sub-pore Scale Events in Two-Phase Flow Through Porous Media," *Transport in Porous Media*, vol. **101**, no. 2, pp. 191–213, (2014).
18. S. Berg *et al.*, "Modelling of Imbibition Relative Permeability by Direct Quasi-Static Approach," *International Symposium of the Society of Core Analysts*, pp. 1–12, (2016).
19. I. Chatzis and F. A. Dullien, "Dynamic Immiscible Displacement Mechanisms in Pore Doublets: Theory Versus Experiments," *Journal of Colloid and Interface Science*, pp. 199-222, January (1983).
20. C. Geuzaine and J. F. Remacle, "Gmsh: a Three Dimensional Finite Element Mesh Generator with Built-in Pre- and Post-Processing Facilities,"

International Journal for Numerical Methods in Engineering, vol. **79**, no. 11, pp. 1309-1331, (2009).

21. J. Bear, *Dynamics of Fluids in Porous Media*, New York: Elsevier, (1972).
22. A. Goebel and K. Lunkenheimer, "Interfacial Tension of Water/n-Alkane Interface," *Langmuir*, vol. **13**, pp. 396-372, (1997).
23. National Center for Biotechnology Information. PubChem Database. Decane CID=15600, "<https://pubchem.ncbi.nlm.nih.gov/compound/Decane>," [Online]. [Accessed July 2019].

Dynamic pore-scale modeling of residual fluid configurations in disordered porous media

Yanbin Gong*, Mohammad Sedghi, and Mohammad Piri

Center of Innovation for Flow through Porous Media, Department of Petroleum Engineering, University of Wyoming, Laramie, Wyoming 82071, United States

Abstract. Fluid trapping in porous media is important in many subsurface flow processes such as enhanced oil recovery and geological sequestration of carbon dioxide. To achieve optimal performance in such applications, a fundamental understanding of residual trapping mechanisms at the pore scale is necessary. In this work, we present a computational study of fluid trapping behaviors in natural porous media under different flow regimes by employing a dynamic pore-network modeling approach. The model incorporates many advanced features that have not been collectively used in previous dynamic platforms. For instance, it rigorously solves for fluid pressure fields from two-phase mass balance equations in each pore element, incorporates a detailed description of pore-scale fluid displacement dynamics of piston-like advance, snap-off, and pore-body filling, and explicitly accounts for flow through wetting layers forming in corners and rough surfaces of pore spaces. Moreover, we extend the ability of our model by including contact angle hysteresis, which is often neglected in existing dynamic models. A heavily-parallelized implementation of this platform is further advanced to achieve an efficient computational performance. We first conduct primary drainage and imbibition simulations in pore networks representing Bentheimer and Berea sandstones. We show that the predicted two-phase relative permeability curves agree well with their experimental counterparts reported in the literature. Afterwards, the validated model is used to systematically probe fluid trapping behaviors in a core-sized pore network that is constructed from high-resolution micro-computed tomography images of a Berea sandstone core sample. The effects of dynamic flow conditions and fluid properties on core-scale two-phase displacement pattern, residual-fluid configuration, and residual oil saturations are examined in detail. Fluid trapping properties such as maximum and average residual-fluid cluster size and capillary-controlled invasion selectivity at the pore scale are analyzed under both capillary- and viscous-dominated flow regimes.

1 Introduction

Residual trapping of the non-wetting fluid in porous media is important in many science and engineering applications such as enhanced oil recovery (EOR), geological sequestration of carbon dioxide, and contaminant removal from groundwater [1–3]. To achieve the optimal performance in these applications, it is crucial to accurately model the flow behaviors and predict the residual fluid configurations. However, multiphase flow systems are exceedingly complex due to, for instance, the complicated pore space geometries and topologies, fluid-fluid capillary interaction, and wettability effects [4–11]. Among many other efforts to better understand the residual trapping behaviors, extensive numerical simulation studies have been conducted at multiple scales. In the conventional continuum models, nevertheless, most of the complex pore-scale processes are significantly simplified and taken into consideration using a series of input functions, e.g., relative permeability, with little physical basis. Yet these properties are expensive and time-consuming to obtain experimentally. Therefore, physics-based models that can predict fluid trapping properties and bridge the gap between the pore and continuum scales flow processes are desperately needed.

Over the years, with the advances in imaging techniques, e.g., micro-computed tomography (micro-CT), different pore-scale simulation techniques have been proposed and investigated to fulfill different purposes. In general, pore-scale models can be categorized into direct pore-level models and pore-scale network models. In the first group, computational fluid dynamics (CFD) methods, such as level-set [12], lattice Boltzmann [13, 14], and volume-of-fluid [15], are utilized to solve the governing flow equations in the pore space obtained through the imaging techniques. The direct models preserve the detailed pore space geometries. However, the complex pore space geometries of naturally-occurring rocks make their computations expensive. The complicated pore-scale fluid dynamics of two-phase system carry the modeling works into a further level of complexity. In the second group of pore-scale models, fluid flow and solute transport are solved in a network of inter-connected pores and throats with idealized geometries. Through this approximation, the fluid interfacial movements can be described by a set of displacement rules with closed-form mathematical expressions to substantially reduce the computational costs. In 1956, Fatt [16] made the pioneering work of modeling drainage process in porous media by using a two-dimensional (2D) network of cylindrical tubes. Since then, tremendous progress has been made in developing

* Corresponding author: ygong@uwyo.edu

different network models, which mainly include quasi-static and dynamic models. In quasi-static models, different fluids are assumed to be at capillary equilibrium and solely the capillary pressure determines the fluid displacement sequence [17–19]. Therefore, the quasi-static models are only applicable to slow flow processes where the capillary number is approximately in the order of 10^{-7} or lower.

To account for the viscous effect, the dynamic models solve the fluid pressure field by writing mass conservation equations for all volume-occupying phases in every pore spaces. In this regard, the computational demand of the dynamic models is orders of magnitude higher than that of the quasi-static simulation. Koplík et al. [20], Dias and Payatakes [21], and Lenormand et al. [22] are among the first to develop the dynamic algorithm for two-phase flow in porous media. They wrote the Washburn equation at the fluid–fluid invasion front to account for the capillary and viscous forces. In these early studies, many pore-scale fluid dynamics such as fluid flow through the wetting layers are neglected, even though they are crucial in maintaining the connectivity of the wetting phase and affecting the residual trapping behaviors of the non-wetting fluid during two-phase flow [23, 24]. Later, Singh and Mohanty [24] proposed a rule-based scheme to implement layer flow for primary drainage displacement. They calculated the wetting phase pressure in layers using a spatial extrapolation approximation and updated the wetting layer volume following a heuristic rule that the amount of wetting phase removed from a layer was proportional to its local capillary pressure drop. Nguyen et al. [25] studied the effect of flow rate on imbibition displacement properties assuming that no viscous pressure drop was associated with the non-wetting phase and the pressure of the wetting phase was constant behind the displacement front. With a similar approach, Wang et al. [26] simulated two-phase imbibition in a regular 2D network consisting of 800 pores and 1540 throats. Thompson [27] introduced a fully dynamic model, in which the local capillary pressure is approximated as a function of the local water saturation in regular cubic pore spaces. To extend the Thompson’s approach, Sheng and Thompson [28] conducted steady-state flow simulations to predict two-phase relative permeability; Joekar-Niasar and Hassanizadeh [29] investigated the non-equilibrium capillary pressure during two-phase flow. More recently, Li et al. [30] studied the effect of viscosity ratio on two-phase imbibition inside a regular 2D pore network consisting of 100×50 pores and a regular three-dimensional (3D) pore network with $20 \times 20 \times 20$ pores. Boujelben et al. [31] presented a new dynamic model to study low-salinity water injection, where the wetting layer was treated as volumeless. Qin et al. [32] extended the model of Joekar-Niasar and Hassanizadeh [29] and studied air-water drainage flow with phase change in two pore networks with 1,163 and 10,619 pores, respectively. Yelkhovskiy and Pinczewski [33] modeled two-phase capillary rise in both round and polygonal capillary tubes by solving an averaged Navier-Stokes equation.

While the geometries of the pore spaces of naturally occurring porous media can be complex [34, 35], to the best of our knowledge, existing fully dynamic models always assume the pore elements have square cross sections. Moreover, factors such as neglecting wettability hysteresis, ignoring throat volumes, and neglecting snap-off

displacements in pore bodies further limit the predictability of the previous developed models.

This study aims at developing a new, generalized dynamic pore-network modeling platform to study fluid trapping behaviors in natural porous media under different flow regimes. We start with an introduction of the representative pore networks used in this work. This is followed by a detailed description of the new dynamic pore-scale modeling algorithm and its parallel implementation. Then, quantitative and qualitative validations of the modeling platform are presented. Afterwards, the model is used to examine the effects of dynamic flow conditions on two-phase displacement patterns, residual oil cluster configurations, and final residual oil saturation during different imbibition displacements. In addition, the impacts of fluid properties including viscosity ratio and wettability are discussed in detail. Finally, the main findings of this work are summarized in the conclusion section.

2 Pore network constructions

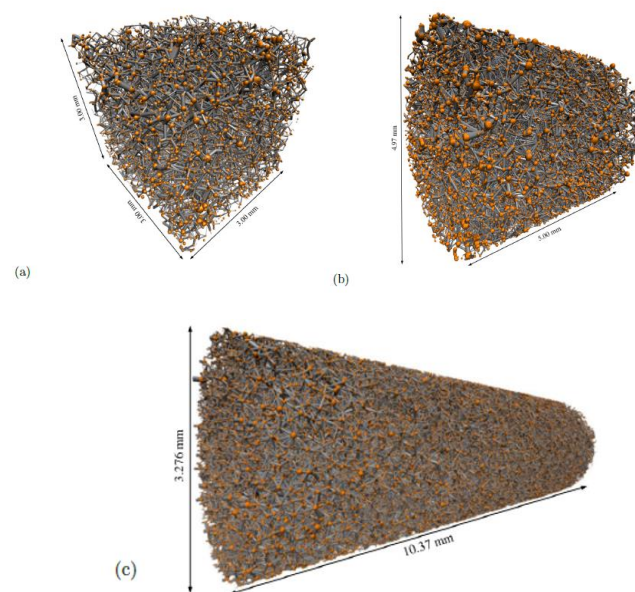


Figure 1. Visualization of (a) the small Berea pore network, (b) the Bentheimer pore network, and (c) the large Berea pore network. Orange and gray colors represent the pores and throats, respectively.

In this work, we utilize four networks for different purposes. For the purpose of validation, we first generate a 2D lattice pore network that is statistically equivalent to the micro-model reported in the experimental study of Lenormand et al. [22]. This 2D pore network consists of 100×100 pores with cross-sectional shape of square. Then, we utilize two pore networks being representative of the Berea and Bentheimer sandstones to predict their two-phase relative permeabilities. The Berea network (see Fig. 1a), having a dimension of $3 \times 3 \times 3 \text{ mm}^3$, is constructed from a process-based technique [36] and has been successfully tested in previous modeling studies [37–39]. The Bentheimer network (see Fig. 1b), having a length of 5.00 mm and a cross-sectional diameter of 4.97 mm, is extracted from the high-resolution (scanning resolution 2.6

μm) micro-CT images of a Bentheimer sandstone rock sample [40]. The Bentheimer rock sample has a measured porosity of 23.42% and an absolute permeability of 2568 mD. To investigate two-phase flow behaviors and residual fluid configurations in disordered porous media, we further extract a longer, cylindrical pore network directly from high-resolution (scanning resolution 2.49 μm) micro-CT images of a Berea sandstone sample with a measured porosity of 21.69% and an absolute permeability of 623 mD [40]. The network (see Fig. 1c) has a length of 10.374 mm and a cross-sectional diameter of 3.276 mm. Hereinafter, we will refer to this network as the large Berea network to distinguish it from the smaller network constructed using the process-based technique. Pores and throats of the three pore networks can have different cross-sectional shapes of square, equilateral and scalene triangles.

3 Model description

3.1 Model assumptions

Fluids are assumed to be Newtonian, incompressible, and immiscible. The flow process is isothermal and there is no interaction between the fluids and the rock material. Also, clay content is assumed to be fully saturated with immobile water. It is worth noting that in our model, both pore and throat elements have their own volume and conductivity. This is distinct from the existing dynamic models, where zero volume or zero conductance are often imposed on either throat elements or pore bodies to simplify the computations. Hereinafter, we will use the terms “water” and “oil” to represent the wetting and non-wetting phases, respectively, and “pore elements” to denote both pore bodies and pore throats.

3.2 Pore-level physics of two-phase flow

Based on the experimental observations of two-phase flow in porous media [41–43], three fundamental pore-level displacing mechanisms are included in this dynamic model: piston-like, cooperative pore-body filling, and snap-off. Their detailed descriptions are presented in our previous work [44]. However, it is worth mentioning that snap-off corresponds to the displacement of the non-wetting phase in the center of a pore element by arc menisci (AMs) formed in the corners and on the rough surfaces of the pore space. When local capillary pressure decreases, the relevant wetting corners gradually swell. Eventually, at a critical threshold capillary pressure, oil at the center is snapped off and the element is spontaneous filled by water. This displacement mechanism significantly contributes to oil entrapment in porous media [45, 46].

3.3 Phase hydraulic conductance

The hydraulic conductance of a pore element filled with a single phase is calculated based on its geometries [18, 47]:

$$g = \begin{cases} \frac{3R^2A}{20\mu}, & \text{for triangular elements} \\ \frac{0.5623GA^2}{\mu}, & \text{for square elements} \end{cases} \quad (1)$$

where R , A , and G are the element’s inscribed radius, cross-sectional area, and shape factor, respectively; and μ is the fluid viscosity.

After a local drainage, it is impossible for oil to completely drain water out of an angular pore element as a certain amount of water remains in the corners. In such fluid configurations, the flow area open to the corner water and the center oil can be computed as:

$$A_w = \begin{cases} r^2 [\cos \theta (\cot \alpha \cos \theta - \sin \theta) + \theta + \alpha - \frac{\pi}{2}], & \text{if } \alpha + \theta \neq \frac{\pi}{2} \\ \frac{b^2}{\tan \alpha}, & \text{if } \alpha + \theta = \frac{\pi}{2} \end{cases} \quad (2)$$

$$A_o = A - A_w \quad (3)$$

$$r = \frac{\sigma_{ow}}{p_c} \quad (4)$$

where α is the corner half angle of the pore element; θ_{ow} is the contact angle of the oil-water-solid system; r is the curvature radius of the AMs; σ_{ow} is the oil-water interfacial tension; p_c is the local capillary pressure; and o and w are the phase indexes denoting oil and water phases. The center oil conductance is then evaluated using A_o and Eq. 1, while the calculation of the corner water conductance can be found in [44, 48, 49].

One should note that at pore scale, the oil conductivity of an element could instantly change from a finite value to zero immediately after the oil phase is snapped off or displaced by water.

3.4 Governing equations

The volume conservation equation of each fluid phase is applied at every pore and throat:

$$V_i \frac{dS_{\alpha,i}}{dt} = \sum_{j=1}^{N_i} \frac{g_{\alpha,ij}}{L_{ij}} (p_{\alpha,j} - p_{\alpha,i}), \quad \alpha = o, w \quad (5)$$

where V_i and N_i are the respective total volume and coordination number of element i ; S_{α} and p_{α} are the saturation and pressure of phase α . The equivalent phase conductance $\frac{g_{\alpha,ij}}{L_{ij}}$ through two neighboring elements, i and j , is considered as the harmonic mean of the phase conductance of i and j . In addition, we know that for any element containing two phases, the pressures of oil and water are related by the local capillary pressure, as:

$$p_{c,i} = p_{o,i} - p_{w,i} \quad (6)$$

and the summation of phase saturations in i follows:

$$S_{o,i} + S_{w,i} = 1 \quad (7)$$

Combining Eqs. 5–7, we obtain the following pressure equation, as:

$$\sum_{j=1}^{N_i} \left(\frac{g_{w,ij}}{L_{ij}} + \frac{g_{o,ij}}{L_{ij}} \right) (p_{w,j} - p_{w,i}) = - \sum_{j=1}^{N_i} \left(\frac{g_{o,ij}}{L_{ij}} \right) (p_{c,j} - p_{c,i}) \quad (8)$$

We choose p_w as the principal unknown because water is hydraulically connected across the entire pore network.

3.5 Local rules

3.5.1 Local displacement

At pore scale, the occurrence of the local displacement is controlled by the threshold capillary pressure, p_c^{th} . In this work, the threshold capillary pressure for piston-like displacement is calculated using the Mayer-Stowe-Princen (MSP) theory [50, 51]. Interested readers are referred to [37, 52] to find the detailed computations of the p_c^{th} for piston-like, cooperative pore-body filling, and snap-off displacements. However, it is worth mentioning that for a given pore element, the threshold capillary pressure for piston-like displacement is always larger than that of the snap-off event. Therefore, piston-like displacement is more favored when the fluid configuration is allowed. However, snap-off does not require the presence of a main terminal meniscus (*MTM*) to occur, meaning that it can take place anywhere in the porous media as long as the fluids are hydraulically connected.

In this work, for a partially invaded element, we assume its local capillary pressure equals to the threshold capillary pressure of the local displacement (i.e., local drainage or imbibition) until the element is fully invaded. By the end of a local imbibition, oil is fully displaced and the local capillary pressure disappears. In contrast, after a local drainage, water layers form in the corners of the angular pore space. In this case, we define a critical saturation corresponding to the point when the entire central pore space is occupied by oil under the threshold drainage capillary pressure of $p_{c,piston}^{th,dra}$. Denoted as $S_{w,piston}^{th,dra}$, this critical saturation can be obtained using Eqs. 2–4 and $p_{c,piston}^{th,dra}$.

Snap-off handling. Immediately after a water element is invaded by oil, we compute its threshold capillary pressure for snap-off, $p_{c,snap}^{th,imb}$, and its critical saturation $S_{w,snap}^{th,imb}$ corresponding to $p_{c,snap}^{th,imb}$ using Eqs. 2–4. In our simulations, as fluid saturations are updated after every time step, a snap-off checking process is performed for all elements containing two phases; if the updated water saturation in an element i exceeds $S_{w,snap}^{th,imb}$, spontaneous snap-off will occur and the oil phase will break into n parts, where n is the coordination number of i . Note that during this process, new *MTMs* will form, resulting in an instant increase in the local capillary pressure. This, in turn, accelerates the retreat of oil from i to its neighbors [53]. Accordingly, we update the local capillary pressure in element i based on the curvature of the newly formed *MTMs*:

$$p_{c,i} = \frac{2\sigma \cos \theta_{ow,i}^{adv}}{R_i} \quad (9)$$

where R_i and $\theta_{ow,i}^{adv}$ are the inscribed radius and advancing contact angle of i .

3.5.2 Contact angle hysteresis and corner interface handling

We assign each pore element a receding (θ_{ow}^{rec}) and advancing (θ_{ow}^{adv}) contact angle for the local drainage and imbibition displacement, respectively. Moreover, within each element, different parts of the solid surface can exhibit different wettabilities. In specific, each element is initially full of water and is considered as strongly water-wet. After it is invaded by oil, the water-filled corners will remain strongly water wet, while the rest of the solid surfaces contacted by oil will become less water-wet (i.e., have higher contact angles).

When a new *AM* forms, its initial location can be uniquely determined by the threshold capillary pressure, contact angle, and the corner half angle of the pore element through a geometrical analysis [37]. As fluid flow continues, the configuration of the *AM* is then subject to the dynamic change of the local capillary pressure. It can stay pinned with a fixed apex-meniscus distance b as the contact angle, θ_{ow}^h , hinges between θ_{ow}^{rec} and θ_{ow}^{adv} or it can move at a constant θ_{ow}^{rec} or θ_{ow}^{adv} . The detailed calculation of the corner interface configuration can be found in [44]. It is evident that such wettability hysteresis behavior results in a non-smooth local capillary pressure–water saturation function.

3.5.3 Local capillary pressure

We note that for a pore element containing two phases, the fluid interface configuration and the phase saturation can be uniquely determined under a given local capillary pressure, as illustrated in Appendix C in [37]. In addition, at a new time step $n+1$, the local capillary pressure, $p_{c,i}^{n+1}$, will be either in the range of $[p_{c,i}^n, p_{c,i}^{max}]$ (or $[p_{c,snap,i}^{th,imb}, p_{c,i}^n]$) for a local drainage (or imbibition) displacement, where $p_{c,i}^n$ is known from the last time step n and $p_{c,i}^{max}$ is a local maximum. In view of these, we propose a bi-sectional iterative method to find the $p_{c,i}^{n+1}$ in any pore element using the newly updated local saturation, $S_{w,i}^{n+1}$. The detailed calculation procedure is illustrated in Fig. 2. It is important to note that this iterative numerical scheme allows our dynamic pore-network modeling platform to work with pore elements with irregular and arbitrary cross-sectional shapes.

3.6 Boundary and initial conditions

At the inlet of the pore network, a Neumann boundary condition is employed to accommodate a constant fluid injection rate. Specifically, the following two equations are added to the linear system of the pressure equations:

$$\sum_{j=1}^{N_{in}} \frac{g_{w,ij}}{\mu_w} (p_{w,j} - p_{w,in}) = -Q_{w,in} \quad (10)$$

$$\sum_{j=1}^{N_{in}} \frac{g_{o,ij}}{\mu_o} (p_{o,j} - p_{o,in}) = -Q_{o,in} \quad (11)$$

where N_{in} is the total number of inlet-connected throats; and $Q_{o,in}$ and $p_{o,in}$ are the fluid injection rate and injection pressure, respectively. At the outlet of the pore network, a constant production pressure $p_{w,out}$ is enforced for the water phase. When oil is also present at the outlet, we adopt the assumption proposed by Joekar-Niasar and Hassanizadeh [29] and set the local capillary pressure gradient in the outlet-connected throats as zero, namely, $\left. \frac{\partial p_c}{\partial x} \right|_{outlet} = 0$. A no-flow condition is applied at the side boundaries of the network.

In our simulations, the pore networks are initially full of water and are gradually drained by oil during the primary drainage displacement. After a steady-state condition (or a targeted initial oil saturation) is reached, the simulation proceeds to the imbibition displacement, during which water is injected at the inlet of the pore network under a constant volumetric flow rate.

$$\sum_{j=1}^{N_i} \left(\frac{g_{w,ij}^n}{L_{ij}} + \frac{g_{o,ij}^n}{L_{ij}} \right) (p_{w,j}^{n+1} - p_{w,i}^{n+1}) = - \sum_{j=1}^{N_i} \left(\frac{g_{o,ij}^n}{L_{ij}} \right) (p_{c,j}^n - p_{c,i}^n) \quad (12)$$

A linear system of pressure equations is then obtained and solved with an algebraic multigrid preconditioned conjugated gradient method using PETSc parallel solver package [54]. Then, we explicitly update the fluid saturations in pores and throats by discretizing the volume balance equation (Eq. 5), as:

$$V_i \frac{S_{\alpha,i}^{n+1} - S_{\alpha,i}^n}{\Delta t^{n+1}} = \sum_{j=1}^{N_i} \frac{g_{\alpha,ij}^n}{L_{ij}} (p_{\alpha,j}^{n+1} - p_{\alpha,i}^{n+1}), \quad \alpha = o, w. \quad (13)$$

To keep the numerical stability, the time step size (Δt) is chosen in a way that at most one pore element can be fully invaded at every time step. Moreover, after every certain number of invasions, we adjust the pore-scale capillary pressures in accordance with the macroscopic capillary pressure distribution to avoid possible numerical oscillations in local p_c . The inherent assumption here is that in a porous medium, the variation of the capillary pressure along the principal flow direction is smooth and continuous. To this end, the macroscopic p_c distribution along the length of the pore network is first calculated as the averages of the pore-scale capillary pressures over the cross-sections of the network. Then, the capillary pressures in different pore elements are updated according to the element's distance from the inlet of the network and the macroscopic p_c distribution.

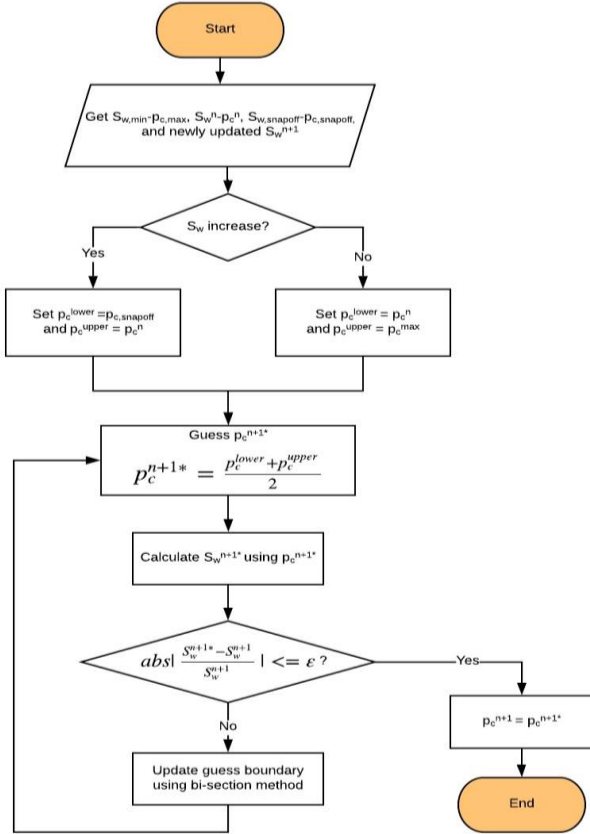


Figure 2. Flow chart of the iterative local capillary pressure finding algorithm.

3.7 Numerical implementation

At a new time step $n + 1$, we first update the fluid pressure field implicitly by listing the pressure equation (Eq. 8) for all connected pores and throats, as:

3.8 Domain decomposition and parallelization

For a fully dynamic pore network model, the computation of phase pressure updating, local capillary pressure iteration, and fluid interface tracking can become significant, particularly for multiphase displacements in a large pore network. In this work, the modeling platform is designed to run on massively parallel computing architectures. To this end, the entire large Berea network is divided into a number of sub-domains. The MVAPICH2 library, a high performance message passing interface (MPI) implementation, is used to communicate information between different computing processors. Please refer to our previous works [44] for more details of parallel computing.

4 Results and discussions

In section 4.1, we first validate our dynamic pore network model. Afterwards, we conduct a series of two-phase displacement simulations to examine the effects of flow rate, viscosity ratio (M), and wettability on dynamic displacement behaviors and residual fluid configurations. Specifically, we conduct five imbibition simulations (simulations 1–5) under elevated water injection rates. Then, another two imbibition simulations (simulations 6 and 7) are performed with enhanced water viscosity to study the viscosity ratio effect. We define the M as the ratio of the viscosity of the invading phase to that of the defending phase. Lastly, four more imbibition simulations (simulations 8–11) are designed with

various oil-water contact angles to study the wettability effect. In all simulations, the imbibition displacements are initiated at an initial oil saturation of $S_{oi} = 0.9$. Properties of the fluids used in these simulations are listed in Table 1. The detailed simulation conditions and residual oil saturations (S_{or}) are summarized in Table 2.

Table 1. Properties of the fluids used in simulations 1–11.

Fluid	No.	Viscosity (cp)	θ_{ow}^{rec}	θ_{ow}^{adv}
Oil	1-11	0.83		
Water	1-5	1.01	0-15	15-30
	6	10.1	0-15	15-30
	7	101	0-15	15-30
	8	1.01	0-15	0-15
	9	1.01	15-30	30-45
	10	1.01	30-45	45-60
	11	1.01	45-60	60-75

Table 2. Fluid injection rates, capillary numbers, and residual oil saturations of simulations 1–11.

No.	$Q_{w,inlet}$ (cc/min)	N_c	S_{or} (%)
1	0.001	2×10^{-7}	43.9
2	0.01	2×10^{-6}	43.3
3	0.1	2×10^{-5}	42.2
4	1.0	2×10^{-4}	34.8
5	10.0	2×10^{-3}	27.0
6	0.1	2×10^{-4}	29.7
7	0.1	2×10^{-3}	9.3
8	0.001	2×10^{-7}	51.2
9	0.001	2×10^{-7}	39.4
10	0.001	2×10^{-7}	36.6
11	0.001	2×10^{-7}	36.3

4.1 Model validation

To validate our model, we first carry out a series of primary drainage simulations in the 2D network over a wide range of capillary numbers and viscosity ratios, following the experimental conditions reported in Lenormand et al. [22]. Figs. 3a–3c show the development of the simulated oil flow paths in the 2D network at flow conditions of (a) $\log M = 2.0$ and $\log N_c = -0.9$, (b) $\log M = -4.7$ and $\log N_c = -3.0$, and (c) $\log M = -4.7$ and $\log N_c = -9.3$. Three important two-phase displacement configurations of stable displacement (Fig. 3a), viscous fingering (Fig. 3b), and capillary fingering (Fig. 3c) are clearly identified and they agree well with the experimental observations presented in [22]. In the stable displacement scenario with a viscosity ratio of $M \gg 1$ and a large capillary number, the invasion front between the fluids is flat and oil invades nearly all of the pore spaces behind of it. In this case, the pore-scale displacements exclusively take place at the invasion front because the viscous pressure drop associated with the invading phase dominates the displacing process (Fig. 3a). As the viscosity ratio becomes much smaller than one, there is almost no viscous resistance to the flow of the invading phase, while the viscous defending phase consumes nearly all the pressure drop. In consequence, as the invading oil creates a small number of fingers with relatively

high conductivities at the inlet, a few of them grow rapidly toward the outlet as the invasions continues, resulting in a quick breakthrough and leaving most of the network uninvaded (Fig. 3b). With the decrease in N_c , the viscous force becomes negligible in both fluids and the pore-scale displacement sequence is largely controlled by the capillary force. In this case, the invading phase selectively takes paths with more favorable capillary pressures and develops capillary fingering, as shown in Fig. 3c. Note that the configurations of the viscous fingering and capillary fingering have distinct differences. The former invasion configuration primarily orient towards the outlet, while the latter one grows anomalously inside the network. This is also in line with the experimental observations reported in [22].

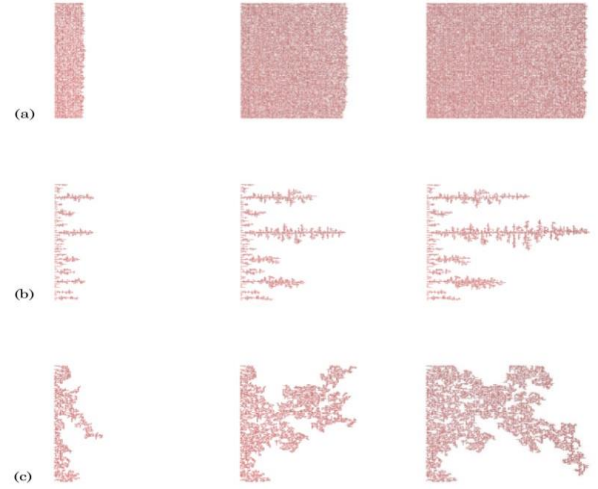


Figure 3. Visualization of the oil configurations in the 100×100 two-dimensional (2D) pore network during primary drainage simulations under different flow regimes: (a) $\log M = 2.0$ and $\log N_c = -0.9$, (b) $\log M = -4.7$ and $\log N_c = -3.0$, and (c) $\log M = -4.7$ and $\log N_c = -9.3$. Pictures are placed from left to right as injection continues. Only elements invaded by oil are shown in red.

We further conduct primary drainage and imbibition simulations in the small Berea and the Bentheimer networks to predict their two-phase relative permeability curves at a low flow rate. During the simulations, the phase relative permeability is computed as:

$$k_{r\alpha} = \frac{\mu_\alpha Q_{\alpha,in} \Delta p_{s\alpha}}{\mu_s Q_{s\alpha,in} \Delta p_{t\alpha}} \quad (14)$$

where the subscripts s and t represent the single- and two-phase flow condition, respectively, and Δp_α is the [33]pressure drop of phase α across the network. A receding contact angle of 0° is used for the primary drainage displacements, whereas advancing contact angles in the ranges of $60-75^\circ$ and $30-50^\circ$ are assigned for the Berea and the Bentheimer networks, respectively, following the works of [37] and [18].

In Figs. 4 and 5, the computed oil and water relative permeabilities versus water saturation for the small Berea and the Bentheimer networks are compared quantitatively against their corresponding measured data collected from the work of Oak [55] and Oren et al. [18]. As shown in these two figures, our predicted relative permeability curves agree closely with

the experimental data for both primary drainage and imbibition displacements. Moreover, the dynamic model accurately predicts the residual oil saturations at the end of the imbibition displacements in both sandstones. We also note that at the early stage of the primary drainage, the predicted water relative permeability underestimates the experimental data. This discrepancy is caused by the fact that phase saturations along the network are not uniform before oil breakthrough. Overall, the simulation results illustrate that our dynamic pore network model is capable of capturing two-phase flow properties under a wide range of flow conditions.

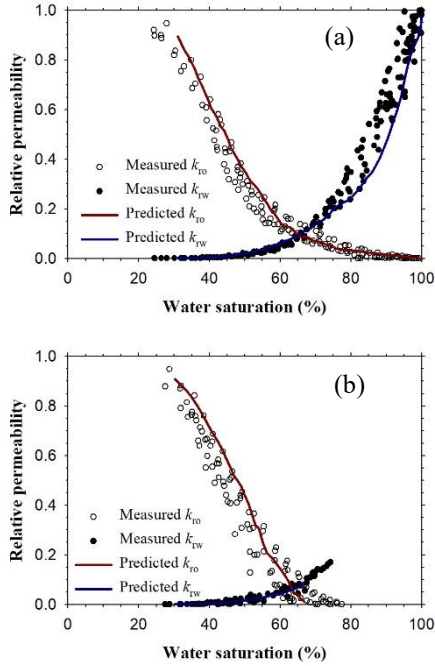


Figure 4. Predicted relative permeabilities (k_r) versus water saturation (S_w) compared against experimental data collected from the literature [55] for (a) primary drainage and (b) imbibition displacements. Both simulations are conducted in the small Berea network.

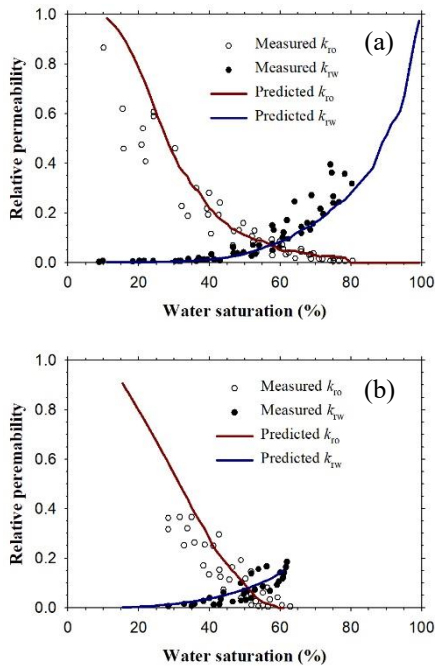


Figure 5. Predicted relative permeabilities (k_r) versus water saturation (S_w) compared against experimental data from the literature [18] for the (a) primary drainage and (b) imbibition displacements. Both simulations are conducted with the Bentheimer network.

4.2 Flow rate effect

4.2.1 Fluid displacement patterns

In this section, simulations 1–5 are conducted with elevated water injection flow rates to achieve different capillary numbers, N_c , ranging from 2.0×10^{-7} to 2.0×10^{-3} . Fig. 6 shows the fluid pressure distribution along the Berea network at early stage of the imbibition process in simulations 1–5. As shown in Fig. 6, the oil pressure is higher than the water pressure in all five simulations due to the positive capillary pressure under the water-wet condition. However, at low capillary numbers ($N_c \leq 2.0 \times 10^{-5}$), the capillary pressure difference (Δp_{cap}) between oil and water is much higher than the viscous pressure drop (Δp_{vis}). In this case, pore-scale displacement is driven by the capillary force, meaning that water prefers to fill the elements with more favorable threshold capillary pressures. Moreover, the low flow rate allows sufficient time for water to penetrate through the wetting layers and do displacement in elements that are ahead of the invasion front. The low capillary number and the hydraulically connected water channels jointly lead to a capillary-dominated imbibition pattern: local invasion can take place throughout the network and they proceeds largely in the order controlled by the size and geometry of the pores, regardless of their locations along the flow direction. As a result, water saturation profile shows a uniform increase across the network in Fig. 7b.

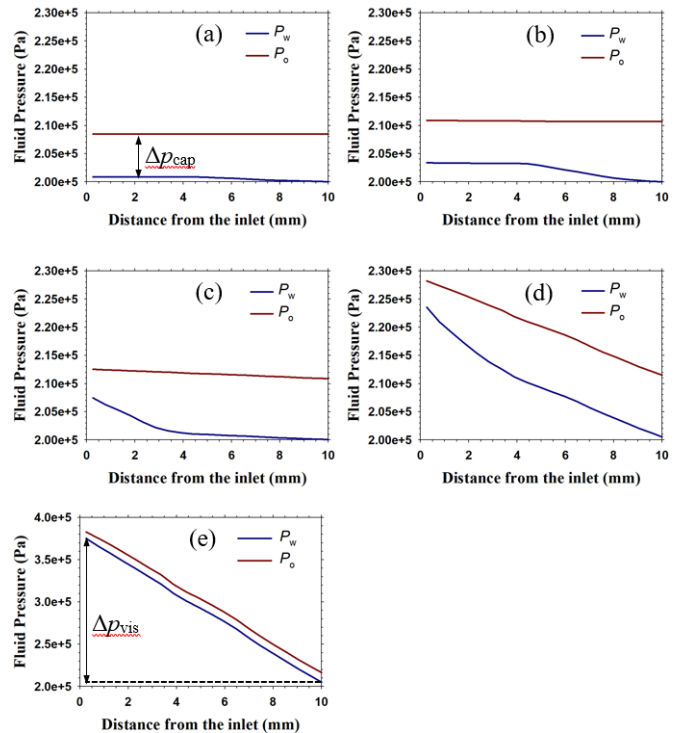


Figure 6. Distributions of water and oil along the large Berea network during the imbibition displacement in simulation (a) #1 (N_c

= 2.0×10^{-7}), (b) #2 ($N_c = 2.0 \times 10^{-6}$), (c) #3 ($N_c = 2.0 \times 10^{-5}$), (d) #4 ($N_c = 2.0 \times 10^{-4}$), and (e) #5 ($N_c = 2.0 \times 10^{-3}$).

In contrast, at high capillary numbers of $N_c \geq 2.0 \times 10^{-4}$, the viscous pressure drop surpasses the capillary pressure difference. In particular, simulation 5 has a pronounced viscous pressure drop of $\Delta p_{vis} = 172$ kPa compared to a capillary pressure difference about $\Delta p_{cap} = 10$ kPa, as depicted in Fig. 6e. This significant viscous pressure gradient favors frontal displacement (piston-like and pore-body filling) close to the water invasion front. Meanwhile, the rapid water injection rate leaves limited time for water flowing through the wetting layers with restricted flow conductance. This further suppresses water invasions ahead of the invasion front. Therefore, a piston-like invasion front develops and gradually moves towards the outlet of the network as the injection continues, as shown in Fig. 7c.

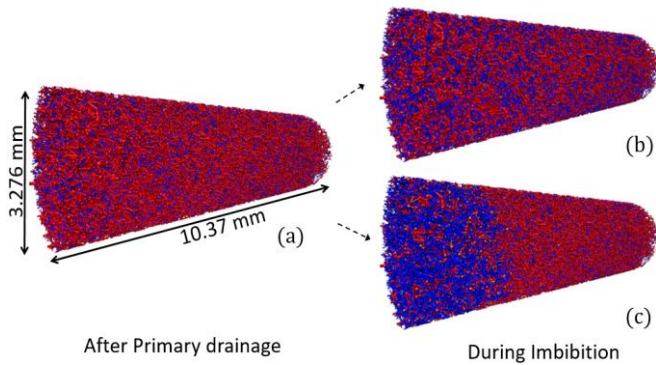


Figure 7. Snapshots of fluid distributions in the large Berea network (a) after the primary drainage process and (b, c) during the imbibition processes with the capillary number of $N_c = 2.0 \times 10^{-7}$ (simulation 1) and $N_c = 2.0 \times 10^{-3}$ (simulation 5), respectively. Oil elements are depicted in red and water elements are depicted in blue. Partially invaded elements are shown in orange.

4.2.2 Trapped oil clusters and residual oil saturations

During imbibition in a water-wet rock, bypassing and snap-off displacement can lead to entrapment of oil and formation of oil clusters with complex structures and a wide range of sizes [23, 56]. This section presents characterizations of the trapped oil clusters, including the volumetric cluster size distribution and the final residual oil saturation, under different capillary numbers. At the end of each imbibition displacement, we calculate a total amount of the trapped oil clusters ($V_{o,total}^{trap}$) and a cumulative volumetric distribution to the $V_{o,total}^{trap}$ from clusters that are smaller than a volume size of $V_{o,i}^{trap}$. Fig. 8 plots the computed cumulative volumetric distribution of trapped oil clusters after the imbibition processes in simulations 1–5. Fig. 9 summarizes the final residual oil saturation of simulations 1–5.

Under the capillary-dominated flow conditions, the injected water has sufficient time to flow through the wetting layers and to swell in the corners of the angular porous space across the network, causing snap-offs in small pore elements. This results in a large amount of hydraulically disconnected oil regions. From Fig. 8, we find that the contributions of oil clusters with sizes up to 0.1 mm^3 are similar in simulations 1–3. Accordingly, Fig. 9 shows that up to a critical capillary

number about 2×10^{-5} , there is a minor drop in the S_{or} with the increase of the capillary number. As N_c increases, the viscous pressure gradient is sufficient to restrain snap-off throughout the imbibition process and favors more piston-like advances, which produce many small-to-medium sized blobs in the vicinity of the invasion front. As a result, in simulations 4 and 5 conducted under the viscous-dominated flow regime, the overall oil cluster sizes significantly decrease (see Fig. 8) and the final residual oil saturation drops sharply (see Fig. 9). The same tendency was also described in experimental studies [57, 58]. Note that all five simulations create many blobs with volumes in the range of $1.0 \times 10^{-9} \sim 1.0 \times 10^{-8} \text{ mm}^3$, which is even smaller than the order of element size. The formation of the sub-pore-sized blobs during imbibition was also observed in previous experimental work [58, 59]. Such isolated sub-pore-sized or pore-sized blobs creates local obstacles for water flow through the narrow pore or throat spaces across the network.

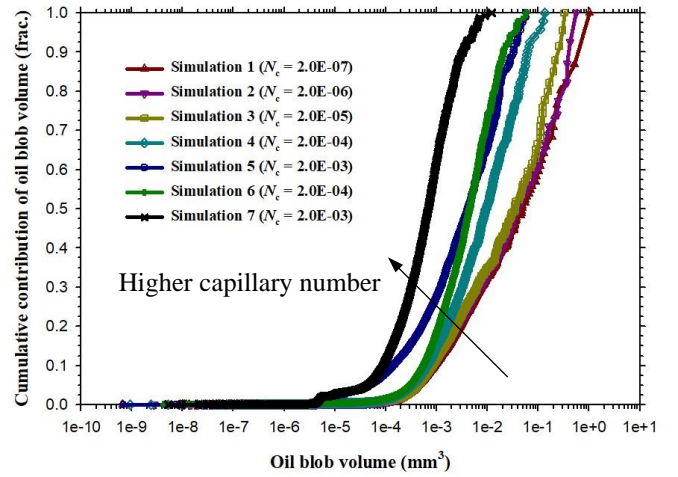


Figure 8. Cumulative volumetric distribution of trapped oil blobs to the overall trapped oil volume after the imbibition displacements in the large Berea pore network in simulations 1–5.

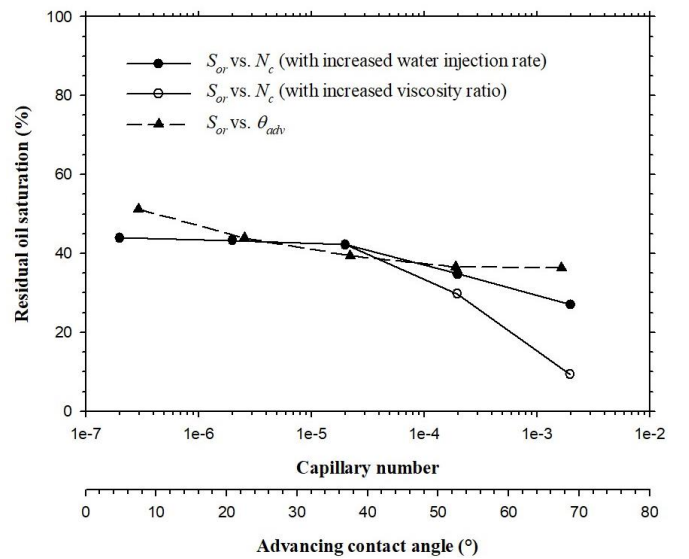


Figure 9. Computed residual oil saturation (S_{or}) versus capillary number (N_c) in simulations 1–7, and computed S_{or} versus contact angle (θ_{ow}^{adv}) in simulations 1 and 8–10. Simulations 1–7 are conducted with a same advancing contact angle distribution ranging

from 15° to 30°, while simulations 1 and 8–10 are performed under a same capillary number of $N_c = 2.0 \times 10^{-7}$.

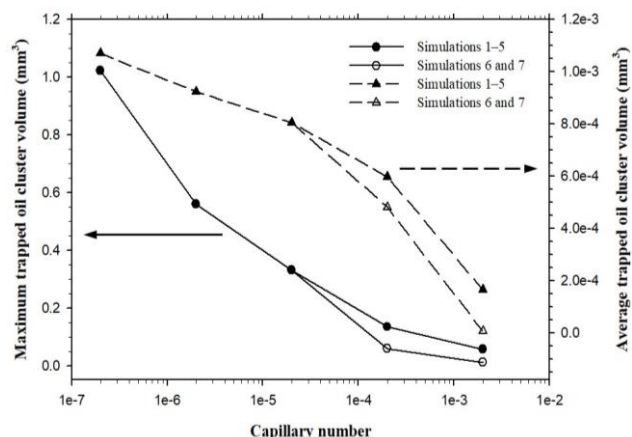


Figure 10. Calculated maximum and average trapped oil cluster sizes after imbibition in the large Berea network in simulations 1–7.

We further plot the maximum trapped oil cluster size, $V_{o,max}^{trap}$, and average trapped oil cluster size, $V_{o,ave}^{trap}$, of simulations 1–5 in Fig. 10. It is found that simulation 1 has a maximum trapped oil cluster volume of $V_{o,max}^{trap} = 1.022 \text{ mm}^3$, which is the largest among the five simulations. As the capillary number increases, both the maximum and the average trapped oil cluster size decreases as the high viscous pressure drop breaks the larger oil clusters. However, it is interesting to note that the variations of the maximum and the average trapped oil cluster sizes with the capillary number are different from the S_{or} – N_c curve shown in Fig. 9; as capillary number increases, both $V_{o,max}^{trap}$ and $V_{o,ave}^{trap}$ show a continuous discernible decrease, although the drop in S_{or} is minor until the capillary number reaches about 2×10^{-5} . This suggests that even under the capillary-dominated flow regime, the configurations of the residual oil clusters experience evident changes as the viscous pressure gradually builds up, although the magnitude of the viscous force is insufficient to push the oil clusters out of the porous media. Previous studies [58, 60] have suggested that the driving force needed to mobilize a trapped oil cluster is inversely proportional to the cluster length. In this respect, the knowledge of the cluster size distribution of the residual oil is an important aid for optimizing the design of EOR processes.

4.3 Fluid property effect

In this section, we first investigate the effects of viscosity ratio on the residual oil saturation by performing simulations 6 and 7. Both simulations are conducted with the same fluid injection rate as that of simulation 3. However, the viscosity of water is increased to 10.10 and 101.0 cP in simulations 6 and 7, respectively. In simulations 8–11, different oil-water contact angles are conducted to examine the wettability effect. In these four simulations, a low capillary number of 2.0×10^{-7} is used to keep them under the capillary-dominated flow regime. The detailed fluid properties, simulation conditions, and the final S_{or} are tabulated in Tables 1 and 2.

4.3.1 Viscosity ratio effect

The cumulative volumetric contribution of trapped oil clusters, and the maximum and the average trapped oil cluster sizes for simulations 6 and 7 are included in Figs. 8 and 10. As the viscosity ratio increases, more contributions to the final S_{or} are from the small-to-medium-sized oil clusters and both the maximum and the average oil cluster sizes are decreased significantly. A closer examination of the spatial distribution map of the trapped oil clusters along the length of the network in simulations 3, 6, and 7 is presented in Fig. 11, where each dot represents the volume-weighted centroid location of an oil cluster. We find that the oil globules distribute uniformly across the network and the majority of the globules' size is in the range of $\delta = 10^{-6} \sim 10^{-3} \text{ mm}^3$. As the viscosity ratio becomes higher, there is an evident narrowing in the range of δ because of the magnified viscous pressure gradient of water. Notably, the population of the sub-pore- and pore-sized oil globules reduces as δ becomes narrower. This can be attributed to the fact that partial invasions are more likely to be completed as the invading water becomes more viscous.

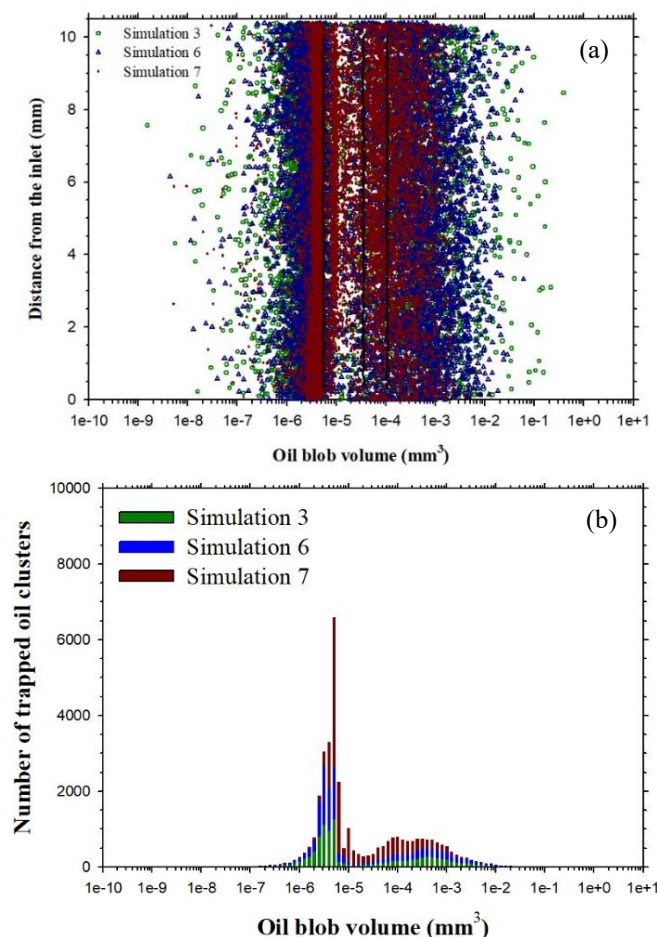


Figure 11. (a) Distribution map of the trapped oil clusters along the length of the large Berea network in simulations 3 (viscosity ratio of $M = 1.22$), 6 ($M = 12.2$), and 7 ($M = 122$). Each dot represents the location of the volume-weighted centroid of an oil cluster. The three vertical lines from left to right show the average volumes of the pore throats, pore elements, and pore bodies, respectively. Stacked histograms of the size distribution of the trapped oil clusters are shown in (b).

The above trend also agrees with that observed from simulations 3–5 as we increase the water injection flow rate. Nevertheless, even under a same capillary number, simulations 6 and 7 exhibit lower final S_{or} and smaller $V_{o,max}^{trap}$ and $V_{o,ave}^{trap}$ than simulations 4 and 5 (see Figs. 9 and 10). This is because the higher water–oil viscosity ratio further confines the occurrence of water invasion within the vicinity of the invasion front and thereby, creates a more stable displacement that leaves less residual oil by the end of the imbibition.

4.3.2 Wettability effect

The residual oil saturations of simulations 8–11 are summarized in Fig. 9. As indicated in Fig. 9, when porous medium is strongly water-wet ($\theta_{ow}^{adv} \leq 45^\circ$), there is a clear reduction in the residual oil saturation as the contact angle increases. When the contact angles are lower than 15° (simulation 8), a large number of snap-off events take place across the network under the capillary-dominated flow condition. Spontaneous snap-offs and water bypassing [23, 61] jointly leave a significant amount of residual oil. As the contact angle increases, it becomes more difficult for snap-off invasion to occur. This is particularly the case for weakly water-wet porous media (simulations 10 and 11), where the majority of oil entrapment solely results from water bypassing. Consequently, much less residual oil is trapped in these two simulations. Similar results have also been reported in the experimental studies of [62, 63].

To further explore the rules of wettability on the residual trapping behavior, we categorize the overall pore elements into three groups based on their inscribed radius (R) and analyze the water saturation of each group. More specifically, water saturations of small ($R < 10 \mu\text{m}$), medium ($10 \leq R \leq 45 \mu\text{m}$), and large ($R > 45 \mu\text{m}$) pore elements are calculated at the end of drainage and imbibition displacements. The results are plotted and compared in Fig. 12.

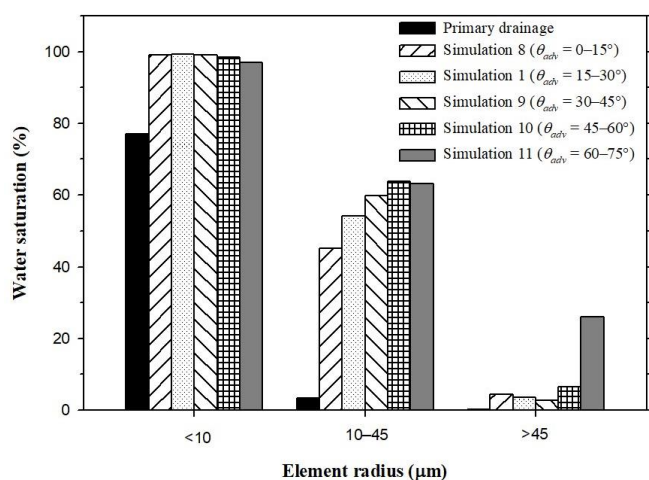


Figure 12. Comparison of the calculated water saturations in various size ranges of elements at the end of the primary drainage and imbibition displacements in simulations 1 and 8–10, all of which are conducted under a same capillary number of $N_c = 2.0 \times 10^{-7}$.

In general, the magnitude of the threshold capillary pressure is lower for larger pore elements assuming uniform contact angles and interfacial tension. Therefore, it is easier for the non-wetting phase to invade into large pores and throats. Accordingly, in Fig. 12, we find that nearly all the medium-to-large elements are invaded by oil while the water saturation is still as high as 77% in small elements after primary drainage. On the other hand, in the following imbibition process, the wetting water phase preferably fill the small elements due to their higher threshold capillary pressures. As shown in Fig. 12, water occupies almost all of the small elements, a fair amount of the medium-sized elements, and a limited amount of the large elements at the end of the imbibition in these five simulations. This selective pore-scale displacement leads to capillary fingering (see section 4.1), resulting in water bypassing and oil entrapment. From Fig. 12, we find that after imbibition displacement in water-wet porous media, the water saturations are always high in small elements. However, as the wettability condition is altered towards neutral wetness and the absolute difference in threshold invasion capillary pressures of pore elements across the pore network shrinks, we see a clear increase in the water saturation (i.e., reduced residual oil trapping) in medium-sized pore elements. In other words, the suppression of the capillary invasion selectivity is more pronounced in the medium-sized pores than in the small elements. For the large pores, however, improved oil recovery is only observed when the porous media have large contact angles of $\theta_{ow}^{adv} = 60-75^\circ$. Note that only a limited number of piston-like invasions can occur in large pores under the strongly water-wet conditions. There is even a slight drop in the water saturation as the contact angle increases from $0-15^\circ$ to $30-45^\circ$, which can be caused by the changes in the water-corner configurations. In summary, the residual oil saturation becomes lower as the fluids-rock system become more neutral wet. The additional oil recovery is mainly attributed to restrained snap-off invasions and suppressed capillary invasion selectivity, particularly in medium-to-large-sized elements.

5 Conclusions

In this work, we developed a new dynamic pore network model that is designed for simulating two-phase flow in disordered porous media. The model has several advantages in comparison with the existing dynamic models: it iteratively solves for local capillary pressure in pore elements with irregular cross-sectional shapes, explicitly accounts for contact angle hysteresis, and rigorously considers pore-scale two-phase flow dynamics including frontal displacement, snap-off, and flow through wetting layers in both pore bodies and throat elements. A heavily-parallelized computing scheme of this model was implemented to achieve computational efficiency.

We performed a series of two-phase primary drainage and imbibition simulations in different pore networks representing two-dimensional (2D) micro-model, three-dimensional (3D) Bentheimer and Berea sandstones. We illustrate that our model is capable of capturing fluid invasion behaviors of stable displacement, viscous fingering, and capillary fingering over a wide range of fluid–fluid viscosity ratios and capillary numbers. The predicted primary drainage

and imbibition relative permeability curves of Bentheimer and Berea sandstones show satisfactory matches with their experimental counterparts.

The validated model is then applied to systematically study the effects of dynamic flow conditions and fluid properties on two-phase displacement patterns, residual oil configurations, and final residual oil saturations. A series of dynamic imbibition simulations are conducted in a core-sized Berea sandstone pore network that is constructed from high-resolution micro-computed tomography (micro-CT) images of a Berea rock sample. Results show that after capillary-dominated imbibition displacement, a large amount of oil is trapped in the form of large-sized oil clusters because of the abundant snap-offs and bypassing. As the water injection flow rate increases up to a critical capillary number of about $N_c = 2 \times 10^{-5}$, there is a minor change in the final residual oil saturation. However, both the maximum and the average residual-oil cluster sizes reduce considerably. With a further increase in the water injection flow rate, a clear piston-like invasion front is formed at the core scale. Under such viscous-dominated flow regime, the significant viscous pressure drop favors frontal displacement in the vicinity of the invasion front, resulting in less amount of large-sized residual oil clusters and a much lower residual oil saturation. Finally, the effects of fluid–fluid viscosity ratio and wettability on residual trapping are investigated. It is found that the overall residual oil cluster sizes are further decreased by enhancing the water-to-oil viscosity ratio, owing to a strengthened frontal displacement. The amount of residual trapping can also be reduced by altering the wettability condition toward neutral wetness, where the pore-scale capillary invasion selectivity is suppressed, particularly in medium-to-large-sized pore elements. In summary, our parallelized dynamic pore network model provides novel insights into residual trapping behaviors in disordered porous media under a wide range of flow conditions and fluid properties. This is vital for optimizing subsurface applications such as enhanced oil recovery, carbon sequestration, and soil remediation.

We gratefully acknowledge the financial support of Thermo Fisher Scientific and the School of Energy Resources at the University of Wyoming.

References

- [1] A. L. Herring, L. Andersson and D. Wildenschild, *Geophysical Research Letters*, vol. 43, no. 18, pp. 9677-9685.
- [2] S. Iglauer, A. Paluszny and M. J. Blunt, *Fuel*, vol. 103, pp. 905-914, 2013.
- [3] H. Ni, B. M. C. Garing and S. M. Benson, *International Journal of Greenhouse Gas Control*, vol. 86, pp. 158-176, 2019.
- [4] Y. Zaretskiy, S. Geiger, K. Sorbie and M. Förster, *Advances in Water Resources*, vol. 33, no. 12, pp. 1508-1516, 2010.
- [5] A. Mehmani, R. Verma and M. Prodanović, *Marine and Petroleum Geology*, vol. 114, p. 104141, 2020.
- [6] J. Cai, T. Jin, J. Kou, S. Zou, J. Xiao and Q. Meng, *Langmuir*, vol. 37, no. 5, pp. 1623-1636, 2021.
- [7] N. Alyafei and M. J. Blunt, *Advances in Water Resources*, vol. 90, pp. 36-50, 2016.
- [8] S. Iglauer, T. Rahman, M. Sarmadivaleh, A. Al-Hinai, M. A. Fernø and M. Lebedev, *Society of Petroleum Engineers Journal*, vol. 21, no. 06, pp. 1916-1929, 2016.
- [9] Y. Gong, M. Sedghi and M. Piri, *Transport in Porous Media*, pp. 1-37, 2021, <https://doi.org/10.1007/s11242-021-01606-1>.
- [10] H. Wang, V. Alvarado, E. Smith, J. Kaszuba, D. Bagdonas, J. McLaughlin and S. Quillinan, *Geophysical Research Letters*, vol. 47, no. 18, p. e2020GL088490, 2020.
- [11] A. Zankoor, M. Khishvand, A. Mohamed, R. Wang and M. Piri, *Journal of Colloid and Interface Science*, vol. 603, p. 356–369, 2021.
- [12] M. Prodanović and S. L. Bryant, *Journal of Colloid and Interface Science*, vol. 304, p. 442–458, 2006.
- [13] Q. Kang, P. C. Lichtner and D. Zhang, *Journal of Geophysical Research: Solid Earth*, vol. 111, 2006.
- [14] S. Bakhshian, S. A. Hosseini and N. Shokri, *Scientific Reports*, vol. 9, p. 3377, 2019.
- [15] A. Q. Raeini, M. J. Blunt and B. Bijeljic, *Journal of Computational Physics*, vol. 231, p. 5653–5668, 2012.
- [16] I. Fatt, *Trans. AIME*, vol. 207, no. 01, pp. 144-181, 1956.
- [17] S. Bryant and M. Blunt, *Physical Review A*, vol. 46, p. 2004, 1992.
- [18] P.-E. Øren, S. Bakke and O. J. Arntzen, *Society of Petroleum Engineers Journal*, vol. 3, p. 324–336, 1998.
- [19] T. W. Patzek, *Society of Petroleum Engineers Journal*, vol. 6, no. 02, pp. 144-156, 2001.
- [20] J. Koplik and T. J. Lasseter, *Society of Petroleum Engineers Journal*, vol. 25, p. 89–100, 1985.
- [21] M. M. Dias and A. C. Payatakes, *Journal of Fluid Mechanics*, vol. 164, p. 305–336, 1986.
- [22] R. Lenormand, E. Touboul and C. Zarcone, *Journal of Fluid Mechanics*, vol. 189, p. 165–187, 1988.
- [23] M. J. Blunt, Cambridge University Press, 2017.
- [24] M. Singh and K. K. Mohanty, *Chemical Engineering Science*, vol. 58, p. 1–18, 2003.
- [25] V. H. Nguyen, A. P. Sheppard, M. A. Knackstedt and W. V. Pinczewski, *Journal of Petroleum Science and Engineering*, vol. 52, p. 54–70, 2006.
- [26] S. Wang, Q. Feng, Y. Dong, X. Han and S. Wang, *Journal of Natural Gas Science and Engineering*, vol. 26, p. 118–129, 2015.
- [27] K. E. Thompson, *AIChE Journal*, vol. 48, p. 1369–1389, 2002.
- [28] Q. Sheng and K. Thompson, *Advances in Water Resources*, vol. 95, p. 92–108, 2016.

- [29] V. Joekar-Niasar and S. M. Hassanizadeh, *International Journal of Multiphase Flow*, vol. 37, p. 198–214, 2011.
- [30] J. Li, S. R. McDougall and K. S. Sorbie, *Advances in Water Resources*, vol. 107, p. 191–211, 2017.
- [31] A. Boujelben, S. McDougall, M. Watson, I. Bondino and N. Agenet, *Journal of Petroleum Science and Engineering*, vol. 165, p. 462–476, 2018.
- [32] C.-Z. Qin, B. Guo, M. Celia and R. Wu, *Chemical Engineering Science*, vol. 202, pp. 194–207, 2019.
- [33] A. Yelkhovsky and W. Pinczewski, *Physical Review Fluids*, vol. 3, no. 4, p. 044003, 2018.
- [34] C. H. Arns, M. A. Knackstedt and K. R. Mecke, in *Morphology of Condensed Matter*, Berlin, Heidelberg, Springer, 2002, pp. 37–74.
- [35] Y. Gong and Y. Gu, *Energy & Fuels*, vol. 29, p. 6213–6223, 2015.
- [36] P.-E. Øren and S. Bakke, *Transport in Porous Media*, vol. 46, p. 311–343, 2002.
- [37] M. Piri and M. J. Blunt, *Physical Review E*, vol. 71, p. 026301, 2005.
- [38] N. A. Idowu and M. J. Blunt, *Transport in Porous Media*, vol. 83, p. 151–169, 2010.
- [39] A. Zolfaghari and M. Piri, *Transport in Porous Media*, vol. 116, p. 1139–1165, 2017.
- [40] A. Aghaei and M. Piri, *Journal of Hydrology*, vol. 522, p. 488–509, 2015.
- [41] R. Lenormand, C. Zarcone and A. Sarr, *Journal of Fluid Mechanics*, vol. 135, p. 337–353, 1983.
- [42] G. Mason and N. R. Morrow, *Journal of Colloid and Interface Science*, vol. 141, p. 262–274, 1991.
- [43] S. Berg, H. Ott, S. A. Klapp, A. Schwing, R. Neitelner, N. Brussee, A. Makurat, L. Leu, F. Enzmann, J.-O. Schwarz and others, *Proceedings of the National Academy of Sciences*, vol. 110, p. 3755–3759, 2013.
- [44] Y. Gong and M. Piri, *Transport in Porous Media*, vol. 135, no. 1, pp. 181–218, 2020.
- [45] J. G. Roof, *Society of Petroleum Engineers Journal*, vol. 10, p. 85–90, 1970.
- [46] Y. Liu, S. Iglauer, J. Cai, M. A. Amooie and C. Qin, *Capillarity*, vol. 2, no. 1, pp. 1–7, 2019.
- [47] T. W. Patzek and D. B. Silin, *Journal of Colloid and Interface Science*, vol. 236, p. 295–304, 2001.
- [48] D. Zhou, M. Blunt and F. M. Orr Jr, *Journal of Colloid and Interface Science*, vol. 187, p. 11–21, 1997.
- [49] M.-H. Hui and M. J. Blunt, *The Journal of Physical Chemistry B*, vol. 104, p. 3833–3845, 2000.
- [50] R. P. Mayer and R. A. Stowe, *Journal of Colloid Science*, vol. 20, pp. 893–911, 1965.
- [51] H. M. Princen, *Journal of Colloid and Interface Science*, vol. 30, pp. 69–75, 1969.
- [52] M. Piri and M. J. Blunt, *Physical Review E*, vol. 70, p. 061603, 2004.
- [53] M. S. Al-Gharbi and M. J. Blunt, *Physical Review E*, vol. 71, p. 016308, 2005.
- [54] S. Balay, S. Abhyankar, M. F. Adams, J. Brown, P. Brune, K. Buschelman, L. Dalcin, A. Dener, V. Eijkhout, W. D. Gropp, D. Karpeyev, D. Kaushik, M. G. Knepley, D. A. May, L. C. McInnes, R. T. Mills, T. Munson, K. Rupp, P. Sanan, B. F. Smith, S. Zampini, H. Zhang and H. Zhang, *Technical Report ANL-95/11-Revision 3.11*, 2019.
- [55] M. J. Oak, in *SPE/DOE Enhanced Oil Recovery Symposium*, 1990.
- [56] S. Iglauer, A. Paluszny, C. H. Pentland and M. J. Blunt, *Geophysical Research Letters*, vol. 38, 2011.
- [57] M. Khishvand, M. Akbarabadi and M. Piri, *Advances in Water Resources*, vol. 94, p. 379–399, 2016.
- [58] I. Chatzis, M. S. Kuntamukkula and N. R. Morrow, *SPE Reservoir Engineering*, vol. 3, p. 902–912, 1988.
- [59] Z. T. Karpyn, M. Piri and G. Singh, *Water Resources Research*, vol. 46, 2010.
- [60] N. R. Morrow, *Journal of Canadian Petroleum Technology*, vol. 18, no. 3, 1979.
- [61] M. J. Blunt, *Journal of Petroleum Science and Engineering*, vol. 20, p. 117–125, 1998.
- [62] H. T. Kennedy, E. O. Burja and R. S. Boykin, *The Journal of Physical Chemistry*, vol. 59, p. 867–869, 1955.
- [63] N. R. Morrow, H. T. Lim and J. S. Ward, *SPE Formation Evaluation*, vol. 1, p. 89–103, 1986.

Oscillating Back Pressure Regulator (OBPR) for High-Pressure Core Flooding

Sanjay Dubey¹, Hossein Khorshidian², Maziyar Mahmoodi, ¹Edison Sripal¹, Lesley James¹,

¹Hibernia EOR Laboratory, Memorial University of Newfoundland, St. John's, Canada

²Opla Energy, Calgary, Canada

Abstract. The challenge in the core analysis industry is the availability of a versatile back pressure regulator (BPR) that can operate efficiently at ultra-low or no flow conditions at very high pressure. The existing models of back pressure regulators are limited to a specific range of operating conditions, automation, and robust core flooding environment. In this work, we developed an initial stage prototype of an Oscillating BPR (OBPR), emphasizing detailed instrumentation and implemented automation. The critical component in an OBPR is the valve that needs to operate within a defined close and open positions based on the feedback received from an encoder, rather than the oscillation created by the flow system or by using a square wave oscillator. The paper investigates the static and dynamic characteristics of the newly designed OBPR instrument. The paper discusses the graphical programming LabVIEW software use to create the feedback control loop using the PID controller. Initial results of the test run were done with the different core flooding systems like Water, Brine, and CO₂. The study also included comparing OBPR pressure performance with the standard back pressure regulator in the market.

1 Introduction

A novel oscillating back pressure regulator (OBPR) was developed to control the backpressure downstream of a two-phase or three-phase core flooding experiment. Core flood experiments are used to investigate the multiphase behaviour of fluid flow in rock cores at reservoir operating conditions. Core flooding technology and instrumentation play a significant role in accurately measuring physical characteristics (relative permeability, connate water content, fluid saturation, pore-space, etc.) and better analyzing the core data. BPRs applied in core flood experiments are subjected to very high pressure (~68 MPa) and temperature conditions (~200°C). Commonly, mechanical regulators accompany all core flooding experiments to provide back pressure and control flow/pressure. The primary purpose of the BPR is to maintain reservoir operating conditions in the core holder and keep a steady low-flow and stable backpressure for in-situ reservoir analysis, reliable displacement of fluid. As fluids are produced, the pressure decreases. The goal is to keep a constant pressure while producing the fluids. BPRs can be used to enhance the downhole pump performance and well productivity in large oil reservoirs [1]. BPRs are especially important in gas injection core flood experiments, core flooding involving live fluids (oil or Brine), or EOR applications such as carbonated water injection (CWI) as in-situ pressures maintained to ensure appropriate phase saturations and relative fractional flow during oil production. BPR applications are also found in the Ion Chromatography analysis of advanced ion management carbonate core-flood experiments [2]. Foam stability is an essential factor in understanding the

displacement of the oil efficiency in porous media, BPR adopted in this chemical flooding experiment

allows setting the desired pressure and temperature [3]. BPR was also applied to build the pressure of 98066.5 Pa to study microbial enhanced oil recovery for the core flood utilizing the model ex-situ bioaugmenting a thermo-, and halo-tolerant rhamnolipid generate using *Pseudomonas aeruginosa* [4]. Gas drainage strategy, such as enhanced coalbed methane, is used to recover the coalbed methane to provide safe conditions for underground coal mining. The lab-scale adsorption investigation was used to observe the displacement of methane by injecting gas (CO₂ or N₂) into intact coal core samples. BPR was used to hold the constant pore pressure during the core flooding experiment [5]. The above applications illustrate that BPR is an important component in core flooding research and justify the need for better BPR design.

Zero flow rate can be challenging to achieve using the conventional BPR. The high flow coefficient makes the system inefficient for the core flood application [6]. The regulator must handle multiphase flow. It can minimize the fluctuation in core outlet pressure. Designing the high precision feedback control system for OBPR can provide highly reliable pressure regulation for core flood applications. Low precision BPRs cannot maintain the core pressure holder at a specific pressure. The precision of BPR is essential in measuring relative permeability, MMP in WAG, apparent viscosity of foam, and many other applications. Imperfect BPR use can cause drastic measurement error, such as distorted breakthrough concentration profiles during the measurement of

* Corresponding author: ljames@mun.ca

dispersion coefficient of CO₂ in CH₄ as part of the CO₂ sequestration for the enhanced gas recovery [7]. Commercial BPRs are complicated in design and to operate, the new OBPR design is easy to use, maintain, clean, and troubleshoot. High dead volume for the regulator will allow more process fluid to be stagnant, which can be a problem in specific applications. Most of the samples are collected and analyzed by using chromatography; hence this can be a severe problem for chemical-sensitive core flood experiments. During the experiment to study the effect of oil saturation on foam propagation, the diaphragm BPR requires to clean the regulator since the experiment is susceptible to undesired chemical reactions and could cause the measurement error [8]. The newly designed OBPR is an improved version of the predecessor OBPR model[6]. Old design uses the square wave oscillator to create oscillation, whereas this OBPR uses nitrogen in the flow system, which causes the feedback loop into the oscillation. This makes the nitrogen to act as a damper for avoiding large pressure fluctuations in the system. According to the literature review, the OBPR design is indistinguishable from another back pressure regulator in the market. The newly designed OBPR is only the adjustable active system in the market. It means that once the set point is given and it is actively controlling the pressure. OBPR automation design can regulate the pressure up to 9,500psi. The BPR in the market is primarily passive. The active system of the OBPR automation is based on the PID LabVIEW design.

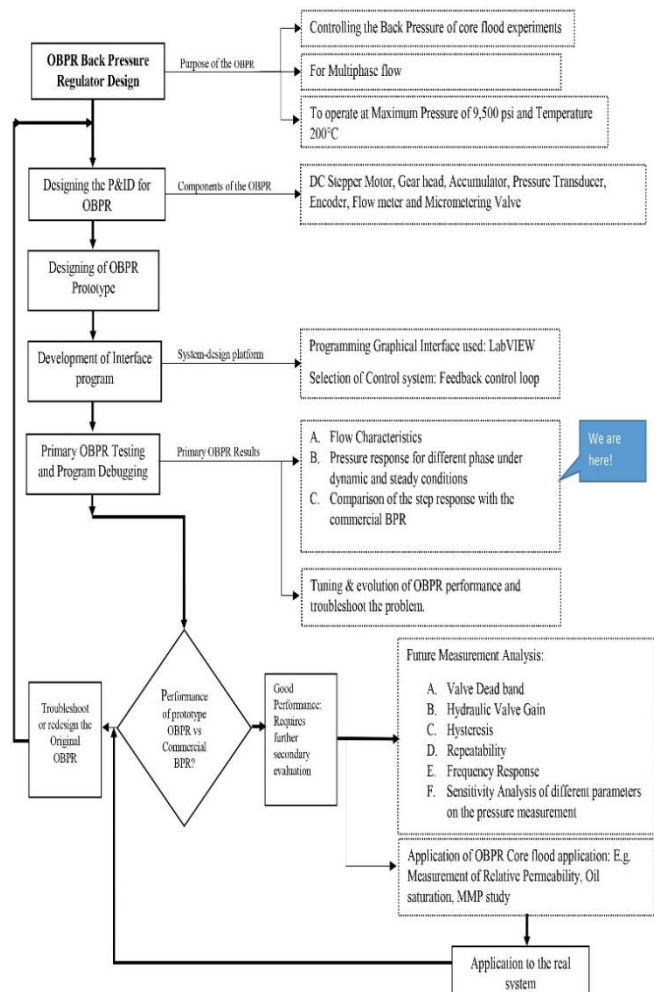
Figure 1a. OBPR Design Algorithm

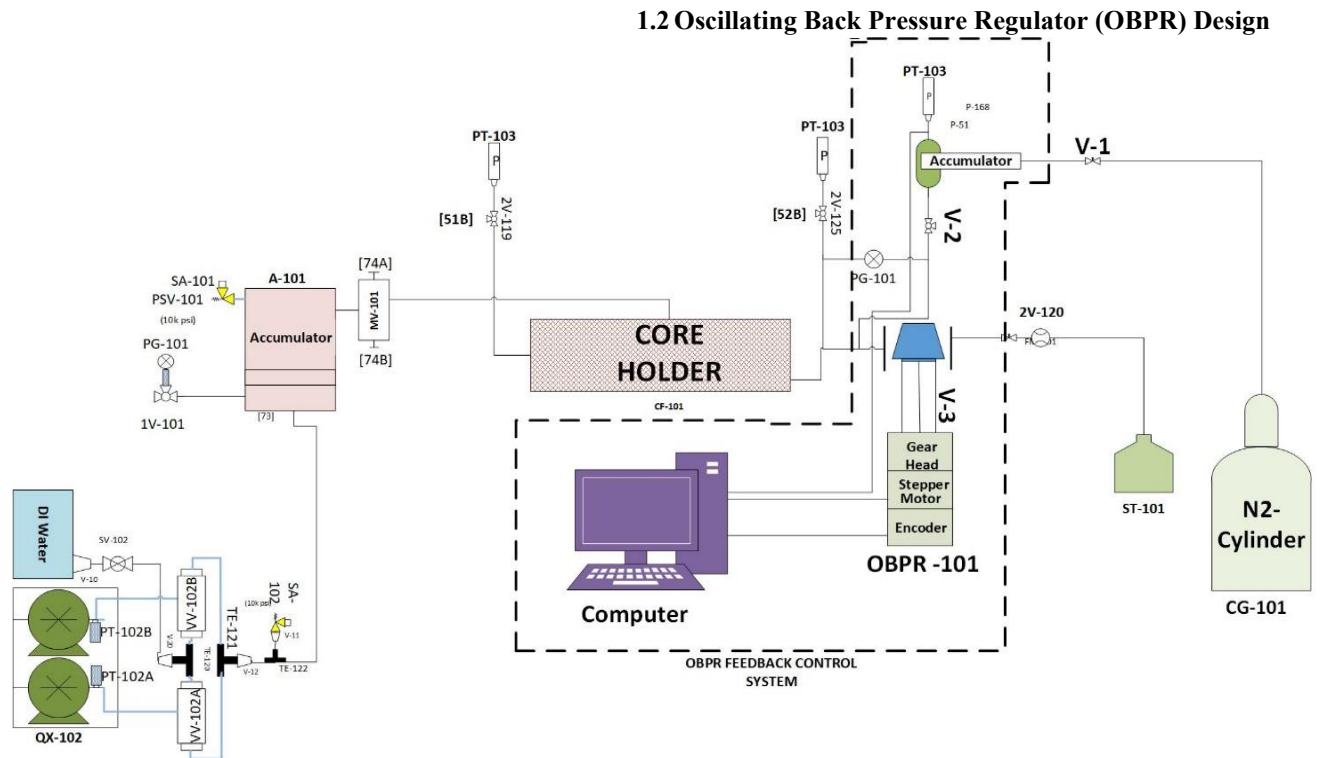
Fig.1 illustrates a research flow diagram for the new OBPR design completed at the Hibernia EOR lab. Initial steps include understanding the desired operating conditions of the OBPR, and construction and assembling the components into the OBPR prototype. The preliminary results obtained at the debugging level were used to compare the OBPR performance of the regulator to the commercial BPRs available in the market and to improve the original design. Preliminary results obtained during the initial run include the core outlet pressure response at different flowrates around 2000 psi, core outlet pressure at different pressure, and core outlet pressure response for the gaseous phase. Understanding the strengths and weakness of the OBPR feedback control system will improve its application to core flooding. Future work shown in the design algorithm includes sensitivity analysis of different components affecting the control performance of the OBPR.

1.1 Back Pressure Regulators

Regulators are different from control valves; generally, a control valve uses an external power system to control the process variable [3]. BPRs are self-actuating valves used for large and small-scale fluid flow experiments. BPRs are classified based on the mechanism (spring load, dome load, air load and diaphragm, etc.), construction material (steel and elastomer), type of fluid, and application. Selection criteria for a BPR are based on the pressure and temperature operating conditions, accuracy and precision, piping sizing, and desired flow rate. Based on the design, the elementary regulator comprises three essential elements: restricting, sensing, and loading. Depending on the type of regulator, the downstream or upstream port communicates with the sensing element like a diaphragm, piston, and spring. All the regulators are self-powered and considered throttling valves as they modulate according to fluid or system pressure.

There are several types of regulators: pressure reducing, pressure relief, pressure switching, vacuum, etc. It is important to understand the BPR and why it is different from other types of valves. Fluids are accumulated at the sampling point using manual, fractional or rotatory collector used for the various displacement study, chemical analysis, which gives more details about the fluid-rock interaction within the core[10, 11]. A BPR can be used as a Low-Pressure Safety Relief Valve (SRV), but the primary goal of an SRV is to self-actuate and safeguard the equipment and life. An SRV only opens when the system's pressure exceeds the design pressure of the material [9]. It is also difficult to control fluid discharge flow through several SRV during blowdowns, making it an inappropriate choice for core flood experiments. The OBPR shown in Figure 2 was designed based on the feedback control system, which may provide a better result for the physical measurement for core flooding experiments. It allows a better pressure dynamic response and handling of ultra-low flow rates. Stepper motors are reliable and durable for open and closed-loop controllers [10]. This paper focuses our discussion on the design, automation, and preliminary pressure response results of this new back pressure regulator.





“Fig 1b. Hibernia core flood experimental setup with newly OBPR feedback control system [13]”

As shown in Figure. 1b, BPRs are generally employed at the downstream position of the core flooding apparatus[11]. The core flooding assembly for this experiment was designed to conduct experiments with single-core plugs for water, Brine, and CO₂. The essential components of the setup are hassler core holder, accumulators, Quizix pumps, quartz pressure sensor, flow meter, oscillating back pressure regulator (OBPR), and sample collector. The flooding system was designed to operate at 150 to 200°C, pore pressure of 9500 psi and overburdened pressure of 10000 psi. Water and brine were injected using the Quizix pump through the floating piston accumulator to the core holder inlet port. CO₂ was injected into the core holder using the booster pump. Core outlet pressure was maintained constant using the OBPR feedback control system, as shown in the dotted box of Fig 1b. Flowmeter was used to measure gas flow, and liquid manual measurement was performed using the standard graduated cylinder. A nitrogen gas tank is placed at the corner of the accumulator to use nitrogen gas as the pressuring gas for the OBPR operation. The biaxial core holder was used with no overburden pressure. Experiments were conducted from ambient conditions to 2000 psi pressure. The initial pressure of the sample core (sandstone core, length: 5.29 cm, diameter: 3.75 cm, area: 11.04 cm², total porosity: 16% sample obtained at a depth of 3862m of Hibernia formation, no overburden pressure) enclosed within in rubber sleeve. Core outlet pressure response was measured at 500, 1000 and 1500 psi. The core flood experiment was designed to understand the core outlet pressure response under static and dynamic conditions. Core outlet pressure response obtained from the OBPR was compare with the core outlet pressure response behavior of the commercial BPR.

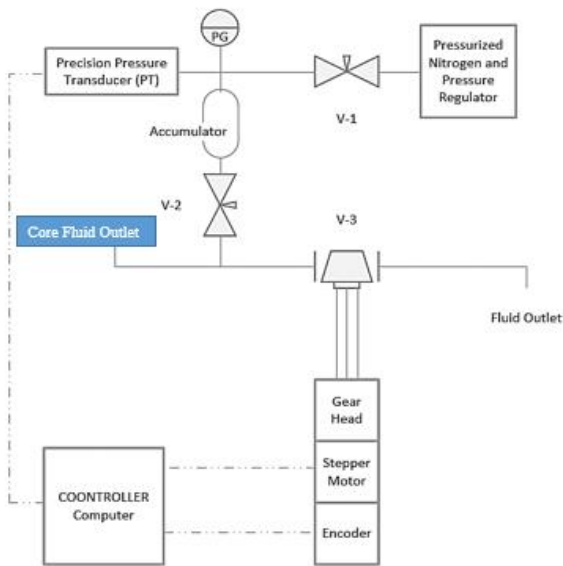


Fig 2. OBPR P&ID Instrumentation Diagram

The OBPR apparatus has been developed to control the backpressure at laboratory core flood equipment outlets, such as core holders. Figure 2 represents a typical embodiment of the OBPR piping and instrumentation diagram. The OBPR consists of a precision needle valve (micro-metering valve), which is actuated by a high-resolution stepper motor (20,000 steps per revolution), to build up intended backpressure by restricting the flow area. During the start of the experiment valve V-3 micro metering valve is closed, and the nitrogen has been charged while keeping the valve V-2 open. As the core fluid pump through the core holder, the pressure at the outlet increases through the line between the V-2 and V-3. The primary fluid enters the accumulator tube, which will increase the nitrogen pressure to the back pressure set point. As the desired back pressure is achieved, the V-3 starts to open and let the excess pressure down by letting some fluid flow out and closing the valve V-3 again to maintain the pressure. This open and close phenomena case at a particular valve location causes the oscillation hence the name of the valve, motor, and feedback control system is given as Oscillating Back Pressure Regulator. Once the desired set pressure is achieved, the flow rate is being controlled. The generated back pressure is measured by a precision pressure transducer, and the data is sent to a controller that sends commands to drive the stepper motor based on the processed data. The stepper motor actuates the stem of the needle valve by a gear head that increases the stepper motor torque and enhances the resolution. The LabVIEW program executes the controlling code using the National Instruments data acquisition system (model no NI PXIe 8430/16).

1.3 OBPR Components and Assembly

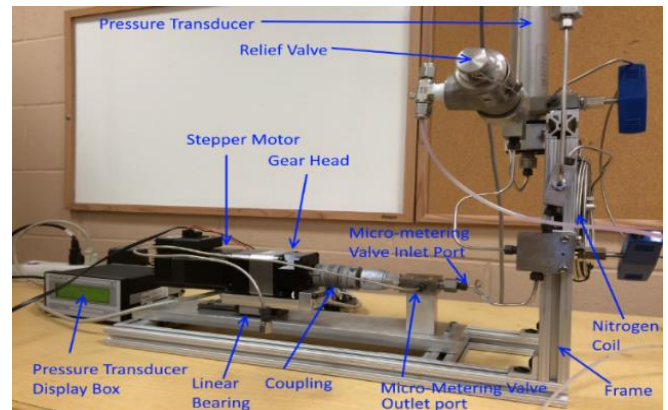


Fig. 3. Assembled OBPR Components

Figure 3 shows the assembled OBPR component. The motor power system provides electricity for the stepper motor. The gearhead is installed on the stepper motor shaft to increase torque and reduce motor speed (70:1). The gear head shaft is connected to the valve stem using a precision coupling. The coupling should be disengaged when the valve positioning is implemented. The linear bearing is mounted beneath the motor since the motor moves back and forth by opening and closing the micro-metering valve. The micro-metering valve inlet (1/8" Autoclave Speed-bite) is connected to a flow line (e.g., the core holder outlet) to control its backpressure.

A tee and valve V-2 in Figure 2 connects the micro-metering valve inlet to the accumulator coil. The coil can be charged with nitrogen up to 10,000 PSIG with the pressurized gas cylinder or a gas booster. The set pressure must be 100 PSIG (50-150 psi is acceptable) lower than the intended backpressure. This causes the controller to keep the micro-metering valve closed before running and receiving any fluid from the core holder. Valve 2 can be opened when nitrogen charging is complete, and valve 1 is closed. Valve 1 disconnects the nitrogen source from the coil accumulator. The coil pressure can be read using the pressure gauge and pressure transducer display box. The OBPR software also displays real-time pressure. The pressure relief valve provides additional safety for the relief of pressure in the case of OBPR failure. The relief valve cracking pressure is at 9500 PSIG. "The OBPR valve can operate up to 5000 psi in a close position, but the maximum allowable pressure is 12,500 psi. The valve stem is not close too tightly to guard the valve seat against getting damage. It is recommended to add an O-ring sealed check valve at the equipment outlet (e.g., core flood unit) to avoid backflow of pressurized nitrogen toward the equipment (e.g., core holder) due to any OBPR malfunction. In addition, using a diaphragm-type accumulator may avoid contact of fluid in the flow line and nitrogen in the coil. The composition of the oil will affect the calculation of the N₂ miscibility with the crude oil. Miscibility of N₂ is relatively high, especially 5000 to 6000 psi for an Alaskan oil[12]. As mentioned earlier, the core flooding experiments were performed with water, brine, and gas (CO₂).

1.4 OPBPR Operation Procedure

The needle valve is positioned in a near-closed condition to build up the intended back pressure inside an accumulator to create backpressure. The accumulator is a long 20ft coiled tube (0.125" OD, 0.04" ID) filled with nitrogen and positioned behind the micro-metering valve. Since pressurized nitrogen is compressible, it allows the core fluids to be charged or discharged in the coil. A higher motor speed reduces the time of the actuation of the system lag. However, it is recommended to set the rate at an intermediate value (e.g., 5 revs/sec) to avoid premature failure of the stepper motor. The pressure transducer at its standard mode provides high-quality pressure data (± 0.25 PSIG) within an acceptable period. The initial valve positioning will dramatically reduce the lag time of the valve operation. This will minimize the time required to shut in a valve from its maximum opened position entirely. The valve closed position should build up the pressure of 5000 PSIG when the core holder is flooded by water at the rate of 5 cc/hr. Although further tightening of the valve stem builds a higher pressure at low flow rates, it will damage the needle valve stem as the valve touches the seat every time it is fully closed. The valve has to be operated within a defined closed and opened position based on the feedback received from an encoder. One rotation of the valve stem is sufficient to increase the flow area for a low-pressure discharge of fluid. The controlling parameters (proportional and derivative terms) have to be set regarding the working conditions. An increase in the volume of the accumulator produces a smoother pressure profile. However, it increases the response time of the pressure transducer and the dead volume. The coil length is currently 20 ft (ID: 0.02"), leading to a magnitude of 1.2 ml. To run the OBPR, the following programs have to run by LabVIEW software. In each program, the required adjustments and commands have to be executed sequentially. In addition, the OBPR hardware has to be prepared to keep the backpressure at the desired value. Adjusting the valve positioning is performed after the software adjustment before charging the accumulator with pressurized nitrogen. In addition, the test script recommends a range of control parameters that the user can execute to obtain the desired back pressure profile. The OBPR performance is affected by different parameters and factors such as:

1. Speed and acceleration of the stepper motor
2. Accuracy of the pressure transducer data
3. Valve opened and closed positions
4. Controlling parameters
5. The volume of the accumulator
6. Pressure response

2 Automation Implementation

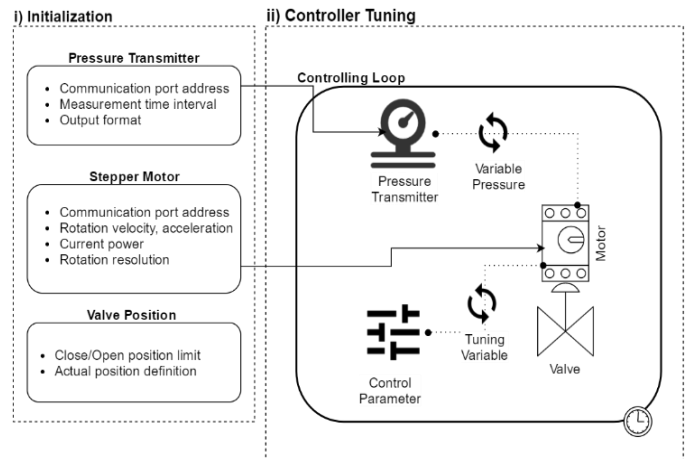


Fig. 4. OBPR Basic Layout Using LabVIEW

The design was automated using the LabVIEW program to make the system work smoothly, as shown in Figure 4. The feedback control system was developed to operate the OBPR. Application of the PID. (Proportional Integral Derivative) a controller can render optimal and robust performance for the stable, unstable, and non-linear processes [15]. The programming platform used in this project is LabVIEW 2015, commercially offered by National Instruments that has an extensive application in the automation and instrumentation industries. The primary controlling code is compatible with the proposed mechanical setup (pressure transmitter and stepper motor) and provides open-source for further upgrades. The logical algorithm is explained as shown in Figure 4. The overall process flow in this algorithm comprises two main steps; I) Initialization and II) Controller Tuning.

The earliest stage in initialization is to establish serial communication with active serial ports of the stepper motor and pressure sensor. The initialization task also includes the primary setting for the pressure sensor and stepper motor parts. As presented in Figure 4, the next phase is to adjust the controlling parameters determined in advance based on flowing phases, flow rate, and operating pressure. The initialization step can be broken into three subsections. First, the pressure sensor properties should be set into desired values. Second, the operation parameters of the stepper motor need to be adjusted before running the main controlling loop. Finally, the valve position, a mechanical part of the equipment, needs to be initially closed and appropriately connected to the motor shaft. After implementing these sequences, the primary controller LabVIEW program is ready to run and execute rotation commands to the motor port based on the pressure difference between set value and recorded value from the pressure sensor. The immediate critical information that constantly is needed through controlling time is the actual encoder and positions. Consequently, the calling program is used for requesting position data and send it to PID. Controller function.

BPR Model	EBPR	VBPR	OBPR
BPR Type	Metal Diaphragm	Piston	Metering valve
Max Temperature (°C)	200	150	200
Max Pressure (psi)	10,000	10,000	9,500
BPR Material	SS316L	SS316L	SS316L
Flow coefficient	1×10^{-09}	2.64×10^{-07}	1×10^{-04}

3 Commercial BPR.

Several studies use pressure response to analyze a regulator's performance [12, 13, 14, 15, 16, 17, 18]. To understand the initial pressure response of the OBPR, the model was compared with the pressure response of two commercial BPRs that are used for similar applications. Water, Brine, and CO₂ were chosen as the primary fluids for these experiments as they are commonly used for experimental studies in geology, oil recovery, and hydrogeology [19].

Table 1. Comparison of different commercial BPR models

Details of the two commercial BPRs, a diaphragm BPR and a piston dome loaded BPR, are provided below and summarized in Table 1. The first commercial BPR used in the comparison is a dome-loaded diaphragm-based regulator (model: ULF EHP SB8) manufactured by Equilibar, referred to as EBPR. The bottom and top dome have O-rings with high yield strain material that renders the liquid-tight seal. In the EBPR case, the elastomer material for the O-ring is stainless steel SS316L. Its sustainability at high pressure and temperature may also affect the regulator selection and internal flow pattern. The diaphragm is placed coplanar to the bottom of the dome surface. The choice of the diaphragm is essential in the core floods. The top dome (reference cap) has a reference fluid that can create uniform hydrostatic pressure over the diaphragm. When the process pressure exceeds the determined pressure, the diaphragm will lift, allowing the fluid to pass across the system.

The second commercial BPR used for the comparison is a needle valve-based BPR (model number C06-003-1), manufactured by Vinci Technologies and referred to as VBPR. It is comprised of two chambers, i.e., top and bottom chambers or dome. The bottom section consists of the needle to enclose the passage for the process fluid. When the bottom fluid pressure is higher than the reference pressure of the top dome, the passage for the fluid is open. Otherwise, it is closed. Uninterrupted flow is secured once the equilibrium between process and reference pressure is attained. The newly developed OBPR feedback control system was used to study the regulator performance under dynamic and steady-state conditions. This is a preliminary study of the OBPR performance based on its design and pressure response. BPR models used for all the core flood systems have been subjected to the limited operating condition (~ up to 1500 psi) to analyze the initial functionality of the OBPR and to ensure safe working conditions. The initial pressure response of the OBPR is a BPR regulator for high-pressure core flood experiments is investigated. Before the experiments, it is necessary to ensure no leakage of the high-pressure fluid from the steam of the valves or the system. This can cause pressure loss resulting in measurement errors and malfunctioning of the valve. It is required to update the position of the stepper motor during the closing of the valve, as over-rotation of the valve handle can cause damage to the valve seating. Motor heating, power outage, or surge can increase or decrease the torque ability of the motor

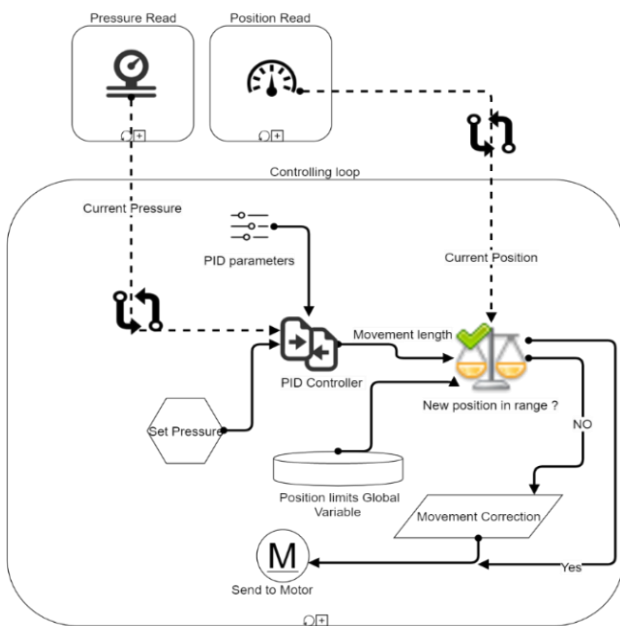


Fig. 5. OBPR Feedback Control System

Figure 5 shows the feedback control system design and its working mechanism. The initial stage of automation for this technique is to obtain the pressure information from the transducer and calculate the difference between the current. **Table 1.** Comparison of different commercial BPR model pressures and reference pressure. PID is used to calculate the proper response based on the pressure difference. Position and pressure variables are read from motor and pressure sensors and inserted into the LabVIEW control panel. The proportional, integral, and derivative terms are also adjustable in this front panel. Derivative of the pressure between two consecutive time steps is measured; it assists in creating controlling command over the stepper motor based on the differential pressure and derivative of the pressure. To correct maximum allowable displacement, the limit test is performed more or less like a trial and error to get the correct limit. The final valve position for the specific command is calculated to check if the valve position is still within the allowable range. Computed movement is then sent to the motor for execution. In the final step, the motor waits for the new pressure value

affecting the pressure response. LabVIEW program complications can also cause trouble in the experimental procedure. Measurement begins with the inspection of the reference pressure. Pressure measurement is continuously streamed on display rendering the real-time value of the pressure in the system. Measurement resolution is essential for this study since our pressure difference across the core holder is relatively low; it is best to use the IIR (infinite impulse response) nano-resolution filter device to report accurate pressure measurement up to 12 digits and acts as an effective in anti-aliasing. To make the stepper motor work properly, it was necessary to configure it or tune the motor. The motor was initially disengaged from the gearhead coupling from the micro metering valve; the motor was also connected to the computer using an RS232 cable. Immediate and buffer types of commands were utilized through the LabVIEW program to communicate with the stepper motor. Critical parameters such as the maximum current, data format, velocity encoder ratio, encoder function, and motor ratio were initially set. The motor response was noted before it was connected for the actual experiment run. The metering valve was adjusted to the closed position to build up the pressure to 5000 PSIG. The position limit controller, which defines the incremental steps that the valve is turned for the maximum opening position (400,000 steps were optimal, sets the entire valve stem rotation at 0.56 turn), was switched on. Once the set position controller defines the current valve position, executes the run, it will communicate the motor and save the initial position of the micro metering valve when the system is at rest with no charge nitrogen flow, the PID. Constant value was input. Once the nitrogen begins to charge into the accumulator coil, the OBPR is set at the desired pressure value. The pressure source is removed once the system is ultimately charged with the nitrogen. As the feedback control system detects the reference pressure, the gearhead rotates to set the new opening position of the micro metering valve. During the initial operation, the valve stem moves in an opening place, creating a sudden pressure drop in the system.

3. Results and Discussion

A feedback control approach was applied to the OBPR system consisting of a micro-metering valve, stepper motor, pressure transducer, and control architecture like PID. During initial experiments, the efficiency of the feedback control system must satisfied the primary goal of holding desired set backpressure under safe conditions. Future work might focus on the feedback control system cost, applicability to the multiphase system, and significant OBPR performance parameters. An ideal feedback control system must have zero steady-state error and constant stability throughout the performance. OBPR results are confined to a controlled variable (pressure response) offset and PID in this discussion. The set point value which was chosen to provide the suitable control performance for given operating conditions. The results show the application of OBPR at ultra-low flow rates initially and preliminary pressure response.

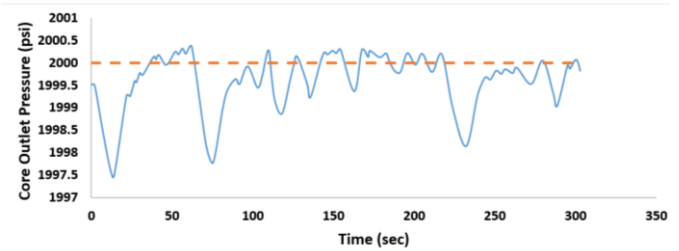


Fig. 6A. OBPR Pressure Response under 2000 psi with Maximum Fluctuation $\pm 0.125\%$ at 50 ml/hr (Primary Fluid: Water)

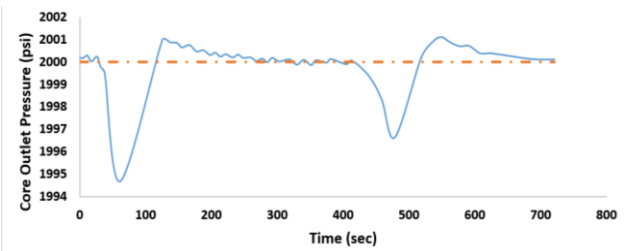


Fig. 6B. OBPR Pressure Response under 2000 psi with Maximum Fluctuation $\pm 0.25\%$ at 10 ml/hr (Primary Fluid: Water)

The OBPR outlet pressure response at different flow rates experiments was completed with water as the primary fluid and using two flow rates, 50 ml/hr (Figure 6A) and 10 ml/hr (Figure 6B). Figure 6A and 6B show the deviation of the core outlet pressure from the set point of the OBPR system that is 2000 psi. This can happen due to various types of elements present in the OBPR feedback control system, such as stem of the valve, pressure sensor, manual tuning, charging gas (nitrogen), stepper motor, gas pressure, etc. Disturbance or deviation seems to be non-periodic and looks like an approximated sine wave function. It is interesting to see that this disturbance frequency is too fast because of quick response from the stepper motor. Figure. 6 A and 6B shows a similar pressure response to the OBPR pressure response shown in Fig.7, but in these experiments, the primary fluid used in core flooding was water. Both the water system in Fig 6 A and B fluctuates around $\pm 0.25\%$ of the reference value. Figure 6B indicates a small number of fluctuations compared to the low volumetric flow rate. High flow rates might cause the system to respond more quickly to maintain the reference point pressure. Hence higher pressure fluctuation can be observed compared to a low flow rate. It was observed that OBPR feedback control system that response too quickly also results in poor performance. The amplitude ratio for the consecutive trough of the pressure response curve in Fig.6A and 6B declines as time progresses; it indicates that the OBPR feedback system reduces the steady-state error between the set point and control process variable. The decay ratio between the neighboring peaks was getting smaller for low flow rates compared to the high flow rate at the same pressure. This indicates that water testing with low flow rates at high pressure has a less settling time than high flow rates. This can cause the outlet core pressure response to reach a steady-state condition with reduced offset error. Fig. 6A & 6B both show the controlled variable overshoot which can cause the long-term degradation of valve.

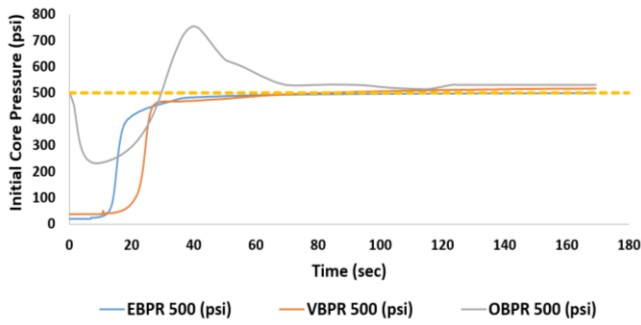


Fig. 7A. BPR Pressure Response for Single Phase Brine at 500 psi

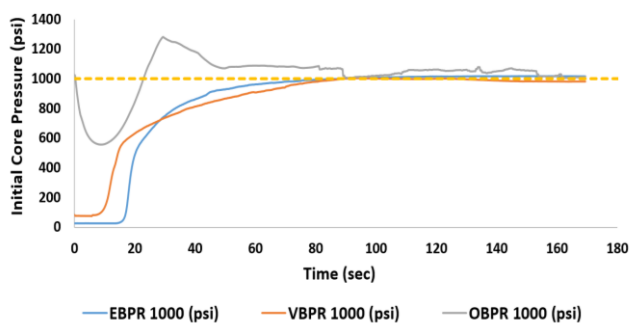


Fig. 7B. BPR Pressure Response for Single Phase Brine at 1000 psi

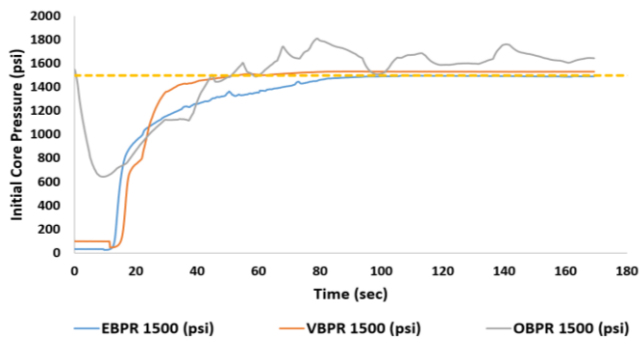


Fig. 7C. BPR Pressure Response for Single Phase Brine at 1500 psi

Dynamic pressure response from the two commercial BPRs (EBPR and VBPR) and the OBPR with initial core pressures of 500, 1000, and 1500 psi, using Brine, are shown in Figures 7A, 7B and 7C. A better understanding of the effects of pressure response dynamics can lead to a better design for the OBPR model with optimizing control and design improvement. The OBPR feedback control system is subjected to a step change disturbance, and the initially controlled pressure variable deviates for few seconds. This category is termed a step response. The pressure response vs time was graphed in Fig 7A, 7B & 7C. It can be seen from all the Fig.7 that the rise time for the OBPR pressure response varies for different pressure, Fig.7C have longest rise time. To judge the control performance of the OBPR with least disturbance, the volumetric flow was kept constant for all the

pressure response. The sudden fall in the pressure for all the OBPR flow system at the early seconds of the operation is shown in Figures 7-A, B and C. Pressure drop can happen to overcome the lock-up conditions which require a fixed amount of torque to rotate the stem of the valve. Lock up is the no-flow state where the regulator has difficulty maintain the initial set pressure [20]. As the feedback control system regains, it re-adjusts the regulator opening position and runs to achieve desired reference value. From Fig. 7A, it is seen that settling time was quite less than another similar system because of the system less overshoot than other two. The core outlet pressure will start to build up and converge around the desired value making the motor run in an oscillatory mode compared to the square wave generator in the predecessor model. It can be observed that OBPR feedback adjustment had an immediate impact on the pressure variable for the initial period as compared to the VBPR and EBPR, which have dead time causing the controller to take action slowly or to get first-order delay response. OBPR feedback control system is quick and holds the least dead time. This can provide better performance compared to other BPR designs for the step disturbance. The algorithm was used for the OBPR feedback control system to get better control performance. However, it can still result in excessive fluctuation or instability for the pressure variable. The final element that can also affect the stability and control performance is the valve. The OBPR pressure instability dampens over the period as the feedback control system approaches the steady-state pressure value. The settling time for the OBPR feed control system starts to get prolonged as the pressure increases due to high rise time—the proportional and integral mode of the PID. Controller tends to get the oscillatory and slow dynamic response. This slight pressure fluctuation can depends on various parameters, such as equilibrium condition between the inlet fluid and nitrogen pressure in the accumulator, regulator opening, PID. Value, phase of the primary fluid, stepper motor, and type BPR regulator. From Figure 7 A, B and C it can be seen that EBPR and VBPR show slow and stable dynamic responses compared to the OBPR. One of the reasons it might be that VBPR and EBPR are better self-regulating the disturbance and approach quickly to attain the desired set point. The sensing parameters (diaphragm and piston) are not significantly affected by the sudden decrease in the dome pressure. The core outlet pressure starts to build up due to restricting elements of the valve. The dome side was already pressurized EBPR and VBPR, causing slow fluid displacement and less pressure drop to cause the instability. In Fig.7 all the set points are represented in the dotted form to understand the system's dynamic and steady state response compared to a reference point. Every system has unique characteristics; the value of PID is obtained on the type of tuning methods. Manual tuning was done on the OBPR system, keeping the oscillation fluctuation at constant amplitude. The stepper motor also adds, such as oscillation or unstable phenomena to overall OBPR feedback control system [21]. It can be observed from Figure 7 that the OBPR is unstable (overshoot) during the initial phase of the operation of the system. This overshoot problem could be resolved with a better PID tuning method. The experimental results illustrated in Figure 7 help us understand the dynamic

response of the pressure compared to the commercial BPR in the market.

To understand the OBPR performance on a gaseous core flood system, experiments were completed using CO₂ as the primary fluid. Figure 8 shows the steady-state pressure response to the gaseous system. A higher oscillation rate is observed compared to the water and brine systems.

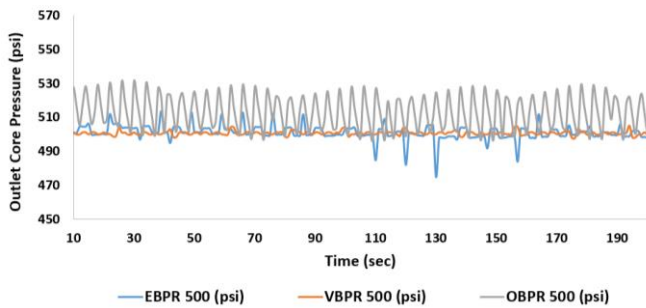


Fig. 8. BPR Pressure Response with Single Phase Gaseous CO₂

The OBPR pressure response was observed to be quick for the gaseous system, and a more periodic disturbance is kept for the OBPR than the commercial BPRs. The PID was designed to reduce the error signal fixing the PID gain and will not reduce the noise signal. This noise signal may arise from the booster pump that is used to pressurize the core holder. Along with this noise fluctuation, the OBPR was able to maintain the steady pressure with ± 50 psi. The OBPR will render limitations for close measurement application with such high delta P across. A more experimental study is required to check the performance of the OBPR for the gaseous system.

The conventional core flood experiment was designed to understand the OBPR feedback control response behavior under static and dynamic conditions. The core outlet pressure response obtained from the OBPR was compared with the core outlet pressure response behavior of the commercial BPR. The pressure fluctuation in the outlet pressure impact the comparison test result for the three BPR, if the OBPR pressure response is compared to the commercial BPR response, it can clearly be seen that the OBPR pressure fluctuation are unstable and respond aggressively to step input disturbance compared to the other two BPR. These fluctuations in OBPR feedback control system are caused by various types of elements present in the OBPR model, such as stem of the valve, pressure sensor, manual tuning, stepper motor, charging gas, primary fluid pressure, etc. All the dynamic response for three different BPR were recorded under the uniform test conditions except at the different pressure. For the high permeable core sample, this small fluctuation can be impactful but all the initial experiments were planned to test the preliminary design of OBPR model and its ability to achieve the desired set backpressure value. This fluctuation also affects the accuracy characteristics of the instrument to measure the core outlet pressure response. Even

though the systematic error is reduced, there still will be some inherent errors in the instrument design. Core outlet pressure was measured with $\pm 0.25\%$ of the setpoint value. These are good initial results. The number of replicates for each experiment was around three or more. There might be chance of precision error which happens due to the analyzing the sets of pressure measurement data for several experiments. It was found that core outlet measurements were reproducible and nearly consistent for desired set point until the tuning parameters were affected. Especially in gas phase, the OBPR system can measure the outlet core pressure response with the tolerance of around $\pm 6\%$ of the original pressure. All the core outlet pressure measurements were only valid under the controlled condition of pressure and temperature. Any variation in the ambient temperature can change the sensitivity for pressure measurement. It's better to ignore such systematic and statistical random error at the initial stage of the designing and testing process.

4. Conclusions

A newly designed oscillating back pressure regulator model for core flood analysis was developed. An experimental study was undertaken to understand the pressure response of the OBPR using different core flood experiments. The OBPR was tested in three fluid flow scenarios using brine, water and CO₂. Results included are the dynamic and steady-state response of the pressure. The OBPR was found to have a faster response than the EBPR and VBPR for the gas and brine systems. The OBPR took some time to achieve the steady-state compared to the EBPR and VBPR for the liquid system. The OBPR was found to suffer from instability in pressure response compared to the commercial regulators. It can also be concluded that the OBPR feedback control performance was assessed based on the magnitude of the step input. The results from the OBPR and comparison with different commercial BPR show that this device can respond well to liquid. More experimental investigation is needed for gas phase system. OBPR system can hold the backpressure similar to another commercial device for core flood application.

5. Future works:

The OBPR requires more rigorous experimental study before applying it successfully to the core flood application. Some of the future works include to:

- Evaluate the OBPR feedback control performance at maximum pressure up to 9,500 psi to and high temperature.
- Improve the feedback control system to reduce the pressure offset and instability.
- Test the OBPR on different gases and multiphase flow systems.
- Use the diaphragm accumulator or floating piston type accumulator to avoid mixing of nitrogen with the primary core fluid such as brine, water, gas and oil.

- e. Perform the sensitivity analysis of different parameter on the OBPR feedback control performance.
- f. Tune the OBPR using the first principle and to use the Mat lab Simulink."
- g. Develop other embodiments for the accurate control of the flow and pressure eliminating the comingle of Nitrogen with the process fluids.
- h. Implement the well-developed OBPR design to measure the physical parameter for core flood applications such as Relative Permeability.

The authors would like to thank Chevron Canada, Hibernia Management and Development (HMDC), Department of Tourism, Culture Industry and Innovation (TCII), Natural Sciences and Engineering Research Council of Canada (NSERC) for funding my research project. Thanks are extended to Equilibar and Vinci Technologies for providing their BPR for our research study.

References

- 1 F. Torabi, B. Yadali Jamaloei, S. Y. Hong, and N. K. Bakhsh, "Improving downhole pump efficiency and well productivity in heavy oil reservoirs utilizing back pressure regulator," *J. Pet. Explor. Prod. Technol.*, vol. 2, no. 4, pp. 181–195, (2012).
- 2 L. T. Vo, R. Gupta, and O. J. Hehmeyer, "Ion Chromatography Analysis of Advanced Ion Management Carbonate Coreflood Experiments," no. Ic, (2012).
- 3 A. Shokrollahi, M. H. Ghazanfari, and A. Badakhshan, "Application of foam floods for enhancing heavy oil recovery through stability analysis and core flood experiments," *Can. J. Chem. Eng.*, vol. 92, no. 11, pp. 1975–1987, (2014).
- 4 S. J. Varjani and V. N. Upasani, "Core Flood study for enhanced oil recovery through ex-situ bioaugmentation with thermo- and halo-tolerant rhamnolipid produced by *Pseudomonas aeruginosa* NCIM 5514," *Bioresour. Technol.*, vol. 220, pp. 175–182, (2016).
- 5 L. D. Connell, R. Sander, Z. Pan, M. Camilleri, and D. Heryanto, "History matching of enhanced coal bed methane laboratory core flood tests," *Int. J. Coal Geol.*, vol. 87, no. 2, pp. 128–138, (2011).
- 6 W. O. Lease and C. F. Van Egmond, "Oscillating Backpressure Regulator for Low Flow Rate, High-Pressure Coreflooding Experiments.," *Soc. Pet. Eng. J.*, vol. 22, no. 6, pp. 899–901, (1982).
- 7 T. J. Hughes, A. Honari, B. F. Graham, A. S. Chauhan, M. L. Johns, and E. F. May, "CO₂ sequestration for enhanced gas recovery: New measurements of supercritical CO₂-CH₄ dispersion in porous media and a review of recent research," *Int. J. Greenh. Gas Control*, vol. 9, pp. 457–468, (2012).
- 8 K. Mannhardt and I. Svorstøl, "Effect of oil saturation on foam propagation in Snorre reservoir core," *J. Pet. Sci. Eng.*, vol. 23, no. 3–4, pp. 189–200, (1999).
- 9 A. P. Spence and R. W. Watkins, "Effect of Microscopic Core Heterogeneity on Miscible Flood Residual Oil Saturation.," *Soc. Pet. Eng. AIME, SPE*, (1980).
- 10 R. J. Hwang and J. Ortiz, "Effect of CO₂ flood on geochemistry of McElroy oil," *Org. Geochem.*, vol. 29, no. 1-3–3 pt 1, pp. 485–503, (1998).
- 11 M. Hellemans, "Overpressure protection," *Saf. Reli. valve Handb. Des. use Process Saf. valves to ASME Int. codes Stand.*, no. 1st edition, pp. 327–434, (2009).
- 12 A. Morar, "Stepper Motor Model for Dynamic Simulation," *Acta Electroteh.*, vol. 44, no. 2, pp. 117–122, (2003).
- 13 R. A. Nasralla and H. A. Nasr-El-Din, "Coreflood study of low salinity water injection in sandstone reservoirs," *Soc. Pet. Eng. - SPE/DGS Saudi Arab. Sect. Tech. Symp. Exhib. 2011*, no. May, pp. 187–199, (2018).
- 14 H. M. Sebastian and D. D. Lawrence, "Nitrogen minimum miscibility pressures," *Eighth Symp. Enhanc. Oil Recover.*, pp. 299–310, (1992).
- 15 V. Rajinikanth and K. Latha, "Tuning and Retuning of PID Controller for Unstable Systems Using Evolutionary Algorithm," *ISRN Chem. Eng.*, vol. 2012, pp. 1–11, (2012).
- 16 M. Mutlu, T. Wassar, M. A. Franchek, and J. A. Gutierrez, "Condition and performance analysis of a subsea BOP control system pressure regulator," *Proc. Annu. Offshore Technol. Conf.*, vol. 2, pp. 1193–1203, (2018).
- 17 R. El Golli *et al.*, "Modelling of a pressure regulator To cite this version : HAL Id : hal-01845776," vol. 84, no. 4, pp. 234–243, (2018).
- 18 B. Delenne, L. Mode, and M. Blaudez, "Modelling and simulation of a gas pressure regulator," in *European simulation symposium. Erlangen, Germany*, (1999).
- 19 H. Ott *et al.*, "Core-flood experiment for transport of reactive fluids in rocks," *Rev. Sci. Instrum.*, vol. 83, no. 8, (2012).
- 20 Bill Menz, "Pressure Regulator Selection Strategy," *Swagelok*, no. August, 2011
- 21 Pickup, I. E. D., and A. P. Russell, "Dynamic instability in permanent-magnet synchronous/stepping motors.," *IEE Proc. B (Electric Power Appl.)*, vol. 134, no. 2, pp. 91–100, (1987)

A Mechanistic Study of Wettability Alterations in Sandstone by Low Salinity Water Injection (LSWI) and CO₂ Low Salinity Water-Alternating-Gas (WAG) Injection

Shijia Ma¹ and L.A. James^{1,*}

¹Hibernia EOR Research Group, Department of Process Engineering, Memorial University of Newfoundland, St. John's, NL, Canada, A1B 3X5

Abstract. Low salinity water injection (LSWI), an emerging Enhanced Oil Recovery (EOR) method, has proven to be effective in increasing oil recovery by wettability alteration. As low salinity water is injected into the reservoir, the pre-established equilibrium is disturbed. The chemical reactions among the oil/brine/rock system alters the existing wettability, resulting in enhanced oil recovery. Water-alternating-gas (WAG) injection is also a leading EOR flooding process in light to medium oil sandstone and carbonate reservoirs. A recently proposed hybrid EOR method, CO₂ low salinity (LS) WAG injection, shows promise based on experimental and simulation studies, compared to LSWI or CO₂ injection alone. Wettability alteration is considered as the dominant mechanism for CO₂ LSWAG injection. In this study, a new displacement contact angle measurement which better mimics the actual displacement process taking place in a reservoir is used, aiming to investigate the effect of monovalent and divalent cations, CO₂, and injection schemes. It is found that the injection of NaCl low salinity water alters the wettability towards slightly water-wet, and the injection of CaCl₂ low salinity water alters the wettability towards slightly oil-wet. The injection of CO₂ promotes water-wetness and geochemical reactions between oil and brine. Injection scheme of CO₂ and NaCl low salinity water is more efficient than WAG cycle of CO₂/NaCl in wettability alteration towards more water-wet. However, the opposite trend is observed with CaCl₂ low salinity water, of which WAG cycle of CO₂/CaCl₂ is more efficient in altering wettability towards water-wet. The oil drop deformation process during LSWI resembles the process of oil removal using surfactant. As CO₂ is introduced, due to the acidic effect of CO₂ and ion exchange, it acts to wet the rock surface, leading to a more water-wet state. With introduction of CO₂, the oil drop deformation resembles the “roll-up” oil removal process.

1 Introduction

Low salinity water injection (LSWI) has been widely investigated and recognized as an effective enhanced oil recovery (EOR) method in both secondary and tertiary mode [1-3]. Compared to other chemical EOR methods, such as polymer or surfactant flooding, LSWI is advantageous due to its lower cost and reduced impact on the environment. Another advantage for LSWI is that it can be combined with other EOR methods to further improve oil recovery [4-6]. According to economic evaluations on chemical EOR methods by Al-Murayri et al. [7] and Muriel et al. [8], LSWI and CO₂ injection generate the highest net present value (NPV) and both methods are effective in increasing oil recovery. Therefore, a hybrid technique termed CO₂ low salinity water-alternating-gas (LSWAG) injection, which combines the EOR effect of both methods, has been developed over the last 15 years. CO₂ LSWAG injection has been studied through core flooding experiments, contact angle and interfacial tension (IFT) measurements, primarily with sandstone, at ambient or reservoir conditions. Most results confirm improved oil recovery using this hybrid technique, in both secondary and tertiary modes, with some

exceptions [9-11]. Studies with negative or neutral outcomes are mainly due to the fact that the cores are strongly water-wet or contain very small amount of clay minerals. Clean water-wet sandstones may not be the most favourable reservoir conditions for CO₂ LSWAG injection [12, 13].

The proposed mechanisms of CO₂ LSWAG injection are a combination of LSWI and CO₂ WAG injection. Al-Abri et al. [14] proposed that the improved oil recovery by immiscible CO₂ LSWAG injection is due to mobility control and wettability alteration. The IFT between high salinity brine and oil reduces as CO₂ is introduced. However, changes in the IFT of low salinity brine and oil are not noticeable, indicating that IFT reduction is not a dominant mechanism in this process. They also suggest multi-component ionic exchange (MIE) in which Na⁺ substitutes the divalent cations (Mg²⁺) accounts for the higher oil recovery when injecting monovalent NaCl brine compared to injection of MgCl₂ brine. Teklu et al. [15] claimed that CO₂ LSWAG injection improved oil recovery of conventional CO₂ WAG injection by forming in-situ carbonated water of higher CO₂ saturation in the brine phase due to the higher CO₂ solubility in low salinity water. This in-situ carbonated water promotes wettability alteration towards more water-wet and CO₂-brine IFT reduction, hence improved oil recovery. They also

* Corresponding author: ljames@mun.ca

compared the CO₂-brine solubility model developed by Enick and Klara [16] and Li and Nghiem [17] with fresh water and 100,000 ppm NaCl at 71°C from 0 to 41 MPa. Both models show that CO₂ solubility in brine increases with pressure and CO₂ solubility is higher in fresh water. Chaturvedi et al. [18] and AlQuraishi et al. [11] suggest that fines migration and wettability alteration, mechanisms of LSWI, might be the dominant mechanisms for increased oil recovery by CO₂ LSWAG injection. The presence of clay minerals, especially kaolinite, is considered essential. However, this proposed mechanism is questioned by Zolfaghari et al. [19] as they achieved oil recovery in sandstone without kaolinite. Wettability alteration towards more water-wet was suggested by Al-Saedi et al. [20-22]. Based on the proposed mechanisms, wettability alteration and mobility control may be considered the dominant mechanisms in CO₂ LSWAG injection.

Wettability alteration taking place during CO₂ LSWAG injection could be ascribed to LSWI or the acidic effect of CO₂ [23, 24] or a combination of both. Drummond and Israelachvili [25] demonstrate wettability alteration indicated by contact angle measurements at ambient conditions for low salinity water varying from oil-wet to water-wet as pH is lower than 9 and from water-wet to intermediate-wet as pH is greater than 9. The pH during a LSWI is mostly below 9 [26], indicating the wettability alteration is more likely to be from water-wet to intermediate-wet [27]. The main functions of injecting CO₂ are oil swelling and viscosity reduction due to CO₂ solubility in oil, miscibility with oil if pressure is above minimum miscible pressure and wettability modification [21]. Since low salinity water and CO₂ both impact wettability, the question remains as to whether the introduction of CO₂ in low salinity water will assist in promoting the geochemical reactions and low salinity effect. Generally, monovalent cations (Na⁺) and divalent cations (Ca²⁺ or Mg²⁺) have different impacts on the rock surface. The MIE mechanism by LSWI proposed by Lager et al. [28] demonstrates that multivalent cations, such as Ca²⁺, act as bridges between the oil polar components and the negatively charged rock surface, promoting oil-wetness. The mechanism of electrical double layer expansion by LSWI suggested by Ligthelm et al. [29] indicates that lowering the electrolyte content, especially reducing the content of multivalent cations, yields expansion of the electrical double layer surrounding the clay and oil, and an increase in zeta potential. This leads to wettability modification of the rock surface towards more water-wet. Wettability characterization is uncertain for CO₂ introduced with low salinity water in the sandstone/oil/brine/rock system since previous experimental data is limited.

To investigate wettability of the rock and fluid systems, direct or indirect and qualitative or quantitative methods can be used. Indirect and qualitative methods for characterizing rock wettability are capillarimetric method [30], spontaneous imbibition [31, 32], capillary pressure curves, and relative permeability method [33, 34]. Indirect and quantitative methods include the Amott and Amott-Harvey index method, USBM (U.S. Bureau of Mines) method, and the combined Amott/USBM method, which measure the average wettability of the rock samples, i.e., a macroscopic mean value of the rock wettability to a given fluid. Direct and quantitative method for characterizing the wettability of a

specific surface is the contact angle measurement [35, 36], as well as the new SEM-MLA method introduced [37, 38]. Contact angle measurement works the best with pure fluids and well-prepared surfaces [39]. It can also be used to determine the effect of crude oil, brine chemistry, temperature and pressure on wettability. According to Arif et al. [40], direct contact angle measurements is a widely recognized technique for wettability characterization of rock/CO₂/brine or rock/oil/CO₂-enriched-brine systems. In this research we used contact angle measurement as a method to evaluate wettability alteration. Our particular interest is understanding the ion exchange and chemical reactions of the rock/oil/brine/ and rock/oil/brine/CO₂ systems by comparing the effect of monovalent and divalent ions and the effect of CO₂ on water-wet and oil-wet sandstone under different injection sequences. Contact angle measurements may indeed be the best choice to differentiate any wettability changes as we are able to 1) conduct measurements with high temperature and pressure, under which the commonly used Amott or USBM method is not applicable [40, 41] and 2) still appreciate the core scale aspects of rock mineralogy and some differences in water-wet and oil-wet "real" surfaces [42].

The data for contact angle measurements on sandstone/crude oil/CO₂-enriched brine system is very limited. Jaeger et al. [43] performed captive bubble contact angle measurements with sandstone samples which were previously aged at room temperature with 1.5 wt% cyclohexanepentanoic acid in decane for two months. They reported a strongly water-wet condition, contact angle of 46°, of such system under 50°C and 20.7 MPa with 32,000 ppm synthetic seawater. Ameri et al. [44] conducted contact angle measurements on Bentheimer sandstones that are initially water-wet and oil-wet at elevated pressure from 0.2 to 14 MPa and with NaCl brine salinity ranging from 5000 to 35,000 ppm. They found that in initially water-wet sandstones, contact angle increases with pressure, and decreases with increasing NaCl brine concentration. The overall contact angle for using NaCl brine salinity ranging from 20,000 to 35,000 ppm is very low, less than 20°. The average contact angle for using 5000 ppm NaCl brine is 40° and the value when distilled water is used is 57°. This indicates that decreasing salinity of NaCl brine leads to a less water-wet state, which differs from the results obtained by Espinoza et al [45]. For initially oil-wet sandstone, samples were aged for 22 months with crude oil at 60°C. In the sub-critical and near-critical state region of CO₂ (0-9 MPa), contact angle increases is slightly higher with 35,000 ppm brine than with distilled water. However, the opposite is observed for super-critical state region of CO₂ (9-13 MPa), Seyyedi et al. [46] reported that contact angle values of the quartz with CO₂-enriched brine are slightly higher than that with brine phase alone, indicating that injection of CO₂ alters wettability towards slightly less water-wet. However, Al-Abri et al. [14] reported contradictory results, showing that the contact angle was reduced with the addition of CO₂, indicating a wettability alteration towards more water-wet. They conducted their contact angle measurements with Berea sandstone discs aged with crude oil at 60° for three weeks. They also found that changes in wettability are greater with divalent ions (Mg²⁺) than monovalent ions (Na⁺ and K⁺).

It is worth mentioning that there are limitations on these contact angle measurements that would result in misleading

interpretations on the effect of CO₂ and low salinity water, and the working mechanisms of CO₂ LSWAG injection. In these measurements, the oil drop is introduced after the rock surface has been in contact with injection brine and CO₂, which is not representative of the actual displacement in a reservoir, where oil exists before the injection fluids. Therefore, in order to better capture and mimic the real displacement procedure taking place in a reservoir to investigate what triggers the wettability alteration during LSWI and CO₂ LSWAG injection, a displacement method developed by Sofla et al. [42] for measuring contact angle was employed in this study. We investigated the dynamic contact angle changes during the displacement process of LSWI, continuous CO₂ and LSWI, and CO₂ LSWAG injection, respectively. With this method, the interactions among crude oil, brine and CO₂ were investigated without the additional effect of capillary imbibition and drainage [47]. The objective is to compare the resulting wettability alteration (through contact angle measurements) due to multi-component ion exchange (MIE), chemical reactions, and injection sequence of low salinity water methods. This paper addresses the question as to whether or not the ionic charge and injection scheme play a role in differentiating LSWI and CO₂ LSWAG injection at the fluid-rock interaction level.

2 Materials

Fluids. The oil phase used in this experiment is an offshore Newfoundland and Labrador (NL) light crude oil. Synthetic brines were prepared to mimic the Hibernia formation water and Grand Banks seawater. The two low salinity brines are 2000 mg/L NaCl and 2000 mg/L CaCl₂. Their chemical compositions and basic properties are presented in Table 1.

Table 1. Compositions and properties of synthetic brines and oil

Component	FB	SW	NaCl	CaCl ₂
Na ⁺ , mg/L	35,671	10,974	786	/
Mg ²⁺ , mg/L	330	1,310	/	/
Ca ²⁺ , mg/L	3,599	420	/	721
K ⁺ , mg/L	255	407	/	/
Cl ⁻ , mg/L	62,371	19,740	1,214	1,279
SO ₄ ²⁻ , mg/L	233	2,766	/	/
HCO ₃ ⁻ , mg/L	/	129	/	/
Total	102,430	35,746	2,000	2,000
pH@22° C	5.9	7.9	6.2	5.8
Density, g/cm ³	1.074	1.023	1.0	1.0
Oil Viscosity, cP	5.0			
Oil Density, g/cm ³	0.878			

Legends: FB – formation brine; SW – seawater; / - not included

Rock sample. Berea sandstone with 80% quartz content and <2% clay content [37] was used in this study. The core samples with an approximate diameter of 2 cm were cut into 5-mm thin slices using MK-370EXP Tile Saw. The dust was blown off with pressurized nitrogen and the core slices were dried in oven overnight. The water-wet samples were immersed in formation brine for one day prior to conducting

contact angle measurements. To obtain an oil-wet initial wettability, the core slices initially immersed in formation brine were removed to a beaker containing NL crude oil and aged at 98°C in the oven for six weeks as suggested by Sripal et al. [37] to obtain oil-wet conditions. Subsequently, the surface of the oil-wet samples was cleaned and immersed in formation water for one day before contact angle measurements.

3 Methods

Figure 1 illustrates the experimental setup used to perform contact angle measurements in this study. All experiments are conducted at ambient conditions. In order to mimic the actual displacement taking place in a reservoir, the cell is initially filled with formation brine. Subsequently, an oil drop with radius ranging from 1.8 to 2.0 mm is introduced through the needle at the bottom of the cell and adheres onto the rock surface. The initial contact angles are measured after the system reached equilibrium, which is 1 hour after it is introduced into the system. This indicates the initial wettability of the rock surface and initial condition of an oil droplet in a reservoir.

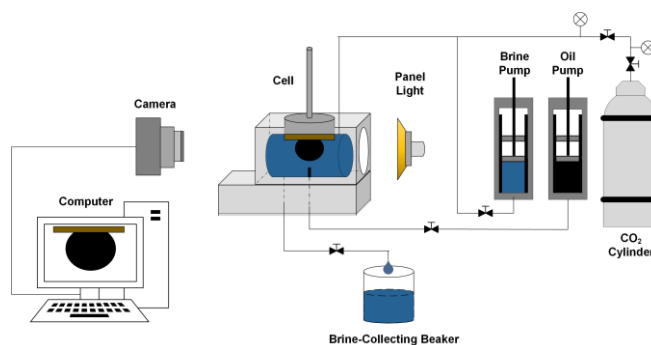


Fig. 1 Schematic diagram of contact angle measurement.

A total of 13 experiments were completed, using the injection schemes outlined in Table 2. Each scenario was completed twice, once using NaCl as the LSW and again using CaCl₂ as the LSW.

Table 2. Injection scheme of experiments

Scenario #	Injection Scheme			
	Cycle 1 (60 mL)	Cycle 2 (20 mL)	Cycle 3 (20 mL)	Cycle 4 (20 mL)
1	SW	SW	SW	SW
2	SW	LSW	LSW	LSW
3	LSW	LSW	LSW	LSW
4	SW	CO ₂ (10ml)	LSW (25mL)	LSW (25mL)
5	SW	CO ₂ /LSW	CO ₂ /LSW	CO ₂ /LSW
6	LSW	CO ₂ (10mL)	LSW (25mL)	LSW (25mL)
7	LSW	CO ₂ /LSW	CO ₂ /LSW	CO ₂ /LSW

Scenario 1 represents seawater injection. Scenario #2 and #3 represent LSWI. Scenarios #4 and #6 represents seawater or low salinity water injection, followed by continuous CO₂

injection and LSWI. Scenario #5 and #7 represent seawater or low salinity water injection, followed by LSWAG injection. Brines and CO₂ were injected through the injection inlet into the cell to displace the existing fluid. The injection speed was controlled so that the oil drop remains attached on the rock surface throughout the experiment.

The total volume of the cell is 20 mL. In cycle 1, 60 mL of seawater or low salinity water is injected to ensure that the initial formation brine is fully displaced. The system is allowed to set for equilibrium for half an hour after every 20 mL of injection fluid and the reading at equilibrium state is taken. Figure 2, as an example, shows the contact angle changes during the half-an-hour equilibrium time of scenario #1, indicating that an equilibrium was gradually established.

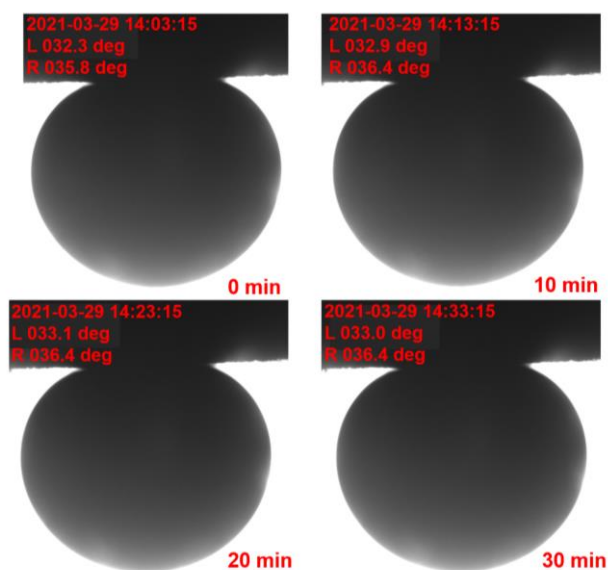


Fig. 2 Contact angle changes after seawater injection during half-an-hour equilibrium time (scenario #1).

After cycle 1, another 60 mL of CO₂ (g), low salinity water and a combination of both are further injected in cycles 2-4 representing the injection schemes of continuous CO₂ and low salinity water injection, and the CO₂ LSWAG process. Contact angles are measured dynamically for each injection cycle and measurements are taken half an hour after each injection cycle. Three distinct measurements are carried out to monitor repeatability. Contact angles are reported as averages of the three measurements. The change in contact angle is calculated using the equation below.

$$\Delta\theta [\%] = (\theta - \theta_{initial}) / \theta_{initial} \times 100 \quad (1)$$

where $\Delta\theta$ refers to the change in contact angle, θ is the value of contact angle measured after each injection cycle, and $\theta_{initial}$ is the initial contact angle measured with the presence of formation water. The reason for comparing changes instead of absolute contact angles is to avoid the influence of the samples and each scenario starts from the same point. Initial contact angle is also reported.

To calculate the uncertainty, or error propagation of $\Delta\theta$, the root-sum square method proposed by Kline and McClintock is used [48]. The effect of uncertainty $\sigma_{\Delta\theta}$ on the calculated $\Delta\theta$ can be expressed as follow:

$$\sigma_{\Delta\theta} = \sqrt{\sigma_{\theta}^2 * \left(\frac{\partial(\Delta\theta)}{\partial\theta}\right)^2 + \sigma_{\theta_{initial}}^2 * \left(\frac{\partial(\Delta\theta)}{\partial\theta_{initial}}\right)^2} \quad (2)$$

Subsequently, changes in contact angle with calculated uncertainty are plotted against injected volume to investigate the effect of low salinity water, injection of CO₂ and WAG injection schemes.

Moreover, in order to validate that the measured contact angle changes are mainly due to the chemical reactions (intermolecular forces) in the oil/brine/rock system, rather than gravitational force, we have estimated the Bond number (B_o) of the oil/seawater/brine system using equation from Li et al. [49].

$$B_o = \frac{\Delta\rho g L^2}{\gamma} \quad (3)$$

where $\Delta\rho$ is the density difference of oil and brine (kg/m³), g is gravitational acceleration (m/s²), L refers to the radius of curvature of oil drop (m), γ is surface tension (N/m). With the measured surface tension (31.5 mN/m), and oil drop radius in seawater (1.86 mm), Bond number is calculated to be 0.154, which is lower than 1, indicating that surface tension dominates.

4 Results and Discussion

As shown in Table 3, section 4.1 investigates the effect of seawater and low salinity water (scenario #1, #2 and #3) on wettability alteration of water-wet and oil-wet Berea sandstone samples. Section 4.2 discusses the effect of CO₂ by comparing scenario #2 and #4, and #3 and #6. Subsequently, the deformation process of the oil drops during the injection of low salinity water and CO₂ is investigated in section 4.3. In the end, section 4.4 studies the effect of different injection schemes by comparing CO₂ + LSW injection scheme to CO₂/LS WAG injection scheme (#4 and #5, and #6 and #7). The effect of monovalent and divalent cations is discussed and compared in all sections.

Table 3. Comparison of different scenarios.

Section	Comparison of different scenarios	
4.1 Effect of Low Salinity Water	#1	SW + SW
	#2	SW + LSW (NaCl and CaCl ₂)
	#3	LSW + LSW (NaCl and CaCl ₂)
4.2 Effect of CO ₂	#2	SW + LSW
	#4	SW + CO ₂ + LSW
	#3 #6	LSW + LSW LSW + CO ₂ + LSW
4.4 Effect of Injection Scheme	#4	SW + CO ₂ + LSW
	#5	SW + CO ₂ /LS WAG
	#6 #7	LSW + CO ₂ + LSW LSW + CO ₂ /LS WAG

4.1 Effect of Low Salinity Water

Contact angle changes due to the injection of seawater alone, low salinity waters alone, and combinations of seawater and low salinity water are shown in Figures 3 and 4 for water-wet and oil-wet sandstones, respectively. These injection schemes mimic the displacement process of (1) seawater injection, (2)

secondary seawater and tertiary LSWI, and (3) LSWI. Overall, changes in contact angle in the oil-wet samples are not as significant as in water-wet samples. However, it is worth comparing and understand the changing trend after each injection cycle, which could be an estimation for the potential changes in a core scale experiment.

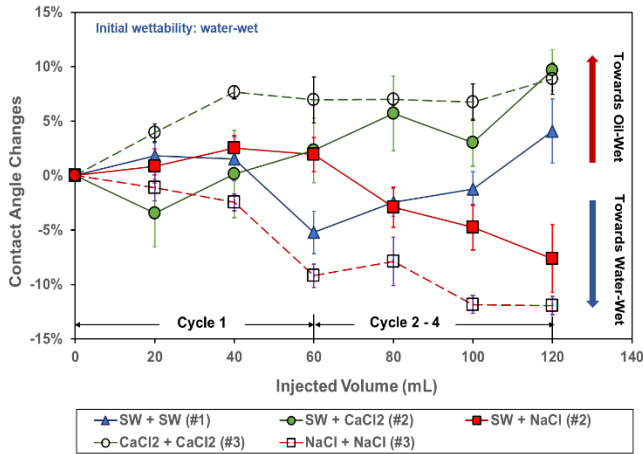


Fig. 3 Contact angle changes during seawater and low salinity water injection in water-wet sandstone (scenario #1, #2, #3).

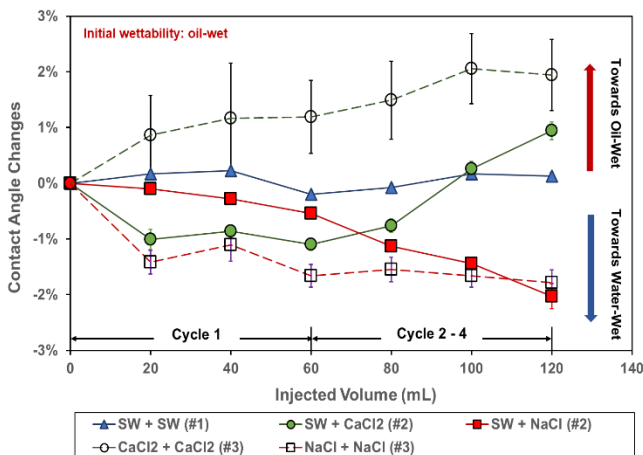


Fig. 4 Contact angle changes during seawater and low salinity water injection in oil-wet sandstone (scenario #1, #2, #3).

In Figure 3, the initial wettability of the rock sample is water-wet, with measured contact angles varying from 34° to 50° (average: 40.6° ± 5.0°). Contact angle changes due to the injection of seawater are within 5%, which is not very significant. This indicates that the injection of seawater has negligible effect on the rock wettability. The trend of using NaCl and CaCl₂ in LSWI shows different impacts on wettability. The red arrow in Figure 2 indicates changing towards more oil-wet and the blue arrow suggests changing towards more water-wet. It is seen that NaCl alters the wettability towards more water-wet, around 10% less compared to initial contact angle, whereas CaCl₂ results in wettability alteration moving to less water-wet. A similar trend is also observed in the combined seawater and LSWI process.

In Figure 4, the initial wettability of the rock sample is oil-wet, with measured contact angle varying from 117° to 155° (average: 133.0° ± 13.5°). For seawater injection (SW + SW), the contact angle remains almost constant throughout the process. The injection of NaCl LSWI alters the rock

wettability towards slightly less oil-wet (SW + NaCl, NaCl + NaCl) and use of CaCl₂ (SW + CaCl₂, CaCl₂ + CaCl₂) alters the wettability towards more oil-wet. This observation agrees with that in the water-wet samples where NaCl promotes water-wetness and CaCl₂ promotes oil-wetness.

Generally, the configuration of water on rock mineral surfaces exist in two ways: (1) pendular-ring on contact points of grains; and (2) thin film on the mineral surfaces [50]. In this study, the oil drop is introduced after formation water and is kept attached to the surface throughout the experiment. Therefore, the model proposed is as shown in Figure 5, where a thin water film is formed between the rock and oil drop. A similar model was also proposed by Lee et al. [51]. They manufactured sand/clay like silica particles using simple anionic surface similar to sand grain and measured the thickness of this water film to be roughly 9-15 nm. According to their measurements on the simple wet system (fabricated simple anionic surface, similar to a sand grain) [51], the thickness of the water film on the silica/clay (sandstone-like) surface is thicker in brines with lower salinities (except for pure water). Therefore, in a system where the substrate is initially oil-wet, in order alter the wettability from oil-wet to intermediate-wet or water-wet, a thicker water film along the pore wall is needed.

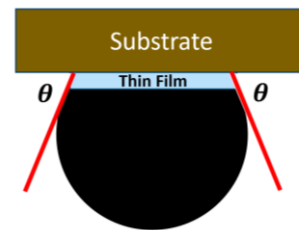


Fig. 5 A proposed model with water thin film forming between the rock/brine and oil/brine interface (Adapted from Lee et al. [51]).

Based on the results from Figure 3 and Figure 4, it is observed that the use of monovalent cations as injection brine alters the wettability towards more water-wet, which agrees with the finding from Xie et al. [52] that monovalent cations (Na⁺) give rise to positive disjoining pressure; however, divalent cations (Ca²⁺) lead to negative disjoining pressure at the same concentration. Negative disjoining pressure between rock surface and oil droplet indicates the attractive force is dominant; thus, more oil-wet is expected for the rock surface. On the other hand, positive disjoining pressure suggests the repulsive force between the rock surface and oil droplet, leading to more water-wet.

4.2 Effect of CO₂

The wettability changes caused by CO₂ after seawater injection and LSWI (NaCl or CaCl₂) were investigated by comparing the contact angle changes in scenarios with CO₂ (#4 and #6) and without CO₂ (#2 and #3). Contact angle changes during cycle 2 – 4 are studied. For LSWI (#2 and #3), cycle 2-4 are injection of LSW. For CO₂ + LSW (#4 and #6), cycle 2 is injection of CO₂, cycle 3-4 are injection of LSW. To calculate the changes, $\theta_{initial}$ in Eq. (1) is not the initial value in cycle 1, but the equilibrium contact angle measured after cycle 1 ($\theta_{cycle\ 1,eq}$). Hence, Eq. (4) was used to calculate

contact angle changes ($\Delta\theta$) and uncertainty was calculated according to Eq. (2).

$$\Delta\theta [\%] = (\theta - \theta_{\text{cycle 1,eq}}) / \theta_{\text{cycle 1,eq}} \times 100 \quad (4)$$

Based on this, all the scenarios investigated in this section will start from the same point in cycle 2 with respect to contact angle change.

Figures 6 and 7 show the results of LSWI and CO_2 + LSWI after seawater injection in water-wet and oil-wet samples respectively. When comparing scenario #2 (SW + LSW) and #4 (SW + CO_2 + LSW), the addition of CO_2 after seawater promotes water-wetness for both water-wet and oil-wet samples. After CO_2 injection, further injection of CaCl_2 changes the wettability towards more oil-wet, and the injection of NaCl changes further more towards water-wet.

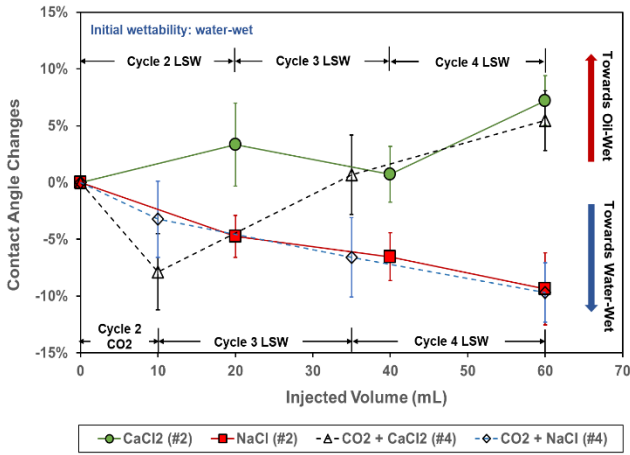


Fig. 6 Comparison of contact angle changes during LSWI and CO_2 + LSWI in water-wet sandstone after 1st cycle of seawater injection (scenario #2 and #4).

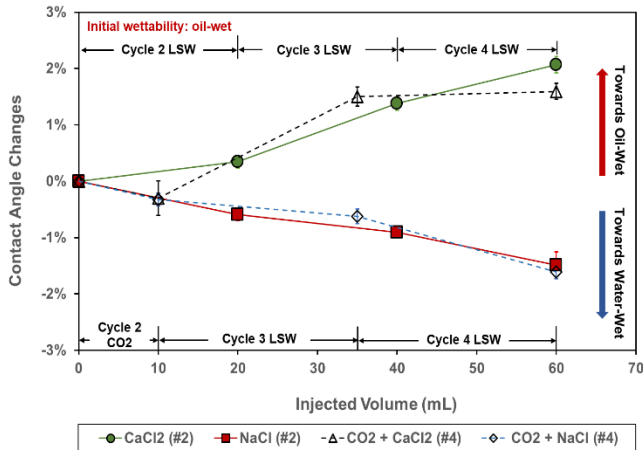


Fig. 7 Comparison of contact angle changes during LSWI and CO_2 + LSWI in oil-wet sandstone after 1st cycle of seawater injection (scenario #2 and #4).

The contact angle changes of LSWI (scenario #3) and CO_2 + LSWI (scenario #6) after LSWI in cycle 1 are shown in Figure 8 and Figure 9. Injection of LSW in cycle 2-4 has no significant impact on contact angle after the 1st cycle of LSWI. However, with the injection of CO_2 in cycle 2 and NaCl in cycle 3-4, CO_2 + NaCl alters wettability towards more water-wet in both water-wet and oil-wet samples (Figure 8 and Figure 9). For scenario #6 (CO_2 + CaCl_2), CO_2

alters wettability towards more water-wet, whereas further injection of CaCl_2 changes the wettability to more oil-wet.

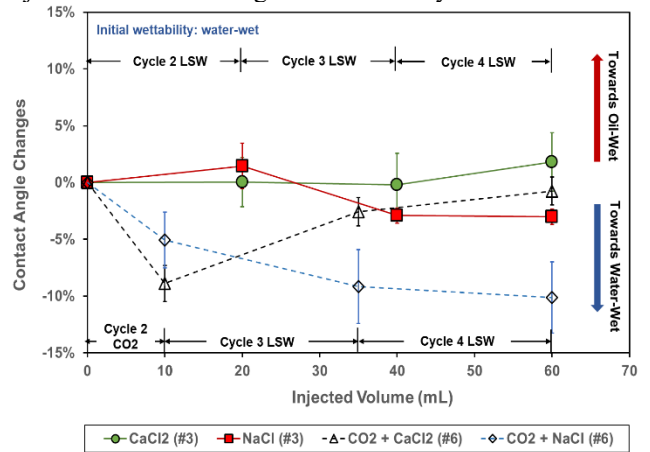


Fig. 8 Comparison of contact angle changes during LSWI and CO_2 + LSWI in water-wet sandstone after 1st cycle of LSWI (scenario #3 and #6).

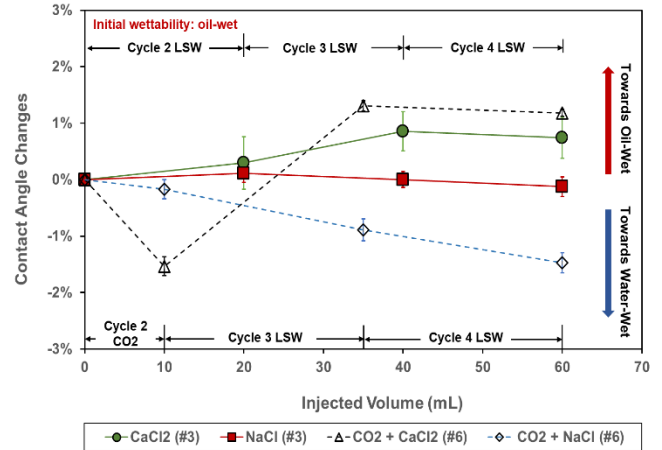
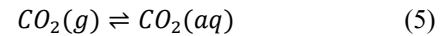


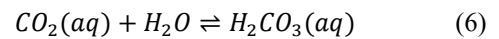
Fig. 9 Comparison of contact angle changes during LSWI and CO_2 + LSWI in oil-wet sandstone after 1st cycle of LSWI (scenario #3 and #6).

It is also observed from Figure 8 and 9 that CO_2 injected after CaCl_2 low salinity water alters wettability towards more water-wet compared to that injected after NaCl low salinity water. As suggested by Lager et al. [53], it is possible that divalent cations are exchanged for monovalent cations during LSWI. Therefore, in our case, more Ca^{2+} on the rock surface is expected in scenario #6 with CaCl_2 .

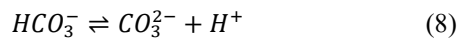
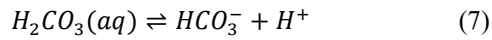
When CO_2 is in contact with water, it first dissolves according to reaction (5):



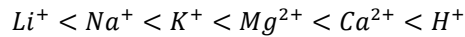
At room temperature, solubility of $\text{CO}_2(g)$ is 0.034 mol/L. Subsequently, reaction (6) takes place to form H_2CO_3 . This reaction is kinetically slow and only a small fraction (0.2 – 1.0%) of dissolved CO_2 , $\text{CO}_2(aq)$, is converted to H_2CO_3 .



However, this carbonic acid dissociates very rapidly at ambient conditions to bicarbonate [54], as shown in reaction (7). The bicarbonate electrolyte in the solution can also form CO_3^{2-} as shown by reaction (8).



With the injection of CO₂, some of the produced CO₃²⁻ would potentially react with the existing Ca²⁺ ions, forming CaCO₃, which results in equation (8) to move to the right direction, leading to slight increase in H⁺. Based on the selectivity of cation affinity to negatively charged surfaces from Velde [55], as shown below, the proton H⁺ has the strongest affinity to be adsorbed onto a negatively charged surface.



Therefore, the generated H⁺ is likely to replace the pre-attached divalent cations, resulting in more water-wetness. In this way, the injection of CO₂ after CaCl₂ low salinity water alters wettability towards more water-wet compared to injection of CO₂ after NaCl low salinity water.

4.3 Surfactant-Like Behavior of Oil Drops

During the injection of LSW and a combination of CO₂ and LSW in the water-wet and oil-wet samples, a surfactant-like deformation process of the oil drop is constantly observed when the initial equilibrium of the system is disturbed. The oil drop deformation with and without CO₂ is discussed respectively in the subsections.

4.3.1 Deformation in the absence of CO₂

Figure 10 and Figure 11 illustrate the deformation process during the injection of NaCl LSW in water-wet and CaCl₂ LSW in oil-wet sandstones, respectively. For NaCl LSWI in water-wet sample, the contact angle varies from water-wet to intermediate-wet and then back to more water-wet while reaching equilibrium. For CaCl₂ LSWI in oil-wet sample, contact angle changes from oil-wet to intermediate-wet and then back to more oil-wet in the end.

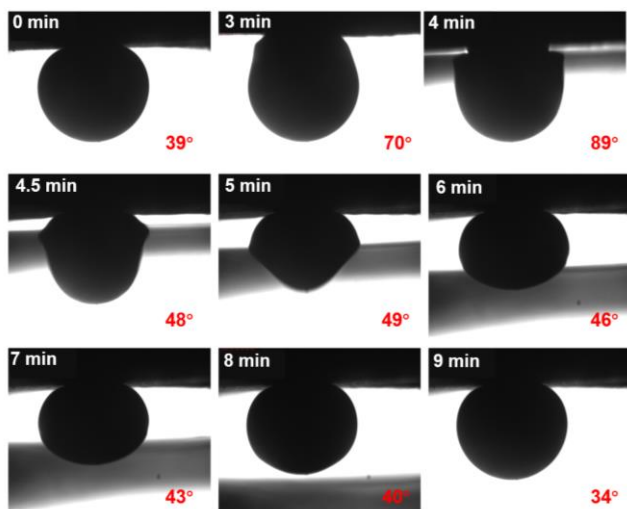


Fig. 10 Oil drop deformation process during NaCl LSWI in water-wet sandstone (scenario #3).

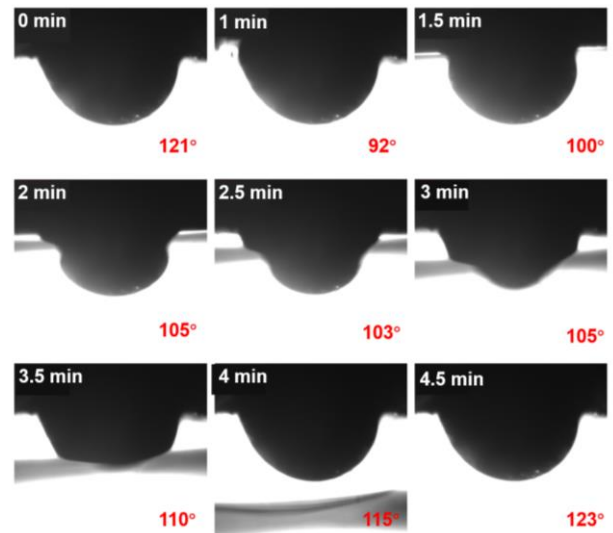
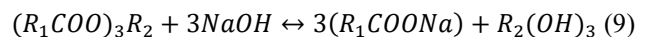


Fig. 11 Oil drop deformation process in time during CaCl₂ LSWI in an oil-wet sandstone system (scenario #3).

Based on Figures 10 and 11, the deformation process during LSWI resembles a surfactant-like behaviour. The potential removal of the droplet exhibits a “necking” or emulsification mechanism. One mechanism for LSWI proposed by McGuire et al. [56] suggests that the changes in wettability during low salinity water injection appear to be similar to the observations from alkaline and surfactant flooding. In this study, the interactions between the oil drop and injection fluids are more dominant due to the presence of just one oil drop. As listed in Table 1, the pH of the injection fluids is higher compared to that of the initial formation water. During the injection of low salinity water, in-situ “surfactants” are generated, as shown in Eq. (9), when the oil drop is in contact with the elevated pH fluid near the rock and oil surfaces. This improves oil recovery [56]. In this way, low salinity water injection is similar to micellar or surfactant flooding.



where R_1 and R_2 represent the R group, which consists of a group of carbon and hydrogen atoms.

According to the study of oil removal from soil surfaces by Miller and Raney [57], two approaches are proposed as mechanisms for oil removal from hydrophobic surfaces using surfactants: (1) roll-up resulting from wetting; and (2) emulsification resulting from reduction in interfacial tension (Figure 12).

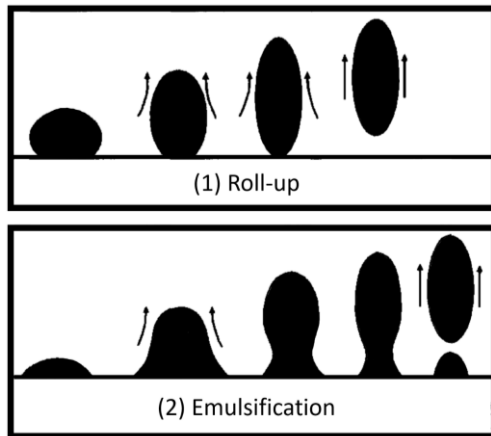


Fig. 12 Mechanisms of oil removal from surface by (1) roll-up and (2) emulsification (adapted from Miller and Raneey [57]).

4.3.2 Deformation with CO₂ present

The top two pictures shown in Figure 13 are the oil drop deformation during injection of CO₂ + CaCl₂, (scenario #4) and the bottom two pictures are during CaCl₂ LSWI (scenario #2). These two deformation processes resemble the two approaches in Figure 12. Without addition of CO₂, the detachment of the oil drop is a saponification or emulsification process. However, the roll-up process is expected with CO₂ due to the geochemical reactions that change the wetting state of the contact point on the rock surface.

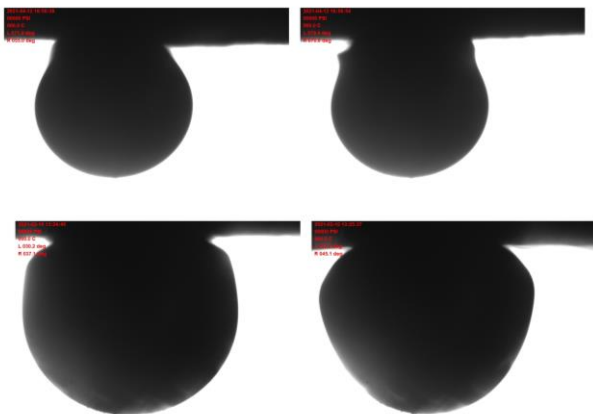


Fig. 13 Comparison of oil drop deformation process: top (scenario #4): during CO₂ and CaCl₂ injection (roll-up); bottom (scenario #2): during CaCl₂ injection (emulsification) after seawater injection in water-wet sandstone.

4.4 Effect of Injection Scheme

The impact of different injection schemes with respect to CO₂ is explored by comparing the scenarios of SW + CO₂ + LSW (#4) and SW + LSWAG (#5), and scenarios of LSW + CO₂ + LSW (#6) and LSW + LSWAG (#7).

Contact angle changes of scenario #4 and #5 are shown in Figure 14 and Figure 15. It is observed that after 1st cycle of seawater injection, further injection of CO₂ + CaCl₂ alters wettability in the direction of more oil-wet, however, CO₂/CaCl₂ WAG injection alters rock wettability towards

more water-wet. Injection schemes of CO₂ + NaCl and CO₂/NaCl WAG both change the rock wettability to more water-wet, whereas changes are more significant for CO₂ + NaCl. The wettability changes by CO₂/LSWAG processes (for both NaCl and CaCl₂) are not as significant as CO₂ + LSW injection when implemented after seawater injection (Figure 14 and Figure 15).

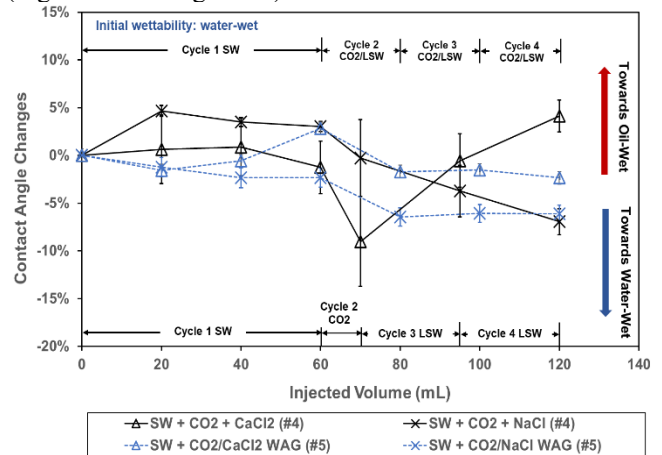


Fig. 14 Comparison of contact angle changes during SW + CO₂ + LSWI and SW + CO₂/LS WAG injection in water-wet sandstone (scenario #4 and #5).

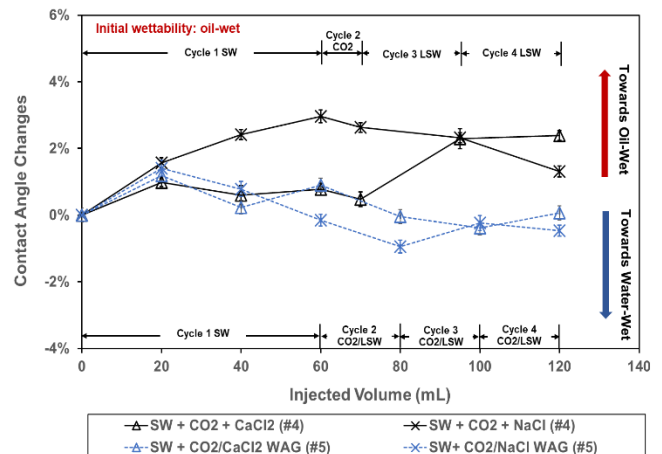


Fig. 15 Comparison of contact angle changes during SW + CO₂ + LSWI and SW + CO₂/LSWAG injection in oil-wet sandstone (scenario #4 and #5), error bars are too small to be seen.

Figure 16 and Figure 17 show the comparison between #6 (LSW + CO₂ + LSW) and #7 (LSW + CO₂/LSWAG) in water-wet and oil-wet samples. The results in the figures show that the addition of CO₂ has a minor effect on the wettability for the CO₂/NaCl WAG process. When comparing CO₂ + CaCl₂ with CO₂/CaCl₂ WAG injection in both water-wet and oil-wet samples, the trend for wettability change is different. For the scheme of CO₂ + CaCl₂ injection, the addition of CO₂ promotes water-wetness of the rock, and the chasing CaCl₂ low salinity water changes the wettability back to more oil-wet. However, in the CO₂/CaCl₂ WAG process, the wettability is altered towards more water-wet.

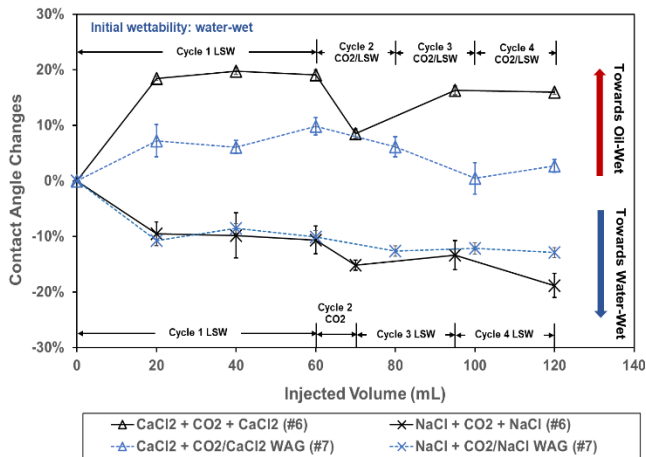


Fig. 16 Comparison of contact angle changes during LSWI, CO₂ and LSWI, and CO₂ LSWAG injection in water-wet sandstone (scenario #6 and #7), some error bars are too small to be seen.

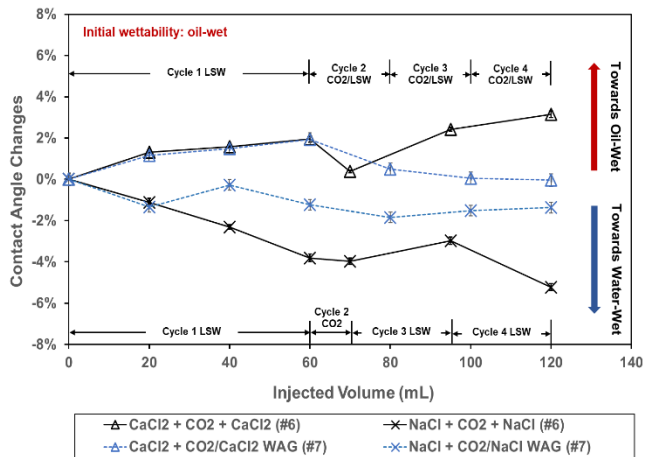


Fig. 17 Comparison of contact angle changes during LSWI, CO₂ and LSWI, and CO₂ LSWAG injection in oil-wet sandstone (scenario #6 and #7), error bars are too small to be seen.

The WAG process of CO₂ and CaCl₂ low salinity water leads to wettability alteration to slightly water-wet. With respect to the scenario of CO₂ + CaCl₂ (#6), even though CO₂ changes wettability to be more water-wet, the generated H⁺ is not sufficient. Thus, subsequent injection of CaCl₂ replaces the monovalent cations and alters the rock wettability towards more oil-wet.

Summarising, if NaCl LSW is used, the continuous CO₂ + NaCl injection scheme is more efficient than WAG cycle of CO₂/NaCl in achieving a more water-wetness condition of sandstone. However, if CaCl₂ LSW is used, WAG cycle of CO₂/CaCl₂ can alter the rock wettability to more water-wet compared to continuous CO₂ + CaCl₂ injection.

5 Conclusion

1. In this study, a displacement method for measuring contact angle changes during the process of seawater injection, LSWI, CO₂ and LSWI, and CO₂ LSWAG injection has been conducted. Seawater, low salinity

water with only monovalent and divalent cations were selected as the injection aqueous phases. The effect of these ions, oil drop deformation process, and the effect of CO₂ and injection scheme have been investigated. It is found that for our Berea sandstone with an initial wettability of either water-wet and oil-wet¹, the injection of 2000 ppm NaCl water alters the wettability towards slightly water-wet, and the injection of 2000 ppm CaCl₂ alters the wettability towards slightly oil-wet. Low salinity water with divalent cation could increase the attraction forces between the oil/rock and oil/brine interfaces, promoting oil-wetness. However, low salinity with monovalent cation reduces the attraction forces, i.e., repulsive force increases, therefore, resulting in more water-wet.

2. The deformation process during LSWI resembles the process of oil removal using surfactant. This “surfactant-like” behaviour lowers the interfacial tension and contributes to increased oil recovery. As CO₂ is introduced, due to the acidic effect of CO₂, it acts to wet the rock surface, leading to a more water-wet state. Therefore, the oil removal or oil drop deformation resembles the “roll-up” oil removal process.
3. The injection of CO₂ promotes water-wetness and geochemical reactions between oil and brine. In the WAG process, more interactions between injection brine, CO₂ and pre-existing brine are expected, and this leads to different wettability alteration trend compared to CO₂ + LSWI. When NaCl LSW is used, continuous CO₂ + NaCl injection scheme is more efficient than WAG cycle of CO₂/NaCl in wettability alteration towards more water-wet. However, with CaCl₂ LSW, WAG cycle of CO₂/CaCl₂ can alter the rock wettability to more water-wet compared to continuous CO₂ + CaCl₂ injection.

6 Future Work

In this study, all the measurements are conducted at ambient condition. The effect of temperature and pressure is not considered. As the temperature and pressure exceeds the critical point for CO₂, the state of CO₂ will become supercritical, with properties midway between a gas and a liquid. Therefore, in order to better understand the wettability alterations with supercritical CO₂, more research with respect to elevated temperature and pressure should be carried out in the future. If wettability alteration is considered as the main mechanism for LSWI or CO₂ LSWAG injection, this displacement contact angle measurement which mimics the real reservoir displacement process could be used as a preliminary screening for brine concentration and composition, as well as injection schemes. However, to achieve a systematic evaluation process, more experimental data with respect to temperature and pressure are required.

¹ Note: wettability was inferred from the contact angle and was not independently verified by measurements like USBM or Amott.

7 Acknowledgements

The authors would like to thank the Hibernia Management and Development Company (HMDC), Chevron Canada Ltd, Petroleum Research Newfoundland and Labrador (PRNL), the Natural Sciences and Engineering Research Council of Canada (NSERC), the Province of Newfoundland and Labrador, and Mitacs for financial support. We thank our colleagues in the Hibernia EOR Research Group for their technical support.

References

1. N. Morrow, and J. Buckley, Improved oil recovery by low-salinity waterflooding. *Journal of petroleum Technology*, **63**(05), pp.106-112, SPE-129421-JPT. (2011).
2. K.J. Webb, C.A. Black, H. Al-Ajeel, Low salinity oil recovery-log-inject-log. In *SPE/DOE Symposium on Improved Oil Recovery*, SPE-89379-MS. (2004).
3. K.J. Webb, C.J.J Black, I.J. Edmonds, Low salinity oil recovery - The role of reservoir condition corefloods. In *IOR 2005-13th European Symposium on Improved Oil Recovery* (pp. cp-12). European Association of Geoscientists & Engineers. (2005).
4. L. Moghadasi, P. Pisicchio, M. Bartosek, E. Braccalenti, P. Albonico, I. Moroni, R. Veschi, F. Masserano, S. Scagliotti, L. Del Gaudio, M. De Simoni, Laboratory investigation on synergy effect of low salinity-polymer water injection on sandstone porous media. In *Offshore Mediterranean Conference and Exhibition, OMC-2019-0868*. (2019).
5. E. Alagic, A. Skauge, Combined low salinity brine injection and surfactant flooding in mixedwet sandstone cores. *Energy & fuels*, **24**(6), pp.3551-3559. (2010).
6. T.W. Teklu, W. Alameri, H. Kazemi, R.M. Graves, A.M. AlSumaiti, Low salinity water - Surfactant - CO₂ EOR. *Petroleum*, **3**(3), pp.309-320. (2017).
7. M.T. Al-Murayri, H.E. Al-Mayyan, K. Moudi, F. Al-Ajmi, D. Pitts, M.J. Wyatt, K.French, J. Surtek, E. Dean, Chemical EOR Economic Evaluation in a Low Oil Price Environment: Sabriyah Lower Burgan Reservoir Case Study. In *SPE EOR Conference at Oil and Gas West Asia*, SPE-190337-MS. (2018).
8. H. Muriel, S. Ma, S.J.D. Sofla, L.A. James, Technical and Economical Screening of Chemical EOR Methods for the Offshore. In *Offshore Technology Conference, OTC-30740-MS*. (2020).
9. H. Jiang, L. Nuryaningsih, H. Adidharma, The effect of salinity of injection brine on water alternating gas performance in tertiary miscible carbon dioxide flooding: experimental study. In *SPE Western Regional Meeting, SPE-132369-MS*. (2010).
10. R. Ramanathan, A.M. Shehata, H.A. Nasr-El-Din, Water Alternating CO₂ Injection Process-Does Modifying the Salinity of Injected Brine Improve Oil Recovery?. In *OTC Brasil, OTC-26253-MS*. (2015).
11. A.A. AlQuraishi, A.M.Amao, N.I. Al-Zahrani, M.T. AlQarni, S.A. AlShamrani, Low salinity water and CO₂ miscible flooding in Berea and Bentheimer sandstones. *Journal of King Saud University-Engineering Sciences*, **31**(3), pp.286-295. (2019).
12. N.R. Morrow, G.Q. Tang, M. Valat, X. Xie, Prospects of improved oil recovery related to wettability and brine composition. *Journal of Petroleum science and Engineering*, **20**(3-4), pp.267-276. (1998).
13. N.R. Morrow, Wettability and its effect on oil recovery. *Journal of petroleum technology*, **42**(12), pp.1476-1484. (1990).
14. H. Al-Abri, P. Pourafshary, N. Mosavat, H. Al Hadhrami, A study of the performance of the LSWA CO₂ EOR technique on improvement of oil recovery in sandstones. *Petroleum*, **5**(1), pp.58-66. (2019).
15. T.W. Teklu, W. Alameri, R.M. Graves, H Kazemi, A.M. AlSumaiti, Low-salinity water-alternating-CO₂ flooding enhanced oil recovery: theory and experiments. In *Abu Dhabi International Petroleum Exhibition and Conference, SPE-171767-MS*. (2014).
16. R.M. Enick, S.M. Klara, CO₂ solubility in water and brine under reservoir conditions. *Chemical Engineering Communications*, **90**(1), pp.23-33. (1990).
17. Y.K. Li, L.X.Nghiem, Phase equilibria of oil, gas and water/brine mixtures from a cubic equation of state and Henry's law. *The Canadian Journal of Chemical Engineering*, **64**(3), pp.486-496. (1986).
18. K.R Chaturvedi, D. Ravilla, W. Kaleem, P. Jadhawar, T. Sharma, Impact of low salinity water injection on CO₂ storage and oil Recovery for improved CO₂ utilization. *Chemical Engineering Science*, **229**, p.116127. (2021).
19. H. Zolfaghari, A. Zebarjadi, O. Shahrokhi, M.H. Ghazanfari, An experimental study of CO₂-low salinity water alternating gas injection in sandstone heavy oil reservoirs. *Iranian Journal of Oil & Gas Science and Technology*, **2**(3), pp.37-47. (2013).
20. H.N. Al-Saedi, S.K. Al-Jaberi, R.E.Flori, W. Al-Bazzaz, Y. Long, A new design of low salinity-CO₂-different chemical matters. In *Abu Dhabi International Petroleum Exhibition & Conference, SPE-197118-MS*. (2019).
21. H.N. Al-Saedi, R.E. Flori, Novel coupling smart water-CO₂ flooding for sandstone reservoirs. *Petrophysics-The SPWLA Journal of Formation Evaluation and Reservoir Description*, **60**(04), pp.525-535. (2019).
22. H.N. Al-Saedi, Y. Long, R.E. Flori, B. Bai, Coupling smart seawater flooding and CO₂ flooding for sandstone reservoirs: smart seawater alternating CO₂ flooding (SMSW-AGF). *Energy & Fuels*, **33**(10), pp.9644-9653. (2019).
23. L.W. Holm, V.A. Josendal, Mechanisms of oil displacement by carbon dioxide. *Journal of petroleum Technology*, **26**(12), pp.1427-1438. (1974).
24. M.S.A. Perera, R.P. Gamage, T.D. Rathnaweera, A.S. Ranathunga, A. Koay, X. Choi, A review of CO₂-enhanced oil recovery with a simulated sensitivity analysis. *Energies*, **9**(7), p.481. (2016).

25. C. Drummond, J. Israelachvili, Surface forces and wettability. *Journal of Petroleum Science and Engineering*, **33**(1-3), pp.123-133. (2002).
26. J.J. Sheng, Critical review of low-salinity waterflooding. *Journal of Petroleum Science and Engineering*, **120**, pp.216-224. (2014).
27. P.P. Jadhunandan, N.R. Morrow, Effect of wettability on waterflood recovery for crude-oil/brine/rock systems. *SPE reservoir engineering*, **10**(01), pp.40-46, SPE-22597-PA. (1995).
28. A. Lager, K.J. Webb, C.J.J. Black, Impact of brine chemistry on oil recovery. In IOR 2007-14th European symposium on improved oil recovery (pp. cp-24). European Associ. of Geoscientists & Engineers. (2007).
29. D.J. Ligthelm, J. Gronsveld, J. Hofman, N. Brussee, F. Marcelis, H. van der Linde, Novel waterflooding strategy by manipulation of injection brine composition. In EUROPEC/EAGE conference and exhibition, SPE-119835-MS. (2009).
30. R.T. Johansen, H.N. Dunning, Relative wetting tendencies of crude oils by capillarimetric method, **5752**. US Department of the Interior, Bureau of Mines. (1961).
31. J.W. Graham, J.G. Richardson, Theory and application of imbibition phenomena in recovery of oil. *Journal of Petroleum Technology*, **11**(02), pp.65-69. (1959).
32. N.R. Morrow, G. Mason, Recovery of oil by spontaneous imbibition. *Current Opinion in Colloid & Interface Science*, **6**(4), pp.321-337. (2001).
33. L.E. Treiber, W.W. Owens, A laboratory evaluation of the wettability of fifty oil-producing reservoirs. *Society of petroleum engineers journal*, **12**(06), pp.531-540, SPE-3526-PA. (1972).
34. J.P. Batycky, F.G. McCaffery, P.K. Hodgins, D.B. Fisher, Interpreting relative permeability and wettability from unsteady-state displacement measurements. *Society of Petroleum Engineers Journal*, **21**(03), pp.296-308, SPE-9403-PA. (1981).
35. A.B.D. Cassie, S. Baxter, Wettability of porous surfaces. *Transactions of the Faraday society*, **40**, pp.546-551. (1944).
36. N. Siemons, H. Bruining, H. Castelijns, K.H. Wolf, Pressure dependence of the contact angle in a CO₂ - H₂O - coal system. *Journal of colloid and interface science*, **297**(2), pp.755-761. (2006).
37. E. Sripal, L.A. James, Application of an optimization method for the restoration of core samples for SCAL experiments. *Petrophysics-The SPWLA Journal of Formation Evaluation and Reservoir Description*, **59**(01), pp.72-81. (2018).
38. E. Sripal, D. Grant, L. James, Application of SEM Imaging and MLA Mapping Method as a Tool for Wettability Restoration in Reservoir Core Samples for SCAL Experiments. *Minerals*, **11**(3), p.285. (2021).
39. W. Anderson, Wettability literature survey-part 2: Wettability measurement. *Journal of petroleum technology*, **38**(11), pp.1246-1262. (1986).
40. M. Arif, S.A. Abu-Khamsin, S. Iglauer, Wettability of rock/CO₂/brine and rock/oil/CO₂-enriched-brine systems: Critical parametric analysis and future outlook. *Advances in colloid and interface science*, **268**, pp.91-113. (2019).
41. N.S. Kaveh, E.S.J. Rudolph, P. Van Hemert, W.R. Rossen, K.H. Wolf, Wettability evaluation of a CO₂/water/bentheimer sandstone system: contact angle, dissolution, and bubble size. *Energy & Fuels*, **28**(6), pp.4002-4020. (2014).
42. S.J.D. Sofla, L.A. James, Y. Zhang, Toward a mechanistic understanding of wettability alteration in reservoir rocks using silica nanoparticles. In E3S Web of Conferences, **89**, p. 03004. EDP Sciences. (2019).
43. P.T. Jaeger, M.B. Alotaibi, H.A. Nasr-El-Din, Influence of compressed carbon dioxide on the capillarity of the gas- crude oil- reservoir water system. *Journal of Chemical & Engineering Data*, **55**(11), pp.5246-5251. (2010).
44. A. Ameri, N.S. Kaveh, E.S.J. Rudolph, K.H. Wolf, R. Farajzadeh, J. Bruining, Investigation on interfacial interactions among crude oil - brine - sandstone rock - CO₂ by contact angle measurements. *Energy & fuels*, **27**(2), pp.1015-1025. (2013).
45. D.N. Espinoza, J.C. Santamarina, Water - CO₂ - mineral systems: Interfacial tension, contact angle, and diffusion — Implications to CO₂ geological storage. *Water resources research*, **46**(7). (2010).
46. M. Seyyedi, M. Sohrabi, A. Farzaneh, Investigation of rock wettability alteration by carbonated water through contact angle measurements. *Energy & Fuels*, **29**(9), pp.5544-5553. (2015).
47. A.B. Dixit, S.R. McDougall, K.S. Sorbie, J.S. Buckley, Pore scale modelling of wettability effects and their influence on oil recovery. In SPE/DOE Improved Oil Recovery Symposium, SPE-35451-MS. (1996).
48. S.J. Kline, F.A. McClintock, Describing uncertainties in single sample experiments. *Mech. Engineering*, **75**, pp.3-8. (1953).
49. S. Li, M. Liu, D. Hanaor, Y. Gan, Dynamics of viscous entrapped saturated zones in partially wetted porous media. *Transport in Porous Media*, **125**(2), pp.193-210. (2018).
50. H. Ding, S. Rahman, Experimental and theoretical study of wettability alteration during low salinity water flooding-an state of the art review. *Colloids and Surfaces A: Physicochemical and Engineering Aspects*, **520**, pp.622-639. (2017).
51. S.Y. Lee, K.J. Webb, I.R. Collins, A. Lager, S.M. Clarke, M. O'Sullivan, A.F. Routh, X. Wang, Low salinity oil recovery - Increasing understanding of the underlying mechanisms. In SPE Improved Oil Recovery Symposium. SPE-129722-MS. (2010).
52. Q. Xie, A. Saeedi, E. Pooryousefy, Y. Liu, Extended DLVO-based estimates of surface force in low salinity water flooding. *Journal of Molecular Liquids*, **221**, pp.658-665. (2016).

53. A. Lager, K.J. Webb, C.J.J. Black, M. Singleton, K.S. Sorbie, Low salinity oil recovery-an experimental investigation1. *Petrophysics-The SPWLA Journal of Formation Evaluation and Res. Descrip.* **49**(01). (2008).
54. H. Wang, J. Zeuschner, M. Eremets, I. Troyan, J. Willams, Stable solid and aqueous H₂CO₃ from CO₂ and H₂O at high pressure and high temperature. *Scientific Reports*, **6**(1), pp.1-8. (2016).
55. B. Velde, *Origin and mineralogy of clays: clays and the environment*. Springer Sci. & Business Media. (2013)
56. P.L McGuire, J.R. Chatham, F.K. Paskvan, D.M. Sommer, F.H. Carini, Low salinity oil recovery: An exciting new EOR opportunity for Alaska's North Slope. SPE-93903-MS. (2005).
57. C.A. Miller, K.H. Raney, Solubilization - emulsification mechanisms of detergency. *Colloids and Surfaces A: Physicochemical and Engineering Aspects*, **74**(2-3), pp.169-215. (1993).